MATERIALS RESEARCH SOCIETY
SYMPOSIUM PROCEEDINGS
VOLUME 339

Diamond, SiC and Nitride Wide Bandgap Semiconductors

EDITORS
Calvin H. Carter, Jr.
Gennady Gildenblat
Shuji Nakamura
Robert J. Nemanich

DTIC
ELECTE
DEC 1 4 1994
S G D

DISTRIBUTION STATEMENT A
Approved for public release;
Distribution Unlimited

MRS

19941209 086

Diamond, SiC and Nitride Wide Bandgap Semiconductors

Accesion For	
NTIS CRA&I	☒
DTIC TAB	☐
Unannounced	☐
Justification	
By	
Distribution /	
Availability Codes	
Dist	Avail and / or Special
A-1	

DISTRIBUTION STATEMENT A
Approved for public release;
Distribution Unlimited

DTIC QUALITY INSPECTED 1

MATERIALS RESEARCH SOCIETY SYMPOSIUM PROCEEDINGS VOLUME 339

Diamond, SiC and Nitride Wide Bandgap Semiconductors

Symposium held April 4–8, 1994, San Francisco, California, U.S.A.

EDITORS:

Calvin H. Carter, Jr.
Cree Research Inc.
Durham, North Carolina, U.S.A.

Gennady Gildenblat
Pennsylvania State University
University Park, Pennsylvania, U.S.A.

Shuji Nakamura
Nichia Chemical Industries Ltd.
Tokushima, Japan

Robert J. Nemanich
North Carolina State University
Raleigh, North Carolina, U.S.A.

MATERIALS RESEARCH SOCIETY
Pittsburgh, Pennsylvania

This work was supported in part by the Office of Naval Research under Grant Number N00014-94-0212. The United States Government has a royalty-free license throughout the world in all copyrightable material contained herein.

Single article reprints from this publication are available through
University Microfilms Inc., 300 North Zeeb Road, Ann Arbor, Michigan 48106

CODEN: MRSPDH

Copyright 1994 by Materials Research Society.
All rights reserved.

This book has been registered with Copyright Clearance Center, Inc. For further information, please contact the Copyright Clearance Center, Salem, Massachusetts.

Published by:

Materials Research Society
9800 McKnight Road
Pittsburgh, Pennsylvania 15237
Telephone (412) 367-3003
Fax (412) 367-4373

Library of Congress Cataloging in Publication Data

Materials Research Society. Meeting (1994 : San Francisco, Calif.). Symposium D.
Diamond, SiC and nitride wide bandgap semiconductors : Symposium D, 1994 Spring Meeting of the Materials Research Society, April 4-8, 1994, San Francisco, California / editors, Calvin H. Carter, Jr., Gennady Gildenblat, Shuji Nakamura, Robert J. Nemanich.
p. cm.—(Materials Research Society symposium proceedings ; v. 339)
Includes bibliographical references and index.
ISBN 1-55899-239-1
1. Wide gap semiconductors—Congresses. 2. Epitaxy—Congresses. 3. Diamond thin films—Electric properties—Congresses. 4. Silicon-carbide thin films—Electric properties—Congresses. 5. Nitrides—Electric properties—Congresses. I. Carter, Jr., Calvin H. II. Gildenblat, Gennady III. Nakamura, Shuji IV. Nemanich, Robert J. V. Title. VI. Series: Materials Research Society symposium proceedings ; v. 339.
QC611.1.W53M38 1994 94-33153
621.3815'2—dc20 CIP

Manufactured in the United States of America

Contents

PREFACE xv

MATERIALS RESEARCH SOCIETY SYMPOSIUM PROCEEDINGS xvi

PART I: PANEL DISCUSSION SUMMARY

SUMMARY OF PANEL DISCUSSION: "SUBSTRATE ISSUES FOR WIDE BANDGAP SEMICONDUCTORS" 3
Max N. Yoder, Peter K. Bachmann, Hiroyuki Matsunami, and Hadis Morkoc

PART II: SURFACES AND SURFACE PREPARATIONS

TIGHT-BINDING STUDY OF THE {211} Σ=3 GRAIN BOUNDARY IN CUBIC SILICON-CARBIDE 9
M. Kohyama and R. Yamamoto

ELECTRONIC STRUCTURES OF β-SiC(001) SURFACES AND Al/β-SiC(001) INTERFACE 15
Xiao Hu, Hong Yan, and Fumio S. Ohuchi

COMPUTER SIMULATION OF Si AND C ATOMS ON SiC SURFACES 21
C.C. Matthai, G.J. Moran, and I. Morrison

DYNAMICS AT A STEP ON THE DIAMOND (111) SURFACE 27
Brian N. Davidson and Warren E. Pickett

INTERACTION OF HYPERTHERMAL HYDROGEN WITH THE DIAMOND SURFACE 33
David Haggerty, Christos Bandis, and Bradford B. Pate

EXPOSURE OF DIAMOND TO ATOMIC HYDROGEN: SECONDARY ELECTRON EMISSION AND CONDUCTIVITY EFFECTS 39
D.P. Malta, J.B. Posthill, T.P. Humphreys, R.E. Thomas, G.G. Fountain, R.A. Rudder, G.C. Hudson, M.J. Mantini, and R.J. Markunas

SURFACE FERMI LEVEL POSITION OF DIAMOND TREATED WITH PLASMA 45
Takashi Sugino, Yoshifumi Sakamoto, Atsuhiko Furukawa, and Junji Shirafuji

SURFACE PREPARATION OF SINGLE CRYSTAL C(001) SUBSTRATES FOR HOMOEPITAXIAL DIAMOND GROWTH 51
T.P. Humphreys, J.B. Posthill, D.P. Malta, R.E. Thomas, R.A. Rudder, G.C. Hudson, and R.J. Markunas

THEORETICAL STUDIES OF C(100) SURFACE RECONSTRUCTION AND REACTION WITH CH_2 57
Z. Jing and J.L. Whitten

SURFACE STUDIES RELEVANT TO THE INITIAL STAGES OF DIAMOND NUCLEATION 63
J.M. Lannon, Jr., J.S. Gold, and C.D. Stinespring

COMPARISON OF SURFACE CLEANING PROCESSES FOR DIAMOND C(001) 69
Peter K. Baumann, T.P. Humphreys, and R.J. Nemanich

ELECTRON EMISSION PROPERTIES OF THE NEGATIVE ELECTRON AFFINITY (111)2×1 DIAMOND-TiO INTERFACE 75
C. Bandis, D. Haggerty, and B.B. Pate

PROPERTIES OF THE HETEROEPITAXIAL AlN/SiC INTERFACE 81
M.C. Benjamin, C. Wang, R.S. Kern, R.F. Davis, and R.J. Nemanich

SURFACE CLEANING, TOPOGRAPHY, AND TEMPERATURE MEASUREMENTS OF SINGLE CRYSTAL DIAMOND 89
Mark P. D'Evelyn, Lisa M. Struck, and Robin E. Rawles

PART III: DEVICES AND DEVICE PROCESSING

*MATERIALS ASPECTS OF DIAMOND-BASED ELECTRONIC DEVICES 97
J.R. Zeidler, C.A. Hewett, and R. Nguyen

*DIAMOND FIELD-EFFECT TRANSISTORS 109
David L. Dreifus, Alison J. Tessmer, Joseph S. Holmes, Chien-Teh Kao, Dean M. Malta, Linda S. Plano, and Brian R. Stoner

TEST OF A DIAMOND-TUNGSTEN SAMPLING CALORIMETER 121
R. Stone, M. Franklin, D. Fujino, K.K. Gan, R. Gilman, S. Han, H. Kagan, S. Kanda, D.R. Kania, R. Kass, S.K. Kim, G. Kumbartski, M.H. Lee, R. Malchow, B. Morozov, W. Palmer, L.S. Pan, P. Rutt, F. Sannes, S. Schnetzer, S.V. Somalwar, Y. Sugimoto, R.J. Tesarek, G.B. Thomson, C. White, and S. Zhao

EXCIMER LASER PLANARIZATION OF DIAMOND FILMS 127
Dong-Gu Lee, S.D. Harkness, and Rajiv K. Singh

*HIGH POWER AND HIGH FREQUENCY SILICON CARBIDE DEVICES 133
John W. Palmour, C.H. Carter, Jr., C.E. Weitzel, and K.J. Nordquist

COMPARISON OF MICROWAVE ECR AND RF PLASMAS FOR DRY ETCHING OF SINGLE CRYSTAL 6H-SiC 145
J.R. Flemish, K. Xie, W. Buchwald, L. Casas, J.H. Zhao, G. McLane, and M. Dubey

ON THE FORWARD CONDUCTION MECHANISMS IN SiC P-N JUNCTIONS 151
Lourdes Pelaz, J. Vicente, M. Jaraiz, L. Bailon, and J. Barbolla

PROPERTIES OF MOS STRUCTURE FABRICATED ON 3C-SiC GROWN BY REACTIVE MAGNETRON SPUTTERING 157
R. Turan, Q. Wahab, L. Hultman, M. Willander, and J.-E. Sundgren

*ELECTRONIC AND OPTOELECTRONIC DEVICES BASED ON GaN-AlGaN HETEROSTRUCTURES 163
M. Asif Khan, J.N. Kuznia, S. Krishnankutty, R.A. Skogman, D.T. Olson, W.J. Schaff, J.W. Burm, M.S. Shur, and T. George

*Invited Paper

InGaN/AlGaN DOUBLE-HETEROSTRUCTURE BLUE LEDS 173
Shuji Nakamura

ION MILLING AND REACTIVE ION ETCHING OF III-V NITRIDES 179
S.J. Pearton, C.R. Abernathy, F. Ren, and J.R. Lothian

CHARACTERIZATION OF CVD DIAMOND FILMS USED FOR RADIATION DETECTION 185
F. Foulon, T. Pochet, E. Gheeraert, and A. Deneuville

PHOTORESPONSE STUDY OF POLYCRYSTALLINE DIAMOND THIN FILM SCHOTTKY DIODES 191
G. Zhao, T. Stacy, E.M. Charlson, E.J. Charlson, M. Hajsaid, R. Roychoudhury, A.H. Khan, J.M. Meese, Z. He, and M. Prelas

AMORPHIZATION AND RECRYSTALLIZATION OF 6H-SiC BY ION BEAM IRRADIATION 197
V. Heera, R. Kögler, W. Skorupa, and J. Stoemenos

OXIDATION AND ION DAMAGE OF DIAMOND BY REACTIVE ION ETCHING 203
T.E. Beerling and C.R. Helms

COMPARISON OF THERMAL GATE OXIDES ON SILICON AND CARBON FACE P-TYPE 6H SILICON CARBIDE 209
Carl-Mikael Zetterling and Mikael Östling

UV-SENSITIVE METAL-SEMICONDUCTOR PHOTODIODES ON 6H-SiC 215
Christer Fröjdh, Göran Thungström, Hans-Erik Nilsson, and C. Sture Petersson

PART IV: CONTACTS

METALLIZATION OF GaN THIN FILMS PREPARED BY ION BEAM ASSISTED MOLECULAR BEAM EPITAXY 223
J.S. Chan, T.C. Fu, N.W. Cheung, N. Newman, X. Liu, J.T. Ross, M.D. Rubin, and P. Chu

COBALT SILICIDE OHMIC CONTACTS TO 6H-SiC 229
Nils Lundberg and M. Östling

CHARACTERIZATION OF MS, MiS, AND MOS CONTACTS TO TYPE IIB DIAMOND BY CAPACITANCE-VOLTAGE AND CURRENT-VOLTAGE 235
Henry A. Wynands, M.L. Hartsell, and Bradley A. Fox

GROWTH OF SINGLE CRYSTAL COPPER FILMS ON DIAMOND USING FCC-IRON SEED LAYERS 241
D.P. Pappas, V.G. Harris, H.A. Hoff, G.L. Watena, and J.W. Glesener

SOLID-PHASE REACTION OF TUNGSTEN THIN FILMS WITH POLYCRYSTALLINE DIAMOND 247
A. Bächli, J.S. Chen, R.P. Ruiz, and M-A. Nicolet

PART V: DIAMOND GROWTH

*CHEMICAL REACTION MECHANISMS OF DIAMOND GROWTH 255
Michael Frenklach

*Invited Paper

*DIAMOND CHEMICAL VAPOR DEPOSITION: GAS COMPOSITIONS AND FILM PROPERTIES 267
Peter K. Bachmann, Hans-Jürgen Hagemann, Hartmut Lade, Dieter Leers, Frederike Picht, Detlef U. Wiechert, and Howard Wilson

DIAMOND HOMOEPITAXY KINETICS: GROWTH, ETCHING, AND THE ROLE OF OXYGEN 279
Robin E. Rawles and Mark P. D'Evelyn

DIAMOND GROWTH RATES AND QUALITY: DEPENDENCE ON GAS PHASE COMPOSITION 285
William D. Cassidy, Edward A. Evans, Yaxin Wang, John C. Angus, Peter K. Bachmann, Hans-Jurgen Hagemann, Dieter Leers, and Detlef U. Wiechert

DIAMOND NUCLEATION STUDIES ON REFRACTORY METALS AND NICKEL 291
S.D. Wolter, B.R. Stoner, P.C. Yang, W. Lui, and J.T. Glass

DEFECTS AND GROWTH OF DIAMOND WAFERS 297
D. Shechtman

DEPOSITION OF DIAMOND USING AN ELECTRON CYCLOTRON RESONANCE PLASMA SYSTEM 301
Donald R. Gilbert, Rajiv Singh, W. Brock Alexander, Doug Gu Lee, and Patrick Doering

CHARACTERIZATION OF A THICK HOMOEPITAXIAL CVD DIAMOND FILM 307
M.A. Plano, M.D. Moyer, M.M. Moreno, D. Black, H. Burdette, L. Robins, L.S Pan, D.R. Kania, and W. Banholzer

DEPOSITION OF FLAME GROWN DIAMOND FILMS IN AN ENCLOSED CHAMBER 313
Kathleen Doverspike, Vasgen A. Shamamian, and Jaime A. Freitas, Jr.

EFFECTS OF METHANE CONCENTRATION AND HYDROGEN TREATMENT ON PREFERRED ORIENTATION IN DIAMOND FILMS GROWN BY CHEMICAL VAPOR DEPOSITION 319
D. Ganesan and S.C. Sharma

PHASE TRANSFORMATION OF SMOOTH DIAMOND FILMS GROWN BY HOT FILAMENT CHEMICAL VAPOR DEPOSITION ON POSITIVELY BIASED SILICON SUBSTRATES 325
G. Popovici, C.H. Chao, M.A. Prelas, E.J. Charlson, and J.M. Meese

EFFECT OF OXYGEN ON THE TEXTURED DIAMOND GROWTH OVER NICKEL SUBSTRATES 329
R. Ramesham, M.F. Rose, R.F. Askew, and M. Bozack

PART VI: BN AND SiC EPITAXIAL GROWTH

CATHODOLUMINESCENCE SPECTROSCOPY OF BORON NITRIDE FILMS 339
C.A. Taylor II, S.W. Brown, V. Subramaniam, S. Kidner, S.C. Rand, and R. Clarke

*Invited Paper

LOW ENERGY THRESHOLD IN THE GROWTH OF CUBIC BORON NITRIDE FILMS BY ECR PLASMA ASSISTED MAGNETRON SPUTTERING 345
C.A. Taylor II, S. Kidner, and R. Clarke

*INITIAL STAGES OF GROWTH OF THIN FILMS OF III-V NITRIDES AND SILICON CARBIDE POLYTYPES BY MOLECULAR BEAM EPITAXY 351
Robert F. Davis, K.S. Ailey, R.S. Kern, D.J. Kester, Z. Sitar, L. Smith, S. Tanaka, and C. Wang

STRUCTURAL STUDY OF SiC/AlN BILAYERS AND TRILAYERS ON Si AND 6H-SiC 363
D. Prasad Beesabathina, K. Fekade, K. Wongchotigul, M.G. Spencer, and L. Salamanca-Riba

*NUCLEATION AND STEP DYNAMICS IN SiC EPITAXIAL GROWTH 369
Hiroyuki Matsunami and Tsunenobu Kimoto

ELECTRON CYCLOTRON RESONANCE PLASMA CHEMICAL VAPOUR DEPOSITION OF SILICON CARBIDE THIN FILMS USING DITERTIARY BUTYL SILANE 381
Mohamed Boumerzoug, Marcel Boudreau, Peter Mascher, and Paul E. Jessop

PROCESS ANALYSIS OF AP-CVD OF SILICON CARBIDE 387
K. Rottner and R. Helbig

DEPOSITION OF EPITAXIALLY ORIENTED FILMS OF CUBIC SiC ON SILICON BY LASER ABLATION OF ELEMENTAL TARGETS 393
L. Rimai, R. Ager, W.H. Weber, J. Hangas, and B.D. Poindexter

STACKING FAULT ENERGY CALCULATIONS IN 6H- AND 15R-SiC 399
F.R. Chien, S.R. Nutt, and W.S. Yoo

CVD-GROWTH OF LOW-DOPED 6H SiC EPITAXIAL FILMS 405
O. Kordina, A. Henry, C. Hallin, R.C. Glass, A.O. Konstantinov, C. Hemmingsson, N.T. Son, and E. Janzén

XPS AND SIMS STUDIES OF CVD-GROWN CUBIC SiC FILMS ON Si(100) 411
A.T.S. Wee, Z.C. Feng, H.H. Hng, K.L. Tan, C.C. Tin, R. Hu, and R. Coston

COMBINED STRUCTURAL AND OPTICAL ASSESSMENT OF CVD GROWN 3C-SiC/Si 417
Z.C. Feng, C.C. Tin, K.T. Yue, R. Hu, J. Williams, S.C. Liew, Y.G. Foo, S.K.L. Choo, W.E. Ng, and S.H. Tang

GROWTH OF EPITAXIAL 2H-SILICON CARBIDE BY PULSED LASER DEPOSITION 423
Mark A. Stan, Martin O. Patton, Hemasiri K.M. Vithana, David L. Johnson, Joseph D. Warner, Nancy D. Piltch, Jinwei Yang, and Pirouz Pirouz

LASER TRANSFORMED SiC THIN FILMS 429
K.G. Kreider, D.R.F. Burgess, Jr., M.J. Tarlov, G. Gillen, S. Wight, R. Lareau, and L.M. Casas

*Invited Paper

REACTIVE MAGNETRON SPUTTERING OF SILICON IN Ar + CH_4: IDENTITY AND ENERGY OF THE SiC GROWTH SPECIES 435
M.P. Fitzner and J.R. Abelson

PART VII: NITRIDE EPITAXIAL GROWTH

*MOVPE GROWTH OF HIGH QUALITY $Al_xGa_{1-x}N/Ga_yIn_{1-y}N$ ($x \geq 0$, $y \leq 1$) HETEROSTRUCTURES FOR SHORT WAVELENGTH LIGHT EMITTER 443
I. Akasaki and H. Amano

GaN ON 6H-SiC—STRUCTURAL AND OPTICAL PROPERTIES 453
C. Wetzel, D. Volm, B.K. Meyer, K. Pressel, S. Nilsson, E.N. Mokhov, and P.G. Baranov

ACCEPTOR BINDING ENERGY AND BAND LINEUP OF III-V NITRIDE ALLOYS MOCVD GROWTH OF GaN ON GaAs- OR GaP-COATED Si 459
Yoshihiro Ueta, Shiro Sakai, Yasushi Kamiya, and Hisao Sato

THERMALLY ANNEALED GaN NUCLEATION LAYERS AND THE MOCVD GROWTH OF Si-DOPED GaN FILMS ON (00.1) SAPPHIRE 465
D.K. Wickenden, J.A. Miragliotta, W.A. Bryden, and T.J. Kistenmacher

GROWTH AND CHARACTERIZATION OF GaN ON Si(111) 471
A. Ohtani, K.S. Stevens, and R. Beresford

EFFECT OF ALUMINUM NITRIDE BUFFER LAYER TEMPERATURE ON GALLIUM NITRIDE GROWN BY OMVPE 477
L.B. Rowland, K. Doverspike, D.K. Gaskill, and J.A. Freitas, Jr.

FUNDAMENTAL MATERIALS—ISSUES INVOLVED IN THE GROWTH OF GaN BY MOLECULAR BEAM EPITAXY 483
N. Newman, T.C. Fu, X. Liu, Z. Liliental-Weber, M. Rubin, J.S. Chan, E. Jones, J.T. Ross, I. Tidswell, K.M. Yu, N. Cheung, and E.R. Weber

STRUCTURAL CHARACTERIZATION OF GaN GROWN BY ELECTRON CYCLOTRON RESONANCE-METALORGANIC MOLECULAR BEAM EPITAXY (ECR-MOMBE) 491
S. Bharatan, K.S. Jones, S.J. Pearton, C.R. Abernathy, and F. Ren

ECR-ASSISTED REACTIVE MAGNETRON SPUTTERING OF InN 497
W.A. Bryden, S.A. Ecelberger, M.E. Hawley, and T.J. Kistenmacher

RAMAN SCATTERING AND X-RAY DIFFRACTION STUDIES OF GALLIUM NITRIDE FILMS GROWN ON (100) GALLIUM ARSENIDE 503
S.W. Brown, S.C. Rand, C.-H. Hong, and D. Pavlidis

BUFFER LAYER THICKNESS AND THE PROPERTIES OF InN THIN FILMS ON AlN-SEEDED (00.1) SAPPHIRE AND (111) SILICON 509
T.J. Kistenmacher, S.A. Ecelberger, and W.A. Bryden

*Invited Paper

DEPOSITION AND CHARACTERIZATION OF CNx FILMS 515
X.T. Cui, Z.H. Zhang, Q.Y. Chen, F. Romero-Borja,
J.R. Liu, Z.S. Zheng, D.W. Pan, L.T. Wood, and
W.K. Chu

PART VIII: DOPING, IMPURITIES AND PROPERTIES

NMR SPIN LATTICE RELAXATION IN NITROGEN-DOPED
6H SILICON CARBIDE 523
J. Stephen Hartman, Arjun Narayanan, and Youxiang Wang

IR-ABSORPTION SPECTRA OF IMPURITIES IN 6H-SiC 529
F. Engelbrecht and R. Helbig

ELECTRON SPIN RESONANCE STUDIES OF DONORS IN BULK
AND THIN FILM β-SiC 535
W.E. Carlos, J.A. Freitas, Jr., J.C. Pazik, L.M. Ivanova,
Yu.M. Altaiskii, and V.L. Zuev

DYNAMICS OF THE NITROGEN BOUND EXCITONS IN 6H
AND 3C SiC 541
J.P. Bergman, C.I. Harris, O. Kordina, A. Henry,
and E. Janzén

RAMAN AND PHOTOLUMINESCENCE STUDIES OF UNDOPED
AND MAGNESIUM-DOPED GaN FILMS ON SAPPHIRE 547
Jaime A. Freitas, Jr. and M. Asif Khan

REDISTRIBUTION OF HYDROGEN IN GaN, AlN, AND InN 553
J.M. Zavada, R.G. Wilson, S.J. Pearton,
and C.R. Abernathy

INFRARED LUMINESCENCE FROM MOCVD GaN 559
M.W. Leksono, C.H. Qiu, W. Melton, and J.I. Pankove

*ELECTRONIC STRUCTURE OF DIAMOND, SILICON CARBIDE,
AND THE GROUP-III NITRIDES 565
Walter R.L. Lambrecht

TUNABLE SECOND-HARMONIC STUDIES OF GaN FILMS NEAR
THE FUNDAMENTAL BANDEDGE 583
Joseph Miragliotta, Wayne A. Bryden, Thomas J. Kistenmacher,
and Dennis K. Wickenden

CORRELATIONS BETWEEN ELECTRICAL AND MATERIAL
PROPERTIES OF CVD DIAMOND 589
C. White, S. Zhao, K.K. Gan, H. Kagan, R. Kass, R. Malchow,
F. Morrow, W. Palmer, S. Han, D. Kania, L.S. Pan, S. Schnetzer,
R. Stone, R. Teserek, J. Angus, S.J. Ma, and Y. Sugimoto

CONDUCTIVITY ANISOTROPY IN EPITAXIAL 6H AND 4H SiC 595
William J. Schaffer, G.H. Negley, K.G. Irvine,
and J.W. Palmour

DIFFUSION OF IMPURITIES UNDER BIAS IN CVD DIAMOND FILMS 601
G. Popovici, T. Sung, M.A. Prelas, S. Khasawinah,
and R.G. Wilson

BAND-OFFSETS BETWEEN GROUP-III-NITRIDES 607
E.A. Albanesi, W.R.L. Lambrecht, and B. Segall

*Invited Paper

PERTURBED-ANGULAR-CORRELATION SPECTROSCOPY ON INDIUM- AND CADMIUM-COMPLEXES IN SILICON CARBIDE 613
J. Meier, D. Forkel-Wirth, T. Licht, U. Reislöhner, M. Uhrmacher, W. Witthuhn, and Isolde Collaboration

A SPIN RESONANCE STUDY OF THE 2.9 eV LUMINESCENCE CENTERS IN NATURAL AND SYNTHETIC DIAMOND 619
D.M. Hofmann, W. Stadler, B.K. Meyer, L. Pereira, L. Santos, and E. Pereira

NICKEL RELATED ABSORPTION LINES IN HIGH-PRESSURE SYNTHETIC DIAMOND 625
M.H. Nazaré, J.C. Lopes, and H. Kanda

FREE CARRIER ABSORPTION IN N-TYPE 6H-SiC 631
F. Engelbrecht and R. Helbig

ELECTRICAL CHARACTERIZATION OF ALUMINUM NITRIDE FILMS ON SILICON GROWN BY CHEMICAL VAPOR DEPOSITION 637
A.H. Khan, J.M. Meese, T. Stacy, E.M. Charlson, E.J. Charlson, G. Zhao, G. Popovici, and M.A. Prelas

CONDUCTIVITY AND FTIR MEASUREMENTS OF THE HYDROGEN CONTENT OF HEAT TREATED DIAMOND FILMS 643
T. Sung, S. Khasawinah, G. Popovici, M.A. Prelas, B.V. Spitsyn, G. Manning, S. Loyalka, and R.V. Tompson

BLUE LIGHT ELECTROLUMINESCENCE FROM DOPED μc-SiC PREPARED BY EXCIMER (ArF) LASER CRYSTALLIZATION 647
S.P. Lau, J.M. Marshall, T.E. Dyer, A.R. Hepburn, and J.F. Davies

THE EFFECTS OF FRICTION AND WEAR ON PECVD DIAMOND FILMS 653
M.L. Languell, J.L. Davidson, J.J. Wert, M.A. George, W.E. Collins, and A. Burger

PART IX: DEFECTS

RECOMBINATION PROCESSES OF THE BROADBAND AND 1.681 eV OPTICAL CENTERS IN DIAMOND FILMS 663
L. Bergman, M.T. McClure, J.T. Glass, and R.J. Nemanich

ON THE NATURE OF THE NATIVE DEFECT ESR IN THIN DIAMOND FILMS 669
J. Shinar, H. Jia, D.P. Lang, and M. Pruski

ON THE STRUCTURE OF THIN DIAMOND FILMS: A ^{1}H AND ^{13}C NUCLEAR MAGNETIC RESONANCE STUDY 675
J. Shinar, M. Pruski, D.P. Lang, S.-J. Hwang, and H. Jia

ENERGIES AND ATOMIC STRUCTURES OF GRAIN BOUNDARIES IN DIAMOND: COMPARISON WITH GRAIN BOUNDARIES IN SILICON 681
M. Kohyama, H. Ichinose, Y. Ishida, and M. Nakanose

NATIVE DEFECTS AND IMPURITIES IN CUBIC AND WURTZITE GaN 687
Jörg Neugebauer and Chris G. Van de Walle

NATIVE DEFECTS IN WURTZITE GaN AND AlN 693
P. Boguslawski, E. Briggs, T.A. White, M.G. Wensell, and J. Bernholc

FAST RECOMBINATION OF EXCESS CARRIER IN 6H-SiC 699
R. Tomashiunas, E. Vanagas, M. Petrauskas, A. Zhindulis,
M. Willander, Q. Wahab, and H. Bergner

RADIATION DEFECTS IN SiC—ELECTRON IRRADIATION WITH
DIFFERENT ENERGIES 705
D. Volm, B.K. Meyer, E.N. Mokhov, and P.G. Baranov

CHARACTERIZATION OF DEFECTS IN N-TYPE 6H-SiC
SINGLE CRYSTALS BY OPTICAL ADMITTANCE
SPECTROSCOPY 711
A.O. Evwaraye, S.R. Smith, and W.C. Mitchel

PROPERTIES OF CRYSTALLINE 3C-SiC GROWN FROM
METHYL TRICHLOROSILANE 717
W.J. Moore, R. Kaplan, J.A. Freitas, Jr., Y.M. Altaiskii,
V.L. Zuev, and L.M. Ivanova

CHARACTERIZATION OF SiC LAYER FORMED BY C ION
IMPLANTATION (ESR AND IR STUDIES) 723
Y. Show, T. Izumi, M. Deguchi, M. Kitabatake,
and T. Hirao

INVESTIGATION OF STRUCTURAL DEFECTS IN 4H
SiC WAFERS 729
M. Tuominen, R. Yakimova, R.C. Glass, T. Tuomi,
and E. Janzén

X-RAY TOPOGRAPHIC STUDIES OF DEFECTS IN PVT 6H-SiC
SUBSTRATES AND EPITAXIAL 6H-SiC THIN FILMS 735
S. Wang, M. Dudley, C.H. Carter, Jr., and H.S. Kong

SOLID-STATE NMR STUDIES OF THE BONDING STRUCTURE
OF DIAMONDLIKE AMORPHOUS CARBON FILMS 741
Susan M. Holl, Robert D. Johnson, Vlad. J. Novotny,
Jeffrey L. Williams, Catherine E. Caley, Mark Hoinkis,
and Robert E. Jones

GROWTH OF BETA SILICON CARBIDE FILMS ON Si BY
HOT-FILAMENT CVD 747
Zhang Rong, Shi Hongtao, Yu Shidong, Zheng Youdou,
He Yuliang, and Liu Xiangna

AUTHOR INDEX 753

SUBJECT INDEX 757

Preface

This volume contains papers presented at the 1994 MRS Spring Meeting on "Diamond, SiC and Nitride Wide Bandgap Semiconductors." The meeting was held in San Francisco, California from April 4-8. This MRS symposium follows several previous MRS symposia also specifically addressing issues related to wide bandgap semiconductors. This volume is organized much as the meeting, but with poster and oral presentations mixed according to the session topics. The meeting ended with a lively panel discussion which focused on substrate issues, and the summary of this panel discussion leads this volume.

This symposium was directed toward the potential of diamond, SiC and nitride wide bandgap semiconductors. The symposium emphasized materials issues related to the semiconducting properties of these wide bandgap materials. Both experimental and theoretical studies were presented. Solid advances were reported in the growth techniques of all three materials groups. Contributions demonstrated the critical importance of surfaces, interfaces, doping, defects, and impurities. Reports demonstrated potential device applications ranging from unique electronic devices to blue/uv light emitters/detectors and even novel structures employing a negative electron affinity. The overall theme of the symposium was that materials research into wide bandgap semiconductors will make possible exciting new applications, and that we are just beginning to understand the potential of the materials.

We wish to thank all of the contributors and participants who made the symposium so successful. We appreciate the efforts of the invited speakers for setting the stage for the program. We also thank the session chairs for coordinating and leading the discussion, and we express our gratitude to the panel moderator and members for stimulating such a lively session on the last day of the symposium.

We appreciate the efforts of the meeting chairs, James M.E. Harper, Alan J. Hurd, and James E. Mark, and the MRS staff for its efforts in making the whole meeting a success. Special thanks to Cecilia Upchurch for her work at coordinating the communications and proceedings.

We gratefully acknowledge the financial support provided by the following organizations: The Office of Naval Research, Cree Research Inc., Kobe Steel USA Inc., Motorola Corp., and Nichia Chemical Industries, Ltd.

Calvin H. Carter, Jr.
Gennady Gildenblat
Shuji Nakamura
Robert J. Nemanich

July 1994

MATERIALS RESEARCH SOCIETY SYMPOSIUM PROCEEDINGS

Volume 316— Materials Synthesis and Processing Using Ion Beams, R.J. Culbertson, O.W. Holland, K.S. Jones, K. Maex, 1994, ISBN: 1-55899-215-4

Volume 317— Mechanisms of Thin Film Evolution, S.M. Yalisove, C.V. Thompson, D.J. Eaglesham, 1994, ISBN: 1-55899-216-2

Volume 318— Interface Control of Electrical, Chemical, and Mechanical Properties, S.P. Murarka, K. Rose, T. Ohmi, T. Seidel, 1994, ISBN: 1-55899-217-0

Volume 319— Defect-Interface Interactions, E.P. Kvam, A.H. King, M.J. Mills, T.D. Sands, V. Vitek, 1994, ISBN: 1-55899-218-9

Volume 320— Silicides, Germanides, and Their Interfaces, R.W. Fathauer, S. Mantl, L.J. Schowalter, K.N. Tu, 1994, ISBN: 1-55899-219-7

Volume 321— Crystallization and Related Phenomena in Amorphous Materials, M. Libera, T.E. Haynes, P. Cebe, J.E. Dickinson, Jr., 1994, ISBN: 1-55899-220-0

Volume 322— High Temperature Silicides and Refractory Alloys, C.L. Briant, J.J. Petrovic, B.P. Bewlay, A.K. Vasudevan, H.A. Lipsitt, 1994, ISBN: 1-55899-221-9

Volume 323— Electronic Packaging Materials Science VII, P. Børgesen, K.F. Jensen, R.A. Pollak, 1994, ISBN: 1-55899-222-7

Volume 324— Diagnostic Techniques for Semiconductor Materials Processing, O.J. Glembocki, S.W. Pang, F.H. Pollak, G.M. Crean, G. Larrabee, 1994, ISBN: 1-55899-223-5

Volume 325— Physics and Applications of Defects in Advanced Semiconductors, M.O. Manasreh, H.J. von Bardeleben, G.S. Pomrenke, M. Lannoo, D.N. Talwar, 1994, ISBN: 1-55899-224-3

Volume 326— Growth, Processing, and Characterization of Semiconductor Heterostructures, G. Gumbs, S. Luryi, B. Weiss, G.W. Wicks, 1994, ISBN: 1-55899-225-1

Volume 327— Covalent Ceramics II: Non-Oxides, A.R. Barron, G.S. Fischman, M.A. Fury, A.F. Hepp, 1994, ISBN: 1-55899-226-X

Volume 328— Electrical, Optical, and Magnetic Properties of Organic Solid State Materials, A.F. Garito, A.K-Y. Jen, C.Y-C. Lee, L.R. Dalton, 1994, ISBN: 1-55899-227-8

Volume 329— New Materials for Advanced Solid State Lasers, B.H.T. Chai, S.A. Payne, T.Y. Fan, A. Cassanho, T.H. Allik, 1994, ISBN: 1-55899-228-6

Volume 330— Biomolecular Materials By Design, M. Alper, H. Bayley, D. Kaplan, M. Navia, 1994, ISBN: 1-55899-229-4

Volume 331— Biomaterials for Drug and Cell Delivery, A.G. Mikos, R.M. Murphy, H. Bernstein, N.A. Peppas, 1994, ISBN: 1-55899-230-8

Volume 332— Determining Nanoscale Physical Properties of Materials by Microscopy and Spectroscopy, M. Sarikaya, M. Isaacson, H.K. Wickramasighe, 1994, ISBN: 1-55899-231-6

Volume 333— Scientific Basis for Nuclear Waste Management XVII, A. Barkatt, R. Van Konynenburg, 1994, ISBN: 1-55899-232-4

Volume 334— Gas-Phase and Surface Chemistry in Electronic Materials Processing, T.J. Mountziaris, G.R. Paz-Pujalt, F.T.J. Smith, P.R. Westmoreland, 1994, ISBN: 1-55899-233-2

Volume 335— Metal-Organic Chemical Vapor Deposition of Electronic Ceramics, S.B. Desu, D.B. Beach, B.W. Wessels, S. Gokoglu, 1994, ISBN: 1-55899-234-0

MATERIALS RESEARCH SOCIETY SYMPOSIUM PROCEEDINGS

Volume 336— Amorphous Silicon Technology–1994, E.A. Schiff, A. Matsuda, M. Hack, M.J. Powell, A. Madan, 1994, ISBN: 1-55899-236-7

Volume 337— Advanced Metallization for Devices and Circuits—Science, Technology, and Manufacturability III, S.P. Murarka, K.N. Tu, A. Katz, K. Maex, 1994, ISBN: 1-55899-237-5

Volume 338— Materials Reliability in Microelectronics IV, P. Børgesen, W. Filter, J.E. Sanchez, Jr., K.P. Rodbell, J.C. Coburn, 1994, ISBN: 1-55899-238-3

Volume 339— Diamond, SiC and Nitride-Wide-Bandgap Semiconductors, C.H. Carter, Jr., G. Gildenblat, S. Nakamura, R.J. Nemanich, 1994, ISBN: 1-55899-239-1

Volume 340— Compound Semiconductor Epitaxy, C.W. Tu, L.A. Kolodziejski, V.R. McCrary, 1994, ISBN: 1-55899-240-5

Volume 341— Epitaxial Oxide Thin Films and Heterostructures, D.K. Fork, J.M. Phillips, R. Ramesh, R.M. Wolf, 1994, ISBN: 1-55899-241-3

Volume 342— Rapid Thermal and Integrated Processing III, J.J. Wortman, J.C. Gelpey, M.L. Green, S.R.J. Brueck, F. Roozeboom, 1994, ISBN: 1-55899-242-1

Volume 343— Polycrystalline Thin Films—Structure, Texture, Properties and Applications, M. Parker, K. Barmak, R. Sinclair, D.A. Smith, J. Floro, 1994, ISBN: 1-55899-243-X

Volume 344— Materials and Processes for Environmental Protection, C. Adkins, P.N. Gadgil, L.M. Quick, K.E. Voss, 1994, ISBN: 1-55899-244-8

Volume 345— Flat Panel Display Materials, J. Batey, A. Chiang, P. Holloway, 1994, ISBN: 1-55899-245-6

Volume 346— Better Ceramics Through Chemistry VI, C. Sanchez, M.L. Mecartney, C.J. Brinker, A. Cheetham, 1994, ISBN: 1-55899-246-4

Volume 347— Microwave Processing of Materials IV, M.F. Iskander, R.J. Lauf, W.H. Sutton, 1994, ISBN: 1-55899-247-2

Volume 348— Scintillator and Phosphor Materials, M.J. Weber, P. Lecoq, R.C. Ruchti, C. Woody, W.M. Yen, R.-Y. Zhu, 1994, ISBN: 1-55899-248-0

Volume 349— Novel Forms of Carbon II, C.L. Renschler, D. Cox, J. Pouch, Y. Achiba, 1994, ISBN: 1-55899-249-9

Volume 350— Intermetallic Matrix Composites III, J.A. Graves, R.R. Bowman, J.J. Lewandowski, 1994, ISBN: 1-55899-250-2

Volume 351— Molecularly Designed Ultrafine/Nanostructured Materials, K.E. Gonsalves, G.-M. Chow, T.D. Xiao, R.C. Cammarata, 1994, ISBN: 1-55899-251-0

Prior Materials Research Society Symposium Proceedings available by contacting Materials Research Society

PART I

Panel Discussion Summary

Summary of Panel Discussion
"Substrate Issues for Wide Bandgap Semiconductors"

Moderator:
Max N. Yoder
Office of Naval Research
Arlington, VA 22217-5660

Panel Participants:
Peter K. Bachmann, Philips GmbH Forschungslaboratorien, Aachen, Germany
Hiroyuki Matsunami, Kyoto University, Kyoto, Japan
Hadis Morkoc, University of Illinois, Urbana, IL

The state-of-the-art in each of the major materials (Diamond, SiC and III-nitrides) was discussed with the advantages, disadvantages, and requirements of each enumerated.

Diamond was shown to exhibit the highest theoretical figures-of-merit in virtually all categories excepting light emission, but experimental progress in achieving electronic grade diamond is lagging. In fact, most homoepitaxial diamond films grown on natural diamond appear to be inferior to the best of natural diamond in terms of charge carrier mobility and defect densities. Only as radiation detectors and heat spreaders has CVD grown polycrystalline material proven superior to natural diamond. The future of CVD diamond looks promising in those areas where defect-free substrates are not mandatory. This includes heat spreaders for both electronics and non-electronic use, electron and particle detector applications, industrial products, applications in sensors, window and membrane applications, low wear applications, and as electron emitting cold cathodes. In fact, the largest projected electronic application of diamond films in the next five years was that of cold cathodes and cold cathode arrays intended for large area flat panel displays. In this application, there is no necessity for large area single crystalline substrates. Another large application is that of polycrystal diamond "coupons" for thermal heat spreaders (if the cost can be brought under control). A secondary electron yield of 38 was reported as being the highest of any known material. Other significant electronic applications were not envisioned until after the year 2010. Post depositional processing steps such as polishing and dicing are seen also seen as bottlenecks for a diamond device technoloy. In the pursuit of non-diamond substrates for heteroepitaxial growth of diamond films, the direct-gap chalcopyrite $BeCN_2$ was proposed.

Mat. Res. Soc. Symp. Proc. Vol. 339. ©1994 Materials Research Society

Silicon carbide (SiC) was adjudged to be the most mature of the materials discussed. It is commercially available with resistivities as high as 10^5 ohm-cm, with p-type doping densities as high 3×10^{18} cm^{-3}, and with n-type doping as high as 2×10^{18} cm^{-3}. Defect density typically is in the low 10^4 cm^{-2} with "killer" micropipe densities as low as 55 cm^{-2} overall and as low as 7 cm^{-2} in selected areas of 4H material. Screw dislocations as low as 280 cm^{-2} have been noted. Wafers of 50 mm diameter will soon be in production and commercially available later this year. SiC diodes have exhibited breakdown voltages of 2000 volts; if 5×10^{14} cm^{-3} background impurity material becomes available, this should increase to 5000 volts. Schottky barrier diode reverse breakdown was shown to be typically reduced by 33% in the presence of micropipe defects. Typically tens of impurities with energy levels within the forbidden gap are found in commercially available SiC. (SiC synthesized at the Baikov Metallurgical Institute in Moscow has been characterized by photoluminesence at NRL and found to exhibit only 2 detectable "impurities". Unfortunately, the sample sizes are very small.) CVD growth of SiC was shown to most assuredly be of a step-flow nature; films grown on vicinal material are much smoother and exhibit fewer defects than those grown on-axis. SiC grown on the "a" axis exhibits much-improved x-ray topography, and is devoid of micropipes, but new types of etch pits appear in this material. The nature and origin of the micropipe defects is still a matter of controversy. Theoretical modelling of global heat transfer and temperature gradients as a function of pressure was shown to hold potential for further improvement of the modified Lely SiC sublimation growth process. There was no debate that current electronic applications of SiC materials exceeds that of the other wide bandgap materials.

Nitride semiconductors (III-N) currently lack a homoepitaxial substrate. While encouraging results are obtained by synthesizing these materials on badly-lattice-mismatched sapphire, this process always requires an amorphous buffer layer; even then, defect densities generally exceed 10^8 cm^{-2}. Somewhat better results are usually obtained by direct nucleation on SiC, but defect densities still significantly exceed that of the substrate. MgO and ZnO have also been tried with equivalent success. Bulk III-N "ingots" are currently known to be grown only in Eastern Europe and independent evaluations of the quality have not yet been published. Not withstanding the rather poor crystalline quality of the III-N materials, some rather impressive device performance has been reported. Microwave insulated gate field effect transistors (IGFETs) were reported wherein f(max) of 35 GHz was achieved; this compares to less than 23 GHz in any SiC device. Arrays of blue light emitting devices (LEDs) were displayed during this conference; the array was so bright that it was painful to the eye to view it directly! Although their operating life is very good, it does not yet compare with that of the much lower efficiency

and lower brightness SiC LEDs. By changing the alloy ratio of the InGaN quantum wells from which the blue LEDs are fabricated, these devices are potentially capable of generating red, green, and yellow light at high efficiency. One hundred of these devices in a cluster array is sufficiently bright to be used as a traffic control signal; in contrast to the 100 watts typical in a traffic light bulb, the LED array would consume but 3.5 Watts! This represents a savings of 845 kWatt-hrs/yr per traffic light. The efficiency of the nitride light emitters derives primarily from their increased thermal conductivity over than of arsenide and phosphide devices and from a second property.

Both the IGFETs and the LEDs exploit a property of III-N semiconductors that is not fully understood: the surface recombination and surface depletion on the GaN surface is virtually non-existent! This contrasts with that of any other known (non-nitride) semiconductor. Closely related to "non-pinned" surface of the III-N materials is their surface robustness. A RHEED pattern taken on a III-N surface after six months exposure to the ambient appears no worse than that taken immediately after growth. Another application envisioned for the nitride materials is that of cold cathodes. For AlGaN alloys of 5.6 eV and higher, the surface is thought to exhibit negative electron affinity (NEA). Unlike diamond films, the nitride films can be deposited pin-hole-free for thicknesses as thin as 3.0 nm.

Each of the three basic material types has unique advantages. Each requires more research. SiC is currently in a dominant sales position, but III-N applications in volume are expected within a few years. Volumetric diamond applications will largely await significant production cost reductions.

Prepared by Max N. Yoder

PART II

Surfaces and Surface Preparations

TIGHT-BINDING STUDY OF THE {211} Σ=3 GRAIN BOUNDARY IN CUBIC SILICON-CARBIDE

M. KOHYAMA* AND R. YAMAMOTO**
* Department of Material Physics, Osaka National Research Institute, AIST, 1-8-31, Midorigaoka, Ikeda, Osaka 563, Japan.
** Institute of Industrial Science, University of Tokyo, 7-22-1, Roppongi, Minato-ku, Tokyo 106, Japan.

ABSTRACT

In grain boundaries in compound semiconductors such as SiC, the interface stoichiometry and the wrong bonds between like atoms are of much importance. Firstly, a general definition of the interface stoichiometry in such grain boundaries has been discussed. Secondly, the atomic and electronic structures of the {211} Σ=3 boundary in SiC have been examined by using the self-consistent tight-binding method, based on the atomic models with bonding networks similar to those in the models of the same boundary in Si or Ge. The wrong bonds have significant effects through the large electrostatic repulsion and the generation of localized states as well as those in the {122} Σ=9 boundary in SiC. And the different bond lengths of the wrong bonds very much affect the local bond distortions at the interfaces, which determines the relative stability among the present models.

INTRODUCTION

There has been increasing interest in SiC as high-temperature devices or high-performance ceramics. It is very crucial to investigate the structures and properties of grain boundaries in SiC, because grain boundaries in sintered ceramics or polycrystalline films have significant effects on the bulk properties. As shown in our previous studies [1], the problems of the interface stoichiometry and the wrong bonds between like atoms are very important in grain boundaries in compound semiconductors such as SiC, similarly to those in the antiphase boundaries [2], and differently from grain boundaries in Si or Ge [3-5]. In our studies, we proposed the definition of the polar and non-polar interfaces of grain boundaries in compound semiconductors. The former and the latter are non-stoichiometric and stoichiometric, respectively. We examined the atomic and electronic structures of polar and non-polar interfaces of the {122} Σ=9 boundary in SiC by using the tight-binding electronic theory [6], and found significant effects of the wrong bonds. We also showed that the relative stability among the interfaces with different stoichiometries can be analyzed by calculating the thermodynamic potentials as a function of the atomic chemical potentials.

In this paper, firstly, we discuss a general definition of the interface stoichiometry of grain boundaries in the zinc-blende structure according to the discussion of the surface stoichiometry [7], and we make clearer the crystallographic analysis in our previous studies. Secondly, we examine theoretically the atomic and electronic structures of the {211} Σ=3 boundary in SiC following our studies of the {122} Σ=9 boundary. The {211} Σ=3 boundary is one of the typical CSL (coincidence site lattice) tilt boundaries frequently observed in CVD-SiC [8] as well as the {111} Σ=3 and {122} Σ=9 boundaries. The {211} Σ=3 boundary is considered to generate only non-polar interfaces, differently from the {122} Σ=9 boundary generating both polar and non-polar interfaces.

Mat. Res. Soc. Symp. Proc. Vol. 339. ©1994 Materials Research Society

INTERFACE STOICHIOMETRY

As discussed in [1], polar and non-polar interfaces in grain boundaries in cubic binary compounds can be defined by the interface stoichiometry. About symmetrical tilt boundaries, non-polar interfaces can be constructed with both non-polar surfaces or by cation-terminated and anion-terminated polar surfaces. Polar interfaces can be constructed with two cation-terminated polar surfaces or with two anion-terminated polar surfaces. On the other hand, a paratwin and an orthotwin [9] can be defined by the relation between the polarity of the two grains for symmetrical tilt boundaries in binary compounds. In a paratwin, the polarity of the two grains displays mirror symmetry to each other with respect to the interface. One additional paratwin can be constructed by inverting the polarity of the two grains. An orthotwin is constructed by inverting the polarity of one of the two grains of the paratwins. Thus, as pointed out in [1], for symmetrical tilt boundaries of which the interface consists of polar surfaces such as {111} and {122}, two polar and one non-polar interfaces can be constructed, which correspond to two paratwins and one orthotwin. And symmetrical tilt boundaries of which the interface consists of non-polar surfaces such as {211} should have only non-polar interfaces.

In configurations without any coordination defects similar to those of the symmetrical tilt boundaries in Si or Ge [3-5], the interface stoichiometry should dominate the relation between the numbers of the two kinds of wrong bonds, cation-cation bonds and anion-anion bonds. The polar interfaces should contain only one kind of wrong bonds or one kind of excess wrong bonds, although non-polar interfaces should contain no wrong bonds or the same numbers of the two kinds of wrong bonds.

The above argument can be proved clearly by Fig. 1, which shows the atomic models of the polar and non-polar interfaces of the {122} Σ=9 boundary in the zinc-blende structure [1]. These contain the bonding network similar to that in the same boundary in Si. These are consistent with the high-resolution transmission electron microscopy (HRTEM) observation in CVD-SiC [10].

In the above argument, only the interfaces consisting of ideal surfaces without any point defects are dealt with, and the interface stoichiometry is considered by the stacking of atomic layers. However, it should be noted that the interface stoichiometry can be defined rigorously even for grain boundaries with point defects or disordered structures by using the method of Chetty and Martin [7]. In this method, surface or interface stoichiometries can be determined by defining the surface or interface regions and counting the atoms in such regions. The surface or interface

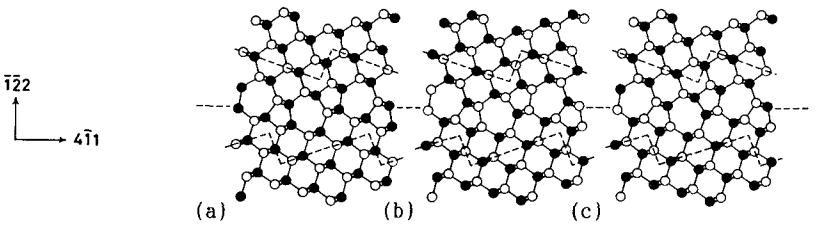

Fig. 1. Atomic models of the {122} Σ=9 boundary in the zinc-blende structure. (a) N-type polar, (b) P-type polar, and (c) non-polar interfaces. Atomic positions are projected along the <011> axis. The open and closed circles are cation and anion atoms, respectively, which correspond to Si and C atoms in SiC. Dashed lines in the crystals indicate the example of interface regions by the method of Chetty and Martin [7].

regions can be defined by boundaries in the interior of the crystals consisting of segments of planes with sufficient symmetries such as {011} or {001} planes in the zinc-blende structure.

Fig. 1 also shows the example of such interface regions. The interface regions of the N-type polar interface and of the P-type polar interface contain 10 cation and 11 anion atoms, and 11 cation and 10 anion atoms in one period, respectively. And the interface region of the non-polar interface contains 10 and 1/2 pairs of cation and anion atoms. These results are consistent with the above crystallographic argument.

THE {211} Σ=3 GRAIN BOUNDARY IN SiC

Atomic models

Figs. 2 and 3 show the atomic models of the non-polar interfaces of the {211} Σ=3 boundary in SiC. These are the p2'mm'(1x2) and pm(1x2) models. These are constructed so as to have the same bonding networks with those in the models of the same boundary in Si or Ge [11,12], because the HRTEM images [8] are not so clear. Two paratwins, Type A and Type B, are constructed for the respective models. In this paper, we deal with only the paratwins. The {211} Σ=3 boundary is connected perpendicularly with the {111} Σ=3 boundary in CVD-SiC [8]. Thus the observed {211} Σ=3 boundary should be a paratwin because the {111} Σ=3 boundary must be a orthotwin with normal Si-C bonds.

The present models contain the same numbers of the two kinds of wrong bonds because of the non-polar interfaces. The wrong bonds exist at the two types of positions. These are the intergranular bonds and the <011> bonds. The intergranular bonds exist on the {011} plane and cross the interface. The <011> bonds connect the two atoms on the neighboring {011} planes, and double the periodicity along the <011> direction as indicated by (1x2). The kinds and positions of the wrong bonds in Type A are inverted in Type B.

In Si or Ge, there exist experimental and theoretical studies [3-5] showing the presence and stability of the <011> bonds in the {211} Σ=3 boundary. And it is considered that the cm(2x2) model is the most stable in Si or Ge, where only the succession of the <011> bonds along the <111> direction is different from the pm(1x2) model and the periodicity along the <111> direction is double in addition to the <011> direction. However, the energy difference between the pm(1x2) and cm(2x2) models seems to be very small in Si [4,5]. Thus, we deal with only (1x2) models for simplicity.

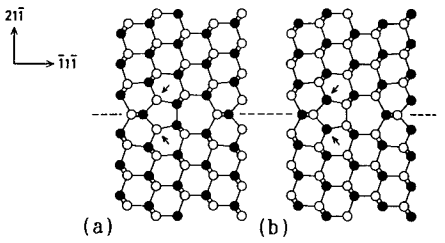

Fig. 2. Atomic models of the {211} Σ=3 boundary in SiC. (a) Type A and (b) Type B of the p2'mm'(1x2) model. Arrows indicate the <011> bonds.

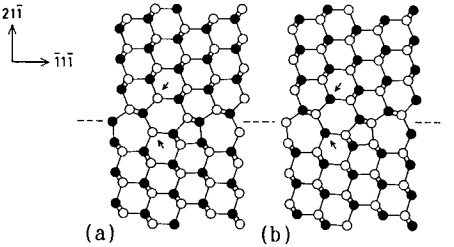

Fig. 3. Atomic models of the {211} Σ=3 boundary in SiC. (a) Type A and (b) Type B of the pm(1x2) model. Arrows indicate the <011> bonds.

The SCTB method

Lattice relaxations have been performed by using the self-consistent tight-binding (SCTB) method [6] following our previous studies. The SCTB method can deal with energies and atomic and electronic structures of complex systems of semiconductors as well as the usual tight-binding method [4,5]. In the SCTB method, the charge transfer effects are included self-consistently into the on-site terms of the Hamiltonian. Thus, self-consistent charge distributions and electrostatic interactions can be dealt with more correctly than the usual method, which are essential in SiC. The binding energy E_B is finally expressed as a sum of the promotion and intra-atomic electrostatic energy E_{pro}, the inter-atomic electrostatic energy E_{Mad}, the covalent energy E_{cov}, and the repulsive overlap energy E_{ov}.

The supercell technique is used to perform band calculations, where periodicity normal to the interface is imposed by stacking symmetric boundary planes alternately in addition to the two-dimensional periodicity of the CSL boundary. In the cases of paratwins, it is necessary to stack both Type A and Type B alternately. However, it is possible to examine respective interfaces, if there exist no significant charge transfer or interactions between the two interfaces in the unit cell. This condition has been shown to be almost satisfied in each case. And in the SCTB method, E_B and the respective energy terms can be given for respective atoms in the unit cell. Thus the energies of respective interfaces can be obtained.

The supercells of the p2'mm'(1x2) model and of the pm(1x2) model contain 192 atoms and 200 atoms, respectively. The interfaces are repeated between 24 atomic layers and 25 atomic layers, respectively, and the distances between the interfaces are about 2.1nm and 2.2nm, respectively. In lattice relaxations, respective three atomic layers in the bulk regions are fixed at the positions containing the rigid-body translations between the two grains. The rigid-body translations have been optimized by iterating relaxations using the Keating-type potential [13] for saving computing time.

Table I. Calculated energy values and bond distortions of the models of the {211} Σ=3 boundary in SiC. Energy increases per one period of interface against the perfect crystal are shown. E_{gb} is the interfacial energy. $\Delta\theta$ and Δr_{Si-C} indicate the ranges of the bond-angle distortions and those of the bond-length distortions of the Si-C bonds. Δr_{Si-Si} and Δr_{C-C} are the bond-length distortions of the Si-Si bonds and of the C-C bonds against the bond lengths in bulk Si and in bulk diamond, respectively. The results of the non-polar interface of the {122} Σ=9 boundary [1] are also shown.

	{211} Σ=3 boundary				{122} Σ=9 boundary
	p2'mm'(1x2)		pm(1x2)		
	Type A	Type B	Type A	Type B	Non-polar
E_{gb}	1.71J/m^2	2.37J/m^2	1.39J/m^2	2.42J/m^2	1.43J/m^2
ΔE_B	4.96eV	6.90eV	4.03eV	7.04eV	2.54eV
$\Delta E_{pro}+\Delta E_{Mad}$	2.48eV	1.45eV	2.19eV	1.09eV	1.12eV
$\Delta E_{cov}+\Delta E_{ov}$	2.48eV	5.45eV	1.85eV	5.95eV	1.42eV
$\Delta\theta$	-23.5° ∿ +21.0°	-19.1° ∿ +27.9°	-14.2° ∿ +21.5°	-23.8° ∿ +17.3°	-23.1° ∿ +24.1°
Δr_{Si-C}	-3.2% ∿ +3.3%	-2.8% ∿ +6.3%	-2.7% ∿ +2.2%	-2.9% ∿ +5.3%	-2.5% ∿ +2.2%
Δr_{Si-Si}	+1.7%,+1.7%	-3.1%,-3.1%	+3.2%,+2.9%	-4.2%,-4.0%	-4.3%
Δr_{C-C}	+1.8%,+1.8%	+5.6%,+5.6%	+2.1%,+1.9%	+9.3%,+8.0%	+3.8%

Results

The rigid-body translation in Type A of the p2'mm'(1x2) model is a dilatation of 0.001nm, and that in Type B is a dilatation of 0.024nm. The rigid-body translation in Type A of the pm(1x2) model is a shift of 0.072nm along the <111> direction with a dilatation of 0.016nm. That in Type B is a shift of 0.068nm along the <111> direction with a dilatation of 0.032nm. In both the models, the interfaces where the Si-Si bonds are the intergranular bonds contain larger dilatations. The translations in the pm(1x2) models are qualitatively similar to those in the pm(1x2) or cm(2x2) models in Si or Ge [3-5].

Table I shows the energies and bond distortions of the relaxed configurations. Type A of the pm(1x2) model is the most stable, where the interfacial energy and the bond distortions are in similar ranges to those in the {122} Σ=9 boundary. Type B of the pm(1x2) model has the largest energy.

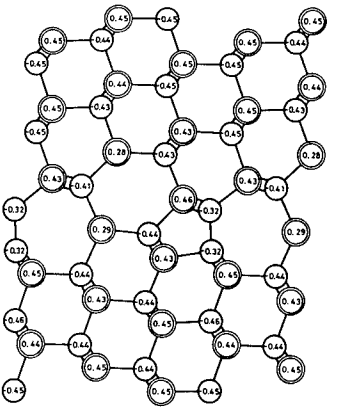

Fig. 4. Relaxed configuration and effective atomic charges of Type A of the pm(1x2) model of the {211} Σ=3 boundary in SiC. The circles and double circles indicate C and Si atoms, respectively. The bulk atomic charges are ±0.45e.

Fig. 4 shows the relaxed configuration and the effective atomic charges of the most stable model. In every interface, the wrong bonds generate no extra carriers, no deep states in the band gap, no charge accumulation, or no macroscopic electrostatic fields. This is because the valence numbers of Si and C are the same and the origin of the atomic charges in SiC is the bond polarization. Thus the absolute values of the effective atomic charges at the wrong bonds are about 3/4 of the bulk values because of three heteropolar bonds. In each interface, the fluctuations of atomic charges and the bond distortions are well localized within several atomic layers at the interfaces. These results are similar to those in the {122} Σ=9 boundary.

However, there exist significant effects of the wrong bonds. Firstly, the wrong bonds very much increase the interfacial energies by the electrostatic repulsion at the wrong bonds. In Table I, the energy increases mainly caused by the electrostatic interactions, $\Delta E_{pro}+\Delta E_{Mad}$, are the substantial parts of the total increases as well as in the {122} Σ=9 boundary. This is consistent with the results in the antiphase boundaries [2]. Secondly, the wrong bonds generate the localized electronic states mainly caused by the different bond lengths. In each interface, the C-C bonds generate the localized states at the bottom of the valence band and above the conduction band, and the Si-Si bonds generate the localized states at the top of the valence band and at the bottom of the conduction band as well as in the {122} Σ=9 boundary.

Thirdly, the wrong bonds very much affect the bond distortions and the distortion energies at the interfaces through the different bond lengths. This point is especially remarkable in the present case as compared with the {122} Σ=9 boundary where this point causes the relative stability of the polar interfaces against the non-polar interface. The wrong bonds tend to have the bond lengths similar to those in bulk Si or bulk diamond. In Type A of both the models, the Si-Si bonds are the <011> bonds, which are inevitably stretched because the distance between the neighboring {011} planes is about 1.6 times larger than the normal Si-C bond length. The C-C bonds are the intergranular bonds, which can be shortened at the interfaces. However, in Type B of both the models, the Si-Si bonds are the intergranular bonds and

the C-C bonds are the <011> bonds. Thus, as shown in Table I, in Type A of both the models, the wrong bonds are well stabilized with the bond lengths nearer to those in bulk Si or bulk diamond, and the distortions of normal Si-C bonds at the interfaces are smaller than those in Type B. Thus, the energy increases $\Delta E_{cov}+\Delta E_{ov}$ mainly caused by the bond distortions, and the total energy increases are much smaller in Type A than in Type B in both the models. About the comparison between Type A of the p2'mm'(1x2) model and Type A of the pm(1x2) model, the bond distortions of the normal Si-C bonds are relatively small in the pm(1x2) model as shown in Table I. Thus, Type A of the pm(1x2) model is the most stable. This is consistent with the results in Si that the pm(1x2) model is more stable than the p2'mm'(1x2) model [4].

CONCLUSION

From the present results of the {211} Σ=3 boundary and the previous results of the {122} Σ=9 boundary, it can be said that the effects of the wrong bonds in grain boundaries in SiC are to make the interfacial energies fairly high by the electrostatic repulsion, to generate the localized states at the band edges, and to influence the local bond distortions by the different bond lengths. Generally, stable interfaces in SiC should be those with as small numbers of wrong bonds as possible and where the different bond lengths of the wrong bonds can be well fitted without any large bond distortions. About the effects of the interface stoichiometry, it dominates the kinds and numbers of the wrong bonds. In SiC, even polar interfaces can exist stably without generating any charge accumulation or extra carriers. And the stability among the interfaces with different stoichiometries depends on the relation between the atomic chemical potentials.

REFERENCES

1. M. Kohyama, S. Kose, M. Kinoshita and R. Yamamoto, J. Phys. Condens. Matter 2, 7809 (1990); M. Kohyama, S. Kose and R. Yamamoto, J. Phys. Condens. Matter 3, 7555 (1991).
2. W.R.L. Lambrecht and B. Segal, Phys. Rev. B41, 2948 (1990); W.R.L. Lambrecht, C.H. Lee, M. Methfessel, M. van Schilfgaarde, C. Amador and B. Segall, in Defects in Materials, edited by P.D. Bristowe, J.E. Epperson, J.E. Griffith and Z. Liliental-Weber, Mat. Res. Soc. Symp. Proc. Vol.209 (MRS, Pittsburgh, 1991), p.667.
3. A. Bourret and J.J. Bacmann, Surf. Sci. 162, 495 (1985).
4. A.T. Paxton and A.P. Sutton, J. Phys. C21, L481 (1988).
5. M. Kohyama, R. Yamamoto, Y. Watanabe, Y. Ebata and M. Kinoshita, J. Phys. C21, L695 (1988).
6. M. Kohyama, S. Kose, M. Kinoshita and R. Yamamoto, J. Phys. Condens. Matter 2, 7791 (1990).
7. N. Chetty and R.M. Martin, Phys. Rev. B44, 5568 (1991).
8. P. Pirouz and J. Yang, in High Resolution Electron Microscopy of Defects in Materials, edited by R. Sinclair, D.J. Smith and U. Dahmen, Mat. Res. Soc. Symp. Proc. Vol.183 (MRS, Pittsburgh, 1990), p.173.
9. D.B. Holt, J. Phys. Chem. Solids 25, 1385 (1964).
10. K. Hiraga, Sci. Rep. Res. Inst. Tohoku Univ. A32, 1 (1984).
11. R.C. Pond, D.J. Bacon and A.M. Bastaweesy, in Microscopy of Semiconducting Materials 1983, Inst. Phys. Conf. Ser. No.67 (IOP, Bristol, 1983), p.253.
12. A.M. Papon and M. Petit, Scripta Metall. 19, 391 (1985).
13. J.L. Martins and A. Zunger, Phys. Rev. B30, 6217 (1984).

ELECTRONIC STRUCTURES OF β-SiC(001) SURFACES AND Al/β-SiC(001) INTERFACE

XIAO HU, HONG YAN AND FUMIO S. OHUCHI

Department of Materials Science and Engineering, FB-10
University of Washington, Seattle, WA 98195, U.S.A.

ABSTRACT

Surface electronic structures of β-SiC reconstructed (001) surfaces and the Al/β-SiC(001) interface have been investigated by employing a tight-binding method. Distinct surface electronic characteristics corresponding to different surface reconstructions are discussed based on the interpretation of surface density of states. The calculations of the Al/β-SiC (001) interface indicate that aluminum deposition on β-SiC(001) surface may induce the substrate to return to the ideal unreconstructed surface and that Al-C interaction is stronger than Al-Si interaction. Al deposition on C-rich surfaces may form a better bonded interface than that on the Si-rich surfaces. Our findings are in good agreement with available experimental and theoretical results.

I. INTRODUCTION

Silicon carbide (SiC) has drawn increasing attention for its important role as a wide band-gap semiconductor. Of the many polytypes of its crystal structures, cubic β-SiC has demonstrated potential applications in high-temperature, high-frequency and high-power semiconductor devices[1,2]. Since interfaces often exert important influence on expected functional performances, an understanding of the mechanism of the Al/β-SiC interface formation and the ability to predict the properties and utilities of this system are obviously very important in this context. On the other hand, surface characteristics play a key role in affecting the properties of the interfaces. In this work, we first investigate the electronic structure of the β-SiC(001) surface of various reconstructions by carrying out an empirical tight-binding calculation. Comparison to the ideal β-SiC(111) and (110) surfaces and the Si(001) (2x1) surface has been made to correlate the (001) surface configuration and chemistry to the resultant surface bonding features[5]. Then, we attempt to uncover the essential difference between Al forming interfaces with the ideal β-SiC(001) surfaces and with the reconstructed surface, as well as between Al-C and Al-Si bonding characteristics, by comparing the structure-related changes in electronic structures and energies of these systems based on similar tight-binding calculations.

II. COMPUTATIONAL METHOD

The method we have employed is based on the LCAO (linear combination of atomic orbitals) theory and utilizes a two-center approximation of atomic orbital interactions[3] coupled with Harrison's universal interatomic distance-dependent functional forms[4] for the construction of Hamiltonian matrix elements. A new set of tight-binding two-center integral parameters, including an excited s* state in the basis set of atomic orbitals, is used to better describe the β-SiC bulk and surface band structure[5]. In order to preserve simplicity and allow easy identification of chemical trends in the band structure, we take only the nearest neighbor atomic interaction into consideration.

Mat. Res. Soc. Symp. Proc. Vol. 339. ©1994 Materials Research Society

The surface electronic structures are calculated by using slab unit cells. For ideal β-SiC(001), (111) and (110) surfaces, the surface atoms on the slabs are in their original bulk atomic positions. For the reconstructed surfaces, the slab surfaces are constructed based on the proposed reconstruction models (to be discussed in the following section) and are subjected to relaxation through an energy minimization method employing a valence-force-field (VFF) model of the Keating type[6,7] before the electronic structure calculations are performed.

For the Al/β-SiC(001) interface, we have calculated the electronic structure by assigning Al atoms on both surfaces of the β-SiC(001) slab unit cell. The positions of the Al atoms are hypothetically chosen so that the differences between Al-Si and Al-C bonding and the effects of the formation of dimers on the bonding characteristics of the Al/β-SiC(001) interface can be studied. The distances between Al, C and Si are assumed to be equal to the sum of Slater's atomic radii[8]. Based on our calculated band structures, distinct surface and interface bonding characteristics corresponding to different surface and interface structures are discussed based on the interpretation of electronic density of states and, for the Al/β-SiC(001) interface, band structure energy changes.

III. RESULTS AND DISCUSSION

3.1 β-SiC(001) reconstructed surfaces

Although literature is available concerning reconstructions of the β-SiC(001) surface[9-13], corresponding models[1,10-15], and their surface electronic structures[16], correlations

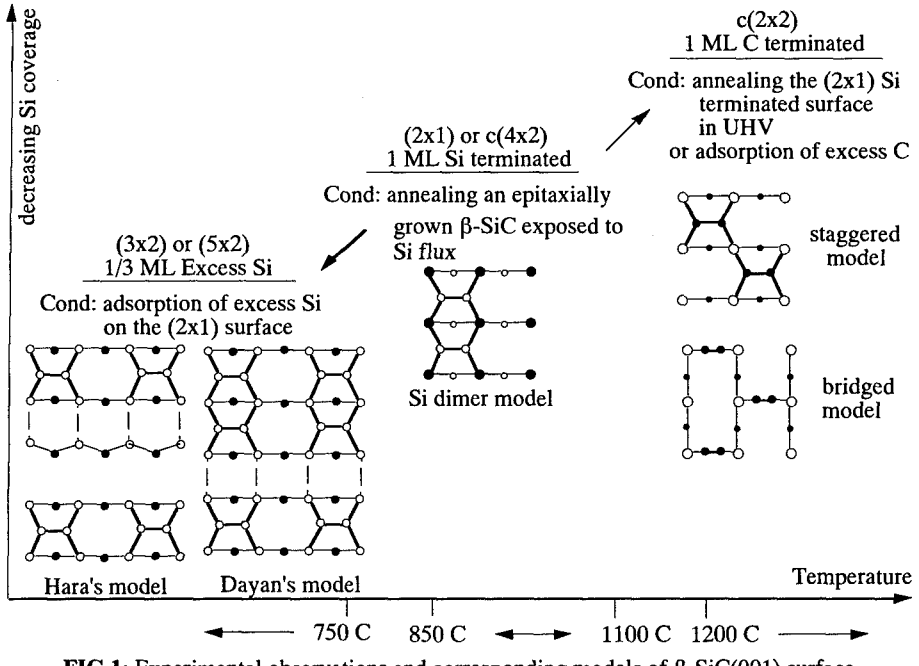

FIG 1: Experimental observations and corresponding models of β-SiC(001) surface reconstructions

between the reconstructions and the associated electronic structures and bonding characteristics have not yet been addressed. Thus, we focus our attention on examining the surface structure related changes in bonding and electronic structures for all the preferred models for β-SiC(001) reconstructed surfaces. The experimental observations of β-SiC(001) surface reconstructions and proposed models are summarized in Fig.1. Note that for the (3x2) surface, careful experiments show that the surface is associated with a 1/3 monolayer (ML) of excess Si atoms rather than 2/3 ML[10,11]. Therefore, the model of Hara et al.[10], as a modification to Dayan's model[1], is adopted in our calculation. For the c(2x2) surface, both two competing models, namely, the 'staggered' model[12] and the 'bridged' model[13], are investigated and compared.

For the (2x1) reconstruction, corresponding to a 1 ML silicon-terminated surface[9-10], there is only one dangling bond left on each surface silicon atom, similar to the ideal β-SiC (111) Si terminated surface[5]. We find that the surface Si exhibits an sp^3 hybridized dangling bond, analogous to that of the (111) ideal Si surface. Surface Si dimerization gives rise to a Si-Si σ bond, lying at about 2.3 eV below the Fermi level, corresponding well to the experimental Si dimer bonding state of the Si (001) (2x1) surface[18]. The overall electronic feature obtained by our calculation resembles that of the Si (001) (2x1) surface by a first principle calculation[5,17], in agreement with the experimental findings that the β-SiC (001) (2x1) surface and the Si (001) (2x1) have similar electronic structures[9,13].

The calculated electronic structure of the β-SiC (001) (3x2) reconstructed surface is close to that of the β-SiC (001) (2x1) surface. However, because of the missing excess Si dimer rows and the sub-layer Si atom dimerization, the surface Si-Si bond lengths and angles differ for different groups of surface atoms, causing the Si-Si σ bond surface states to shift and broaden in response to respective bonding environment. For the same reason, the hybridized Si sp^3 dangling bond states are also shifted and broadened[5]. The findings in the experiment of Parrill and Chung[9] that the overall features of the (3x2) surface are close to those of the (2x1) surface and that both Mg-excited and Zr-excited Si 2p spectra are shifted and broadened for the (3x2) surface agree with our calculation.

For the β-SiC (001) c(2x2) surface, it is found in our calculations that the surface presents a hybridized C sp^3 dangling bond for the staggered model whereas the bridged model predicts a strong C 2p dangling bond pairing which gives rise to pπ bonding and pπ* antibonding states. The C dimer bond of the staggered model is a single σ bond. It is weaker than that of the bridged model, which is considered to be a C=C double σ bond[5]. There is no Si dangling bond on the staggered model surface while a hybridized Si dangling bond shows up on the bridged model surface. This provides additional evidence that the C dimer of the bridged model is so strong that its bonding to the sublayer Si is greatly weakened, thereby causing the sublayer Si to present a dangling state. The experiments of ELS, AES and LEED etc.[12] and the calculation of Craig and Smith[15] strongly support the staggered model, while other calculations favor the bridged model[13,14].

3.2 Al/β-SiC(001) interface

We have studied four systems for the Al/β-SiC (001) interface, i.e. Al/unreconstructed surface and Al/reconstructed surface for both Al/C terminated and Si terminated surfaces, by interpreting the electronic density of states of the interfaces to elucidate their respective bonding characteristics and by investigating the band structure energy changes to reveal their relative interfacial stabilities.

3.2.1 Interfacial density of states and bonding

The atomic structures of the slab unit cells of Al/C terminated ideal and reconstructed surfaces are depicted in Fig.2A. After the deposition of Al on the unreconstructed C surface, the significant change compared to the ideal C terminated surface is that the C dangling 2p state and the surface hybridized resonance states disappear, and there is no surface state in the fundamental gap. Instead, an Al 3p dangling bond shows up prominently.

For the Al on the reconstructed C surface, the Al 3p dangling bond remains; but its intensity is lower than that of the Al on the unreconstructed C surface. The C dimer bonding states $p\sigma$ and $s\sigma$ and the antibonding states $p\sigma^*$ and $s\sigma^*$, respectively, are analogous to those of the clean C reconstructed surface of the bridged model. We compare to the bridged model because the C dimer length of the bridged model is closer to the C dimer length of this surface. The significant difference between this surface and the C clean surface of the bridged model is that $p\pi$ and $p\pi^*$ states disappear on this surface because Al reacts with C, eliminating the C 2p dangling bond and the dangling bond pairing which originally induces $p\pi$ and $p\pi^*$ states.

Comparing these two interfaces, we find that the Al-C σ bonding and the σ^* anti-bonding states of the Al/reconstructed C surface stay closer than those of the Al/unreconstructed C surface, indicating that the Al-C interaction of the former interface is weaker. In addition, the more localization of the bands associated with the Al-C interaction at the Al/reconstructed C surface also suggests that the Al-C interaction of the Al/unreconstructed C terminated surface is stronger.

The atomic configurations of the slab unit cells of Al/β-SiC (001) Si terminated unreconstructed and reconstructed surfaces are shown in Fig.2B. Compared to the Al/unreconstructed C terminated surface, the Al-Si $p\sigma$ and $p\sigma^*$ on the Al/unreconstructed Si surface are closer and stay in higher energy states, indicating that Al-Si bond is much weaker and less energetically favorable with respect to Al-C bond. This is also supported by the fact that there is no Al-Si $s\sigma$ bonding state; thus the covalent energy of the Al-Si bond should be very high.

On the Al/reconstructed Si surface, the Al-Si bonding and anti-bonding states get even closer than those of the Al/Si unreconstructed surface, indicating weaker Al-Si bonding in this case. A significant difference between this surface and the Al/C reconstructed surface is that, on this surface, a Si sp^3 dangling state appears, in analogy to both that on the β-SiC(111) Si terminated surface and that on the β-SiC (001) Si terminated (2x1) surface[5]. This is strong evidence that Al-Si bonding is rather weak at the interface of Al/reconstructed Si surface, leaving the Si sp^3 dangling bond little influenced by the deposited Al.

So far, we have discussed the surface electronic structures and bonding of four Al/β-SiC interfacial systems through qualitative interpretations of the electronic density of states. However, in order to more quantitatively elucidate the interfacial bonding strength and the difference in Al bonding to a C terminated surface and to a Si terminated surface in response to surface dimerizations, it is more desirable to investigate the total energy differences between these systems. In this work, we have performed band structure energy change calculations to approximate the total energy changes.

3.2.2 The changes in band structure energy

For either Al/C terminated surface or Al/Si terminated surface system (Fig.2A and 2B), the Al-Si or Al-C distance remains fixed. Again, Slater's atomic radii are used to determine Al-C and Al-Si distances as well as C and Si dimer lengths. Thus the band structure energy change from Al/unreconstructed surface to Al/reconstructed surface should approximate the total energy change to the first order.

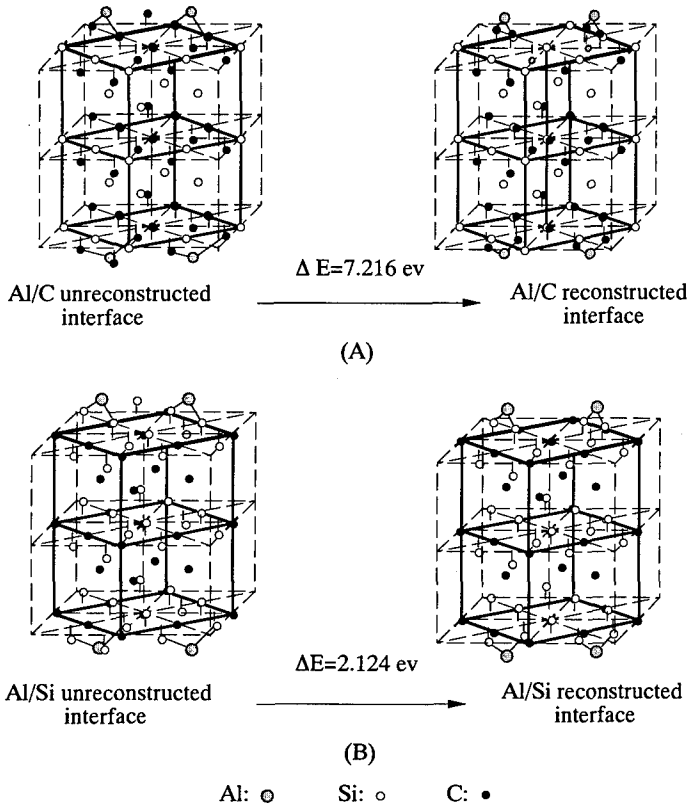

FIG. 2 Band structure energy changes of the system of (A) Al/C interface (B) Al/Si interface

The calculated band structure energy changes for Al/C terminated surface and Al/Si terminated surface systems are +7.216 eV and +2.124 eV, respectively. The results give an indication that the Al/reconstructed surface system will be energetically unfavorable compared to the Al/unreconstructed surface system in both Al/C terminated and Al/Si terminated cases. Thus Al deposition on a β-SiC (001) reconstructed surface may induce the substrate to return to the unreconstructed surface. Another indication from these results is that the tendency for Al inducing C reconstructed surface to C ideal surface is stronger than that for Si terminated surface.

These two findings are consistent with our previous analysis of band structures and other experimental and theoretical conclusions[19, 20].

IV. SUMMARY

We have shown that the present empirical tight-binding method can represent quite well the β-SiC (001) surface bonding and electronic structure characteristics associated with their corresponding surface structures. The work investigating the Al/β-SiC(001) interface converges to the conclusion that Al bonding to an unreconstructed surface is much stronger and more energetically favorable than Al bonding to a reconstructed surface for both Al/C terminated β-SiC (001) and Al/Si terminated β-SiC (001) systems. Thus Al deposition on β-SiC (001) surface may induce the substrate to return to its ideal unreconstructed surface. Moreover, it is found that Al-C interaction is much stronger than Al-Si interaction. It is therefore expected that the Al deposition on C-rich surface may form a better bonded interface than that on the Si-rich surface.

REFERENCE

[1] M. Dayan, J. Vac. Sci. Technol. A **3**, 361 (1985); A **4**, 38 (1986)
[2] W.J.Choyke, in Proceedings of Novel Refractory Semiconductors, ed. by David Emin, T.L.Aselage, and Charles Wood, MRS Symposia Proceedings, No.**97** (Material Research Society, Pittsburgh, 1987), p.207
[3] J.C.Slater and G.F.Koster, Phys. Rev. B **94**, 1498 (1954)
[4] W.A. Harrison, Electronic Structure and The Properties of Solids (Freemen, San Francisco, CA, 1980)
[5] X.Hu, H.Yan, F.S.Ohuchi and M.Kohyama, preprint, 1994
[6] P.N.Keating, Phys. Rev. B **145**, 637 (1966)
[7] J.C.Martins and A. Zunger, Phys. Rev. B **30**, 6217 (1984)
[8] J.C.Slater, Quantum Theory of Molecules and Solids, Vol.2, (McGraw-Hill, New York, 1965) p.307
[9] T.M.Parrill and Y.W.Chung, Surf. Sci. **243**, 96 (1991)
[10] S.Hara, Y.Aoyagi, M.Kawai, S.Misawa, E.Sakuma and S.Yoshida, Surf. Sci. **273**, 437 (1992)
[11] R.Kaplan and T.M.Parrill, Surf. Sci. **165**, L45 (1986)
[12] V.M.Bermudez and R.Kaplan, Phys. Rev. B **44**, 11149 (1991)
[13]J.M.Powers, A.Wander, P.J.Rous, M.A.Van Hove and G.A.Somorjai, Phys. Rev. B **44**, 11159 (1991); Surf. Sci. Lett. **260**, L7 (1992)
[14] Badziag, Phys. Rev. B **44**, 11143 (1991)
[15] B.I.Craig and P.V.Smith, Surf. Sci. **233**, 255 (1990); Surf. Sci. Lett. **256**, L609 (1991)
[16] H.Hoechst, M.Tery, B.C.Johnson, J.M.Meere, G.W.Zajac and T.H.Fleish, J. Vac. Sci. Technol. **A**, **5**, 1640 (1987)
[17] P.Kruger, A.Mazur, J.Pollmann and G.Wolfgarten, Phys. Rev. Lett. **57**, 1468 (1986)
[18] R.I.G.Uhrberg, G.V.Hansson, J.M.Nicholls and S.A.Flodstrom, Phys. Rev. B **24**, 4684 (1991)
[19] V.M.Bermudez, Appl. Phys. Lett. **42** 70 (1983)
[20] W.Lu, K.Zhang and X.Xie, Phys. Rev. B, **45**, 11048 (1991)

COMPUTER SIMULATION OF Si AND C ATOMS ON SiC SURFACES

C C MATTHAI, G J MORAN AND I MORRISON
Department of Physics and Astronomy
UWCC, Cardiff CF2 3YB, UK

ABSTRACT

The molecular dynamics method employing an empirical potential energy function to describe the Si-C interaction has been used to determine the minimum energy sites for Si and C adatoms on C-terminated SiC (001) substrates. It is found that whereas a single C adatom lies on the carbon dimer bond, this site only becomes energetically favourable for silicon adatoms when they interact to form a dimer pair.

INTRODUCTION

Silicon Carbide (SiC) has long been considered a suitable material for devices requiring wide-gap semiconductors. Recent progress in growing high quality single crystal SiC on Si(001) substrates has provoked much interest in this system. However, because of the large lattice mismatch and different thermal expansion, numerous defects are found on the SiC surface. The Si and C terminated cubic SiC (001) surfaces have been studied by many groups using a variety of techniques[1,2]. Theoretical studies of this system have included a molecular orbital technique investigation of the SiC/Si interface [3] and a semi-empirical tight-binding study of surface relaxations of the SiC surface[4]. To our knowledge there has been no theoretical investigation of the potential energy contours of the SiC(001) surface. As such information is valuable in determining both the adsorption sites and activation energies for surface diffusion, we have performed simulations of the C-terminated SiC(001) surface with Si and C adatoms. However, for understanding the growth process, it is important to determine how the interactions between adatoms affects the subsequent adsorption site. We have therefore extended our simulations to include two adatoms on the surface.

CALCULATIONAL PROCEDURE

The cubic SiC substrate was constructed with the (001) face representing the surface of the zincblende structure. The C-terminated SiC (001) surface reconstructs to a (2x1) structure with the carbon atoms dimerising in a manner akin to the Si(001) (2x1) surface. To determine the possible adsorption sites, a Si or C adatom was placed on the surface in some initial configuration and the forces on all the atoms calculated. With the exception of the adatom all the atoms were allowed to move until an energy minimum was achieved. The adatom was constrained to move in a direction perpendicular to the surface. The minimum energies for each lateral position of the atom resulted in a potential energy surface map. In order to avoid the system getting trapped in local minima, the adatom was periodically given a small temperature. The minimum energy was then obtained by the process of quenching the system so that the kinetic energy was reduced to zero.

In order to move the atoms it is necessary to have a scheme to enable the forces on

Mat. Res. Soc. Symp. Proc. Vol. 339. ©1994 Materials Research Society

each atoms to be calculated. Although it now possible to perform such calculations using ab initio total energy techniques these are rather computer intensive and so restrict the number of geometries that can be investigated. Semi-empirical total energy functionals have been shown to give a good description of the surface reconstructions found in semiconductor structures and also to be useful in giving information about the growth processes[5]. We have therefore chosen to use similar potential energy functions to that used to study the Si-Ge system. These interatomic potentials reported by Tersoff[6] have a coordination dependent bonding term which is a requisite for describing reconstructed surfaces.

RESULTS

Bulk

Before the surface simulations were performed calculations on the bulk SiC system were carried out. The interatomic potential used gave a minimum lattice energy of -6.2 eV /atom at a lattice parameter of 4.3Åfor the ordered $Si_{0.5}C_{0.5}$ alloy. To ensure that this ordered phase was the lowest energy, a silicon crystal was first constructed and then randomly chosen Si atoms were converted to C atoms until there were an equal number of Si and C atoms. The energies of these systems were found to be on average 0.1 eV/atom higher than in the ordered phase. Thus it was concluded that the cubic SiC structure favoured the ordered phase with this potential energy function.

C-terminated surface

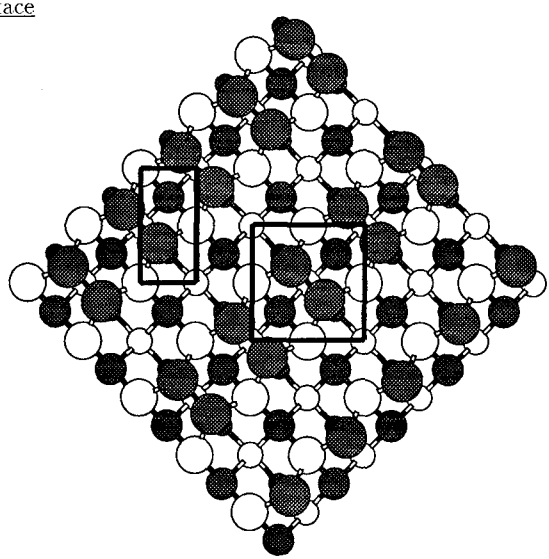

Figure 1: Schematic diagram of the areas scanned in determining the potential energy surfaces for the (001) (2x1) SiC and Si reconstructions. In the case of the SiC reconstruction filled circles represent C atoms and unfilled Si atoms. The square area represents the scan on SiC and the rectangle the scan on Si.

The surface was modelled by allowing the C atoms on the surface to relax to form dimer bonds. the dimer bond length was found to be 1.5Åcompared to a Si dimer bond length of 2.25Åon the Si(001) (2x1) reconstructed surface. The C atoms on the surface also undergo a substantial downward relaxation of 0.5Åcompared to the bulk terminated unrelaxed surface.

Adatoms

Once the relaxed (001) surface structure was established, an adatom was placed on the surface and the relaxed energy and adatom height for that particular position was determined in the manner described above. This was done for for a mesh of 121 points in the region indicated in Figure 1. Two sets of simulations were performed; one for a C-adatom and one for a Si-adatom. From the potential energy surfaces shown in Figure 2, it may be observed that as might be expected there is a minimum energy configuration with the adatom above the C-C dimer. When this happens the dimer opens out and the C atoms move to their bulk sites. However, unexpectedly the Si adatom was found to have a higher energy at this site than the C adatom. Although this is the global minimum for the C adatom, the Si adatom has its global minimum at the edge of the square indicated in figure 1. By way of comparison we have also calculated the potential energy surface for a Si adatom on the Si(001) (2x1) reconstructed surface for the rectangular region in Figure 1. From these results, shown in Figure 3, it may be noted that the minimum energy site is not on the dimer bond.

Figure 2(a): Potential energy surface for the Si adatom on the SiC (001) surface. Dark regions represent areas of low energy.

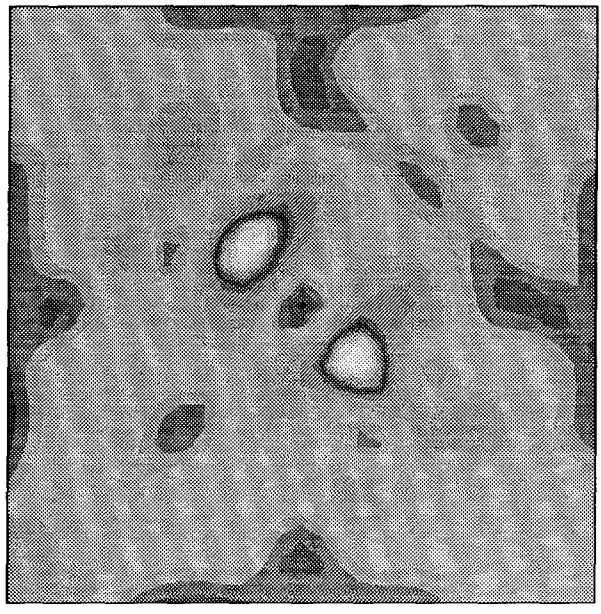

Figure 2(b): Potential energy surface for the C adatom on the SiC (001) surface.

Figure 3: Potential energy surface for the Si adatom on the Si (001) surface.

Adatom pair

Following the calculations with one adatom, the simulations were carried out for two adatoms. These were placed on adjacent sites on the C-dimer bonds and the atoms allowed to relax. Immediately the adatoms were found to move towards each other forming a dimer in the opposite direction to the surface C-dimers (Figure 4) For the Si pair, the dimer bond length was found to be 2.34Åwhich is very close to the interatomic spacing in bulk silicon but larger than the dimer bond length on the Si(001) (2x1) surface.

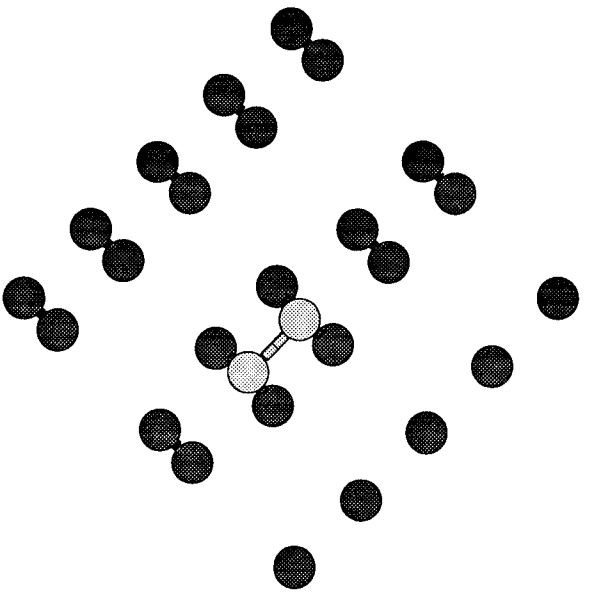

Figure 4: The minimum energy atomic configuration for the pair of Si adatoms on the SiC (001) surface.The light shaded circles represent the Si adatom pair in a plane above the C dimers (dark shaded circles).

CONCLUSION

We have performed simulations of Si and C adatoms on the SiC (001) C-terminated surface. The main finding is that the C adatom is more strongly bound to the surface at the bulk continued site than the Si adatom with the latter having a global minimum away from the dimer bond. This result is similar to that found for homoepitaxial growth of Si(001). However, once a second adatom is placed on the surface it is energetically favourable for the adatoms to pair up and form a dimer in an orthogonal direction. The usefulness of these potentials in describing the early stages of growth of SiC suggests that they can be used to study the evolution of extended defects in this system.

ACKNOWLEDGEMENTS

This work has been supported by the SERC and DRA, Malvern.

REFERENCES

1. P A Ivanov and V E Chelnokov, Semicond Sci Technol 7 863 (1992)

2. M Dayan, J Vac Sci Technol A3 361 (1985)

3. B I Craig, Semicond Sci Technol 8 172 (1993)

4. S P Mehandru and A P Anderson, Phys Rev B42 9040 (1992)

5. P Ashu and C C Matthai, Appl Surf Sci 48/49 39 (1991)

6. J Tersoff, Phys Rev B39 5566 (1989)

DYNAMICS AT A STEP ON THE DIAMOND (111) SURFACE

BRIAN N. DAVIDSON AND WARREN E. PICKETT
Complex Systems Theory Branch, Naval Research Laboratory, Washington DC

ABSTRACT

Using an accurate tight-binding method, we examine the structure and dynamics at a C(111) step. We find the H vibration frequencies at a step are distinguishable from the flat surface. Removal of H from the surface creates an unstable bulk terminated diamond structure which relaxes to a graphitic layer and pulls away from the bulk. The explanation for these results can be given in terms of the relationship of the band structure to the relaxed geometries. The addition of H stabilizes this surface and reverts it back to sp^3 bonding. The addition of CH_3 near a step is also discussed. These results are important towards the understanding of possible diamond growth mechanisms that occur at a step.

INTRODUCTION

Even cleaved and polished diamond surfaces in reality are not flat, but are rough, and may contain height variations of hundreds of Angstroms. It is not surprising then that the C(111) surface of diamond films, grown by chemical vapor deposition (CVD), contains grooves [1], hillocks and steps [2, 3]. Hu *et al.* [1] used reflection electron microscopy to determine that not only did their surface consist of single atom steps, but that epitaxial growth involved the lateral motion of these steps. In fact, diamond growth mechanisms have been proposed that begin with the formation of a single atom step on the C(111) surface [4, 5]. Until recently, quantum mechanical treatments of surface steps have been performed using small clusters, which cannot realistically incorporate the steric freedom introduced by a step. The purpose of this work is to develop a better understanding of the physics and chemistry of diamond at a surface step.

Incorporation of a step on the surface in a model calculation lowers the symmetry as compared to the flat surface. The resulting increase in unit cell size severely limits the use of *ab-initio* methods for a two-dimensional periodic cell. To overcome this difficulty, we employ a parameterized tight binding energy functional (PTBF) that has been optimized for both the diamond and graphite phases of carbon [6]. This approach is much faster than *ab-initio* methods without much loss in accuracy and allows us to consider the large unit cells required to model surface steps. Our PTBF uses a parameterized Hamiltonian matrix to generate the electronic levels and an analytical function to model the remaining repulsive terms. The total energy is written as:

$$E_{total} = E_{rep} + E_{bs} + E_{charge}. \quad (1)$$

The repulsive energy, E_{rep}, is a functional of a pair potential between the ions. The band-structure energy, E_{bs} is a sum of the occupied eigenvalues of an orthogonal sp^3 basis Hamiltonian. A positive charge term, E_{charge} is added to account for charge transfer. The forms of the functions and the parameters for C are described in detail in ref. [6]. We have successfully applied this parameterization to the study of the C(111), C(100) and C(110) surfaces [7] and found that it is in good agreement with density functional (DF) results, where they exist. The additional C-H parameters were calculated from a fit to DF forces and energies [8] of

Mat. Res. Soc. Symp. Proc. Vol. 339. ©1994 Materials Research Society

small hydrocarbons over a range of C-H bond lengths. The parameters for the C-H bond are given in ref. [7] along with a comprehensive description of how we obtained them. These parameters accurately reproduce the vibrations and anharmonicity of the H bond on the C(111) surface.

The surfaces are modeled as slabs (infinite in two dimensions) with at least 60 C atoms per unit cell. The steps in our periodic cells are separated by seven surface C bond lengths. The supercells have inversion symmetry about the middle. The thickness was chosen such that the surface states on the top and bottom would not significantly mix. For the band structure energy, a 28 $\vec{k}$ point integration mesh in the reduced Brillion zone is used for the bare surfaces and an eight $\vec{k}$ point integration mesh is used for the H covered surface. Since the bare surface is metallic, we smear the occupation of the levels with a Fermi-Dirac distribution with a width of 0.01 eV.

HYDROGENATED SURFACE STEP

The surface of a diamond film during CVD growth is believed to be predominately H covered due to the presence of a H atmosphere. Sun *et al.* [3] observed the relative density of the atomic steps on their surface by monitoring the H stretch modes both parallel and perpendicular to the surface. They assumed the parallel component of the stretch mode could be attributed to the H bond attached to the edge of a surface step. Since a step on the (111) surface exposes a (110) face, the frequency of the stretch modes for these H atoms should be different. Unlike the (111) surface, the (110) direction has H bonds attached to nearest neighbor atoms. In this geometry, the localized stretching modes can still couple, so we'd expect a splitting of states.

Shown below in Fig. 1 are the four H sites in our unit cell. Atoms 1 and 2 on the "terrace" of the steps have local geometries consistent with the C(111) surface. Atoms 3 and 4 are on the (110) step face. We calculate the H vibrations from the eigenvalues of the dynamical matrix whose components are determined by finite differencing of the forces. The 8 $\vec{k}$ point band structure integration was necessary mostly for convergence of the highly coupled H bend modes. Our previous calculations [7] on the flat surfaces had indicated that the H stretching modes on the C(110) had a 8 cm^{-1} splitting between nearest neighbors and was 6 cm^{-1} and 14 cm^{-1} higher than the C(111) surface, which showed no mixing of neighboring H modes. In Fig. 1 we plot a histogram of the stretch modes weighted by the relative magnitudes of the H eigenvectors. H atoms 3 and 4 contribute equally to the higher frequency modes at 2857 and 2865 cm^{-1}. The lower modes are from the terrace H atoms, but are not split due to coupling. The small frequency difference arises from the slight difference in the local geometry between sites 1 and 2. The H stretch mode at 2850 cm^{-1} is from H bond 1, at the base of the step and the mode at 2847 cm^{-1} is from H atom 2, in the middle of the terrace. Since slight variations in local bonding would cause a spread in these frequencies, this 3 cm^{-1} difference may not be experimentally differentiable.

The H bending motion modes are more difficult to isolate since they couple strongly to the C lattice phonons. Hamza *et al.* [9] reported monohydride H bend frequencies near 1290 cm^{-1} on the "flat" C(111) surface. Our calculations [7] on the flat surface had the H bend modes centered around 1210 cm^{-1} with a splitting of $\pm$ 162 cm^{-1}. Fig. 2 show the H bending modes at a step. These modes are more detailed than the stretch modes due to the additional degrees of freedom and the phonon coupling. A step breaks the symmetry in one of the two directions defining the plane of the surface. The H motions can be distinguished

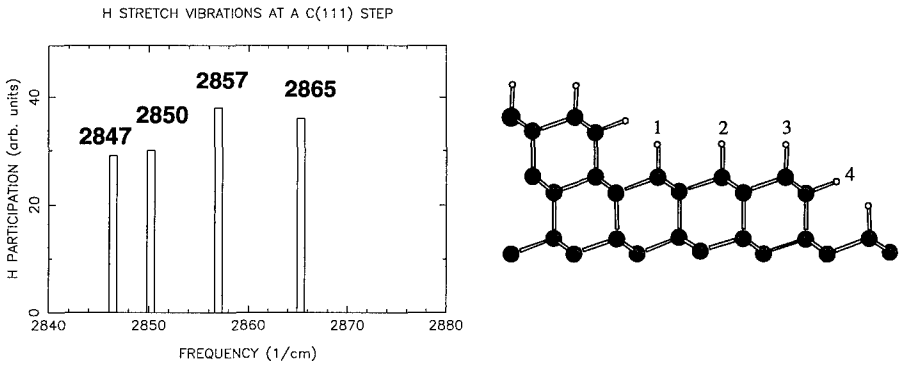

Figure 1: H stretching frequencies at a step. The magnitudes of the peaks are proportional to the magnitude of the H eigenvectors of the dynamical matrix. See text for identification of the modes.

as bending in the direction across a step or along a step (in/out of the page of figure 1). The higher frequencies at 1361 and 1320 cm^{-1} are across the step and are from the H atoms on the (110) and (111) planes respectively. The bending motion in the direction along the steps are split for the (110) H atoms at 1005 and 1190 cm^{-1}. The bending frequency of the terrace atoms are not as dispersive and are centered around 1090 cm^{-1}.

REMOVAL OF H

In order to add a hydrocarbon to the diamond surface, a H atom needs to be removed to open a surface site. The H can be eliminated by heating or by abstraction from a collision with a gas-phase molecule. We removed one of the 4 hydrogens labeled in Fig. 1 and found that the structure with either H atoms 3 or 4 removed is slightly higher in energy by 50 to 70 meV than the relaxed structure with one of the terrace atoms missing [10]. At the high temperatures used for film growth, it is possible that many more H bonds could be broken.

The starting configuration for the bare surface, shown at the top of Fig. 3, has bulk terminated, ideal bond lengths and angles. We allow this surface to relax using steepest descents. Upon complete relaxation at T=0 (no input of additional energy), we find that the top layer forms a graphitic-like sheet (bottom of Fig. 3). The relaxed step terrace is nearly flat and sp^2 bonded. Fig. 3 has a side view of the step, indicating the new bond lengths. The average bond length in the surface plane is 1.437$\AA$, which is close to the bond length of graphite (1.42$\AA$). With the exception of the one stretched bond of 1.62$\AA$ attached to the bottom of the step, the second layer has an average bond length of 1.50$\AA$, approximately half-way between graphite and diamond. The spacing between the first and second layer has increased to $\sim$ 2.0$\AA$. The atoms in the second layer are now essentially 3-fold coordinated since the upper bond has stretched by almost 30%, but their bonding has remained sp^3 in character. It is of interest to note that transmission electron microscopy images indicate that when diamond is heated, the graphite that appears is oriented with the c axis along the (111) direction and the a axis along the (110) direction [11].

The explanation for this relaxation is given in detail in ref. [10]. In summary, the band

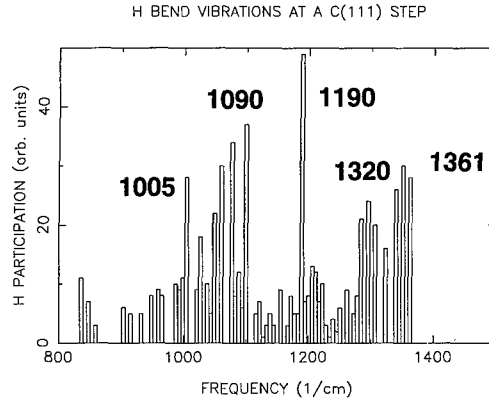

Figure 2: H bending frequencies at a step. The magnitudes of the peaks are proportional to the magnitude of the H eigenvectors of the dynamical matrix. See text for explanation of the modes.

structure energy of the surface is lowered by the second layer atoms pushing up into the surface plane. This forces an increase in splitting between the bonding and antibonding surface states and lowers the energy of the occupied levels. This phenomena is not observed on the flat C(111) surface because the cost of forming a graphite plane is an increase in the repulsion between the atoms. Having a step on the surface provides the steric freedom to overcome this cost. A Si stepped surface would not show this behavior since Si does not have as strong π bonding. New gap states appear, which are localized "surface" states in the next layer, due to the increase in spacing between the first and second layer. It is possible that the lower layer would continue to graphitize for the same physical reasons as we describe for the surface, and could be tested with a much larger unit cell.

Exposure of a (2x1) reconstructed C(111) surface to atomic H will revert the surface back to (1x1) [12, 13]. Similarly, we placed H atoms above the graphitized step approximately above the original (bulk ideal) surface bonds. This configuration was allowed to relax using steepest descents. The H bonds that formed on the terrace and steps transformed the surface back to sp^3 bonding. This result is consistent with the calculations of Mehandru *et al.* [15] who reported that the addition of H to a planar graphite cluster can cause the C atoms to buckle into chair configurations associated with sp^3 bonding. All the carbon bond lengths have returned to approximately the bulk diamond value.

ADDITION OF CH_3

Diamond growth can proceed by the addition of methyl groups to the surface. *Ab-initio* cluster calculations have been performed comparing the addition of methyl and acetylene groups on the C(111) surface [14] . Fig. 4 shows the top half of our unit cell for the relaxed configurations of a methyl group added to one of the four distinct sites near the step. The CH_3 molecules were placed on the surface so as to minimize the H-H repulsions. Of the configurations shown, the highest energy structure has the methyl group at the edge of the step (configuration *c*). Configurations *a* and *b*, with the methyl group at the top of

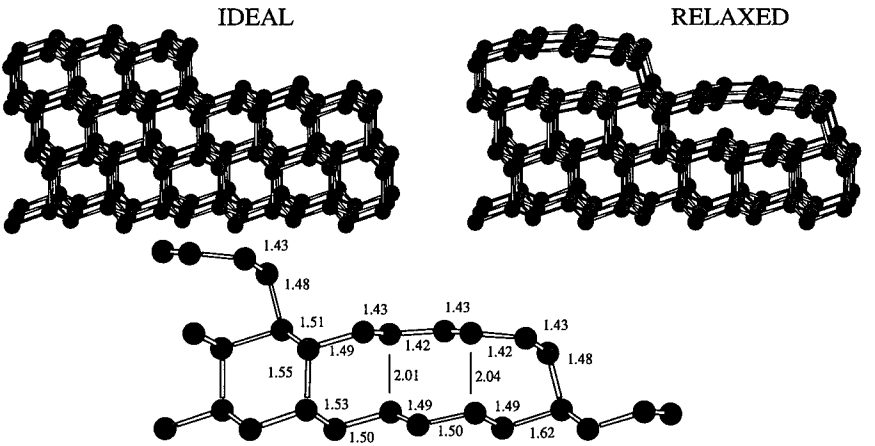

Figure 3: Graphitization of C(111) step upon relaxation. The ideal surface (top) has diamond bond lengths. The relaxed surface has surface bond lengths less than 1.45 $\AA$. Atoms are darkened to highlight the transformation of the sp^3 chair configuration into graphitic hexagons indicating sp^2 like bonding. Bottom figure is side view of the fully relaxed bare step with. bond lengths in Ångstroms.

the step, are only slightly lower in energy by 0.18 and 0.17 eV respectively as compared to configuration *c*. In these three configurations, the bond length between the methyl group and the surface carbon are $\sim$ 2% longer than the diamond bond lengths in qualitative agreement with *ab-initio* results on the C(111) flat surface [14].

The structure with the CH_3 at the bottom of the step is part of the diamond growth sequence proposed by Huang and Frenklach [5] and is significantly lower in energy than the other configurations by $\sim 2.75eV$. This unusually large decrease in energy, as compared with the other 3 structures, is driven by the lowering of the electronic energy of the H atom at the step edge. This H atom is attracted to the methyl carbon atom $\sim 1.5\AA$ away and has moved away from the step edge by 5%. We report this finding since it appears that the H atom could be pulled away from the step at finite temperatures by the methyl carbon, opening another site for additional hydrocarbons to attach, but we would emphasize that this result needs to be tested by more precise *ab-initio* methods to insure that it is not an anomaly of our C-H parameterization.

ACKNOWLEDGMENTS

The authors would like to thank Mark Pederson and Jeremy Broughton for their helpful discussions. B.N.D. acknowledges support from the National Research Council. This work was supported by Office of Naval Research Contract # N00014-93-WX-2C023.

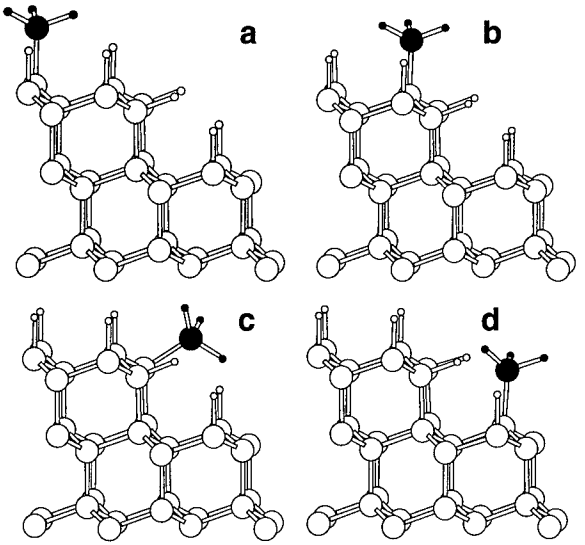

Figure 4: The relaxed positions of four possible attachments of a methyl group near a step. The atoms shown are exactly half the thickness of unit cell used in the calculation, which is periodic in two dimensions.

REFERENCES

1. Z.W. Hu, S.S. Jiang, P.Q. Huang, S.H. Li, Z.M. Zhang, C.Z. Ge, X.N. Zhao and D. Feng, J. Phys. Condens. Matt. **4**, 3753 (1992).
2. W.J.P. van Enckervort, G. Janssen, W. Vollenberg, J.J. Schermer and L.J. Giling, Diamond and Related Materials **2**, 997 (1993).
3. B. Sun, X. Zhang and Z. Lin, Phys. Rev. B **47**, 9816 (1993).
4. M. Frenklach, K.E. Spear, J. Mater. Res. **3**, 133 (1988).
5. D. Huang and M. Frenklach, J. Phys. Chem. **95**, 3692 (1991).
6. C.H. Xu, C.Z. Wang, C.T. Chan and K.M. Ho, J. Phys. Condens Matt. **4**, 6047 (1992).
7. B.N. Davidson and W.E. Pickett, to appear in Phys. Rev. B April 15 (1993).
8. M.R. Pederson and K.A. Jackson, Phys. Rev. B **41**, 7453 (1990).
9. A. V. Hamza, G. D. Kubiak and R. H. Stulen, Surf. Sci. Lett. **206**, L833 (1988).
10. B.N. Davidson and W. E. Pickett, submitted to Phys. Rev. B. (1994).
11. T. Evans and P. F. James, Proc. Roy. Soc. A **277**, 260 (1963).
12. P.G. Lurie and J.M. Wilson, Surf. Sci. **65**, 453 (1977).
13. R.P. Chin, J. Y. Huang, Y. R. Shen, T.J. Chuang, H. Seki and M. Buck, Phys. Rev. B **45**, 1522 (1992).
14. M.R. Pederson, K.A. Jackson and W.E. Pickett in New Diamond Science and Technology, edited by R. Messier, J. T. Glass, J.E. Butler and R. Roy (Mater. Res. Soc. Proc., Pittsburgh PA, 1991) pp 29-38; J.W. Mintmire, D.W. Brenner, B.I. Dunlap, R.C. Mowrey and C.T. White , ibid., pp. 57-62.
15. S.P. Mehandru, A.B. Anderson and J.C. Angus, J. Phys. Chem. **96**, 10978 (1992).

INTERACTION OF HYPERTHERMAL HYDROGEN WITH THE DIAMOND SURFACE

DAVID HAGGERTY, CHRISTOS BANDIS, AND BRADFORD B. PATE
Physics Department, Washington State University, Pullman, WA 99164

ABSTRACT

A mass-selected low kinetic energy (1-50 eV) ion source is used to expose the diamond (111) surface to ionized atomic hydrogen (H^+) at controlled impact kinetic energy. We report the result of 20 eV and 50 eV kinetic energy exposures as measured by ultraviolet photoelectron spectroscopy (UPS). UPS is found to be a useful probe of hydrogen adsorption on diamond.

INTRODUCTION

A clean diamond C(111) surface is unstable and is known to reconstruct to a surface phase in the form of Pandey's π-bonded chain structure with 2x1 symmetry,[1] whereas the hydrogen terminated surface (freshly polished or otherwise hydrogenated) is monohydride terminated[2] and shows 1x1 symmetry in its LEED pattern. In addition, the surface termination by hydrogen removes surface state emission near the valence band maximum.[1]

Hydrogen stabilization of the diamond surface against reconstruction is thought to be a key element enabling diamond growth by means of low pressure chemical vapor deposition (CVD). However, if every surface atom were terminated by hydrogen, carbon deposition (i.e. diamond growth) would be hindered due to a lack of chemically active sites. The steady state fraction of hydrogen free sites is thought to be directly related to growth rate. The production of active sites during growth is attributed to the abstraction of surface-bound hydrogen by gas-phase atomic hydrogen (activation energy ≈ 8 kcal/mole).[3] In a typical diamond CVD apparatus, chemisorption of atomic hydrogen competes with hydrogen abstraction to maintain an almost completely hydrogenated surface, with an active surface site density[4,5,6] in the range of 1-20% monolayer (ML). On the other hand, it has been found by Mitsuda and coworkers that complete reversion to the 1x1 surface phase occurs at 5% ML coverage.[7] Ancilotto and Selloni have found similar results in a first-principles molecular dynamics study of hydrogen on Si(111).[8] These results suggest that a better understanding of the mechanisms of hydrogen adsorption and abstraction that are active in the growth environment will lead to improvements in growth rates and/or film quality.

EXPERIMENT

The sample used in this study is a natural type IIb diamond,[9] polished on a cast iron scaife with diamond grit in olive oil.[1] Following the polish, the sample was ultrasonically cleaned in organic solvents and mounted in a platinum holder in the UHV analysis chamber. A chromel-alumel thermocouple, spot welded to the platinum holder near the front of the sample, was used to monitor sample temperature. During anneals, the sample was heated by direct e-beam bombardment of the rear of the platinum holder.

Mat. Res. Soc. Symp. Proc. Vol. 339. ©1994 Materials Research Society

The hydrogen beam was produced by a Colutron gun system Model G2 connected to the analysis chamber so that the source was located approximately 1 meter from the sample. The hydrogen ion beam was accelerated to 950 eV and then passed through the integral Einzel focusing lens and ExB velocity filter. After entering the analysis chamber the beam energy was reduced to the desired level using a simple two element electrostatic retarding lens and a retarding bias applied to the sample. The kinetic energy is reported as the difference between the voltages applied to the source and the sample. Typical mass-selected hydrogen ion beam currents (H^+) before the retardation stage are in the range of 100-150 nA. After the beam is retarded to 50 eV or 20 eV kinetic energy, the current drops to approximately 20-30 nA. The ultraviolet photoemission spectra (UPS) were collected using monochromatized He I light (21.2 eV) from a resonance lamp and a 100 mm radius hemispherical electron energy analyzer.

RESULTS AND DISCUSSION

The first figure shows a spectrum typical of an as-polished diamond C(111):H surface and one for the same surface after a 1000° C anneal. The spectrum for the as-polished sample shows the low kinetic energy spike characteristic of the negative electron affinity (NEA) of C(111):H. The annealed surface has positive electron affinity,[10] and its spectrum is seen to lack the low

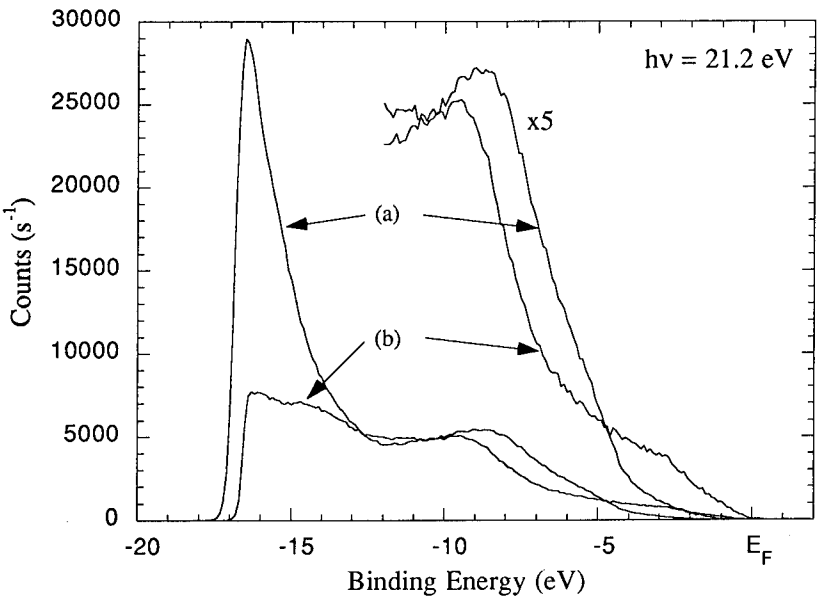

Figure 1 - UPS spectra of the diamond surface before hydrogen exposures: (a) As-polished C(111)1x1:H and (b) After anneal to T > 1000° C to remove hydrogen.

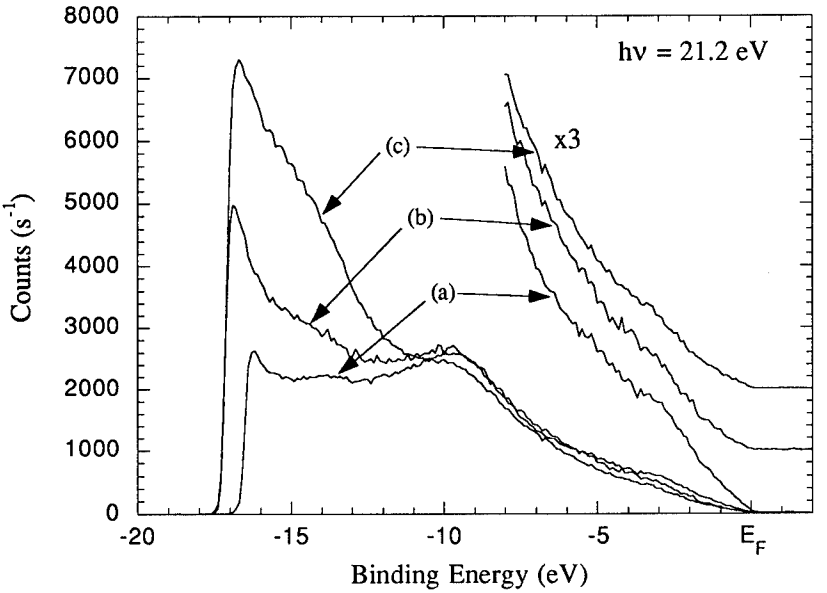

Figure 2 - UPS spectra showing the effect of hydrogen beam exposures on the annealed C(111) surface: (a) After anneal to T > 1000° C (b) After 1.5 L 50 eV H^+ exposure and (c) After subsequent 1.5 L 20 eV H^+ exposure.

kinetic energy spike. Also this spectrum shows enhanced emission 2.5 eV below the Fermi level which is attributed to surface state emission.[1] The intensity of both the surface state emission and the low kinetic energy spike can be used to determine the state of surface hydrogenation.

The second figure shows the change in the UPS when the annealed (hydrogen free) surface is exposed to low kinetic energy hydrogen. Both the 1.5 Langmuir (L) 50 eV exposure and the subsequent 1.5 L 20 eV exposure cause the spectrum to become more like the UPS spectrum of the fully hydrogenated surface; the low kinetic energy spike is emerging and the surface state emission somewhat decreases.

The third figure continues the sequence of spectra. Spectrum (a) in this figure is the spectrum of the 1.5 L, 20 eV hydrogen beam-exposed surface previously shown in figure 2. Spectrum (b) shows the change when the beam-exposed sample is subjected to an exposure of atomic hydrogen produced by the conventional hot filament technique. Hydrogen gas is leaked into the chamber to a pressure of $1x10^{-5}$ Torr and then cracked into atomic species by a tungsten filament heated to 2100° C. Spectrum (c) shows a further increase in the low kinetic energy spike and another slight decrease in the surface state emission. By comparing this spectrum to the as-polished spectrum (Figure 1) we conclude that the hot filament exposure did not fully hydrogenate the surface. In contrast, the spectrum taken after a subsequent hydrogen beam exposure (20 eV, 1.5 L) closely resembles the spectrum from the as-polished sample, and we conclude that the beam exposure has fully hydrogenated the surface.

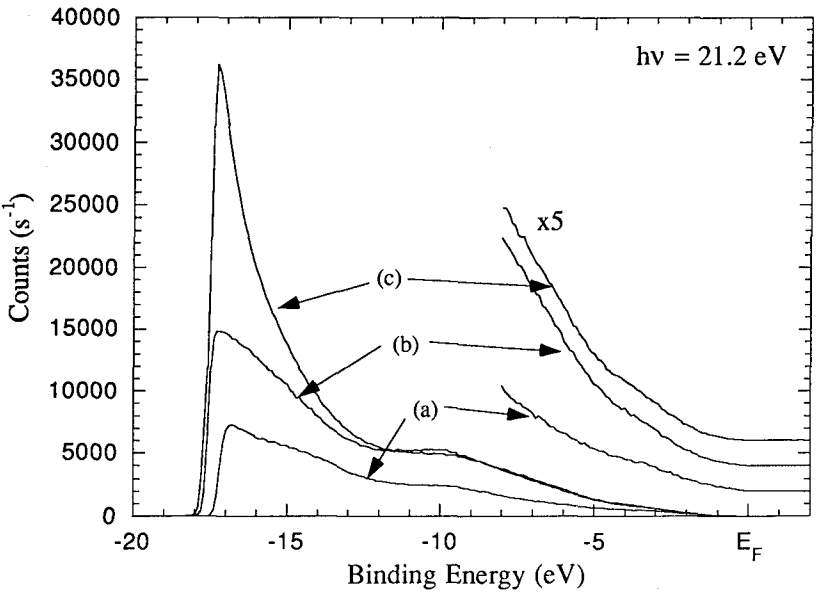

Figure 3 - UPS spectra showing the successful hydrogenation of the C(111) surface: (a) Same as Fig. 2 spectrum C (c) After hot-filament hydrogen exposure (c) After 1.5 L 20 eV H^+ exposure.

CONCLUSIONS

We have demonstrated the adsorption of hydrogen on diamond C(111) from a low kinetic energy, mass-selected ionized atomic hydrogen beam. We find that UPS is useful as a fingerprint of the hydrogen adsorption.

ACKNOWLEDGEMENTS

This work was supported in part by the National Science Foundation under grant number ECS-9222368 and by Washington State University. D.H. wishes to thank the Department of Education for fellowship support.

REFERENCES

1. B. B. Pate, Surf. Sci. **165**, 63 (1986).
2. A. V. Hamza, G. D. Kubiak, and R. H. Stulen, Surf. Sci. **206**, L833 (1988).

3. D. W. Brenner, D. H. Robertson, R. J. Carty, D. Srivastava and B. J. Garrison in Computational Methods in Material Science, edited by J. E. Mark, M. E. Glicksman and S. P. Marsh (Mater. Res. Soc. Proc. **278**, Pittsburgh, PA, 1992), pp.255-261.
4. M. Frenklach, Phys. Rev. B, **45** (16), 9455 (1992).
5. J. C. Angus, *et. al.*, Phil. Trans. R. Soc. Lond. A, **342**, 195 (1993).
6. J. E. Butler and R. L. Woodin, Phil. Trans. R. Soc. Lond. A, **342**, 209 (1993).
7. Y. Mitsuda, *et. al.*, Surf. Sci. **257**, L633 (1991).
8. F. Ancilotto and A. Selloni, Phys. Rev. Lett. **68**, 2640 (1992).
9. The single crystal sample, diamond D5, was provided on loan by Dr. F. A. Raal of the DeBeers Diamond Laboratory, Johannesburg, South Africa.
10. F. J. Himpsel, J. A. Knapp, J. A. Van Vechten and D. E. Eastman, Phys. Rev. B, **20**, 624 (1979).

EXPOSURE OF DIAMOND TO ATOMIC HYDROGEN: SECONDARY ELECTRON EMISSION AND CONDUCTIVITY EFFECTS

D.P. Malta, J.B. Posthill, T.P. Humphreys, R.E. Thomas, G.G. Fountain, R.A. Rudder, G.C. Hudson, M.J. Mantini and R.J. Markunas
Research Triangle Institute, P.O. Box 12194, Research Triangle Park, NC 27709

ABSTRACT

Secondary electron (SE) yield was enhanced by a factor of ~30 and surface conductance increased up to 10 orders of magnitude when O-terminated or non-terminated natural diamond (100) surfaces were exposed to atomic H. The SE yield from atomic H-exposed surfaces was spatially dependent on near-surface microcrystalline perfection enabling defect-contrast imaging in the conventional SE mode of the scanning electron microscope (SEM). Ultraviolet photoelectron spectroscopy (UPS) on atomic H-exposed surfaces revealed an intense low energy peak attributed to photoexcitation of secondary electrons into unoccupied hydrogen-induced states near the conduction band edge and their subsequent escape into vacuum. The low energy photoemission peak, enhanced SE yield and enhanced surface conductivity were completely removed via high temperature annealing or exposure to atomic O creating the denuded or O-terminated surfaces, respectively.

INTRODUCTION

The interaction of gas species with diamond surfaces has previously been studied in an effort to better understand diamond growth from the gas phase[ie.1]. Hydrogen and oxygen have been of particular interest since they are often used in chemical vapor deposition (CVD) diamond growth processes including recently developed water/alcohol processes[2]. In addition to the key roles H and O play as chemical reactants in the diamond growth process, studies indicate that the presence of either H or O as a surface adsorbate and/or as an absorbed species can dramatically alter the physical properties of the surface. For example, UPS studies on a C(111) surface exposed to atomic hydrogen[3] have indicated that the surface exhibited negative electron affinity (NEA) such that the vacuum energy level was positioned below the conduction band minimum. In this condition, free electrons could essentially "spill" out of the surface without an energy barrier to overcome. This situation would be favorable in applications such as cold cathode emitters where enhanced electron emission is desired provided a sufficient supply of free electrons is available. Other recent results indicate that SE emission from CVD-grown polycrystalline diamond can be reduced by annealing and suggest that the emission reduction is due to removal of hydrogen from the diamond film[4]. Others have observed higher electrical conductivity associated with the presence of hydrogen in CVD-grown polycrystalline diamond films[5].

Mat. Res. Soc. Symp. Proc. Vol. 339. ©1994 Materials Research Society

We have investigated the effects of subjecting various diamond surfaces to atomic H, atomic O and annealing on electronic structure, secondary electron yield and surface conductance. Our results show that these physical properties strongly depend on the presence or absence of H on or near the surface and, therefore, define means by which these physical properties can be controlled. We propose a mechanism based on these observations and energy band considerations.

EXPERIMENTAL

Four commercially polished, nominally (100)-oriented diamond crystals, types Ia, Ib, IIa and IIb, and a CVD-grown diamond homoepitaxial layer were examined. The homoepitaxial layer was grown on a type Ia C(100) substrate by rf-plasma-enhanced CVD using an ethanol/water process at 1Torr and 80W rf power and a sample temperature of ~600°C. All diamond surfaces were exposed to atomic H for 1 min by immersion in a H rf-plasma at 50W with a hydrogen partial pressure of 7mTorr and sample temperature of 380°C. The samples were examined by UPS to observe electronic structure, SEM for imaging and to measure secondary electron yield and two-point probe to measure surface conductance. Samples were then subjected to one of the following: (a) annealing at ~1000°C for 15 mins in ultra-high vacuum (UHV), (b) exposure to a 20%O/Ar rf-plasma at 50W and 7mTorr with a sample temperature of 380°C for 1 min or (c) immersion in hot CrO_3/H_2SO_4 for 15 min followed by boiling aqua regia for 15 min. The UPS, SEM and conductance measurements were then repeated. Transfers to the UPS chamber following rf-plasma and annealing processes were done in-vacuo via an integrated UHV transfer system.

RESULTS and DISCUSSION

UPS on the type IIb (100) diamond surface following H plasma exposure for 1 min revealed an intense low-energy emission peak. Shown in Fig. 1 are the energy distribution spectra for the H-exposed (Fig. 1a) and clean (annealed, Fig. 1b) C(100) surfaces. Spectra were recorded in the angle-integrated mode with a 21.2eV light source and an analyzer energy resolution of ~0.2eV. The presence of the low-energy emission peak has been attributed to the photoexcitation of secondary electrons into unoccupied H-induced states located near the conduction band edge. These states are believed to be created by chemisorbed H on the surface which was desorbed upon annealing at ~1000°C in UHV. Upon annealing, the low-energy emission peak was extinguished (Fig. 1b).

Observation of diamond surfaces in the SEM revealed that electron emission was greatly enhanced following H-plasma exposure relative to surfaces that have been exposed to an O-plasma, oxidizing acid or annealed.

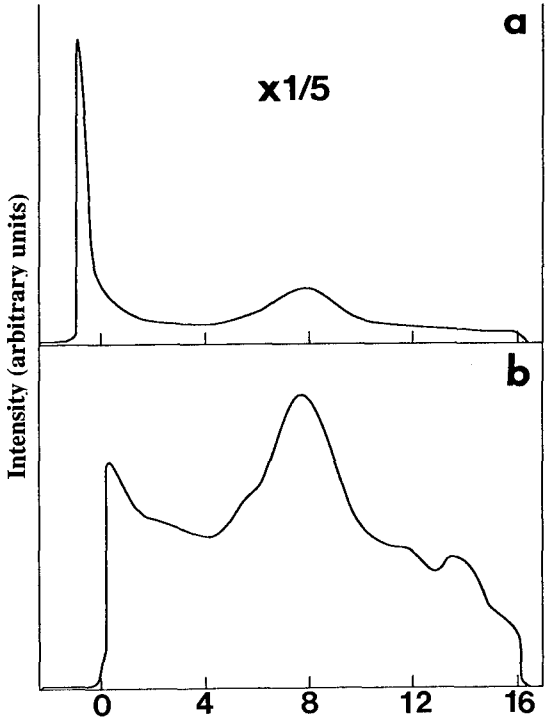

Figure 1 - Ultraviolet photoelectron emission spectra from a type IIb (100) diamond surface (a) following 1 min H plasma exposure and (b) following a 15min anneal in ultrahigh vacuum.

Comparison of backscattered electron (BSE) (high energy electrons) and secondary electron (predominantly E<50eV) images indicated that the enhancement was of the lower energy secondary electrons. The total electron yield, σ, was deduced by measuring the beam current, I_b with a Faraday cup and the specimen current, I_s, with an electrometer, and using the current balance relation:

$$I_b = \sigma I_b + I_s \quad (1)$$

where

$$\sigma = \delta + \eta \quad (2)$$

η is the BSE yield and δ is the SE yield. η is small for low atomic number materials and on the order of 0.09 for carbon at 3keV[6]. For large values of σ and assuming η didn't change upon atomic H exposure which is supported by BSE images,

$$\delta = (\sigma - \eta) \sim \sigma \text{ since } \eta << \sigma \quad (3)$$

Total electron yield (and therefore secondary electron yield) was enhanced by up to a factor of 30 upon atomic H exposure over annealed or O-treated surfaces. Enhancement was greatest on the type IIb diamond (Fig. 2) and to a lesser extent on the homoepitaxial film and nitrogen-containing types Ia and Ib crystals (not shown). σ was as high as 37.7 on one type IIb crystal after H exposure. Although the type IIa crystal showed strong enhanced emission following H exposure as evidenced by qualitative observation in the SEM, σ values measured before and after H exposure showed little change. It is believed that poor conduction through the highly insulating type IIa crystal prohibits the use of this method for deriving accurate yield measurements. The scatter observed in the upper curve is believed to be caused by some degree of charging in the semiconducting type IIb diamond. Emission enhancement was reversed by either high temperature annealing, O-plasma exposure or immersion in oxidizing acid creating either a denuded or oxygenated surface. The enhanced yield observations are consistent with UPS observations on type IIb diamonds.

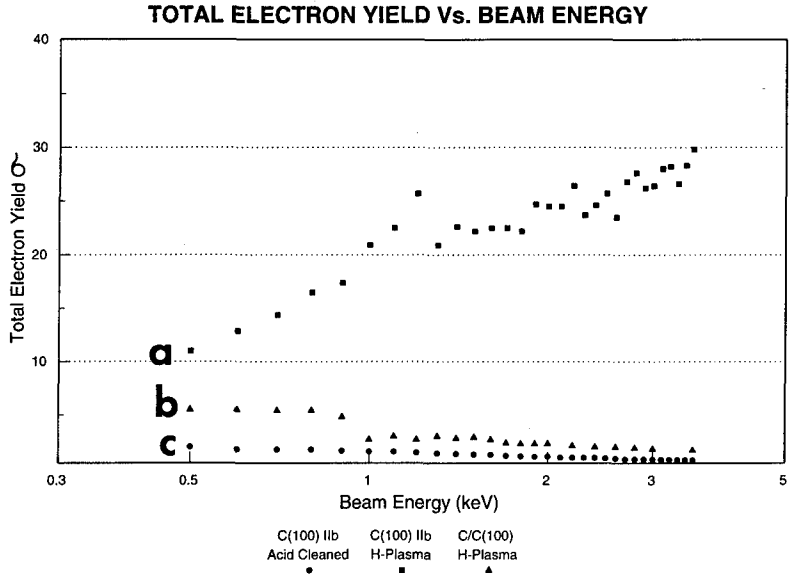

Figure 2 - Total electron yield (σ) as a function of incident electron beam energy as measured in the scanning electron microscope on (a) a H plasma-exposed type IIb (100) diamond, (b) a H plasma-exposed homoepitaxial diamond layer and (c) an acid-cleaned type IIb (100) diamond.

Surface conductance on a type IIa diamond following high temperature annealing was extremely low (<1fA at 100V) and increased 10 orders of magnitude following a 1 min H-plasma exposure (10μA at 100V) consistent with recent results obtained from polycrystalline and homoepitaxial diamond samples[5,7]. Enhancement of surface conductance is attributable to the creation of unoccupied H-induced surface states. It is hypothesized that there is a re-alignment of the surface Fermi level of the H-exposed diamond surface upon metal contact allowing tunneling of electrons from the metal into the H-induced states.

The SE yield on H-exposed diamond surfaces was found to depend on the local near-surface crystalline perfection. Imaging of these H-exposed surfaces in the conventional SE mode of the SEM resulted in large area sub-micron resolution maps of near-surface defect structures (Fig. 3). The characteristic cellular dislocation structure of the type IIb (100) crystal (Fig. 3a) had been previously observed using other techniques[8]. The defect structure of the type IIa (100) crystal consisted of an orthogonal array of rows of clustered defects (Fig. 3b). Plan view transmission electron microscopy (TEM) on a similar type IIa (100) crystal (Fig. 3c) identified the defects as dislocations and determined the row directions to be <011>. It is believed that defects lying near the surface act as trap sites for free electrons thus reducing the SE yield in their immediate vicinity thereby producing contrast in the SE image. SE imaging on annealed or atomic O-exposed surfaces shows only typical topographical polishing scratches (not shown).

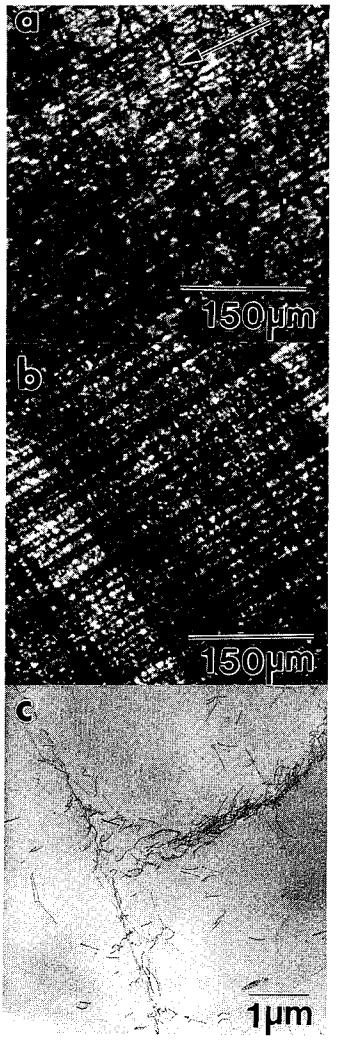

CONCLUSION

Exposure of diamond surfaces to atomic H via immersion in an rf-plasma discharge has been found to significantly alter several physical properties of the surface. In particular, secondary electron emission was enhanced by a factor of ~30 and near-surface defect imaging was possible using secondary electrons in the SEM. Surface conductance was enhanced by up to 10 orders of magnitude. The presence of a low energy emission feature in the UPS spectrum indicates the creation of H-induced states near the conduction band edge associated with H chemisorption on the surface. Removal of the H by high temperature annealing, exposure to atomic O or immersion in oxidizing acid removes the low energy UPS emission peak and reverses the secondary electron emission and surface conductance enhancement. These results have provided insight into the mechanism by which these physical properties are altered as well as means by which they can be controlled. Future work to further investigate these mechanisms will employ secondary electron emission spectroscopy and further UPS analysis.

Figure 3 - Secondary electron SEM images (a and b) and a plan-view TEM image (c) of (100) natural diamond crystals. (a) H plasma-exposed type IIb surface shows dislocations clustered into cell walls (arrow). (b) H plasma-exposed type IIa surface shows orthogonal rows of clustered defects. (c) TEM on type IIa (001) identifies defects as dislocations and determines row directions to be <011>.

ACKNOWLEDGEMENTS

The authors gratefully acknowledge the support of this work by the BMDO/IST through ONR (Contract No. N00014-92-C-0081) and we thank Dr. David C. Joy and Mr. Max N. Yoder for insightful discussions.

REFERENCES

1. R.E. Thomas, R.A. Rudder, and R.J. Markunas, J. Vac. Sci. **10**,2451(1992)
2. R.A. Rudder, G.C. Hudson, J.B. Posthill, R.E. Thomas, R.C. Hendry, D.P. Malta, R.J. Markunas, T.P. Humphreys and R.J. Nemanich, Appl. Phys. Lett. **60** 329 (1992)
3. J. van der Weide and R.J. Nemanich, Appl. Phys. Lett. **62** 1878 (1993)
4. R. Ramesham, M.F. Rose, R.F. Askew, T.L. Bekker, J.A. Dayton Jr., I.L. Krainsky, J. Mearini, L. Vanzant, D.M. File, A.S. Gilmour Jr., and V. Ayres, Surface and Coatings Technology, in press.
5. M.I. Landstrass and K.V. Ravi, Appl. Phys. Lett. **55** 975 (1989)
6. P. Palluel, Compt. Rendu, **224**, 1492 (1947)
7. H. Nakahata, T. Imai, and N. Fujimori, Proc. of the 2nd Intl. Symp. on Diam. Mat., Washington, DC, 1991 (The Electrochemical Society, Pennington, NJ), Vol. 91-8, p. 487
8. D.P. Malta, J.B. Posthill, E.A. Fitzgerald, R.A. Rudder, G.C. Hudson, and R.J Markunas, Proc. of the 3rd Intl. Symp. on Diam. Mat., Honolulu, Hawaii, 1993 (The Electrochemical Society, Pennington, NJ), Vol. 93-17, p. 647

SURFACE FERMI LEVEL POSITION OF DIAMOND TREATED WITH PLASMA

TAKASHI SUGINO, YOSHIFUMI SAKAMOTO, ATSUHIKO FURUKAWA
AND JUNJI SHIRAFUJI
Department of Electrical Engineering, Faculty of Engineering, Osaka University, 2-1 Yamadaoka, Suita, Osaka 565, Japan

ABSTRACT

The surface Fermi level position of undoped epitaxial diamond layers is estimated from contact potential difference between Au reference and diamond measured by Kelvin probe method. The surface Fermi level position of the as-grown layer is located at the energy of 0.75 eV above the valence band edge. O_2 plasma treatment leads to an upward shift of the surface Fermi level position to an energy of 1.89 eV from the valence band edge. The surface Fermi level is located at an energy of 0.97 eV above the valence band edge after H_2 plasma treatment. Reversible change in the surface Fermi level position is found between O_2 and H_2 plasma treatments. A change in the band bending is observed at the surface of polycrystalline diamond films treated with various ways by X-ray photoelectron spectroscopy (XPS) analysis. A variation in the current-voltage characteristics of epitaxial and polycrystalline diamonds treated with O_2 and H_2 plasmas can be qualitatively explained in terms of a change in the band bending due to the shift of the surface Fermi level position.

1. INTRODUCTION

There has been an increasing interest in realizing electronic devices which can be operated at high temperatures since success in synthesis of diamond films by chemical vapor deposition (CVD)[1]. This is because diamond has superior properties such as wide band gap and high thermal conductivity in addition to semiconducting property due to boron doping. Moreover, an achievement of epitaxial diamond films on diamond substrates has suggested a high potentiality of fabricating electronic devices such as field effect transistors (FET's)[2]. It is of great importance to improve not only bulk electrical characteristics but also surface properties in order to realize high device performances. The surface Fermi level position determines the electrical characteristics of semiconducting thin layer. Electrical characteristics of metal-diamond Schottky junctions and metal-insulator-diamond diodes which are necessary for FET's are also influenced by surface Fermi level pinning. It is substantial to evaluate the surface Fermi level position in order to understand those electrical properties. However, there are very few investigations on the role of the surface Fermi level of diamond.

This letter describes a variation in the surface Fermi level position of epitaxial and polycrystalline diamond films treated with various processes including annealing and plasma treatment. It is also demonstrated that the surface Fermi level position can be connected to the change in the current-voltage (I-V) characteristics due to such treatments.

2. EXPERIMENTAL

Single crystal and polycrystalline diamond films were used in the present experiment. Undoped epitaxial diamond films were grown on (100) high-pressure synthesized diamond substrates by microwave plasma-assisted chemical vapor deposition method using methane (CH_4) and H_2 mixture gas. The diamond films were 8 μm thick. The epitaxial films were used to estimate the contact potential difference by Kelvin probe method and to measure I-V characteristics. Polycrystalline diamond films were prepared on (111) p-Si (4-6 Ωcm) or Si_3N_4 ceramic substrates by hot-filament chemical vapor deposition. The mixture gas of methanol (CH_3OH) and H_2 was utilized as a source material. Boron doping was carried out by

Mat. Res. Soc. Symp. Proc. Vol. 339. ©1994 Materials Research Society

adding a proper amount of boron trioxide (B_2O_3) to methanol, by which volatile $(CH_3O)_3B$ is formed. Detailed deposition conditions have been presented elsewhere[3]. Diamond films deposited on Si substrates were used for XPS analysis. On the other hand, the electrical characteristic was measured on boron-doped diamond films deposited on insulating Si_3N_4 ceramic substrates.

As-grown epitaxial diamond films were treated with O_2 or H_2 plasma in an inductively coupled remote-plasma reactor at 13.56 MHz. The plasma chamber was evacuated to 3×10^{-6} Torr after setting the sample. The gas pressure and the rf power were regulated at 0.2 Torr and 35 W. The treatment temperature was 368 K. In the case of polycrystalline diamond films, on the other hand, the as-deposited films were annealed at 873 K for 60 min in the flowing N_2 gas prior to the plasma treatment. This process was necessary because of unstable electrical properties of as-deposited polycrystalline films as have been observed in the measurement of the temperature dependence of the electrical conductance[4]. After the preannealing, O_2 or H_2 remote plasma treatment was carried out at 0.5 Torr, 50 W and 370 K. The treatment time was 10 min.

The Kelvin probe method was used to measure the contact potential difference (CPD) between an Au probe and the diamond surface. The probe was vibrated at 200 Hz. The CPD signal was measured by a lock-in detection technique. If we assume the work function of Au, ϕ_M(Au), and the electron affinity of diamond, χ(dia) to be 5.1 and 2.3 eV, respectively[5,6], the surface Fermi level position, E_f-E_v, with respect to the valence band edge can be estimated from the relationship

$$E_f-E_v=E_g(\text{dia})+\chi(\text{dia})-\phi_M(\text{Au})-\text{CPD} \qquad (1)$$

It should be noted here that CPD includes a variation in the work function due to adatom-induced surface dipole.

XPS analysis was performed on polycrystalline diamond films deposited on Si in order to study chemical bond scheme of carbon atoms at the surface and surface band bending.

Ti ohmic contacts were provided on the epitaxial diamond films by electron beam evaporation. The current-voltage characteristics were measured for the coplanar samples, the surface of which was treated with plasma.

3. RESULTS AND DISCUSSION

Figure 1 shows the variation in the surface Fermi level position (E_f-E_v) of an epitaxial film with various treatments. An as-grown sample was treated with O_2, H_2, and O_2 plasmas in sequence. Kelvin probe measurement was carried out every each plasma treatment. The measurement error was ±0.05 eV. The surface Fermi level is located around 0.75 eV above the valence band edge in the as-grown sample. After O_2 plasma treatment, the surface Fermi level moves upward to 1.89 eV above the valence band edge. When the sample is subsequently treated with H_2 plasma after the O_2 plasma treatment, the surface Fermi level shifts back to the valence band and is located at E_v + 0.97 eV. The second round of the O_2 plasma treatment allows to locate the surface Fermi level at 1.54

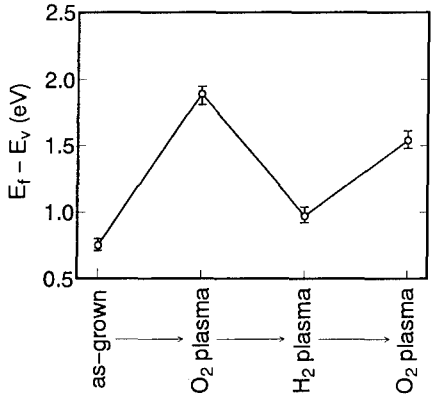

Fig.1. Surface Fermi level position of epitaxial diamond layers treated in sequence with plasma.

eV above the valence band edge. Thus it seems that the change in the surface Fermi level position is reversible between O_2 and H_2 plasma treatments. The incomplete recovery of the surface Fermi level position seen in Fig.1 is possibly due to shortage of the treatment time.

Surface analysis of polycrystalline films was performed by XPS measurement since Kelvin probe measurement was useless due to differently oriented facets. The C_{1s} core level spectra measured every 0.1 min during Ar ion etching for the undoped diamond films treated with O_2 or H_2 plasma after annealing are shown in Fig.2. The binding energies of the main peak are 286.9 and 285.8 eV at the surfaces treated with O_2 and H_2 plasma after annealing, respectively. On the other hand, the peak energy is shifted to 284.4 eV when both samples treated with O_2 and H_2 plasmas suffer Ar ion etching for 0.4 min. As Mg K_α (1253.6 eV) line was used as an excitation X-ray, C_{1s} photoelectrons excited in the region about 2 nm deep from the surface can be detected for the escape angle of 90°. This shift of the binding energy means that the surface Fermi level position of the sample treated with O_2 or H_2 plasma is different from that of the Ar ion etched sample, resulting in the different band bending. The band bending of the samples treated with various ways can be estimated in comparison with that of the Ar ion etched sample as a reference.

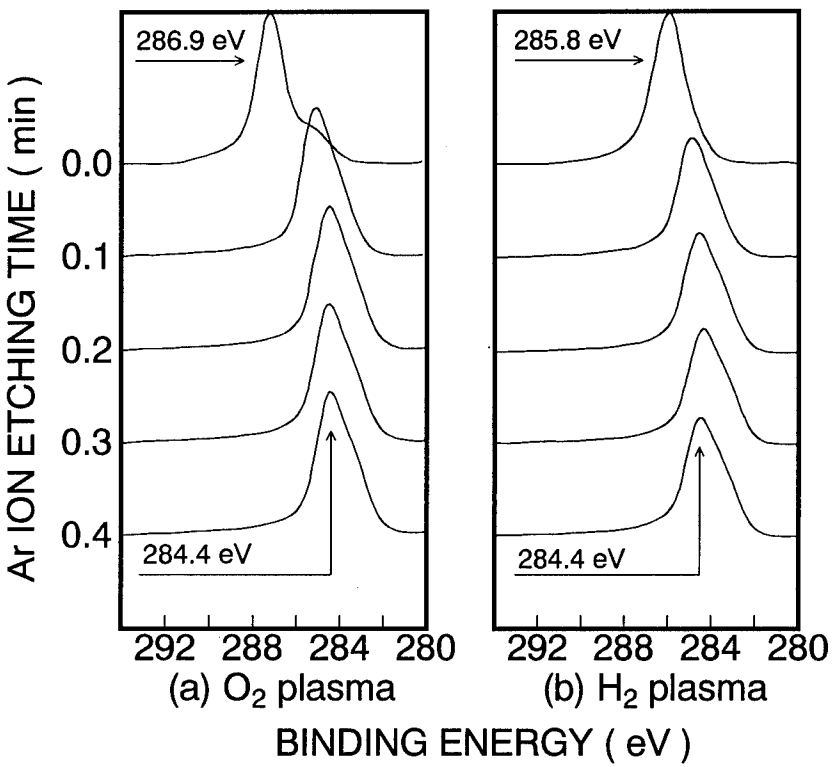

Fig.2. XPS spectra from C_{1s} core level of (a) O_2- and (b) H_2-plasma-treated samples. XPS measurement was carried out after Ar ion etching of 0, 0.1, 0.2, 0.3 and 0.4 min.

Figure 3 indicates the change in the band bending caused by various treatments with reference to that of Ar ion etched sample. The surface Fermi level position is not estimated yet for Ar ion etched diamond films. The surface Fermi level of the preannealed sample moves away from the valence band edge in comparison with the case of as-deposited one. When additionally treated with H_2 plasma after preannealing, the surface Fermi level sits between those of the as-deposited and preannealed samples. There is no difference of the surface Fermi level position between the preannealed and O_2-plasma-treated samples. It is noted that the behavior of the surface Fermi level with O_2 and H_2 plasma treatments is qualitatively the same between polycrystalline and epitaxial films. The surface Fermi level of boron-doped diamond films varied similar to those shown in Figs.2 and 3.

Figure 4 indicates the I-V characteristics of the epitaxial diamond films treated with O_2 and H_2 plasmas in comparison with that of the as-grown one. The conduction is ohmic in the voltage range from 10^{-2} to 10 V. A remarkable variation in the I-V characteristics after these treatments is possibly due to chemisorption of hydrogen or oxygen atoms rather than diffusion of these atoms into the layer, because the plasma process is carried out at a temperature as low as 368 K and a short treatment time of 10 min. In other words, no variation in the resistance occurs due to hydrogen passivation of traps in the film[7]. The values of the resistance are estimated to be 2.9 x 10^2, 3.3 x 10^4 and 1.7 x 10^3 Ω, respectively, for the samples as-grown, treated with O_2 plasma and treated with H_2 plasma subsequently after O_2 plasma treatment.

The variation in the I-V characteristics with plasma treatments indicated in Fig.4 can be discussed in relation to the results of surface analysis. The electrical resistance is increased by O_2 plasma treatment in comparison with that of the as-grown sample. O_2 plasma has been used as an efficient reactive ion etching process for diamond films[8]. A simple inspection showed that no significant variation in the thickness of the diamond film was found after O_2 plasma treatment for 10 min. The resistance increase caused by O_2 plasma treatment in Fig.4 is not associated with a decrease in the geometry of the sample. Another candidate for explaining the results of Fig.4 is a contribution of graphite phase. Graphite phase at the surface can be electrically conductive. However, the XPS analysis demonstrated that there existed no graphite phase at the surface of the as-deposited and O_2 plasma treated polycrystalline diamond films.

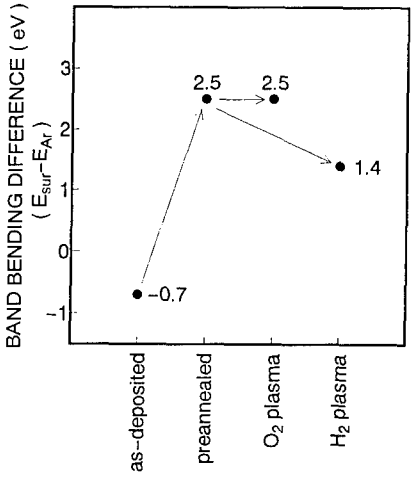

Fig.3. Difference of band bending from that of Ar ion etched sample.

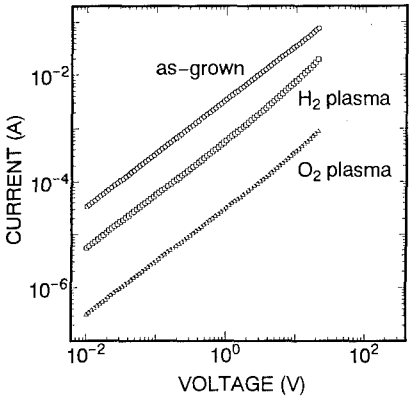

Fig.4. Room temperature I-V characteristics of epitaxial diamond layers as-grown, treated with O_2 plasma and treated with H_2 plasma after O_2 plasma treatement.

Most plausible effect which gives a direct influence on the surface electrical conduction is surface band bending due to the plasma treatment as obtained by Kelvin probe measurement. The surface Fermi level position is located at 0.75, 1.89 and 0.97 eV above the valence band edge for the samples as-grown, treated with O_2 plasma and treated with H_2 plasma after O_2 plasma treatment, respectively. The change in the I-V characteristics can be explained qualitatively by the surface Fermi level position even though other properties of the diamond epitaxial layer are not known. In the case that the bulk Fermi level position is not changed by plasma treatment, the hole concentration in the surface region where the surface band bending occurs as shown in Fig.5 reduces with increasing value of E_f-E_v, resulting in an increase of the surface resistance. The value of E_f-E_v for the O_2-plasma-treated sample increases in comparison with that of as-grown one. This means an increase of the resistance in the surface region of the O_2-plasma-treated sample. In the case when H_2 plasma treatment is carried out after O_2 plasma treatment, on the other hand, the surface Fermi level position comes between two values of the as-grown and the O_2-plasma-treated samples in the present experiment. The I-V characteristic of the H_2-plasma-treated sample can be explained consistently due to the surface resistance, the value of which is between those of the as-grown and the O_2-plasma-treated samples. A variation in the resistance between O_2- and H_2-plasma-treated polycrystalline films can be also explained by the band bending.

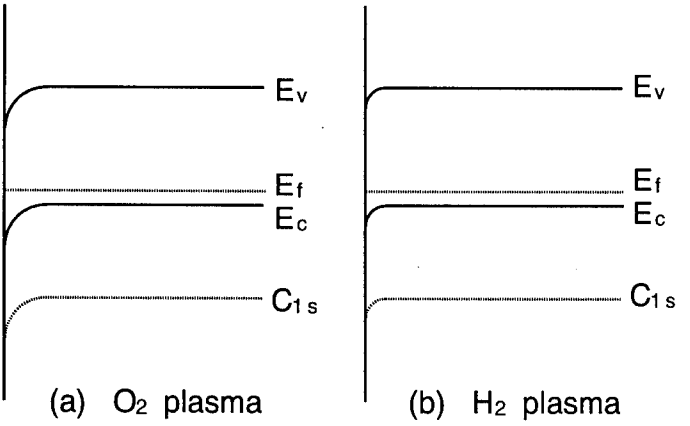

Fig.5. Band diagrams of (a) O_2-plasma-treated and (b) H_2-plasma-treated samples.

4. SUMMARY

It is observed for the epitaxial and polycrystalline diamond films that the surface Fermi level position shifts far away from the valence band edge due to O_2 plasma treatment in comparison with that due to H_2 plasma treatment. I-V characteristics have been measured for the epitaxial diamond films treated with O_2 and H_2 plasmas. A variation in the resistance can be explained by a change of the band bending.

ACKNOWLEDGMENTS

The authors are much indebted to Mr. N. Fujimori, Mr. S. Shikata, and Dr. Y. Nishibayashi of Sumitomo Electric Industries, Inc. for supplying epitaxial diamond films and to Dr. K. Kobashi and Mr. K. Nishimura of Kobe Steel, Ltd. for supplying Si_3N_4 substrates.

REFERENCES

1. B.V.Spitsyn, L.L.Bouilov and B.V.Derjaguin, J. Cryst. Growth **52**, 219 (1981).
2. H.Shiomi, Y.Nishibayashi and N.Fujimori, Jpn. J. Appl. Phys. **28**, L2153 (1989).
3. T.Sugino, K.Karasutani, F.Mano, H.Kataoka, J.Shirafuji and K.Kobashi, Diamond and Related Materials to be published.
4. Y.Muto, T.Sugino, K.Kobashi and J.Shirafuji, Appl. Phys.Lett. **59**, 843 (1991).
5. H.B.Michaelson, J. Appl. Phys. **48**, 4729 (1977).
6. M.W.Geis, J.A.Gregory and B.B.Pate, IEEE Trans. Electron Devices **36**, 619 (1991).
7. M.I.Landstrass and K.V.Ravi, Appl. Phys. Lett. **55**, 975 (1989).
8. P.D.DeGraff and D.C.Flanders, J. Vac. Sci. Technol. **16**, 1906 (1979).

SURFACE PREPARATION OF SINGLE CRYSTAL C(001) SUBSTRATES FOR HOMOEPITAXIAL DIAMOND GROWTH

T.P. HUMPHREYS, J.B. POSTHILL, D.P. MALTA, R.E. THOMAS, R.A. RUDDER, G.C. HUDSON AND R.J. MARKUNAS

Research Triangle Institute, Research Triangle Park, North Carolina 27709-2194

ABSRACT

A novel substrate preparation procedure which can be employed to remove the original surface from as-received C(001) natural diamond substrates has been developed. A description of the various substrate processing steps which includes, low-energy ion implantation of C and O, high-temperature annealing, electrochemical etching and surface plasmas treatments is presented. Also demonstrated is the growth of topographically excellent homoepitaxial films by rf-plasma-enhanced chemical vapor deposition using water/ethanol mixtures on C(001) substrates.

INTRODUCTION

Semiconducting homoepitaxial diamond films are being considered for the construction of electronic devices which can operate at high-temperature and in high radiation environments. At present, the growth of single crystal diamond films with smooth topographies and low defect densities depends largely upon the commercial availability of suitable single crystal substrates For-instance, some previous attempts to grow homoepitaxial diamond layers on various chemically prepared C(001) substrates have resulted in surface morphologies which are not ideal [e.g.,1,2]. It is thought to be desirable to upgrade the surface quality of the diamond substrates prior to homoepitaxial growth. In an attempt to address this issue, we have developed a novel substrate preparation procedure in which we can effectively remove the surface and near-surface diamond layer associated with the original as-received surface. We have simultaneously undertaken to establish rigorous diamond growth protocols so as to best test our diamond substrate preparation methods. In this paper we present a detailed account of the various processing steps and techniques that have been used to modify the diamond surface. An assessment of the substrate surface quality includes an investigation of the grown homoepitaxial diamond films using water/alcohol mixtures on appropriately prepared substrates. For comparison, corresponding epitaxial films have also been grown on as-received C(001) substrates.

EXPERIMENTAL PROCEDURE

Specific low-energy implants of C and O ions at room temperature have been used to amorphize the near-surface region of several low-defect density C(001) high resistivity type Ia (2mm x 2mm) natural diamond substrates. Type Ia crystals were chosen primarily because they have been shown to have lower dislocation densities than type II diamonds [3,4,5]. A summary of the corresponding ion-implantation conditions are presented in Table I. Both single and double

Mat. Res. Soc. Symp. Proc. Vol. 339. ©1994 Materials Research Society

implants of C and O ions with energies of 70 keV and 180 keV and a fluence of 5E16 ions-cm^{-2} have been employed in this study. Two distinct implant energies were selected such that the position of the implant damage peak could be varied, thereby controlling the thickness of diamond removed.

Table I. Ion implantation conditions and corresponding diamond thicknesses removed upon annealing and EC etching.

SAMPLE NUMBER	ION SPECIES	IMPLANT ENERGY (keV)	ION DOSE (ions/cm^2)	DIAMOND LAYER THICKNESS REMOVED UPON ANNEALING AND EC ETCHING (nm)
K1	C	70	5E16	130
K2	C	180	5E16	190
K3	C	70 + 180	5E16 + 5E16	250
K4	O	70	5E16	115
K5	O	180	5E16	119
K6	O	70 + 180	5E16 + 5E16	220

Following implantation, the crystals were subsequently annealed for 1 hour at 1000 ^{o}C in flowing N_2 to graphitize the implanted layer. Both Raman spectroscopy and current-voltage (I-V) techniques were employed to characterize the diamond surface following the high-temperature annealing step. In particular, an inspection of the corresponding Raman spectrum showed the presence of two prominent spectral features at 1332 cm^{-1} and 1580 cm^{-1} indicative of graphite formation. In addition, a significant reduction in the surface resistivity of the diamond surface was also measured upon I-V probing of the newly formed non-diamond layer. For-instance, typical surface resistivity values of 10^4 - 10^5 Ω m^{-1} were routinely measured for the graphitized layer compared to 10^{17} - 10^{20} Ω m^{-1} for the untreated surfaces [6,7]. In order to remove the graphitized layer a contactless electrochemical (EC) etching technique was utilized [8]. EC etching was performed by placing the diamond crystal in deionized water between two Pt electrodes at a potential of typically 200V - 400 V. After etching for a period of typically 24 - 36 hrs, the crystals became optically transparent from visual inspection. Further I-V measurements and Raman analysis confirmed the removal of the graphite layer with an appropriate increase in the surface resistivity, typically 10 ^{12} -10 ^{14} Ω m^{-1}, and the observation of the 1332 cm^{-1} phonon peak of diamond in the Raman spectrum. Prior to homoepitaxial growth, the EC etched surfaces were exposed to consecutive Ar/20% O_2 and H_2 plasmas treatments of 50 W power at a pressure of 7 x 10^{-3} Torr and a substrate temperature of 380^{o}C.

Each processing step was monitored using scanning electron microscopy (SEM), atomic force microscopy (AFM) and low-energy electron diffraction (LEED) techniques. Homoepitaxial films were subsequently grown on the prepared substrates by rf-plasma enhanced chemical vapor deposition (CVD) using water/ethanol mixtures similar to that described previously [9]. The

growth rate is typically 0.5 μm-hr^{-1} at a pressure of 1 Torr and a substrate temperature of ~600°C. Corresponding flow rates for water and ethanol are 12 sccm and 18 sccm, respectively.

RESULTS AND DISCUSSION

Illustrated in Fig. 1(a) is the surface morphology of the O ion, 70 keV energy implanted substrate (sample No. K4) following annealing and subsequent EC etching. For comparison, the micrograph also shows a non-implanted ('clip') region of this substrate which was masked during ion implantation. Since this region was unaffected by EC etching, a distinct step exists whose height indicates the depth of diamond removed upon processing. From stylus profilometer measurements, a step height of ~115 nm was recorded The respective diamond layer thicknesses that have been successfully removed from each of the ion-implanted samples are compiled in Table I. Clearly, the EC etched surface still exhibits a degree of surface roughness. Further examination of the EC etched surface by AFM showed the presence of etch pits and striations of the order of ~50 nm rms which appeared to mimic the surface topography of the as-received crystal. Indeed, similar surface topographies have also been observed for each of the implanted crystals.

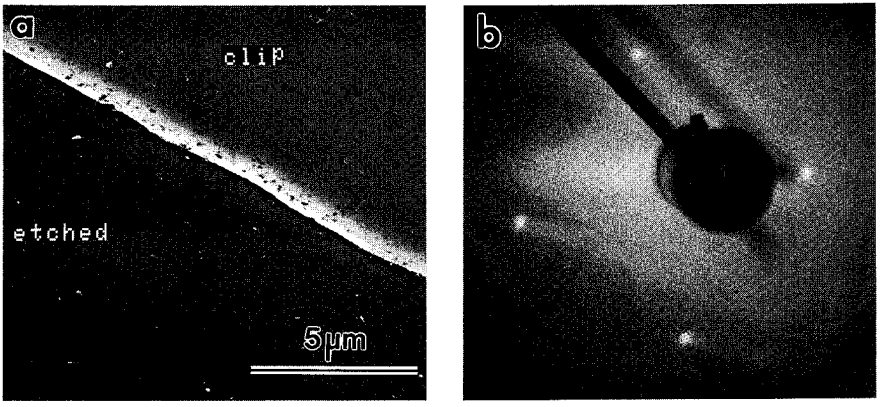

Fig. 1(a) Typical substrate surface morphology following ion implantation, annealing and EC etching (sample No. K1), (b) (1x1) LEED pattern following consecutive Ar/20%O_2 and H_2 plasma treatments for 75 mins and 5 mins, respectively.

Most apparent was the absence of a LEED pattern following EC etching. It is suggested that ion-straddling damage from the tail of the implanted region which cannot be removed upon EC etching is responsible for the surface disorder. However, by exposing the EC etched surfaces to an Ar/20%O_2 plasma for typically 75 - 90 mins duration and a consecutive 5 mins H_2 plasma exposure, the surface crystallinity can be restored as evidenced by the presence of a sharp (1x1) LEED pattern shown in Fig 1 (b). Clearly, the diamond surface is aggressively etched by the Ar/20%O_2 plasma which subsequently removes the remaining non-diamond layer. The short H_2 plasma exposure is primarily employed to make the surface of the diamond more conductive, thereby preventing charging during LEED analysis [7].

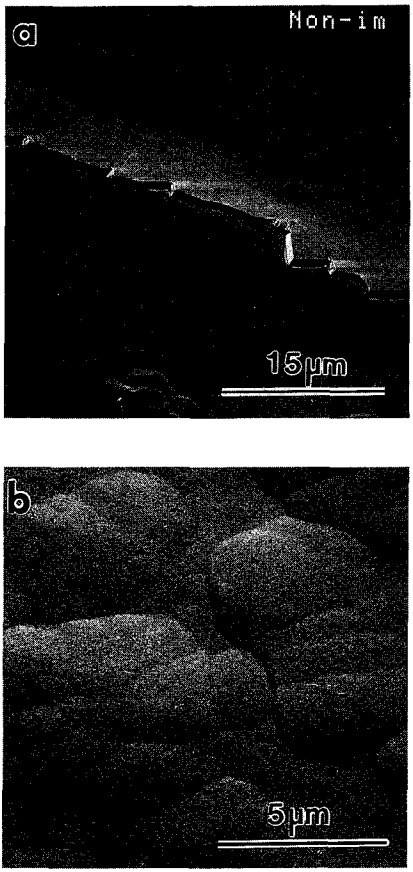

Homoepitaxial diamond films of different thicknesses were deposited on each of the processed samples. A representative example of the epilayer surface morphology that has been routinely observed for each crystal is shown in Fig. 2. Clearly evident is a degree of surface roughness which is associated with the presence of flat-top, crystallographically-oriented hillocks that are ~5µm in lateral size. These features are quite distinct from the pyramid-like hillocks observed in some previous studies [1,2]. In comparison, these morphological features are apparently absent from the untreated or non-implanted surfaces where the epitaxial layer appears to be smoother. However, as illustrated in Fig 2(c), by continuing the growth sequence for an additional 48 hrs (total epilayer thickness ~26um), the flat hillock growth features appear to coalesce resulting in a smooth surface morphology. The observed morphological growth features may be attributed to the nucleation on residual impurities that results from implantation. It is not currently known how these flat hillocks relate to the microstructure of the diamond epilayer, and it is possible that they are benign.

Fig. 2 SEM micrograph of a homoepitaxial diamond layer grown on sample No. K6: (a) Epilayer of ~2µm thickness showing corresponding morphologies on both the processed and untreated surfaces, (b) processed surface only, and (c) following ~26µm of growth.

For comparison, epitaxial diamond films have be grown on as-received untreated C(001) substrates. Shown in Fig. 3 is the smooth surface morphology obtained after ~0.5μm of growth as well as after ~10μm growth. We have observed smooth diamond homoepitaxial topographies after 50+μm of growth.

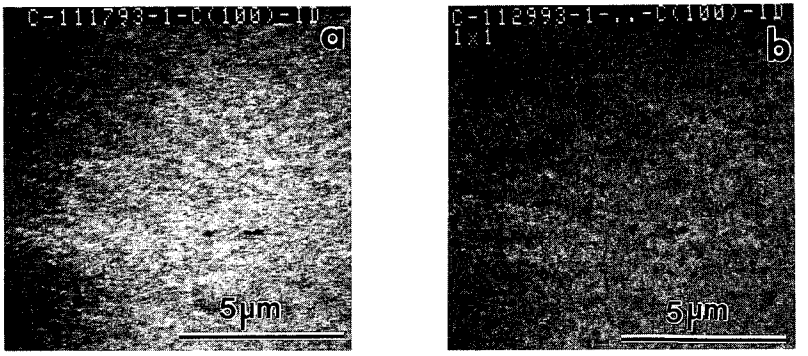

Fig. 3 SEM topographical image of a diamond homoepitaxial film grown on an as-received C(001) substrates with epilayer thicknesses of (a) ~0.5 μm and (b) ~10 μm, respectively

CONCLUSIONS

We have demonstrated that our low-temperature, water/ethanol diamond homoepitaxial growth process requires minimal substrate preparation to achieve excellent surface topographies. Additionally, we have shown how to damage, remove, and recover a single crystal diamond surface which will be suitable for homoepitaxy. This could be an important process for diamond single crystal recycling or for manufacture of well-controlled step heights. The presence of flat hillocks on such a grown surface is, however, still an issue that requires resolution. Nevertheless, the planarizing effect of extended diamond homoepitaxial growth does eliminate these hillocks.

ACKNOWLEDGEMENT

The authors gratefully acknowledge support of this work by BMDO/IST through ONR (Contract No. N00014-92-C-0081).

REFERENCES

1. W.J.P. van Enckevort, G. Janssen, W. Vollenberg, M. Chermin, L.J. Giling, and M. Seal, Surf. and Coating Tech., 47, 39 (1991).

2. J.B. Posthill, D.P. Malta, R.A. Rudder, G.C. Hudson, R.E. Thomas, R.J. Markunas, T.P. Humphreys, R.J. Nemanich, Proc. 3rd Inter. Symp. on Diamond Materials, The Electrochemical Society, 93-17, 303 (1991).

3. T. Evans and C. Phaal, Proc. Royal Society of London A, 270, 538 (1963).

4. J.B. Posthill, T. George, D.P. Malta, T.P. Humphreys, R.A. Rudder, G.C. Hudson, R.E. Thomas and R.J. Markunas, Proc. 51st Ann. Meet. Electron Microsc. Soc. of America, 1196 (1993).

5. J.B. Posthill, R.A. Rudder, G.C. Hudson, D.P. Malta, G.G. Fountain, R.E. Thomas, R.J. Markunas, T.P. Humphreys, R.J. Nemanich and D.R. Black, Proc. 2nd Inter. Symp. on Diamond Materials, The Electrochemical Society, 91-8, 274 (1991).

6. M.I. Landstrass and K.V. Ravi, Appl. Phys. Lett., 55, 975 (1989).

7. D.P. Malta, J.B. Posthill, R.E. Thomas, G.G. Fountain, R.A. Rudder, G.C. Hudson, M.J. Mantini, R.J. Markunas and T.P. Humphreys, this proceedings.

8. M. Marchywka, P.E. Pehrsson, S.C. Binari and D. Moses, J. Electrochemical Soc., 140, L19 (1993).

9. R.A. Rudder, G.C. Hudson, J.B. Posthill, R.E. Thomas, R.C. Hendry, D.P. Malta, R.J. Markunas, T.P. Humphreys and R.J. Nemanich, Appl. Phys. Lett., 60, 329 (1992).

THEORETICAL STUDIES OF C(100) SURFACE RECONSTRUCTION AND REACTION WITH CH_2

Z. JING,* AND J. L. WHITTEN**

*Department of Physics, Box 8202, North Carolina State University, Raleigh, NC, 27695.

**Department of Chemistry, Box 8201, North Carolina State University, Raleigh, NC, 27695.

ABSTRACT

The reconstruction of the C(100) surface and its reaction with CH_2 are studied by a cluster model at several theoretical levels [1-13]. For the reconstruction of the C(100) surface, the calculated surface dimer bond length is found to be very sensitive to the level of theoretical treatment and the spin state. A single-determinant SCF treatment gives a closed-shell singlet state, higher in energy than the triplet state, and with a dimer length of 1.401 Å, 0.279 Å shorter than the triplet. The correct ground state is a singlet, but a multi-determinant wavefunction is required for its description. At the CI level, the surface dimer bond length in the ground state is found to be 1.508 Å and the energy decrease on dimer formation with respect to the ideal C(100)-1×1 surface is 2.28 eV per dimer. For the reaction of CH_2 with C(100), no barrier is found for the chemisorption of CH_2 on the surface and the reaction is highly exothermic. The surface is converted from C(100)-2x1 to C(100)-1x1 upon CH_2 chemisorption.

1. INTRODUCTION

The openness of the ideal C(100) surface and the nature of its surface sites would make this a preferred surface for diamond film growth. However, the ideal 1x1 surface readily undergoes reconstruction to form a dimerized C(100)-2x1 structure. This dimerized surface can readily add one hydrogen per carbon, but unlike Si(100), the distance between adjacent carbon atoms on the surface is too short to accommodate two additional hydrogens. The dimerized surface apparently does not readily add carbon from hydrogen rich CVD processes, for example, from typical sources containing 95% hydrogen and 5% methane. Dosing the C(100)-2x1 surface with oxygen has been investigated as a means of preventing surface dimerization in order to achieve low temperature epitaxial growth of diamond.

It is important to determine whether there are fundamental energy barriers to the reaction of CH_x species with C(100)-2x1 or whether difficulties in the growth of films of high quality are due to other factors. In this paper, we consider the reaction of CH_2 with the C(100)-2x1 surface and calculate from first-principles quantum mechanics the energetics of the adsorption process and determine whether energy barriers exist.

Although LEED experiments have shown dimer formation on the clean C(100) surface, questions regarding the details of the dimerization remain to be answered [14-17], e.g., the C-C dimer bond length and whether the dimer is symmetric or asymmetric. Several theoretical calculations on the C(100) surface reconstruction have been carried out [18-30]. The results vary considerably, with calculated dimer bond lengths ranging from 1.38 Å to 1.67 Å and calculated dimer bond energies from 0.82 eV to 7.86 eV. It would be desirable to carry out *ab initio* calculations, treating the electron correlation properly, on the surface reconstruction of the C(100) surface. The present study describes the C(100) surface by a cluster model and treats the system using self-consistent-field (SCF) and configuration interaction (CI) methods.

The paper is organized as follows. Section 2 gives a brief review of the general theory. Section 3 and 4 report the results of C(100) surface reconstruction and its reaction with CH_2, respectively, and Section 5 summarizes the conclusions.

Mat. Res. Soc. Symp. Proc. Vol. 339. ©1994 Materials Research Society

2. THEORY AND COMPUTATIONAL METHOD

In this work, calculations are carried out for the full electrostatic Hamiltonian of the system, with wavefunctions constructed by SCF and CI expansions. There are no empirical parameters in all calculations.

For N electrons, Q nuclei

$$H = \Sigma_i^N -1/2\,\nabla_i^2 \quad + \quad \Sigma_i^N \Sigma_k^Q -Z_k/r_{ki} \quad + \quad \Sigma_{i\,j}^N \; 1/r_{ij}$$

SCF and CI calculations are performed. CI wavefunctions are generated from an initial SCF configuration, or from multiple parent configurations in the case of stretched or broken bonds, by one- and two-particle excitations from the main components of the wavefunction to give expansions of the form

$$\Psi = \Sigma_k \lambda_k A(x_1^k x_2^k \cdots x_n^k)$$

In the latter treatment, the objective is to treat the surface region with sufficient accuracy to describe bond formation, while at the same time coupling the surface region to the bulk lattice. In the CI calculations, the occupied and virtual orbitals of the SCF solution are transformed separately to obtain orbitals with varying degrees of localization about the surface carbon atoms undergoing dimerization. This unitary transformation of orbitals which is based upon exchange maximization with the valence orbitals of atoms in the dimer region of the cluster enhances convergence of the configuration interaction (CI) expansion. In the CI expansion, all configurations arising from single and double excitations with an interaction energy greater than 2×10^{-6} Hartree with the parent configuration are explicitly retained; contributions of excluded configurations are estimated using second-order perturbation theory. Details of the theory have been reported elsewhere [31-33].

3. RECONSTRUCTION OF THE C(100) SURFACE

The cluster $C_{12}H_{20}$, shown in Fig. 1, is used to model the C(100) surface and is studied by the SCF and multi-parent configuration interaction method using orbital localization. In the calculations, all atoms beneath the first layer are fixed which leaves only one variable, the C_1-C_3 rotation angle α. Unless mentioned explicitly, the C_1-C_3 bond length is fixed at the constant value of 1.544 Å, the nearest neighbor C-C bulk distance.

The cluster is first treated at the SCF level. The energy change on reconstruction, as a

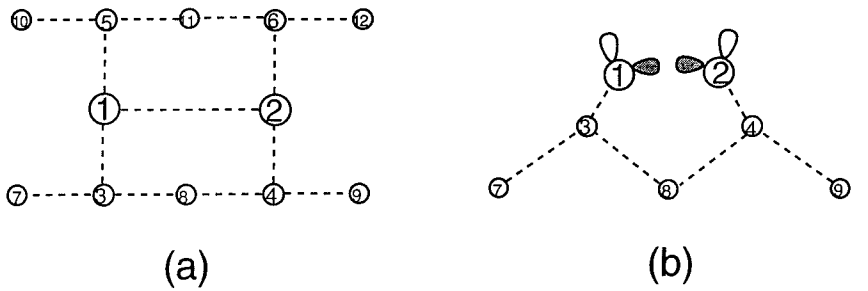

Fig. 1a,b Top and side views the C_9H_{12} cluster. All the peripheral dangling bonds of the boundary atoms are saturated by H atoms (not shown in the figures).

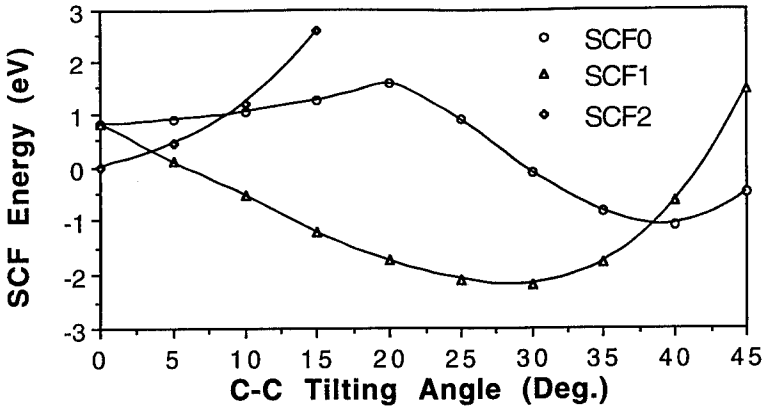

Fig. 2 The SCF energies as a function of α and spin states. SCF0, SCF1 and SCF2 represent the SCF energies for the spin states S=0, 1 and 2, respectively.

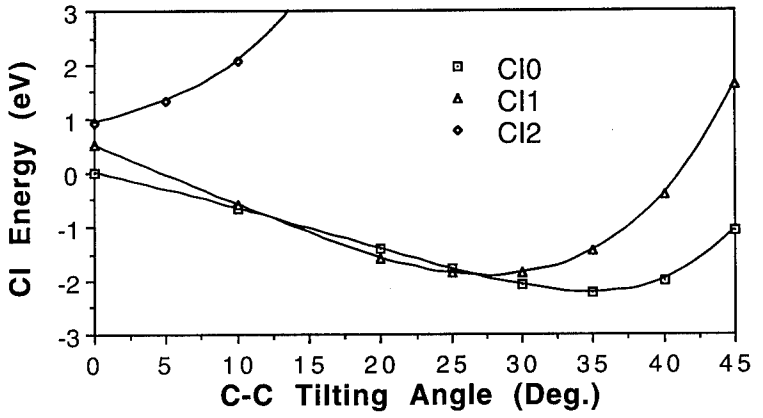

Fig. 3 The CI energies as a function of α and spin states. CI0, CI1 and CI2 represent the CI energies for the spin states S=0, 1 and 2, respectively.

function of the angle of rotation about the second layer atoms, α, is shown in Fig. 2 for three spin states, S=0, S=1 and S=2, of the pair of carbon atoms C_1 - C_2. For the ideal, unreconstructed C(100)-1x1 surface where $\alpha=0$, the lowest energy is that of the high spin state S=2. The singlet and triplet states are 0.78 eV and 0.81 eV higher in energy than the high spin state S=2 at the SCF level. In the calculation of a dimer bond energy, the lowest energy at $\alpha=0$ is taken as the reference. Because of the number of broken bonds and the interaction of the dangling bond orbitals at $\alpha=0$, the SCF treatments are not expected to produce accurate energies, but these values are interesting to compare with the CI results.

When α increases, the energy of the singlet state S=0, as shown in Fig. 2, increases at first and then decreases to a minimum at $\alpha=39.0°$. The corresponding dimer bond length is 1.401 Å.

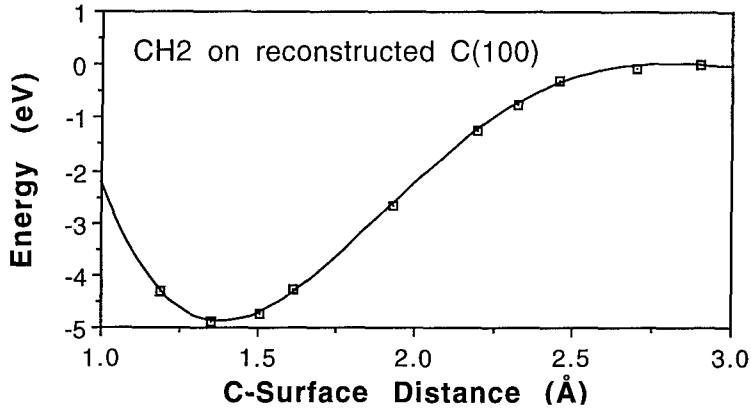

Fig. 4 The CI energy as a function of C-surface distance for the chemisorption of CH_2 on the reconstructed C(100)-2x1 surface.

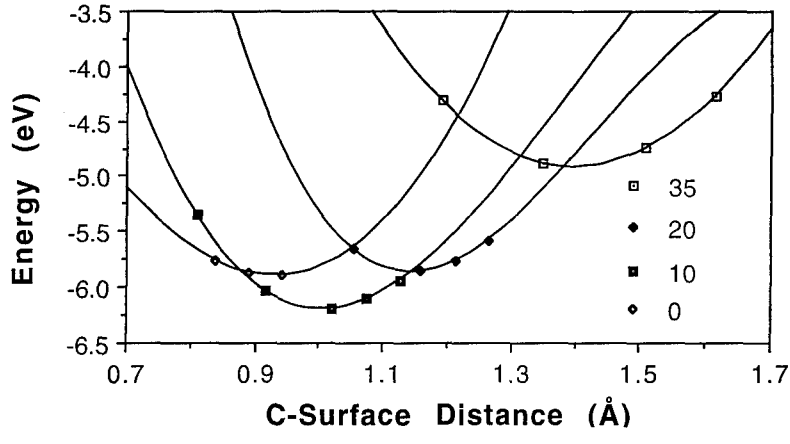

Fig. 5 The CI energies as a function of α and C-surface distance.

The increase in energy at the beginning of the rotation is an artifact of the SCF calculation which will disappear in the CI treatment. For the triplet state S = 1, the energy decreases monotonically and reaches a minimum at α=28.2°. The corresponding dimer bond length of 1.680 Å is also close to the value of 1.698 Å found in the previous section. For the high spin state S=2, the energy increases sharply with the C_1-C_3 rotation, suggesting that no dimers can be formed for this high spin state.

Next, the cluster is treated at the CI level with emphasis on the dimer C_1-C_2 region. The energy change on reconstruction, as a function α, is depicted in Fig. 3. Compared to the SCF result shown in Fig. 2, the configuration interaction treatment gives similar results for S=1 and S=2 states, but a dramatically different result for the S=0 state.

For the ideal, unreconstructed C(100)-1x1 surface where $\alpha = 0$, the lowest energy is that of the singlet state. The triplet and the higher spin state S=2 are 0.51 eV and 0.95 eV higher in energy than the singlet state at the CI level. When α increases, the CI energy of the singlet state S=0 decreases monotonically and reaches a minimum of -2.23 eV at $\alpha = 34.3°$. The lowest state is for S=0 corresponding to a strong interaction between the interior dangling bonds and a weak coupling of the exterior dangling orbitals. If the latter two orbitals are triplet coupled, the energy increases by 0.31 eV and the minimum is shifted to $\alpha = 27.5°$. Similar to the S=2 curve in Fig. 2, as α increases, the energy of the high spin state S=2 increases sharply due to the Pauli repulsion of electrons in the inward directed hybrid orbitals, suggesting that no dimers can be formed for this high spin state, whereas the energies of the S=1 and S=0 spin states decrease,

The results above are calculated with the fixed C_1-C_3 distance. We now relax this parameter and calculate the change in the cluster structure and energy. The C_1-C_3 distance is optimized to be 1.564 Å and the dimer bond length C_1-C_2 1.508 Å. Compared to the result for the fixed C_1-C_3 distance, the relaxed C_1-C_3 distance increases by 0.02 Å and the dimer bond length decreases by less than 0.01 Å. The total energy is lower by 0.05 eV, shifting the dimer bond energy to 2.28 eV. Most of the calculated dimer bond energies reported in the literature [18,20,23,28-30] are around 4 eV, which is considerably larger than our value of 2.28 eV. Probably, one of the main reasons for the discrepancies with larger calculated dimer bond energies, lies in the extraordinary stability of the singlet-coupled dangling orbitals in the unreconstructed geometry which is the reference state for the dimer bond energy calculation. Singlet-coupling of these orbitals lowers the energy by 0.95 eV from the high spin, S=2, state of the unreconstructed C(100)-1x1 geometry. The present CI calculations show that a minimum of four determinants with optimized orbitals are required to describe this state.

4. REACTION OF CH_2 WITH C(100)

For the chemisorption of CH_2 on C(100), we first calculate the total energy of the system as a function of C-surface distance on the reconstructed C(100)-2x1 surface and then relax the surface atoms to their equilibrium geometry. As a CH_2 approaches the reconstructed surface, the CI energy, shown in Fig. 4, decreases monotonically by 4.7 eV and then increases at the C-surface distance of 1.4 Å, suggesting that there is no barrier to the chemisorption of CH_2 on the C(100)-2x1 surface.

Fig. 5 shows the CI energy of $CH_2/C_{12}H_{20}$ as a function of C-surface distance and α, the C_1-C_2 rotation angle. The energy decreases considerably when α is changed from 35° to 20° and to 10°, suggesting that the surface is de-reconstructed with the chemisorption of CH_2. The lowest energy is 6.2 eV with respect to the reference energy of $CH_2 + C_{12}H_{20}$ at $\alpha = 9.2°$, corresponding to a dimer bond length of 2.23 Å. The energy increases slightly when α is decreases from 10° to 0°, the ideal C(100)-1x1 surface. It is the singlet coupling of the dangling bond orbitals that prevents a complete return to the 1x1 geometry for this single CH_2 dimer system.

5. CONCLUSION

The conclusions of our C(100) surface reconstruction studies can be summarized as follows: the calculated dimer bond length is sensitive to spin state and to the level of theoretical treatment. The correct ground state is a singlet, but a multi-determinant wavefunction is required for its description. The calculated dimer length in the ground state is 1.508 Å and the energy decrease on dimer formation with respect to the ideal C(100) surface is 2.28 eV per dimer. The important conclusion of this work is that there is no activation barrier for the addition of CH_2 to the C(100)-2x1 surface, neither in the approach of the fragment toward the surface nor in breaking the C-C surface dimer. However, full coverage of the surface by addition of CH_2 to parallel surface dimers is not possible without strong steric repulsion of hydrogen and thus hydrogens must be stripped from the surface for epitaxial growth to continue. This difficulty

would be avoided in the carbon rich limit of CH and C deposition and activation barrier calculations for these species are planned.

Acknowledgment

This research was supported by a grant from the U.S. Department of Energy. One of the authors (Z. J.) would like to thank Dr. G. Lucovsky for his support.

References

(1) R. Messier, J. T. Glass, J. E. Butler, and R. Roy, eds. "New Diamond Science and Technology", MRS, Pittsburgh, 1991.
(2) R. A. Rudder, G. C. Hudson, J. B. Posthill, R. E. Thomas, R. J. Markunas, T. P. Humphreys and R. J. Nemanich, Appl. Phys. Lett., 60, 329 (1992).
(3) R. F. Davis, Z. Sitar, B. E. Williams, H. S. Kong, H. J. Kim, J. W. Palmour, J. A. Edmond, J. Ryu, J. T. Glass, and C. H. Carter, Jr. Mater. Sci. Eng. B1, 77 (1988).
(4) R. A. Rudder, J. B. Posthill, and R. J. Markunas, Elect. Letters. 25, 1220 (1989).
(5) K. E. Spear, J. Am. Ceram. Soc. 72, 171 (1989).
(6) H. Kawarada, J. S. Ma, T. Yonehara, and A. Hiraki, MRS Symp. Proc. 162, 195 (1990).
(7) H. Itoh, T. Nakamura, H. Iwahara, and H. Sakamoto, in "New Diamond Science and Technology", p. 929, eds. R. Messier, J. T. Glass, J. E. Butler, and R. Roy, 1991.
(8) W. A. Yarbrough, J. Vac. Sci. Technol. A9, 1145 (1991).
(9) J. F. Prins, and H. L. Gaigher, in "New Diamond Science and Technology", p.561, eds. R. Messier, J. T. Glass, J. E. Butler, and R. Roy, MRS, Pittsburgh, 1991.
(10) R. A. Rudder, G. C. Hudson, Y. M. LeGrice, M. J. Mantini, J. B. Posthill, R. J. Nemanich and R. J. Markunas, 1989 MRS Meeting, San Diego, CA, EA-19, 89 (1989).
(11) W. S. Verwoerd, Surf. Sci., 108, 153 (1981).
(12) X. M. Zheng and P. V. Smith, Surf. Sci., 256, 1 (1991).
(13) R. E. Thomas, R. A. Rudder, R. J. Markunas, D. Huang, M. Frenklach, J. Chem. Vapor Dep., 1, 6 (1992).
(14) R. E. Thomas, R. A. Rudder, R. J. Markunas, J. Vac. Sci. Technol., A 10, 2451 (1992).
(15) A. V. Hamza, G. D. Kubiak and R. H. Stulen, Surf. Sci., 237, 35 (1990).
(16) P. G. Lurie and J. M. Wilson, Surf. Sci., 65, 453 (1977).
(17) B. B. Pate, Surf. Sci., 165, 83 (1986).
(18) W. S. Verwoerd, Surf. Sci., 103, 404 (1981); 108, 153 (1981).
(19) F. Bechstedt, and D. Reichardt, Surf. Sci., 202, 83 (1988).
(20) S. P. Mehandru, and A. B. Anderson, Surf. Sci., 248, 369 (1991).
(21) J. A. Appelbaum, and D. R. Hamann, Surf. Sci. 74, 21 (1978).
(22) Y. L. Yang and M. P. D'Evelyn, J. Am. Chem. Soc., 114. 2796 (1992); J. Vac. Sci. Technol. A 10, 978 (1992).
(23) T. Takai, T. Halicioglu, and W. A. Tiller, Surf. Sci. 164, 341 (1985).
(24) D. W. Brenner, Phys. Rev. B 42, 9458 (1990).
(25) X. M. Zheng and P. V. Smith, Surf. Sci. 256, 1 (1991).
(26) D. Huang and M. Frenklach, J. Phys. Chem. 96, 1868 (1992).
(27) M. Tsuda, S. Oikawa, S. Furukawa, C. Sekine, and M. Hata, J. Electrochem. Soc. 139, 1482 (1992).
(28) Th. Frauenheim, U. Stephan, P. Blaudeck, D. Porezag, H.-G. Busmann, W. Zimmermann-Edling, and S. Lauer, unpublished.
(29) S. H. Yang, D. A. Drabold, and J. B. Adams, unpublished.
(30) S. Skokov, C. S. Carner, B. Weiner, and M. Frenklach, unpublished.
(31) J. L. Whitten and T. A. Pakkanen, Phys. Rev. B 21 (1980) 4357.
(32) P. Cremaschi and J. L. Whitten, Surf. Sci. 149 (1985) 273.

SURFACE STUDIES RELEVANT TO THE INITIAL STAGES OF DIAMOND NUCLEATION

J.M. LANNON, JR.*, J.S. GOLD*, AND C.D. STINESPRING**
*Department of Physics, West Virginia University, Morgantown, WV 26506-6101
**Department of Chemical Engineering, West Virginia University, Morgantown, WV 26506-6101

ABSTRACT

Studies of diamond heteroepitaxy on silicon indicate that C-C surface species act as nucleation precursors. We have investigated the conversion of the Si(100) 2x1 surface to SiC using C_2H_4 to obtain an understanding of how C-C species may be formed and to determine the effect of an O-adlayer on enhancing or selecting the reaction channel which leads to these species. Under appropriate conditions, the interaction between C_2H_4 and the clean silicon surface yields both SiC and C-C species. The presence of an O-adlayer significantly reduces the activity of silicon and enhances the formation of sp^2 and sp^3 C-C species. These results provide key insights into diamond nucleation conditions in conventional growth processes.

INTRODUCTION

The initiation and control of nucleation are central issues in the heteroepitaxial growth of diamond on silicon. Numerous studies have suggested that C-C species formed on the surface during the initial stage of deposition play a critical role in the nucleation process.[1,2] The research described in this paper is aimed at understanding the nature of these C-C species and the factors controlling their formation. Ultimately, this information may provide a key to controlling nucleation and improving thin film quality.

Evidence of the importance of C-C species in diamond nucleation is provided by the work of Stoner et al.[2] In studies of bias enhanced nucleation of diamond on silicon, they performed x-ray photoelectron spectroscopy (XPS) analyses as a function of bias time. Following the evolution of the Si 2p and C 1s XPS peaks, they observed the formation of SiO_x and SiC within the first minute, but after 5 minutes, the SiO_x species disappeared, and a C-C species was formed. The estimated thickness of the C-C species was never greater than ~0.9 nm, and its concentration (relative to the SiC peak) remained approximately constant over the next 1.5 hrs until it dramatically increased. Based on Auger electron spectroscopy and Raman analyses, this increase coincided with the formation of diamond nuclei.

Stoner et al.[2] hypothesized that the C-C species was "responsible for the nucleation of diamond and that the SiC merely acted as a temporary but critical host on which the carbon could accumulate until clusters of the appropriate size and structure required for diamond nucleation developed." Although not conclusive, the results of Stoner et al. suggest that the C-C species was due to the selective removal of Si from the SiC film by hydrogen ions in the plasma.

Mat. Res. Soc. Symp. Proc. Vol. 339. ©1994 Materials Research Society

Motivated by these results, we have performed ultrahigh vacuum (UHV) studies to investigate the conversion of the Si(100) 2x1 and oxygen covered silicon (Si/O-adlayer) surfaces to SiC using C_2H_4. We have also investigated the formation of C-C species resulting from the interaction of hydrogen ions with SiC. These results will be reported elsewhere.[3] This paper focuses on the silicon conversion studies. To some extent, this represents a reexamination of previous work by one of us (CDS)[4] and Yates and coworkers.[5] This paper, however, describes new results which are relevant to the formation of the C-C nucleation precursors, the use of an O-adlayer to enhance or select the reaction channel leading to the formation of C-C surface species, and the nucleation of diamond.

EXPERIMENTAL

The experimental apparatus used in these studies comprises a UHV growth and analysis chamber with multiple effusive molecular beam sources for introducing reactive gases and a heated sample manipulator. Analytical techniques available within the chamber include Auger electron spectroscopy (AES) and low energy electron diffraction (LEED).

Considerable attention was given to establishing AES analysis conditions which minimize electron beam damage and to obtaining reliable standard spectra for SiC, graphite, and diamond. These results will be discussed in detail elsewhere.[6] C-KLL spectra obtained after a growth sequence were acquired in the N(E) mode and integrated numerically after background subtraction to provide the peak area. In addition, the C-KLL spectra were resolved into SiC, sp^2-C and/or sp^3-C components using factor analysis and standard spectra for SiC, graphite, and diamond. In a similar application, factor analysis has been used recently by Fuchs et al.[7] to determine the sp^2/sp^3 ratio in diamond and diamond-like carbon films.

The Si samples were n-type electronic grade materials with a (100) orientation and a resistivity of 5 ohm-cm. Prior to growth, samples were cleaned using Ar^+ bombardment and annealed for 15 min at 1100 K to restore crystal order and produce the 2x1 surface reconstruction.[8] The C_2H_4 used in these experiments was research purity (99.99%) supplied by Matheson.

In a typical growth experiment, the Si sample was cleaned and annealed, heated to the desired temperature, exposed to C_2H_4 for a specified time, and analyzed using AES. Following analysis, the exposure to C_2H_4 was continued, or the sample was cleaned, annealed, and reexposed to C_2H_4. Because analyses could not be performed while maintaining the sample temperature, experiments were performed to verify that thermal cycling did not appreciably alter the results.

For growth on the Si/O-adlayer surface, the adlayer was formed using electron stimulated adsorption.[9] Under normal AES analyses conditions, the partial pressure of H_2O ($\sim 10^{-10}$ Torr) was not a significant contributor to surface contamination. When the electron beam current was increased by a factor of 10 to 100, however, physisorbed H_2O was dissociated and reacted to form the O-adlayer. Using the scanning capability of the electron gun, the O-adlayer was formed over small areas (~500 μm x 500 μm), while the rest of the surface remained in the 2x1 configuration. Thus, multiple experiments, on the 2x1 surface and on the O-adlayer, could be performed simultaneously.

RESULTS

Figure 1 shows a plot of the C-KLL Auger peak area versus C_2H_4 fluence obtained for growth at 1000 K and a C_2H_4 flux of 13 ML s^{-1} (1 ML = 10^{15} cm^{-2}). Previous XPS studies[4] for temperatures in this range have shown the interaction between the Si(100) and C_2H_4 forms SiC by a two-dimensional, layer-by-layer growth process. This reaction was found to be first order in C_2H_4 fluence with a reaction efficiency of 1.6 x10^{-3}. The Si required for continued reaction and growth in this process is provided by out-diffusion and segregation. Based on these considerations, the thickness of the SiC film represented in Figure 1 is 5 nm (~ 10 times the C-KLL electron mean free path) after the first exposure (1x10^4 ML) indicated. Thus, this plot represents changes in composition of the near-surface-layers of the growing thin film rather than changes in film thickness. The nature of these changes can be understood by examining the Si-LMM and C-KLL Auger transitions.

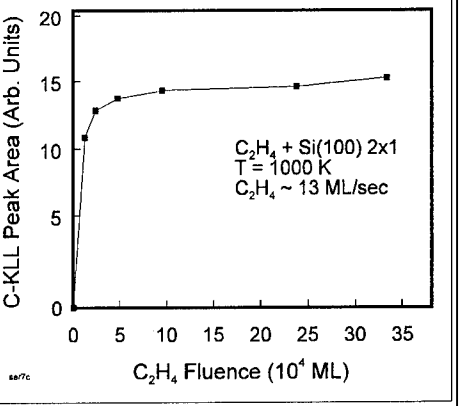

Figure 1. C-KLL peak area versus fluence for growth at 1000 K on the Si(100) 2x1 surface.

Si-LMM Auger peaks (not shown here for brevity) are representative SiC with an adlayer due to segregated silicon. The C-KLL spectra shown in Figure 2, in comparison with the SiC reference spectrum, are enhanced and broadened on the low kinetic energy side of the main peak. Based on analyses of C-KLL spectra of graphite and diamond, this is consistent with the formation C-C species.[6,10] Thus, for growth at 1000 K, the C-KLL spectra indicate that SiC is the dominant reaction product. However, C-C species are also formed in the near-surface-layers, even at relatively low fluences, and, as growth continues, the contribution from these C-C species increases.

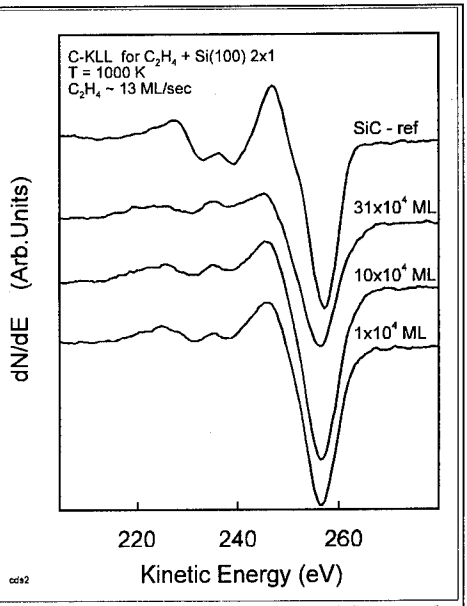

Figure 2. C-KLL spectra for selected fluences for the growth sequence shown in Figure 1.

Insight into the nature of the C-C species may be obtained through factor analysis of the C-KLL peak shapes. These results are given in Figure 3 which shows the carbon species distribution as a function of C_2H_4 fluence. Initially, the distribution is a nearly equal mixture of SiC and sp^2-C bonds. As growth continues, however, the SiC component decreases and the sp^2-C

component increases, reaches a maximum, and decreases. For fluences greater than ~5 x10^4 ML, sp^3-C species, appear and continue to increase.

Although a significant fraction of the carbon bonds formed at 1000 K may be characterized as sp^2 or sp^3 species, SiC formation is still a dominant reaction channel. As a means of reducing the activity of Si and enhancing the formation of C-C species, the effect of an O-adlayer, formed on the clean Si(100) 2x1 surface prior to the beginning of the growth process, has been investigated.

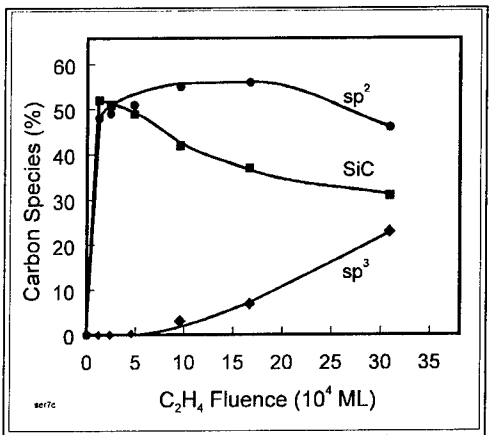

Figure 3. C-species distribution versus fluence for the growth sequence shown in Figure 1.

Figure 4 shows a plot of C-KLL Auger peak area versus C_2H_4 fluence for a typical growth sequence on the Si/O-adlayer. From these data, differences in growth on the Si(100) 2x1 and Si/O-adlayer are immediately apparent. The nature of these differences can be understood by examining the Si-LMM spectra shown in Figures 5.

As seen in Figure 5, the Si-LMM spectra are characteristic of the silicon substrate with an SiO_x overlayer and indicate only very limited SiC formation. Although the intermediate spectra are not shown, the Si/SiO_x peaks are uniformly attenuated as the fluence increases to a value of ~12x10^4 ML. Beyond this, the Si-LMM intensity remains essentially unchanged. Continued observation of the substrate Si-LMM peaks throughout the growth sequence is an indication that AES is sampling the entire thickness of the growing film. Thus, the attenuation of the Si-LMM peaks may be used to calculate the reaction efficiency. If the growing film is assumed to have a uniform thickness, this leads to an initial (i.e. < 5x10^4 ML) reaction efficiency of ~7.9x10^{-7}. This is clearly a function of fluence based on the shape of the C-KLL area versus fluence plot.

The "turnover" in the C-KLL area versus fluence plot (for fluences greater than ~20x10^4 ML) may be due to desorption of C-species from the surface. This does not seem likely, however, since the resultant increase in intensity of the Si-LMM substrate peaks is not observed. A more probable explanation is the coalescence and subsequent growth of three-dimensional clusters. This would reduce the rate of increase of the C-KLL peak area, while the accompanying increase in surface roughness would decrease the observed C-KLL area.

From the onset of growth on the Si/O-adlayer, the C-KLL spectra shown in Figure 6 are dominated by C-C species, and as the C_2H_4 fluence increases, the C-C contribution appears to increase. The nature of these peak shape changes is illustrated in

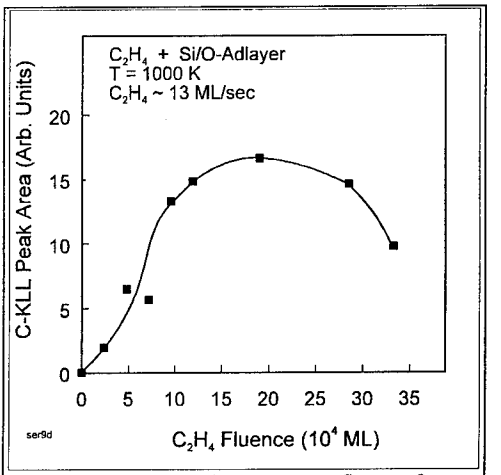

Figure 4. C-KLL peak area versus fluence for growth at 1000 K on the Si/O-adlayer surface.

Figure 7 which shows the factor analyses of the C-KLL peak shapes. In this case, the equivalent peak area rather than the percentage of each species has been plotted as a function of C_2H_4 fluence.

Throughout the growth sequence on the O-adlayer, these data indicate that the sp^2 and sp^3 species account for ~90% of the C-species formed. The sp^2 component increases with C_2H_4 fluence, reaches a maximum at ~$12x10^4$ ML, and then decreases. The sp^3 component shows similar behavior, however, the initial rate is somewhat slower and the turnover occurs at a slightly higher C_2H_4 fluence. As indicated above, the decrease in C-KLL peak area for each of these species is most likely due to the conversion to cluster growth and surface roughening rather than desorption of C-species. The SiC component accounts for about 10% of the C-species formed and remains essentially constant throughout the growth sequence. This is consistent with a low level of SiC formation indicated by the Si-LMM spectra.

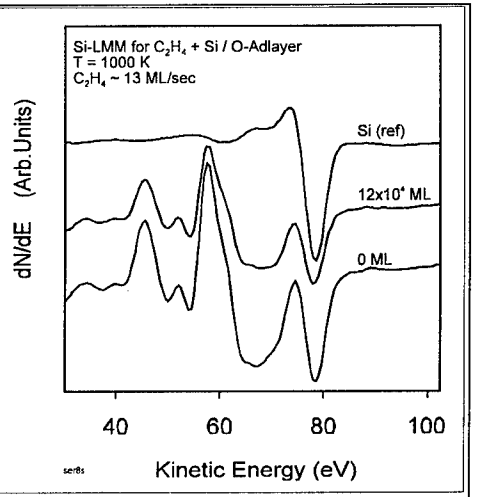

Figure 5. Si-LMM spectra for selected fluences for the growth sequence shown in Figure 4.

CONCLUSIONS

This study provides three key results. First, for growth at 1000 K on the Si(100) 2x1 surface, C-C species are a component of the reaction product. Further, a non-negligible fraction of these species are sp^3-C bonds. Second, the O-adlayer, in limiting the activity of Si, has opened a new reaction channel or allowed the observation of a channel which is normally obscured by SiC formation. Third, after initially reacting to form a uniform layer, the sp^2 and sp^3 species coalesce and grow as clusters. This, combined with the accompanying increase in surface roughness, accounts for the subsequent reduction in C-KLL peak area.

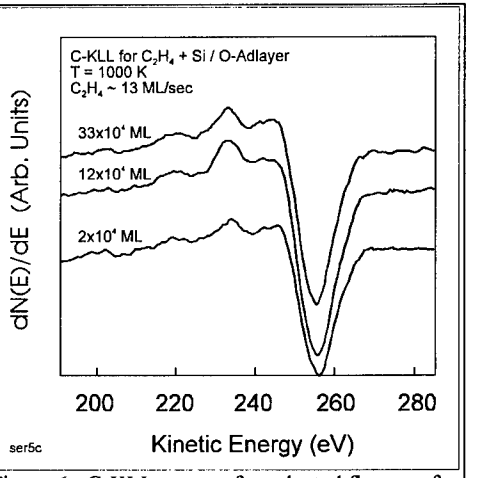

Figure 6. C-KLL spectra for selected fluences for the growth sequence shown in Figure 4.

Based on the diffusion/segregation model of SiC formation,[4,11] silicon is depleted from the near surface layers to support the segregated Si-adlayer. It is this adlayer which reacts with the incident hydrocarbon to form SiC. The silicon then segregates (presumably by place exchange) and the reaction continues. When the film is sufficiently thin or the temperature sufficiently high, silicon depletion from the near surface layers is compensated by bulk or grain boundary diffusion, and stoichiometry is maintained. For thicker films and/or lower temperatures (e.g. 1000 K), silicon depletion can not be made-up, and

the near-surface-layers become increasingly C-rich. The C-C species observed for growth on the Si(100) 2x1 are formed, we believe, as a result of this process.

The reaction on the Si/O-adlayer surface is distinctly different. The activity of silicon is substantially reduced, and SiC formation is not a factor. The C-C species are formed by direct interaction of the hydrocarbon with the surface. The fact that coalescence and conversion to a cluster growth mechanism are observed emphasizes the importance of adspecies-adspecies interactions. Further, since adspecies-adspecies interactions are enhanced by increased surface coverage, this suggests the importance of high activity hydrocarbon species (e.g. produced in a conventional deposition plasma).

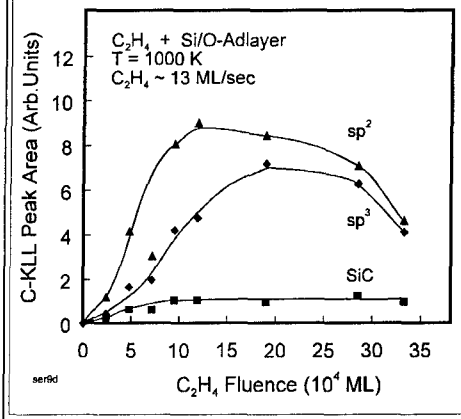

Figure 7. C-species distribution versus fluence for the growth sequence shown in Figure 4.

In the work of Stoner et al.,[2] the formation of C-C nucleation precursors may have been enhanced by silicon depletion (from SiC) by the hydrogen plasma. Our studies of hydrogen ion interactions with SiC indicate that this does occur.[6] The present work, however, indicates that C-C species would be formed directly as a result of the formation of the SiC layer, and the brief appearance of an SiO_X layer may have played an important role in initiating or enhancing the formation of the C-C nucleation precursors. Indeed, had the oxide layer not been rapidly removed, nucleation and growth may have been much different. The presence of an oxide layer might have reduced the induction period or altered the film morphology.

ACKNOWLEDGMENTS

This research was supported by the Office of Naval Research and Advanced Research Programs Administration under grant numbers N00014-92-1438 and N00014-92-2006, respectively.

REFERENCES

1. Z. Feng, K. Komvopoulos, I.G. Brown, and D.B. Bogy, J. Appl. Phys. 74, 2841 (1993).
2. B.R. Stoner, G.-H.M. Ma, S.D. Woltner, and J.T. Glass, Phys. Rev. B45, 11067 (1992).
3. J.M. Lannon, J.S. Gold, and C.D. Stinespring, (to be published).
4. C.D. Stinespring and J.C Wormhoudt, J. Appl. Phys. 65, 1733 (1989).
5. F. Bozso, J.T. Yates, Jr., W.J. Choyke, and L. Muehlhoff, J. Appl. Phys. 57, 2771 (1985).
6. J.M. Lannon, J.S. Gold, and C.D. Stinespring, (to be published).
7. A. Fuchs, J. Scherer, K. Jung, and H. Ehrhardt, Thin Solid Films 232 (1993) 51.
8. G. Schulze and M. Henzler, Surface Sci. 124, 336 (1983).
9. R.E. Kirby and M. Lichtman, Surface Sci. 41, 447 (1974).
10. J.T. Grant and T.W Haas, Surface Sci. 23, 347 (1970).
11. C.D. Stinespring and W.F. Lawson, Surface Sci. 150, 209 (1985).

COMPARISON OF SURFACE CLEANING PROCESSES FOR DIAMOND C(001)

PETER K. BAUMANN, T.P. HUMPHREYS AND R.J. NEMANICH
Department of Physics, North Carolina State University, Raleigh, North Carolina 27695-8202

ABSTRACT

Two wet chemical cleaning processes (a conventional chromic acid clean and an electrochemical etch) and a H-plasma exposure have been employed to clean natural type IIb semiconducting diamond C(001) wafers. The effects of these processes on the diamond surface have been assessed and compared. As evidenced by Auger electron spectroscopy (AES), an oxygen free surface could be obtained following annealing to 900°C for the electrochemical process compared to 1050°C for the chromic acid etch. In addition, the technique of Atomic Force Microscopy (AFM) demonstrated the presence of oriented pits on the surface of samples electrochemically etched for long times at high currents. Furthermore, heteroepitaxial Cu films have been grown on the diamond substrates cleaned by a process as described above. By means of Ultraviolet Photoemission Spectroscopy (UPS) a Schottky barrier height of $\Phi_B \cong 1.0$ eV was measured. Furthermore, the presence a negative electron affinity (NEA) has been determined.

INTRODUCTION

The goal for the preparation of diamond surfaces is to remove non diamond carbon and any surface contaminants. A commonly used cleaning method involves boiling of the samples in chromic acid and aqua regia. Recently, a different approach based on electrochemical etching to remove conductive surface layers has been proposed [1]. Each of these processes is indeed suitable to remove non diamond carbon [1, 7, 8]. However, both procedures lead to an oxygen terminated diamond surface. In order to remove these surface contaminations it is therefore necessary to employ an additional cleaning technique. A very common approach involves annealing of the diamond crystals in UHV. Indeed, several publications have examined the effects of annealing on the diamond C(001) surface [2-5]. Furthermore, temperature programmed desorption studies have investigated the correlation of the removal of oxygen and hydrogen with surface reconstruction [2-4]. Two different configurations for the bonding of oxygen on a (1x1) surface have been suggested [3]. Arguments for a monohydride terminated surface [4, 5] or a hydrogen free surface [2] after annealing to ~ 1000°C have been presented.

Semiconductor surfaces with a work function such that the vacuum level lies below the conduction band minimum exhibit a negative electron affinity (NEA). Therefore, electrons in the conduction band can escape freely from such a surface. For wide bandgap semiconductors (like diamond) the conduction band minimum is likely to be close to the vacuum level. In particular, different surface preparation methods can influence whether a diamond surface exhibits a NEA [5]. Photoemission spectroscopy is found to be a suitable method to detect a NEA. Electrons that get excited from the valence band into the conduction band by photoemission may quasi-thermalize to the conduction band minimum. In case of an NEA surface they can readily be emitted. Photoemission spectra display these NEA electrons as a sharp feature at the low energy end of the spectrum [9, 10].

In this study we performed comparative annealing studies of natural diamond C(001) crystals cleaned by either of the two wet chemical procedures. Following the anneal, a H plasma clean at 370°C has been employed. Indeed, the environment of a H plasma may be comparable to the one of diamond growth at low temperatures [6]. Furthermore, interfacial properties of hetero-epitaxially grown Cu films on diamond C(001) are presented.

EXPERIMENTAL DETAILS

Several natural type IIb single crystal diamond C(100) substrates have been used in this study on the influence of different cleaning techniques on the surface properties. The two

Mat. Res. Soc. Symp. Proc. Vol. 339. ©1994 Materials Research Society

chemical cleaning processes are described: A clean employing chromic acid (CrO_3:H_2SO_4) (boiling for 15 min.), aqua regia (3HCl:1HNO_3) (boiling for 15 min.) followed by deionized (DI) water (rinsing). Or an electrochemical etching procedure [1]. For this process the samples were suspended between two Pt electrodes in DI water as electrolyte. A DC-voltage of 350 V was applied between the two electrodes. A typical etch lasted 3 hours. A constant current of about 0.5 mA was measured. After each of the two cleaning processes the samples were blown dry with N_2, mounted on a molybdenum sample holder and transferred into the UHV system. In addition, the diamond wafers were annealed successively to temperatures of 900°C and 1050°C for 15 minutes each. The base pressure in the annealing chamber was ~ 1x 10^{-10} Torr and rose to ~ 4 x 10^{-9} Torr and 6 x 10^{-9} Torr during the two anneals, respectively. Following the latter anneal, a hydrogen plasma etch has been employed. For this purpose the diamond crystal was heated to 370°C and exposed to a remotely excited H plasma. The details of the plasma system are described elsewhere [13]. The H pressure in the plasma chamber was held at 50 mTorr. A number of techniques have been employed to analyze the samples subsequent to each cleaning step including *in-situ* low energy electron spectroscopy (LEED), *in-situ* Auger electron spectroscopy (AES) *in-situ* ultraviolet photoemission spectroscopy (UPS) and *ex-situ* atomic force microscopy (AFM). In particular, 21.21 eV HeI radiation has been used to facilitate the photoemission measurements. In order to overcome the work function of the electron analyzer, a bias of 2.0 V has been applied to the sample. Therefore it was possible to detect low energy electrons emitted from a NEA surface.

Furthermore, thin Cu films of 1, 2, 4 Å thickness were grown on diamond crystals cleaned by chromic acid. For this purpose a Cu filament has been employed. In order to desorb adsorbed gas contaminants the sample was annealed to 800°C for 15 minutes. Prior to deposition 50Å of Cu has been evaporated to liberate any foreign material from the filament. During growth the temperature of the sample was maintained at 500°C (pressure ~ 2 x 10^{-9} Torr). The deposited thickness of the Cu was determined by a quartz crystal oscillator.

RESULTS AND DISCUSSION

Following either of the two wet chemical cleaning procedures the as-loaded diamond crystals exhibited a comparable unreconstructed (1x1) LEED pattern. Furthermore, AES spectra showed peaks indicative of the presence of oxygen on all samples. Upon heating to 900°C a reduction of the surface oxygen (Fig. 1a) was observed for diamond substrates cleaned by employing chromic acid. However, the LEED pattern remained unchanged. Following an anneal to 1050°C the amount of oxygen on the surface dropped below the detection limit of the AES instrument. A reconstructed (2x1) LEED pattern appeared. In addition, a sharp low energy peak attributed to a NEA surface was seen in UPS spectra following the last annealing step. The reconstructed (2x1) LEED pattern and the NEA could be retained following a hydrogen plasma exposure (Fig. 2).

In comparison, AES spectra of the as-loaded electrochemically etched samples displayed features indicative of the presence of SiO_2 surface impurities. However, following a UV ozone exposure and an HF dip these contaminations could no longer be detected (Fig. 1b). Also the amount of fluorine was below the detection limit of the AES equipment. After annealing to 900°C no oxygen could be observed by means of AES. Again, a 2x1 surface reconstruction could be observed. Furthermore, a NEA effect was detected by means of UPS. No changes in the AES spectrum nor in the LEED pattern were seen upon heating to 1050°C. Also, the NEA surface could be retained.

It is reasonable to assume that the appearance of a NEA and a reconstructed (2x1) surface can be attributed to the removing of oxygen as discussed in other studies [2-4]. Indeed, it is remarkable that an oxygen free diamond C(001) surface can be obtained at lower temperatures following an electrochemical etch and a HF dip compared to a conventional approach. The higher annealing temperature required to remove the surface oxygen from the samples cleaned conventionally may be attributed to oxidization of the diamond surface by chromic acid. Although the mechanism of the electrochemical etch is not well-understood it may be suggested from these experiments that this process in combination with the HF dip is less

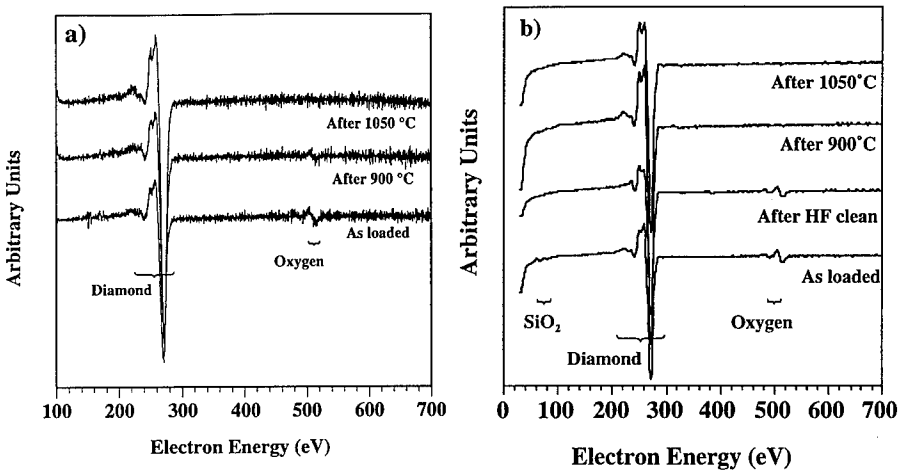

Fig.1. Auger spectra as a function of annealing temperature. a) Diamond C(001) following chromic acid clean. The as loaded surface exhibits features indicative of oxygen which can be reduced at 900°C and removed at 1050°C. b) Diamond C(001) following electrochemical etching. The as loaded surface exhibits features indicative of oxygen which can be removed at 900°C.

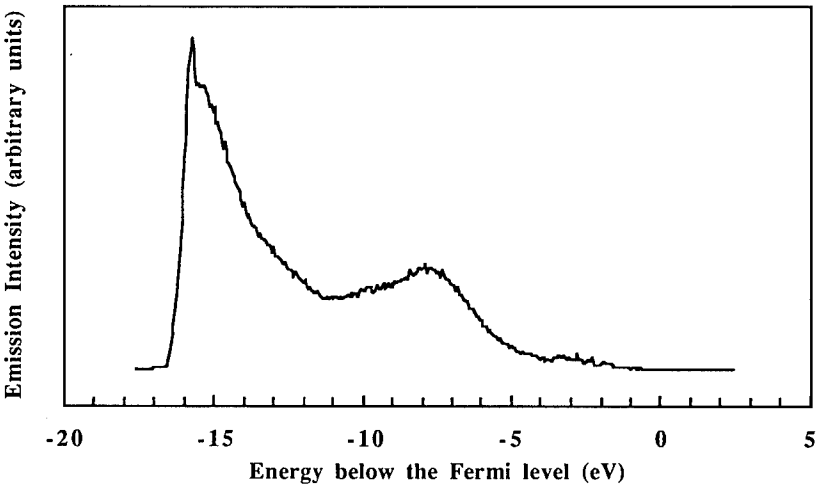

Fig. 2. Photoemission spectrum of diamond C(001) (cleaned by chromic acid) subsequent to 1050°C anneal and H-plasma exposure.

oxidizing than a conventional chromic acid clean. However, we have not established whether fluorine plays a role in lowering the annealing temperature required to remove oxygen from the diamond C(001) surface.

Since the diamond crystals still exhibit a (2x1) reconstructed configuration and a NEA following a H-plasma etch, it can be suggested that the (2x1) reconstruction is associated with a monohydride terminated surface. Previously Hamza et al. suggested a monohydride terminated surface following annealing to ~ 1000°C based on electron-simulated desorption time-of-flight measurements [4]. Indeed, the results presented here provide further evidence for this explanation. However, Yang et al. argue that a dihydride terminated surface is energetically unlikely due to stearic hindrance of the H atoms. Therefore, they propose that a monohydride terminated surface evolves into a free surface upon heating to ~ 1000°C [2].

Due to polishing with diamond grit all the samples used in this study exhibited straight groves with a depth of ~ 30 Å as evidenced by AFM (Fig. 3a). Features of this kind are common for polished diamond substrates. Following a chromic acid clean no changes in surface morphology of the wafers could be detected. Even after boiling the substrates in chromic acid and aqua regia for 2 hours each no altering of the surface was seen. Also, AFM images of electrochemically etched crystals did not reveal any changes either. However, after an extended electrochemical etch lasting 12 hours at ~ 50 mA scattered pits could be detected on the diamond surface. These etch pits were found to be oriented along the <110> crystallographic directions, as shown in Fig. 3b. In addition, larger amounts of SiO_2 were detected on these surfaces by means of AES. In other experiments it has been demonstrated that layers of graphite and damaged amorphized diamond could be removed from surfaces by means of this electrochemical etching procedure [7, 8]. Therefore, we suggest that the etch pits mark the location of defects in the diamond. These defects may be intrinsic to the natural diamond or due to damage from polishing. It can be suggested that this electrochemical etching procedure may be employed to assess the crystalline quality of other wide bandgap semiconductors.

As evidenced by UPS the crystals annealed to 800°C exhibited a positive electron affinity (PEA). However, following deposition of Cu a distinctive low energy peak could be observed (Fig. 4). This feature has been attributed to a negative electron affinity (NEA) surface. Furthermore, a value $\Phi_B \cong 1.0$ eV for the Schottky barrier height has been measured from the UPS spectra. The electron affinity χ induced after Schottky barrier formation can be calculated according to the equation [14]:

$$\chi = (\Phi_M + \Phi_B) - E_G \qquad (1)$$

By using the values for the metal work function of copper $\Phi_M = 4.65$ eV for the (001) surface, the bandgap of diamond $E_G = 5.45$ eV and the measured Schottky barrier height, an electron affinity of $\chi \cong + 0.2$ eV is determined. This finding obviously stands in contrast to the appearance of a metal induced NEA feature found in the UPS spectra. Indeed, for Ti or Ni grown on diamond C(111) a metal induced NEA has been observed by means of UPS that could be explained according to the simple work function model [11, 12]. Possible explanations may include non uniformities in the Cu films due to epitaxial growth, changes in the Cu work function for thin layers and impurities. Indeed, these Cu layers were shown to be epitaxial and exhibited an island morphology [7, 8]. Clearly, future experiments will have to determine the actual work function of these thin Cu films, and the relation of surface preparation to the Schottky barrier and diamond electron affinity.

CONCLUSIONS

A conventional chromic acid clean and an electrochemical etch have been compared as surface preparation processes for p-type semiconducting natural diamond C(001) substrates. Following a 900°C anneal the removal of surface oxygen, a (2x1) reconstruction pattern and a NEA effect were observed. However, for samples cleaned using chromic acid these effects were seen only upon heating to 1050°C. The (2x1) configuration and the NEA were retained

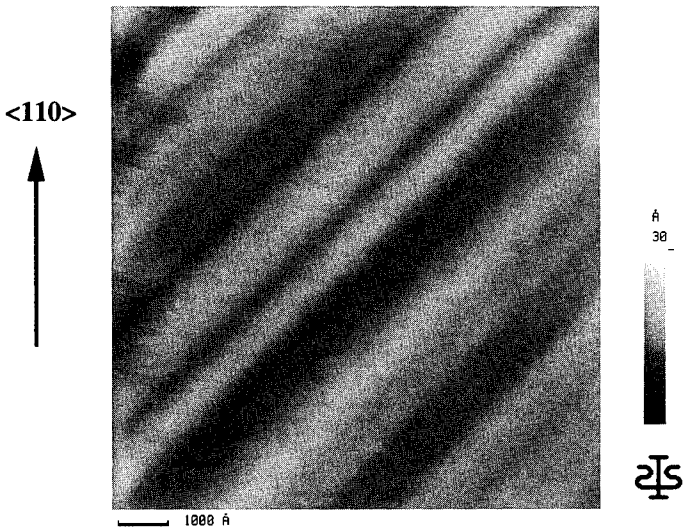

Fig. 3a. AFM micrograph of diamond C(001) following polish.

Fig. 3b. AFM micrograph of diamond C(001) after electrochemical etching for 12h at 50 mA.

subsequent to a H-plasma etch. Furthermore, samples electrochemically etched for long times at high currents displayed oriented pits on the surface as evidenced by AFM. Following Cu deposition a metal induced NEA and a Schottky barrier height of $\Phi_B \cong 1.0$ eV have been observed by means of UPS.

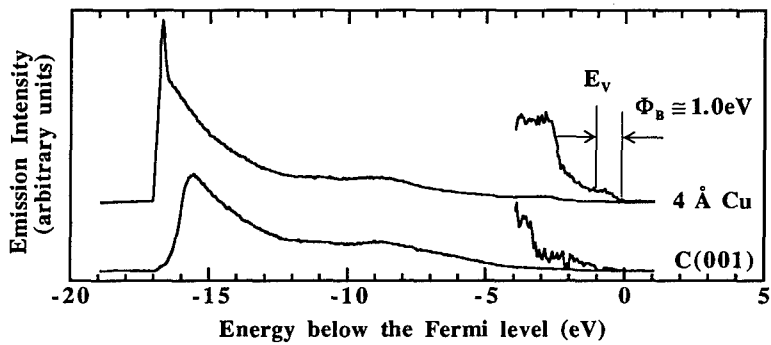

Fig. 4. UPS spectra of diamond C(001) cleaned by chromic acid and of Cu deposited on C(001).

ACKNOWLEDGMENTS

We wish to thank J. van der Weide for helpful discussions and technical assistance. Also, we acknowledge support from the Office of Naval Research (Contract No. N00014-92-J-1477).

REFERENCES

1. M. Marchywka, P.E. Pehrsson, S.C. Binari and D. Moses, J. Electrochem. Soc., Vol. **140**, No. 2 (1993) L19.
2. Y.L. Yang, L.M. Struck, L.F. Scutcu and M.P. D'Evelyn, Thin Solid Films **225,** 203 (1993)
3. R.E. Thomas, R.A. Rudder and R.J. Markunas, J. Vac. Sci. Technol. A **10**, 2451 (1992).
4. A.V. Hamza, G.D. Kubiak and R.H. Stulen, Surf. Sci. **237**, 35 (1990).
5. J. van der Weide, Z. Zhang, P.K. Baumann, M.G. Wensell, J. Bernholc and R.J. Nemanich, submitted for publication.
6. Y. Muranaka, H.Yamashita and H. Miyadera, J. Vac. Sci. Technol. A **9**, 76 (1991).
7. P.K. Baumann, T.P. Humphreys, R.J. Nemanich, K. Ishibashi, N.R. Parikh, L.M. Porter and R.F. Davis, Proceedings of the Fourth European Conference on Diamond, Diamond-like and Related Materials, (J. Diamond Rel. Mat., Vol. 3/4-6, 1994) pp. 883-886, in press.
8. P.K. Baumann, T.P. Humphreys, R.J. Nemanich, submitted for publication.
9. F.J. Himpsel, P. Heimann and D.E. Eastman, Solid State Commun. **36,** 631 (1980).
10. B.B. Pate, W.E. Spicer, T. Ohta and I. Lindau, J. Vac. Sci. Technol. **17,** 1087 (1980).
11. J. van der Weide and R.J. Nemanich, J. Vac. Sci. Technol. B **10**, 1940 (1992).
12. J. van der Weide and R.J. Nemanich, Phys. Rev. B, in press.
13. T.P. Schneider, J. Cho, Y.L. Chen, D.H.Mahler and R.J. Nemanich, in Surface Chemical Cleaning and Passivation for Semiconductor Processing, edited by G.S. Higashi, E.A. Irene, T. Ohmi (Mater. Res. Soc. Proc. **315,** Pittsburgh, PA, 1993) pp.197-209.
14. E.H. Rhoderick and R.H. Williams, Metal-Semiconductor Contacts (Clarendon, Oxford, 1988).

ELECTRON EMISSION PROPERTIES OF THE NEGATIVE ELECTRON AFFINITY (111)2x1 DIAMOND-TiO INTERFACE

C. BANDIS, D. HAGGERTY AND B. B. PATE
Physics Department, Washington State University, Pullman, WA 99164-2814.

ABSTRACT

We report photoemission measurements from the (111)2x1 diamond-titanium monoxide (TiO) interface. Submonolayer deposition of TiO on the (111)2x1 diamond surface modifies the electron affinity of the surface from positive to negative. No change in the band bending was observed as a result of the TiO deposition. Total electron yield measurements from the diamond-TiO interface were also performed. The yield spectra, as expected for a negative electron affinity (NEA) surface, have emission thresholds that are in good agreement with the absorption coefficient of diamond. To further understand the emission properties of NEA (111) diamond surfaces we also compare the electron yield photo-excitation spectra of the diamond-TiO interface with the yield spectra of hydrogenated (111)1x1:H diamond surfaces.

INTRODUCTION

Negative electron affinity (NEA) semiconductor surfaces, that is surfaces with the vacuum level lying below the conduction band minimum (CBM), have been used over the years to create efficient electron emitters for use in devices such as photo-cathodes and electron multipliers which are essential tools to both science and technology. Semiconductor surfaces (e.g. Si, GaAs, GaP) have been engineered to have NEA by combining heavy p-type doping and thin cesium surface coatings.[1] A NEA semiconductor surface makes it possible to observe conduction band electrons with kinetic energies as low as the conduction band minimum escaping into the vacuum. This gives us the opportunity to study the electronic properties of the semiconductor for near band gap excitation photon energies.

The as-polished (111)1x1:H diamond surface, which is known to be hydrogen terminated[2,3,4], was found to exhibit NEA over a decade ago.[5] In contrast the hydrogen-free (111)2x1 reconstructed diamond surface has positive electron affinity.[6] Van der Weide et. al.[7] have recently showed that the argon plasma treated, hydrogen-free, (111) diamond surface can be activated to NEA by deposition of a thin layer of Ti.

Total electron yield measurements (number of emitted electrons per incident photon) from the as-polished (111)1x1:H diamond (type IIa) surface reveals an oscillatory structure for near band gap excitation photon energies.[8] The oscillations are approximately evenly spaced by 160 meV. In order to better understand the mechanism responsible for this oscillatory structure we recently performed additional experiments[9] which are briefly summarized here. We found that close examination of the total electron yield thresholds suggests that a significant component of the electron yield is due to exciton induced electron emission; that is that excitons break up at the surface due to the NEA potential step and emit their electrons. The photo-excited electrons thermalize via a Fan phonon cascade mechanism[10] to the CBM or to exciton levels depending on the excitation photon energy. We concluded that the oscillatory structure is due to the difference in the surface escape probabilities between CBM electrons and electrons originating from exciton states, and is present only when the band bending is small (~ 0.1 eV).

In order to further test previous experimental observations from the (111) diamond surface, we attempted to activate the extensively studied[11] (111)2x1 diamond surface to NEA by deposition of a thin layer of TiO. The choice of TiO was made based on the experiments by van

Mat. Res. Soc. Symp. Proc. Vol. 339. ©1994 Materials Research Society

der Weide,[7] and the fact that addition of oxygen on a cesium activated NEA surface enhances its NEA properties.[1]

It is the purpose of this paper to present the results of our photoemission experiments from the diamond-TiO interface. The experiments include electron energy distribution curves (EDC) and total electron yield measurements. Data taken from the diamond-TiO surface are compared with those from the (111)1x1:H and (111)2x1 diamond surfaces. Analysis of our data finds that the (111)2x1 diamond-TiO surface has negative electron affinity with 0.5 eV downward band bending.

EXPERIMENTAL CONDITIONS

The experimental results discussed in this paper are from work performed on the (111) surface of a type IIb diamond single crystal[12]. The surface was mechanically polished on a cast iron wheel using diamond grit and olive oil, and cleaned ultrasonically with methyl-ethyl-ketone, acetone, and alcohol.[11] The photoemission experiments were performed in our ultra high vacuum system with a working pressure of $7x10^{-10}$ Torr (with He-lamp operation) and a base pressure of $3x10^{-10}$ Torr. The sample was mounted in platinum foil suspended by a single platinum wire. Heating up to 1100 °C could be accomplished via electron bombardment from a tungsten filament mounted behind the diamond by the application of a positive voltage (about 1 KV) to the sample. The NEA of the as-polished (111) diamond surface was transformed to a positive electron affinity when we reconstructed the surface.

Deposition of TiO was achieved by resistive heating of a Ti wire-wrapped tungsten filament. The film thickness was monitored with a quartz crystal rate monitor. XPS (Al Ka) was used to monitor the surface cleanliness and TiO stoichiometry. The substrate was at room temperature during the evaporations.

A Hg-Xe arc-lamp was employed as a source for near band gap radiation. The photon energy was selected with the use of a 1 m normal incidence monochromator (McPherson 225) and refocused at the sample position into a 1 mm x 2 mm rectangular spot. The excitation spectra are always normalized with respect to the photo-yield of sodium salicylate[13]. The energy resolution of the monochromator was less than or equal to 50 meV. The UPS measurements were made using UV light from a He resonance lamp (hv=21.218 eV). The He lamp radiation was refocused at the sample position into a spot approximately 1.5 mm in diameter.

The total electron yield measurements were performed at room temperature, using a retarding field analyzer equipped with a position sensitive multi-channel plate detector. The electron energy distribution measurements were taken with a hemispherical electron energy analyzer, operated with 0.16 eV resolution.

RESULTS AND DISCUSSION

In figure 1 we show electron EDCs from the as-polished (111)1x1:H diamond surface, and the (111)2x1 reconstructed diamond surface. The EDC from the as-polished (111) diamond surface is consistent with results reported elsewhere,[11] with the key characteristic being the high intensity peak at the low kinetic energy (about -16 eV binding energy) which indicates a NEA surface. It also shows the absence of surface state emission in the part of the spectrum corresponding to the top of the valence band. The position of the valence band maximum (VBM) is found to be 0.4 eV below the Fermi level. Heating of the sample up to 1000 °C results in hydrogen desorption, surface reconstruction, and surface state emission at an energy 2.5 eV below the Fermi level (fig.1). The low kinetic energy emission threshold increases by 0.7 eV as compared to the (111)1x1:H as-polished surface indicating that the electron affinity has become

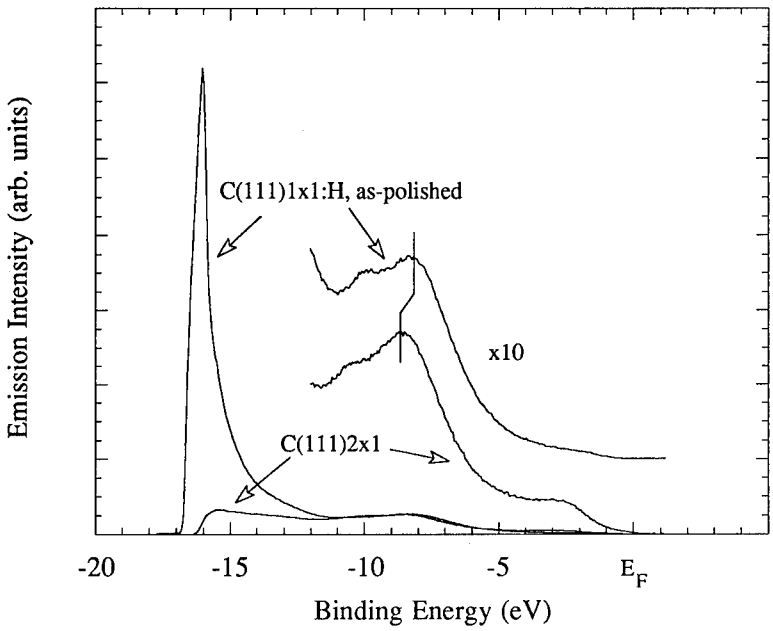

Figure 1. Comparison of the EDCs from as-polished (111)1x1:H and reconstructed (111)2x1 diamond surfaces at hν=21.218 eV. Note both the change in the downward band bending and the shift of the low energy emission threshold.

positive. By taking into account the increase in the Fermi level pinning position by 0.5 eV upon reconstruction of the surface, we calculate an increase in the electron affinity of 1.2 eV.

Successive evaporations of TiO onto the positive electron affinity (111)2x1 reconstructed diamond surface resulted in lowering of the electron affinity. Figure 2 shows the variations of the EDCs from the diamond-TiO interface with the thicknesses of the TiO film. Our data show that the low kinetic energy threshold moves towards lower energies, while simultaneously the intensity of the threshold emission increases as the TiO film thickness becomes higher. No change in the band bending was observed during the TiO deposition. Therefore, the valence band maximum lies 0.9 eV below the Fermi level as in the case of the (111)2x1 diamond surface. After a total of 3.5 Å TiO deposition, the low energy threshold is about 16.1 eV below the VBM emission. Therefore the low energy threshold lies below the CBM ($h\nu-E_{gap}$=15.73 eV, where E_{gap}=5.49±0.005 eV[14]), indicating a NEA surface. Furthermore, we see that for increasing TiO thickness the Fermi level emission becomes more pronounced. At the same time, the diamond features (e.g. surface states) become weaker due to the small inelastic mean free path of the emitted electrons.

It is known that re-hydrogenation of the (111)2x1 reconstructed diamond surface removes the surface states and restores both the symmetry and the electron affinity of the surface back to that seen from the as-polished (111)1x1:H diamond surface[15]. However, re-hydrogenation of the (111)2x1 surface does not restore the increase of the downwards band bending seen upon reconstruction. This behavior of the Fermi level pinning position has also been observed by Pate

et. al.[15] in C 1s spectra. Therefore, much like the TiO results reported here, the re-hydrogenated (111)1x1:H diamond surface has NEA and an additional downward band bending of 0.5 eV when compared to the as-polished (111)1x1:H diamond surface.

In fig. 3 total electron yield measurements from the NEA diamond-TiO surface (curve B) are presented and compared with yield spectra from both the as-polished (111)1x1:H diamond surface (curve A) and the re-hydrogenated (111)1x1:H surface (curve C). In both cases A and B, which exhibit the additional 0.5 eV downward band bending, the electron yield does not have the oscillatory structure observed from the as-polished (111)1x1:H diamond surface. Close examination of the diamond-TiO yield thresholds shows that they are in good agreement with the diamond photo-absorption coefficient reported by Clark et. al..[16] This verifies that indeed the surface is NEA. The strongest threshold observed in the total electron yield curves is at 5.54 eV. This value corresponds to excitation of a valence band electron to the exciton level with simultaneous emission of a transverse optical (TO) phonon. The emission at hν<5.5 eV from the diamond-TiO surface (curve B) is thought to be due to direct photoemission from the TiO layer.

The insert in figure 3 shows the curves A and B normalized to the same intensity at about hν=5.6 eV (curves A' and B' respectively), just below the threshold for electron excitation to the conduction band with simultaneous emission of a TO phonon. Curve C was not included in the insert for presentation purposes; its normalization results in a curve very similar to B'. The normalized curves demonstrate that data taken from surfaces with similar downward band

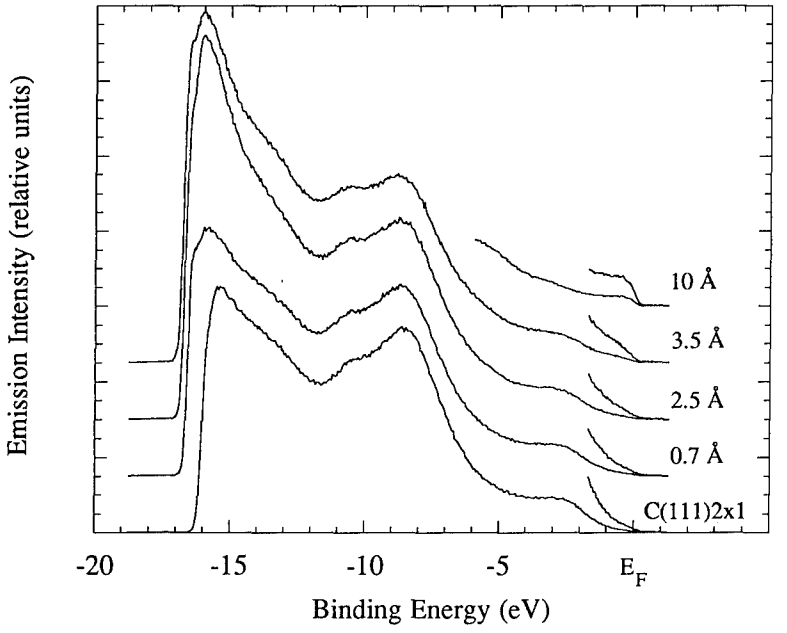

Figure 2. Effect of TiO deposition on the positive electron affinity (111)2x1 diamond surface. Note the variation in the low energy emission threshold with the TiO film thickness, which demonstrates the change of the electron affinity from positive to negative. No additional change of the surface band bending as a result of the TiO deposition is observed.

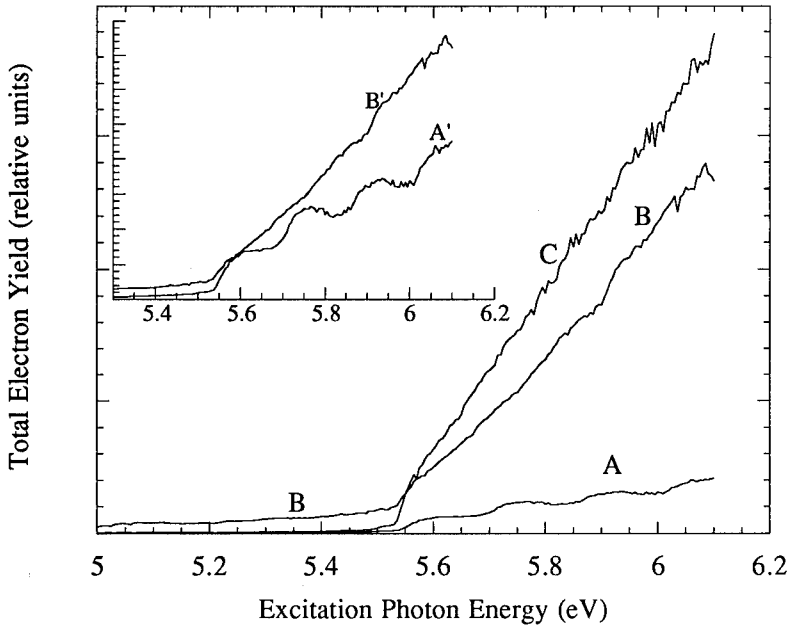

Figure 3. Total electron yield spectra from the A) as-polished (111)1x1:H diamond surface, B) the TiO-(111)2x1 diamond interface, and C) the re-hydrogenated (111)1x1:H diamond surface. In the insert the curves A' and B' show the yield spectra A and B normalized to the same intensity at 5.6 eV. Note that besides the absence of the oscillations in the curve B', the yield spectra A' and B' also differ in shape.

bending have very similar shape; the yield curve from the as-polished surface is found to have a different shape, besides exhibiting an oscillatory structure. The shape of the electron yield spectrum from the as-polished diamond surface is consistent with exciton induced emission being the dominant yield component.[9] A more detailed analysis of the functional form of the electron yield will be included in a future publication.

CONCLUSIONS

Deposition of TiO on the positive electron affinity (111)2x1 reconstructed diamond surface results in a NEA. This was verified by observing that the low energy emission threshold of the electron EDCs moved toward lower energies, and below the CBM, upon deposition of TiO. In addition, as expected for electron emission from a NEA surface, the total electron yield thresholds are found to be in good agreement with the diamond photo-absorption thresholds. Comparison of the yield spectra taken from the diamond-TiO interface with those taken from the as-polished (111)1x1:H, and the re-hydrogenated (111)1x1:H diamond surfaces showed a great similarity with the latter only. Both the diamond-TiO interface and the re-hydrogenated (111)1x1:H diamond surface exhibit an additional 0.5 eV downward band bending as compared to the as-polished (111)1x1:H diamond surface. We suggest that the characteristic difference in the

functional form of the electron yield of the as-polished diamond surface arises from the fact that, in this case, the dominant component of the total electron yield is solely due to exciton induced electron emission.

ACKNOWLEDGEMENTS

The authors acknowledge the research support of the National Science Foundation under grant number ECS-9222368.

REFERENCES

1. R.L. Bell, Negative Electron Affinity Devices, (Clarendon Press - Oxford, 1973).
2. B.J. Waclawski, D.T. Pierce, N. Swanson and R.J. Celotta, J. Vac. Sci. Technol. **21**(2), 268 (1982).
3. B.B. Pate, M.H. Hecht, C. Binns, I. Lindau and W.E. Spicer, J. Vac. Sci. Technol. **21**(2), 268 (1982).
4. A.V. Hamza, G.D. Kubiak and R.H. Stulen, Surface Sci. **206**, L833, (1988).
5. F.J. Himpsel, J.A. Knapp, J.A. Van Vechten and D.E. Eastman, Phys. Rev. **B20**, 624 (1979).
6. B.B. Pate, P.M. Stefan, C. Binns, P.J. Jupiter, M.L. Shek,I. Lindau and W.E. Spicer, J. Vac. Sci. 19 (3), 349 (1981).
7. J. van der Weide and R.J. Nemanich, J. Vac. Sci. Technol. **B10** (4), 1940 (1992).
8. B.B. Pate, I. Lindau, and W.E. Spicer, Proceedings of the 17th International Conference on the Physics of Semiconductors, edited by J.D. Chadi and W.A. Harrison (Springer Verlag 1985), p. 1201.
9. C. Bandis and B.B. Pate (in preparation).
10. H.Y. Fan, Radiat. Eff. **4**, 7 (1970).
11. B.B. Pate, Surf. Science **165**, 83 (1986), and references therein.
12. The diamond single crystal, our sample D5, was provided on loan by Dr. F.A. Raal from DeBeers Diamond Laboratory, Johannesburg.
13. J. Samson, Techniques of Vacuum Ultraviolet Spectroscopy (John Wiley & Sons, Inc., New York, 1967), pp. 214-216.
14. P.J. Dean, E.C. Lightowlers and D.R. Wight, Phys. Rev. **140**, A352 (1965).
15. B.B. Pate, M. Oshima, J.A. Silberman, G. Rossi, I. Lindau and W.E. Spicer, J. Vac. Sci. Technol. **A2** (2), 957 (1984).
16. C.D. Clark, P.J. Dean and P.V. Harris, Proc. Roy. Soc. (London) **A277**, 312 (1964).

PROPERTIES OF THE HETEROEPITAXIAL AlN/SiC INTERFACE

M.C. Benjamin, C. Wang, R.S. Kern,
R.F. Davis, and R.J. Nemanich
Department of Physics and Department of Materials
Science and Engineering,
North Carolina State University,
Raleigh, NC 27695-8202

ABSTRACT

This study presents the results of surface investigation of the heteroepitaxial AlN/SiC interface. The analytical tools employed included UPS, XPS, Auger spectroscopy, and LEED. The surface electronic states were characterized by uv photoemission obtained at surface normal. Conclusions drawn from this study are that the AlN/SiC structure results in a negative electron affinity surface which is extremely sensitive to defect density. The surface Fermi level is found to be near the middle of the AlN gap, and a possible band alignment between the AlN and SiC is presented.

A. INTRODUCTION

The semiconductor industry is presently limited in device application by the materials used in device fabrication. Novel materials are being sought to replace Si and Ge based devices. Devices are needed which operate at higher temperatures, powers, and frequencies than before. Radiation hardness is also a valued trait. Potential materials are diamond, SiC, AlN, and GaN. These wide bandgap semiconductors have the properties needed to realize these goals. Of these materials SiC appears most advantageous [1]. This material which can be readily grown and working devices have been made of SiC [2].

The material studied was an aluminum nitride (AlN) film grown epitaxially on a 6H silicon carbide (SiC) substrate. AlN has a direct optical band gap of 6.2 eV and a wurtzite hexagonal structure with an a-axis lattice constant of 3.11 Å. The growth was achieved by molecular beam epitaxy (MBE). The epitaxial growth is confirmed by RHEED measurements [3]. SiC can be used as a substrate for the growth of AlN due to the close lattice match (3.08Å vs. 3.11Å). This allows for the manufacturing of novel structures such as Negative Electron Affinity (NEA) surfaces for UV and X-ray detectors and cold cathode emitters. The possibility for NEA based vacuum collector-emitters also exists [4]. The phenomenon of a negative electron affinity (NEA) occurs at a semiconductor surface when the vacuum energy level lies below the conduction band edge. Since the bonding of common semiconductors are based on sp^3 hybridization, the valance band develops from bonding levels and the conduction band from the antibonding atomic orbitals. Since wide band gap semiconductors have common bonding origin, the NEA phenomenon is more likely to occur for these materials. The consequence of a NEA surface is that any electrons from the valence band promoted into the conduction band can escape from the material. Thus, having an NEA surface enhances cathode operation (emission).

B. EXPERIMENTAL PROCEDURE

The presence of a NEA can be determined by ultraviolet photoemission spectroscopy (UPS).[5-7] This technique involves directing 21.2 eV light (the He I resonance line) to the surface of the sample and detecting the spectrum of the emitted photo excited electrons as a function of electron kinetic energy. Typically, UPS is used to obtain a profile of the valence band (VB) electronic states. As such, most studies of UPS of semiconductors present data of the most energetic electrons emitted from the surface. Electrons scattered to lower energy and secondary electrons will be displayed in the spectra at lower kinetic energies. In addition, for a semiconductor which exhibits a NEA surface, a distinctive peak may be observed at the low kinetic energy (highest binding energy) end of the photoemission spectra. Fig. 1 depicts a schematic representation of the

Mat. Res. Soc. Symp. Proc. Vol. 339. ©1994 Materials Research Society

photoemission spectra from a semiconductor with a negative or positive electron affinity. The low kinetic energy feature is due to secondary electrons which (quasi) thermalize to the conduction band minimum.

The sharp features typical of a NEA have been observed from spectra of (111) and (100) diamond surfaces [5-9]. In the studies of diamond, a correlation was made between the presence of hydrogen and the NEA peak [6,7]. In addition, it was also shown that thin metal layers such as Ti or other low workfunction metals could induce a NEA on the diamond surface [9,10]. These measurements verify that the surface dipole can be influenced by surface processing and that the effects contribute to the observation of a NEA.

For the AlN UPS studies presented here, the SiC substrate is important for two reasons. The first is that from wide bandgap semiconductors there would be charging problems, and the photoemission would be quickly quenched. The reason for this is that with such a large band gap, the AlN acts as an insulator and will charge up. This problem is avoided by growing a thin layer of AlN on a conducting doped SiC substrate. The n-type SiC substrates used in this study, being more conductive than bulk AlN, provide a source of electrons for photoemission. The second benefit of the SiC substrate is the small lattice mismatch between SiC and AlN (3.08 Å vs. 3.11 Å). The small lattice mismatch enables heteroepitaxial growth.

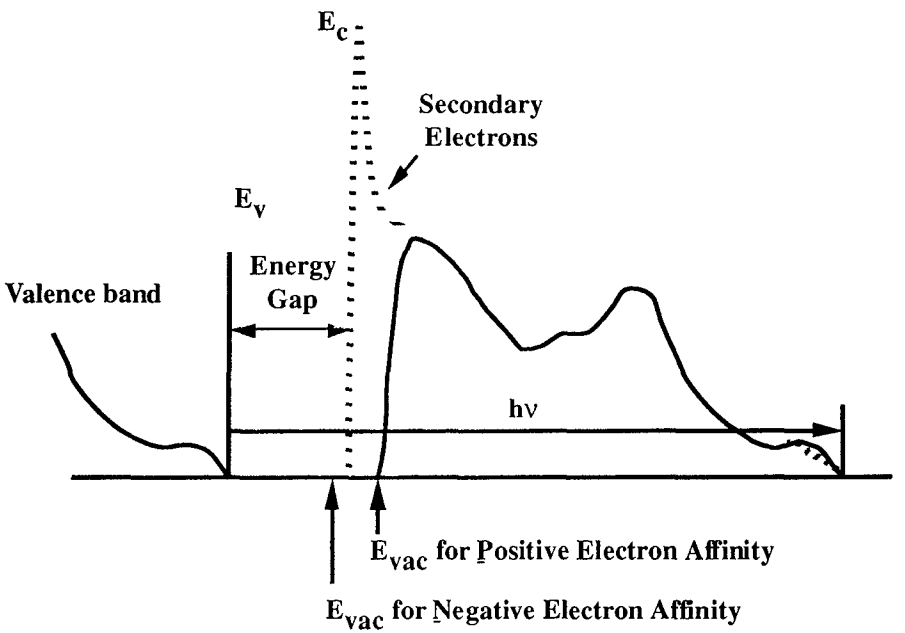

1. A schematic of the difference in the photoemission spectra of a semiconductor with a positive or negative electron affinity.

The AlN/SiC sample was deposited on the SiC substrate by a modified gas source MBE system. The substrate was a vicinal wafer of 6H polytype (0001) (oriented 3-4 degrees towards [1120])

SiC which resulted in the growth of hexagonal (2H) AlN. The MBE system consists of three parts: a load lock (base pressure of 5 x10^{-8} Torr), a transfer tube (base pressure of 1x10^{-10} Torr), which also was used for degassing the substrates, and the growth chamber (base pressure of 5x 10^{-11} Torr). Knudson effusion cells with BN crucibles and Ta wire heaters were charged with 6N pure aluminum. Ultra-high purity nitrogen, further purified by a chemical purifier, was used as the source gas. The nitrogen gas was excited by an ECR plasma source, which was designed to fit inside the 2.25 inch diameter tube of the source flange cryoshroud. The details of the system can be found elsewhere. [11]

The SiC substrates were obtained from Cree Research Inc. Prior to loading into the chamber, the substrates were cleaned by a standard degreasing and RCA cleaning procedure. After undergoing a degassing procedure in UHV (700 °C for 30 minutes), the substrates were transferred into the deposition chamber. Epitaxial AlN films were deposited under the conditions shown below in Table I. The films examined were roughly 100 Å thick.

Table I. Deposition Conditions for MBE AlN film growth.

Nitrogen pressure:	2x10^{-4} Torr
Microwave power:	50W
Aluminum cell temp:	1120 °C
Substrate temperature:	1100 °C
Deposition Rate:	1000Å/hr

The samples were transported in air to the surface analysis system. The analysis system is made up of several chambers linked by a linear UHV transfer line. The details of the system are described elsewhere.[8,10] Among the capabilities available are UPS, XPS, LEED, hydrogen and argon plasma cleaning, thermal programmed desorption, and Auger Spectroscopy.

The UPS chamber has a base pressure of 2x10^{-10} Torr. Operating conditions involve pressures up to 1x10^{-9} Torr, but the higher pressure is due to the helium inflow and does not contaminate the sample. The UPS system utilizes a helium resonance lamp (the He I line) to provide a source of 21.2 eV light. Photoemitted electrons are measured with a 50 mm mean radius hemispherical electron analyzer operated at a 0.15 eV energy resolution and a 2° angular resolution. The analyzer (VSW HA50) is mounted on a double goniometer and can be tilted with respect to the sample in two independent directions. The AlN/SiC samples were fastened with tantalum wire to a molybdenum sample holder. The sample holder is biased by up to 4 V to allow low energy electrons to overcome the work function of the analyzer. The Fermi level of the system (sample and analyzer) is determined by UPS measurement of the sample holder with no sample bias (i.e. grounded). The sample holder can be heated to 1150 °C.

C. RESULTS

The UPS measurements were carried out on the AlN/SiC sample as loaded, and after anneals of 700 °C and 1000 °C. Auger Electron Spectroscopy (AES) and Low Energy Electron Diffraction (LEED) were also performed on the sample as-loaded, and after the anneals. The UPS data for the as-loaded AlN/SiC sample are displayed in Fig. 2. The spectra were obtained with different sample bias to overcome the workfunction of the analyzer. In the figure, all spectra have been displaced by the applied bias so that the Fermi level aligns. Two aspects indicate the presence of the NEA. The first is the detection of a low energy peak clearly observable with a sample bias of 3.0 Volts, with onset occurring at a bias of 1.5 Volts. The two low energy peaks of roughly the same height present at the 3.0 Volt bias are attributed to the normal secondary emission typical of UPS while the low energy feature is attributed to electrons thermalized to the conduction band minimum. This second peak is considered as the NEA peak since the electron count drops off so quickly. The large (~3V) bias is needed because the workfunction of the AlN is apparently less than that of the analyzer. The analyzer workfunction is between 4 and 5 eV.

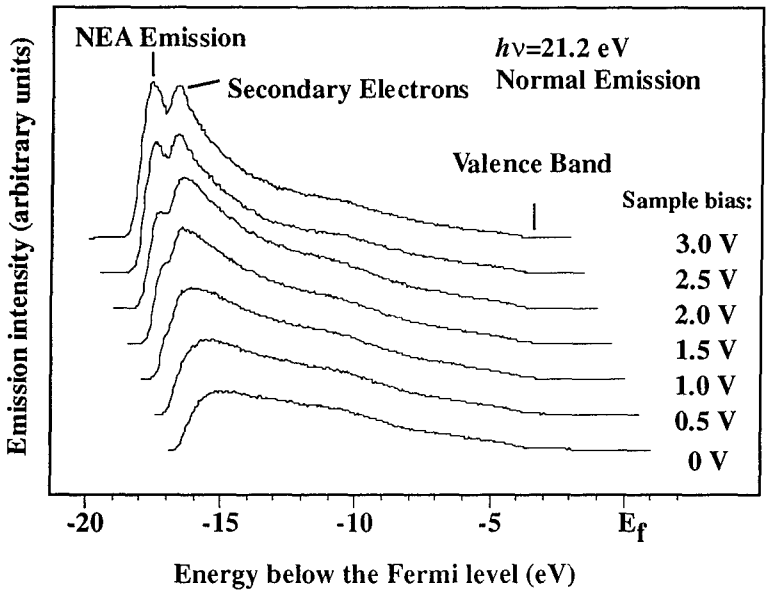

2. The uv-photoemission of from AlN on 6H-SiC. The spectra were obtained at different sample bias to overcome the workfunction of the electron analyzer.

The second indication of the NEA is that the width of the photoemission spectra are consistent with the model described in Fig. 1. Here the width $W = h\nu - E_g$ where W extends from the low energy limit to the valence band maximum. We have used this relation to determine the position of the valence band maximum in the spectrum obtained with a 3V bias. The low energy limit was determined by linear extrapolation of the back edge to zero intensity. Then using the band gap of AlN as 6.2 eV and the 21.2 eV photon energy, the valence band maximum should then occur at 15.0 eV above this limit. The vertical line labeled Valence Band was obtained in this way. As is evident from the spectra, the valence band emission extends to this energy. We also note that the results indirectly verify that the band gap of the AlN film is the same as the bulk value of 6.2 eV. As mentioned earlier, the Fermi level is determined from the onset of electron emission from a metal sample.

The effect of annealing in vacuum was explored. After annealing to 700 and 1000 °C the photoemission spectra showed a decrease in the relative intensity of the NEA related peak (Fig. 3). Auger Electron Spectroscopy (AES) of the as-loaded surface showed oxygen and carbon contaminates in addition to the Al and N signals. After an anneal of 700 °C the AES showed a small reduction of the oxygen and a similar scale increase in the surface carbon, a trend that continued with the 1000 °C anneal. A LEED pattern was not visible from the sample as loaded or after the anneals of 700 °C and 1000 °C . We note that after a short H-plasma clean a faint 1x1 pattern was visible with an electron beam energy of 80 eV and the C signal was removed. The lack of a LEED pattern for the as-loaded and the annealed samples is possibly related to the carbon and oxygen on the surface. The reduction of the NEA related features indicates that the effect is related to the surface structure and termination of the AlN.

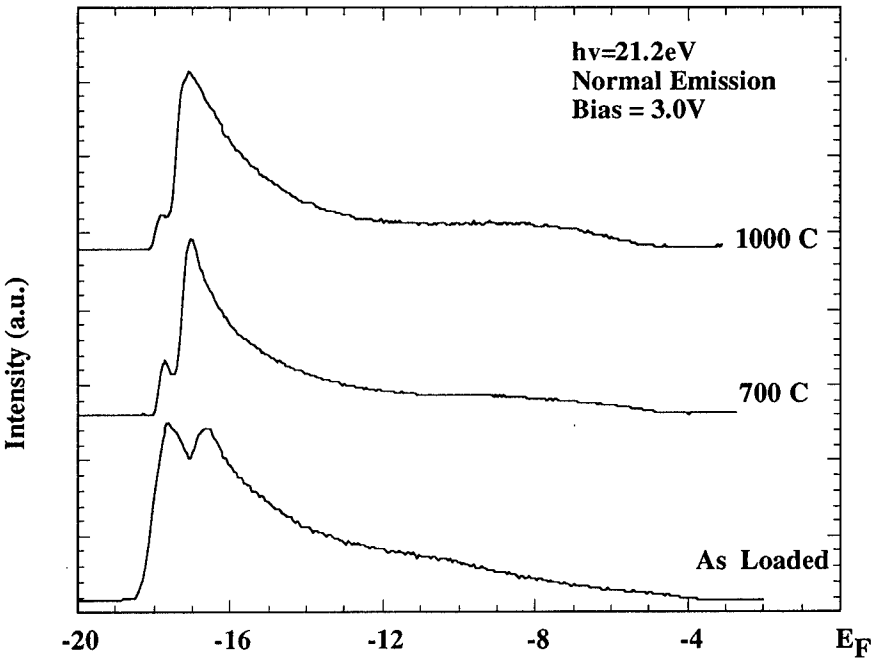

3. The uv-photoemission spectra of the AlN on 6H-SiC as-loaded and after vacuum annealing at the indicated temperatures. All spectra were obtained with a sample bias of 3.0 V.

The second sample investigated was capped with a thin (<10Å) layer of silicon to prevent oxidation during transit. While the processing parameters were similar [14], the photoemission spectra were different as can be seen in fig. 4. A peak sharper than that of the NEA surface in fig.2 appeared with a bias of 3.0 Volts, but the width of the spectra was not consistent with the known band gap. As such we do not believe this to be a NEA surface. We attribute this to the presence of the silicon. Even after two plasma exposures, one of which was a deep etching exposure, we were unable to remove all of the silicon.

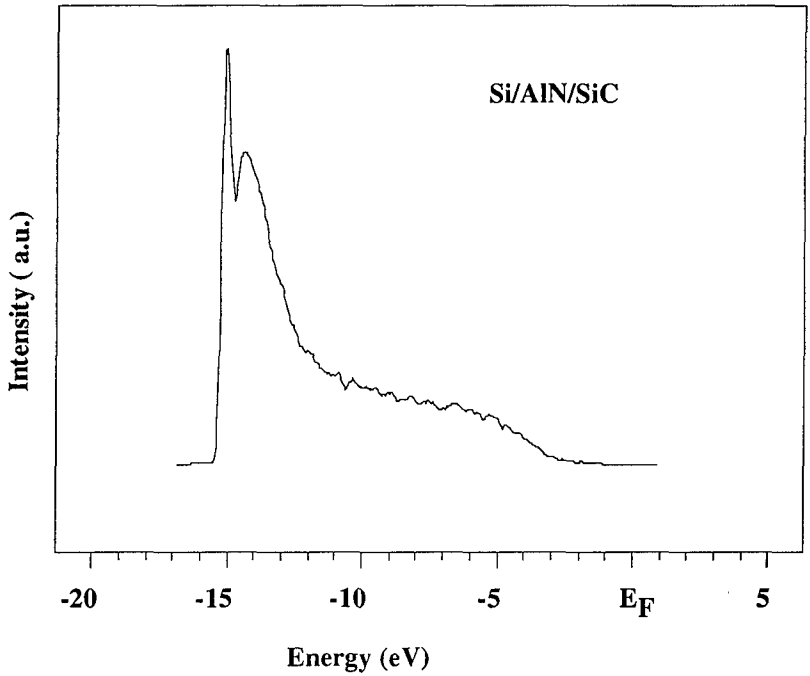

4. The uv-photoemission spectra of the second AlN on 6H-SiC sample studied. This spectrum was obtained with a sample bias of 3.0 V

In comparison to the UPS spectra obtained from diamond surfaces which exhibit a NEA, [3-8] the feature in diamond is significantly sharper than that observed here for the AlN. There are several possible causes that could contribute to a broader signature. These could be related to a more disordered surface or to the intrinsic properties of the AlN (e.g. direct bandgap). Future research will explore these issues.

The last point that we address in this report is the position of the Fermi level in the AlN. From Fig. 1, it is evident that the surface Fermi level occurs at ~3.5 eV above the valence band maximum. This is near the center of the 6.2 eV bandgap. From this data we suggest a possible band alignment of AlN and SiC. Here we have assumed that there is no band bending in the AlN or in the SiC near the interface. Because of the wide band gap of the AlN, it seems unlikely that there is significant band bending in the thin film. The bulk Fermi level of the SiC has been determined from the doping level of the substrates to be ~0.3 eV below the SiC conduction band edge[12]. The results are summarized in Fig. 5. The band offsets are -0.8 eV at the valence band and 2.4 eV at the conduction band. The largest uncertainty in this proposed band offset is probably in the band bending in the SiC. Such band bending would result in an increase in the magnitude of the valence band offset and a decrease in the conduction band offset. While we are not aware of any calculations of the heterojunction band offsets of wurtzite AlN on 6H-SiC, there

has been a calculation of the offsets of the (110) interfaces of cubic AlN/SiC [13]. The theoretical results also indicate a type I offset with band discontinuities of 1.5 eV at the valence band and -1.2 eV at the conduction band. This is qualitatively similar to the results presented in Fig. 5.

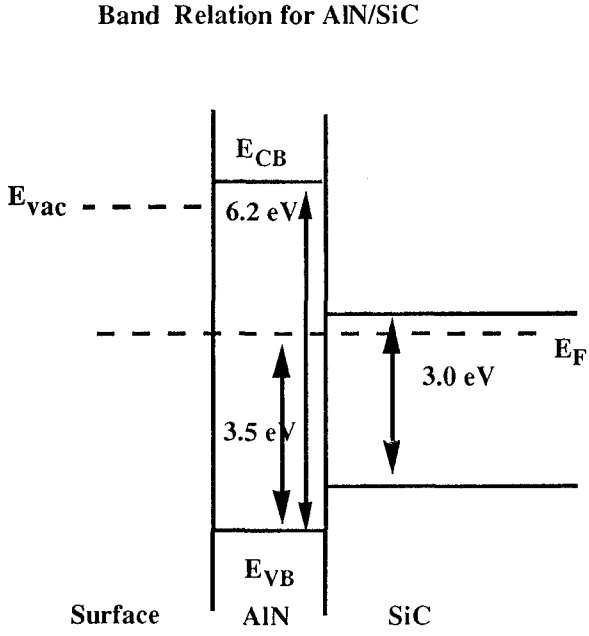

5. A schematic of the possible band alignment of AlN on 6H-SiC. The text describes the assumptions and related measurements.

D. CONCLUSIONS

In summary, we have observed features in the UPS spectra indicative of a NEA surface on as-loaded and annealed AlN on SiC. The measurements were made possible by the development of MBE heteroepitaxial growth of AlN on 6H-SiC. The NEA features are dependent on surface processing. The surface Fermi level of the AlN is found to be ~3.5 eV above the valence band maximum, and we have suggested a model for the band offsets assuming no band bending.

Acknowledgment

This work was supported in part by the Office of Naval Research through grants N0014-92-J-1477 and N0014-92-J-1604.

F. REFERENCES

1 J.H. Edgar, J. Mater. Res., **7**, 235 (1992)

2 H.S. Kong, J.W. Palmour, J.T. Glass, and R.F. Davis, Appl. Phys. Lett. **51**, 442 (1987)

3 C. Wang, R.F. Davis, Appl. Phys. Lett. **63**, 990 (1993).

4 M.D. Williams, M.D. Feuer, S.C. Shunk, N.J. Sauer, and T.Y. Chang, **J.** Appl. Phys. **71**, 3042 (1992).

5 F.J. Himpsel, J.A. Knapp, J.A. van Vechten and D.E. Eastman, Phys. Rev. B **20**, 624 (1979).

6 B.B. Pate, Surf. Sci. **165**, 83 (1986).

7 B.B. Pate, M.H. Hecht, C. Binns, I. Lindau and W.E. Spicer, J. Vac. Sci. Technol. **21**, 364 (1982).

8 J. van der Weide and R.J. Nemanich, J. Vac. Sci. Technol. B **10**, 1940 (1992).

9 J. van der Weide and R.J. Nemanich, Appl. Phys. Lett. **62**, 1878 (1993).

10 J. van der Weide and R.J. Nemanich, Phys. Rev. **B** (in press).

11 Z. Sitar, M.J. Paisley, D.K. Smith and R.F. Davis, Rev. Sci.Instrum.. **61**, 2407 (1990).

12 J. Pelletier, D. Gervais, and C. Pomot, J. Appl. Phys. **55**, 994 (1983)

13 Walter R.L. Lambrecht and Benjamin Segall, Phys. Rev. **B43**, 7070 (1991).

14 L.B. Rowland, R.S. Kern, S.Tanaka, and R.F. Davis, in Proceedings of the Fourth International Conference on Amorphous and Crystalline Silicon Carbide, edited by C.Y. Yang, M.M. Rahman, and G.L. Harris (Springer, Berlin, 1992) p. 84.

SURFACE CLEANING, TOPOGRAPHY, AND TEMPERATURE MEASUREMENTS OF SINGLE CRYSTAL DIAMOND

MARK P. D'EVELYN,* LISA M. STRUCK,** AND ROBIN E. RAWLES**
*General Electric Corporate Research and Development, P.O. Box 8, Schenectady, NY 12301 and Departments of Chemistry and Materials Engineering, Rensselaer Polytechnic Institute, Troy, NY 12180-3590
**Department of Chemistry and Rice Quantum Institute, Rice University, Houston, TX 77251-1892

ABSTRACT

Application of surface science methods to single crystal diamond surfaces requires the preparation of clean, well-ordered surfaces and accurate measurement of substrate temperature. Cleaning of diamond (100) in $H_2SO_4/HNO_3/HClO_4$ produced several infrared absorption features between 1025 and 1275 cm^{-1}, as observed by infrared multiple-internal-reflection spectroscopy. These modes are assigned to surface hydroxyl and bridge-bonded oxygen. Heating an oxidized surface to ca. 1130 °C caused disappearance of a surface hydroxyl mode centered at 1080 cm^{-1}. We show by atomic force microscopy that an as-polished diamond (100) sample is covered by grooves and ridges several nm in height, implying a modest density of atomic steps. The surface of a diamond that underwent etching via numerous adsorption/desorption experiments in ultrahigh vacuum and was acid cleaned several times was essentially unchanged, indicating a minimal perturbation of the surface topography. The capability of Fizeau interferometry for accurate measurement of single-crystal diamond temperatures is demonstrated.

INTRODUCTION

Surface science methods have contributed greatly toward an atomic level understanding of the growth and processing of semiconductor materials, particularly silicon, and methods for preparation of clean, well-ordered surfaces are well established. Diamond presents a number of technical challenges for surface science studies. Surface preparation is difficult because diamond cannot be sputtered without extensive, irreversible surface damage.[1,2] Several groups have applied mechanical polishing followed by heating to ca. 1400 K in ultrahigh vacuum (UHV) to removed adsorbed gases.[2-7] However, polishing leads to a surface of complex topography[8] whose annealing behavior in ultrahigh vacuum has not been adequately characterized. Several groups have included an acid treatment in the cleaning procedure in order to remove graphite and metal contaminants,[9-12] but the effect of these treatments on the surface chemistry of diamond has received only limited attention to date.[13,14]

Measurement of accurate sample temperatures poses an additional problem for diamond, as direct attachment of a thermocouple is difficult and optical pyrometry is inapplicable. Typically a thermocouple is attached to the sample support. However, the desorption temperatures for hydrogen from diamond (100) and (111) reported by various groups[4-6,9,11,12] differ by as much as several hundred degrees, and variable thermal contact with the sample seems the most likely explanation for the discrepancies. Two methods for measuring accurate diamond temperatures have been demonstrated recently, although each has drawbacks. Yang *et al.* obtained calibrated sample temperatures by optical pyrometry on a sputter-deposited tungsten film on the back side of a diamond sample,[6,15] and Smentkowski and Yates obtained accurate temperature readings using a thermocouple embedded in a hole drilled sideways in a diamond sample.[16]

Mat. Res. Soc. Symp. Proc. Vol. 339. ©1994 Materials Research Society

In this paper we report the effect of acid treatments on the surface chemistry and topography of diamond (100), as studied by infrared spectroscopy and atomic force microscopy, and demonstrate an alternative method for obtaining calibrated temperatures via Fizeau interferometry.

ACID CLEANING: INFRARED SPECTROSCOPY

We have investigated the surface chemistry of acid cleaning of diamond (100) by infrared multiple-internal-reflection spectroscopy. The apparatus and procedures have been described elsewhere.[6,7,17] Briefly, collimated light from a Fourier-transform infrared spectrometer is focused through a differentially-pumped KBr window onto one beveled edge of a 15×3×0.22 mm^3 diamond internal reflection element (IRE) inside an ultrahigh vacuum chamber. After undergoing approximately 33 internal reflections from each face to enhance sensitivity to surface species, the infrared light is transmitted through the opposite beveled edge of the diamond IRE and is collected and focused onto a detector. Diamond is effectively opaque at this long path length for frequencies between 1600 and 2800 cm^{-1}, preventing the observation of C=O stretching modes, and the sensitivity is greatest at frequencies below 1500 cm^{-1}.

In one experiment, the diamond IRE became slightly graphitized following experiments in UHV and was removed from the apparatus and boiled in a 3:4:1 solution of $H_2SO_4/HNO_3/HClO_4$[18] for 50 minutes. The ratio of FTIR spectra taken before and after the acid treatment is shown in Fig. 1(a). The primary band at 1020-1150 cm^{-1} is assigned to surface hydroxyl (-OH) groups,[7,17] based on the spectrum of 1-adamantanol.[19] The weaker feature near 1230 cm^{-1} is assigned to surface ether (C-O-C) groups, based on *ab initio* self-consistent-field calculations[20] of 2-oxaadamantane and bioxaadamantane.[17]

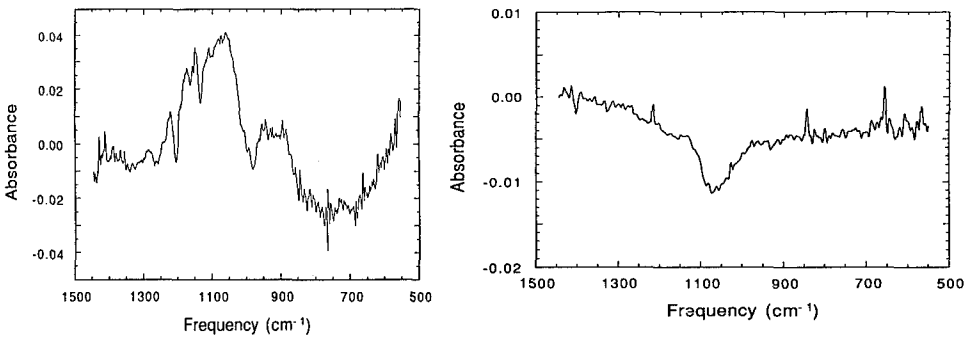

(a) (b)

FIG. 1. Infrared spectra of species: (a) formed by boiling slightly graphitized diamond (100) in 3:4:1 $H_2SO_4/HNO_3/HClO_4$ or (b) removed by heating oxidized sample to ≈1400 K in UHV.

In a second experiment, the diamond IRE was treated with the same acid solution and then placed in the UHV chamber. The chamber was baked out and the sample was heated to approximately 1400 K in UHV. The ratio of FTIR spectra taken before and after the final heating step is shown in Fig. 1(b). The primary mode centered near 1080 cm^{-1}, assigned to hydroxyl groups, corresponds to surface species most likely formed during the acid treatment that desorbed upon heating. The sharp features in the spectrum are not reproducible and presumably are scanning artifacts.

Figs. 1(a) and 1(b) indicate that acid treatment results in formation of surface oxides on diamond (100), in agreement with earlier infrared[13] and x-ray photoelectron spectroscopy[14] results on powder and polycrystalline diamond. We attribute the disappearance of surface hydroxyl groups upon heating to 1400 K to desorption as CO, CO_2 and H_2, based on previous temperature-programmed desorption studies of diamond (100)[9] and diamond powder.[21] Each cycle of oxidation and heating in UHV therefore results in etching of roughly one monolayer of diamond.

SURFACE TOPOGRAPHY: ATOMIC FORCE MICROSCOPY

We have examined the surface topography by atomic force microscopy (AFM) on two separate diamond (100) samples: one as received from the vendor (Harris Diamond Corp.) and the other after extensive experiments over the course of two years, including heating in ultrahigh vacuum (UHV), numerous adsorption/desorption cycles, and several acid treatments to remove graphitic carbon and metal contamination.[7,17] AFM scans were performed with a Park Scientific Instruments AFM using a 2.5 μm piezoelectric scanner under null force conditions with a Si_3N_4 tip. The tip radius is estimated as 300 nm, and the force constant was approximately 0.37 N/m. Images of the two specimens are shown in Fig. 2.

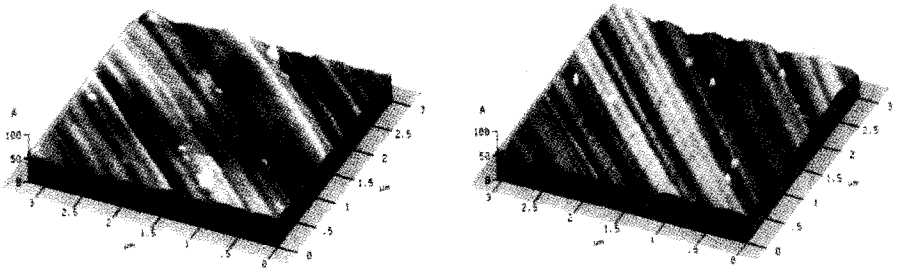

(a) (b)

FIG. 2. Atomic force microscopy images of diamond (100) samples: (a) as received from vendor; (b) after UHV and acid cleaning experiments over the course of several years.

The as-received diamond (100) sample is seen to be covered by grooves and ridges with a peak-to-peak amplitude of 10-30 Å. Local slopes were found to be in the range of 1-2°. These local slopes imply terrace widths in the range of 30-50 Å *if* surface roughness on a lateral length scale of 1-100 nm is small. The observation of CH_2 modes by Struck and D'Evelyn[7] on the sample shown in Fig. 2(b) is suggestive of additional roughness on the atomic scale, but we were unable to achieve the resolution necessary to observe atom-high steps in the present study. The groove-and-ridge morphology is strongly suggestive of a chemical polishing mechanism.[8,22]

The surface of the diamond (100) sample that had undergone prolonged treatments both in UHV and in hot acid (Fig. 1(b)) is qualitatively the same as the as-received specimen. The fact that it is not greatly smoother indicates that very little annealing of diamond (100) occurs in UHV at temperatures up to 1400 K. Surface oxides are formed both by the acid treatments and by water adsorption in UHV[7] which desorb upon heating to 1400 K as CO and/or CO_2,[9,21] thus etching the surface by up to a monolayer (0.9 Å). The fact that the character of the surface topography is essentially unchanged indicates either that at most several nm diamond were removed by the series of treatments or that the material removal was approximately conformal, i.e., the amount of diamond etched was essentially the same at terrace and step sites across the surface.

The surface topography shown in Fig. 1 is qualitatively similar to that reported by Couto *et al.*[8] by scanning tunneling microscopy on boron-doped diamond (100), polished in a direction of easy abrasion, but is much smoother. The latter authors observed peak-to-peak amplitudes about a factor of ten larger and reported local slopes as high as 30°. The discrepancy is presumably due to differences in the extent of polishing applied to the diamonds. This variability also implies that different polishing procedures may result in surfaces of very different atomic step density. We note that even smoother diamond (100) surfaces can be grown by chemical vapor deposition (CVD), although care must be taken to avoid formation of penetration twins and growth hillocks.[23-27] Flat diamond (100) facets have also been prepared by treatment in a hydrogen plasma.[28]

TEMPERATURE MEASUREMENT BY FIZEAU INTERFEROMETRY

We have applied optical Fizeau interferometry to the measurement of sample temperature of three separate natural diamond substrates, with (100), (110), and (111) orientation. The diamond substrates were held inside a hot-filament CVD reactor between two mullite tubes and heated by rhenium wires embedded in the mullite in 10 Torr of H_2. The sample temperature was monitored independently by a chromel-alumel thermocouple cemented to the mullite support.

Collimated light from a HeNe laser was reflected at near-normal incidence from the back side of the diamond substrate. The existence of a slight wedge angle between the back and front faces of the substrate causes interference in the light reflected from the two faces, producing a spatial fringe pattern. At each lateral position on the substrate, a fringe index $m = 2nd \cos\theta / \lambda$ can be defined, where $n = 2.39$ is the index of refraction of diamond, d is the local thickness, which was about 100 μm for these samples, θ is the angle of incidence ($\approx 0°$), and λ is the wavelength of light (633 nm). The local value of m determines the degree of constructive versus destructive interference between the two reflected beams: the intensity is a minimum if m is an integer and a maximum at half-integer values of m. Changes in d and/or n due to a change in temperature (or to growth[29,30]) alter the local value of m across the substrate, causing the fringe pattern to propagate laterally. In these experiments the fringe pattern image was projected onto a CCD video array and the output recorded on videotape. Analysis of the data was performed by measuring the fringe positions as displayed on a video monitor as a function of temperature. The results from the three samples are summarized in Fig. 3.

Movement of the Fizeau fringes is seen to be quite sufficient for temperature measurement: the ca. 100-μm-thick samples yielded motion of 0.01 - 0.06 fringe/degree for temperatures between 25 and 1100 °C. A shift of 0.1 fringe can readily be measured with a stable system, resulting in a temperature resolution of 2-10 °C for a. 100-μm-thick sample, or 0.2-1 °C for a 1-mm-thick sample. Even with modest temperature resolution, this technique could be used to calibrate a thermocouple attached to a sample support, as with pyrometry.[6]

The rate of fringe movement with temperature is directly related to changes in the thickness and index of refraction: $\lambda/(2nd \cos\theta)\, dm/dT = \alpha + n^{-1} dn/dT$, where α is the thermal expansion coefficient. The data shown in Fig. 3 imply values of 1.7×10^{-5} at 25 °C to 6×10^{-5} at 1000 °C for this quantity, substantially larger than literature values.[31,32] The reason for this discrepancy is not understood, but is most likely due to the behavior of $n(T)$. We are also unable at present to determine whether the differences in the rate of fringe movement between the samples reflect real differences in their physical properties or merely variations in the thermal contact between the heated mullite tubes and the diamonds. Further experiments will be necessary to determine the behavior of $n(T)$ at elevated temperature, but it is clear that Fizeau interferometry can be used to obtain calibrated temperature measurements of diamond.

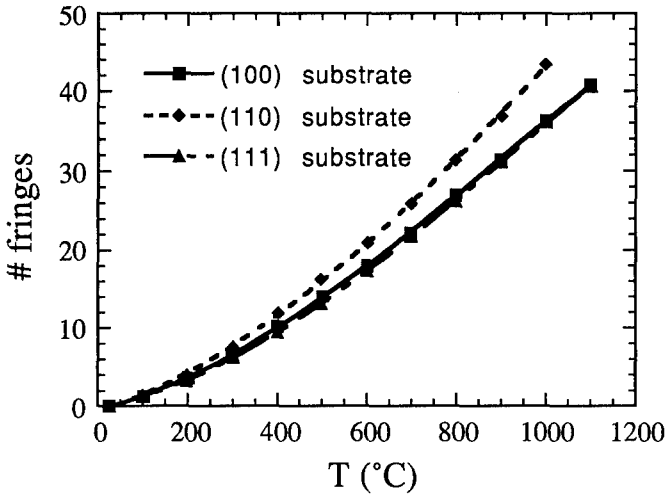

FIG. 3. Movement of Fizeau fringes upon heating of diamond substrates with (100), (110), or (111) orientation.

ACKNOWLEDGMENTS

The authors gratefully acknowledge the National Science Foundation (Grant CHE-9214328) and the Office of Naval Research for support of this work, and thank Dr. W. G. Morris for performing the atomic force microscopy.

REFERENCES

1. J. B. Marsh and H. E. Farnsworth, Surf. Sci. **1**, 3 (1964).
2. P. G. Lurie and J. M. Wilson, Surf. Sci. **65**, 453 (1977).
3. G. Vidali and D. R. Frankl, Phys. Rev. B **27**, 2480 (1983).
4. B. Pate, Surf. Sci. **165**, 83 (1986).
5. (a) A. V. Hamza, G. D. Kubiak, and R. H. Stulen, Surf. Sci. **206**, L833 (1988); (b) A. V. Hamza, G. D. Kubiak, and R. H. Stulen, Surf. Sci. **237**, 35 (1990); G. D. Kubiak, M. T. Schulberg, and R. H. Stulen, *ibid.*, **277**, 234 (1992).
6. Y. L. Yang, L. M. Struck, L. F. Sutcu, and M. P. D'Evelyn, Thin Solid Films **225**, 203 (1993).
7. L. M. Struck and M. P. D'Evelyn, J. Vac. Sci. Technol. A **11**, 1992 (1993).
8. M. Couto, W. J. P. van Enckevort, B. Wichman, and M. Seal, Appl. Surf. Sci. **62**, 263 (1992).
9. R. E. Thomas, R. A. Rudder, and R. J. Markunas, J. Vac. Sci. Technol. A **10**, 2451 (1992).
10. J. J. Lander and J. Morrison, Surf. Sci. **4**, 241 (1966).

11. T. Mitsuda, T. Yamada, T. J. Chuang, H. Seki, R. P. Chin, J. Y. Huang, and Y. R. Shen, Surf. Sci. **257**, L633 (1991).
12. S.-T. Lee and G. Apai, Phys. Rev. B **48**, 2684 (1993).
13. (a) T. Ando, S. Inoue, M. Ishii, M. Kamo, Y. Sato, O. Yamdada, and T. Nakano, J. Chem. Soc. Faraday Trans. **89**, 749 (1993); (b) T. Ando, M. Ishii, M. Kamo, and Y. Sato, J. Chem. Soc. Faraday Trans. **89**, 1783 (1993).
14. P. E. Pehrsson, in *Diamond Materials*, edited by J. P. Dismukes and K. V. Ravi (The Electrochemical Society, Pennington, New Jersey, 1993), p. 668.
15. Y. L. Yang, Ph.D. Dissertation, Department of Chemistry, Rice University, 1992 (unpublished).
16. V. S. Smentkowski and J. T. Yates, Jr., J. Vac.Sci. Technol. A **11**, 3002 (1993).
17. L. M. Struck, Ph.D. Dissertation, Department of Chemistry, Rice University, 1993 (unpublished).
18. J. F. Prins, J. Phys. D: Appl. Phys. **22**, 1562 (1989).
19. T. J. Broxton, L. W. Deady, M. Kendall, and R. D. Topsom, Appl. Spectrosc. **25**, 600 (1971).
20. M. J. Frisch, G. W. Trucks, M. Head-Gordon, P. M. W. Gill, M. W. Wong, J. B. Foresman, B. G. Johnson, H. B. Schlegel, M. A. Robb, E. S. Replogle, R. Gomperts, J. L. Andres, K. Raghavachari, J. S. Binkley, C. Gonzalez, R. L. Martin, D. J. Fox, D. J.Defrees, J. Baker, J. J. P. Stewart, and J. A. Pople, *Gaussian 92*, Revision A, (Gaussian, Inc., Pittsburgh, 1992).
21. (a) S. Matsumoto, H. Kanda, Y. Sato, and N. Setaka, Carbon **15**, 299 (1977); (b) S. Matsumoto and N. Setaka, Carbon **17**, 485 (1979).
22. M. Seal, Proc. Roy. Soc. London A **248**, 379 (1958).
23. (a) T. Tsuno, T. Imai, Y. Nishibayashi, K. Hamada, and N. Fujimori, Jpn. J. Appl. Phys. **30**, 1063 (1991); (b) T. Tsuno, T. Tomikawa, S.-I. Shikata, T. Imai, and N. Fujimori, Appl. Phys. Lett. **64**, 572 (1994).
24. L. F. Sutcu, C. J. Chu, M. S. Thompson, R. H. Hauge, J. L. Margrave, and M. P. D'Evelyn, J. Appl. Phys. **71**, 5930 (1992).
25. G. Janssen, W. J. P. van Enckevort, W. Vollenberg, and L. J. Giling, Dia. Relat. Mater. **1**, 789 (1992).
26. J. B. Posthill, D. P. Malta, R. A. Rudder, G. C. Hudson, R. E. Thomas, R. J. Markunas, T. P. Humphreys, and R. J. Nemanich, in *Diamond Materials*, edited by J. P. Dismukes and K. V. Ravi (The Electrochemical Society, Pennington, New Jersey, 1993), p. 303.
27. M. P. Everson, M. A. Tamor, D. Scholl, B. R. Stoner, S. R. Sahaida, and J. P. Bade, J. Appl. Phys. **75**, 169 (1994).
28. K. V. Ravi, P. I. Oden and D. R. Yaniv, in *Diamond Materials*, edited by J. P. Dismukes and K. V. Ravi (The Electrochemical Society, Pennington, New Jersey, 1993), p. 766.
29. R. E. Rawles, C. Kittrell, and M. P. D'Evelyn, in *Diamond Materials*, ed. by J. P. Dismukes and K. V. Ravi (The Electrochemical Society, Pennington, New Jersey, 1993), p. 269.
30. C. Pan, C.J. Chu, J. L. Margrave, and R. H. Hauge, submitted to Diamond and Related Materials.
31. G. A. Slack and S. F. Bartram, J. Appl. Phys. **46**, 89 (1975).
32. J. Fontanella, R. L. Johnston, J. H. Colwell, and C. Andeen, Appl. Optics **16**, 2949 (1977).

PART III

Devices and Device Processing

MATERIALS ASPECTS OF DIAMOND-BASED ELECTRONIC DEVICES

J.R. ZEIDLER*, C.A. HEWETT**, and R. NGUYEN**
*NCCOSC RDTE DIV 804, 53570 Silvergate Ave. RM 2070, San Diego, CA 92152-5070.
**NCCOSC RDTE DIV 555, 49285 Bennett ST. RM 111, San Diego, CA 92152-5791.

ABSTRACT

An overview of enabling materials technologies required for fabrication of electronic devices on diamond is presented. Emphasis is placed on electronic doping of diamond by boron ion implantation. Van der Pauw resistivity and Hall Effect measurements were used to determine the net carrier concentration, carrier mobility and resistivity of natural and synthetic diamonds implanted under various conditions. The measured results for a range of implantation conditions and post-annealing temperatures are discussed in the context of a model developed by J.F. Prins[1]. The requirements placed on ohmic contacts to diamond, and a process for fabricating ohmic contacts, is discussed briefly. Finally, current-voltage characteristics of a simple MISFET fabricated on ion implanted natural diamond are presented and analyzed.
[1]J.F. Prins, Physical Review **B**, 38 (1988) 5576.

INTRODUCTION

The potential use of semiconducting diamond as an electronic material has been discussed by several authors. In this paper we present an overview of two fundamental issues in the fabrication of diamond electronic devices, dopant incorporation via ion implantation (specifically boron ion implantation to produce a p-type), and ohmic contact formation (particularly with respect to the measurement of specific contact resistance). We conclude with an evaluation of the electrical characteristics of both a single insulated gate FET and a simple source-follower circuit fabricated in diamond using these technologies.

p-TYPE DOPING BY BORON ION IMPLANTATION

Prins[1] proposed that, by performing the implantation at low temperature (77 K)[1-4] to inhibit the migration of the interstitials out of the implanted region, the percentage of implanted boron atoms incorporated into the diamond lattice on substitutional sites can be increased. Prins[1] has further noted that a low temperature implantation of carbon ions in a prescribed ratio relative to the boron ion dose would create a vacancy rich region for the subsequent boron implantation and annealing procedures. (Although mechanisms may differ, co-implantation has been used to improve the implantation doping process for other materials, *e.g.* the use of Be/F co-implantation has been shown[5] to increase the activation efficiency of Be dopants in AlGaAs/GaAs structures). During a rapid post implant anneal, the recombination of carbon self-interstitials and vacancies reduces radiation damage while boron combining with vacancies produces electrically active dopant incorporation. This was indicated[1] by optical transmission and electrical resistance measurements of diamonds implanted with various ratios of carbon and boron ions. Further confirmation was obtained by Sandhu, *et al*[6] by using additional optical absorption and electrical resistance

Mat. Res. Soc. Symp. Proc. Vol. 339. ©1994 Materials Research Society

measurements of natural insulating (Type IIA) diamonds that were co-implanted with boron and carbon ions.

More recently, Prins[2,3] has shown that the carbon self-interstitial/vacancy recombination rate and the boron interstitial/vacancy combination rate exhibit different dependencies on the annealing temperature, rather than the simple equi-rate models assumed previously[1,4]. The sheet resistance for diamond implanted with a fixed carbon dose was demonstrated to increase by over seven orders of magnitude as the annealing temperature was increased from 850°C to 1075°C. The self-interstitial/vacancy recombination rates increased continuously with increasing annealing temperature throughout this temperature interval. For boron-implanted diamond, however, the sheet resistance is at a minimum for an annealing temperature of approximately 1000°C, and increases by over five orders of magnitude as the annealing temperature is increased from 1000°C to 1100°C. This indicates that the boron acceptor activation efficiency is maximized by annealing the implanted samples at approximately 1000°C. Subsequent annealing at higher temperatures can then provide for further reductions in the radiation damage.

We have directly measured both the carrier concentration and the hole mobility as a function of temperature for natural type IIa diamond implanted with either boron or carbon, or co-implanted with boron and carbon, at substrate temperatures of 77, 300, or 800 K. Natural type IIa diamonds, 5mm x 5mm x 0.25mm or 4mm x 4mm x 0.25mm in size, with a (100) orientation, were used throughout this study. The implantation conditions were selected to allow verification of the approach suggested by Prins [1]. In both cases a tri-level implant procedure was used to provide an approximately uniformly doped p-type layer of about 2000 Å in thickness, as subsequently confirmed by SIMS measurements performed at Charles Evans & Associates on a separately implanted test sample. Implantation of ^{11}B and ^{12}C was performed in a 400 kV custom ion implanter at Hughes Research Laboratories. ^{11}B ions were produced from BF_3 gas in an electron-bombardment ion source; ^{12}C ions were produced from a CO gas source. The ion beam was mass separated at full energy by using a double focussing magnet. Neutrals were removed and the beam electrostatically scanned to provide a uniform implant at 7° from the (100) axis. The fluence was determined by integrating the net positive charge striking the target, which is biased and isolated from ground potential through a current integrator. The target chamber was evacuated to about 10^{-6} Torr using a cryopump. The diamonds were mounted on a temperature controlled sample holder for the specified implantation conditions. Six diamonds were implanted at the temperatures, doses, and conditions indicated in Table I. Ion current densities were controlled to complete the desired implantation dose in time intervals between 60 and 600 s.

After implantation, the samples were immediately removed from the implantation stage, placed in a quartz furnace preheated to 990°C and annealed under flowing dry nitrogen to remove implantation damage and activate the implanted boron. In all but one case the annealing time was 10 min. For the low dose, low temperature boron implantation, a 60 min anneal was used to determine whether additional annealing time would improve the activation efficiency and mobility. The samples were cleaned by etching in a boiling saturated solution of CrO_3 in sulfuric acid to remove any potential graphitized layers resulting from the implantation process. The diamonds were then rinsed in deionized water, boiled in acetone, rinsed with methanol, then blown dry by using dry nitrogen. The samples were then loaded into an ultra-high vacuum chamber (base pressure $\sim 1x10^{-8}$ Torr) for ohmic contact metallization.

Contacts were defined on the sample corners by using a stainless steel shadow mask. The contact metallization consisted of 100 Å of Mo deposited by electron beam evaporation, followed by 1500 Å of Au deposited from a resistively heated boat. After removal from the vacuum chamber, the samples were baked at 120°C for 20 min, then annealed for 6 min at 960°C in a dry hydrogen ambient (dew point < -60°C). This process, discussed below, has previously been shown to yield ohmic contacts[7]. Gold wires were then wire bonded between the Mo/Au evaporated contacts and the gold contact pads of a chip carrier and mounted in the high temperature van der Pauw resistivity/Hall effect measurement apparatus.

Table I. Ion Implantation Conditions

Implant Species	Ion Energy (keV)	Implant Dose (cm^{-2})	Implant Temperature (K)	Anneal Time (min)
$^{12}C^+$	120 60 30	3.0×10^{14} 2.1×10^{14} 1.5×10^{14}	77	10
$^{12}C^+ + {}^{11}B^+$	120 60 30 100 50 25	3.0×10^{14} 2.1×10^{14} 1.5×10^{14} 3.0×10^{14} 2.1×10^{14} 1.5×10^{14}	77	10
$^{11}B^+$	100 50 25	3.0×10^{14} 2.1×10^{14} 1.5×10^{14}	77	10
$^{11}B^+$	100 50 25	3.0×10^{13} 2.1×10^{13} 1.5×10^{13}	77	60
$^{11}B^+$	100 50 25	3.0×10^{14} 2.1×10^{14} 1.5×10^{14}	300	10
$^{11}B^+$	100 50 25	3.0×10^{14} 2.1×10^{14} 1.5×10^{14}	800	10

Electronic transport measurements were made in a specially constructed quartz chamber (described in reference 8) with a high purity argon ambient maintained at a dew point of less than -60°C (as monitored by a hygrometer in the gas exhaust line). The sample was radiatively heated by furnace coils surrounding the quartz chamber to a maximum temperature of 790°C. Hall/resistivity measurements were then made as a function of sample temperature. Measurements were carried out in a magnetic field of 0.95 Tesla with injected currents of between 1 nA and 10 μA.

The sheet resistance data shown in Fig. 1 indicate that the lowest resistance is achieved by co-implanting with carbon and boron at low temperature. The resistance for this sample is more than an order of magnitude lower than that of the sample implanted with boron at low temperature. The sample implanted with an order of magnitude lower boron dose, but annealed for 60 min, exhibited a significantly increased resistance but was still superior to that obtained for the sample implanted with a full boron dose at 300 K. The room temperature boron implant produced a lower sheet resistance than the low temperature carbon implant, while the 800 K boron implant exhibited the highest sheet resistance among all the implanted samples. The fact that the high temperature boron

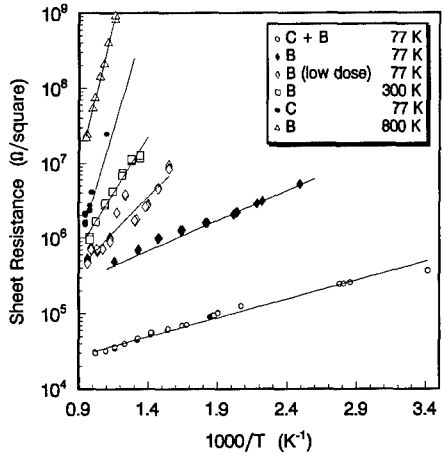

Fig 1. Sheet resistance as a function of inverse temperature for the implantation conditions specified in Table I.

implant produces the highest resistance corroborates nuclear reaction analysis results[9] which showed, by direct boron depth profiling, that most of the boron implanted at 670 K migrated out of the implant region. Additionally, it has been shown[9] that while boron implantation at 370 K results in a somewhat greater concentration of boron in the implant region than does implantation at 670 K, implantation of boron at 90 K results in significantly greater boron concentrations than either the 370 or 670 K implantations. The increased sheet resistance of the 800 K boron implantation over the low temperature carbon implantation observed in this work is presumably caused by a reduction in electrically active lattice defects produced in the course of the high temperature implant, an indication that the 10 min activation anneals do not remove all residual lattice damage. Prins[1-4] has shown that after activating the boron, a higher temperature anneal over a longer time period will further reduce the number of residual defects.

The carrier concentration data, summarized in Fig. 2, indicates that the low temperature carbon plus boron co-implantation procedure produces an increase in the total number of holes of almost two orders of magnitude over that obtained with boron alone. The reduced dose boron implant does provide fewer carriers, but due to the increased annealing time, the amount of reduction is less than the order of magnitude decrease expected from the decrease in the dose. The 300 K boron implant produced a measurable

hole concentration, but the density was approximately an order of magnitude lower than that of the sample implanted with an equal boron dose at 77 K. Neither the sample that was implanted with carbon at 77 K nor the sample implanted with boron at 800 K produced a measureable carrier concentration.

Measurements of the carrier mobility showed that the carbon plus boron co-implanted sample exhibits a significant decrease in the hole mobility relative to samples implanted with boron alone. In all cases the measurements showed considerable variation, but repeated trials and repeated measurements at each temperature were used to obtain reliable data. As with measurements of the carrier concentration, neither the carbon only implant nor the 800 K boron implant produced a measurable hole mobility.

In initial calibration runs of the system, Hall/van der Pauw resistivity measurements were made on a natural type IIb semiconducting diamond. The temperature dependence of the free hole concentration vs temperature was equivalent to that obtained by Collins *et. al.*[10,11] and indicated a hole activation energy of 0.33 eV. The measured mobility of

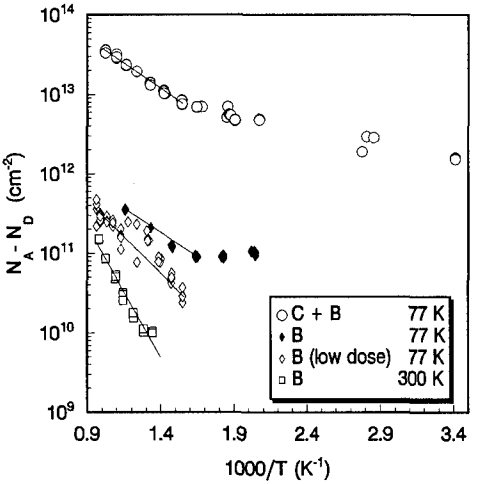

Fig 2. Net carrier concentration as a function of inverse temperature for the implantion conditions specified in Table I.

this sample was 400 cm^2/V-s at 300 K. This is lower than the values previously reported[10,11], but within the range reported by others[12,13] for synthetic diamond. The lower mobility values may be indicative of a higher defect density in our sample relative to that measured by Collins[11]. Vavilov, *et. al.*[14] reported room temperature mobilities of between 200-700 cm^2/V-s for natural diamond implanted with 40 keV boron ions at room temperature and vacuum annealed at 1400°C for two hours. Consequently, it is reasonable to expect that a better optimized set of implantation and annealing conditions would improve the hole mobility. This was subsequently tested by annealing an implanted sample at 1450°C for one hour. Figure 3 shows the measured sheet resistance as a function of inverse temperature for the implanted and annealed samples. The sheet resistance is significantly lower for the sample receiving the 1450°C anneal, in agreement with the observations of Prins[15]. The net carrier concentration determined by the Hall effect

measurements is plotted in Fig. 4 as a function of inverse temperature. The effect of the 1450°C anneal is to increase the net carrier concentration by approximately one order of magnitude. Prins[15] has suggested that the reduction in sheet resistance following a second higher temperature anneal is due to a reduction in compensating donors. We observe only a relatively small change in mobility (105 cm^2/V-s *vs.* 55 cm^2/V-s), indicating that the primary effect is indeed one of reduced compensation.

Since the sample implanted with carbon plus boron received a total implant dose twice that of the sample implanted with boron alone this reduction in mobility is not surprising. With the increase in activation associated with the carbon pre-implant, however, this might be controlled by reducing both the carbon and boron implant doses. Alternatively, it is possible to design an equally effective implantation scheme using suitably tailored multi-energy boron implants. This has also been noted by Prins[3].

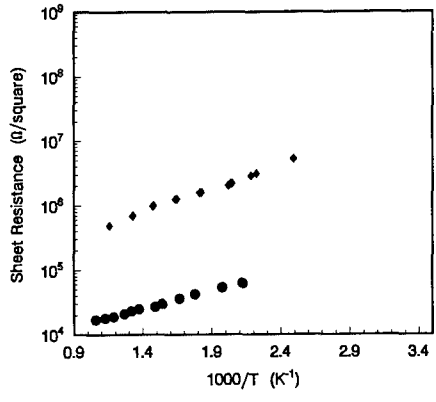

Fig 3. Sheet resistance as a function of inverse temperature for a diamond implanted with boron at 77 K and annealed at 990°C (♦) and subsequently annealed at 1450°C (•).

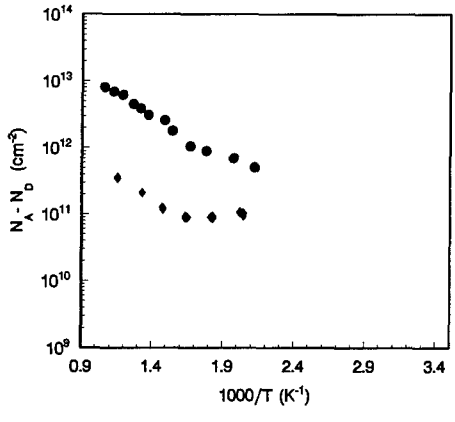

Fig 4. Net carrier concentration as a function of inverse temperature for a diamond implanted with boron at 77 K and annealed at 990°C (♦) and subsequently annealed at 1450°C (•).

OHMIC CONTACT CHARACTERIZATION

The development of ohmic electrical contacts is an integral stage in the growth of a new materials technology. A low contact resistance is the primary requirement for such contacts. However, strong adhesion and the ability to withstand the high temperatures for which diamond devices are intended are also required. The formation of low resistance ohmic contacts to any wide bandgap semiconductor is a difficult problem due to the large potential barrier which arises when a metal is deposited on the semiconductor. To further complicate the problem, diamond has a large surface state density, effectively pinning the Fermi level far from the band edges. In spite of these difficulties, techniques have been developed to produce ohmic contacts to p-type semiconducting diamond. Ohmic contacts produced via a solid state annealing process have been studied extensively[7] and are believed to satisfy the requirements noted above. In this process a thin film of a transition metal carbide forming metal is deposited on the diamond surface. Annealing at high temperature (950°C) leads to the formation of a carbide layer at the interface. This layer provides an intimate contact to the diamond and promotes good adhesion.

Ohmic contacts may be characterized by measuring the series resistance arising at the contact-semiconductor junction, R_c. Normalizing the contact resistance to the contact area gives rise to the specific contact resistance, r_c. For the ideal case of uniform current flow perpendicular to the contact, we have $r_c = R_c/A$, with A being the contact area. In reality, however, the current flow is rarely perpendicular, and the finite resistance of the semiconductor leads to current crowding[16-18]. Measurement techniques[18,19] have been developed to allow the current crowding and bulk resistance of the semiconductor to be deconvolved from R_c, thereby uniquely determining the specific contact resistance. Conceptually, the simplest technique is that of Cox and Strack[19] in which contacts are made to both the front and back sides of the sample. The primary advantages of this technique are the ease in processing the contacts and the simplified analysis due to the geometry. However, due to the semi-insulating nature of bulk diamond, there is a large series resistance contribution to the total resistance from the substrate itself. In practice, this limits the method of Cox and Strack to contact resistances of 10^{-1} Ω-cm^2 or greater on typical type IIb diamond. A second technique utilizes an array of contact pads of equal size, but varying separation, contacting a thin conducting layer. The contact resistance in these structures is analyzed using the transmission line model[18]. The primary drawback to transmission line model measurements is the need to perform a mesa etch in order to reduce the analysis of current flow between contacts to a two dimensional problem.

A technique for eliminating the mesa etch requirement from the transmission line model measurement has been demonstrated[20]. This approach is based on use a circular test pattern consisting of a central dot and concentric ring contacts. The measurements are interpreted using a circular transmission line model. We have chosen to use this method for determining r_c. The geometry of the circular transmission line test pattern is outlined in Fig. 5.

Two heavily doped diamond samples were obtained by growing homo-epitaxial layers with a large boron concentration on type IIa insulating diamond substrates. The first sample consisted of a diamond film with a high boron concentration and about 4 μm in thickness grown epitaxially on a <100> type IIa insulating diamond substrate with the dimensions of 5 x 5 x 0.25 mm^3. The second sample consisted of a 6 μm thick diamond film with a high boron concentration grown epitaxially on a <110> type IIa substrate, also 5 x 5 x 0.25 mm^3. These films were grown at MIT Lincoln Labs. The lightly doped

samples consisted of two irregularly shaped type IIb (naturally boron doped) diamonds thinned to 44 and 50 μm thickness, and a 5 x 5 x 0.25 mm^3 type IIb diamond window.

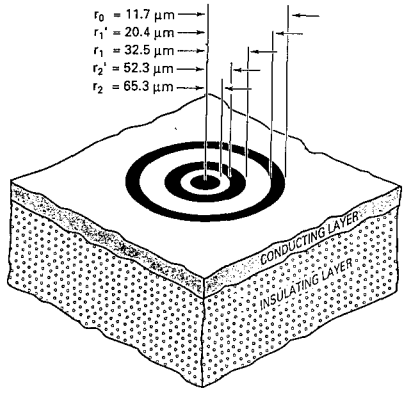

Fig. 5. Schematic representation of the circular transmission line contact pattern used in determination of the specific contact resistance.

The samples were cleaned using Decontam, deionized water, and methanol, sequentially. The samples were then coated with photoresist and patterned using standard photolithographic techniques. Samples were baked at 120°C for 20 minutes following photoresist patterning and loaded into an ion pumped ultra-high vacuum system (base pressure 1 x 10^{-8} Torr). Electron beam evaporation was used for deposition of the carbide forming metal (either Ti or Mo). The thickness of the carbide forming metal was ~100 Å. Subsequently, 1500 Å of Au was deposited from a resistively heated boat onto the surface of the Ti or Mo without breaking vacuum to prevent oxidation prior to annealing, as well as to reduce the resistance in the contact metallization. The pressure during evaporation was 2 x 10^{-7} Torr. Film thicknesses were determined using a crystal monitor during deposition. After deposition a lift-off process was used to remove undesired metal, leaving contact structures as shown in Fig. 5. The dimensions (in the notation of Reeves[20]) were $r_1'=1.74r_0$, $r_1=2.78r_0$, $r_2'=4.47r_0$, and $r_2=5.58r_0$ with $r_0=11.7$ μm.

Following patterning, the contact structures were characterized using a current source and digital multimeter. The measurements consisted of placing tungsten probes on the inner dot, the central ring, and the outer ring. The total resistance between the central ring and the inner dot, and the central ring and the outer ring were measured. The end resistance was determined by passing a current through the central ring and the inner dot and measuring the voltage between the central ring and the outer contact. This result was checked by switching contact pairs and remeasuring. Using these three results, the specific contact resistance can be calculated as described by Reeves[20]. After probing, the samples were baked at 120°C for approximately 20 minutes and then annealed in a purified hydrogen ambient at 950°C. Anneal times were 2 minutes for Ti and 6 minutes for Mo. After annealing, the samples were remeasured.

The results of the specific contact resistance measurements are summarized in Table II. As expected, contacts to the highly doped epitaxial films (epi-<100> and epi-<110>) exhibit the lowest specific contact resistances. Both the titanium- and molybdenum-based metallizations showed excellent results as deposited, with little or no improvement upon

annealing. Contacts formed by placing tungsten probe tips on the diamond surface showed only a slight deviation from linearity. Contacts formed by the Ti films were highly linear. This may be due to the highly doped nature of these layers. The measured value of specific contact resistances after annealing are more than satisfactory for device fabrication. Lightly doped diamond (represented by the "thin" and "thick" samples) are much more difficult to contact, but are still adequate for larger devices. Fig. 6 shows the contribution of the contact resistance to the total device resistance for two different sized devices. Clearly, for larger devices the requirements on the specific contact resistance are much less stringent. Non-ohmic behavior was observed for the as-deposited contacts in these samples, with ohmic behavior observed after annealing.

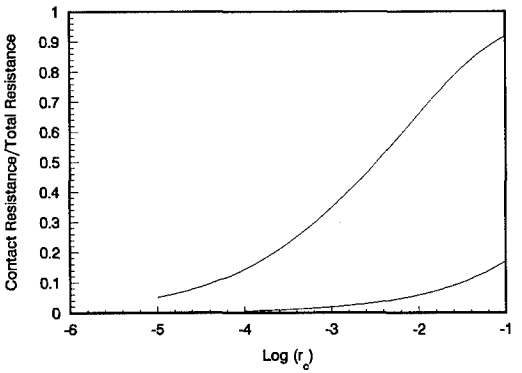

Fig 6. The contribution of the contact resistance to the total device resistance for two different sized devices. The top curve is for a circular MISFET with a source to drain separation of 12 μm, a gate length of 2 μm and a gate width of 314 μm. The bottom curve is for a circular MISFET with a source to drain separation of 400 μm, a gate length of 200 μm and a gate width of approximately 2460 μm. In both cases the channel was assumed to be undepleted (V_g= 0 V). The sheet resistance was assumed to be a uniform $10^4\ \Omega\square^{-1}$.

Table II
Specific Contact Resistance Results for Various Samples

Sample	Conducting layer thickness (μm)	Metal	N_A (cm^{-3}) at 300 K	r_c (Ω-cm^2) as deposited	r_c (Ω-cm^2) Post Anneal
epi-<100>	4	Ti, Mo	$5x10^{19}$	$3.2x10^{-6}$	$1.8x10^{-5}$
epi-<110>	6	Ti, Mo	$7x10^{19}$	$7.6x10^{-5}$	$2x10^{-5}$
thin type IIb	44, 50	Mo	(a) 10^{14}	over-ranged	$1.2x10^{-3}$
thick type IIb	250	Mo	(a) 10^{14}	over-ranged	$1.4x10^{-2}$

(a) Representative value from other type IIb diamond samples.

FABRICATION AND TESTING OF A MISFET

To investigate the effectiveness of ion implantation for electronic device applications, an implanted diamond was used to fabricate a Metal Insulator Gate Field Effect Transistor (MISFET). This structure was selected to eliminate the gate leakage problem observed in diamond MESFET fabrication[21]. A circular geometry that consisted of a central drain contact 400 μm in diameter, with concentric 200 μm wide gate and source contacts 1000 μm and 1600 μm in diameter was chosen to eliminate the need for a mesa etch.

A tri-level boron implant procedure was used to provide an approximately uniformly doped p-type layer of about 2000 Å in thickness in a natural type IIa diamond sample. The implantation energies were 100 keV, 50 keV and 25 keV, with doses of 3.0 x 10^{14}/cm^2, 2.1 x 10^{14}/cm^2, and 1.5 x 10^{14}/cm^2, respectively. The substrate was maintained at 77 K during the implantation procedure. After implantation, the sample was annealed under flowing dry nitrogen at 990°C to remove implantation damage and activate the implanted boron. The annealing time was 10 min. The sample was then cleaned by etching in a heated saturated solution of CrO_3 in sulfuric acid to remove any potential graphitized layers resulting from the implantation process. The diamond was then rinsed in deionized water, acetone, and methanol, and blown dry using dry nitrogen.

MISFETs were then fabricated using procedures described elsewhere[22]. In brief, source and drain ohmic contacts, consisting of a bilayer structure of 100 Å of Mo deposited on the diamond and capped with 1600 Å of Au, were defined by a lift-off process[7,22], and annealed at 960°C in a dry hydrogen environment. The gate insulator, consisting of an SiO_2 film approximately 1000 Å thick, was deposited by indirect plasma enhanced chemical vapor deposition at a temperature of 300°C. The gate metal, also defined by a lift-off process was a 100 Å Ti/1600 Å Au bilayer structure[22]. Ti was selected as the gate metal to provide good adhesion to the gate insulator, with the Au cap to prevent oxidation of the Ti and to lower the gate resistance. All metallizations were deposited in an ultra-high vacuum system with a pressure during deposition of less than $7x10^{-8}$ Torr.

Four devices were fabricated on the sample. The room temperature depletion mode transistor characteristics were obtained for gate voltages between 0 and 12 V. Three devices showed nearly identical performance, the fourth device had a drain current roughly a factor of two higher for a given drain and gate bias condition. As shown in Fig 7, drain current saturation is observed over the entire range of V_G and current pinch-off is achieved between gate voltages of 10 to 12 V. The transconductance was measured to be 28 μS/mm. Although not shown here, the source-to-drain resistance increased from 8.3 kΩ to 1.1 MΩ following deposition of the gate oxide, indicating that the deposited oxide causes the channel layer to be partially depleted. This allows "enhancement" mode operation of the device under negative gate bias conditions. The "enhancement" mode transistor characteristics are shown in Fig. 7b for gate bias between 0 and -6 V. The transconductance in this mode was measured to be 48 μS/mm.

Two of the devices, operating in the depletion mode, were contacted with probes and connected in the driver-active load configuration.[23] An active load is employed in place of a passive load (resistor) whenever it is desired to operate at a high current (for example, in order to obtain a high transconductance) with small power dissipation. If both transistors have identical I-V characteristics, the voltage gain of the pair is
where g_m is the transconductance and ρ_o is the output resistance in saturation. A parasitic

$$A_v = \frac{g_m \rho_o}{2} \quad (1)$$

resistance, shown with dashed lines in the figure, is a consequence of the blanket implant process doping the diamond between devices, and has a value of approximately 10 kΩ. (The sheet resistance of the implanted layer is about 10 kΩ$\square^{-1}$.) The transistors were connected in such a way as to place this parasitic resistor across the power supply rather than across the output. The circuit was tested at room temperature under dc conditions. A gain (V_{out}/V_{in}) of approximately 2 was measured over a wide range of V_{DD}. This gain was lower than had been expected, based on the individual device characteristics shown in Fig. 7 and equation (1). The most likely cause for the lower than expected gain is mechanical damage to the gate oxide resulting from the contacting probes.

Currently, efforts are under way to reduce the parasitic resistance, primarily by utilizing a selective area implant.

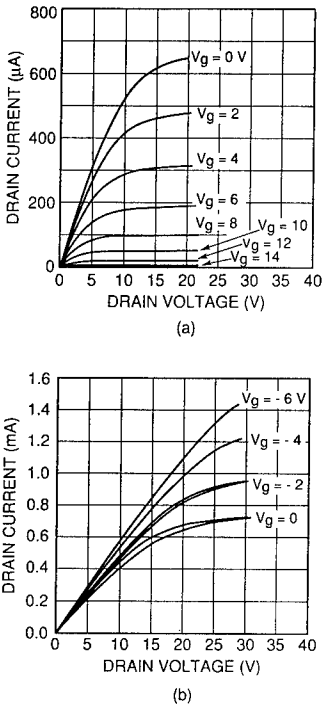

Fig. 7 (a) Room temperature current-voltage characteristics of a diamond MISFET operating in depletion mode. (b) Room temperature current-voltage characteristics of the device with negative gate bias applied, operating in "enhancement" mode.

CONCLUSIONS

Although further development is needed, the enabling technologies of ion implantation into diamond, and ohmic contact formation to semiconducting diamond have been demonstrated. These technologies have been used in the fabrication of MISFET devices exhibiting both current saturation and complete channel pinch-off, with two such devices being connected to form a simple demonstration circuit.

ACKNOWLEDGEMENTS

The work discussed here was supported by the Naval Command, Control, and Ocean Surveillance Center RDT&E Division Independent Research program (Dr. Alan Gordon) and the Office of Naval Research (Mr. Max Yoder) under BMDO/IST funding.

REFERENCES

1 J.F. Prins, Phys. Rev. B, **38**, 5576 (1988).
2 J.F. Prins, Phys. Rev. B, **44**, 2470 (1991).
3 J.F. Prins, Nuc. Instr. and Meth., **B59**, 1387 (1991).
4 J.F. Prins, Phys. Rev. B, **39**, 3764 (1989).
5 G.S. Sandhu, M.L. Swanson, and W.K. Chu, Appl. Phys. Lett. **55**, 1397 (1989).
6 R.A. Kiehl, P.E. Hallali, J. Yates, M.A. Tischler, R.M. Potemski, and F. Cardone, IEEE Electron Device Lett., **12**, 530 (1991).
7 K.L. Moazed, J.R. Zeidler, and M.J. Taylor, J. Appl. Phys., **68**, 2246 (1990).
8 J.R. Zeidler, C.A. Hewett, and R.G. Wilson, Phys. Rev. B, **47**, 2065 (1993).
9 R.A. Spits, T.E. Derry, J.F. Prins, and J.P.F. Sellschop, Nucl. Instr. and Meth. **B59/60**, 1366 (1991).
10 A.T. Collins and E.C. Lightowlers, in **The Properties of Diamond**, edited by J.E. Field (Academic Press: New York, 1979), pp 79-109.
11 A.T. Collins and A.W.S. Williams, J. Phys. C: Solid St. Phys., **4**, 1789 (1971).
12 N. Fujimori, H. Nakahata, and T. Imai, Jap. J. Appl. Phys., **29**(5), 824 (1990).
13 P.I. Baranskii, V.G. Malogolovets, V.I. Torishnii, and G.V. Chipenko, Sov. Phys. Semicond., **21**(1), 45 (1987).
14 V.S. Vavilov, M.A. Gusasyan, M.I. Guseva, T.A. Karatygina, and E.A. Konorova, Sov. Phys. Semicond., **8**(4), 471 (1974).
15 J.F. Prins, Materials Science Reports, **7**, 271 (1992).
16 S.S. Cohen and G.Sh. Gildenblat, in VLSI Electronics Microstructure Science, Vol.13, ed. N.G. Einspruch, Academic Press, Inc., New York, pp. 87-133 (1986).
17 C.-Y Ting and C.Y. Chen, Solid-State Electronics, **14**, 433-438 (1971).
18 H.H. Berger, Solid-State Electronics, **15**, 145-158 (1972).
19 R.H. Cox and H. Strack, Solid-State Electronics, **10**, 1213-1218 (1967).
20 G.K. Reeves, Solid-State Electronics, **23**, 487-490 (1980).
21 G. Sh. Gildenblat, S.A. Grot, C.W. Hatfield, and A.R. Badzian, IEEE Elect. Dev. Lett., **12**, 37 (1991).
22 C.R. Zeisse, C.A. Hewett, R. Nguyen, J.R. Zeidler, and R.G. Wilson, IEEE Elect. Dev. Lett., **12**, 602 (1991).
23 J.R. Zeidler, C.A. Hewett, R. Nguyen, C.R. Zeisse, and R.G. Wilson, Diamond and Related Materials, **2**, 1341 (1993).

DIAMOND FIELD-EFFECT TRANSISTORS

DAVID L. DREIFUS, ALISON J. TESSMER, JOSEPH S. HOLMES, CHIEN-TEH KAO, DEAN M. MALTA, LINDA S. PLANO, AND BRIAN R. STONER
Kobe Steel USA Inc., Electronic Materials Center, 79 TW Alexander Drive, Research Triangle Park, NC 27709

ABSTRACT

Metal-oxide-semiconductor field-effect transistors (FETs) have been fabricated using B-doped diamond thin films deposited on polycrystalline, (100) highly-oriented, and single crystal diamond insulating substrates. Diamond films were grown using a microwave plasma chemical vapor deposition technique. Various electrical and materials characterization techniques were employed to confirm that the films exhibited properties suitable for FET fabrication. Devices with gate lengths and widths of 2 μm and 314 μm respectively, were processed using standard photolithography. Silicon dioxide was used as the gate dielectric. Current-voltage characteristics of these devices have been measured during variable temperature cycling in air. Devices fabricated on the randomly oriented polycrystalline diamond substrates have been operated to 285°C. Field-effect transistors fabricated using the highly-oriented diamond substrates have been characterized to 400°C. Single crystal diamond devices exhibited saturation and pinch-off of the channel current at temperatures up to 500°C. These devices have been biased in amplifier circuit configurations that have been characterized from 20 Hz to 1 MHz. Single crystal FETs exhibited voltage gain over an extended temperature range. Transconductances as large as 1.7 mS/mm have been observed. The electronic properties, fabrication technologies, and performance of devices fabricated on the three diamond substrate materials will be discussed and compared.

INTRODUCTION

There have been many publications describing the virtues of diamond's unique combination of properties such as its wide bandgap, high breakdown field, high thermal conductivity, high electron and hole mobilities, and radiation hardness.[1-6] Several theoretical analyses suggest that diamond devices could potentially exhibit performance superior to that of devices fabricated from other materials such as Si and GaAs.[3, 6] Hence, diamond has been regarded as a suitable material for electronic devices operating under hostile conditions such as high temperature, high power, high radiation, and high frequencies.[1-3] A great deal of excitement has been generated by reports of working transistors fabricated from single crystal diamond.[1, 2, 4, 7-11] The performance of diamond transistors, however, has varied greatly, depending on device structure, starting material, doping technique, and device processing technologies. Many of the reported devices were fabricated on material grown by chemical vapor deposition (CVD) on single crystal, natural diamond substrates. In-situ doping[1, 2, 7, 9], ion implantation[4, 10], and solid-state diffusion[11] methods have all been employed to form the device active areas.

In contrast, there have been reports that refute the optimistic outlook for diamond electronic devices.[12-14] In these latter reports, authors indicate that many unresolved issues need to be addressed, such as the availability of a suitable large-area substrate, the lack of low activation energy dopants, the state of diamond device process technologies, and the growth of high quality doped diamond layers.

To date, the combination of elevated temperature operation, saturation, and complete pinch-off of the active channel has not been reported. On planar devices, gate electrode failure and peripheral leakage currents have prevented proper device operation above 100°C,[4] although some modulation has been seen at temperatures up to 350°C.[2] Device transconductance has been limited to less than 100 μS/mm.

Another limiting factor for the previously reported devices is that they are all fabricated using single crystal diamond substrates. While this is not a problem as far as device operation itself is

Mat. Res. Soc. Symp. Proc. Vol. 339. ©1994 Materials Research Society

concerned, it is a severe limitation in terms active device area and cost. This is due to the small size and high cost of available high quality natural and synthetic diamond substrates. Ideally, large area single crystal diamond or alternate substrates on which diamond can be grown heteroepitaxially would be desirable. Although initial hetero-nucleation results on SiC[15] and Ni[16] indicate that this may be possible, true heteroepitaxy has not yet been realized except on single crystals of cubic-BN.[17, 18] Unfortunately, cubic-BN is currently as difficult to produce in large-area single crystals as diamond. Thus, natural and synthetic high-temperature, high-pressure material remain the sole sources of substrates for monocrystalline diamond films.

The economic viability and the availability of polycrystalline diamond films have many groups trying to fully characterize the electronic properties of these films.[5, 19-24] Polycrystalline diamond films have been deposited over large areas using a variety of deposition techniques.[25-27] Boron-doped semiconducting diamond films can be easily obtained.[5, 19, 20, 28-31] The doping concentrations can be accurately controlled by changing the gas phase chemistry in CVD processing. Although the effects of grain boundaries upon electrical properties have not been fully assessed, it is worthwhile to investigate the possibilities of electronic devices made of polycrystalline diamond films, and also interesting to compare electrical properties between polycrystalline and single crystal diamond films. Promisingly, the first operation and subsequent enhanced performance of FETs fabricated using polycrystalline diamond films has been reported.[32, 33] Furthermore, an engineered polycrystalline material in which the individual grains are highly-oriented with respect to the substrate and adjacent grains has been recently synthesized. This (100)-oriented material shows promise for becoming a potential substrate material for diamond electronic devices.[34] The individual grains in highly-oriented polycrystalline diamond are aligned such that only low-angle grain boundaries are present. The electrical properties of this material have already been shown to be superior to randomly-oriented polycrystalline diamond.

In this work, depletion-mode metal-oxide-semiconductor field-effect transistors (MOSFETs) have been demonstrated for single crystal and highly-oriented polycrystalline, and randomly-oriented polycrystalline diamond. The devices exhibit well-behaved characteristics, including saturation and complete pinch-off of the channel current. Variable temperature operation has been observed and single crystal devices have been operated at temperatures as high as 500°C. Large drain-to-source currents and transconductances have also been demonstrated. These results provide experimental evidence in support of the viability of active diamond electronic devices.

EXPERIMENTAL

In order to bench-mark the performance of diamond FETs, a systematic approach was undertaken in which device modeling and electrical and materials characterizations were used to provide iterative feedback for the growth of device-quality p-type diamond layers. Device modeling was employed to determine the effects of materials parameters and device structure. The materials parameters required for the simulations were obtained from the published literature.[3, 35] Sensitivity analyses were performed and correlated with existing published data and the measured electrical properties. Initially, single crystal diamond material was selected for the proof of concept devices in order to eliminate the effects of grain boundaries on device performance. Growth conditions were optimized using feedback from measurements such as variable-temperature van der Pauw Hall-effect and capacitance-voltage (C-V) techniques. Device fabrication technologies were standardized to reduce process-induced variations on device performance. Polycrystalline diamond layers were grown separately in earlier experimentation. Again, the layers were characterized and then processed into FETs. Boron-doped layers were grown on single crystal diamond substrates and characterized prior to device fabrication. Transistors were processed and characterized using variable-temperature current-voltage (I-V) measurements. A second set of diamond thin films were then grown on single crystal substrates along with several highly-oriented substrates. Devices were characterized individually and then configured to form simple circuits.

Growth and Characterization of Diamond Films

Highly-oriented and randomly-oriented polycrystalline diamond and natural single crystal diamond substrates were used. The highly-oriented and randomly-oriented polycrystalline substrates consisted of 15-40 μm of undoped diamond growth on 5 mm x 5 mm high-resistivity Si substrates. The techniques for producing these films have been published previously.[15, 34] Insulating, type IIa, (100)-oriented, 4 mm x 4 mm x 0.25 mm natural stones were purchased from Harris Diamond. Boron-doped diamond thin films were deposited on all three diamond substrates using a microwave plasma assisted CVD technique. Highly-oriented polycrystalline insulating diamond substrates were placed adjacent to single crystal diamond substrates and were exposed to identical deposition conditions. In a separate experiment, B-doped layers were deposited on the randomly-oriented diamond substrates used for FET fabrication.[33] Scanning electron, Raman, and secondary ion mass spectroscopic techniques were used to evaluate the structural properties of the homoepitaxial films. The thicknesses of the deposited layers were measured using cross-sectional scanning electron microscopy (SEM) and surface profilometry of selected-area deposited regions on single crystal diamond. Thickness measurements were not performed on either the highly-oriented or randomly oriented diamond layers.

Electrical characterization of the B-doped layers was performed using variable temperature van der Pauw Hall-effect measurements. The doped layers were selectively deposited using sputtered SiO_2 to mask the edges of the substrate so that the p-type layer would be isolated in the center of the samples to avoid peripheral current leakage currents at the sample edges. The SiO_2 was removed in HF following growth, and the films were subsequently annealed at 600 °C for 30 min. under vacuum at 10^{-7} Torr in order to dissociate hydrogen from the film surface. After annealing, the sample was boiled in a solution of $CrO_3 + H_2SO_4$ at 200 °C to remove graphite which may have formed during growth or annealing. Finally, the film was cleaned in Aqua Regia and standard RCA[36] solutions to prepare the surface prior to deposition of the electrical contacts. A van der Pauw contact configuration was used for Hall-effect measurements which were performed between -193 °C and 325°C. Device layers were screened such that only the ones with the expected properties were processed into FETs. After the devices were completed, capacitance-voltage (C-V) measurements were performed on the gate electrodes in order to determine the local electronic properties within the active channel region beneath the device. A Hewlett-Packard 4284A LCR Meter was employed for C-V measurements.

Device Fabrication

Devices were fabricated using a three-step photolithographic process. Concentric-ring geometry devices were employed to avoid the need for a mesa definition step and eliminate the possibility of peripheral surface leakage currents. A schematic cross-section of the fabricated device is shown in Figure 1. As indicated, current flows radially in the device. Patterning of the device structures was achieved using standard UV contact lithography. Source and drain contacts

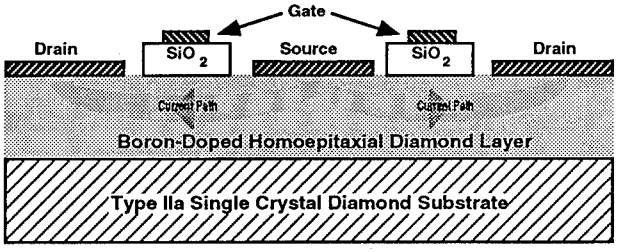

Figure 1. Schematic cross-section of a single crystal concentric-ring diamond field-effect transistor. Note that the current flows radially from the Source to the Drain contacts.

were made using 2000Å-thick Au metallization. The gate dielectric layer consisted of 750 Å of SiO_2 which was deposited using a low-temperature CVD process. The gate electrode consisted of 2000Å of Al. A lift-off technique was employed to delineate the metal electrodes. The gate length, width, and source-to-drain spacing were 2 μm, 314 μm, and 12 μm respectively.

Device Characterization

Diamond FETs were characterized as a function of temperature. A probe station with a custom-built hot stage was used to characterize the devices from room temperature to 550°C. Static I-V measurements of the ohmic and insulating contacts, as well as the overall device behavior, were made using a Hewlett-Packard 4145B Semiconductor Parameter Analyzer. Devices were then configured into amplifier and digital logic circuits. The ac behavior was observed on a Tektronix 2232 digital storage oscilloscope. A Philips PM5138 Function Generator and the HP4284A LCR Meter were used to provide sinusoidal inputs for the amplifier circuits. Variable frequency measurements of diamond amplifiers were made from 20 Hz to 1 MHz. Synchronous TTL logic signals were generated using custom-built circuits formed from commercially available Si digital logic circuits. Digital signals were observed using the Tektronix oscilloscope and a Hewlett Packard 1661AS Portable Logic Analyzer on loan from HP. The behavior of the various circuits was measured as a function of temperature up to 400°C.

RESULTS AND DISCUSSION

Device Modeling

A schematic representation of a simulated diamond FET is shown if Figure 2(a). The contour lines beneath the gate electrode represent the depletion region resulting from drain and gate biases of -40 V and 20 V, respectively. An example of simulated room temperature I-V characteristics is shown in Figure 2(b). Sensitivity analyses were performed and the results are to be published elsewhere.[37]

Growth and Characterization of Diamond Films

Post deposition analyses of the diamond layers were performed. Scanning electron, Raman, and secondary ion mass spectroscopic techniques were used. The surface morphologies of the various diamond materials were viewed using scanning electron microscopy (SEM). For the case of homoepitaxial diamond layers, the surface was practically featureless. The morphology of the randomly-oriented layers exhibited well-faceted polycrystalline diamond with grain sizes on the order of a few microns. A smoothing of the surface was observed for the case of the highly-oriented diamond material as grains coalesced in the final stages of growth. Micrographs of surface morphology of the two polycrystalline materials are shown in Figures 3 (a) and (b). In all three materials, a well-defined peak at 1332 cm^{-1} was observed in the Raman spectra, indicating the presence of diamond. A photoluminescence background was observed in both the highly-oriented and randomly-oriented diamond layers, but was non-existent in the homoepitaxial diamond layers. Secondary ion mass spectroscopy (SIMS) was used to determine the impurity concentration of the randomly-oriented polycrystalline diamond layers grown at the same time as the FET active layers. Uniform atomic B concentrations throughout the p-type layers were obtained.

Electrical Characterization

Prior to device fabrication, the samples were evaluated such that only the those with the expected electrical properties were used in the device fabrication. Hall-effect measurements were

performed to correlate the electronic transport with the crystallographic properties. The measured temperature-dependent carrier concentrations and mobilities were consistent with the properties published for polycrystalline[19, 20, 31, 38] and homoepitaxial[24, 39, 40] diamond. For the first set of single crystal films, room temperature carrier mobilities of 400-500 $cm^2/V \cdot s$ were measured for

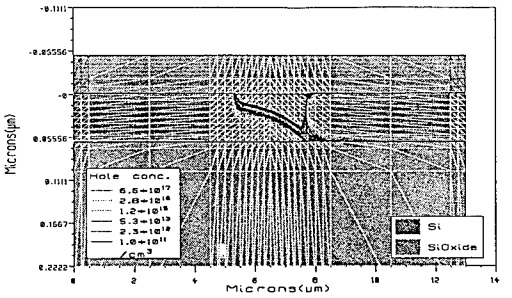

Figure 2(a). Two-dimensional schematic diagram of a diamond FET.

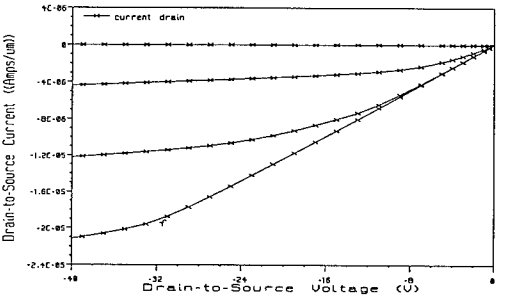

Figure 2(b). Simulated current-voltage characteristics of a diamond FET.

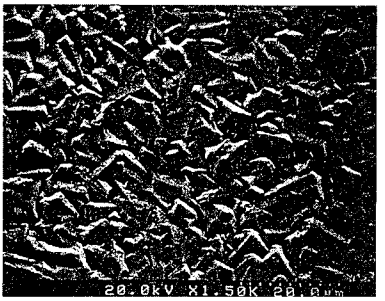

(a) randomly-oriented diamond

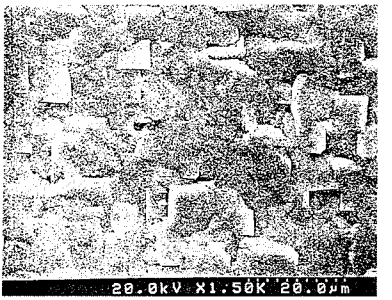

(b) highly-oriented polycrystalline diamond

Figure 3. The surface morphology of B-doped diamond layers deposited onto (a) randomly-oriented, (b) highly-oriented insulating diamond substrates.

single crystal films with atomic B concentrations in the range between 1-10x10^{17} cm^{-3}. Room temperature measurements on similar polycrystalline and highly-oriented diamond layers yielded mobilities in the range of 20-50 $cm^2/V•s$ and 125-175 $cm^2/V•s$ respectively. The larger carrier mobilities measured in the highly-oriented diamond layers are attributed to the presence of only low-angle grain boundaries.[24, 34] A comparison of the temperature dependent behavior of the carrier concentrations and mobilities for p-type diamond layers deposited simultaneously on all three substrates is shown in Figures 4(a) and (b). Note that the carrier concentration is very similar among the three materials, however, the mobility varies significantly. Growth conditions were subsequently optimized to provide higher quality epitaxial device layers. The carrier mobilities of the homoepitaxial samples used in the device fabrication were all above 1000 $cm^2/V•s$. Carrier mobilities in excess of 1300 $cm^2/V•s$ for films containing atomic B concentration of 2x10^{17} cm^{-3} have since been achieved on type IIa substrates.[41] Additionally, carrier mobilities as large as 280 $cm^2/V•s$ have been measured for highly-oriented diamond layers.

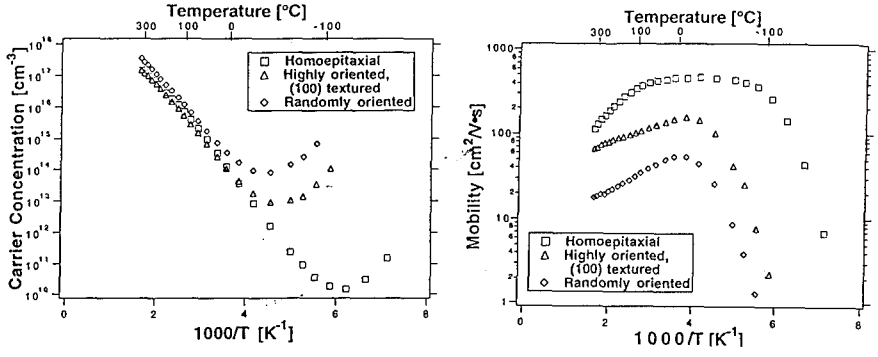

(a) carrier concentrations (b) carrier mobilities

Figure 4. Comparisons of (a) carrier concentrations and (b) carrier mobilities for randomly-oriented, single crystal, and highly-oriented B-doped diamond layers that were deposited onto the various substrates at the same time.

Device Characteristics

Current-voltage measurements were made on the processed devices. Optical micrographs of completed devices fabricated on all three substrates are shown in Figures 5(a-c). It is apparent from the micrographs that the substrate morphology has been replicated in the subsequent depositions of the doped active layers. The drain-to-source and gate-to-source currents between electrodes were measured to evaluate the properties of the ohmic contacts and the insulating properties of the gate dielectric. Linear I-V behavior was observed for the ohmic contacts, while the gate current was less than 1nA in all cases. Capacitance-voltage measurements were made on selected MOS gates on homoepitaxial diamond layers. From the slope of $1/C^2$ vs. V, uncompensated acceptor concentrations were determined. These results were in good agreement with the values for atomic B concentration as determined by SIMS.

The FET dc characteristics for devices fabricated from the three materials were measured as a function of temperature on a probe station with a custom-built hot stage. Devices fabricated from randomly-oriented polycrystalline diamond were measured from room temperature to 285°C, where they failed due to catastrophic breakdown of the gate dielectric. This failure mechanism had been reported previously.[2] The current-voltage characteristics of randomly-oriented polycrystalline diamond FETs operating at 150°C and 250°C are shown in Figures 6(a) and(b) respectively.

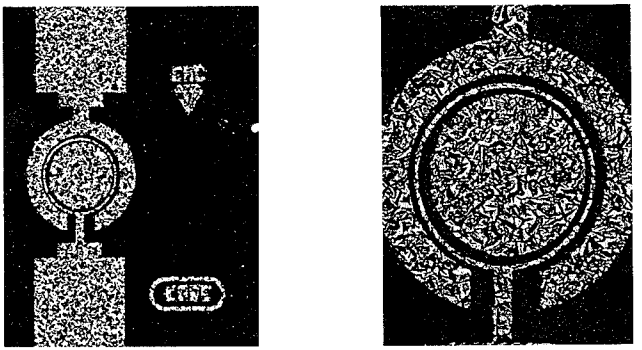

(a) randomly-oriented diamond

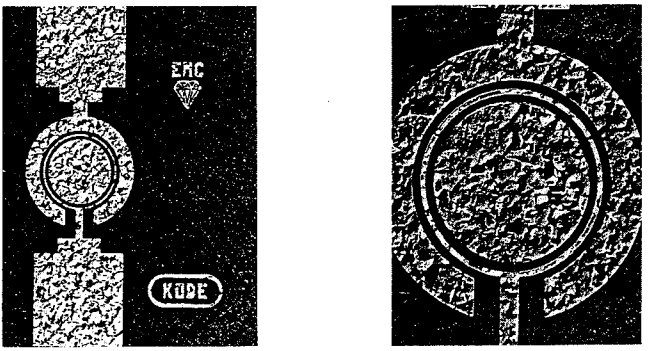

(b) highly-oriented diamond

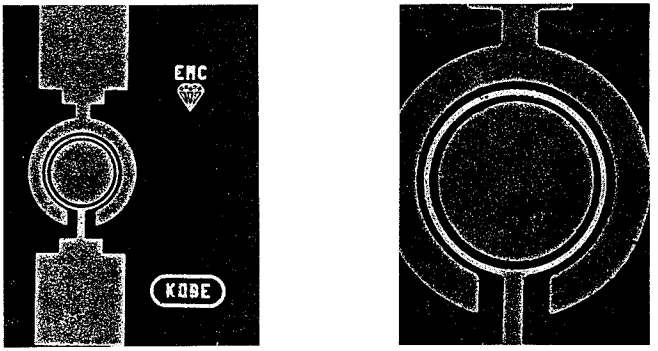

(c) single crystal diamond

Figure 5. Optical micrographs of diamond field-effect transistors fabricated using (a) randomly-oriented, (b) highly-oriented diamond layers, and (c) type IIa single crystal.

Complete pinch-off of the channel current was not possible above room temperature. A parasitic leakage path through the underlying Si substrate was suspected. An activation energy of 1.0 eV was determined for the temperature dependence of the parallel resistance. This is typical of values observed for conduction in undoped polycrystalline diamond.[42-46]

The first active device fabricated using HOD films has been demonstrated. The individual grain sizes are much larger than the gate length of the device. Thus the drain-to-source current is expected to traverse only one or perhaps two grain boundaries as it flows radially in the device. MOSFETs have been shown to exhibit operation consistent with depletion-mode devices. Maximum transconductance of 100 μS/mm was determined from the measured characteristics. Although the drain-to-source currents are low, the characteristics of highly-oriented polycrystalline diamond MOSFETs are significantly improved as compared to devices fabricated from randomly-oriented polycrystalline diamond.[32, 33] Transistors fabricated from the highly-oriented diamond were characterized to a temperature of 400°C before gate failure was observed. Drain-to-source characteristics for devices operating at 25°C and 325°C are shown in Figures 7(a) and (b).

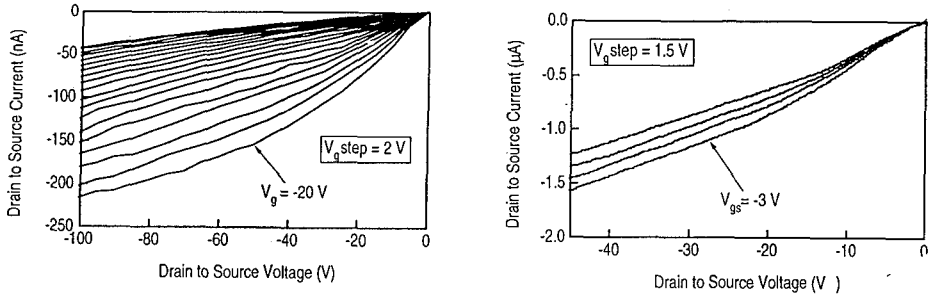

Figure 6. Drain-to-source current-voltage characteristics of a randomly-oriented polycrystalline diamond field-effect transistor operating at (a) 150°C and (b) 250°C.

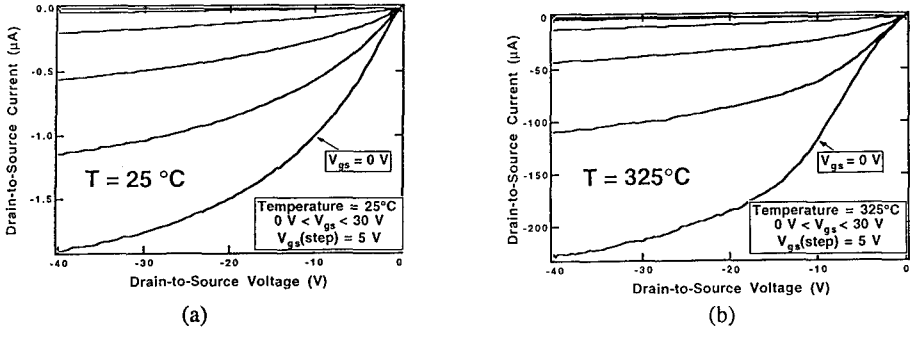

Figure 7. Drain-to-source current-voltage characteristics of a highly-oriented polycrystalline diamond field-effect transistor operating at (a) 25°C and (b) 350°C.

Devices fabricated from single crystal diamond were tested to a temperature 550°C before current leakage prevented proper device operation. This represents the highest temperature

operation reported for an active electronic device fabricated from diamond. For the case of the single crystal and highly-oriented polycrystalline diamond devices, both saturation and pinch-off of the channel current were observed at elevated temperatures. Current-voltage characteristics for single crystal diamond FETs operating at 350°C and 500°C are shown in Figures 8(a) and (b) respectively. Other MOSFETs fabricated on similar single crystal diamond films exhibited drain-to-source currents of 8 mA and a maximum transconductance in excess of 1.7 mS/mm. It is interesting to note that similar characteristics were observed for early demonstrations of SiC FETs.[47]

Devices were tested during multiple temperature cycling. After several cycles, thermal expansion of the probe tips relative to the substrate resulted in scratching and subsequent removal of contact metallizations. To avoid damage to the device patterns in subsequent experimentation, the probes were removed prior to changes in temperature. Removal of the probes from the contact pads was adopted whenever the temperature was changed to avoid damage to the device patterns.

Single crystal diamond FETs were also biased in simple amplifier and digital logic circuit configurations. A schematic diagram of a common-source diamond amplifier is shown in Figure 9(a). The time-dependent sinusoidal input and resultant output voltages for a diamond amplifier operating at 300°C are shown in Figure 9(b). The gain characteristics were measured at various temperatures and frequencies. The frequency response for a diamond amplifier operating

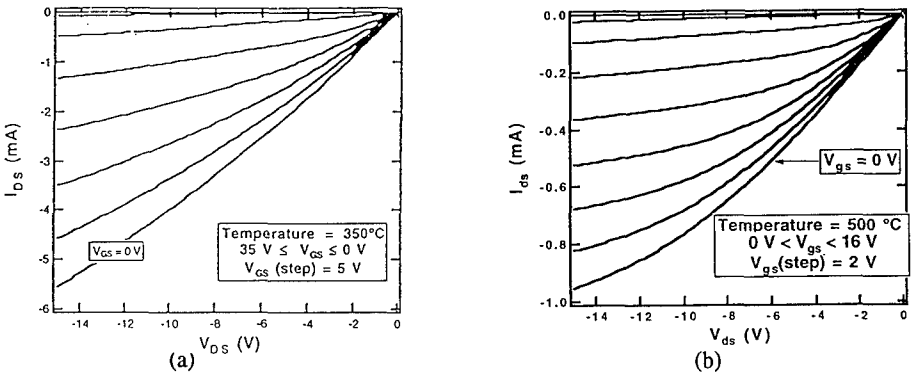

Figure 8. Drain-to-source current-voltage characteristics of single crystal diamond field-effect transistor operating at (a) 350°C and (b) 500°C.

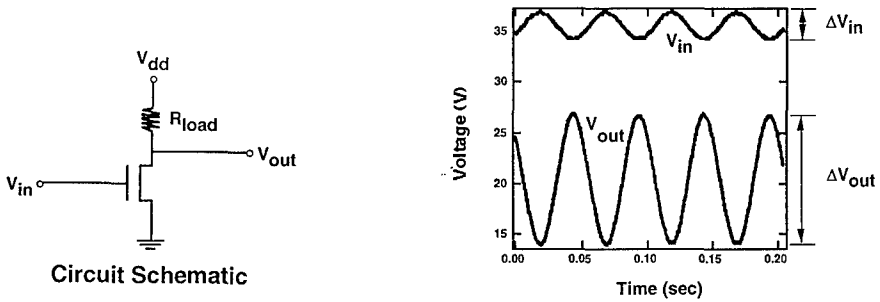

Figure 9. Single crystal diamond amplifier circuit showing (a) a schematic diagram of a common-source diamond amplifier and (b) the input and output voltages as a function of time at 250°C.

at 75°C and 250°C is shown in Figure 10. Note that the characteristics follow a well-behaved roll-off at 20 dB/decade. This behavior is seen in amplifiers fabricated from other materials in which the frequency-dependent behavior is dominated by a resistance-capacitance time constant.

Multiple diamond MOSFETs were configured into digital logic circuits and operated to 400°C. Circuit behavior will be presented elsewhere.[48]

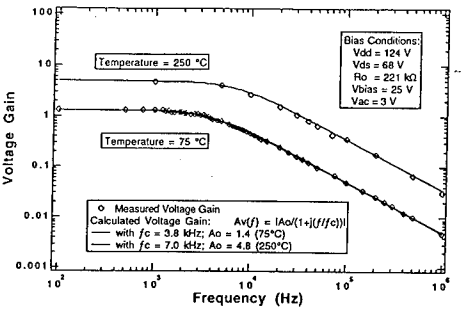

Figure 10. Voltage gain as a function of frequency for a diamond amplifier operating at 75°C and 250°C.

SUMMARY

Metal-oxide-semiconductor field-effect transistors (FETs) have been fabricated using B-doped diamond thin films deposited on randomly-oriented polycrystalline, (100) highly-oriented polycrystalline, and single crystal insulating diamond substrates. Devices fabricated on the randomly-oriented polycrystalline diamond substrates have been operated to 285°C. Field-effect transistors fabricated using the highly-oriented diamond substrates have been characterized to 400°C. Single crystal diamond devices exhibited saturation and pinch-off of the channel current at temperatures up to 500°C. These devices have been biased in amplifier circuit configurations that have been characterized from 20 Hz to 1 MHz. Single crystal FETs exhibited voltage gain over an extended temperature range. Transconductances as large as 1.7 mS/mm have been observed that are similar to the early demonstrations of SiC FETs. The high temperature operation of active diamond electronic devices supports the claims that diamond could be used at elevated temperatures.

ACKNOWLEDGMENTS

The authors would like to acknowledge the assistance of Michelle Hartsell, Henry Wynands, Brad Fox, and Dean Malta for electrical characterization of the films used in this work, Glenn Tessmer for his support in the growth of the diamond active layers, and Robert Henard for metallization support.

REFERENCES

1. M.W. Geis, Proc. of the IEEE **79**, 669-677 (1991).
2. S.A. Grot, G.S. Gildenblat and A.R. Badzian, IEEE Elec. Dev. Lett. **13**, 462-464 (1992).
3. R.J. Trew, J.-B. Yan and P.M. Mock, Proc. of IEEE **79**, 598-620 (1991).
4. C.A. Hewett, C.R. Zeisse, R. Nguyen and J.R. Zeidler, Proceedings of the First International High Temperature Electronics Conference, Albuquerque, NM (1991)

5. K. Kobashi, K. Nishimura, K. Miyata, R. Nakamura, H. Koyama, K. Saito and D.L. Dreifus, 2nd International Conference on the Applications of Diamond Films and Related Materials, Tokyo, Japan MYU, Japan (1993) 35-42.
6. K. Shenai, R.S. Scott and B.J. Baliga, IEEE Trans. Elect. Dev. **36**, 1811-1823 (1989).
7. G.G. Fountain, *et al.*, The Second International Symposium on Diamond Materials, Washington, DC The Electrochemical Society (1991) 523-529.
8. M.W. Geis, D.D. Rathman, D.J. Ehrlich, R.A. Murphy and W.T. Lindley, IEEE Elec. Dev. Lett. **EDL-8**, 341-343 (1987).
9. H. Shiomi, Y. Nishibayashi and Fujimori, Jpn. J. Appl. Phys. **28**, L2153-L2154 (1989).
10. J.R. Zeidler, C.A. Hewett, R. Nguyen, C.R. Zeisse and R.G. Wilson, Dia. and Rel. Mat. **2**, 1341-1343 (1993).
11. W. Tsai, M. Delfino, D. Hodul, M. Riazat, L.Y. Ching, G. Reynolds and C.B. Cooper III, IEEE Elect. Dev. Lett. **12**, 157-159 (1991).
12. I.M. Buckley-Golder and A.T. Collins, Dia. and Rel. Mat. **1**, 1083-1101 (1992).
13. A.T. Collins, Semicond. Sci. Technol. **4**, 605-611 (1989).
14. A.T. Collins, Mat. Sci. and Eng. **B 11**, 257-263 (1992).
15. B.R. Stoner and J.T. Glass, Appl. Phys. Lett. **60**, 698-700 (1992).
16. Y. Sato, H. Fujita, T. Ando, T. Tanaka and M. Kamo, Phil. Trans. R. Soc. Lond. **342**, 31-37 (1993).
17. S. Koizumi, T. Murakami, T. Inuzuka and K. Suzuki, Appl. Phys. Lett. **57**, 563-565 (1990).
18. M. Yoshikawa, H. Ishida, A. Ishitani, S. Koizumi and T. Inuzuka, Appl. Phys. Lett. **58**, 1387-1389 (1991).
19. K. Nishimura, K. Das, J.T. Glass, K. Kobashi and R.J. Nemanich, (1989).
20. G. Gildenblat, S. Grot and A. Badzian, Proc. of IEEE **79**, 647-668 (1991).
21. R. Harper, C. Johnston, N. Blamires, P. Chalker and I. Buckleygolder, Surf. and Coating Tech. **47**, 344-355 (1991).
22. M. Werner, V. Schlichting and E. Obermeier, Dia. and Rel. Mat. **1**, 669-672 (1992).
23. L.M. Edwards and J.L. Davidson, Dia. and Rel. Mat. **2**, 808-811 (1993).
24. D.M. Malta, J.A. von Windheim and B.A. Fox, Appl. Phys. Lett. **submitted**, (1993).
25. H. Kawarada, K.S. Mar and A. Hiraki, Jap. J. Appl. Phys. **26**, L1032-L1034 (1987).
26. Y. Liou, A. Inspektor, R. Weimer and R. Messier, Appl. Phys, Lett. **55**, 631-633 (1989).
27. M. Kamo, H. Yurimoto and Y. Sato, Appl. Surf. Sci. **33/34**, 553-560 (1988).
28. J.F. Prins, Thin Solid Films **212**, 11-18 (1991).
29. K. Okano, H. Naruki, Y. Akiba, T. Kurosu, M. Iida, Y. Hirose and T. Nakamura, Jpn J. Appl. Phys. **28**, 1066-1071 (1989).
30. N. Fujimori, The Centennial memorial Issue of The Ceramic Society of Japan **99**, 1063-1068 (1991).
31. N. Fujimori, T. Imai and A. Doi, Vacuum **36**, 99-102 (1986).
32. A.J. Tessmer, K. Das and D. Dreifus, Dia. and Rel. Mat. 89-92 (1992).
33. A.J. Tessmer, L.S. Plano and D.L. Dreifus, IEEE Elec. Dev. Lett. **14**, 66-68 (1993).
34. B.R. Stoner, D.M. Malta, A.J. Tessmer, J.S. Holmes, D.L. Dreifus, R.C. Glass, A. Sowers and R.J. Nemanich, SPIE, San Diego, CA SPIE (1994)
35. J.E. Field, in *The Properties of Diamond* 1- Eds. (Academic Press; Harcourt Brace Jovanovich, Publishers, New York, 1979), pp. 674.
36. W. Kern and D.A. Puotinen, RCA Review **31**, 187 (1970).
37. A.J. Tessmer and D.L. Dreifus, to be published
38. M. Aslam, I. Taher, A. Masood, M.A. Tamor and T.J. Potter, Appl. Phys. Lett. **60**, 2923-2925 (1992).
39. G.S. Gildenblat, S.A. Grot, C.W. Hatfield, C.R. Wronski, A.R. Badzian, T. Badzian and R. Messier, MRS (1989).
40. J.R. Zeidler, C.A. Hewett and R.G. Wilson, Phys. Rev. **B 47**, 2065-2071 (1993).
41. L.S. Plano, D.M. Malta, J.A. von Windheim, C.-t. Kao and B.A. Fox, to be published (1994).
42. K. Miyata, D.D. L., K.D. Das, J.T. Glass and K. Kobashi, The Second International Symposium on Diamond Materials, Washington DC The Electrochemical Society (1991) 543-550.

43. K. Miyata, Y. Matsui, K. Kumagai, S. Miyauchi and K. Kobashi, New Diamond Science and Technology, Washington DC Materials Research Society (1991) 981-986.
44. K. Miyata, D. Dreifus and K. Kobashi, Appl. Phys. Lett. **60**, 480-482 (1992).
45. Y. Mori, N. Eimori, J. Ma, T. Ito and A. Hiraki, Appl. Surf. Sci. **56-58**, 89-93 (1992).
46. J. Mort, M.A. Machonkin and K. Okumura, Appl. Phys. Lett. **59**, 455-457 (1991).
47. R.F. Davis, G. Kelner, M. Shur, J.W. Palmour and J.A. Edmond, Proc. of the IEEE **79**, 677-701 (1991).
48. J.S. Holmes, A.J. Tessmer and D.L. Dreifus, The Second International High Temperature Electronics Conference, Charolette, North Carolina to be published (1994)

TEST OF A DIAMOND-TUNGSTEN SAMPLING CALORIMETER

R. Stone[a], M. Franklin[b], D. Fujino[c], K. K. Gan[c], R. Gilman[a], S. Han[d], H. Kagan[c], S. Kanda[e], D. R. Kania[d], R. Kass[c], S. K. Kim[f], G. Kumbartski[a], M. H. Lee[f], R. Malchow[g], B. Morozov[h], W. Palmer[c], L. S. Pan[d], P. Rutt[a], F. Sannes[a], S. Schnetzer[a], S. V. Somalwar[a], Y. Sugimoto[i], R. J. Tesarek[a], G. B. Thomson[a], C. White[c], S. Zhao[c].

[a]Department of Physics and Astronomy, Rutgers University, Piscataway, NJ 08855-0849
[b]Physics Department, Harvard University, Boston, MA 02138
[c]Department of Physics, The Ohio State University, Columbus, OH 43210
[d]Laser Division, Lawrence Livermore National Laboratory, Livermore, CA 94550
[e]Department of Physics, University of Hawaii, Honolulu, HI 96822
[f]Physics Department, Seoul National University, Seoul 151-742, Korea
[g]Physics Department, Colorado State University, Ft. Collins, CO 80523
[h]Joint Institute for Nuclear Research, Dubna, USSR
[i]KEK National Laboratory, Tsukuba-shi, Ibaraki-ken 305, Japan

ABSTRACT

Diamond is suitable for use as an ionizing particle detector for high rate, high radiation, and/or chemically harsh environments. A sampling calorimeter, a detector measuring the total energy of an incident particle, consisting of 20 alternating layers of diamond and tungsten has been constructed and tested. The diamond for the detector layers was grown by chemical vapor deposition with an averaged thickness of 500 μm. The active area of each layer was 3×3 cm^2 with ohmic contacts on opposite faces forming a metal-insulator-metal structure. The calorimeter was tested with electrons of energies up to 5.0 GeV. The response of the diamond/tungsten calorimeter was found to be linear as a function of incident energy. A direct comparison of diamond/tungsten and silicon/tungsten calorimeters was made.

I. INTRODUCTION

High luminosity hadron colliders such as CERN's LHC will require high performance detectors with fast rise and recovery times that can survive in an extreme radiation environment. Detectors based on diamond hold great promise for calorimeters and tracking detectors for this purpose. Diamond has a large bandgap (5.5 eV) and is radiation hard. High carrier mobilities (1800 cm^2/V-s for electrons and 1200 cm^2/V-s for holes) provide a very fast charge collection time (2 ns over 300 μm)[1]. As an added advantage, polycrystalline diamond grown by chemical vapor deposition (CVD) in large area wafers is potentially inexpensive.

Figure 1 illustrates the principle of operation of diamond as an ionizing radiation detector. An electric field is applied across the diamond via electrodes in ohmic contact[1] with the surface. A charged particle passing through the diamond creates electron-hole (e-h) pairs in the material. The e-h pairs separate due to the applied field, inducing a signal on the electrodes. Since diamond is an excellent insulator, the leakage current is negligible even for fields $> 10^4$ V/cm. As a result, the fabrication of a device is very simple with no need for a reverse biased p-n junction. We present performance measurements of a calorimeter using diamond detectors based on the principles described above.

Mat. Res. Soc. Symp. Proc. Vol. 339. ©1994 Materials Research Society

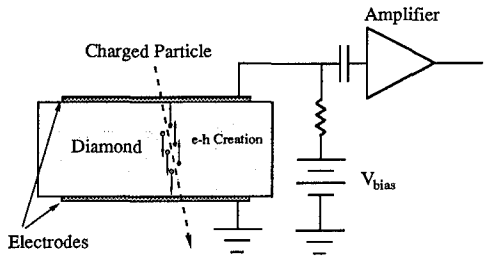

FIG. 1: Schematic of diamond detector operation.

These measurements are compared with measurements of a silicon-tungsten calorimeter of similar configuration.

II. CALORIMETER DESIGN AND BEAM CONDITIONS

A sampling calorimeter counts the number of electron-positron pairs produced via photons from bremsstrahlung interactions occurring in the layers of material used as a radiator. The energy of an electron or photon incident on the calorimeter can be shown to be proportional to the total number of pairs sampled in the electromagnetic shower.

The diamond and silicon calorimeters used in these tests were constructed with twenty layers of alternating 3.2 mm thick pieces of tungsten radiator ($1.0\,X_0$) and detector planes. Each detector plane was made of either a diamond or silicon assembly mounted on a 1.6 mm thick G-10 PC board with associated amplifier electronics. The diamond detectors were grown by Norton Diamond Films, Inc. [2] with an average thickness of $500\,\mu$m. The silicon detectors were uniformly $300\,\mu$m thick. The active area of each detector assembly measured $3.0 \times 3.0\,\mathrm{cm}^2$ and was segmented into three channels defined by $1.0 \times 3.0\,\mathrm{cm}^2$ strips. Two additional planes of silicon were mounted in front of each calorimeter with their strips oriented perpendicular to each other. These two planes were used to align the calorimeters in the beam and to provide coarse beam position information. The diamond and silicon detectors were coupled to charge-sensitive amplifiers having a gain of 30 mV/fC. The amplifier signal was then shaped using a $2.7\,\mu$s peaking time. The resulting pulses were digitized in a LeCroy 1885F Fastbus ADC [3].

The data presented in this report were taken at the IT4 beam line at the TRISTAN accumulator ring at KEK. The energy response of the calorimeter was measured by using six different beam momenta over the entire available range 0.5–5.0 GeV/c. The fractional momentum resolution (σ_P/P), determined from a previous experiment, varied between 4.9% for the 0.5 GeV/c beam and 1.3% for the 5.0 GeV/c beam.

III. CALIBRATION

The absolute gain of individual detector elements was determined by removing the tungsten from between the detector planes and using the electron beam as a source of minimum ionizing particles (MIP's). The calibration events were carefully selected to ensure that no showering occurred at or before the detector layer undergoing calibration. Figure 2 shows typical pedestals and signals (hatched regions) for both detectors after calibration.

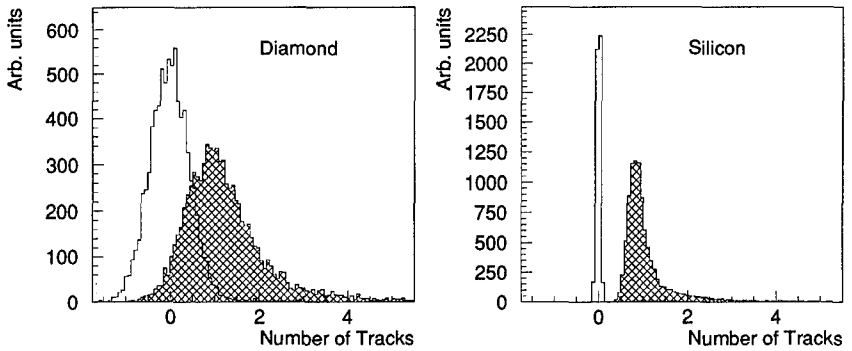

FIG. 2: Single particle signals for typical diamond and silicon detectors (shaded regions) in units of MIP's. The unshaded regions are noise signals from empty events.

Signals from diamond detectors are intrinsically smaller than those for silicon due to the higher electron-hole (e-h) creation energy (13.0 eV for diamond versus 3.6 eV for silicon). This is somewhat compensated by diamond's greater density ($3.5\,g/cm^3$ for diamond, $2.3\,g/cm^3$ for silicon). Therefore, the mean energy loss of 0.5 GeV electrons, as calculated from the restricted energy loss formula [4], implies 3600 and 7800 e-h pairs are created for each $100\,\mu m$ of diamond and silicon traversed, respectively. Furthermore, for the diamonds used, not all the charge was collected. The collection distance is a measure of the amount of charge collected and is defined as the average distance electrons and holes separate due to the applied field. The average collection distance over all diamond layers was $42\,\mu m$.

The average measured signal/noise for the two detector types was 2.1:1 for diamond and 26:1 for silicon. Combining the signal/noise information, the number of electrons produced and the collection distance (for the diamond detectors) gives an average electronic noise of 712 and 450 electrons for diamond and silicon, respectively.

IV. DATA ANALYSIS

The response of the calorimeter for each event was determined by summing the pedestal-subtracted, gain-corrected signals from all the channels. By accepting events where only the center strips in the front two pieces of silicon were hit, a maximum accepted spot size of $1.0 \times 1.0\,cm^2$ was defined which ensured that the shower was roughly centered in the calorimeter. Figure 3a shows the calorimeter response distributions for both calorimeters to 4 GeV electrons. As shown, there was a small constant background evident on the low side of the peak of the calorimeter response spectrum. This background was attributed to scraping of the beam in the collimator upstream of the calorimeter. Therefore, in the final calculation of the mean and rms, events were rejected where the calorimeter response was more than three standard deviations below the mean. Also, an estimate was made of the broadening of the response spectrum due to this scraping effect ($\approx 2.5\%$). After determining the mean and rms for the data at each energy, the beam energy spread [6] and the broadening due to scraping were subtracted in quadrature from the rms. Both calorimeters were treated in the same manner except for the corrections presented below.

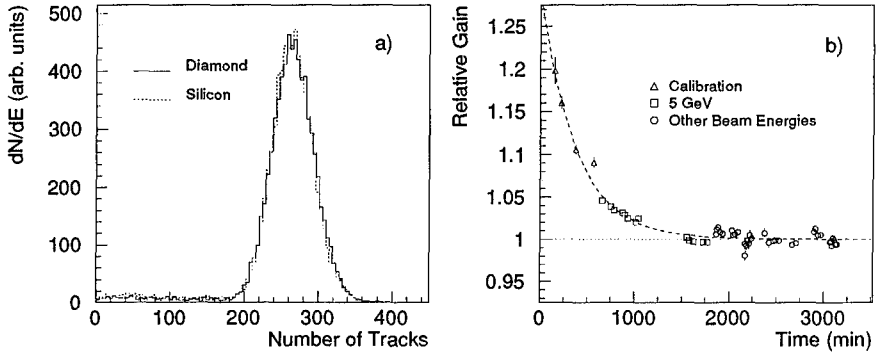

FIG. 3: Calorimeter response to 4 GeV electrons for both calorimeters (a) and relative calorimeter gain as a function of time since the application of the bias voltage (b). The solid line corresponds to a fit to an exponential (τ=380 min) plus a constant.

Two effects were observed in the diamond calorimeter which required corrections. First, one of the side strips in layer 16 (16 X_0 deep in the calorimeter) was very noisy. Therefore, the signal from this channel was replaced by the average of the signals in the corresponding strips in layers 14 and 18. Second, there was a systematic variation of the diamond calorimeter gain in the first part of the electron calibration and in the 5 GeV data that immediately followed. Figure 3b shows the normalized calorimeter response as a function of time after the diamond bias voltage was turned on for data taking[1]. The data were corrected for this time dependence resulting in a 3% shift in the mean calorimeter response at 5 GeV. The time dependent correction was negligible for data at other energies which were taken later. The effect of this time dependence on the energy resolution fit parameters was less than their uncertainties.

The response of each calorimeter was found to be linear in the electron beam energy. Linear fits of the energy response yield the following results:

$$\begin{aligned} \epsilon_{\text{diamond}}(\text{MIP's}) &= (66.19 \pm 0.26) \cdot E_{beam} \quad \chi^2 = 10.84/5\, dof \\ \epsilon_{\text{silicon}}(\text{MIP's}) &= (65.96 \pm 0.26) \cdot E_{beam} \quad \chi^2 = 8.35/5\, dof. \end{aligned}$$

Plots of the energy resolution (σ_E/E) as a function of incident electron energy are shown for the diamond and the silicon calorimeters in Figure 4. The solid lines are fits to a function of the form:

$$\frac{\sigma_E}{E} = \sqrt{\frac{A^2}{E^2} + \frac{B^2}{E} + C^2} \equiv \frac{A}{E} \oplus \frac{B}{\sqrt{E}} \oplus C \qquad (1)$$

The values for the fit parameters along with their χ^2 are summarized Table 1.

V. CALORIMETER SIMULATION

A simulation of each calorimeter using EGS4 [7] was performed to compare with the measured resolutions and to determine the amount of lateral and longitudinal energy loss.

[1]For 8 hours prior to data taking, the diamond bias voltage was cycled on and off repeatedly to test the calorimeter and fix minor problems with the electronics.

TABLE 1: Fitted resolutions for the diamond and the silicon calorimeters.

Detector	A (%GeV)	B (%GeV$^{\frac{1}{2}}$)	C (%)	$\chi^2/D.O.F.$
Diamond(data)	8.35 ± 0.73	19.20 ± 0.52	2.2 ± 1.3	0.04/3
Diamond(EGS)	2.94 ± 0.56	18.62 ± 0.15	1.33 ± 0.49	3.26/3
Silicon(data)	4.00 ± 0.85	19.73 ± 0.19	0.0 ± 1.6	2.21/3
Silicon(EGS)	1.6 ± 0.67	20.578 ± 0.047	0.00 ± 0.91	2.82/3

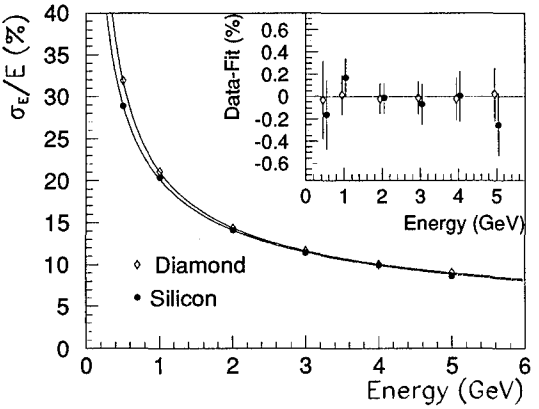

FIG. 4: Energy resolution (σ_E/E) of diamond-tungsten and silicon-tungsten calorimeters as a function of energy. Inset contains residuals for the fits discussed in the text.

Since, in the analysis, events were accepted where the incident beam struck a $1.0 \times 1.0\,\mathrm{cm}^2$ square centered in each calorimeter, the simulation generated events where the incident electrons were uniformly populated over this region. The resolutions given by the EGS simulation are given in Table 1. The lateral energy leakage was 18% and independent of the beam energy. Fluctuations on the lateral leakage varied approximately as $3.4\%/\sqrt{E}$ (1.6% at 5 GeV). The longitudinal energy leakage depended on the beam energy reaching 1.4% at 5 GeV. The fluctuations on the longitudinal leakage were 1.1% and independent of the beam energy.

VI. DISCUSSION

Both the diamond and the silicon calorimeter resolutions as a function of incident electron energy were fit to the resolution function given in equation 1. The three parameters determined from the fits describe terms which vary as $1/E$, $1/\sqrt{E}$ and a constant.

The $1/E$ term arises from effects which produce a constant width to a calorimeter response (σ_E). The simulations of both calorimeters indicate approximately $2\%/E$ which is attributed to the high energy tail of the Landau distribution for single tracks [5]. An additional contribution arises from electronic noise in each of the detector channels.

By adding the single channel noise for all the channels in quadrature, we estimate the contribution to the $1/E$ term due to electronic noise at $(7\pm1)\%/E$ and $(0.9\pm0.1)\%/E$ for diamond and silicon, respectively. Adding the electronic noise contributions in quadrature to the EGS results bring the $1/E$ term in the diamond and silicon EGS resolutions into reasonable agreement with the data.

The $1/\sqrt{E}$ dependence arises from counting statistics on the number of particles passing through the detector layers. As noted above, the lateral leakage also contributes to this term, however, its contribution of $3.4\%/\sqrt{E}$ to the overall resolution is negligible when compared with the $\approx 19\%/\sqrt{E}$ of the contained portion of the shower.

The constant term arises from sources whose contributions to the width of the energy distributions vary linearly with the energy. From the simulations, fluctuations in the longitudinal leakage are seen to contribute approximately 1.1%. In both calorimeters, there is good agreement between the simulation and data for the constant term.

VII. SUMMARY OF RESULTS

We have constructed and successfully operated simple diamond-tungsten and silicon-tungsten calorimeters with 1.0 X_0 sampling frequency. Results from exposure of these calorimeters to electron beams ranging between 0.5–5.0 GeV show that both detectors have a linear response in beam energy and comparable energy resolutions. The energy resolutions of the diamond and the silicon calorimeters were found to be:

$$\text{Diamond} \quad \frac{\sigma_E}{E} = \frac{(8.35 \pm 0.73)\%}{E} \oplus \frac{(19.20 \pm 0.52)\%}{\sqrt{E}} \oplus (2.2 \pm 1.3)\% \tag{2}$$

$$\text{Silicon} \quad \frac{\sigma_E}{E} = \frac{(4.00 \pm 0.85)\%}{E} \oplus \frac{(19.73 \pm 0.19)\%}{\sqrt{E}} \oplus (0.0 \pm 1.6)\% \tag{3}$$

When the electronic noise and beam related backgrounds are taken into account these results are in agreement with EGS simulations of both calorimeters.

We gratefully acknowledge the Texas National Research Laboratory Commission and the Superconducting Supercollider Laboratory for sponsoring this research.

REFERENCES

[1] L.S. Pan, *et al.*, "Journal of Applied Physics," **74** (1993) 1086.

[2] Norton Diamond Film, Northboro, MA 01532–1545.

[3] LeCroy Research Corporation, Chestnut Ridge, NY 10977.

[4] Particle Data Group "Physical Review D" **45** (1992) III–14.

[5] H. G. Fischer, "Nuclear Instruments and Methods," **156** (1978) 81.

[6] K. Ogawa, *et al.*, KEK internal memo 85–2.

[7] R. L. Ford and W. R. Nelson, SLAC–0210 (1978).

EXCIMER LASER PLANARIZATION OF DIAMOND FILMS

DONG-GU LEE, S.D. HARKNESS, AND RAJIV K. SINGH
University of Florida, Department of Materials Science and Engineering, Gainesville, FL32611

ABSTRACT

The planarization of rough polycrystalline diamond films synthesized by DC arc discharge plasma jet CVD was attempted using KrF excimer laser pulses. The effects of laser incidence angle and reaction gases (ozone and oxygen) on etching rate were studied. The temperature change of diamond and graphite with different laser fluences was calculated by computer simulation to explain the etching behavior of diamond films. The calculated threshold energy density for etching of pure crystalline diamond was about 1.7 J/cm^2. However, the threshold energy density was affected by the angle of laser incidence. Preferential etching of a particular crystallographic plane was observed through scanning electron microscopy. The etching rate of diamond with ozone was lower than that with oxygen. Also, the etching rate of diamond films at normal laser incidence was lower than that of films tilted at 45° for laser fluences above 2.3 J/cm^2. When the angle of incidence was 80° to the diamond surface normal, the peak-to-valley surface roughness was significantly reduced, from 30 μm to 0.5 μm.

INTRODUCTION

CVD diamond has recently received much attention for its remarkable properties. It is the hardest natural material and is chemically inert, has high wear resistance, high optical transparency from the infrared to the ultraviolet, and the highest thermal conductivity at room temperature. Therefore, diamond films have great potential in mechanical, optical, and microelectronic applications.

Planarization of the diamond surface is essential for its applications because CVD diamond films generally have high roughness. The conventional method for planarization of diamond is mechanical polishing with diamond powder. But this technique requires a long time to achieve planarization. Many alternative techniques, such as gas ion beam [1,2], polishing with hot plate [3], and laser irradiation [4-6] have been reported. Among these many techniques, planarization of diamond films by laser irradiation is particularly effective due to its fast processing at room temperature without any contacts and the size and shape limitations.

A general etching mechanism for diamond using laser pulses has been proposed by Rothschild [7]. This involves a combined photochemical and thermal transformation of the initial diamond crystal to graphite followed by sublimation or chemical reaction of the transformed solid.

The photon energy of the KrF laser (λ=248 nm, E=5.0 eV) is lower than the bandgap energy of diamond (E=5.4 eV). Therefore, diamond can not absorb the incoming laser energy on its surface effectively. However, impurities [8] and defects in or around the diamond crystal grains as well as graphitization of the diamond surface during laser irradiation [7] can absorb more energy, leading to an increase in the etching rate of diamond.

In this experiment, the effects of laser incidence angle and reaction gases (oxygen, ozone) on etching rate, surface morphology, and roughness of diamond films were studied. Also, the surface temperature change with respect to laser fluence was calculated by computer simulation.

Mat. Res. Soc. Symp. Proc. Vol. 339. ©1994 Materials Research Society

EXPERIMENTAL

A free-standing diamond film (~500 μm thick) synthesized by arc discharge plasma jet CVD procured from Westinghouse Electric Co. is shown in Fig. 1. The peak-to-valley surface roughness of the free-standing diamond films was about 30 μm.

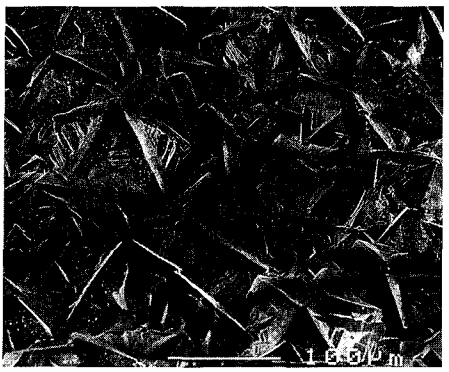

Fig. 1. Surface morphology of the original free-standing diamond.

The diamond films were irradiated with 20 ns pulses from a KrF excimer laser at a repetition rate of 20 Hz with fluences of 1~4 J/cm^2. The size of the rectangular beam spot was 2 mm x 1 mm. Laser irradiation of the diamond surface occured at 45° to the surface normal. The camber was held at 100 torr, but since the diamond surface was so close to the gas nozzle and the gas was directly blown onto the film surface, we neglected the pressure effects on the laser processing. Other irradiations, taken at normal incidence and at 80° to the film surface normal, were done outside chamber. Oxygen gas was directly blown onto the sample surface through a flexible tube.

Surface roughness was measured by a Dektak surface profilometer, which uses a mechanical stylus. The etching rate was obtained from the value of the etching depth divided by the number of laser pulses. The film surfaces were examined by scanning electron microscope.

RESULTS AND DISCUSSION

Effect of angle of laser incidence

Figure 2(a) shows the surface of a CVD diamond film irradiated at normal incidence with a laser fluence of 3.5 J/cm^2 for 2 min. 5 sec.. The irradiated surface was much smoother than the original diamond surface. A laser-induced periodic structure, which is called 'ripple', was developed on the film surface. The period of the surface ripple was approximately 10 μm, which is much wider than the wavelength of the laser. Irradiation with lower fluence of 1.5 J/cm^2 did not result in a periodic structure. The reason for ripple formation might be that interference of the incident laser beam and scattered light on the irregular surface produces a sinusoidal component of spatial variation in the light intensity falling on the diamond surface, resulting in a variation in etching rate [9]. The ripple surface is more readily developed at higher beam intensities. As shown in Fig. 2(b), formation of graphite or amorphous carbon, which did not fully react with oxygen during illumination, took place around the irradiated area. When laser incidence was set at 45° to the diamond surface normal with laser fluences of 1 to 4 J/cm^2, roughness of the irradiated surfaces was not significantly improved.

Shown in Fig. 3 is the etching rate of the CVD diamond films plotted versus laser fluence for films irradiated at different angles (0°, 45°) using different gases (oxygen and ozone). The etching rate of diamond irradiated at 45° using oxygen was higher than that at normal incidence above fluence of 2.3 J/cm^2. The measured threshold energy for etching at 45° incidence was around 1.7 J/cm^2. Different etching rates at different angles appear as a result of preferential etching. Most crystals have an octahedral shape formed by (111) planes. Compared to the

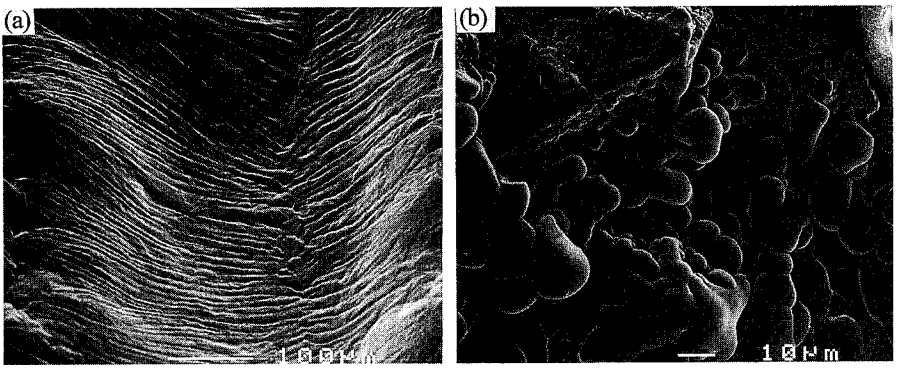

Fig. 2. Surface morphologies of diamond films observed by scanning electron microscope. (a) normal irradiation to the diamond surface(E=3.5 J/cm^2, 2 min. 5 sec), (b)boundary area of (a).

relatively defect-free (100) planes, the (111) planes have many more defects and impurities which can absorb more laser energy, causing more heating and sublimation, which results in faster etching rates. Microscopically, the laser light at 45° incidence shines more intensively (111) planes than at normal incidence.

To explain the lower threshold energy at normal incidence than at a 45° incidence, a geometrical factor should be taken into consideration. Laser light at 45° to the diamond surface normal shines flat on the surface of diamond facets on which thermal energy can diffuse any directions. Normally incident laser light shines on a non-planar surfaces having a cone shape which results in a geometrical limitation of heat flow. Therefore, normal incidence causes heat confinement as well as intensified absorption near tips, leading to higher local temperature [6] and resulting in initiation of etching of materials at lower laser fluences.

Consequently, etching rate of diamond films with lower laser fluences (below 2.3 J/cm^2) was

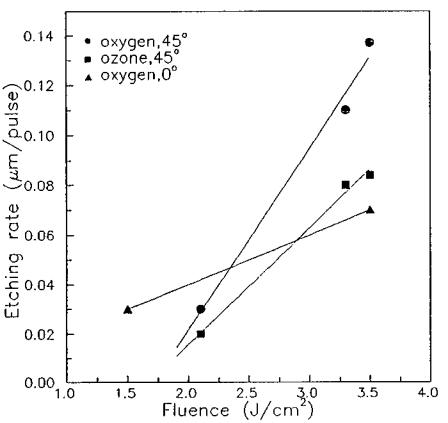

Fig. 3. Etching rate of diamond films versus laser fluence at different angles (0°: normal incidence, 45°) under different gas atmospheres (oxygen, ozone).

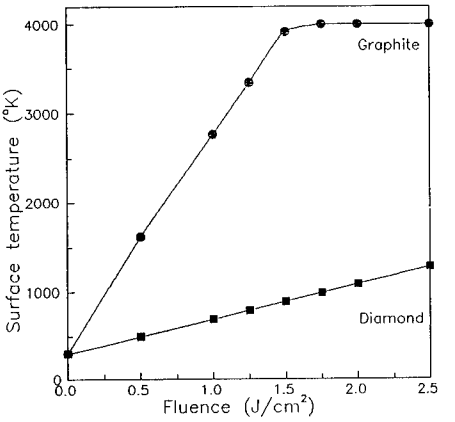

Fig. 4. The calculated surface temperature of diamond and graphite versus laser fluence by computer simulation.

mainly controlled by geometrical factor causing heat confinement, but above 2.3 J/cm^2, by energy sensitivity of a plane.

Figure 4 shows surface temperature plotted versus laser fluence calculated using SLIM (Simulation of Laser Interactions with Materials), a software package developed by John Viatella and Rajiv Singh [10]. The simulation assumed a single laser pulse and a planar surface, which is similar to the condition at 45° incidence. The sublimation temperature of graphite is around 4000 K and the graphitization temperature of diamond is around 900 K. The laser fluence satisfying both these surface temperature which we call the threshold energy density, was 1.7 J/cm^2. This calculated value perfectly matched the experimental data at 45° laser incidence as seen in Fig. 3. Based on the data in Fig. 4, we theorize that diamond is not directly etched away but transforms to graphite, which then sublimates, thereafter forming CO and CO_2.

Fig. 5 presents SEM images showing how the diamond surface changed as a function of time. A fluence of 2.1 J/cm^2 was applied at an angle of incidence of 80° to the surface normal. The original rough surface of the CVD diamond film (Fig. 1) was progressively more etched away as time passed, as shown in Fig. 5(a, b, and c). The peak-to-valley surface roughness was significantly reduced, going from 30 μm to 0.5 μm. As shown in Fig. 5(d), which is a magnified image of Fig. 5(c), preferential etching in accordance with crystal plane orientation was observed.

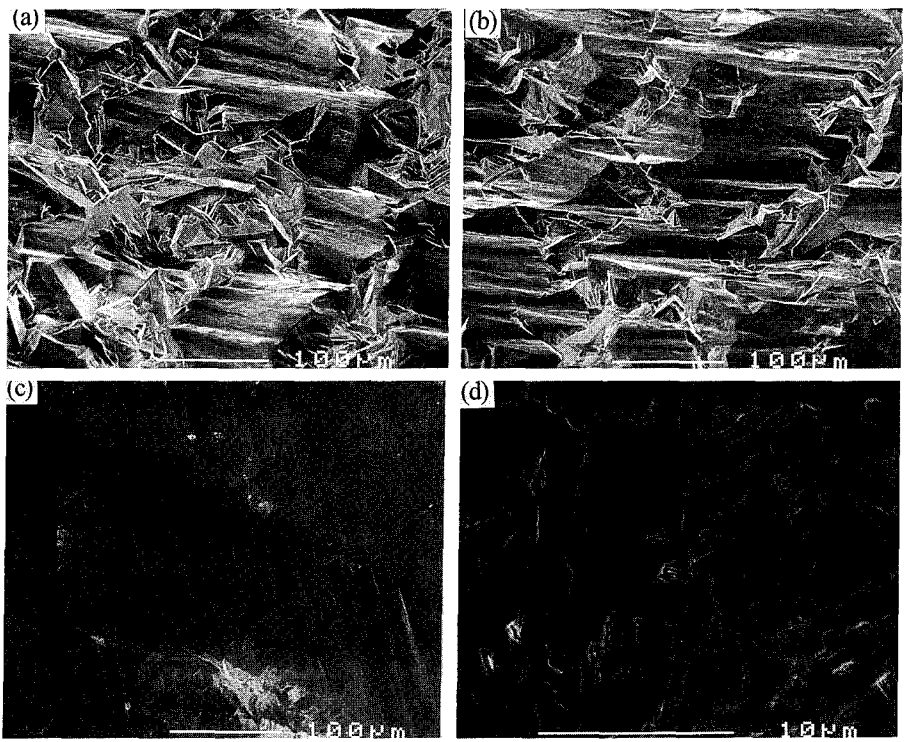

Fig. 5. Surface morphology changes of diamond films as a function of time of (a) 2 min., (b) 4 min., and (c) 6 min. with fluence of 2.1 J/cm^2 at 80° incidence to the diamond surface normal. (d) is the magnified image of (c).

Effect of ozone gas

Etching rates of diamond tilted at 45° were measured with fluences of 1 to 4 J/cm^2 (shown in Fig. 3) using ozone produced by an ozonizer. The oxygen feed gas flowed through a narrow gap between two concentric tube electrodes with a high DC voltage (6 kV) applied to these two electrodes to produce the ozone.

The etching rate using ozone was lower than that using oxygen. The surface of the diamond film processed in ozone, shown in Fig. 6(a), was rougher in comparison with that processed in oxygen (Fig. 6(b)). There are several possible reasons for this; Under oxygen atmosphere, the incident photon energy can be delivered to the film surface without much energy loss because the KrF laser energy (E=5.0 eV) is not used up for the dissociation of the O_2 bond (E=5.1 eV). Few amounts of atomic oxygen, if any, are near the film surface. On the other hand, under ozone atmosphere, some of the incident photon energy is absorbed by ozone due to its high absorption coefficient (α=290 cm^{-1}) [11]. Namely, ozone gas blocks some amounts of the incoming laser light and lowers the laser energy density on the surface, which results in an decrease of etching rate. Also, ozone (O_3) begins to thermally decompose at temperature above 50°C and completely decomposes at 230°C [12]. This means that ozone simply plays a role of supplying atomic oxygen, because the surface temperature of the diamond is very high during illumination. The etching rate of (111) planes will be more enhanced by atomic oxygen compared to using oxygen. In other words, use of ozone will promote the preferential etching of certain planes, resulting in a rough surface.

CONCLUSIONS

The planarization of rough polycrystalline diamond films synthesized by DC arc discharge plasma jet CVD was attempted using KrF excimer laser pulses. The calculated threshold energy density for etching of pure crystalline diamond was about 1.7 J/cm^2. The threshold energy density was affected by the angle of laser incidence. Preferential etching of a particular crystallographic plane was observed. The etching rate of diamond films at normal laser incidence was lower than that of films tilted at 45° for fluences above 2.3 J/cm^2. Also, the etching rate of diamond with ozone was lower than that with oxygen. When the angle of incidence was 80° to the film surface normal under oxygen atmosphere, the peak-to-valley roughness was significantly reduced, from 30 μm and 0.5 μm.

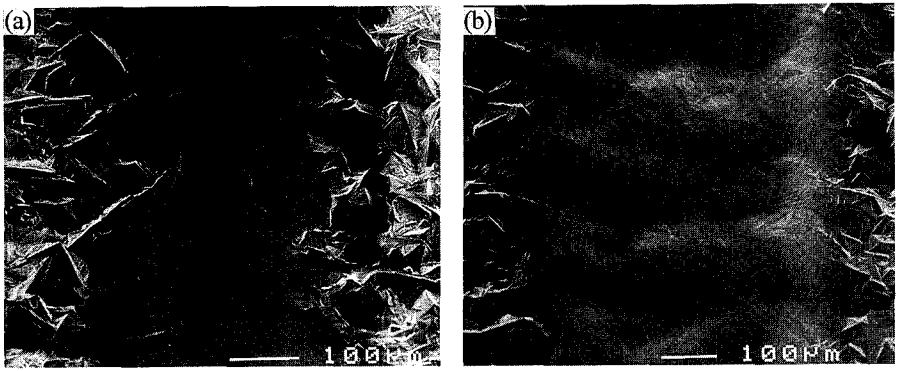

Fig. 6. SEM images of diamond surfaces at 45° incidence under (a) ozone and (b) oxygen atmospheres with fluence of 2.2 J/cm^2.

REFERENCES

1. T. Zhao, D.F. Grogan, B.G. Bovard, and H.A. Macleod, in *Diamond Optics III*, edited by A. Feldman and S. Holly (Proc. Soc. Phot-Opt. Instrum. Eng. **1325**, 1990) pp. 142-151; Appl. Opt. **31**, 1483 (1992).
2. A. Hirata, H. Tokura, and M. Yoshikawa, Thin Solid Films **212**, 43 (1992).
3. H. Tokura, C.-F. Yang, and M. Yoshikawa, Thin Solid Films **212**, 49 (1992).
4. S. Tezuka and M. Yosikawa, J. Jpn. Soc. Precision Eng. **56**, 2255 (1990).
5. A. Blatter, U. Bögli, L.L. Bouilov, N.I. Chapliev, V.I. Konov, S.M. Pimenov, A.A. Smolin, and I.V. Spitsyn, J. Eletrochem. Soc. **91**, 357 (1991).
6. U. Bögli, A. Blatter, S.M. Pimenov, A.A. Smolin, and V.I. Konov, Diamond & Rel. Mater. **1**, 782 (1992).
7. M. Rothschild, C. Arnone, and D.J. Ehrlich, J. Vac. Sci. Technol. B, **4** (1), 310 (1986).
8. V.P. Ageev. L.L. Builov, V.I. Konov, A.V. Kuzmichev, S.M. Pemenov, Acedemician A.M. Prokhorov, V.G. Ral'chenko, B.V. Spitsyn, and B.I. Chapliev, Sov. Phys. Dokl. **33** (11), 840 (1988).
9. A.E. Siegman and P.M. Fauchet, IEEE J. Quantum Electon. **QE-22** (8), 1384 (1986).
10. R.K. Singh and J. Viatella, J. Met. **44**, 22 (1992).
11. *CRC Handbook of Marine Science*, edited by F.G. Walton Smith (CRC press, Cleveland, Ohio, vol I, 1974), p.218
12. C. Coste, in *Ozonization manual for water and wastewater treatment*, edited by W.J. Masschelein (John Wiley & Sons, New York, 1982), pp. 206-214.

HIGH POWER AND HIGH FREQUENCY SILICON CARBIDE DEVICES

JOHN W. PALMOUR*, C.H. CARTER, JR.*, C.E. WEITZEL**, AND K.J. NORDQUIST**
*Cree Research, Inc., 2810 Meridian Parkway, Durham, NC 27713
**Phoenix Corporate Research Laboratories, Motorola, Inc., Tempe, AZ 85284

ABSTRACT

The breakdown electric field of 4H-SiC as a function of doping was measured using pn junction rectifiers, with maximum voltages of 1130 V being achieved. 4H-SiC vertical power MOSFET structures have shown specific on-resistances of 33 $m\Omega$-cm^2 for devices capable of blocking 150 V. A current density of 100 A/cm^2 was achieved at a drain voltage of 3.3 V. Thyristors fabricated in SiC have also shown blocking voltages of 160 V and 100 A/cm^2 at 3.0 V. High temperature operation was measured, with the power MOSFETs operating to 300°C, and the thyristors operating to 500°C.

Submicron 6H- and 4H-SiC MESFETs have shown good I-V characteristics to $V_d = 40$ V, with an I_{dss} of 200-300 mA/mm. The maximum operating frequencies (f_{max}) achieved for 6H-SiC MESFETs is 13.8 GHz, with small-signal power gains of 9.8 dB and 2.9 dB at 5 GHz and 10 GHz, respectively. 4H-SiC MESFETs have demonstrated an RF output power density of 2.8 W/mm at 1.8 GHz. This is the highest power density ever reported for SiC and is 2-3 times higher than reported for comparable GaAs devices.

INTRODUCTION

Silicon carbide has been projected to have tremendous potential for high voltage solid-state power devices with very high voltage and current ratings because of its high electric breakdown field of 4×10^6 V/cm[1] and high thermal conductivity of 4.9 W/cm-K.[2] The high breakdown field allows the use of much higher doping and thinner layers for a given voltage than is required in Si devices, resulting in much lower specific on-resistances for unipolar devices.[3] 6H-SiC has received the most attention for high power devices since it was the first commercially available polytype in wafer form. Another polytype that shows even more potential for high power operation is 4H-SiC, because the electron mobility in 4H-SiC is about twice as high as that of 6H-SiC.[4] Moreover, 6H-SiC exhibits a high degree of mobility anisotropy, having a mobility in the (0001) direction that is 1/5th that in the basal plane,[5] yielding a 10× advantage for 4H-SiC over 6H-SiC for vertical power devices.

Silicon carbide has also received increased attention because of its potential for high power microwave devices. The combination of high electric breakdown field, high saturated electron drift

Mat. Res. Soc. Symp. Proc. Vol. 339. ©1994 Materials Research Society

velocity of 2.0×10^7 cm/sec,[6] and high thermal conductivity will allow very high power operation at high frequency, and the wide bandgap should also allow SiC FETs to have significant RF output power at high temperatures.[7] Submicron MESFETs in 6H-SiC have recently demonstrated desirable microwave performance.[8,9] As is the case for power devices, the higher electron mobility of 4H-SiC makes it even more promising for high power, high frequency operation.

This paper presents recent data on several types of power devices that have been fabricated in both 6H-SiC and 4H-SiC that confirm the potential of this material for both high power and high frequency applications. Both 4H and 6H-SiC diodes have demonstrated breakdown voltages greater than 1100 V. High voltage rectifiers and switches such as power MOSFETs and thyristors have been demonstrated for high temperature applications. All these devices had relatively small active areas in order to insure good yield because of the presence of micropipe defects (about 100 cm^{-2}) that can cause device failure.[10] However, they show promise for much larger power devices as the material quality is improved. High frequency MESFETs have been fabricated in both 4H and 6H-SiC and have demonstrated very high RF output power densities.

POWER DEVICE STRUCTURES

PN Junction Rectifiers

Vertically oriented pn junction diodes have been previously fabricated in 6H-SiC and have been characterized as a function of doping,[1] with blocking voltages as high as 2000 V being reported.[11] The forward bias characteristics show that the 6H-SiC rectifiers have a built-in potential of about 2.6 V and the rated current of 100 mA (68 A/cm^2) was obtained at 3.0 V. A 1400 V 6H-SiC pn junction rectifier exhibited about 1 μA leakage current at a reverse voltage of about 1375 V, near the onset of avalanche breakdown.[12] The reverse bias leakage current at 1300 V was 140 nA (9.3×10^{-5} A/cm^2), and was 15 nA (1.0×10^{-5} A/cm^2) at 1100 V. Although both the pn junction diodes and packages need further improvement for high voltage passivation, they have been proven to be reliable at high temperature. These devices have successfully passed 1000 hour reverse blocking tests at 350°C.

In this research, 4H-SiC substrates were used to study the electric breakdown field of 4H pn junction diodes. The 4H substrates were n-type ($4\text{-}10\times10^{18}$ cm^{-3}) and both Si-face and C-face wafers, as well as p^+n and n^+p diode structures were investigated. The low doped epitaxial layer thicknesses ranged from 0.5 μm to 15 μm, with corresponding doping levels in the range of 2.2×10^{18} to 8×10^{15} cm^{-3}. The diodes were mesa terminated by RIE, using NF_3, through the epitaxial layers. The wafers were oxidized to form a passivating SiO_2 layer. Al/Ti ohmic contacts[13] were then patterned on the top p-layer and Ni ohmic contacts deposited on the n-type substrate, after which the contacts were annealed. Good avalanche breakdown characteristics were observed for all of the diode data points shown in Fig. 1, except for the lowest doped sample.

While there is some scatter in the data, no statistical difference was observed in the breakdown fields of either Si- or C-face samples, or p^+n or n^+p samples. As shown in Fig. 1, a doping of 1.4×10^{16} should have a breakdown voltage of 1000 V, corresponding to an electric breakdown field of 2.2×10^6 V/cm. The highest breakdown field, 5.2×10^6 V/cm, was observed at high doping. The I-V characteristics of the highest voltage 4H-SiC diode are shown in Fig. 2. In forward bias, the built-in potential was 2.8 V. In reverse bias, this diode showed low leakage rectification to 1130 V. The doping near the junction was 8×10^{15} cm^{-3} and the layer was 15 μm thick, which should have supported a higher voltage. However, it is possible that the doping decreased through the epilayer, causing the depletion region to punch-through to the n^+ substrate.

Power MOSFETs

Silicon carbide vertical power MOSFETs possess a strong advantage over those made in silicon because the high voltage layer (drain-drift region) may use a 10× higher doping level and one-tenth the thickness for a given voltage due to the much higher breakdown field of SiC. Ultimately, this could translate into specific on-resistances that are as low as 1/300th that of equivalent Si devices.[3] The first vertical UMOS power MOSFET structures fabricated in 6H-SiC were recently reported by Palmour, et al.[12] These devices had specific on-resistances ($R_{ds(on)}$) of 38 $m\Omega$-cm^2 and could operate at drain voltages of 50 V. The devices failed at higher voltages due to gate oxide breakdown. The 6H-SiC MOSFETs withstood current densities of 190 A/cm^2 (0.32 A/cm of gate periphery). The maximum transconductance (g_{max}) was 6.75 mS/mm and the

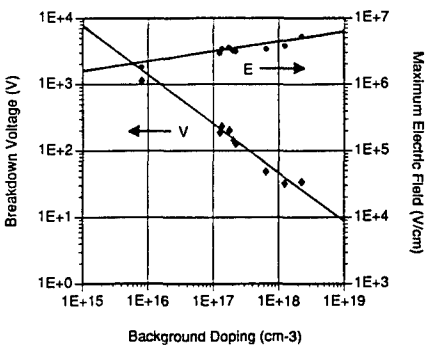

Figure 1: Breakdown voltage and electric breakdown field as a function of background doping for 4H-SiC pn junction diodes.

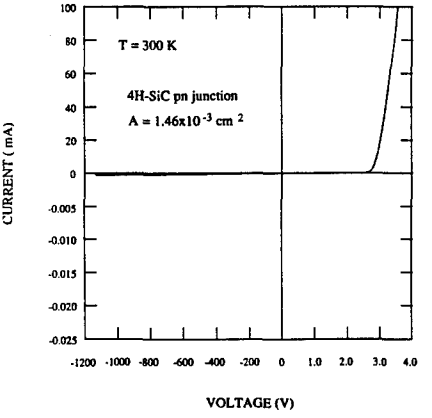

Figure 2: I-V characteristics of an 1130 V 4H-SiC mesa p^+n diode.

threshold voltage was V_g = 3.7 V. These devices were operated to 300°C, with good I-V characteristics throughout that range.

This same UMOS design, shown in Fig. 3, has now been applied to 4H-SiC. The design utilized n^+ source fingers ion implanted into an epitaxially grown p-type channel layer. The n^- drain epilayer was isolated using a reactive ion etched mesa. The active area of this device was 6.7×10^{-4} cm^2 and the gate periphery was 4 mm.

The I-V characteristics of one of these devices is shown in Figure 4. This device blocked 80 V on the drain and could withstand current densities as high as 368 mA (550 A/cm^2 and 0.92 A/cm of gate periphery) and power densities greater than 10 kW/cm^2. A drain current of 134 mA (200 A/cm^2) was obtained at V_d = 3.5 V, which corresponds to an $R_{ds(on)}$ of 17.5 mΩ-cm^2 at a gate bias of +16 V. The g_{max} for this device was about 40 mS (10 mS/mm). The channel mobility for the device shown in Fig. 6 was about 20 cm^2/V-sec.

A higher voltage 4H-SiC UMOS device is shown in Figure 5. This device blocked 150 V and could achieve a drain current of 67 mA (100 A/cm^2) at V_d = 3.3 V and V_g = +18 V. This corresponds to an $R_{ds(on)}$ of 33 mΩ-cm^2. The g_{max} of this device was about 20 mS (5 mS/mm). The channel mobility for this device was about 7-12 cm^2/V-sec. The highest blocking voltage achieved to date with these 4H devices was 180 V, but the devices on that wafer had a higher $R_{ds(on)}$ of 74 mΩ-cm^2.

The 4H-SiC UMOS devices were characterized as a function of temperature. The I-V curves for a different 80 V MOSFET at room temperature are shown in Fig. 6(a). This particular device had a much higher $R_{ds(on)}$ of 55 mΩ-cm^2 at room temperature than the best devices shown in Figs. 4 & 5, because it had a higher threshold voltage of about 6.3 V. The drain current and transconductance at V_g = +18 V increased dramatically with a temperature increase from room

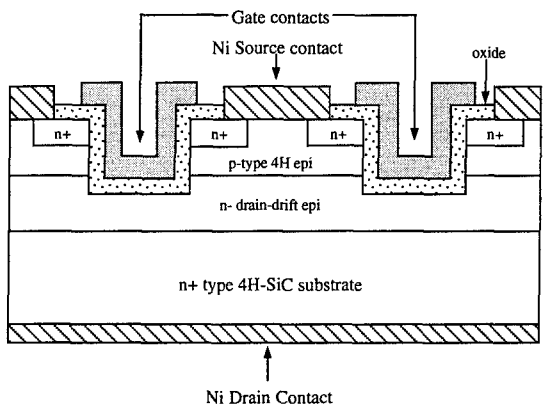

Figure 3: Cross-sectional view of the n-channel 4H-SiC UMOS vertical MOSFET device design. The drain-drift layer was mesa isolated.

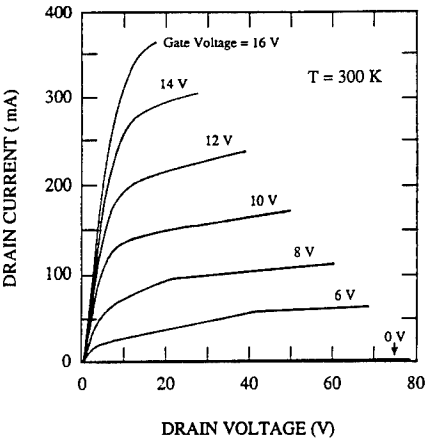

Figure 4: I-V characteristics of an 80 V 4H-SiC vertical UMOS power MOSFET structure. (A = 6.7×10^{-4} cm^2).

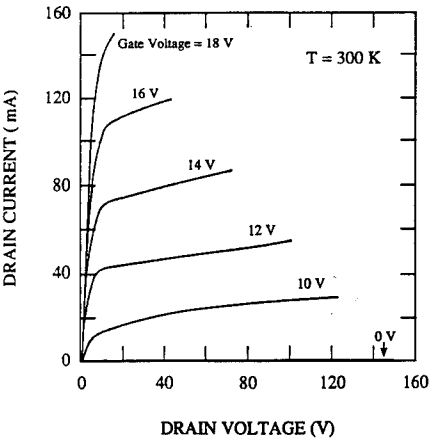

Figure 5: I-V characteristics of a 150 V 4H-SiC vertical UMOS power MOSFET structure. (A = 6.7×10^{-4} cm^2).

temperature to 150°C, as shown in Fig. 6(b). These increases were primarily due to the decrease in threshold voltage to 4.9 V. The drain current increased by a factor of almost two and the transconductance increased from 11.9 mS (2.98 mS/mm) to 18 mS (4.5 mS/mm). It is assumed that these increases were due to the reduction in threshold voltage to 4.8 V because the $R_{ds(on)}$ remained very stable, showing a very slight decrease to 53 mΩ-cm^2. These trends continued up to 300°C, as shown in Fig. 6(c). The threshold voltage decreased to 4.4 V at this temperature, which resulted in increases in the drain current and transconductance to about 174 mA and 25 mS (6.25 mS/mm), respectively. The $R_{ds(on)}$ actually increased to 86 mΩ-cm^2 at 300°C. It was found that these devices had low lifetimes at temperatures above 300°C, exhibiting gate oxide failure during measurement. This problem will require further development.

Thyristors

Bipolar power device structures have also been recently reported in 6H-SiC.[12] Bipolar junction transistors (npn) had collector voltages as high as 200 V and current gains as high as 10.4. Additionally, pnpn thyristors were also demonstrated to have forward breakover voltages as high as 100 V, with a 500 μA trigger current required for an 8 V breakover. Unfortunately, the thyristors had a very high specific on-resistance of 126 mΩ-cm^2 once the breakover voltage was reached. This was due to the high resistivity of the p-type substrate used. Both the BJTs and thyristors operated very well, if not better, at elevated temperatures up to 400°C. As the temperature of the thyristors was raised, both the required trigger current and the resistance reduced

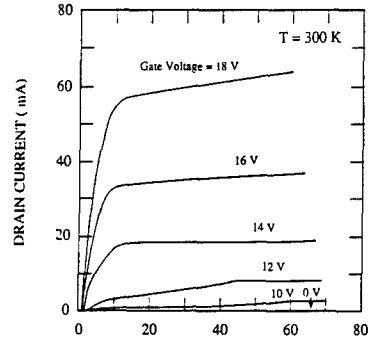

(a)

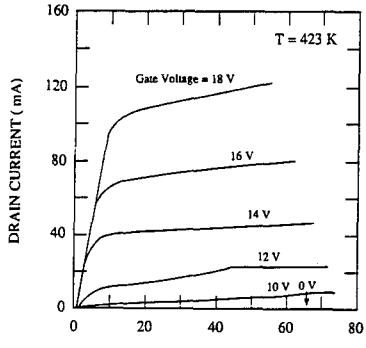

(b)

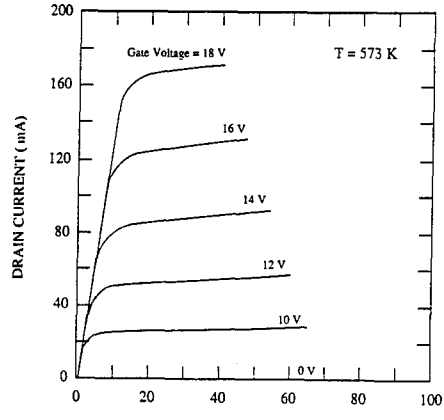

(c)

Figure 6: Current-voltage characteristics of a 4H-SiC vertical UMOS power MOSFET structure at (a) 27°C, (b) 150°C , and (c) 300°C.

dramatically. At 350°C, the thyristors showed much better operation, with a trigger current of 150 μA for an 8 V breakover and a specific on-resistance of 11 mΩ-cm^2. It is assumed that the greatly decreased resistance was due to a much higher carrier concentration in the p-type substrate at high temperatures, because the Al p-type dopant is not fully ionized at room temperature.

Subsequently, the same structure was applied to the opposite polarity thyristor, which allows the use of much lower resistivity n-type substrates.[14] The device structure of the 6H-SiC npnp thyristors is shown in Figure 7. They utilized a mesa structure, with all of the doping being done in-situ during epitaxy. The area of the device was 1.05×10^{-3} cm^2 and the device periphery was terminated using a reactive ion etched mesa. These devices showed forward and reverse voltages of 160 V with no gate current. As shown in Figure 8, the forward breakover voltage was reduced to -6 V with a trigger current of -200 μA. The improved performance of this device is revealed by the much lower voltage drop of 3.0 V for 105 mA (100 A/cm^2). With a built-in voltage of 2.65 V, this corresponds to a specific on-resistance of 3.6 mΩ-cm^2.

These npnp devices have now been successfully operated at high temperatures. The I-V characteristics of an npnp thyristor as a function of temperature are shown in Fig. 9. This device required a gate trigger current of -250 μA for a breakover voltage of -7 V at room temperature, as shown in Fig. 9(a). The forward breakover voltage with no gate current was about -120 V, and the voltage drop for 100 A/cm^2 was 3.0 V. When the device was heated to 350°C, the gate current required for a -7 V breakover dropped to -150 μA, as shown in Fig. 9(b). The built-in voltage at 350°C decreased to about -2.0 V, but the bulk resistance increased 10 mΩ-cm^2 due to decreasing mobilities with increasing temperature. These offsetting effects meant that the voltage drop for 100 A/cm^2 was still about -3.0 V. This thyristor operated well to as high as 500°C, as shown in

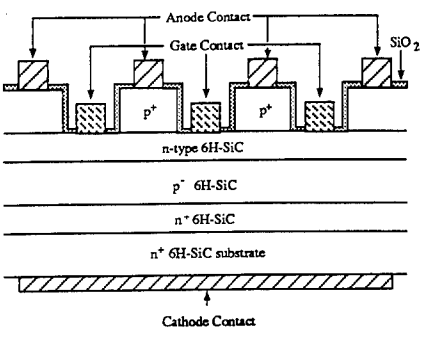

Figure 7: Cross-sectional view of the npnp 6H-SiC thyristor device design. The outer perimeter was mesa isolated.

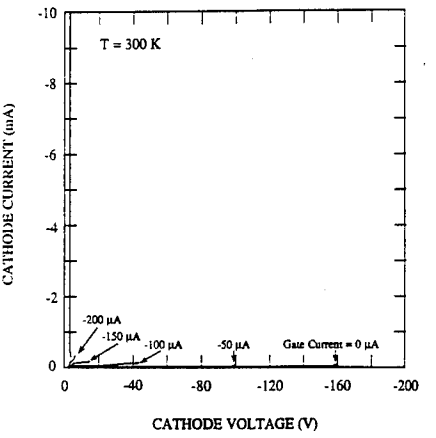

Figure 8: Forward bias I-V characteristics of a vertical 6H-SiC npnp thyristor at 25°C. The active area was 1.05×10^{-3} cm^2.

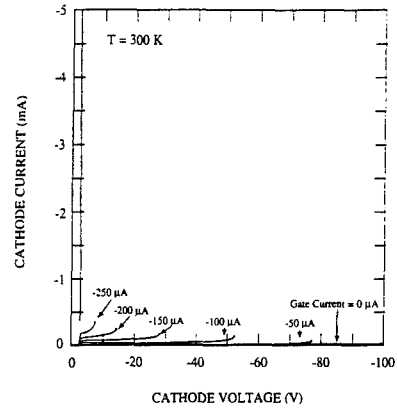

(a)

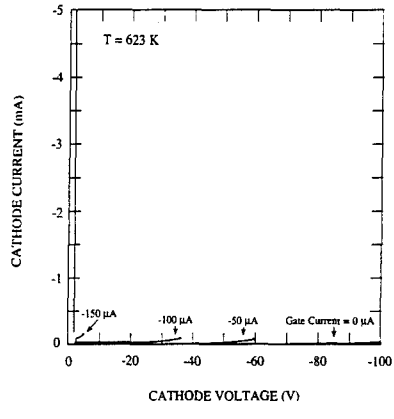

(b)

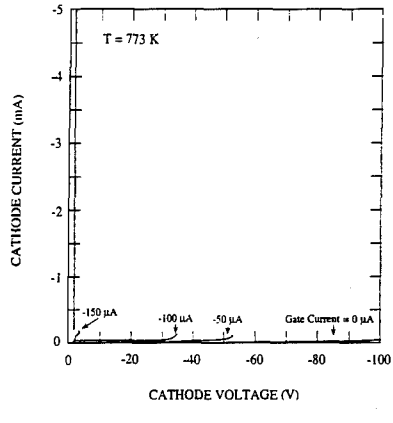

(c)

Figure 9: Forward bias current-voltage characteristics of a 6H-SiC npnp thyristor at (a) 27°C, (b) 350°C, and (c) 500°C. The area of the device was 1.05×10^{-3} cm^{-2}.

Fig. 9(c). The forward breakover voltage with no gate current was still above -100 V and the leakage current at -100 V was only -43 μA (4×10^{-2} A/cm^2). The forward breakover voltage with a gate current of -150 μA was reduced to about -3.0 V. The built-in voltage at 500°C was further decreased to -1.8 V and the specific on-resistance was still about 10 mΩ-cm^2, resulting in a voltage drop of -2.75 V for a current density of 100 A/cm^2.

HIGH FREQUENCY SiC MESFETs

Both 6H- and 4H-SiC MESFETs have been fabricated using the same basic device design. The MESFET utilized a two fingered design with each gate finger being 166 μm, for a total gate width of 332 μm. The cross-sectional design, shown in Figure 10, was also similar for both polytypes, with n$^+$ source and drain regions formed by epitaxial growth and reactive ion etching and annealed Ni source and drain contacts. The n-type channel doping was 1-2.5$\times10^{17}$ cm^{-3} and was isolated from the substrate by a p-type epilayer with a doping of about 1-5$\times10^{15}$ cm^{-3}.

As mentioned previously, 4H-SiC shows more promise for power microwave devices than 6H-SiC because of the much higher electron mobility. The typical I-V characteristics of the first reported 4H-SiC high frequency MESFETs are shown in Fig. 11(a). The drain current density at V_{ds} = 25 V is about 300 mA/mm, with a maximum transconductance in the range of 38-42 mS/mm. The high frequency characteristics of one of these devices is shown in Fig. 11(b). The gate length was 0.7 μm, and the source-gate and gate-drain spacing were 0.3 μm and 0.8 μm, respectively. As shown in Fig. 11(b), the f_{max} for this device was 12.9 GHz and the f_t was 6.7 GHz. The small-signal power gain was 9.3 dB at 5 GHz, and 2.2 dB at 10 GHz. The measurement conditions were V_{ds} = 30 V, I_{ds} = 78 mA, V_{gs} = +1 V, and I_{gs} < 1 pA.

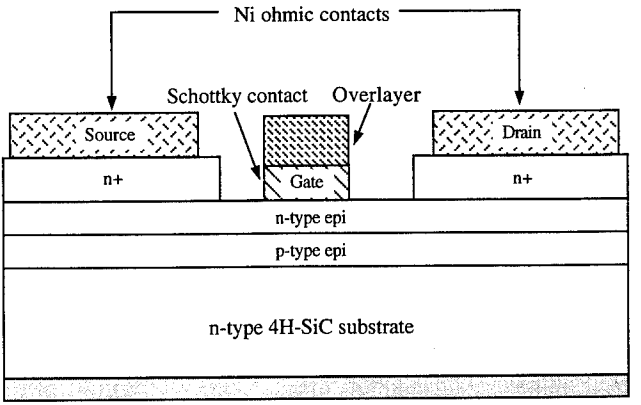

Figure 10: Cross-sectional view of a 4H-SiC MESFET utilizing epitaxially grown n$^+$ source and drain mesas.

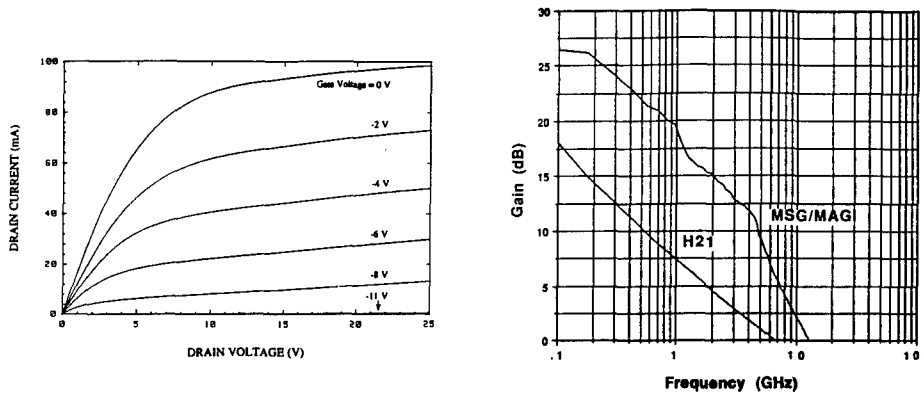

(a) (b)

Figure 11: (a) Current-voltage characteristics of a 4H-SiC MESFET and (b) small-signal parameters, MSG/MAG and H_{21}, as a function of frequency, for a 4H-SiC MESFET with a gate length and width of 0.7 μm and 332 μm, respectively.

The output power was also measured in Class A operation on-wafer using an ATN LP1 On-Wafer Load Pull System. The measured gain, output power, and power added efficiency at 1.8 GHz are plotted in Fig. 12. The maximum output power 29.72 (0.937 W) was achieved with 6.7 dB gain, 12.7% power added efficiency, and 15.4% drain efficiency using an input power of 23 dBm. The maximum power density was 2.8 W/mm which is the highest reported to date for a SiC MESFET. By reducing the drive level to 21 dBm the gain, power added efficiency, and drain efficiency improved to 8.15 dB, 14.8%, and 17%, respectively, but the output power decreased to 29.15 dBm (2.5 W/mm).

Small-signal RF measurements were also performed on some earlier 6H-SiC devices, which demonstrated a lower f_{max} of 10 GHz.[8] However some more recent 6H-SiC devices with smaller dimensions and improved fabrication have yielded small-signal RF results that are superior even to those of the 4H-SiC devices. The typical I-V characteristics of one of these devices is shown in Fig. 13(a). The gate length of this device was 0.5 μm, and the source-gate and gate-drain spacing were 0.3 μm and 0.8 μm, respectively. The drain current density at V_{ds} = 30 V is about 240 mA/mm, with a maximum transconductance in the range of 38 mS/mm. The high frequency characteristics of one of these devices is shown in Fig. 13(b). The f_{max} for this device was 13.5 GHz and the f_t was 8.1 GHz. The small-signal power gain was 9.8 dB at 5 GHz, and 2.9 dB at 10 GHz. The measurement conditions were V_{ds} = 40 V, I_{ds} = 74.1 mA, V_{gs} = -3 V, and I_{gs} = 9.6 μA. RF power measurements have not yet been performed for these newer 6H-SiC devices, but it is anticipated that it will be significantly higher than the 1 W/mm measured on the older 6H-SiC MESFETs. However, it is likely that they will still not have as high a power density as was observed for the 4H-SiC.

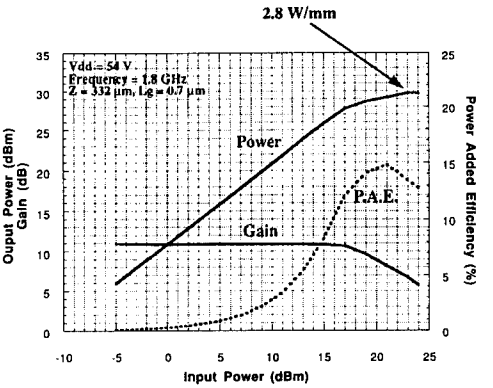

Figure 12: RF power performance of a 0.332 mm gate width 4H-SiC MESFET at 1.8 GHz. The measurement conditions were V_{ds}= 54 V, V_{gs} = -2 V, and I_{ds} = 77.4 mA.

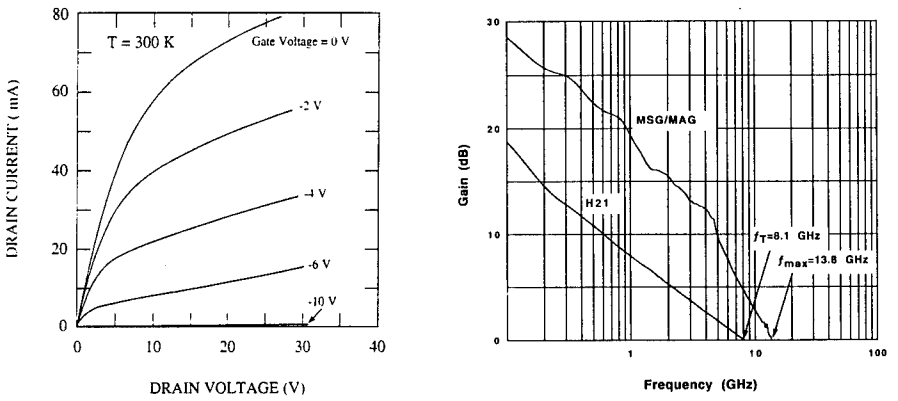

Figure 13: (a) Current-voltage characteristics of a 6H-SiC MESFET and (b) small-signal parameters, MSG/MAG and H_{21}, as a function of frequency for a 6H-SiC MESFET with a gate length and width of 0.5 µm and 332 µm, respectively.

CONCLUSIONS

A variety of power device structures have now been demonstrated in both 6H and 4H-SiC, showing promise for both DC and RF operation. For pn junction rectifiers, power MOSFETs, and thyristors in SiC, the level of doping allowed for a given voltage is much higher than in Si and the layer thickness is about 1/10th that required for Si. This is a particularly strong advantage for unipolar power MOSFETs, where it will eventually result in dramatically lower on-resistances than for Si devices of equivalent size, or allow dramatically smaller SiC device sizes for the same on-

resistance. All of these devices have the ability to operate at high temperatures, although the power MOSFETs are currently limited by oxide breakdown at temperatures above 300°C.

Very promising results have now been demonstrated for both 6H and 4H-SiC MESFETs for microwave operation. The f_{max} for MESFETs fabricated in 4H-SiC is 12.9 GHz and an RF power density of 2.8 W/mm was measured at 1.8 GHz, surpassing the output power capability of comparable GaAs MESFETs by a factor of 2-3. More recent 6H-SiC MESFETs have now reached an f_{max} of 13.8 GHz, the highest value reported to date for a SiC FET. When a comparable 4H-SiC design is completed it should surpass the frequency of these 6H devices because of the higher electron mobility of 4H-SiC.

ACKNOWLEDGEMENTS

The 4H-SiC rectifier and power MOSFET research was performed at Cree with funding from BMDO and the Dept. of the Air Force, Wright Labs (Contr. F33615-93-C-2340), monitored by C. Severt. The thyristor research was performed at Cree and was funded by NASA (Contr. NAS3-26927), monitored by G. Schwarze. The high frequency MESFET research was performed as a collaborative effort between Cree and Phoenix Corporate Research Laboratories, Motorola, Inc. It was funded in part by the ONR, Contr. N00014-92-C-0083, monitored by Dr. Y.S. Park.

REFERENCES

1. J.A. Edmond, D.G. Waltz, S. Brueckner, H.S. Kong, J.W. Palmour, and C.H. Carter, Jr., Proc. First International High Temp. Electron. Conf., edited by D.B. King and F.V. Thome (Sandia National Labs, Albuquerque, NM, 1991) pp. 500-505.
2. G.A. Slack, J. Phys. Chem. Solids **34**, 321 (1973).
3. M. Bhatnagar and B.J. Baliga, IEEE Trans. on Electron Devices **40**, 645 (1993).
4. W.J. Schaffer, H.S. Kong, G.H. Negley, and J.W. Palmour, to be published, Proc. of 1993 Intnl. Conf. SiC & Related Matls, edited by M. Spencer & G. Harris, (Intnl. Proc. in Phys.).
5. W.J. Schaffer, G.H. Negley, K.G. Irvine, and J.W. Palmour, Diamond, SiC, and Nitride Wide-Bandgap Semiconductors, edited by C.H. Carter, Jr., G. Gildenblatt, S. Nakamura, and R.J. Nemanich, (Mater. Res. Soc.Proc., this volume, Pittsburgh, PA, 1994).
6. W. von Muench and E. Pettenpaul, J. Appl. Phys. **48**, 4823 (1977).
7. M.W. Shin, G.L. Bilbro, and R.J. Trew, 1993 IEEE/Cornell Conference (IEEE).
8. J.W. Palmour, C.E. Weitzel, K. Nordquist, and C.H. Carter, to be published, Proc. of 1993 Intnl. Conf. SiC & Related Matls, edited by M. Spencer & G. Harris, (Intnl. Proc. in Phys.).
9. S. Sriram, R.C. Clarke, M.H. Hanes, P.G. McMullin, C.D. Brandt, T.J. Smith, A.A. Burk, Jr., H.M. Hobgood, D.L. Barrett, and R.H. Hopkins, to be published, Proc. of 1993 Intnl. Conf. SiC & Related Matls, edited by M. Spencer & G. Harris, (Intnl. Proc. in Phys.).
10. P.G. Neudeck and J.A. Powell, IEEE Electron Device Lett. **15**, 63 (1994).
11. P.G. Neudeck, D.J. Larkin, J.A. Powell, L.G. Matus, and C.S. Salupo, Appl. Phys. Lett. **64** (11), 1386 (1994).
12. J.W. Palmour, J.A. Edmond, H.S. Kong, and C.H. Carter, Jr., 1993 Proc. 28th Intersociety Energy Conversion Conference, (Amer. Chem. Soc., 1993) pp. 1.249-1.254.
13. J. Crofton, P.A. Barnes, J. Williams, and J.A. Edmond, Appl. Phys. Lett. **62**, 384 (1993).
14. J.W. Palmour, J. Edmond, H.S. Kong, and C.H. Carter, Jr., to be published, Proc. of 1993 Intnl. Conf. SiC & Related Matls, edited by M. Spencer & G. Harris, (Intnl. Proc. in Phys.).

COMPARISON OF MICROWAVE ECR AND RF PLASMAS FOR DRY ETCHING OF SINGLE CRYSTAL 6H-SiC

J. R. FLEMISH*, K. XIE**, W. BUCHWALD*, L. CASAS*,
J. H. ZHAO**, G. McLANE*, AND M. DUBEY*

* Army Research Laboratory–EPSD, Fort Monmouth, NJ 07703
** ECE Dept., Rutgers University, Piscataway, NJ 08855

ABSTRACT

Electron cyclotron resonance (ECR) plasma etching of single crystal 6H-SiC has been investigated using a CF_4/O_2 gas mixture and compared to conventional reactive ion etching (RIE) in a radio frequency (13.56 MHz) reactor. The use of ECR results in higher etch rates, lower levels of bias and smoother etched surfaces than rf-RIE. ECR etch rates exceeding 100 nm/min have been obtained at a substrate bias of –100 V. Etch rate and surface morphology have been studied as a function of pressure, bias and power. Auger electron spectroscopy shows that ECR etching leaves no residues unlike rf-RIE which leaves residues containing Al, F, O and C. The current-voltage and capacitance-voltage measurements of Schottky diodes show that there is far less damage induced by ECR etching compared to rf-RIE.

INTRODUCTION

An important issue for SiC device fabrication is the development of suitable dry etching techniques, since SiC is relatively inert to most chemical solutions. In the past decade, conventional reactive ion etching (RIE) of SiC has been demonstrated in capacitively-coupled, radio frequency (rf) plasma reactors. There are many reports on rf-RIE of SiC in a variety of fluorinated gas mixtures [1-5]. However, some problems are typically encountered. In particular, rough surface morphologies often result due to micromasking effects. While, addition of H_2 to the gas mixture can suppress the formation of micromasking residues, it also suppresses SiC etching [4]. Moreover, the high rf power densities needed for obtaining adequate etch rates lead to high biases on the substrate, which in turn causes lattice damage to the underlying semiconductor material due to energetic ion bombardment. Recently, electron cyclotron resonance (ECR) plasmas have received attention for electronic materials processing applications [6], as they offer advantages such as high plasma density and low ion energy. A preliminary study has shown that ECR plasmas provide an attractive means of etching SiC [7]. In this paper we report on ECR plasma etching of single crystal 6H-SiC using a CF_4/O_2 mixture and compare these results to rf-RIE. Etch rate, surface morphology and selectivity have been evaluated. The surface composition after etching was studied by Auger electron spectroscopy. The degree of etch-induced damage was assessed by current-voltage (I-V) measurements of Schottky diodes fabricated on the etched surfaces.

EXPERIMENTAL

This study employed a load-locked multipolar ECR plasma system utilizing a 2.45 GHz excitation source with an rf (13.56 MHz) substrate biasing capability. This system can perform in an ECR plasma mode or in a capacitively-coupled rf plasma mode. In the ECR mode, substrate bias is adjusted independently of the microwave plasma power by varying the rf power, and the substrates sit approximately 15 cm below the ECR discharge. In the RIE mode the plasma is generated by rf power applied to an aluminum substrate holder. The chamber was evacuated below $1x10^{-6}$ Torr prior to initiating gas flow. The etch gas was pre-mixed CF_4/O_2 (5:1) at a flow of 50 sccm. Two different masking materials, Al and indium-tin-oxide (ITO), have been tested. The patterns were defined photolithographically using a lift-off process.

Mat. Res. Soc. Symp. Proc. Vol. 339. ©1994 Materials Research Society

Etch depths were measured using a Dektak stylus profilometer. The surface morphology after etching was examined by scanning electron microscopy. The surface composition of etched SiC samples were analyzed by Auger electron spectroscopy (AES) and scanning Auger microscopy (SAM). The samples were loaded into the AES system immediately after being taken from the etching chamber to minimize exposure to air. An unetched control sample was cleaned by a standard RCA process [8] and dipped in a dilute HF immediately before analysis. Elemental concentrations were quantified using tabulated relative sensitivity factors.

The samples used for electrical measurements consisted of a 10 μm thick 6H-SiC epilayer ($n=5x10^{15}/cm^3$) grown on a (0001) Si-terminated 6H-SiC substrate with $n=2x10^{18}/cm^3$. Ta ohmic contacts were evaporated onto the sample backsides and annealed at 850°C. After plasma etching the samples were transferred to an ultra-high vacuum metallization system where 250 μm diameter Pd Schottky contacts were deposited by e-beam evaporation through a stainless steel shadow mask. A control sample was RCA-cleaned and dipped in dilute HF before deposition. Schottky barrier height and ideality factor were determined from I-V measurements.

RESULTS AND DISCUSSIONS

Al has been widely used in conventional rf-RIE as an etch mask, as it is not reported to etch significantly in typical F-containing plasmas. However, in our ECR experiments Al did not endure well for deep etching. ITO films endured far better, particularly at low levels of bias. In the ECR plasma at –100V bias the selectivities of SiC etching with respect to ITO and Al are approximately 40:1 and 10:1, respectively. Because the ECR process uses considerably lower bias than rf-RIE, the erosion of Al is likely to be due to a chemical effect rather than to sputtering. Perhaps either the ECR plasma creates F-containing species which are more reactive or in much larger concentration than do typical rf plasmas, or residues which form in the rf-RIE processes effectively protect the Al mask from attack by reactive species.

The etch rates of SiC using rf-RIE at 25 mTorr are shown in Fig. 1 for rf power varying from 100W to 300W (0.20 W/cm^2 to 0.59 W/cm^2). These results are comparable to what has been reported previously for rf-RIE of SiC [1–5]. A rough surface morphology results at all power levels, as shown in Fig. 2a, due to a high density of micromasked regions. This micromasking is also consistent with previous reports which have shown that the micromasking is caused by Al which sputters from the reactor electrode and redeposits in clusters on the etched surface [4, 5]. These reports also show that micromasking can be suppressed by H_2 addition to the gas mixture. Similarly, we obtain smooth surfaces (Fig. 2b) by using a gas mixture of $CF_4/O_2/H_2$ in a ratio of 5:1:1. This H_2 addition leads to nearly a three-fold reduction in the etch rate as shown in Fig. 1. For a given power density, the addition of H_2 had no effect on the substrate potential which was approximately –270 V and –520 V at power densities of 0.20 and 0.59 W/cm^2, respectively.

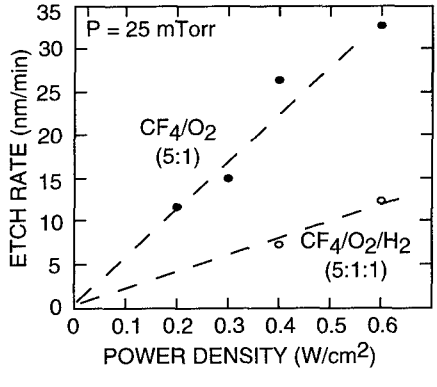

Fig. 1. Variation in SiC etch rate with power for rf-RIE at 25 mTorr.

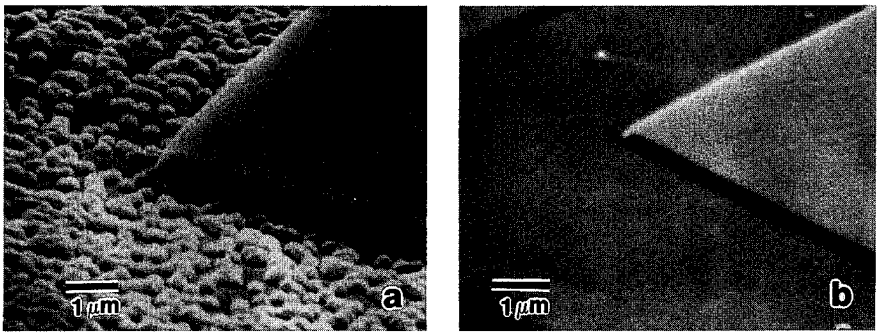

Fig. 2. SiC with ITO mask etched by rf-RIE in CF_4/O_2 (a) without H_2, (b) with H_2 added.

Results for ECR etching are shown in Fig 3. The etching rate is directly proportional to the applied microwave power as shown in Fig. 3a for two different levels of substrate bias. The increase in etch rate with microwave power can be attributed to two factors: (1) Higher power leads to a higher density of excited species which react with the SiC surface, and (2) higher power results in higher ion densities, which in turn leads to enhanced energetic ion bombardment and removal of etch products adsorbed on the SiC surface. Most notable about ECR etching compared to rf-RIE is that dramatically higher rates are obtained at much lower levels of bias.

The variation in the SiC etch rate with applied bias for the ECR plasma (2 mTorr and 500 W) is shown in Fig. 3b. The rate is approximately proportional to the substrate bias in the range of –20 to –150 V. Further increases in bias appear to have less of an effect on the etch rate. This result may be explained if the desorption of etch products is rate-limiting at low bias. In this case the increase in bias leads to a proportional increase in the energy of ions bombarding the sample surface, and therefore to an increase in the rate of sputter-induced desorption of the etch products. At high levels of bias the desorption of etch products may become less rate-limiting and the increase in rate may also be due to the onset of physical sputtering of the SiC.

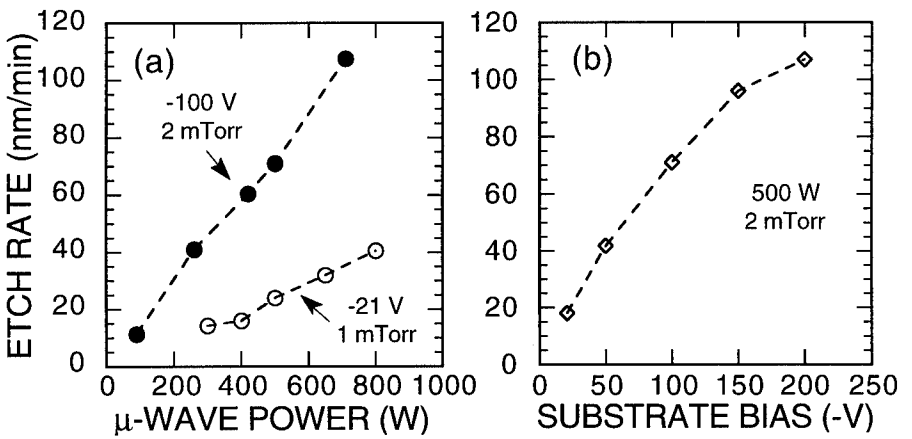

Figure 3. ECR etch rate of SiC, variation with (a) power and (b) applied bias.

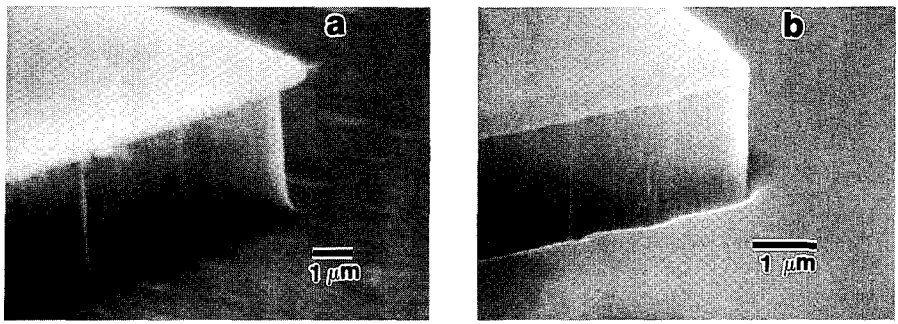

Fig. 4. ITO masked SiC etched by CF_4/O_2 ECR plasma with bias of (a) –40 V and (b) –100 V.

Figure 4 shows SEM micrographs of SiC samples etched by ECR plasmas at 500 W with two different levels of applied bias, –40 V and –100 V. The surfaces are smooth and the pattern profiles show highly anisotropic etching. Moreover, we have observed no micromasking effects in the ECR etching experiments over the entire range of parameters tested. This result is attributable to the low pressure which is characteristic of the ECR process and which facilitates the effective desorption and removal of etch products with negligible redeposition. At high substrate bias, a notable feature is the formation of a trenched region at the base of the etched side-walls. This trenching effect is strongly dependent on the bias and can be attributed to enhanced ion bombardment at the base of the side-wall pattern due to the deflection of ions impinging on the sidewalls at low angles [9]. In our experiments trenching has not been observed at bias of less than approximately –50 V. Trenching is readily observable at –70 V and is acute at –100 V. Bias also increases the etch anisotropy. At low bias significant undercutting of the mask occurs, while at –100V etching is highly anisotropic.

The AES results are summarized in Table I. AES spectra of SiC etched by rf-RIE at a power density of 0.6 W/cm^2 show significant amounts of Al, F, O and C on the sample surface. Furthermore, these impurities are localized at the top of the micromasked protrusions, indicating that a residue which contains these elements is responsible for the micromasking effect. Large amounts of Al, F and O are also detectable on the sidewalls of the etched patterns. SAM measurements show that Al and F are uniformly distributed over the ITO mask, unlike on the etched surface where they are clustered. With addition of H_2, there is large reduction of the surface Al content from 26% to 8.8% and the F signal disappears. The reduction of these impurities coincides with an improvement in surface morphology and the suppression of micromasking. However, significant amounts of Al, F and O are still detectable on the sidewalls, indicating that even with H_2 addition there is still a tendency for residue formation.

Table I. AES atomic concentration data (%) for unetched, ECR-etched, and rf-RIE SiC surfaces.

Method	Sample	C	Si	O	F	Al	N
unetched	SiC surface	53.4	40.8	3.1	–	–	2.6
rf-RIE	SiC surface	43.8	25.1	3.3	1.8	26.0	–
(no H_2)	SiC side-wall	38.6	16.1	3.8	2.4	39.1	–
rf-RIE	SiC surface	45.4	39.4	6.4	–	8.8	–
(H_2 added)	SiC side-wall	39.9	27.7	9.7	2.0	20.1	–
ECR etched	SiC surface	58.1	41.9	–	–	–	–
(–20 V)	SiC side-wall	63.0	34.9	2.1	–	–	–

Residual O and N impurities are observed on the unetched sample surface and most likely originate from the cleaning solutions. No impurities other than Si and C are detectable on the ECR etched surface. The ECR etched surface appears to be carbon-rich, but contamination from atmospheric hydrocarbons during sample exposure to air may in part be the origin of the excess C. The sidewalls are much more carbon-rich with 63 at% carbon and 35 at% silicon. Interestingly, no Al or F, and very little O are detected on the sidewalls, which indicates that there is not an appreciable tendency for residues to form during ECR etching.

Schottky diode I-V characteristics are very sensitive to the metal-semiconductor interface quality. Assuming a thermionic emission model [10], the barrier height (Φ) was determined from the measured diode saturation current. The effective Richardson constant for SiC was taken to be 72 A-K^2/cm^2 based on an electron effective mass of 0.60. For each sample approximately 15 to 20 diodes were measured. Out of these a small number on each sample exhibited unusually high leakage currents which were presumed to be related to defects in the as-grown SiC layers. Disregarding the outlying characteristics, Fig. 5 shows I-V characteristics which are representative of Schottky diodes fabricated on as-grown, rf-RIE (–510 V, 0.59W/cm^2) and ECR (–100 V, 800W) etched surfaces. For these samples approximately 500 nm of material was etched away, and for rf-RIE H_2 was added to obtain a smooth surface. Most notable is the large increase in the reverse bias leakage current for the etched samples. This increase is approximately two orders of magnitude for ECR etched samples and approximately six orders of magnitude for the rf-RIE samples. The Schottky diodes on the as-grown sample show average values of $\Phi = 1.05 \pm 0.02$ eV and $n = 1.34 \pm 0.08$, with the errors representing the standard deviations. The high ideality factor may arise from the presence of a thin interfacial layer between the Schottky contact and the SiC. The existence of such a layer is consistent with AES results showing O and N on the RCA-cleaned SiC surface. Schottky diodes on the rf-RIE sample all show high leakage currents with average values of $\Phi = 0.637 \pm 0.004$ and $n = 1.27 \pm 0.03$. The very high leakage current and low barrier height are consistent with the occurrence of significant lattice damage to the SiC caused by rf-RIE. In contrast, Schottky diodes on the ECR etched surface show values of $\Phi = 0.874 \pm 0.002$ and $n = 1.09 \pm 0.05$. The barrier height is lower than that of the as-grown sample, but much higher than that of the rf-RIE sample. This result together with the fact that less degradation is seen in the leakage currents suggests that the ECR etching process is far less damaging to the underlying SiC than the rf-RIE process.

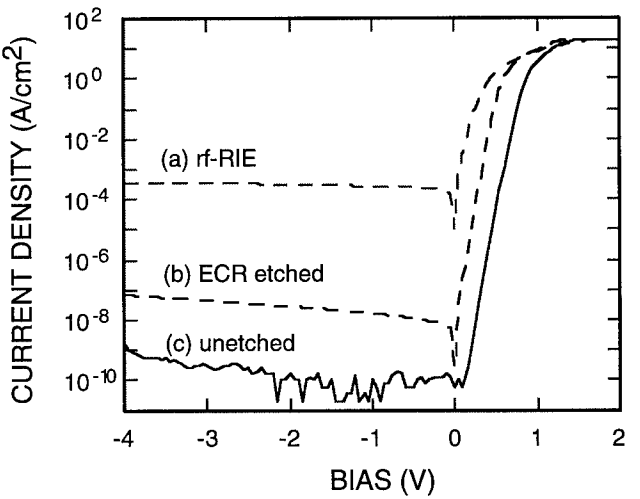

Fig. 5. Current-voltage characteristics of Pd Schottky diodes on (a) RIE etched, (b) ECR etched at –100 V, and (c) unetched SiC samples.

SUMMARY

Smooth, anisotropic, residue-free dry etching of 6H-SiC has been demonstrated using ECR plasmas with a CF_4/O_2 gas mixture. ECR plasma etching of SiC is far more selective with respect to ITO masks than Al masks. Etch rates in excess of 100 nm/min are obtained with relatively low bias (–100 V). Etching at bias higher than –70 V is highly anisotropic, but trenches form at the bases of the etched sidewalls. Etching at low bias (less than –50 V) is less anisotropic and without trench formation. High bias ECR etching appears to be useful for processes such as deep mesa etching, while low bias etching is well suited for shallow recess etching of active device layers. The AES analysis of etched surfaces show that there are no residues on the ECR etched surfaces. In contrast, conventional rf-RIE processes using the same gas mixture yields residues which contain Al, F, O, and C. Upon addition of H_2 to this process residue formation is suppressed on the etched surfaces but persists on the side-wall features. Current-voltage measurements of Pd Schottky diodes indicate that ECR etching induces far less damage to the SiC than conventional rf-RIE.

REFERENCES

1. J. Sugiura, W. J. Lu, K. C. Cadien, and A. J. Steckl, J. Vac. Sci. Technol. B 4, 349 (1986).
2. J.W. Palmour, R.F. Davis, T.M. Wallett, and K.B. Bhasin, J. Vac. Sci. Technol. A 4, 590 (1986).
3. W.S. Pan, and A.J. Steckl, J. Electrochem. Soc. 137, 212 (1990).
4. P.H. Yih and A.J. Steckl, J. Electrochem. Soc. 140, 1813 (1993).
5. A. J. Steckl and P. H. Yih, Appl. Phys. Lett. 60, 1966 (1992).
6. J. Asmussen, J. Vac. Sci. Technol. A 7, 883 (1989).
7. J. R. Flemish, K. Xie and J. H. Zhao, Appl. Phys. Lett. 64, in press (1994).
8. W. Kern and D.A. Puotinen, RCA Rev. 31, 187 (1970).
9. C. M. Melliar-Smith and C. J. Mogab, in Thin Film Processes, edited by J. L. Vossen and W. Kern (Acedemic, San Diego, 1978) p. 540.
10. S. M. Sze, Physics of Semiconductor Devices, 2nd ed. (Wiley, New York 1981) p. 255.

ON THE FORWARD CONDUCTION MECHANISMS IN SiC P-N JUNCTIONS

LOURDES PELAZ, J. VICENTE, M. JARAIZ, L. BAILON AND J. BARBOLLA
Universidad de Valladolid, Departamento de Electricidad y Electrónica, Facultad de Ciencias, E-47011 Valladolid, Spain

ABSTRACT

In SiC junctions, it is usual to find the ideality factor $n=2$ (or slightly higher) in 6H-SiC and $n>2$ and temperature dependent for 3C-SiC. However, the recombination current yields an ideality factor no higher than 2. This value can be slightly increased by considering the Poole-Frenkel effect (PFE), so that the 6H-SiC junction characteristics can be properly fitted. On the other hand, 3C-SiC junction characteristics, which are quite different from the ideal ones, cannot be satisfactorily explained on the basis of this model and the multitunnel capture-emission mechanism is proposed as the responsible for this behavior.

INTRODUCTION

Silicon Carbide is a wide bandgap semiconductor for all of its polytype structures; the most common are 3C-SiC and 6H-SiC with 2.2 and 2.9 eV, respectively. This property, along with other excellent physical and electronic properties [1], render it a promising material for use in high-temperature and high-power devices among many other applications. Superior electrical device results have been reported about 6H-SiC because the technology for producing substrates and epitaxial layers in this polytype is more advanced compared to 3C polytype [2].

Since SiC is a large gap semiconductor, the recombination process is expected to be predominant over diffusion in a p-n junction at room temperature and low forward voltages. Therefore, it is expected the current-voltage relationship given by [3]:

$$J = q\frac{W}{\tau}n_i \exp(qV/nkT) \tag{1}$$

where q is the electron charge, W the depletion-layer width, τ the effective lifetime, n_i the intrinsic carrier density, k the Boltzmann's constant, T the absolute temperature and n the ideality factor whose value should be 2.

THE POOLE-FRENKEL EFFECT ON 6H-SIC JUNCTIONS

The Poole-Frenkel effect (PFE) [4] is the enhancement of the carrier emission rate from the traps by the electric field due to the lowering of the effective potential barrier as illustrated in Fig. 1. This effect is present only when the trap behaves like a Columbic well, i.e., the emission of electrons or holes ionizes the trap.

This effect can be modeled through the modification of the hole recombination time for an acceptor-like trap (equivalently the electron recombination time for a donor-like trap):

Mat. Res. Soc. Symp. Proc. Vol. 339. ©1994 Materials Research Society

$$\tau_p = \tau_p(0) \exp\left[-\frac{q(q/\pi\epsilon)^{1/2}F^{1/2}}{kT}\right] \qquad (2)$$
$$\tau_n = \tau_n(0)$$

where $\tau_p(0)$ and $\tau_n(0)$ are the hole and electron recombination time in absence of electric field, ϵ is the dielectric constant of the material and F the electric field.

Simulation results are been carried out by using MEDICI [5] with the introduction of the expressions given by the equation 2 in the classical Shockley-Read-Hall generation-recombination rate. Both experimental data [6] and simulation results with and without PFE are shown in Fig. 2.

The recombination current dominates up to 2.3 V at 300 K. The dominance of this current occurs up to lower voltage bias as the temperature increases since the diffusion current increases faster than the recombination current. In the range where the recombination mechanism plays a significant role in determining the forward characteristics, a difference between the characteristics with and without the PFE can be pointed out but when the diffusion current is important no difference is observed. In all curves, the best agreement with experiments is

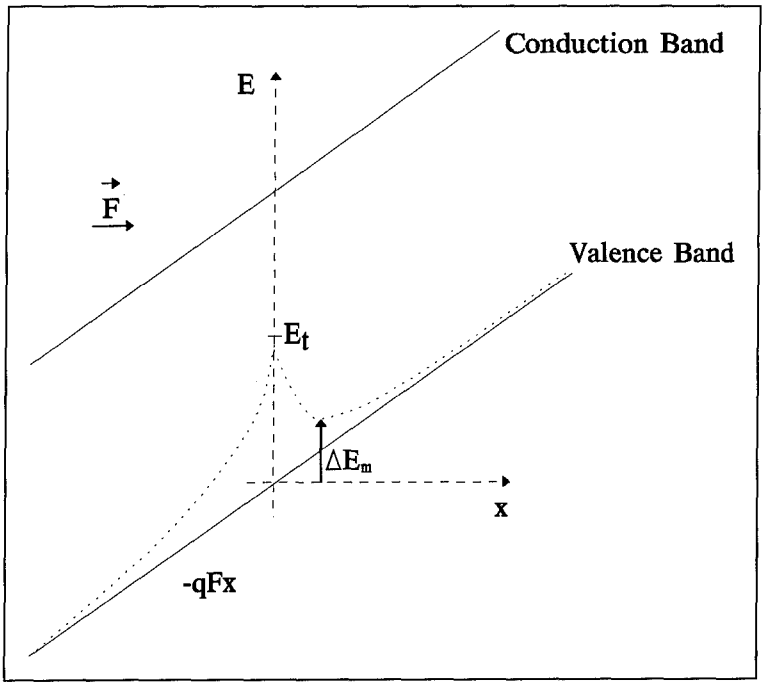

Figure 1. Energy-band diagram around a trap. The dashed line denotes the effective potential well of an acceptor-like trap.

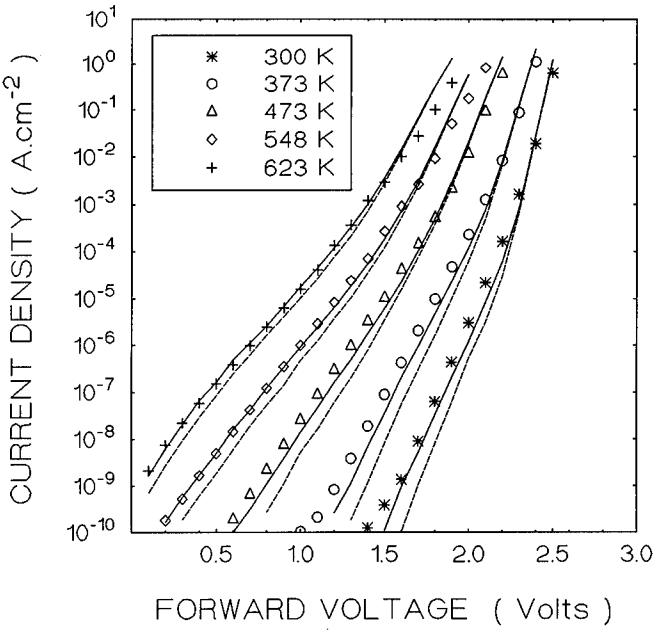

Figure 2. Forward characteristics of a 6H-SiC diode as a function of temperature. Measured data (symbols) are taken from [6]. The lines are simulation results with (solid lines) and without (dashed lines) the Poole-Frenkel effect.

obtained when the PFE is included. PFE has more importance at low temperature and low forward bias (the electric field is higher) as expected from the equation (2). At room temperature, unless PFE is considered, the computed level of the current at low forward bias is up to one order lower than the experimental values; this difference diminishes as the temperatures increases and even at high temperature, experimental and simulated results are in good agreement and there is no significant difference between including PFE or not.

PFE can adequately justify the J-V characteristics of 6H-SiC, that almost follow the ideal curves. However, 3C-SiC junction characteristics [7] do not correspond to the expected from the classical mechanisms, even including PFE; any other mechanism associated to the large gap of 3C-SiC cannot be accepted as the responsible for this behavior since 6H-SiC possesses a larger gap and exhibits a quasi-ideal behavior. It seems more probable that this anomalous behavior in 3C-SiC can be related to localized states, since a relationship between the general crystal quality and the ideality factor has been observed and it is well known that the 3C-SiC technology generates a large amount of defects which do not appear in 6H-SiC [8]-[9].

THE MULTITUNNEL CAPTURE-EMISSION EFFECT ON 3C-SIC JUNCTIONS

It can be thought that high levels of current can be obtained if a very active recombination mechanism as a consequence of, for example, a large density of traps is assumed. This can be modeled by a very small recombination time ($\tau \to 0$) that, according to the equation (1), gives rise to large current density. However, we have previously proved [10] that the

generation-recombination rate, and as a consequence the current density, saturates and the limit value lies below the experimental current density data. Therefore, a different conduction mechanism should be considered in order to explain these characteristics.

Several aspects can be mentioned in the 3C-SiC junction characteristics [7], [11]-[12]. The ideality factor is much higher than 2 and depends on temperature but the magnitude of q/nkT shows a slight temperature dependence and, moreover, a large excess of current is exhibited at low forward bias and room temperature. These facts, which can also be found in tunnel diode, suggest that the dominant mechanism in 3C-SiC diodes should involve tunneling. Several models based on tunneling processes have been proposed in the literature. Band-to-band tunnelling [13] can be discarded because it is neither energetically probable in the structures considered here nor fits the appropriate functional dependence. Since it is widely recognised that a large amount of defects are present in 3C epilayers which may deeply affect the diode characteristics, trap-assisted tunneling is suggested to explain the behavior of these diodes. In particular, the multitunnel capture-emission process [14] could be the cause for the behavior of 3C-SiC junctions. In this process, shown in Fig. 3, the carriers use the localized energy levels in the gap as steps to tunnel through the gap and when the tunneling rate from one step to other is smaller than the emission or capture coeficient, the carrier is released from a localized state to the band or recombinated with another carrier.

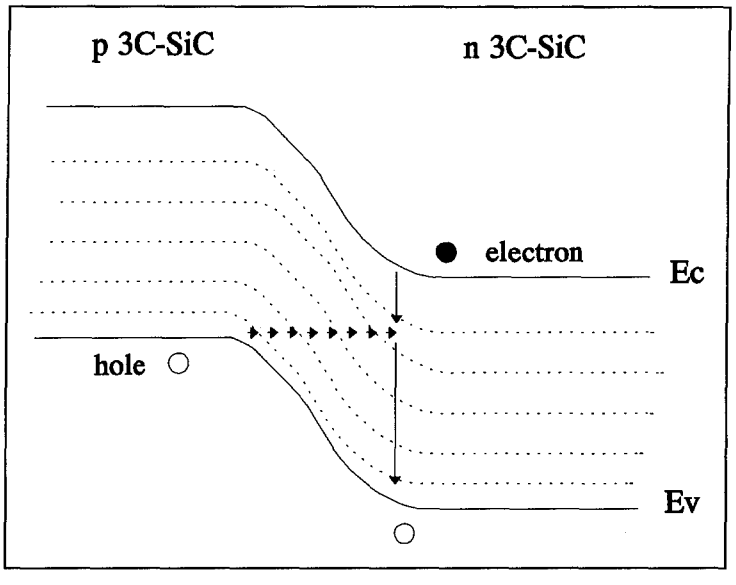

Figure 3. Energy-band diagram of the multitunneling capture-emission.

The current-voltage relationship based on the multitunneling capture-emission process is given by:

$$J = B \exp\left[-\frac{\Delta E}{kT}\right] \exp(A V) \tag{3}$$

where B is a constant, ΔE is related to the energy level of the traps (when the emission process is involved) or to the Fermi level position (when a capture process is involved) at the point where the carriers are released from a localized state to the bands and, finally, A is a temperature-independent constant.

Experimental J-V curves along with the ones corresponding to equation (3) are plotted in Fig. 4. The linear region in the semilogarithmic plot can be fitted to this exponential curve with these parameters:

$A = 9.00\ V^{-1}$
$B = 5.22\ A.cm^{-2}$
$\Delta E = 0.42\ eV$

The values of ΔE are deep enough to be related to the Fermi level in this structure where the carrier concentration is about $10^{17}\ cm^{-3}$. Therefore, it should be admitted that this value corresponds to an effective the trap energy level in the gap from where, after tunnelling through many other traps, the emission of the carrier to the band occurs. The ΔE values are related to energy levels of impurities or, more probably, to defects and imperfections associated with the cubic structure of 3C-SiC. This situation may be possible in the 3C-SiC since its cubic network is considered as a 'strained' crystal which grows on Si or hexagonal SiC and, as a consequence, many crystallographic defects are expected to be present [15].

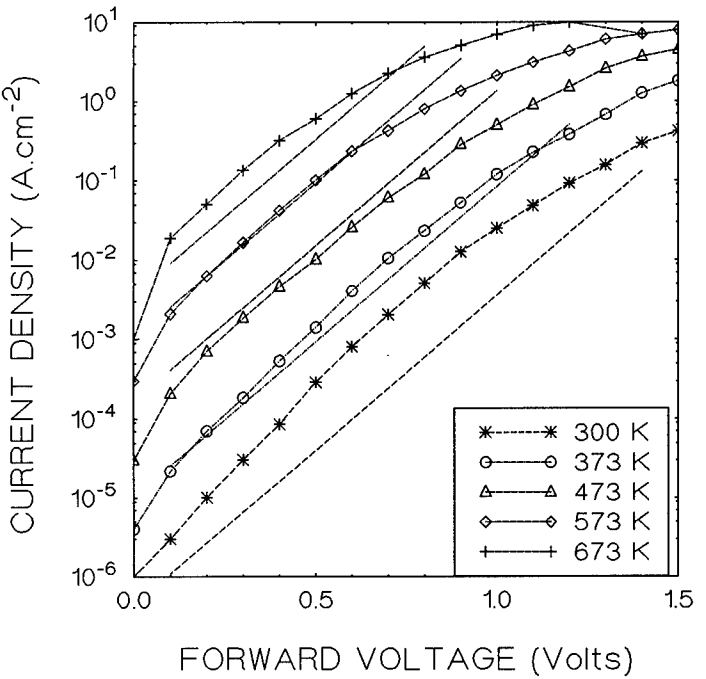

Figure 4. Forward characteristics of a 3C-SiC diode as a function of temperature. Measurement data (symbols) are taken from [7]. Dashed lines are the analitycal curves calculated according equation (3).

CONCLUSIONS

Crystallographic defects appear to be a possible cause for the non-ideal behavior of 3C-SiC p-n diodes since, in comparison, 6H-SiC p-n diodes exhibit normal characteristics. In order to improve the diode characteristic, a technological effort should be done so that the amount of defects and crystal imperfections can be reduced.

The authors wish to acknowledge to TMA (Technology Modeling Associates, Inc.) for software facilities.

This work has been funded by CICYT (Comisión Interministerial de Ciencia y Tecnología).

REFERENCES

1. Landolf-Börnstein, Physics of Group IV Elements and III-V compounds (Springer-Verlag, Berlin, 1982), p. 132.
2. R.F. Davis, J.W. Palmour and J.A. Edmond, Mat. Res. Soc. Symp. Proc. **162**, 463 (1990).
3. S.M. Sze, Physics of Semiconductor Devices, 2nd. ed. (John Wiley & Sons, New York, 1981) p. 92.
4. J. Frenkel, Phys. Rev. **54**, 657 (1938).
5. MEDICI, *Technology Modeling Associates, Inc.*,1991.
6. J.A. Edmond, D.G. Waltz, S. Brueckner, H. Kong, J.W. Palmour and C.H. Carter Jr., Proc. 1st. Int. Hi. Temp. Electron. Conf., 500 (1991).
7. J.A. Edmond, K. Das and R.F. Davis, J. Appl. Phys. **63**, 922 (1988).
8. H.J. Kim, R.F. Davis, X.B. Cox and R.W. Linton, J. Electrochem. Soc. **134**, 2269 (1987).
9. A.J. Steckl and J.P. Li, IEEE Trans. Electron Devices **39**, 64 (1992).
10. L. Pelaz, J.L. Orantes, L. Enríquez, L. Bailón and J. Barbolla, (to be published).
11. A. Suzuki, A. Uemoto, M. Shigeta, K. Furukawa and S. Nakajima, Extended Abstracts of the 18th Conference on Solid Stade Devices and Materials, 101 (1986).
12. P.G. Neudeck, D.J. Larkin, J.E. Starr, J.A. Powell, C.S. Salupo and L.G. Matus, IEEE Electron Device Letters **14**, 136 (1993).
13. E.O. Kane, J. Phys. Chem. Solids **12**, 181 (1959).
14. H. Matsuura, T. Okuno, H. Okushi and K. Tanaka, J. Appl. Phys. **55**, 1012 (1984).
15. N.E. Jepps and T.F. Page, Progress in Crystal Growth and Characterization **7**, 259 (1983).

PROPERTIES OF MOS STRUCTURE FABRICATED ON 3C-SiC GROWN BY REACTIVE MAGNETRON SPUTTERING.

R. Turan*, Q. Wahab, L. Hultman, M. Willander and J. -E. Sundgren
Department of Physics, Linköping University, S-581 83 Linköping, Sweden

ABSTRACT

We report the fabrication and the characterization of Metal Oxide Semiconductor (MOS) structure fabricated on thermally oxidized 3C-SiC grown by reactive magnetron sputtering. The structure and the composition of the SiO_2 layer was studied by cross-sectional transmission electron microscopy (XTEM) Auger electron spectroscopy (AES). Homogeneous stoichiometric SiO_2 layers formed with a well-defined interface to the faceted SiC(111) top surface. Electrical properties of the MOS capacitor have been analyzed by employing the capacitance and conductance techniques. C-V curves shows the accumulation, depletion and deep depletion phases. The capacitance in the inversion regime is not saturated , as usually observed for wide-bandgap materials. The unintentional doping concentration determined from the $1/C^2$ curve was found to be as low as 2.8×10^{15} cm^{-3}. The density of positive charges in the grown oxide and the interface states have been extracted by using high-frequency C-V and conductance techniques. The interface state density has been found to be in the order of 10^{11} cm^{-2}-eV^{-1}.

INTRODUCTION

Cubic type silicon carbide (SiC) and its heterojunction with silicon are attracting a great deal of attention due to its potential applications in semiconductor science and technology. The growing interest for SiC stems from its advantageous properties such as high electron mobility, high breakdown electric field, large bandgap, high thermal and chemical stability. High temperature gas sensors[1], heterojunction bipolar transistors[2], solar cells [3] and power devices[4] are among the most commonly proposed applications for cubic silicon carbide layers.

For the production of cubic SiC layers, several deposition techniques such as CVD[5], PECVD[6] and MBE[7] have been used. In spite of the large lattice mismatch (20 %), the epitaxial 3C-SiC layers have been grown by using these techniques. As an alternative method, the ultra high vacuum reactive magnetron sputtering (RMS) has proven to be successful in growing 3C-SiC layers on the silicon substrate[8,9]. RMS offers low temperature growing conditions which is highly desirable for integration of 3C-SiC devices with silicon based technology. The electrical and structural properties of 3C-SiC layers grown by RMS have been well investigated and shown to be suitable for device production[9,10,11]. P-n junction diodes[12], heterojunction diodes[13] and light emitting diodes[14] have already been produced and operated successfully.

This paper presents the first report on the metal oxide semiconductor capacitor fabricated on 3C-SiC layer produced by the RMS technique. Successful operation of MOS devices is crucial particularly in high temperature gas sensors which make use of the shift in the flat band voltage as a result of the gas detection. Similarly, the electrical properties of the oxide/semiconductor interface play important roles in the metal-oxide-field effect transistors (MOSFET). In addition, the interface properties of SiO_2/SiC is important for the surface

* Permanent address : Department of Physics, Middle East Technical University, 06531 Ankara, Turkey.

Mat. Res. Soc. Symp. Proc. Vol. 339. ©1994 Materials Research Society

passivation in devices like heterojunction bipolar transistors. It is now well known that SiO_2 layers can be thermally grown on SiC without degrading the underlying crystal[15-19]. It has been reported that good quality interfaces with relatively low density of defect states could be produced for both CVD grown 3C-SiC[16-18] and bulk 6H-SiC[15]. In this paper, we present the chemical, structural and electrical properties of MOS structure produced on RMS-grown 3C-SiC.

EXPERIMENTAL

3C-SiC layers were deposited on Si(111) substrates by reactive magnetron sputtering of elemental silicon in mixed Ar/CH_4 plasmas. The films were deposited on Si(111) substrates kept at a temperature of 850 °C. The base pressure in the deposition chamber was less than $2x10^{-8}$ Torr. Details of the growth technique and the analysis of the grown SiC layers were published previously[9]. It was already shown that shown that the SiC layer grown at this temperature has a relatively sharp interface to the silicon substrate and a good crystal quality. In order to get a smooth surface prior to oxidation, the samples were first mechanically polished using 0.1 μm diamond paste. Following a standard RCA cleaning process in the clean room environment, the oxidation process was carried out at 1200 °C for 45 minutes. This oxide layer was etched away using buffered HF in order to remove the mechanical damage created by polishing. The samples were then again cleaned and oxidized at 1200 °C for 90 min. Following the oxidation the samples were annealed at the same temperature for 30 min. The thickness of the oxide layer was determined by ellipsiometry. Part of the oxide layer was removed by buffered HF and $TaSi_2$ was then sputtered as ohmic contact. Small pieces from the same sample were cut and prepared for XTEM and AES study. In order to define the electrodes, a shadow mask with circular holes with an area of $4.42x10^{-3}$ cm^{-2} was used and Al was then evaporated on the oxide layer. The composition of the SiO_2 layer was characterized by Plasma Therm scanning Auger electron spectroscopy in combination with sputter etching to remove surface contaminant. For AES analysis, four different samples were oxidized in similar conditions. These samples are (1) 3C-SiC grown by CVD, (2) 3C-SiC grown by RMS, (3) 6H-SiC from CREE and (4) a Si substrate piece. For XTEM analysis a Philips CM 20 UT microscope was used.

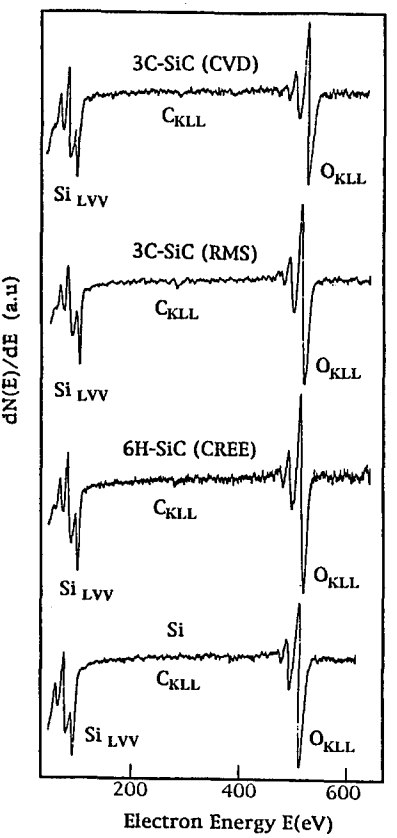

Figure 1 AES spectrum of four different SiC samples

RESULTS AND DISCUSSION

For the MOS capacitors studied in the present work, the oxide thickness was

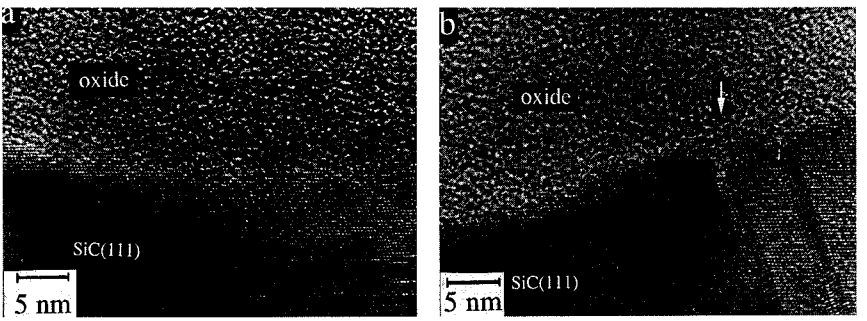

Figure 2 XTEM images showing two representative regions of SiO_2/SiC interface.

measured to be 160 nm by ellipsiometry. Figure 1 shows the AES spectrum for the similarly processed four different samples. As can be seen from Fig. 1, only intense peaks belonging tc Si and O were observed. The tiny carbon peaks observed in all samples are just above the noice level of the measurement and indicate small amount of carbon presence in the grown layers. Some of the carbon signal is likely to result from the system contamination since we observe the carbon signal in Si sample in which carbon concentration is expected to be below the detection limit of AES. These results show that chemically good quality SiO_2 layer were grown on SiC samples and C atoms were flushed out probably in the form of CO[20]. The Si_{LVV} to O_{KLL} peak height ratios were observed to be same for all samples, indicating same chemical composition.

Figure 2a and 2b are high resolution XTEM images from representative areas of the interface between SiO_2/SiC film with {111} stacking faults a) parallel to the film/substrate surface and b) inclined to the surface and emerging through the film. In both cases, the oxide was homogeneous with an atomically rough interface to SiC. The interface was continuos, except at emerging stacking faults where local dents of oxide formed in the SiC as indicated by the arrow in Fig. 2b. This is probably the reason for relatively high oxidation rate observed in this work. The presence of the stacking faults were observed in the nonoxized SiC prepared in similar condition. Their amount was almost equal to that measured in the sample used here. It is therefore most likely that these stacking faults formed during the deposition of SiC, and not related to the oxidation process.

Figure 3a shows typical C-V and G-V curves measured at 1MHz for the MOS capacitor. From the C-V curves we see that the sample is n-type and accumulation and depletion are present as expected. Unlike the silicon MOS capacitors the C-V curve is not saturated at a constant value for negative biases, showing that SiC is not completely inverted due to the low minority carrier generation rate of SiC. This behavior was consistently observed in MOS capacitors produced on CVD grown 3C-SiC and 6H-SiC[15-19]. As shown in Figure 3b, the plot of 1/C2 vs gate voltage yielded a straight line confirming the deep depletion behavior for the negative biases. The dopant concentration in the SiC layer was found to be 2.8×10^{15} cm^{-3} from $1/C^2$ vs V_G curve analyzed in the deep depletion region.

The expected flat band capacitance for the present SiO_2/SiC MOS capacitor was calculated by using the method described in ref.[22]. In this calculations, the intrinsic carrier

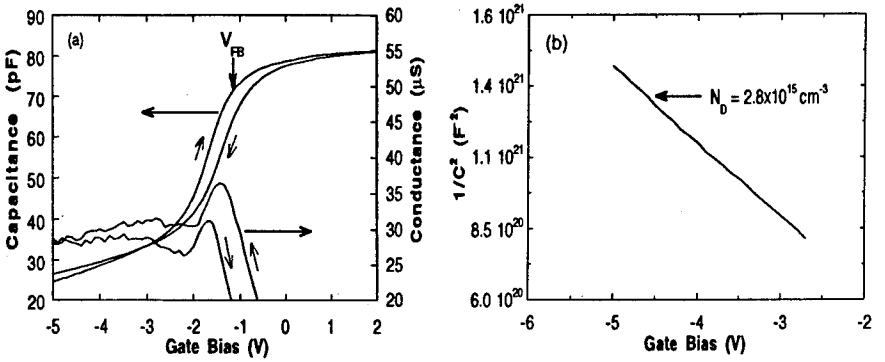

Figure 3. a) Plot of 1MHz C-V and G-V curves from SiC-MOS capacitor. b) $1/C^2$ plot from the same sample.

concentration of SiC at room temperature was taken to be 6 cm^{-3}[19]. As denoted in Figure 2 the shift in the flat band voltage is along the negative voltage direction, indicating that oxide layer contains positive ion charges as usually observed in silicon MOS devices. On the other hand the C-V curve exhibits a hysteresis indicating that there are significant amounts of electron trap centers in the grown oxide layer[23]. Since the effect of trapped electrons and the positive oxide charges cancels each other in a C-V curve their amount can not be determined exactly from the shift in the flat band voltage. However, an estimation for the positive oxide charges could be made by taking the curve that sweeps the voltage axis from the negative values to the positive ones. The effect of trap centers on the C-V characteristics is expected to be minimum for this sweep direction. By using the relation[22] $Q_o=C_{ox}(W_{ms}-\Delta V_{FB})$ the amount of positive oxide charges was found to be $1.5x10^{11}$ cm^{-2}. In the above equation, Q_o represents the density of the oxide charges per square cm, C_{ox} is the oxide capacitance per square cm, W_{ms} is the work function difference between Al gate and SiC and ΔV_{FB} is the shift in the flat band voltage. Wms was taken to be -0.3 eV in this calculation[22].

Interface states located at the SiO_2/SiC interface play important roles in device operations. In many devices their density should be kept below certain values in order to have successful operation. Th conductance technique, which is known to be most accurate in the such analysis, was used to determine the density of interface states in the present SiO_2/SiC structure. In this calculation, the density of interface states was derived from the relation[24] $D_{it} = (G_{it}/w)_p/(qAf_D)$, where D_{it} is the interface-state density, w is the frequency of the measurements and A is the gate area. f_D is a parameter that depends on the fluctuation in the surface potential. By following the method described by J. R. Brews [24] and using this equation, the interface-state density was found to be 3.4 10^{11} $cm^{-2}eV^{-1}$ at a point 0.14 eV below the conduction band edge. In this calculation, the surface potential for each applied bias was derived from the 1MHz C-V curve[22]. This interface state value is close to what have been measured for CVD grown 3C-SiC and 6H-SiC. Although the measured interface density may be sufficiently low for the operation of certain devices, it is highly desirable to pull its value below 10^{11} cm^{-2} eV^{-1}. In order to do this, the oxidation, annealing and processing conditions should be investigated and optimized. Such an investigation for the RMS grown SiC layers is under way.

SUMMARY

This work has shown that MOS capacitors could be fabricated and operated successfully on 3C-SiC layers produced by reactive magnetron sputtering. No contamination has been detected at the SiO_2/SiC interface within the resolution of TEM and AES. A relatively high oxidation rate was observed at the region where stacking faults were located. The electrical properties of the grown oxide layer and its interface with SiC have been studied by capacitance and conductance techniques. The amount of positive charges located in the oxide has been estimated by using the flat band voltage of the high frequency C-V curve. The density of interface states determined for one single point in the bandgap was shown to be in the same order with those measured for SiC grown by other techniques.

REFERENCES

1. A. Arbabm, A. Spetz, Q. Wahab, M. Willander and I. Lundstrom, J. Sensors and Materials, **4** , 174 (1993)
2. T. Sugii, T. Yamazaki and T. Ito, IEEE Trans. Electron Devices, **ED-37**, 2331(1990).
3. A. Solangi and M. I. Chaudry, in Amorphous and Crystalline Silicon Carbide, (Springer Proc. Physics. **71**, Springer, Berlin, 1992).
4. M. Bhatnagar and B. J. Baliga, IEEE Trans. Electron Devices, **ED-40**, 645 (1993).
5. S. Nishino, J. A. Powell and H. A. Will, Appl. Phys. Lett. **42**, 460 (1983).
6. S. Nishino and J. Saraie, in Amorphous and Crystalline Silicon Carbide, (Springer Proc. Physics. **34** , Springer, Berlin, 1989), p. 186.
7. S. Motoyoma, N. Morikawa, M. Nasu and S. Kaneda, J. Appl. Phys. **68**, 101 (1990).
8. Q. Wahab, L. Hultman, J.-E Sundgren and M. Willander, J. Mater. Sci. Eng. **B 11**, 61 (1992).
9. Q. Wahab, R. C. Glass, I. P. Ivanov, J. Birch, J.-E. Sundgren and M. Willander, J. Appl. Phys., **74,** 1663 (1993).
10. R. Tomasiunas, M. Petrauskas, M. Willander, Q. Wahab and J.-E. Sundgren, J. Semicond. Sci. Technol., **7**, 1257 (1992).
11. R. Tomasiunas, M. Petrauskas, M. Willander, Q. Wahab and J.-E. Sundgren, in Proceeding of 15th Nordic Semiconductor Meeting,Edited by S. Fransilla and R. Paananen (Finland, June 8-11, 1992), p.35.
12. M. Karlsteen, Q. Wahab, M. Willander, J.-E. Sundgren and G. Holmen, J. Diamond and Related Mater. **1**, 486 (1992).
13. M. Karlsteen, Q. Wahab, O. Nur, M. Willander, and J. -E Sundgren, Accepted in 3rd Int. SiC and related materials, 2-5 November , Washington DC. (1993).
14. Q. Wahab, M. Karlsteen, M. Willander and J.-E. Sundgren , J. Electronic Materials, **11**, 899 (1991).
15. N. Singh and A. Rys, J. Appl. Phys., **73**, 1279 (1993).
16. S. M. Tang, W. B. Berry, R. Kwor, M. V. Zeller and L. G. Matus, J. Electrochem. Soc., **137**, 221 (1990).
17. S. Zaima, K. Onoda, Y. Koide and Y. Yasuda, J. Appl. Phys., **68**, 6304 (1990).
18. M. I. Chaudry, J. Appl. Phys., **69**, 7319 (1991).
19. K. Shibahara, S. Nishino and H. Matsunami, Jpn. J. Appl. Phys., **23**, L862(1984).
20. R. W. Kee, K. M. Geib, C. W. Wilmsen and D. K. Ferry, J. Vac. Sci. Technol., **15** 1520 (1978).
21. H. Du, M. Libera, Z. Yang and Po-Jen lai, D. C. Jacobson, Y. C. Wang and R. F. Davis., Appl. Phys. Lett., **62**, 423 (1993).
22. E. H. Nicollian and J. R. Brews, MOS (Metal Oxide Semiconductor) Physics and Thechnology (Wiley, New York, 1982).
23. F. P. Heiman and Warfield, IEEE Trans. Electron Devices, **ED-12**, 167 (1965).
24. J. R. Brews, Solid-State Electronics, **26**, 711 (1983).

ELECTRONIC AND OPTOELECTRONIC DEVICES BASED ON GaN-AlGaN HETEROSTRUCTURES

M. ASIF KHAN*, J.N. KUZNIA*, S. KRISHNANKUTTY*, R.A. SKOGMAN*, D.T. OLSON*, W.J. SCHAFF**, J.W. BURM**, M.S. SHUR+ AND T. GEORGE++

* APA OPTICS INC., 2950 N.E. 84th Lane, Blaine, MN 55449

** School of Electrical Engineering, Cornell University, Ithaca, NY 14853

+ Department of Electrical Engineering, University of Charlottesville, VA 22903

++ Jet Propulsion Laboratory, California Institute of Technology, Pasadena, CA 91109

ABSTRACT

Availability of optoelectronic components operating in the UV-Visible part of the spectrum opens several exciting and important system applications. Solid state ultraviolet and blue-green lasers can increase the optical data storage density of CDROM/WORM and magneto-optical disks by a factor of four. They are also ideally suited for environmental pollutant identification and monitoring. On the other hand, solid state ultraviolet detectors that do not respond to visible or IR radiation are highly desirable for various commercial systems. These include medical imaging, industrial boiler systems, fire/flame safeguard systems around oil and gas installations and several military applications. A key requirement for these ultraviolet laser and sensor devices is the availability of a semiconductor material system with high quality controlled doping and fabrication technology.

$Al_xGa_{1-x}N$ and $In_xGa_{1-x}N$ for which the direct bandgap can be tailored from the visible to the deep UV is such a material system. Ours and several other research groups (nationally and internationally) have been developing $Al_xGa_{1-x}N$ materials and processing technologies over the past several years. Recently, by employing innovative approaches, significant advances have been made in heteroepitaxy of $Al_xGa_{1-x}N$ on sapphire substrates. Also, controlled n and p-type doping has been achieved. Several high performance devices that form the basis of exciting future research have been demonstrated. These include high responsivity visible blind ultraviolet sensors, basic transistor structures and high power blue light emitting diodes. These pave the way for future research leading to exciting products such as blue-green lasers and UV-imaging arrays. The demonstrated transistor structures are foundation for building $Al_xGa_{1-x}N$

Mat. Res. Soc. Symp. Proc. Vol. 339. ©1994 Materials Research Society

-GaN based high power, high frequency and high temperature electronic components. In this paper, we will summarize some of our recent work and reflect on the potential and the issues in $Al_xGa_{1-x}N$-$In_xGa_{1-x}N$ based device development.

Introduction

$Al_xGa_{1-x}N$ and $In_xGa_{1-x}N$ are wide direct bandgap III-V semiconductors with bandgaps varying from 6.2eV (x = 1) to 3.4eV (x = 0) for $Al_xGa_{1-x}N$ and 3.4eV (x = 0) to 1.95eV (x = 1) for $In_xGa_{1-x}N$.

Pioneering research was carried out by Pankove and coworkers in the 1970's aimed at developing the materials and device technologies for GaN and $Al_xGa_{1-x}N$ [1]. We have recently demonstrated MESFET and HEMT devices based on the AlxGa1-XN material system [2]. Recent Monte Carlo simulations predict high values for peak velocity, vp, saturation velocity, v_s, and electron mobility, μ, in GaN ($v_p = 2.7 \times 10^5$ m/s, vs $\approx 1.5 \times 10^5$ m/s, and $\mu \approx 1000\ cm^2V^{-1}s^{-1}$ at room temperature in GaN doped at $10^{17}\ cm^{-3}$) [3]. These values combined with a wide energy gap and fairly good thermal conductivity make GaN/AlGaN heterostructures quite attractive for microwave and millimeter wave devices with a wide operation temperature range.

$In_xGa_{1-x}N$ is an ideal candidate for active layers in optical devices such as light emitting diodes (LED's) and lasers in the blue-green regions of the electromagnetic spectrum. Using high quality GaN layers, we have previously demonstrated photopumped ultraviolet stimulated emission in both the edge emitting (cavity length 2 mm) and vertical cavity (cavity length 1.5 μm) configuration [4]. Amano et al. have also demonstrated stimulated emission at room temperature from optically pumped 2.15 mm long GaN cavities in the edge-emitting configuration [5]. Nakumara et al. have recently reported on the fabrication of an efficient blue LED based on a GaN/InGaN double heterostructure [6]. Very recently Amano et al. reported on stimulated emission from InGaN/GaN double heterostructures [7]. They used edge emission geometry and their cavities were 1 mm long.

In this paper, we now describe our recent efforts in developing electronic and optoelectronic devices based on the $Al_xGa_{1-x}N$/$In_xGa_{1-x}N$ material systems. This includes (a) the demonstration of a 0.25 μm gate length AlGaN/GaN HFET with the cutoff frequency $f_T \approx 11$ GHz and the maximum oscillation frequency $f_{max} \approx 35$ GHz and (b) the observation of vertical cavity (perpendicular to the epilayer i.e surface emission) stimulated emission from an $In_{0.25}GaN_{0.75}N$/GaN single heterojunction (SH).

HFET based on GaN-AlGaN Heterostructures

The AlGaN/GaN heterostructure for this work, shown in Figure 1, was grown in a low pressure MOCVD reactor operating at 76 torr. Triethylaluminum (TEA),

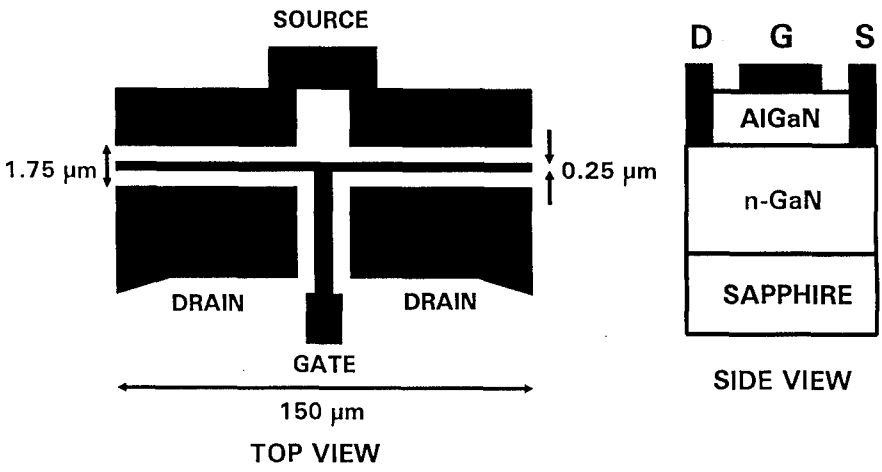

Figure 1. AlGaN/GaN HFET structures.

triethylgallium (TEG), and ammonia (NH_3) were used as the precursors. Typical growth conditions were similar to those described earlier [2]. As before[2] we used refractory metals (TiAu & TiW) for the source-drain and gate contacts. The GaN layer was unintentionally doped with a background carrier concentration of 1×10^{17} cm^{-3}. The thickness of the AlGaN layer in our heterojunction was 250 Å. From the measured device threshold voltage $V_T = -2V$, we estimate the doping of the AlGaN layer to be of the order of 3.5 to 4×10^{18} cm^{-3}. The nominal gate length L_g was 0.25 μm and the distances between the source and drain and the gate contact were 0.75 μm each.

For a device with a gate length and width of 0.25 and 150 μm respectively, Figures 2(A) and 2(B) show the measured source-drain current voltage characteristics and the transconductance as a function of the gate bias at different drain biases. As seen from Figure 2(A), the device conductance at low drain biases is only weakly dependant on the gate bias for a wide range of values. This implies large source and drain series resistances, R_s and R_d, which we estimate to be 30 Ω/mm from the source-drain I-V characteristics. We also observe a nonlinearity in the drain I-V curves indicating a

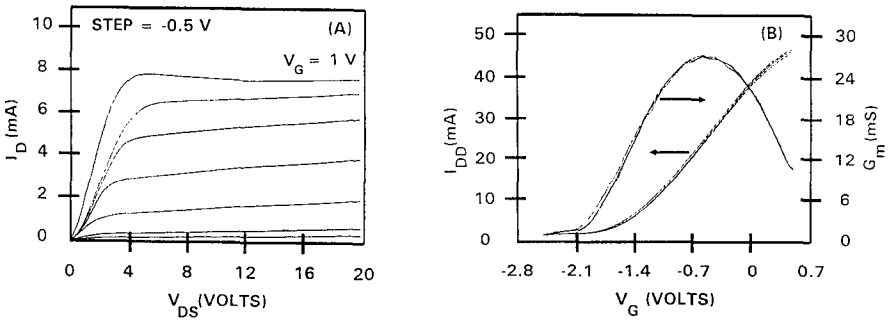

Figure 2. (A) Source to drain ouput current - voltage characteristics (-2 < V_G < 1 V step = -0.5 V) and (B) transconductance versus gate bias.

non-ohmic behavior for low drain biases. The device characteristic curves were analyzed using the universal HFET model[3] (which was modified in order to account more accurately for very large series resistances). The fitting of the model to experimental data yielded $R_s = R_d = 28\ \Omega$/mm width which was in good agreement with the simple estimate made above. The model also shows the maximum current in our device to be limited to approximately 60 mA/mm gate width. This limitation may be caused either by defect states at or near the AlGaN/GaN interface or by the properties of the non-ideal source and drain contacts. In Figure 3 we plot the measured gate current-voltage characteristics. As seen the turn-on voltage for the gate leakage current is around 4 V. This makes possible the design of normally-off devices for applications in digital integrated circuits operating at elevated temperature.

From the estimated values of the source resistances for our device, the maximum device transconductance (g_{max}) must be smaller than or equal to $1/R_s$ = 33 mS/mm. This number is in a good agreement with the maximum measured transconductance of 27 mS/mm (at room temperature). Hence, we conclude the extrinsic transconductance for our 0.25 μm gate device to be limited by the series resistance. Also from Figure 2(B), the maximum measured transconductance corresponds to the extrinsic gate-to-source bias V_{gs} = -0.5 V. The threshold voltage, V_T, is approximately equal to

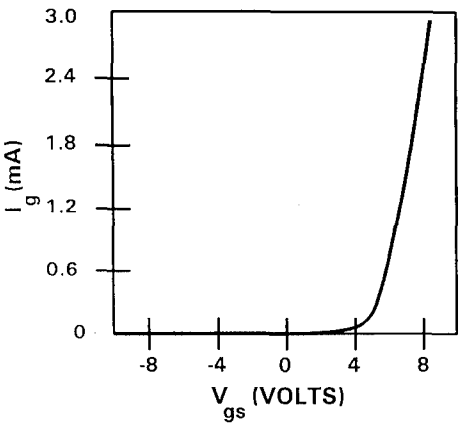

Figure 3. Gate current - voltage characteristics.

-2 V. The drain saturation current (I_{sat}) at V_{gs} = -0.5 V is roughly 4 mA (= 27 mA/mm). Such a current leads to the voltage drop of 0.75 V across the series resistance. Hence, the intrinsic gate-source voltage swing, $V_{GT} = V_{gs} - V_T - I_{sat}R_s$ = - 0.5 + 2 - 0.75 = 0.75 V. Using this we estimate the concentration of the two dimensional electron gas, n_s, at the source as:

$$n_s = (\varepsilon V_{GT})/q(d_i + \Delta d) = 1.24 \times 10^{16}\ m^{-2} \qquad \text{Eq. (1)}$$

Here q is the electronic charge, ε and d_i are the dielectric permittivity and thickness of the AlGaN layer, and Δd is the effective thickness of the two dimensional electron gas which we estimate to be approximately 50 Å. At V_{GT} = 0.75 V, the effective electron velocity v_{eff} at the source end of the device is given by:

$$v_{eff} = I_{ds}/qn_sW = 13{,}500\ (m/s) \qquad \text{Eq. (2).}$$

Since electron velocity increases from the source to drain the above value of v_{eff} translates to a minimum cutoff frequency f_T of:

$$f_T = v_{eff}/2\pi L = 12000/(2\pi \times 2.5 \times 10^{-7}) = 8.5(GHz) \qquad \text{Eq. (3)}$$

In Figure 4(A) we plot the measured values of the current gain as a function of frequency for our 0.25 μm gate length HFET device. As seen the measured f_T value of 11 GHz (using 6 dB/octave rolloff) agrees well with the estimated lower bound of 8.5 GHz. From the data of Figure 4(B), describing the measured gain versus frequency, we also estimate a value of 35 GHz for the maximum oscillation frequency for our

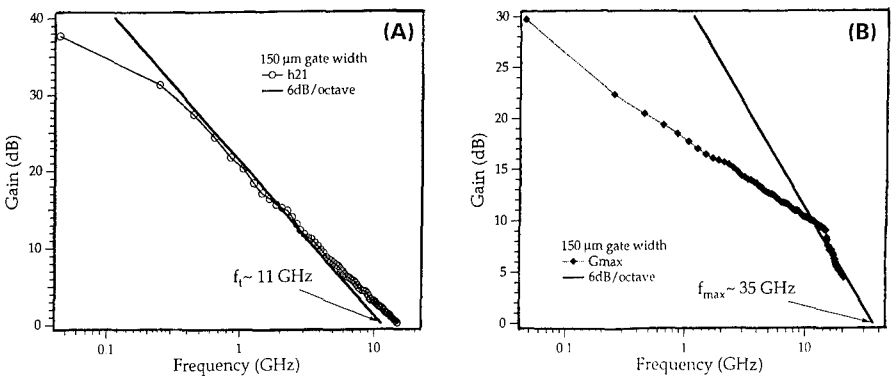

Figure 4. Results of the measurements of (A) f_T and (B) f_{max}.

device. The relatively high value of f_{max} is explained by a very low parasitic output conductance in the saturation regime (see Figure 2(B)).

Stimulated Emission from InGaN-GaN Heterojunctions

Samples in this study were deposited using a low pressure MOCVD system. Triethylgallium, trimethylindium and ammonia were used as the precursors. Prior to deposition of the heterostructure a thin 50 nm AlN buffer layer was grown on the sapphire substrate. The heterojunction for the study, as shown in Figure 5, consisted of a 4 μm thick GaN layer followed by a 0.1 μm thick $In_{0.25}Ga_{0.75}N$ layer. The GaN layer was deposited at 1050° C and 76 torr and the $In_{0.25}Ga_{0.75}N$ layer at 875° C.

Cross-section transmission electron microscopy (XTEM) was used to establish the single crystal nature of the heterojunction layers. The In mole fraction 'x' of our $In_xGa_{1-x}N$ films was determined using X-ray diffraction spectra shown in Figure 6. Room temperature low power (10 mW cw) photoluminescence measurements using a HeCd laser (325 nm) showed a characteristic emission spectra peaking at 415 nm (violet). The peak emission energy corresponds to a band-edge transition from $In_{0.25}Ga_{0.75}N$ assuming a linear interpolation of bandgap energies between GaN (3.4 eV) and InN (1.95 eV). The alloy compositions from x-ray and photoluminescence

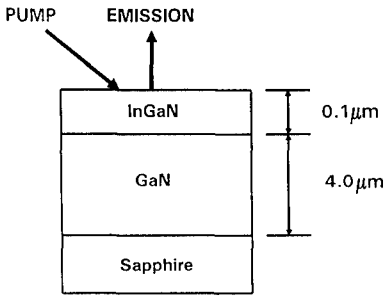

Figure 5. Schematic and lasing geometry for InGaN/GaN hetero-structure.

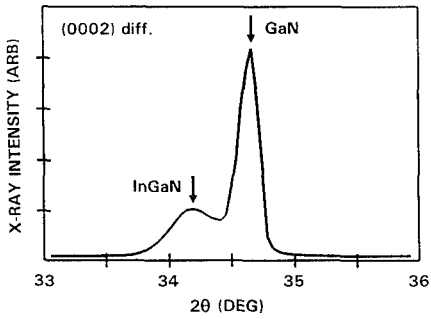

Figure 6. X-ray spectra for an InGaN/ GaN single heterostructure.

measurements are in good agreement.

Pulsed photopumping measurements were performed on the as-grown samples at room temperature using the geometry of Figure 5. A nitrogen laser at 337.1 nm with a peak power of 1.5 mJ per pulse and a pulse length of 0.5 ns with a repetition rate of 10 Hz was used for these measurements. Emission spectra were detected perpendicular to the epilayer surface using a synchronous monochromator and boxcar integrator system. For the surface emitting configuration, the dependence of the violet emission intensity (at 415 nm) on pump power intensity is shown in Figure 7. This is similar to that observed in high quality, single crystal GaN deposited on sapphire substrates [4,5]. Similar to Amano et.al. [7] we feel this nonlinear rise in emission intensity is indication of onset of stimulated emission. For our 0.1 μm thick $In_{0.25}Ga_{0.75}N$ film, the threshold for stimulated emission (at 415 nm) is estimated to be about 2 MW/cm^2. In Figure 8 we plot the spontaneous (using a 10 mW cw HeCd laser) and the room temperature stimulated emission signal (at a pump power of 5 MWcm^{-2}). As seen the linewidth of the purple emission also narrows dramatically, from 20 to 1.5 nm, at the onset of stimulated emission.

Summary

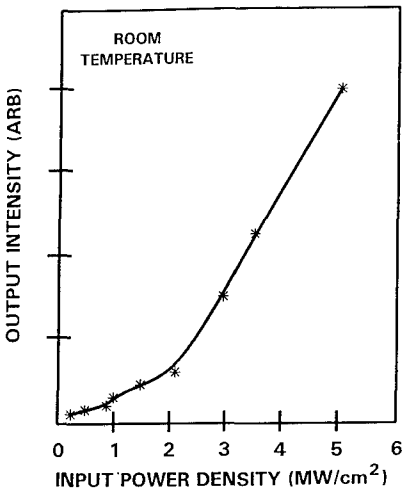

Figure 7. Total optical output power from a single InGaN/GaN heterostructure as a function of excitation power.

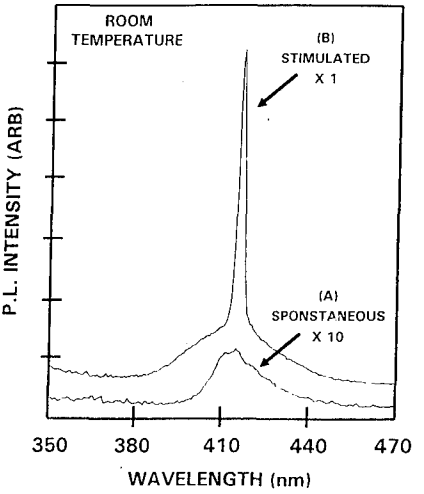

Figure 8. Plotted are the (A) spontaneous surface emission and (B) stimulated surface emission.

In summary we report the fabrication and the high frequency characterization of a GaN/AlGaN heterojunction FET. For a 0.25 μm gate length device (gate width 150 μm) and a source-drain separation of 2 μm we measured f_T and f_{max} values of 11 and 35 GHz respectively. To the best of our knowledge this is the first report of high frequency characterization for a GaN/AlGaN HFET device.

We have also demonstrated for the first time room temperature violet stimulated emission from a $In_{0.25}Ga_{0.75}N$/GaN heterojunction in the surface emitting configuration. The quality of the material was high enough to yield stimulated emission with a cavity length of 4.1 μm (0.1 μm $In_{0.25}Ga_{0.75}N$ on 4 μm GaN) and mirror reflectivities of about 20%. This work represents a significant step toward the realization of high frequency devices based on GaN/AlGaN heterostructures and violet/blue injection lasers based on GaN/InGaN heterojunctions. This work was partially supported by Air Force Contract F49620-93-C-0059 and F33615-92-C-1078 monitored by Dr. Gernot Pomrenke and Dr. Paul Shriver. It was also supported by Office of Naval Research Grant N00014-92-C-0090 and N00014-91-c-0065 and was monitored by Mr. Max Yoder.

References

1. J.I. Pankove, E.A. Miller and J.E. Berkeyheiser, RCA Rev. **32**, 383 (1971).

2. M. Asif Khan, J.N. Kuznia, A.R. Bhattarai and D.T. Olson, Appl. Phys. Lett. **62**, 1786 (1993), also, M. Asif Khan, A. Bhattarai, J.N. Kuznia and D.T. Olson, Appl. Phys. Lett. **63**, 1214 (1993).

3. B. Gelmont, K. S. Kim, and M. Shur, J. Appl. Phys., **74**, 1818 (1993).

4. M. Asif Khan, D.T. Olson, J.M. Van Hove and J.N. Kuznia, Appl. Phys. Lett. **58**, 1515 (1991).

5. H. Amano, T. Asahi and I. Akasaki, Jpn. Jour. Appl. Phys. **29**, L205 (1990).

6. S. Nakamura, M. Senoh and T. Mukai, Appl. Phys. Lett. **62**, 2390 (1993), also, S. Nakamura, T. Mukai and M. Senoh, Appl. Phys. Lett. **64**, 1687 (1994).

7. H. Amano, T. Tanaka, Y. Kunii, S.T. Kim and I. Akasaki, Appl. Phys. Lett. **64**, 1377 (1994).

InGaN/AlGaN DOUBLE-HETEROSTRUCTURE BLUE LEDS

SHUJI NAKAMURA
Department of Research and Development,
Nichia Chemical Industries, Ltd.,
491 Oka, Kaminaka, Anan, Tokushima 774, Japan

ABSTRACT

High-brightness InGaN/AlGaN double-heterostructure (DH) blue-light-emitting diodes (LEDs) with a luminous intensity of 1.2 cd were fabricated successfully for the first time. As an active layer, a Zn-doped InGaN layer was used. The peak wavelength and the full width at half-maximum of the electroluminescence were 450 nm and 70 nm, respectively. The forward voltage was as low as 3.6V at 20 mA.

INTRODUCTION

Much research has been done on high-brightness blue-light-emitting diodes (LEDs) for use in full-color displays or full-color indicators with the characteristics of high-reliablility and high-speed. For those purposes, II-VI materials such as ZnSe, SiC and III-V nitride semiconductors such as GaN have been investigated intensively for a long time. However, it was impossible to obtain high-brightness blue LEDs with a brightness over 1 cd. Among these semiconductors there has recently been great progress in the crystal quality, p-type control and growth method of GaN films and GaN devices [1-5]. For practical applications of short-wavelength optical devices, such as laser diodes (LDs), a double heterostructure (DH) is indispensable for III-V nitrides. The ternary III-V semiconductor compound, InGaN, is one candidate as the active layer for blue emission because its band gap varies from 1.95 eV to 3.40 eV, depending on the indium mole fraction [6]. Recently, relatively high-quality InGaN films were obtained by Yoshimoto et al., using a high growth temperature (800 °C) and a high indium source flow rate ratio [7]. We succeeded in obtaining high-quality InGaN films which could be used as an active layer of DH LEDs [8]. Thus, the first successful InGaN/GaN DH blue LEDs were fabricated using the above-mentioned InGaN films [9,10]. In this paper, InGaN/AlGaN DH blue LED which has a Zn-doped InGaN layer as an active layer is described. Also, we describe Zn doping into InGaN films. Zn doping into GaN has been intensively investigated to obtain blue emission centers for application to blue LEDs by many researchers because strong blue emissions have been obtained by Zn doping into GaN [11-13]. However, there are no reports on Zn doping into InGaN.

EXPERIMENTAL

InGaN/AlGaN DH structures were grown by the two-flow MOCVD method. Details of two-flow MOCVD are described in other papers [14,15]. The growth was conducted at atmospheric pressure. Sapphire with (0001) orientation (C face) and two-inch diameter, was used as a substrate. Trimethylgallium (TMG), trimethylaluminum (TMA), trimethylindium (TMI), monosilane (SiH_4), bis-cyclopentadienyl magnesium (Cp_2Mg), diethylzinc (DEZ) and ammonia (NH_3) were used as Ga, Al, In, Si, Mg, Zn and N sources, respectively. First, the substrate was heated to 1050 °C in a stream of hydrogen. Then, the substrate temperature was lowered to 510 °C to grow the GaN buffer layer. The thickness of the GaN buffer layer was about 200 Å. Next, the substrate temperature was elevated to 1020 °C to grow GaN films. The Si-doped GaN films were grown for 60 minutes. The thickness of the Si-doped GaN film was approximately 4 μm. After GaN growth, a $Al_{0.15}Ga_{0.85}N$ layer was grown to a thickness

Mat. Res. Soc. Symp. Proc. Vol. 339. ©1994 Materials Research Society

of 0.15 μm by flowing TMA and TMG. After $Al_{0.15}Ga_{0.85}N$ growth, the temperature was decreased to 800 °C, and the Zn-doped $In_{0.06}Ga_{0.94}N$ layer was grown for 15 minutes. The thickness of the Zn-doped InGaN layer was about 500Å. After the Zn-doped InGaN growth, the temperature was increased to 1020 °C to grow Mg-doped p-type $Al_{0.15}Ga_{0.85}N$ and GaN layers by flowing TMA, TMG and Cp_2Mg gases. The thicknesses of Mg-doped p-type $Al_{0.15}Ga_{0.85}N$ and GaN layers were 0.15 μm and 0.5 μm, respectively. The details of growth conditions of GaN and InGaN films are described in other papers [9,10]. After the growth, N_2-ambient thermal annealing was performed to obtain a highly p-type GaN layer at a temperature of 700 °C [16]. This thermal annealing technique to obtain highly p-type GaN is much better than the low-energy electron beam irradiation treatment because the entire p-type GaN layer becomes a uniform highly p-type GaN layer [17]. Fabrication of LED chips was accomplished as follows: the surface of the p-type GaN layer was partially etched until the n-type GaN layer was exposed. Next, a Ni/Au contact was evaporated onto the p-type GaN layer and a Ti/Al contact onto the n-type GaN layer. The wafer was cut into a rectangular shape. These chips were set on the lead frame and were then molded. The characteristics of LEDs were measured under DC-biased conditions at room temperature.

RESULTS AND DISCISSION

Figure 1 shows the double-crystal X-ray rocking curve (XRC) for the (0002) diffraction of Zn-doped InGaN films grown on GaN films. Curve (a) shows the Zn-doped InGaN film which was grown at a temperature of 800 °C and a DEZ flow rate of 8.0 nmol/min (sample A). Curve (b) shows the Zn-doped InGaN film which was grown under the same conditions as sample A, except for the growth temperature and DEZ flow rate which were changed to 810 °C and 2.7 nmol/min (sample B). Both curves clearly show two peaks. One is the (0002) peak of X-ray diffraction of GaN and the other is that of InGaN. We can estimate the indium mole fraction of the InGaN films by calculating the difference in peak position between the InGaN and GaN peaks, assuming that the (0002) peak of the X-ray diffraction of GaN is constant at 2θ=34.53 degrees and that Vegard's law is valid. These calculated values of the indium mole fraction are 0.16 for sample A and 0.11 for sample B, as shown in Fig. 1.

The full width at half-maximum (FWHM) of the double-crystal XRC for the (0002) diffraction from the Zn-doped InGaN film was 6.3 min and that from the GaN film was 5.6 min for sample A. The FWHM of the XRC for the (0002) diffraction from the Zn-doped InGaN film was 6.2 min and that from the GaN film was 5.4 min for sample B. The values of FWHM of Zn-doped InGaN films are almost the same as those of the GaN films used as substrates. We already reported the FWHM of XRC of undoped InGaN films [8]. When we compare the FWHM of XRC of Zn-doped InGaN films with that of undoped InGaN films, the value of FWHM of Zn-doped InGaN films is almost the same as that of undoped InGaN films [8]. Therefore, in this Zn doping range, the crystal quality of InGaN films is minimally affected by Zn doping, judging from the FWHM of XRC measurements.

Figure 2 shows typical results of room-temperature photoluminescence (PL) measurements of the Zn-doped InGaN films. The PL measurements were performed at room temperature. The excitation source was a 10 mW He-Cd laser. These samples of spectra (a) and (b) correspond to samples A and B of Fig.1, respectively. Both spectra clearly show two peaks and many small oscillations caused by optical interference effects are seen. The appearance of interference effects shows that the surface of the Zn-doped InGaN film is smooth and uniform. Spectrum (a) shows the peak emissions at 410 nm (3.02 eV) and 494 nm (2.52 eV). Spectrum (b) shows the peak emissions at 398 nm (3.12 eV) and 462 nm (2.68 eV). The shorter-wavelength peak is the band-edge (BE) emission of InGaN, and the longer-wavelength peak is Zn-related emission which has a large value of FWHM (about 66 nm). The difference in peak emission energy between the BE and Zn-related emissions is 0.50 eV for spectrum (a) and 0.44 eV for spectrum (b).

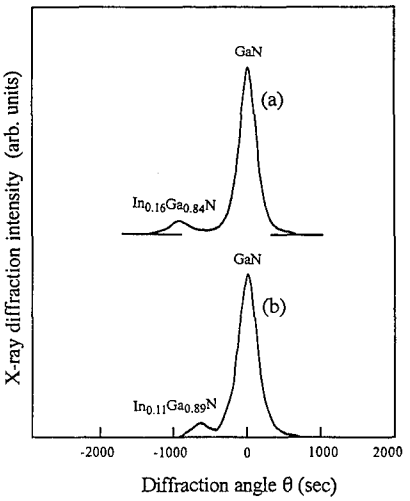

Fig. 1. The XRC for (0002) diffraction from Zn-doped InGaN films grown under the same conditions except for the InGaN growth temperatures and DEZ flow rates. The growth temperatures of InGaN were (a) 800 °C and (b) 810 °C. The flow rates of DEZ were (a) 8.0 nmol/min and (b) 2.7 nmol/min.

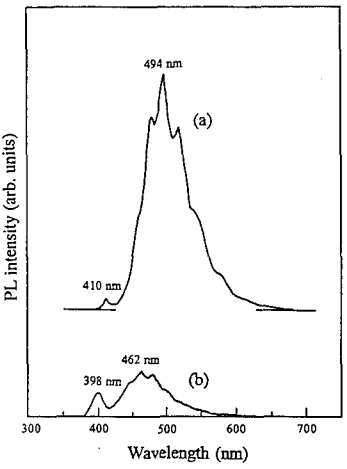

Fig. 2. Room-temperature PL spectra of Zn-doped InGaN films grown under the same conditions except for the InGaN growth temperatures and DEZ flow rates. The growth temperatures of InGaN were (a) 800 °C and (b) 810 °C. The flow rates of DEZ were (a) 8.0 nmol/min and (b) 2.7 nmol/min.

Next, we describe InGaN/AlGaN DH LEDs. Figure 3 shows the structure of the InGaN/AlGaN DH LEDs. Figure 4 shows the electroluminescence (EL) spectra of the InGaN/AlGaN DH LEDs at forward currents of 10, 20, 30 and 40 mA. The peak wavelength is almost constant at 450 nm and the FWHM of the peak emission is 70 nm.

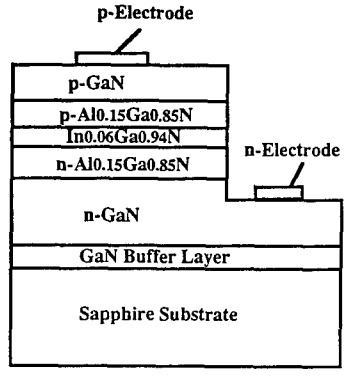

Fig. 3. The structure of the InGaN/AlGaN DH LEDs.

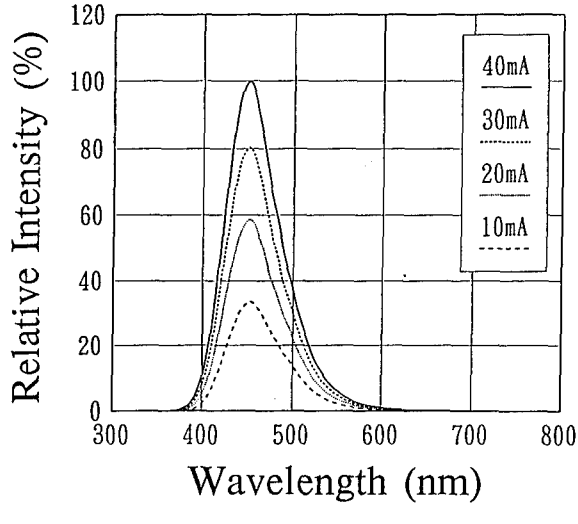

Fig. 4. Electroluminescence spectra of the InGaN/AlGaN DH LEDs under different forward currents.

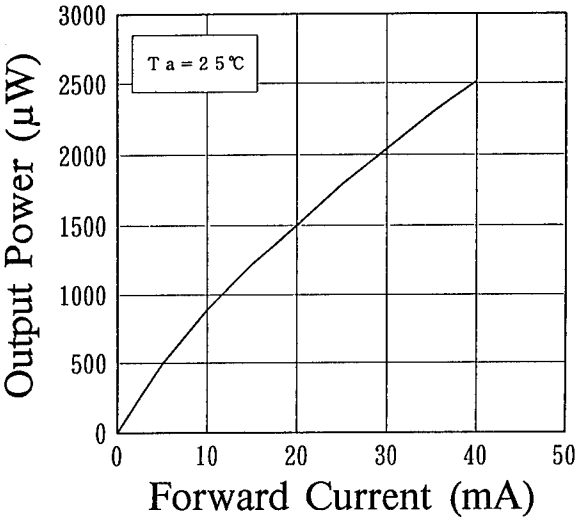

Fig. 5. The output power of the InGaN/AlGaN DH LEDs as a function of the forward current.

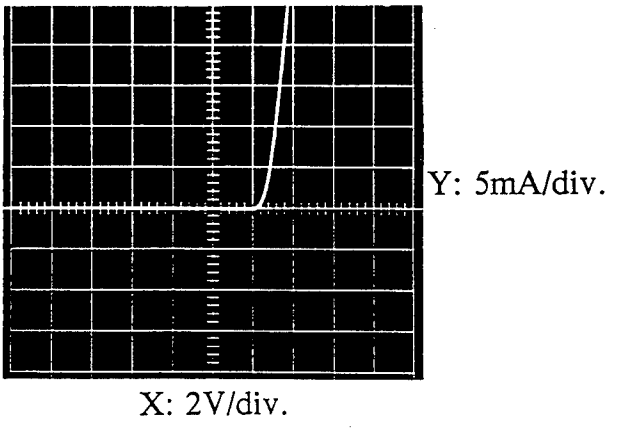

Fig. 6. Typical I-V characteristics of the InGaN/AlGaN DH LEDs.

The output power is shown as a function of the forward current in Fig. 5. The output power increases slightly sublinearly up to 40 mA as a function of the forward current. The output power of the InGaN/AlGaN DH LEDs is 0.8 mW at 10 mA, 1.5 mW at 20 mA and 2.5 mW at 40 mA. The external quantum efficiency is 2.7 % at 20 mA. A typical on-axis luminous intensity of DH LEDs with a 15° cone viewing angle is 1.2 cd at 20 mA. This luminous intensity is the highest value ever reported for blue LEDs. It is shown that the forward voltage is 3.6 V at 20 mA in Fig. 6. This forward voltage is the lowest value ever reported for III-V nitride LEDs. In the previous reports of InGaN/GaN DH LEDs, the forward voltage was as high as about 10 V and the output power was not very high (about 125 μW) [9,10]. In previous study, electron beam irradiation was performed for as-grown InGaN/GaN epilayers in order to obtain a highly p-type GaN layer, instead of thermal annealing. Therefore, the forward voltage was as high as 10 V and the output power was not very high because the entire p-layer was not rendered a uniform highly p-type GaN layer by electron beam irradiation. Thermal annealing can easily change the entire high-resistivity p-type GaN layer into low-resistivity p-type GaN layer uniformly [16,17].

SUMMARY

In summary, candela-class high-brightness InGaN/AlGaN DH blue LEDs with luminous intensity over 1 cd were fabricated for the first time. The peak wavelength and the FWHM of the EL were 450 nm and 70 nm, respectively. This value of luminous intensity was the highest ever reported for blue LEDs. Using these high-brightness blue LEDs, high-brightness full-color indicators and flat panel displays will be developed in the near future.

REFERENCES

1. S. Strite and H. Morkoç, J. Vacuum Sci. & Technol. B**10**, 1237 (1992).
2. I. Akasaki, H. Amano, Y. Koide, K. Hiramatsu and N. Sawaki, J. Cryst. Growth **98**, 209 (1989).
3. H. Amano, M. Kito, K. Hiramatsu and I. Akasaki, Jpn. J. Appl. Phys. **28**, L2112 (1989).
4. M. A. Khan, J. N. Kuznia, J. M. Van Hove, D. T. Olson, S. Krishnankutty and R. M. Kolbas, Appl. Phys. Lett. **58**, 526 (1991).
5. S. Nakamura, T. Mukai and M. Senoh, Jpn. J. Appl. Phys. **30**, L1998 (1991).
6. K. Osamura, S. Naka and Y. Murakami, J. Appl. Phys. **46**, 3432 (1975).
7. N. Yoshimoto, T. Matsuoka, T. Sasaki and A. Katsui, Appl. Phys. Lett. **59**, 2251 (1991).
8. S. Nakamura and T. Mukai, Jpn. J. Appl. Phys. **31**, L1457 (1992).
9. S. Nakamura, M. Senoh and T. Mukai, Jpn. J. Appl. Phys. **32**, L8 (1993).
10. S. Nakamura, M. Senoh and T. Mukai, Appl. Phys. Lett. **62**, 2390 (1993).
11. J. I. Pankove and J. A. Hutchby, Appl. Phys. Lett. 24, 281 (1974).
12. G. Jacob, M. Boulou and M. Furtado, J. Cryst. Growth **42**,136 (1977).
13. P. Bergman, G. Ying, B. Monemar and P. O. Holz, J. Appl. Phys. **61**, 4589 (1987).
14. S. Nakamura, Jpn. J. Appl. Phys. **30**, 1620 (1991).
15. S. Nakamura, Y. Harada and M. Senoh, Appl. Phys. Lett. **58**, 2021 (1991).
16. S. Nakamura, T. Mukai, M. Senoh and N. Iwasa, Jpn. J. Appl. Phys. **31**, L139 (1992).
17. S. Nakamura, N. Iwasa, M. Senoh and T. Mukai, Jpn. J. Appl. Phys. **31**, 1258 (1992).

ION MILLING AND REACTIVE ION ETCHING OF III-V NITRIDES

S. J. Pearton, C. R. Abernathy, F. Ren* and J. R. Lothian*
Dept. Materials Science & Eng., University of Florida, Gainesville, FL
*AT&T Bell Laboratories, Murray Hill, NJ

ABSTRACT

Dry patterning of GaN, InN, AlN and InGaN grown by MOMBE on GaP, Al_2O_3 or GaAs substrates was performed with 100-500 eV Ar^+ ions at beam angles of incidence ranging from 0-75° from the normal, or with ECR discharges of BCl_3/Ar, CH_4/H_2 or Cl_2/H_2. The mill rates normalized to the Ar^+ beam current were typically a factor of 2 lower than for GaAs and InP (i.e. maximum values of 300-500 $Å \cdot min^{-1} \cdot mA^{-1} \cdot cm^{-2}$ at 400 eV Ar^+ beam energy and 60° angle with respect to the beam normal). The surface morphology of the ion milled nitrides was smooth even at 500 eV Ar^+ energy, with no evidence for preferential sputtering of N as determined by AES. The ECR dry etch rates were fastest with elevated temperature Cl_2/H_2 discharges, although both of the other chemistries investigated provide smooth, anisotropic pattern transfer. Since the ion mill rates are slow for single-crystal nitrides and less than the mill rates of common masking materials (SiO_2, SiN_x, photoresist) it appears this technique is useful only for shallow-mesa applications, and that dry etching methods involving an additional chemical component or ion implantation isolation are more practical alternatives for device patterning.

INTRODUCTION

There is great current interest in the InGaAlN system for blue light-emitting devices and high temperature electronics [1-7]. Several groups have recently reported the fabrication of p-n junction LED's, MESFETs and HEMTs. Due to the wide bandgap of the nitrides it is difficult to achieve good ohmic contacts and wet and dry etching processes are still quite crude for these materials. In particular, controlled etching techniques are necessary for reproducible fabrication of small dimension or multi-element photonic and electronic circuits.

In this paper we report a study of the Ar^+ ion milling characteristics of GaN, AlN, InN and InGaN. Ion milling is commonly employed in GaAs technology for mesa etching applications and it is necessary to establish the milling characteristics of the III-V nitrides. We also demonstrate highly anisotropic ECR dry etching of the nitrides in ECR Cl_2/H_2 or $CH_4/H_2/Ar$ discharges.

EXPERIMENTAL

The nitride layers were grown using group III metalorganics (triethylgallium, trimethylamine alane or trimethylindium, respectively for GaN, AlN and InN) and atomic nitrogen from an ECR plasma disk source operating at 200W applied power.[8] The growth temperature was ~500°C for each of the nitrides, and layers up to 1.5 μm thick were deposited.

Mat. Res. Soc. Symp. Proc. Vol. 339. ©1994 Materials Research Society

The InN was n-type (10^{20} cm^{-3}) with mobility ~100 $cm^2 V^{-1} sec^{-1}$, while the GaN and AlN were undoped ($<10^{16}$ cm^{-3}) and these epitaxial layers were fully depleted. AZ 1350J photoresist was spun onto the samples and lithographically patterned in a resolution test array. The etch rates were obtained from stylus profilometry of the features after removal of the resist.

Ion milling was performed in a Technics Micro Ion Mill [Model MIM (TLA 20)] using an Ar^+ ion beam at 100-500V whose angle of incidence was varied between 0 and 75° from the vertical. The samples were mounted on a wafer-cooled plate held at 10°. Typical neutralized Ar^+ ion current densities were 0.5-0.8 mA · cm^{-2} at the sample position.

The dry etching was performed in a Plasma Therm SL720 system with an Astex 1500 high profile ECR source (2.45 GHz). The top magnet in this source was operated at 135A, corresponding to a field >875 Gauss, and the bottom collimating magnet at 100A, producing calculated nearly vertical ion trajectories at the sample position. The ion energies were controlled by application of 13.56 MHz power to the sample chuck, and the resulting dc bias was varied from −150 to −250V. The process pressure for both plasma chemistries was 1 mTorr, and the applied microwave power was varied from 100-1000W. Scanning electron microscopy (SEM) was used to examine the etched surface morphologies, and Auger Electron Spectrometry (AES) was employed to measure the near-surface stoichiometry before and after the plasma processing of the nitride layers.

RESULTS AND DISCUSSION

Figure 1 shows the average mill rate for InN, GaN, AlN and InGaN normalized to the Ar^+ ion beam current as a function of Ar^+ ion energy at 0° (vertical) incidence angle. For the single crystal samples (InN, GaN, InGaN) the mill rate depends linearly on the ion energy, with a slope of ~0.75. The absolute rates are approximately a factor of two slower than those reported previously for single crystal GaAs and InP.[9] The sputtering yields were ~0.3 atoms per ion at 500 eV Ar^+ ion energy. The lower mill rates for the single-crystal nitrides reflect their stronger bond strengths relative to GaAs and InP. For the polycrystalline InN the ion mill rates were higher than for the single crystal samples. To the best of our knowledge these are the first reported data for ion milling of III-V nitrides.

Figure 2 shows the experimentally observed mill rate dependence on the angle of incidence of the Ar^+ ion beam for all four nitrides at 400V. The fundamental dependence of mill rate on beam angle is similar in each case, and is similar to that reported previously for GaAs and InP.[9] As predicted from linear cascade theory, the ion mill rate increases with increasing incidence angle up to ~60° and then decreases. The sputtering yields ranged from ~0.25 atoms per ion for GaN to 0.5 atoms per ion for InN at normal (0°) incidence, and from ~0.37 atoms per ion for GaN to ~0.75 atoms per ion for InN at 60° angle of incidence.

Surface morphologies for GaN, AlN and InN after 35 minute ion milling treatment at 400V Ar^+ beam voltage (0° normal incidence) are shown in the SEM micrographs of Figure 3. The milled surfaces are similar in morphology to those of the masked areas, and suggest that there is no preferential sputtering of the lighter element N under these conditions. This is somewhat different from the case of InP reported previously, where P was preferentially sputtered under these conditions, leading to the presence of In droplets on the surface.

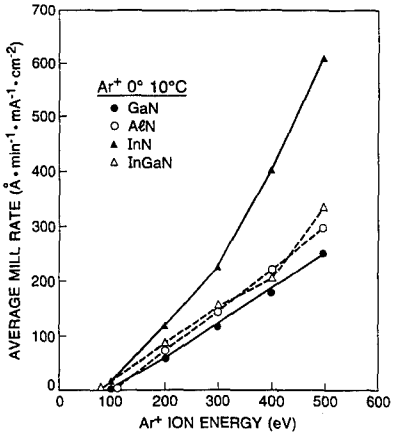

Fig. 1. Mill rates averaged over a 5 min period and normalized to ion current for Ar^+ ion milling of GaN, AlN, InN and InGaN, as a function of ion energy. The beam was normally incident, and the sample temperature was 10°C.

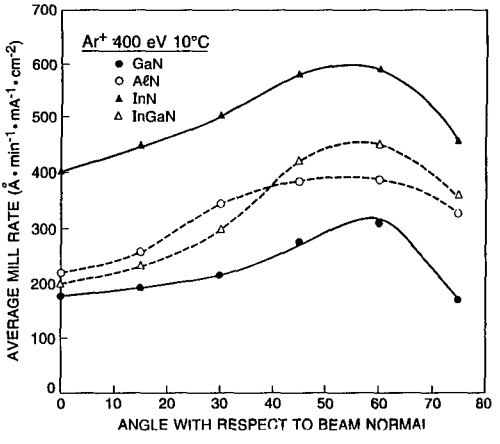

Fig. 2. Average mill rate normalized to ion current for 400 eV Ar^+ ion milling of the III-V nitrides, as a function of beam incidence angle measured from the normal.

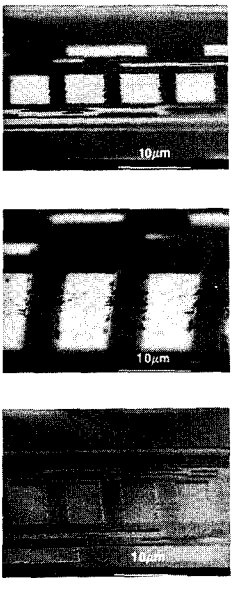

Fig. 3. SEM micrographs of features ion milled into GaN (top), InN (center) or AlN (bottom) at 0° incidence angle for 35 minutes using 400 eV Ar^+ ions.

AES analysis showed there was no significant change in near-surface stoichiometry of any of the nitrides after ion milling and ion chanelling showed there was no amorphous layer formation.

Figure 4 shows the etch rates of GaN, AlN and InN in 10 Cl_2/15 H_2 (total flow rate 25 standard cubic centimeters per minute, sccm) discharges with a fixed dc bias of −150V on the samples, as a function of the applied microwave power. For both GaN and AlN the etch rates increase by approximately a factor of five between 100 and 1000W as more reactive chlorine and atomic hydrogen becomes available due to a greater dissociation efficiency in the discharge, a fact confirmed by optical emission spectroscopy of the 656.3 nm atomic hydrogen and 837.6 nm atomic chlorine lines, and by microwave (35 GHz) interferometric measurements of the electron densities at different applied microwave powers. The etch rates of InN are much smaller than those of the other two materials because of the low volatility of $InCl_x$ species. The resulting surface morphologies of etched InN layers were rough due to In enrichment.

Figure 5 shows SEM micrographs of features etched ~1 μm deep in GaN at either 500W (top) or 1000W (center) microwave power in Cl_2/H_2 discharges. In both cases the etching is smooth and anisotropic with a very slight undercut observable on the 1000W sample. The bottom of Fig. 5 shows features etched into AlN at 500W microwave power using the Cl_2/H_2 mixture, and once again there is high fidelity pattern transfer.

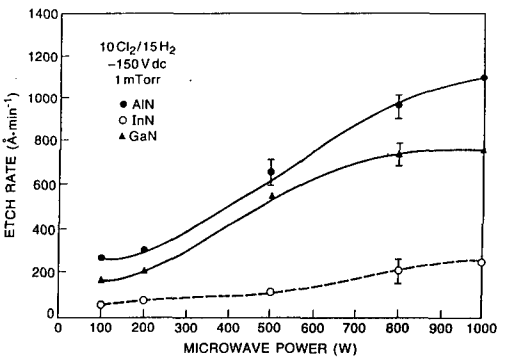

Fig. 4. Etch rates of GaN, AlN and InN in Cl_2/H_2 microwave discharges (1 mTorr, −150V dc) as a function of applied microwave power.

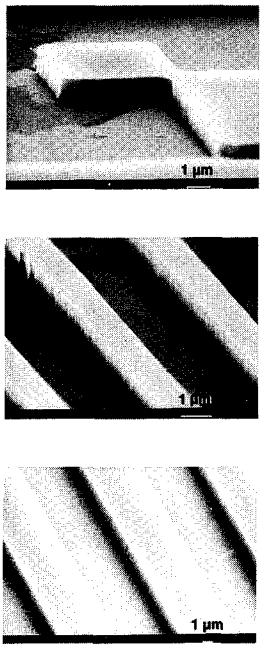

Fig. 5. SEM micrographs of features etched in GaN using either 500W (top) or 1000W (center) microwave power Cl_2/H_2 discharges (1 mTorr, −150V dc), and into AlN (bottom) under the same conditions at 500W microwave power.

The dry etching of InN was much more successful in CH_4/H_2 based discharges (we always add Ar to this chemistry to facilitate plasma ignition and aid in desorption of the group III etch products). Figure 6 shows the etch rates of the III-V nitrides in $CH_4/H_2/Ar$ discharges (1 mTorr, −250V dc) as a function of applied microwave power. Now the InN displays the fastest etch rate, as expected from past results on group III arsenides and antimonides. The only drawback of this chemistry for etching of III-V nitrides is the relatively high dc self-bias (−250V) required. We found a threshold bias of −175V needed to initiate etching of InN under our conditions. All three materials display a saturation in etch rate at the highest microwave power employed, indicating that the etching is not reactant-limited at 1000W. The etch rates for GaN, AlN and InN in $CH_4/H_2/Ar$ were linearly dependent on dc self-bias over the range −175 to −400V, suggesting that desorption of the etch products by ion assistance is playing a significant role.

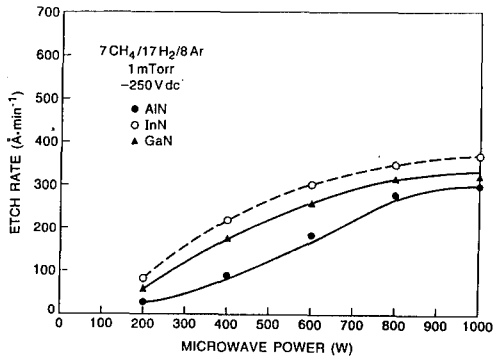

Fig. 6. Etch rates of GaN, AlN and InN in $CH_4/H_2/Ar$ discharges (1 mTorr, −250V dc) as a function of applied microwave power.

SEM micrographs of InN etched in $CH_4/H_2/Ar$ at 500W (top) or 1000W (center) microwave power showed there is still some texture to the surfaces, but they are much smoother than those obtained with Cl_2/H_2 etching. Features etched into GaN using $CH_4/H_2/Ar$ at 1000W, showed a smooth anisotropic pattern transfer into this material, albeit at slower rates than with Cl_2/H_2.

CONCLUSION AND SUMMARY

In summary we find that ECR discharges of Cl_2/H_2 provide practical etch rates and smooth pattern transfer in GaN and AlN, while CH_4/H_2 performs the same function for InN.

The ion milling rates of GaN, InN, AlN and InGaN were measured as a function of Ar^+ ion energy and beam angle of incidence. The single-crystal samples have milling rates approximately a factor of two slower than for GaAs and InP under the same conditions.

REFERENCES

1. T. L. Tansley and R. J. Egan, Physica B*185* 190 (1993).
2. H. Amano, M. Kito, K. Hiramatsu and I. Akasuki, Jap. J. Appl. Phys. *28* L2112 (1989).
3. J. S. Foresi and T. D. Moustakas, Appl. Phys. Lett. *62* 2859 (1993).
4. B. Goldenberg, J. D. Zook and R. J. Ulmer, Appl. Phys. Lett. *62* 381 (1993).
5. M. A. Kham, A. Bhattarai, J. N. Kuznia and D. T. Olson, Appl. Phys. Lett. *63* 1214 (1993).
6. S. Nakamura, Y. Harada and M. Seno, Appl. Phys. Lett. *58* 2021 (1991).
7. M. A. Khan, J. N. Kuznia, A. R. Bhattarai and D. T. Olson, Appl. Phys. Lett. *62* 1786 (1993).
8. C. R. Abernathy, S. J. Pearton, F. Ren and P. Wisk, J. Vac. Sci. Technol. B*11* 179 (1993).
9. C. I. H. Ashby, Properties of GaAs EMIS Data Review 15422 (IEE, London 1985).

CHARACTERIZATION OF CVD DIAMOND FILMS USED FOR RADIATION DETECTION.

F. FOULON[1], T. POCHET[1], E. GHEERAERT[2], A. DENEUVILLE[2]
[1]LETI (CEA - Technologies Avancées) / DEIN / SPE, Centre d'Etudes de Saclay, 91191 Gif-sur-Yvette, France.
[2]Laboratoire d'Etudes des Propriétés Electroniques des Solides, CNRS, B.P. 166, 38042 Grenoble Cedex 9, France.

ABSTRACT

Diamond films produced by microwave plasma enhanced chemical vapor deposition (CVD) technique and used to fabricate radiation detectors have been characterized. The polycrystalline diamond films have a measured resistivity of 10^{12} Ω.cm and a carrier lifetime of about 530 ps. The carrier mobility - lifetime product depends on the density of photogenerated carriers. The carrier mobility decreases from 160 to 13 $cm^2/V.s$ for a carrier density increase from 2×10^{11} cm^{-3} to 3.7×10^{13} cm^{-3}. The detector response to laser pulses (λ = 355, 532 and 1064 nm), X-ray flux (2.5 - 16 keV) and alpha particles (^{241}Am, 5.49 MeV) has been investigated. The response speed of the detector is in the 100 ps range. X-ray photon flux measurements and alpha particle counting capabilities of the CVD diamond detectors are demonstrated.

INTRODUCTION

The interest of diamond stems from its unique set of electrical, chemical and physical properties. Natural diamond is a semiconductor with a wide band gap (5.5 eV)[1], a high intrinsic resistivity (up to 10^{20} Ω.cm)[2,3], high electron and hole mobilities (~ 2000 and 1200 $cm^2/V.s$, respectively)[1] and the highest electrical breakdown field (10^7 V/cm)[4]. Thus, it is well suited for electronic applications and radiation detector fabrication. Its radiation hardness [5,6] and resistance to acides, allow its use in hostile environnement. Moreover, the diamond atomic number matches relatively well that of the biological tissues (Z ~ 6.7) making diamond an ideal material for the fabrication of dosimeters for personnel exposed to radiations. So far, diamond detectors have been fabricated either from natural or synthetic bulk diamond [7-9]. Progresses made in diamond thin film growth by chemical vapor deposition (CVD) techniques [10-12] allow their used for the fabrication of radiation detectors[13].

In this paper, we report the fabrication and the characterization of detectors made from diamond thin films deposited by microwave plasma enhanced CVD technique. The electrical response of the detectors to fast laser pulses (λ = 355, 532 and 1064 nm, τ_L = 30 ps at FWHM), X-ray photons (2.5 to 16 keV) produced by an X-ray tube and alpha particles (^{241}Am, 5,5 MeV) was investigated in order to characterize the carrier photogeneration and recombination processes. These measurements showed that CVD diamond detectors can be used for the characterization of the intensity and temporal shape of ultrafast (~ 100 ps) light, X-ray, gamma-ray and charged particle pulses, for X-ray flux and dose measurements and for alpha particle counting.

Mat. Res. Soc. Symp. Proc. Vol. 339. ©1994 Materials Research Society

EXPERIMENTAL

Polycrystalline diamond films have been synthesized by microwave plasma CVD at 2.45 GHz [14]. The films were deposited on low resistivity (1 Ω.cm) silicon (100) wafers at a rate of about 0.5 μm/h. Deposition was carried out at a temperature of 750°C on the wafer surface. The average size of the crystallites was of about one micron. On some samples, the silicon substrate has been etched giving free standing diamond films. Light transmission measurements (190-1100 nm) were made through these films. Gold pads, 1 mm in diameter, were deposited on the diamond surface to form the electrical contacts. These contacts were characterized by measuring the dark current on sandwich structures versus bias voltage. The electrical resistivities of the films were deduced from these measurements. Photocurrent measurement under steady state monochromatic light illumination (λ = 600 nm, P = 1.4 x 10^{-5} W/cm²) was also carried out.

The detectors were tested under pulsed Nd:Yag laser irradiation (λ = 355, 532 and 1064 nm, τ_L = 30 ps at FWHM). The generated photocurrent and its transient decay were measured as an output voltage by connecting the detector to an ultrafast oscilloscope with a 50 Ω input resistance and a 7 GHz bandwidth.

The detector response to X-rays produced by Bremsstrahlung effect was studied using an X-ray tube providing X-ray photons with an average energy that could be set from 2.5 to 16 keV. The X-ray flux linearly increased with the tube current which could be varied from 0.1 to 2 mA. This provided a maximum flux of 3.4 x 10^4 and 1.9 x 10^7 photons/cm².s at 2.5 and 16 keV, respectively, on the detector surface. The 10 μm thick diamond film absorbs 52 % and 0.11 % of the incident energy at 2.5 and 16 keV, respectively.

The response to alpha particles emitted by an ^{241}Am source (5.49 MeV) has also been investigated. In this experiment, the detector output was connected to a preamplifier whose output was fed into a shaping amplifier with a shaping time of 2 μs. The signal was recorded on a multichannel analyzer.

RESULTS AND DISCUSSION

Diamond film transmission spectra showed that for wavelengths in the range 500 to 1100 nm, about 35 % of the light is transmitted through a 10 μm thick film. At these wavelengths, strong light diffusion in the polycrystalline film is believed to result in low film transmission. Below 500 nm, the film transmission strongly decreases, toward a value of 10 % at 355 nm. The diamond surface reflecting about 20 % of the light, this shows that the film is absorbing even at wavelengths longer than 225 nm, corresponding to the energy band gap (5.5 eV).

Figure 1 shows the dark current and photocurrent of a CVD diamond detector versus bias voltage. The dark current versus applied voltage curve shows that the electrical contacts are ohmic for bias voltages up to 40 V. The resistivity of the CVD diamond is of about 10^{12} Ω.cm. The photocurrent at 50 V, 68 pA, is twenty times greater than the dark current, 2.8 pA. Photoconductive effects are observed even at wavelengths longer than that related to the band gap energy. Photogenerated carriers are believed to be excited from energy states located in the semiconductor gap and caused by impurities and defects present in the material [15].

The response of the detectors to laser pulses reflects the change in conductivity due to the generation of laser induced photoexcited carriers in the diamond film. The voltage signal on the 50 Ω input of the oscilloscope is proportional to the product detector bias voltage V by carrier density and carrier mobility. Figure 2 shows the voltage signal for a diamond detector polarized at 50 V under laser pulse irradiation (λ = 1064 nm) at an energy density of 12 mJ/cm². The pulse

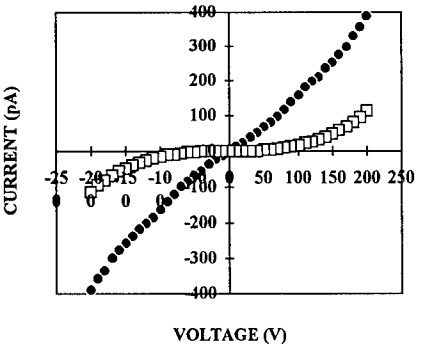

Fig.1 : Dark current (□) and photocurrent (•) versus detector bias voltage

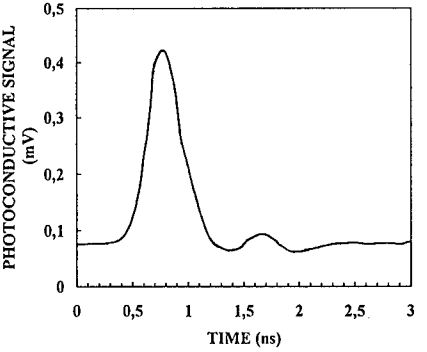

Fig.2 : Voltage signal of a detector polarized at 50 V under laser irradiation (λ = 1064 nm, τ_L = 30 ps).

risetime, duration at FWHM and decay time are of about 180, 280 and 530 ps, respectively. The decay time is larger than the RC constant of the electrical circuit at the oscilloscope input : ~190 ps. Thus, the CVD diamond carrier lifetime τ is assumed to be equal to the pulse decay time : τ = 530 ps. We did not observe any significant variation in the temporal characteristics of the photoconductive signal with the detector polarization (in the range 10 to 200 V), neither with the laser energy density (i.e the carrier density), nor with the laser wavelength. These results are comparable to those obtained with devices fabricated from type IIa natural diamonds [16]. It has been shown[17] that carrier lifetime is independent of the bias voltage for electric fields in excess of 1.5 kV/cm, which correspond to a bias voltage of 1.5 V for our 10 µm thick detectors. Note that the electrical properties of CVD diamond films depend on the deposition conditions. Pan and al. [18] have measured carrier lifetimes below 60 ps in 6 µm thick polycrystalline diamond films deposited by microwave-assisted CVD.

Figure 3 shows the evolution of the peak voltage of the photoconductive signal as a function of the laser energy density (λ = 1064 nm) for various bias voltages. The peak voltage increases linearly with the energy density before saturation is reached at energy densities above 3 mJ/cm². This effect will be discussed in the next paragraph. Identical evolution of the peak voltage versus energy density was observed at all laser wavelengths.

Figure 4 shows the X-ray (E = 8 keV) induced detector current as a function of the number of incident photons on the detector surface. The dark current has been substracted from the total current. The detector was polarized at 50 volts. The current increases non-linearly with the number of incident photons similarly to what was observed under laser irradiation. This effect is believed to result from the decrease of the carrier mobility - lifetime ($\mu\tau$) product with the density generated per second in the diamond film. This phenomenon has already been observed both for bulk natural and thin film CVD diamonds [22-24]. The evolution of $\mu\tau$ on the carrier photogenerated carrier density, N_C,can be deduced from the theoretical expression of the X-ray induced detector current, I_X, given by :

$$I_X = q.V.\mu.\tau.N_C.A / d \qquad (1)$$

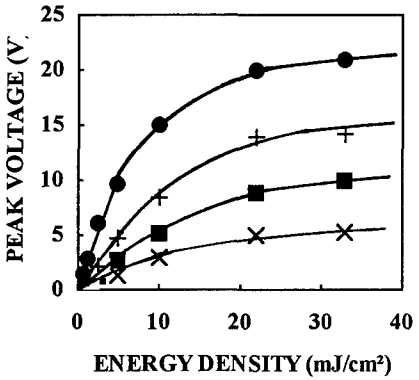

Fig.3 : Photoconductive peak voltage as a function of laser energy density (λ = 1064 nm) for : (x) 30 V, (□) 50 V, (+) 80 V and (•) 100 V bias voltages.

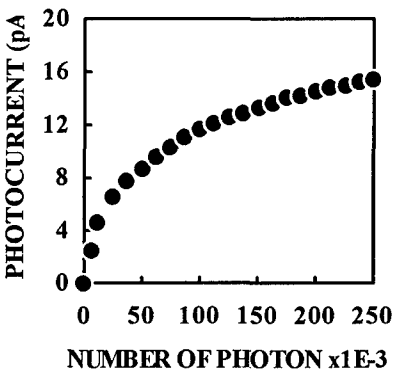

Fig. 4 : Detector photocurrent versus the number of incident X-ray photons (E = 8 keV) on the detector surface.

where q is the electron elementary charge, V the detector bias voltage , A and d the area and thickness of the detector. Equation (1) assumes that the electrical contacts are ohmic and that one type of carrier dominates the charge transport process in the film. N_c can be calculated from the number N_i of incident X-ray photons on the detector surface, taking into account the energy attenuation coefficient in carbon, μ_{en}, that depends on the photon energy[19]. N_c is given by :

$$N_c = N_i.[1 - \exp(-\mu_{en}(E).d)].E / \omega.A.d \qquad (2)$$

where E is the X-ray photon energy and ω the electron-hole pair generation energy (~ 13 eV)[20]. The evolution of μτ on the carrier density, deduced from equation (1) and (2) has been reported in figure 5. μτ decreases from 8 x 10^{-10} cm²/V at a carrier density of 2 x 10^{11} cm^{-3} to 7 x 10^{-9} cm²/V at 3.7 x 10^{13} cm^{-3}. Since no variation of the carrier lifetime, i.e. photoconductive decay time, on energy density was observed under laser irradiation, one could assume that the μτ decrease with carrier density only results from a decrease of the carrier mobility. Thus, μ decreases from 160 cm²/V.s at a carrier density of 2 x 10^{11} cm^{-3} to 13 cm²/V.s at 3.7 x 10^{13} cm^{-3}. In the 10 μm thick diamond film polarized at 50 volts, the average carrier path before capture is of about 42 μm for μ = 160 cm²/V.s and τ = 530 ps. Thus, the overall carrier mobility is likely to be limited by carrier trapping at the grain boundary rather than by carrier mobility in the crystallites themselves.

The influence of the detector bias, in the range 10 to 100 V, on the detector current was investigated. The detector current increases linearly with the bias voltage. This behavior is in good agreement with equation (1).

Preliminary results were obtained on alpha particle counting with the CVD diamond detectors. Qualitative information on the charge collection efficiency as a function of bias voltage is given in figure 6. It gives the alpha peak channel on a multichannel analyzer versus detector bias voltage. The peak channel continuously increases with the bias voltage. There is no saturation of the collected charges for voltages up to 260 V. This shows that even at 260 volts, only a fraction of the generated carriers are collected. Thus, the collection distance, μτV/d, at 260 volts is smaller than the detector thickness (d =10 μm). Taking τ = 530 ps and V = 260 volts, this gives a

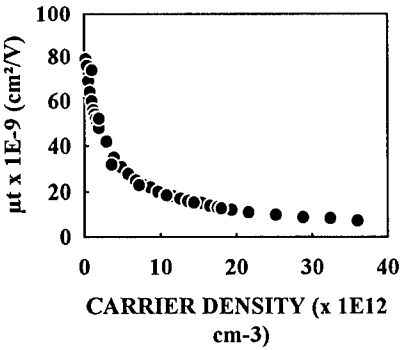

Fig. 5 : μτ versus carrier density at a bias voltage of 50 V.

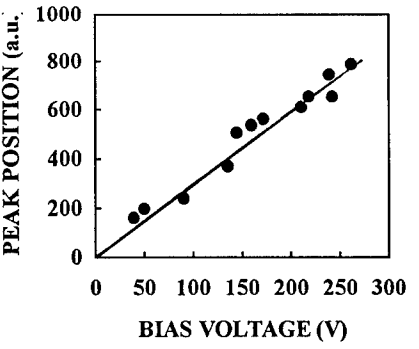

Fig.6 : Alpha peak position, i.e charge collection efficiency (a.u.) as a function of bias voltage.

mobility $\mu < 7$ cm²/V.s. Local high carrier density ($N_c > 4 \times 10^{13}$ cm^{-3}) along the track of the alpha particle in the diamond film could explain this low carrier mobility. Further experiments are in progress to characterize charge generation and collection in CVD diamond detectors.

CONCLUSION

CVD diamond films used for the fabrication of radiation detectors were characterized. The films have a resistivity of 10^{12} Ω.cm and a carrier lifetime of 530 ps. The carrier mobility - lifetime product was found to depend on the density of photogenerated carriers. The carrier mobility decreases from 160 to 13 cm²/V.s for a carrier density increase from 2×10^{11} cm^{-3} to 3.7×10^{13} cm^{-3}. We have also shown that CVD diamond photodetectors can be used for various purposes. They allow the characterization of ultrafast (~ 100 ps) laser, X- and Gamma-ray pulses. By a fine tuning of the diamond film deposition parameters, which set the film properties, one could control the carrier lifetime and thus of the time response of the detector is made available. CVD diamond detectors can also be used for X-ray flux measurements and alpha particle counting.

ACKNOWLEDGEMENTS

F. Lainé and J.C. Vuillemin are greatfully acknowledged for their technical support.

REFERENCES

1 S.M. Sze, Physic of semiconductor devices, New York : John Wiley, 1981.
2 W.B. Wilson, Phys. Rev., **127**, 1549 (1962).
3 P. Denham, E.C. Lightowlers and P.J. Dean, Phys. Rev.**161**, 762 (1967).
4 G.A. Baraff, Phys. Rev. **A26**, 133 (1964).
5 S.P. Kozlov, E.A. Konorova, A.L. Barinov and V.P. Jarkov, IEEE Trans. Nuc. Sci. NS-**22**, 171 (1975).

[6] S.P. Kozlov, A.V. Bachurin, S.S. Petrusev and Y.P.Fedorovsky, IEEE Trans. Nuc. Sci. **NS-24**, 240 (1977).
[7] D.R. Kania, L.S. Pan, P. Bell, O.L. Landen, H. Kornblum,P. Pianetta and M.D. Perry, J. Appl. Phys. **68**, 124 (1990).
[8] S. Han and al., MRS Symp. Proc. **302**, 305 (1993).
[9] J.H. Grobbelaar, R.C. Burns, T.L. Nam and R.J. Keddy, Nucl. Inst. and Meth. **B61**, 553 (1991).
[10] B.E. Williams and J.T. Glass, J. Mater. Res. **2**, 373 (1989).
[11] J.L. Kaae, P.K. Gantzel, J. Chin, W.P. West, J. Mater.Res. **5**, 1480 (1990).
[12] PK. Bachmann, D. Leers and D.U. Wiechert, Ber. Bunsenges. Phys. Chem. **95**, 1390 (1991).
[13] C.P. Beetz, B. Lincol, D.R. Winn, K. Segall, M. Vasas and D. Wall, IEEE Trans. Nuc. Sci. **38**, 107 (1991).
[14] A. Deneuville, P. Gonon, E. Gheeraert, A.T. Collins and Y.L. Khong, Diamond and Related Materials **2**, 737 (1993).
[15] D.G. Jeng, H.S. Tuan, R.F. Salat, G.J. Fricano, Appl. Phys. Lett. **58**, 1271 (1991).
[16] T. Pochet, B. Brullot, R. Galli and C. Rubbelynck, MRS Symp. Proc. , **302**, 281 (1993).
[17] L.S. Pan et al., MRS Symp. Proc. **302**, 245 (1993).
[18] L.S. Pan, D.R. Kania, P. Pianetta, M. Lanstrass, J.W. Ager, S. Han and O.L. Landen, J. Appl. Phys. **73**, 2888 (1993).
[19] J.H. Hubbell, Int. J. Appl. Radiat. Isot. **33**, 1269 (1982).
[20] C. Canali, E. Gatti, S.F. Kozlov, P.F. Manfredi, C. Manfredotti, F. Nava and A. Quirini, Nuc. Instr. and Meth. **160**, 73 (1979).

PHOTORESPONSE STUDY OF POLYCRYSTALLINE DIAMOND THIN FILM SCHOTTKY DIODES

G. Zhao*@, T. Stacy*, E. M. Charlson*, E. J. Charlson*, M. Hajsaid*, R. Roychoudhury*, A. H. Khan*, J. M. Meese*, Z. He** and M. Prelas**

* *Department of Electrical and Computer Engineering, University of Missouri, Columbia, Missouri 65211*
** *Department of Nuclear Engineering, University of Missouri, Columbia, Missouri 65211*

ABSTRACT

We are reporting the first quantitative photoresponse characteristics of boron doped hot-filament CVD (HFCVD) diamond based Schottky diodes using semi-transparent aluminum contacts in the spectral range of 300-1050 nm. Quantum efficiencies, obtained without correction for surface reflection in the visible and near UV region, were between 5% and 10% when the diodes were unbiased. Effect of reverse bias on the photoresponse was investigated at selected photon energies. Reverse biased diodes exhibit increasing photoresponse and ultimately saturation. Quantum efficiency as high as 30% was also obtained at 500 nm, when a reverse bias of over 1 volt was applied. The photoresponse mechanism of CVD diamond Schottky diodes is also discussed. A Schottky barrier height of 1.15 $\pm$ 0.02 eV for Al-HFCVD diamond contacts was determined using the d.c. photoelectric method.

INTRODUCTION

Photonic devices based on semiconducting CVD diamond thin films are of great interest due to diamond's unique properties. However, the majority of research on CVD diamond optical applications focuses on coatings for infrared windows.[1-3] Several properties of diamond, such as large band gap, high electron and hole mobilities, wide optical transmission band and high thermal conductivity, offer the feasibility of high-power, high-speed optoelectronic devices. Many applications require detection setups with high responsivity to UV light and small or negligible responsivity to visible light. Photodetectors made from wide bandgap materials are expected to exhibit this feature.[4] However, the work related to photodetection which has been reported so far, has concentrated on studies of bulk diamond photoconductivity and the a.c. photoemission of metal-diamond structures.[5-10] Therefore, it is important to study the photoresponse of HFCVD diamond Schottky diodes, and further optimize the design to make this new class of photodiodes feasible.

In this work, photoresponse studies are presented on p-type HFCVD diamond Schottky diodes with semi-transparent Al contacts, whose electrical characteristics are reported elsewhere.[11] These include two parts: (1) quantitative photoresponse characterization in the spectral range of 300-1050 nm, (2) determination of Schottky barrier heights of Al contacts to HFCVD diamond films using d.c. photoelectric measurements. The studies were done utilizing a photoresponse measurement setup which produces fine focused monochromatic incident light using a 200 W mercury arc lamp as a source. D.C. photocurrent was used as the output for these characterizations.

Quantum efficiencies, obtained without correction for surface reflection in the near UV and visible region (300 - 800 nm), were 5 % - 10 % when the diodes were unbiased. The effect of reverse bias on the photoresponse was also studied at selected photon energies.

@ Current address: R&D Center, ENDEVCO, 355 North Pastoria Avenue, Sunnyvale, CA 94086

Mat. Res. Soc. Symp. Proc. Vol. 339. ©1994 Materials Research Society

Reverse biased diodes exhibit increasing photoresponse and ultimate saturation for each incident photon energy due to the broadening of the depletion region. The effect of reverse bias on the photoresponse increases with higher incident photon energy, because of the rapid absorption of high energy photons in the depletion region. Quantum efficiencies as high as 30 % were obtained near the peak of the spectrum, i.e. 500 nm irradiation, when a reverse bias of over 1 volt was applied. Eleven Schottky diodes were fabricated and tested. The variation of the photoresponse obtained on these diodes was within 26 % for each irradiation. The photoresponse of these diodes in the spectral range investigated is attributed to photoelectric emission between metal and semiconducting diamond, and/or extrinsic photoexcitation of impurities in CVD diamond, as well as crystal defects. Further studies on the UV response and some improvement of the diode structure are needed to exploit the full features of this new kind of photodiode.

In addition, using the d.c. photoelectric method, the extrapolated Schottky barrier height of 1.15 $\pm$ 0.02 eV was determined for Al-HFCVD diamond thin film Schottky diodes, which agrees with the values obtained on these diodes by our C-V measurements.[12] These results are also consistent with those obtained on microwave plasma assisted CVD (MPACVD) diamond film using the a.c. photoelectric method.[5] Therefore, we confirm the occurrence of Fermi-level pinning at the CVD diamond-metal interface.

EXPERIMENTAL

Boron doped polycrystalline diamond thin films used for Schottky diodes were deposited on p-type (100) silicon substrates using a modified four-hot-filament CVD method with hydrogen and methane as the reaction gases and with acetone vapor as the carrier gas for the boron dopant (trimethyl borate). The acetone also is an additional carbon source. X-ray diffraction, scanning electron microscopy and Raman spectroscopy studies indicated that high quality boron doped polycrystalline diamond films were obtained. Details regarding the growth technique, process parameters and material characterization are reported earlier.[13] Prior to the metal deposition, two treatments, (i.e. dehydrogenation and surface chemical cleaning), were utilized to provide a stable diamond bulk film and a clean surface, according to the procedures described in Ref. 11. Schottky diodes were then fabricated by thermal evaporation of semi-transparent aluminum contacts on boron doped diamond thin films whose thickness was about 7-8 μm. The circular Schottky contact area was 4.5 mm^2. Figure 1 is a micrograph of the diamond film surface morphology taken near the edge of the top Al contact. A typical rectifying current-voltage characteristic of an Al-HFCVD diamond thin film based Schottky diode is shown in Figure 2.

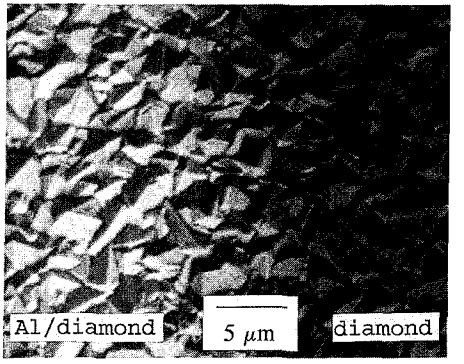

Fig.1 A typical micrograph of the diamond film surface morphology taken near the edge of the top Al contact.

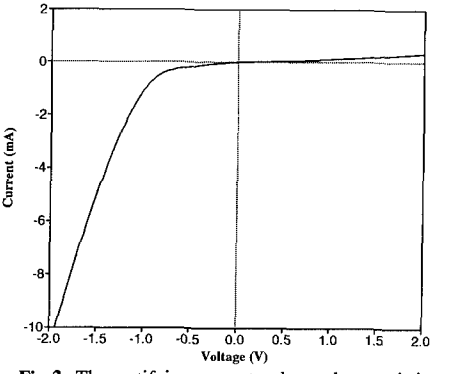

Fig.2 The rectifying current-voltage characteristic of CVD diamond thin film based Schottky diode.

The photoresponse measurements were performed with an experimental system that operated in air and covered the spectral range from 300 to 1200 nm. This system consists of a 200 Watt mercury arc lamp as the light source, an Oriel double monochromator, two quartz convex lenses for light convergence, a calibrated Hamamatsu silicon photodiode, a Keithley model 617 electrometer, and a sample holder with a three dimensional micro-manipulator. Before the measurement, the system was carefully aligned to obtain maximum output light intensity, as judged by the silicon detector. All photoresponse measurements were made at room temperature. For each measurement, the monochromatic light focus on the sample was achieved by moving the micro-manipulator successively in three dimensions until the photocurrent was maximized. The photocurrent was taken to be the difference between the device current with and without illumination. The silicon photodetector was used to calculate the incident monochromatic light intensity before and after each spectral measurement.

QUANTITATIVE PHOTORESPONSE CHARACTERIZATION

A metal-semiconductor diode can be used as a high-efficiency photodetector for visible and ultraviolet light detection.[14] Depending on incident photon energies and diode biasing conditions, Schottky diodes can be operated in various modes. Normally a photodiode can be characterized in either a photovoltaic (unbiased) mode or reverse biased mode (with the reverse bias voltage less than diode's breakdown voltage). One of the most important figures of merit for photodiodes is quantum efficiency, which is defined as the number of electron-hole pairs generated per incident photon:[14]

$$\eta = \frac{I_p / q}{P_{opt} / h\nu} \qquad (1)$$

where I_p is the photo-current generated by the absorption of incident optical power P_{opt} at a wavelength λ (corresponding to a photon energy $h\nu$). Since a calibrated silicon photodiode was used to measure the incident light power, P_{opt} was calculated from $(I_d \times A_p)/ (S_d \times A_d)$, where I_d is the detector's photocurrent, S_d is the calibrated radiation sensitivity, and A_p and A_d are the effective areas of our sample and detector, respectively.

Figure 3 shows the spectral photoresponse of Al-HFCVD diamond Schottky diodes in the spectral range of 300 - 1050 nm. Quantum efficiencies obtained without correction for surface reflection in the near UV and visible region (from 300 to 800 nm) were 5 % to 10 %, when the measurements were taken in the photovoltaic mode, i.e without any bias. At zero bias, the junction depletion region, which separates photon-generated electron-hole pairs and hence contributes to photocurrent, is very narrow unless an extremely lightly doped or intrinsic semiconductor is used. Any photon-generated carrier, which is created deeper than a diffusion length from the depletion region (i.e. field-free region), will not contribute to the photocurrent. However, the junction depletion region can be broadened to collect photons more efficiently, if the diode is reverse biased. Therefore, in order to study the origin of the photocurrent, another kind of spectral photoresponse was characterized when the diamond Schottky diodes were reverse biased. Figure 4 shows the effect of reverse bias on the photoresponse of Al-HFCVD diamond Schottky diodes at selected photon energies. Quantum efficiencies obtained were normalized with respect to the corresponding unbiased values. As expected, the reverse biased diodes exhibit increasing photoresponse and ultimately saturate around 1 volt for each value of incident photon energy. In addition, the effect of reverse bias on the increase in photoresponse is larger when higher energy photons are used. The reason for a larger effect on high energy photoresponse under reverse bias is the rapid absorption of high energy photons in the depletion region. Overall, quantum efficiency as high as 30 % for Al-HFCVD diamond Schottky diodes was obtained near the peak of the spectrum (i.e. 500 nm), when a reverse bias of over 1 volt was applied.

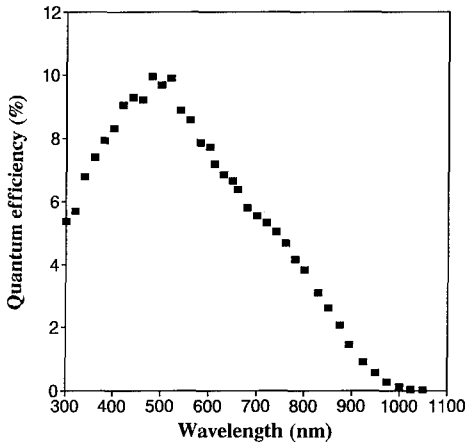

Fig.3 Quantum efficiency vs. wavelength measured on an unbiased polycrystalline diamond Schottky diode without the correction of reflection.

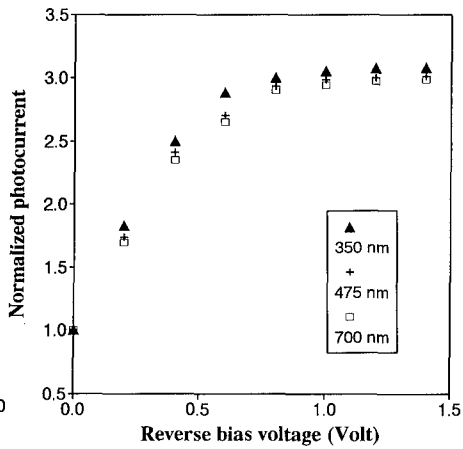

Fig.4 Effect of reverse bias on the photoresponse of Al-HFCVD diamond Schottky diodes at three selected photon energies.

The photoresponse of these HFCVD Schottky diodes to visible and near UV light is attributed to several mechanisms including photoelectric emission between metal and semiconductor, extrinsic photoexcitation of impurities, i.e. nitrogen and boron, in CVD diamond films, as well as crystal defects.[7]

Although a useful visible and near UV photoresponse of Al-HFCVD diamond Schottky diodes was obtained, further characterization of the UV photoresponse to study band-to-band excitation, and the improvement of diode structure are needed, in order to exploit fully the features of this new kind of photodiode.

SCHOTTKY BARRIER HEIGHT DETERMINATION

Basically, four methods can be used to measure the Schottky barrier height (SBH) of a rectifying metal-semiconductor contact[14]: the current-voltage, activation energy, capacitance-voltage and photoelectric methods. However, for polycrystalline CVD diamond Schottky diodes, none of the diamond research groups to date has been able to determine SBH with sufficient accuracy from the current-voltage and the activation energy methods, due to the high ideality factor and the fact that under forward bias the diodes are bulk resistance limited.[5] The first study on the determination of the SBH of polycrystalline CVD diamond based diode was reported in 1989 by Hicks et al, using the a.c photoelectric method, where a sophisticated synchronous detection system was utilized.[5] In this work, we were able to determine the SBH of HFCVD diamond Schottky diodes using the d.c. photoelectric method.

In order to perform the photoelectric measurements to determine Schottky barrier height, the incident photon energy, $h\nu$, must be less than the semiconductor band gap, Eg, so that band-to-band excitation in the semiconductor can be avoided. According to Fowler's theory, the photocurrent per absorbed photon (yield) as a function of photon energy, $h\nu$, is given by[15]

$$Yield = B\,T^2\left[\frac{x^2}{2}+\frac{\pi^2}{6}-\left(e^{-x}-\frac{e^{-2x}}{4}+\frac{e^{-3x}}{9}-\cdots\right)\right] \qquad for\ x \geq 0 \qquad (2)$$

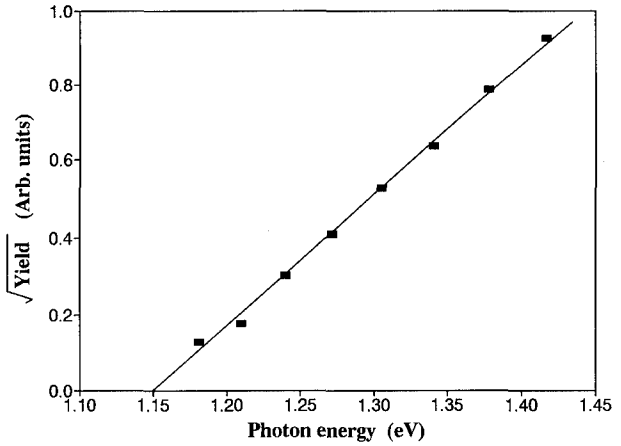

Fig.5 Square root of the photoresponse per incident photon vs. photon energy measured on Al-HFCVD diamond Schottky diode.

where B is a constant and $x = h(\nu-\nu_0)/KT$. The threshold energy, $h\nu_0$, is equal to the barrier height, $q\phi_b$. Under the condition of $x > 3$, equation (2) reduces to:

$$\sqrt{Yield} \sim h(\nu - \nu_0) \qquad for\ h(\nu - \nu_0) > 3KT. \tag{3}$$

When the square root of the photoresponse is plotted as a function of photon energy, a straight line should be obtained, and the extrapolated value on the energy axis should give the barrier height directly.

The photoelectric experimental results for an Al Schottky contact to a p-type polycrystalline HFCVD diamond thin film are shown in Figure 5. One can easily see that the yield vs. photon energy obeys the Fowler relation. Therefore, the extrapolated barrier height of 1.15 $\pm$ 0.02 eV was determined for Al-HFCVD diamond Schottky diodes. This result agrees very well with the data reported by Hicks, which is 1.13 $\pm$ 0.03 eV for both Al and Au rectifying contacts to p-type microwave assisted CVD diamond films. Moreover, the barrier height obtained using the d.c. photoelectric measurements is very close to the barrier height determined in the C-V measurements on these diodes,[12] where a Schottky barrier height of 1.04 eV was obtained. Our SBH measurements using either the photoelectric or capacitance-voltage method indicate that the barrier height of HFCVD diamond Schottky diodes is controlled by a high density of defect states, and hence is independent of the metal work function. This phenomenon is known to occur in silicon as well as in single crystal diamond.[15] Our results indicate that the Schottky barrier height is pinned approximately 0.2 Eg from the top of the valence band, which is consistent with results obtained on microwave plasma CVD diamond films.[5,8] Although the origin of such pinning has not been identified for CVD diamond, it is likely to be due to damage introduced during growth and/or to an oxygen-terminated CVD diamond surface introduced during the surface cleaning.[16]

CONCLUSIONS

The quantitative photoresponse characteristics of boron doped polycrystalline diamond thin film Schottky diodes were studied in the spectral range of 300-1050 nm. Semi-transparent aluminum contacts were used to obtain useful photoresponse in this range. Quantum

efficiencies obtained without correction for surface reflection in the visible and near UV region (300 - 800 nm) were between 5 % and 10 %, when the diodes were unbiased. Quantum efficiency as high as 30 % was also obtained at 500 nm, when a reverse bias of over 1 volt was applied. The photoresponse of these diamond Schottky diodes to visible and near UV light is attributed to photoelectric emission, extrinsic photoexcitation of impurities, i.e. nitrogen and boron, and crystal defects. The Schottky barrier height between aluminum and p-type polycrystalline diamond was also determined to be 1.15 eV using the d.c. photoelectric method. The result agrees with the barrier height determined using C-V measurements, and is also consistent with those obtained on microwave plasma assisted CVD diamond film using the a.c. photoelectric method. Therefore, Fermi-level pinning at the CVD diamond-metal interface is confirmed.

ACKNOWLEDGEMENTS

This study is supported by the Department of Energy under Contract DE FG02-91ER12107. The authors would like to thank Mr. Louis M. Ross and Mr. Naiyu Zhao for their assistance in the XRD and SEM studies.

REFERENCES

[1] C. Willingham, T. Hartnett, C. Robinson and C. Klein, in proc. of 1st Intl. Conf. on Applications of Diamond Films and Related Materials, edited by Y. Tzeng, M. Yoshikawa, M. Murakawa and A. Feldman (elsevier, Newyork, 1991) p.157

[2] W. D. Partlow, R. E. Witkowski and J. P. McHugh, in proc. of 1st Intl. Conf. on Applications of Diamond Films and Related Materials, edited by Y. Tzeng, M. Yoshikawa, M. Murakawa and A. Feldman (elsevier, Newyork, 1991) p.163

[3] P. Koidl, C. Wild, R. Locher and R. Kohl, in Proc. of 2nd Intl. Conf. on Diamond Films and Related Materials, edited by M. Yoshikawa, M. Murakawa, Y. Tzeng and W. A. Yarbrough, (MYU, Tokyo, 1993) p. 87

[4] M. Marchywka, J. K. Hochedez, M. W. Geis, D. G. Socker, D. Moses and R. T. Goldberg, Appl. Opt. **30** 5011(1911)

[5] M. C. Hicks, C. R. Wronski, S. A. Grot, G. Sh. Gildenblat, A. R. Badzian, T. Badzian and R. Messier, J. Appl. Phys. **65** 2139(1989)

[6] J. Mort and K. Okumura, Appl. Phys. Lett. **56** 1898(1990)

[7] D. G. Jeng and H. S. Tuan, Appl. Phys. Lett. **58** 1271(1991)

[8] S. A. Grot, S. Lee, G. Sh. Gildenblat, C. W. Hatfield, C. R. Wronski, A. R. Badizan, T. Badzian and R. Messier, J. Mater. Res. **5** 2497(1990)

[9] L. S. Pan, S. Han, D. R. Kania, S. Zhao, H. Kagan, K. K. Gan and R. Kass, in Proc. of 2nd Intl. Conf. on Diamond Films and Related Materials, edited by M. Yoshikawa, M. Murakawa, Y. Tzeng and W. A. Yarbrough, (MYU, Tokyo, 1993) p. 71

[10] R. Vaitkus, T. Inushima and S. Yamazaki, in Proc. of 2nd Intl. Conf. on Diamond Films and Related Materials, edited by M. Yoshikawa, M. Murakawa, Y. Tzeng and W. A. Yarbrough, (MYU, Tokyo, 1993) p. 95

[11] G. Zhao, E. M. Charlson, E. J. Charlson, T. Stacy, J. Meese, G. Popovici and M. Prelas, J. Appl. Phys., **73** 1832(1993)

[12] G. Zhao, et al (unpublished)

[13] G. Zhao, E. M. Charlson, B. Y. Liaw, E. J. Charlson, T. Stacy, J. M. Meese and M. Prelas, in Proc. of 2nd Intl. Conf. on Diamond Films and Related Materials, edited by M. Yoshikawa, M. Murakawa, Y. Tzeng and W. A. Yarbrough, (MYU, Tokyo, 1993) p.515

[14] S. M. Sze, Physics of Semiconductor Devices, 2nd ed. (John Wiley & Sons, New York,1981)

[15] G. Sh. Gildenblat, S. A. Grot and A. Badzian, Proc. of IEEE, **79** 647(1991)

[16] M. Aoki, G. Shishikura, I. Ohdomari and H. Kawarada, in Proc. of 2nd Intl. Conf. on Diamond Films and Related Materials, edited by M. Yoshikawa, M. Murakawa, Y. Tzeng and W. A. Yarbrough, (MYU, Tokyo, 1993) p. 341

AMORPHIZATION AND RECRYSTALLIZATION OF 6H-SiC BY ION BEAM IRRADIATION

V. HEERA[1], R. KÖGLER[1], W. SKORUPA[1] AND J. STOEMENOS[2]
[1] Research Center Rossendorf Inc., P.O.B. 510119, D-01314 Dresden, Germany
[2] Aristotle University of Thessaloniki, Physics Dep., 54006 Thessaloniki, Greece

ABSTRACT

The evolution of the damage in the near surface region of single crystalline 6H-SiC generated by 200 keV Ge^+ ion implantation at room temperature (RT) was investigated by Rutherford backscattering spectroscopy/chanelling (RBS/C). The threshold dose for amorphization was found to be about $3 \cdot 10^{14}$ cm^{-2}. Amorphous surface layers produced with Ge^+ ion doses above the threshold were partly annealed by 300 keV Si^+ ion beam induced epitaxial crystallization (IBIEC) at a relatively low temperature of 480°C. For comparison, temperatures of at least 1450°C are necessary to recrystallize amorphous SiC layers without assisting ion irradiation. The structure and quality of both the amorphous and recrystallized layers were characterized by cross-section transmission electron microscopy (XTEM). Density changes of SiC due to amorphization were measured by step height measurements.

INTRODUCTION

SiC is a promising semiconductor material for high temperature, high power and high speed electronic applications [1], which has attracted increasing attention since high quality single crystalline 6H-SiC wafers have been commercially available [2]. In addition, there exist many other polytypes of SiC [3] which differ in their physical properties and may be transformed into each other by thermal and ion beam processing [4,5,6]. This makes SiC to also be an attractive candidate for heterostructure applications.

However, some basic problems still have to be solved before this material can be widely used. One of these problems is associated with the annealing of radiation damage formed during ion implantation into SiC [7,8,9]. In particular, ion beam amorphized SiC is known to be very stable against thermal annealing, and temperatures higher than 1450°C are necessary for its recrystallization [7,9,10]. Such extremely high temperatures are not suitable for most technological processes. In order to overcome this problem, amorphization must be avoided or, alternatively, a recrystallization procedure must be found which operates at lower temperatures. Such a process could be the ion beam induced epitaxial crystallization (IBIEC) [11], which has been shown to occur in several semiconductor materials at temperatures well below the threshold temperature for thermally stimulated solid phase epitaxy (SPE) [12,13].

With this aim in view, we have carried out a series of experiments regarding ion beam induced amorphization and recrystallization of SiC. In a first attempt we succeeded in performing IBIEC of 6H-SiC at a temperature as low as 480°C [14]. In this paper further results on amorphization of 6H-SiC by 200 keV Ge^+ ion implantation and subsequent IBIEC with 300 keV Si^+ ion irradiation at about 480°C are presented. The influence of the amorphization dose on the structure and morphology of both the recrystallized and the remaining amorphous layer has been studied by XTEM. Particular attention has been directed to a possible polytype transformation during the IBIEC regrowth.

Mat. Res. Soc. Symp. Proc. Vol. 339. ©1994 Materials Research Society

EXPERIMENTAL

1" wafers of single crystalline 6H-SiC ((0001) orientation, n-type, Si surface) from Cree Research [2] were used as substrate material in our investigations. Damaged surface layers were produced by 200 keV Ge^+ ion implantation into 6H-SiC at RT. The ion doses ranged from $1 \cdot 10^{13}$ to $1 \cdot 10^{15}\,cm^{-2}$, and the ion fluxes were in the range of 1 to $5 \cdot 10^{11}\,cm^{-2}s^{1}$. The damage evolution was investigated by 1.2 MeV He^+ RBS/C. Two sets of samples with amorphous surfaces layers were prepared by $5 \cdot 10^{14}$ $Ge^+/\ cm^2$ and $1 \cdot 10^{15}$ $Ge^+/\ cm^2$ implantation , respectively. Ge^+ ions were chosen for the amorphization, because their mass is sufficiently high to produce completely amorphous layers at RT. In addition, the isovalent Ge^+ ions should not dope SiC.

The wafer was cut into pieces of about 1 cm^2 and half-capped by Si wafer pieces to preserve unirradiated reference regions for the RBS/C and XTEM analysis after the IBIEC irradiation. After a surface cleaning procedure the SiC specimens were mounted on a heating stage in the implantation chamber and pre-heated to a temperature of about 400°C. Then the specimens were subjected to 300 keV Si^+ irradiation in the dose range between $1 \cdot 10^{16}cm^{-2}$ and $3 \cdot 10^{17}\,cm^{-2}$. The ion flux was about $3 \cdot 10^{12}cm^{-2}\,s^{-1}$ and led to an additional temperature increase. During the ion irradiation the nominal temperature was monitored within 477 ± 5°C. The amorphous surface layers were analyzed by RBS/C before and after Si^+ irradiation. The structure and quality of both the amorphous and recrystallized layers were characterized by cross-section transmission electron microscopy (XTEM). Density changes of SiC due to amorphization were determined by step height measurements with a surface profilometer (DEKTAK 8000).

RESULTS AND DISCUSSION

RBS/C results on the evolution of irradiation damage in 6H-SiC generated by 200 keV Ge^+ implantation at RT are shown in Fig. 1. Compared to the spectrum of the virgin material only a slight increase in the dechanneling yield can be seen for the dose of $1 \cdot 10^{13}cm^{-2}$. With increasing ion dose a damage peak appears in the spectra which reaches the random level for a dose of about $3 \cdot 10^{14}cm^{-2}$. The RBS/C results reveal that a complete amorphous surface layer with a fairly sharp interface at a depth of 143 nm has been formed after implantation of $5 \cdot 10^{14}cm^{-2}$. For the highest amorphization dose used in our experiments ($1 \cdot 10^{15}cm^{-2}$) the amorphous layer thickness increases to 148 nm and the interface becomes a little sharper. The maximum Ge concentration in the amorhous SiC layer is estimated to be less than 0.1%.

According to Spitznagel et al. [8], the critical energy density for amorphization of 6H-SiC at RT is $2 \cdot 10^{21}$ keV/cm^3. In Fig. 2 the depth distributions of the damage energy calculated by TRIM [15] (version 92.14, considering complete damage cascades) are shown together with this amorphization threshold. It can be seen, that the buried amorphous layer ($3 \cdot 10^{14}cm^{-2}$) is closer to the surface and the thickness of the amorphous surface layers is smaller than that found in the RBS/C measurements when using the density of unirradiated crystalline SiC (3.21 g/cm^3) in the TRIM calculations. However, it has bee demonstrated by McHargue et al. [9] that the density of SiC decreases linearly with deposited damage energy during ion irradiation and saturates at 2.72 g/cm^3 for amorphous SiC. Indeed, a better agreement between our experimental results and the TRIM calculations has been obtained for this atomic density (see solid lines in Fig. 2).

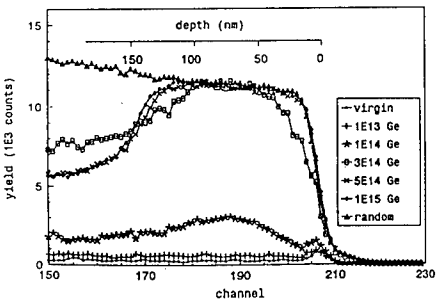

1. RBS/C spectra of the damage evolu- ...on during 200 keV Ge^+ implantation into SiC.

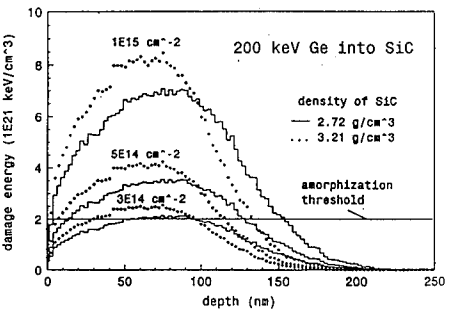

Fig.2 TRIM results of the damage energy of 200 keV Ge^+ implantation into SiC.

The density reduction during amorphization is confirmed by measuring the step height between an amorphous and a virgin region on 6H-SiC with a surface profilometer (DEKTAK 8000). A surface step of about 20 nm has been found. This corresponds exactly to the density change mentioned above if a linear swelling perpendicular to the surface is assumed.

In the next set of experiments the 6H-SiC samples with amorphous surface layers produced by $5 \cdot 10^{14}$ and $1 \cdot 10^{15}$ Ge^+/cm^2 were irradiated with fluences from $1 \cdot 10^{16}$ to $3 \cdot 10^{17}$ cm^{-2} of 300 keV Si^+ ions at a sample temperature of about 480°C. TRIM calculations show that the maxima of the ion and damage distribution in crystalline SiC (3.21 g/cm^3) are located at a depth of 340 nm and 270 nm, respectively. For the highest silicon dose the concentration of excess silicon atoms in SiC is less than 2% in the amorphous region and about 20% at the maximum. In this case the total deposited damage energy is more than 30 times the amorphization threshold energy for RT implantation.

XTEM micrographs of the structure before and after Si ion irradiation with $3 \cdot 10^{17}$ Si^+/cm^2 through the amorphous layer produced by $5 \cdot 10^{14}$ Ge^+/cm^2 implantation are shown in Fig. 3. The thickness of the initial amorphous layer is determined to be 146 nm. This is in very good agreement with our RBS/C results and TRIM predictions. The amorphous surface layer is followed by a heavily damaged zone of about 13 nm thickness. After the Si^+ ion irradiation at 480°C a shrinkage of the amorphous surface layer is observed. RBS/C results [14] reveal that the recrystallization is due to both a thermal recrystallization [10], which stops after about 20 nm, and additional IBIEC. The XTEM micrograph shows the following layer sequence: (i) An amorphous surface layer of about 80 nm thickness which contains many crystalline grains of 10 to 30 nm in size. These grains are randomly oriented and therefore they can only originate from a spontaneous nucleation. Any grain growth due to microcrystalline inclusions remaining after the amorphization implantation may be ruled out. (ii) A 40 nm thick defective crystalline zone, and (iii) a nearly perfect crystalline layer

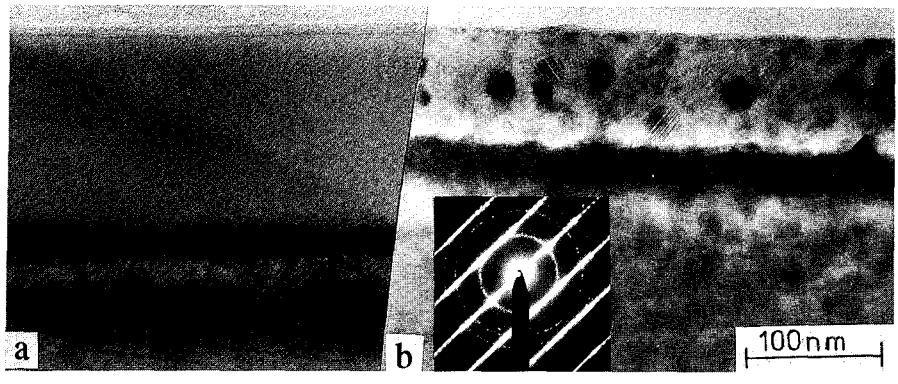

Fig. 3. XTEM micrographs of the structure before (a) and after (b) Si ion irradiation with $3 \cdot 10^{17}$ Si^+/cm^2 at 480°C through the amorphous layer produced by $5 \cdot 10^{14}$ Ge^+/cm^2 implantation. A selected area diffraction pattern taken from the first 200 nm is shown in the inset.

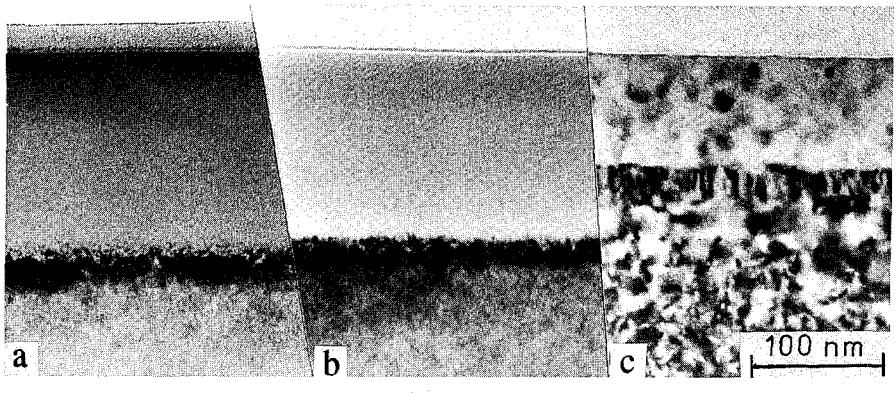

Fig. 4. XTEM micrographs of the structure before (a) and after anneling at 480°C without (b) and with (c) Si ion irradiation through the amorphous layer produced by $1 \cdot 10^{15}$ Ge^+/cm^2 implantation .

extending to the initial amorphous/crystalline interface. It should be noted, that this region is just the one which has also been recrystallized at 480°C without IBIEC irradiation. A selected area diffraction (SAD) pattern from this layer structure is shown in the inset of Fig.3. It consists of the diffraction pattern of single crystalline 6H-SiC overlapped by broken diffractions rings which stem from the randomly oriented crystalline grains in the amorphous surface layer. The interpretation of the diffraction rings is not quite unambigous. It seems, that the grains are mainly of 3C-polytype. This is in agreement with other results showing that after annealing of sputtered amorphous SiC polycrystalline material of 3C-SiC has been formed [16]. However, polycrystallization has been found only above temperatures of 1000°C for stoichometric SiC, whereas in our experiments the crystallization occurs at 480°C. A possible explanations for this observation could be that either the ion irradiation enhances the nucleation rate dramatically, or the Ge content influences the recrystallization behavior. In order to clarify this question, we investigated the effect of the Si irradiation on an amorphous surface layer produced with a dose twice as high than the previous amorphization dose.

In Fig. 4. XTEM micrographs of the structure before and after anneling without and with Si ion irradiation through the amorphous layer produced by $1 \cdot 10^{15}$ Ge^+/cm^2 implantation are presented. The thickness of the as- amorphized layer is about 166 nm. This is somewhat thicker than that found in our RBS/C measurements, but is in reasonable agreement with the TRIM calculations (Fig. 2). After thermal annealing of 5 hours at 480°C there is only a slight shrinkage of the amorphous layer. However, the width of the defective zone behind the amorphous layer has been decreased from 30 nm to 22 nm. No crystalline inclusions within the amorphous layer can be identified. The situation is quite different when there is an additional ion irradiation. In this case about 100 nm of the amorphous surface layer has been partly converted to polycrystalline material. The amorphous content of this layer amounts to only about 20%. This layer is followed by 36 nm defective and 35 nm nearly perfect single crystalline material. Insofar, the final layer structures formed by IBIEC are very similar for the two amorphous surface layers produced with $5 \cdot 10^{14}$ Ge^+/cm^2 and $1 \cdot 10^{15}$ Ge^+/cm^2 implantation, respectively. Thus, we can conclude that polycrystallization is substantially enhanced by the ion irradiation. However, it cannot be stated, whether this is due to solely the energy deposited in the layer or to the content of excess Si atoms in the SiC matrix enhancing this effect.

CONCLUSIONS

Completly amorphous surface layers thicker than 140 nm can be formed in 6H-SiC by 200 keV Ge^+ implantation at RT with doses equal to or higher than $5 \cdot 10^{14}$ cm^{-2}. The amorphization results are in good aggreement with the threshold energy for amorphization found by Spitznagel et al. [8] and TRIM calculations when cosidering a density reduction from 3.21 g/cm^3 for crystalline SiC to 2.72 g/cm^3 for amorphous SiC.

Crystallization of the amorphous surface layer can be stimulated by 300 keV Si^+ ion irradiation at a temperature as low as 480°C. The layer regrows epitaxially from the crystalline 6H-SiC substrate into the amorphous material by both, thermally induced recrystallization, which stops after a short distance less than 20 nm, and additional IBIEC effect. The mean IBIEC rate is about 1.5 nm/ 10^{16} cm^{-2} [14]. The IBIEC regrown layer is

of 6H-polytype as the underlying substrate, too. However, it includes defects of high density as dislocation loops and various precipitates. The remaining amorphous layer is partly transformed into polycrystalline material. The crystalline grains are likely the 3C polytype. The polycrystallization is enhanced with increasing Ge concentration and occurs only under ion irradiation.

As our results demonstrate, low temperature recrystallization of amorphous SiC is possible by means of ion irradiation. However, polycrystallization competes with epitaxial crystallization. Therefore, single crystalline material of high quality is difficult to obtain from the amorphous state.

ACKNOWLEDGEMENTS

We would like to thank E. Glaser of FSU Jena for RBS/C analysis and J.Petzoldt of TU Ilmenau for the helpful discussions concerning the polytype transformations. Part of this work was supported by the Bundesministerium für Forschung und Technologie (Contract 03-SK3ROS-5)

REFERENCES

1. J.A. Powell, P.G. Neudeck, L.G. Matus and J.B. Petit, Mat.Res.Soc.Symp.Proc. **242**, 495 (1992).
2. Cree Research, Inc., Durham, NC 27713, USA.
3. R.F. Davies and J.T. Glass, Advances in Solid State Chemistry **2**, 1 (1991).
4. W.S. Yoo and H. Matsunami, Jap.J.Appl.Phys. **30** (1991) 545
5. J. Pezoldt, A.A. Kalnin and W.D. Savelyev, Nucl.Instr.Meth. **B65**, 361 (1992).
6. J. Pezoldt, A.A. Kalnin, D.R. Moskwina and W.D. Savelyev, Nucl.Instr.Meth. **B80/81**, 943 (1993).
7. J.A. Edmond, S.P. Withrow, H.S. Kong and R.F. Davies, Mat.Res.Soc.Symp.Proc. **51**, 395 (1986).
8. J.A. Spitznagel, S. Wood, W.J. Choyke, N.J. Doyle, J. Bradshaw and S.G. Fishman, Nucl.Instr.Meth. **B16**, 237 (1986).
9. C.J. McHargue and J.M. Williams, Nucl.Instr.Meth. **B80/81**, 889 (1993).
10. H.G. Bohn, J.M. Williams, C.J. Mc Hargue and G.M. Begun, J.Mater.Res. **2**, 107 (1987).
11. F. Priolo and E. Rimini, Mater.Sci.Rep. **5**, 319 (1990).
12. J.S. Williams, M.C. Ridgway, R.G. Elliman, J.A. Davies, S.T. Johnson and G.R. Palmer, Nucl.Instr.Meth. **B55**, 602 (1991).
13. N. Kobayashi, H. Kobayashi and Y. Kumashiro, Nucl.Instr.Meth. **B40/41**, 550 (1989).
14. V. Heera, R. Kögler, W. Skorupa and E. Glaser, Mat.Res.Soc.Symp.Proc. **316,** (1994) 229 and **321**, (1994) 387
15. J.F. Ziegler, J.P. Biersack and U. Littmark, The Stopping and Range of Ions in Solids, vol. 1 (Pergamon, New York, 1985).
16. K. Yoshi, Y. Suzaki, A. Takeuchi, K. Yasutake and H. Kawabe, Thin Solid Films **199**, 85 (1991).

OXIDATION AND ION DAMAGE OF DIAMOND BY REACTIVE ION ETCHING

T. E. BEERLING AND C. R. HELMS
Stanford University, Department of Electrical Engineering, Stanford, Ca. 94035.

ABSTRACT

Oxygen is a commonly used etchant of carbon materials, including diamond. In this work, we examine the effects of oxygen ion bombardment to diamond surfaces, as might be encountered in a reactive ion etching (RIE) process. Surfaces were characterized using Electron Energy Loss Spectroscopy (EELS) and Auger Electron Spectroscopy (AES). EELS was used to determine the presence of non-diamond carbon at the surface which may form due to ion damage. AES was used to determine the presence of oxygen on the diamond surface from oxygen ion bombardment. The effect of ambient molecular oxygen present during inert ion bombardment is also addressed. EELS was also used to determine the state of diamond surfaces that were bombarded with hydrogen ions, as might be used in the removal of adsorbed oxygen.

INTRODUCTION

Reactive ion etching (RIE) is currently used in industry to etch semiconductors, dielectrics, and metals during electronic device fabrication. It is expected that diamond electronic device fabrication will borrow heavily from the mature processing technologies, such as RIE. Oxygen is logical choice as the etchant gas for diamond and other carbon films. The etch products of oxygen ion etching are volatile (CO_2 or CO). Oxygen etching does not carry the same sort of safety issues often found halogen based chemistries.

Ion energies for RIE are typically in the 10^2 eV range. For these ion energies, chemical bonds can be broken and atoms displaced, creating a damage region. However, the damage layer is limited to a very narrow region, on the order of tens of angstroms, and damage regions are soon sputtered or etched away. Damage cannot significantly accumulate, as in the case of ion implantation, where the ion ranges are much larger. Other etching techniques, such as reactive ion beam etching (RIBE), employ ions of approximately the same energy range (10^2-10^3 eV) as RIE. Physical sputtering also employs ions in a similar energy range. Surface damage is of special importance in the RIE of diamond, due to diamond's metastable nature. If sufficient energy is supplied to diamond, a sp^3 to sp^2 transformation can occur. In addition, long range order may also be lost, creating an amorphous layer. Annealing will not recover the diamond structure, except for the most minimal damage.

Most solid state electrical devices rely on good surfaces. The state of the surface controls the behavior of metal contacts and surface conduction devices. Therefore, it is imperative that processing leave a surface free of non-diamond carbon. We have undertaken a study where diamond surfaces have been exposed to energetic ions in an ultra high vacuum environment, so that *in situ* characterization could be performed. The quality of the surface, that is, whether diamond, graphite, or amorphous carbon is present, was determined using Electron Energy Loss Spectroscopy (EELS). EELS is well suited for these studies, as the electron scattering lengths used in these studies (10-20 Å) are of the same order as the ion ranges for the ion energies employed. The presence of residual etchant atoms (oxygen) was determined using Auger Electron Spectroscopy.

EXPERIMENTAL

We performed the experiments in an ultra high vacuum chamber with base pressures in the 10^{-10} torr range, achieved using an ion pump. Ion bombardment was achieved using a

Mat. Res. Soc. Symp. Proc. Vol. 339. ©1994 Materials Research Society

differentially pumped ion gun. The ion angle of incidence was 54° from normal. The chamber pressures during ion bombardment were typically in the 10^{-6} torr range, achieved using a 170 l/sec turbomolecular pump. The effect of background neutrals during ion bombardment could be determined as the operating pressures were low enough that gas phase collisions were negligible.

(100) 2b diamond samples (from Doubledee Harris), 2 mm x 2 mm x 0.25 mm in size, were used in these studies. 2b samples were used as they have a lower resistivity than 2a diamond. The lower resistivity eliminated charging problems during electron irradiation. Boron doped CVD diamond, courtesy of the Crystallume Corp., was also used in these studies. CVD diamond samples were boron doped (~10^{17} cm^{-3}) to avoid charging problems during electron spectroscopy. Raman spectra of the CVD diamond displayed the characteristic peak at 1332 cm^{-1}, with a much smaller feature attributable non-diamond carbon.

The spectroscopies were performed using a single pass cylindrical mirror analyzer of 0.3% resolution, with a concentric electron gun. Incident electron energies were 3 keV for AES, and either 200 or 500 eV for EELS, where EELS data was collected in reflection mode. Derivative spectrum were obtained for EELS and AES using a lock-in amplifier. In performing electron spectroscopies, low current densities were used (~10 $\mu A/cm^{-2}$), as it was found that electron stimulated desorption of oxygen became problematic at higher beam densities. In order to better resolve peaks in the EELS spectrum, second derivative EELS spectrum were obtained by numerically differentiating the first derivative spectrum during data analysis. For qualitative observation of EELS data, the second derivative spectrum is advantageous to the first derivative spectrum as the position of the second derivative spectrum peaks in energy are nearly the same as that of the true peaks of N(E). This is not the case for first derivative spectrum, where the position of the N(E) peaks are denoted by a zero point in dN(E)/dE.

RESULTS

I. Energetic ion damage

Shown in Figure 1 are a EELS spectrum for 2b diamond, highly ordered pyrolitic graphite (HOPG), and an amorphous carbon surface created by 1 keV ion bombardment of diamond. The diamond surface was treated by etching the surface to 200 eV oxygen ions. The dominant features for diamond are the bulk and surface plasmons, located at 34.5 and 22.5 eV, respectively. There is a strong loss feature at 9 eV. We believe this feature is attributable to adsorbed oxygen on the diamond surface [1], as has been suggested by other researchers [2]. Using a lower EELS primary beam energy, and higher resolution, we observe a π loss feature at ~4 eV, attributable to the small degree of damage possible with 200 eV oxygen ion bombardment. HOPG has a strong π like plasmon at 6.5 eV, and weaker peaks at 13, 19.5 eV, and 26 eV. None of the loss features of diamond are observed, and so graphite and diamond are easily distinguishable. During diamond ion bombardment, if the ion energy is sufficiently high, an amorphous region of sp^3 and sp^2 carbon is created. This can be observed for 1 keV oxygen ion bombardment. The dominant loss feature is the $\sigma+\pi$ amorphous plasmon at ~25 eV [3], and a π-like plasmon located at 4.5 eV (some interference from the elastic peak is occurring). There may also weak contributions from purely graphitic features at 13, 19.5, and 26 eV. We can therefore distinguish between diamond, graphite, and amorphous carbon.

As the surface is being etched/sputtered, the damage cannot accumulate, and so the surface retains many sp^3 bonds, although long range order is lost. The fact that sp^3 carbon is still present at the surface is important when attempting to the remove damage regions. Ion damage in silicon is often removed with acid etching. Oxidizing acids are often used to remove non-diamond carbon from diamond surfaces as the selectivity is extremely good. We have damaged CVD diamond with 2 keV argon ions, and then exposed to acids, or performed a low temperature anneal in N_2 (285 °C) to argon ion damaged diamond before the acid treatment. The acid solution was 3:4:1 H_2SO_4:HNO_3:$HClO_4$ at 100 °C, and samples were immersed for 20 minutes. Figure 2 shows the EELS spectrum of CVD diamond that was damaged, annealed, and then exposed to acids. The

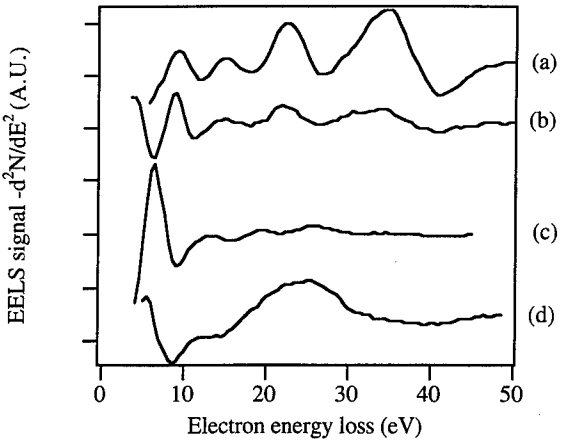

Figure 1: EELS of different states of carbon. (a): EELS of 2b diamond exposed to 200 eV oxygen ions, EELS primary beam energy = 500 eV. (b): 2b diamond exposed to 200 eV oxygen ions, EELS primary beam energy = 200 eV. (c): Highly ordered pyrolitic graphite (HOPG), EELS primary beam energy = 500 eV. (d): 2b diamond exposed to 1 keV oxygen ions, EELS primary beam energy = 500 eV.

change in the loss spectrum after acid treatment is subtle at best; there is no recovery of the diamond bulk plasmon. The diamond sample that was not annealed before acid treatment did not show any signs of recovering diamond loss features after acid etching either. The amount of sp^3 carbon in the film must be high enough as to protect sp^2 carbon that is contained within the damage layer. Low temperature annealing was unable to prevent sufficient graphitization to make the ion damaged region susceptible to acid attack. The only sp^2 carbon that could be removed would have to be at or very near the surface; we have seen an increase in the damage layer sheet resistance (<10 increase) after acid etching. For studies on ion implantation to create ohmic contacts, ion damaged regions for boron implanted diamond (35 keV) were annealed at 1200 °C before they were removed with oxidizing acids [4]. Annealing temperatures this high will often be incompatible with previous processing steps.

II. Oxidation during oxygen ion bombardment

Residual etchant atoms are often found on the surface after etching, as is the case for oxygen ion etching of diamond. For oxygen ion bombardment of diamond surfaces, we have typically found approximately 0.5 monolayers of oxygen present during and after bombardment, as determined by AES.

Efremow *et al* found that they could etch diamond by 2 keV xenon ion bombardment in either an O_2 or NO_2 ambient [5]. Etching of silicon by argon ion bombardment in a reactive ambient (Cl_2) has also been shown to occur [6]. Cl_2 can spontaneously adsorbs to the silicon surface to create surface species with reduced binding energies, which are removed by the ion bombardment. For diamond etching by oxygen, the behavior is different. Molecular oxygen will not strongly adsorb to the diamond surface [7, 8]. We exposed 1 keV argon ion damaged diamond to molecular oxygen to determine if strong adsorption occurs without inert ion stimulation. After exposures of >1000 Langmuirs of O_2, the largest oxygen concentration ever observed seen was 0.1 monolayers (see Figure 3). This same oxygen surface concentration was observed after argon bombardment and before the O_2 exposure (some background oxygen could have entered into the ion gun during argon bombardment). The fact that there was no increase in the oxygen

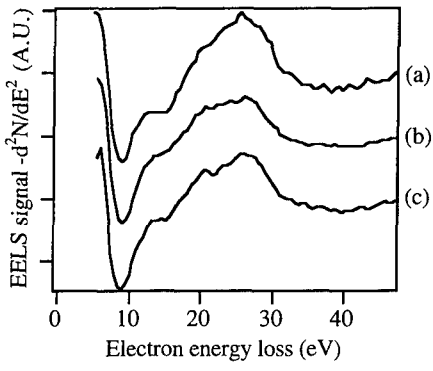

Figure 2: EELS spectrum for argon ion damaged CVD diamond before and after annealing and $HClO_4$:HNO_3:H_2SO_4 treatment. (a): 2 keV argon ion bombarded CVD diamond, (b): after 285 °C anneal in N_2, (c): after acid treatment. EELS primary beam energy = 500 eV.

concentration with O_2 exposure suggests that strong molecular oxygen adsorption does not occur on ion damaged diamond surfaces.

The oxygen concentration becomes appreciable during inert ion bombardment in an oxygen ambient (see Figure 3). For the same background O_2 pressure, the steady state oxygen concentration is comparable, but slightly lower (~20%) than 200 eV oxygen ion bombardment. Diamond samples were initially damaged with 1 keV argon to determine how much improvement is made in the surface and subsurface region. The damaged layer was chemically etched by argon ion bombardment in molecular oxygen, as good diamond loss features are recovered at the surface. The diamond layer underneath was also etched. If it were not, the EELS spectrum would be identical to that of 200 eV argon bombardment without a molecular oxygen ambient, which shown evidence of non-diamond carbon, as shown in Figure 3. The small amount of oxygen that makes its way into the ion gun to contribute to ion current cannot account for the etching seen, and gas phase collisions were negligible. We suggest that oxygen physisorbs on the diamond surface and thus possesses a brief residence time on the diamond surface before escaping to the gas phase. Therefore, there is some probability of an interaction of a physisorbed oxygen molecule and an incoming ion. If an incoming ion can dissociate a physisorbed oxygen molecule, reactive atomic oxygen is available at the diamond surface. The residence time of molecular oxygen is so brief that weakly bound oxygen does is not significant in the total oxygen coverage.

III. Oxygen removal from diamond surfaces

It may be desired to remove residual oxygen from diamond surfaces with hydrogen ion exposure. EELS spectrum for 200 eV H_2^+ ion bombardment of oxygenated diamond (by 200 eV oxygen ion bombardment) is shown in Figure 4. Good diamond surfaces have been degraded; a π like plasmon has developed at ~5 eV. The EELS spectrum for 200 eV H_2^+ ion bombarded ions is similar to 200 eV argon bombarded diamond (shown in figure 3), which has no chemical effect. Therefore, in the etching of diamond, H_2^+ ion beam does not appear to have as strong of a chemical component as oxygen ion bombardment (in a molecular oxygen background).

For oxygen etching, the primary etch products are CO or CO_2. It has been shown that the dominant hydrocarbon etch product during hydrogen ion etching of diamond compacts is CH_4 [9]. Therefore, more hydrogen is required to remove a carbon atom than is needed for oxygen etching. This translates into slower etch rates and therefore larger steady state damage layers. In addition, the penetration of hydrogen ions will be higher than that of oxygen ions. The increased

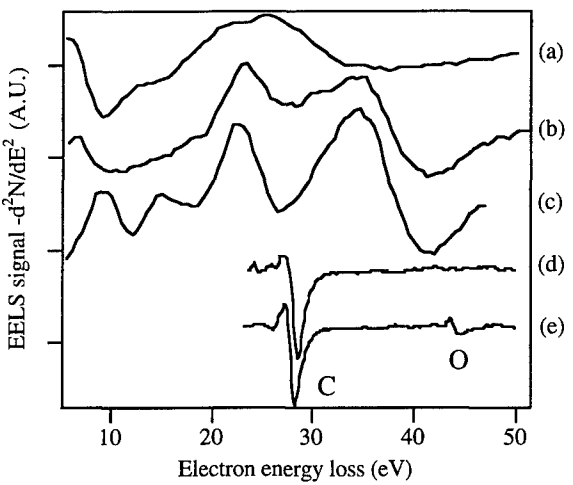

Figure 3: EELS and AES spectrum for ion treated 2b diamond. (a): 2b diamond exposed to 1 keV argon ions, (b): 2b diamond exposed to 200 eV argon ions, (c): 2b diamond exposed to 200 eV argon ions, in a $2x10^{-6}$ torr molecular oxygen ambient. (d): Argon ion damaged surface exposed to 1500 langmuir of molecular oxygen, (e): Typical AES scan for oxygen ion bombarded surface or argon bombarded surface in a molecular oxygen ambient.

.ion range of hydrogen will lead to a larger amorphous layer [10]. The hydrogen ions may penetrate too deeply into the diamond to be effective in forming C-H products at the surface

It is unknown how reactive molecular hydrogen ions are with diamond surfaces. If they are not reactive, and molecular ions do not dissociate upon impact, molecular hydrogen ions will be inert with diamond surfaces. We have found that the concentration of atomic ions in the oxygen ion beam (~30% O^+) is higher than for the hydrogen ion beam (<10% H^+). It might be argued that better diamond surfaces were achieved during oxygen ion bombardment due to the higher concentration of atomic ions, which may be more reactive. However, we obtained good diamond surfaces by inert ion bombardment in an O_2 ambient, where the ions have no chemical effect. Background gases can be important in etching and it appears that molecular hydrogen had little effect in etching, unlike molecular oxygen.

CONCLUSIONS

For most electronic applications, an amorphous region containing non-diamond carbon will not be acceptable. For example, ion damage has been shown to change the behavior of metal/diamond contacts [11]. If non-diamond carbon cannot be tolerated, it is important to be aware of the potential for ion damage. If an RIE etch is performed with an high self bias, it may be necessary to reduce the self bias near the end of the etch, as low temperature annealing and acid etching may be ineffective in removing damage. Lowering the self bias will act to reduce the non-diamond region present at the surface. Etching will be less anisotropic with the reduction of the self bias. However, only a very thin layer of material needs to be removed so anistropically etched features will not be appreciably changed. Similar rules will apply to other processing steps involving energetic ions, such as RIBE and sputtering.

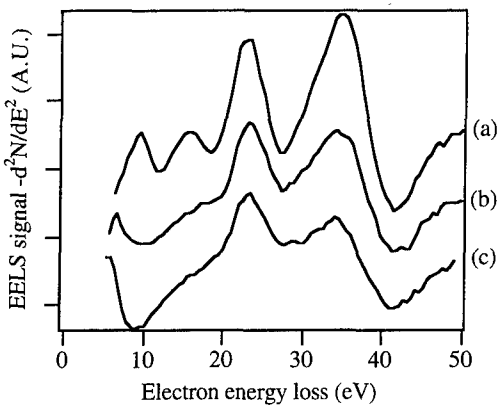

Figure 4: EELS spectrum for H_2^+ ion bombardment to 2b diamond. (a): oxygenated diamond before molecular hydrogen ion bombardment, (b): $1x10^{16}$ cm^{-2}, 200 eV dose, (c): $2.5x10^{16}$ cm^{-2}, 200 eV dose. EELS primary beam energy = 500 eV.

We have observed residual oxygen on the diamond surface after oxygen ion bombardment, with surface concentrations of approximately 0.5 monolayers. Background molecular oxygen is playing a strong role in the etching of diamond, as good diamond surfaces were recovered by inert ion bombardment in a molecular oxygen ambient. In addition, the oxygen surface concentration during inert ion bombardment in a molecular oxygen ambient is comparable to that seen for oxygen ion bombardment. Hydrogen ion bombardment does not leave as ideal a surface as oxygen ion bombardment of the same energy. This is believed to be due to the increased number of atoms necessary to create volatile etch products, and due to the inactivity of background molecular hydrogen during ion bombardment.

REFERENCES

[1] T. E. Beerling, C. R. Helms, to be submitted to Applied Phys. Lett.
[2] Y. Mori, Y. Show, M. Deguchi, H. Yagi, H. Yagyu, N. Nobuhiro, T. Okada, A. Hatta, K. Nishimura, M. Kitabatake, T. Ito, T. Hirao. T. Izumi, T. Sasaki, A. Hiraki, Jap. J. Appl. Phys., Letters, **32**, pt.2, no. 7b, L989, (1993).
[3] Y. Wang, H. Chen, R. W. Hoffman, J. C. Angus, J. Mater. Res., **5**, no. 11, 2387, (1990).
[4] J. F. Prins, J. of Phys D., **22**, no. 10, 1562, (1989).
[5] N. N. Efremow, M. W. Geis, D.C. Flanders, G. A. Lincoln, N. P. Economou, J. Vac. Sci. Technol. B, **3**, no. 1, 416, (1985).
[6] T. M. Mayer, R. A. Baker, J. Vac. Sci. Technol, **21**, no. 3, 757, (1982).
[7] R. E. Thomas, R. A. Rudder, R. J. Markunas, J. Vac. Sci. Technol. A, **10**, 2451, (1992).
[8] A. Freedman, C. D. Stinespring, Appl. Phys. Lett., **57**, 1194, (1990).
[9] R. Yamada, J. Vac. Sci. Technol. A, **5**, no 4, 2222, (1987).
[10] A. Hoffman, P. J. K. Paterson, S. Prawer, Nucl. Instr. and Meth., **B52**, 63, (1990).
[11] T. Tachibana, B.E. Williams, J.T. Glass, Phys. Rev. B, **45**, no. 20, 11968, (1992).

COMPARISON OF THERMAL GATE OXIDES ON SILICON AND CARBON FACE P-TYPE 6H SILICON CARBIDE

CARL-MIKAEL ZETTERLING AND MIKAEL ÖSTLING*
Royal Institute of Technology, Solid State Electronics, Kista-Stockholm, Sweden
*Present adress: Stanford University, CIS, Stanford, CA 94305, USA

ABSTRACT

Monocrystalline 6H silicon carbide samples (n-type and p-type) with both carbon face and silicon face have been used to investigate gate oxide quality. The oxides were thermally grown in a dry oxygen ambient at 1523 K with or without the addition of TCA (Trichloroethane), or in wet pyrogenic steam at 1473 K. $POCl_3$ doped polysilicon gates were used for electrical characterisation by capacitance-voltage measurements and breakdown field measurements. Large flatband voltage shifts indicate fixed oxide charges up to 10^{13} cm^{-2}. The incorporation of aluminum in the oxides was monitored using SIMS (Secondary Ion Mass Spectrometry). Surprisingly high signals were interpreted as evidence of an aluminum-oxygen compound having been formed (ie Al_2O_3).

INTRODUCTION

Silicon carbide has been suggested as the material for high power and high temperature electronic devices, such as power MOSFETs [1]. The progress that has been achieved in materials and process technology has inspired further device research related to silicon carbide [2, 3]. The 6H polytype is commercially available today in wafers, with either the silicon or the carbon face polished, and with either p- or n-type doping. Several kinetic studies have been made on the oxidation of n-type (nitrogen doped) silicon carbide, and the oxide quality is satisfactory[4, 5]. Further investigations are needed on p-type substrates (aluminum doped), since difficulties have been reported in obtaining high quality oxides [6]. It is suspected that the large amounts of aluminum detected in the oxides after thermal oxidation [7] will influence both the threshold voltage and the gate oxide breakdown of MOSFETs. A previous study of dopant redistribution during oxidation has been made on 3C silicon carbide [8]. In this study we compare electrical characteristics of oxides and their corresponding aluminum concentration versus depth profiles.

EXPERIMENTAL

The starting material was monocrystalline 6H silicon carbide samples with the silicon face or the carbon face polished (from Cree Research Inc.). Wafers were supplied with at least 3 μm thick epilayers to reduce the concentration of defects and accurately control the doping. The initial concentration of aluminum was $1.3 \cdot 10^{15}$ cm^{-3} in the Si face wafer and $5.5 \cdot 10^{15}$ cm^{-3} in the C face wafer (uniform net doping levels, measured by capacitance-voltage measurements using a Hg probe). The nitrogen concentration was $8.7 \cdot 10^{15}$ cm^{-3} in the Si face wafer, and $5.8 \cdot 10^{15}$ cm^{-3} in the C face wafer.

Three different methods were used for the oxidation:

1. Dry oxidation at 1523 K
2. Dry oxidation at 1523 K with the addition of TCA (Trichloroethane) to yield 2-3% chlorine
3. Wet oxidation in pyrogenic steam at 1473 K

Mat. Res. Soc. Symp. Proc. Vol. 339. ©1994 Materials Research Society

TABLE I. Oxidation results

CREE specifications:				
Wafer type:	n-type	p-type	n-type	p-type
Polished face:	silicon	silicon	carbon	carbon
Net doping (cm^{-3}):	$8.7 \cdot 10^{15}$	$1.3 \cdot 10^{15}$	$5.8 \cdot 10^{15}$	$5.5 \cdot 10^{15}$
Oxidation time (min):	50	50	10	10
Oxide thickness (nm):				
Dry (1523 K)	44	40	51	48
Dry + TCA (1523 K)	43	42	49	50
Wet (1473 K)	40	48	130	131

Wafers with the Si face were oxidized for 50 minutes and the C face for 10 minutes, in order to obtain comparable oxide thicknesses. After oxidation a 60 minutes nitrogen anneal was performed at the same temperature as the oxidation, in the same furnace. Both n-type and p-type samples were oxidized simultaneously, and silicon (100) samples were used as control wafers to monitor the oxidation process. Oxide thickness was measured using ellipsometry, with a wavelength of 632.8 nm and an incident angle of 70° (the index of refraction for SiC was assumed to be 2.636). All oxides were between 40 and 50 nm thick, except the wet oxidized C face samples, which were 130 nm. This shows that oxide growth at these temperatures is diffusion limited on the C face only.

The gates were formed by depositing 450 nm polysilicon in a LPCVD process, and doped using $POCl_3$. Aluminum was e-gun evaporated to a thickness of 200 nm. Wet etching and dry etching with CF_4 were used in a lithographic process to form circular contacts in the aluminum and polysilicon thin films respectively. The diameters of the contacts were 100 μm, 200 μm, 400 μm and 1000 μm. The backsides were coated with aluminum (p-type) and nickel (n-type). Prior to electrical characterisation an anneal at 773 K was performed in a vacuum furnace.

RESULTS

Electrical characterisation

Capacitance-voltage measurements were made at room temperature and in darkness using a HP4280A CV-meter with 1 MHz measuring frequency. Voltage sweeps were made at equilibrium from inversion/depletion to accumulation. No significant hysteresis occurred when the gate voltages were swept in both directions, and both 200 μm and 400 μm diameter capacitances were measured to ensure identical curve forms. To ensure that the series resistance was of minor importance, the oxide capacitance of 100 μm and 1000 μm diameter gates were measured and found to scale with gate area. CV-curves for the different oxides with 400 μm diameter polysilicon gates can be seen in figure 1a-d, with capacitance values normalised to that of the oxide. Theoretical curves were calculated using the method by Brews [9], with oxide thickness, gate area and substrate doping as input parameters. The workfunction, however, was set to 0 eV. Separate theoretical curves were obtained for the dry (50 nm) and wet oxides (130 nm) on the C face (fig 1b).

The oxide thickness which was calculated from the capacitance in accumulation agreed well with the oxide thickness measured by ellipsometry, except for the p-type C face oxides. In this case the series resistance was too high for accurate measurements, see fig 1d. This problem has recently been reported by Ouisse et al [6] with the remedy of measuring at low frequencies.

However, the p-type Si face oxides (fig 1c) were surprisingly good. The low capacitance part of all the curves are not completely in inversion if compared to the theoretical curves. Instead deep depletion occurs, which may be attributed to the wide bandgap of silicon carbide, with the resulting low thermal generation of minority carriers. This has been reported previously in literature [4, 10, 11].

From the large flatband voltage shifts in the curves in fig 1a-c the fixed oxide charge is estimated to be between 10^{12} and 10^{13} cm^{-2} which is extremely high. From fig 1a and 1b it can be seen that the wet oxides display a smaller flatband voltage shift than the dry oxides on n-type substrates, but this effect is less obvious on the p-type, fig 1c. The region with a large slope (onset of depletion) is a good indication of surface states when different curves with the same oxide thickness are compared. In fig 1a and 1b (and weakly in 1c) the dry oxidation with TCA added displays less surface states than a standard dry oxide. The wet oxide on n-type Si face (fig 1a) also exhibits some possible surface states.

The oxides were unfortunately very leaky, especially the p-type oxides, which made CV-measurements difficult to perform. Consequently, proper breakdown field measurements of the oxides could not be undertaken. Even at 100 Volts some oxides would not break, since the leakage current was around 1 μA. However, since CV-measurements could be made at high gate voltages, the breakdown was approximated to 8-10 MV/cm, which is high enough for MOSFETs (although the leakage itself causes failure).

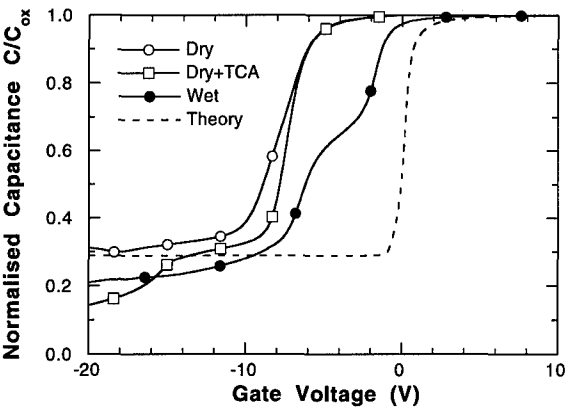

Figure 1a. Capacitance vs gate voltage for n-type silicon face SiC MOS capacitor. Gate area is 0.00126 cm^{-2}.

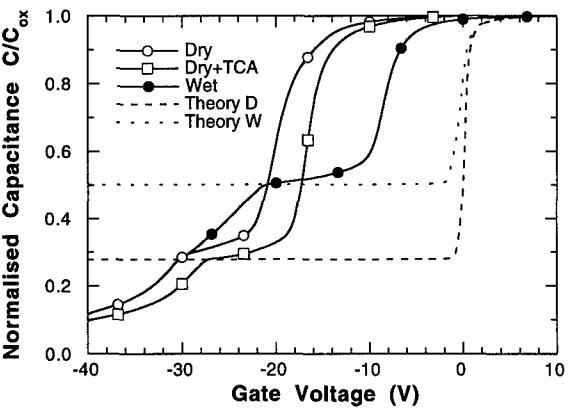

Figure 1b. Capacitance vs gate voltage for n-type carbon face SiC MOS capacitor. Gate area is 0.00126 cm^{-2}.

Figure 1c. Capacitance vs gate voltage for p-type silicon face SiC MOS capacitor. Gate area is 0.00126 cm^{-2}.

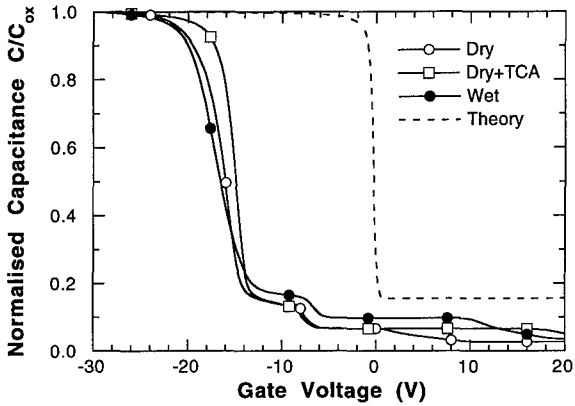

Figure 1d. Capacitance vs gate voltage for p-type carbon face SiC MOS capacitor. Gate area is 0.00126 cm^{-2}.

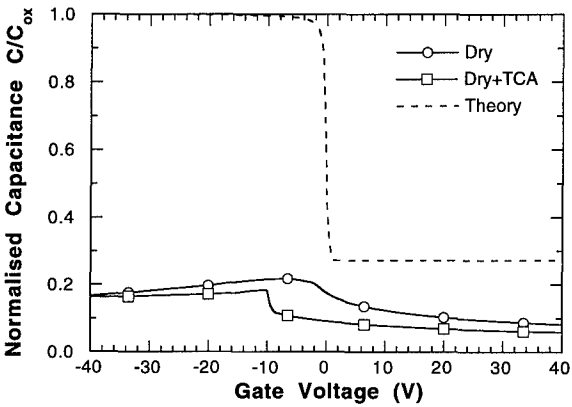

Aluminum incorporation

Secondary Ion Mass Spectrometry (SIMS) measurements were carried out using a Cameca ims4f instrument with an 8.0 keV O_2^+ ion beam. Positive secondary ions of ^{27}Al was detected, and as a monitor of the depth profiling silicon ions were used (^{30}Si). The sputter craters were 125 x 125 μm^2 in size, and the diameter of the analyzed area was 8 μm. Crater depths were measured using an Alpha step 200 surface stylus profilometer. Aluminum implantation standards for both SiC and SiO_2 samples were measured consecutively to determine the absolute concentration of aluminum. Both the standards and the samples were sputter coated with a 10-15 nm thick film of gold prior to analysis, to reduce charging effects. The surface was also flooded with electrons during profiling for charge compensation.

SIMS depth profiles in figure 2 show the concentration of aluminum in oxides grown by dry oxidation. For these measurements, structures without an aluminum contact was used, but in the case of the C face there was large amounts of aluminum left. This caused rough sputtering and broadening of the signals, as seen in fig 2b. It is not clear if the aluminum level in the polysilicon is significant, or caused by the surface aluminum still present. Signal intensities were converted to aluminum concentration with the following calibration factors: $3 \cdot 10^{14}$ atoms/cm^3 per c/s in SiC and $2 \cdot 10^{14}$ atoms/cm^3 per c/s in SiO_2. In the bulk SiC the aluminum levels were compared to the

specifications from CREE for the p-type substrates, and they were about 4 times higher, indicating low activation of dopants. The signal for the n-type substrates is most likely due to background noise.

The aluminum signal in the oxides is very interesting, since it indicates that trace amounts of aluminum are present even in the n-type substrates from CREE. Possible molecular interference on mass number 27 is very scarce, and the signal intensity is predominantly attributed to aluminum. However, an aluminum concentration of 10^{18} cm^{-3} in the oxides is unreasonable if the aluminum originates from the oxidized SiC bulk. Although the ionisation of aluminum is enhanced in the presence of oxygen, especially when using oxygen ions for sputtering, this is not seen in the reference implanted with aluminum. One possible explanation may be that aluminum occurs in the form of Al_2O_3 and not as an isolated atomic impurity in the SiO_2 matrix. The intensity of the ^{30}Si is probably enhanched by $(^{28}Si^{16}O_2)^{2+}$ ions, which facilitates the detection of the oxide layer.

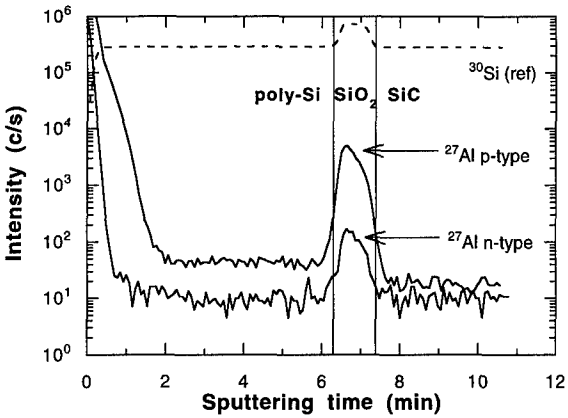

Figure 2a. SIMS depth profiles of aluminum in silicon face SiC samples. The samples were oxidized in dry oxygen at 1523 K for 50 minutes, and have a 450 nm top layer of polysilicon.

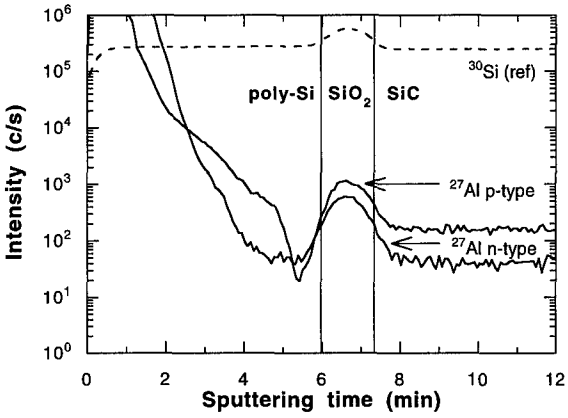

Figure 2b. SIMS depth profiles of aluminum in carbon face SiC samples. The samples were oxidized in dry oxygen at 1523 K for 10 minutes, and have a 450 nm top layer of polysilicon.

CONCLUSION

Four different silicon carbide samples have been thermally oxidized. The oxides have been characterized using capacitance-voltage measurements and SIMS (Secondary Ion Mass Spectrometry). It was found that wet oxidation on n-type results in less fixed oxide charge, but possibly with a higher density of surface states. Oxides on p-type were difficult to characterize, especially on the C face wafers. Large amounts of aluminum was found in the oxides, even n-type samples, possibly in the form of Al_2O_3.

ACKNOWLEDGEMENTS

We gratefully acknowledge Dr. M. Linnarsson and Dr. B. G. Svensson for the SIMS analysis and helpful discussions. This work was partly supported by the Swedish National Board for Industrial and Technical Development (NUTEK).

REFERENCES

1. M. Bhatnagar and B. J. Baliga, IEEE Trans. Electron Devices, **40**, 645, (1993).
2. R. F. Davis, G. Kelner, M. Shur, J. W. Palmour and J. A. Edmond, Proc. IEEE, **79**, 677, (1991).
3. P. A. Ivanov and V. E. Chelnokov, Semicond. Sci. Technol., **7**, 863, (1992).
4. N. Singh and A. Rys, J. Appl. Phys., **73**, 1279, (1993).
5. Z. Zheng, R. E. Tressler and K. E. Spear, J. Electrochem. Soc., **137**, 854, (1990).
6. T. Ouisse, N. Bécourt, C. Jaussaud and F. Templier, J. Appl. Phys., **75**, 604, (1994).
7. C.-M. Zetterling and M. Östling, Presented at ICSCRM '93, Washington D. C., 1993 (In press).
8. J. W. Palmour, R. F. Davis, H. S. Kong, S. F. Corcoran and D. P. Griffis, J. Electrochem. Soc., **136**, 502, (1989).
9. E. H. Nicollian and J. R. Brews, MOS Physics and Technology, 1st ed. (Wiley, New York, 1982)
10. J. B. Petit, P. G. Neudeck, L. G. Matus and J. A. Powell, 4th International Conference on Amorphous and Crystalline Silicon Carbide and Other IV-IV Materials, (Springer Proceedings in Physics, Vol 71, 190, Springer-Verlag, 1991).
11. A. Suzuki, H. Ashida, N. Furui, K. Mameno and H. Matsunami, Jpn. J. Appl. Phys., **21**, 579, (1982).

UV-SENSITIVE METAL-SEMICONDUCTOR PHOTODIODES ON 6H-SIC.

CHRISTER FRÖJDH*, GÖRAN THUNGSTRÖM*, HANS-ERIK NILSSON*, AND C. STURE PETERSSON
Royal Institute of Technology, Dept of Solid State Electronics, Electrum 229, S-164 40 KISTA, SWEDEN
* Also: Mid-Sweden University, Dept. of Electronics, S-851 70 SUNDSVALL, SWEDEN

ABSTRACT

Schottky diodes on Silicon Carbide (SiC) are of interest for many applications because of the relatively simple fabrication process. In this work we have fabricated Schottky diodes by evaporation of Ti on 6H-SiC and measured their electrical and optical properties. Most of the diodes show good rectifying behaviour with low reverse current and an ideality factor below 1.20. The photoresponse of the diodes has been measured in the range 200 - 400 nm. The peak sensitivity was found to be at 270 nm.

INTRODUCTION

Silicon Carbide is normally considered as a promising material for high power and high frequency applications because of its wide bandgap (Eg=2.9 eV for 6H-SiC), high saturation velocity for electrons and high thermal conductivity. A review of the properties of the material can be found in [1].

The wide bandgap also makes the material interesting for measuring UV-radiation. Photodiodes made on 6H-SiC are only sensitive to radiation at wavelengths below 400 nm, the wavelength where the photon energy corresponds to the bandgap energy. Their advantage as compared to Silicon photodiodes is that they can be used to measure the UV-radiation in visible light without extra filtering.

Photodiodes with pn-junctions have already been fabricated by ion implantation [2],[3]. High quality photodiodes fabricated by mesa etching of epitaxial layers were presented in [4].

The absorption coefficient for light in SiC is strongly wavelength dependent varying from about 10^2 to 10^6 cm^{-1} from 400 nm down to 200 nm. In order to make efficient diodes for short wavelengths the window of the diode must be very thin. The other important property is that the leakage current must be low.

Many metals form diodes with high Schottky barriers when deposited on silicon carbide. A number of reports on diodes made from Pt and Ti [5], Co [6] and other metals exist in the literature. The advantage of using a Schottky diode as a photodiode is the simple fabrication process and that no inactive window exists at the surface, since the light enters through finger shaped openings in the metal. The disadvantage is of course that one part of the diode area is shielded from light by the metal.

In this project we fabricated finger shaped Schottky diodes by evaporating Ti on a 6H-SiC wafer. The metal Ti was chosen because of its good adhesion to SiC and that the expected barrier height is sufficient to give low leakage currents.

PROCESSING

The starting material was a n-type 6H-SiC wafer with a n-type epitaxial layer on top of it. The doping in the bulk was specified to be $N_D=2*10^{18}$ cm^{-3}. The epitaxial layer had a thickness

Mat. Res. Soc. Symp. Proc. Vol. 339. ©1994 Materials Research Society

of 10 μm and a specified doping concentration of $N_D=2.5*10^{16}$ cm^{-3}. The wafers were fabricated by Cree Research Inc.

Prior to processing the wafers were degreased by subsequent dipping in trichlorethylene, acetone and 2-propanol and finally dipped in HF. A pattern with a number of finger shaped openings was formed on the wafer. The finger widths were in the range 1 - 2 μm. Four different diode areas were used: 100 x 100 μm, 75 x 75 μm, 50 x 50 μm and 25 x 25 μm. A SEM-micrograph of a part of the pattern is shown in Fig 1. The left part of the metal area is used for probing. The total size of the metal area for one diode is 120 x 220 μm. Each diode is surrounded by an opening with a width of 10 μm. Fig 2 shows the fingers of a single diode with a finger width of 1,2 μm. A cross section of one part of a diode is shown in Fig 3.

Titanium was evaporated on the wafers using an electron gun evaporator with a residual pressure of $1*10^{-7}$ Torr. The resulting layer thickness was 2000 Å. A standard lift-off procedure was used to remove excess metal. A back contact was made by evaporation of 5000 Å of Al on the back side of the wafer. After metallisation the samples were annealed in a furnace at 550 °C for 30 minutes. No additional surface passivation was done.

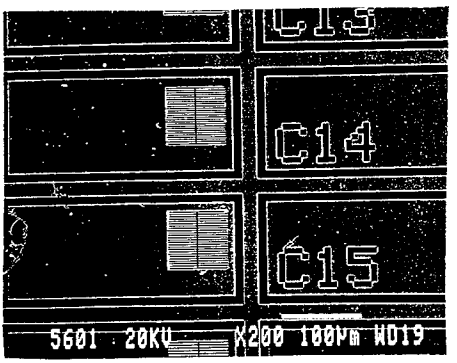

Fig 1. SEM micrograph of part of the mask showing a number of diodes. One diode consists of a rectangular metal area with the square finger area inside it and the surrounding opening isolating it from other diodes.

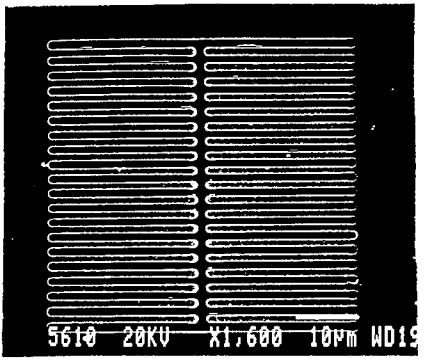

Fig 2. SEM micrograph showing the finger area of one diode.

ELECTRICAL CHARACTERISATION

After processing the diodes were placed on a probe station and characterised electrically by IV and CV measurements. A probe tip was placed on the metal area on the left side of the opening in the diode. The back side of the wafer was used as the second electrode.

CV-measurements were performed using a HP4279A CV-meter at a frequency of 1 MHz and varying the bias voltage from 0 to -10 V. Fig 4 contains the results from the CV-measurements. The doping concentration in the epitaxial layer was found to be $N_D=2.6*10^{16}$ cm^{-3} and the Schottky barrier height was ϕ_B= 0.88 eV.

IV-characteristics were measured in a computerised measurement system using HP3245A Universal Source and HP3458A Multimeter.

Most of the diodes show good rectifying behaviour with an ideality factor generally below 1.20 and with a reverse leakage current at -10 V bias varying from 50 pA for the best diodes up to 2 nA for an average diode. Reverse current as a function of reverse voltage for a typical diode is presented in Fig 5.

The ideality factor for the same diode was extracted from the data in Fig 6. The ideality factor was n=1.15 and the Schottky barrier height was Φ_B=0.83 eV. The somewhat lower value of the barrier height obtained from IV-measurements than from CV-measurements can easily be explained by defects lowering the barrier at local spots.

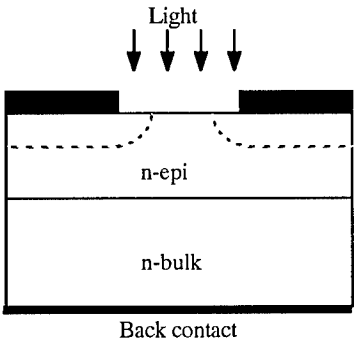

Fig 3. Cross section of one finger. The dotted line shows the shape of the depletion region in the opening.

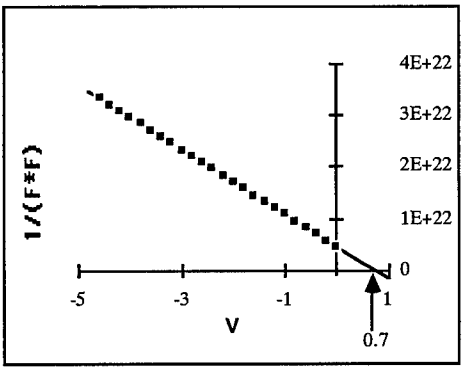

Fig 4. $1/C^2$ versus reverse voltage for a diode. The intercept with the voltage axis shows the built in voltage of the diode (V_{BI} = 0,7 V).

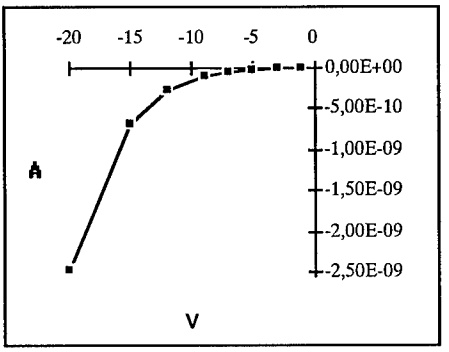

Fig 5. Reverse current as a function of reverse voltage for a typical diode.

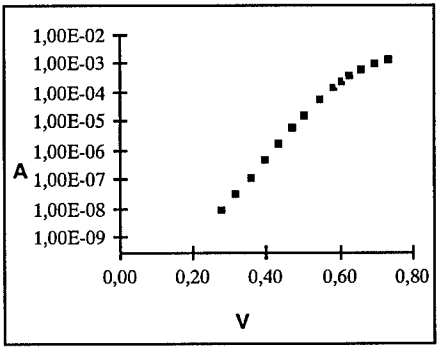

Fig 6. Forward current as a function of forward voltage for the same diode

OPTICAL CHARACTERISATION

Optical measurements were made using an ORIEL 1/8 m single monochromator equipped with an UV-enhanced 150 W Xenon arc lamp. Relative responsitivity was measured from 400 to 200 nm in steps of 10 nm with a spectral bandwidth of 10 nm. The total beam area during this measurement was 10 x 3 mm and the intensity of the light varied from 1200 μW at

400 nm down to 4 μW at 200 nm. The response of a diode with an area of 100 x 100 μm and a finger width of 1.5 μm, measured at 0V bias, is presented in Fig 7. The peak responsitivity is encountered at 270 nm. A number of measurements were made for diodes with different finger widths. No significant difference in the photoresponse caused by different finger widths could be observed.

In order to see the scaling effects the responsitivity of a series of diodes with four different areas was measured. The results from this measurement are presented in table 1. Since the beam was not confined to the fingers of the diodes some response from the periphery of the diode has to be expected. In order to match the photoresponse to the diode area the response from 1.7 μm of the area surrounding the diode (Fig 1) had to be included.

Diode size	Area factor	Response factor	Area factor including 1.7 μm of pheriphery
100x100μm	16	4.2	4.2
75x75μm	9	2.7	2.7
50x50μm	4	1.6	1.8
25x25μm	1	1	1

Table 1. Photoresponse for diodes with various sizes.

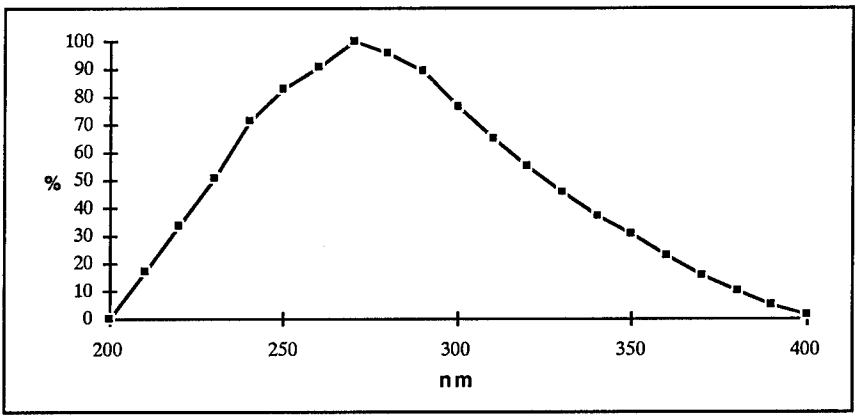

Fig 7 . Relative response of a diode with 1.5 μm finger width at 0V bias.

The dependence of photocurrent on reverse bias was also investigated. The photoresponse as a function of reverse bias at a wavelength of 300 nm is presented in Fig 8.

SIMULATIONS AND DISCUSSION

In order to investigate the theoretical sensitivity a segment of one diode was simulated using the program MEDICI. The simulated diode had a finger width of 1,5 μm. The direction of the radiation is perpendicular to the surface of the semiconductor and the metal is considered opaque to the radiation. All generation of photocarriers then takes place in the semiconductor below the opening in the metal. The intensity of the radiation in this simulation was $5*10^{15}$ photons/cm^2/s corresponding to 3.3 mW/cm^2 at 300 nm. Fast surface recombination was assumed.

The results for different carrier lifetimes and different reverse biases are presented in Fig 9. As can be seen from the figure the carrier lifetime is of great importance for making an efficient photodiode. Simulations for other wavelengths give similar results but with the difference that the dependence on carrier lifetime decreases as the absorption constant increases giving shallower absorption depths. For carrier lifetimes of at least 100 ns almost all radiation entering the finger opening contributes to the photocurrent.

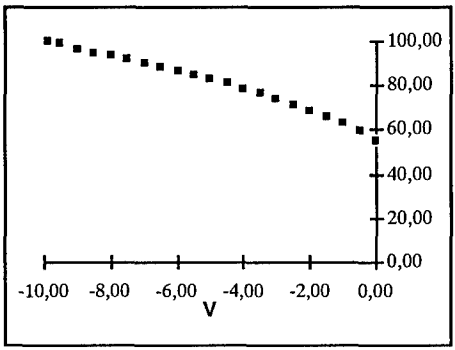

Fig 8. Photoresponse as a function of reverse bias at 300 nm normalised to the response at-10 V.

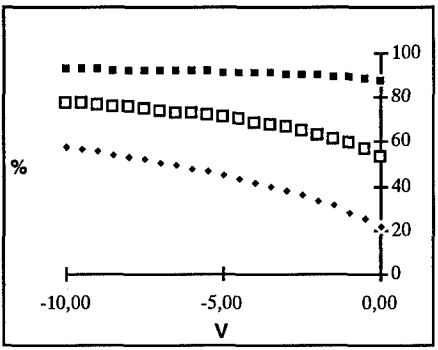

Fig 9. Simulated photoresponse at 300 nm of a diode with 1,5 μm fingers for three different carrier life times. Upper: 100ns, middle: 10ns, lower: 1 ns

In order to see the effects of the open area around the diode another simulation was done for an opening with a width of 10 μm. The data from that simulation are presented in Fig 10.

The measured dependence of photoresponse on reverse bias (Fig 8) is compared to simulations for different carrier lifetimes (Fig 10). The closest matching is found for a lifetime of 10 ns. However the low dependence of photoresponse on finger width indicates a somewhat higher lifetime.

In order to get efficient collection of photocarriers the depletion width and the diffusion length should be large. A realistic low doping concentration available today is $N_D=1*10^{14}$ cm^{-3}.

If we assume a carrier lifetime of 100 ns in the material and a fixed width of the metal fingers an optimal finger spacing could be calculated by multiplying the detection efficiency for the light entering the openings with the fraction of the total area occupied by the openings. The results from that simulation are presented in Fig 11. The width of the metal fingers was set to 1 μm. A reverse bias of 3 V was assumed.

The results of Fig 11 indicate that the optimum finger spacing in this case is around 5 μm. The theoretical quantum efficiency can then be as high as 80 % excluding effects of reflection at the semiconductor surface. The exact size is not critical since the maximum is fairly broad.

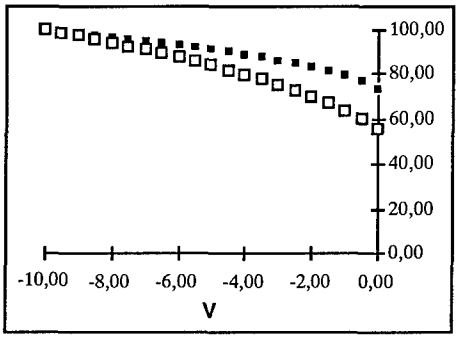

Fig 10. Simulated photoresponse at 300nm for carrier lifetimes of 100ns (upper curve) and 10 ns (lower curve) normalised to the response at -10 V The absolute response at 10ns is about 3 times lower.

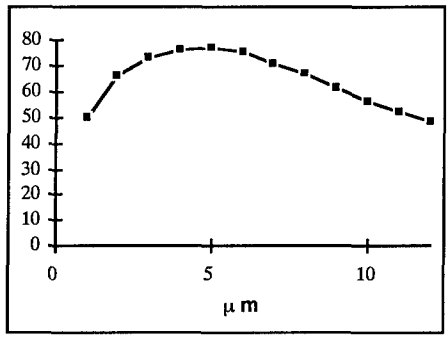

Fig 11. Calculated photoresponse as a function of finger spacing for a metal finger width of 1 μm at $N_D=1*10^{14}$ cm^{-2} and t=100 ns. Units are percent of radiation falling on the diode area.

CONCLUSIONS

Schottky diodes on 6H-SiC can be used as efficient photodetectors. The sensitivity can be optimised by using material with low doping concentration and by tailoring the finger widths to minimise the area covered by metal without significantly reducing the collection efficiency for photocarriers. Simulations indicate that diodes with a doping concentration of $N_D=1*10^{14}$ cm^{-3}, a carrier lifetime of at least 100 ns, a finger width of 1 μm and a finger spacing of 5 μm can have a quantum efficiency of 80 % at a wavelength of 300 nm excluding effects of reflection. This could be further improved by reducing the doping concentration or increasing the lifetime.

REFERENCES

1. P. A. Ivanov and V. E. Chelnokov, Semicond. Sci. Technol 7 (1992) 863-880

2. P. Glasow, G. Ziegler, W. Suttorp, G. Pensl, R. Heibig, SPIE, vol 868, pp. 40-45, 1987

3. C. Fröjdh, Q. Wahab, M. Willander, C. S. Petersson, G. Holmén, Presented at the 15th Nordic Semiconductor meeting, 1992 (unpublished)

4. D. M. Brown, E. T. Downey, M. Ghezzo, J. W. Kretchmer, R. J. Saia, Y. S. Liu, J. A. Edmond, G. Gati, J. M. Pimbley, W. E. Schneider, IEEE Trans on Electron Devices Vol 40 No 2 February 1993.

5. M. Bhatnagar, H. Nakanishi, P. K. Mclarty, B. J. Baliga, B. Patnaik, and N. Parikh, IEDM 92 pp 789-792, 1992

6. N. Lundberg, M. Östling, Appl. Phys.Lett Vol 63 pp 3069-3071 1993.

PART IV

Contacts

Metallization of GaN Thin Films Prepared by Ion Beam Assisted Molecular Beam Epitaxy

J.S.Chan, T.C.Fu and N.W.Cheung
Department of Electrical Engineering & Computer Sciences
UC-Berkeley, CA 94720

N. Newman, X. Liu, J.T. Ross and M.D.Rubin
Lawrence Berkeley Laboratory
UC-Berkeley, CA 94720

P. Chu
Center for Advanced Materials
Hong Kong City Polytechnic, Hong Kong

Abstract

Gallium nitride has generated much interest due to its ability to emit light in the blue to UV range [1]. We have investigated the ohmic contact properties of various metals evaporated onto highly auto-doped n-type GaN thin films which were grown on basal sapphire substrates by ion-assisted molecular beam epitaxy (IAMBE). Electrical measurements of transmission line structures with the metals In, InSn and AuGeNi revealed a wide range of contact resistivity (10^{-2} to 10^{-6} Ω-cm^2) which changed with annealing.

Introduction

Metallization on GaN is an important topic because efficient and reliable electroluminescent devices require ohmic contact resistivity of 10^{-4} Ω-cm^2 or better. In addition, the thermal stability of these metal contacts is an important factor in device fabrication. Therefore, the identification and optimization of the processing conditions for suitable ohmic contacts is crucial. In this study, we investigated the metals In, InSn and AuGeNi.

Experiment

The auto-doped n-type GaN films used in this investigation were prepared by the ion-assisted MBE method detailed in an earlier paper by this group [2]. The resistivity ρ for these films is 2×10^{-2} Ω-cm, which gives a doping concentration between 10^{18}-10^{19} cm^{-3}. Different metals were evaporated onto the GaN films using a Veeco evaporator system.

Mat. Res. Soc. Symp. Proc. Vol. 339. ©1994 Materials Research Society

The nominal thickness for the metals In and InSn was 3000 Å, whereas for the AuGeNi system, the thicknesses for the layers Au/Ni/AuGe were 1000 Å/400 Å/1000 Å, respectively. Electrical measurements using the transmission line model (TLM) were carried out on the n-GaN films to measure contact resistance [3]. The samples were rapid thermal annealed (RTA) in a forming gas overpressure for 15 seconds.

The transmission line structures used GaN mesa formed by ion-milling. An Ar ion beam accelerated to -800 V with a beam current of 1 mA cm^{-2} was used. The etch rate was 1000 Å / min. After the mesa was formed, contact metals were evaporated and patterned on the GaN using the lift-off technique. The TLM model is a one-dimensional treatment of the current flow between two adjacent ohmic contacts. Contact widths (W) of 400 μm and length (L_c) of 40 μm are separated by distances L_i. A current of known quantity (I_s) is sourced between two contacts. The resulting potential is measured, and the total resistance R calculated. Figure 1 is the current-voltage (I-V) plot of the InSn/GaN sample, which shows ohmic behavior. Figure 2 shows the resistance versus contact spacing plot for the same sample at different annealing temperatures. This resistance consists of the contact resistance component as well as the GaN bulk resistance R_s, and is expressed as:

$$R = 2R_c + (R_s/W)L_i \qquad \text{(EQ 1)}$$

where R_c denotes contact resistance. These values can be extrapolated directly from the R versus L_i plot. From the plot, R_c and the transmission length L_t could be deduced.

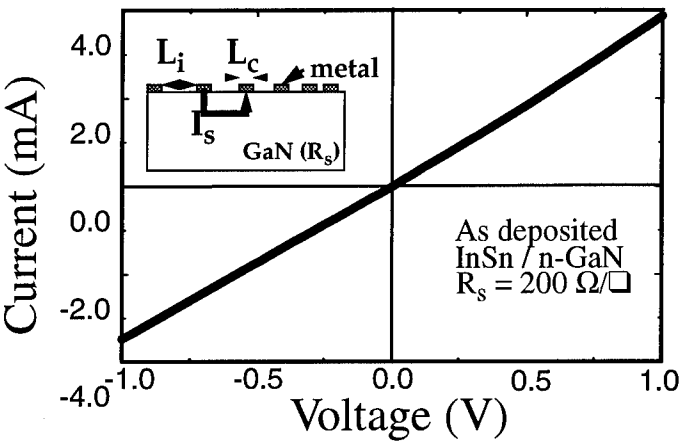

FIGURE 1. Current-Voltage Characteristic of the InSn/GaN sample, which indicates ohmic behavior.

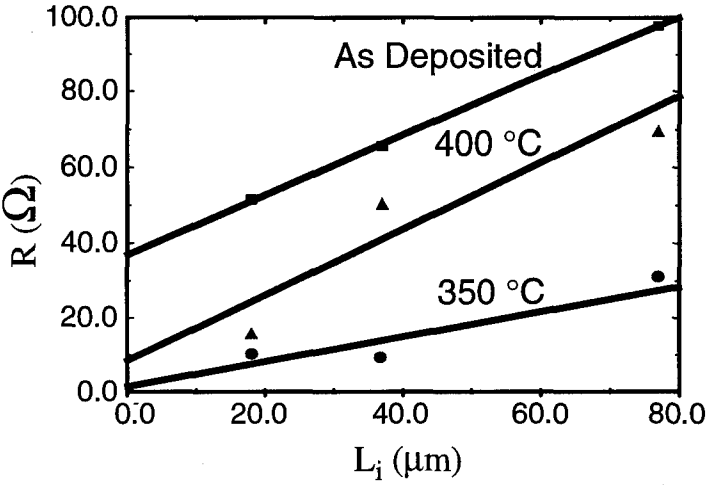

FIGURE 2. TLM Resistance vs. contact spacing for InSn/GaN. Lowest contact resistivity is observed after rapid thermal annealing at 350 °C.

The calculated contact resistivity ρ_c (where $\rho_c = R_c L_t W$) is plotted as a function of annealing temperatures for the metals In, InSn and AuGeNi in Figure 3.

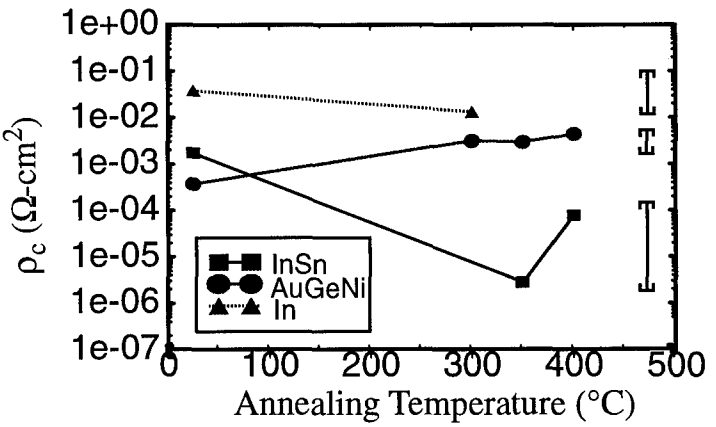

FIGURE 3. Contact resistivity vs. annealing temperature for the metals In, InSn and AuGeNi. InSn is shown to give the lowest contact resistivity.

Results and Discussion

From the electrical data, InSn was the only metal to show dramatic improvement in contact resistivity with annealing. After annealing at 350 °C, ρ_c dropped by three orders of magnitude from $2x10^{-3}$ Ω-cm^2 to $3x10^{-6}$ Ω-cm^2. However, in a subsequent annealing at 400 °C, the resistance increased again. The metallization was found to form separated islands after annealing above 350 °C, indicating that the determination of ρ_c for this temperature is inaccurate because the metal does not form a continuous conducting layer.

Similar to InSn, the In contact formed islands upon annealing at 300 °C.The metal In is not a satisfactory ohmic contact for devices. The lower ρ_c when Sn was present and the constant ρ_c when only In is present suggests that Sn doping at the metal-semiconductor (M/S) interface is the dominant factor in reducing ρ_c, rather than bandgap narrowing near the interface. Assuming that current transport is governed by the field emission, the tunneling model predicts that contact resistivity ρ_c is proportional to $\exp(\phi_b/N_d^{1/2})$, where ϕ_b denotes the barrier height, and N_d is the doping level at the M/S interface. The combination of a decrease in ϕ_b and an increase of N_d will lower the contact resistivity.

The AuGeNi contact showed slight electrical degradation with annealing. Rutherford Backscattering Spectrometry (RBS) revealed a rough AuGe/Ni interface with the as-deposited sample (See Figure 4). This interface smoothed out considerably upon annealing at 300 °C and 350 °C, but roughened again at 400 °C. (See Figure 5). However, the contact was found to remain planar and continuous after the annealing treatment, in contrast to InSn. Also, the Ni layer did not migrate to the GaN surface.

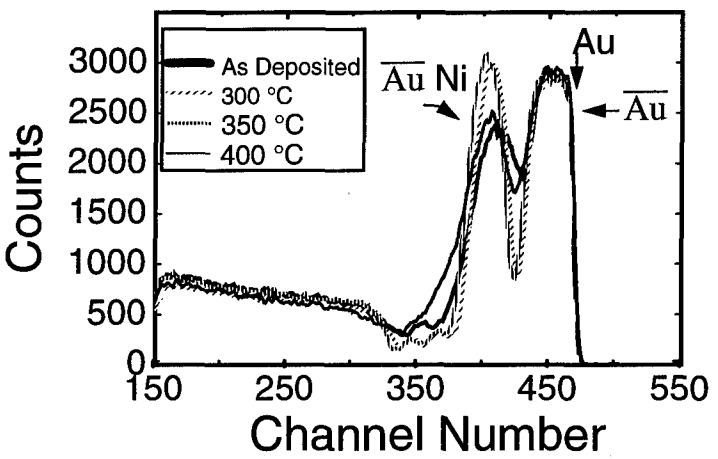

FIGURE 4. Rutherford Backscattering Spectrometry of the AuGeNi/GaN system. The AuNi signal revealed a smoothing of the AuGe/Ni interface with annealing between 300 - 350 °C, and a subsequent roughening at 400 °C.

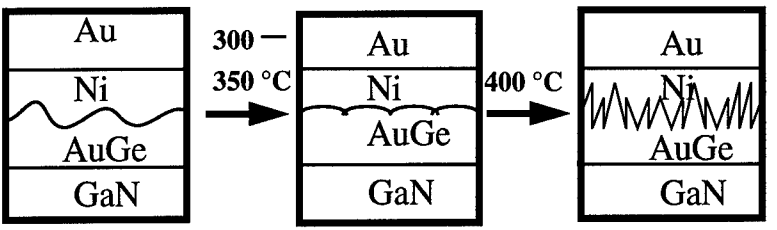

FIGURE 5. Schematic of the AuGe/Ni layer reaction with annealing (From RBS spectrum in Figure 4).

Conclusion

Electrical measurements of the ohmic contact resistivity of metal-GaN films indicated that the InSn contact performed better than the In contact probably due to Sn doping of GaN film at the metal-semiconductor interface. On the other hand, the AuGeNi system did not observe improvement with annealing. The InSn and AuGeNi contacts both gave adequate contact resistivity even with low temperature annealing (< 350 °C). However, higher processing temperature will lead to thermal instability.

References

[1] S.Strite and H. Morkoc, J.Vac.Sci.Technol.B, **10**, 1237 (1992).

[2] M.Rubin, N.Newman, J.S.Chan, T.C.Fu and J.T.Ross, Appl. Phys.Lett., **64**, 64 (1994).

[3] D.C.Look, Electrical Characterization of GaAs Materials and Devices, 1st ed. (John Wiley and Sons, New York, 1989), pp.132-136.

[4] J.G.J. Chern and W.G.Oldham, IEEE Elect.Dev.Lett., **5**, 178 (1984).

Acknowledgments

We acknowledge Kin Man Yu for his assistance in performing RBS analysis. We would also like to thank the Microfabrication Lab and the Device Characterization Lab of UC-Berkeley for providing the usage of their equipments for this work. This research is supported in part by the Air Force Office of Scientific Research (AFOSC/JSEP) under contract # F49620-90-C-0029, by the NSF under contract # ECS-9202993, and by the U.S. Department of Energy under contract # DE-AC03-76SF00098.

COBALT SILICIDE OHMIC CONTACTS TO 6H-SiC

Nils Lundberg and M. Östling*
Royal Institute of Technology, Department of Solid State Electronics,
E229, S-164 40 Kista-Stockholm, Sweden
*Present address: Stanford University, CIS, CIS-105, Stanford, Ca, 94305-4070

ABSTRACT

Materials and electrical evaluation were performed to determine the characteristics of ohmic contacts to 6H-SiC. Both elemental metal (Co) and silicides (CoSi and $CoSi_2$) were studied following heat treatments at 500 °C and 900 °C for 5 hours and 2 hours, respectively. Materials analysis by Rutherford Backscattering Spectrometry (RBS) and X-ray Diffraction (XRD) monitored the temperature stability of the contacts after the annealings. Current density-voltage measurements at elevated temperatures established the specific contact resistance ρ_c.

INTRODUCTION

Realisation of high temperature and high power applications for silicon carbide demand stable electrical contacts. The contacts should preferably withstand 500 °C for extended periods of time and still maintain stable electrical characteristics. Refractory metals and their silicides have been suggested as contact materials because of their unique thermal stability [1]. A low specific contact resistance ρ_c is crucial for most device structures in silicon carbide. Cobalt disilicide ($CoSi_2$), with its low resistivity (15 μΩcm) should have a potential to fulfill most of the criteria required for such a contact.

In this study ohmic contacts of cobalt and cobalt silicides were investigated. The contacts were formed on n-type heavily doped Si-face SiC epitaxial layers on p-type bulk 6H SiC wafers. A systematic investigation of the symmetric behaviour of the current density-voltage (JV) characteristics was performed at elevated temperatures. The temperature stability of the contacts was examined by consecutive heat treatments.

The addition of a thin Ti layer interposed between the Co and the SiC was investigated. Both the solid state reactions occurring at elevated temperatures and the JV-characteristics were studied.

EXPERIMENTAL

All samples were fabricated on single crystal 6H-SiC wafers purchased from Cree Research , Inc. The electrical carrier concentration of the p-type (Al) bulk substrate was $1 \cdot 10^{18}$ cm^{-3} and the 2 μm thick n-type (N) silicon face epilayer had a donor concentration of $7 \cdot 10^{18}$ cm^{-3}. The pre-deposition cleaning procedure consisted of degreasing in trichloromethyl ethylene, acetone and propanol, followed by an etching in a H_2SO_4:H_2O_2 (3:1) solution and a 30 second dip in a dilute HF solution. Subsequent rinsing in de ionised water was done after both the degreasing and the two acids. The different contact structures were deposited by e-gun

Mat. Res. Soc. Symp. Proc. Vol. 339. ©1994 Materials Research Society

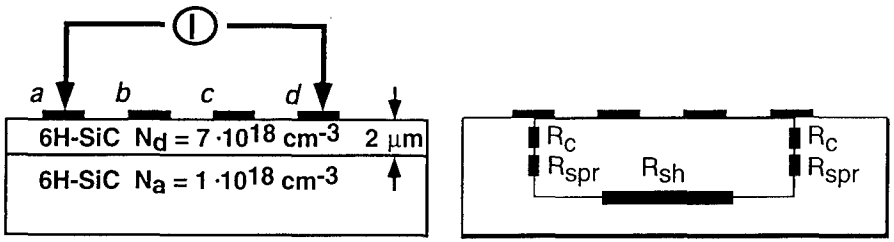

Figure 1. Four point probe arrangement used to determine the specific contact resistance ρ_C and the system equivalent circuit.

evaporation: Co (50 nm) / SiC substrate, Si (165 nm) / Co (50 nm) / SiC substrate. Additionally, two samples had a 5 nm thick Ti layer interposed between the SiC substrate and the previously described structures. Ti reacts on β-SiC at 350°C with carbon to form TiC [2], resulting in an improved adhesion. The base pressure during all evaporations was $8 \cdot 10^{-6}$ Pa. Patterning of the contact structures were done by a standard lift-off technique. Annealing of the contacts were performed in a vacuum furnace with a base pressure of $2 \cdot 10^{-5}$ Pa, at 500 °C and 900 °C, for 5 hours and 2 hours, respectively.

Specific contact resistance ρ_c was measured using a four point probe method described by Kuphal [3] and most recently by Shor et al. [4]. As shown in figure 1, the total resistance between two ohmic contacts consists of: the contact resistance R_c; the spreading resistance R_{spre}; and the sheet resistance R_{sh} of the material under the contact. A current I_{ad} is applied between contact *a* and *d*, and the voltages V_{ab} and V_{bc} are measured. For contact *a* one finds

$$\rho_c = A / I_{ad} [V_{ab} - R_{spre} - V_{bc} \{\ln((3s / d) - 1 / 2) / (2 \ln 2)\}] \quad (1)$$

where d is the contact diameter and s is the spacing between the contacts. In our experiments the ratio between d^2 and the thickness of the conducting layer w was small allowing us to neglect R_{spre} while minimising the error [3]. JV-characteristics of the ohmic behaviour were obtained for current levels ranging from 1 mA to 100 mA between two 100 µm in diameter contacts 400 µm apart. The forward resistance R_F corresponds to the inverse slope of the JV-curve.

RESULTS

Materials characterisation.

No homogenous reaction between the SiC substrate and the contact structures occurred during the annealing at 500°C for two hours as can be seen in the RBS-spectra for the Co/Ti-structure in figure 2. The Co signal remains at its surface position and the trailing edge of the signal does not extend significantly into the sample. Additionally, the Ti- and the Si-signals have not reached their surface positions, indicating no reaction. However, analysis by XRD of

have not reached their surface positions, indicating no reaction. However, analysis by XRD of both the Co- and the Co/Ti-structure revealed peaks corresponding to Co_2Si (d = 2.75 Å) suggesting an intermixing of the Co and the Ti films. XRD-analysis of the Co/Ti-structure also reveals the formation of TiC (d = 2.16 Å). As the movement of Ti was not observed in the RBS-spectrum the TiC formation must be at the SiC/Ti interface.

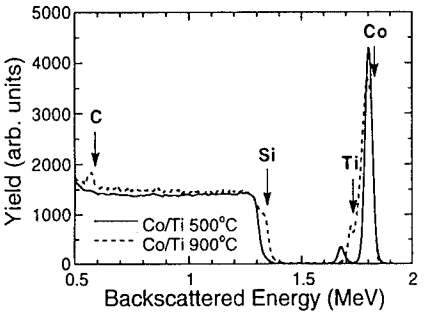

Figure 2. RBS-spectra of the Co/Ti-structure after annealings at 500°C and 900°C. The arrows indicate the surface position of the elements.

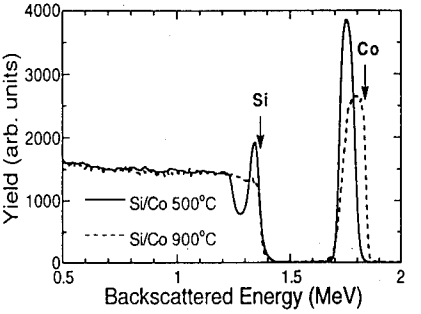

Figure 3. RBS-spectra of the Si/Co-structure after annealings at 500°C and 900°C.

On the other hand, when a Si layer was incorporated, at 500°C, the formation of Co_2Si and CoSi was observed with and without the additional Ti layer. All the Co had reacted but a film of Si, 115 nm in thickness, remained unreacted at the surface as can be seen in figure 3. In good agreement with the Co/Ti-structure the Ti signal in the RBS spectrum of the Si/Co/Ti-structure was positioned at the SiC interface.

After annealing at 900°C for 2 hours Co silicides were formed in all contact structures indicative of reaction with the SiC substrate. In the Co/Ti-structure, C and Ti migrated to the surface as shown in figure 2, yielding a 4:1 C:Ti ratio at the surface. Analysis by RBS and XRD revealed the silicides in the Ti containing structures to be more Co rich, indicating the TiC formed at 500°C to slow down the silicidation growth at the SiC interface.

In figure 3 it can be seen that $CoSi_2$ was formed homogeneously through the film in the Si/Co-structure. All the Co in the structure have reacted to form $CoSi_2$, thereby making the structure extremely temperature stable since $CoSi_2$ melts at 1599 K[5]. The Si/Co/Ti-structure displayed a 2:3 Co:Si stoichiometry. In contrast to the Co/Ti-structure no carbon signal could be seen at the surface.

Electrical characterisation.

The Co/Ti-structure displays a nearly linear and symmetric respons at room temperature for all current densities, shown in figure 4. When the temperature is elevated the ohmic characteristics is improved, yielding a lower forward resistance R_F. R_F is lowered from 190 Ω at 300 K to 140 Ω at 350 K. Further increase of the temperature to 450 K lowers R_F to 110 Ω. The lowered R_F at increased temperature can be attributed to a more complete ionisation of the n-type dopants in the epi-layer.

JV-characteristics for the Co structure reveals a quite different behaviour. For currents between 10 mA to 100 mA R_F was 170 Ω at 300 K and decreased to 150 Ω at 450 K. However,

for currents lower than 1 mA, R_F was roughly 2.5 kΩ at 300 K and decreased to 1.5 kΩ at 450 K. The high R_F values for low currents suggest the presence of a thin insulating layer at the interface, which supports the observations by RBS that only a limited reaction with the SiC substrate occurred during the 500°C anneal.

Both the Si/Co/Ti and the Si/Co structures displayed a slightly non-linear JV-characteristic with a slight benefit for the Si/Co-structure, shown in figure 4. For low currents (less than 1 mA), the Si/Co/Ti-contact structure revealed a high R_F value, 840 Ω at 300 K. It was lowered to 470 Ω at 450 K.

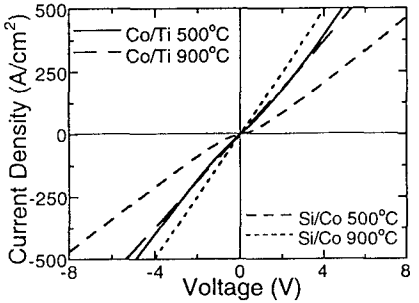

Figure 4. JV-characteristics of both the Co/Ti- and the Si/Co-structure after the different annealings.

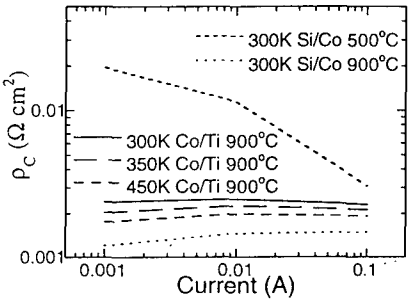

Figure 5. Specific contact resistance as a function of current for both the Co/Ti- and Si/Co-structures. The Co/Ti-structure was annealed at 900°C and operated at various temperatures, and the Si/Co-structure was operated at 300 K after different annealings.

Corresponding data for the Si/Co contacts were 690 Ω and 220 Ω, respectively. These high values of R_F at low currents for these two contacts indicate a high resistivity material in the contact, which is consistant with the findings of a non-reacted Si layer in the RBS-spectra of these samples.

Results from the ρ_c measurements of the contact structures are displayed in table 1. Only a slight dependence of current density on the ρ_c can be seen for the Co/Ti-structure, as could be expected from the linear JV-behaviour. ρ_c is lower than $4 \cdot 10^{-3}$ Ωcm² for temperatures ranging from 300 K to 450 K. In contrast to the Co/Ti contact the Co contact displays a strong ρ_c dependence on the current density which is in good agreement with the observations done by the JV-method.

Both the Si/Co/Ti and the Si/Co contacts display a strong dependence on the current density. However, at 100 mA the specific contact resistance is not higher than $3 \cdot 10^{-3}$ Ωcm², shown in figure 5. Operating at 450 K lowers the ρ_c of the contacts to $2 \cdot 10^{-3}$ Ωcm².

Followed by annealing at 900°C linear JV-characteristics were obtained for both the Co/Ti and the Co contacts. Currents smaller than 1 mA yielded R_F values of 138 Ω and 165 Ω for the Co and the Co/Ti contacts, respectively. At 450 K the corresponding values had further decreased to 110 Ω and 135 Ω , respectively. The R_F value at currents larger than 10 mA for the Co and the Co/Ti contact were 123 Ω and 161 Ω, respectively at 300 K, indicating only a weak dependence on the current density.

The two contact structures with a Si layer incorporated revealed the best ohmic characteristics. They displayed the lowest R_F values, 111 Ω and 100 Ω, for currents smaller than 1 mA, and the resistance-decrease at higher currents was less than 1 Ω! Extending the operating

temperature to 450 K lowered the resistances to 91 Ω and 83 Ω, for the Si/Co/Ti and the Si/Co structures, respectively. See figure 6.

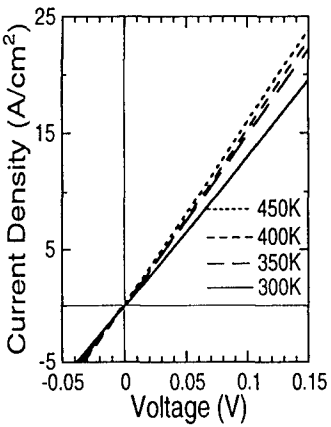

Figure 6. JV-characteristics of the Si/Co- structure annealed at 900°C, measured at various operating temperatures

All structures operated with ρ_c lower than $3 \cdot 10^{-3}$ Ωcm² for the various currents at 300 K and the values decreased as the operating temperature was elevated to 450 K. Minimum ρ_c ($9.2 \cdot 10^{-4}$ Ωcm²) was observed for the Si/Co structure.

Table I

Specific contact resistance ρ_C (Ω cm²) for contacts to n-type SiC with a carrier concentration of $7 \cdot 10^{18}$ cm^{-3}, after annealings at 500°C and 900°C for 5 and 2 hours, respectively. In the column **CONTACT** the four different contact structures appear. **TEMP** corresponds to the operating temperature in Kelvin. I = 100 mA corresponds to a current density of 1490 A/cm² and 1310 A/cm² for the Co-, Co/Ti- and Si/Co-, Si/Co/Ti-contacts, to SiC respectively.

ANNEALING (C°)	CONTACT	TEMP (K)	ρ_C / (Ω cm²) for I = 1 mA	for I = 10 mA	for I = 100 mA	REMARKS
500°C	Co	300	$2.7 \cdot 10^{-2}$	$5.6 \cdot 10^{-3}$	$1.4 \cdot 10^{-3}$	strongly
		450	$1.4 \cdot 10^{-2}$	$4.4 \cdot 10^{-3}$	$1.6 \cdot 10^{-3}$	non-linear
	Co/Ti	300	$3.7 \cdot 10^{-3}$	$2.4 \cdot 10^{-3}$	$8.9 \cdot 10^{-4}$	linear
		450	$1.8 \cdot 10^{-3}$	$1.7 \cdot 10^{-3}$	$1.1 \cdot 10^{-3}$	
	Si/Co	300	$2.0 \cdot 10^{-2}$	$1.1 \cdot 10^{-2}$	$3.1 \cdot 10^{-3}$	non-linear
		450	$6.7 \cdot 10^{-3}$	$6.5 \cdot 10^{-3}$	$1.9 \cdot 10^{-3}$	
	Si/Co/Ti	300	$1.5 \cdot 10^{-2}$	$5.0 \cdot 10^{-3}$	$2.5 \cdot 10^{-3}$	non-linear
		450	$6.5 \cdot 10^{-3}$	$4.0 \cdot 10^{-3}$	$2.4 \cdot 10^{-3}$	
900°C	Co	300	$2.5 \cdot 10^{-3}$	$2.5 \cdot 10^{-3}$	$1.8 \cdot 10^{-3}$	linear
		450	$1.5 \cdot 10^{-3}$	$1.6 \cdot 10^{-3}$	$1.5 \cdot 10^{-3}$	
	Co/Ti	300	$2.4 \cdot 10^{-3}$	$2.5 \cdot 10^{-3}$	$2.3 \cdot 10^{-3}$	linear
		450	$1.8 \cdot 10^{-3}$	$2.0 \cdot 10^{-3}$	$1.9 \cdot 10^{-3}$	
	Si/Co	300	$1.2 \cdot 10^{-3}$	$1.5 \cdot 10^{-3}$	$1.5 \cdot 10^{-3}$	linear
		450	$9.2 \cdot 10^{-4}$	$1.3 \cdot 10^{-3}$	$1.5 \cdot 10^{-3}$	
	Si/Co/Ti	300	$2.0 \cdot 10^{-3}$	$2.0 \cdot 10^{-3}$	$1.9 \cdot 10^{-3}$	linear
		450	$1.4 \cdot 10^{-3}$	$1.7 \cdot 10^{-3}$	$1.7 \cdot 10^{-3}$	

These results clearly show the advantage of depositing nearly stoichiometric Co and Si layers prior to silicidation in forming temperature stable contacts. During the annealing process, the amount of carbon incorporated in the contact is reduced compared to elemental Co layer reacting with the substrate. The reduction in carbon content results in an improved electrical characteristic.

The weak dependence on both current density and elevated temperature indicates that electron tunnelling through the Schottky barrier is the dominant current mechanism in the contact; consequently, an increase of the carrier concentration in the SiC epi-layer would lead to lower value of specific contact resistance. Addition of a thin Ti layer interposed between the SiC substrate and the Co improved the adhesion before annealing; however, TiC was formed at the interface during annealing acting as a barrier to the silicidation process.

CONCLUSION

Stoichiometric deposited cobalt silicide ohmic contacts displaying a minimum dependence on the current density were fabricated on n-type 6H-SiC. The specific contact resistance ρ_c decreased as the operating temperature was increased from 300 K to 450K. A temperature stable $CoSi_2$/SiC contact revealed the lowest value of ρ_c ($9.2 \cdot 10^{-4}\ \Omega cm^2$). No improvement in the electrical characteristics was observed by the addition of a thin Ti ahesion layer. Further investigations are under way to establish the long term stability at operating temperatures in the excess of 500°C.

ACKNOWLEDGEMENTS

James Doyle and Dr. Bengt G. Svensson at the Department of Solid State Electronics are greatly acknowledged for valuable comments. The investigation was partly funded by the Swedish National Board for Technical and Industrial Development (NUTEK).

REFERENCES

1. G. Kelner, in *Proc. of the 15th Nordic Semiconductor Meetings*, edited by S. Fransilla and R. Paananen Hämeelinna, Finland (1992)
2. J. J. Bellina, M. V. Zeller, Mat. Res. Soc.Symp. **97**, 265 (1987)
3. E. Kuphal, Solid State Electron. **24**, 69 (1981)
4. J. S. Shor, R. A. Weber, L. G. Provost, D. Goldstein and A. D. Kurtz, Mat. Res. Symp. **242** 573 (1992)
5. M-A Nicolet and S. S. Lau, in *VLSI Electronics: Microstructure Science*, edited by N. Einspruch and G. Larrabee, (Academic, New York, 1983), Vol. 6, Chap. 6.

CHARACTERIZATION OF MS, MiS, AND MOS CONTACTS TO TYPE IIB DIAMOND BY CAPACITANCE-VOLTAGE AND CURRENT-VOLTAGE

HENRY A. WYNANDS, M. L. HARTSELL, AND BRADLEY A. FOX,
Kobe Steel USA Inc., Electronic Materials Center, 79 TW Alexander Dr., P.O. Box 13608, Research Triangle Park, NC 27709, USA..

ABSTRACT

Three types of electrical contacts on natural type IIb single crystal diamonds have been studied by current-voltage (IV) and capacitance-voltage (CV) measurements. Vertical structures were fabricated with the metal-diamond (MS), metal-undoped diamond-doped diamond (MiS), or metal-SiO_2-doped diamond (MOS) contacts and ohmic contacts on the opposite face of the diamond. The MS contact was rectifying and both the MiS and MOS were blocking contacts. While very high leakage currents were measured on the MiS structure in forward bias (>10^6 times the reverse bias), an accumulation region was observed in the MiS CV data. The uncompensated acceptor concentration values calculated from the CV data were in good agreement for different structures fabricated on the same samples and with the secondary ion mass spectroscopy (SIMS) measurements of the bulk boron concentration. Extreme stretch out was observed in the CV of the MiS and MOS due to interface traps. The density of interface traps was estimated to be in the 10^{12} cm^{-2} eV^{-1} range for these structures.

Introduction

Application of diamond as an electronic material requires an understanding of the properties of electrical contacts. Three types of contact structures (MS, MiS, and MOS) on natural type IIb semiconducting diamond are compared in this study. The characterization of Schottky contacts on natural, synthetic, and CVD diamond[1-8] has been reported. To improve the characteristics of rectifying contacts, insulating diamond layers between the semiconducting diamond and contact metal (MiS structures) have been used.[9-13] Likewise, MOS structures have been fabricated for capacitors, and for use as gate structures in field-effect electronic devices.[14-16] The electrical characterization of these contact structures on natural semiconducting diamond provides a baseline of reference data to be used for comparisons with similar contacts fabricated on epitaxial or polycrystalline CVD diamond, and assists in determining the best high temperature contact structures.

Experimental

The MS and MiS or MOS vertical structures were sequentially fabricated on the frontside of natural (100) type IIb semiconducting single crystal diamonds. Backside, low contact impedance, ohmic contacts were fabricated with a heavily boron ion implanted region.[17, 18] In the MiS structure a ~90 nm thick homoepitaxial insulating diamond layer was deposited by microwave plasma CVD. The oxide layer of the MOS structure was a ~75 nm film of SiO_2 deposited by a low temperature deposition technique. The Al electrodes were

Mat. Res. Soc. Symp. Proc. Vol. 339. ©1994 Materials Research Society

evaporated through a shadow mask as 420 μm diameter dots (MS and MiS), or were photolithographically defined 250 μm dots on the MOS structures.

The Current-Voltage (IV) characteristics were measured using a HP 4145B meter. The onset voltage of forward bias conduction was defined by extrapolation of the linear portion of a ln(I) vs. V plot to the voltage where the current was 10^{-13} A (sensitivity limit). Capacitance measurements were made using computer controlled HP 4284A LCR and Keithley 595 meters. Six spatially distributed electrodes with low leakage currents ($<3x10^{-5}$ A/cm^2) were chosen for testing on the MiS and MOS structures, whereas the six MS electrodes were spatially distributed but were chosen at random. For comparison purposes, secondary ion mass spectroscopy (SIMS) measurements of the bulk boron concentration were made on several samples. A calibration standard, a boron ion implanted diamond sample, was measured in the same analysis sequence. The measured values are considered accurate to within 30%[19] in the measured concentration range.

Results

The forward bias and reverse bias current characteristics, displayed in Fig.1, clearly illustrate the differences between the MS, MiS, and MOS structures. Low reverse bias currents were measured for all samples. For the MOS and MiS structures the values were 1-2 orders of magnitude lower than the MS structures. In the forward bias region high conduction was exhibited by both the MS and MiS structures, whereas the conduction in the MOS structure was limited by the SiO_2. The onset voltages of the MS and MiS structures were ~0.5 V and 1.75 V respectively. The calculated rectification ratios (measured at ± 5 V) remained greater than 10^6 for temperatures up to 150°C. The values reported are an average of 6 of the best structures. Leakage currents as high as 4-6 orders of magnitude larger than the best values reported in Table I were measured on other MiS or MOS electrodes.

In addition to IV measurements, differential capacitance (C) was measured as a function of both bias (V) and frequency. Representative plots of both C vs. V and C^{-2} vs. V at several frequencies are shown in Fig. 2 a-c. The use of the low impedance boron implanted back contact minimized the frequency dispersion.[17, 18] The limited frequency dispersion, evident at frequencies above 100 kHz for the MiS and MOS structures, results from bulk series resistance.

The CV data of the MiS and MOS structures reveal a clear accumulation region in forward bias where the capacitance is constant. Because conduction through the insulator is limited, the carriers that move to the semiconductor-insulator interface under forward bias are blocked; as a result the capacitance was independent of bias. The extreme hysteresis of the CV with scan direction, shown in Fig. 2d, was present for both the MiS and MOS structures. Due to this hysteresis, the observation of the accumulation region required scanning the bias from depletion to accumulation. Once the electrode had been forward biased, and carriers had accumulated at the semiconductor-insulator interface, any subsequent CV was stretched out along the voltage axis. For both structures the measured high frequency capacitance in this region was approximately a factor of two lower than the geometric capacitance, calculated from the electrode area and insulator thickness.

Since the probable cause of the CV hysteresis is the presence of the interface traps, the density of interface traps, D_{it}, was estimated for both the MiS and MOS structures. No significant differences were noted between the three samples; the D_{it} was on the order of 10^{12} cm^{-2} eV^{-1} for each, as can be seen in Table I.

The uncompensated acceptor concentration (N_A-N_D) was determined from the slope of the linear portion of the C^{-2} vs. V plot.[20] The N_A-N_D values calculated for the three types of structures are shown in Table I. The values were averaged over all measured frequencies and at least 5 electrodes on each sample.

Figure 1: The current voltage data of the MS, MiS, and MOS structures showed very different forward bias characteristics.

Figure 2: The CV data of a) MS, b) MiS, and c) MOS structures, and d) the hysteresis of the MiS data. The MiS and MOS structures exhibited accumulation regions in forward bias. The frequency dependence for each structure was evident primarily at 1 MHz. The CV data of the MiS (Fig. 2d) and MOS (not shown) structures exhibited extreme hysteresis with scan direction.

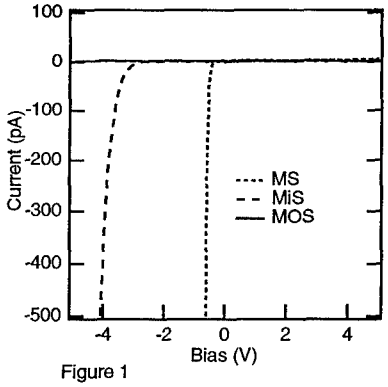

Figure 1

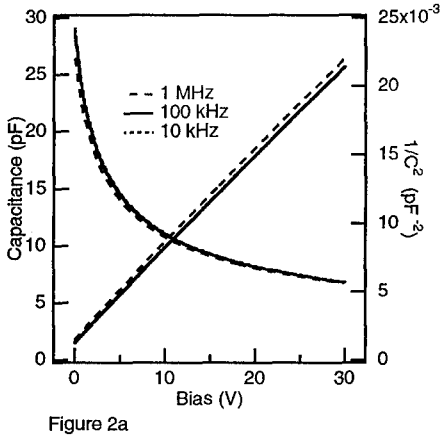

Figure 2a

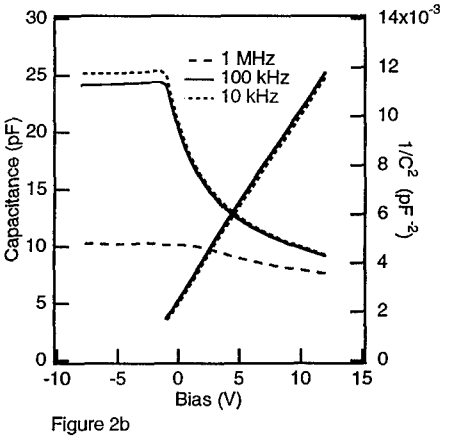

Figure 2b

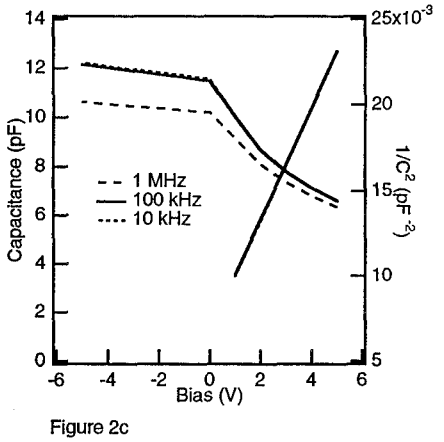

Figure 2c

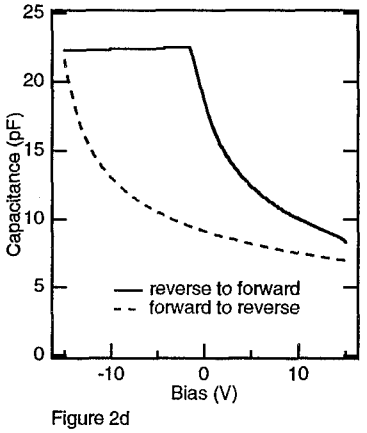

Figure 2d

Table I: Comparison of the reverse bias leakage currents, the uncompensated acceptor concentration (N_A-N_D) and the boron concentration ([B]) as determined by CV and SIMS measurements, and the density of interface traps (D_{it}) values of MS, MiS, or MOS structures.

Sample Number (structure)	Rev. Bias Current (A)	CV (N_A-N_D) (10^{16} cm^{-3})	SIMS [B] (10^{16} cm^{-3})	Density of interface traps (10^{12} cm^{-2} eV^{-1})
1 (MS)	8×10^{-10}	1.75 ± 0.25	---	
1 (MiS)	1×10^{-12}	1.76 ± 0.19	---	0.3-2.4
2 (MS)		3.01 ± 0.15	---	
2 (MOS)		3.13 ± 0.15	---	0.8-3.8
3 (MOS)	3×10^{-11}	1.6 ± 0.2	---	> 1
4 (MS)		1.98 ± 0.27	2.5 ± 0.8	
5 (MS)		2.91 ± 0.04	3.5 ± 1.0	
6 (MS)		2.84 ± 0.17	3 ± 0.9	

Two comparisons are made in Table I. First, a comparison of different contact structures which were sequentially fabricated on the same sample is made. Sample 1 was studied as MS and MiS structures and Sample 2 as MS and MOS structures. The insensitivity of the N_A-N_D values to the type of contact structure is a good indication that the CV is actually probing the diamond depletion layer. Second, N_A-N_D values from MS CV are compared with SIMS measurements of the bulk boron concentration (samples 4-6). While differences between the techniques are expected, the good agreement of these measurements already been established.[21] If it can be assumed that the SIMS value of the boron concentration really is a measure of N_A, the CV value (N_A-N_D) would be expected to be lower by an amount equal to N_D. Since the N_D in type IIb natural diamond is typically in the 10-20% range,[22, 23] the comparison of CV and SIMS is a good one. Viewing the entire data set the overall agreement of the values is evident, regardless of contact structure or measurement technique.

The barrier height of a Schottky contact can be calculated from the x-intercept of the C^{-2} vs. V plot.[20] The values measured for the MS samples in Table I averaged 2.3 ± 0.2 eV. This value agrees with previously measured MS diode barrier heights on natural type IIb diamonds.[20, 23]

Discussion

The current-voltage data in Fig. 1 presents clear evidence for the nature of the three types of electrical contacts to the semiconducting diamond. Current rectification by the MS structure is demonstrated by the greater than 10^6 rectification ratios and by the reverse bias leakage currents. The current blocking characteristic of the MOS capacitor structure is verified by the very low leakage currents in both forward and reverse bias. The high resistance SiO_2 layer limited the current for the entire bias range. Similarly the MiS reverse bias currents were reduced, compared to the MS structure, due to the additional resistance of the insulating diamond layer. However, the high forward bias conduction of the MiS sample, greater than 5000 times that of the MOS structure, was distinctly different than the MOS samples. In fact,

the MiS IV data is very similar to the MS data, except that the currents were decreased by two orders of magnitude. Therefore on the basis of the IV data, the insulating diamond contributed additional resistance to a rectifying contact, but the contact was not current blocking.

The interpretation of the CV data for the MS and MOS structures is consistent with the picture derived from the IV data. With increased reverse bias the width of the depletion layer in the semiconducting diamond is increased and the capacitance is decreased. The rate of capacitance change is related to the dopant concentration [20] and the values of N_A-N_D derived from the CV data are consistent with the SIMS values of the boron concentration. The MOS capacitance is lower due to the series capacitance contributed by the thickness of the dielectric SiO_2. In the forward bias region the depletion layer in the semiconductor disappears and the MS junction no longer acts as a capacitor. The MOS CV has a constant capacitance in this region because the insulating SiO_2 layer remains as a dielectric.

However, the MiS CV data requires a somewhat different interpretation than the MiS IV data, which suggested the MiS contact was rectifying. Like the MOS case, the MiS CV data, shown in Fig. 2b, reveals both a depletion region, as expected, and a very clear accumulation region. The forward bias leakage through the insulating diamond layer, although significant ($>5 \times 10^{-9}$ A), was not sufficient to remove the charge carriers accumulated at the semiconducting diamond-insulating diamond interface. Together the IV and CV data suggest that the MiS structure may be viewed as a current blocking contact with very high leakage currents.

The uncompensated acceptor concentrations determined from CV data were consistent for different structures. The N_A-N_D values for the MS/MiS and MS/MOS structures fabricated on the same crystals agreed within the standard deviations (see Table I). This supports the premise that the properties of the semiconducting diamond are being studied for each structure. The N_A-N_D values presented here are also consistent with 1-3 x 10^{16} cm^{-3} range published [3, 14, 23] for other natural type IIb single crystal diamonds. As noted above, the difference between the SIMS and the CV values is a measure of N_D. The calculated N_D values fall in the 10-20% range typically noted for type IIb diamond. [22, 23]

The hysteresis of the MOS and MiS CV data, shown in Fig. 2d, is consistent with a relatively high trap density at the semiconductor-insulator interface. With the electrode forward biased and holes accumulated at the interface, the interface traps could be occupied by the carriers. With subsequent bias changes the trapped carriers remained at the interface and the charge on the metal electrode was therefore balanced by both the trapped charge and the charge at the edge of the depletion region. Greater bias changes were necessary to effect similar depletion layer changes [24] and the CV became stretched-out along the voltage axis. The density of interface traps was estimated for these samples to be in the 10^{12} cm^{-2} eV^{-1} for both MiS and MOS samples. With the insulating diamond layer being a homoepitaxial film, it may have been expected that the D_{it} values would be lower than that for the MOS structures. While this may be the case when fabrication conditions are optimized, in this case the values are quite similar.

In summary, this study reports a comparison of MS, MiS, and MOS electrical contacts on natural type IIb single crystals. Overall the measured impurity concentrations determined by CV were in good agreement with the boron concentration values determined by SIMS. On the two samples which were characterized with different contact structures, the measured N_A-N_D values were within the experimental uncertainties. This indicates that the diamond is being probed without major interference from other effects. In addition, this is believed to be the first known reported measurement of D_{it} on diamond structures and the first known report of the carrier accumulation in an MiS diamond structure.

We would like to thank Chien-teh Kao for the growth of the homoepitaxial diamond film utilized in the MiS structure, Robert Henard for growth of the MOS oxide layer and for metallization, and Koichi Miyata and David Dreifus for insightful discussions.

References

1. M. D. Bell, and W. J. Leivo, *Phys. Rev.* **111**, 1227 (1958).
2. G. H. Glover, *Solid-State Electronics* **16**, 973 (1973).
3. E. C. Lightowlers, and A. T. Collins, *J. Phys. D: Appl. Phys.* **9**, 951 (1976).
4. C. A. Mead, and T. C. McGill, *Phys. Letts.* **58A**, 249 (1976).
5. M. W. Geis, D. D. Rathman, D. J. Ehrlich, R. A. Murphy, and W. T. Lindley, **EDL-8**, 341 (1987).
6. M. C. Hicks, C. R. Wronski, S. A. Grot, G. S. Gildenblat, A. R. Badzian, T. Badzian, and R. Messier, *J. Appl. Phys.* **65**, 2139 (1989).
7. G. S. Gildenblat, S. A. Grot, and A. Badzian, *Proc. IEEE* **79**, 647 (1991).
8. T. Tachibana, B. E. Williams, and J. T. Glass, *Phys. Rev. B* **42**, 11972 (1992).
9. H. Shiomi, Y. NIshibayashi, and N. Fujimori, *Jap. J. Appl. Phys.* **29**, L 2163 (1990).
10. N. Fujimori, and Y. Nishibayashi, *Diamond Rel. Mat.* **1**, 665 (1992).
11. K. Miyata, D. Dreifus, and K. Kobashi, *Appl. Phys. Lett.* **60**, 480 (1992).
12. K. Miyata, and D. Dreifus, *J. Appl. Phys.* **73**, 4448 (1993).
13. K. Miyata, K. Kobashi, and D. L. Dreifus, *Diam. Rel. Mat.* **2**, 1107 (1993).
14. M. Geis, J. Gregory, and B. Pate, *IEEE Trans. Electron Dev.* **38**, 619 (1991).
15. S. A. Grot, G. S. Gildenblat, and A. R. Badzian, *IEEE EDL* **13**, 462 (1992).
16. A. J. Tessmer, K. Das, and D. Dreifus, *Diam. Rel. Mat.* 89 (1992).
17. V. Venkatesan, K. Das, J. A. von Windheim, and M. W. Geis, *Appl. Phys. Lett.* **63**, 1065 (1993).
18. V. Venkatesan, D. M. Malta, K. Das, and A. M. Belu, *J. Appl. Phys.* **74**, 1179 (1993).
19. Personal Communication: Charles Evans and Associates (1993).
20. D. K. Schroder, *Semiconductor Material and Device Characterization* (John Wiley and Sons, Inc., New York, 1990) Chap. 2.
21. H. A. Wynands, D. M. Malta, B. A. Fox, J. A. von Windheim, J. P. Fleurial, D. Irvine, and J. Vandersande, *Phys. Rev. B* **49**, 5745 (1994).
22. A. T. Collins, and E. C. Lightowlers, in *The Properties of Diamond* , edited by J.E. Field, (Academic Press, London, 1979).
23. J. A. von Windheim, V. Venkatesan, D. M. Malta, and K. Das, *J. Electron. Materials* **22**, 391 (1993).
24. E. H. Nicollian, and J. R. Brews, *MOS Physics and Technology* (John Wiley & Sons, New York, 1982) Section 8.

GROWTH OF SINGLE CRYSTAL COPPER FILMS ON DIAMOND USING FCC-IRON SEED LAYERS

D.P. PAPPAS[1], V.G. HARRIS[2], H.A. HOFF[2], AND G.L. WATENA[2], J.W. GLESENER[2]
[1]VIRGINIA COMMONWEALTH UNIVERSITY, RICHMOND, VA 23284-2000
[2]NAVAL RESEARCH LABORATORY, WASHINGTON, DC 20375

ABSTRACT

Copper films were grown on a single crystal diamond substrate using an iron seed layer. The effect of the crystalline structure of the iron seed on the Cu films was studied with extended x-ray absorption fine structure (EXAFS) and scanning electron microscopy (SEM). The EXAFS study shows that the 10 Å Fe seed layer is in an fcc structure, and has collapsed into a bcc structure by the time 20 Å of Fe has been deposited. In the SEM pictures it is observed that subsequent layers of Cu grow as continuous films for thin fcc-Fe seeds, and grow in an island mode for the thick, bcc-Fe seeds.

INTRODUCTION

Epitaxial growth of metastable phases of matter on lattice matched substrates has opened an entirely new field of experimental and theoretical physics [1]. The use of diamond substrates is especially appealing due to the unique properties of diamond, i.e. its large band gap, high thermal conductivity, extreme hardness, and desirable optical properties [2, 3]. In in the past few years there has been a strong interest in developing applications of diamond films and surfaces. The characterization of the interfacial properties between diamond and various metals used for contacts (e.g. copper) is a necessary step in the development of diamond-based electronic devices. In addition, an understanding of the magnetic properties of transition metal films such as iron, cobalt, and nickel on diamond may also provide a means of developing high temperature, non-volatile magnetic storage devices and sensors based on diamond.

The epitaxial growth of these transition metals on C(100) is feasible due to the close lattice match (a=3.57 Å for diamond vs. 3.59, 3.52, and 3.61 for fcc-Fe, Ni, and Cu, respectively), and the fact that the symmetry of the (100) face of the diamond and fcc structures is the same. Recent scanning electron microscopy (SEM) and low energy electron diffraction (LEED) work by Humphreys, *et. al* [3], has shown that it is possible to grow continuous, single crystal films of Ni(100) on C(100) by e-beam epitaxy. In addition, it has been shown using reflection high energy diffraction (RHEED) and Auger electron electron diffraction (AED) that thin films of Fe can also be stabilized on the C(100) surface [4, 5]. However, we note here that since Fe is normally bcc at low temperature (T< 973° C), the fcc-Fe films which are grown on the C(100) surface are in a meta-stable state. Therefore, it can be expected that the Fe will only maintain an fcc structrure up to some critical thickness. This is analogous to the case of fcc-Fe grown on the Cu(100) face, which collapses into a bcc structure at thicknesses of ≈20 Å [6]. Copper, on the other hand, is difficult to grow on the diamond surface due to its tendency to grow in a polycrystalline fashion at room temperature, and ball up into islands at high temperature annealing temperatures or growth conditions [7].

In the present work we have used thin Fe seed layers in order to grow subsequent layers of epitaxial Cu films on the C(100) surface. We have measured the macroscopic properties of Cu/Fe/C(100) multilayers using SEM and the microscopic properties of the Fe seed layer in these structures using EXAFS. We have found that as long as the Fe maintains an fcc-structure, it is

Mat. Res. Soc. Symp. Proc. Vol. 339. ©1994 Materials Research Society

possible to grow epitaxial, smooth layers of Cu on this surface. However, once the Fe has made the transition to bcc, the Cu tends to form islands on the surface.

SAMPLE PREPARATION AND STRUCTURAL CHARACTERIZATION

The films in this study were grown on single crystal, polished synthetic diamond substrates using the (100) surface. The details of the substrate preparation are given in Ref. [4]. The substrate was then inserted into an ultra-high vacuum chamber, and Fe was deposited from an e-beam source, and the pressure stayed below 5×10^{-10} Torr during growth, and thus it was possible to obtain very pure Fe seed layers, as monitored by Auger electron spectroscopy. The Fe thickness was determined using a vibrating quartz crystal microbalance. During the Fe growth the C(100) substrate was left at room temperature in order to achieve a continuous covering of Fe on the substrate [4]. The films were then annealed to 350° C while the electron diffraction pattern was monitored. After the anneal, depending on the thickness of the Fe, it was found that the films crystallize into either (a) an single crystal structure (with an electron diffraction pattern oriented with respect to the diamond substrate) for d<20 Å, or (b) into a polycrystalline film (with a ringed electron diffraction pattern) for d≥20 Å. These results are similar to the the behavior of fcc-Fe which is grown on Cu(100), which undergoes a martensitic transition to bcc-Fe at ≈18-20 Å [6].

In the present study we have investigated the effect of the Fe seed layer structure on the subsequent epitaxy of Cu layers. In order to achieve this, we have grown 100 Å of Cu onto a thick and a thin Fe seed layer, with thicknesses of 10 Å and 20Å, respectively. The Cu was evaporated from a W basket at a pressure of 1×10^{-9} Torr, and the thickness was again measured with a quartz crystal thickness monitor. The Fe/C(100) substrate was held at 300° C during the Cu evaporation. As shown in Ref. [4], the Cu grown on the thin Fe seed is epitaxial and oriented with respect to the diamond substrate, however the Cu grown on the thick, polycrystalline Fe seed showed a ringed diffraction pattern, similar to that of the Fe.

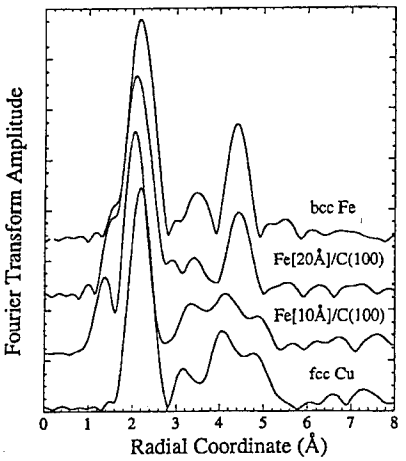

Figure 1: Fourier transformed Fe K-edge EXAFS data for Cu/Fe/Diamond with a 10 Å Fe seed and a 20 Å Fe seed. The top and bottom spectra are from bulk bcc-Fe and fcc-Cu standards.

In order to determine the local structure of the Fe seeds we have conducted an EXAFS study on the Fe K-absorption edge of two different thickness seed layers, as shown in Fig 1. The details of the data collection and analysis are presented elsewhere [4, 11]. Figure 1 is a plot of Fourier transformed Fe EXAFS data collected from the two Cu/Fe/Diamond(100) samples and bulk bcc-Fe and fcc-Cu standards. Although these data have not been corrected for electron phase shifts and therefore do not represent true radial distances, both sets have undergone similar analysis procedures which allow direct comparisons to be made. Comparisons between the data sets reveal strong differences between the EXAFS from the 20 Å Fe seed layer vs. the 10 Å seed. The most important difference is the appearance of a distinct peak at 4.4 Å in the spectrum of the thick Fe seed layer. This peak is prominent in the bcc-Fe standard, and is due to

constructive interference along the cube diagonal of the bcc-structure. On the other hand, the thin Fe seed shows the triple hump structure around the 4 Å peak which is a signature of an fcc-structure, as demonstratedby the fcc-Cu standard spectrum. The first two peaks in the thin Fe EXAFS spectrum, at 1.3 Å and 2.1 Å, are attributed to the carbon nearest neighbors (at the interface) and the Fe nearest neighbors (in the film). The Cu nearest neighbors at the top layer of the seed also contribute to the broadening of the 2.1 Å peak. Fitting the near neighbor environment of Fe atoms [12] in the Fe/C sample gives bond lengths of 2.50(.005), 2.65(.005), and 2.1(.05) Å for the Fe-Fe, Fe-Cu, and Fe-C correlations, respectively. The measured Fe-Cu distance is larger than expected from the summation of Goldschmidt radii (2.55Å). This can be attributed to a reconstruction observed in the epitaxial growth of Cu/Fe(100) due to, e.g., the mismatch between the fcc-Cu and the fcc-Fe(100) lattice constant.

It has been shown in Ref. [4] with reflection high energy electron diffraction (RHEED) that Cu can be grown epitaxially on the thin, fcc-Fe seed layers. The electron diffraction is sensitive to ordering for length scales comparable to the coherence length of the electron beam, which is on the order of 100 - 200 Å. In the present study we are concerned with the long-range smoothness and quality of the film from a macroscopic point of view, i.e. on the order of microns. This will provide information regarding the merits of the samples from an application point of view. In Fig. 2(a) and (b) we show a comparison of SEM pictures of the diamond surface before and after the preparation of the first sample, 100 Å of Cu grown on the thin fcc-Fe seed layer. All of the SEM pictures in this study were taken at 25 keV. Contact to the the surface was made with silver paint which ran to the ground plane in order to minimize charging of the diamond substrate. Fig. 2(a) shows an edge-on view of the bare substrate, where the sample is being viewed at an angle of 68° from the normal. The ripples on the surface of the cleaned substrate which are evident in Fig. 2(a) are typical of all of the substrates. These ripples are on the order of .05 μm, and most likely left from the vendors' polishing procedure. RHEED patterns observed from this surface [4] shows that the surface gives a high quality, single crystal diffraction pattern.

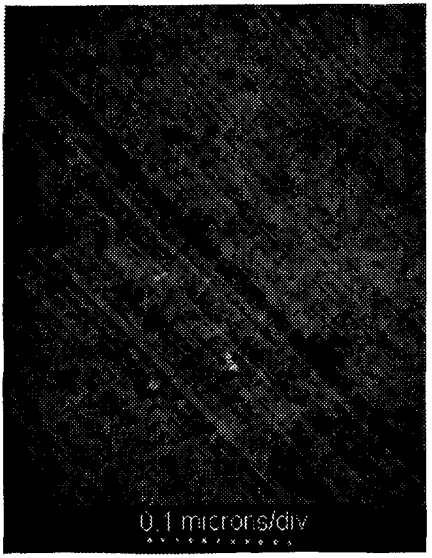

Figure 2(a): SEM image of the polished diamond surface before the film growth.

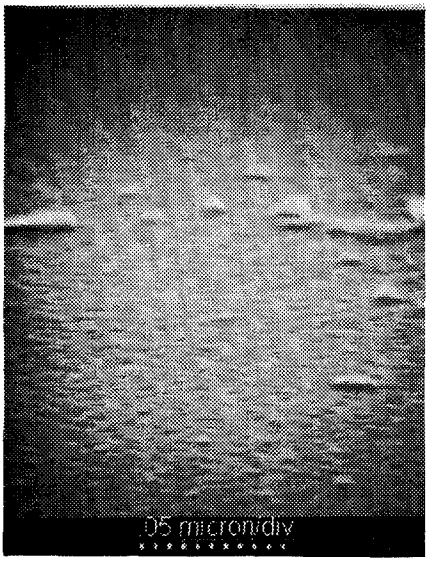

Figure 2(b): SEM image of 100 Å Cu/10 Å Fe/C(100).

In Fig. 2(b), we show a similar edge-on SEM image which was obtained from the surface of a 100 Å Cu film grown on the fcc-Fe/C(100). The electron diffraction shows a single-crystal pattern, with no trace of C or Fe in the Auger spectrum. In the SEM image it can be seen that the .05 μm ripples are still evident, with some larger-scale contamination which is due to transferring *ex-situ* from the growth facilities to the SEM. From Fig. 2(b) in conjunction with the RHEED data of Ref. [5] and the Cu EXAFS data of Ref. [4], it is clear that the copper layer grown on the thin, fcc-Fe/C(100) is a continuous, oriented, single crystal layer.

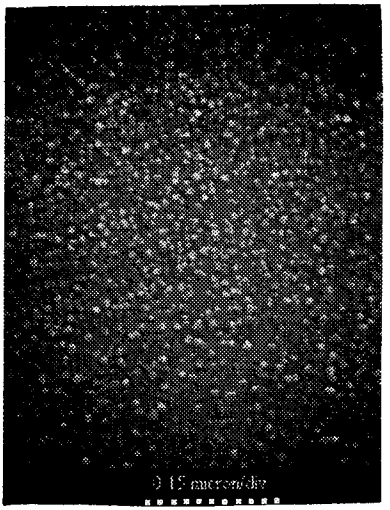

Figure 3(a):4.5 $\times$ 5.7μ SEM image, top view, of 100 Å Cu/20 Å Fe/C(100).

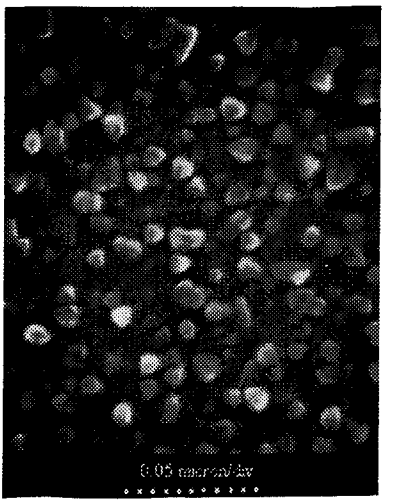

Figure 3(b): 1.5 $\times$ 1.9μmSEM image, top view, of 100 Å Cu/20 Å Fe/C(100).

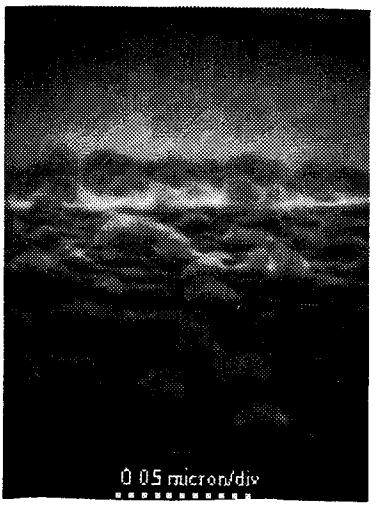

Figure 3(c): SEM image, edge view, of 100 Å Cu/20 Å Fe/C(100).

For growth of Cu on the thick, polycrystalline, bcc-Fe seed layers, however, a much rougher surface is evident in the SEM images. Images from this surface are shown in Fig. 3(a)-(c). In Fig. 3(a) a top view of the surface is shown, and it can be seen that a film with a uniform granularity has formed. A higher magnification of this same top view is shown in Fig. 3(b). Here, the crystalline nature of the granules is evident as straight edges on the grain boundaries. The measurement of the grain orientation is limited by the current resolution of this SEM study, however, and a higher resolution study with, e.g., scanning tunneling microscopy, may be able to correlate the orientation of the Cu grains to the structure of the underlying Fe seed. A side view of the Cu film grown on the thick, bcc-Fe seed is shown in Fig. 3(c). This image was taken with the SEM beam at 90° to the sample normal. The profiles of

the Cu islands can be seen at the horizon of the picture, while the foreground shows Cu islands in a slight dip on the edge of the crystal. From this view it can be seen that a few of the Cu islands are up to 1000 Å high, while most of the islands are much lower. Since the total Cu thickness is only 100 Å, this indicates that there is considerable mobility at this growth temperature (300° C) of the Cu atoms on the surface. An interesting aspect of the Cu islands in Fig. (3) is that the width of the islands appears to be quite uniform ($\approx 0.1\mu$m), while the height varies. We are currently conducting studies into the relationship between the structure of the Fe seed and the dynamics of the Cu growth in order to understand this aspect of the data.

Summary

EXAFS data shows that fcc-Fe can be grown up to at least 10 Å thick on C(100) by deposition at low temperature and subsequent annealing to 350° C, while 20 Å of Fe forms a polycrystalline bcc film. These two thicknesses of Fe were used as seed for the subsequent growth of a Cu cap layer. The Cu cap layer was studied with SEM, and is observed to grow as a single layer on the thin, fcc-Fe seed, and in islands on the thick, bcc-Fe seed layer. From this study it can be concluded that fcc-Fe seeds are useful for growth of lattice matched materials such as Cu(100). We expect the use of synthetic diamond substrates for the growth of such transition metal films and multilayers to become more widespread for economic purposes because they are inexpensive and reusable, and from a scientific aspect because they have desirable optical properties, high thermal conductivity, and a high resistivity.

REFERENCES

1. L.M. Falicov, D.T. Pierce, S.D. Bader, R. Gronsky, K.B. Hathaway, H. Hopster, D.N. Lambeth, S.S.P. Parkin, G. Prinz, M. Salamon, I.K. Schuller, and R.H. Victora, J. Mater. Res. **5**, 1299 (1990).
2. M.W. Geis, J.C. Angus, Scientific American **267**, 84 (1992).
3. T.P. Humphreys, *et. al*, Mat. Res. Soc. Symp. Proc. **202**, 463, 1991.
4. D.P. Pappas, J.W. Glesener, V.G. Harris, J.J. Krebs, Y.U. Idzerda, A.A. Morrish, and G. A. Prinz, Mat. Res. Soc. Symp. Proc. **313**, 369 (1993).
5. D.P. Pappas, J.W. Glesener, V.G. Harris, Y.U. Idzerda, J.J. Krebs, and G.A. Prinz, Appl. Phys. Lett., **64**, 28 (1994).
6. D.D. Chambliss, K.E. Johnson, K. Kałki, S. Chiang, and R.J. Wilson, Mat. Res. Soc. Symp. Proc. **313**, 713 (1992).
7. C. Wan-rong and W.U. Zi-qin, Chinese Physics **3**, 299 (1983).
8. S.A. Chambers, T.J. Wagener, and J.H. Weaver, Phys. Rev. B **36**, 8992 (1987).
9. C. Liu, E.R. Moog, and S.D. Bader, Phys. Rev. Lett. **60**, 2422 (1988).
10. C.S. Wang, B.M. Klein, H. Krakauer, Phys. Rev. Lett. **54**, 1852 (1985).
11. In *X-Ray Absorption Principles, Applications, Techniques of EXAFS, SEXAFS, and XANES*, ed. by C.C. Koningsberger and R. Prins (Wiley, New York 1988).
12. J.J. Rehr and R.C. Albers, Phys. Rev. B **41**, 8139 (1990).

SOLID-PHASE REACTION OF TUNGSTEN THIN FILMS WITH POLYCRYSTALLINE DIAMOND

A. BÄCHLI, J. S. CHEN, R. P. RUIZ* AND M-A. NICOLET
California Institute of Technology, Pasadena, CA 91125
* Jet Propulsion Laboratory, California Institute of Technology, CA 91109

ABSTRACT

The thermally induced solid-phase reaction of 135 nm thick sputter-deposited W films with polycrystalline CVD-grown diamond substrates is investigated. The samples are annealed in vacuum ($5x10^{-7}$ torr) at temperatures between 700 °C and 1100 °C for 1 hour and examined by 2 MeV $^4He^{++}$ backscattering spectrometry, x-ray diffraction, and scanning electron microscopy.

The as-deposited W films contain roughly 5 at.% oxygen. After annealing the samples at 800 °C this oxygen concentration falls below the detection limit of less than 1 %. Incipient W_2C phase formation occurs during annealing at 900 °C. The final state, the WC phase, is reached after annealing at 1100 °C.

I. INTRODUCTION

Films of polycrystalline diamond are now commercially available. The fabrication of electronic devices, thermal conductors, grinding tools, optical windows as well as other anticipated applications require that such diamond films be bonded at one place or another to metals. The question thus arises how polycrystalline diamond films react thermally with various metals.

The properties of the interfaces thus formed are of great interest. Some work has been published on the mechanical and electrical properties of thin film diamond-metal contacts.[1] Understanding and control of such contacts, however, will necessitate a detailed clarification of the reactions that occur upon thermal treatments. So far such reactions have been investigated on polycrystalline diamond only for few metals.[2,3]

While no reaction is expected for some metals (Al, Au, ...), the formation of compounds should occur with carbide-forming metals. The identification of the newly-formed phases is straight forward, since the carbides have been extensively studied for over a century and are now widely used, mostly because of the high melting points of the carbides and their extreme hardness.[4]

In the present study we investigate the solid-state reaction between sputtered tungsten films and two different types of polycrystalline diamond substrates at temperatures between 700 °C and 1100 °C to determine the phases formed during the annealing.

Mat. Res. Soc. Symp. Proc. Vol. 339. ©1994 Materials Research Society

II. EXPERIMENTAL PROCEDURES

The two different types of diamond films used as substrates in this study vary in their surface morphology, as can be seen in Fig. 1: The majority of the experiments reported here were performed with 350 µm thick free-standing square-shaped diamond films with a side lengths of 5 mm (type "A"). For comparison, the experiments were repeated with 1.3 µm thick diamond films on Si wafers (type "B"). The free standing type A films had been obtained by removing them from their substrate after chemical vapor deposition. It is the side originally facing the substrate that was used for the W deposition because this face is macroscopically smooth. Microscopically, the surface morphology consists of flat-topped mesas which are about 0.5 µm in diameter and separated by many deep interstices as seen in Fig. 1a. The type B diamond films were grown by the tantalum hot-filament-assisted chemical vapor deposition on Si (100) wafers. At the surface the size of the grains ranges from 50 to 1000 nm (Fig. 1d) and this surface appears shiny and smooth to the eye.

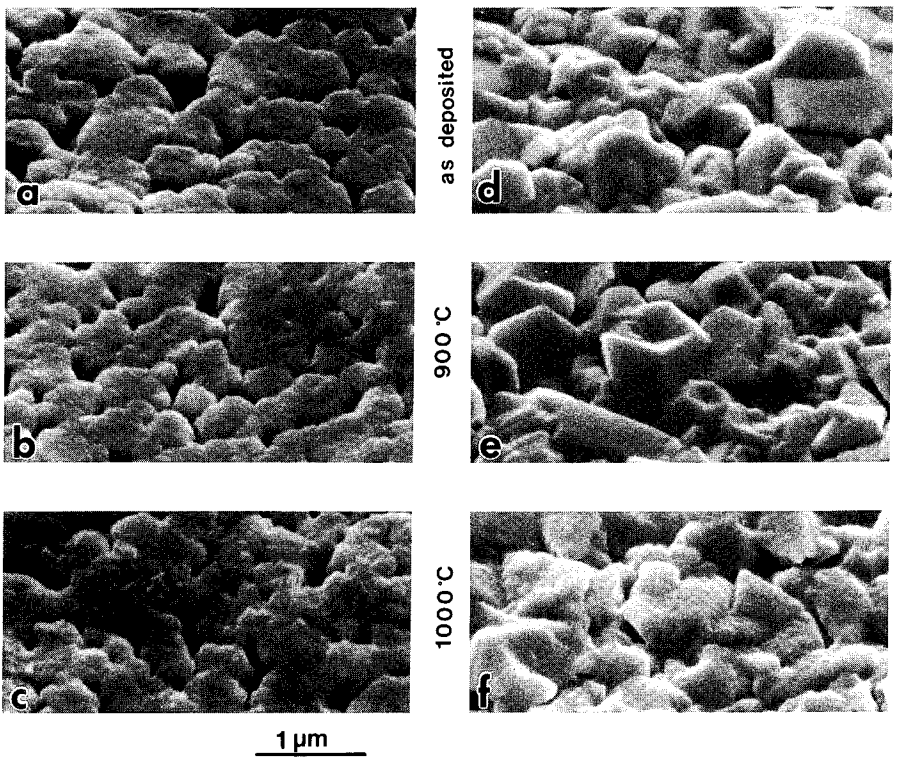

Figure 1 Scanning electron micrographs of diamond samples with a 135 nm thick W layer viewed at an angle of 45 °: after metal deposition (a,d), after annealing at 900 °C (b,e), and after annealing at 1000 °C (c,f), each for one hour. The diamond substrates of the samples on the left are free-standing 350 µm thick plates ("type A "), those on the right are 1.3 µm thick layers grown on Si (100) wafers ("type B").

Prior to the tungsten deposition the diamond films were degreased in ultrasonically agitated organic solvent baths. Tungsten films of 135 nm thickness were deposited by rf-magnetron sputtering with Ar gas in an oil-free vacuum of $2x10^{-7}$ Torr base pressure. The samples were annealed in a vacuum tube furnace ($5x10^{-7}$ Torr) at 700, 800, 900,1000, or 1100 °C for one hour.

Compositional analysis was carried out by 2 MeV $^4He^{++}$ backscattering spectrometry. Structural information was obtained by x-ray diffraction with a collimated Co K_α beam incident on the sample at a glancing angle of 15 ° and an Inel position-sensitive dedector. Morphological changes were observed by scanning electron microscopy.

III. RESULTS

The phase diagram of the W-C system[5] shows two phases at 2000 °C. At this temperature, the hexagonal α-W_2C phase exists over a 2 at.% range around 38.5 at.% C. For lower temperatures the stability of W_2C is uncertain as some phase diagrams show an eutectoid $W_2C \leftrightarrow W+WC$ at 1250 °C while others suggest that the W_2C phase is stable down to low temperatures. The hexagonal WC is a stoichiometric compound. There is a small carbon solubility in W with its maximum of 0.7 at.% at 2715 °C.

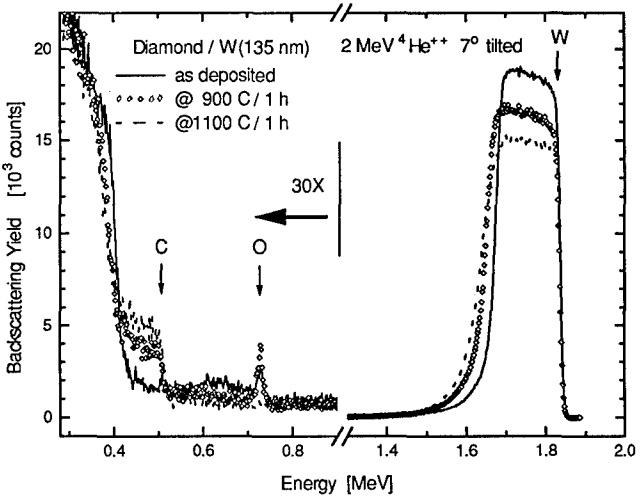

Figure 2 2 MeV $^4He^{++}$ backscattering spectra of type A diamond samples with an overlain 135 nm thick W film before and after annealing at 900 and 1100 °C. The samples were tilted 7 ° against the incident beam direction. The scattering angle of the detected particles is 170 °.

Fig. 1 shows the surface of the different samples viewed at an angle of 45 ° after W deposition (a, d) and after annealing at 900 °C (b, e), and annealing at 1000 °C (c, f). The overall appearance is dominated by the morphology of the respective diamond substrates and does not change during annealing. However, there is a discernible roughening of the surface after annealing at 900 °C that becomes even further pronounced after annealing at 1000 °C, which can be explained by the volume expansion of 30 % that goes along with the transformations from W to WC.

The backscattering spectra of the W on type A diamond as-deposited, annealed at 900 °C, and annealed at 1100 °C are shown in Fig. 2. The data extracted from such backscattering spectra are given in Table I.

Table I Oxygen content and carbon concentration in the reacted metal layer on type A diamond extracted from backscattering spectra such as the ones shown in Fig. 2, and the phases detected by x-ray diffraction.

temperature [°C] (1 hour duration)	O [at.%]	C [at.%]	x-ray
as-deposited	5	-	W, W_3O
700	5	-	W, W_3O
800	-	6	W
900	-	34	α-W_2C, WC
1000	-	45	WC, α-W_2C
1100	-	47	WC

The spectrum of the as-deposited sample (solid line) reveals no detectable amount of C in the film. However, there is some O at the surface as well as in the bulk of the W film. Comparing the areas under the W and O signal (omitting the surface peak), we calculate[6] an O content in the metal of about 5 at.%. From the energy width of the W signal we infer the film's thickness of the as-deposited W film to be 135 nm, assuming bulk density. The W deposited in the interstices between the grains (see Fig. 1a) generates the low-energy tail seen in the W signal of every backscattering spectrum. Annealing at 700 °C leaves the spectrum unchanged. First changes can be observed after the annealing at 800 °C. There is now C in the film whose concentration in the surface layer (30 nm) is about 6 at.%. Oxygen in the bulk of the W can not be detected any longer but the signal which stems from oxygen at the surface remains. The backscattering spectrum of the sample annealed at 900 °C (diamonds in Fig. 2) reveals considerable interdiffusion of C and W. The C concentration is about 34 at.%. This result suggest that W_2C has formed. After a 1000 °C annealing the composition of the film changes once more uniformly throughout its thickness to a carbon content of 45 at.% and all the O has disappeared from the surface. Annealing at 1100 °C modifies the spectrum only by a small increase of the carbon content in the film from 45 to 47 at.%. This atomic composition is very near that of WC. We therefore conclude that the final state is reached by annealing at 1100 °C for one hour.

The x-ray diffraction patterns shown in Fig. 3 confirm that the formed compounds are W_2C and WC. For all spectra in this figure, the main peaks at 2Θ = 51.5 °, 90.4 °, and 112.7 ° originate from the diffraction of the 350 µm thick polycrystalline diamond substrate. The other peaks are labeled W (+), W_2C (o), and WC (*). The diffraction peaks in the spectrum of the as-deposited sample are those of α-W.[7] The presence of oxygen in the as-deposited films, which is obvious in the backscattering spectrum (Fig. 2), can be seen here as well: the intense peaks of the W_3O (β-tungsten) which don't interfere with diamond or with α-W peaks can be detected in the background. The most visible of these peaks is marked β in Fig. 3. No new peaks appear after annealing the sample at 800 °C, but the W peaks sharpen as the grains grow and the W_3O peaks disappear. Most of the peaks in the spectrum of the sample annealed at 900 °C can be assigned to the α-W_2C phase. Some of the intense WC peaks show that a next phase has already started to grow at 900 °C. In the sample annealed at 1000 °C some α-W_2C peaks are still detectable, but the WC phase dominates clearly. Annealing at 1100 °C leads to an increased intensity of the WC peaks.

The experiments presented so far were all performed on type A diamond samples. Backscattering and x-ray analyses showed that the reaction evolves on type B diamond samples in the same way as described so far. Only the corresponding temperatures change slightly as follows (the numbers in parenthesis give the corresponding tempera-

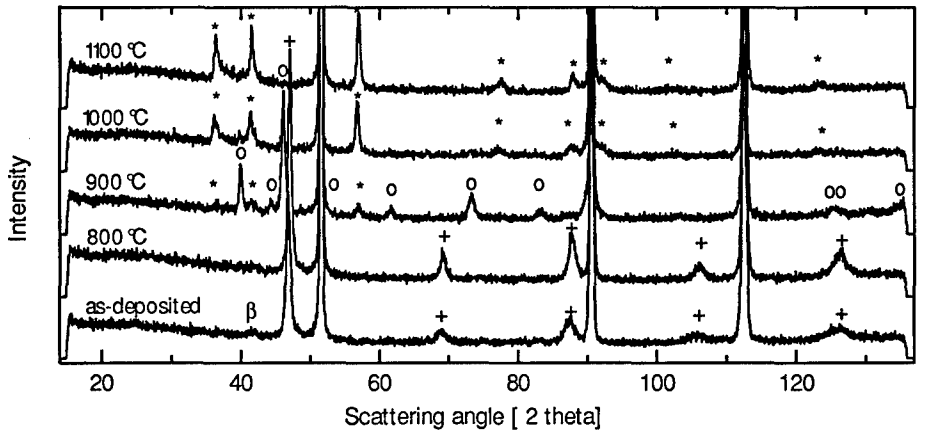

Figure 3 X-ray diffraction spectra for Co K_α radiation of Type A diamond samples with an overlain 135 nm thick W film annealed for 1 hour at the indicated temperatures. The peaks of the W (+), W_2C (o), and WC (•) phase are labeled. The three unmarked intense peaks stem from the polycrystalline diamond substrate. The β stands above the most visible W_3O (β-tungsten) peak .

tures for the reaction on type A diamond): The first forming phase is W_2C which starts to form at 800 °C/ 1h (900 °C). This phase dominates clearly after annealing at 900 °C/ 1h (900 °C) and the final state is reached after annealing at 1100 °C/ 1h (1100 °C). The measurements on type B diamond give different snapshots of the same evolving reaction pattern. A noteworthy detail in the backscattering spectrum of the type B sample annealed at 800 °C is the presence of a distinct step at the top of the W signal near 1.78 MeV. Its lower level coincides with that of W_2C and clearly indicates that the largest amount W_2C phase initially formed begins to grow at the surface of the sample.

IV. DISCUSSION

Why the oxygen initially present in the tungsten film disappears upon annealing of the sample between 700 °C and 800 °C can be explained by several thermal processes and reactions with volatile products : (i) At 725 °C the W_3O decomposes into W and the two volatile oxides WO_2 and WO_3.[4] (ii) Carbon may be involved in the reaction, since some C has diffused throughout the W film already at 800 °C (see Table I). Reactions such as $WO_3 + C \leftrightarrow WC + (CO \text{ and/or } CO_2)$ are well known to people producing WC by carburization of WO_3 with solid carbon.[8] (iii) Oxygen is known to diffuse rapidly in W and in Mo films even at temperatures below 800 °C.[9]

Silicon and diamond are both group IVB elements, have the same type of bonding and the same crystal structure. Thus we can expect similarities in the thermal reaction behaviour between metal/diamond and between metal/Si couples. The latter have been investigated extensively during the last two decades. The Walser-Bené rule,[10] which holds for the majority of the metal-Si combinations, says that the first silicide that forms is the highest congruently melting compound next to the lowest-melting eutectic in the

phase diagram. In the system investigated here, the lowest melting eutectic is at 22 at.% C and the highest (and only) congruently melting compound next to it is the W_2C. This compound is indeed observed first. The Walser-Bené rule holds for the tungsten-diamond reaction, too.

However, the reaction of a W film with diamond is expected to also differ from the way a metal film reacts with Si. A major difference relates to the ratio of the species' size: the metallic radius of Si is within about 15 % of all transition metal radii except Zr, Hf and the IIIB metals, but the radius of C is 35 % smaller than that of W. A consequence of this size ratio is the very high diffusivity of C in W.[11] We observed that W_2C initially grows inward, starting from the open tungsten surface, which shows that C diffuses through the tungsten film more rapidly than the rate at which the carbide nucleates and grows at the tungsten-diamond interface. Although it takes the results of an experiment performed with an inert marker on a laterally uniform sample to unambiguously support the claim, it is obvious that carbon must be the dominant moving species in the W_2C reaction, and probably in the transformation of W_2C to WC as well.

V. CONCLUSION

Isothermal annealing of thin tungsten films on polycrystalline CVD diamond for one hour leads to solid-state reactions in the temperature range from 800 °C to 1100 °C. Oxygen impurities disappear from the bulk of the film at 800 °C. The first phase detected is W_2C, as predicted by the Walser-Bené rule. W_2C forms first at the open metal surface and not at the metal-diamond interface. The final phase WC is reached after annealing at 1100 °C for one hour.

Acknowledgments

This project was supported in part by the Swiss National Science Foundation. The diamond substrates have been supplied by the Norton Company (Northboro, Ma) and by CSEM (Neuchâtel, Switzerland). Their generous and essential contribution to this work is thankfully acknowledged. We thank R. Gorris and M. Easterbrook for their technical assistance.

1 K. Das, V. Venkatesan, K. Miyata, D.L. Dreifus, J.T. Glass, Thin Solid Films, **212** 19 (1992).
2 J.S. Chen, E. Kolawa, F.S. Pool, M-A. Nicolet, Thin Solid Films, **236** 72 (1993).
3 C.R. Guarnieri, F.M.d'Heurle, J.J.Cuomo and S.J. Whitehair, Appl. Surf. Sci., **53** 115 (1991).
4 H.J. Goldschmidt, Interstitial Alloys, 1st ed. (Butterworths, London, 1967).
5 H. Okamoto, Binary Alloy Phase Diagrams Updating Service, Dec. 1992 Supplement.
6 W.K. Chu, J.W. Mayer and M-A. Nicolet, Backscattering Spectrometry (Academic Press, New York, 1978).
7 JCPDS Cards (1993) W: 4-0806; α-W_2C: 35-776; WC: 25-1047; W_3O: 2-1138
8 P. Schwarzkopf and R. Kieffer, Refractory Hard Metals, (The Macmillan Company, New York, 1953) pg. 51.
9 G. Bomchil, G. Göltz and J. Torres, Thin Solid Films **140** 59 (1986).
10 R. Walser and R. Bené, Appl. Phys. Lett. **28** 624 (1976).
11 Landolt-Börnstein, New Series **III/26** 495 (1990).

PART V

Diamond Growth

CHEMICAL REACTION MECHANISMS OF DIAMOND GROWTH

MICHAEL FRENKLACH
Department of Materials Science and Engineering, The Pennsylvania State University, University Park, PA 16802

ABSTRACT

It is becoming increasingly apparent that future progress in diamond chemical vapor deposition depends on deeper understanding of the underlying mechanism of surface processes. Substantial efforts toward this goal have led to several conclusions on which consensus is beginning to emerge. Among them are the mediating role of hydrogen atoms, generic features of the growth kinetics, thermodynamic stability of reconstructed (100) surfaces, and the insertion reaction of methyl into (100)–(2×1) dimers. Despite these efforts, an overall picture of diamond growth in terms of elementary processes is still lacking. In this paper, the current state of mechanistic understanding is reviewed, emphasizing common themes, and new results are presented. Among the latter are the effect of reaction reversibility on surface morphology, surface migration, and a new mechanism for diamond growth from acetylene.

INTRODUCTION

In spite of substantial progress in technological aspects of chemical vapor deposition (CVD) of diamond films,[1,2] the underlying chemical reaction mechanism of diamond growth remains poorly understood. It is becoming increasingly apparent that future progress in diamond chemical vapor deposition depends on deeper understanding of the fundamental surface processes. Substantial efforts toward this goal have led to several conclusions on which consensus is beginning to emerge. The objective of the present paper is to review the current state of mechanistic understanding, to identify the key problems, and to present new theoretical findings.

The discussion is organized into two principal parts: the first has its focus on generic features of diamond growth kinetics, where nearly complete consensus has been approached, and the second on elementary surface reactions, an area of uncertainty and scientific challenge.

GENERAL KINETIC FEATURES

Independent of specific surface reactions which govern the incorporation of a gaseous precursor into the diamond lattice, there appears to be growing consensus on the general feature of diamond growth reaction kinetics: the formation of an active diamond growth site by H abstraction followed by the addition of a carbonaceous gaseous species to this surface radical. Suggested first by Frenklach and co-workers[3-6] and now reiterated by others,[7-10] the process can be schematically represented by the following set of reactions

$$C_dH + H \xrightarrow{k_1} C_d^{\bullet} + H_2 \qquad (1)$$

$$C_d^{\bullet} + H \xrightarrow{k_2} C_dH \qquad (2)$$

Mat. Res. Soc. Symp. Proc. Vol. 339. ©1994 Materials Research Society

$$C_{d}\bullet + C_nH_m \xrightarrow{k_3} \text{products} \qquad (3)$$

where C_dH denotes C–H surface sites on a diamond surface and $C_d\bullet$ their radicals.

The significance of this generic reaction scheme is several-fold: first, the nature of the active site for diamond growth is identified to be a surface radical, $C_d\bullet$; second, the formation rate of these surface radicals is determined by the rate of H abstraction, reaction 1; and third, the formation of the surface radicals is balanced by their recombination with gaseous H atoms, reaction 2. The latter proceeds with an essentially collisional rate and no other reactions of gaseous species can compete with it. The balance of reaction fluxes of (1) and (2) leads to the following expression for the surface fraction of radicals $C_d\bullet$

$$r \equiv \frac{\chi_{C_d\bullet}}{\chi_{C_dH} + \chi_{C_d\bullet}} \approx \frac{\chi_{C_d\bullet}}{\chi_{C_dH}} = \frac{k_1}{k_2} \qquad (4)$$

where $\chi_{C_d\bullet}$ and χ_{C_dH} are the number of radical and non-radical surface sites per unit area, respectively, and k_1 and k_2 are the rate coefficients of reactions 1 and 2, respectively. This result, first noted by Frenklach and Wang,[6] implies that the fraction of surface radicals, defined by r in Eq. 4, is essentially independent of H atoms and is a function of temperature only. At 1200 K, the surface fraction r is equal to about 0.1.

Following further the reaction scheme 1–3, the rate of adsorption of a gaseous precursor on a diamond surface is given as

$$\text{Rate} = k_3 [C_nH_m] \chi_{C_d\bullet} \qquad (5)$$

where k_3 is the rate coefficient of reaction 3 and $[C_nH_m]$ the gas-phase concentration of a hydrocarbon precursor in the diamond deposition zone. Dividing Eq. 5 by χ_{C_dH}, we obtain

$$R_{C_nH_m} = k_3 [C_nH_m] \frac{\chi_{C_d\bullet}}{\chi_{C_dH}} = r\, k_3 [C_nH_m] \qquad (6)$$

This defines the *per-site* rate of hydrocarbon adsorption, $R_{C_nH_m}$. Similarly, we define per-site rates of H-abstraction $R_{abs} = k_1[H]$ and H-addition $R_{add} = k_2[H]$. These per-site rates provide critical time scales for the analysis of specific reaction mechanisms, as will be demonstrated later in the text.

The incorporation into the diamond lattice of the species adsorbed in reaction 3 is initiated either by H abstraction[11] or H-addition,[12] depending on the nature of the adsorbate. In either case, the rate of diamond growth should depend on the flux of hydrogen atoms arriving at the growing surface. This provides a unifying feature exposed in a recent analysis of Cappelli and Loh[13] and that of Goodwin.[10]

There is also a general agreement on the *parallel* reaction kinetics for the formation of non-diamond phase,[6,9,10,14] in this sense following the ideas of Fedoseev and co-workers.[15] The specific form differs from author to author, perhaps reflecting the uncertain nature of the defects which may include voids, amorphous carbon, graphite, or combinations of them. Thus, for instance, Goodwin[10] suggested second-order surface kinetics for the formation of defects, while Frenklach and Wang[6] introduced a reversible $sp^3 \Leftrightarrow sp^2$ transformation,

$$C_d\bullet \rightleftharpoons C_g + H \qquad (7)$$

and surface condensation of aromatics[16] to account for the non-diamond phase. In Eq. 7, C_g denotes an sp^2-type carbon site. The reversibility of reaction 7, on a global scale, has been observed in theoretical calculations of Davidson and Pickett[17] and the reverse of reaction 7 has been explored by Angus and co-workes[18] for diamond nucleation on graphite edges. Several surface reactions discussed in the next section provide specific examples for the type of processes reaction 7 may represent.

The kinetic features discussed above seem to provide a generic mathematical form for the rate of diamond growth. Nonetheless, individual reaction mechanisms may alter specific details and thus affect the predictive capabilities of such models. Furthermore, mechanistic details may affect the predicted surface morphology of the growing film. This is illustrated in Fig. 1, which depicts the results of sterically-resolved dynamic Monte Carlo simulations for diamond growth. The process of diamond growth was modeled[19] as a Markovian sequence of collisions between gas-phase species and the growing surface. The outcome of an individual collision between a given gaseous species and a given surface site was determined by its probability, which was assumed to be equal to the product of the conditional probability of reaction to occur upon this collision and the probability of the collision to occur. Each simulation started with a 100×100 carbon site ideal diamond (001) plane. The growth was assumed to follow a combined methyl-and-acetylene reaction mechanism:[19] the addition of gaseous methyl radicals and acetylene molecules to surface radical sites, when such additions were allowed sterically, i.e., when the repulsion exerted on the atoms of the chemisorbing species was not substantial.

Shown in Fig. 1 are the results of two runs performed under exactly identical conditions, except that the addition of methyl was assumed to be reversible in one run and irreversible in the other. The film growth rates, averaged over the model surface, were computed to be the same in the two cases. However, the two results differ markedly in the predicted surface roughness: a much smoother film is obtained when the methyl addition is assumed to be reversible (see Fig. 1). This is explained as follows. During the deposition, the surface is saturated with chemisorbed methyl groups. Some of these groups are adsorbed at surface sites at which incorporation of the groups into the diamond lattice is not possible. At the same time, each adsorbed CH_3 inhibits, due to steric repulsion, adsorption of other CH_3 groups at near-by sites. Thus, when the adsorption of CH_3 is assumed to be irreversible, parts of the surface remain permanently blocked, resulting in a rough surface morphology. When the adsorption of CH_3 is assumed to be reversible, such blocking CH_3 groups are eventually desorbed, thus providing another opportunity for CH_3 adsorption at sites capable of incorporating the incoming CH_3 into the diamond lattice.

Although these results are obtained for a specific reaction mechanism, the phenomenon observed should be rather of general nature. This underscores further the necessity of establishing surface reaction mechanisms at a detailed, elementary level. A brief review of the subject is given below.

SURFACE REACTION MECHANISMS

Methyl radicals and acetylene molecules are the most abundant gaseous species present in the deposition zone of hot-filament, flame, and plasma-assisted diamond CVD reactors as determined experimentally[20-28] and predicted computationally[6,29-32]. Hence, those surface reaction mechanisms which employ either CH_3 or C_2H_2 as a growth species were given the most attention and are reviewed below.

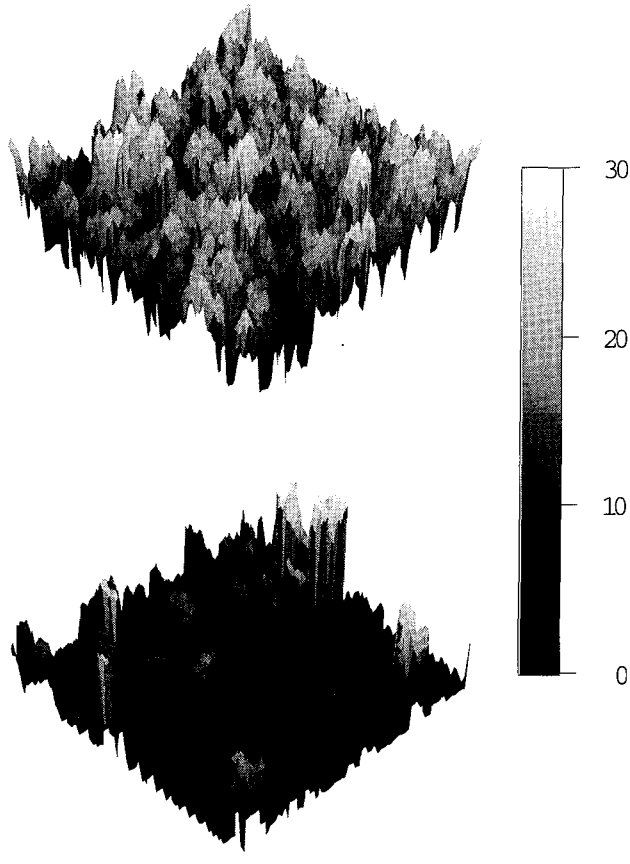

Figure 1. Surfaces obtained in sterically-resolved dynamic Monte Carlo simulations of diamond growth on a (001) plane composed of 100×100 carbon atom sites using a methyl-and-acetylene-addition reaction mechanism and assuming the methyl addition step to be reversible (top panel) or irreversible (bottom panel). The color scale on the right is the number of carbon layers in the [001] direction.

Methyl Growth Mechanisms

Generally, C_1-hydrocarbons have been assumed to be the sole growth species simply following a one-carbon-at-a-time picture. Recent isotope labeling experiments,[33,34] reporting that about 90 % of deposited diamond originates with methane and its radicals, support this point of view. A series of less direct experiments[35] echo this conclusion.

Proposals have been made invoking CH_5^+ ions[15] and CH_4 molecules[36] but without suggesting possible reactions. The mechanism suggested by Tsuda et al. that implicated either gaseous methyl cations[37] or the presence of a positive charge on the surface,[38] faces two major difficulties. First, the critical role of ions or electrostatic charges has not been corroborated by experiment; and second, a prohibitively strong repulsion exists among methyl groups required to be adsorbed at three neighboring sites of the (111) surface. This repulsion has been computed at different levels of theory: empirical, using Brenner potential;[39] quantum semiempirical, using AM1[40] and ASED-MO[41] methods; and local density approximations.[42]

While the adsorption of three neighboring methyl groups seems to be essentially forbidden, the adsorption of two neighboring methyl groups meets only a moderate repulsion.[41-43] The formation of a C–C bond between these two methyls encounters a substantial potential energy barrier, ~50 kcal/mol, if only one of the two is activated by H abstraction.[43] Such relatively large barriers are typical for the addition of a primary hydrocarbon radical to a hydrogen-saturated carbon atom.[44,45] When both methyl groups undergo H abstraction, the C–C bond should be formed quickly and irreversibly as is typical of radical combination.[43] However, the produced $-CH_2-CH_2-$ adspecies is kinetically unstable under the conditions of diamond CVD.[12] Abstraction of an H atom from one of these CH_2 sites will be followed by a β-scission and ultimate desorption of the $-CH=CH_2$ group. This sequence of events limits the rest of the proposed CH_3-based mechanisms of diamond growth on (111) and (110) surfaces.[8,46,47]

The most promising in terms of mechanistic understanding appears to be the growth on (100) surfaces. The growth on (100) surfaces by incorporation of C_1H_X hydrocarbon radicals has been advocated from considerations of surface morphology.[48,49] Harris[7] proposed a specific reaction mechanism in which the growth is initiated by the addition of CH_3 to a radical created on a dihydride surface. After an H atom is abstracted from the adsorbed CH_3 and another H is abstracted from the neighboring surface site, the two radicals combine, forming a next-layer diamond site. The principal difficulty with this mechanism is the strong repulsion exerted on the incoming CH_3.[50] In fact, due to the repulsion between closely spaced hydrogen atoms, the dihydride surface itself was suggested to be thermodynamically unstable at typical CVD conditions and to reconstruct to a monohydride phase.[51] Such reconstruction was observed experimentally[52-56] and supported by theoretical calculations.[50,51,57-60]

Based on these considerations, it has been proposed[50,61] that the growth takes place on a reconstructed, (100)-(2×1) surface, initiated by the addition of CH_3 to a radical site of the surface dimer unit. Following an H abstraction from the adsorbed CH_3, the produced CH_2 adradical is incorporated into the diamond lattice by opening the dimer and forming a bridge between the dimer carbons. We will refer to such a site as a CH_2-bridge site or simply, in the context of the present discussion, a *bridge* site. In one of the proposed mechanisms,[50] the CH_2 adradical forms a C–C bond with the second carbon site of the dimer simultaneously with the cleavage of the dimer bond. This one-step reaction was found to possess a substantial potential energy barrier. In the other mechanism,[61] the reaction proceeds in two steps

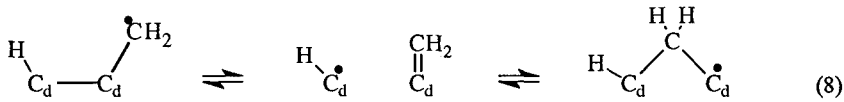

(8)

This two-step reaction mechanism appears to be energetically and kinetically feasible, as determined by using empirical,[61] quantum ab initio,[11] and quantum semiempirical[12] potentials. The feasibility of this reaction is further supported by the thermodynamic stability of the dimer monoradical,[12,59] defying in this case the β-scission rule.

However, reaction 8 alone cannot explain propagation of diamond growth, as it only "fills in" the dimer sites and does not address the growth between the nascent bridge sites. Two proposals were made regarding this issue. In the mechanism of Harris and Goodwin,[11] after one CH_3 group is inserted into a dimer, another CH_3 is chemisorbed to a nearby radical of the next-row dimer. A subsequent H abstraction forms a bridge site next to the first one. However, as will be dicussed later, once CH_3 is chemisorbed to a dimer radical, it is more likely to insert into that dimer than to bridge to the adjacent bridge site. To resolve this difficulty, Zhu et al.[62] suggested that after the first step of reaction 8 and before the second one, surface radical migration

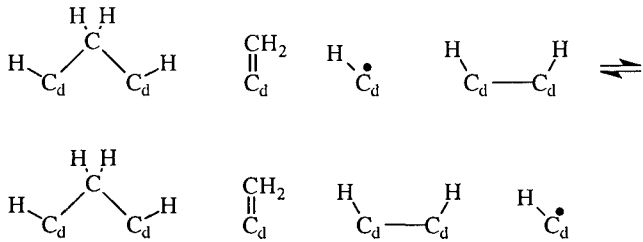

(9)

takes place, followed by the eventual addition of the lone chemisorbed CH_2 group at the initial bridge site. That reaction 9 is facile was based on a relatively small endothermicity, 6 kcal/mol, computed[62] using MM3 molecular mechanics.[63] However, a thermochemical analysis[64] indicates that reaction 9 is not effective in competing with the second step of reaction 8. Furthermore, neither the mechanism of Harris and Goodwin[11] nor that of Zhu et al.[62] can resolve the difficulty arising with CH_3 being adsorbed not at the near-by site but at the remote site of the dimer, as e.g. shown below

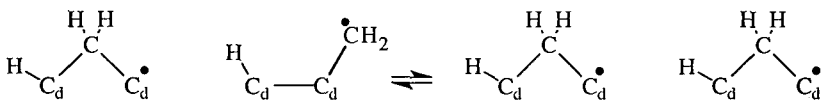

(10)

The configuration formed in such a case—two bridge sites separated by a *void* site—has the geometry of a dihydride (100) site and, as mentioned above, exerts a large steric repulsion on the adsorption of CH_3. Thus, the occurrence of reaction 10 should result in a highly defective film or cease the growth altogether, contrary to the experimental evidence reviewed by Harris and Goodwin[11] and Zhu et al.[62] A remedy to such disruptive growth, suggested by the latter authors,[62] is the removal of undesirable bridge sites by the reverse of reaction 8. This

requirement, however, should substantially slow down the growth, again contrary to experiment. Another possibility would be to fill in the void sites by species other than methyl. For instance, Imai et al.[65] performed PM3-level quantum chemical calculations and found no potential energy barriers for the addition of CH or CH_2 to a $C_{11}H_{18}$ cluster simulating such a dehydrogenated void site. Yet, the concentrations of these species are expected to be orders of magnitude lower than that of CH_3 in the deposition zone of hot-filament reactors,[6,21,24,29] i.e., under the conditions capable of producing high quality diamond films.

Recently, chemical reactions of methyl radicals on (100) diamond surfaces have been investigated by quantum-mechanical calculations at the PM3 semiempirical level performed on a series of small and large size clusters.[64] Among a variety of possible chemisorption sites considered, surface dimer radicals were found to be not only the most favorable on kinetic grounds, but the only type capable of sustaining the subsequent incorporation of adsorbed methyl groups into the diamond lattice. Migration of a hydrogen atom from one surface site to another, like

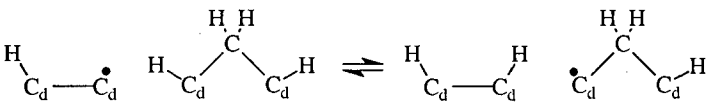

(11)

or from a chemisorbed CH_3 group to a neighboring surface radical, like

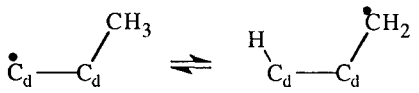

(12)

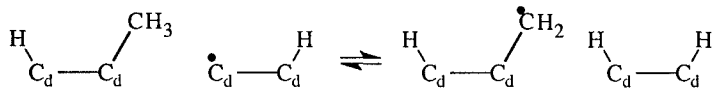

(13)

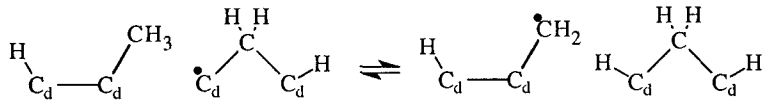

(14)

was found to be faster than the H addition and H abstraction reactions and therefore to provide redistribution of radical sites on the reacting surface. For instance, due to fast H migrations, the probability of having a dimer radical near a bridge site is decreased by more than one order of magnitude. The decreased lifetime of a dimer radical when it neighbors a bridge site decreases the rate of the CH_3 incorporation into void sites as compared to the CH_3 insertion into dimers. In other words, these results do not support the "trough" mechanism suggested by Harris and Goodwin[11] to explain the growth of diamond.

One of the most important findings of our recent study[64] is the migration of CH_2 groups on diamond (100) surfaces,

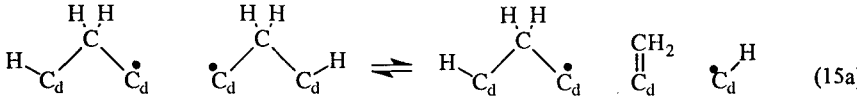

(15a)

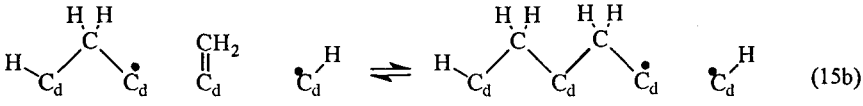

(15b)

The migration was found to be feasible on both kinetic and thermodynamic grounds and offers the most likely explanation for the formation of smooth surfaces observed experimentally. Being an essential part of the diamond growth mechanism, the migration of CH_2 can be viewed as surface "diffusion" of bridge sites, whose rate is limited by the H addition and H abstraction reactions.

The general implication of the CH_2 migration is that the reaction mechanism of diamond (100) growth consists of two principal features:[64] conversion of dimer sites into bridge sites and surface migration of the bridge sites towards continuous bridge chains. This mechanism does not require any particular order of dimer formation (which may include reactions of gaseous species other than methyl, like, e.g., acetylene; see next), but establishes the governing role of surface diffusion. This conclusion is in harmony with those drawn from experimental observations.[66]

Acetylene Growth Mechanisms

Ever since the initial proposal that acetylene can be a major growth species in chemical vapor deposition of diamond,[4] the subject has been surrounded with controversies. Until very recently, numerous experimental studies have been reported claiming that acetylene cannot possibly be an efficient growth species. The new evidence presented by Loh and Cappelli[9] demonstrates unambiguously that high-quality diamond can be grown from acetylene as a sole hydrocarbon source and with a rate comparable to that from methane. Similar results have been also reported by Martin.[67]

Part of the problem has been associated with the difficulty of visualizing a plausible reaction mechanism that can convert a presumably unreactive acetylene molecule into a diamond lattice. Several reaction mechanisms have been proposed, each being criticized and none so far accepted universally. The initial mechanism of Frenklach and Spear,[4] proceeding through sequential H-abstraction and acetylene-addition reaction steps, was found to possess substantial potential-energy barriers.[68-70] A similar reaction pathway via concerted transition states[68] appeared to encounter no energy barriers, but was criticized for its first step being highly reversible and estimated to proceed in the reverse direction under the conditions of diamond CVD.[71,72] Instead, Belton and Harris[71] suggested that acetylene adds to the same site as proposed by Frenklach and Spear[4] but with both its carbon atoms, not just one as in the original proposal,[4] dehydrogenated. Although such addition resolves the thermodynamic stability of the chemisorbed acetylene, in that its desorption rate—the reverse of the addition—is negligible, the difficulty resides in its kinetic stability, i.e., in the relatively short lifetime of the adsorbate in the presence of bombardment by H atoms, as compared to the time required to incorporate the chemisorbed acetylene into the diamond lattice.

The proposal of Belton and Harris[71] continues with a similar addition that places another acetylene molecule just near the first one. The two chemisorbed molecules are then converted into the diamond lattice by a reaction with atomic hydrogen. Besler, Hase and Hass[69] found, through semiempirical quantum-chemical calculations, that such conversion can proceed as molecular addition between the neighboring chemisorbed acetylenes, without the mediating role of hydrogen. Thus, the minimum requirement for this growth mechanism is that the first chemisorbed acetylene remains adsorbed until the second acetylene adsorption takes place.

The per-site rate for the adsorption of acetylene at a biradical site is $R_{C_2H_2} = r^2 k_{C_2H_2}[C_2H_2]$. Considering typical CVD conditions[22]—temperature 1200 K, $r \sim 0.1$, $[C_2H_2]=[H] \sim 10^{-9}$ mol/cm^3—and assigning a conceivable upper limit of 10^{13} cm^{3}mol^{-1}s^{-1} to $k_{C_2H_2}$, we obtain $R_{C_2H_2}$ of the order of 10^2 s^{-1}; with $k_{C_2H_2} = 3\times10^9$ cm^{3}mol^{-1}s^{-1}, as estimated by Belton and Harris[71] for 1200 K, the acetylene adsorption is even slower, $R_{C_2H_2} = 0.03$ s^{-1}.

Let us now consider a situation where one C_2H_2 molecule has already been adsorbed and a second C_2H_2 molecule is being adsorbed with the per-site rate of $R_{C_2H_2} \sim 10^2$ s^{-1}. During this time, however, the initially adsorbed C_2H_2 is being continuously bombarded by H atoms and some of them are added to the chemisorbed acetylene. We estimate the per-site rate for this addition as $R_H \sim 10^4$ s^{-1}, basing it on a rate constant[73] of $\sim 10^{13}$ cm^{3}mol^{-1}s^{-1} for H addition to C_2H_4. The surface radical formed is unstable and undergoes rapid thermal decomposition

$$C_d\text{–}\dot{C}H\text{–}CH_2\text{–}C_d \rightarrow C_d\text{–}C_2H_3 + C_d\bullet \qquad (16)$$

with a rate of $\sim 10^7$ s^{-1} (at 1200 K), typical[73] for such β-scissions of C–C bonds. The resulting chemisorbed vinyl desorbs either through thermal decomposition, with a rate[73] of ~ 0.1 s^{-1}, or through the addition of H to the inner carbon of the vinyl group followed by β-scission of C_2H_4, with respective rates of 10^4 and 10^7 s^{-1}. Comparing these rates with the much lower rate of acetylene addition, $R_{C_2H_2}$, we must conclude that during the time required for the adsorption of the second C_2H_2, the first one is likely to desorb. The same conclusion still holds if instead of the H-addition reactions we would invoke tenfold slower H-abstraction steps.

The above analysis points out the general feature—the kinetic instability of acetylene bonded to two isolated lattice carbons. This places a prohibitive restriction on many of the proposed mechanisms creating $-CH_2-CH_2-$ pattern, as mentioned earlier for the methyl-based reaction mechanisms. Recent kinetic Monte Carlo simulations demonstrated that the growth rate of diamond can be accounted for by considering combined CH_3 and C_2H_2 additions, in which two-center additions of acetylene are disallowed and only three-center additions permitted.[74] This may resolve the prohibition of the two-center reactions; however, serious doubts still remain regarding the detailed mechanism proposed for the three-center acetylene addition. Although the transition state determined for this reaction in semiempirical quantum-chemical calculations of Huang et al.[68] was found to possess no potential energy barrier, it is not clear that such a concerted transition state can be attained dynamically with sufficient frequency. Furthermore, calculations confined to a more realistic geometry of the surface appeared to produce substantial barriers.[50]

Recently, a new class of reactions was introduced[12] which includes the addition of acetylene to a biradical on (001) diamond surface. For example, the reaction pathway shown in Fig. 2 was computed to be kinetically and thermodynamically feasible. The reaction begins with the addition of acetylene to one of the radical sites, with a potential energy barrier of 8.4 kcal/mol and the rate coefficient of 2.4×10^{11} cm^{3}mol^{-1}s^{-1} at 1200 K. The resulting acetylene adduct is thermodynamically stable, with a chemisorption energy of 95.0 kcal/mol. The overall addition of acetylene to a biradical is essentially irreversible, with the equilibrium constants of $\sim 10^{10}$.

Incorporation of the chemisorbed acetylene into a diamond lattice is initiated by H atom addition to an sp^2 carbon atom, which is immediately, with the per-site rate of $\sim 10^7$ s^{-1}, followed by β-scission, similarly to reaction 16. However, under the present circumstances, the formed C_2H_3 group, chemisorbed to one of the (100)-(2×1) dimer sites, undergoes a rapid insertion reaction upon either H abstraction from its inner C atom, H addition to its outer C atom, or H migration to a neighboring radical site. For the conditions stated, T = 1200 K and [H] = 10^{-9} mol/cm^3, H migration is estimated to be the fastest. The migration of the inner H atom of the chemisorbed C_2H_3 to a carbon radical of the adjacent-row dimer (see Fig. 2) is estimated to occur with the rate of 1.4×10^9 s^{-1}, i.e., about 5×10^5 times faster than the abstraction of the inner H from the adsorbed C_2H_3 and about 5×10^4 times faster than the addition of an H to the dimer radical site. The reverse migration of H is estimated to be tenfold slower than the forward reaction. The (100)-(2×1) dimer with the $H_2C{=}C\bullet$ adspecies formed at one of its sites undergoes a rapid dimer opening, shown as the bottom reaction sequence in Fig. 2. These reactions are similar to those for a methylene adspecies, reaction 8, but with an additional advantage of ending with the chemisorbed $=CH_2$ group, which also can be incorporated into a diamond lattice by the migration mechanism, reaction 15. Assuming that the initial addition of acetylene to a radical site is rate limiting[12] leads to event probability of the order of 10^{-2}. Multiplying the latter by r = 0.1, the probability for the neighboring site to be a radical, we obtain 10^{-3}, which is within the range tested in recent dynamic Monte Carlo simulations[19] and close to the experimental sticking probability determined by Loh and Cappelli.[75] The proposed mechanism for acetylene addition is also consistent with recent experimental findings of Thomas et al.[55] that acetylene chemisorbs onto a room-temperature diamond surface after it was subjected to adsorption of oxygen followed by thermal desorption of carbon monoxide. The latter should leave behind dehydrogenated radical sites,[76] some of which may be biradical.

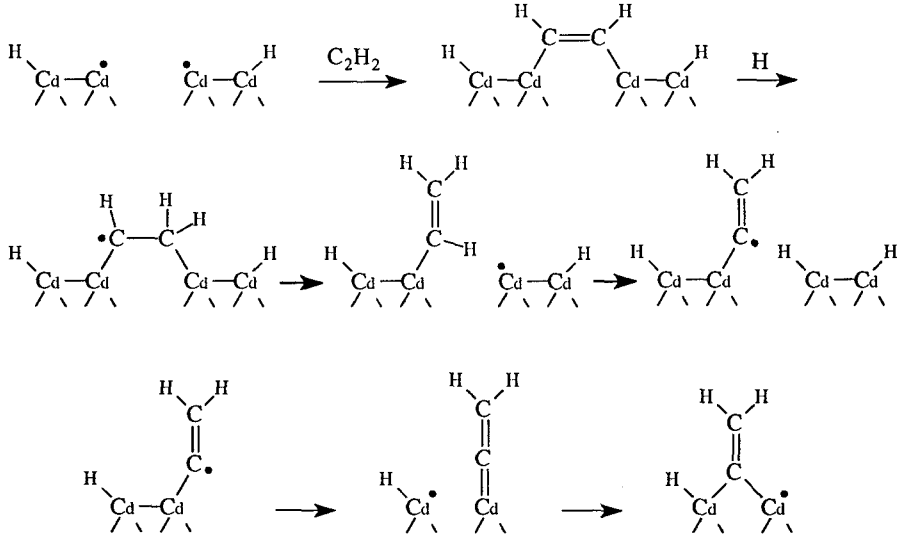

Figure 2. Reaction pathway for acetylene addition between dimers of adjacent rows.

CONCLUSIONS

The main conclusion that follows from the recent findings reviewed above is that the reaction mechanism of diamond (100) growth consists of two principal features: conversion of dimer sites into bridge sites and surface migration of the bridge sites towards continuous bridge chains. The mechanism does not require any particular order of dimer formation, but establishes the governing role of the surface migration of CH_2 groups on diamond (100) surfaces. The migration was found to be feasible on both kinetic and thermodynamic grounds and offers the most likely explanation to the formation of smooth surfaces and preferential growth at steps observed experimentally.

ACKNOWLEDGMENTS

The work was supported by the Innovative Science and Technology Program of the Ballistic Missile Defense Organization via the U.S. Office of Naval Research, under Contract No. N00014-92-J-1420. The author wishes to thank the anonymous reviewer for a thorough review of the manuscript and many helpful suggestions on the text.

REFERENCES

1. K. E. Spear and J. P. Dismukes, Eds., *Synthetic Diamond: Emerging CVD Science and Technology* (Wiley, New York, 1994).
2. J. P. Dismukes and K. V. Ravi, Eds., *Proceedings of the Third International Symposium on Diamond Materials* (The Electrochemical Society, Pennington, NJ, 1993).
3. M. Frenklach, in *Molecular processes in diamond formation*, A. J. Purdes, J. C. Angus, R. F. Davis, B. M. Meyerson, K. E. Spear, and M. Yoder, Eds. (The Electrochemical Society, Pennington, NJ, 1991), p. 142.
4. M. Frenklach and K. E. Spear, J. Mater. Res. **3**, 133 (1988).
5. M. Frenklach, in *A Unifying Picture of Gas Phase Formation and Growth of PAH, Soot, Diamond and Graphite*, J. C. Tarter, S. Chang, and D. J. DeFrees, Eds. (NASA Conference Publication 3061, 1990), p. 259.
6. M. Frenklach and H. Wang, Phys. Rev. B **43**, 1520 (1991).
7. S. J. Harris, Appl. Phys. Lett. **56**, 2298 (1990).
8. J. E. Butler and R. L. Woodin, Phil. Trans. R. Soc. Lond. A **342**, 209 (1993).
9. M. H. Loh and M. A. Cappelli, Diamond Relat. Mater. **2**, 454 (1993).
10. D. G. Goodwin, J. Appl. Phys. **74**, 6888 (1993).
11. S. J. Harris and D. G. Goodwin, J. Phys. Chem. **97**, 23 (1993).
12. S. Skokov, B. Weiner, and M. Frenklach, J. Phys. Chem. **98**, 8 (1994).
13. M. A. Cappelli and M. H. Loh, presented at the 4th Europian Conference on Diamond, Diamond-like and Related Materials, Albufeira, Portugal, 1993.
14. M. E. Coltrin and D. S. Dandy, J. Appl. Phys. **74**, 5803 (1993).
15. D. V. Fedosayev, B. V. Deryagin, and I. G. Varasavskaja, Surf. Coatings Technol. **38**, 9 (1989).
16. M. Frenklach, J. Appl. Phys. **65**, 5142 (1989).
17. B. N. Davidson and W. E. Pickett, Nature (1994, submitted).
18. W. R. L. Lambrecht, C. H. Lee, B. Segall, J. C. Angus, Z. Li, and M. Sunkara, Nature **364**, 607 (1993).
19. M. Frenklach, J. Chem. Phys. **97**, 5794 (1992).
20. C. H. Wu, M. A. Tamor, T. J. Potter, and E. W. Kaiser, J. Appl. Phys. **68**, 4825 (1990).
21. S. J. Harris, A. M. Weiner, and T. A. Perry, Appl. Phys. Lett. **53**, 1605 (1988).
22. W. L. Hsu, Appl. Phys. Lett. **59**, 1427 (1991).
23. W. L. Hsu, J. Appl. Phys. **72**, 3102 (1992).
24. F. G. Celii and J. E. Butler, Annu. Rev. Phys. Chem. **42**, 643 (1991).
25. P. B. Davies and P. M. Martineau, J. Appl. Phys. **71**, 6125 (1992).
26. K. L. Menningen, M. A. Childs, P. Chevako, H. Toyoda, L. W. Anderson, and J. E. Lawer, Chem. Phys. Lett. **204**, 573 (1993).
27. P. Joeris, C. Benndorf, and S. Bohr, J. Appl. Phys. **71**, 4638 (1992).
28. A. Campargue, M. Chenevier, L. Fayette, B. Marcus, M. Mermoux, and A. J. Ross, Appl. Phys. Lett. **62**, 134 (1993).
29. D. G. Goodwin and G. G. Gavillet, J. Appl. Phys. **68**, 6393 (1990).

30. E. Kondoh, K. Tanaka, and T. Ohta, J. Appl. Phys. **74**, 4513 (1993).
31. E. Meeks, R. J. Kee, D. S. Dandy, and M. E. Coltrin, Combust. Flame **92**, 144 (1993).
32. M. A. Cappelli and P. H. Paul, J. Appl. Phys. **67**, 2596 (1990).
33. M. P. D'Evelyn, C. J. Chu, R. H. Hauge, and J. L. Margrave, J. Appl. Phys. **71**, 1528 (1992).
34. C. E. Johnson, W. A. Weimer, and F. M. Cerio, J. Mater. Res. **7**, 1427 (1992).
35. For Example: S. J. Harris and L. R. Martin, J. Mater. Res. **5**, 2313 (1990); S. J. Harris, A. M. Weiner, and T. A. Perry, J. Appl. Phys. **70**, 1385 (1991); W. A. Yarbrough, K. Tankala, and T. DebRoy, J. Mater. Res. **7**, 379 (1992); Y. Wang, E. A. Evans, L. Zeatoun, and J. C. Angus, Presented at the Third IUMRS International Conference on Advanced Materials, 1993.
36. Harris, J. Appl. Phys. **65**, 3044 (1989).
37. M. Tsuda, M. Nakajima, and S. Oikawa, J. Am. Chem. Soc. **108**, 5780 (1986).
38. M. Tsuda, M. Nakajima, and S. Oikawa, Jpn. J. Appl. Phys. **26**, L527 (1987).
39. D. W. Brenner, Phys. Rev. B **42**, 9458 (1990).
40. S. M. Valone, M. Trkula, and J. R. Laia, J. Mater. Res. **5**, 2296 (1990).
41. S. P. Mehandru and A. B. Anderson, J. Mater. Res. **5**, 2286 (1990).
42. M. R. Pederson, K. A. Jackson, and W. E. Pickett, Phys. Rev. B **44**, 3891 (1991).
43. D. Huang and M. Frenklach, J. Phys. Chem. **95**, 3692 (1991).
44. R. A. Back, Can. J. Chem. **61**, 916 (1983).
45. K. Tabayashi and S. H. Bauer, Combust. Flame **34**, 63 (1979).
46. P. Deak, J. Giber, and H. Oechsner, Surf. Sci. **250**, 287 (1991).
47. W. A. Yarbrough, in *Diamond growth on the (110) surface*, S. Holly and A. Feldman, Eds. (SPIE–The International Society of Optical Engineers, Bellingham, WA, 1991), p. 90.
48. J. C. Angus and C. C. Hayman, Science **241**, 913 (1988).
49. K. E. Spear and M. Frenklach, presented at First International Symposium on Diamond and Diamond-like Films, May 7-12 1989, 1989.
50. D. Huang and M. Frenklach, J. Phys. Chem. **96**, 1868 (1992).
51. Y. L. Yang and M. P. D'Evelyn, J. Vac. Sci. Technol. A **10**, 978 (1992).
52. P. G. Lurie, Surf. Sci. **65**, 453 (1977).
53. B. B. Pate, Surf. Sci. **165**, 83 (1986).
54. A. V. Hamza, G. D. Kubiak, and R. H. Stulen, Surf. Sci. **237**, 35 (1990).
55. R. E. Thomas, J. B. Posthill, R. A. Rudder, R. J. Markunas, and M. Frenklach, in *Diamond surface studies of growth mechanisms from water-alcohol deposition chemistries*, J. P. Dismukes and K. V. Ravi, Eds. (The Electrochemical Society, Pennington, NJ, 1993), p. 71.
56. K. Okada, S. Komatsu, T. Ishigaki, S. Matsumoto, and Y. Moriyoshi, Appl. Phys. Lett. **60**, 959 (1992).
57. W. S. Verwoerd, Surf. Sci. **103**, 404 (1981).
58. S. H. Yang, D. A. Drabold, and J. B. Adams, Phys. Rev. B **48**, 5261 (1993).
59. S. Skokov, C. S. Carmer, B. Weiner, and M. Frenklach, Phys. Rev. B **49**, 5662 (1994).
60. T. Frauenheim, U. Stephan, P. Blaudeck, D. Porezag, H. G. Busmann, W. Zimmermann-Edling, and S. Lauer, Phys. Rev. B. in press (1994).
61. B. J. Garrison, E. J. Dawnkaski, D. Srivastava, and D. W. Brenner, Science **255**, 835 (1992).
62. M. Zhu, R. H. Hauge, J. L. Margrave, and M. P. D'Evelyn, in *Mechanism for diamond growth on flat and stepped diamond (100) surfaces*, J. P. Dismukes and K. V. Ravi, Eds. (The Electrochemical Society, Pennington, NJ, 1993), p. 138.
63. N. L. Allinger, Y. H. Yuh, and J. Lii, J. Am. Chem. Soc. **111**, 8551 (1989).
64. S. Skokov, B. Weiner, and M. Frenklach, J. Phys. Chem. (1994, submitted).
65. T. Imai, T. Ueda, and N. Fujimori, presented at Japan Applied Physics Conference, Kansai University, Japan, September 16-19,1992.
66. W. J. P. van Enckevort, G. Janssen, W. Vollenberg, J. J. Schermer, L. J. Giling, and M. Seal, Diamond Related Mater. **2**, 997 (1993).
67. L. R. Martin, J. Mater. Sci. Lett. **12**, 246 (1993).
68. D. Huang, M. Frenklach, and M. Maroncelli, J. Phys. Chem. **92**, 6379 (1988).
69. B. H. Besler, W. L. Hase, and K. C. Hass, J. Phys. Chem. **96**, 9363 (1993).
70. X. Y. Chang, D. L. Thompson, and L. M. Raff, J. Phys. Chem **97**, 10112 (1993).
71. D. N. Belton and S. J. Harris, J. Chem. Phys. **96**, 2371 (1992).
72. S. J. Harris and D. N. Belton, Jpn. J. Appl. Phys. **30**, 2615 (1991).
73. W. G. Mallard, F. Westley, J. T. Herron, R. F. Hampson, and D. H. Frizzell, *NIST Chemical Kinetics Database 5.0* (National Institute of Standards and Technology, Geithersburg, MD, 1993).
74. M. Frenklach, Phys. Rev. B **45**, 9455 (1992).
75. M. H. Loh and M. A. Cappelli, in *Study of precursor transport during diamond synthesis in a supersonic flow*, J. P. Dismukes and K. V. Ravi, Eds. (The Electrochemical Society, Pennington, NJ, 1993), p. 17.
76. M. Frenklach, D. Huang, R. E. Thomas, R. A. Rudder, and R. J. Markunas, Appl. Phys. Lett. **63**, 3090 (1993).

DIAMOND CHEMICAL VAPOR DEPOSITION : GAS COMPOSITIONS AND FILM PROPERTIES

PETER K. BACHMANN, HANS-JÜRGEN HAGEMANN, HARTMUT LADE, DIETER LEERS, FREDERIKE PICHT, DETLEF U. WIECHERT, AND HOWARD WILSON
Philips Research Laboratories, P.O.Box 1980, D-52021 Aachen, Germany.

ABSTRACT

Rate, crystallinity and phase purity of vapor-grown diamond deposits are discussed. Emphasis is on microwave plasma CVD of diamond from C/H-, C/H/O–, C/H/F-, C/H/Cl- and C/H/N-gas mixtures.
The manufacture of wear-resistant diamond thin films, diamond vacuum window membranes and thick diamond heat spreader plates are used as examples to outline the influence of various deposition parameters on the performance of finished products and to describe the use of ternary gas phase compositional diagrams as tools for minimization of deposition technology and product optimization efforts.

INTRODUCTION

Since the revitalization of diamond chemical vapor deposition in the late 1970s [1-3], numerous CVD processing variants were added to the list of possible ways to grow diamond films (see, e.g., [4, 5] for an extensive list of references and a critical comparison of the methods). The driving force for inventing new ways of diamond making was and is to grow better quality, more uniform, homogeneous diamond layers onto larger substrate areas at higher rates and lower deposition temperatures. While some of the methods are merely of scientific interest, others, especially microwave plasma CVD (applied by, e.g. Crystallume, DeBeers, Philips), DC arc jet deposition (applied by, e.g., Norton Diamond Films, Fujitsu), RF plasma CVD (applied by, e.g., Toyota) or hot filament diamond deposition (applied by General Electric, Diamonex) emerged into industrially applicable manufacturing technologies with potential for scale-up and volume production of high quality material.
In addition to new means of initiating the CVD reactions, such as filaments, low pressure non-isothermal or higher pressure thermal plasmas, new gas compositions were tested in order to improve on the quality and phase purity of the deposit, to reduce the thermal load on the substrate and to increase the deposition rates (see [4-6] for

Mat. Res. Soc. Symp. Proc. Vol. 339. ©1994 Materials Research Society

references). Additives to the carbon carrier gases as well as their concentrations were often selected by trial-and-error or are more or less directly connected to the specifics of the deposition process used, as, e.g., the use of acetylene/oxygen-mixtures in the combustion flame diamond growth [7]. The scientific as well as the patent literature of the 1980s contain a wealth of methods and recipes to grow diamond from the vapor phase.

In an effort to develop a unifying scheme for, at least, the various CVD approaches to grow diamond, we analyzed the data provided in the literature by over 30 years of diamond CVD research as well as the results of our own plasma and flame growth experiments. This resulted in the development of a ternary C/H/O-gas phase compositional diagram [6] that, indeed, provides a common roof for all diamond CVD methods known to date and helps to explain, optimize and correlate deposition conditions, experimental results and film properties.

GAS PHASE COMPOSITIONAL DIAGRAMS FOR DIAMOND CVD

The principles of constructing a ternary C/H/O-diagram and its use to predict experimental trends and specific properties of the deposited material are outlined in [6]. In its first version, the triangular diagram comprises a wedge-shaped region where diamond growth is, at least with respect to the gas composition, feasible. This "diamond domain" extends along the H-CO tie line of the diagram and is limited by a region of oxygen-rich gas compositions from which no deposit forms and by a region of carbon-rich gas mixtures that result in the deposition of dominantly amorphous, non-diamond carbon phases.

The basic principles of this diagram stood the test of time and the existence of the diamond domain was confirmed by many authors [8-10]. Its position and shape are surprisingly accurately explained by fairly straight-forward thermodynamical calculations [11].

Since its first publication, additional experiments in previously unexplored regions of the diamond domain, namely gas compositions with very high oxygen and carbon partial pressures with almost no hydrogen (i.e. neither added H_2 nor H as part of the carbon carrier, led to modifications of its shape and revealed additional trends [8]. If solely based on microwave plasma CVD experiments at 1.5 kW and 50-110 mbar performed on the same deposition unit, the diamond domain exhibits a lens shape as shown in Fig. 1 [8]. The most import modifications compared to the earlier version [6] of this diagram are:

- a lens-shaped rather than a wedge-shaped diamond domain.
  This includes the fact that the domain narrows down to a single point at its right side near the C-O side line of the diagram. Carefully performed experiments [8] indicate that diamond growth without <u>any</u> hydrogen in the system (neither in the carbon carrier nor added H_2) is not feasible and at least 0.5% H needs to be present in the C/H/O-mixture to enable diamond growth.

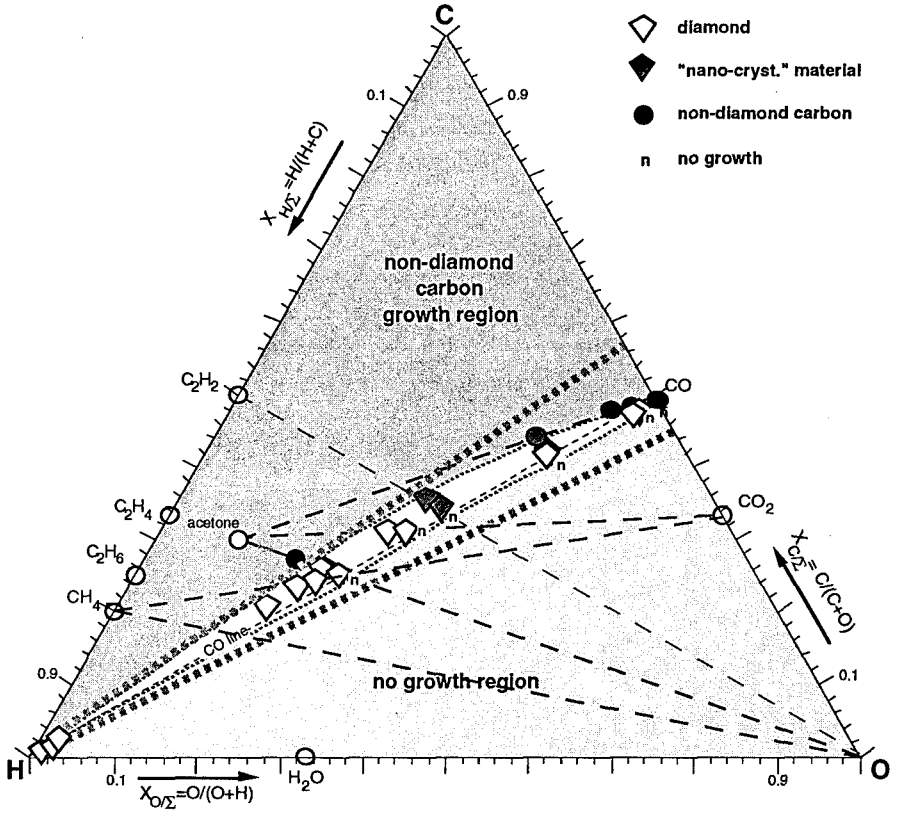

Fig. 1: Updated C/H/O-gas phase compositional diagram of diamond CVD [8]. The data are solely based on our own MW-plasma CVD experiments at power levels of up to 1.5 kW and pressures of 50-110 mbar.

- the straight oxygen-rich border of the diamond domain is very close to the CO-H-tie line of the diagram. Its position was not only confirmed in many growth experiments, but is also nicely illustrated by the complete vanishing of any C-related optical plasma emission when crossing over from the diamond domain into the no-growth region of the diagram. Interestingly, both the sharpness of the oxygen-rich domain border as well as the lens shape of its C-rich border are confirmed by thermodynamics calculations [11]. For high power densities, calculated and experimental domain shape seem to match even closer than for low power/low pressure plasmas, indicating that at least under high power density conditions the system can be close to thermodynamical equilibrium.

Of course, the correct gas phase composition is not the only requirement for diamond CVD. If no energy is provided to the system in order to sufficiently radicalize the gas phase, diamond growth will not proceed, i.e. the diamond domain will disappear. For microwave energies of only 500 W, the domain is narrower than indicated in Fig.1 and does not extend over the full width of the triangular diagram, as shown by P. Paroli [9]. Therefore, being a necessary but not a sufficient prerequisite, the diamond domain indicates where to search for diamond and hence provides a strategy tool to optimize the deposition process and the quality of the deposit. In connecting the experimental results of over 30 years of worldwide research, it also illustrates that specific starting materials are not required for diamond growth and that many CVD diamond patents related to gas phase compositions are most likely obsolete.

It is, of course, possible to construct other ternary gas phase compositional diagrams. In order to evaluate the proposed [12-17] benefits (lower deposition temperature and/or higher rates) of adding halogen compounds to the diamond CVD gas phase, we performed a series of microwave plasma deposition experiments using C/H/Cl- and C/H/F-gas mixtures [18]. We were able to confirm diamond growth from both gas systems and plotted our results [18] along with literature data [12-17] into C/H/Cl- and C/H/F-gas phase compositional diagrams. The hydrogen-rich corner of the C/H/Cl-diagram is shown in Fig. 2. The respective diamond domain is limited to an area very close to the H-corner of the diagram. High chlorine concentrations seem to foster the deposition of non-diamond carbon phases. In our microwave experiments we were, however, unable to locate a region inside the C/H/Cl-growth domain that would provide an advantage in terms of rate, phase purity or deposition temperature over the C/H/O-gas compositions we tested. This, along with the problems asso-

ciated with the handling of chlorine-containing gas mixtures forced us to terminate further exploration chlorine-assisted diamond CVD.

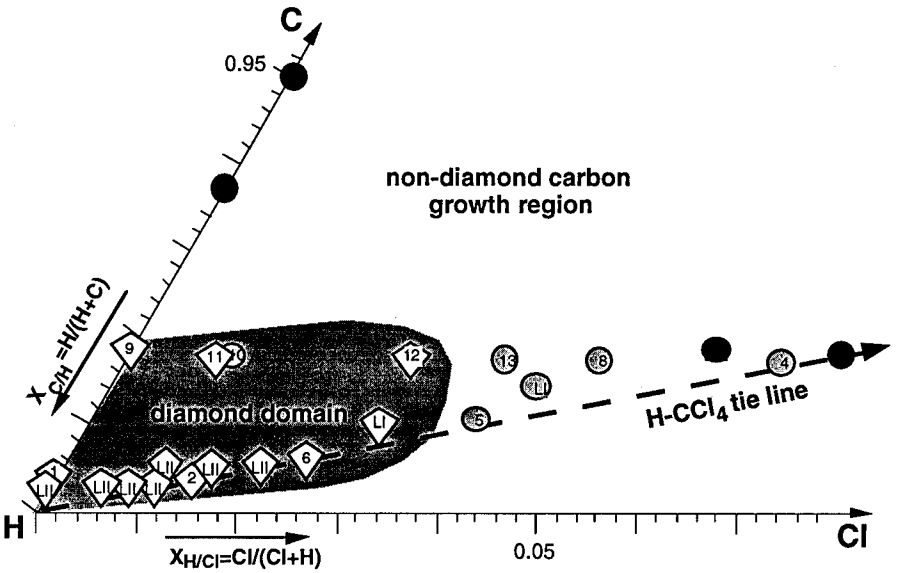

Fig. 2: H-rich corner of the C/H/Cl-gas phase compositional diagram of diamond CVD [24].

In the case of fluorine-assisted diamond CVD, evaluation of the literature [12-17] and our own experimental data in the form of a C/H/F-diagram indicates that the diamond domain extends well into the fluorine-rich region of the ternary system (see also W. Cassidy et al, this proceedings for corresponding thermodynamical calculations of the C/H/F system). However, again we could not find any advantage of fluorine-assisted diamond CVD over growth from C/H/O-mixtures and, in addition, the use of fluorine severely restricts the type substrate materials. Silicon, e.g, is always damaged, even if only small quantities of fluorine are present in the plasma activated gas phase. We, therefore, terminated further investigation of halogen-containing diamond CVD gas mixtures.

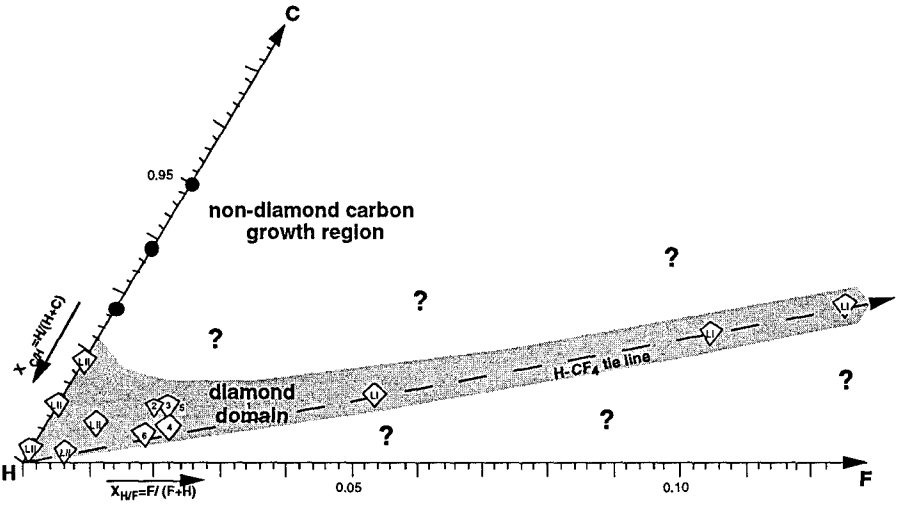

Fig. 3: Status of the H-rich corner of the C/H/F-gas phase compositional diagram.

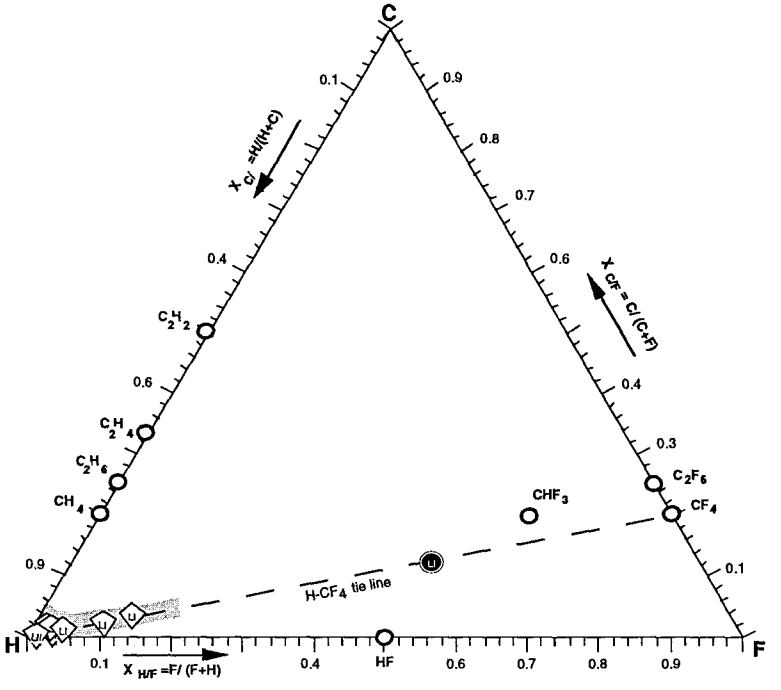

Fig. 4: Present status of the full size C/H/F-gas phase compositional diagram.

A C/H/N-gas phase compositional diagram is not worth plotting, because diamond growth is basically limited to a region very close to its C/H-side line. Addition of only 1% nitrogen gas to a mixture of 1% CH_4/H_2 results in severe deterioration of the crystalline structure and poor phase purity of the deposited material [19]. As detected by emission spectroscopy, nitrogen-containing compounds in the source material were also responsible for the poor quality of our microwave plasma deposited films grown from acetylene-oxygene mixtures [8] (see Fig.1).

DIAMOND FILM PROPERTIES

The C/H/O- or C/H/X-diagrams are not only helpful in exploring new gas compositions but also to optimize the start-up or shut down procedure of deposition experiments, and to help minimizing the effort needed to optimize the properties of the deposit and hence of the final product. With the no-growth region bordering the diamond domain on the carbon-lean side and the region of non-diamond carbon growth on the C-rich side it is obvious that the rate has to drop when cutting across the domain at any position from the C-rich to the C-lean side [6]. It is also obvious that the phase purity has to improve in the same direction. This allows to optimize rate versus phase purity for any given application according to the limitations imposed by the specific product.

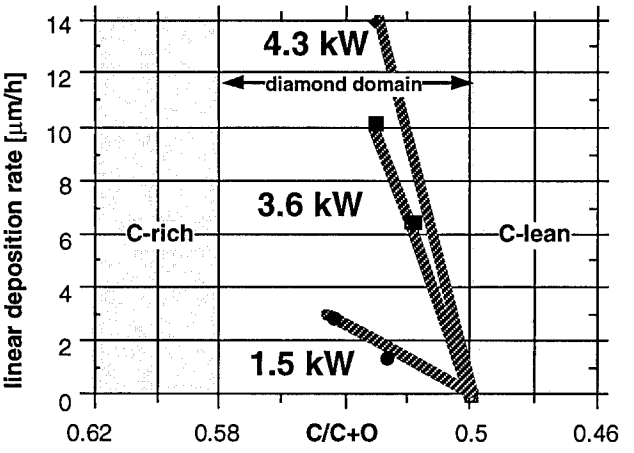

Fig. 5 : Deposition rate across the diamond domain for three different microwave power levels at 100 mbar (4 cm Ø Si; T ≈ 800 °C).

Fig. 5 delineates the experimentally determined rate variation across the diamond domain along the acetone-oxygen tie line of the C/H/O-diagram for three different microwave power levels at approximately 800 C and 100 mbar for microwave plasma CVD experiments onto 4 cm diameter silicon wafers. This graph also nicely confirms the expected rate increase for higher plasma power densities (i.e. higher gas phase temperatures) already discussed in [6].

In the course of developing vacuum windows based on thin diamond membranes [20], we were able to clearly correlate the occurrence of membrane damage during the required wet etching procedure with the CVD gas phase composition. Attempts to correlate the membrane destruction with crystal size, texture, phase purity or other deposition parameters failed. TEM data of our films [21] indicate that, although the crystalline perfection of individual diamond grains grown from gas mixtures with high oxygen levels, i.e. in the center of the C/H/O-diagram, is better and the dislocation densities are lower than for C/H-grown material, connectivity between the grains seems to be a problem and small pores are likely to form. Such O-induced structural differences seem to be responsible for the observed film damage during the window fabrication process.

Wear resistant coatings can be grown from C/H- and C/H/O-gas mixtures. We were able to demonstrate that if the nucleation density is high enough, a layer of only 50 nanometer of CVD diamond grown from either acetone/oxygen- or from methane/hydrogen-mixtures converts the wear performance of the soft surface of a silicon wafer to that of a tungsten carbide cutting tool insert [22]. In this case, optimization of the film properties along the diamond domain is not required and the deposition rate advantage of C/H/O- over C/H-gas mixtures can be fully exploited. However, choosing the proper position across the width of the diamond domain allows to optimize the wear performance of a film versus its friction properties and its growth rate. While high friction, well-facetted material grows closer to the oxygen-rich border, low friction, fine grain material precipitates closer to the C-rich border of the diamond domain.

Gas phase induced crystallinity and phase purity changes also seem to affect the thermal and optical properties of the deposit:

The thermal conductivity of C/H/N-grown diamond is usually low due to the formation of amorphous components during the deposition process. It is also well known that the presence of nitrogen in the CVD gas phase quenches the diamond A-band lumi-

nescence at 445 nm. In that sense, avoiding any nitrogen to be present in the system will help to improve the performance of the deposited material.

Preliminary results of a comparison of thermal diffusivity data of a large number of our C/H- and C/H/O-grown diamond thin and thick films reveals that it is difficult to grow high quality heat sink material from oxygen-containing gas mixtures. Although we were able to grow 250 μm thick white diamond disks with a thermal conductivity as high as 22±2 W/cm K, the thermal conductivity of material grown from gas mixtures with high oxygen partial pressures never exceeded 10 W/cm K [23].

CONCLUSION

The composition of the CVD gas phase plays a vital role for the diamond deposition process, its optimization with respect to rate, phase purity, substrate temperature and substrate material. It is equally important for the mechanical, optical, thermal and electrical properties of the deposited material.
Ternary gas phase compositional diagrams are not only scientifically interesting but are helpful tools that provide a strategy to minimize the effort needed for optimization, and thus reduce diamond CVD process and product development costs.

ACKNOWLEDGEMENTS

Support of this work by the German Ministry of Research and Technology is gratefully acknowledged.

REFERENCES

[1] B.V. Spitsyn, L.L. Bouilov, and B.V.Derjaguin, J. of Crystal Growth, 52, 219 (1981).

[2] S. Matsumoto, Y. Sato, M. Kamo, and N. Setaka, Jpn. J. of Appl. Phys. 21, L183 (1982).

[3] M. Kamo, Y. Sato, S. Matsumoto, and N. Setaka, J. of Crystal Growth, 62, 642 (1983).

[4] P.K. Bachmann, in "Thin Film Diamond" edited by A. Lettington and J.W. Steeds, Chapman and Hall Royal Society London, ISBN 0-412-49630-5 (1994).

[5] P.K. Bachmann, W. v. Enckefort, Diamond and Related Materials, Vol.1, 1021 (1992).

[6] P.K. Bachmann, D.Leers, and H. Lydtin, Diamond and Related Materials, Vol. 1, No.1, 1 (1991).

[7] Y. Hirose, S. Ananuma, N. Okada, K. Komaki, "1st Intl. Symp.on Diamond and Diamond-Like Films", The Electrochem. Soc. Pennington, NJ, Proceedings,Vol. 89-12, 80 (1989).

[8] P.K. Bachmann, D. Leers, and D.U. Wiechert, presented at DIAMOND 1992, paper 4.2 (unpublished) Aug. 31-Sept. 4, 1992, Heidelberg, Germany

[9] P. Paroli, presented at, ADC´93, 2. Intl. Conference on the Applications of Diamond Films and Rel. Materials Aug. 25-27, 1993, Omiya, Saitama, Japan.

[10] M. Fryda, C.P.Klages,Diamond and Rel. Mat.,in press, (1994)

[11] N.A. Prijaya, J. C. Angus, P.K. Bachmann Diamond and Rel. Mat., Vol. 3, No.1-2, 129 (1993)

[12] D.E. Patterson, B.J. Bai, C.J. Chu, R.H. Hauge,and J.L. Margrave in "New Diamond Science and Technology", edited by R.F. Messier, J.T. Glass, J.E. Butler, and R. Roy, Mater. Res. Soc. Pittsburgh, PA, 433 (1991).

[13] M.S. Wong, C.H. Wu, Diamond and Related Materials, 1,369 (1992)

[14] M. Kadono, T. Inoue, M. Miyanaga, S. Yamazaki, Appl. Phys. Lett. 61,7,772 (1992).

[15] R.A. Rudder , G.C. Hudson, D.P. Malta, J.B. Posthill, R.E. Thomas, R.J. Markunas, in "Applications of Diamond and Related Materials, edited by Y. Teng, M. Yoshikawa, M. Muranaka, A. Feldman, Elsevier Science Publishers, 583 (1991).

[16] C.H. Chu, M.H. Hon, presented at DIAMOND 1992, Heidelberg, Germany (unpublished) (1992).

[17] F.C. Hong, J. C. Hsieh, J.J. Wu, presented at DIAMOND 1992, Heidelberg, Germany (unpublished) (1992).

[18] P.K. Bachmann, H.J. Hagemann, H. Lade, D.Leers, F. Picht, D.U. Wiechert, presented at "Diamond Films´93", paper 2.2 (unpublished) , Albufeira, Portugal, Sept. 20-24, 1993.

[19] P.K. Bachmann and D.U. Wiechert, Diamond and Related Materials, Vol. 1, 422 (1992).

[20] P.K. Bachmann, H. Lade, D.Leers, D.U. Wiechert presented at "Diamond Films´93", paper 16.2 (unpublished), Albufeira, Portugal, Sept. 20-24, 1993.

[21] P. Pongratz, M. Joksch, P.K. Bachmann, D.Leers to be published.

[22] P.K. Bachmann, H. Lade, D.Leers, D.U. Wiechert presented at "Diamond Films´93", paper 12.062 (unpublished), Albufeira, Portugal, Sept. 20-24, 1993.
Diamond and Related Materials, in press, (1994)

[23] P.K.Bachmann, H.J.Hagemann, H.Lade, D.Leers, D.U.Wiechert, H. Wilson, submitted for presentation at "Diamond Films ´94", (unpublished) Castelvecchio Pascoli, Italy, Sept. 25-30, 1994.

DIAMOND HOMOEPITAXY KINETICS: GROWTH, ETCHING, AND THE ROLE OF OXYGEN

Robin E. Rawles* and Mark P. D'Evelyn**
*Rice University, Department of Chemistry, Houston, TX, 77251-1892
**General Electric Corporate Research and Development, P.O. Box 8, Schenectady, NY 12301; Departments of Chemistry and Materials Engineering, Rensselaer Polytechnic Institute, Troy, NY 12180-3590

ABSTRACT

Growth and etch rates for diamond homoepitaxy have been measured *in situ* using Fizeau interferometry. Experiments were conducted in a hot-filament reactor using hydrogen, methane, and oxygen feed gases at a reactor pressure of 25 torr. The substrate temperature dependence for growth on diamond(100) was studied for 0.5% and 1% CH_4 and 0-0.44% O_2. Apparent activation energies of 17 and 5 kcal/mol were determined for growth from 0.5% and 1% CH_4 in hydrogen, over the ranges of 700 - 1000 °C and 800 - 1050 °C, respectively. When a minimal amount of oxygen was added to the feedstock, the growth-rate behavior was similar for that with pure methane. With greater amounts of added oxygen, growth rates were higher than those without oxygen at low temperatures, proceeded through a maximum, and then decreased until etching was observed at high temperatures. Similar behavior was observed for growth from 1% CH_4 with and without oxygen. We also measured the temperature dependence for etching of homoepitaxial diamond films in hydrogen with 0 - 0.1% O_2, and observed etch rates of 0.01 - 0.1 microns/hr in the range of 950 - 1150 °C. We propose that oxygen facilitates diamond growth at low temperatures by enhancing the removal of both sp^2- and sp^3-bonded "errors" and/or by increasing the efficiency of carbon incorporation by roughening the diamond surface, and that these etching processes become dominant at high temperatures.

INTRODUCTION

The addition of oxygen-containing precursors to the gas mixture in diamond chemical vapor deposition (CVD) has been shown to have a number of important effects. These effects include increasing or decreasing growth rate depending on sample temperature and carbon-oxygen ratio, and improvements in film quality [1-7]. The mechanistic role that oxygen plays in diamond CVD is unclear, however, and we have undertaken to explore that role by studying the kinetics of homoepitaxial diamond growth and etching by *in situ* Fizeau interferometry. This technique provides a very sensitive monitor of thickness changes as well as gives an indication of morphological changes, and allows us to systematically investigate diamond CVD rapidly and efficiently. We have found that the addition of oxygen enhances growth rates at lower substrate

Mat. Res. Soc. Symp. Proc. Vol. 339. ©1994 Materials Research Society

temperatures but results in etching at higher temperatures, and is more effective than hydrogen alone at removal of sp^2 and sp^3 carbon.

EXPERIMENTAL

We have measured the substrate temperature dependence for growth/etching of diamond(100) [8] in a hot-filament reactor under the growth conditions described in Table I. Raman spectroscopy performed on selected samples after several growth experiments showed a sharp peak at 1332 cm^{-1} but no evidence for sp^2 carbon. Substrates were held between two mullite tubes and heated by tungsten or rhenium wires embedded in the mullite. The sample temperature was monitored by a chromel-alumel thermocouple cemented to the mullite support.

I. Growth Conditions

Substrate:	type 2a diamond (100)
Filament:	0.127 mm W wires (3)
Flow rates:	H_2, 150 sccm
	CH_4, 0.75, 1.0 sccm
	O_2, 0 - 0.67 sccm
Reactor pressure:	25 torr
Filament temperature:	2050 °C
Filament - Substrate Distance:	5.0 - 7.0 mm

Separate etching experiments were performed with 0 - 0.1% O_2 in 150 sccm H_2 and no CH_4. The remaining parameters in the etching experiments were identical to those listed in Table I.

Growth and etch rates were monitored *in situ* by optical Fizeau interferometry using 633 nm light from a HeNe laser reflected at near-normal incidence from the back side of the natural diamond substrate [9,10]. The existence of a slight wedge angle between the back and front faces of the substrate causes interference in the light reflected from the two faces, producing a *spatial* fringe pattern with a spacing of 131 nm. Deposition or removal of diamond causes the pattern to propagate laterally, shifting by one fringe for a thickness change of 131 nm. In these experiments the fringe pattern image was projected onto a CCD video array and the output recorded on videotape. Analysis of the data was performed by measuring the fringe positions as displayed on a video monitor as a function of time. Thickness changes as small as 10 nm were observable.

RESULTS

The dependence of the growth rate on substrate temperatures at a CH_4 concentration of 0.5% is shown in Fig. 1. For the sample grown without oxygen we measured an apparent activation energy of 17 kcal/mol. Addition of 0.05% O_2 produced no significant change in the growth-rate behavior from that of pure methane in hydrogen. For the remaining samples grown with oxygen the growth rate is enhanced relative to that from pure methane at low temperatures, increases to a

maximum, and then decreases until etching is observed at high temperatures. For 0.09 and 0.14% O_2 the behavior is similar, with maximum rates of 0.33 and 0.30 microns/hr at 800 °C, respectively, and etching is observed at $T_S \geq 1000$ °C. For 0.21% O_2 this behavior is more pronounced, with a growth-rate maximum of 0.54 microns/hr measured at 900 °C and etching observed at $T_S \geq 950$ °C.

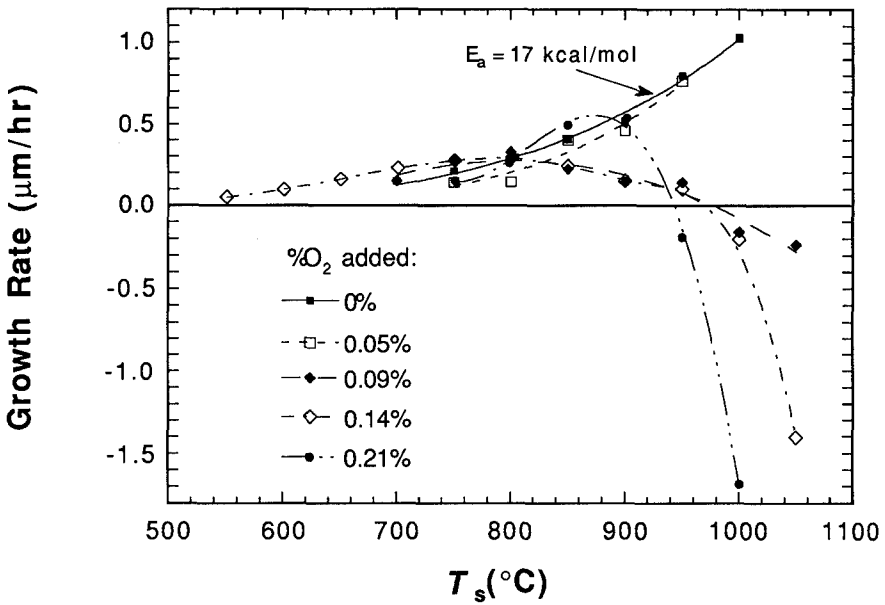

Fig. 1. Dependence of homoepitaxial [100] growth/etch rate on substrate temperature, 0.5% CH_4.

The dependence of the growth rate on substrate temperatures at a CH_4 concentration of 1% is shown in Fig. 2. For the sample grown without oxygen we measured an apparent activation energy of 5 kcal/mol. For the sample grown with 0.44% oxygen we observe a maximum growth rate of 0.87 microns at 900 °C and etching above 1050 °C.

The dependence of etch rate on substrate temperature with 0 - 0.1% O_2 in 150 sccm H_2 (T_f = 2050 °C, P = 25 torr) is shown in Fig. 3. For etching in hydrogen alone, we observed rates of 0.01 - 0.1 microns/hr for sample temperatures of 1050 - 1150 °C. Similar etch rates were observed for mixtures of oxygen and hydrogen between 950 and 1050 °C. At 1050 °C the etch rate with 0.05% and 0.1% O_2 is roughly two and four times the etch rate in hydrogen alone.

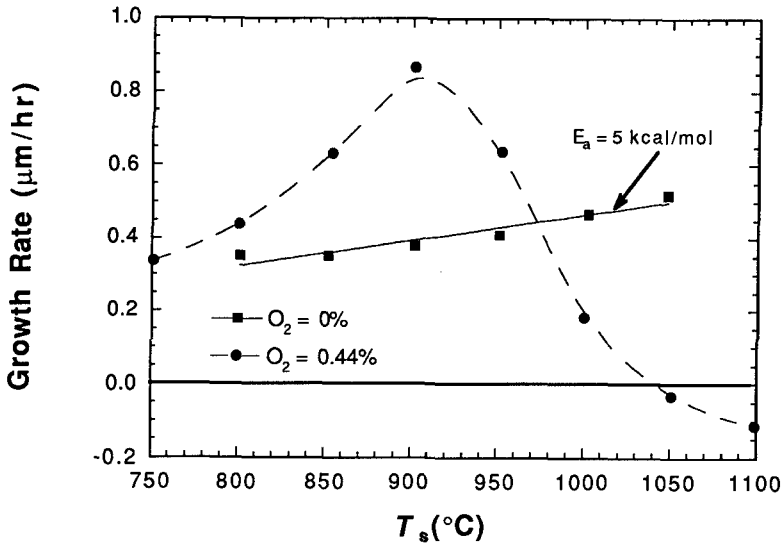

Fig. 2. Dependence of homoepitaxial [100] growth/etch rate on substrate temperature, 1% CH_4.

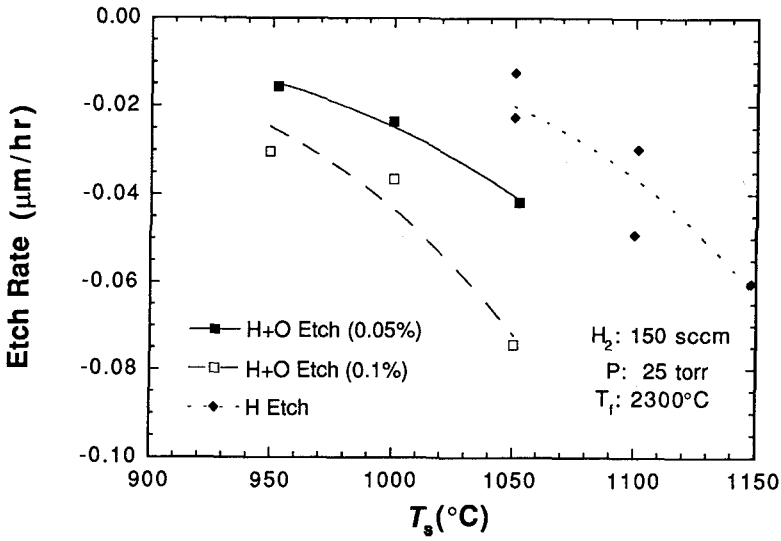

Fig. 3. Dependence of homoepitaxial [100] etch rate on substrate temperature.

DISCUSSION

The growth-rate behavior for pure methane in hydrogen shown in Fig. 1 and Fig. 2 is qualitatively similar to that reported previously on diamond (100) [9,11] and for growth of polycrystalline films [12-14]. Further work will be necessary to understand the differences in apparent activation energies between the 0.5% and 1% methane results, but changes in effective activation energy with methane concentration have been reported previously for polycrystalline films [12,13]. Unlike the reported growth kinetics for polycrystalline films without oxygen [12-14], however, we do not observe a decline in growth rates at temperatures above 850 - 950 °C.

The addition of oxygen to the gas mixture produces striking effects which cannot be attributed to gas-phase chemistry [15] alone. The enhanced growth rate at lower substrate temperatures is consistent with the qualitative observations reported previously [1-7]; however, the transition from growth to etching as the substrate temperature rises as seen in Figs. 1 and 2 has significant implications. This result suggests that growth and etching are competing processes over the entire temperature range, with growth dominating at low substrate temperatures and etching at high substrate temperatures. The kinetics data in Fig. 1 also shows that the addition of more and more oxygen pushes this transition to subsequently lower temperatures while increasing the maximum growth rate. Further experiments are needed to explore how far this trend will continue with yet higher oxygen-carbon ratios.

The etching kinetics data shown in Fig. 3 shows that addition of oxygen results in a higher etch rate than with (atomic) hydrogen alone. We have also conducted experiments in etching of polycrystalline CVD diamond films in pure hydrogen and in H_2+O_2 which demonstrated that the addition of oxygen resulted in more efficient removal of sp^3 *and* sp^2 carbon [9]. These results suggest that the enhancement in growth rate at lower temperatures is due to enhanced etching with oxygen as opposed to hydrogen alone, and that at higher substrate temperatures the dominance of etching over growth is due not only to the addition of oxygen but also to the increased rate of etching by atomic hydrogen. However, the etch rate due to atomic hydrogen is much less than the growth rate so that no decline in the net growth rate is observed.

The growth/etching kinetics presented here support the proposition that high quality diamond homoepitaxy requires simultaneous growth and etching [16, 17], and indicate that these competing processes have different effective activation energies which need to be determined in order to model this behavior. Efforts are underway in our laboratory to further explore the effects of oxygen addition on diamond growth and etching through the study of homepitaxial growth kinetics simultaneously with gas-phase chemistry.

ACKNOWLEDGMENTS

The authors acknowledge the National Science Foundation (CHE-9214328) and Office of Naval Research for support of this work, and thank Prof. L. V. Interrante for his hospitality.

REFERENCES

1. Y. Hirose and Y. Terasawa, Jpn. J. Appl. Phys. **25**, 519 (1986).
2. C.-P. Chang, D. L. Flamm, D. E. Ibbotson, and J. A. Mucha, J. Appl. Phys. **63**, 1744 (1988).
3 Y. Saito, K. Sato, H. Tanaka, K. Fujita, and S. Matsuda, J. Mater. Sci. **23**, 842 (1988).
4. Y. Liou, A. Inspektor, R. Weimer, D. Knight, and R. Messier, J. Mater. Res. **5**, 2305 (1990).
5. J. Wei, H. Kawarada, J. Suzuki, and A. Hiraki, J. Cryst. Growth **99**, 1201 (1990).
6. P. K. Bachmann, D. Leers, and H. Lydtin, Diamond Rel. Mat. **1**, 1 (1991).
7. R. A. Rudder, G. C. Hudson, J. B. Posthill, R. E. Thomas, R. C. Hendry, D. P. Malta, R. J. Markunas, T. P. Humphreys, and R. J. Nemanich, Appl. Phys. Lett. **60**, 329 (1992).
8. Dubbeldee Harris Diamond Corp., Mt. Arlington, New Jersey, USA.
9. R. E. Rawles, C. Kittrell, and M. P. D'Evelyn, in Diamond Materials, edited by J. P. Dismukes and K. V. Ravi (The Electrochemical Society, Pennington, New Jersey, 1993), pp. 269-275.
10. C. Pan, C.J. Chu, J. L. Margrave, and R. H. Hauge, submitted to Diamond Rel. Mat.
11. C. J. Chu, R. H. Hauge, J. L. Margrave, and M. P. D'Evelyn, Appl. Phys. Lett. **61**, 1393 (1992).
12. D. -W. Kweon, J. -Y. Lee, and D. Kim, J. Appl. Phys. **69**, 8329 (1991).
13. E. Kondoh, T. Ohta, T. Mitomo, and K. Ohtsuka, J. Appl. Phys. **72**, 705 (1992) and **73**, 3041 (1993).
14. J. W. Kim, Y. -J. Baik, K. Y. Eun, and D. N. Yun, Thin Solid Films **212**, 104 (1992).
15. W. A. Weimer, F. M. Cerio, and C. E. Johnson, J. Mater. Res. **6**, 2134 (1991).
16. B. V. Spitsyn and L. L. Bouilov, in Diamond and Diamond-Like Materials Synthesis, edited by G. U. Johnson, A. R. Badzian, and M. W. Geis, (Materials Research Society, Pittsburgh, PA, 1988), pp. 3-14.
17. M. Zhu, R. H. Hauge, J. L. Margrave, and M. P. D'Evelyn, in Diamond Materials, edited by J. P. Dismukes and K. V. Ravi (The Electrochemical Society, Pennington, New Jersey, 1993), pp. 138-145.

DIAMOND GROWTH RATES AND QUALITY: DEPENDENCE ON GAS PHASE COMPOSITION

William D. Cassidy*, Edward A. Evans*, Yaxin Wang*, John C. Angus*
Peter K. Bachmann**, Hans-Jurgen Hagemann**, Dieter Leers** and Detlef U. Wiechert**
*Case Western Reserve University, Cleveland, OH 44106-7217, USA
**Philips Research Laboratories, Aachen, D52021, Aachen, Germany

ABSTRACT

Diamond growth rates and quality were studied as a function of source gas composition and correlated with position on the ternary C-H-O diagram. The chemical potentials of carbon and oxygen change dramatically on either side of the H_2-CO tie line, leading to large differences in the equilibrium distribution of species. These differences are reflected in the species flux reaching the diamond surface, and hence in the quality and growth rate of the diamond. *In situ* microbalance measurements in a hot-filament reactor show that the reaction rate is independent of the CO concentration, but decreases with increasing O_2. Quality, as measured by Raman spectroscopy, increases as the C/C+O ratio in the source gases is reduced to approach the critical value of 0.5. The stability of the filaments to decarburizing and oxidation are correlated with the carbon and oxygen chemical potentials and hence to the position on the C-H-O diagram. A preliminary ternary diagram for the C-H-F system is presented.

GAS PHASE COMPOSITIONS

Since its introduction [1], the ternary C-H-O diagram has proven to be a very useful tool for study of the chemical vapor deposition of diamond [1]. A thermochemical explanation of the diagram has been given by Prijaya *et al.* [2].

Gas phase compositions for diamond growth are slightly undersaturated with solid carbon at the gas activation temperature. As the gas cools, it becomes supersaturated with carbon and solid carbon can precipitate. Gases containing only the elements C, H and O in equilibrium with solid carbon are dominated by H_2 and CO at high temperatures. Therefore, diamond growing gas compositions are close to the H_2-CO tie line on the ternary C-H-O diagram.

Solubility curves calculated using the methods of Prijaya *et al.* [2] are shown in Fig. 2. The solubility curves for the C-H-O system are a generalization of the results of Sommer and Smith [3,4], Lersmacher *et al.* [5] and Anthony [6]. In Fig. 1, and throughout this paper, we use the nomenclature of Bachmann *et al.* [1], in which the number of gram atoms of carbon, hydrogen and oxygen in the source gases are represented by C, H and O.

Equilibrium calculations show that the concentrations of secondary species change dramatically near the H_2-CO tie line [2]. Results of such calculations are shown in Fig. 2. Large changes in mole fraction occur at the critical concentration C/C+O = 0.5.

Gas phase compositions in the diamond growing domain were studied by mass spectroscopy and by optical emission spectroscopy. The ratio of the mass spectrometer signals for CH_4 and C_2H_2 in a hot-filament reactor is shown in Fig. 3. Note that as the O/C+O ratio increases, the ratio of CH_4 to C_2H_2 increases. This is in qualitative agreement with the calculations shown in Fig. 2. The measured change in CH_4/C_2H_2 ratio is less than one would infer from Fig. 2 because of mixing and deviation from equilibrium at points removed from the filament.

Mat. Res. Soc. Symp. Proc. Vol. 339. ©1994 Materials Research Society

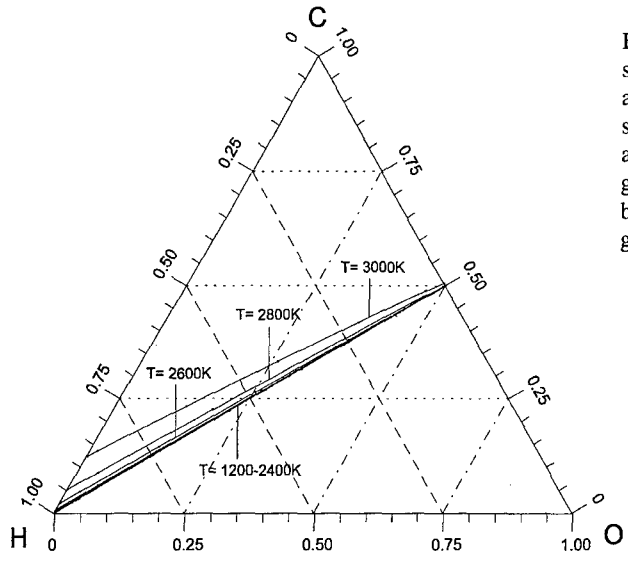

Figure 1. Calculated carbon solubility curves at 30 torr for a series of temperatures. The solubility curves delineate the approximate boundaries of gas compositions that have been successfully used to grow diamond [1].

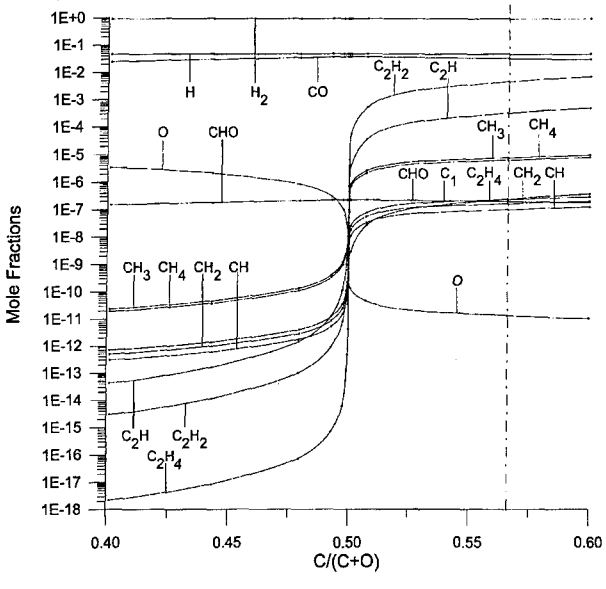

Figure 2. Calculated mole fractions versus C/C+O at 2300K and 30 torr. The partial pressure of H_2 was fixed at 27.5 torr. The vertical dashed line shows the carbon solubility limit at 2300K. The diamond domain extends from that point down to a value of C/C+O of approximately 0.5. Note that the C_2H_x molecules, e.g., C_2H_2, undergo greater changes than the CH_x molecules, e.g., CH_4.

Figure 4 shows optical emission spectra from an oxygen/acetone plasma during microwave assisted diamond deposition. The strong emissions from the CH, C_2 and C_3 bands are quenched as the C/C+O ratio is decreased to less than 0.5. This result is in agreement with the prediction of the equilibrium calculations for CH shown in Fig. 2 and for C_2 and C_3 given in reference [2].

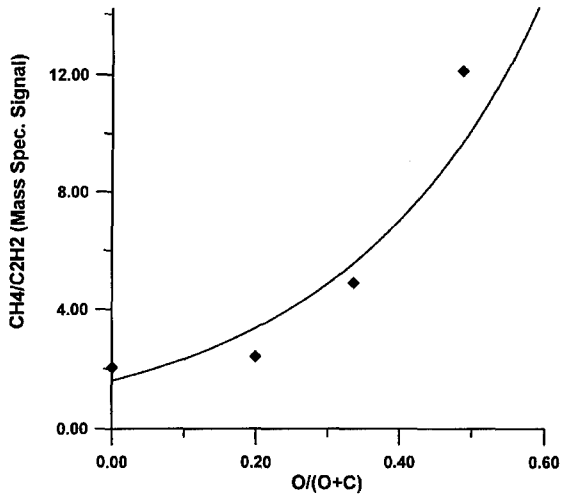

Figure 3. Ratio of mass spectrometer signals of CH_4 to C_2H_2 vs. O/C+O during hot filament assisted deposition of diamond at 30 torr. Gas mixtures made up from 0.5% CH_4 in H_2 and 1.5% O_2 in H_2.

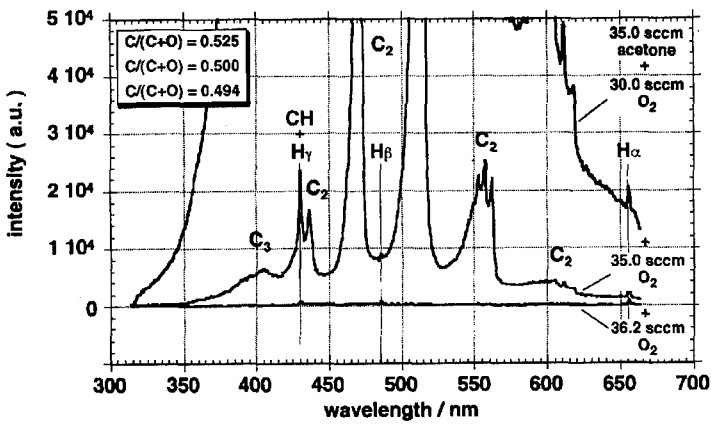

Figure 4. Optical emission spectra for CH, C_2 and C_3 during microwave plasma assisted deposition of diamond from acetone and oxygen at 100 torr and power of 3.6 kW.

DIAMOND GROWTH RATES AND QUALITY

The growth rate of diamond was studied during hot-filament assisted deposition using the *in situ* microbalance described by Wang and Angus [7]. The source gas was comprised of CH_4, H_2 and O_2. The growth rate is plotted as a function of O/C+O ratio in Fig. 5.

The growth rates for each individual methane concentration approach zero as the ratio O/C+O in the gas phase approaches 0.5. This result is consistent with the thermochemical analysis, which shows that the gas becomes undersaturated with respect to carbon at this point [2].

The results also agree with the conclusion that in hot-filament reactors CO acts as an unreactive sink for carbon in the gas phase. This was confirmed by experiments in which CO was added to the hot-filament microbalance reactor after steady-state diamond growth had been achieved. No measureable decrease in rate was observed. However, successful growth of diamond from CO/H_2 gas mixtures by microwave assisted plasma deposition indicates that the effective temperatures in plasmas are high enough to decompose CO.

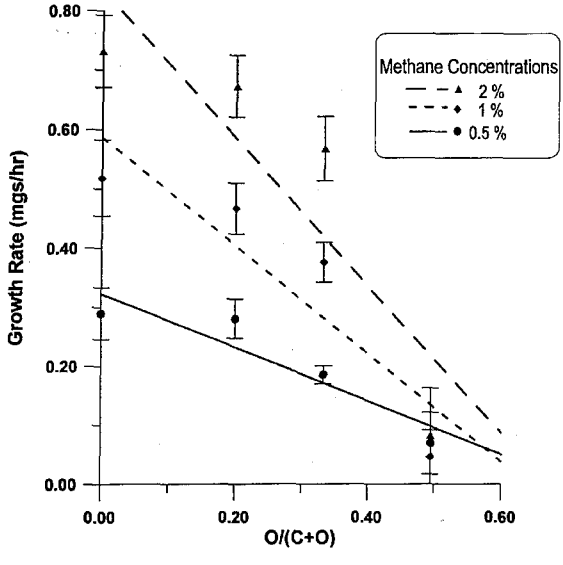

Figure 5. Growth rate of diamond during hot filament assisted deposition. Pressure was 30 Torr. Each data point is the average of several runs. The error bars show plus and minus one standard deviation.

The Raman spectra of diamond grown from acetone/oxygen mixtures in a microwave-assisted reactor at two different values of C/C+O are shown in Fig. 6. The spectra are much cleaner at the carbon-lean edge of the diamond domain (C/C+O = 0.48) than at the carbon-rich edge (C/C+O = 0.57).

DIAGRAMS FOR C-H-F AND C-H-Cl

The same technique described by Prijaya *et al.* [2] was used to generate carbon solubility curves for the C-H-F and C-H-Cl systems. Solubility curves for the former are shown in Fig. 7.

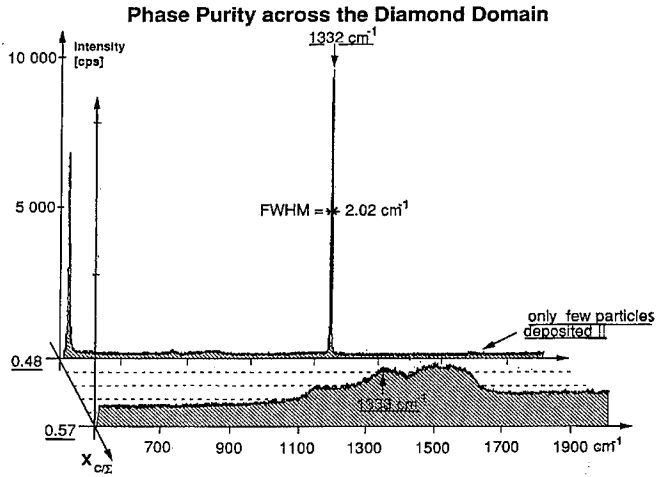

Figure 6. Raman spectra of diamond grown by microwave assisted deposition from acetone/oxygen. Compositions are : $X_{C/\Sigma}$ = C/C+O = 0.48 (carbon lean) and 0.57 (carbon rich).

The carbon solubility curves in the C-H-F system start near the H corner, approach the HF side of the triangular diagram near the point H/H+F ≈ 0.5 and terminate on the C-F side near C/C+F ≈ 0.2. This effect arises because the gas phase compositions in equilibrium with solid carbon are dominated by HF because of its stability. The carbon solubility curves for the C-H-Cl system (not shown) show low carbon solubilities in the gas phase except at very high temperatures.

The results of several experiments using $H_2/CF_4/CH_4$ mixtures in a conventional microwave diamond deposition system are plotted in Fig. 7. The limited results support the conclusions from the calculations that in the C-H-F and C-H-Cl systems the diamond growing compositions are at compositions leaner in carbon than in the C-H-O system.

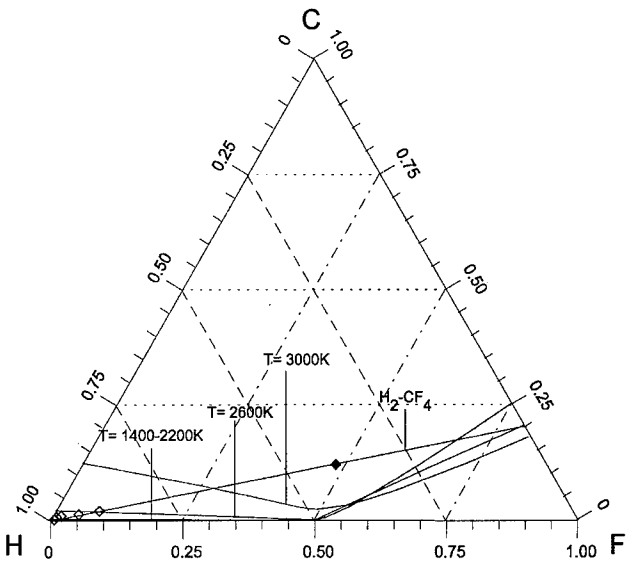

Figure 7. Computed solubility curves for the C-H-F system at temperatures from 1400 to 3000K. Total pressure is 30 torr. The H_2-CF_4 tie line is also shown. Successful diamond growing compositions are indicated by open symbols; the experiment that gave non-diamond carbon by a filled symbol.

FILAMENT STABILITY

The rate of generation of atomic hydrogen decreases as the extent of carburization of the filament increases [3,8]. Furthermore, the rate of diamond formation is believed to be proportional to the local hydrogen atom concentration. Therefore, the state of carburization of the filament is an important variable in determining the efficiency of a hot filament diamond deposition system.

Tungsten and tantalum filaments can exist as metals or carbides, or can become oxidized if the chemical potential of oxygen is sufficiently high. The equilibrium state of the filament can be plotted on the C-H-O diagram. The line for the equilibrium reaction $W + C = WC$ lies close to the H_2-CO tie line; but the line for the reaction $W + 3/2O_2 = WO_3$ is at much higher oxygen contents. On the other hand, for tantalum the line for the reaction $Ta + 5/2O_2 = Ta_2O_5$ is very close to the H_2-CO tie line. This means that tantalum filaments will be prone to oxidation if the source gas compositions deviate slightly below a ratio of C/C+O = 0.5. We have found this effect experimentally. Tantalum filaments oxidize rapidly with very small excursions of C/C+O ratio below 0.5.

SUMMARY

The diamond growing domain originally described by Bachmann and co-workers [1] is defined by overall source gas compositions that are close to the carbon solubility limit at gas activation temperatures. Equilibrium calculations delineate the approximate boundaries of the diamond domain for the C-H-O system. Similar methods are used to predict feasible overall source gas compositions in the the C-H-F and C-H-Cl systems. The ternary diagrams can also be used to correlate diamond growth rates and quality, which are a strong function of the overall elemental C/C+O ratio in the source gases. Growth rates decrease and quality of individual crystals increases as the C/C+O ratio is decreased to approach a value of 1.

ACKNOWLEDGEMENTS

The authors would like to acknowledge the support of the National Science Foundation (USA), Case Western Reserve University, Philips and the German Ministry of Research and Technology.

REFERENCES

1. P.K. Bachmann, D. Leers and H. Lydtin, Diamond and Related Materials **1**, 1 (1991).
2. N. Prijaya, J.C. Angus and P.K. Bachmann, Diamond and Related Materials **3**, 129 (1993).
3. M. Sommer, K. Mui and F.W. Smith, Sol. State Comm. **69**, 775 (1989).
4. M. Sommer and F. W. Smith, J. Mater. Res. **5**, 2433 (1990).
5. B. Lersmacher, H. Lydtin, W.F. Knippenberg and A.W. Moore, Carbon **5**, 207 (1967).
6. T. Anthony, in The Physics and Chemistry of Carbides, Nitrides and Borides, edited by R. Freer (Kluwer Academic Publishers, Norwell, MA, USA, 1990) p. 133.
7. Y. Wang and J.C. Angus, Proc. 3rd Int. Symp. on Diamond Materials, Honolulu, May, 1993; Proc. Vol. 93-17, J.P. Dismukes and K.V. Ravi, Eds., p.249, Electrochemical Society, Pennington, NJ, 1993.
8. R.R. Rye, submitted, J. Appl. Phys.

DIAMOND NUCLEATION STUDIES ON REFRACTORY METALS AND NICKEL

S. D. Wolter, B. R. Stoner*, P.C. Yang, W. Lui, and J. T. Glass
Department of Materials Science and Engineering, North Carolina State University, Raleigh, NC 27695-7919

*Electronic Materials Research Center, Kobe Steel USA Inc., Research Triangle Park, NC, 27709

ABSTRACT

Diamond nucleation has been investigated on a variety of potential heteroepitaxial substrate materials. Previous work in this laboratory has demonstrated heteroepitaxial nucleation on both Si and SiC substrates via bias-enhanced nucleation (BEN). In this study the effects of BEN of diamond on refractory metal substrates is investigated in detail. Initial data suggest a strong correlation between the carbide forming nature of the substrate material and the rate of nucleation during biasing. Our second avenue of research involves low pressure diamond growth on nickel. This material is a promising material due to its close lattice match and recent evidence of epitaxy reported by other researchers. To form heteroepitaxial diamond on nickel a high temperature pretreatment routine has been established and is the basis for this area of research. The relative importance of hydrogen absorption during this routine is explored and correlated to the formation and degree of diamond epitaxy.

Introduction

The understanding as to how the formation of a carbide influences diamond nucleation is important. Results from the initial diamond research on silicon indicated that a silicon carbide interlayer formed which was detected via transmission electron microscopy and observed to be typically less than a few hundred angstroms in thickness.[1] Also, surface analytical studies on diamond scratched silicon substrates have been undertaken to confirm the formation of this carbide and to determine its relevance on diamond nucleation.[2, 3] Previous work[2, 3] indicated the creation of a carbide prior to detecting the presence of diamond, which suggests that diamond may be nucleating on the resultant carbide. It should be noted though that very early during nucleation the presence of diamond is difficult to observe since the quantity of diamond present may be below the sensitivity of the typical analytical instrumentation. This stipulation makes it difficult to altogether rule out the possibility that diamond may be nucleating on the silicon rather than the carbide phase. This also holds true for other carbide forming substrates such as the refractory metals. Although, in a work involving diamond deposition on refractory metal substrates Joffreau et al.[4] observed a correlation between diamond nucleation and the kinetic properties of the resulting carbides. This eludes to the possibility that the resultant carbide is a principle component for influencing diamond nucleation. In this study and others the thickness of the carbide overlayer formed via the CVD environment is on the order of a few microns and was confirmed via XRD. Although silicon and the refractory metals are similar in that they both form carbides, these materials are different in that they possess unique carbide structures and material properties. Much may be gained from a better understanding of diamond nucleation if one were to study and compare the attributes of diamond nucleation on these materials such as that performed by Joffreau[4] and his colleagues.

The use of nickel as a substrate in the low pressure growth regime typically results in the formation of graphite rather than diamond. Sato et al.[5] have indicated that it is possible under certain conditions to form diamond on nickel at low pressure. There has been recent success in not

Mat. Res. Soc. Symp. Proc. Vol. 339. ©1994 Materials Research Society

only forming diamond on nickel but also obtaining highly oriented diamond.[6, 7] This has been readily obtained on both Ni(100) and Ni(111) surfaces and does not show a preference for the ease at which the oriented particles are attained with respect to the substrate surface orientation. The mechanism(s) responsible for the formation of diamond rather than graphite (in appreciable amounts) as well as the attainment of oriented diamond is not fully understood but there have been speculations for these possible mechanisms.[8]

This study was undertaken to investigate the influence of bias-enhanced nucleation (BEN) on the refractory metals. BEN has been observed to enhance the diamond nucleation density on unscratched silicon(100) substrates[9, 10] and it was later discovered that epitaxial diamond may form on this substrate via a carburization step followed by BEN.[13] This process involves applying a negative bias to the substrate holder while it is immersed in a CH_4/H_2 plasma in order to promote diamond nucleation. In a study of BEN on copper substrates the negative substrate bias was found to be relatively ineffective in promoting diamond nucleation.[11] These researchers used similar experimental conditions to a study performed by Stoner et al.[9] in which enhanced nucleation densities were evidenced on Si(100). It should be noted, although, that the ideal biasing conditions to obtain enhanced diamond nucleation densities may vary depending upon the substrate. However, it is speculated that the carbide forming nature of the substrate may strongly influence the nucleation efficiency during the biasing process. The variation in the carbide forming nature of the refractory metals should thus reveal a correlation with the nucleation phenomena via BEN. This should make it possible to gain further insight into BEN and diamond nucleation in general as well as investigating potential heteroepitaxial substrates using this pretreatment technique. With regard to the work undertaken on nickel an ex situ high temperature pretreatment was performed under vacuum as opposed to a previous study utilizing an in situ high temperature pretreatment in a hydrogen ambient. This study will investigate the relevance of hydrogen for carbon dissolution and possible diamond heteroepitaxy on nickel.

Experimental

I. Bias-enhanced nucleation of diamond on refractory metals

Bias-enhanced nucleation (BEN) and diamond deposition was performed in a microwave plasma CVD chamber purchased from Applied Science and Technology, Inc. The growth system has been discussed in greater detail previously.[9] BEN was performed as a pretreatment routine to promote diamond nucleation. In short, a negative dc bias is applied to a tantalum can and substrate holder, while the positive potential is connected to ground. Table I indicates the BEN and diamond deposition conditions utilized in this study.

The refractory metals used in this study were hafnium, titanium, tantalum, niobium, and tungsten and were studied within a short time span so that effects from growth system variations or other external influences would be minimized. These substrates were chosen arbitrarily with the exception of hafnium, which was used in the later phase of this experimental sequence to confirm possible correlations to be discussed later. The substrates were polished using SiC followed by diamond media and further polished using 0.05μm alumina powder suspended in deionized water. The substrates were then solvent cleaned using trichloroethylene, acetone, methanol, and 2-propanol, consecutively. A deionized water rinse was performed on the substrates just prior to entering into the growth chamber. Each of the refractory metal substrates were subjected to varying BEN times followed by 30 minutes of diamond deposition to obtain data of the nucleation density versus bias time. The short deposition period enabled an accurate account of the density of diamond nuclei that were observed by scanning electron microscopy (SEM). The initial diamond was found to have formed on the edges of these substrates and proceeded towards the center. The nucleation density measurements were undertaken at the center portion of the substrates and multiple sampling areas were examined to ensure consistent results. The nucleation density versus

bias time plot will provide insight into the effectiveness of BEN among the refractory metal substrates. This data will be referenced to previous BEN data obtained on silicon and copper. X-ray diffraction (XRD) was then used to confirm the formation of a carbide following BEN and diamond deposition.

Table I.	BEN	Diamond Deposition
Power	900 watts	900 watts
Plasma position	immersed	remote
CH_4/H_2	5%	1%
Pressure	15 torr	15 torr
Temperature	720°C	690°C
Time	variable	30 min.

Table II.	Pretreatment: STEP 1. Vacuum	STEP 2. HF CVD	Diamond Deposition STEP 3. HF CVD
CH_4/H_2	N/A	H2 only	0.5%
Pressure	1x10-6 torr	25 Torr	35
Temperature	~1050°C	~1050°C	900°C
Time	1 - 5 min.	15 min.	~3 hr.

II. High-temperature high-vacuum carbon dissolution in nickel

Polycrystalline nickel was highly polished using 0.1μm diamond grit. The substrates were solvent cleaned and thoroughly rinsed in de-ionized water. Following the cleaning procedure these substrate were seeded using 1.0μm diamond. The samples were sealed under a vacuum of roughly 1x10-6 torr in quartz ampoules. The ampoule containing the sample was then inserted into a furnace for 1, 3, and 5 minutes. The ampoules subsequently were removed and air cooled to room temperature before removing the samples from the ampoule. After removal the samples were ultrasonically cleaned in 2-propanol and entered into a hot filament chemical vapor deposition (HF CVD) chamber. A high temperature pretreatment as discussed previously[6, 7] was employed to condition the surface where upon highly oriented diamond may form. Following this pretreatment a diamond deposition routine was undertaken to grow out the diamond particles. Table II lists the conditions used for the three steps undertaken in this experimentation.

Results

I. Bias-enhanced nucleation of diamond on refractory metals

The plot of nucleation density versus bias time for the refractory metals compared to silicon and copper is shown in Figure 1. The diamond nucleation density on copper substrates as discussed previously is relatively unaffected by the application of a negative substrate bias.[11] In contrast silicon has proven to be an ideal substrate for BEN.[9] The individual plots of these materials were curve fitted with correlation coefficients greater than 0.85 and is meant to give a general interpretation of the relative influence of the negative substrate bias for establishing diamond nuclei. The nucleation densities at 60 minutes of substrate biasing were used to formulate a sequential ordering of the refractory metals according to their effect on diamond nucleation via BEN. The nucleation density at this bias time was chosen since any further substrate biasing did not appreciably increase the nucleation density. The initial experiments revealed that titanium

substrates resulted in a diamond nucleation density approaching $1x10^{10}/cm^2$ at this bias time. The niobium, tantalum, and tungsten provided decreasing nucleation densities, respectively. This initial survey study of these elements revealed a possible correlation to refractory metal material properties to be discussed shortly. This led to the addition of hafnium to this study in order to confirm these possible correlations. In short the hafnium was speculated to surpass the titanium nucleation densities at prolonged BEN times and was confirmed via experimentation.

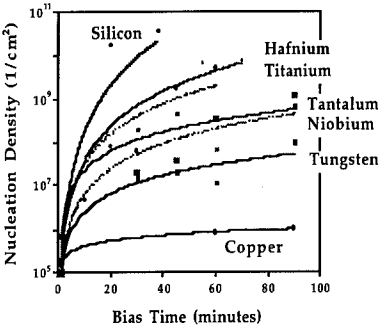

Figure 1. Nucleation density versus bias time for the refractory metals compared to silicon and copper.

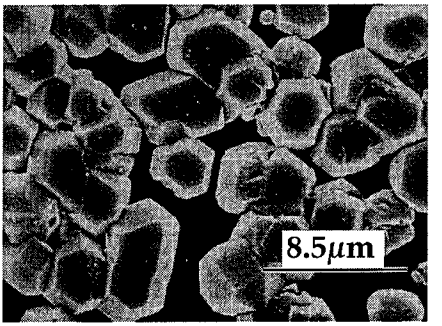

Figure 2. Diamond particles on nickel after performing the high-temperature high-vacuum carbon dissolution step.

II. High-temperature high-vacuum carbon dissolution in nickel

The nickel substrates were observed to have reacted with the diamond seeds during the high temperature vacuum pretreatment (the white haze over the surface from the diamond seeds prior to this pretreatment had notably darkened). The samples were subsequently removed from the ampoule and ultrasonically cleaned in 2-propanol revealing a shiny, mirror-polished surface. The high temperature pretreatment routine and diamond deposition were then undertaken via HFCVD. Figure 2 shows that for the 5 minute vacuum pretreatment, highly oriented diamond was formed. The 1 and 3 minute pretreatments resulted in oriented particles although much less in quantity than for the 5 minute sample. The nickel had presumably absorbed carbon during the high temperature vacuum pretreatment that was utilized during the deposition procedures performed in the HFCVD system.

Discussion

I. Bias-enhanced Nucleation on Refractory Metals

It has been speculated that an important attribute for enhanced diamond nucleation via the negative substrate bias is the carbide forming nature of the substrate. Thus, the refractory metals were chosen because of their carbide forming nature. The extreme nucleation densities plotted in Figure 1 confirmed this speculation and also indicated a preferential ordering of these metals according to their carbide forming traits.

The periodic trends of the refractory metal and carbide material properties are generally known to those who have studied these materials. With respect to diamond nucleation it may not

be unreasonable to expect the nucleation processes to be influenced by a similar manner. Typical pretreatment techniques to enhance diamond nucleation utilize diamond media as a precursor to diamond formation. This directly influences diamond nucleation in that nucleation densities pretreated with diamond media are approximately 3 orders of magnitude higher than when compared to non-pretreated substrates. BEN does not require a deleterious pretreatment or carbon precursor that may influence diamond nucleation; nucleation may be enhanced on pristine substrates via this process. Therefore, it is fortuitous to have at our disposal this class of material with well-defined periodic attributes that allow the authors to use BEN to study diamond nucleation.

The properties associated with the elements or various compounds may be explained by their (i) thermodynamic or (ii) kinetic attributes. A correlation was determined with regard to the thermodynamic attributes of these materials. The thermodynamic data that was investigated was the heat of formation of the carbide (ΔHf^{298}) and these values show a strong correlation to the nucleation density values at 60 minutes of biasing (Figure 1) as shown in Figure 3. This figure includes the data for both the monocarbides and the subcarbides, when relevant. Both data were included since the XRD observed these phases on the applicable metals. In short the refractory metals with a more stable carbide formation (i.e. more negative ΔHf^{298}) resulted in the greatest nucleation density of diamond.

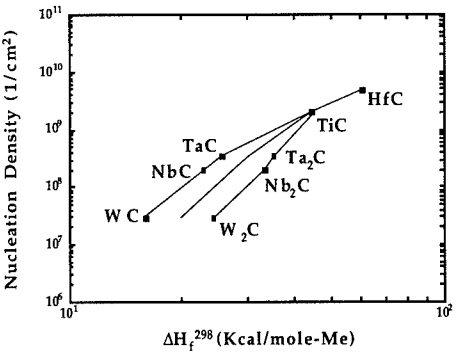

Figure 3. Plot of the nucleation density at 60 minutes of BEN versus the carbide heat of formation. This graphic reveals a correlation between BEN and this material property.

II. High-temperature high-vacuum carbon dissolution in nickel

Recently, it has been uncovered that by employing a high temperature substrate pretreatment in hydrogen, highly oriented diamond was possible.[6, 7] This pretreatment was implemented to first dissolve carbon into the nickel and second to condition the surface so that highly oriented diamond may be formed. The relevance of hydrogen on carbon dissolution in nickel and the role this species plays for influencing the surface for heteroepitaxial diamond formation has not been established.

The approach in this present research effort has been to first investigate the influence of hydrogen on carbon dissolution. During experimentation it was observed that the carbon dissolution rate was comparable to previous work when undertaken in a hydrogen ambient. Also, following the high temperature carbon dissolution pretreatment performed in vacuum (Step 1) and employing the high temperature pretreatment in the HFCVD chamber (Step 2) carbon was observed to diffuse out of the nickel. This suggests that the solubility of carbon in nickel may be decreased in the presence of hydrogen. A continuation of this research would expand into

performing both Step 1 and Step 2 in vacuum. It is speculated that since the solubility of carbon appears to be greater in nickel when the high temperature dissolution pretreatment is performed in the absence of hydrogen that higher nucleation densities may result.

Conclusion

BEN has lead to heteroepitaxy on β-SiC[12] and Si(100)[13]. It is speculated that the carbide forming nature of silicon may be an important attribute for this pretreatment technique. Thus, the motivation for studying the refractory metals is linked to their carbide forming traits. The refractory metals did show a correlation to the carbide heat of formation. The thermodynamic data referenced to the nucleation density at 60 minutes of biasing indicates very strongly that the substrates are influencing the nucleation mechanisms. The relatively high nucleation densities (with no scratching pretreatment) reveals that, provided a high quality carbide may be formed, these substrates are potential candidates for BEN of heteroepitaxial diamond.

Also, highly oriented diamond was obtained on nickel via a high-temperature high-vacuum carbon dissolution pretreatment. The role of hydrogen on carbon dissolution and for obtaining highly oriented diamond particles has not yet been well established. In this study it was observed that the carbon solubility in nickel may be increased in the absence of hydrogen.

Acknowledgments

The authors wish to acknowledge the financial support of this research which was provided in part by BMDO/IST through ONR and the Kobe Steel, Ltd. Professorship at NCSU.

References

1. B. E. Williams and J. T. Glass, 4:2 (1989) 373.
2. B. E. Williams, B. R. Stoner, D. A. Asbury and J. T. Glass, presented at*Diamond and Diamond-Like Films and Coatings, NATO Advanced Study Institute, Series B: Physics , Castelvecchio Pascoli, Italy, 1990*, Plenum, New York, 1990.
3. D. N. Belton, S. J. Harris, S. J. Schmieg, A. M. Wiener and T. A. Perry, **Appl. Phys. Lett.**, 54:5 (1989) 416.
4. P. O. Joffreau, R. Haubner and B. Lux, **Int. J. of Ref. Hard Metals**, 7:4 (1988) 186.
5. Y. Sato, I. Yashima, H. Fujita, T. Ando and M. Kamo, presented at*Materials Research Society , Pittsburgh, PA, 1991*, p. 371.
6. W. Zhu, P. C. Yang and J. T. Glass, **Appl. Phys. Lett.**, 63:12 (1993)
7. P. C. Yang, W. Zhu and J. T. Glass, **J. Mater. Res.**, 8:8 (1993)
8. W. Zhu, P. C. Yang and J. T. Glass, presented at*Proc. of the 2nd International Conference on Applications of Diamond Films , Tokyo, Japan, 1993.*
9. B. R. Stoner, G.-H. M. Ma, S. D. Wolter and J. T. Glass, **Phys. Rev. B**, 45:19 (1992) 11067.
10. S. Yugo, T. Kanai, T. Kimura and T. Muto, **Appl. Phys. Lett.**, 58:10 (1991) 1036.
11. S. D. Wolter, B. R. Stoner and J. T. Glass, **Dia. Rel. Mat.**, In print (1994).
12. B. R. Stoner and J. T. Glass, **Appl. Phys. Lett.**, 60:6 (1992) 698.
13. S. D. Wolter, B. R. Stoner, J. T. Glass, P. J. Ellis, D. S. Buhaenko, C. E. Jenkins and P. Southworth, **Appl. Phys. Lett.**, 62:11 (1993) 1215.

DEFECTS AND GROWTH OF DIAMOND WAFERS

D. SHECHTMAN
Department of Materials Engineering, Technion, Haifa, Israel.
Currently at JHU, NIST and NRL.

ABSTRACT

Crystallographic defects which form during growth of CVD diamond were studied and their effect on the surface structure of the growing wafer evaluated. The most abundant defects are $\Sigma=3$ twins boundaries whose density is very high at the nucleation side and as low as one twin per 10 μm at the growth surface. The intersection of these twin boundaries with one another results in a formation of higher order twin boundaries. $\Sigma=9$ as well as $\Sigma=27$ and $\Sigma=81$ boundaries have been analyzed. The surface crystallography of optical quality diamond wafers reveals the role of $\Sigma=3$ twins in promoting fast growth.

INTRODUCTION

As diamond wafers become a commercial product, their properties and growth rate will determine their market success. Since structural defects affect both, it is crucial to define them and to understand the way they interact with one another. It is also important to understand the role they play in promoting fast growth on the one hand and harming some properties on the other. Since the lattice parameter of diamond is as small as 0.356 nm, the proper tool to study structural defects in diamond is a transmission electron microscope (TEM) with resolving power of better than 0.2 nm. This allows resolving the {111} planes on which $\Sigma=3$ boundaries occur. The morphology and crystallography of the surface of a diamond wafer can be studied by scanning electron microscopy (SEM).

EXPERIMENTAL

A large number of samples were prepared by three methods: Microwave Plasma Assisted CVD, Hot Filament and Plasma Jet. The thickness of the specimens ranges from 1 μm to 1.5 mm. Thin films made of the bulk wafers were studied by high resolution transmission electron microscopy and the surfaces by SEM. Although quantitatively the microstructure varies from one specimen to the other, depending on the deposition method and parameters, the crystallography of the defects and their interaction was the same for all the specimens studied.

RESULTS AND DISCUSSION

$\Sigma=3$ Twins

The microstructure of a wafer consists of columnar grains with a cross section that grows from about 1 μm at the nucleation side of the wafer to about 100 μm at the growth side (see figure 1). The most abundant crystallographic defects found in the films and wafers were $\Sigma=3$ twins. The mean free path between them ranges from about 10 nm at the nucleation side, to about 10 μm at the growth side. These $\Sigma=3$ twins are coherent in most cases and thus the twin boundary matches the {111} twin plane. Non-coherent $\Sigma=3$ twin boundaries are found too, but in diamond, unlike the case of silicon, they tend to form on a {111} plane of the twin (not the common {111}). The non-coherent $\Sigma=3$ boundaries may effect the properties of the diamond, but this will be discussed elsewhere.

Mat. Res. Soc. Symp. Proc. Vol. 339. ©1994 Materials Research Society

High Order Twins

As twinned parts of the crystal grow contiguously, a higher order twin boundary is formed. The intersection line of two $\Sigma=3$ twin boundaries becomes this way the nucleation line of a $\Sigma=9$ boundary. Because $\Sigma=3$ twin boundaries are in most cases planar and form on the {111} twin habit plane, the $\Sigma=9$ twin nucleates along a straight line. Two more high order boundaries that have been observed and studied are $\Sigma=27$ and $\Sigma=81$ [1,2]. These high order twin boundaries can be considered as grain boundaries with a special orientation between the grains.

Growth Features

We shall now deal with the role of twins in the growth of CVD diamond wafers, and start at the nucleation side. Figure 2 illustrates an early stage of growth of diamond nuclei by Hot Filament CVD. Similar observations were made on the nucleation of Microwave Plasma assisted CVD. The one distinctly large crystal is heavily facetted and its surface is rich in reentrant corners. The other relatively large crystals, marked with arrows, are twinned and their morphologies contain reentrant corners.

Figure 1
The fractured section of a diamond wafer reveals the development of the grains.

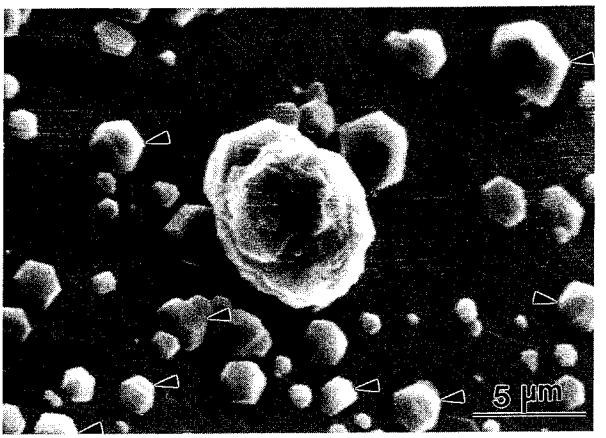

Figure 2
In the early stage of the nucleation, the larger crystals are heavily twinned, the medium sized (marked) contain several twins each and the smaller crystals contain no twins.

Faceted untwinned crystals are relatively small and usually grow to about 1 μm in size. The growth sequence that emerges is the following: as the small facetted crystals develop twins to relieve elastic stress, reentrant corner can form in them and growth rate increases. The twinned crystals have therefore an advantage over the other ones and while growing further they twin more and increase their edge. The selection of the winners in the growth race is done therefore in an early stage of the wafer's growth process, which matches our observations on cross sections of wafers.

As the growth process continues, only very few of the initial nuclei survive to grow from about 1 μm to 100 μm on the side. Survival rate is thus 10-4 and the fittest, twinned crystals win the race to stay at the surface. The many others are shadowed and cease to grow [3]

Figure 3
The growth morphology of the wafer is characterized by parallel steps formed along laminar $\Sigma=3$ twins. The growth planes are {111} and {001}.

We shall consider now the growth surface of a thick wafer. The surface morphology of an optical quality unpolished diamond wafer is illustrated in figure 3. The wafer is 1.5 mm thick and the grain size at the surface is several hundred μm. It is clear that the crystals are composed of parallel twinned sections which form reentrant and convex corners on the surface. The planar twins vital for the formation of this morphology are of the $\Sigma=3$ type and they can exist at the top because they run parallel to the growth direction. This is shown in the polished and etched cross-section, figure 4. $\Sigma=3$ twins which form in directions other than the one shown in the figure, run into the grain boundary and stop growing. The laminar twins thus divide each crystal into two interlocking orientations. While reentrant corners in a diamond single crystal can form only at the intersection line of the twin with the surface, convex corners can form along any line of facet plane intersection. Reentrant corners are important for the nucleation of new planes on the growth surface [3] and facilitate fast growth by promoting new plane nucleation. The laminar twins become this way an important surface feature for fast growth.

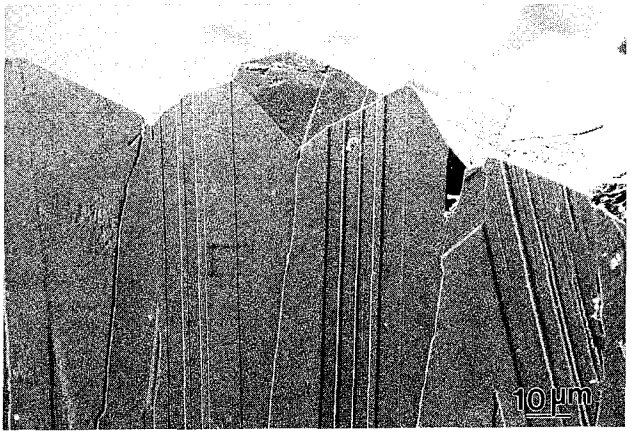

Figure 4
The survival of $\Sigma=3$ twins during the growth process depends on their orientation. Only twins that form parallel to the growth direction can make it to the surface.

CONCLUSION

While high order twins may be harmful to diamond wafer properties, $\Sigma=3$ twins play a beneficial role by releasing stress at the first growth stages and by promoting fast wafer growth. A diamond wafer which features laminar twins on its growth surface may actually be the product of choice as it grows relatively fast and possesses good optical and other properties.

ACKNOWLEDGEMENT

The study is sponsored by ARPA/NRL.

REFERENCES

1. D. Shechtman, J.L. Hutchison, L.H. Robins, E.N. Farabaugh and A. Feldman, "Growth defects in diamond films" J. Mater. Res., Vol. 8, No. 3, (1993) 1.

2. D. Shechtman, A. Feldman and J.L. Hutchison, "High order twin boundaries in CVD diamond films", Materials Letters 17 (1993) 211-216.

3. A. van der Drift, "Evolutionary selection a principle governing growth orientation in vapour-deposited layers", Philips Res. Reports 22 (1967) 267-288. Press, New York, 1991 p. 611.

4. R.G. Seidensticker and D.R. Hamilton, "Growth mechanisms in germanium dendrites" J. Appl. Phys. 34 (1963) 3113.

DEPOSITION OF DIAMOND USING AN ELECTRON CYCLOTRON RESONANCE PLASMA SYSTEM

DONALD R. GILBERT*, RAJIV SINGH*, W. BROCK ALEXANDER*, DONG GU LEE*, AND PATRICK DOERING**
*Department of Materials Science and Engineering, University of Florida, Gainesville, FL 32611
**LMA, Inc., 93 West Tech Center, Medfield, MA 02052

ABSTRACT

We have used an electron cyclotron resonance plasma system to perform chemical vapor deposition experiments on single-crystal, (110) oriented diamond substrates. The depositions were carried out at 0.060 Torr using mixtures of methanol in hydrogen. Substrate temperatures were varied from approximately 620 to 800 °C. The film morphology was examined using SEM and microstructural phase determination was attempted using micro-Raman spectroscopy. Based on the results of these experiments, we have determined general trends for the characteristics of films deposited on diamond from the ECR plasma at low pressures and temperatures.

INTRODUCTION

In recent years, a great deal of effort has been put into investigating the chemical vapor deposition (CVD) process of diamond formation. Diamond has the widest bandgap (5.45 eV) of the Group IV semiconductors and is optically transparent well into the infrared region of the spectrum. It has the highest thermal conductivity of any natural material at room temperature. It is extremely hard, has a low coefficient of friction and is relatively inert. All of these qualities make diamond very attractive for a host of potential applications.

A fundamental obstacle to deposition of diamond on non-diamond substrates is the difficulty with which diamond nucleates. This is due in part to the high surface energy of diamond, which acts as a barrier to nucleation. As a result, this requires pretreating the non-diamond substrate, usually by scratching with some form of diamond grit.[1-5] In contrast, deposition of diamond on a pre-existing diamond surface avoids the problem of a nucleation barrier, facilitating the formation of new diamond and allowing growth to occur readily. Ideally, deposition will occur epitaxially, forming a continuous single crystal. However, there is a high probability that the new diamond will nucleate and grow with some degree of misorientation to the substrate, resulting in a polycrystalline film.

Current standard diamond CVD systems (such as hot-filament and microwave plasma) typically operate at pressures above 10 Torr and substrate temperatures above 800 °C. This general range of operating conditions has been fairly well surveyed using a variety of chemical vapor mixtures (commonly CH_4 or CO in H_2, often with O_2 added).[6] Extension of the characterized deposition conditions to lower pressure and temperature regimes may provide added insight into the fundamental processes which occur during growth. One system which is well suited to this task is the electron cyclotron resonance (ECR) enhanced plasma CVD system.

Mat. Res. Soc. Symp. Proc. Vol. 339. ©1994 Materials Research Society

EXPERIMENT

Experiments were carried out in a Plasma-Therm BECR6 electron cyclotron resonance plasma system. This system uses an external ring of rare-earth permanent magnets to produce the necessary magnetic field for the ECR condition inside the aluminum reaction chamber. Figure 1 shows a schematic of the system. A standard 1.5 kilowatt microwave source operating at 2.45 GHz was used to produce the plasma.

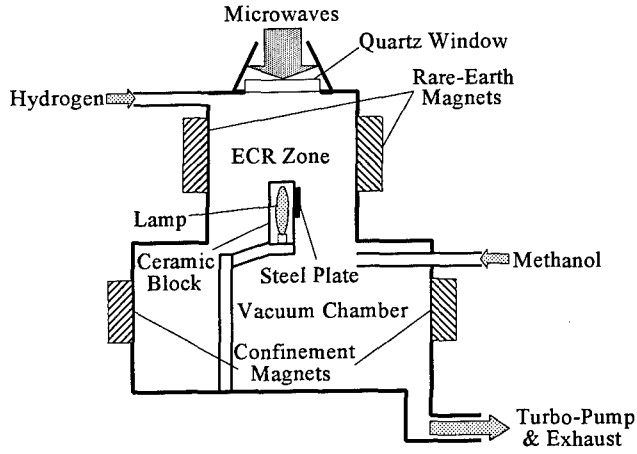

Figure 1. Schematic of ECR deposition system

Single crystal (110) oriented diamond substrates of approximately 1.5 to 2.5 mm average diameter were mounted on a stainless steel plate using colloidal silver paste. The plate was fitted to a ceramic block containing a quartz heat lamp. The substrate position relative to the plasma region was adjustable. An electrical bias was applied to the steel mounting plate with the intention of modifying the ion/electron impingement onto the substrate.

In preparation for deposition, the (110) substrates were sonicated in acetone, washed in a hot acid solution (3:1 HNO_3:H_2SO_4), and rinsed with methanol. Substrates were also exposed to a hydrogen plasma for 30 to 40 minutes before beginning deposition.

A vacuum system base pressure of less than 2×10^{-5} Torr was achieved prior to each experiment. All depositions were conducted at 0.060 Torr. Gas mixtures of methanol and hydrogen, ranging from 1.0% to 5.5% methanol, were used for deposition. Input microwave power was 1000 watts with a typical reflected power of 5% or less, depending on the reactor conditions chosen. The substrate temperatures were varied from approximately 620 to 800 °C, as determined by a pre-established calibration of the power applied to the quartz heat lamp. A positive bias voltage of 40 volts, relative to ground, was supplied to the steel mounting plate. All depositions reported here occurred inside the active (luminous) plasma region.

Following deposition, the surface morphology was observed using scanning electron microscopy. Determination of the phase of the deposited films was attempted using micro-Raman spectroscopy. SIMS was used to examine the constituent make-up of the film as a function of depth.

RESULTS

The small size of the substrates complicated investigation of the processed samples. SEM observation of film morphology was the most readily obtained method of characterization. Using SEM, along with other microstructural characterization techniques, we have developed some basic outlines for the behavior of film evolution in the ECR under different process conditions.

Figure 2 shows three SEM views of a clean substrate surface. The predominant surface is very smooth, although some particulate coverage is clearly evident. All substrates demonstrated some irregular features due to damage caused during fabrication, as seen in Figure 2(b) and 2(c).

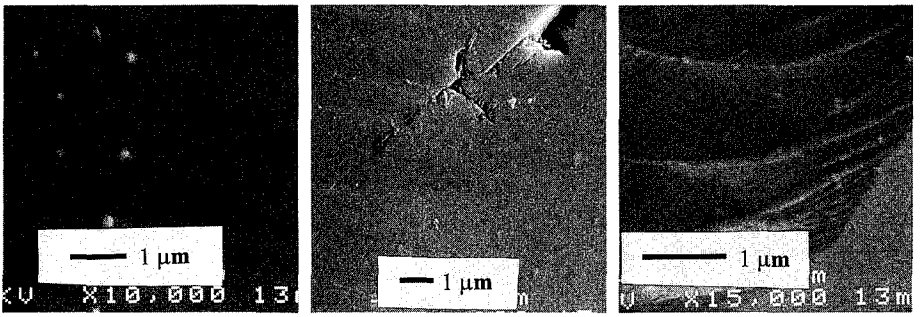

(a) (b) (c)

Figure 2. Typical morphology of a diamond substrate showing (a) surface, (b) crack and (c) chip features.

After twenty minutes of deposition, the surface still appeared relatively smooth, as seen in Figure 3(a), although there was visual evidence of thin, continuous film coverage. SIMS depth analysis of incorporated impurities of the 20 minute sample confirmed the presence of a film. After 40 minutes of deposition, Figure 3(b), we saw a significant alteration of the surface morphology. The predominant surface became much rougher. The deposition conditions used for this investigation were 3% methanol in hydrogen with a substrate temperature of approximately 680 °C.

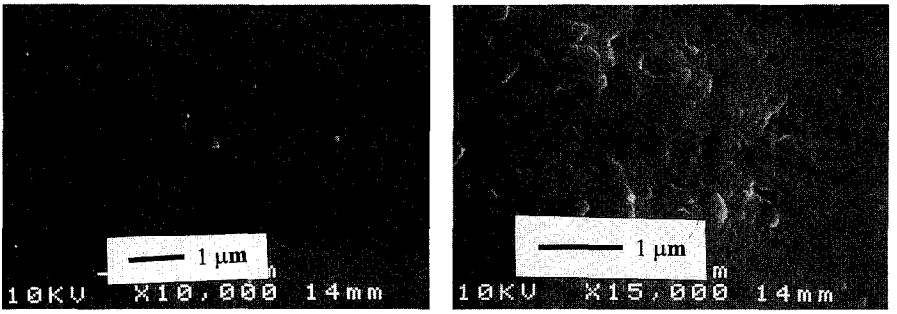

(a) (b)

Figure 3. Film morphology after (a) 20 and (b) 40 minutes of deposition.

Observation of the film morphology after 4 hours of deposition showed a very uniform coverage of all surfaces, as seen in Figure 4. The film displayed a relatively fine texture, with average features of approximately 100 nm.

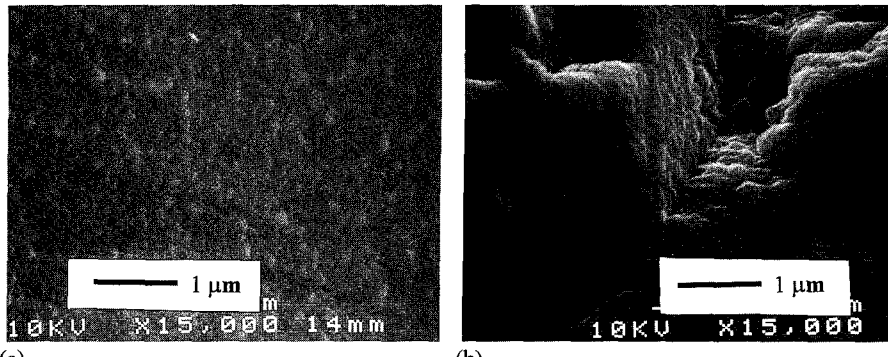

(a) (b)

Figure 4. Morphology after 4 hour deposition showing (a) surface and (b) edge coverage.

The substrate temperature was found to play a critical role in the determination of the deposited film characteristics. Figure 5 shows films which were deposited at 620, 720 and 800 °C. All depositions were made for four hours using 3% methanol in hydrogen. At 620 °C, we observed an irregular surface with a prevailing island-like morphology. A predominantly smooth film was obtained at 720 °C. The highly irregular area seen in Figure 5(b) is the result of a substrate fabrication feature. When deposition was attempted at 800 °C, a non-adherent, flaky coating resulted. The surface beneath the flaky coating was relatively irregular, with a great deal of small scale (~200-300 nm) pitting.

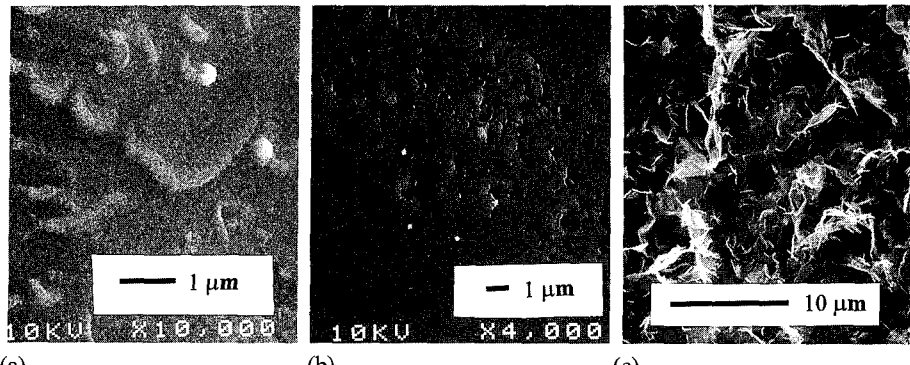

(a) (b) (c)

Figure 5. Film morphology from (a) 620, (b) 720 and (c) 800 °C deposition.

The gas phase chemistry is also critical to the resulting deposited film morphology. Figure 6 shows the effects of varying the relative amount of methanol in hydrogen in the gas mixture when using a substrate temperature of approximately 720 °C. Figure 6(a) shows the results of a four hour deposition from a 1% methanol mixture. The predominant surface was extremely smooth with some particulate coverage, which is very similar to the plain substrate shown in Figure 2. Nucleation and growth is evident at surface irregularities, as is seen along the crack feature shown. The film shown in Figure 5(b) (above) serves as an example of deposition from 3% methanol at the stated conditions. Figure 6(b) shows the surface of a film deposited from 5.5% methanol after four hours. The same type of uniform, flaky, non-adherent coating as was seen in Figure 5(c) was obtained.

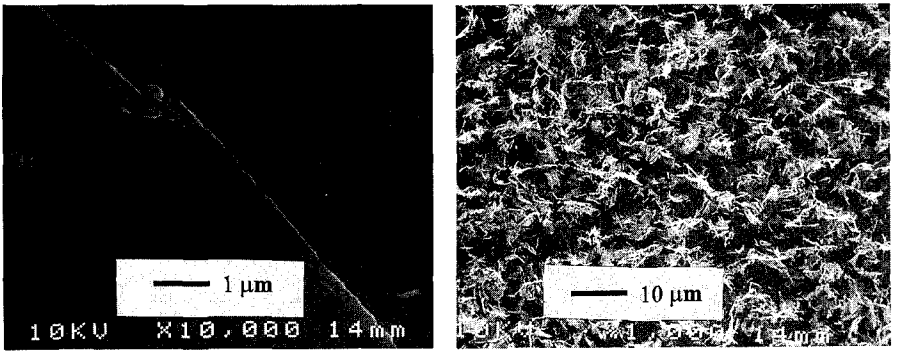

(a) (b)

Figure 6. Deposited film morphology from (a) 1% and (b) 5.5% methanol mixtures.

The results of micro-Raman spectroscopy have been relatively inconclusive thus far. Figure 7 shows a typical film spectrum, which was taken from the film shown in Figure 4 (4 hour deposition at 700 °C from 3% methanol in hydrogen). The sharp diamond peak at 1333.4 cm^{-1} with a full-width-at-half-maximum of 2.9 cm^{-1} is clearly evident. However, there has been a lack of significant variation in spectrum characteristics for different experimental conditions. We theorize that we may be seeing a significant influence from the substrate material which may obscure observation of the film characteristics. Analysis of a bare substrate yielded a peak at 1332.7 cm^{-1} with a full-width-at-half-maximum of 2.8 cm^{-1}. Our most significant observation based on the Raman spectra has been the notable lack of non-diamond-phase features, which have a much higher scattering efficiency than diamond.

CONCLUSIONS

We have shown that variation of gas composition over a fairly narrow range (1-5% methanol) has a very significant effect on the deposited film morphology. Substrate temperature is also an important parameter, with excessive heating (≥800 °C) yielding poor film structure. Also, film evolution in the ECR appears very uniform over the substrate surface.

Work is in progress to further determine the microstructural characteristics of diamond films produced under these unique conditions.

Figure 7. Micro-Raman spectrum of film deposited at 700 °C from 3% methanol in hydrogen on a (110) diamond substrate.

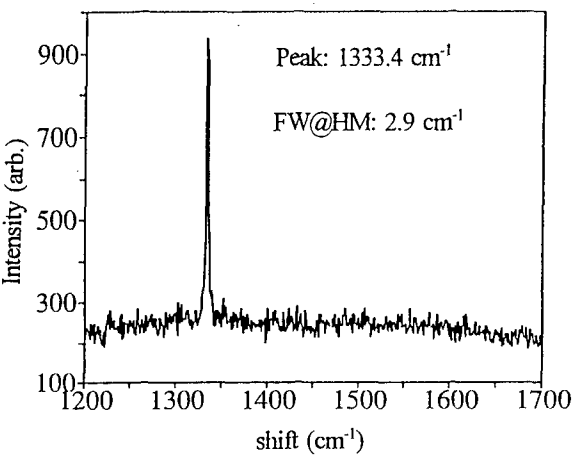

ACKNOWLEDGEMENTS

This work was supported by BMDO/IST and managed by ONR.

REFERENCES

1. H. Itoh, T. Osaki, H. Iwahara, and H. Sakamoto, J. Mat. Sci. **26**, 3763 (1991).

2. R. Polini, J. Appl. Phys. **72**, 2517 (1992).

3. P. A. Dennig, H. Shiomi, and D. A. Stevenson, Thin Solid Films **212**, 63 (1992).

4. H. Maeda, S. Ikari, T. Okubo, K. Kusakabe, and S. Morooka, J. Mat. Sci. **28**, 129 (1993).

5. P. E. Pehrsson, F. G. Celii, and J. E. Butler, in Diamond Films and Coatings, edited by R. F. Davis (Noyes Publications, Park Ridge, New Jersey, 1993) pp. 71-108.

6. P. K. Bachmann, D. Leers, and H. Lydtin, Diamond and Related Materials **1**, 1 (1991)

CHARACTERIZATION OF A THICK HOMOEPITAXIAL CVD DIAMOND FILM

M. A. PLANO, M. D. MOYER AND M. M. MORENO
Crystallume, Menlo Park, CA 94025
D. BLACK, H. BURDETTE AND L. ROBINS
National Institute of Standards and Technology, Gaithersburg, MD
L. S. PAN AND D. R. KANIA
Lawrence Livermore National Laboratory, Livermore, CA
W. BANHOLZER
G. E. Superabrasives, Worthington, OH

ABSTRACT

A thick homoepitaxial CVD diamond film was grown on a large high temperature, high pressure (HTHP) IIa diamond to study the defects present in the CVD film. The HTHP diamond had dimensions of 6 mm x 6 mm x 0.44 mm. The thickness of the diamond was increased to 0.84 mm by microwave plasma CVD. X-ray topographs were taken before and after growth to compare the defects in CVD diamond to those in the HTHP diamond. Prior to growth the substrate was unstrained and the characteristic microstructure of stacking faults and dislocations was observed. There was also a surface relief, visible optically, on the substrate of lines along the [100] which are probably due to polishing. After deposition of the CVD film, the crystal was strained with the film in tension. The defect structure observed throughout the CVD film followed the surface relief of the substrate. Cathodoluminescence spectra indicate that the film contains nitrogen defect complexes which are not present in the substrate. Cathodoluminescence also indicates that there are more non-radiative recombination centers in the film than in the substrate. Electrical results from transient photoconductivity measurements indicate that while the mobilities of the film and the substrate are comparable, the lifetime is much shorter in the film, possibly reflecting the higher concentration of non-radiative recombination centers.

INTRODUCTION

Diamond semiconductor electronic applications depend critically on the ability to grow low-defect, high-quality, single crystal diamond layers [1]. One technique to study defects in single crystals is X-ray topography[2]. By comparing topographs of a diamond substrate and a chemical vapor deposited (CVD) thick film grown on the same substrate a study can be made of the defects both in the substrate and in the film. Also, one can determine if defects in the substrate affect the formation of defects in the film. The presence of defects in the diamond films can also be detected by observing their indirect effect on electrical and luminescence measurements. The ability to control defect formation and impurity incorporation in single crystal CVD diamond films would make them superior to natural diamonds.

EXPERIMENTAL DETAILS AND RESULTS

A thick, undoped homoepitaxial CVD diamond film was grown on a large high temperature, high pressure (HTHP) [3,4] IIa diamond to study the defects present in the CVD film. The HTHP diamond had dimensions of 6 mm x 6 mm x 0.44 mm and the thickness of the diamond was increased to 0.84 mm by microwave plasma CVD[5]. Figure 1 is an optical micrograph of

Mat. Res. Soc. Symp. Proc. Vol. 339. ©1994 Materials Research Society

the sample and the diamond is highly transparent and smooth. The defect in the center of the crystal is a metal inclusion in the HTHP substrate.

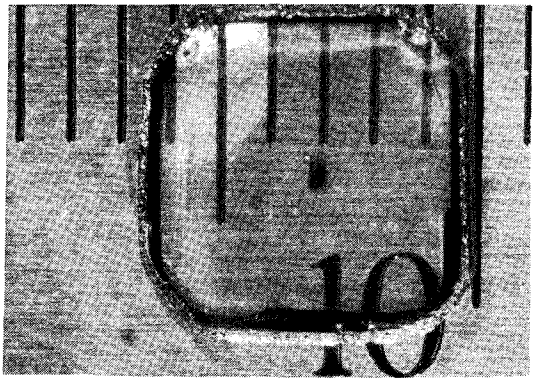

Figure 1. Optical micrograph of a diamond sample consisting of a HTHP substrate with a 400μm film of CVD homoepitaxial diamond on the surface.

X-ray topographs were taken before and after growth to compare the defects in CVD diamond to those in the HTHP diamond. Prior to growth the substrate was unstrained and the characteristic microstructure of stacking faults and dislocations was observed. There was also a surface relief, visible optically, on the substrate of lines along the [100] which are probably due to polishing. These lines are visible in the center of the crystal in the x-ray topograph shown in Fig. 2.

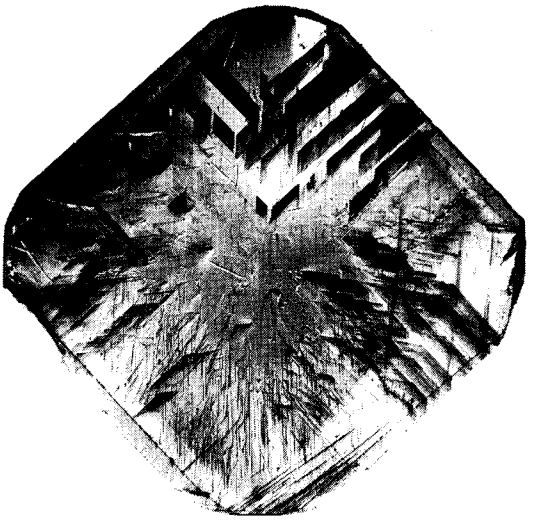

Figure 2. A $(\bar{2}20)$ asymmetric transmission image of the HTHP substrate. The dark-planar features are stacking faults and the fine linear features seen at the bottom of the image are dislocations. This crystal has a series of lines seen on the surface of the crystal, parallel to [100], which probably resulted from polishing.

After deposition of the CVD film, the crystal was strained with the film in tension. Five separate images were required to image the whole crystal at a fixed Bragg angle, as can be seen in Fig. 3. It is possible that the strain observed in the diamond after deposition of the CVD film results from a change in lattice spacing in the film due to the incorporation of hydrogen. There is a high defect density in the film and it is probable that there are many dislocations. The defect microstructure of the film was observed to follow the surface "relief" as seen in Fig. 3. Since the deposited film was comparable in thickness to the substrate crystal a narrow x-ray beam was used to differentiate the image from the film and from the substrate. Figure 4 shows an image using this narrow beam technique. In this case the high defect density in the film is apparent from the increase in diffracted intensity compared to the substrate image.

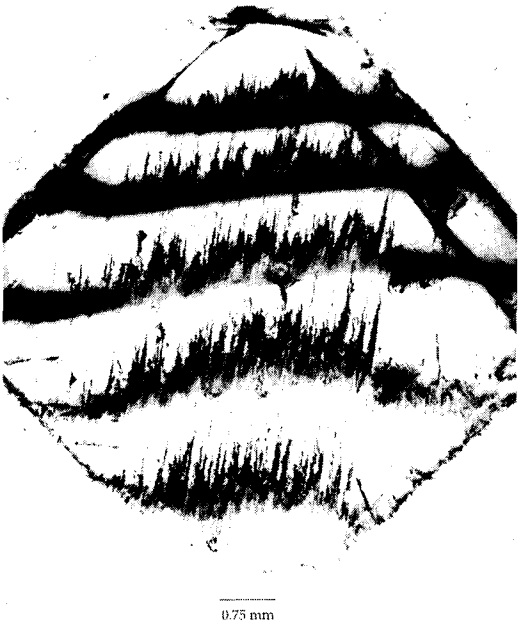

Figure 3. A $(\bar{2}20)$ asymmetric transmission image of the crystal after deposition of the CVD film. The stress in the deposited film caused the sample to become warped. In this case, the stress was large enough that 5 separate diffraction images, differing by 0.04° in Bragg angle, were required to obtain an image of the entire crystal. The "mossy" structure in the image is due to the film which can be seen to follow the surface structure in the [100] direction.

This same homoepitaxial CVD diamond film on the HTHP substrate was also evaluated electrically, by transient photoconductivity measurements, and with cathodoluminescence. Transient photoconductivity measurements [6] were done on both the back, substrate side and the front, epitaxial side of the diamond. Also, two sets of contacts were placed orthogonal to each other on both surfaces to see if there was a directional effect due to the surface relief pattern. No difference was observed between the two sets of contacts on the same surfaces, however differences were observed between the substrate and epitaxial side of the crystal. The combined electron-hole mobility at low excitation densities and low electric field was similar for both the substrate side and the epitaxial side and had a value of about 1000 cm^2/V-sec, see Fig. 5a.

However, there was a big difference between the decay times of the substrate and the epitaxial film. The HTHP substrate had a lifetime which increased with excitation density and had a value of about 10 ns at high excitation densities, whereas the epitaxial film had lifetimes of about 40 ps which was constant with excitation density, see Fig. 5b. The lower lifetime observed for the CVD epitaxial layer may be directly related to the higher concentration of defects present in the CVD film as compared to the HTHP substrate.

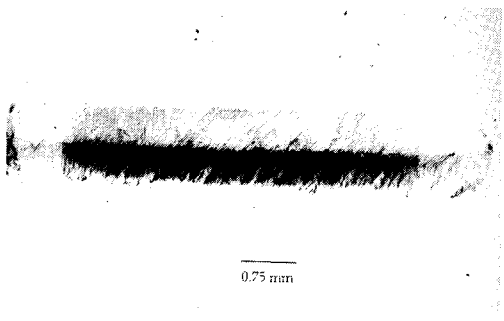

Figure 4. A $(0\bar{2}2)$ symmetric transmission image of the CVD film on the HTHP substrate taken with a narrow beam so as to differentiate between the film and substrate images. The film image is on the bottom and the substrate image is on top. The higher diffracted intensity observed from the film is indicative of a much higher defect density than in the single crystal substrate.

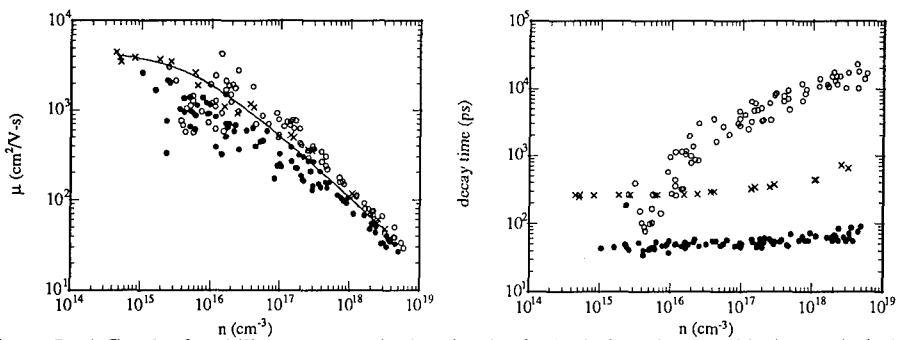

Figure 5. a) Graph of mobility versus excitation density for both the substrate side (open circles), the epi side (closed circles) and a natural IIa (crosses) as measured by transient photoconductivity. b) Graph of the decay time versus excitation density for both the substrate side (open circles), the epi side (closed circles) and a natural IIa (crosses).

Cathodoluminescence (CL) was taken on both the epitaxial side and the substrate side of 2 CVD epi/HTHP diamond samples labelled 189 and 191. The X-ray topographs and electrical results shown earlier were for sample 189 only. The CL spectra for the energy range 1.5 eV to 4.0 eV are shown in Figure 6a and 6b. A broad band at 2.2-2.3 eV is observed on the substrate side for both samples. This broad band has been observed in other diamonds and is associated

with B doped diamond. The center that causes this luminescence is not necessarily due to boron doping, but it is a center which may be activated due to a change in the electronic configuration. If boron were present in the HTHP substrates an exciton line should be observed at 5.2 eV and this is not observed in the substrates. Another broad band, band A[7], which is commonly observed in diamond at 2.85 eV is not observed in these two HTHP diamonds. That band is attributed to dislocations.

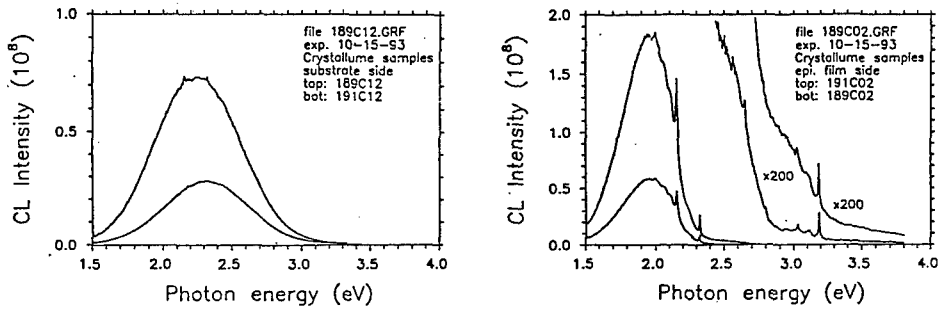

Figure 6. a) CL spectra for two HTHP single crystal IIa diamonds. The broad luminescence at 2.2 - 2.3 eV has been associated with B doped diamond. b) CL spectra of the epitaxial CVD film side of two samples grown on HTHP substrates. The peaks observed at 2.156 eV, 2.33 eV and 3.188 eV are due to nitrogen defect complexes.

The CL spectra for the epitaxial films is completely different than the HTHP substrate in the 1.5 eV to 4.0 eV range and are shown in Fig. 6b. Many peaks are observed only on the film side which have been correlated with nitrogen defect complexes. There is a narrow line observed at 3.188 eV which is attributed to a complex of nitrogen paired with an interstitial carbon atom. The line at 2.33 eV is due to a nitrogen containing center and the 2.156 eV line is due to nitrogen complexed with one or two atomic vacancies. CL is not quantitative in nature so that concentrations of nitrogen in the CVD film cannot be determined from this data. However, the lowest detectable limit for a CL narrow peak is about 1 ppb which is equivalent to several times $10^{14}/cm^3$.

The CL spectra for the exciton region (4.5 eV to 6.0 eV) [8] are shown for the substrate side in Fig. 7a and for the epitaxial side in Fig. 7b. For both sides of the sample the phonon replicas are observed, the main difference between the two sides of the sample is the intensity of the peaks. The lower intensity for the epitaxial film side indicates that there are more non-radiative recombination centers in the film. Lifetime is shortened by non-radiative centers and could explain the electrical behavior described earlier where the film lifetime was shorter than the substrate lifetime.

CONCLUSIONS

Prior to growth the HTHP substrate was unstrained and the characteristic microstructure of stacking faults and dislocations was observed. After deposition of the CVD film, the crystal was strained with the film in tension. A high defect density was observed in the film and it is probable that there are many dislocations. Cathodoluminescence indicates the presence of nitrogen-defect complexes and non-radiative recombination centers in the homoepitaxial diamond film. Electrical measurements of the film and substrate indicate that they have a comparable combined electron-hole mobility, but that the CVD film has a lower lifetime than the

HTHP substrate. The lower lifetime observed for the CVD epitaxial layer is probably related to the higher concentration of defects present in the CVD film as compared to the HTHP substrate. The higher defect concentration and poorer electrical performance of undoped CVD homoepitaxial diamond films indicates that diamond film quality is not yet limited by the quality of the diamond substrate.

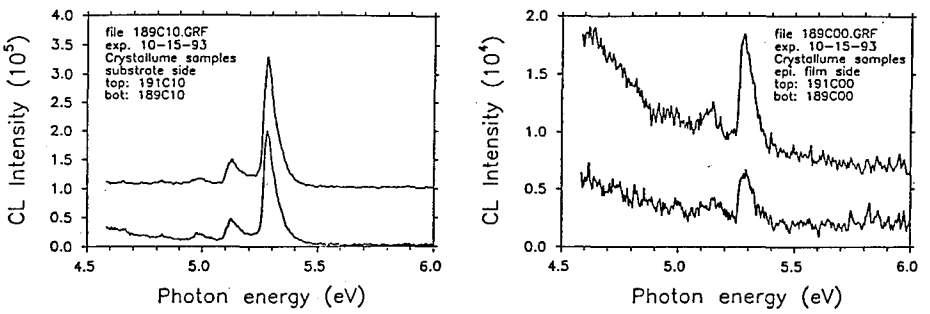

Figure 7. a) Cathodoluminescence spectra for the HTHP IIa substrates in the exciton region from 4.5 eV to 6.0 eV. b) Cathodoluminescence spectra for the CVD epitaxial films grown on two HTHP substrates.

ACKNOWLEDGMENTS

Crystallume would like to acknowledge BMDO through ONR and the Army Research Laboratory at Fort Monmouth for partial support of this work.

REFERENCES

1. M. I. Landstrass, M. A. Plano, S. McWilliams, M.A. Moreno, D.R. Kania, L.S. Pan, S. Han and J. R. Flemish, Proc. of Third Int. Symposium on Diamond Materials, ECS, 920 (1993).

2. B.K. Tanner, X-Ray Diffraction Topography (Paragammon Press, New York, 1976).

3. R. H. Wentorf, J. of Phys. Chem. **75**, 1833 (1971).

4. H. M. Strong and R. H. Wentorf, Am. J. Phys. **59**, 1005 (1991).

5. M. Kamo, Y. Sato, S. Matsumoto, N. Setaka, J. Cryst. Growth **62**, 642 (1983).

6. L. S. Pan, D.R. Kania, S. Han, J. W. Ager II, M.I. Landstrass, O. L. Landen and P. Pianetta, Science **255**, 830 (1992).

7. J. Ruan, Appl. Phys. Lett. **60**, 3138 (1992).

8. A. T. Collins, J. Phys. Condensed Matter **1**, 4029 (1989).

DEPOSITION OF FLAME GROWN DIAMOND FILMS IN AN ENCLOSED CHAMBER

KATHLEEN DOVERSPIKE*, VASGEN A. SHAMAMIAN*, AND JAIME A. FREITAS, JR.**
* Naval Research Laboratory, Washington D.C. 20375-5000
**Sachs-Freeman Associates, Landover,MD 20785-5396

ABSTRACT

Polycrystalline diamond films were synthesized using an oxy-acetylene flame in the open atmosphere and in an enclosed chamber. In the present work, we have shown that the 2.16eV defect band seen in the photoluminescence spectra from the central portion of the films grown in the open atmosphere show a dependence on the growth temperature. Films grown in the open atmosphere all exhibit a decrease in the crystalline quality when moving to the outside edge most likely due to the entrainment of nitrogen into the films.

The present study was done in the enclosed chamber using an oxygen atmosphere via an oxygen flow around the torch. Films have been grown in the enclosed chamber that show only trace amounts of the 2.16eV band. Both the Raman and the photoluminescence spectra show that the films grown in the enclosed chamber are very uniform over the deposition area, which suggests that the degradation of the outer portion of the open atmosphere films may be the result of room air entrainment, and not a temperature variation across the substrate. In addition, when either lower purity oxygen is used or lower growth temperatures, we easily observe the 2.16eV band which may be the result of nitrogen impurities in the source gases.

INTRODUCTION

The combustion flame technique has been demonstrated at several laboratories to be a viable technique to obtain high quality diamond films with a high growth rate[1-5]. Diamond growth using an oxy-acetylene torch occurs in the fuel rich acetylene feather just outside the primary flame front. The overall combustion reaction in the inner cone is [6]:

$$C_2H_2 + O_2 \rightarrow 2CO + H_2 \quad (1)$$

with many intermediates (eg. H, OH, C_2, and C_2H) involved in the overall reaction. If the torch is run in a fuel rich mode, the unburnt hydrocarbons, reactive intermediates, CO, and H_2 form a region (feather) bounded by another flame front caused by oxygen diffusion from the surrounding atmosphere. Laser-induced fluorescence and mass spectroscopy have shown the feather region also contains an appreciable amount of nitrogen[6] from diffusion of room air into the flame. Although, nitrogen is not electrically active (the substitutional nitrogen donor level is believed to be about 1.7eV below the conduction band)[7], nitrogen incorporation may be detrimental. Besides the substitutional nitrogen donor level, nitrogen also forms complexes with vacancies and, depending on their location in the bandgap, may compensate p-type films[8], or act as deep trapping centers. Therefore, controlling the atmosphere around the flame is of interest in order to control the incorporation of unwanted dopants, such as nitrogen.

In this paper, we report on the growth of free standing polycrystalline diamond films by the combustion process using a pre-mixed oxy-acetylene torch operated in the open atmosphere,

Mat. Res. Soc. Symp. Proc. Vol. 339. ©1994 Materials Research Society

and in an environmentally controlled enclosed chamber. Previously, we had reported on growth in an enclosed chamber using both argon and oxygen as the auxiliary gas [9]. The highest quality films in that study (determined by the FWHM of the Raman line, the ratio of the diamond first order phonon line to the amorphous carbon peak, and the intensity of the nitrogen-vacancy complexes seen in the photoluminescence spectra) were obtained when oxygen was used as the auxiliary gas. In the present study we have grown films in the enclosed chamber using oxygen as the auxiliary gas, while also using various grades of oxygen to determine if there is any correlation between the oxygen source used and the nitrogen-vacancy complexes seen in the photoluminescence spectra.

EXPERIMENTAL

All of the diamond films were synthesized using a premixed oxy-acetylene welding torch with a nozzle diameter of 1.00 mm. The flow rates of the oxygen and acetylene (99.6%) were controlled by mass flow controllers with the total flow rate being held constant at approximately 4 SLM. Three different grades of oxygen were used ranging from 99.5% to 99.998% with nitrogen concentration ranging from 500 ppm to 15 ppm respectively. Slight variations in the oxygen flow were made in order to adjust the O_2/C_2H_2 ratio. Both the enclosed chamber and open atmosphere films were grown on molybdenum screws that were placed in a threaded hole in a water-cooled copper block. The temperature of the screw was controlled by the depth of penetration into the copper block and was monitored using a two-color pyrometer for the open atmosphere experiments, while a one-color pyrometer (calibrated using the two-color pyrometer) was used for the enclosed chamber experiments. The film growth temperature was approximately 990°C (±20°) unless otherwise noted. In order to enhance initial surface nucleation, the molybdenum screw was polished with 600 mesh silicon carbide, and then ultrasonically cleaned in acetone and methanol. Because of the large difference between the thermal expansion coefficients of diamond and molybdenum, films delaminated as the substrate cooled. All the samples discussed in this paper were thus free standing diamond films.

A similar apparatus to that described above was placed in an enclosed chamber in order to control the atmosphere around the flame. Prior to lighting the torch, the chamber was evacuated to several torr and then filled with argon(99.98%). A slight positive pressure, with respect to ambient, was maintained to avoid nitrogen leaking into the chamber. An auxiliary flow of 8 SLM oxygen was introduced in the chamber via a shroud (2 inches in diameter) around the torch tip.

The Raman measurements were performed in the photoluminescence apparatus using the 488.0 nm line of an argon ion laser focused to approximately 100 μm diameter spot size[10]. The photoluminescence experiments were carried out at 6 K in a Janis supervaritemp cryostat. Scanning electron microscopy (SEM) was performed on these samples using a Leica 360 field emission microscope.

RESULTS

For the films grown in the open atmosphere, the O_2/C_2H_2 ratio was about 1.12 while for the films grown in the enclosed chamber, the O_2/C_2H_2 ratio was about 1.07. Assuming 100% combustion, an auxiliary flow of approximately 3 SLM would be needed to completely oxidize the reactants (2 SLM C_2H_2 in our case), therefore our auxiliary flow of 8 SLM was chosen to ensure an ample supply of oxygen. The growth time for these samples were 40 minutes. Figure 1a and 1b are SEM micrographs showing the morphology of the films grown in the open atmosphere and the enclosed chamber respectively. Compared to the clean well-faceted morphology seen in figure 1a, the morphology of films grown in the enclosed chamber (figure 1b) exhibited many pits on the crystallites. Fig 2 shows the Raman spectra of two films with each spectrum being normalized to the diamond Raman line (1332 cm^{-1}). Curve A (figure 2) is a typical Raman spectrum of a film grown in the enclosed chamber, while curve B and C are spectra taken of a film grown in the open atmosphere (2b is of the central region and 2c is of the outer portion of the film). The corresponding photoluminescence spectra of these films are shown in figure 3 (curve A from the enclosed chamber, curve B and C from the center and outer

portion of the film grown in the open atmosphere). These photoluminescence spectra were also normalized to the diamond first order phonon line (labeled "a" in figure 3).

DISCUSSION

The well crystallized faces typical of growth in the open atmosphere is shown in figure 1a. In figure 1b, the morphology of the film grown in an enclosed chamber is slightly different. While the overall size of the grains appear very similar, the surface of the films grown in the enclosed chamber exhibit many pits. We believe these may be etch pits, and are related to an increase in the amount of OH and atomic O species that are expected when entraining 100% oxygen into the flame. OH, and to a lesser extent atomic O, are believed to be effective carbon etchants[11]. Fewer pits are found on the (100) face which is known to be the slowest etched face in both natural and synthetic diamond[12]. In addition to the observed preferential etching, crystallites from the films grown in the enclosed chamber appear to have rounded edges as compared to the sharp, well-defined edges on those grown in the open atmosphere.

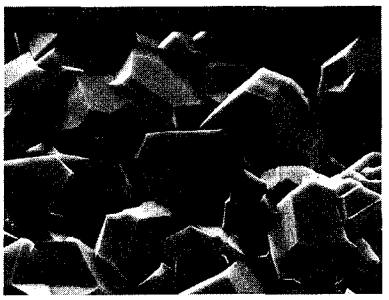

1(a)

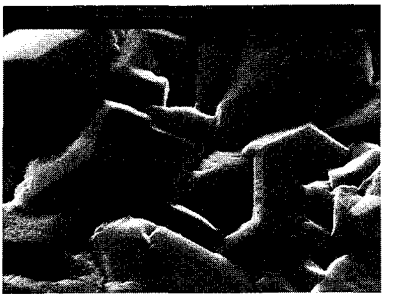

1(b)

Figure 1. Morphology of films grown in the open atmosphere(1a) and in an oxygen atmosphere in the enclosed chamber(1b).

The Raman spectrum (figure 2, curve A) of a film grown in the enclosed chamber with oxygen as the auxiliary gas, shows a relatively low background luminescence and a very small amount of amorphous carbon at 1500 cm^{-1}. The Raman spectra which were taken at various places on the film, including the outside portion, all yielded a spectra similar to that shown in figure 3a. The FWHM over the entire growth was about $3.8 \pm .3$ cm^{-1}. Because of the large spot size (100 μm), the Raman signal, and hence the FWHM, consists of contributions from many crystallites and intergranular material. For growths in the enclosed chamber, film to film variation in the Raman FWHM was found to be less than 1 cm^{-1}.

The Raman spectrum taken of a film grown in the open atmosphere shows that the central portion (figure 2, curve B) of the film contains higher quality diamond as compared to the outer edge (curve C). The Raman background luminescence of the central portion is much smaller than that of the outer portion and the component at 1500 cm^{-1}, which is attributed to amorphous carbon, is also smaller. High resolution Raman of the central area yields a FWHM of about 2.7cm^{-1}, while that of the outer portion of the film is about 6.9 cm^{-1}.

Figure 3 (curve A) is a photoluminescence spectrum of a film grown in the enclosed chamber. Defect bands which commonly occur in the photoluminescence spectra of diamond are observed at 2.16 and 1.95 eV. The defect band at 1.95 eV has been assigned to a nitrogen-vacancy pair[13], while the defect band at 2.16 eV may be associated with a nitrogen-double vacancy complex[14]. As can be seen in figure 3, a peak at 1.95 eV was not observed, and only with magnification of the background can the defect band at 2.16 eV be observed. The

photoluminescence spectra taken across the film showed no variation, indicating good crystalline uniformity. This suggests that the degradation across the films grown in the open atmosphere is probably not the result of any temperature gradient across the film, but rather the result of the entrainment of room air, and subsequent incorporation of nitrogen in the films.

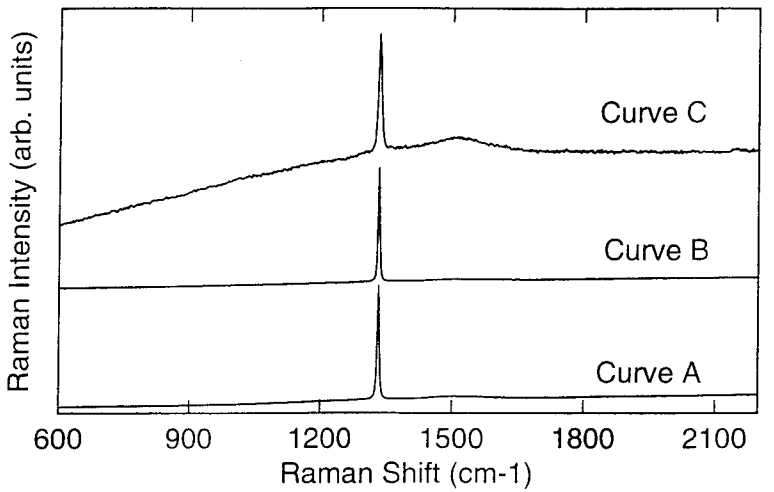

Figure 2. Raman spectra of films grown in the enclosed chamber (Curve A), the center of an open atmosphere film (Curve B), and the outside edge of an open atmosphere film (Curve C).

Also shown in figure 3 are the photoluminescence spectra of a film grown in the open atmosphere. In agreement with the Raman spectra which showed a better FWHM of the central region, the photoluminescence data also indicate higher quality diamond in the central region(curve B) as compared to the outer portion (curve C). The photoluminescence spectrum taken near the outside edge of this film, indicates lower quality diamond both by the ratio of the diamond first order phonon line (a) to the amorphous carbon peak (a*), and also the enhanced presence of the 2.16 eV band (b) and the 1.95 eV band(c). In all the films examined that were grown in the open atmosphere, the 2.16 eV band was the dominant defect observed in the photoluminescence spectra of the central region of the film. Spectra that were taken progressively closer to the outer edge show an increase in the 1.95 eV band intensity that equals that of the 2.16 eV band.

It has been previously reported that a decrease in the nitrogen complexes seen in the photoluminescence spectra of films grown in the open atmosphere can be achieved if turbulent flame conditions are used[15]. In this study, we have determined that even under the present laminar conditions, one can also achieve a decrease in the nitrogen complexes simply by using higher temperatures (approximately 990°C). By changing the growth temperature from 990 to 930°C, we have observed an increase of the 2.16 eV band in the photoluminescence spectra from the central portion of the film.

The quality of films grown in the open atmosphere were not found to be dependent on the quality of oxygen used. In films grown in the enclosed chamber, when lower grades of oxygen were used, a small amount of the 2.16 eV band was observed in the photoluminescence spectra, but no signs of the 1.95 eV band was observed in any these films. These results indicate that there may be a correlation between the nitrogen complexes seen in the photoluminescence

spectra with the oxygen purity, but further experiments need to be done to discard any effects due to temperature variations in the growth. We also used the high purity oxygen (99.998 %) at lower deposition temperatures (approximately 930°C) in the enclosed chamber and were also able to observe the 2.16 eV band in the photoluminescence spectrum without enlarging the background. This is an indication that some of the nitrogen incorporation in the diamond films is coming from the acetylene, which is not surprising since the highest grade commercially available, 99.6 %, contains approximately 1000 ppm nitrogen. It has also been reported that nitrogen contamination in acetylene is also a problem in SiC growth where acetylene is used as one of the gas sources[16].

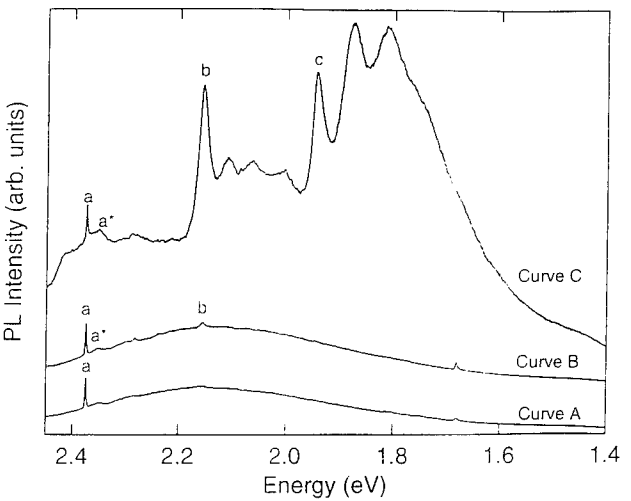

Figure 3. Photoluminescence spectra of films grown in the enclosed chamber (Curve A), the center of an open atmosphere film (Curve B), and the outside edge of an open atmosphere film (Curve C).

CONCLUSIONS

In the present work, we have shown that in the open atmosphere films there appears to be a growth temperature dependence on the 2.16 eV band seen in the photoluminescence spectra of the central portion of the film. Higher growth temperatures, 990°C, result in a smaller 2.16eV defect band in the photoluminescence spectra. Toward the outer portion of the films, both the 2.16 and the 1.95eV band increase in intensity. In films grown in the enclosed chamber with oxygen as the auxiliary gas, we have made films that show only a trace amount of any nitrogen complexes. Both the Raman and the photoluminescence spectra indicate that the films grown in the enclosed chamber show uniform crystalline quality over the deposition area indicating that the degradation of the outer portion of the open atmosphere films may be the result of room air entrainment, and not a temperature variation across the substrate. When either lower purity oxygen is used, or lower growth temperatures, we do observe a small peak at 2.16 eV in the photoluminescence spectrum, which may be the result of nitrogen impurities in the source gases. In the near future, we plan to perform secondary ion mass spectroscopy (SIMS) on these samples to determine if there is a correlation between the actual nitrogen incorporation and the nitrogen complexes in the photoluminescence spectra.

ACKNOWLEDGEMENTS

We would like to thank D.K.Gaskill and K.Hobart for some helpful discussions, and L.Shirey for assistance on the SEM. One of us (JAF) performed this work under the contract #N00014-93-C-2227 at the Naval Research Laboratory.

REFERENCES

1. Y.Hirose and N.Kondo, Program and Book of Abstracts, Japan Applied Physics 1988 Spring Meeting, March 29,1988,p.95.
2. L.M.Hannssen, W.A.Carrington, J.E.Butler and K.A.Snail, Mat. Lett., **7** (7,8), 289 (1988).
3. Y.Tzeng, C.Cutshaw, R.Phillips, T.Srivinyunon, A.Ibrahimand B.H.Loo, Appl. Phys. Lett. **56** (2), 134 (1990).
4. M.A.Cappelli and P.H.Paul, J.Appl.Phys. **67** (5), 2596 (1990).
5. K.V.Ravi, C.A.Koch, H.S.Hu and A.Joshi, J. Mater. Res., **5** (11), 2356 (1990).
6. Y.Matsui, A.Yuuki, M.Saharaand Y.Hirose, Jap. J. Appl. Phys. 28 (9), 1718 (1989).
7. G.Farrer, Solid State Commun. **7**, 685 (1969).
8. J.Mort, M.A.Machonkin, and K.Okumura, Appl. Phys. Lett. **59** (24) 3148 (1991).
9. K.Doverspike, J.E.Butler, and J.A.Freitas, Jr. in Wide Band Gap Semiconductors, edited by T.D.Moustakas, J.I.Pankove, and Y.Hamakawa (Mat. Res. Soc. Proc. **242**, Pittsburgh, PA, 1992)p. 37.
10. J.A.Freitas, J.E.Butler, U.Strom, J. Mater. Res. **5** (11), 2502 (1990).
11. S.J.Harris and A.Weiner, Appl. Phys. Lett. **55** (21), 2179 (1989).
12. K.Tankala and T.Debroy, New Diamond Science and Technology , edited by R.Messier, J.T.Glass, J.E.Butler and R.Roy (Mater. Res. Soc. Proc., Pittsburgh, PA 1991) pp. 827-831.
13. G.Davies and M.F.Hamer, Proc. Royal. Soc. London A, **348**, 285 (1976).
14. J.Walker, Rep. Prog. Phys. **42,** 1605 (1979).
15. J.A.Freitas,Jr., U.Strom, K.Doverspike, C.M.Marks and K.A.Snail in Wide Band Gap Semiconductors, edited by T.D.Moustakas, J.I.Pankove, and Y.Hamakawa (Mat. Res. Soc. Proc. **242**, Pittsburgh, PA, 1992) p. 139.
16. J.D.Parsons, R.F.Bunshah, and O.M.Stafsudd, J. Electrochem. Soc., **140** (6), 1756 (1993).

EFFECTS OF METHANE CONCENTRATION AND HYDROGEN TREATMENT ON PREFERRED ORIENTATION IN DIAMOND FILMS GROWN BY CHEMICAL VAPOR DEPOSITION

D. Ganesan and S. C. Sharma
Department of Physics and Materials Science & Engineering Program
The University of Texas at Arlington, Arlington, Texas 76019

ABSTRACT

We have conducted x-ray diffraction, Raman spectroscopy, and scanning electron microscopy analyses of diamond films grown by hot filament assisted chemical vapor deposition (HFCVD). We present results on the relative abundance of the (111), (220) and (400) faces in polycrystalline diamond films as functions of CH_4 concentration. The intensity of the (111) peak can be varied from about 20% to 60% by adjusting CH_4 in CH_4/H_2 mixtures. We also present results on preferred orientation in films grown under varying hydrogen treatments. We discuss correlations between the preferred orientation, FWHM of the diamond peak in the Raman spectrum, and surface morphology of the films.

INTRODUCTION

There has been an increasing interest in the growth and characterization of polycrystalline diamond films because of their exceptional properties.[1,2] The growth of these films by a variety of low-pressure techniques and their properties have been discussed in numerous articles.[3-5] Whereas significant progress has already been made in understanding the growth of polycrystalline and homoepitaxial single crystal diamond films, the heteroepitaxy of diamond films remains to be developed. Attempts have also been made to grow highly oriented polycrystalline diamond films.[6] To our knowledge, there has not been any attempt to systematically study the effects of growth parameters on the relative abundance of different orientations present in diamond films grown by HFCVD. The only other study, known to us, has been on the plasma grown films.[7] In this paper, we present results on the effects of CH_4 concentration in CH_4/H_2 mixtures and of hydrogen treatment on the relative abundance of the crystalline faces in HFCVD grown diamond films.

EXPERIMENTAL DETAILS

Polycrystalline diamond films were deposited by using a hot filament assisted CVD system that has been discussed in detail elsewhere.[5] The deposition parameters for these experiments were from our so called *regime-2* and they were as follows: CH_4/H_2 mixture flow rate ~ 60 sccm, system pressure ~ 25 Torr, filament temperature ~ 2300 K, substrate temperature ~ 1100 K, and filament to substrate separation ~ 1 cm. Diamond films were grown at seven different CH_4 concentrations ranging from 0.5% to 4% in CH_4/H_2 mixtures. The growth rates for these samples were typically 1 μm/hr. These films were examined by using Raman spectroscopy, scanning electron microscopy, and X-Ray Diffraction (XRD). Our Raman spectrometer consists of an argon ion laser (λ = 5145 Å), a SPEX 14018 double monochromator, and computer control data acquisition unit. A Cambridge Stereo Scan-120 scanning electron

Mat. Res. Soc. Symp. Proc. Vol. 339. ©1994 Materials Research Society

microscope was used to observe and photograph surface morphology of the films. The x-ray diffraction measurements were made by using a computer-controlled Philips PW1729 x-ray diffractometer equipped with Cu-K_α monochromatic x-ray beam (45 keV @ 35 mA) and operated with a step size of 0.02° (2θ) and @ 0.5 sec per step.

RESULTS AND DISCUSSION

The Raman spectra of two films grown at CH_4 concentrations of 1.4 % and 3.0 % are shown in Fig. 1. The Raman spectra clearly show that the film grown at 1.4 % CH_4 concentration is a high quality diamond film; the sharp peak at 1332 cm^{-1} is well known to be the characteristic line of crystalline diamond. The film grown at 3.0 % CH_4 concentration contains significantly less sp^3 bonded diamond structure; the additional features around 1350 cm^{-1}, 1550 cm^{-1}, and 1580 cm^{-1} are due to polycrystalline diamond, diamond-like carbon, and amorphous carbon. Details on the evolution of these features, as functions of growth conditions, in HFCVD diamond films have been discussed elsewhere.[5]

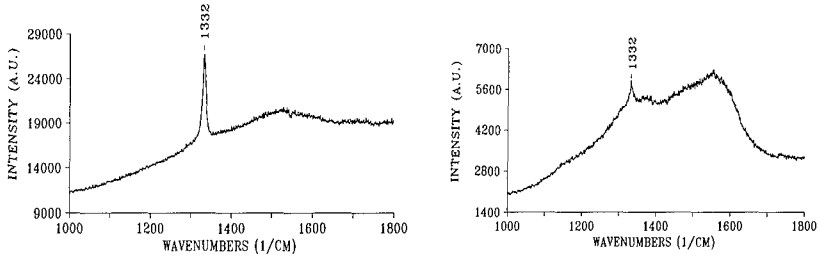

Figure 1. Raman spectra of films grown at 1.4 % and 3.0 % CH_4 in CH_4/H_2 Mixtures.

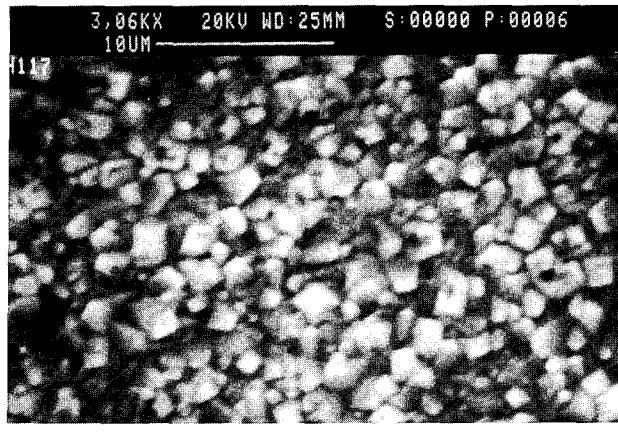

Figure 2 (a). SEM of films grown at 1.4 % CH_4 in CH_4/H_2 Mixtures.

The surface morphology of the films is shown by the SEM micrographs of Figure 2. The Raman and SEM features and their dependence on CH_4 concentration are in excellent agreement with our previous results.[5]

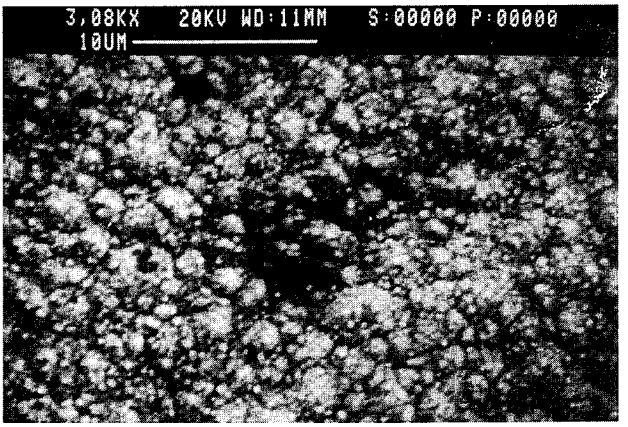

Figure 2 (b). SEM of films grown at 3.0 % CH_4 in CH_4/H_2 Mixtures.

XRD spectra of two films grown, with and without H_2 treatment, are shown in Fig. 3.

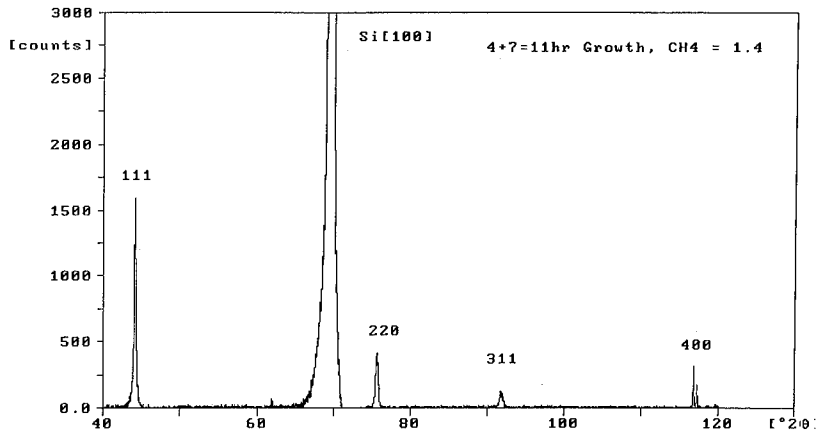

Figure 3 (a). XRD spectra of films grown without H_2 treatment.

A standard computer software calculates quantities of interest, like peak position (2θ), area under each peak, d spacing, size of the crystallites, lattice strain, etc. We observe peaks in the x-ray diffraction spectra of these films corresponding to the (111), (220), (311), (400) and (331) faces.[8] We have also measured a spectrum for diamond powder and its results are within one standard deviation of the values given in JCPDS card 6-0675.[8] The abundance of the (111) and (220) faces in our diamond films are shown *vs* CH_4 concentration in Fig. 4. The abundance of each orientation is defined to be the ratio of the area under the peak originating from that particular orientation to the sum of the peak areas of all other faces. The error bars represent standard deviations calculated from ten different XRD measurements on each sample. A comparison between the XRD spectra of the 1.4 % CH_4 concentration film and diamond powder shows that this film resembles randomly oriented diamond powder.

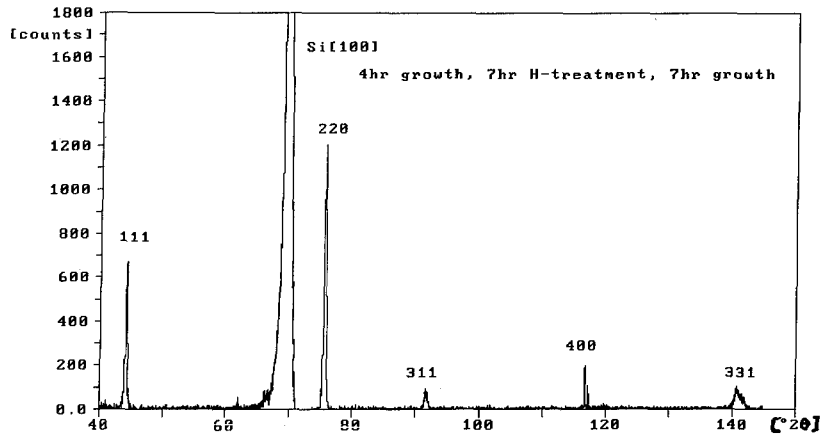

Figure 3 (b). XRD spectra of films grown after H_2 treatment.

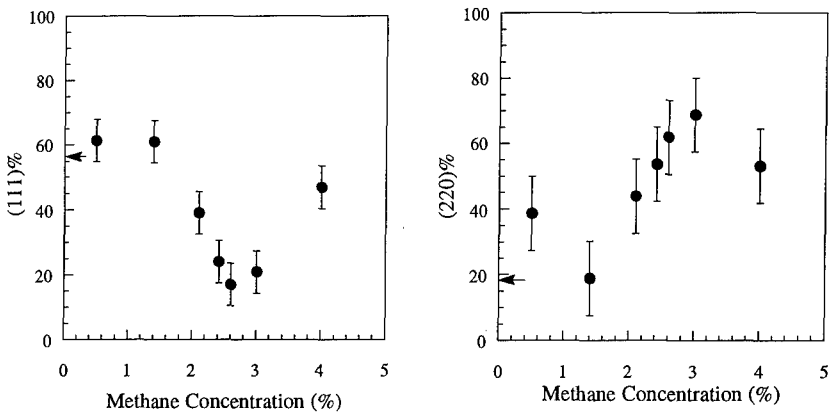

Figure 4. Relative abundance of the (111) and (220) faces *vs* CH_4 concentration. The diamond powder results are shown by arrows.

It is observed that the composition of the CH_4/H_2 mixture has an important effect on the growth of preferred crystallographic orientation in the film. The abundance of the (111) face remains at around 60% for CH_4 concentrations upto 1.4%. Between 1.4% and 2.6% CH_4 concentrations, the abundance of this face drops sharply with increasing CH_4 concentration. For higher CH_4 concentrations, the abundance of the (111) face increases. Since the abundance of the (400) face is comparatively small (ranging from 0 to 5%), the abundance of the (220) face shows an expected behavior with the composition of the CH_4/H_2 mixtures. These results clearly show that the growth of a preferred orientation in HFCVD grown polycrystalline films can be controlled, albeit within reasonable limits, by adjusting CH_4 concentration. In order to study whether the abundance of the preferred orientation could be further influenced by hydrogen treatment, we have conducted an experiment in which the following sequence is adopted: 1) first a diamond film is grown by using 1.4% CH_4 concentration, 2) this film is examined by Raman, SEM, and XRD, 3) the film is exposed to continuous flow of H_2 for a certain period of time by keeping all other growth conditions the same as they were during the original growth in step (1), 4) additional growth of diamond is accomplished on the H_2-treated film, 5) the film is reanalyzed by Raman, SEM, and XRD, and 6) steps (3) - (5) are repeated. The results from these experiments are shown in Figure 5, where the ratio of the relative abundance of the (220) and (111) faces is plotted *vs* deposition time for different conditions of H_2 treatment.

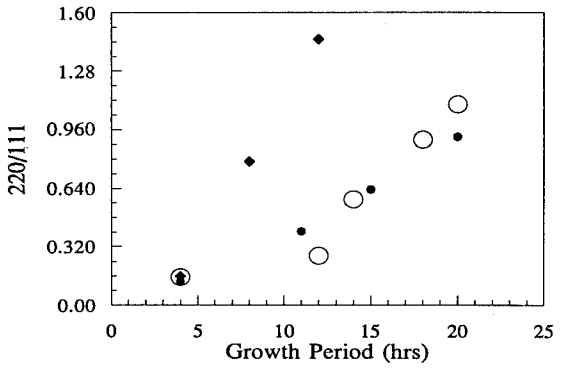

Figure 5. Ratio of the abundance of the (220) and (111) faces *vs* growth period for different H_2 treatments; (●, growth without H_2 treatment), (○, growth after 7 hrs H_2 treatment once following 4 hrs growth), (◆, 1 hr. H_2 treatment after each growth).

It is observed that hydrogen treatment influences growth of a particular orientation ((220), in this case) at the expense of the growth of other faces. There is almost a three-fold increase in the rate of growth of the (220) face when the sequence, diamond growth *plus* H_2 treatment, is repeated. We observe a correlation between the abundance of the (220) faces, graphitic contents, and FWHM of the diamond peak; as the relative abundance of the (220) faces increases, the Raman spectrum shows an increase in the graphitic contents of the film and the 1332 cm^{-1} Raman line broadens.

CONCLUSION

In conclusion, we have presented results from a study of the effects of CH_4 concentration and H_2 treatment on preferred orientation in polycrystalline diamond films. Both methane concentration and hydrogen treatment are found to significantly influence the growth of the (220) face at the expense of the growth of the (111) face. We observe a three-fold increase in the growth rate for the (220) face of diamond by repeatedly subjecting "freshly grown" diamond films to H_2 treatment. There appears to be a correlation between the preferred growth of the (220) face, graphitic contents in the film, and the sharpness of the 1332 cm^{-1} diamond peak in the Raman spectrum.

ACKNOWLEDGMENT

We wish to thank Dr.'s R. C. Hyer and M. Green for assistance in the growth and Raman analysis of the films.

REFERENCES

1. See excellent papers in, Thin *Film Diamond,* eds. A. H. Lettington and J. W. Seeds, Philos. Trans.: Phys. Scien. Eng., **342**, 193 (1993).
2. *New Diamond Science and Technology*, eds. R. Messier, J. T. Glass, J. Butler, and R. Roy, Mater. Res. Soc., (1990).
3. K. E. Spear, J. Amer. Ceram. Soc., **72**, 171 (1989).
4. A. R. Badzian, T. Badzian, R. Roy, R. Messier, and K. E. Spear, Mat. Res. Bull., **23**, 531 (1988).
5. S. C. Sharma, M. Green, R. C. Hyer, C. A. Dark, T. D. Black, A. R. Chourasia, D. R. Chopra, and K. K. Mishra, J. Mater. Res. **5**, 2424 (1990).
6. M. W. Geis, Appl. Phys. Lett. **55**, 550 (1989).
7. K. Kobashi, K. Nishimura, K. Miyata, K. Kumagai, and A. Nakaue, J. Mater. Res. **5**, 2469 (1990).
8. See Powder Diffraction File, Set 6-10, Published by the Joint Committee on Powder Diffraction Standards, Card Number : 6-0675, 1967.

PHASE TRANSFORMATION OF SMOOTH DIAMOND FILMS GROWN BY HOT FILAMENT CHEMICAL VAPOR DEPOSITION ON POSITIVELY BIASED SILICON SUBSTRATES.

G. POPOVICI,* C. H. CHAO,** M. A. PRELAS,* E. J. CHARLSON,** AND J. M. MEESE**

*Nuclear Engineering Department, **Electrical Engineering Department, University of Missouri, Columbia, MO 65211

ABSTRACT

Smooth diamond films have been grown by hot filament chemical vapor deposition under d.c. bias on mirror-polished Si substrates. Films a few micrometers thick were obtained in 30 minutes. Raman spectra showed very broad diamond peaks. X-ray diffraction showed the presence of diamond and also other carbon phase with a line 2.11 Å. With time, the films apparently underwent a phase transformation.

INTRODUCTION

Diamond films produced by low pressure chemical vapor deposition (CVD) are hard, chemically inert, and transparent over 0.225 to 25 mm. Such films have already been used as protective coatings for infrared optics. One major limitation in optical coatings is their surface roughness due to crystalline grains. The light scattering on the rough surface, rather than the absorption, is responsible for optical losses in diamond films. [1] Therefore, smooth diamond films should be of interest for optical applications.

This paper reports the synthesis and properties of microscopically smooth diamond films grown by hot filament CVD on Si (100) substrates by nucleation and growth under d.c. bias.

EXPERIMENTAL

The diamond films were grown by hot filament CVD with a d.c. electric bias applied between filament and substrate. The substrates were as-received mirror-polished Si (100) wafers, chemically cleaned. They were mounted on a large (4x4x1 cm^3) graphite holder biased positively with respect to the filament. The distance between the coil tungsten filament and the substrates was 2 to 4 mm. The chamber pressure during deposition was maintained at 30-40 torr. Flow rates (measured by MKS flowmeters) of 1 sccm of methane and 99 sccm of hydrogen were used. The coil tungsten filament was carburized before deposition to reduce the tungsten contamination in films. The filament temperature varied for different runs between 1950 ^{o}C and 2200 ^{o}C (measured by a Micron digital two-wavelength optical pyrometer). The substrate temperature was maintained at 800 ±20 ^{o}C (measured by a chromel-alumel thermocouple placed under the Si substrate). This was, most probably, the temperature of the graphite holder. The real temperature on the growing surface of the film could be much higher, as occasional melting of the silicon surface was observed.

Mat. Res. Soc. Symp. Proc. Vol. 339. ©1994 Materials Research Society

Bias potentials between 50 V and 150 V were applied (50, 80, 100, 120, and 150 V). The bias current varied between 0.19 and 2.30 A, being dependent on the applied potential and also on the filament temperature, the chamber pressure, and the distance from filament to substrate. As the bias voltage was applied, a bright plasma ball formed around the filament. The nucleation/growth time was 30 min. Smooth, visually transparent films approximately 5 μm thick were obtained as detailed below.

Scanning electron microscopy (SEM) with energy dispersive spectroscopy (EDS), X-ray diffraction (XRD), Raman and Auger spectroscopy measurements were used to characterize the samples.

RESULTS AND DISCUSSION

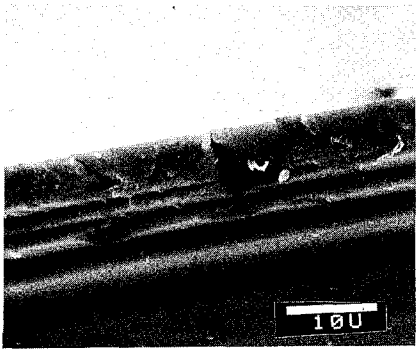

Fig. 1. A cleavage of the smooth film grown under bias V=50 V, I=0.20 A

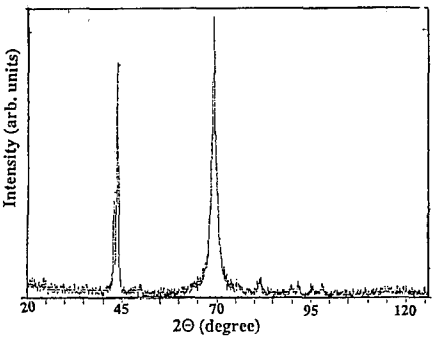

Fig. 2 The typical X-ray diffraction pattern of smooth films

The SEM pictures of the film cleavage (Fig.1) shows a film with thickness ~5 μm. The surface is smooth. No element heavier than Na, except silicon, was detected by energy dispersive spectroscopy.

Fig. 2 shows a typical X-ray diffraction patterns for smooth films, as measured two-three weeks after growth. The films have a strong (111) reflection (dominant peak at 44.07^{o}, interplanar spacing d=2.055 A). The XRD patterns also show a weaker non-diamond peak at $2\Theta=42.9^{o}$ (d=2.11 Å). No graphite lines were observed.

The range from 42^{o} to 45^{o} of a typical pattern is shown expanded in Fig. 3. The pattern has a strong line at 44.07^{o} (d=2.055 A), an adjacent line at 43.8^{o} (d=2.065 A) and a line at 42.9^{o} (d=2.11 A). For all samples grown in various conditions, these three peaks were present, their intensity, as measured a short time (two-three weeks) after growth, varied from sample to sample, the peak at 44.07^{o} being always dominant, and the peak at 42.9 the weaker one.

A carbon atom can be bound to another carbon atom by a single, double or triple bond. This allows the existence of an array of different carbon lattices: diamond, graphite, buckyballs and a large number of graphite and diamond polytypes.

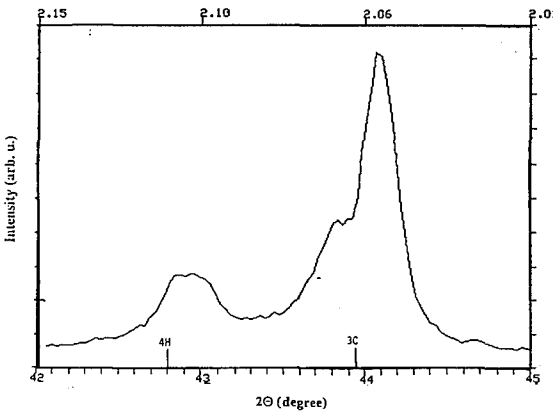

In the cubic diamond structure each carbon atom is located at the center of a regular tetrahedron and is singly bonded to the four neighbour atoms at the tetrahedron corners. Diamond polytypes have hexagonal (2H - lonsdaleite, 4H, 6H, 8H and so on) or rhombohedral (15R, 21R) structures. [2] The structures of hexagonal and cubic diamond differ only in the stacking of double -buckled layers.

Fig. 3 XRD pattern in the range of 42-45 ° typical for films grown under bias

XRD patterns for hexagonal diamond polytypes were calculated by Ownby et al. [2] The line with spacing d=2.11 Å might belong to the 4H polytype, but no other lines belonging to diamond polytypes were present in XRD pattern. Badzian and Badzian [3] have observed, besides the usual (111) diamond reflection (d=2.06 A), a peak with d=2.12 A in epitaxial films grown on (111) facets of natural diamond. They have suggested that the peak is due to interplanar distance of a new form of tetrahedral carbon. The splitting of the 2.06 A line in two lines with 2.055 A and 2.065 A can be attributed to the presence of stacking faults. Planar defects, like stacking faults and twins, were found indeed to be present with high density in the <111> growth direction.[3]

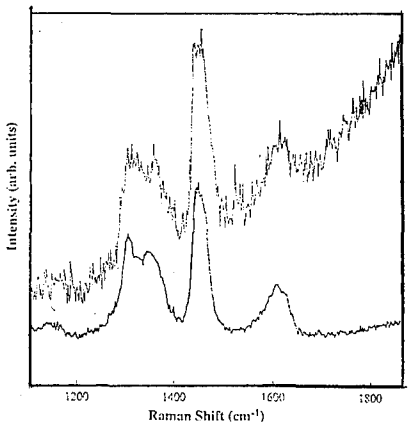

Fig. 4 Raman spectra

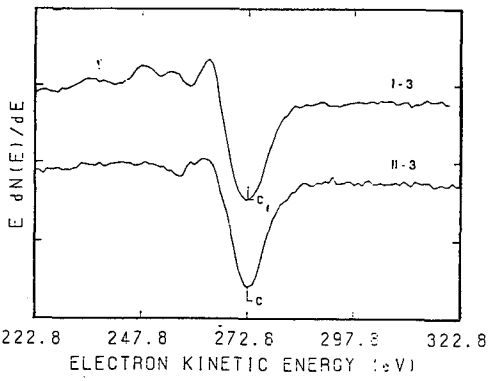

Fig. 5 Differential Auger spectra.

A series of quite strange Raman spectra, like those shown in Fig. 4, were obtained on some samples. There is a diamond line, although widened and displaced. Diamond lines for the different samples was displaced from 1332 cm-1 to larger or smaller wave numbers indicating the presence of stresses in the films. The line at ~1450 cm^{-1} is usually assigned to amorphous carbon. However, in our case the line is too narrow to be explained in this way. For amorphous carbon it should have been much broader. Differential Auger spectra (Fig. 5) have diamond features.

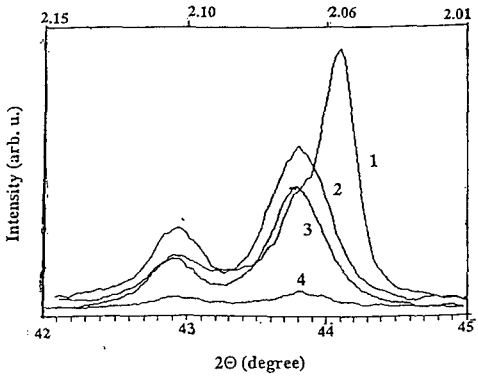

Figure 6 presents the change of XRD line intensities that occurred with time. The narrow line with d=2.054 A has disappeared and the lines with d=2.65 A and d=2.11 A have first become relatively stronger, then decreased and after four month hardly any line could be observed. Changes in XRD patterns similar to those shown in Fig. 4 were observed for the other smooth films too.

Fig. 6 Evolution in time of XRD pattern. Time of the measurements after the film was grown: 1) two weeks 2) three weeks 3) two months 4) four month

It is quite possible that the carbon phases obtained under electric field are unstable and can have polymorphic changes. Polymorphic transformations are known to happen with metal lattices even at room temperature .[4]

CONCLUSIONS

Microscopically smooth diamond films, with preferential (111) orientation have been grown under d.c. bias on mirror polished Si substrates by hot filament CVD, without surface pre-treatment to enhance nucleation. Thicknesses of a few micrometers were obtained in 30 minute depositions. Changes in the relative diffraction line intensities occurred in time. A possible explanation of these observations is that the carbon phases obtained under electric field are unstable and can undergo polymorphic transformations.

References

1 C. Wild, W. Muller-Sebert, T. Eckermann, and P. Koidl, Applications of Diamond Films and Related Materials, Materials Sci. Monographs, vol.73, (Elsevier Sci. Publishers, 1991) p.197
2. P. D. Ownby, X. Yang, and J. Liu, J. Amer. Ceram. Soc. 75, 1876 (1992)
3. A. R. Badzian and T. Badzian, Diamond and Related Materials, 2, 147 (1993)
4. C. Barrett and T. B. Massalski, Structure of Metals, Pergamon Press, N. Y. 1980, pp.486-507

EFFECT OF OXYGEN ON THE TEXTURED DIAMOND GROWTH OVER NICKEL SUBSTRATES

R. RAMESHAM*, M.F. ROSE, R.F. ASKEW, and M. BOZACK[1]
Space Power Institute, 231 Leach Center, [1]Physics Department, Auburn University, Auburn, AL 36849-5320

ABSTRACT

Microwave plasma has been used to grow diamond films using CH_4 and H_2 over nickel substrates. Nucleation of the diamond has been achieved by manual scratching and ultrasonic agitation of the substrates. The substrate was left in the H_2 microwave plasma to remove any oxide film present prior to the diamond growth. According to SEM the morphology of the grown films was (100) textured over the entire surface. Our interest is to study the effect of O_2 on the growth rate and the morphology of as-deposited diamond films. Infact, O_2 has a tendency to preferentially etch the diamond (etch rate: 111 > 110 >100). Injection of O_2 into the reaction mixture could enhance the 100 texture further. Raman analysis confirms the deposited films as diamond. Effect of O_2 on the nature of the films and the characterization of as-deposited films is described.

INTRODUCTION

Diamond is a remarkable material for innumerable applications because of its unusual properties [1,2] and therefore, several potential applications can be anticipated in electronics and protective coatings. However, the progress in diamond technology is hindered to a large extent because of the inability to grow heteroepitaxially and the difficulties of incorporating n-type carriers.

There have been some reports on the growth of heteroepitaxial diamond over the Si, ß-SiC, and c-BN substrates [3-11]. Heteroepitaxial growth of diamond on non-diamond substrates is potentially significant especially for electronics applications. Heteroepitaxy is largely depend on the nature of the crystal structure of the substrate and the deposited diamond film. Suitable candidate materials to yield the heteroepitaxial diamond growth are Mo, W, Pt, Pa, Ta, Ni, Cu, c-BN, œ-SiC, ß-SiC, etc., based on their lattice parameters. The lattice misfit should be small in order to produce epitaxial films. The larger the lattice misfit, the greater the defect density and more likely the film will be polycrystalline. Stoner et al., [3,7,11] and Wolter et al., [6] have reported the heteroepitaxial growth of diamond on the ß-SiC (lattice misfit with respect to ß-SiC is 18.1%) and (100) silicon surface via carbonization process, respectively. The defects caused by the lattice misfit may be responsible for the observed low electrical mobility values with respect to homoepitaxial diamond films [11]. Thermal expansion coefficient of silicon is twice to that of diamond. Therefore, the diamond grown over the silicon substrate has good adhesion strength as reported in the literature. If one could get the similar diamond growth [3,6,7,11] over the nickel or copper substrate (best lattice match), those films may have minimal defects and higher mobilities. Copper may at presently be ruled out since the melting point is in the vicinity of diamond growth conditions. Alternatively, nickel is the most appropriate substrate to envision the heteropitaxial diamond growth and there are two major problems associated with the nickel substrate. They are the formation of graphite prior to the diamond growth and adhesion failure of the film due to the higher thermal expansion coefficient of nickel.

Belton and Schmieg [12] have reported the growth of diamond over Ni (100) substrates and observed loss of epitaxial growth due to the formation of disordered carbon such as glassy carbon and graphite. Such interfacial layers prevent the formation of diamond film from seeding

Mat. Res. Soc. Symp. Proc. Vol. 339. ©1994 Materials Research Society

the order of the nickel substrate. A graphite intermediate layer is formed over the nickel substrate whereas carbide intermediate layer is formed over the silicon substrate. Chemical and structural effects of the substrate are important for predicting the type of carbon forms as an intermediate layer. Eimori et al., [13] have reported the formation of significant graphitization upon annealing of the nickel deposited polycrystalline diamond film in vacuum at temperatures of 200 - 900°C. Nickel film has completely diffused mostly into the grain boundaries of the film when the sample was annealed at 900°C. Rudder et al., [14] have reported on the nucleation of thin single crystal (<100 Å) on Ni (100) surfaces using remote plasma enhanced CVD. Badzian and Badzian [15] have reported that nickel may not be a good substrate for diamond heteroepitaxy because graphite would be formed in an environment of H_2 and CH_4. A mechanism has been proposed to avoid the graphite formation by forming a nickel-carbon-hydride layer just before the CVD diamond growth is initiated using hydrogen and hydrocarbons. A ternary phase of Ni-C-H melts at 1150°C and has a characteristic Raman line at 1000 cm^{-1}. Yang et al., [16] have communicated an approach involves seeding and multistep CVD process to overcome the adverse effects such as graphite formation in the plasma. There have been some reports on the growth mechanism and texture development that results in via randomly oriented nuclei and higher growth rate direction that is perpendicular to the growth surface [8,17,18]. Epitaxial growth of diamond on single crystal diamond substrates and the exploration of the diamond electronic devices are feasible, but the cost and size factors of single crystal diamond dictate the research on heteroepitaxial diamond growth. We have employed the two-step process in ref. [16] and growth process proposed in refs. [8,17, 18] to enhance the texture. We have provided the results on the deposition and characterization of polycrystalline diamond films grown on various nickel-base alloys in ref. [19]. In this paper we provide the effect of oxygen on the textured growth of diamond thin films over Ni 200 and single crystal nickel substrates.

EXPERIMENTAL DETAILS

Substrates were ultrasonically damaged in methanol containing 90 μm monocrystalline diamond particles [20]. H_2 microwave plasma treatment was performed at high temperature to reduce the oxides present on the substrates and to recrystallize the surface to prepare for the diamond growth. Microwave plasma (2.45 GHz) assisted CVD system (ASTeX, Woburn, MA) has been used to grow diamond films. Schematic diagram of the diamond deposition system is described earlier [21]. Nickel 200 alloy (Ni: 99.5%, C: 0.06%, and Cu: 0.05%) and single crystal nickel substrates have been chosen in this study to grow diamond films. Hydrogen and methane flow rates employed in all the experiments of diamond growth were 500 and 3.6 sccm, respectively.

RESULTS AND DISCUSSION

Figure 1 show SEM micrographs of diamond grown over (100) oriented single crystal nickel substrate (#121593-1): (a) typical morphology and (b) magnified view of the single particle. This substrate was treated with H_2 microwave plasma for 30 minutes at 1248°C prior to CVD diamond growth. Typical diamond deposition parameters are as follows: Pressure: 34.4 Torr, FP: 707 watts, RP: 9 watts, Temperature of the substrate: 914°C, Deposition time: 7.5 hours. Figure 1c and d show SEM micrographs of diamond grown in the presence of O_2 over the Ni 200 substrate (#112393-1). (c) Typical morphology and (d) magnified view of "c." This sample was treated with H_2 microwave plasma for 30 minutes at 1316°C. Percentage of the oxygen in hydrogen is 1. Temperature of the substrate and deposition time are 953°C and 8 hours, respectively. Very sparse deposits of faceted diamond crystals were observed on the Ni 200 substrate. The morphologies of the single particle in figure 1b and d are different. Infact addition of O_2 into the reaction mixture should enhance the (100) texture of diamond films [22]. Percentage of O_2 in H_2 may be too high in order to yield textured diamond films. Subsequently, reduced the flow rate of O_2 to 2 sccm (#091793-1, Pressure: 34.3 Torr, FP: 801 watts, RP: 12

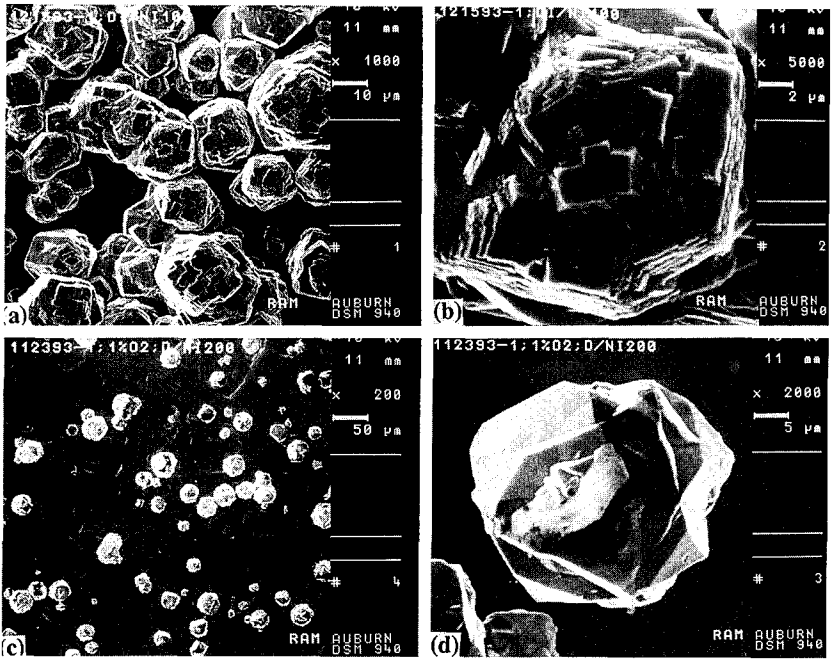

Figure 1: SEM micrographs of diamond grown over H_2 microwave plasma treated(100) oriented single crystal nickel substrate (#121593-1) (a) typical morphology (b) magnified view of single particle. Diamond grown over the Ni 200 substrate (#112393-1) in the presence of O_2. (c) Typical morphology and (d) magnified view of "c".

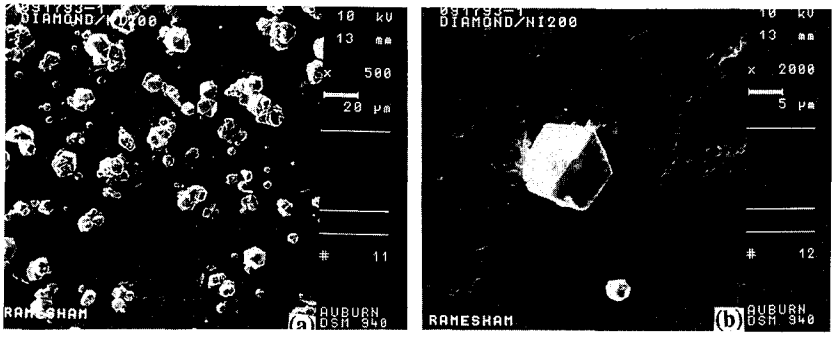

Figure 2: SEM micrographs of the diamond grown over the ultrasonically damaged and H_2 microwave plasma treated Ni 200 substrate using a gas mixture of $H_2/CH_4/O_2$.(500/3.6/2 sccm) Percent of O_2 in hydrogen: 0.4%. (#091793-1)

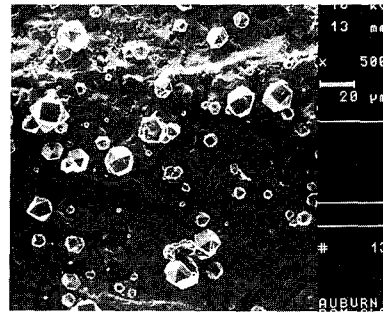

Figure 3: SEM micrographs of the diamond grown over H_2 microwave plasma treated Ni 200 substrate using a gas mixture of $H_2/CH_4/O_2$(500/3.6/0.5 sccm) . Percent of O_2 in hydrogen: 0.1%. (#092093-1)

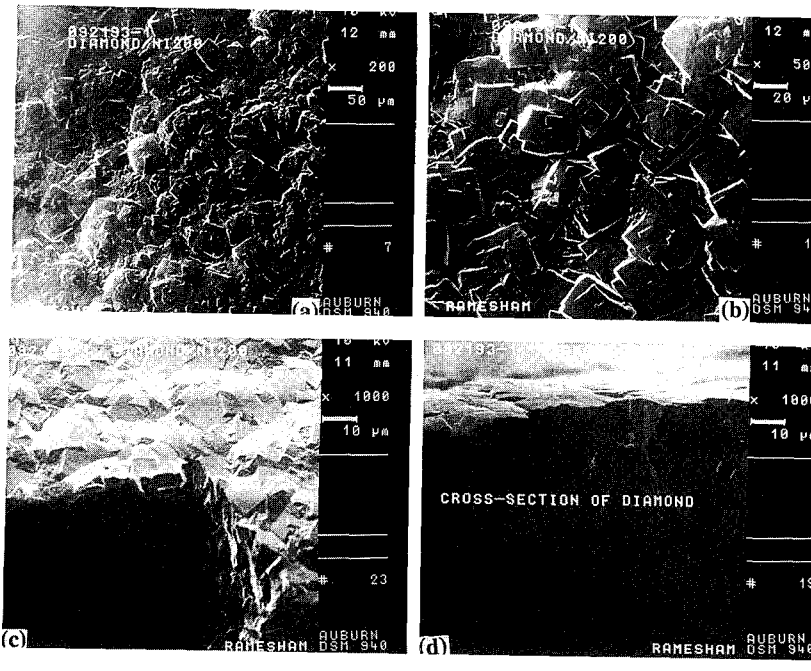

Figure 4: SEM micrographs of (a) typical morphology of CVD diamond grown over Ni 200 (b) magnified view of (a), (c and) cross-sectional views of the diamond. Oxygen was injected into the reactor for five times (each time 2 to 5 minutes) during the growth period with a flow rate of 0.5 sccm.(#092193-1)

watts, Temperature of the substrate: 970°C, Deposition time: 7.25 hours.) and 0.5 sccm (#092093-1) and the corresponding SEM micrographs of diamond grown on ni substrates are shown in figure 2 and 3, respectively. Very sparse deposits were observed in both the experiments. Therefore, it is decided to admit the oxygen into the reaction mixture intermittently in order to etch the non-diamond carbon and enhance the texturing of diamond films. Typical diamond deposition parameters for the data shown in the Figure 3 (#092093-1) are as follows: Pressure: 35 Torr, FP: 803 watts, RP: 6 watts, Temperature of the substrate: 966°C, Deposition time: 5 hours. We have added oxygen (0.05% - 1.0%) to the reaction mixture (H_2 and CH_4) in order to observe its effect on the quality of diamond thin films. Preliminary observations indicate that the growth of diamond is completely inhibited.

A virgin Ni 200 (#092193-1)sample was treated with H_2 microwave plasma and subsequently deposited diamond films (Pressure: 30.2 Torr, FP: 650 watts, RP: 9 watts, Temperature of the substrate: 942°C, Deposition time: 31 hours.). O_2 was injected into the reactor five times during the complete deposition period with a flow rate of 0.5 sccm for 2 to 5 minutes to investigate texturing of diamond films. Addition of oxygen into the plasma could enhance the growth rate of diamond as reported earlier [23,24]. Our observations did not show any increase in the diamond growth rate either on silicon or on nickel alloys. Figure 4a and b show the textured diamond films grown over Ni 200 alloy. Columnar growth of diamond films may be seen vividly from the cross-sectional micrographs shown in figure 4c and d. One may infer from this experiment scratching and/or seeding with diamond particles are not necessary to initiate the growth of diamond. One could infer based on the data observed in AES and XPS that there was an increase in the carbon content upon hydrogen microwave plasma treatment. That carbon might be acting as a nucleation site for the diamond growth. The formation of graphite on the surface of the nickel in the initial stages of the deposition and it may be acting as a nucleation center for the diamond to grow in the subsequent duration of the experiment.

Figure 5 show SEM micrographs of the diamond films grown over the ultrasonically damaged for 2 hours and manually scratched with 90 μm diamond particles and finally H_2 microwave plasma (20 minutes at 1300°C) treated Ni 200 substrate (#092393-1, Pressure: 31.9 Torr, FP: 700 watts, RP: 10 watts, Temperature of the substrate: 1013°C, Deposition time: 52 hours.). Oxygen was injected (0.2 sccm) into the reactor 8 times (each time for 5 minutes) during the deposition period. Typical morphologies of (100) texture is shown in figure a, b, and c.

Ni 200 substrates were cleaned with acetone, 2-propanol, and distilled water. Samples were analyzed with AES and XPS and found the presence of numerous surface contaminants. The contaminants are as follows: Si, S, Cl, Ar, Ca, Pd, C, O, and possibly Mn and Zn. The C, O, N originates from atmospheric gases and is observed on nearly all surfaces exposed to the atmosphere. A cleaned Ni 200 sample was left in H_2 microwave plasma for 1 hour at 1200°C and analyzed the sample by AES and XPS. It was surprising to note that the surface was completely cleaned and observed only carbon and oxygen signals with no traces of the contaminants present before cleaning. The carbon signal is significant and higher than the chemically cleaned surface. This may be attributed to the contamination of substrate base (Quartz) with carbon such as diamond from the earlier experiments. We speculate that the H_2 microwave plasma treatment deposits carbon while removing most other surface contaminants. AES and XPS spectra from the diamond covered surface show the surface nearly all carbon. The binding energy of the C1s peak is 284.6 eV, precisely the expected binding energy of C-C bonds. H_2 microwave plasma treatment did show the enrichment of nickel surface with carbon and that could be due to formation of Ni-C-H as proposed earlier [15,16]. Our studies did not show any nickel film on the diamond crystallites as observed in ref. 16. We have observed the droplets of nickel only in some experiments.

Raman analysis of the as-deposited films on all the substrates was performed by Renishaw 2000 Ramascope using HeNe (633 nm, red) laser. All the films were confirmed to be diamond that contains non-diamond carbon (graphite, disordered carbon, and glassy carbons) inclusions

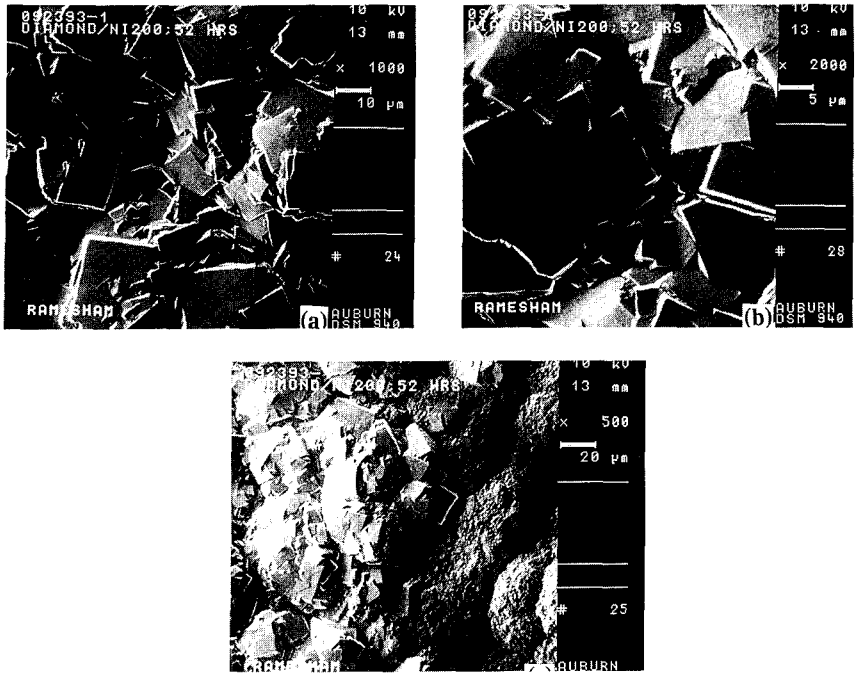

Figure 5: SEM micrographs of the diamond films grown over ultrasonically damaged (2 hours), manually scratched with 90 µm diamond particles, H_2 microwave plasma treated Ni 200 substrate. (a and b) Typical morphology and (c) variable morphology. Oxygen was injected into the reactor for eight times (each time 5 minutes) during the growth period with a flow rate of 0.2 sccm.(#092393-1)

present in the films. Raman spectrum of the backside of the diamond film grown on a single crystal of (100) orientation Ni substrate clearly shows a peak at 1584 cm^{-1} apart from the diamond peak at 1326.2cm^{-1}. The former peak may be due to the presence of graphite that means graphite is being formed even before the diamond growth in contrast to ref. 16 though the sample was provided H_2 microwave plasma treatment. Though the texture is (100) but the Raman signature corresponding to diamond is either shifted towards the lower wave numbers and/or even broad. We could only say at this stage based on the data obtained that the (100) texture is misleading when investigated by Raman spectroscopy. We have not observed any Raman signature (1000 cm^{-1}) corresponding to Ni-H-C in our studies as observed in [15].

We have performed the diamond growth on single crystal (100), (111), and (110) oriented nickel substrates. The nickel crystals were not surface damaged, but provided H_2 microwave plasma treatment. We have observed (100) textured growth on all the substrates. It was quite surprising to note that the (100) texture resulted in on the (111) oriented single crystal nickel substrate. This indicates that the film is not following the order of the substrate. The morphology was solely manipulated with the diamond deposition conditions. Detailed investigation of diamond growth on single crystal nickel substrates by x-ray analysis and other techniques is under progress.

CONCLUSIONS

Ni 200 substrate has yielded <100> textured diamond growth. Nickel droplets were observed over the diamond crystals grown on Ni 200 substrate. Continuous injection of oxygen into the diamond reaction mixture is not assisting in texturing the diamond films as anticipated. Intermittent addition of oxygen may be helping to enhance the texturing of diamond deposited over the nickel substrates. Raman analysis of the backside of the diamond film shows the signatures of diamond and graphite. Surface damage or seeding is not necessary to grow diamond over the nickel. We have grown textured (100) diamond films on (100), (111), (110) oriented single crystal nickel substrates. Though the diamond films were 100 texture the corresponding Raman signature was not satisfactory. Long period of growth with and without H_2 microwave plasma treatment has yielded the (100) texture.

ACKNOWLEDGMENTS

This work is carried out at the Space Power Institute of the Auburn University and was supported in part by the Naval Surface Warfare Center, Crane, IN through Port Hueneme, CA and by the Center for Commercial Development of Space Power (CCDS) and Advanced Electronics, located at Auburn University, with funds from NASA Grant NAGW-1192-CCDS-AD, Auburn University, Center's Industrial Partners, and in part by the Office of Innovative Science and Technology (SDIO/TNI) of the Strategic Defense Initiative Organization's Office through Navy Contract #N60921-91-C-0078 with the Naval Surface Warfare Center.

REFERENCES

1. J.E. Field, ***The Properties of Diamond***, Academic Press, London, 1979.
2. J.H. Edgar, ***J. Mater. Res.***, **7,** 237 (1992).
3. B.R. Stoner and J.F. Glass, ***Appl. Phys. Lett.***, **60,** 698 (1992).
4. X. Jiang and C.P. Klages, ***Diamond and Related Materials,*** **2,** 1112 (1993).
5. W. Zhu, X.H. Wang, , B.R. Stoner, G.H. Ma, H.S. Kong, M.W.H. Braun, and J.T. Glass, ***Phys. Rev.,*** **B15, 47**, 6529 (1993).
6. S.D. Wolter, B.R. Stoner, J.T. Glass, P.J. Ellis, D.S. Buhaenko, C.E. Jenkins, and P. Southworth, ***Appl. Phys. Lett.,*** **62,** 1215 (1993).
7. B. Stoner, S. Sahaida, J.P. Bade, P. Southworth, and P. Ellis, J. ***Mater. Res.,*** 8, 1334 (1993).

8. C. Wild, W. Muller-Sebert, T. Eckermann, and P. Koidl, "Textured growth and twinning in polycrystalline CVD diamond films," ***Electrochem. Soc. Proc.,*** Edited by A.J. Purdes, J.C. Angus, R.F. Davies, B.M. Meyerson, K.E. Spear, M. Yoder, **91-8, 224** (1991).
9. M. Yoshikawa, H. Ishida, A. Ishitani, T. Murakami, S. Koizumi, and T. Inuzuka, ***App. Phys. Lett.,*** **57,** 428 (1990).
10. S. Koizumi, T. Murakami, T. Inuzuka and K. Suzuki, ***Appl. Phys. Lett.,*** **60,** 698 (1992).
11. B.R. Stoner, S.R. Sahaida, D.M. Malta, A. Sowers, and R.J. Nemanich, "Heteroepitaxial nucleation nucleation and growth of highly oriented diamond films on silicon via in-situ carburization and bias-enhanced nucleation," in ***Proceedings of 2nd International Conference on the Applications of Diamond Films and Related Materials***, Edited by M. Yoshikawa, M. Murakawa, Y. Tzeng, and W.A. Yarbrough, MYU publishers, Tokyo, Japan, 1993, p.825.
12. D.N. Belton and S.J. Schmieg, ***J. Appl. Phys.,*** **66,** 4223 (1989).
13. N. Eimori, Y. Mori, J. Moon, A. Hatta, J.S. Ma, T. Ito, and A. Hiraki, ***Diamond and Related Materials,*** **2,** 537 (1993).
14. R.A. Rudder, D.J. Vitkavage, and R.J. Markunas, "Nucleation studies of diamond on Ni(100) surfaces," ***Materials Research Society Extended Abstracts,*** Edited by G.H. Johnson, A.R. Badzian, M. Geis, **EA-15** (1988) 19.
15. A. Badzian and T. Badzian, "Nickel hydride assistance in CVD diamond growth," in ***Diamond Films, The Electrochemical Society Proceedings,*** Edited by J.P. Dismukes, K.V. Ravi, K.E. Spear, B. Lux, N. Setaka, **PV93-17** (1993) 441.
16. P.C. Yang, W. Zhu, and J.T. Glass, ***J. Mater. Res.,*** **8,** 1773 (1993).
17. R.E. Clausing, L. Heatherly, E.D. Specht, and K.L. Moore, "Texture development in diamond films grown by hot filament CVD processes," in ***New Diamond Science and Technology,*** Edited by R. Messier, J.T. Glass, J.E. Butler, and R. Roy, Vol. No. NDST-2, Materials Research Society, Pittsburgh, PA, 1991, p. 575.
18. Y. Sato, I. Yashima, H. Fujita, T. Ando, and M. Kamo, "Epitaxial growth of diamond from the gas phase," in ***New Diamond Science and Technology,*** Edited by R. Messier, J.T. Glass, J.E. Butler, and R. Roy, Vol. No. NDST-2, Materials Research Society, Pittsburgh, PA, 1991, p. 371.
19. R. Ramesham, M.F. Rose, and R.F. Askew, "Growth of Textured Diamond Thin Film on Ni-Base Alloys," Submitted to Proceedings of International Conference on Metallurgical Coatings and Thin Films," San Diego, CA, April 25-29, 1994.
20. R. Ramesham and T. Roppel, ***J. Mater. Res.,*** **7,** 1144 (1992).
21. R. Ramesham, T. Roppel, C. Ellis, D.A. Jaworske, and W. Baugh, ***J. Mater. Res.,*** **6,** 1278 (1991).
22. R. Ramesham and B.H. Loo, ***J. Electrochem. Soc.,*** **139,** 1988 (1992).
23. J.A. Mucha, D.L. Flamm, and D.E. Ibbotson, ***J. Appl. Phys.,*** **65,** 3448 (1989).
24. C.P. Chang, D.L. Flamm, D.E. Ibbotson, and J.A. Mucha, J. ***Appl. Phys.,*** **63,** 1744 (1988).

PART VI

BN and SiC Epitaxial Growth

CATHODOLUMINESCENCE SPECTROSCOPY OF BORON NITRIDE FILMS

C. A. TAYLOR II, S. W. BROWN, V. SUBRAMANIAM, S. KIDNER,
S. C. RAND, and R. CLARKE
Harrison M. Randall Laboratory of Physics,
University of Michigan, Ann Arbor, MI 48109-1120

ABSTRACT

We report results from cathodoluminescence spectroscopy of boron nitride films grown on Si (100) substrates by ECR ion source assisted magnetron sputtering of a hexagonal BN target. Three main peaks are observed in the near-bandgap region for hexagonal boron nitride films at energies of 4.90 eV, 5.31 eV, and 5.50 eV. In addition, deep-level emission spectra of predominantly cubic boron nitride films are correlated with sample growth conditions. In particular we show that the emission intensity, position, and linewidth are strongly dependent on the substrate bias voltage used during sample growth.

INTRODUCTION

The development of III-V nitride materials is of considerable interest for semiconductor electronic and optical device applications [1]. The bandgaps of III-V nitrides range from 1.9 eV for wurtzitic InN to greater than 6.2 eV for cubic BN, making these materials well suited for optical applications throughout the visible and into the near-ultraviolet (UV) region. The polytypes of boron nitride, having some of the largest bandgaps of the III-V nitrides, are technologically important materials for deep-blue and UV applications, yet their luminescence properties are not well characterized. While several researchers have reported unidentified defect- and impurity-related deep-level luminescence from both hexagonal and cubic boron nitride [2-7], there has been only one report of luminescence at wavelengths near the band edge in this compound, namely the work of Lukomskii, et al. [8], which was performed with single crystal hexagonal BN. In this paper, we report the first observations of near-bandgap luminescence from hexagonal boron nitride films and also discuss correlations between growth conditions and selected spectral features of cubic boron nitride films.

EXPERIMENTAL DETAILS

Boron nitride films were grown on Si (100) substrates by an RF magnetron sputter deposition process. During growth, the substrates were biased negatively with respect to ground and were immersed in a nitrogen plasma produced by an electron cyclotron resonance (ECR) source. Our previous work determined the existence of a sharp threshold in the substrate bias voltage beyond which cubic BN is formed [9]. The growth process was studied in detail using reflection high energy electron diffraction (RHEED). The threshold, which occurs at bias voltages on the order of -100 V, was revealed by distinct differences in the RHEED ring patterns of hexagonal and cubic BN. Furthermore, the structural quality of the cubic BN films, as monitored by the ring width of the RHEED patterns, was found to be optimized in a very narrow window of voltages just beyond the threshold.

Cathodoluminescence (CL) measurements were performed in a UHV chamber at a base pressure of 5×10^{-10} torr. Samples were mounted with either indium or silver paint on a UHV compatible open-flow liquid helium cryostat capable of temperature control from 4.2 K to 400 K. Sample temperature was monitored with a silicon diode and controlled to within 0.05 K using a Lakeshore 91C temperature controller. The CL was excited with a Vieetech VE-052 electron gun operated at an acceleration voltage of 30 keV and a filament current of 60 μA producing a beam current at the sample of ~3.0 μA. The spot size at the sample was maintained at 2 mm or larger to reduce effects of sample heating. The CL was focused onto the slits of an ISA THR1000 spectrometer equipped with a grating blazed at 250 nm. The spectrometer was operated in first order with a spectral resolution of 0.02 eV. A UV sensitive photomultiplier tube (RCA C31034a-02)

Mat. Res. Soc. Symp. Proc. Vol. 339. ©1994 Materials Research Society

operating in photon-counting mode was used to detect the CL signal. Spectra were not corrected for instrumental response [10].

RESULTS AND DISCUSSION

A hexagonal BN film, of ~ 8000 Å thickness, was grown at 850 °C without substrate bias and was characterized by infra-red (IR) absorption measurements and high resolution transmission electron microscopy (HRTEM). As shown in Figure 1, the film was characterized by strong IR absorptions at 788 cm^{-1} and 1383 cm^{-1} from hexagonal BN TO phonons [11]. In this film, there was no evidence of sp^3 bonding, which would generate a feature near 1065 cm^{-1} corresponding to cubic BN TO phonon absorption [12]. HRTEM (not shown) confirmed that this film is highly oriented hexagonal BN, with the hexagonal BN (002) planes aligned perpendicular to the silicon [110] direction. This highly oriented growth mode of hexagonal BN on silicon (100) substrates has been observed previously [13].

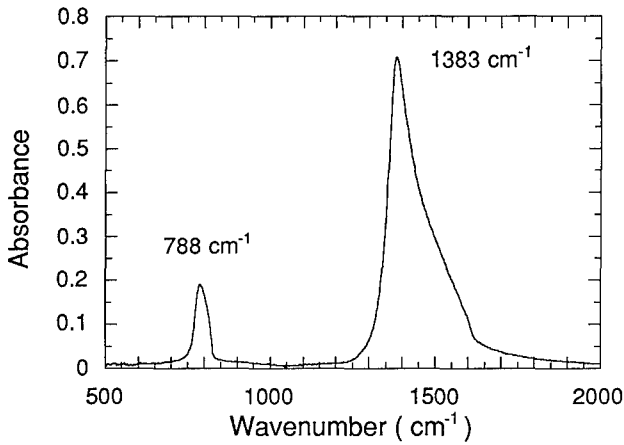

Fig. 1. Infrared absorption spectrum of hexagonal BN film grown without substrate bias. The peaks at 788 cm^{-1} and 1383 cm^{-1} correspond to A_{2u} and E_{1u} vibrational modes, respectively.

The low temperature CL spectrum of this hexagonal BN film, shown in Figure 2(a), was dominated by three deep-level emission bands centered at 3.40 eV, 3.84 eV, and 4.40 eV. In addition, three near-bandgap UV emission peaks centered at energies of 4.90 eV, 5.31 eV, and 5.50 eV were observed (Figure 2(b)). To our knowledge, these near-bandgap features have not been reported previously in any type of boron nitride film. Recent cathodoluminescence studies of single crystals of hexagonal BN showed similar UV luminescence features, as well as additional features at energies as high as 5.8 eV [8]. The widths of UV emission lines from our hexagonal BN film were approximately a factor of 2 greater than those reported for single crystal BN. This increased linewidth was attributed to inhomogeneous broadening due to the polycrystalline nature and small grain size of the film. Similar effects have been observed, for example, in the near-bandgap emission from polycrystalline diamond films [14,15]. The exact origin of the observed peaks is currently under investigation.

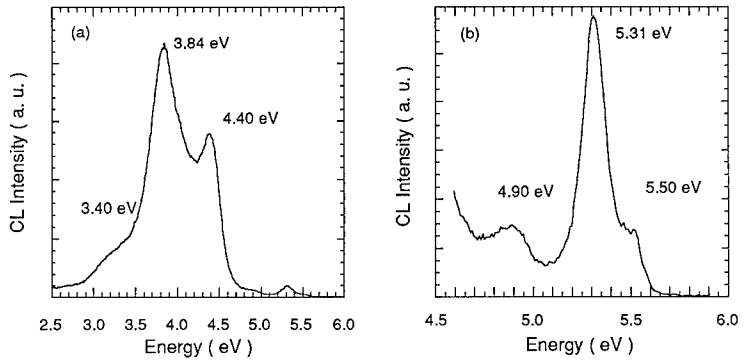

Fig. 2. (a) Deep-level and (b) near-bandgap UV emission spectra taken at 4.2 K from a hexagonal BN film.

The temperature dependence of the near-bandgap CL features is shown in Figure 3. As can be seen in the figure, the intensities of the peaks decreased rapidly with increasing temperature above 60 K. In addition, the peak positions were not strongly temperature dependent, which is consistent with both experimental measurements and theoretical expectations of the bandgap temperature dependence of hexagonal BN [16]. The measured shift of the hexagonal BN bandgap with temperature is lower by at least an order of magnitude compared to shifts in cubic III-V materials.

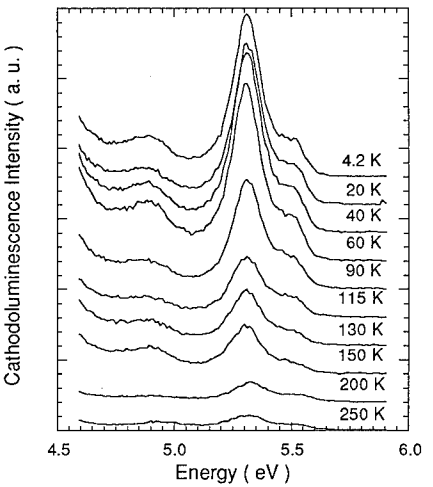

Fig. 3. Temperature-dependent CL spectra from a hexagonal BN film in the near-bandgap region.

We have also examined the deep-level emission from a series of 2000 Å thick polycrystalline cubic BN films grown with varying substrate bias. These cubic BN films were grown

under identical conditions except for substrate bias voltage which was varied systematically from -108 V to -116 V. This range of substrate bias voltage is just beyond the threshold value for cubic BN formation with our current growth conditions, which results in optimization of the cubic BN crystalline quality near -116 V [9]. HRTEM measurements confirmed that the films have a thin amorphous layer adjacent to the silicon substrate followed by a ~ 200 Å hexagonal BN layer with the remainder of the film being cubic BN. A thin amorphous layer has been reported previously for cubic BN films on silicon (100) substrates [13].

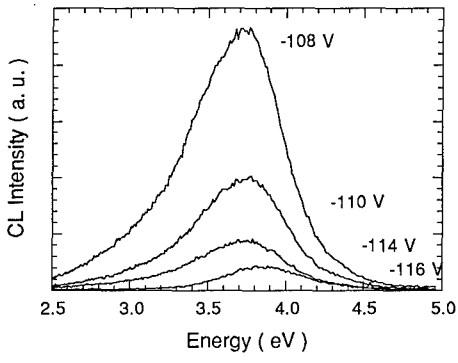

Fig. 4. Deep-level emission spectra of cubic BN films grown at bias voltages ranging from -108 V to -116 V.

The deep-level defect-related CL, shown in Figure 4, diminished significantly in samples grown with increasing substrate bias voltage. Normalized CL spectra for samples grown at -108 V and -116 V, shown in Figure 5(a), demonstrated that, in addition to the decrease in intensity, the emission linewidth narrowed substantially and shifted to higher energy as the cubic BN crystal quality was optimized. The IR absorbance of the two samples is shown in Figure 5(b). The relative increase in absorbance at 1065 cm^{-1} reflects the improved crystallinity of the cubic BN film grown with a substrate bias of -116 V.

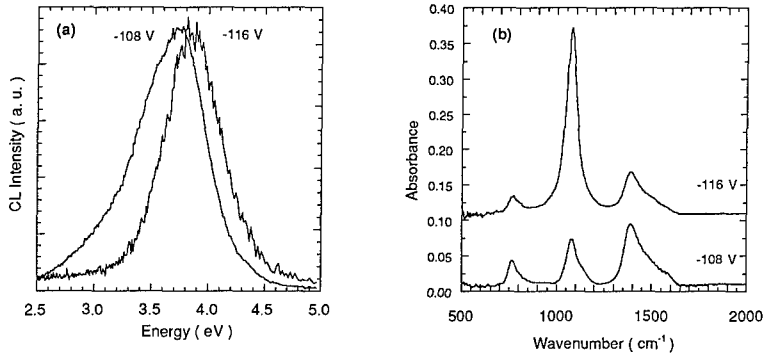

Fig. 5. (a) Normalized CL spectra and (b) IR absorption spectra of cubic BN films grown with substrate bias voltages of -108 V and -116 V.

CONCLUSIONS

In summary, we have presented the first near-bandgap UV emission from a hexagonal BN film. Three main peaks were observed in the UV emission spectrum at energies of 4.90 eV, 5.31 eV and 5.50 eV. In addition, we examined cubic BN films and found strong correlations in the intensity, linewidth, and position of defect-related visible emission with substrate bias voltage used during growth. In particular, the defect-related emission was found to decrease in intensity and shift to higher energy as the cubic BN growth conditions were optimized. We are currently investigating the origin of the near-bandgap emission from hexagonal BN films and extending our research to examine near-bandgap emission from cubic BN.

ACKNOWLEDGEMENTS

This work was supported by ONR Grant No. N0014-91-J-1398 and the NSF Center for Ultrafast Optical Science (STC PHY 8920108). The authors gratefully acknowledge the encouragement and support of Max Yoder.

REFERENCES

1. Wide Band Gap Semiconductors, T. D. Moustakas, J. I. Pankove, and Y. Hamakawa, eds., (Mat. Res. Soc. Symp. Proc. **242,** San Francisco, CA, 1991).
2. S. Larach and R. E. Shrader, Physical Review **104**, 68 (1956).
3. N. J. Pipkin, J. Mat. Sci. **15**, 2651 (1980).
4. V. B. Shipilo, E. M. Shishonok, A. M. Zaitsev, A. A. Melnikov, and A. I. Olekhnovich, Phys. Stat. Sol. (a) **108**, 431 (1988).
5. O. Mishima, K. Era, J. Tanaka, and S. Yamaoka, Appl. Phys. Lett. **53**, 962 (1988).
6. E. M. Shishonok, V. B. Shipilo, A. I. Lukomskii, and T. V. Rapinchuk, Phys. Stat. Sol. (a) **115**, K237 (1989).
7. V. B. Shipilo, A. I. Lukomskii, and L. M. Gameza, Zhur. Prikl. Spektr. **55**, 567 (1991).
8. A. I. Lukomskii, V. B. Shipilo, and L. M. Gameza, Zhur. Prikl. Spektr. **57**, 100 (1992).
9. S. Kidner, C. A. Taylor II, and R. Clarke, Appl. Phys. Lett. **64**, 1859 (1994).
10. System response, measured with a deuterium lamp source, indicates that our current optical system has a wavelength limit of ~210 nm (~5.9 eV).
11. D. M. Hoffman, G. L. Doll, and P. C. Eklund, Phys. Rev. B **30**, 6051 (1984).
12. P. J. Gielisse, S. S. Mitra, J. N. Plendl, R. D. Griffis, L. C. Mansur, R. Marshall, and E. A. Pascoe, Phys. Rev. **155**, 1039 (1967).
13. D. J. Kester, K. S. Ailey, R. F. Davis, and K. L. More, J. Mater. Res. **8**, 1213 (1993).
14. J. Ruan, K. Kobashi, and W. J. Choyke, Appl. Phys. Lett. **60**, 1884 (1992).
15. A. T. Collins, M. Kamo and Y. Sato, J. Mater. Res. **5**, 2507 (1990).
16. A. Zunger, A. Katzir, and A. Halperin, Phys. Rev. B **13**, 5560 (1976).

LOW ENERGY THRESHOLD IN THE GROWTH OF CUBIC BORON NITRIDE FILMS BY ECR PLASMA ASSISTED MAGNETRON SPUTTERING

C. A. TAYLOR II, S. KIDNER, and R. CLARKE
Harrison M. Randall Laboratory of Physics,
University of Michigan, Ann Arbor, MI 48109-1120

ABSTRACT

We report the growth of cubic boron nitride (cBN) films by magnetron sputtering on Si (100) substrates. The films are grown in the presence of negative substrate bias voltages and a nitrogen plasma produced by an electron cyclotron resonance source. We find evidence for a sharp low-voltage threshold in the substrate bias (-105 V) beyond which the samples are predominantly cBN. The structural quality of the cBN films is optimized in a narrow range of voltages near this threshold. We discuss the important role of energetic ions in the formation of cBN in light of recent theoretical findings.

INTRODUCTION

The growth of high quality cubic boron nitride (cBN) has been of technological interest for many years. First demonstrated by Wentorf [1] in 1957, cBN has attractive properties such as extreme hardness, high thermal conductivity, and low chemical reactivity. More recently, cBN has been gaining attention as a III-V nitride material for semiconductor device applications. The relatively wide band gaps of the III-V nitrides make them particularly well suited for blue to ultraviolet optical devices as well as for high power/high temperature electronic applications [2,3].

The challenges encountered in growing epitaxial BN films arise in part from the lack of a suitable lattice matched substrate. Perhaps more important is the difference in equilibrium phases for BN and its III-V nitride counterparts. Unlike the other III-V nitrides, which tend to stabilize in the wurtzitic structure, BN prefers to stabilize in a hexagonal phase (hBN) similar to the graphitic phase of carbon.

The growth of cBN films has been demonstrated using a variety of deposition processes [4-10] which all employ an energetic plasma to promote cBN growth. From these investigations it is clear that the kinetics of the plasma plays an important role in the synthesis of cBN. In this report we present new results of BN films deposited on (001) silicon by RF sputtering using both a low energy electron cyclotron resonance (ECR) ion source and negative substrate bias to promote cBN formation. We find evidence for a very sharp bias voltage threshold above which cBN is formed. Moreover, the structural quality of the cBN is optimized near this threshold. The range of bias voltage over which cBN is formed is much narrower than previous reports in the literature would indicate [5,10].

EXPERIMENTAL DETAILS

Sputtering of a hot pressed hBN target was carried out in an RF magnetron sputter deposition system with a base pressure of 5×10^{-10} Torr. The cryopumped ultrahigh vacuum

Mat. Res. Soc. Symp. Proc. Vol. 339. ©1994 Materials Research Society

chamber is equipped with an Astex compact ECR source and a 30 kV reflection high energy electron diffraction (RHEED) system.

The substrate oxide layer was removed thermally at base pressure following a modified Shiraki [11] clean. The samples were brought to the growth temperature of 850° C and dc-biased negatively with respect to ground. The RF magnetron source-to-substrate distance is approximately 20 cm and the ECR is mounted at 45° with a source-to-substrate distance of 8 cm. At these distances the substrate surface is completely immersed in the ECR plasma but is well removed from the plasma confinement region of the sputtering source. During growth the chamber pressure was 1.0 mTorr with flow rates of 10 sccm Ar into the chamber and 10 sccm N_2 through the ECR. Both gases were ultrahigh purity (99.999+ %) and were passed through additional point-of-entry purifiers before entering the gas manifold. The samples were examined in-situ immediately after growth using RHEED.

RESULTS

With the RF magnetron power fixed at 600 W and the microwave ECR power fixed at 200 W, the substrate bias was varied systematically from -100 V to -120 V. With these operating conditions our growth rate is approximately 0.1 Å/s. Although all of the samples are polycrystalline films there is clear evidence in the RHEED pattern of a sharp threshold in the bias voltage at -105 $\pm$ 1.0 V beyond which the samples are cubic. This threshold is revealed by the distinct differences in the RHEED ring patterns of hBN and cBN. Furthermore, the structural quality of the films as monitored by the ring width of the RHEED patterns is optimized in a very narrow window of voltages just beyond the threshold. Figure 1 shows intensity profiles taken along the shadow edge of the RHEED ring patterns for a series of samples grown near the threshold voltage.

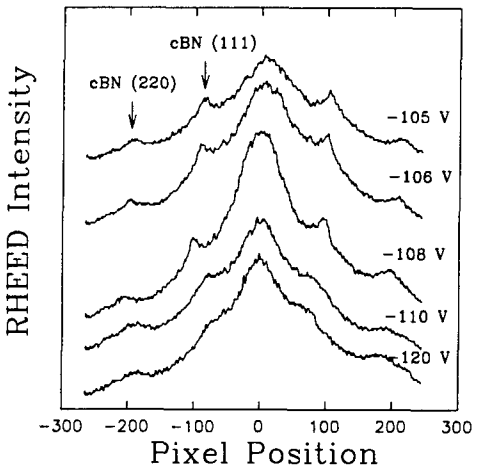

Fig. 1. Intensity profiles of RHEED ring patterns grown near the threshold voltage. The cBN (111) ring width becomes noticably sharper and more intense at -108 V. Beyond -108 V the rings quickly broaden.

Table I. RHEED ring width vs. substrate bias for samples grown near the threshold voltage. Diffraction ring widths are obtained from fitting the intensity profile to Gaussian line shapes.

Substrate Bias (V)	Diffraction Ring Width (Pixels)	Structure and Ring Index
-100	51.6	hBN (002)
-104	42.3	hBN (002)
-105	27.5	cBN (111)
-106	25.2	cBN (111)
-108	23.7	cBN (111)
-110	38.1	cBN (111)
-120	57.2	cBN (111)

The first set of peaks, to either side of the central diffuse scattering peak, correspond to the cBN (111) diffraction ring. The next set (further out from the diffuse central peak) correspond to the cBN (220). The width of the cBN diffraction rings is strongly dependent on the bias voltage (see Table I). At the threshold value of approximately -105 V the RHEED pattern indicates cBN, while below this value (less negative bias voltage) only hBN is formed. In the region between -106 V and -108 V the rings in the RHEED pattern are much sharper and brighter indicating larger grain sizes and a generally more ordered structure. Beyond -108 V the rings begin to noticeably broaden indicating a significant decrease in structural quality.

Shown in Figure 2 is the infrared spectrum of a 2000 Å film grown at -108 V, three volts beyond the threshold. The cBN TO-mode is observed at the accepted value of 1065 cm^{-1}. The hBN A_{2u} and E_{1u} modes at 770 cm^{-1} and 1380 cm^{-1} indicate a small amount of hBN in the film. These results are confirmed by plan-view transmission electron microscopy (Fig. 3). The diffraction pattern shows sharp rings which index to cBN. The diffuse partial rings in the pattern are due to the small amount of hBN in the film. This small fraction of hBN is not detectable in the RHEED diffraction pattern.

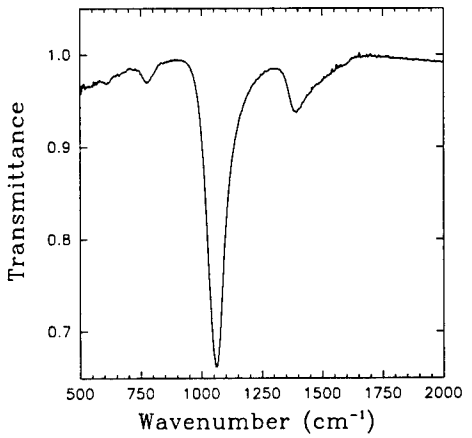

Fig. 2. Infrared spectrum of a cBN film grown with a substrate bias voltage of -108 V. The cBN TO-mode is at 1065 cm^{-1} and the small peaks at 770 cm^{-1} and 1380 cm^{-1} indicate a small amount of hBN in the films.

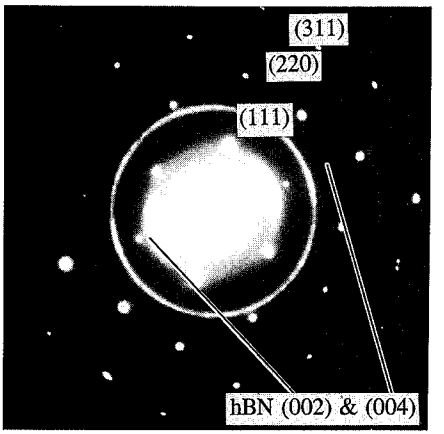

Fig. 3. Plan view transmission electron diffraction pattern of a BN film grown with a substrate bias voltage of -108 V. The spot pattern is from the [110] zone of silicon. The very faint and diffuse partial rings index to the (002) and (004) of hBN. All other rings index to cBN.

DISCUSSION

The existence of some type of threshold or range of parameters for cBN formation has been reported in several investigations utilizing plasma assisted deposition [5-7,9,10], nearly all of which have employed high energy ion bombardment from a Kaufman type source to control the formation of cBN. Using ion bombardment of this type the "window" for cBN formation, whether it be defined in terms of a substrate bias [5,10], an ion energy [6,7,11,12] or momentum/atom [9], exists over a wide range of the controlling parameter. Studies in the

literature have shown cBN formation with ion energies as high as 7 keV with a typical window of formation on the order of hundreds of eV. Several investigations have claimed optimized growth with N_2/Ar ion beams with ion energies of 500 eV [6,9,12]. Our finding, to the best of our knowledge, is the first evidence of a sharp low-energy threshold (on the order of 100 eV).

The existence of an energy threshold for cBN formation can be understood by considering how BN transforms from the thermodynamically stable hexagonal structure to the higher energy cubic structure. In general, this transformation requires a hybridization change from sp^2 to sp^3 accompanied by a reduction of the interplanar spacing which cannot be accomplished without both bond breaking and a change in the chemical nature of the bond. It is clear that without energetic species, the BN film will stabilize in the hexagonal structure on substrates other than diamond and cBN itself. While it has been suggested [12] that cBN formation is the result of the build up of biaxial film stress, our findings suggest that the role of the energetic ions is to break the bonds of surface atoms and provide the kinetics necessary for cBN formation.

Although our threshold energy is much lower and sharper than previous work would indicate, it is surprising that film growth is possible in the presence of such high kinetic energies. In most material systems collision energies in this range would cause considerable lattice damage. To understand why cBN can withstand such energies the case of diamond (a similar sp^3 bonded material) provides considerable insight. Recent theoretical investigations of radiation damage in diamond have shown that the impulse energy required to permanently displace a single atom on the surface of a diamond lattice is approximately 50 eV [13]. In terms of an incident ion of similar mass this would correspond to kinetic energies in the range of 100 eV which is strikingly similar to our findings [14]. The authors attribute this extremely high damage threshold in diamond (approximately 3.5 times the cohesive energy) to the large speed of sound in diamond. In effect, there is a rapid dissipation of kinetic energy into the surrounding crystal via incoherent lattice vibrations, in agreement with values derived from experiments using high energy electron bombardment of diamond [15].

CONCLUSIONS

In light of our experimental findings and the recent theoretical work, we conclude that cBN formation requires the arrival of energetic species on the order of 100 eV to facilitate bond breakage of surface atoms during growth. We expect this energy value to be strongly dependent on deposition rate for a given incident flux of ions since at some point the deposition rate will saturate the kinetic effects provided by the ions and hBN will be formed. Once this point is reached either the ion flux must be increased or the energy must be increased to provide additional collision kinetics. We believe this may account for the widely varying energy ranges reported in the literature for cBN growth. Furthermore, our work suggests that an extremely slow deposition rate combined with ions on the order of 100 eV will optimize not only the fraction of cBN formation but the crystal quality as well.

ACKNOWLEDGEMENTS

The authors thank S. Fahy and G. Doll for many valuable discussions regarding our findings. This work was supported by ONR Grant No. N0014-91-J-1398. The authors gratefully acknowledge the encouragement and support of Max Yoder.

REFERENCES

1. R. H. Wentorf, J. Chem. Phys. **26**, 956 (1957).
2. R. F. Davis, Proc. IEEE **79**, 702 (1991).
3. S. Strite and H. Morkoc, J. Vac. Sci. Technol. B **10**, 1237 (1992).
4. M. Mieno, T. Yoshida, and K. Akashi, J. Japan Inst. Metals **52**, 199 (1988).
5. M. Mieno and T. Yoshida, Surface and Coatings Technol. **52**, 87 (1992).
6. T. Wada and N. Yamashita, J. Vac. Sci. Technol. A **10**, 515 (1992).
7. N. Tanabe, T. Hayashi, and M. Iwaki, Diamond and Related Materials **1**, 883 (1992).
8. A. K. Ballal, L. Salamanca-Riba, G. L. Doll, C. A. Taylor and R. Clarke, J. Mater. Res. **7**, 1618 (1992).
9. D. J. Kester, K. S. Ailey, R. F. Davis, and K. L. More, J. Mater. Res. **8**, 1213 (1993).
10. A. Weber, *et al.*, J. Phys. III (Paris) **2**, 1931 (1992).
11. A. Ishizaka and Y. Shiraki, J. Electrochem. Soc. **133**, 666 (1986).
12. D. Kester and R. Messier, Mat. Res. Soc. Symp. Proc. **235**, 721 (1992); J. Appl. Phys. **72**, 504 (1992).
13. W. Wu and S. Fahy, Phys. Rev. B **49**, 3030 (1994).
14. The 100 eV energy range assumes that the incident ion will recoil from the lattice upon collision, transfering approximately 50% of its kinetic energy.
15. C. D. Clark and E. W. J. Mitchell, Institute of Physics Conference Series, Dubrovnik Conference "Radiation Effects in Semiconductors", p.45 (Institute of Physics, London, 1977).

INITIAL STAGES OF GROWTH OF THIN FILMS OF III-V NITRIDES AND SILICON CARBIDE POLYTYPES BY MOLECULAR BEAM EPITAXY

Robert F. Davis, K. S. Ailey, R. S. Kern, D. J. Kester, Z. Sitar, L. Smith, S. Tanaka and C. Wang, North Carolina State University, Department of Materials Science and Engineering, Box 7907, Raleigh, NC 27695-7907, USA

ABSTRACT

The morphology and interface chemistry occurring during the initial deposition of BN, AlN and GaN films via metal evaporation and N_2 decomposition under UHV conditions have been determined. FTIR spectroscopy and TEM revealed the consecutive deposition of an initial 20Å layer of a-BN, 20-60Å of oriented h-BN, and a final layer of polycrystalline c-BN. This sequence is attributed primarily to increasing intrinsic compressive stress in the films. XPS analysis revealed the growth of GaN on sapphire to occur via the Stranski-Krastanov mode; growth on SiC showed characteristics of three-dimensional growth. AlN grew layer-by-layer on both substrates. Vicinal 6H-SiC(0001) substrate surfaces contain closely spaced, single bilayer steps. During deposition of Si and C at 1050°C, 6H layers initially form and step bunching occurs. The latter phenomenon results in more widely spaced steps, the nucleation of 3C-SiC both on the new terraces and at the larger steps and formation of double position boundaries. The C/Si ratio in the gaseous reactants also affects the occurrence of these three phenomena.

INTRODUCTION

Boron nitride, like C, forms in three crystalline structures: layered hexagonal (h-); zincblende (c-); and wurtzite (w-), which are analogous to graphite, diamond and Lonsdaleite, respectively. The interest in c-BN films stems from their potential applications as hard coatings and from their electronic and thermal properties. Unlike diamond, c-BN does not react with ferrous metals, and it can be used at higher temperatures before the onset of structural transformation to h-BN. These properties make it an excellent cutting tool material. Electronic applications of c-BN would take advantage of its very wide band gap ($E_g \approx 6.4$ eV) [1], its ability to be doped both p-type(Be) and n-type(Si) [2], and its very high thermal conductivity.

Several groups have successfully grown c-BN using various techniques including ion beam assisted deposition [3–5], r.f. sputtering [6], ion plating [7], laser ablation [8,9], ECR plasma [10] and chemical vapor deposition (CVD) [11]. Cracking and loss of adhesion of deposited c-BN films are frequently reported phenomena, which have been attributed to a high level of intrinsic compressive stress in the films.[12,13] However, recent research strongly indicates that a high stress level in the film is a necessary condition for the formation of the cubic phase [13,14].

An area of research where significant progress has been made is in determining the deposition conditions necessary for c-BN growth. The work of Kester and Messier [15] established that for a given substrate temperature, the momentum transferred into the growing film by the bombarding ions is the single parameter which controls the formation of c-BN. As long as sufficient N is present, a threshold value of momentum transfer exists for the formation of c-BN. This controlling parameter incorporates the values of ion energy, ion flux, and ion species. As a result of the present study described below, a better understanding of both the conditions required for c-BN growth and of the mechanisms responsible for that growth have been developed.

Successful commercialization of infrared and selected visible light-emitting optoelectronic devices simultaneously stimulated research in the wide-band gap semiconductors for similar devices operable in the blue and ultra-violet regions of the spectrum. Much attention has been given to GaN and AlN, since they form a continuous range of solid solutions [16–18] which possess direct bandgaps from 3.45 to 6.28 eV, respectively.

Bulk single crystals of these nitrides are not available, thus films must be grown heteroepitaxially. Sapphire remains the most commonly used substrate, despite its huge lattice mismatch. A variety of other substrates including α-SiC, β-SiC, GaAs, ZnO, MgO, and Si have been employed. The research reported below has been concerned with the mode of epitaxial

Mat. Res. Soc. Symp. Proc. Vol. 339. ©1994 Materials Research Society

growth and interface chemistry of AlN and GaN on sapphire and 6H-SiC via gas source molecular beam epitaxy (GSMBE) and investigated using X-ray photoelectron Spectroscopy. Epitaxial growth is normally divided into three thermodynamically-controlled modes. In two-dimensional layer-by-layer or Frank-van der Merwe (F-M) growth, material initially forms a complete monolayer on the substrate and subsequently grows in sequential monolayers. In the second mode, the overgrowth nucleates at random positions on the surface, or at favorable surface sites produced by different defects. Stable nuclei then grow three dimensionally in all directions. They may subsequently coalesce and form a continuous film, with or without orientational coherence between individual surface crystallites. This growth mode is known as the three-dimensional or Volmer-Weber (V-W) mode. The third or Stranski-Krastanov (S-K) mode can be viewed as a composite of the previous two. Firstly, one or a few monolayers completely covers the substrate. Subsequent growth occurs via random nucleation and V-W growth.

Silicon carbide exhibits polytypism, a one-dimensional polymorphism derived from the many possible stacking sequences of the Si/C bilayers along the closest packed direction. The lone cubic polytype, β-SiC, crystallizes in the zincblende structure and is also referred to as 3C-SiC. There are also approximately 250 other rhombohedral and hexagonal polytypes that are collectively known as α-SiC. The most common of the α-SiC polytypes is 6H-SiC, where the 6 refers to the number of Si/C bilayers along the closest packed direction in the unit cell and the H indicates the hexagonal nature of the unit cell. The 4-H polytype has also recently become commercially available. The 3C, 4H and 6H materials are presently undergoing a significant revival in interest for microelectronic and optoelectronic applications because of the high breakdown electric fields ((2.5-3.0) x 10^6 V/cm), high thermal conductivity (3.9 W/cm°C), high saturated drift velocity (2-3 x 10^7 m/s) and reasonable low field electron mobility at room temperature (300 - 1000 $cm^2/V/s$). Most SiC films are currently deposited via CVD on 6H wafers at temperatures exceeding 1500°C. However, because of the interest in the controlled deposition of different polytypes and the fabrication of heterostructures with hyper-abrupt junctions and closely controlled solid solution compositions with, e.g., AlN, MBE has been employed in our laboratories to investigate the achievement of these goals. The results to date regarding the first objective are presented below.

The following sections describe the procedures used to deposit and analyze these several materials as well as detail the results and conclusions of this research.

EXPERIMENTAL PROCEDURES

Boron nitride

Ion beam assisted deposition involving electron beam evaporation of B with simultaneous bombardment by nitrogen and argon ions from a Kaufman source was used for the growth of BN films. The substrates were infrared-transparent, high resistivity (ρ>50 Ω-cm) on-axis Si(100) wafers and cut and polished natural diamond(100). The Si substrates were cleaned using a standard RCA procedure[19]. The final step was a 5 min dip in 10% HF. The surface was H terminated, as determined by XPS. The diamond substrates were etched in a boiling 3:4:1 H_2SO_4:HNO_3:$HClO_4$ solution for 45 minutes to remove any graphitic phase. These substrates were subsequently loaded through a vacuum lock into the UHV deposition chamber. Base pressures in the chamber were typically 5-8 x 10^{-10} Torr.

Each substrate was heated under UHV conditions at 700°C for 20 min to remove residual H_2O and hydrocarbon species. Boron was deposited using a rate of 0.5 Å/s. The Ar/N_2 flow ratio through the ion gun was 1:1. The ionization potentials of these two gases are similar; thus, the ion ratio was also close to 1:1. The ion source was operated at 500 eV; based on the studies of Van Vechten et al.[20], the N ions were predominantly N_2^+. The discharge voltage of this source was maintained at a sufficiently low value to prevent double ionization of either species. Both the ion beam and the boron evaporation were started and allowed to stabilize before deposition. During this period, the substrate was covered by a movable shutter. To eliminate the potential for surface damage, there was no pre-deposition ion bombardment of the substrates. The ion current densities for the deposition on Si ranged from 0.20 to 0.30 mA/cm^2; 0.24 mA/cm^2 was employed for growth on diamond. The temperature of the Si wafers ranged from 400 to 700°C; the diamond substrates were heated at 400 and 600°C.

Fourier transform infrared spectroscopy (FTIR) was the primary method of characterization due to the ability to distinguish between the cubic and hexagonal or amorphous forms of BN. Cubic BN has a transverse optical mode absorption peak at 1075 cm^{-1}; amorphous and hexagonal BN have a primary absorption peak at 1367 cm^{-1} and a secondary peak at 783 cm^{-1} [21, 22]. The film crystallography and the film-substrate interface were studied via high resolution cross sectional transmission electron microscopy (HRTEM) using a JEOL 4000EX operated at 400kV. The images were recorded using a 1 mr convergence semi-angle at a Scherzer defocus of ≈47nm.

Aluminum and gallium nitrides

A Perkin-Elmer 430 MBE containing standard effusion cells for the evaporation of Ga and Al and an ECR microwave plasma source operated at 50 W to activate/dissociate ultra-high-purity N_2 was used to deposit AlN and GaN on polished wafers of (6H)-SiC(0001) and sapphire(0001). These substrates were heated in UHV to 700°C for 30 min. They were subsequently transferred *in vacuo* to the analytical chamber and examined via XPS for surface contamination. The intensities and shapes of several characteristic peaks were also measured and later used as references. Prior to growth, the substrates were heated to the 600°C deposition temperature and subsequently exposed to a flux of activated nitrogen species. An 0.5 - 1 monolayer layer of GaN or AIN was then deposited and the samples transferred to the analytical chamber. These steps were repeated until a total of 5–12 monolayers were grown.

For the study of AIN growth, Mg Ka X-rays (1253.6 eV) were used; for GaN growth, both Mg and Al (1486.6 eV) anodes were employed. Both X ray sources was required for the GaN because of the overlap of important photoelectron peaks by the intense Ga LMM Auger electron emission. The Mg anode was used for examining the O_{1s} and N_{1s} photopeaks, while the Al anode was used for examining the C_{1s}, Si_{2s}, Al_{2p} and Ga_{3d} peaks. For GaN, the Si_{2s} photopeak at 153 eV was used, rather than the more commonly used Si_{2p} peak. The Ga_{3p} peak at 107 eV lies very close to the Si_{2p} peak at 103 eV and overwhelms the emission of the latter, as the Ga signal increases with the thickness of GaN film. The Si_{2s} peak is also near the Ga_{3s} at 160 eV but is located farther from the nearby Ga peak than the Si_{2p} peak is from its Ga neighbor.

Silicon carbide

Silicon carbide monolayers were deposited on the Si(0001) face of 6H-SiC wafers via gas source MBE in the temperature range of 950-1150°C using C_2H_4/Si_2H_6 rates(sccm) and ratios of 0.3/0.3 - 1.0/0.1. All substrates were chemically cleaned in 10% HF for five minutes prior to loading. The RHEED pattern of the cleaned substrate was 1 x 1. The samples were subsequently annealed in vacuum at 1050°C for 30 minutes to remove the residual silicon dioxide and hydrocarbon species; the RHEED pattern remained 1 x 1. Transmission electron microscopy was employed to determine the nature of the steps and terraces on the 6H-SiC surface as a result of degree of off-axis preparation and heating.

RESULTS AND DISCUSSION

Boron nitride

The FTIR spectra for films deposited on Si(100) under identical conditions except for growth time are shown in Fig. 1. The relative amount(s) of non-cubic phase(s) was high for very thin films (<200Å). As the deposition time and resulting thickness increased, the relative percentage of the cubic phase increased. All FTIR spectra reported in the literature and containing c-BN have also indicated the presence of some non-cubic phase(s). Several explanations for this phenomenon can be postulated: (1) the occurrence of the non cubic phase(s) on the grain boundaries within the c-BN matrix; (2) separate h-BN or a-BN micro-regions distributed throughout the films; and (3) a layered sequence of these various phases. The increase in the concentration of c-BN with thickness observed in the present study would favor the layered sequence. To test this hypothesis cross-

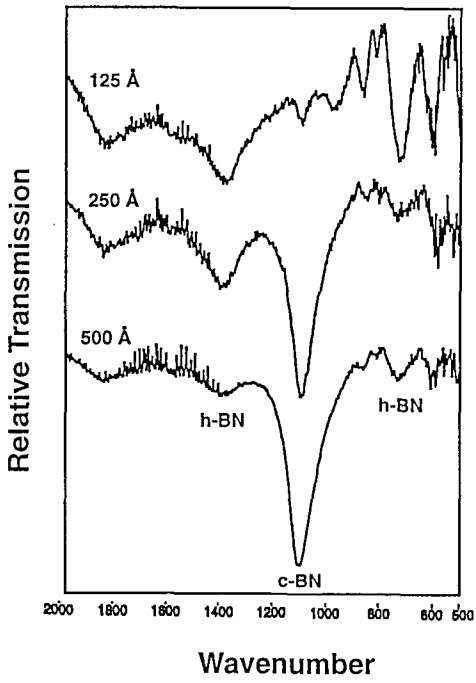

Figure 1. FTIR spectra of BN films of various thicknesses deposited on Si(100) substrates under the following conditions: boron deposition rate: 0.26 Å/s; ion energy: 500eV; ion flux density: O.5mA/cm^2; ion bombardment by 50:50 Ar:N_2; substrate temperature: 400°C.

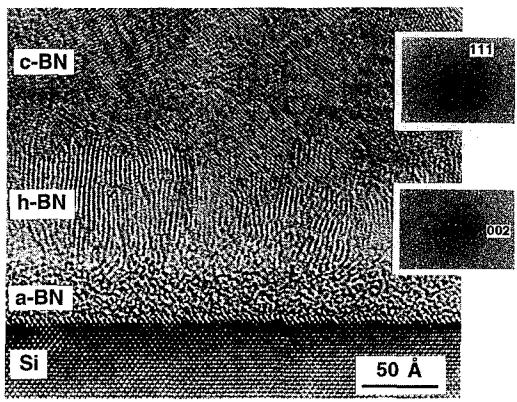

Figure 2. Cross-sectional HRTEM image of BN film deposited under the same conditions as noted in Figure 1 and showing the Si substrate and regions of amorphous BN (a-BN), hexagonal BN (h-BN), and cubic BN (c-BN).

sectional HRTEM images were obtained, an example of which is shown in Fig. 2 for deposition at 400°C. The images supported the hypothesis in that they revealed the sequential deposition of three distinct regions: an initial layer of ≈20 Å of a-BN at the Si (100) interface, a layer of 20-60 Å of h-BN, and a top layer of polycrystalline c-BN. The c-axis of the h-BN was oriented parallel to the Si (100) surface; however, it was oriented randomly around this axis. An optical diffraction pattern was obtained by performing a fast Fourier transform on the HRTEM image to obtain the diffraction information shown. The lattice spacings for the top layer matched that of c-BN, while those within the middle layer matched that of hBN. These images also showed that the c-BN is single phase and that it grows without further transformation, at least to the maximum layer thickness deposited to date (~1000Å). To study the effect of substrate temperature on the nature of 150Å thick BN films, depositions were conducted from 200–700°C. No other variables were changed. The results of one of these series of depositions are shown in Fig. 3. Within the range of 200–400°C, the films were a mixture of the cubic and the hexagonal/amorphous phases. The relative amount of cubic phase increased with increasing temperature. Above 400°C, the amount of c-BN dropped rapidly; it was not observed in the films deposited at 600 and 700°C.

The thickness of the films deposited on diamond(100) were 1000 Å. A sharp c-BN peak was observed at ≈1080 cm^{-1}. The h (or a-)-BN peak was very small. The spectrum of this relatively thick film had a sharper c-BN peak and a better c-BN/h-BN ratio than any of the films deposited on Si. For the film grown at 600°C, the FTIR spectrum was essentially the same.

A second significant parameter investigated was the ion flux which has a linear relationship to the momentum transferred to the growing film. The FTIR spectra of Fig. 4 shows that at 600°C, only a small concentration of the cubic phase is observed until the flux reaches 30 mA. This confirms that there is a minimum momentum transfer level, and therefore ion flux, necessary to grow the cubic phase at a given temperature.

To understand why the sequence of BN phases occurs, it is necessary to examine the nature of the substrate/film interface and the gradual changes in stress which occur within the growing film. The two primary factors which control whether a given bulk inorganic solid can be produced in an amorphous form are chemical composition and cooling rate from the melt. Additional factors such as surface roughening [23] and residual stress may result in the deposition of an amorphous films. It may be argued that the significant differences between lattice parameter and crystal structure between Si and h-BN and c-BN prevent the formation of either phase directly on this substrate. However, a-BN also deposits on diamond(100) under the same conditions with approximately the same thickness, and the lattice parameters of this substrate and c-BN are very close. Thus, it may be postulated that it is the cooling rate of the deposited atoms which controls both the formation and the extent of the a-BN phase. This cooling rate is controlled initially by the substrate temperature and subsequently by the thermal conductivity of the a-BN layer. McKenzie, et al. [24] and Cuomo, et al. [25] have shown that substrate temperature has an important effect of the nature of the amorphous C film which deposits during ion assisted deposition. At high (including room) temperatures a predominantly sp^2 bonded glassy film results; as the temperature is lowered, a predominantly sp^3 material emerges. As the thermal conductivity of the amorphous binary BN phase is lower than either the Si or diamond substrates, its occurrence as a series component in the thermal circuit quickly becomes the controlling factor in the conduction of heat away from the interface.

The essentially identical FTIR spectra of a- and h-BN indicate that they are closely related by bonding and, perhaps, to some extent by structure. Thus it may also be postulated that the small amount of residual stress produced during the initial deposition results in a very thin, randomly oriented h-BN layer. This increasing stress is partially relieved by the formation of the preferentially oriented crystalline h-BN phase which subsequently forms. McKenzie et al. [12,13] have presented a thermodynamic argument based on the Gibbs free energy function in which a biaxial stress term has been included which explains the orientation dependence of the h-BN. A substantial reduction in free energy occurs when the c-axis of the h-BN lies in the plane of the stress field. However, the stress in the growing film continues to increase primarily via ion bombardment and the consequent defect creation on the BN lattice and incorporation of Ar and excess N_2. This eventually takes the film beyond the P-T threshold where c-BN becomes the stable phase.

Figure 3 indicates that increasing the substrate temperature above 400°C slows the rate of residual stress generation via increased surface mobilily of the deposited species and therefore

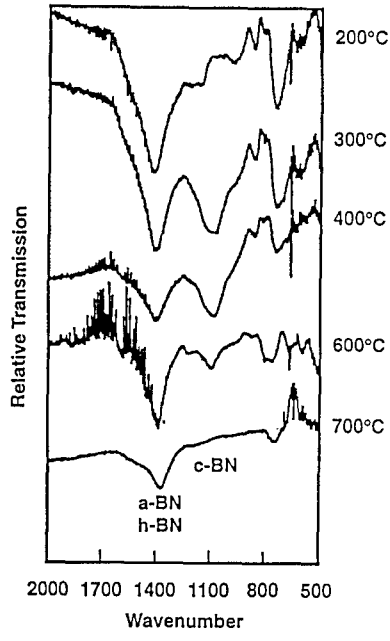

Figure 3. FTIR spectra of BN films deposited at various substrate temperatures on Si(100) under the following conditions: film thickness: 200 Å; ion flux density: 0.32 mA/cm^2; B deposition rate: 0.5 Å/s; ion energy: 500 eV; ion bombardment by 50:50 Ar:N_2.

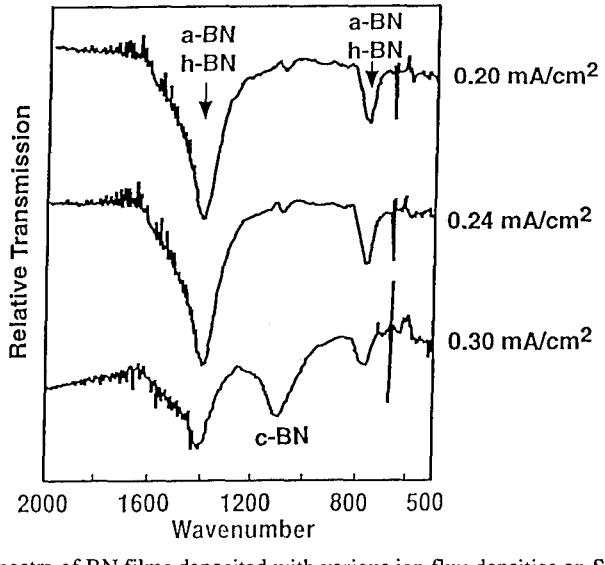

Figure 4. FTIR spectra of BN films deposited with various ion flux densities on Si(100) substrates at 600°C under the following conditions: film thickness: 250Å; boron deposition rate: 0.5 Å/s; ion energy: 500 eV; ion bombardment by 50:50 Ar:N_2.

relaxation of the surface, reduction in both lattice defects and the incorporation of gas molecules and possibly some bulk annealing. By contrast, an increase in ion momentum results in a more rapid increasing stress which negates the effect of increased temperature, as shown in Fig. 4.

Aluminum and gallium nitrides

The initial Si_{2p} signal, in the sequence of peaks acquired between deposition steps during the growth of AlN on α(6H)-SiC, from the bare substrate was a peak characteristic of clean SiC with only slight asymmetry due to spin-orbit splitting. With the first AlN growth step, significant shouldering of the peak appeared on the high binding energy side, indicating the presence of a more oxidized state of silicon. This shoulder persisted throughout the film deposition process and remained as the SiC component and the overall Si intensity diminished with film growth. A Gaussian curve fitting algorithm using chi-square minimization was applied to the most intense shouldered peak, obtained after the first growth step, to resolve the position of the high binding energy component. The results of curve fitting are shown in Figure 5. The Gaussian fit closely matched most of the peak except for exponential tailing on the low binding energy side. The high binding energy shouldering was found to be primarily due to a single component shifted 1.4 eV from the main SiC peak. This component has been attributed to the formation of silicon nitride during the initial stages of AlN growth. This behavior shows that the Si-face of SiC initially undergoes nitridation.

The peak areas were measured for the growth on both substrates and the relative peak intensities calculated. Figure 6 shows the change in XPS peak intensities of the substrate components during the growth of AlN on α-SiC and sapphire. Theoretical curves representing layer-by-layer growth and calculated for two escape depths, namely, 18 Å (C_{1S},Si_{2S}) and 12 Å (O_{1S}), are shown for comparison. These two curves correspond to the growth on SiC and sapphire, respectively.

The experimental data matched the corresponding theoretical curves very closely, with progressively better fit to the theoretical curves as the AlN thickness increased. From this dependence, AlN appeared to grow two-dimensionally on both substrates. This is in agreement with several reports, which indicate that the morphology of GaN films is affected beneficially when they are grown on an AlN buffer layer previously deposited on the sapphire substrate.

A similar conclusion regarding initial silicon nitride formation could not be made for the growth of GaN on SiC, although there is little reason to expect that in this case a completely different chemistry occurred at the interface. However, the shouldering effect was not apparent due to a poorer signal-to-noise ratio. The close proximity of the Ga_{3s} peak on the high energy side could have obscured the evidence of the silicon nitride formation as well.

Figure 7 shows a plot of relative peak intensities of the substrate components vs. film thickness. The plots show that the substrate peak intensity diminished faster initially for the growth of GaN on SiC than on sapphire (compare O_{1s} to C_{1s} and Si_{2p} signals). This is most likely due to a faster initial nucleation process on SiC, as well as due to the formation of a thin silicon nitride layer at the interface. The O_{1s} signal also decreased rapidly, once initial nucleation occurred, and with the same slope as the Si_{2p} and C_{1s} signals at the very beginning of the growth. Furthermore, an earlier study in the authors' laboratory of the growth rate of GaN on different substrates did not indicate a substantial difference between the growth rates on SiC and sapphire within experimental conditions. The growth rate was controlled by the Ga arrival rate rather than by any other factors. Similar behavior for the change in the intensity of the Si_{2S} and C_{1s} photoemission was anticipated, since they both originated from the same SiC substrate. However, this was not observed. As shown in Figure 7, the C_{1s} peak intensity shows a faster initial drop and also saturates at a lower value. This can also be explained by the formation of a thin layer of silicon nitride. Since the Si-face of the SiC substrates was used, a silicon nitride layer formed on the surface during exposure to the reactive nitrogen species prior to film deposition. This resulted in burying the C layer more deeply under the Si. The difference in the initial intensity drop approximately corresponds to the formation of one monolayer of silicon nitride.

All three curves assumed a more gradual behavior after the initial rapid drop. The slopes of the C_{1s} and Si_{2S} signals in this region were considerably lower than the slope of the corresponding theoretical curve, which indicates an early saturation, while the slope of the O_{1s} signal exhibits a closer match to its theoretical curve. However, none of the experimental curves resembled the

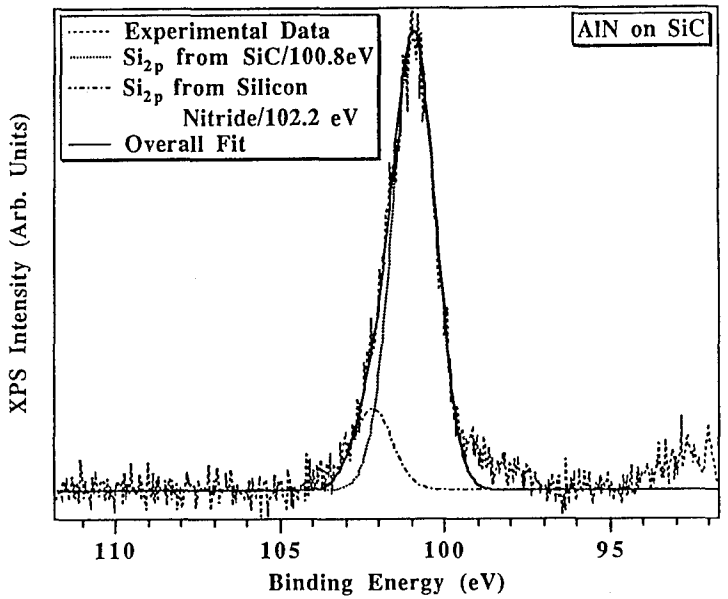

Figure 5. Gaussian curve fit of Si2p photoemission from AlN deposited on α(6H)-SiC showing component atributed to silicon nitride shifted 1.4 eV from SiC peak.

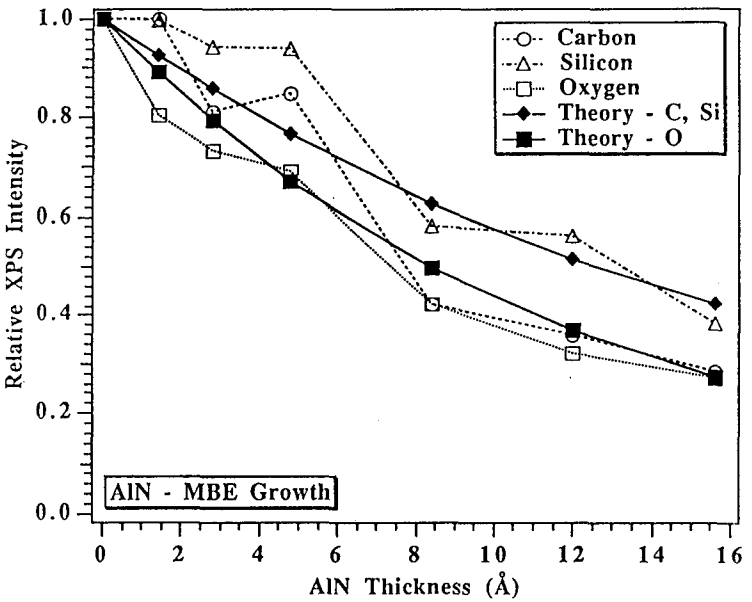

Figure 6. Change of XPS photoelectron intensity during growth of AlN on α(6H)-SiC and sapphire.

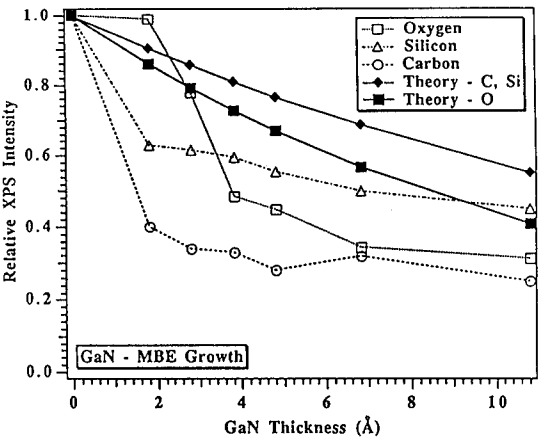

Figure 7. Change of XPS photoelectron intensity during growth of GaN on α(6H)-SiC and sapphire.

corresponding calculated curves for layer-by-layer growth. The early saturation in both cases indicated island formation at some stage in the growth process. As such, the growth of GaN on (0001) α-SiC and sapphire appears to follow the Stranski-Krastanov mode.

Silicon carbide

The chemically cleaned surface of the off-axis SiC samples cut 3.5° toward [11$\bar{2}$0] showed a continuous series of periodically and closely spaced single Si/C bilayer steps, the collection of which sloped downward along the surface when observed along the [1$\bar{1}$00] zone axis. By contrast very few steps were observed in the on-axis material; they were also single steps but which oscillated up an down across the surface. Heating both samples to 1200°C for 30 minutes did not result in any observable change in the nature of these surface microstructures.

Deposition on the off-axis material at 950, 1050 and 1150°C using a C_2H_4/Si_2H_6 flow ratio of 0.2/0.1 resulted in the initial growth of a 1-2 unit cells of 6H-SiC via step flow. Evidence that step bunching occurred is shown in Fig. 8 which shows that the single step planes of the as-received material have migrated to become collections of steps having approximately 1-3 unit cell heights (6-18 bilayers) which are now further displaced from each other than the single bilayer steps noted above. According to the theory of Heine and coworkers [26], the internal energy of the 6H structure undergoes a larger reduction if atoms deposit such as to extend the A-plane. Thus initial deposition in our experiments may have occurred primarily on the B and C planes such as to extend the 6H structure. The higher the temperature of deposition, the more rapid movement of atoms on the surface, the greater the extension of the B and C planes and the more widely spaced the steps and the wider the terraces. At some point, the distance between steps becomes sufficiently large that the kinetics of surface migration do not allow the depositing atoms to reach the steps in sufficient numbers to continue the step flow growth of 6H. At this point β-SiC is nucleated on the terraces. Evidence for this theory is shown in Fig. 8 which shows that the distance between the islands of 3C increased as the temperature of the deposition was increased.

On the basis of the films obtained at three different temperatures and the determination of the mean growth rate of each 3C component of the film, the activation energy was calculated to be 0.4 eV. This may be indicative of a surface-diffusion controlled process.

As noted and shown above, the use of a flow rate ratio of 0.2/0.1 resulted in the deposition of 6H followed by 3C on the off-axis films. Increasing this ratio to 1.0/0.1 at 1050°C resulted in an insignificant amount of deposition (a much reduced growth rate--only a few islands of 3C were

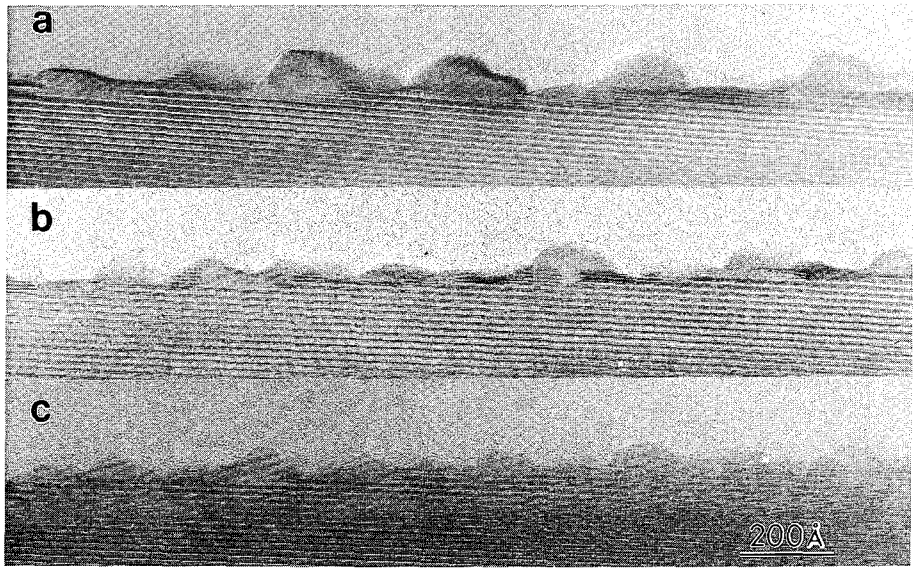

Figure 8. TEM micrographs showing the initial stage of 3C-SiC growth on 6H-SiC substrates at 950, 1050 and 1150°C. Note the step bunching in proximity to each 3C island.

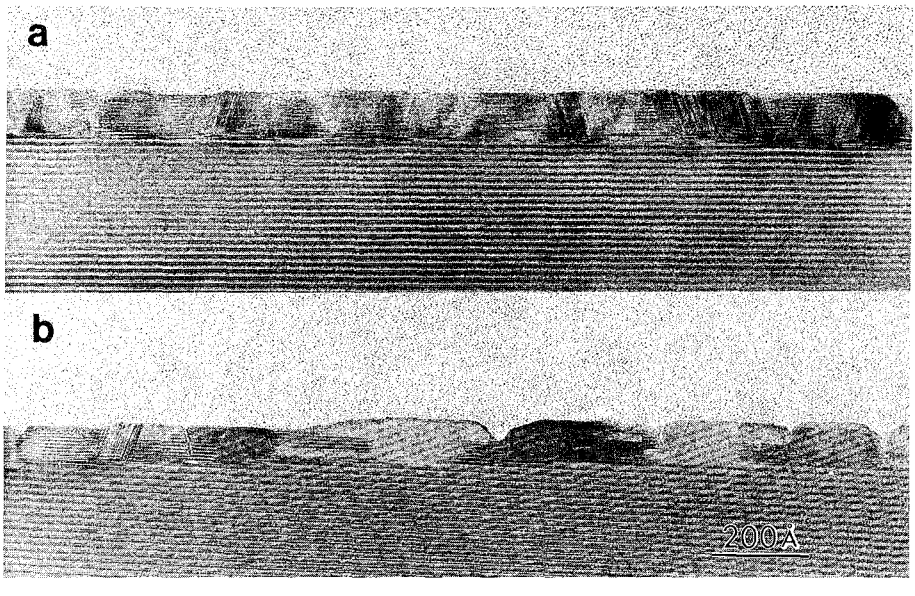

Figure 9. TEM micrographs showing that a larger density of islands have coalesced on the on-axis 6H-SiC substrate than on the off-axis. Note the presence of double positioning boundaries at the steps in the off-axis substrate.

observed). Increasing the flow rate ratio to 0.1/0.1 on off-axis materials at 1050°C resulted in the deposition of only 6H. Step bunching and the simultaneous extension of the terrace distance continued to occur during this deposition. Thus the absence of the 3C phase must be explained by reasons other than kinetic. The increased terrace width is strong evidence for step flow growth. Under these conditions, the as-received substrate immediately reconstructed, as shown by the change in the RHEED pattern from (1x1) to (3x3). Kaplan[27] has proposed a model for this reconstruction which consists of an adsorbed Si bilayer. If true, our results indicate that the energy of the growing surface is reduced due to this reconstruction and that the surface mobilities of adatoms are enhanced on such a reconstructed surface, leading to step flow growth over a much larger period of time.

Using a combination of initially high (0.2/0.1) (for 30 min) and subsequently lower (0.3/0.3) (for 60 min) C/Si ratios to deposit SiC films revealed that on the off-axis material, 6H was again formed initially with the concomitant step-bunching followed by the nucleation of the 3C phase on the terraces. Most of the time of deposition in the off-axis material was expended in step bunching rather than 3C nucleation. Thus, the density of nuclei on these off-axis planes should be lower or much lower than on the on-axis plane where step bunching does not occur. As such the size of the islands at the time of coalescence with adjacent islands on the off-axis material should be notably larger than on the on-axis material. This phenomenon is shown in Fig. 9. In Fig 9(a), the concentration of nuclei is very large; however, changing to a 1/1 C/Si ratio allows for step flow growth to now occur for the reasons noted above. In the off-axis material, the islands continued to grow under the influence of the high C/Si ratio. However changing to the 1/1 ratio resulted in a change to either layer-by-layer or step flow growth of 3C-SiC from the islands such that they meet and form double position boundaries. Step flow is believed to become the growth mode for these 3C films as shown by the increasing smoothness of the off-axis film--it is essentially becoming very similar in surface character as the on-axis films.

SUMMARY

Single phase c-BN has been achieved as the last stage in a sequential deposition involving layers of a-BN and h-BN produced by IBAD on Si(100) and diamond(100) substrates. The a-BN is believed to result from the rapid cooling of the depositing species, though stress-related phenomena cannot be ruled out. The c-axis of the h-BN is preferentially oriented perpendicular to the growth direction to relieve the increasing residual stress produced by lattice defect formation and gas incorporation. The equilibrium P-T threshold for the formation of c-BN is eventually exceeded, and this phase grows without further transformation. Raising the temperature results in surface and possibly bulk annealing and a significant delay in the formation of the c-BN. Increasing the ion momentum tends to cancel the effect of increased temperature.

Sequential gas source MBE and XPS have been employed to determine the mode of initial growth of GaN and AlN on α(6H)-SiC(0001) and sapphire(0001) substrates. Evidence for silicon nitride formation on the SiC substrates was obtained. No significant chemical changes at the interface were observed when films were grown on sapphire. The growth of GaN on sapphire appeared to occur via the Stranski-Krastanov mode. The growth on SiC showed characteristics of three-dimensional growth. At present, it is unclear whether or not this latter result was due to formation of the thin interfacial layer of silicon nitride. The growth of AlN on both substrates showed a better initial morphology and appeared to grow layer-by-layer within the thickness range of the deposited film.

The as-received wafer of vicinal α(6H)-SiC(0001) contains a series of closely spaced single bilayer steps which do not move after heating to 1200°C for at least an hour. The distance between steps increases as the degree of off-axis decreases. Deposition on the vicinal surface with C_2H_4/Si_2H_6 >1.0 results in the initial growth of a few monolayers of 6H-SiC with the concomitant action of step bunching . The latter process moves the steps apart such that the kinetics of atom motion become unfavorable to step flow growth and nucleation of 3C-SiC occurs on the terraces. This phase grows and coalesces, often at the steps where double position boundaries are often produced. Increasing the temperature causes more rapid step-bunching. With the C_2H_4/Si_2H_6 =1.0 the only phase which deposits is α-SiC.

ACKNOWLEDGEMENTS

This research was sponsored in part by SDIO/IST and managed by ONR under contracts N00014-92-J-1720 (BN) and N00014-92-J-1720 (AlN and GaN); by Kobe Steel, Ltd. (BN); and ONR under contract N00014-92-J-1500 (SiC). A portion of the BN TEM research was supported by the U. S. Dept. of Energy, Assistant Secretary for Energy Efficiency and Renewable Energy, Office of Transportation Technologies as part of the HTML user program, contract DE-AC05-840R21400, managed by Martin Marietta Energy Systems, Inc. The authors also express their appreciation to Cree Research, Inc. for the SiC wafers, to Professor D. R. McKenzie of the University of Sydney and to L. S. Porter, M. J. Paisley and R. C. Glass of NCSU for helpful discussion.

REFERENCES

1. L. Vel, G. Demazeau and J. Etourneau, Materials Science and Engineering B10, 149 (1991)
2. K. Era, O. Mishima, Y. Wada, J. Tanaka and S. Yamaoka in Electroluminescence, edited by Shionoya and H. Kobayashi, Springer Proceedings in Physics Vol. 38 (Springer-Verlag, Berlin, 1989), p. 386.
3. K. Inagawa, K. Watanabe, H. Ohsone, K. Saitoh, and A. Itoh, J. Vac. Sci. Technol. A5, 2696 (1987).
4. D. J. Kester and R. Messier, in Phase Formation and Modification by Beam-Solid Interactions, edited by G. S. Was, L. E. Rehn and D. Follstaedt (Mater. Res. Soc. Proc. 235, Pittsburgh, PA, 1992) 721.
5. T. Wada and N. Yamashita, J. Vac. Soc. Technol. A10, 515 (1992).
6. K. Bewilogua, J. Buth, H. Hübsch, and M. Grischke, Diamond and Related Mater. 2, 1206 (1993).
7. M. Murakawa, S. Watanabe and S. Miyake, Diamond Films and Technol. 1, 55 (1991).
8. G. L. Doll, J. A. Sell, C. A. Taylor II, and R. Clarke, Phys. Rev. B 43, 6816 (1991).
9. T. A. Friedmann, K. F. McCarty and E. J. Klaus, App. Phys. Letts 61, 2406 (1992).
10. Y. Osaka, M. Okamoto and Y. Utsumi, in Low Energy Ion Beam and Plasma Modification of Materials, edited by J. M. E. Harper, K. Miyake, J. R. McNeil and S. M. Gobatkin (Mater. Res. Soc. Proc. 223, Pittsburgh, PA, 1991) 81.
11. H. Saitoh and W. Yarborough, App. Phys. Lett. 58, 2228 (1991).
12. D. R. McKenzie, W. D. McFall, W. G. Sainty, C. A. Davis and R. E. Collins, Dia. Rel. Mater. 2, 970 (1993).
13. D. R. McKenzie, J. Vac. Sci. Technol. B11, 1928 (1993).
14. D. J. Kester, K. S. Ailey, R. F. Davis and K. L. More, J. Mater. Res. 8, 1213 (1993).
15. D. J. Kester and R. Messier, J. Appl. Phys. 72, 504 (1992).
16. S. Yoshida, S. Misawa and S. Gonda, J. Appl. Phys. 53, 5844 (1982).
17. M. R. H. Khan, Y. Koide, H. Itoh, N. Sawaki and I. Akasaki, Solid State Comm. 60, 509 (1986).
18. Y. Koide, H. Itoh, M. R. H. Khan, K. Hiramatsu, N. Sawaki and I. Akasaki, J. Appl. Phys. 61, 4540 (1987).
19. W. Kern and D. A. Puo-tinen, RCA Rev. 31,187 (1970).
20. D. Van Vechten, G. K. Hubler and E. P. Donovan, Vacuum 36, 841 (1986).
21. R. Geick and C. H. Perry, Phys. Rev. 146, 543 (1966).
22. P. J. Gielisse, S. S. Mitra, J. N. Plendl, R. D. Griffis, L. C. Mansur, R. Marshall and E. A. Pascoe, Phys. Rev. 155, 1039 (1967).
23. D. Eaglesham, H.-J Gossman and M. Cerallo, J. Appl. Phys. 65, 1227 (1990).
24. D. R. McKenzie, D. A. Muller, E. Kravtchinskaia, D. Segal, D. J. H. Cockayne, G. Amaratunga and R. Silva, Thin Solid Films 206, 198 (1991).
25. J. J. Cuomo, J. P Doyle, J. Bruley and J. C. Liu, Appl. Phys. Lett. 58, 466 (1991).
26. V. Heine, C. Cheng and R. J. Needs, J. Am. Ceram. Soc. 74, 2630 (1991).
27. R. Kaplan, Surf. Sci. 215, 111 (1989).

STRUCTURAL STUDY OF SIC/AIN BILAYERS AND TRILAYERS ON SI AND 6H-SIC

D. PRASAD BEESABATHINA*, K. FEKADE**, K. WONGCHOTIGUL**
M.G. SPENCER**, AND L. SALAMANCA-RIBA*

* Department of Materials and Nuclear Engineering, University of Maryland, College Park, MD 20742.
** MSRCE, School of Engineering, Howard University, Washington DC 20059.

ABSTRACT

The growth morphology and microstructure of SiC/AlN/6H-SiC, SiC/AlN/SiC/Si, and SiC/AlN/Si heterostructures grown by LPCVD were studied using transmission electron microscopy. The SiC/AlN bilayers grown on 6H-SiC substrates were single crystalline and comprised of 3C-SiC and 2H-AlN. The epitaxial relationship between 2H-AlN and 6H-SiC is [0001]AlN//[0001]SiC. The SiC/AlN/SiC trilayers and the SiC/AlN bilayer grown on (001)Si were composed of 3C-SiC and 2H-AlN. However, the 2H-AlN layer was polycrystalline even though the (001)3C-SiC was single crystalline. The preferred orientation of the AlN layers in SiC/AlN/SiC/Si and SiC/AlN/Si are [0112] and [0002], respectively. The AlN/3C-SiC interface is relatively sharp compared to the AlN/Si interface in which an amorphous layer close to the interface was observed. In general, the polycrystalline AlN structure has two distinct layers: (1) nucleation layer and (2) bulk layer. High resolution lattice images of the polycrystalline AlN showed amorphous areas and small misoriented crystallites in the nucleation layer. The bulk layer consists of preferentially oriented large columnar grains.

INTRODUCTION

Wide band gap semiconductors such as SiC and AlN show great promise in electro-optical and high temperature applications [1-5]. AlN has a band gap of 6.28 eV and cubic 3C-SiC has a band gap of 2.28 eV. Thin films of AlN have potential use in optical and surface-acoustic-wave devices. The chemical and thermal stability as well as the high resistivity of AlN films make them suitable as insulating and passivating layers in semiconductor devices. The combination of excellent physical, thermal and electronic properties of cubic SiC have resulted in device applications involving high temperatures and high power. The synthesis and properties of these materials have been the subject of intense study due to their wide applicability. Remarkable progress in single crystal growth of 3C-SiC and 2H-AlN has been made in recent years. Thin films of AlN and SiC have been grown on several substrates. Successful growth of cubic SiC on Si and 6H-SiC has been reported [6,7]. Single crystalline AlN films have been deposited on (111)Si[8], SiC[9] and sapphire[10]. Recently, Rowland et al. [11] obtained single crystalline SiC/AlN multilayers using molecular beam epitaxy (MBE) technique. The electronic structure and bonding at the SiC/AlN interface have been calculated by Lambrecht et al.[12]. In this work, we present a study of the structure and growth morphology of individual layers in SiC/AlN/6H-SiC, SiC/AlN/SiC/Si, and SiC/AlN/Si heterostructures.

EXPERIMENTAL PROCEDURE

Layers of AlN and SiC were grown in a commercial, low pressure vertical chemical vapor deposition (CVD) reactor. The details of the SiC growth have been reported elsewhere[13]. The AlN films were grown on 6H-SiC(0001), 3C-SiC(100)/Si(100) and 2^{o} off-axis (100)Si substrates. The

Mat. Res. Soc. Symp. Proc. Vol. 339. ©1994 Materials Research Society

reactant gases used were SiH_4, C_3H_8, NH_3 and Trimethylaluminium (TMA). The AlN growth was performed at substrate temperatures of 1260-1300°C while the 3C-SiC growth was performed at temperatures of 1250-1350°C. Hydrogen was used as the carrier gas. The flow rate of SiH_4 was fixed at 10 sccm whereas the flow rate of C_3H_8 was fixed at 20 sccm. The TMA and NH_3 flow rates were fixed at 50 and 100 sccm, respectively. The system pressure was 10 Torr for all the growth process except for the growth of 3C-SiC film grown on Si in the 3C-SiC/AlN/3C-SiC/Si system. There was no interruption of the growth process until all layers were deposited. However, in the case of the SiC/AlN/SiC/Si the first layer of 3C-SiC film grown on Si substrates was deposited using a horizontal CVD reactor at a pressure of 200 Torr. The AlN and SiC layers grown on this 3C-SiC film were then deposited using the vertical reactor.

Cross-sectional transmission electron microscope (TEM) specimens were prepared by conventional mechanical thinning procedure to about 10 μm followed by Ar++ ion milling at 5 kV and 1 mA gun current to obtain perforation. Additional milling at 3 kV was performed for half an hour to remove any damage induced at the higher energy. TEM observations were made using a JEOL 2000 FX-II, and a Philips 400T electron microscopes operating at 200 KV, and 400 KV, respectively.

Results and Discussion

Figure 1 shows relatively low-magnification high resolution images of a) the AlN/6H-SiC and b) the 3C-SiC/AlN interfaces of a SiC/AlN/6H-SiC heterostructure. The corresponding selected area diffraction (SAD) patterns shown as insets reveal that both layers are single crystalline and composed of 2H-AlN and 3C-SiC. The AlN layer has uniform thickness and the AlN/6H-SiC interface is relatively sharp. The A1N layer has a thin nucleation or transition layer of ≈ 200 Å adjacent to the 6H-SiC as indicated by arrows in Fig 1(a). The 3C-SiC layer consists of large-faceted columnar grains with a high density of planar defects, especially near the interface (see Fig 1(b)). The lattice mismatch between 3C-SiC and 2H-AlN at room temperature is low (≈1%). However, the coefficients of thermal expansion α, of 3C-SiC at 300°K and 1000°K are $2.9X10^{-6}$ K^{-1} and $4.5X10^{-6}$ K^{-1}, respectively. In contrast, α of 2H-A1N remains approximately $4.5X10^{-6}$ K^{-1} in this temperature range [14]. Therefore, we attribute the high density of planar defects observed in the 3C-SiC layer to the large (≈30%) mismatch in α between these two materials. This is also consistent with the defect density variation from the interface (high density) to the film surface (low density). Also, the continuation of grain boundaries across this interface is clearly seen in Fig.1(b) and only one type of {111} planar defects exists in each grain. The epitaxial relationships obtained from the diffraction pattern of Fig. 1(b) are [0001]6H-SiC//[0001]2H-A1N and [0110]6H-SiC//[0110]2H-A1N.

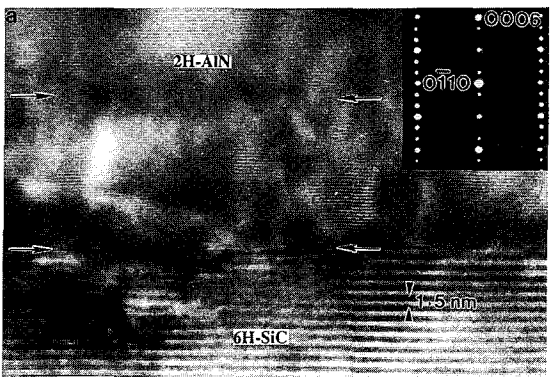

Fig. 1(a) Low magnification high-resolution image of 2H-AlN/6H-SiC interface of a SiC/AlN/6H-SiC structure. The nucleation layer is marked between arrows.

In the case of the 3C-SiC/2H-AlN interface, the orientation relationship is [111]3C-SiC // [0001]2H-AlN. Occasionally, grains with another {111} type of stacking faults as well as micro twins were observed in the 3C-SiC layer as shown in Fig. 2. However, the density of these planar defects is low compared to the planar defects lying parallel to the interface. Streaks observed in the diffraction pattern along [111] and 1/3[115] directions in Fig. 2 (indecated by arrow) are due to stacking faults on these planes. The (111) spot becomes the 1/3(115) (in terms of matrix reciprocal lattice) spot due to twinning. Figure 3 shows a cross-sectional high resolution lattice image of the 3C-SiC/Si interface of a SiC/AlN/SiC/Si multilayer structure. The corresponding SAD pattern is shown as inset.

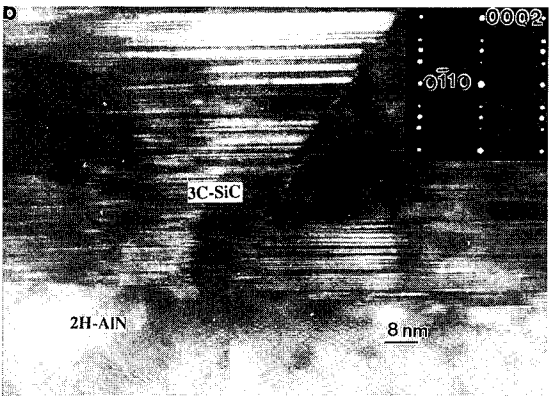

Fig. 1(b) low-magnification high-resolution image of 3C-SiC/2H-AlN interface of a SiC/AlN/6H-SiC structure. Note the high density of planar defects in 3C-SiC layer.

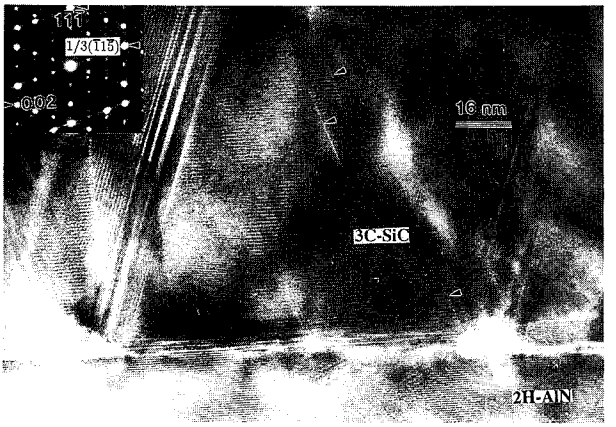

Fig. 2 Low-magnification high-resolution image of the 3C-SiC/2H-AlN interface region of a SiC /AlN/6H-SiC structure showing another type of {111} stacking faults.

Cubic SiC films have successfully been grown on (100)Si by several groups [15,16]. The epitaxial relationships between cubic SiC and Si are [001]SiC//[001]Si, [111]SiC//[111]Si, [111]SiC//[111]Si, and [220]SiC//[220]Si which are consistent with previous reports[16]. Stacking faults in the SiC layer originating at the SiC/Si interface are attributed to the large lattice mismatch of 20% between 3C-SiC and Si as well as to errors in deposition [15,17]. The defect density decreased away from the interface. A thin amorphous layer is observed adjacent to the Si substrate. This layer is attributed to ion beam damage during ion milling [15] since it becomes narrower away from the edge of the TEM sample

(see left side of Fig. 3). The 3C-SiC/Si interface is relatively sharp. The AlN/SiC interface in this sample is shown in Fig 4. The nucleation layer adjacent to the interface is indicated by arrows. The columnar grain in the bulk AlN layer are clearly seen in the bright field image of Fig. 4. Figure 5 shows a cross-sectional high resolution lattice image of the 2H-AlN/3C-SiC interface along with the corresponding SAD pattern.

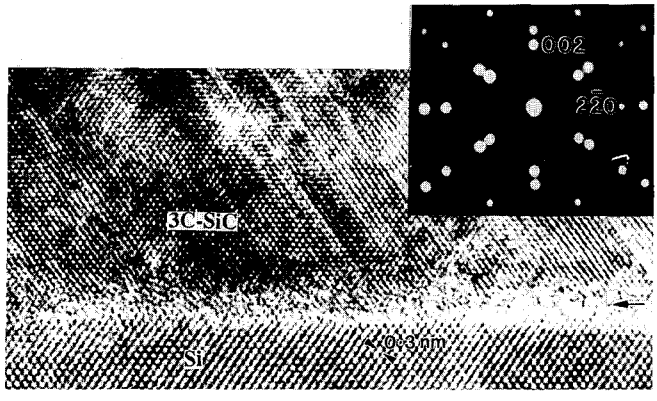

Fig. 3 Atomic resolution lattice image of the 3C-SiC/Si interface of a SiC/AlN/SiC/Si structure depicting planar defects on {111} planes of SiC. A thin amorphous layer adjacent to the interface is marked by arrow. The corresponding SAD pattern is shown as inset.

The AlN layer has small crystallites close to the interface. The 2H-AlN layer in this case is polycrystalline and contains columnar grains exhibiting a particular orientation with the 3C-SiC layer. The preferred orientation in the AlN layer is identified as [0112] which is parallel to [002] of 3C-SiC (reflections from (0112) are indicated by an arrow-head in Fig. 5). In addition, amorphous like and disordered regions were observed in this layer. The top 3C-SiC on the polycrystalline 2H-AlN was also polycrystalline.

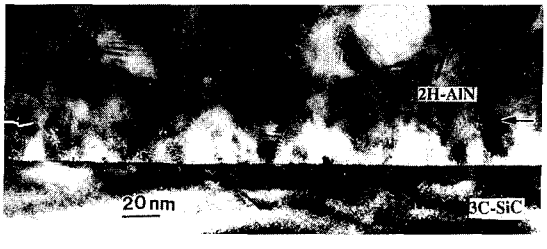

Fig. 4 Bright field image of the 3C-SiC/2H-AlN interface of a 3C-SiC/2H-AlN/3C-SiC/Si heterostructure showing the columnar grain growth over the nucleation layer.

Figure 6 shows a bright field image of a cross section which includes the (001)Si substrate and the 3C-SiC/AlN layers of a SiC/AlN/Si structure. Both SiC/AlN layers consist of a dense columnar microstructure without any voids along the columnar grain boundaries. The AlN/Si interface is relatively rough and contains an amorphous layer formed by interdiffusion between the two layers. On the other hand, the SiC/AlN interface is not well discernible because of intermixing at the interface. The bulk AlN columnar grains have a [0002] preferred orientation, which is consistent with previous

results[18]. In contrast, Azema et al. [19] observed [0110] preferred orientation in their 2H-AlN layers grown on (100)Si. High resolution lattice images of the AlN/Si interface showed ≈160 Å thick amorphous layer in the AlN film adjacent to the interface. The subsequent SiC layer grown on the polycrystalline AlN layer was also polycrystalline. The diffraction pattern obtained only from the bulk SiC layer is shown as inset to Fig. 6. The interplanar spacing obtained from the first ring of spots corresponds to (111) planes of SiC indicating the preferred orientation of the SiC layer on AlN layer.

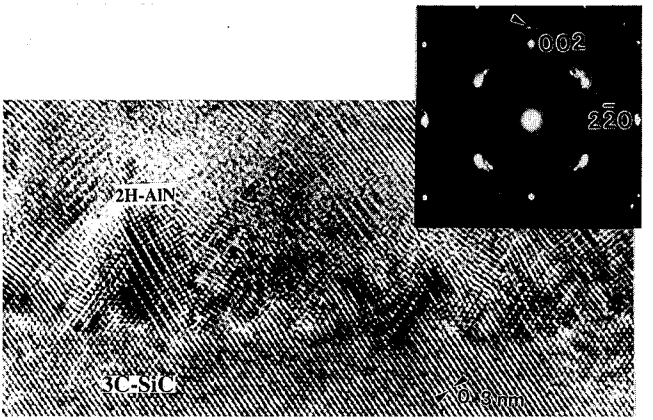

Fig. 5 [110] high resolution lattice image of the 3C-SiC/2H-AlN interface of a 3C-SiC/ 2H-AlN/3C-SiC/Si heterostructure. The SAD pattern is shown as inset. (0112) reflection from AlN layer (arrowhead) is parallel to the growth direction. .

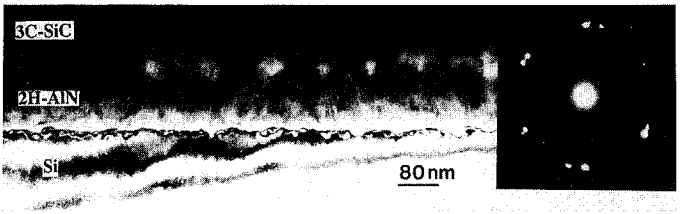

Fig. 6 Bright field image of a SiC/AlN/Si cross section.

In the multilayer structures studied here, the AlN layers grown on (100)Si and (100)3C-SiC are polycrystalline with columnar grains possessing a preferred orientation. However, AlN is single crystalline when grown on 6H-SiC. This difference in AlN growth morphology can be attributed to the activation energy for the formation of AlN on chemically and crystallographically different surfaces. In general, the polycrystalline structure of AlN consist of two distinct layers: (1) a nucleation layer of ≈ 200Å and (2) a bulk layer. Columnar grains in the bulk layer develop a preferred orientation from the randomly oriented nucleation layer. However, the nucleation layer in the case of AlN grown on Si consists of a thin amorphous layer. This characteristic AlN growth can be attributed to the zone T region in the Thornton model [20]. It is interesting to note that the nucleation layer is also observed when the AlN layer is single crystalline. However, the nucleation layer in this case is well oriented with respect to the substrate

CONCLUSIONS

A detailed microstructural characterization of 3C-SiC/2H-AlN/6H-SiC, 3C-SiC/2H-AlN/3C-SiC/Si, and 3C-SiC/2H-AlN/Si heterostructures was carried out using high resolution and conventional electron microscopy. SiC/AlN bilayers were single crystalline when grown on 6H-SiC substrates. However, they were polycrystalline when grown on monocrystalline (001) 3C-SiC/(001)Si and (001)Si. Also, a polycrystalline AlN layer was found with a different preferred orientation on 3C-SiC/Si than on Si. In general, the polycrystalline AlN growth consists of two distinct layers. The first thin nucleation layer near the interface is polycrystalline followed by the growth of large aligned columnar grains. However, the nucleation layer in the single crystalline AlN layer on 6H-SiC is epitaxially well oriented. A high density of planar defects was observed in single crystalline 3C-SiC layers grown on 2H-AlN/6H-SiC due to the large thermal expansion coefficient mismatch.

ACKNOWLEDGMENT

This work was support by the National Science Foundation (Grant # HRD9255378) & the Office of Naval Research (Grant # N00014/93/1/0954). We also like to thank Dr. P. Pirouz, and Dr. Jinwewi. Yang of Case Western Reserve University for the use of their facility and helpful discussions.

REFERENCES

1 A. Fathimulla and A.A. Lakhani, J. Appl. Phys. 54, 4586 (1983).
2 T. Shiosaki and A Kawabata, Ferroelectrics 42, 219 (1982).
3 K. Tsubouchi and N. Mikoshiba, IEEE Trans. Sonics Ultrason. 32, 634 (1985).
4 J.W. Palmour, H.S. Kong and R.F. Davis, Appl. Phys. Lett. 51, 2028 (1987).
5 G. Kelner, M. Shur, S. Binari, K. Sleger, and H.S. Kong in Amorp. and Cryst. SiC and Related Materials II, (edited by Rahman et.al. Springer Verlag, Berlin, 1989) p. 184.
6 H. Matsunami, S. Nishino and H. Ono, IEEE Trans. Electron Devices, 28, 1253 (1981).
7 K.L. More, S.P. Withrow, T.E. Haynes, and R.A. Zuhr, Mat. Res. Soc. Symp. Proc. 162, 451 (1989).
8 M. Morita, S. Isogal, N.Shimizu, K. Tsubouchi, and N. Mikoshiba,. Jpn. J. Appl. Phys. 20, 173 (1981).
9 L. Chu, D.W. Ing, and A.J. Norieka, Solid State Electron. 10, 1023 (1967).
10 S. Yoshida, S. Mizawa, Y. Fujii, S. Takada, H. Hayakawa, S. Gonda, and A. Itoh, J. Vac. Sci. Technol. 16, 990 (1979).
11 L.B. Rowland, R.S. Kern, S.Tanaka, and R.F. Davis, Apply Phys. Lett. 62, 3333 (1993)
12 W.R. L. Lambrecht and B. Segall, Phys. Rev B 43, 7070 (1991).
13 K.G. Irvine, I. Jenkins, W. Givens, M.G. Spencer and M. Aluko, Mater Sci. Eng. B11, 93 (1992).
14 R.Poerschke & O. Madelung, Data in Science and Technology (Semiconductor group IV elements & III-V compound),(Springer-Verlag, Berlin 1991)
15 S.R. Nutt, D.J. Smith, H. J. Kim, and R. F. Davis, Appl. Phys. Lett. 50, 203 (1987).
16 Q. Wahab, L. Hultman, J.E. Sundgren, and M.Willander, Mat. Sci. Eng. B11, 61 (1992).
17 P. Pirouz, F. Ernest, and T.T. Chang, Mat.Res. Soc. Symp. Proc. Vol. 116, 57 (1988).
18 M. Morita, S.Isogal, N. Shimizu, K. Tsubouchi, and N. Mikoshiba, Jpn. J. Appl. Phys. 20, 1 173 (1990).
19 N.Azema, J.Durand, R. Berjoan, C. Dupuy, J. L. Balladore, and L. Cot,. J. Crystal Growth 129, 621 (1993).
20 A. Thornton, J.Vac. Sci. Technol. 12, 830 (1975).

NUCLEATION AND STEP DYNAMICS IN SiC EPITAXIAL GROWTH

HIROYUKI MATSUNAMI AND TSUNENOBU KIMOTO
Department of Electrical Engineering, Kyoto University
Yoshidahonmachi, Sakyo, Kyoto 606-01, Japan

ABSTRACT

Recent progress in homoepitaxial growth of 6H-SiC by step-controlled epitaxy utilizing off-angle substrates is discussed in detail. Features of step-controlled epitaxy and its growth mechanism are described based on experimental results. The growth mode on off-angle substrates is explained by a stagnant layer model. The diffusion length of adatoms on a surface is calculated using a simple surface diffusion model. The critical conditions of two-dimensional nucleation and step-flow growth are predicted based on theoretical calculation and experimental results. Microscopic surface processes such as nucleation and step motion are made clear by observing the grown layer after short-time growth.

INTRODUCTION

In recent years, single-crystalline wafers of silicon carbide (SiC) larger than 1 inch diameter are available based on a modified Lely (sublimation) method [1]. In addition, progress in homoepitaxial growth of SiC utilizing step-controlled epitaxy has given superior single crystalline layers and easy control of in-situ impurity doping [2,3]. Step-controlled epitaxy implies high-quality homoepitaxy of SiC at rather low temperatures using SiC off-angle substrates. This is, now, a key technology of SiC epitaxial growth for electronic applications. Much attention to this attractive material is widely expanding to realize advanced electronic devices.

In this report, homoepitaxial growth of SiC on SiC at low temperatures by step-controlled epitaxy, utilizing step-flow growth from surface atomic steps, is discussed in detail. Its growth mechanism is elucidated based on detailed experiments for off-angle and surface polarity effects on epitaxial growth. To explain the substrate temperature dependence of epitaxial growth, a stagnant layer model is proposed. To make clear the surface kinetics, the diffusion length of adatoms on a surface is determined using a simple surface diffusion model. Then, microscopic surface processes such as nucleation and step motion are characterized by observing the grown surface after short-time growth.

STEP-CONTROLLED EPITAXY

Crystal growth has been carried out by atmospheric-pressure chemical vapor deposition (CVD) in a horizontal reaction tube using SiH_4, C_3H_8 and H_2. Substrates were heated by radio frequency induction, and the growth temperature was varied in the range of 1100~1600℃. The growth procedure consists of two steps, etching with HCl and epitaxial growth at a required temperature. The flow rates of SiH_4, C_3H_8 and H_2 during epitaxial growth were 0.15~0.30 sccm, 0.10~0.40 sccm and 3.0 slm, respectively.

Single crystals of 6H-SiC {0001} faces were used as substrates. The

Mat. Res. Soc. Symp. Proc. Vol. 339. ©1994 Materials Research Society

surface polarity, either (0001)Si or (000$\bar{1}$)C face, was identified by thermal oxidation (dry O_2 at 1000℃ for 5 h) utilizing the difference in oxidation rates between both faces. Substrates were angle-lapped to get off-orientation within 0 to 10° toward <11$\bar{2}$0>.

In Fig.1, Nomarski microphotographs are shown for layers grown at 1500℃ on well-oriented and 6° off-oriented {0001} faces using a standard growth condition (SiH_4: 0.3 sccm, C_3H_8:0.2 sccm, growth rate:2.5μm/h). On well-oriented (0001)Si faces, although the surface is very flat, the layer has a mosaic pattern in which boundary lines divide the layer into several regions. By reflection high-energy electron diffraction (RHEED), the layer was identified as 3C-SiC including <111> symmetrical twins. Molten KOH etching also revealed the layer as 3C-SiC, and the boundary lines are twin boundaries known as double positioning boundaries. On (000$\bar{1}$)C faces, the surface has bumpy structure including many islands. The layer has been identified as 3C-SiC by RHEED.

On the contrary, on off-oriented substrates, very flat and mirror-like layers are grown independent of surface polarity. The layers were identified as 6H-SiC by RHEED and molten KOH etching. The polytypes were also characterized by photoluminescence and Raman scattering analysis. Concerning homoepitaxial growth of 6H-SiC by CVD, temperatures over 1800℃ had been necessary to get good surface morphology on well-oriented 6H-SiC (0001)Si faces [4-6]. The temperature required for epitaxy was reduced by more than 300℃.

Schematic images of the relationship between growth modes and polytypes of grown layers are shown in Fig.2. On well-oriented surfaces, two-dimensional nucleation does occur on terraces under high supersaturation owing to low temperature (1500℃). The polytypes of grown layers are governed by environmental growth conditions, especially temperature, and the

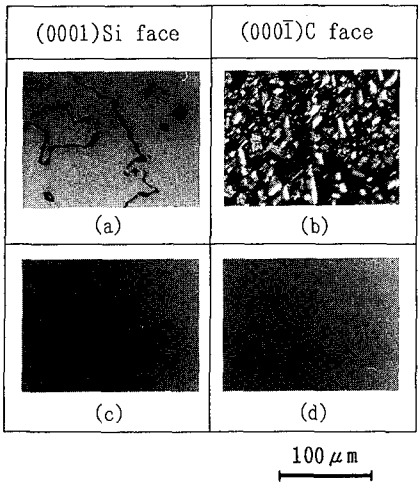

Fig.1. Surface morphology of layers grown on well-oriented faces [(a) and (b)] and off-oriented faces [(c) and (d)].

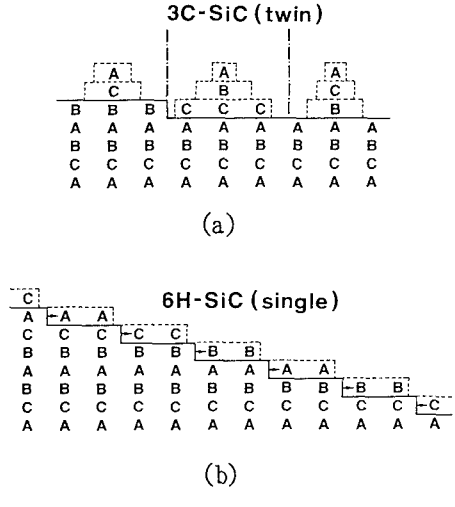

Fig.2. Schematic images of growth modes. 3C-SiC by two-dimensional nucleation (a) and homoepitaxy of 6H-SiC by step-flow growth (b).

grown layer becomes 3C-SiC which is stable at low temperatures. Since the stacking order of 3C-SiC and 6H-SiC is different, the 3C-SiC grown layer becomes a twin structure as shown in Fig.2(a). By the introduction of off-orientation, the surface step density is increased, and 6H-SiC is grown laterally from the steps inheriting the stacking order of the substrate as in Fig.2(b). Hence the author's group named the growth method "step-controlled epitaxy" [2,3].

The dependence of growth rate on C/Si ratio is shown in Fig.3 [7]. The substrates are 6H-SiC (000$\bar{1}$)C faces with 6° off-angle. Solid and open circles are the results for SiH_4 flow rates of 0.15 and 0.30 sccm at 1500℃. In the region of C/Si<1.4, the growth rate increases remarkably with increase in the C/Si ratio, which may be caused by the increase of C source. In the region of C/Si>1.4, the growth rate does not change with the C/Si ratio and it increases proportionally with the flow of SiH_4, which shows that the supply of SiH_4 limits the growth under enough C source. Quite similar results were obtained in the growth on off-oriented (0001)Si faces. These results suggest that Si-related species are preferentially adsorbed on a surface, and may diffuse on terraces terminated with C atoms. Crystal growth proceeds through carbonization of adsorbed Si by hydrocarbon molecules or their fragments.

GROWTH MECHANISM

To make clear the polarity effects, the off-angle dependence of growth rate at 1500℃ on both (0001)Si and (000$\bar{1}$)C faces is shown in Fig.4 [7]. Open and closed triangles indicate 3C-SiC grown on well-oriented (0001)Si and (000$\bar{1}$)C faces, respectively. Open and closed circles indicate 6H-SiC grown on off-oriented (0001)Si and (000$\bar{1}$)C faces. The flow rates of SiH_4 and C_3H_8 are 0.30 and 0.20 sccm. On well-oriented substrates, higher growth rates were obtained on (000$\bar{1}$)C faces than on (0001)Si faces, which is ascribed to the high nucleation rate on (000$\bar{1}$)C terraces. As the terrace

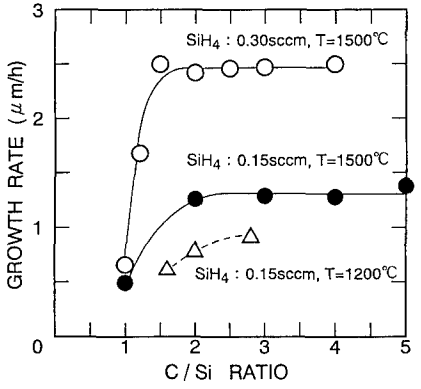

Fig.3. Dependence of growth rate on C/Si ratio for different SiH_4 flow rates at different temperatures (on off-oriented (000$\bar{1}$)C faces) [7].

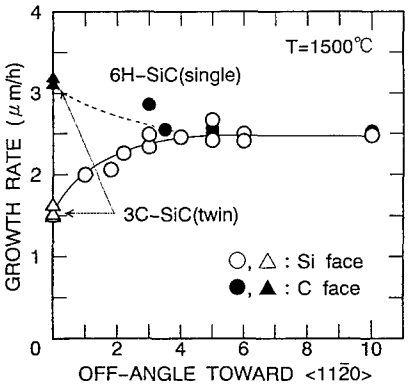

Fig.4. Dependence of growth rate (at 1500℃) on substrate off-angle [7].

width becomes narrower with the increase of off-angle, step-flow growth becomes dominant, which yields 6H-SiC grown layers. 6H-SiC can be homoepitaxially grown on substrates with more than 1° off-angle. With increasing off-angle, the growth rates on both faces approach each other and become almost the same value for off-angles higher than 5° .

Figure 5 shows the temperature dependence of growth rate between 1200℃ and 1600℃ using substrates with an off-angle of 6° , in which step-controlled epitaxy of 6H-SiC occurs [7]. Homoepitaxial growth on 6H-SiC {0001} faces can be realized even at 1200℃, indicating a reduction of 600℃ for homoepitaxy. With increasing temperature, the growth rate increases showing a very small activation energy of 3.0 kcal/mol. In SiC growth on well-oriented {0001} faces using CVD, activation energies of 22 [4] or 20 kcal/mol [8] were reported. The activation energy of 22 kcal/mol has been explained as that for Si adsorption based on thermodynamic consideration.

To explain the small activation energy, the growth mechanism was analyzed. In CVD, the growth is governed by (1)surface reaction control or (2)mass transport control (or diffusion control). In surface reaction control, the activation energy is given as the sum of those required for various processes (evaporation from kinks onto a surface, desorption from a surface to vapor and surface diffusion) or at least one of them which dominates the growth. These activation energies, however, seem to be higher than 10~20 kcal/mol [9], though a detailed study has not been done. Thus, the surface reaction cannot explain the small activation energy.

The temperature dependence of growth rate was analyzed based on a stagnant layer model [10], in which the crystal growth is controlled by mass transport. The diffusion of reactants from the main gas stream through a stagnant layer to the crystal surface controls the growth. As described above, the growth rate of SiC is determined by the supply of Si-related species. Thus, the model proposed for Si growth in CVD using a horizontal

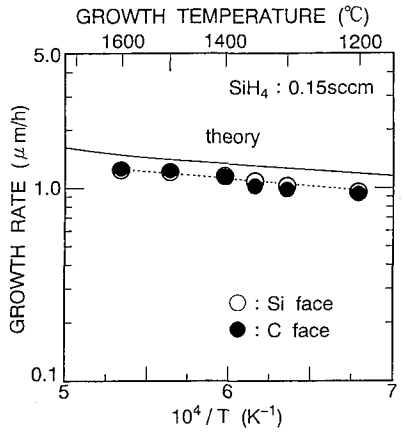

Fig.5. Temperature dependence of growth rate on off-oriented (0001)Si and (000$\bar{1}$)C faces. Solid curve shows a calculated result [7].

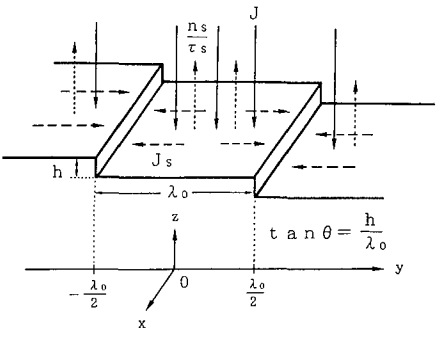

Fig.6. Schematic illustration of simple surface diffusion model, with steps of height h separated by equal terrace width λ_0.

reactor can be applied to SiC growth with some modification. The growth rate at a position x_0 from the front edge of a susceptor in the reactor is given by the following equation [10].

$$R(x_0) = [cD_0T_sP_0/\{n_0kT_0^2\delta(x_0)\}]\exp[\{-D_0T_s/(T_0v_0b)\}\int\{dx/\delta(x_0)\}]. \quad (1)$$

The integration should be carried out from 0 to x_0. Here, D_0 is the diffusion coefficient of SiH_4 in H_2 at 300 K, T_s the substrate temperature, P_0 the partial pressure of SiH_4, v_0 the mean velocity of nonheated gas, b the reactor free height, $\delta(x)$ the stagnant layer thickness, c the spacing of 6H-SiC {0001} faces, n_0 the density of surface atomic sites, and T_0=300K. In the ideal case (laminar flow with uniform velocity), $\delta(x)$ is given by $(\mu x/v_0\rho)^{1/2}$, where μ and ρ are the gas viscosity and density [11].

Using appropriate values for individual variables and constants, the growth rates were calculated neglecting the complex flow by heating [7]. The result is shown by a solid curve in Fig.5. The absolute values of calculated growth rate surprisingly well agree with experimental results, in spite of a simple model. The growth rate can be predicted within an error of 20%, which is ascribed to the underestimation in $\delta(x)$ and some factor in complex gas flow. The growth rate increases gradually with temperature increase owing to the enhancement of diffusion in a stagnant layer. Although the stagnant layer model does not give an activation-type formula, the calculated curve in the range of 1200~1600℃ yields an apparent activation energy of 3.0 kcal/mol, which corresponds to the diffusion in a stagnant layer. Therefore, the growth is limited by mass transport in step-controlled epitaxy, which gives no polarity dependence of growth rate.

SURFACE KINETICS

Step-controlled epitaxial growth of 6H-SiC on off-oriented 6H-SiC{0001} was quantitatively analyzed [12] based on a simple surface diffusion model proposed by Burton, Cabrera and Frank (BCF model [13]) to determine the surface diffusion length and step-flow growth conditions.

In a model shown in Fig.6, some adatoms on a surface can reach steps and are incorporated into the crystal, and others reevaporate to vapor. Some adatoms coalesce to form nuclei on terraces if supersaturation on the surface is high enough.

By solving the continuity equation of adatoms under the boundary condition of perfect sinks at steps, the adatom concentration $n_s(y)$ per unit area on a terrace is given as

$$n_s(y) = J\tau_s + (n_{s0} - J\tau_s)\{\cosh(y/\lambda_s)/\cosh(\lambda_0/2\lambda_s)\}, \quad (2)$$

where J is the flux of reactants arriving onto a surface, τ_s the mean residence time of adatoms, n_{s0} the adatom concentration in equilibrium, and λ_s the surface diffusion length.

The growth rate R is the product of the step velocity, proportional to the derivative of $n_s(y)$, and $\tan\theta$ ($=h/\lambda_0$, θ: off-angle) in step-flow growth, and is given by

$$R = (2h\lambda_s/n_0\lambda_0)\{J - (n_{s0}/\tau_s)\}\tanh(\lambda_0/2\lambda_s). \quad (3)$$

Here, h is the step height, λ_0 step width, and n_0 the density of surface atomic sites on the surface.

Since the supersaturation ratio $\alpha(y)$ defined as $n_s(y)/n_{s0}$ is a maximum

α_{max} at the center of a terrace, two-dimensional nucleation occurs easily at this position. The growth mode is determined according to the following relation:

$$\alpha_{max} > \alpha_{crit} : \text{two-dimensional nucleation,}$$

$$\alpha_{max} < \alpha_{crit} : \text{step-flow growth.}$$

Under the critical condition, α_{max} is equal to α_{crit}. Therefore, the following equation is given [12],

$$(\lambda_0/4\lambda_s)\tanh(\lambda_0/4\lambda_s) = \{(\alpha_{crit} - 1)h/(2n_0R)\}(n_{s0}/\tau_s). \quad (4)$$

In the equation, R is determined by growth conditions, λ_0 and h are obtained by preparation condition of substrates, and n_0 an inherent parameter of the material. If the values of n_{s0}/τ_s (desorption flux in equilibrium) and α_{crit} are known, λ_s can be calculated.

Although the individual estimation of n_{s0} and τ_s is difficult, n_{s0}/τ_s can be expressed by the equilibrium vapor pressure in chemical reactions between Si and hydrocarbon gases [14]. Among different chemical reactions, the reaction of Si and C_2H_2 (a product from C_3H_8) is most active and dominant in SiC growth [15,16]. The temperature dependence of n_{s0}/τ_s was calculated by the use of equilibrium vapor pressure obtained from this reaction [12]. The n_{s0}/τ_s increases exponentially with the increase in temperature.

In principle, α_{crit} is intrinsic to a material at a fixed temperature. When the critical nucleation rate is assumed to be 10^{12} $cm^{-2}s^{-1}$, which corresponds to one nucleus per unit time on a 10 nm x 10 nm terrace (average terrace width in the present off-angle substrate), α_{crit} for a disk-shaped nucleus is given by [17]

$$\alpha_{crit} = \exp[\pi h\sigma^2\Omega/\{(65 - \ln 10^{12})k^2T^2\}], \quad (5)$$

where Ω and σ are the volume of the Si-C pair and the surface free energy. Using Ω for 6H-SiC and assuming the surface energy of (0001)Si and (000$\bar{1}$)C faces as 2220 and 300 erg/cm^2 obtained for 3C-SiC (111)Si and ($\bar{1}\bar{1}\bar{1}$)C faces [18], the temperature dependence of α_{crit} for (0001)Si and (000$\bar{1}$)C faces was calculated, and the result is shown in Fig.7 [12]. The value decreases with the increase in temperature, which means that a lower supersaturation ratio is enough for nucleation at higher temperature. However, in real crystal growth, nucleation easily occurs at lower temperatures owing to a significant decrease in n_{s0}/τ_s. The polarity dependence of α_{crit} is significant. The α_{crit} for (000$\bar{1}$)C faces takes quite low values of almost unity, which indicates that nucleation occurs more frequently on (000$\bar{1}$)C faces under the same supersaturation.

To estimate the surface diffusion length of adatoms, the critical growth conditions were found experimentally by observing the polytypes of grown layers [12]. Some of the critical conditions at which the growth mode changes from step-flow growth to two-dimensional nucleation are shown in Table I. The critical conditions do not depend on the substrate polarity.

Figure 8 shows the calculated temperature dependence of surface diffusion length on both faces using several data obtained from the experiments [12]. The surface diffusion length decreases at high temperatures due to enhanced desorption. The values on (000$\bar{1}$)C faces are longer than those on (0001) Si faces by more than one order of magnitude. Although nucleation occurs much more easily on (000$\bar{1}$)C faces, the longer surface diffusion length may

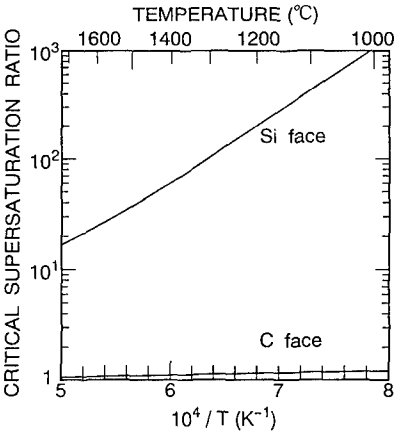

Fig.7. Temperature dependence of critical supersaturation ratio for (0001)Si and (000$\bar{1}$)C faces [12].

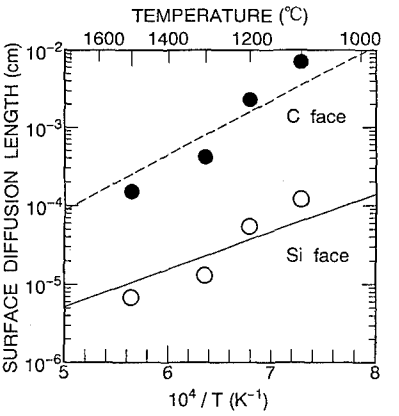

Fig.8. Temperature dependence of surface diffusion length of adatoms on (0001)Si and (000$\bar{1}$)C faces [12].

Table I. Some of critical growth conditions at which growth mode changes from two-dimensional nucleation to step-flow growth.

Growth temperature (℃)	Off-angle (°)	Terrace width (nm)	Growth rate (μm/h)
1100	6	2.4	0.80
1200	3	4.8	0.95
1300	6	2.4	2.50
1500	1	14.4	2.00

compensate frequent nucleation on the terraces. This brings no polarity dependence of surface morphology in step-controlled epitaxy.

Since the temperature dependence of n_{s0}/τ_s, α_{crit} and λ_s have been obtained, the critical growth conditions can be predicted using eq.(4). If the growth temperature and off-angle are fixed, the critical growth rate (maximum growth rate for step-flow growth) can be calculated. In Fig.9, the critical growth conditions are shown for substrate off-angles of 0.2, 1, 3,

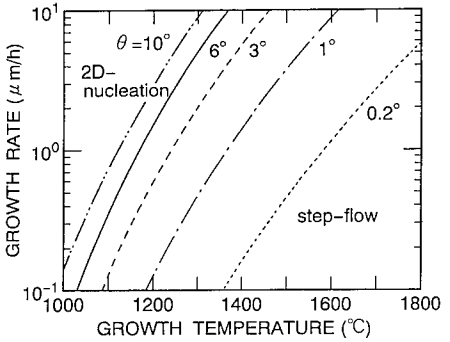

Fig.9. Critical growth conditions as a function of growth temperature, growth rate, and substrate's off-angle. Top-left and bottom-right regions of each curve correspond to two-dimensional nucleation and step-flow growth conditions [12].

6 and 10° [12]. The top-left and bottom-right regions separated by individual curves indicate two-dimensional nucleation and step-flow growth conditions, respectively. Almost no difference in the critical conditions was obtained on (0001)Si and (000$\bar{1}$)C faces. A higher growth rate and lower off-angle can be taken for step-flow growth at higher growth temperatures. At 1800℃, a very small off-angle of 0.2° , which indicates almost well-oriented faces, is enough to get step-flow growth with a moderate growth rate of 6μm/h. On the contrary, a large off-angle more than 5° is necessary to realize step-flow growth (homoepitaxy of 6H-SiC) at 1200℃.

NUCLEATION AND STEP MOTION

In addition to the growth mechanism and surface kinetics, microscopic surface processes such as nucleation and surface diffusion of adatoms should be made clear [19]. The formation of nuclei and the lateral growth rates of steps in SiC growth were studied. The effects of growth temperature, substrate polarity and off-orientation on the surface processes were investigated.

Crystal growth was carried out in atmospheric CVD in the temperature range of 1200~1600℃. Single crystals of 6H-SiC, both (0001)Si and (000$\bar{1}$)C faces, grown by the Acheson method were used as substrates. Since nucleation is sensitive to surface conditions including impurities and defects introduced during polishing, as-grown natural faces were used. The density and size of nuclei were characterized by observing the surface with a Nomarski microscope after short-time growth. To investigate step-motion, circular mesa-tables, 120 nm height and 20~300μm diameter, were formed on SiC substrates by conventional photolithography and reactive ion etching. The lateral growth rates were measured from the advance of a table-edge after short-time growth using a similar method as in the literature [20].

Figure 10 shows a Nomarski microphotograph of a (0001)Si face with circular mesa-tables after growth for 60 s at 1600℃ with the flow rates of SiH_4: 0.15 sccm and C_3H_8: 0.10 sccm (growth rate: 1.2μm/h) [19]. The formation of many nuclei on the terraces and lateral advance of table edges are observed. For growth at higher temperatures of 1500~1600℃, most nuclei showed distorted hexagonal shape (size: 20~50μm) with facets of all nuclei parallel to {1$\bar{1}$00} faces. The distorted hexagonal nuclei showed 3C-SiC component in micro-Raman spectroscopy, but it is not clear why the nuclei had distorted hexagonal shape. On the other hand, for growth at lower

temperatures of 1200~1300℃, many small-size (<5μm) triangular-shaped nuclei showing 3C-SiC feature were formed. Although the facets of all nuclei are parallel to {1$\bar{1}$00} faces, they are rotated by 180° to each other, corresponding to double positioning domains.

In Fig.11, the temperature dependence of the nucleus density (number of nuclei per unit area) on well-oriented (0001)Si and (000$\bar{1}$)C faces is shown [19]. The nucleus density significantly increases at low temperatures, which is attributed to higher supersaturation owing to the reduced equilibrium vapor pressure and suppressed surface diffusion of adatoms. The nucleus density is higher on (000$\bar{1}$)C faces than on (0001)Si faces by more than one order of magnitude. This remarkable polarity dependence can be explained by

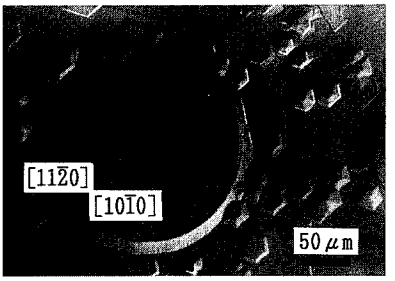

Fig.10. Microphotograph of (0001)Si faces with circular mesa-tables after growth at 1600℃ for 60 s [19].

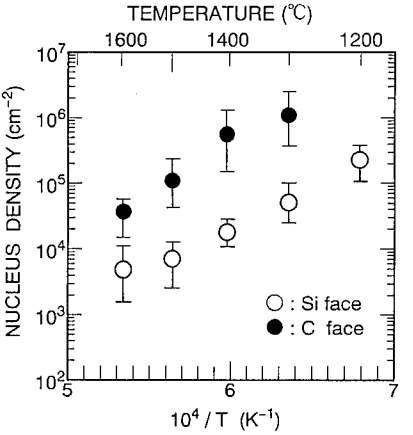

Fig.11. Temperature dependence of nucleus density on well-oriented (0001)Si and (000$\bar{1}$)C faces [19].

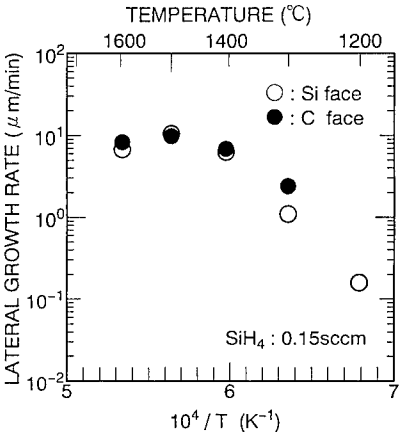

Fig.12. Temperature dependence of lateral growth rate on well-oriented (0001)Si and (000$\bar{1}$)C faces [19].

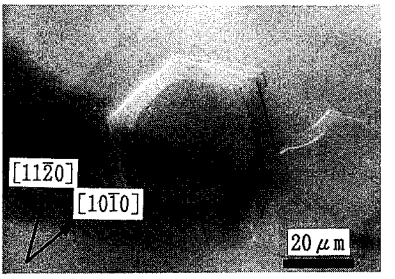

Fig.13. Microphotograph showing anisotropy in lateral growth rate after growth at 1600℃ for 60 s [19].

the difference in surface energy between both faces. Preferential nucleation may occur at screw dislocations on the substrate surface. This becomes important when the nucleus density is low ($<10^5$ cm^{-2}).

The lateral growth rate estimated from the advance of the table edge is almost independent of the table diameter. Figure 12 shows the temperature dependence of lateral growth rate toward <11$\bar{2}$0> on well-oriented (0001)Si and (000$\bar{1}$)C faces [19]. The lateral growth rates ($\sim 10\,\mu$m/min above 1400℃) are very large compared with the vertical growth rate (1.2μm/h at 1600℃). This results because adatoms diffuse on a surface and are preferably incorporated into a crystal at steps and/or kinks. The lateral growth rate considerably decreases at low temperatures, which is attributed to the reduction in surface diffusion length of adatoms.

As shown in Fig.13, the original circular mesa-table deforms into a hexagonal shape, which is caused by anisotropy in lateral growth rates [19]. The fastest growth direction is <11$\bar{2}$0> and the lowest <1$\bar{1}$00>. The anisotropy may be originated from the difference in the arrangement of atoms and bond configuration at table edges. Microscopically, the table edges consist of very small straight steps and kinks. Since the straight steps align parallel to the crystal facets ((1$\bar{1}$00) faces), the table edges perpendicular to <1$\bar{1}$00> can be regarded as straight macro steps. The kink density increases with the deviation of direction from <1$\bar{1}$00>, and becomes maximum in <11$\bar{2}$0>. Hereafter, the growth along <1$\bar{1}$00> and <11$\bar{2}$0> is referred as step growth and kink growth. The ratio of incorporation of migrating adatoms at steps and kinks gives the ratio of lateral growth rates for steps and kinks. The ratio is 0.85 at 1600℃, and decreases down to 0.45 at 1200℃, which indicates the enhanced anisotropy in the growth at low temperatures.

To investigate the effects of off-orientation on surface kinetics, the growth on off-oriented faces (5° off) with similar mesa-tables was done at 1500℃ [19]. In this case, however, no nuclei were observed even after growth for 300 s. This result can be attributed to quite low supersaturation caused by high density of steps on the surface. The formation of {0001} facets along the off-direction was observed at the upstream sides of table edges. The formation of facets can be explained by the fact that the growth proceeds through the step-flow mode.

SUMMARY

Recent progress in homoepitaxial growth of 6H-SiC by step-controlled epitaxy utilizing off-angle substrates was discussed in detail. Features of step-controlled epitaxy and its growth mechanism were described based on experimental results. The growth on well-oriented substrates was found to be surface-reaction controlled, whereas that on off-oriented substrates mass-transport controlled. The temperature dependence of growth rate was analyzed by a stagnant layer model, and the small activation energy was explained as the required energy for diffusion of Si-related species in a stagnant layer. The diffusion length of adatoms on a surface is calculated using a simple surface diffusion model. The critical conditions of two-dimensional nucleation and step-flow growth were predicted based on theoretical calculation and experimental results. Microscopic surface processes such as nucleation and step motion were made clear by observing the grown layer after short-time growth. The nucleus density and the lateral growth rate were determined.

ACKNOWLEDGMENT

This work has been continuously supported by a Grant-in-Aid for Scientific Research from the Ministry of Education, Science and Culture, Japan.

REFERENCES

[1] Yu.M.Tairov and V.F.Tsvetkov, J. Cryst. Growth **52**, 146(1981).
[2] N.Kuroda, K.Shibahara, W.S.Yoo, S.Nishino, and H.Matsunami, Ext. Abstr. 19th Conf. on Solid State Devices and Materials (Business Center for Academic Societies, Tokyo, 1987), p.227.
[3] H.Matsunami, T.Ueda and H.Nishino, Mat. Res. Soc. Symp. Proc. **162**, 397 (1990).
[4] B.Wessels, H.C.Gatos, and A.F.Witt, in Silicon Carbide 1973 (University of South Carolina Press, Columbia, SC, 1974), p.25.
[5] W.von Muench and I.Pfaffeneder, Thin Solid Films **31**, 39 (1976).
[6] S.Nishino, H.Matsunami, and T.Tanaka, J. Cryst. Growth **45**, 144 (1978).
[7] T.Kimoto, H.Nishino, W.S.Yoo, and H.Matsunami, J. Appl. Phys., **73**, 726 (1993).
[8] V.J.Jennings, A.Sommer, and H.C.Chang, J. Electrochem. Soc. **113**, 728 (1966).
[9] D.W.Shaw, in Crystal Growth: Theory and Techniques (Plenum, New York, 1974) Vol.1, Chap.1.
[10] F.C.Eversteyn, P.J.W.Severin, C.H.J.van den Brekel, and H.L.Peek, J. Electrochem. Soc. **117**, 925 (1970).
[11] R.M.Olsen, Essentials of Engineering Fluid Flow (International Textbook, Scranton, PA, 1966).
[12] T.Kimoto and H.Matsunami, J. Appl. Phys. **75**, 850 (1994).
[13] W.K.Burton, N.Cabrera, and F.C.Frank, Philos. Trans. R. Soc. London A **243**, 299 (1951).
[14] J.O.Hirschfelder, F.Curties, and R.B.Bird, Molecular Theory of Gases and Liquids (Wiley, New York, 1954).
[15] C.D.Stinespring and J.C.Wormhoudt, J. Cryst. Growth **87**, 481 (1988).
[16] M.D.Allendorf and R.J.Kee, J. Electrochem. Soc. **138**, 841 (1991).
[17] J.P.Hirth and G.M.Pound, Condensation and Evaporation, Nucleation and Growth Kinetics (Pergamon, Oxford, 1963), Chap.D.
[18] E.Pearson, T.Takai, T.Halicioglu, and W.A.Tiller, J. Cryst. Growth **70**, 33 (1984).
[19] T.Kimoto and H.Matsunami, to be published in Proc. Int. Conf. SiC and Related Materials -ICSCRM-93.
[20] J.Nishizawa, T.Terasaki, and M.Shimbo, J. Cryst. Growth **17**, 241 (1972).

ELECTRON CYCLOTRON RESONANCE PLASMA CHEMICAL VAPOUR DEPOSITION OF SILICON CARBIDE THIN FILMS USING DITERTIARY BUTYL SILANE

Mohamed Boumerzoug, Marcel Boudreau, Peter Mascher, and Paul E. Jessop, Centre for Electrophotonic Materials and Devices, Department of Engineering Physics, McMaster University, Hamilton, Ontario, Canada L8S 4L7.

ABSTRACT

Silicon carbide films were deposited by electron cyclotron resonance plasma chemical vapour deposition, using Ditertiary Butyl Silane ($SiH_2(C_4H_9)_2$), a non-corrosive organic compound, liquid at room temperature and stable in air, as precursor. Depositions were carried out in an Ar/H_2 plasma at relatively low temperatures, below 400 ^oC. The influence of deposition parameters such as substrate temperature, gas flow rates, pressure, and microwave power, was systematically investigated and related to the Si:C ratios and the refractive index. The film composition was measured by Auger electron spectroscopy and the surface morphology was examined by scanning electron microscopy. The deposition rates and refractive indexes were extracted from the conventional ellipsometric functions, psi and delta. The results show that high quality silicon carbide of variable Si:C ratios and with very low levels of impurities are obtained.

INTRODUCTION

Silicon carbide (SiC) possesses interesting mechanical, optical, thermal, and electrical properties [1,2]. It has drawn great interest in the recent years for applications such as light emitting diodes [3] and electronic devices in high temperature and radiation environments [4]. Our own research effort is directed mainly at exploring the applications of high quality SiC films in optoelectronic devices and for semiconductor passivation. Several techniques of processing have been used including chemical vapour deposition (CVD) [5], plasma enhanced CVD [6] and electron cyclotron resonance CVD [7]. The latter method is the most advantageous due to the possibility of generating a plasma with high ion density at low pressures [8]. This method is becoming even more attractive with the increasing need for low-temperature thin-film processing for very large scale integration technology. In general, SiC is deposited from a combination of two or more gas sources, where methane is the commonly used carbon gas source [9], although other sources have been studied by different laboratories [10]. For the conventional silicon source, silane (SiH_4), there are some concerns regarding the safe handling of this material. SiH_4 is toxic and spontaneously flammable in air, requiring special handling procedures. Organic compound sources are receiving considerable attention from the plasma processing laboratories mainly due to the need for less hazardous materials than the volatile inorganic gas sources. Recently, organic sources that contain direct Si-C bonds were suggested as a monosource for Si and C. Among the suggested compounds is Ditertiary Butyl Silane (DTBS), also known under its commercial name CONSI™ 4000 . A schematic of the molecule structure is given in Figure 1. The compound is liquid at room-temperature and stable in air. The advantage of using DTBS is that, in addition to all elemental constituents being contained in the molecule and the Si already bonded to C, this

Mat. Res. Soc. Symp. Proc. Vol. 339. ©1994 Materials Research Society

precursor is relatively easy to handle. In fact, it has already been used for the deposition of SiC in a PECVD reactor [11]. In a recent paper we have shown that good quality SiN:H can be deposited in an ECR-CVD reactor using DTBS as a silicon source [12]. In this paper, we report ECR-CVD of SiC with DTBS as a monosource for Si and C. The effect of processing conditions, such as substrate temperature and microwave power on the film composition and refractive index will be discussed. We show that DTBS is capable of producing silicon carbide of variable Si:C ratios and with very low levels of impurities . To our knowledge this is the first time that DTBS was used for the preparation of SiC in an ECR-CVD reactor.

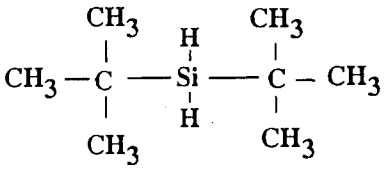

Figure 1: Schematic of the Ditertiary Butyl Silane ($SiH_2(C_4H_9)_2$) molecule.

EXPERIMENTAL DETAILS

The experiments were performed on a custom designed ECR-CVD system. A detailed schematic of the system is shown elsewhere [13]. The system is connected to a load-locked stainless steel chamber evacuated with a turbo pump to a base pressure of $1x10^{-7}$ torr. A high capacity diffusion pump provides a base pressure in the processing chamber below $1x10^{-7}$ torr. The gases for plasma generation, Ar and H_2, are introduced to the ECR chamber through a dispersion ring. The DTBS was delivered to the processing chamber through a second dispersion ring maintained 10 cm above the substrate holder. DTBS was obtained from Olin Hunt and has a chemical purity higher than 99%, a boiling point of 128 ^oC and a vapour pressure of 20.5 torr at 20^oC . It was loaded in a standard 200 ml stainless steel bubbler under flowing argon. In all experiments, the temperature of the bubbler was maintained at 20 ^oC. A low vapour pressure mass flow controller allows accurate control of the DTBS flow. A throttle valve is used for adjusting the pressure in the processing chamber at a given gas flow rate. An Ar/H_2 plasma cleaning of the processing chamber was done after each deposition to ensure the reproducibility of the film characteristics.

The microwave power supply is capable of delivering up to 1000 Watts, and the input power was systematically varied between 300 to 1000 Watts. The magnet currents were set to obtain a stable, uniform plasma mode and were maintained at 180 A and 115 A for the upper and lower magnet currents during all experiments. At such optimized conditions a reflected power as low as 5 Watts was typically obtained. Real time film optical properties and deposition rates were calculated using a Rudolph i1000 *in situ* rotating compensator ellipsometer. The ellipsometer is

interfaced to a personal computer with an RS-232 serial communication link . A dedicated software is used to collect data and to determine the film thickness and index of refraction from the conventional ellipsometric parameters. Samples were mounted on a heatable stage and placed so as to allow measurements of the ellipsometric parameters during the deposition. The substrate temperature was measured using a thermocouple attached to the sample holder, and was systematically varied from 350 °C to 650 °C in steps of 50 °C .

All the films were deposited on (100) silicon substrates which were ultrasonically degreased in trichloroethylene, acetone and methanol, rinsed in water and dried with nitrogen. Just prior to loading the samples into the load-lock they were deoxidized in HF:H_2O (1:10), rinsed with dionized water and dried with nitrogen. Auger electron spectroscopy (AES) was performed on 1000 Å thick SiC deposited on low resistivity (100) Si . The Si:C ratio was determined from the Si and C peak to peak ratio. AES was also used for the detection of contaminants such as oxygen.

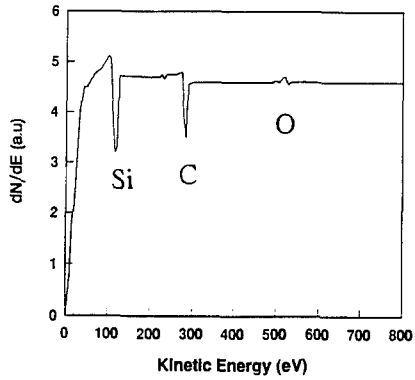

Figure 2: Auger spectrum of a typical ECR-CVD SiC film.

RESULTS AND DISCUSSION

Figure 2 shows an Auger electron spectrum of a SiC film deposited at a microwave power of 400 Watts and a substrate temperature of 350°C with an H_2/Ar gas flow ratio of 0.5. These measurements of the sputter cleaned film surface show very low levels of incorporated oxygen, typically less than 2 at. %. The residual oxygen likely is a contaminant species in the vacuum system. Scanning electron microscopy of films processed under various conditions shows that the films are uniform over a 2" wafer. We did not investigate the structural properties of these films, but for such low deposition tempera-

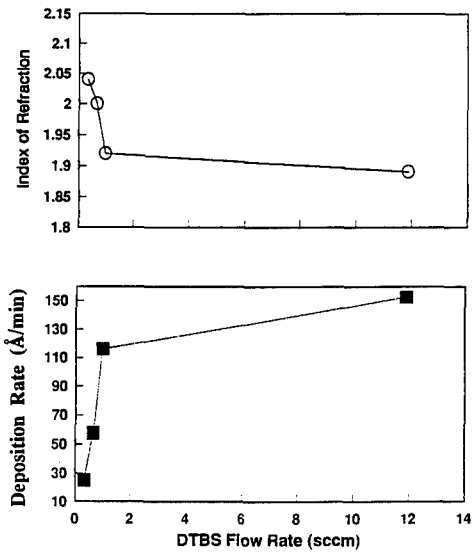

Figure 3: Deposition rate and index of refraction vs. DTBS flow rate.

tures they are expected to be amorphous.

The SiC film deposition rate and the index of refraction versus DTBS flow rate are plotted in Figure 3. During this experiment, the pressure was kept constant at 2.5 mtorr, the substrate temperature was held at 350°C, and the microwave power at 400 Watts. The deposition rate increases with the DTBS flow, reaching values higher than 140 Å/min. for a DTBS flow as low as 12 sccm. The DTBS flow was intentionally kept below 14 sccm in order to avoid the coating of the chamber wall. A thicker coating will lead to the incorporation of deposits from the wall into the films and will affect the reproducibility and hence the quality of the as-deposited films. A practical upper limit on the deposition rate then is approximately 100 Å/min. The carbon content in the film increases with the DTBS flow rate, as confirmed by AES, while the index of refraction was decreasing. This could be explained by the fact that with higher flow, relatively fewer of the Si-C bonds are broken. As is shown in Figure 1 , in the DTBS molecule, the silicon is bonded to two carbons. In order to obtain stoichiometric SiC (Si:C ≈ 1) one of the two bonds needs to be broken. The high deposition rate indicates that a significant number of Si-C molecular bonds remain intact in an Ar/H_2 plasma and are directly incorporated into the film.

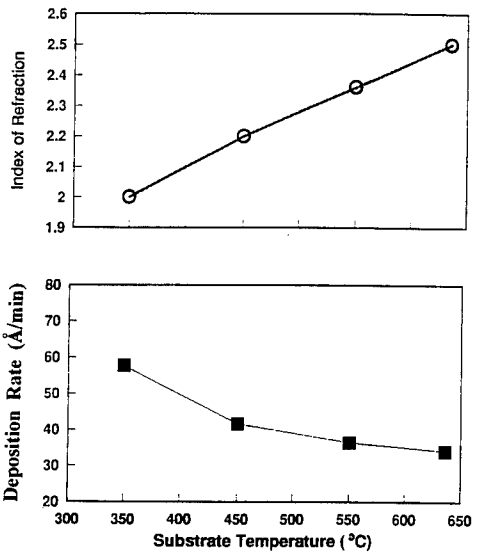

Figure 4. Deposition rate and index of refraction vs. substrate temperature.

The deposition rate and refractive index of the SiC films as a function of the substrate temperature, using a fixed DTBS flow at a constant microwave power and total pressure is shown in Figure 4. The deposition rate decreases with increasing temperature. This could be due to an increase of the desorption rate of the DTBS at the substrate surface. The index of refraction was found to increase with the deposition temperature, suggesting that denser films are obtained at higher temperatures. While the film density seems to increase with the deposition temperature, we did not observe a significant change in the Si/C ratio suggesting that the film composition is independent of its density. A deposition temperature that gives a practical deposition rate was found to be about 400 °C. A similar behavior of the refractive index with the substrate temperature was observed earlier for various processes using vapour sources [14,15].

The effect of the microwave power on the deposition rate and refractive index is displayed in Figure 5. A significant change in the deposition rate is observed for a microwave power higher than 500 Watts at fixed gas and DTBS flow rates. The amount of incorporated carbon has also increased with the microwave power. The silicon to carbon ratio could then be varied from about 0.75 to about 1 with increasing the microwave power. This could be due the fact that under higher microwave power the CH_3 radicals are broken further and carbon is

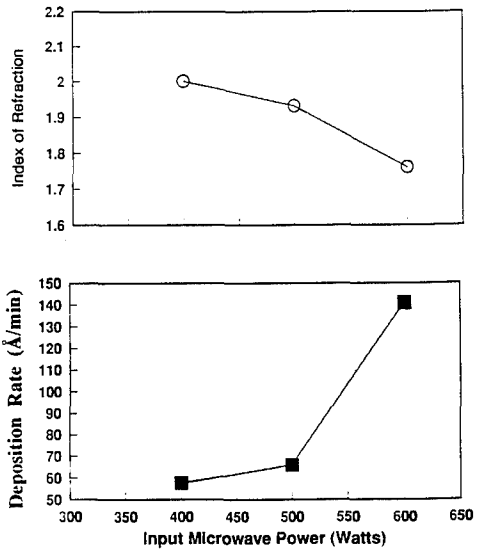

Figure 5: Deposition rate and index of refraction vs. microwave power.

reincorporated into the deposited films. It could also be due to the type of precursors generated from the DTBS molecule being different from those generated at low microwave power . With such precursors the carbon deposition is enhanced relative to the silicon deposition. Studies of the respective plasma characteristics using optical emission spectroscopy are in progress and should help to clarify this point.

CONCLUSIONS

We have described first results obtained using DTBS as a silicon-carbon monosource in an ECR-CVD reactor . High quality SiC films can be deposited at a relatively high deposition rate, in excess of 140 Å/min. This high deposition rate is attributed to the direct Si-C bonds in the DTBS molecule. The levels of incorporated carbon from the organic silicon source depend strongly on the processing conditions, leading to many possibilities of controlling the film's composition and optical properties.

ACKNOWLEDGMENTS

This work is supported through grants from the Natural Sciences and Engineering Research Council of Canada (NSERC) and the Ontario Centre for Materials Research (OCMR).

REFERENCES

1. R. F. Davis, J. Vac. Sci. Technol. A, **11**, 829 (1993).
2. N. Bécourt, J. L. Ponthenier, A. M. Papon, C. Janssaud, Physica B, **185**, 79 (1993).
3. S. M. Paasche, T. Toyoma, H. Okamoto, Y. Hamakawa, IEEE Trans. Elect. Dev., **36,** 2895(1989).
4. R. F. Davis, G. Kelner, M. Shur, J. W. Palmour, J. A. Edmond, Proceed. IEEE, **79**, 677 (1991)
5. Y. Ohshita, Mat. Res. Soc. Symp. Proc., **162**, 433 (1989).
6. Y. L. Chen, J. Bentley, C. Wang, G. Lucovsky, D. M. Maher, Mat. Res. Soc. Symp. Proc. **297**, 711 (1993).
7. T. Futagi, M. Katsuno, N. Ohtani, Y. Ohta, H. Mimura, K. Kawamura, Appl. Phys. Lett., **58**, 2948 (1991).
8. S. Matsuo, Y. Adachi, Jpn. J. Appl. Phys., **21**, L4 (1982).
9. A. V. Zherzdev, V. G. Karpov, A. B. Pevtsov, A. G. Pilatov, N. A. Feoktistov, Sov. Phys. Semicond. **26**, 421 (1992).
10. J. Chen, W. Sah, S. Lee, J. Appl. Phys., **70**, 125 (1991).
11. J. M. Garow, R. A. Levy, M. Bhaskaran, H. J. Boeglin, R. Shalvoy, J. Electrochem. Soc., **140**, 3001 (1993).
12. M. Boudreau, M. Boumerzoug, R. V. Kruzelecky, P. Mascher, P. E. Jessop, D. A Thompson, Can. J. Phys. **70**, 1104 (1992).
13. M. Boudreau, M. Boumerzoug, R. V. Kruzelecky, P. Mascher, P. E. Jessop, D. A Thompson, Mat. Res. Soc. Symp. Proc. **300**, 183 (1993).
14. C. Bourreau, Y. Catherine, P. Garcia, Mater. Sci. Eng. A, **139**, 376 (1991).
15. B. L. Chin, E. P. Van den Ven, Solid State Technol., **31**, 119 (1988).

PROCESS ANALYSIS OF AP-CVD OF SILICON CARBIDE

K.ROTTNER AND R.HELBIG
UNIVERSITY OF ERLANGEN, INSTITUTE OF APPLIED PHYSICS, GERMANY

Abstract

The growth of SiC epilayers by atmospheric pressure CVD (AP-CVD) is influenced by many chemical gas phase reactions and transport phenomena, and is difficult to study directly due to the high growth temperatures (up to 2100 K). To grow epilayers of good quality, it is necessary to control the silicon and carbon supply, each affected by different mechanisms. The use of graphite as the susceptor material causes a remarkable change in the carbon balance due to reactions between the graphite and the hydrogen carrier gas. This graphite-hydrogen reaction enriches the gas phase with carbon and above a certain critical temperature it is impossible to control the Si:C-ratio in the gas phase by a variation of the carbon containing input gas. The silicon supply is usually treated as transport through a stagnant layer in the gas phase determined by the transport properties of the carrier gas and the temperature gradient in the reactor. A numerical solution of the flow-equations in the reactor shows that the flow characteristics and temperature gradients in the reactor are hardly affected by the gas flow velocity.

Introduction

SiC is rapidly becoming the semiconductor material of choice for high temperature and high power electronic devices. The growth of epitaxial layers by CVD is a key step for electronic device development. The high temperatures of about 1600°C, necessary to grow α-SiC layers in a reasonable quality, make it difficult to gain insight into the physical and chemical processes responsible for the growth. Lack of experimental methods implies that the process can best be analysed by numerical studies of fluid dynamics and reaction kinetics.

The first step is to determine the influence of the reactor design on the deposition process, which involves the temperature and gas flow dynamics in the reactor tube.

Another important factor is the stoichiometry of the gas phase necessary to grow stoichiometric single crystalline epilayers.

The epitaxial growth is only one technological step in manufacturing electronics, so one of the important aspects of theoretical and experimental work in the field of crystal growth is the performance and properties. The simplest device structure necessary for nearly all electronic applications is the pn junction. Mesa pn diodes were fabricated and the results of current voltage measurements were compared with those reported by other groups.

Experiment

The CVD-system we used is nearly identical to most of the horizontal systems used by other groups. The material source gases silane and propane are diluted in hydrogen carrier gas with a $1{:}10^4$ mixture. The standard gas flow rates are 3 slm of hydrogen, 0.5 sccm of silane and for

Mat. Res. Soc. Symp. Proc. Vol. 339. ©1994 Materials Research Society

propane 0.3 sccm. The 6H-SiC substrates (2° off axis mod. Lely wafers) are grown by a sublimation process by the material research group at Siemens AG, Erlangen[1] and are placed on a wedge-shaped inductive heated graphite susceptor. The reactor is a water cooled horizontal quartz tube with an inner diameter of 2 inches [2].

The device structure for the mesa diodes is p^+-n^- on n^+-substrate (Fig.1). The donor and acceptor impurities are aluminum and nitrogen, the doping concentrations are $N_A=10^{18}$ cm^{-3}, $N_D=10^{16}$ cm^{-3} and $N_D=5\cdot10^{17}$ cm^{-3}, respectively. Each epilayer is 2μm thick. Electrical passivation of the mesa surface was achieved by dipping the sample in silicone oil.

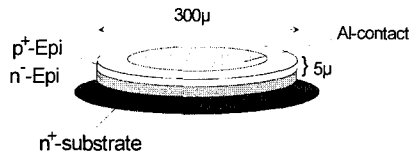

Fig.1
Mesa structure schematically.

Results and Discussion

A. Numerical simulation of gas flow and temperature distribution

To learn about the fluid mechanics in the reactor, the transport equations of mass and heat transfer were solved numerically by a finite elements method multigrid solver[3]. The reactor geometry was analysed using a two dimensional non-orthogonal grid consisting of different blocks describing the thermal properties of the reactor materials (i.e. quartz and graphite). Heat transfer by radiation was considered by the calculation of "view-factors". For the gas transport properties the small silane and propane concentrations (one part in 10^4) where neglected and only the hydrogen considered.

The computed stream lines and isotherms are shown in Fig.2 a). The used parameters are the same as our standard growth parameters: T = 1800K and 2.5 cm/s gas flow velocity at the inlet. As shown the temperature gradient is extremely high at the leading edge of the susceptor. Within a few millimetres the gas temperature increases from 300 K to 1600 K with a corresponding rapid expansion of the gas volume. It can be seen that both behind and in front of the susceptor there are strong recirculations due to convection, which causes a lower temperature gradient in the upper part of the reactor.

In addition, in the region in front of the susceptor these recirculations form a gas buffer due to the small amount of gas exchanged between the circulation currents in the upper part of the tube and the remaining gas stream in the lower part.

This gas flow recirculation must be eliminated in order to grow layers with sharp doping profiles without an interruption of the growth process. We have studied variations of both geometry and gas flow to determine the optimum conditions to avoid these effects. The first attempt was to increase the gas flow velocity to make the forced convection term dominating. The computed stream lines and isotherms for higher carrier gas flow rates are shown in Fig.2b).

The isotherms show a strong increase of the temperature gradient in the gas phase above the susceptor and begins to form of a 'cold finger'. Another way to avoid circulations is to make the reactor smaller. We computed a scaled down geometry without changing the gas flow velocity of 2.5 cm/s. The result is given in Fig.2c). The velocity profile above the susceptor is not affected by the scaling, due to the linear dependence of the flow equations on the length. However, the velocity gradient is inversely scaled. At a scaling of 1:4 the circulations begin to

disappear. The isotherms also change: they get more elliptical and symmetrical at the middle of the susceptor. In addition the temperature gradient increases in the entire reactor.

B Analysis of the carbon balance

The stoichiometry of the gas phase is reported to have a strong influence on the quality and the morphology of the grown epilayer. The reported growth dependence on the input gas flow rates is not consistent. Our own results, and those of some other groups show a linear increase of the growth rate with the silane flow rate, but no variation with the carbon containing input gas rate[4]. Minagwa et al[5] (using Ta-susceptors) report opposite results: variation of the growth rate only with the propane flow rate, but not with the silane flow. For some intermediate cases Kimoto et al[6] (using SiC-coated susceptors) found a strong dependence on the C:Si-ratio of the input gases. These three different results need to be explained. Since we used graphite as the susceptor, we studied the effect of this material in the reaction system. The graphite can react with the hydrogen to supply hydrocarbons with the dissociation of hydrogen being the limiting step in the reaction. The production rate of hydrocarbons and the equilibrium partial pressures of the formed species are given by Clarke[7] and Duff[8].

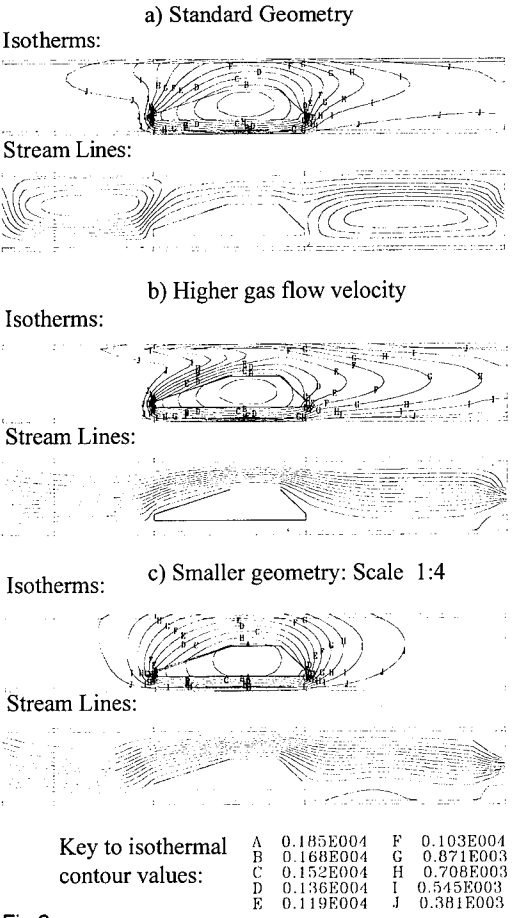

Fig.2
Computed isothermes and stream lines for 1800 K susceptor temperature.
a) standard parameters 2.5 cm/s gas flow vel.
b)12.5 cm/s gas flow velocity
c) Scaled geometry: 25% of original dimensions

Due to the porosity of the graphite the effective area of a susceptor is much larger than the geometric one. We assumed the susceptor surface to be 10 cm² geometric and 100 cm² effective. The results of the numerical calculation for the carbon supply by different species is shown in Fig.3. By assuming that all emitted hydrocarbons mix in the whole reactor cross section and that they are allowed to reach equilibrium conditions and composition, it can be seen that the entire rate of emission of hydrocarbons exceeds at relative low temperatures the input carbon concentration determined by the propane gas flow rate of 0.3 sccm. The dominant species is up

to 2000 K methane, above 2000K acetylene is the molecule with the highest production rate. The radicals CH_2 and C_2H are the next most abundant species.

The critical temperature T_c can be defined by setting the emitted hydrocarbon rate equal to the molar flow rate of the carbon containing input gas, assuming again that all hydrocarbons can mix uniformly in the reactor cross section. The result of this calculation is shown in Fig.4 for an input carbon flow rate of $5 \cdot 10^{-7}$ moles/sec assuming 0.3 sccm propane. It can be seen that at our growth conditions the system is well within the graphite dominated region. To achieve growth independent of the graphite hydrogen reactions without changing the susceptor material, we had to use a susceptor with a geometric area about 1 cm².

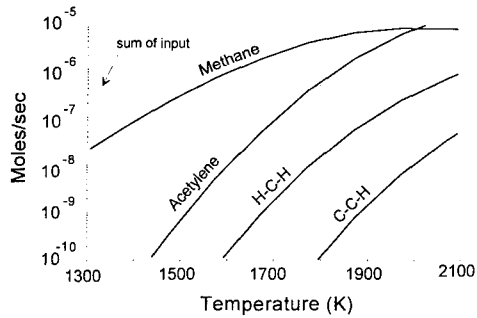

Fig.3
Molar emission rate of hydrocarbons from graphite hydrogen reactions. Equilibrium composition of most abundant species.

The variations of reactor geometry described in section A have different effects on the carbon balance: When enlarging the gas flow rate of hydrogen the carbon flow rate must be increased, to maintain a constant partial pressure of carbon but T_c increases. When scaling down the reactor geometry while keeping constant the gas flow velocity, the susceptor area and the gas flow rate decrease with the square of the scaling factor. On the other hand, the mixing of the hydrocarbons becomes faster and the estimation for T_c becomes more realistic.

The fact that there is a strong influence of the graphite on the growth conditions shows that the reported results of those groups using graphite susceptors cannot be compared to the results of experiments done by groups using metal as the susceptor material. The results of growth experiments using SiC-coated susceptors[6] show differences to that reached by pure graphite and metal[5] as susceptor material. A further conclusion is, that the SiC-ratio in the gas phase is not a factor limiting monocrystalline layer growth as suggested by Harris[9]. We did growth experiments up to 2100 K and found smooth monocrystalline layers could be grown, even at this temperature the excess of carbon is nearly one order of magnitude. This large amount of hydrocarbons compared to the propane produced by the uncoated graphite causes the gas phase to get independent of the input carbon concentration.

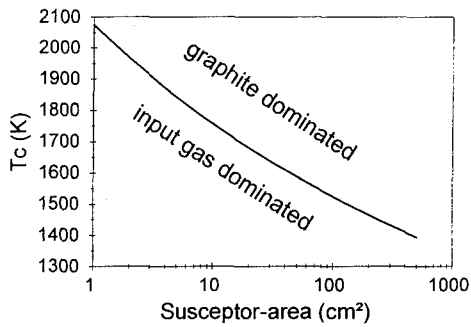

Fig.4
Critical susceptor temperature versus the effective susceptor area. Above T_c the gas phase is independent of the input hydrocarbon and dominated by the graphite reactions.

The thermodynamical calculations done by Allendorf[10] show that when considering the sticking coefficients the more stable molecules, like methane, contribute less to the growth process than reactive radicals with lower partial pressures but high sticking coefficients.

C. Device performance: Characteristics of pn-diodes.

The mesa diodes where manufactured as described in the introduction. We determined the current voltage characteristics in the temperature range between 300 K and 900K. The J-V-

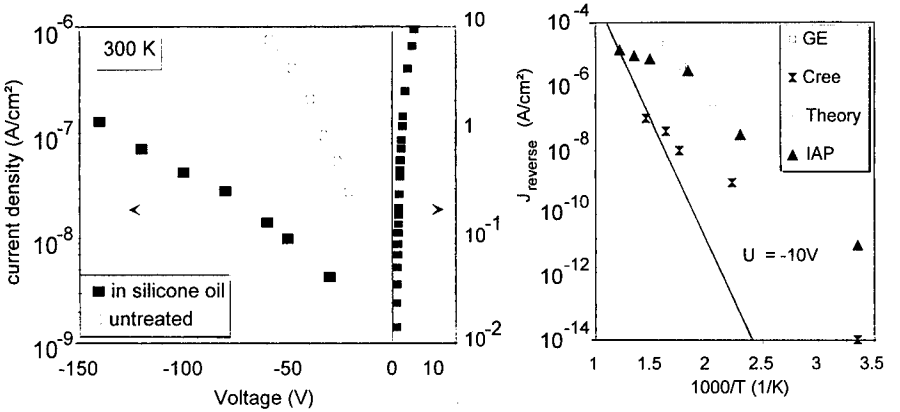

Fig.5 (a) (b)

a) J-V Characteristics of the 6H-mesa diode. Reverse current measured with silicone oil and without any passivation. The forward current is unaffected by the passivation material.
b) Temperature dependence of reverse current density at bias voltage 10 V. The comparison between our sample and samples of other groups show, that at room temperature the theoretical current is not reached, but at higher temperatures.

curve is shown in Fig.5a) with silicone oil used for surface passivation (■) and without (o).

The results achieved without silicon oil show the strong influence of the surface leakage currents even at low voltages. The use of silicone oil decreases the reverse currents about two orders of magnitude. The curve shows that our diodes can be compared to that reported by Edmond[11]. To reach higher voltages the thickness of the n^--epilayer has to be increased. In the forward direction we reached current densities up to 100 A/cm², but the high currents are limited by the contact resistance which is not optimised for this diode.

The current densities at higher temperatures are shown in Fig. 5b) is comparable to results reported by other groups[12]. The theoretical I-V curve has been calculated by Ruff[13]. All diodes exceed at room temperature the theoretical value of the reverse current density be some orders of magnitude demonstrating the influence of surface or other technological defects. At higher temperatures the theoretical values are reached. Certainly the main effect is the leakage current at the surface of the pn-junction. As shown in Fig. 5a) the dipping of the diode in silicon oil decreases strongly the leakage current. Silicone oil is certainly not the perfect passivation, more improvement could be achieved be "turning off" the surface currents when using better passivation materials.

Conclusions

We have studied numerically the gas flow and temperature parameters in a AP-CVD reactor. At standard growth conditions there are strong recirculations due to free convection in front of the susceptor which acts as gas buffer, making it impossible to grow sharp doping profiles. By increasing the gas flow velocity these recirculations can be eliminated, but the formation of a cold finger is evident. Making the whole geometry smaller terminates the recirculations but enlarges the temperature and gas flow velocity gradients and reduces the area of the susceptor where the substrate can be placed. The best way to avoid these difficulties seems to be the mixture of both approaches. Our calculations predict that a reactor diameter of 25 mm and a gas flow velocity of 5 cm/s should be the best way to reach the goal.

The gas phase composition is hardly affected by the use of graphite as susceptor material for temperatures above 1500K. In our experiments the silicon supply is found to be the limiting growth factor and the hydrocarbons are always present in excess quantities. At temperatures below 2000 K the major carbon species is methane which is not affected by the hydrocarbon species selected as the input gas.

The prepared mesa diodes show good performance in current voltage characteristics, but the results point out that even at low bias voltages the leakage current is mainly due to surface effects. This shows the need of suitable passivation even at low voltages and of better substrate material with lower defect densities to manufacture larger diodes and so decrease the surface effects.

Acknowledgement

We like to thank J. Kabs for I-V-measurements, L. Kadinski (Lehrstuhl für Strömungsmechanik, Erlangen) for supporting the numerical simulations and Siemens AG (ZFE Erlangen) for financial support and the device processing.

REFERENCES

[1] G. Ziegler, P. Lanig, D. Theis and D. Weyrich, *IEEE Trans. Elecon. Devices* **30** (1983) p. 277

[2] S.Karmann, W. Suttrop, A. Schöner, M. Schadt, C. Haberstroh, F. Engelbrecht, R. Helbig, G. Pensl, R.A. Stein, S. Leibenzeder, *J. Appl. Phys.* **72** (1992) p. 5437

[3] F. Durst, L. Kadinski, M. Peric, M. Schäfer, *J. Cryst. Growth*, **125** (1992) p. 612

[4] S. Karmann, *PhD-thesis*, Erlangen (1992)

[5] S. Minagwa, H.C. Gatos, *Jpn. J. Appl. Phys.***10** (1971), p.1680

[6] T. Kimoto, S. Nishino, W.S. Yoo, H. Matsunami, *J. Appl. Phys.* **73** (1993) p. 726

[7] J.T. Clarke and B.R. Fox, *J. Chem. Phys.* **46** (1967) p.827

[8] R.E. Duff and S.H Bauer, *J. Chem. Phys.* **36** (1962) p.1745

[9] J.M. Harris, H.C. Gatos, A.F. Witt, *J. Electrochem. Soc.*: Solid State Science **2** (1971) p. 338

[10] M.D. Allendorf, *J. Electrochem. Soc.*: Solid State Science, **140**, (1993) p.747

[11] J.A. Edmond, D.G. Waltz, S. Brueckner, H.S. Kong, J.W. Palmour, C.H. Carter, Jr., *Proc 1st Int. High Temperature Electronic Conf.*, Albuquerque, New Mexico 1992, p. 500

[12] W.J. Choyke, G. Pensl, *Physikal. Blaetter* **47** (1991), p. 212

[13] M. Ruff, accepted for publication in *Proc. IEEE, Electron. devices.*

DEPOSITION OF EPITAXIALLY ORIENTED FILMS OF CUBIC SiC ON SILICON BY LASER ABLATION OF ELEMENTAL TARGETS.

L. Rimai, R. Ager, W. H. Weber, J. Hangas and B. D. Poindexter.
Ford Research Laboratory, P.O.Box 2053 MD3028, Dearborn MI48121-2053

ABSTRACT

Silicon carbide films are grown epitaxially on crystalline silicon substrates heated above 1000 °C, by laser ablation of pure carbon targets to thicknesses between 300 and 400 nm. These films grow on top of the silicon substrate from the carbon in the ablation plume and from the silicon of the substrate. By using a method of alternate ablation of a pure carbon and a pure silicon target, similar epitaxial films can be grown to thicknesses in excess of 1 μm with part of the silicon being supplied by the ablation plume of the silicon target.

INTRODUCTION

The most frequently used method for the growth of crystalline SiC films is that of Chemical Vapor Deposition (CVD) onto a heated Si wafer, from a stream of carbon and silicon containing molecules. These molecules also contain hydrogen, and in addition the depositions are usually carried out in a hydrogen atmosphere. Often the process is initiated with a carbonization step, where a thin SiC layer (2 to 30 nm) is grown by reacting at high temperature the hydrocarbon with the Si substrate.[1-4] This "buffer" layer is epitaxially aligned SiC, at least under certain conditions, and its growth induces a characteristic morphology to the underlying Si surface.[4-7] Crystalline SiC films can be grown on Si wafers by pulsed laser ablation of a ceramic SiC target,[8-10] and under suitable conditions these films exhibit substantial degree of epitaxial orientation.[9,10] One disadvantage of this procedure is that ceramic SiC targets usually contain additives needed for their preparation, which will get transferred as impurities to the growing film. Also, the ablation rate of SiC is relatively low, thereby yielding slow film growth when used as targets. Here it is shown that epitaxial films of SiC can be deposited on Si wafers, by laser ablation of targets of pure elemental materials, either C alone, the films growing by direct reaction of the plume carbon with the Si substrate, or, Si and C ablated alternately. The ablation rate of these targets is higher than that of the ceramic SiC and correspondingly the film growth rate is also faster.

FILM PREPARATION

The depositions are carried out in a vacuum system of 5×10^{-6} Torr base pressure. The excimer laser beam impinges onto the target at an angle adjustable between 20 and 45°, where it illuminates a rectangular area on the order of 0.2 cm^2. Surface pitting is minimized by scanning the illuminated spot in a predetermined pattern generated by computer control of the angular position of a near 45° deflection mirror ahead of the laser beam's focusing lens. When Si and C are used, the relative amounts of material ablated from each target are controlled by an appropriate scanning pattern. The plume of atoms and ions emerges in a cone normal to the

Mat. Res. Soc. Symp. Proc. Vol. 339. ©1994 Materials Research Society

target, and impinges onto the heated substrate located about 7 cm away. The laser wavelength is 351 nm, pulsed at rates in the range 5-20 Hz. The 20 ns long 200 to 350 mJ pulses yield a fluence of 1 to 3 J/cm^2 at the target.

The substrate ([100] or [111] oriented Si wafer) is heated to between 1000 and 1200° C by a resistive heater. The flux distribution in the plume is sharply peaked in the forward direction causing non-uniform deposition over the substrate. Increased uniformity, i.e., a uniform film over larger areas of the substrate, is obtained by a target scanning procedure, as the plume moves with respect to the substrate. For sufficiently low pressure during the deposition (large mean free path) the substrate to target distance can also be increased. The front surface of the substrate can be covered by a patterned Ta contact mask to obtain a correspondingly patterned SiC film. The depositions performed with these masks clearly showed that the SiC film is formed on top of the Si substrate, and the gross average film deposition rate can be estimated by profilometer measurements of the edge thickness as a function of deposition time. Figures 1 and 2 summarize the results of growth rate on [001] Si wafers, for a carbon target only and alternate 1:1 Si and C targets, respectively.

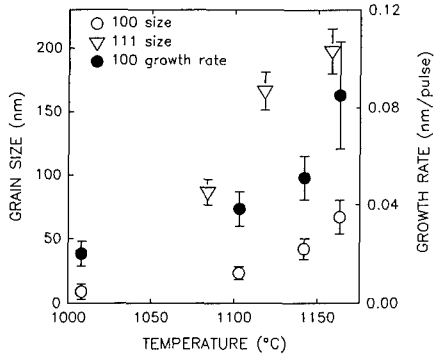

Figure 1. XRD derived grain size and average growth rate for 350 mJ pulses, of SiC deposited from a C target on Si substrates oriented as indicated.

The SiC films deposited with a C target alone grow as stoichiometric SiC on top of the Si wafer, for thicknesses somewhat over 300 nm. Beyond this thickness, a carbon layer starts to form over the SiC film. This is clearly shown by Raman spectroscopy (see below) and is also confirmed by preliminary Auger profiling.

With the use of alternate Si and C targets the maximum film thickness limitation of 300 nm is removed. SiC films were grown with thickness up to 1μm. For the data in Fig. 2, the time spent on each target was 2 s, which corresponds to 40 laser pulses, or about 4 nm average deposition of each element at the fastest growth rate. The angle of incidence of the plume onto the substrate seems to affect the average deposition rate much more than the expected geometric effect, as indicated by the data in Fig. 2.

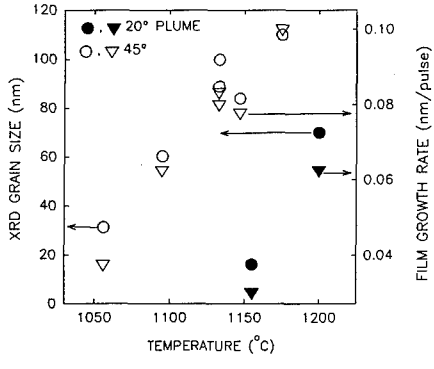

Figure 2. SiC deposited from alternating C and Si targets, at two plume angles, on [001] Si. Circles: grain size. Triangles: growth rate.

FILM CHARACTERIZATION

Figure 3 shows examples of Θ-2Θ X-ray diffraction scans, which were used to examine the crystalline nature of the films. These scans exhibit the diffraction peaks from lattice

spacings normal to the film plane.[10] The SiC films on [100] Si wafers show strong peaks at spacings of 2.18 and 1.0893 Å (2Θ = 41.5 and 89.96°, respectively) which correspond to the 200 and 400 reflections of crystalline cubic (3C) SiC. On some of the films we also observe an extremely weak peak at 2Θ = 35.6°. This peak corresponds to the 2.52 Å (111) spacing of SiC, and it would be the strongest diffraction peak in a polycrystalline sample. These results, illustrated by the bottom trace of Fig. 3, indicate that this film consists essentially of 3C SiC oriented with its {100} planes parallel to those of the Si substrate. From the small relative intensity of the 111 peak we estimate the misoriented fraction of the SiC to be at most a few percent. The top trace of Fig. 3 shows diffraction bands of a film deposited under similar conditions on a [111] Si wafer, where the very strong peak at 2Θ=35.6° (spacing of 2.52Å corresponding to (111) planes parallel to film) again indicates alignment with the substrate.

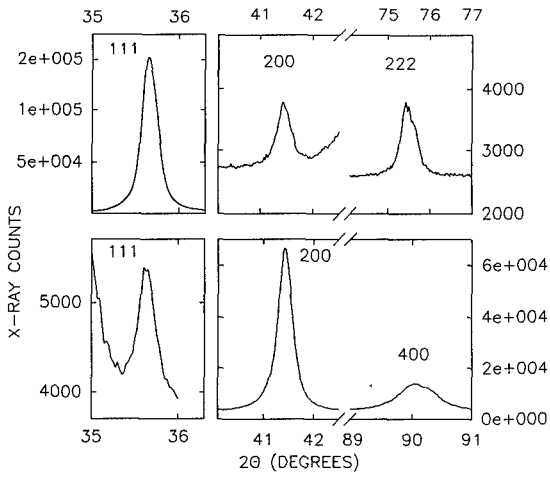

Figure 3. X-ray diffraction bands. Bottom: [001] substrate. Top: [111] substrate. Note the reversal in the (200)/(111) band intensity ratio between the two substrates.

The shape of the diffraction bands, after deconvolution from the instrumental bandshape can be analyzed to yield an average crystallite dimension along the film normal.[10] This grain size is a strong function of the deposition temperature as shown in Figs. 1 and 2, for films deposited under similar conditions (20 Hz, 4 minutes). There are substantial variations in XRD linewidth, even if substrate temperature, pulse energy and repetition rate, and total deposition time are kept the same. These fluctuations are larger for the films from C targets alone than for those deposited from alternate targets, as indicated in the error bars of Fig. 1, where the data correspond to results from a large number of depositions at each temperature. These fluctuations are possibly due to variations in the energy flux distribution across the laser beam, even if the total pulse energy is constant. The crystallite dimensions are smaller than the thickness of the films, but the orientation of the grains must be generally close to that of the substrate, as indicated by the weakness of the 111 peak for the [100] films and the 200 peak for the [111] films.

Confirmation of the crystallographic alignment of the [100] films was obtained from recording of selected area electron diffraction (SAED) patterns. A planar section of SiC film on [001] substrate was core drilled from the wafer, ground and dimpled from the Si side to less than 25 μm thick at center and then ion milled until perforated. Figure 4A is the SAED pattern obtained with a JEOL 2000FX AEM at 200 keV. It shows that the {200} and {220} planes from the cubic SiC are parallel to the corresponding planes of the Si substrate, indicating mostly epitaxial grains. The extra reflections, particularly from {111} planes indicate the presence of twins. The grains are columnar with width ranging from 50 to 150 nm, as shown in Fig. 4B,

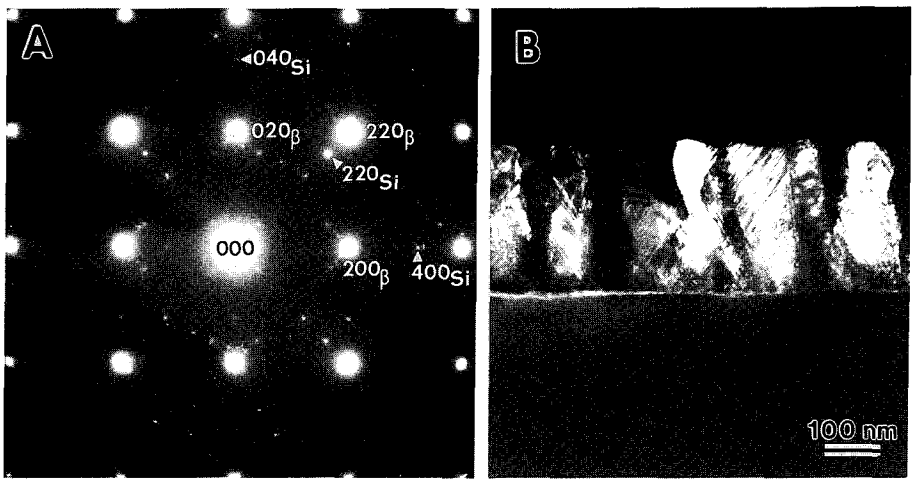

Figure 4. A: Planar section SAED of a SiC film on [001] Si showing epitaxial relation between film and substrate. B: Dark Field TEM micrograph of a cross section of the same film showing columnar grains with stacking faults.

which is the dark field TEM micrograph of a cross section of the film. Stacking faults are visible within the grains. This SiC film was 260 nm thick.

It might be expected that films deposited using only the C target would contain some graphitic or amorphous carbon material. It is found that for deposition temperatures between 1010 and 1200° C for the first 6000 to 8000 pulses (300±50 mJ/pulse) there is no observable carbon overlayer. However, at lower deposition temperatures or for longer deposition a carbon overlayer starts to form. As the number of pulses is increased beyond 8000, the integrated intensity of the SiC XRD peak tends to saturate with respect to the increase of the edge thickness of the film and eventually a dark carbon layer becomes evident on inspection. Films deposited with the dual target method, in the same temperature range, do not show any sign of carbon even up to 1μm in thickness.

Raman spectra are quite sensitive to the presence of carbon.[10,11] The Raman intensities for graphitic (sp^2) carbon bonds are expected to be substantially stronger than those for either sp^3 carbon or SiC bonds, and at the substrate temperatures here the carbon is expected to be graphitic.[12-13] Figure 5 shows Raman spectra of two [001] films, deposited from a single carbon target, with 20000 (spectra C and E) and 5000 pulses (spectra A and D). The intensities of the SiC zone center transverse optic (TO) band near 790 cm^{-1} are within a factor of 2 in the two films as are the integrated X-ray intensities of the SiC 200 and 400 bands. The Raman intensity of the graphitic bands at 1350 and 1580 cm^{-1} relative to that of the SiC TO band is very large in spectra C, E and zero in spectra A, D. The latter is the case in all the films deposited with less than about 8000 pulses from carbon alone (with maximum edge thicknesses less than 400 nm) and in all spectra of films deposited from the two alternating targets. Figure 6 shows

Raman spectra from a SiC film deposited on [001] Si from alternate targets, the top spectrum being that of the film on the substrate, as are spectra A and C of Fig. 5. These spectra show clear evidence of the presence of Si, by the presence of the strong Si zone center fundamental near 520 cm^{-1} (Fig. 6, top spectrum) and the broad second order Si band near 950 cm^{-1} especially obvious in spectrum C of Fig. 5. The bottom spectrum of Fig. 6 as well as spectrum B of Fig. 5 are taken from small delaminated flakes of the corresponding films, and show no significant evidence of residual Si, within the deposited films indicating that they consist, to good approximation, of stoichiometric SiC. The observed Raman frequency shifts between the film on the substrate and the delaminated film, and those between these pulsed laser deposited films, the thick CVD films and the bulk crystals or thick films might be due to the presence of different strain fields.[14]

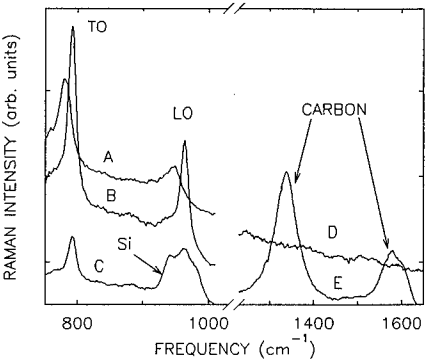

Figure 5. Raman spectra of two of the SiC films deposited from a C target at 1100°C. Traces B, D and A are from the same film deposited with 5000 pulses, A taken from a small delaminated piece. C and E are from a film deposited with 20000 pulses

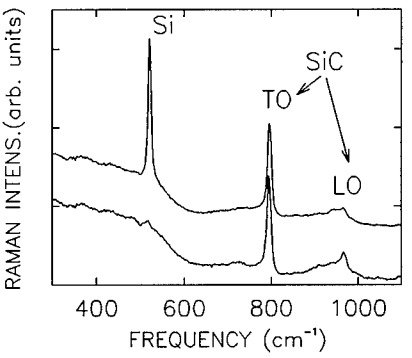

Figure 6. Raman spectra of SiC film on [001] Si deposited from alternating Si and C targets. Top: Film on substrate. Bottom: Delaminated piece of same film. The spectra are displaced vertically for clarity.

The intensities of the SiC TO band and the zone center longitudinal optic (LO) band are comparable to those of the corresponding bands for SiC films deposited on Si by ablating stoichiometric SiC targets.[9,10] All these films show a strong TO band and a weak, often broadened LO band, at times obscured by the Si substrate's second order Raman band near 950 cm^{-1}. The breadth and weakness of the LO bands might be related to the large carrier concentration in these films, probably due to the presence of a large concentration of electrically active defects and to irregularities in the structure of the Si/SiC interface.

CONCLUDING COMMENTS

The results presented above show that crystalline SiC films up to a few hundered nm in thickness can be deposited on top of [100] and [111] Si wafers in a vacuum chamber, from a plume generated by laser ablation from a pure carbon target. If during deposition the substrate is held at a sufficiently high temperature, XRD indicates that the SiC film is aligned with the substrate crystallographic orientation, but that the crystallite dimensions along the film normal are somewhat smaller than the film thickness. The rate of deposition of the SiC film as well as the

crystallite dimension increase with temperature. However at least for substrate temperatures up to 1200° C the maximum SiC film thickness that can be achieved is around 400 nm. Beyond this thickness the film is covered by an overlayer of graphitic carbon. The growth of such SiC films implies the existence of two processes: a reaction between the carbon in the plume and the Si in the substrate to form carbidic bonds, and the diffusion of either Si or C or both through a finite thickness of SiC even at such relatively low temperatures as 1100° C. It is also shown that this maximum film thickness limitation can be removed by using an alternatingly ablated dual target system of carbon and silicon targets with no deterioration of the crystallographic properties of the film. In this manner SiC films can be grown to thickness in excess of 1μm. In all cases the films consist essentially of stoichiometric SiC with no significant excess of free carbon or silicon.

REFERENCES

1. J. A. Powell and L. G. Matus in *Amorphous and Crystalline Silicon Carbide and Related Materials*, Springer Proceedings in Physics, edited by G. L. Harris and C. Y.-W. Yang (Springer, Berlin, 1989), Vol. 34, p. 2.
2. L. G. Matus and J. A. Powell in *Amorphous and Crystalline Silicon Carbide and Related Materials*, Springer Proceedings in Physics, edited by G. L. Harris and C. Y.-W. Yang (Springer, Berlin, 1989), Vol. 34, p. 40.
3. S. Nishino and J. Saraie in *Amorphous and Crystalline Silicon Carbide and Related Materials*, Springer Proceedings in Physics, edited by G. L. Harris and C. Y.-W. Yang (Springer, Berlin, 1989), Vol. 34, p. 45.
4. P. Liaw and R. F. Davis, J. Electrochem. Soc. **132**, 642 (1985).
5. T. T. Cheng, P. Pirouz and J. A. Powell, in *Chemistry and Defects in Semiconductor Heterostructures*, edited by M. Kawabe, T. D. Sands, E. R. Weber and R. S. Williams, Mat. Res. Soc. Symp. Proc. Vol.148, PA, (1989) p.229.
6. A. J. Steckl and J. P. Li, IEEE Trans. on Electron Devices,**39**, 64, (1992).
7. A. J. Steckl and J. P. Li in *Wide Band Gap Semiconductors*, edited by T. D. Moustakas, J. I. Pankove and Y. Hamakawa, Mat. Res Soc. Symp. Proc. Vol 242, (1992), p. 537.
8. M. Balooch, R. J. Tench, W. J. Sielhous, M. J. Allen, A. L. Connor and D. R. Olander, Appl. Phys. Lett. **57**, 1540 (1990).
9. L. Rimai, R. Ager, E. M. Logothetis, W. H. Weber and J. Hangas, Appl. Phys. Lett. **59**, 2266 (1991).
10. L. Rimai, R. Ager, E. M. Logothetis, W. H. Weber and J. Hangas in *Wide Band Gap Semiconductors*, edited by T. D. Moustakas, J. I. Pankove and Y. Hamakawa, Mat. Res Soc. Symp. Proc. Vol 242, (1992), p. 549.
11. F. Tuinstra and J. L. Koenig, J. Chem. Phys. **53**, 1126 (1970).
12. H. Richter, Z. P. Wang and L. Ley, Solid State Commun. **39**, 625 (1981).
13. D. S. Knight and W. B. White, J. Mater. Res. **4**, 385 (1989).
14. Z. C. Feng, W. J. Choyke and J. A. Powell, J. Appl. Phys. **64**, 6827 (1988).

STACKING FAULT ENERGY CALCULATIONS IN 6H- AND 15R-SiC

F.R. CHIEN*, S.R. NUTT** AND W.S. YOO***
*Division of Engineering, Brown University, Providence, RI 02912
**Department of Materials Science, University of Southern California, Los Angeles, CA 90089
***Advanced Technology Materials, Inc., Danbury, CT 06810

ABSTRACT

As-grown SiC single crystals and as-deposited SiC epilayers often exhibit stacking faults. The most probable fault configurations that occur in 6H- or 15R-SiC crystals are deduced from calculations of the stacking fault energies using a modified Ising model with the Ising parameters taken from earlier *ab initio* calculations. In this study, experimental TEM observations reveal stacking fault configurations in 6H- and 15R-SiC, and the observed configurations are compared with calculated stacking fault energies.

INTRODUCTION

Silicon carbide (SiC) is well known for polytypism, or one-dimensional polymorphism,[1] and more than 200 polytypes have been documented. One common polytype is β-SiC, a zinc blende structure with cubic (C) symmetry. All other polytypes are denoted as α-SiC and occur in hexagonal (H) or rhombohedral (R) structures. Several nomenclatures have been used to describe these polytypes. For example, in Ramsdell notation,[2] simple polytypes are labeled 4H, 6H, 15R, 3C .... etc., while in the Zhdanov notation[3] these same polytypes denoted by (22), (33), $(32)_3$ and (∞), respectively. The most abundant naturally occurring SiC polytype is the (33) structure, followed by the (22) and $(32)_3$ structures, suggesting that these are the most stable polytypes.[4]

A number of theories have been advanced to explain this curious behavior, but so far nearly all of these have been based on non-equilibrium mechanisms such as crystal growth from dislocations[5]. However, there is considerable evidence to suggest that polytypism is, at least partially, an equilibrium phenomenon. In this paper, the essential features follow from the equilibrium properties are described by a modified ANNNI (Axial Next Nearest Neighbor Ising) model, an inter-layer interaction model proposed by Cheng, Needs and Heine.[6,7]

The present paper investigates the most probable fault configurations in SiC (33) and $(32)_3$ polytypes. Calculations of stacking fault energies (SFEs) in several possible stacking fault configurations are carried out based on a model of inter-layer interactions, and direct experimental observations of stacking faults by TEM are compared with the calculated SFEs. In this study, we show that (33) and $(32)_3$ SiC polytypes exhibit low SFEs, and thus SiC single crystals generally include stacking faults.

REVIEW OF ENERGY EVALUATION IN SiC POLYTYPES

The growth of SiC polytypes can be envisioned as stacking Si-C double layers on top of one another in various sequences to achieve growth in the [111] or [0001] direction. Cheng *et al.*[7] modeled the energy of a polytype in terms of the interaction between Si-C double layers and treated the polytypes as consisting of identical double layers arranged in different stacking sequences. In this treatment, each double layer can be stacked in two different orientations on the layer below it, and the orientation (σ) for the n-th layer is designated by the symbol $\sigma_n = \pm 1$. For example, designation of the common structures (∞), (22), (33) and $(32)_3$ are:

$$\langle 3C \equiv \infty \rangle \quad = \cdots + + + + + + + + \cdots \quad \text{or} \quad \cdots - - - - - - - - \cdots \tag{1a}$$

$$\langle 4H \equiv 2 \rangle \quad = \cdots + + - - + + - - + + - - \cdots \tag{1b}$$

$$\langle 6H \equiv 3 \rangle \quad = \cdots + + + - - - + + + - - - \cdots \tag{1c}$$

$$\langle 15R \equiv 32 \rangle \quad = \cdots + + + - - + + + - - \cdots \text{ or } \cdots - - - + + - - - + + \cdots \tag{1d}$$

Mat. Res. Soc. Symp. Proc. Vol. 339. ©1994 Materials Research Society

where the + (spin up ↑) and – (spin down ↓) indicate the possible orientations of SiC_4 tetrahedra. The total energy (E_{TOT}) for a system of N layers can be written by the Hamiltonian[7-9]

$$E_{TOT} = NE = NE_0 - \frac{1}{2}\sum_{i,n} J_n(\sigma_i\sigma_{i+n} + \sigma_i\sigma_{i-n}) \qquad (2)$$

where $\sigma_i = +1$ or -1 according to whether the layer has spin up or down. The Ising parameters, J_n, are the energies of interaction between n-th neighbor planes, and E_0 is the energy of the crystal without interaction between layers. Note that in the above model, interactions beyond the third nearest layer are neglected, i.e., $J_n = 0$ for $n > 3$.

According to equation (2), the energies (per SiC pair) of four simple polytypes (including up to third neighbor interactions) are

$$\begin{aligned} E_{<\infty>} &= E_0 - J_1 - J_2 - J_3 \\ E_{<2>} &= E_0 + J_2 \\ E_{<3>} &= E_0 - 1/3\, J_1 + 1/3\, J_2 + J_3 \\ E_{<32>} &= E_0 - 1/5\, J_1 + 3/5\, J_2 + 3/5\, J_3 \end{aligned} \qquad (3)$$

At ground state (T = 0 K)

Cheng et al.[7] have investigated, up to the fourth-nearest neighbor, the interaction energies J_1 to J_4 between SiC double layers by calculating the total energies of five SiC polytypes, (11), (22), (33), (∞) and (1122), with norm-conserving pseudopotentials (*ab initio* quantum mechanical calculations of total energies) at T = 0 K. The calculated J_n values (per SiC pair) up to the third-nearest neighbors are listed below.[7]

$$J_1 = 5.41 \text{ meV} \quad J_2 = -3.49 \text{ meV} \quad J_3 = -0.46 \text{ meV} \quad \text{(per SiC pair)}$$

With this approximation, (22) is predicted to be the most stable phase at the ground state.

At higher temperatures

At higher temperatures the Ising parameters $J_1(T)$, $J_2(T)$ and $J_3(T)$ will vary with T. The phonon free energy was calculated by Cheng, Heine and Jones[10] for several silicon carbide polytypes using the calculations of the interatomic displacement-displacement correlation (valence overlap shell model). The three most commonly observed polytypes, i.e., (33), (22) and $(32)_3$, were shown to be thermodynamically stable, with (22) and (33) as the low- and high-temperature phases, respectively, and $(32)_3$ stable at intermediate temperatures. The long-range phonon effect splits the multiphase degeneracy between phases (33) and (22), to which SiC is extremely close at T = 0 K, and it stabilizes $(32)_3$ with a significantly large stability region of 200 ~ 500 K. The transition temperature for (22) to (33) is about 2300 - 2400 K.

STACKING FAULT ENERGY CALCULATIONS

Pandey et al.[11] determined relative SFEs corresponding to different faulted configurations based on the essential pair potential model. Unfortunately, the magnitudes of the SFEs were not available in this work. In the present study, calculations of SFEs in several possible faulted configurations are carried out based on the previously described modified Ising model. For these calculations, it is important to point out that the SFE is a function of temperature. As described before, (33) and $(32)_3$ are stabilized in different temperature ranges. Furthermore, in the temperature range of the $(32)_3$ phase, specific SFEs for the (33) phase may become negative. A negative SFE would provide a driving force for a phase transformation of $(32)_3 \leftrightarrow (33)$.

In the following section, stacking fault energy calculations for the $(32)_3$ and (33) polytypes will be carried out using the following definition[12]

$$\gamma = E_{TOT}(N, \text{defect}) - E_{TOT}(N, \text{perfect}) \qquad (4)$$

in which E_{TOT} indicates the total energy of N layers calculated from a defect and a perfect structure. The energies of the perfect and defect $(32)_3$ and (33) polytypes can be obtained from the energy expression (2). The calculation and the results are described in the next section.

RESULTS AND DISCUSSION

Stacking faults in $(32)_3$

Using the relation for the Ising parameters as a function of temperature derived from Cheng et al.[10], we can find the interaction parameters J_n for $(32)_3$ in the temperature range of maximum stability, i.e., at 2100 K.

$$J_1 = 5.570 \text{ meV} \qquad J_2 = -3.47 \text{ meV} \qquad J_3 = -0.457 \text{ meV} \qquad \text{(per SiC pair)}$$

These values can be used in expression (2) for the total energy of the structure, yielding $E_{<32>} = E_0 - 1/5\, J_1 + 3/5\, J_2 + 3/5\, J_3 = E_0 - 3.470$ meV per SiC pair. This expression will be altered when a defect is introduced into the structure. For example, a possible twin in $(32)_3$ can be expressed as

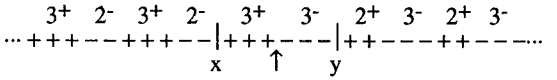

where the arrow indicates the twin plane. Because we only take the third-nearest neighbor into account, the left side of x ($<3^+2^->$ semi-infinite layers) and the right side of y ($<2^+3^->$ semi-infinite layers) are not affected by the disorder between x and y. Therefore, calculation of the energy difference between the 6-layer defect structure and the 6-layer perfect structure is sufficient. Thus,

$$E_{TOT}(6, \text{defect}) = 6E_0 - 2J_1 + 2J_2 + 4J_3 = 6E_0 - 19.91 \text{ meV}$$
$$E_{TOT}(6, \text{perfect}) = 6E_{<23>} = 6E_0 - 20.82 \text{ meV}$$

and

$$\gamma = E_{TOT}(6, \text{defect}) - E_{TOT}(6, \text{perfect}) = 0.91 \text{ meV per SiC pair}$$

An alternative expression for stacking fault energy is

$$\gamma = \frac{\text{stacking fault energy (per SiC pair)}}{\text{atomic area per SiC pair}} \qquad (5)$$

where the effective atomic area per SiC pair on the (111) or (0001) plane is 8.22×10^{-20} m^2/per SiC pair. Therefore, 1 meV per SiC pair corresponds to 1.94 mJ/m^2.

Simple stacking faults in $(32)_3$ can be formed by inserting (extrinsic) or removing (intrinsic) one layer. In addition, twins are also possible in this structure. Some of these configurations and their corresponding SFEs are summarized in Table 1.

Regarding the stacking faults in bulk crystals, the most frequently observed faulted configuration, $(3^+2^-3^+\underline{3}^-3^+2^-)$, is shown in Fig. 1(a). This configuration is represented by (c) in Table 1, and exhibits a minimum SFE. However, in epitaxial 15R films, high-resolution images reveal twins and stacking faults. Twins are often arranged in configuration (a) in Table 1. A typical example of this configuration is shown in Fig. 1(b). In the same image, one of the most frequently observed stacking fault configurations is (g), exhibiting 5 faulted layers expressed as $(3^+2^-) \rightarrow (2^+3^-)$. This type of stacking fault was also frequently observed in bulk crystals. The formation of 5 faulted layers could be related to spiral growth along a giant screw dislocation, or possibly a step flow mechanism[13] involving a 5-layer step such as (3^+2^-) or (2^+3^-). Thus, the number of possible growth faults are limited with the 5-layer step. However, the one-layer band (example (f) in Table 1) is extremely unstable, and the faulted configuration of (1^+4^-), originating from a (3^+2^-) or (2^+3^-) step, was not observed.

Table 1. Possible twins and stacking faults in $(32)_3$. The arrows (↑) indicate the twin planes and underlines indicate bands of disorder in $(32)_3$.

	stacking faults	stacking fault energy (γ)	
(a)	$3^+\ 2^-\ 3^+\ 2^-\ 3^+\ 3^-\ 2^+\ 3^-\ 2^+\ 3^-$ $\cdots+++--+++--\vert+++---\vert++--+++---\cdots$ x ↑ y	0.91 meV	1.77 mJ/m^2
(b)	$3^+\ 2^-\ 3^+\ 2^-\ 3^+\ 2^-\ 2^+\ 3^-\ 2^+\ 3^-$ $\cdots+++--+++--++\vert+--++-\vert--++---\cdots$ x ↑ y	6.03 meV	11.70 mJ/m^2
(c)	$3^+\ 2^-\ 3^+\ 2^-\ 3^+\ 3^-\ 3^+\ 2^-\ 3^+\ 2^-$ $\cdots+++--+++--\vert+++---+++\vert--+++---\cdots$ x y	0.91 meV	1.77 mJ/m^2
(d)	$3^+\ 2^-\ 3^+\ 2^-\ 4^+\ 2^-\ 3^+\ 2^-\ 3^+\ 2^-$ $\cdots+++--++\vert+--++++--+\vert++--+++---\cdots$ x y	7.85 meV	15.23 mJ/m^2
(e)	$3^+\ 2^-\ 3^+\ 2^-\ 2^+\ 2^-\ 3^+\ 2^-\ 3^+\ 2^-$ $\cdots+++--++\vert+--++--+\vert++--+++---\cdots$ x y	6.03 meV	11.70 mJ/m^2
(f)	$3^+\ 2^-\ 3^+\ 2^-\ 3^+\ 1^-\ 3^+\ 2^-\ 3^+\ 2^-$ $\cdots+++--+++--\vert+++-+++\vert--+++---\cdots$ x y	14.47 meV	28.07 mJ/m^2
(g)	$3^+\ 2^-\ 3^+\ 2^-\ 2^+\ 3^-\ 3^+\ 2^-\ 3^+\ 2^-$ $\cdots+++--++\vert+--++---+++\vert--+++---\cdots$ x y	3.47 meV	6.73 mJ/m^2

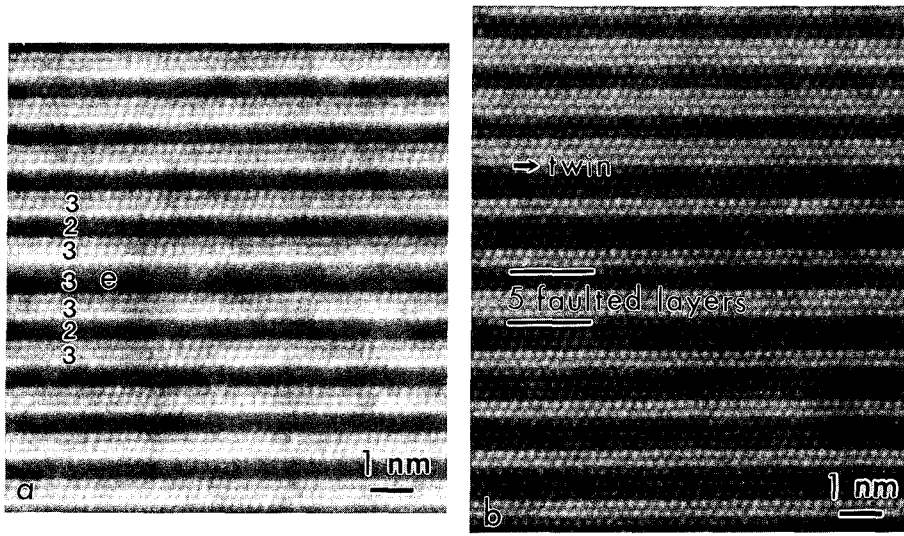

Fig. 1. (a) An extrinsic "e" stacking fault in a bulk $(32)_3$, and (b) twinned and faulted configurations in $(32)_3$ epilayers.

Table 2. Possible stacking faults in (33). The underlines indicate bands of disorder in (33).

	stacking faults	stacking fault energy (γ)	
(a)	$3^+\ 3^-\ 3^+\ 3^-\ 2^+\ 3^-\ 3^+\ 3^-$ $\cdots +++--- \underline{++} ---+++--- \cdots$ x y	0.96 meV	1.86 mJ/m^2
(b)	$3^+\ 3^-\ 3^+\ 3^-\ 4^+\ 3^-\ 3^+\ 3^-$ $\cdots +++--- \underline{++++} ---+++--- \cdots$ x y	1.77 meV	3.43 mJ/m^2
(c)	$3^+\ 3^-\ 3^+\ 3^-\ 1^+\ 3^-\ 3^+\ 3^-$ $\cdots +++--- \underline{+} ---+++--- \cdots$ x y	13.98 meV	27.12 mJ/m^2

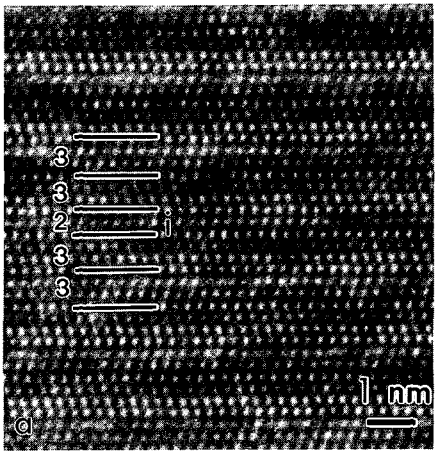

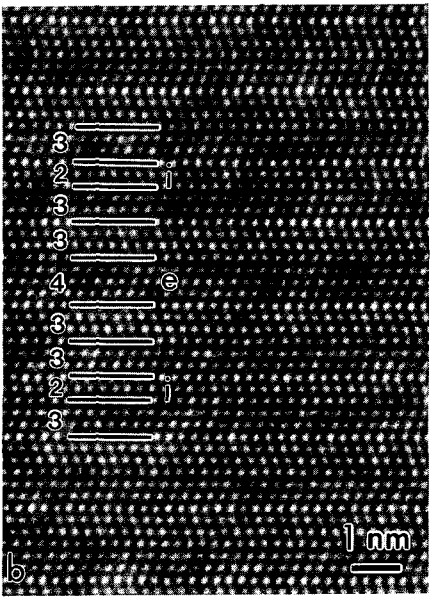

Fig. 2. (a) An intrinsic "i" stacking fault in a bulk (33), and (b) intrinsic "i" and extrinsic "e" stacking faults coexist in (33) epilayers.

Stacking faults in (33)

The structure of (33) is crystallographically symmetric. Unlike the $(32)_3$, (33) does not present twin structures. When (33) is the most stable phase, the interaction parameters J_n are given below (for 2500 K).[10]

$J_1 = 5.65$ meV $\quad J_2 = -3.468$ meV $\quad J_3 = -0.466$ meV $\quad$ (per SiC pair)

Using these values, we find $E_{<3>} = E_0 - 1/3\ J_1 + 1/3\ J_2 + J_3 = E_0 - 3.505$ meV per SiC pair. Possible stacking fault configurations and corresponding stacking fault energies for the (33) structure are listed in Table 2.

The most frequently observed stacking fault configuration in bulk (33) is sequence (a) in Table 2, corresponding to the lowest stacking fault energy. A TEM image of this configuration is shown in Fig. 2(a), where the fault is indicated by "i". However, in epitaxial (33) thin films, the most frequently observed faulted configurations are sequences (a) and (b) in Table 2, corresponding to intrinsic (i) and extrinsic (e) faults, respectively. A TEM image of these structures in a thin film is shown in Fig. 2(b), where "e" and "i" designate the fault types. As discussed in a previous study,[13] epitaxial growth mechanisms may be different from bulk growth. If the substrate surface is intentionally off-cut, creating atomic steps, the step bunching phenomenon (step flow) can dominate the growth and force the epilayer to replicate the stacking structure of the substrate.[13] Thus, the number of layers in the epilayer must be the same as the substrate steps, even if stacking faults take place, e.g., $(3^-3^+3^-3^+3^-3^+)$ in the substrate steps $\rightarrow$ $(3^-4^+3^-3^+2^-3^+)$ stacking fault in the epilayers. Therefore, (33) films exhibit mixed intrinsic (i) and extrinsic (e) faulted configurations, despite the fact that the extrinsic fault has a slightly higher SFE.

CONCLUSIONS

During crystal growth of SiC, the observed stacking fault configurations are ones of minimum or close to minimum energies. However, some of the stacking fault configurations observed in 6H- and 15R-SiC have higher energies, and these are consequences of the particular growth mechanism involved. Temperature is also an important factor affecting the magnitude of stacking fault energy. During crystal growth, temperature fluctuations may sometimes result in negative SFEs, causing a phase transformation to occur. For example, the extrinsic fault of $(3^+2^-3^+3^-3^+2^-)$ in $(32)_3$, (c) in Table 1, exhibits a relatively low stacking fault energy, but the SFE may become negative when the temperature is increased to the stability range of (33). When this happens, a phase transformation from $(32)_3$ to (33) may occur. Negative SFEs in $(32)_3$ can be obtained by using the Ising parameters within the stability region of (33). Similarly, the intrinsic fault of $(3^+3^-3^+2^-3^+3^-)$ in (33) can be stabilized at lower temperatures within the stability range of $(32)_3$. Although phonon contributions can stabilize the $(32)_3$ phase, the energy differences between (33) and $(32)_3$ are extremely small, and thus the control of polytypes is difficult. Small temperature fluctuations and/or low levels of impurity are known to affect SiC polytype formation.

ACKNOWLEDGMENT

The authors (FRC and SRN) are grateful for support from Advanced Technology Materials, Inc., and the Office of Naval Research (contract number N00014-90-J-4051). Helpful discussions with Dr. Rob Phillips of Brown University are gratefully acknowledged.

REFERENCES

1. A.R. Verma and P. Krishna, in Polymorphism and Polytypism in Crystals, (John Wiley, New York, 1966)
2. L.S. Ramsdell, Am. Mineral. **32**, 64 (1947)
3. G.S. Zhdanov, C.R. (Dokl.) Acad. Sci. USSR, **48**, 39 (1945)
4. G.C. Trigunayat and G.K. Chadha, Phys. Stat. Sol. **4**, 9 (1971)
5. D. Pandey and P. Krishna, Prog. Crystal Growth Charact., **7**, 213 (1983)
6. C. Cheng, R.J. Needs, V. Heine and N. Churcher, Europhys. Lett., **3**, 475 (1987)
7. C. Cheng, R. J. Needs and V. Heine, J. Phys. C, **21**, 1049 (1988)
8. J. Yeomans, in Solid State Physics, Vol. 41, edited by H. Ehrenreich and D. Turnbull, Academic Press (1988)
9. G.D. Price and Y. Yeomans, Acta Cryst. **B40**, 448 (1984)
10. C. Cheng, V. Heine and I.L. Jones, J. Phys.: Condens. Matter, **2**, 5097 (1990)
11. D. Pandey and P. Krishna, Phil. Mag. **31**, 1133 (1975)
12. A.F. Wright, M.S. Daw and C.Y. Fong, Phil. Mag. A. **66**, 387 (1992)
13. F.R. Chien, S.R. Nutt, W.S. Yoo, T. Kimoto and H. Matsunami, J. Mater. Res. **9**, 940 (1994)

CVD-GROWTH OF LOW-DOPED 6H SIC EPITAXIAL FILMS

O. KORDINA, A. HENRY, C. HALLIN, R.C. GLASS*, A.O. KONSTANTINOV, C. HEMMINGSSON, N.T. SON AND E. JANZÉN
Department of Physics and Measurement Technology, Linköping University, 581 83 Linköping, Sweden.
*Present adress, Westinghouse Electric Corporation, Science and Technology Center, 1310 Beulah Road, Pittsburgh, PA 15235, USA

ABSTRACT

We present a method for growing low-doped 6H SiC films using chemical vapour deposition in a hot-wall system. The study discusses the influence of temperature, growth rate and C/Si ratio on the purity of the layers. Furthermore, we make a comparison between methane and propane as carbon source, and investigate the influence of bake-out prior to growth. The films are characterised using low temperature photoluminescence. The relative intensity of the free exciton related luminescence as compared to impurity related bound exciton recombination is discussed in terms of material purity. A capacitance-voltage technique is used to determine the doping concentration.

INTRODUCTION

SiC possesses properties such as a large bandgap, high breakdown electric field and high thermal conductivity making it suitable as a high power device material. In order to realize high voltage rectifying properties it is necessary to produce thick low-doped active layers. For instance, a 5 kV rectifier needs a 40 μm thick active layer with a doping concentration in the low 10^{15} cm^{-3} range.

The aim of this work is to produce thick (up to 50 μm) n-type layers with residual doping concentrations in the 10^{14} cm^{-3} range by Chemical Vapour Deposition (CVD). In order to reduce nitrogen incorporation to a minimum, great care must be taken in the procedures prior to- and during growth. We have investigated the influence of bake-out, growth rate, C/Si ratio and different carbon precursors on the purity of the epitaxial films.

EXPERIMENTAL

The films were grown in a hot-wall reactor, previously described elsewhere [1], with a SiC-coated graphite susceptor. The precursors used were silane and propane both diluted to 1% in hydrogen, or silane and methane the latter diluted to 10% in hydrogen. The reason for using methane as an alternative carbon source is that it is commercially available in a much purer form than propane. The substrates (Cree research, research grade, Si-face, off-axis, n-type ≈ 10^{18} cm^{-3}) were cut into four or six pieces prior to growth. The precursors were diluted in a high flow of purified hydrogen. Growth temperatures varied from 1450°C to 1650°C and the C/Si ratio was varied from 1.2 to 6 and 3 to 30 when propane and methane were used as carbon precursor, respectively. The growth rate was kept between 1 to 2 μm/h.

CHARACTERISATION

The grown samples were analyzed with low temperature photoluminescence (PL) and

Mat. Res. Soc. Symp. Proc. Vol. 339. ©1994 Materials Research Society

Capacitance versus Voltage (CV) techniques. PL measurements were performed at liquid helium temperature (4.2 K) with an argon ion laser emitting in the UV region (333.6 - 363.8 nm) as excitation source. The power density of the moderately focused laser beam was typically 0.6 mW/cm^2. The luminescence was dispersed by a double grating monochromator equipped with 1200 grooves/mm gratings blazed at 0.5 μm, and detected by a GaAs photomultiplier tube. Schottky diodes for CV measurements were made by evaporating gold Schottky contacts (0.36 or 0.58 mm in diameter) on the epitaxial layer and alloying a nickel-gold ohmic backside contact. Layer thickness measurements were made by observing the room temperature luminescence from a cleaved edge through a microscope with UV laser excitation.

RESULTS

Effects of bake-out

One of the most apparent effects we observe, growing material in our reactor, is the long time required at elevated temperatures before any low-doped material can be produced. We grew three runs in succession at 1600°C for 10 h with the same set of growth parameters. The growths were preceeded by a normal bake-out procedure in vacuum at 1200°C - 1300°C for a few hours in addition to 20 runs made on Si substrates at 1200°C or 1250°C with a total time of approximately 35 h. The first sample obtained an impurity concentration just below 10^{17} cm^{-3}. The second sample grown in this series had one order of magnitude lower impurity concentration, and the third had additionally 5 times lower impurity concentration. It is apparent that nitrogen is held within the system and released only at high temperatures in spite of the long time above 1200°C prior to these runs.

Effects of temperature, C/Si ratio and silane flow

To establish the effects of different growth parameters on the impurity concentrations a series of short runs were made according to a reduced factorial experimental design. The silane flow, temperature and C/Si ratio were varied between 10 - 30 ml/min, 1550°C - 1650°C and 10 - 20 respectively, and the carbon precursor in this series was methane. The outcome of this set of runs shows that the growth rate depends only on the silane flow. The impurity concentration depends mainly on the silane flow in such a way that a high flux of silane gives a low impurity concentration. High temperatures and high C/Si ratios also give lower impurity concentration, however the influence of the C/Si ratio was surprisingly small in view of the site-competition mechanism proposed by Larkin et al [2]. It is uncertain to what extent the growth rate influences the impurity concentration, it could equally be so that a certain thickness is required to obtain the same effect. By just varying the C/Si ratio it is possible to produce layers ranging from the mid 10^{14} cm^{-3} n-type, without any noticeable compensating acceptors, to extremely low-doped p-type, provided there is some aluminium present in the system.

The influence of the C/Si ratio when propane is used is even smaller. An important difference between methane and propane is that methane decomposes less readily than propane. Since we have a high decomposition efficiency in our reactor, being a hot-wall reactor, it is important to compare the effective C/Si ratio. In other words, when propane is used, we may even at relatively low C/Si ratios have an effective C/Si ratio exceeding those reported by Larkin et al [2]. Thus, it is possible that we are working in a different growth regime. Evidence of this is given by the fact that when we attempted to decrease the amount of nitrogen incorporation in our layers by raising the C/Si ratio to 6 at 1450°C and a growth rate of 2 μm/h, the produced layer showed extremely bad morphology and clear indications of 3C inclusions. This indicates that in our case, already at relatively moderate C/Si ratios, the surface of the growing crystal becomes disturbed on account of the high carbon pressures. Finally, when propane is used as carbon precursor, it is difficult to

grow layers below the 10^{15} cm^{-3} range without the aid of compensating acceptors, due to the high nitrogen content of this source.

The choice of temperature for growth of epitaxial layers is, in our case, determined by the morphology. The morphology of the layer is greatly improved when the temperature is raised from 1450°C to 1550°C. Higher temperatures provide even better morphology, but the life-time of the susceptors is greatly reduced in this case. Additionally, the graphite releases more aluminium and boron at temperatures above 1550°C which is not desireable unless compensated layers are preferred. The crystalline quality determined by PL studies is also enhanced by higher temperatures. In the films grown at lower temperatures it is possible to detect small amounts of 3C inclusions even in films with relatively low growth rates.

There exists a difference between the propane and the methane precursor with regard to morphology. The methane precursor always gives slightly worse morphology. Propane gives excellent morphology for C/Si ratios below 3-4 [3]. Above this value the morphology gradually becomes worse. Using methane, the morphology is bad for low C/Si ratios, quite good for C/Si ratios above 5, and becomes slightly worse at higher C/Si ratios.

Photoluminescence and CV results

All films were characterised by PL at liquid helium temperatures and CV measurements. A correlation between the ratio of the nitrogen bound exciton lines to the I_{77} Free Exciton (FE) line and the residual doping concentration of the layers has been established by Pensl and Choyke, and Clemen et al [4,5]. Figure 1 shows the ratio between the nitrogen bound exciton P-line to the I_{77} FE line as a function of doping concentration. It is difficult to draw any firm conclusions between our data points and the data points presented by Clemen et al since the experimental conditions

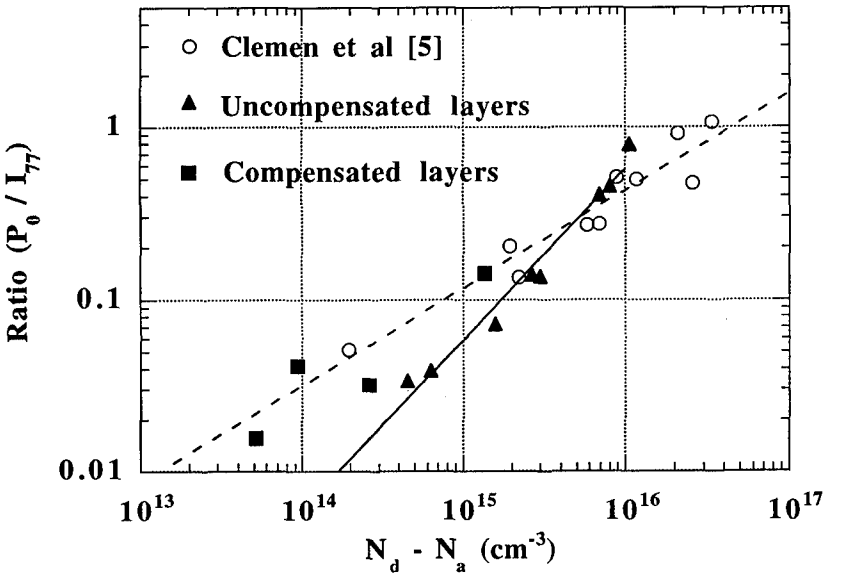

Figure 1. Open circles and dashed line: data points and corresponding slope obtained by Clemen et al, triangles and solid line: data points from our CVD grown layers with no observable compensation, squares: data points from our CVD layers showing clear indications of compensation.

were not exactly the same. The open circles are data points taken from Clemen et al [4], wheareas the triangles and squares are data points from our epitaxial layers. A major difference between the measurements done by Clemen et al and our measurements is the wavelength of the excitation source. Since our wavelength is somewhat longer we penetrate into the epitaxial film further. This is important since free excitons produced near the surface may diffuse to the surface and recombine nonradiatively, whereas on the other hand free excitons produced deep inside the material may diffuse to the interface between the substrate and the epitaxial layer and recombine there.

All our points in the figure are from undisputable n-type material, but the squares represent points showing clear indications of acceptor compensation in the PL spectra. At doping levels above 10^{15} cm^{-3} our data points coincide with the results by Clemen et al, however, as the doping levels decrease, the scatter between the points increases. A normal scatter can be expected due to the uncertainty CV measurements give at very low doping levels with small diode areas. Additionally, at low impurity levels there exists some inhomogeneity in doping concentration over the surface of the crystal. Since we can not measure at the same spot with CV as with luminescence this inhomogeneity will contribute to the scatter in the data points. However, we believe that the compensation mechanism also plays a role. When only the triangles are taken into account, which represent points where no traces of the Al bound exciton lines are seen by PL, the slope of the curve becomes steeper.

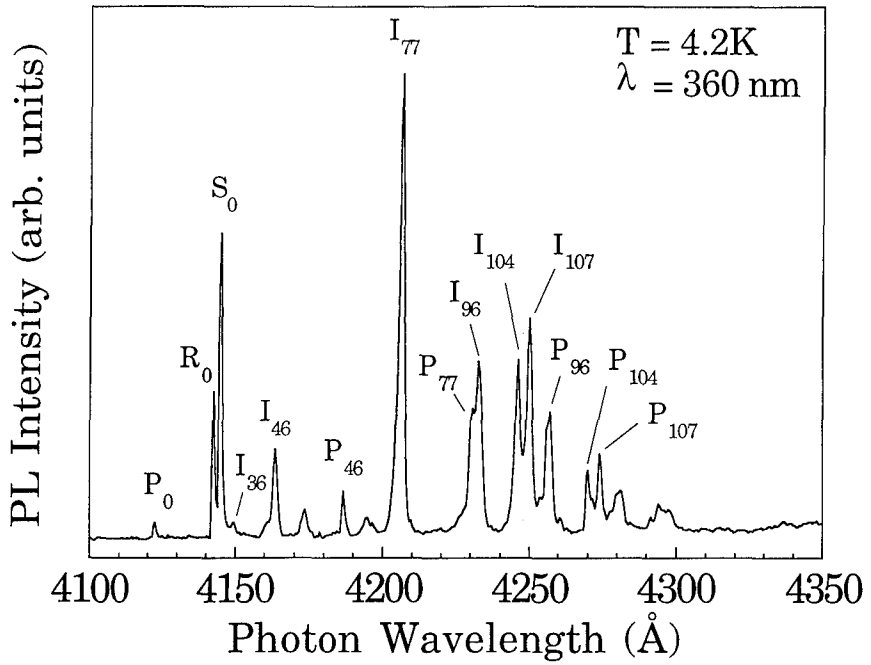

Figure 2. Near bandgap luminescence observed from a 60 μm thick film grown with methane as carbon precursor. The spectrum shows no indications of any acceptor compensating defects.

Figure 2 and 3 shows PL spectra taken from a low-doped uncompensated n-type layer and a low-doped p-type epitaxial layer respectively. Though the spectrum in figure 2 by no means represents our highest ratio between the FE and the nitrogen bound exciton (BE) related lines on an n-type sample, it is a sample which shows no indications of any compensating Al defects. This

particular sample was grown at 1550°C using methane as carbon precursor, the C/Si ratio was 3 and the growth rate was 2 μm/h. The layer was grown for 30 h thus giving a total thickness of 60 μm. The doping concentration of this sample has been measured by CV to be in the mid 10^{14} cm^{-3} range. In this sample the C/Si ratio was kept deliberately low to prevent the film from turning p-type which is the normal case for high C/Si ratios using methane due to the much lower nitrogen

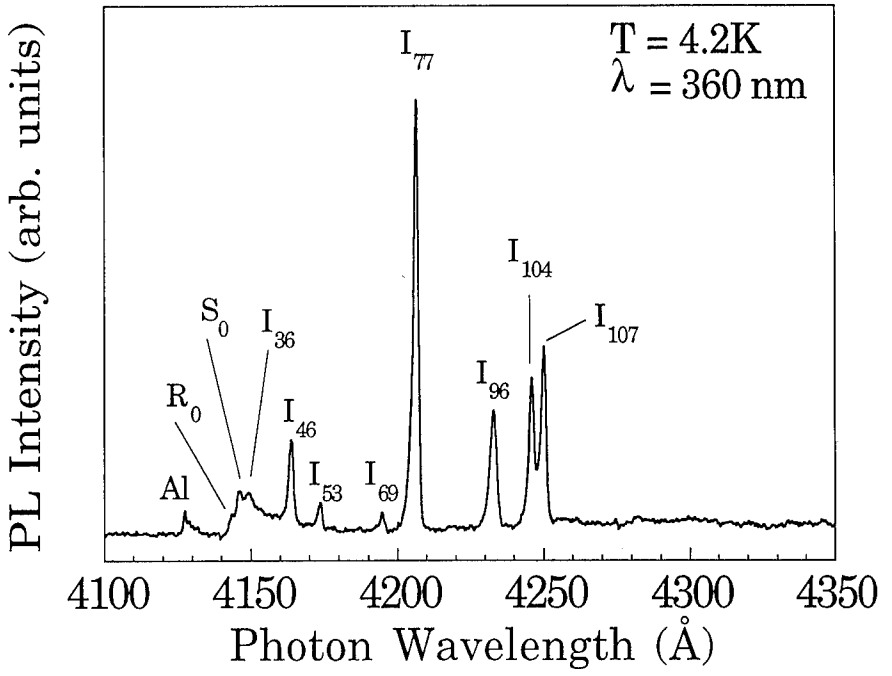

Figure 3. Near bandgap luminescence observed from a very low-doped p-type film grown with methane as carbon precursor using a high C/Si ratio. The spectrum is completely dominated by FE related lines.

content in this precursor. Figure 3 shows a spectrum of a sample grown with methane using a C/Si ratio of 30. As can be seen the spectrum is completely dominated by FE related lines. Though the ratio between the I_{77} FE line and the nitrogen bound exciton S-line represents the highest reported value to our knowledge, the relevance of such a comparison is highly doubtful. We have noticed that the ratio between the I_{77} FE line to the nitrogen bound S-line appears insensitive to changes in excitation power in n-type samples, whereas for p-type samples this ratio decreases consederably with increasing power densities. The explanation we propose for this behaviour is that in the p-type sample it is necessary to produce sufficient amount of free electrons to neutralise the ionized nitrogen donors before these can capture a FE to form a BE. The relevant comparison in this case would be between the aluminium BE and the FE related lines.

High power device material

The object of this study is to provide material of high quality suitable for high power devices. We have grown the following structure: On top of a high-doped n-type substrate, we grew a 45 μm thick n-type layer in the low 10^{15} cm^{-3} range, and finished off with a high doped p-type layer

approximately 10^{18} cm^{-3}, and 1.5 µm thick. The carbon precursor we used in this case was propane on account of the better morphology. The growth temperature, C/Si ratio and growth rate was 1550°C, 3 and 1.7 µm/hr respectively. Aluminium doping of the p-type layer was accomplished by a small addition of trimethylaluminium (TMA). The film showed excellent morphology, with the exception for a barely noticable corrugated structure when the sample was studied at 400 times magnification with Normarski optics. The corrugated structure we beleive arise from step bunching effects. PL data confirm that the doping concentration of the layer is between $4 \cdot 10^{14}$ cm^{-3} according to the calibration slope proposed by Clemen et al or just above $1 \cdot 10^{15}$ cm^{-3} according to the slope recommended in this paper for uncompensated material.

CONCLUSIONS

Using methane or propane as carbon precursors it is possible to grow low-doped epitaxial films with residual carrier-concentrations below 10^{15} cm^{-3}. Using propane the limit of uncompensated layers is just below 10^{15} cm^{-3}, whereas with methane uncompensated epitaxial layers can be produced in the mid 10^{14} cm^{-3} or lower, however with a slightly worse morphology. If compensated layers are acceptable both n- and p-type doping below 10^{14} cm^{-3} can be obtained with both carbon precursors. Changing the C/Si ratio when propane is used in our reactor provides unnoticable effects on the nitrogen incorporation of the layers, whereas when methane is used some effects are noticed. Moderate to high C/Si ratios with methane as carbon precursor turns the layer low-doped p-type. Optimal growth temperatures we found to be between 1550°C to 1600°C on account of the good morphology and high crystalline quality obtained at these temperatures. At 1600°C or higher, impurities from the graphite susceptor and graphite felt become disturbing since they can provide unwanted compensating defects.

ACKNOWLEDGEMENTS

Al Burk jr is acknowledged for helpful discussions. Financial support for this work was provided by the Swedish board for Industrial and Technical Development (NUTEK)/Asea Brown Boveri (ABB) Power Device Program, the Swedish Council for Engineering Sciences (TFR), NUTEK, the NUTEK/Swedish Natural Research Council (NFR) Material Consortium on Thin Film Growth and the Swedish Institute.

REFERENCES

[1] O. Kordina, C. Hallin, R.C. Glass, A. Henry and E. Janzén, A Novel Hot-Wall CVD Reactor for SiC Epitaxy, presented at the ICSCRM, nov 1-3 1993, Washington DC, in press.

[2] D.J. Larkin, P.G. Neudeck, J.A. Powell, L.G. Matus, Site-Competition Epitaxy for Controlled Doping of CVD Silicon Carbide, presented at the ICSCRM, nov 1-3 1993, Washington DC, in press.

[3] T. Kimoto, H. Nishino, W.S. Yoo and H. Matsunami, J. Appl. Phys. **73** (2), 1993.

[4] G. Pensl, W.J. Choyke, Electrical and Optical Characterization of SiC, Physica B, 185 (1993), 264-283.

[5] L.L. Clemen, M. Yoganathan, W.J. Choyke, R.P. Devaty, H.S. Kong, J.A. Edmond, D.J. Larkin, J.A. Powell, A.A. Burk jr, Calibration Procedure to Determine the Nitrogen Impurity Concentration in 6H SiC at Low Concentration Levels, presented at the ICSCRM, nov 1-3 1993, Washington DC, in press.

XPS AND SIMS STUDIES OF CVD-GROWN CUBIC SiC FILMS ON Si(100)

A.T.S. WEE*, Z.C. FENG*, H.H. HNG*, K.L. TAN*, C.C. TIN**, R. HU**, AND R. COSTON**
*Department of Physics, National University of Singapore, S0511, Singapore
**Department of Physics, Auburn University, Auburn, AL 36849-5311, USA

ABSTRACT

A series of CVD-grown 3C-SiC/Si(100) films of different growth times, and hence film thicknesses, are studied by X-ray photoelectron spectroscopy (XPS) and secondary ion mass spectrometry (SIMS). XPS showed that the surfaces of the samples consist of Si oxides (SiO_2 and SiO_x where $x < 2$) and unreacted CH. Unreacted elemental Si is also present and its amount decreases with increasing growth time. This surface overlayer is further investigated by changing the photoelectron take-off angle and from chemical etching studies. Compositional variations of the SiC films are also studied using SIMS.

INTRODUCTION

There has recently been renewed interest in the development of silicon carbides due to the successful epitaxial growth of 3C-SiC films on Si substrates by chemical vapour deposition (CVD) [1-3]. In the growth of single-crystal 3C-SiC by CVD, a major obstacle is the large mismatch of about 20% between the deposited SiC [4.359 Å at room temperature (RT)] and the underlying Si substrate (5.430 Å at RT). However, epitaxial growth can be achieved by imposing an initial temperature ramp on the Si substrate in the presence of a hydrocarbon which decomposes to form an initial layer of SiC which acts as a buffer for the subsequent epitaxial growth of SiC [4].

For electronic device applications, an understanding of the characteristics of the surface exposed to air is also important. From this point of view, surface oxide and carbonaceous contaminants on the SiC produced by CVD have been studied by Auger electron spectroscopy (AES) and XPS [5-7].

In this work, XPS and SIMS are used to investigate the surface overlayers and the buffer SiC interfacial layer in a series of CVD-grown 3C-SiC films on Si(100). The SiC films are grown for different amounts of time and are hence of varying thicknesses.

EXPERIMENTAL

A series of single crystalline 3C-SiC with the growth times of 2, 15, 45 minutes, 2, 3 and 4 hours were grown on Si(100) at atmospheric pressure and at a temperature of 1350°C using a vertical chemical vapour deposition (V-CVD) system [8]. The growth rate under these conditions as measured by FTIR [9] was found to be 3.2 μm h^{-1}. Hence the thicknesses of the above six films are 0.1 μm (0.06 μm, determined by RBS), 0.8 μm, 2.4 μm, 6.4 μm, 9.6 μm and 12.8 μm respectively.

XPS measurements were made in a VG ESCALAB MKII spectrometer (base pressure < 2 x 10^{-10} mbar) using a Mg Kα X-ray source (1253.6 eV, 120 W) at a constant analyser pass energy of 20 eV. All XPS binding energies are calibrated to the C1s peak of CH at 284.6 eV [10]. Take-off angles (angle between the detected

Mat. Res. Soc. Symp. Proc. Vol. 339. ©1994 Materials Research Society

photoelectrons and surface) of 75° and 20° were used to vary the sampling depth, the smaller take-off angle being the more surface sensitive.

The SIMS experiments were performed in a VG SIMSLAB (base pressure < 2 x 10^{-10} mbar) which is connected to the XPS chamber via a preparation chamber. A 9 keV Ar^+ beam produced from a differentially pumped VG DP50B duoplasmatron ion gun was incident at 45° to the sample normal. Energy pre-filtered secondary ions were detected normally by a VG MM12-12 quadrupole mass spectrometer (0-800 amu). The mass spectra were obtained using a beam current of 10 nA with the beam rastered in TV mode. The depth profiles were obtained using a 80 nA beam in reduced-area-scan (RAS) mode with electronic gating to minimize crater edge effects. The sample bias (approximately 10 V for positive ions) was chosen to optimize yields at cluster ions.

RESULTS AND ANALYSIS

High resolution XPS spectra from Si2p, C1s and O1s were obtained for all the SiC samples, no other elements being detected in significant amounts by XPS. The Si2p and C1s spectra for the 3h sample, both before and after (see later) etching, are presented in Figure 1. The Si2p spectra can be fitted with four Gaussian peaks which are assigned to elemental Si (98.9 ± 0.3 eV), SiC (100.1 ± 0.2 eV), SiO_X (x < 2) (101.3 ± 0.3 eV) and SiO_2 (102.9 ± 0.2 eV). The C1s spectra exhibit two main peaks assigned to CH (284.6 eV) and SiC (282.3 ± 0.3 eV), the higher binding energy tail being attributed to C-O and C=O atmospheric contaminant species. The O1s spectra are found to be composed mainly of a single peak with a binding energy which corresponds to SiO_2 (532.0 ± 0.2 eV).

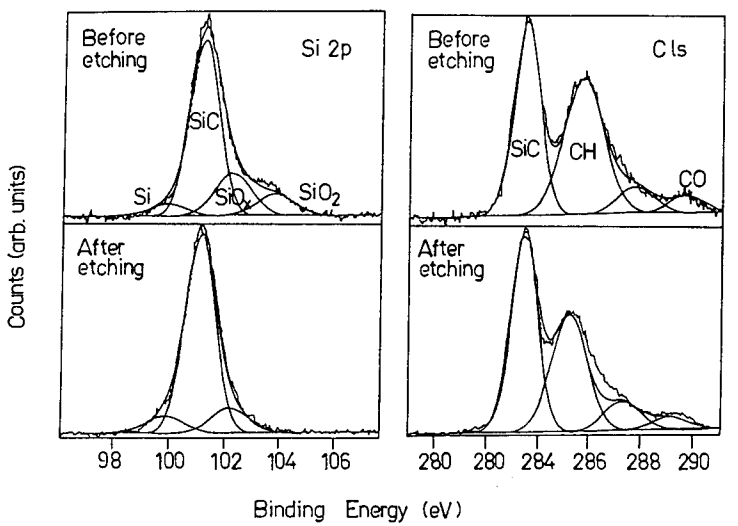

Figure 1. Si2p and C1s XPS spectra for the 3 h (#122B) SiC/Si samples.

Quantification of the XPS data was performed by determining the area of each peak and correcting using the manufacturer's relative sensitivity factors (RSF) [11]. The RSFs used were 0.37, 0.32 and 0.72 for Si2p, C1s and O1s respectively. Ratios of selected elements/compounds of interest are summarized in Table 1.

Sample		Si2p region			C1s region	
Growth Time	Sample No.	Si/SiC	$\frac{Si}{(SiO_2+SiO_x)}$	$\frac{(SiO_2+SiO_x)}{SiC}$	CH/SiC	$(SiC)_{Si}/(SiC)_C$
2 min	#125D	0.3	0.51	0.60	1.3	0.9
15 min	#125C	0.1	0.24	0.59	0.9	0.8
45 min	#125A	0.09	0.19	0.48	0.6	0.8
2 h	#120	0.05	0.21	0.21	5.8	1.1
3 h	#122B	0.08	0.19	0.50	1.1	0.9
4 h	#328B	0.1	0.11	0.85	2.3	0.8

Table 1. Ratios of elements/compounds of interest obtained from the XPS data (take-off angle is 75°).

It is observed from Table 1 (last column) that the Si:C ratio for SiC is 1.0 ± 0.2, i.e. the SiC compound is indeed stoichiometric. The Si/SiC ratio shows that SiC film that was grown for 2 min has the largest amount of unreacted elemental Si, while that grown for 2 h has the least. As the growth time increases, the $Si/(SiO_2+SiO_X)$ ratio decreases. This suggests that as the growth time increases, more elemental Si will be reacted to form SiC or Si oxides. Table 1 also shows that the sample that is grown for 45 min has the minimum amount of CH contaminants [CH/SiC ratio], while the 2 h sample has the minimum amount of oxides [(SiO_2+SiO_X)/SiC ratio]. These XPS results show that the 3 h sample is quite similar to the 45 min sample except that it has more CH contaminant.

These observations can be rationalized by considering the CVD growth process with C_3H_8 and SiH_4 as source gases. The initial SiC interfacial layer contains relatively large amounts of unreacted Si as indicated by the 2 min sample. This suggests that the initial SiC formed is not crystalline, consistent with previous observations [1,2] which showed the presence of dislocations, stacking faults, microcracking, etc., at the SiC/Si interface. At the end of the growth, there appears to be a layer of unreacted CH and Si on top of the SiC film. This is related to the gas flow shut-down and sample cooling procedure in the CVD system. The Si oxides were formed upon subsequent exposure of the samples to atmosphere.

In order to increase the surface sensitivity of XPS, the take-off angle of samples #120 and #122B of growth times 2 and 3 h respectively was changed from 75° to 20°. Figure 2 compares the Si2p and C1s spectra obtained at take-off angles of 75° and 20° for the 3 h sample. Table 2 shows the ratios for selected elements or compounds of interest at a take-off angle of 20°

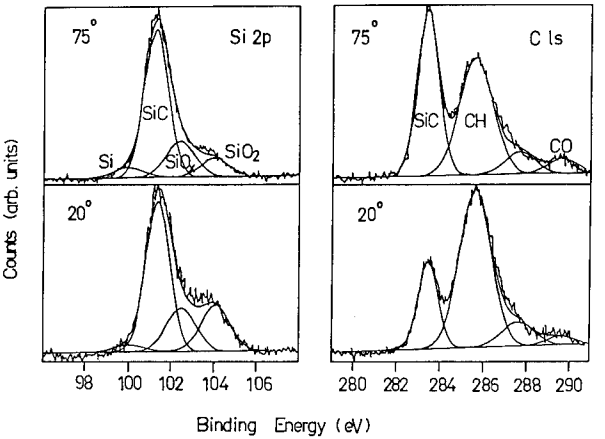

Figure 2. (a) Si2p and (b) C1s XPS spectra for the 3 h sample (#122B) obtained with take-off angles of 20° and 75°.

Sample		Si2p region			C1s region	
Growth time	Sample No.	Si/SiC	$\frac{Si}{(SiO_2+SiO_x)}$	$\frac{(SiO_2+SiO_x)}{SiC}$	CH/SiC	$(SiC)_{Si}/(SiC)_C$
2 h	#120	0.1	0.38	0.32	9.5	1.3
3 h	#122B	0.06	0.087	0.73	2.8	1.1

Table 2. Ratios of elements/compounds of interest obtained from the XPS data (Take-off angle = 20°)

When the angle is decreased from 75° to 20°, the intensity of the CH/SiC ratio in the C1s peak increases by ~100%. On the other hand, the $(SiO_X+SiO_2)/SiC$ ratio in the Si2p peak increases by only ~50% (Tables 1 and 2). This indicates that the CH contaminant is deposited on the surface with the SiO_2 and SiO_X layer underneath it. The origin of the CH group can be attributed to unreacted C_3H_8 or its intermediate products (such as C_2H_2 or C_2H_4) on the surface.

Chemical etching was also performed on the 2, 3 and 4 h samples to remove any unreacted Si, CH and Si oxides. A mixture of HF and HNO_3 (1:1) was used as the etching solution. The samples were placed in the solution for about 10 seconds. They were then rinsed with deionized water followed by methanol and dried with paper. XPS spectra of these samples were then obtained immediately. The widescan XPS spectra show a decrease in the height of the C1s and O1s peaks. This indicates that the etching is efficient in removing the contaminant CH and the oxides that exist on the sample surface. A comparison of Si2p and C1s peaks of the etched and unetched 3 h sample is presented in Figure 1. Table 3 shows the ratios for elements or compounds of interest obtained from the Si2p and C1s regions for the three etched samples at a take-off angle of 75°

Sample		Si2p region			C1s region	
Growth time	Sample No.	Si/SiC	$\frac{Si}{(SiO_2 + SiO_x)}$	$\frac{(SiO_2 + SiO_x)}{SiC}$	CH/SiC	$(SiC)_{Si}/(SiC)_C$
2 h	#120	0.26	1.2	0.21	2.1	1.1
3 h	#122B	0.11	0.68	0.16	0.79	0.86
4 h	#328B	0.036	0.18	0.20	0.31	0.85

Table 3. Ratios of elements or compounds of interest for the etched samples at a take-off angle of 75°

On all the etched samples, the Si:C ratio for SiC remains the same after the samples were chemically etched indicating that etching does not change the SiC stoichiometry. The etched surfaces show negligible SiO_2 and some SiO_x and CH, suggesting that HF preferably etches SiO_2, and to a lesser extent SiO_x and carbonaceous contaminants. What is particularly interesting is that removing the topmost layers causes an increase in the Si/SiC ratio for the 2 and 3 h samples, the increase being larger than when the take-off angle was reduced to 20°. This suggests that an elemental Si overlayer exists atop the SiC film since its signal increased when the CH and Si oxides are partially etched away. It was reported in literature that the Si overlayer exists in CVD-grown SiC films at temperatures above 940°C [12]. However, for the 4 h sample, the elemental Si signal decreases. This may be due to the longer etching time which resulted in some of the Si overlayer being etched away as well.

Positive SIMS depth profiles of all the samples were performed to investigate the compositional variations of the SiC films with depth. A typical profile (#125C) is shown in Figure 3. The SiC/Si substrate interface is clearly shown in this depth profiles as judged by the sharp decrease in the SiC^+ and C^+ signals. Positive SIMS mass spectra of (a) the sample surface; (b) inside the SiC film, and (c) inside the Si substrate for the same sample are presented in Figure 4. It is observed that there is an increase in N^+ as one goes deeper into the sample. The mass spectrum of a control Si substrate was performed and it showed negligible amounts of nitrogen in it. A possible explanation is that there may be incorporation of nitrogen during the growth of the SiC film. The high temperature that was used in the CVD method may facilitate the diffusion of nitrogen into the substrate from the growth chamber ambient.

CONCLUSION

The following can be concluded from the surface analytical studies of a series of CVD-grown 3C-SiC/Si(100) films of different growth times (film thicknesses):

(1) The results obtained from XPS showed that the surfaces of the samples consist of Si oxides (SiO_2 and SiO_x where $x < 2$) and unreacted CH. Unreacted elemental Si is also present and its amount decreases with increasing growth time. The 45 min sample was found to have the least amount of CH while the 2 h. sample had the least amount of Si oxides.

(2) By changing the photoelectron take-off angle and from chemical etching studies, it was found that an unreacted elemental Si overlayer exists atop the stoichiometric SiC film, followed by Si oxides and finally a carbonaceous species on the surface.
(3) Positive SIMS mass spectra showed an increase in the N^+ signal as one goes deeper inside the samples. This is attributed to the diffusion of nitrogen from the growth chamber ambient during high temperature SiC growth.

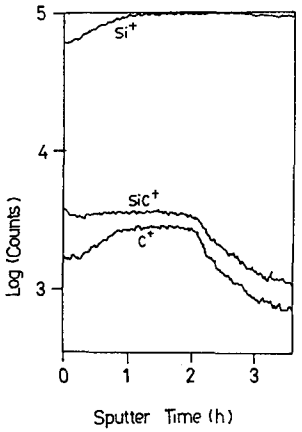

Figure 3. Positive SIMS depth profile of the 15 min. SiC sample (#125C)

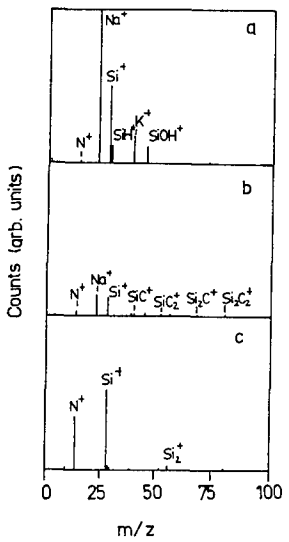

Figure 4. Mass spectra of (a) sample surface; (b) SiC region; and (c) Si region of sample #125C.

REFERENCES

1. S. Nishino, J.A. Powell and H.A. Will, *Appl. Phys. Lett.*, **42**, 460, (1983)
2. A. Addamiano and J.A. Sprague, *Appl. Phys. Lett.* , **44**, 525, (1984)
3. J.A. Powell, L.G. Matus, M.A. Kuczmarski, C.M. Chorey, T.T. Cheng and P. Pirouz, *Appl. Phys. Lett.*, **51**, 823, (1987)
4. J.A. Powell, L.G. Matus and M.A. Kuczmarski, *J. Electrochem. Soc.*, **134**, 1558, (1987)
5. M. Dayan, *J. Vac. Sci. Technol. A*, **4**, 38, (1986)
6. Y.Mizokawa, S. Nakanishi, O. Komoda, S. Miyase, H.S. Diang, C. Wang, N. Li and C. Jiang, *J. Appl. Phys.*, **67**, 264, (1990)
7. J.M. Powers and G.A. Somorjai, *Surf. Sci.*, **244**, 39, (1991)
8. C.C Tin, R. Hu, J. Williams and Z.C. Feng, *Bull. Am. Phys. Soc.* **38**, 566 (1993)
9. Z.C. Feng, C.C. Tin, K.T. Yue, R. Hu, J. Williams, S.C. Liew, Y.G. Foo, S.K.L. Choo and W.E. Ng, this issue.
10. C.D Wagner et.al., *Handbook of X-ray Photoelectron Spectroscopy*, G.E. Mailenberg (Ed), Perkin-Elmer Corporation (1979)
11. VG Scientific Technical Document TD8618
12. F. Bozso, T.J. Yates, Jr., W.J. Choyke and L. Muchlhoff, *J. Appl. Phys.*, **57**, 2771, (1985)

COMBINED STRUCTURAL AND OPTICAL ASSESSMENT OF CVD GROWN 3C-SiC/Si

Z. C. FENG,* C. C. TIN,** K. T. YUE,+ R. HU,** J. WILLIAMS,** S. C. LIEW,* Y. G. FOO,* S. K. L. CHOO,* W. E. NG* AND S. H. TANG*
*Department of Physics, National University of Singapore, S0511, Singapore
**Department of Physics, Auburn University, Auburn, AL 36849-5311, USA
+Department of Physics, Emory University, Atlanta, GA 30322, USA

ABSTRACT

A combined structural and optical assessment of cubic (3C-) SiC thin films grown on Si (100) substrates by chemical vapor epitaxy (CVD) is presented. The CVD growth was performed at both atmospheric and low (100 Torr) pressure, using a vertical reactor. The CVD-grown 3C-SiC films with different growth time were characterized by X-ray diffraction, Raman scattering and Fourier transform infrared (FTIR) spectroscopy to be single crystalline with a high degree of crystal perfection. The film thickness was determined from FTIR spectra. Variations of X-ray, FTIR and Raman spectra with different growth conditions and film thicknesses are studied comparatively. Related problems are discussed.

INTRODUCTION

In recent years, much attention has been focused on the research and development of silicon carbides because of their unique electrical, optical and thermal properties. In particular, cubic silicon carbide (3C-SiC) which possesses a wide band gap of 2.2 eV at room temperature (RT), high breakdown electric field, high melting point and high thermal conductivity, are suitable for device applications at high temperature, high power and high radiation environment in electronics and optoelectronics. Since the first report of the success of large area epitaxial growth of 3C-SiC films on Si substrates by chemical vapor deposition (CVD) [1], a great deal of effort has been made in this field [2-4]. We have previously made optical studies on CVD-grown 3C-SiC/Si (100) by low temperature photoluminescence (PL) and Raman scattering techniques [5-6].

Here, a combined structural and optical assessment on CVD-grown 3C-SiC epilayers on Si (100) substrates is presented. The CVD growth was performed at both normal (1 atm.) and low (100 Torr) pressure, using a vertical reactor. Different growth conditions were used. The samples were characterized by x-ray diffraction (XRD), Raman scattering and Fourier transform infrared (FTIR) spectroscopy. Information of the structural and optical properties for SiC films were obtained from these complementary analyses. Variations in X-ray, FTIR and Raman spectra with different growth conditions, film thicknesses and other parameters are studied comparatively.

EXPERIMENT

The epitaxial cubic SiC films were prepared at Auburn University, using a new chemical vapor deposition (CVD) system. This system employs a vertical reactor configuration with a rotating susceptor and is capable of operating in both atmospheric and low pressure modes. The silicon carbide-coated susceptor is heated by a RF

Mat. Res. Soc. Symp. Proc. Vol. 339. ©1994 Materials Research Society

induction power supply. The gases used for the experiments in this paper were hydrogen, 2% propane in hydrogen, 2% silane in hydrogen and 10% hydrogen chloride in hydrogen. General substrate cleaning procedure involve successive rinses in trichloroethylene, acetone, methanol and deionized water. The outline of the growth procedure for the epitaxial growth of 3C-SiC on both on- and off-axis (100) Si substrates is generally similar to that reported by Powell et al. [7]. Generally, the growth procedure consists of in-situ etching of the substrate by 3% HCl at about 1200°C, a buffer growth initiated by a temperature ramp to 1350°C followed by a growth at 1350°C.

We present here only the results from samples on on-axis (100) Si substrates and grown at both 1 atmosphere and 100 Torr pressure. A series of 3C-SiC/Si(100) with different deposition time ranging from 0.5 - 4 hours were studied.

X-ray diffraction and Fourier transform infrared (FTIR) measurements were performed at National University of Singapore (NUS). A Philips PW1729 x-ray generator with *Cu Kα* radiation and a PW1710 diffractometer were used for the x-ray patterns with digital data output for computer interfacing. FTIR transmission measurements were made using a Perkin Elmer PE1710 spectrometer. Raman scattering measurements were performed at room temperature (RT), in a near-backscattering geometry with the 4880 Å excitation from an Ar^+ laser, using a triple spectrometer - optical multichannel analyzer (OMA) system at Emory University.

TABLE I Sample information from CVD-grown 3C-SiC/Si (100)

sample No.	growth time τ (hr)	XRD (400) w/2 (°)	Raman scattering FWHM (cm^{-1}) ω_{LO}	ω_{TO}	I_{TO}/I_{LO}	FTIR d (μm)
1 atmosphere:						
#413	0.5	0.217	11	10	0.23	1.5
#409	1	0.160	9	9	0.18	3.2
#414B	2	0.133	8	8	0.15	6.2
#419	4	0.109	7	7	0.12	12.7
100 Torr:						
#721A	1	0.160	9	9	0.15	3.0
#720A	2	0.142	8	8	0.11	5.7

RESULTS AND DISCUSSION

X-Ray Diffraction

All the films were examined by XRD. Figure 1 shows a typical XRD θ-2θ pattern, consisting of only Bragg diffraction from the (200) and (400) planes of the 3C-SiC film, and the (200) diffraction from the Si substrate. There is no signal from crystal planes other than (200), (400), etc. This indicates the single crystallinity of the structure and

its (100) surface of the SiC film.

Slow and high resolution scans were made around the (400) diffraction 2θ angles of Si (~69°) and 3C-SiC (89-90°), shown as in Figs. 2 and 3. The diffraction patterns due to the x-ray source radiation from *Cu Kα1* (λ=1.54051 Å) and *Kα2* (λ=1.54433 Å) are well-resolved. The line width at the half maximum intensity, w/2, is only 0.08° due to the Si substrate and 0.16° or 0.19° due to the 3C-SiC film. Such narrow widths of XRD patterns show the good crystalline quality of our films [8]. The values of w/2 for samples with different growth time, τ, are listed on Table I and shown in Fig. 4 (1 atm. only). With increasing τ, from 0.5 to 4 hours, corresponding to the film thickness, d, from 1.7 to 12.7 μm, which were determined by FTIR and will be shown later, w/2 (filled square symbols with the Y-axis scale multiplied by 0.02°) decreases, indicating an improvement in the crystalline perfection of the 3C-SiC films with τ.

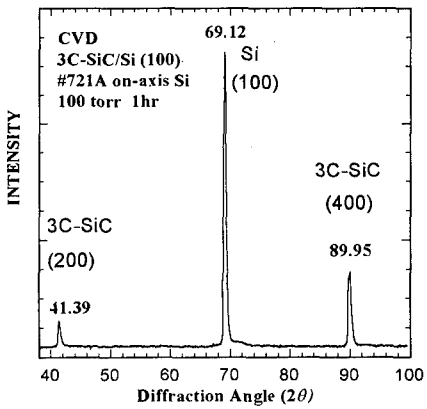

Fig. 1 X-ray diffraction θ-2θ scan (38-100°) of a CVD 3C-SiC/Si (100).

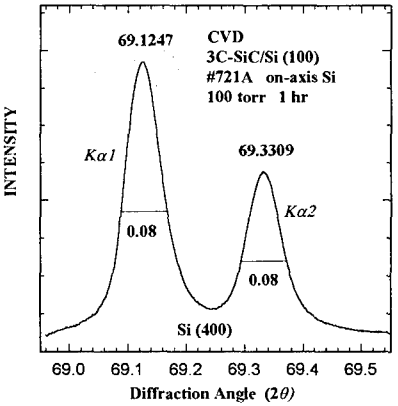

Fig. 2 XRD θ-2θ pattern from substrate Si (400) planes.

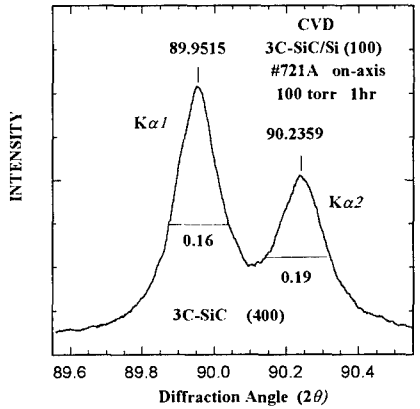

Fig. 3 XRD θ-2θ pattern from film 3C-SiC (400) planes.

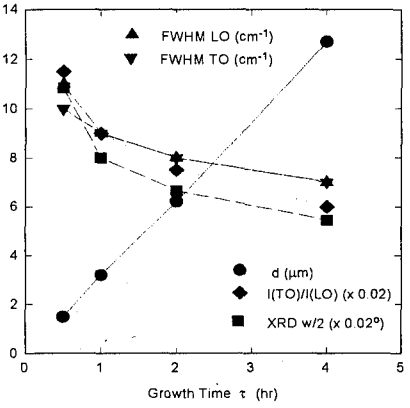

Fig. 4 XRD w/2, LO and TO FWHM, I(TO)/I(LO), and d (μm) versus τ.

Raman scattering

Fig. 5 shows the Raman spectra from three of these SiC samples with τ = 0.5, 1 and 2 hours and grown at 1 atm. pressure. Raman signal from the Si substrate is located predominantly at 520 cm^{-1} (RT). The longitudinal optical (LO) and transverse optical (TO) phonons from 3C-SiC appear near 970 and 796 cm^{-1}, respectively. Their intensities increase with respect to that of the Si mode with increasing τ. Their peak positions in wavenumber are shifted down 1-2 cm^{-1} in comparison with the published data of bulk 3C-SiC because of the effect of the biaxial tension within the film [6].

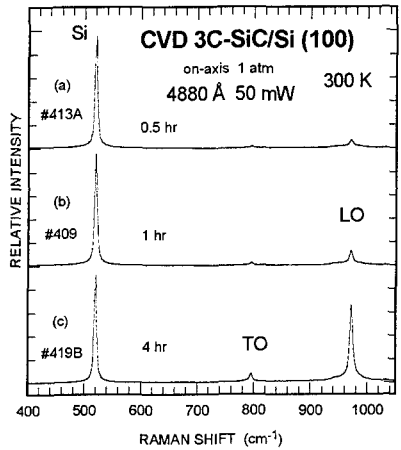

Fig. 5 Raman spectra of three CVD 3C-SiC/Si (100).

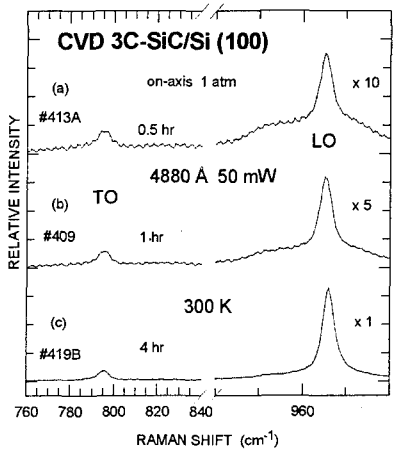

Fig. 6 Expanded Raman spectra of Fig. 5.

Fig. 6 displays the expanded Raman spectra of the 3C-SiC LO and TO modes from these three samples. As shown, the line shapes of LO and TO modes vary among the different samples, from which more information about the film quality can be obtained. The full width at half maximum (FWHM) values for these modes are listed in Table I and illustrated with filled triangle and reversed triangle symbols, respectively, in Fig. 4 (1 atm. samples only). They are decreasing, indicating the improvement in the film quality, with increasing τ. Moreover, for the τ=0.5 hr sample, there exist extra features at the left and right sides of the LO mode, which are probably due to the defects or other non-cubic SiC polytypes, and partially the second order phonons from the Si substrate. As τ increases, these features at frequencies higher and lower than ω_{LO} decrease in intensity, and almost disappear for the τ=4 hr sample.

Raman scattering from the (100) surface of a cubic crystal is allowed for LO and forbidden for TO according to the selection rule. The appearance of TO in Figs. 5 and 6 are mainly due to two reasons. One is from the non-perfect backscattering geometry arrangement (~ 60° incidence with respect to the normal direction of the sample surface in the present Raman measurements), and another is due to the disorder of the measured crystal. The intensity ratios of the forbidden TO to the allowed LO, I(TO)/I(LO) are plotted in Fig. 4 (filled rhombus symbols), and also listed in Table I. This ratio decreases with increasing τ and approaches a saturated value as τ

increases beyond 4 hr. When the measurements were made in a real backscattering geometry, this ratio was less than 1% for the τ=4 hr thick film (not shown here). Therefore, it is reasonable to assign the saturation ratio, η_s, for very large τ (~11%) as the base line for the effect from the quasi-backscattering alone. The value η = I(TO)/I(LO) - η_s should be the ratio due to the effect from the disorder of film 3C-SiC, which can be used as a figure of merit to characterize the crystalline quality of the 3C-SiC film, together with FWHM. From Table I, I(TO)/I(LO) values for low pressure samples are lower than those for 1 atm samples with the same growth time, indicating an improvement of the quality of 3C-SiC films under low pressure growth.

FTIR and film thickness

Figs. 7 and 8 exhibit two typical FTIR transmission spectra for CVD 3C-SiC grown on on-axis Si, #409 with τ=1 h at 1 atm pressure and #720 with τ= 2 h at low (100 Torr) pressure, respectively. A deep and flat band exists for both samples between 790 and 960 cm^{-1}, which is due to the strong lattice absorption from SiC. This reststrahlen band represents the range of the phonon dispersion curve with the edge frequencies characteristic of TO and LO phonons. Multi-phonon absorptions are responsible to three dips at 1310 cm^{-1} (2LA), 1520 cm^{-1} (LO+LA), and 1625 cm^{-1} (LO+LA), where LA is the longitudinal acoustic phonon [9]. The dip at 1065 cm^{-1} is due to the Si-O-Si stretching vibration. A small dip near 3000 cm^{-1}, which is almost covered by the strong noise level, is due to the stretching of O_2-C complex.

Other features in Figs. 7 and 8 are the interference fringes from the thin cubic SiC film. Obvious oscillations are observed beyond 1700 cm^{-1}. The intervals between maxima or minima vary from sample to sample with thicker film having denser oscillation fringes (comparing Fig. 8 for a τ=2 film with Fig. 7 for a τ=1 h film). This can be used to determine the thickness, d, of the 3C-SiC film. The values of d, determined from FTIR spectra, for a set of samples grown on on-axis substrates are listed in Table I and shown in Fig. 4. From these data, we obtain a growth rate of 3.2 ($\pm$0.1) μm/hr for 1 atm growth [10]. The growth rate for low pressure is slightly lower than 3 μm/hr.

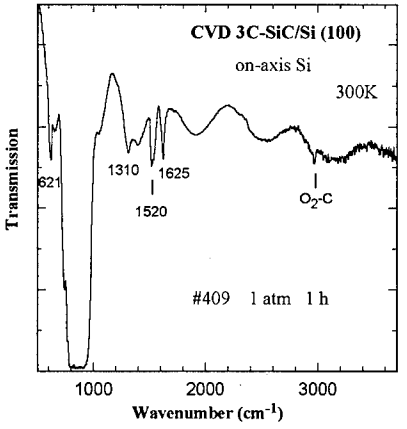

Fig. 7 FTIR spectra of a CVD-grown 3C-SiC/Si (100), #409, τ=1 h.

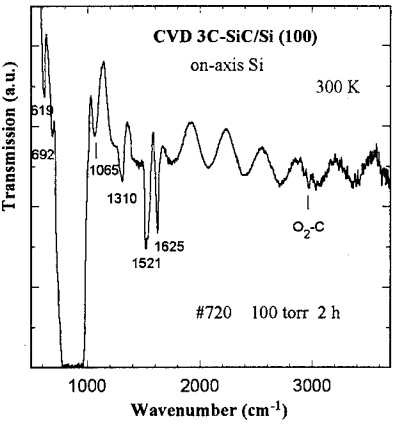

Fig. 8 FTIR spectra of a CVD-grown 3C-SiC/Si (100), #720, τ=2 h.

CONCLUSION

In summary, we have successfully grown cubic SiC thin films on Si (100) substrates by a newly developed CVD system with a vertical reactor and a rotating susceptor at both normal atmosphere and low pressure environment, and under different growth conditions. The CVD epitaxial films were characterized by X-ray diffraction, Raman scattering and Fourier transform infrared (FTIR) spectroscopy. XRD showed the 3C-SiC (200)/(400) and Si (200) lines only, characteristic of the single crystalline structure. FTIR spectra exhibited the strong reststrahlen bands due to the SiC optical phonons. The sharp interference fringes varied with films, showing the uniformity of film thickness, and were used to determine the film thickness. Raman spectra showed the characteristic 3C-SiC LO phonon mode which is strong and allowed for the (100) surface. The existence of the forbidden TO mode reveals the disordered structure particularly in the very thin films. The analysis on the variations of X-ray, FTIR and Raman spectra with different film thicknesses and other parameters confirm that the CVD-grown 3C-SiC films on Si (100) thicker than 13 μm or with 4 hours growth time possess high quality of crystalline perfection. It also shows that low pressure growth achieves an improvement of the quality of 3C-SiC films. This combined structural and optical study on CVD-cubic SiC/Si enhances our understanding of the CVD growth of SiC. Further studies on CVD 3C-SiC grown under different conditions, including on off-axis Si substrates, are in progress.

ACKNOWLEDGMENT

Prof. S. Perkowitz and Dr. A. T. S. Wee are acknowledged for support and help. We are grateful to the assistance from Y. J. He, Y. M. Goh and H. J. Du. This work was partially supported by NASA contract no. NAGW-1192 through the Center for Commercial Development of Space Power and Advanced Electronics at Auburn University.

REFERENCES

1. S. Nishino, J. A. Powell and H. A. Will, Appl. Phys. Lett. **42**, 460 (1983).
2. J. A. Powell, P. Pirouz and W. J. Choyke, in Z. C. Feng ed., Semiconductor Interfaces, Microstructures and Devices: Properties and Applications, Institute of Physics Publishing, 1993, Bristol, pp 257-293.
3. R. F. Davis and J. T. Glass, Advances in Solid-State Chemistry, **2**, 1 (1991).
4. C. Y. Yang, M. M. Rahman and G. L. Harris ed. Amorphous and Crystalline Silicon Carbide IV, Springer-Verlag, 1992, Berlin.
5. W. J. Choyke, Z. C. Feng and J. A. Powell, J. Appl. Phys. **64**, 3163 (1988).
6. Z. C. Feng, A. J. Mascarenhas, W. J. Choyke and J. A. Powell, J. Appl. Phys. **64**, 3176, 6827 (1988).
7. J. A. Powell, L. G. Matus and M. A. Kuczmarski, J. Electrochem. Soc. **134**, 1558 (1987).
8. A. J. Steckl, C. Yuan, J.P. Li and M.J. Loboda, Appl. Phys. Lett., **63**, 3347(1993).
9. H. J. Kim and R. F. Davis, SPIE Vol. **794**, Modern Optical Characterization Techniques for Semiconductors and Semiconductor Devices, 183 (1991).
10. Y. G. Foo, Honours research report, supervised by Z. C. Feng, National University of Singapore, Materials Science, 1993/94.

GROWTH OF EPITAXIAL 2H-SILICON CARBIDE BY PULSED LASER DEPOSITION

Mark A. Stan, Martin O. Patton, Hemasiri K. M. Vithana, and David L. Johnson; Physics Department; Kent State University; Kent, Ohio 44242, Joseph D. Warner and Nancy D. Piltch; NASA-Lewis Research Center; Cleveland, Ohio 44135, Jinwei Yang and Pirouz Pirouz; Department of Materials Science, Case-Western Reserve University, Cleveland, Ohio 44106

ABSTRACT

Silicon carbide films have been grown on 6H-SiC (0001) and Si (001) wafers by laser ablation using an excimer laser. The films were deposited at heater plate temperatures between 970° C to 1270° C. Film composition, morphology and polytypism were determined by Auger electron spectroscopy, atomic force microscopy and high resolution transmission electron microscopy (TEM). In the course of these experiments growth of 2H-SiC on 6H-SiC was observed at the highest heater plate temperatures. Cross-sectional TEM images clearly show the symmetry of a film grown at 1270° C as c-axis oriented 2H-SiC containing columnar grains with average diameter of 20 nm and length of 100 nm.

INTRODUCTION

Silicon carbide has been of wide interest as a potentially important semiconducting material for a long time[1]. Silicon carbide has a large band-gap (2.4 to 3.3 eV), high thermal conductivity (5 W/cm-°C), high electric breakdown (4 x 10^6 V/cm), good radiation resistance, and excellent stability at temperature in excess of 1000 °C. These properties make it an attractive material for high temperature electronic and UV optical applications. More than a hundred different polytypes of SiC have been identified, all which are different stackings of two variants of a basic tetrahedral SiC unit along an unique direction, the c-axis[2]. SiC polytypes have cubic (C), hexagonal (H), or rhombohedral (R) symmetry and following Ramsdell are identified by the periodicity of the Bravais lattice of the crystal[3]. To date many different polytypes have been grown in thin film form (6H, 4H, 3C, and 15R) by various methods, such as atmospheric and low pressure chemical vapor deposition (CVD)[4], and molecular beam epitaxy (MBE)[5]. The growth of these different polytypes depends on the orientation of the crystal surface, the temperature and substrate surface cleanliness[6], and the growth technique. For example, thin film growth by CVD on 6H-SiC substrates lapped several degrees off the {0001}direction toward the $\{11\bar{2}0\}$ result in the formation of 6H-SiC thin films[6] at 1200 °C. On the other hand, gas source MBE growth on similarly prepared 6H substrates resulted in the formation of 3C-SiC in the temperature range of 1050 °C to 1250 °C[5]. However, no technique in the past has been able to produce in thin film form the SiC polytype, 2H-SiC, with the highest bandgap and lowest repeat order. 2H-SiC in the past has only been grown as extremely small whisker crystals of no more than 400 μm in diameter[7].

2H-SiC is an important polytype for electronic and optical properties, if usable quantities and geometric form can be produced. It has the highest bandgap (3.3 eV)[8], the largest bi-refringency[9], and may have the highest electron mobility[10] of any of the SiC polytypes. Furthermore its structure, wurzite, and its lattice parameter matches those of 2H-AlN. The

Mat. Res. Soc. Symp. Proc. Vol. 339. ©1994 Materials Research Society

possibility of growth of 2H-SiC on AlN/sapphire enhances the usefulness of the material. The AlN/sapphire system offers potential growth of films over areas greater than 75 cm^2 on high resistivity substrates. Furthermore, this method avoids the difficulties associated with the micropipes common to SiC substrates grown by the modified sublimation method.[11] Possible applications of 2H-SiC are UV LEDS, high speed and high frequency devices, optically active devices, 2H-AlN/2H-SiC hetro-structures and a wide variety of photonic applications.

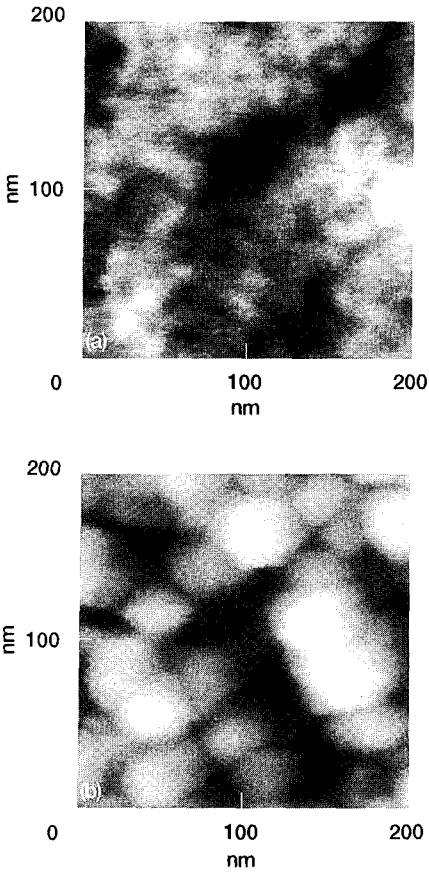

Figure 1.—Atomic force micrographs of SiC films grown on 6H-SiC at 1125 °C (a), and 1270 °C (b). The RMS roughness is 0.32 nm (a) and 6.3 nm (b).

EXPERIMENT

One growth method that has not been extensively applied to SiC is that of pulsed laser deposition (PLD). This method has recently proved to be very successful for the epitaxial growth of a wide variety of compounds. Examples include the high temperature superconductors YBCO and BKBO, as well as insulators such as MgO, $LaAlO_3$ and $SrTiO_3$. Under conditions typical for laser deposition of materials the initial plasma temperature is of the order of 10^4 K, whereas the species in the CVD or MBE processes have energies which are several orders of magnitude lower. In the course of investigation into the use of PLD for SiC thin film growth, we discovered conditions necessary for the growth of epitaxial 2H-SiC on (0001) 6H-SiC.[12] The 6H-SiC and Si substrates were mounted on the front of a molybdenum plate which was heated from the backside resistively by tantalum coils. The substrate was held onto the molybdenum plate by a molybdenum clip. The surface of the heated plate was placed parallel to the surface of a poly-crystalline SiC (purity 99.999%) target. The laser beam was focused onto the target through a fused-silica window on the vacuum chamber. The fluence of the laser beam at the target surface was approximately 2.5 J/cm^2. The repetition rate was 2 pulses per second. The chamber pressure was approximately 5 x 10^{-6} torr during deposition. The laser beam was scanned over the target using a conventional beam steerer. The temperature of the plate was measured by a type R-thermocouple welded to the molybdenum plate. SiC was deposited on Si with the Mo plate temperature held at 970 °C and 1125 °C while the plate temperature for SiC films on SiC was

970 °C, 1125 °C and 1270 °C. The growth rate was approximately 0.05 nm per second. After deposition the samples were analyzed by X-ray diffraction (XRD), atomic force microscopy (ATM), Auger electron spectroscopy (AES), electron diffraction, and high-resolution transmission electron microscopy (HTREM).

CHARACTERIZATION

All of the SiC films described here (both on Si and SiC substrates) were specular and featureless under an optical microscope at magnification to 400x. Examination of the films by a scanning electron microscopy revealed a featureless surface at 25Kx, with the presence of an occasional particulate believed to originate from the ablation target. To reveal the SiC film surface morphology, AFM was employed using a Digital Instruments Nanoscope III apparatus. Films grown on Si and 6H-SiC at 970 °C and those on Si at 1125 °C were featureless by AFM. The films grown on 6H-SiC, as seen in Fig. 1., at 1125 ° C and 1270 °C were granular with average grain size and roughness of 0.32 nm and 15 nm, and 6.3 nm and 65 nm, respectively. The grains of the film grown at 1270 °C have a hexagonal symmetry as shown in Fig. 1b.

X-ray diffraction measurements revealed that only the films grown on 6H-SiC at 1125 °C and 1270 °C were crystalline. Reflections corresponding to d-spacings of 0.126 nm and 0.252 nm were observed. The X-ray rocking curve performed on the film grown at 1270 °C indicated that substrate was lapped 2.5° off-axis. The full-width-at-half-maximum of the rocking curve about the d=0.252 nm film reflection was 3 degrees. This result may be attributed to both the small grain size and a slight variation of the grain orientation.

The AFM data along with the XRD data suggests that the film grown at 1270 °C is crystalline with hexagonal symmetry, but can not reveal the polytype. In order to determine the polytype of the film grown at 1270 °C a cross-sectional specimen was prepared by the sandwich technique and was investigated using a JEOL 4000EX electron microscope. Fig. 2 shows a low magnification high resolution electron micrograph of the film. Inset in this figure is a diffraction pattern corresponding to the film. The symmetry and measurements on the diffraction pattern of the film both correspond to 2H-SiC. The data in fig. 2 were obtained with the incident beam in the microscope accurately aligned with the [11$\bar{2}$0] axis of the film. From this diffraction data we conclude that the 2H grains have parallel

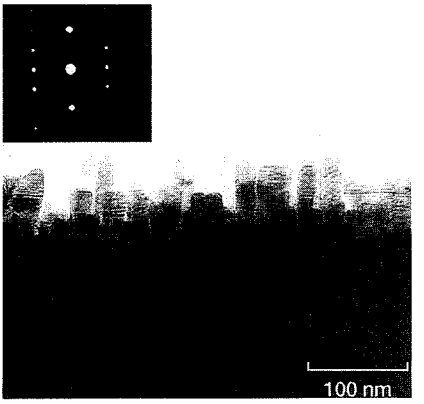

Figure 2.—Cross-sectional TEM micrograph of the 2H-SiC/6H-SiC interface with the electron beam along the [11$\bar{2}$0] zone-axis of the film. Inset is the diffraction pattern of the film.

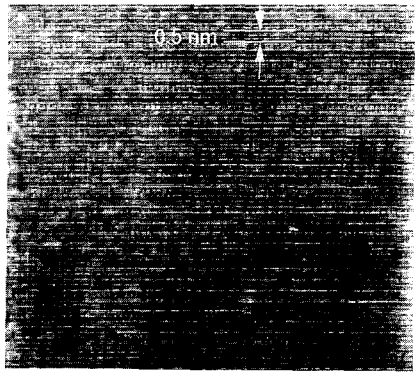

Figure 3.—A high magnification HREM of a 2H-SiC grain.

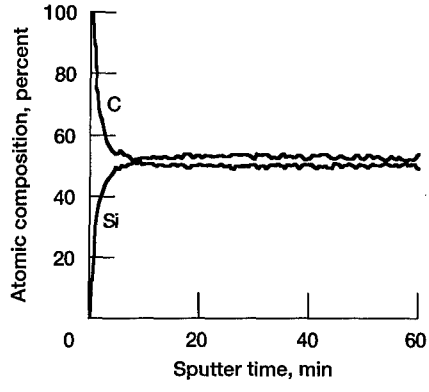

Figure 4.—Augér electron spectroscopy depth profile of the backside of a 6H-SiC wafer held at 1270 °C during deposition.

c-axis, and their [10$\bar{1}$0] axis are aligned with the [10$\bar{1}$0] axis of the 6H substrate. However, the film c-axis was tilted by 3° to 4° away from the substrate normal.

Fig. 3 shows a high magnification micrograph of two of the 2H-SiC grains and the interface between them. The faces of the basal planes, (0002) are nearly horizontal and have a spacing of 0.5 nm, as marked on the figure. Except for a few faults (especially near the top of the grains) where small regions have the 3C structure, the grains are relatively defect free.

AES was performed on the SiC films grown on both Si and 6H-SiC and bare 6H-SiC substrates. The Si(KLL) and the C(KLL) peaks were used to determine the ratio of Si to C. The ratio of the peak heights from the bare 6H-SiC substrate (69:30) was used to calibrate the findings for the thin films. In all the films, we observed an oxygen signal (0.5 % to 3%) at or below the noise level for the system; therefore, no conclusion regarding the effect of the background gases in the chamber on the growth of 2H-SiC can be made. At 970 °C and 1125 °C the films grown on silicon and at 970 °C the film grown on 6H-SiC had the same Si:C ratio as in the calibration sample. The SiC film grown at 1270 °C had a Si:C ratio which was carbon rich. The backside of the substrate which had SiC deposited on it at 1270 °C was analyzed by AES and was found to be carbon rich on the surface and then approach the calibrated values deeper into the crystal as can be seen in Fig. 4. AES data on the SiC film grown at 1125 °C was inconsistent. One AES depth profile showed a carbon rich surface while two others did not. These data suggest that silicon is partially volatile at higher growth temperatures and result in the 2H-SiC films on SiC being carbon rich.

CONCLUSIONS

We have discovered that epitaxial 2H-SiC thin films can be grown on off-axis 6H-SiC using PLD in a high-vacuum environment with the substrate holder plate temperatures at least 1125 °C. The size of the 2H-SiC grains increases with deposition temperature and is 65 nm in diameter for a growth temperature of 1270 °C. All the grains have their c-axis nearly aligned and are aligned with the substrate along the $[10\bar{1}0]$ direction. There is a tilt of approximately 3° between the substrate c-axis and that of the film. Silicon carbide grows amorphously on silicon up to temperatures of at least 1125 °C.

Acknowledgements

Useful discussions with J. A. Powell and S. Nishino are acknowledged. We appreciate the help of R. M. Dickerson in the TEM sample preparation. The work of M. A. S., H. K. M. V., D. L. J. and M. O. P. was supported by NASA-Lewis Research Center's cooperative grant NCC3-222, and the work of J. W. Y. was supported by NASA grant number NAG3-758.

REFERENCES

1. W. Shockley, in *Silicon Carbide: A High Temperature Semiconductor,* edited by J.R. O'Conner and J. Smiltens, (Pergamon, Oxford, 1960), pp. I-IV.
2. P. Pirouz and J.W. Yang, Ultramicroscopy 51, 189 (1993).
3. L. Ramsdell, Am. Mineral. 32, 64 (1947).
4. *Amorphous and Crystalline Silicon Carbide IV,* edited by C.Y. Yang, M.M. Rahman, and G.L. Harris, 71, (Springer-Verlag, Berlin, 1992).
5. S. Kaneda, Y. Sakamoto, T. Mihara, and T. Tanaka, J. Crystl Growth 81, 536 (1987).
6. T. Kimoto, H. Nishino, A. Yamashita, W.S. Woo, and H. Matsunami, in *Amorphous and Crystalline Silicon Carbide IV,* edited by C.Y. Yang, M.M. Rahman, and G.L. Harris, 71, (Springer-Verlag, Berlin, 1992), p. 31.
7. J.A. Powell, J. Appl. Phys. 40, 4660 (1969).
8. L. Patrick, D.R. Hamiliton and W.J. Choyke, Phys. Rev., 143, (1966).
9. J.A. Powell, J. of Optical Society of America, 62, 341 (1972).
10. L. Patrick, J. Appl. Phys., 37, 4911 (1966).
11. K. Koga, Y. Fujikawa, Y. Ueda and T. Yanaguchi in *Amorphous and Crystalline Silicon Carbide IV,* edited by C.Y. Yang, M.M. Rahman, and G.L. Harris, 71, (Springer-Verlag, Berlin, 1992).
12. M.A. Stan, M.O. Patton, J.D. Warner, J.W. Yang, and P. Pirouz, to appear in May 16, 1994 issue of Appl. Phys. Lett, 64.

LASER TRANSFORMED SiC THIN FILMS

K.G. Kreider, D.R.F. Burgess, Jr., M.J. Tarlov, G. Gillen, S. Wight
National Institute of Standards and Technology
Gaithersburg, MD 20899

R. Lareau and L.M. Casas
EPS-Army Research Laboratory
Ft. Monmouth, NJ 07703

ABSTRACT

Silicon carbide has excellent physical and electronic properties for use in devices when higher temperatures or higher power densities are required. We have investigated a direct laser conversion technique to create electrical conductors on the high band-gap silicon carbide. Thin films of silicon carbide (SiC) were sputter deposited on Al_2O_3, SiO_2, and Si substrates using a SiC target with an RF planar magnetron. These films were irradiated at 308 nm with multiple 15 ns excimer laser pulses creating 0.5 to 2 mm wide electrically conducting paths. Both the irradiated and unirradiated films were evaluated as a function of substrate type, deposition temperature, finish, stoichiometry, annealing temperature, sputter gas, film thickness, and laser processing conditions. The lowest resistivity films, originally 10 ohm-m, were calculated to be 160 μohm-m obtained after irradiation, which compares to a value of 50 μohm-m obtained after irradiating bulk SiC. The films were characterized using XPS, SIMS, AES, SEM, and Raman spectroscopy. We were able to characterize the composition of the films and conducting traces, the surface oxide, the critical binding energies, the lattice structure, and the morphology of the microstructure. Models for the phase transformations and conductivity have been formulated.

INTRODUCTION

Many of the limitations of semiconductor devices are a result of the properties of silicon. To achieve higher performance devices, gallium arsenide (GaAs) and silicon carbide (SiC) are being evaluated. Of these two leading candidates silicon carbide has the higher bandgap energy (2.2 eV for ß SiC; 2.9 eV for 6H SiC); the higher breakdown electrical field (2.5 x 10^6 V/cm for 6H; 2 x 10^6 V/cm for ß); and the higher thermal conductivity (4.9 W/cm-K). These advantages permit the use of silicon carbide at high temperatures without intrinsic conduction effects, under high voltage gradients, and in situations requiring high heat dissipation. If the application technology is developed for silicon carbide, this will enable new levels of power in semiconductor devices. Because of its high saturated electron drift velocity, SiC would also be favored at high (microwave) frequencies. These properties suggest that silicon carbide could be used in devices as a high temperature semiconductor, a blue light emitting diode, a p-doped window for solar cells, an ultraviolet radiation detector, and in high temperature sensors and actuators.

Silicon carbide has been considered for use in electronic devices in three different forms. These include single crystal SiC in both ß cubic and hexagonal phases, high temperature chemical vapor deposited ß SiC, and low temperature sputter deposited amorphous thin films. Our research has focussed on the low temperature sputter deposited form. The fabrication parameters for these films have been studied by Wasa et al[1,2] and Tohda et al[3] in order to produce wear resistant films and temperature sensors. They established parameters for producing amorphous films (substrate temperature below 500°C) and ß SiC films (above 700°C). Further work by Seaward, Barbee, and Tiller[4] using magnetron sputtering was used to optimize the optical properties and band gap. Suzaki et al[5] established that the properties of RF sputtered SiC films making them useful for p-doped windows for Si solar cells. As the technology of the sputter deposited films advances, it is expected that more applications will be established.

In order to fabricate silicon carbide semiconductor devices, several technologies must be developed. For example, to construct a junction field-effect transistor, other FETs or light emitting diodes, the planar technologies of doping, oxidation, and metallization are needed as well as patterning technologies. One of the limiting processing steps with silicon carbide-based devices pertains to the metallization for the source, drain, and gate contacts. These contacts must be free of oxidation and unreactive with materials in contact, including silicon carbide for long times at 350°-

Mat. Res. Soc. Symp. Proc. Vol. 339. ©1994 Materials Research Society

400°C. Aluminum is unsatisfactory and much of the preliminary testing of these devices has been performed in nitrogen to prevent oxidation of the metal electrodes. A recent discovery by Quick[6,7] may result in a new method of forming electrical contacts on SiC without the need for (external) metallization. He has used Nd:YAG lasers to (thermally) irradiate silicon carbide, producing tracks which are highly conductive. We report on testing those materials and make comparison to laser irradiated silicon carbide films produced here at NIST.

Silicon carbide (SiC) is a line compound with little solubility for carbon or silicon and does not melt congruently, but is characterized[8] by a peritectic reaction at 2545±40°C. Therefore, upon heating by laser irradiation beyond 2545°C, SiC will form solid carbon and liquid silicon with 27% atomic carbon dissolved. After sufficient heat is supplied for the latent heat of fusion, the temperature of the two phase mixture will increase further, and more carbon will dissolve until Si gas is formed above 3500°C. In the presence of oxygen, both CO and SiO could form rapidly which also would change the carbon to silicon ratio of the remaining condensed phase. However, due to the rapid heating and cooling during a laser pulse (<15 ns), there is little time for segregation by diffusion. This investigation was intended to find optimal processing conditions for laser transformed thin film silicon carbide and explain the resultant structures.

Experimental Procedure

Thin films were sputter deposited from CVD SiC (99.5%) onto substrates of silicon wafers, fused quartz, α SiC, and alumina with a 0.1 μM and 1 μM finishes. Power levels of 50-200W rf and 125 W dc were supplied to a 10 cm target in 0.4 Pa of argon and also argon + 4% hydrogen sputtering gas after a pump down to 10^{-3} Pa. Additional graphite or silicon targets were used simultaneously to produce films with excess carbon or silicon. The target to substrate distances used were 5-10 cm and the substrate temperatures were varied between 40°C to 380°C to investigate the relationship between processing parameters and film properties. A range of laser intensities were used to convert the SiC to conductive layers. Typically, the XeCl excimer laser (308 nm, 15 ns) was operated at 10 Hz and a 7.5 mm diameter (0.5 cm^2) center portion of the laser beam was selected. This light was spatially filtered by focusing through a pinhole and then recollimated using f1.5 optics. A 3 mm diameter uniform center portion of the beam was then selected and focused down to beam sizes of 0.5-1.0 mm diameter. This procedure was found to produce a relatively uniform distribution in the irradiated area. Typically, the incident energy in the irradiated area was about 5-10 mJ/pulse, corresponding to about 600-1200 mJ/cm^2/pulse (for a 1 mm diameter irradiated area). The sample to be irradiated was mounted on a stepper motor driven stage allowing the laser spot to be translated across the sample surface at a controlled rate.

Four point resistance measurements were made with osmium points at temperatures ranging from 22°C to 120°C to evaluate the conductivity of the films and the thermal coefficient of resistivity. Depth profiling by Auger electron spectroscopy was performed using a Perkin-Elmer PHI 660 scanning Auger microprobe with 3 keV electron beam to stimulate Auger transitions and a 4 keV Ar^+ ion beam to sputter-etch the surface. Secondary ion mass spectrometry (SIMS) was performed using a Cameca IMS 4F instrument with a 14.5 keV Cs^+ beam and monitoring negative secondary ions. Sputtered crater depths for both Auger and SIMS measurements were determined using a surface profilometer. XPS Spectra were acquired using a nonmonochromatized Al anode operated at 240 W as the excitation source. A hemispherical analyzer was operated in the retarding mode at a pass energy of 20 eV for electron energy analysis. Raman spectra were acquired by exciting at 514 nm (argon ion laser), irradiating the sample with typically 250 mW in a 60 μm diameter spot at near grazing incidence (<15°) and vertically polarized light, collecting the scattered light at near surface normal (>75°) with roughly f6 optics, dispersing the Raman shifted light using a 0.5 m monochromator, and detecting with a 512x512 CCD array.

Results

Our investigation of the optimization of electrical conductivity of the laser converted tracks focussed on film fabrication parameters and laser processing parameters. The laser power density was varied by either attenuating the laser beam with glass and quartz plates or by varying the distance between the focusing lens (more typical). A variety of laser intensities were used: from low intensities where little visible change in the irradiated area was observed (as well as little conductivity change) to significant visible change to clear ablation (where a 2-4 mm long plume was ejected). In general, visible changes in the irradiated area would occur at low intensities, but with little

change in conductivity. Visible emission from the surface was observed upon laser irradiation. This was dependent upon laser intensity, the specific surface, and whether the surface had been irradiated previously. For the SiC on polished silicon surfaces at low intensities, no visible emission was observed. For all of the other SiC samples (α, reaction-bonded, SiC thin films on alumina and quartz) even at very low intensities, an initial "spark" was observed that went away after a few pulses. This was interpreted as a "cleaning" or ablation of the surface layer, such as removing a thin surface oxide (SiO_x) layer. For all of SiC surfaces it was determined that there was an optimum laser intensity for best conversion to conductive layers; that is, at low intensities (<500 mJ/cm^2/pulse) little change in the conductivity was measured and at high intensities (>1500 mJ/cm^2/pulse) material was ablated. It was also found that there was also a optimum rate of translation of the irradiated area along the surface. Very fast rastering (<4 repeat pulses/spot) resulted in non-uniform conversion. Very slow rastering (>25 repeat pulses/spot) resulted in good conversion, but loss of some material. Rastering at a rate corresponding to effectively about 11-16 repeat pulses on each spot resulted in the best conversion. Good conductivity (50-60% of best values) was obtained even at very fast rastering and only slowly improved as the rate of rastering decreased until an optimum value was reached. After this point was reached, the resistance of the laser transformed film abruptly increased, consistent with partial ablation of the transformed film (from optical microscopy and visible emission from a 2-4 mm plume from the irradiated area).

Table 1 is a presentation of some of the results and parameters of the investigation of fabrication variables. An optimization of these parameters after laser irradiation for resistance permits the following conclusions. (1) Alumina substrates were superior to silicon, silica, or SiC. (2) Better results were accomplished with an optical finish on the Al_2O_3. (3) A substrate temperature of 330-380°C was better than 50°C. (4) Excess silicon in the deposit was inferior to stoichiometric SiC. (5) Excess carbon (20%) produced the best results. (6) Annealing the sputtered film at 930°C (to crystallize β SiC) was not useful. (7) Pure argon sputtering gas was better than argon plus 4% H_2. (8) The thickness of the SiC thin film should be 3 μm or more to obtain the best results. The best laser irradiated tracks on sputter deposited SiC were made using polished Al_2O_3 substrates at 330°C and 3.4 μm thick with excess carbon in an argon sputter gas and had a resistance of 800Ω. This compares to 10^8-10^9 ohms for the as deposited films.

In addition to the room temperature 4 point probe resistance tests, we tested the resistance of the laser transformed tracks as a function of temperature between 20°C and 120°C. The thermal coefficient of resistivity was negative in all the laser transformed thin films indicating semiconductor behavior. The coefficient was approximately 1500 ppm per K for low resistance (1400 ohm) films and higher for films with greater resistance (3000 ppm per K for 12000 ohm).

A series of diagnostic techniques were employed to characterize the laser irradiated silicon carbide. Optical microscopy and scanning electron microscopy were used to characterize the morphology and topology of the phases, X-ray photoelectron spectroscopy (XPS) was used to monitor the surface composition and carbon to silicon ratios, SIMS depth profiling and Auger depth profiling were used to determine changes in composition with depth and Raman analysis was

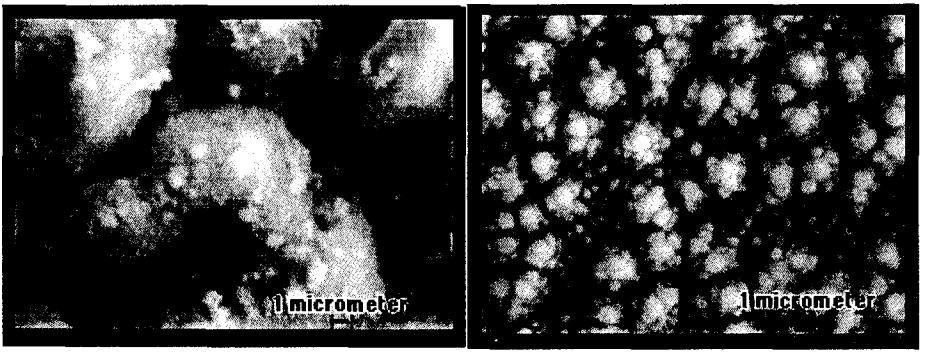

Figure 1. SEM photographs of laser transformed silicon carbide samples (a) hot pressed SiC (b) thin film SiC on alumina

used to identify bonding pairs in the transformed material.

The microscopic topology of the highly conductive films is presented in the SEM photographs Figures 1a and 1b. Fig. 1a illustrates the coarse, 5 μm "globules" solidified from the molten particle on hot pressed SiC. Fig. 1b shows the smaller agglomerated globules solidified from the laser melted thin (3 μm) films. These structures appear very similar at 1000x using optical microscopy although the depth of focus is significantly inferior. Films which were transformed to lower electrical conductivity either had more widely spaced globules (lower power) or had sections where the film was ablated. In general, we could correlate high conductivity films with the appearance of uniform and complete melting of the surface of the laser track.

One key issue in explaining the high conductivity of the laser transformed material is identifying the phase or phases in Fig. 1a and 1b. The irradiation includes a heating to the point of vaporization and melting of the silicon carbide. The peritectic melting at 2545°C should produce molten silicon with 27 atomic percent carbon plus solid carbon according to the phase diagram. However, because the heating is so rapid (10 ns) diffusion distances would be very small (<10 nm, assuming a liquid-like diffusivity of 10^{-4} cm^2/s) and a melt of 50% carbon could be produced above 3000°C which would require little or no phase separation. We expect the cooling to be similarly rapid and therefore phase separation is also severely constrained during solidification.

The stoichiometric ratio of silicon and carbon in the silicon carbide thin films was measured by Auger depth profiling. We measured silicon, carbon, and oxygen signals as a function of depth on areas of high conductivity and on areas of as deposited films. The silicon-carbon ratio was 1:1 (±5%) throughout all the films tested and was not affected by the hydrogen in the sputtering atmosphere. We did not see significant differences between high conductivity and low conductivity traces and the oxygen signal was within the noise level (5%).

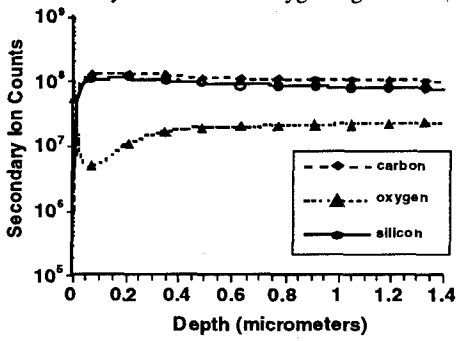

Figure 2. SIMS depth profile of a high conductivity laser irradiated SiC thin film

It was felt that secondary ion mass spectrometry (SIMS) would be more sensitive to the low concentration levels of oxygen. Several thin films were analyzed by sputter depth profiling with SIMS. Fig. 2 shows SIMS depth profiles of an high conductivity track (resistance of 800 ohm) in a laser irradiated film. The unirradiated films show flat depth profiles with signals identical to that observed at the largest depths in the irradiated films. The irradiated film shows the presence of a thin surface oxide. Similar surface spikes in the oxygen signal were observed in other irradiated SiC samples (but not in the unirradiated samples). The SIMS depth profiles also indicate a depleted region of oxygen that reaches a minimum value at a depth of about 0.05 micrometers. The oxygen secondary ion signal at the minimum values is about 4 times lower than in the unirradiated film. The oxygen variation in the irradiated films occurs over a depth of about 0.0 to 0.3 micrometers. Beyond 0.3 micrometers, the oxygen signal is comparable to the unirradiated sample. We associate the dip in oxygen with the laser transformed zone with high conductivity. Combining our estimate of 0.2 μm from the SIMS profile and the 800 ohm resistance on the 4 point probe, the apparent resistivity of the transformed track is 0.016 ohm-cm.

The presence of a surface oxide was also apparent on the XPS intensity traces (as well as with AES). XPS was useful in measuring the excess carbon and silicon in the films deposited from multiple targets, but not in identifying changes in the bonding nature of the irradiated layers. Twenty percent excess carbon was measured on the sample tested with 7000 ohms resistance and permitted estimation of all of the compositions of the samples with excess carbon. Similarly 14% excess silicon was measured on sample 18B but all samples with excess silicon had poor conductivity after laser irradiation.

Raman spectroscopy can be used to identify interatomic bonding. We were particularly interested in characteristic Si-C, Si-Si, and C-C bonds that would indicate the presence of the peritectic reaction of SiC=Si(C) + C. The Raman spectra for both unirradiated and irradiated

silicon carbide and sputtered thin film silicon carbide are presented in Fig. 3. In the hot pressed SiC, as expected there are two strong peaks at 785 and 975 cm^{-1} indicative of ordered silicon carbide[9], while in the as-deposited films their absence suggests an amorphous state. In the irradiated films, there is a sharp peak at 520 cm^{-1}, indicative of ordered silicon[11] and broad peaks at 1580 and 1360 cm^{-1}, indicative of graphite and disordered carbon, respectively.[10] Although Fig. 3 seems to imply that there is little silicon or carbon in the irradiated, hot pressed SiC, other Raman spectra obtained at lower irradiation indicate the presence of silicon and carbon. There are several significant observations, consistent with the reaction SiC = Si(C) + C. (1) Si-C bonds were reduced in α SiC upon irradiation. (2) Si-Si bonds increased in laser irradiated α SiC and SiC films. (3) C-C bonds increased the films (but decreased in α SiC).

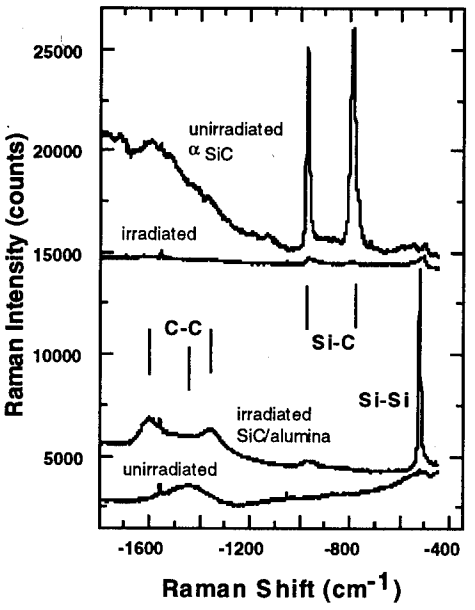

Figure 3. Raman spectra from hot pressed SiC and thin film SiC on alumina before and after laser irradiation.

The reduction in Si-C bonds at the surface of the highly conductive tracks in α SiC coupled with the increase of Si-Si bonds indicates the progression of the peritectic reaction SiC=Si(C) + C in the α SiC. The increase in Si-Si bonds and C-C bonds in the film also indicates the peritectic reaction. In the case of the films, there was no excess carbon before irradiation and the melting cycle was faster as evidenced by the microstructure (Fig. 1a, 1b), suggestive of increased C-C bonds with the laser processing. Note the apparent photoluminescence at lower energies ("scattered" light at >1300 cm^{-1} shift from 514 nm, consistent with a bandgap of ~2.3 eV) in the insulating, unirradiated α SiC material. In summary, some peritectic phase separation of carbon and silicon are apparent by Raman spectroscopy.

Summary

It was found that laser irradiation of sputter deposited amorphous silicon carbide films could cause a resistance drop from 10^8-10^9 ohms to 800 ohms in a 4 point test. A 0.2 μm thick conducting film within the sputtered film was created by melting and solidification which had very little change in composition. These results are similar to that previously reported for laser transformed hot pressed alpha SiC. Although some evidence of phase separation into carbon and silicon was observed by Raman spectroscopy it is unlikely that major segregation has taken place because of the rapid (15 ns) thermal treatment. Some surface silicon dioxide is formed and some material loss due to vaporization was also noted.

The technique of laser writing conducting paths on silicon carbide may lead to important applications as harsh environment sensors and electronic devices.

TABLE 1				
Laser Transformed Silicon Carbide Sputtered Thin Films				
Run	Substrate	Thickness (μm)	Resistance (kΩ)	Note
15	Si, SiC	1.6	30.	50°C*
16	Al_2O_3	2.4		50°C*
17	Al_2O_3**	1.6	4.5	
	Al_2O_3	1.6	70.	+930°C 2h
18	Al_2O_3	1.4	>100.	xs Si
19	Al_2O_3**	1.3	7.	xs C
	$A1_2O_3$	1.7	6.	xs C
	Al_2O_3	1.7	35.	+930°C 2h
20	Al_2O_3	4.8	6.5	xs C
	Al_2O_3**	3.4	0.8	xs C
	Al_2O_3	3.4	1.6	+930°C 2h
21	Al_2O_3	4.0	1.7	
	Al_2O_3**	2.9	1.4	
	Si	3.1	4.2	
22	Al_2O_3	3.3	24.	Ar + $4H_2$
	Al_2O_3**	2.5	14.	Ar + $4H_2$
	Si	2.9	20.	Ar + $4H_2$
23	Al_2O_3	2.7	4.0	Ar + $4H_2$
	Al_2O_3**	3.7	7.	and
	Si	2.0	2.0	xs C
* Substrate temperature, all others 300 - 370°C ** Optical polish				

Acknowledgments

This work was supported by NIST Director's Reserve funds. We gratefully acknowledge helpful discussions with Nat Quick and assistance from Walt Bowers, Wilbur Hurst, and Jim Maslar in some of the Raman experiments and James Cline for X-ray analysis.

References

1. K. Wasa, T. Nagai, and S. Hayakawa, *Thin Solid Films* **31**, 235 (1976)
2. K. Wasa, T. Tohda, and S. Hayakawa, *Rev. Sci. Inst.* **50**, 10834 (1979)
3. T. Tohda, K. Wasa, and S. Hayakawa, *J. Electrochem Soc.* **127**, 44 (1980).
4. K.L. Seeward, T.W. Barbee, and W.A. Tiller, *J. Vac. Sci. Tech.* **A4**, 31 (1986)
5. Y. Suzaki, S. Inoue, I. Hasegawa, K. Yoshii, and H. Kawabe, *Thin Solid Films* **173**, 235 (1989).
6. N.R. Quick and R.J. Matson in Proceedings of the International Symposium on Microelectronics '91, F.J. Duarte and D.G. Harris (ed), STS Press, McLean, 1992, p 545.
7. N.R. Quick, U.S. Patent No. 5,145,741, 8 Sep. 1992
8. Binary Allo Phase Diagrams, ed. T.B. Massalski, American Society from Metals, Cleveland, OH, 1986, p. 589.
9. F. Adar, *Microchem. J.* **38**, 50 (1988).
10. F. Tuinstra and J.L. Koenig, *J. Chem. Phys.* **53**, 1126 (1970)
11. J. Gerault, R. Morancho, G. Constant and M. Alnot, *Thin Solid Films* **101**, (1983)

REACTIVE MAGNETRON SPUTTERING OF SILICON IN AR + CH_4: IDENTITY AND ENERGY OF THE SIC GROWTH SPECIES

M. P. FITZNER AND J. R. ABELSON
Coordinated Science Laboratory and the Department of Materials Science and Engineering, University of Illinois, Urbana IL 61801

ABSTRACT

Double-modulation mass spectrometry is used to analyze the identity and energy distribution of the particle flux during low-temperature growth of $Si_{1-x}C_x$ by reactive magnetron sputtering of a silicon target in 3 mTorr argon and 0 - 0.35 mTorr methane. The ion fluxes, methane consumption, film deposition rate, and film composition are determined as a function of the methane partial pressure at fixed target current. Argon, silicon, carbon and hydrocarbon ions are detected at the substrate position. The argon and hydrocarbon ions have a narrow energy distribution consistent with the plasma potential. The silicon and carbon ions have a broad energy spread, consistent with that of sputtered neutrals which are post-ionized by the plasma. The film composition (C/Si) varies in the same manner as the arrival ratio of (C^+/Si^+) ions, but does not correlate well with the arrival ratio of ($\Sigma CH_x^+/Si^+$) ions or the methane consumption rate. We conclude that the main source of carbon in $Si_{1-x}C_x$ films is the sputtering of C atoms from the Si target surface.

INTRODUCTION

Cubic silicon carbide (SiC) is receiving much attention as a semiconductor for power devices because of its wide band gap (2.3 eV) and high thermal stability (T_m = 2800 °C). However, device fabrication has been limited by the high temperatures (~ 1200 °C) required to grow epitaxial films using chemical vapor deposition. Recently, Ivanov and Sundgren have successfully grown SiC films at lower temperatures (800 °C) using DC reactive magnetron sputtering (RMS) of a Si target in an (Ar + CH_4) atmosphere. Little direct evidence exists concerning the particle fluxes that reach the growing film surface, or the mechanism(s) by which carbon is transferred from CH_4 molecules to the SiC film in the absence of thermal pyrolysis. Quantitative information is desirable for process optimization, since low energy ion bombardment can be used to promote crystallinity at low temperatures[1], and the defect chemistry will depend on the relative fluxes of C to Si. During reactive magnetron sputtering of Si in an (Ar + CH_4) plasma, C will arrive at the growing SiC surface in several forms. Hydrocarbon radicals and ions are generated by fast electron collisions with methane molecules. The production rates for these species are highest in the intense plasma near the target. Some of the C-bearing species will chemisorb on the Si target surface and then be sputtered off by argon ions. The hydrocarbons may also chemisorb directly onto the growing film surface. Since a weak plasma escapes the magnetic trap and extends to the substrate,

Mat. Res. Soc. Symp. Proc. Vol. 339. ©1994 Materials Research Society

local production of radicals and ions is potentially significant compared with transport from the target region.

This work reports the ion fluxes, CH_4 consumption, film deposition rate, film composition, and plasma parameters near the substrate (potential, density, and electron energy distribution function) as a function of the CH_4 partial pressure at fixed target current. These data provide a nearly complete and quantitative understanding of the SiC growth fluxes during RMS.

EXPERIMENTAL

The deposition system is of high vacuum construction, turbo-pumped to a base pressure of 5×10^{-7} Torr. The deposition source is a 5 cm diameter planar magnetron (AJA International) with a polycrystalline silicon target, 7 cm from the substrate. Amorphous, hydrogenated $Si_{1-x}C_x$ films are deposited in a plasma of 3 mTorr Ar and 0 - 0.35 mTorr CH_4 onto electrically grounded crystalline silicon substrates held at 235°C. The plasma current is maintained at 50 mA (~ 12.8 ma/cm^2); the cathode voltage ranges from 407 - 385 V, decreasing as methane is added to the system.

Plasma ions are analyzed using the double modulation mass spectrometry (DMMS) technique as previously described[2] but with the electron-impact ionizer turned off. DMMS samples particles line-of-sight from a point on the erosion "racetrack" of the sputter target, through a pair of 2 mm diameter collimating orifices and the quadrupole mass filter. Particle energy distributions are provided by an AC modulated retarding field between the last grid of the ion optics and the quadrupole rods, i.e., a "pole bias." The DMMS can also be operated as a standard mass spectrometer to determine the fractional consumption (depletion) of CH_4 by the plasma. In order to detect thermal and nearly thermal plasma ions, it is necessary to accelerate them into the first orifice of the DMMS by raising the plasma potential. A disc electrode, 11.4 cm in diameter with a 1.9 cm hole in the middle, is placed above the orifice and biased positively with respect to the (grounded) orifice and chamber walls. This electrode becomes the plasma anode, and the plasma potential equals the anode potential plus ~ 2 V. For anode biases of > + 27 V, all ion signals saturate. Unless noted otherwise, an anode bias of + 27 V was used for all DMMS measurements. Film compositions (C/Si) are determined by Rutherford backscattering spectrometry (RBS). To improve the resolution for C, samples were deposited on C (graphite) substrates.

RESULTS AND DISCUSSION

Figure 1 shows a mass scan of the hydrocarbon ions produced by the plasma and accelerated into the DMMS. The quadrupole has been adjusted for maximum sensitivity for fast ions, at the expense of mass resolution.[3,4] However, the individual hydrocarbon peaks can be accurately determined by a gaussian fitting procedure. For reference, the inset shows the Ar^+ ion signal and a fit with 1 amu full width at half maximum. For the hydrocarbon peaks, the mass locations are fixed and the widths are held constant at 1 amu full width at half maximum; only the signal heights are adjusted to produce the fit to the data shown by the solid line.

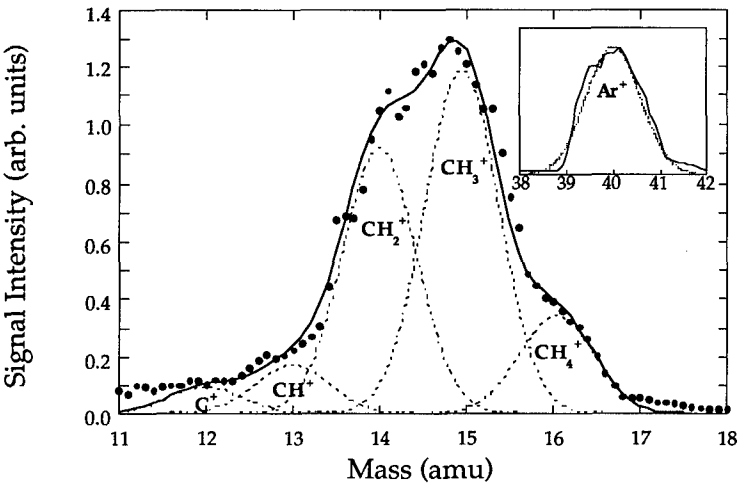

Fig. 1. A mass scan of the hydrocarbon ions produced by the plasma and accelerated into the DMMS. Gaussian fits (dashed lines) are used to resolve individual hydrocarbon peaks. The overall fit is excellent (solid line).

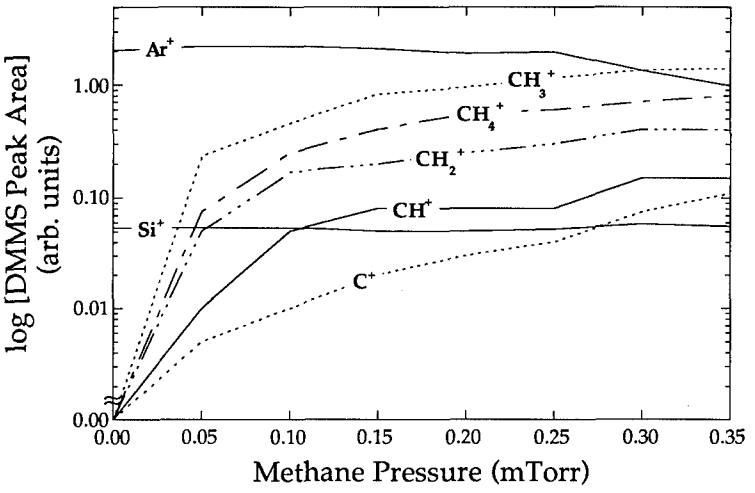

Fig. 2. The area of each ion peak in figure 1 as a function of the CH_4 partial pressure.

Figure 2 shows the area of each ion peak as a function of the methane partial pressure. The hydrocarbon ion signals increase linearly with methane pressure across the range investigated. By contrast, the carbon ion signal increases more rapidly. A possible source of C^+ ions is the sputtering of C atoms from the Si target surface, followed by post-ionization as these atoms traverse the plasma. This is the mechanism that produces the Si^+ ion flux. We performed Langmuir probe measurements near the substrate and determined that the plasma density and electron energy distribution do not vary strongly with methane pressure; hence the ionization probability for sputtered atoms is essentially constant, and the C^+ and Si^+ signals are proportional to the sputtered C and Si atom fluxes. Note that the Si^+ signal remains constant, indicating that the target surface does not become heavily covered ("poisoned") by C even at high CH_4 pressure.[5,6]

Three experiments establish the origin of the C^+ signal. In the absence of anode bias, plasma ions are not accelerated into the DMMS. But when we grounded the anode, all signals fell below the detection limit, except for C^+, which decreased by only a factor of ~ 2. This is strong evidence that many of the C^+ ions have a directed velocity that allows them to enter the DMMS. Note that the collection probability for fast ions increases with anode bias, since a greater sheath potential will re-direct a greater fraction of the ion velocity vectors into the narrow acceptance angle of the collimating orifices. Thus the drop in C^+ signal cannot be interpreted simply in terms of fast vs. slow ions. In a pure Ar discharge, only Si^+, Ar^+ and Ar^{++} ions are detected.

Because of the narrow acceptance angle into the DMMS, we can block any signal originating from the Si target surface by inserting a small (1 cm^2) insulated beam stop in the line-of-sight from the target to the DMMS. As a result the Ar^+ and hydrocarbon ion signals remained nearly constant, while the C^+ and Si^+ signals fell below the range of detection. This is further proof that C^+ signal is mostly comprised of sputtered carbon. Finally, figure 3 shows the energy distributions of the Ar^+, CH_3^+, Si^+ and C^+ ions, obtained by differentiating DMMS retarding potential scans. Both Ar^+ and CH_3^+ have relatively narrow distributions consistent with near-thermal ions that fall through the plasma sheath. The Si^+ and C^+ distributions are significantly broader, as expected for sputtered species. The fact that C^+ has the broadest distribution is consistent with the sputtering of atoms of low binding energy, i.e., C chemisorbed on the Si target surface. The data from these three experiments conclusively demonstrate that the majority of the C^+ signal originates from sputtered C atoms.

The relative importance of sputtered C in determining the $Si_{1-x}C_x$ film composition is suggested by the data of figure 4. The ratio of arriving C^+/Si^+, of all hydrocarbon ions $\Sigma CH_x^+/Si^+$, and of C/Si in the films is plotted as a function of methane pressure. The film composition and C^+/Si^+ ratio track each other very well, whereas the integrated hydrocarbon arrival and depletion have a different pressure dependence. Since a large flux of hydrocarbon ions and neutrals reach the film surface, these data imply that the reactive sticking coefficient for sputtered C is much higher than for these species.

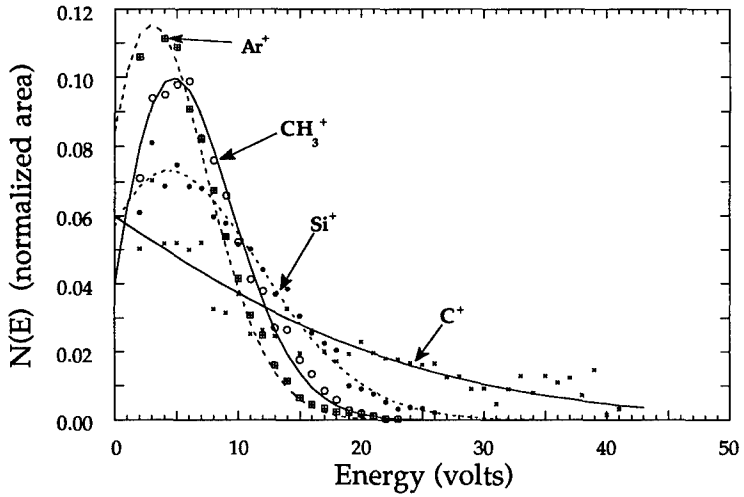

Fig. 3. Energy distributions of the Ar^+, CH_3^+, Si^+ and C^+ ions, obtained by differentiating DMMS retarding potential scans. Gaussian fits are shown.

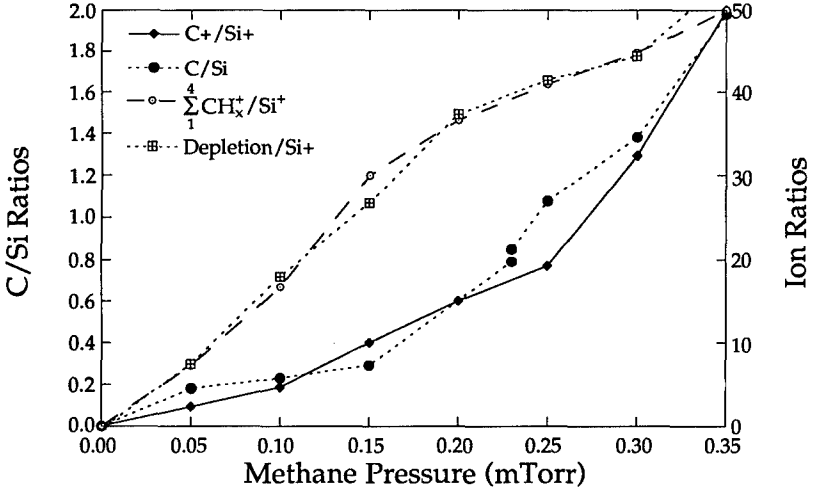

Fig. 4. The ratio of arriving C^+/Si^+, of all hydrocarbon ions $\Sigma CH_x^+/Si^+$, and of C/Si in $Si_{1-x}C_x$ films grown under identical conditions, as a function of methane pressure.

CONCLUSIONS

The ratio of C/Si sputtered from the target surface correlates exactly with the film composition over a wide range of CH_4 pressures. By contrast, the flux of hydrocarbon ions and neutrals follow a different dependence. These data imply that the reactive sticking coefficient for sputtered C is much higher than for hydrocarbon species, i.e., sputtered C dominates the growth process.

ACKNOWLEDGMENTS

The work was supported by the Electric Power Research Institute. Analyses of $Si_{1-x}C_x$ film composition were performed in the Center for Microanalysis of Materials, Materials Research Laboratory at UIUC. The authors thank Dr. Ivan Petrov (University of Illinois) and Dr. Ivan Ivanov (Linköping University) for many stimulating discussions and their assistance with this project.

REFERENCES

1. I. Ivanov, S. Statev, I. Petrov and V. Orlinov, *Vacuum* **00**, 1 (1992)
2. A. M. Myers, D. N. Ruzic, R.C. Powell, N. Maley, D.W. Pratt, J.E. Greene, J.R. Abelson, *Journal of Vacuum Science and Technology* A8, p. 1668, (1990)
3. D. Rapp, Englander-Golden and D. Briglia, *The Journal of Chemical Physics* **42**, 4081, (1965)
4. D. Rapp and Englander-Golden, *The Journal of Chemical Physics* **43**, 1464, (1965)
5. Q. Wahab, L. Hultman, J.-E. Sundgren and M. Willander, *Materials Science and Engineering* **B11**, 61, (1992)
6. Q. Wahab, R. C. Glass, I. Ivanov, J. Birch, J.-E. Sundgren and M. Willander, *Journal of Applied Physics* **74**, 1663, (1993)

PART VII

Nitride Epitaxial Growth

MOVPE GROWTH OF HIGH QUALITY $Al_xGa_{1-x}N/Ga_yIn_{1-y}N$ ($x \geq 0$, $y \leq 1$) HETEROSTRUCTURES FOR SHORT WAVELENGTH LIGHT EMITTER

I.Akasaki and H.Amano,

Meijo University, Department of Electrical and Electronic Engineering,
1-501 Shiogamaguchi, Tempaku-ku, Nagoya 468, Japan.

ABSTRACT

High-quality AlGaN/GaN and AlGaN/GaInN DHs were fabricated by MOVPE using low-temperature deposited AlN buffer layer. We applied the newly designed dual-flow-channel reactor, by which high-quality and well-controlled AlGaN and GaInN alloys and their heterostructures have been grown. AlGaN/GaN-DH shows low-threshold stimulated emission by optical pumping at room temperature for both edge and surface modes. The peak wavelength of stimulated emission for edge mode was 369.5nm. The peak wavelength of stimulated emission was affected by the strain due to heterostructure as well as the many body effect under high excitation. The wavelength for stimulated emission can be widely changed by using GaInN as the active layer. AlGaN/GaInN DH with InN molar fraction of the active layer of 0.09 shows room temperature low-threshold stimulated emission for edge mode by optical pumping with peak wavelength of 402.5nm. A few mW-class symmetrical AlGaN/GaN DH LED and antisymmetrical AlGaN/GaInN/GaN DH LED using low energy electron beam irradiation (LEEBI) treated Mg-doped P-AlGaN cladding layer were fabricated. These results show that column-III nitrides are promising for the realization of practical short wavelength LED and LD.

INTRODUCTION

AlN, GaN, InN and their alloys AlGaN ,GaInN and AlGaInN are promising for the application to short wavelength light emitter, because they possess direct large band gaps of 1.95eV for InN to 6.2eV for AlN. The elastic constants of column-III nitrides are about twice as large as those of II-VI compounds, such as ZnSe and ZnS. Therefore, these nitrides are physically harder and more stable than II-VI compounds. However, because of the lack

Mat. Res. Soc. Symp. Proc. Vol. 339. ©1994 Materials Research Society

of the substrate materials the lattice constant and thermal expansion coefficient of which are close to those of column-III nitrides, it had been quite difficult to grow high-quality films. We succeeded in growing high-quality GaN and AlGaN epitaxial layers on the sapphire substrate using AlN buffer layer[1,2] by metalorganic vapor phase epitaxy (MOVPE). Afterwards, some research groups showed similar effects either using GaN buffer layer by MOVPE[3] or using initial nitridation of the sapphire and GaN buffer layer by electron cyclotron resonance plasma assisted molecular beam epitaxy (ECR-MBE)[4].

Control of n-type conductivity has been achieved in the GaN, AlGaN and GaInN by us for the first time by doping with Si[5-7] from the undoped level up to near $10^{19}cm^{-3}$.

On the other hand, it had been fairly difficult to grow nitrides having p-type conductivity. Among many candidates, Mg is thought to be one of the best candidates as the shallow acceptor impurity in GaN, AlGaN and GaInN. In the early 1970's, some research groups attempted to grow GaN doped with Mg by hydride vapor phase epitaxy(HVPE). Maruska et al. succeeded in fabricating MIS-type violet light emitting diode using Mg-doped highly resistive GaN as the insulating layer[8]. In 1989, we used bis-cyclopentadienylmagnesium (Cp_2Mg) as the Mg source gas in MOVPE and found that Mg concentration changed linearly with the flow rate of Cp_2Mg[9]. As-grown GaN:Mg showed high resistivity. We realized, for the first time, that GaN:Mg with distinct p-type conductivity by low energy electron beam irradiation (LEEBI)[10] . Dehydrogenation process of the hydrogen passivated Mg is proposed[11,12]. Later, another groups also succeeded in obtaining GaN:Mg with p-type conductivity by thermal annealing of the as-grown GaN:Mg[11] under nitrogen atmosphere, or by growing GaN:Mg with hydrogen-free atmosphere[13-16].

For the design of the structure of the devices such as light emitting diode (LED) and laser diode (LD) using alloys and heterostructures, understanding the basic physical, optical and luminescence properties, in particular impurity-related luminescence and many-body effects under high excitation are essential as well as the control of electrical properties. In this paper, (1) control of conductivity for p-type GaN and AlGaN, (2) dispersion of refractive indices of GaN, AlGaN and GaInN, (3) properties of stimulated emission at room temperature from AlGaN/GaN DH and AlGaN/GaInN DH, and (4) characteristics of P-

AlGaN/GaInN DH are discussed.

EXPERIMENTAL

Horizontal type MOVPE reactor was used in this study. To reduce parasitic reactions between organometallic sources and NH_3, dual-flow channel reactor was used[17]. TMAl, TMGa, TMIn and NH_3 were used as Al, Ga and In and N source gases, SiH_4 and Cp_2Mg as the Si and Mg source gases, respectively. Sapphire was used as the substrate. Just before the growth of GaN, AlGaN or GaInN, AlN buffer layer about 50nm was deposited at 600°C. The effects of AlN buffer layer has been published elsewhere[18]. Both Si and Mg were doped during growth. Mg-doped GaN and AlGaN were treated with LEEBI. Electrical properties of Mg-doped p-type films after the LEEBI treatment were characterized by Hall effect measurement using van der Pauw method. Refractive indices were measured by spectroscopic ellipsometry using Δ-tanΨ method. Linearly polarized light was incident on the film with angle of 70° , which means that approximately E$\perp$c components of the refractive indices was measured. Optical pumping measurement was performed at room temperature using pulsed nitrogen laser as the excitation source. In order to form electrodes for both n-type and p-type layer in DH, selective growth method was used[5].

RESULTS AND DISCUSSION

Conductivity control for p-type GaN and AlGaN

Conductivity of Mg-doped film is more depend on the treatment condition rather than on the concentration of Mg. Hole concentration up to $2\times10^{18}cm^{-3}$, and resistivity of 0.2 Ωcm at room temperature was achieved for GaN:Mg. The Mg-shallow acceptor ionization energy in GaN was found to be about 160meV from the temperature dependence of the intensity of D-A pair emission[19] and from that of the hole concentration[13]. The ionization energy in $Al_xGa_{1-x}N$ is larger than that in GaN by about (0.4×x)eV, where x is the AlN molar fraction in AlGaN. Figure 1 shows the temperature dependence of the hole concentration of Mg-doped $Al_{0.08}Ga_{0.92}N$. Fitting parameter to obtain activation energy E_A is also shown in the figure. Free hole concentration does not saturate even at high temperature, which is promising for the fabrication of devices operating at high temperature.

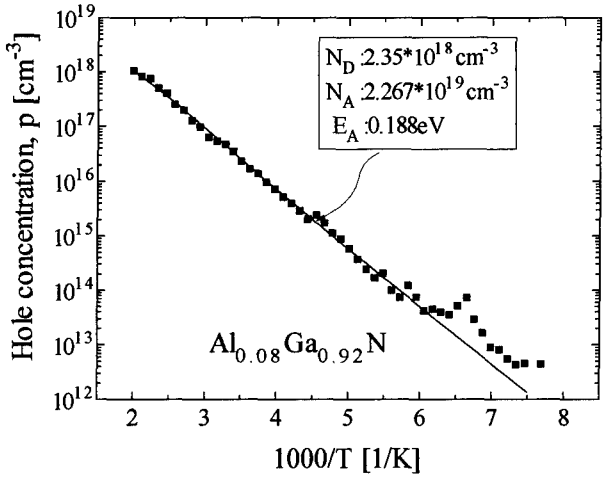

Figure 1. *Temperature dependence of the hole concentration in $Al_{0.08}Ga_{0.92}N$:Mg*

Dispersion of the refractive indices

Figure 2 shows the dispersion of the refractive indices of the E⊥c components in AlGaN, GaN and GaInN alloys. Refractive index of all the sample tends to have a maximum at M0 specific points in a photon energy range studied here. Figure 3 summarizes

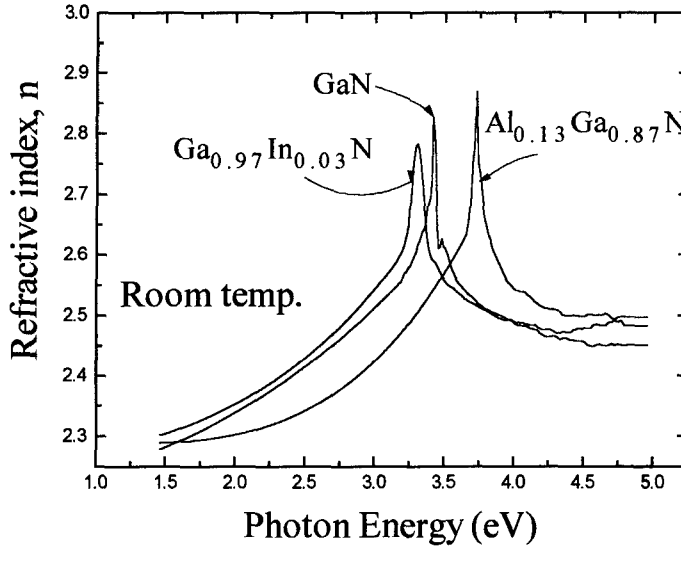

Figure 2 *Dispersion of refractive indices of E⊥ c components for GaN, AlGaN and GaInN at room temperature.*

compositional dependence of the refractive indices as a function of wavelength. The difference in refractive index between GaN and alloys indicate the possibility of the fabrication of waveguide using heterostructure.

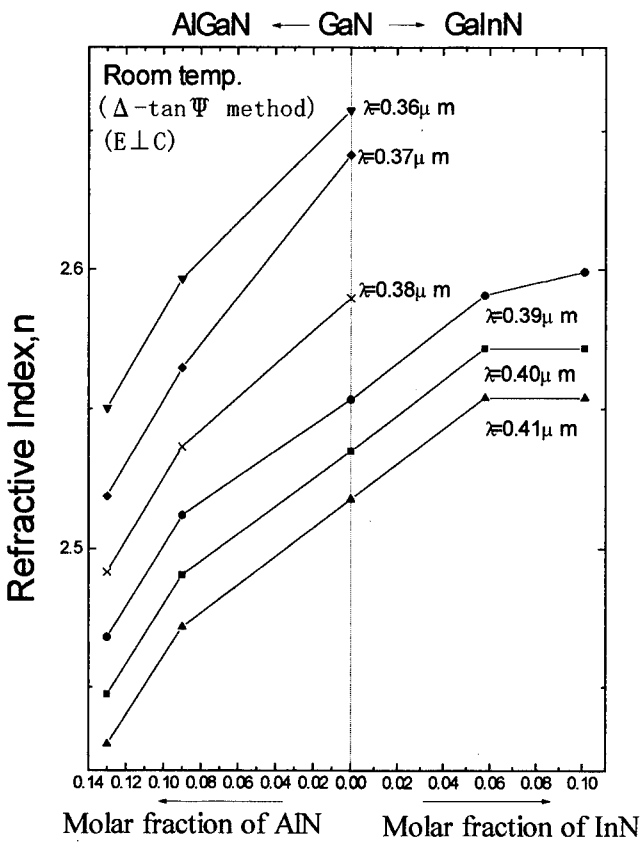

Figure 3 *Compositional dependence of the refractive indices for AlGaN and GaInN at various wavelengths*

Critical layer thickness of AlGaN and GaInN grown on GaN is estimated by using the theory of Matthews and Blakeslee[20]. In the calculation, elastic constants of the alloys are assumed to vary linearly with the alloy composition. Figures 4(a) and 4(b) show critical layer thickness of AlGaN and GaInN on GaN as a function of alloy composition, respectively. It is clear that the critical layer thickness is very thin even at low molar fraction of AlN or InN. AlGaN/GaN quantum wells have been fabricated on the basis of this calculation. Quantum size effect has been clearly observed[21].

Optically pumped stimulated emission

Figure 5 shows the emission spectra at room temperature from optically pumped AlGaN/GaN DH(Fig.5(a)) and AlGaN/GaInN DH(Fig.5(b)) excited above threshold power density(P_{th}). Clear stimulated emission can be observed from both structures. P_{th} is about 0.11MW/cm^2 for AlGaN/GaN DH, and 0.13MW/cm^2 for AlGaN/GaInN DH. P_{th} from AlGaN/GaN DH is in good agreement with the estimated value obtained using the measured refractive indices of the alloys shown in Fig.2[22]. P_{th} from AlGaN/GaInN DH is slightly larger than that from the estimated value. This may be caused by the poorer crystalline quality of GaInN active layer than that of GaN active layer. Further developments for the fabrication of these heterostructures will surely lead to the realization of low threshold violet LDs. In either case, peak wavelength of stimulated emission is lower than that of spontaneous emission. Cingolani et al. also observed the red shift of the stimulated emission at 80K from needle GaN crystals[23]. They explained this phenomenon using electron-hole plasma model. In this measurement at RT, however, at the present time, it is unclear whether this red shift is caused by the electron-hole plasma or other effects, for example, excitonic.

Properties of mW-class LEDs based on column-III nitrides

GaN p-n homojunction LED with output power of 1.5mW at a forward current of 30mA and peak wavelength of 0.37μm and 0.42μm at room temperature had been fabricated[24]. Figure 6 shows EL spectrum at a forward current of 10mA from P-GaN/GaInN/N-GaN DH. Clear band-to-band transition in GaInN layer can be observed. Peak wavelength is 0.40μm and FWHM is 0.09eV which is the narrowest EL from column-III nitride-based LED[25]. P-AlGaN/GaInN/N-GaN antisymmetrical DH was also fabricated. Peak wavelength is about 445nm, and output power is a few mW at a forward current of 20mA.

Critical layer thickness

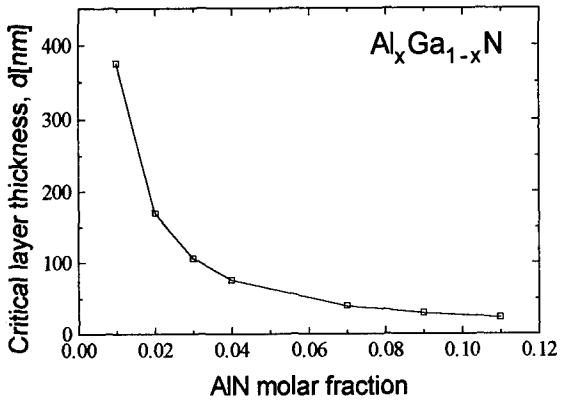

(a)

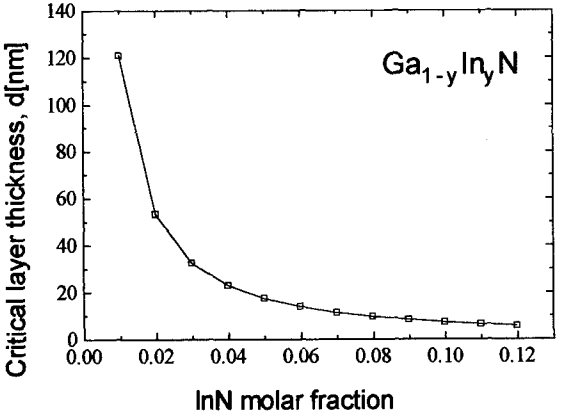

(b)

Figure 4 *Critical layer thicknesses for AlGaN(Fig.4(a)) and GaInN(Fig.4(b)) grown on GaN.*

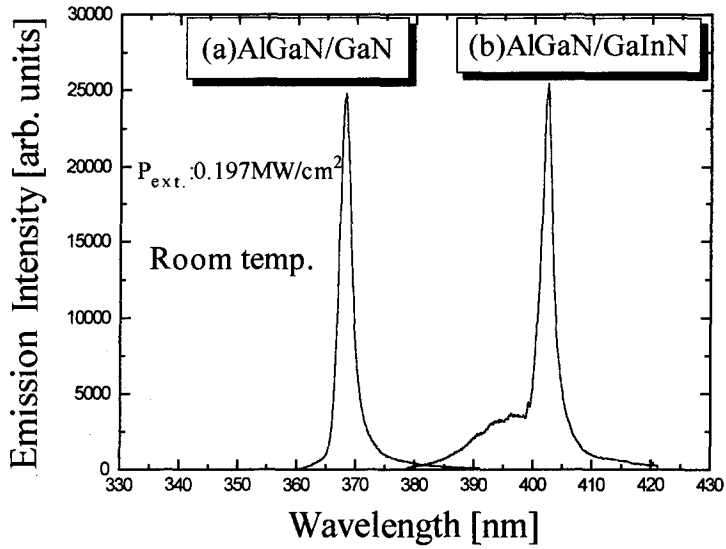

Figure 5 *The emission spectra at RT from optically pumped AlGaN/GaN DH(Fig.5(a)) and AlGaN/GaInN DH(Fig.5(b)) excited above threshold power density.*

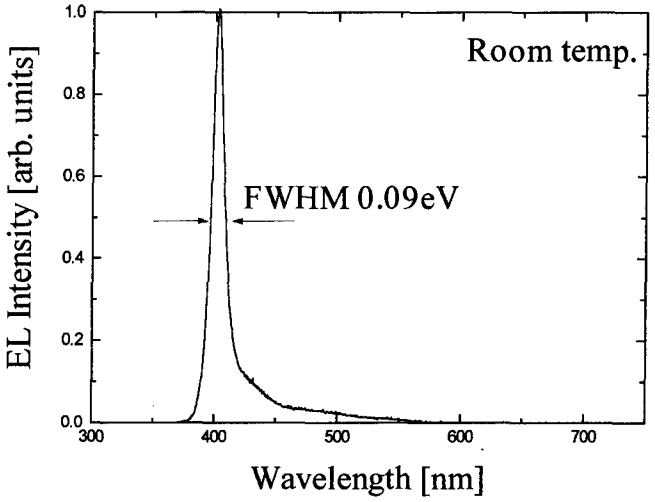

Figure 6 *EL spectrum at a forward current of 10mA from P-GaN/GaInN/N-GaN DH.*

SUMMARY

By MOVPE using the AIN buffer layer, crystalline quality as well as the electrical and luminescence properties of GaN, AlGaN and GaInN films have been remarkably improved. Utilizing such high-quality nitrides, conductivity control for n-type GaN, AlGaN and GaInN has been achieved. By combining with the LEEBI treatment, both GaN and AlGaN with distinct p-type conduction have been realized for the first time. Basic optical properties are clarified with use of such a high quality nitride layer. High-quality AlGaN/GaN DH and AlGaN/GaInN DH showing stimulated emission with low threshold power by optical pumping at room temperature have been fabricated. High power of 1.5mW UV/blue light emitting p-n diodes with homodiode, P-GaN/GaInN/N-GaN symmetrical DH with narrow band-to-band transition, and P-AlGaN/GaInN/N-GaN anti-symmetrical DH with output power of a few mW have been fabricated.

Acknowledgments

The authors would like to thank T.Tanaka for help with the experiments. This work was partly supported by the Grant-in-Aid for Scientific Research on Priority Areas, "Crystal Growth Mechanism in Atomic Scale" No. 03243107 from the Ministry of Education, Science and Culture of Japan. Special Research Grants for the Development of Characteristic Education of Japan, The Murata Science Foundation, and HOSO-BUNKA FOUNDATION.

REFERENCES

1.H.Amano, N.Sawaki, I.Akasaki and Y.Toyoda, Appl.Phys.Lett. **48**, 353(1986).
2.I.Akasaki, H.Amano, Y.Koide, K.Hiramatsu and N.Sawaki, J.Cryst. Growth **98**, 209(1989).
3.S.Nakamura, Jpn.J.Appl.Phys., **30**,L1705(1991).
4.T.D.Moustakas, R.J.Molnar, T.Lei, G.Menon and C.R.Eddy Jr., Mat.Res.Soc.Symp.Proc. **242**, 427(1992).
5.H.Amano, and I.Akasaki, Ext.Abs.Mater.Res.Soc.Fall Meeting,**21**, 165(1990).
6.H.Murakami, T.Asahi, H.Amano, K.Hiramatsu, N.Sawaki and I.Akasaki, J.Cryst.Growth, **115**,648(1991).
7.N.Koide, H.Kato, M.Sassa, S.Yamasaki, K.Manabe, M.Hashimoto, H.Amano, K.Hiramatsu and I.Akasaki,J.Cryst.Growth, **115**,639(1991).
8.H.P.Maruska,W.C.Rhines and D.A.Stevenson, Mat.Res.Bull. **7**,777(1972).
9.H.Amano, M.Kito, K.Hiramatsu and I.Akasaki, J.Electrochem.Soc., **137**, 1639(1990).
10.H.Amano, M.Kito, K.Hiramatsu and I.Akasaki, Jpn.J.Appl.Phys. **28**,L2112(1989).
11.S.Nakamura, N.Iwata, M.Senoh and T.Mukai, Jpn.J.Appl.Phys., **31**,1258(1992).

12.J.A.Van Vechten, J.D.Zook, R.D.Horning and B.Goldenberg, Jpn.J.Appl.Phys. **31**,3662(1992).

13.R.J.Molnar and T.D.Moustakas, Bull.Am.Phys.Soc.,**38**,445(1993).

14.M.E.Lin, G.Xue, G.L.Zhou, J.E.Greene and H.Morkoc, Appl.Phys. Lett., **63**,932(1993).

15.C.Wang and R.F.Davis, Appl.Phys.Lett., **63**,990(1993).

16.M.Rubin, N.Newman, J.S.Chan, T.C.Fu and J.T.Ross, Appl.Phys. Lett., **64**,64(1994).

17.K.Hirosawa, K.Hiramatsu, N.Sawaki and I.Akasaki, Jpn.J.Appl. Phys., **32**,L1039(1993).

18.H.Amano, I.Akasaki, K.Hiramatsu, N.Koide and N.Sawaki, Thin Solid Films, **163**,415 (1988).

19.I.Akasaki, H.Amano, M.Kito and K.Hiramatsu, J.Lumin.,**48&49**, 666(1991).

20. J.W.Matthews and A.E.Blakeslee, J.Cryst.Growth **27**, 118(1974).

21.K.Itoh, T.Kawamoto, H.Amano, K.Hiramatsu and I.Akasaki, Jpn.J. Appl.Phys. **30**, 1924(1991).

22.I.Akasaki, H.Amano, N.Koide, M.Kotaki and K.Manabe, Physica B **185**, 428(1993).

23.R.Cingolani, M.Ferrara and M.Lugara, Solid State Commun., **60**, 705(1986).

24.I.Akasaki, H.Amano, K.Itoh,N.Koide and K.Manabe, Inst.Phys.Conf.Ser. ,**129**, 851(1993).

25.S.Nakamura, M.Senoh and T.Mukai, Appl.Phys.Lett., **62**,2390 (1993).

GaN ON 6H-SiC -- STRUCTURAL AND OPTICAL PROPERTIES

C. Wetzel [a], D. Volm, B.K. Meyer, K. Pressel[+], S. Nilsson[+],
E.N. Mokhov*, and P.G. Baranov*
Physik-Department E16, TU München, 85747 Garching, Germany,
[+]Institut für Halbleiterphysik, 15230 Frankfurt/Oder, Germany
*Ioffe Physico-Technical Institute, 194021 St. Petersburg, Russia

ABSTRACT

Recent progress in the growth of high quality 6H-SiC single crystals has led to an ideal substrate material for GaN epitaxial films. Nearly matching lattice constants of wurzite GaN to 6H-SiC in the hexagonal plane can reduce strain effects at the interface. We employed the sublimation sandwich method to grow single crystal layers at reasonable growth rates with free carrier concentrations of $2x10^{17}$ cm^{-3}. Very sharp x-ray diffraction peaks of the GaN (0002) plane are obtained indicating the high quality of this system ($\Delta(2\theta) < 0.1$ degrees). These findings are directly reflected in the optical properties. The photoluminescence is dominated by a single sharp exciton line, impurity related donor acceptor transitions are seen with very weak intensities. However, at lower energies the internal luminescence transitions of the 3d transition metal ions Fe and V are observable. The incorporation of Fe is confirmed by electron paramagnetic resonance.

INTRODUCTION

The potential of GaN as a blue light emitter is intimately connected to the substrate material used in the epitaxial growth [1]. One of the key issues is lattice matching, but also the difference in thermal expansion and conductivity of substrate and epitaxial layer has to be taken into consideration. Growth of GaN on 6H-SiC offers distinct advantages over the commonly used sapphire substrate [2]. The lattice mismatch is only 3.5 % and this should reflect in the structural and optical properties of the layers. This has been demonstrated quite recently [2]. Molecular beam epitaxy (MBE) and metal organic chemical vapor deposition (MOCVD) are two commonly used techniques to achieve GaN layers of high crystalline quality [4,5]. The sublimation growth technique is an alternative method. It achieves very high growth rates, typically 300 μm per hour, and offers a great freedom in doping. The potential of this technique is best demonstrated by the growth of SiC epitaxial layers on various polytypes of SiC substrates, having outstanding quality [6,7]. In this report we present results from photoluminescence and X-ray reflection measurements of GaN layers grown on 6H-SiC using the sublimation growth technique [8]. The structural and optical properties are compared to samples grown by MBE and MOVCD.

EXPERIMENTAL DETAILS

The GaN epilayers are grown from metallic Ga and activated ammonia on SiC. The substrates of the 6H polytype (6H-SiC) have been grown by the LELY method and are oriented in the [0001] plane. The growth of the GaN layers is performed using a modification of the sandwich method as originally described in Ref. [8]. The quartz reactor contains several deposition cells in a row

Mat. Res. Soc. Symp. Proc. Vol. 339. ©1994 Materials Research Society

that share the same gas stream of ammonia. Each cell consists of a Ga source and SiC substrate separated by a gap of 5 mm. The heating is performed by a high frequency generator on a graphite rod. The surface of this rod is covered by a layer of SiC to prevent the evaporation of C into the reactor volume. The gradient of the resulting temperature field across the narrow gap is perpendicular to the surface of the substrate. Through this gap ammonia flows with a speed of 25 to 50 l/min. Under these conditions there is an efficient mass transport of Ga vapor and activated nitrogen towards the substrates. Prior to deposition the 6H-SiC substrates are etched in molten KOH. At growth temperatures between 1170 and 1270 ^{o}C single crystal layers of GaN are obtained at a growth rate up to 300 μm/h. These GaN layers showed n-type conduction, the electron mobility ranged from 30 to 80 cm^2/Vs. The layer thickness was 60 μm. The GaN epitaxial layers were characterized by temperature dependent photoluminescence in the spectral range from 3.5 to 0.5 eV using a grating monochromator or a Fourier Transform spectrometer. Standard absorption or reflection measurements were performed to determine the free electron concentration. For further details see Ref. [7]

EXPERIMENTAL RESULTS

For the X-ray diffraction the Cu K_α line was used. The sample was oriented along a high symmetry axis in the basal plane. One hence expects reflections from the planes perpendicular to the c-axis [0001] as shown in Fig. 1. At 34.5 degrees the GaN (0002) reflection occurs with a half width of 6 minutes. X-ray reflection data for GaN grown on sapphire using MBE or MOCVD are of the same order. At 73 degrees the second order of the (0002) reflection is seen. Simultaneously the reflections from the 6H-SiC can be observed in first order (0006) and in second order (000 12). Measuring the backside of the sample, i.e. the substrate, a reversed intensity ratio for GaN and SiC reflections is found. A matching of the lattice constant cannot be observed since mainly reflections from the c-axis are seen. However, within the deformation potential model a change of the lattice constant **a** within the plane is directly connected with changes in **c**. For the analysis the following lattice constants were used: SiC a=3.0806 Å, c=15.1173 Å and GaN a=3.186 Å, c=5.176 Å; accordingly the lattice mismatch amounts to 3.5 %.

In Fig. 2 we show the low temperature photoluminescence results. In this particular sample the donor bound exciton recombination at 3.47 eV [10] is rather weak and the luminescence is dominated by the impurity related transitions (donor-acceptor or band-acceptor) around 3.26 eV. Not shown in Fig. 2 is the deeper luminescence band at 2.2 eV which according to other groups is related to intrinsic defects [11]. The ratio of exciton to donor-acceptor pair recombination can be taken as a measure of the quality of the samples. In the best ones it was 30:1 and the donor bound exciton had a line width of 4 meV thus comparable to MBE- or MOCVD-grown layers. A second transition with rather strong intensity is seen 100 meV below the exciton line. It is not a phonon replica of the 3.47 eV line. The temperature dependence of this line could be followed up to 40 K, where the intensity had decreased beyond detection limit. The activation energy is 5 meV which points to excitonic behavior. In a recent publication [12] it was reported that the 3.37 eV line appeared after hydrogen passivation of the Mg acceptors in GaN. If this is true the recombination could be explained by exciton recombination at neutral acceptor hydrogen complexes. Another less intense line appears at 3.31 eV. Its temperature dependence allows to distinguish whether it is an independent transition or a phonon replica of the 3.37 eV line. From 5 K up to 30 K its intensity decreases more or less linearly being reduced by 30 % at 30 K. At higher temperatures it merges into the transition centered around 3.26 eV

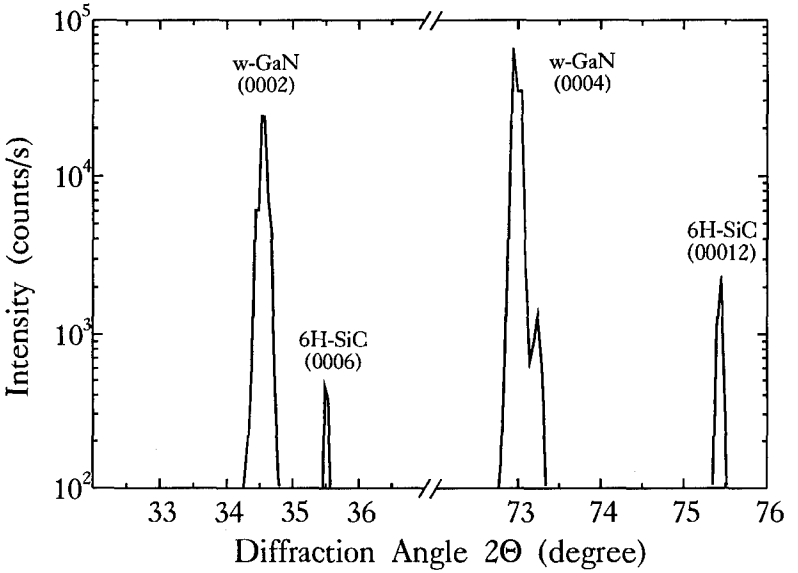

Fig. 1: X-ray diffraction along the c-axis. GaN and SiC substrate reflect in first and second order.

and could not be followed any more. Assuming band acceptor transitions which is plausible for the high carrier density of $4x10^{17}$ cm^{-3} a binding energy of 190 meV is calculated (the band gap of GaN at low temperatures is 3.5 eV). Such a shallow acceptor level has to our knowledge not been reported before. The acceptor binding energies in GaN span a very wide range from 220 meV down to 800 meV (Mg, Zn) [1]. In Zn doped GaN [13] four Zn related acceptor levels have been observed, the shallowest one being 340 meV above valence band. Zn belongs to the group II acceptors amongst Be, Mg and Cd. Since the epitaxial layers were undoped and the group II acceptors are not common trace impurities we disregard them as the source of the 3.31 eV line. On the other hand Zn is sometimes used as a dopant and may remain in the reactor. The group IV elements C, Si and Ge are also shallow acceptors in III-V compounds, possibly also in GaN. Carbon doped GaN as well as GaN implanted with C have been investigated earlier [11,14]. In the implantation study [14] no near band gap luminescence due to C could be found, only the deep center at 2.2 eV appeared. Doping with C [11] enhanced this particular luminescence and it was concluded that the recombination is between a shallow donor level and a deep acceptor complex involving C as a constituent. We can speculate that C induces also a shallow level but more experiments are needed to clarify the role of C in GaN.

The recombination at 3.26 eV is often observed in undoped GaN. The zero phonon line is followed by up to 4 phonon replicas with average energies of 92 meV. The peak positions agree well with values reported by Khan et al.[15]. They studied the influence of Si on the photoluminescence of GaN and concluded that the 3.26 eV donor acceptor recombination is due to Si as unintentional dopant. The intensity of the luminescence was proportional to the amount of Si in the sample. For GaN on SiC grown at temperatures around 1100 °C Si can evaporate from the substrate and diffuse into the epilayer. The amphoteric character of Si is well established in GaAs and it points that Si shows a similar behavior in GaN.

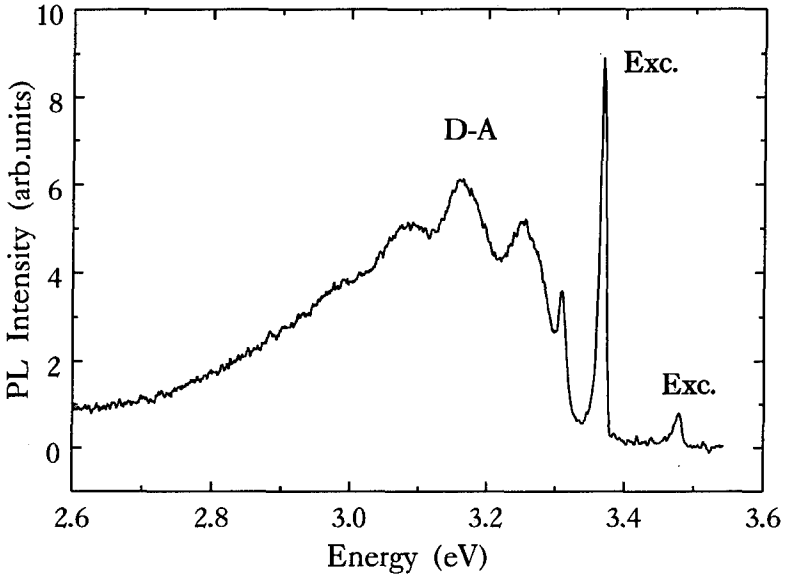

Fig. 2: Photoluminescence in the bandgap region consists of donor bound excitons and impurity related transitions.

Most previous researchers in photoluminescence investigations concentrated on the spectral range from the band gap region down to 1.5 eV. They thus missed the characteristic internal luminescence lines of the 3d transition metal elements in the near infrared. Baur et al. [16] were the first to report on infrared luminescence of the iron acceptor in undoped epitaxial GaN layers. We confirm their results and show the presence of vanadium in addition. In Fig. 3 the luminescence spectrum from 11000 cm^{-1} to 7000 cm^{-1} is shown. In order to achieve the high resolution a Fourier Transform spectrometer was used. Three prominent zero phonon lines (ZPL) are seen at 10480, 9629 and 8450 wave numbers followed by phonon replicas. The transition at 10480 cm^{-1} corresponds to the internal $^4T_1(G) \rightarrow {}^6A_1(S)$ recombination of Fe^{3+} on Ga site, the $3d^5$ configuration [16]. The origin of the ZPL at 9628.8 cm^{-1} deserves further investigations. In Ref. [16] it is tentatively assigned to the $^3T_2(F) \rightarrow {}^3A_2(F)$ transition of Cr^{4+} The iron acceptor level has been determined to be 2.6 eV above the valence band [17]. According to the Langer Heinrich rule [18] the energy levels of the transition metal elements can be used as a measure of the band offset. Knowing the energy level of $Fe^{3+/2+}$ in GaAs and in GaN allows us to conclude where the energy level position of other 3d elements will be. It predicts for chromium the 3+/2+ level to be located around 0.6 eV below the conduction band. In n-type material the Cr^{2+} charge state will be present and excitation will start from the 2+ charge state, i.e. $Cr^{2+} \rightarrow Cr^{3+} + e_{cb}$. So the internal luminescence of Cr^{3+} is expected to be seen. For an internal transition of a 3d element the 9628.8 cm^{-1} line has an unusual temperature dependence, it can be seen up to 150 K whereas the other lines disappear around 80 K. Also hardly any broadening of the line is observed. The full width at half maximum is below 1 cm^{-1} and thus narrow enough to perform Zeeman spectroscopy and to conclude about spin and hence charge state of the impurity. These experiments are currently underway.

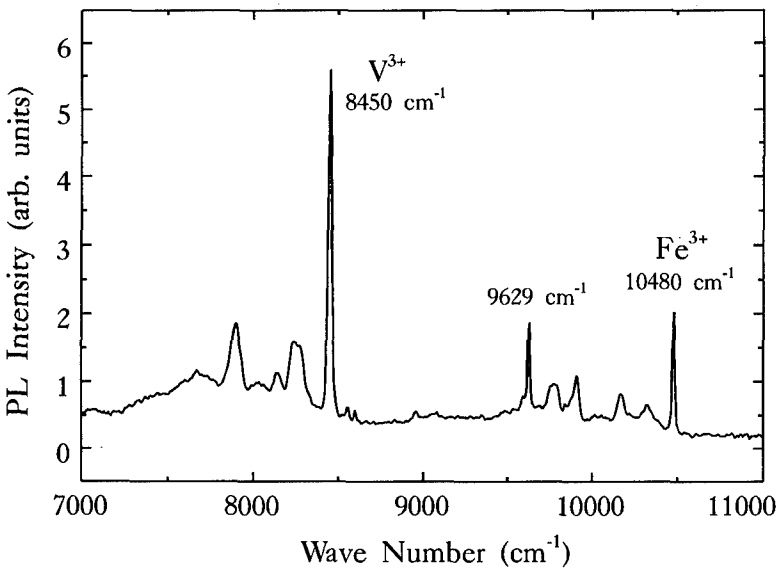

Fig. 3: Photoluminescence in the infrared of V and Fe internal transitions. The line at 9629 cm^{-1} is tentatively assigned to Cr.

The third line at 8450 cm^{-1} is attributed to the internal luminescence of V^{3+} on Ga site. The internal luminescence of V^{3+} in III-V semiconductors is a well-known feature [19]. V^{3+} has the $3d^2$ configuration, the identical configuration as Cr^{4+} mentioned above. In each compound GaAs [20], GaP [20] and InP [21] the luminescence of V^{3+} is dominated by a ZPL ("cold" line) and a "hot" line 10 to 15 wave numbers at higher energies. This line appears at higher temperatures (>8 K). The identical behavior is seen on the 8450 cm^{-1} line. More details will be presented in a forthcoming publication [9]. The three ZPLs were strongest when illuminating the sample with above band gap light, but also could be seen under the excitation of the green line of an Ar ion laser (514 nm). All three impurities hence are electrically active inducing energy levels in the band gap of GaN. The high free electron concentration did not allow us to perform magnetic resonance experiments which could clarify which impurity in what charge state is present. We could however compensate the layers by fast neutron irradiation. For a dose around 10^{18} n/cm^2 the layers became transparent in the infrared. In the electron paramagnetic resonance (EPR) experiments the Fe^{3+} resonance [17] was seen meaning that the Fermi level is at least 1 eV below the conduction band. It also shows that by neutron irradiation acceptors probably gallium vacancies, are formed in an amount to compensate the action of nitrogen vacancies, the shallow donors, in GaN.

CONCLUSION

GaN grown on 6H-SiC by the sandwich sublimation technique has excellent crystalline and optical properties comparable to MBE- and MOCVD-grown layers. The residual impurities acting in GaN on SiC as shallow acceptors are tentatively assigned to Si and C. The presence

of three 3d transition elements with their characteristic luminescence bands between 1.3 and 1 eV in GaN is shown.

ACKNOWLEDGEMENT

One of us (C.W.) thankfully acknowledges the financial support from the Deutsche Forschungsgemeinschaft for a post-doctorial stay at LBL.

REFERENCES:

[a]Present adress: Materials Science Division, Lawrence Berkeley Laboratory, Berkeley, CA 94720

1. For a recent review see: S. Strite and H. Morkoc, J. Vac. Sci. Technol. B 10, 1237 (1992)
2. M.E. Lin, B. Sverdlov, G.L. Zhou and H. Morkoc, Appl. Phys. Lett. 62, 3479 (1993)
3. M.E. Lin, B.N. Sverdlov and H. Mokoc, Appl. Phys. Lett. 63, 3625 (1993)
4. H. Amano, M. Kito, K. Hiramatsu, and I. Akasaki, Jap. J. Appl. Phys. 28, L2112 (1989)
5. S. Nakamura, M. Senoh and T. Mukai, Jap. J. Appl. Phys. 30, L1708 (1991)
6. Y.A. Vodakov, M.I. Karklina, E.N. Mokhov and A.D. Roenkov, Inorganic Materials 17, 537 (1980) in russian
7. Y.A. Vodakov, E.N. Mokhov, A.D. Roenkov and D.T. Saidbekov, phys.stat.sol. (a) 51, 209 (1979)
8. Y.A. Vodakov, E.N. Mokhov, M.G. Ramm and A.D. Roenkov, Kristall und Technik, 14, 729 (1979)
9. C. Wetzel, D. Volm, B.K. Meyer, K. Pressel, S. Nilsson, E.N. Mokhov and P.G. Baranov, unpublished
10. O. Lagerstedt and B. Monemar, J. Appl. Phys. 45, 2266 (1974)
11. T. Ogino and M. Aoki, Jap. J. Appl. Phys. 19, 2395 (1980)
12. M.S. Brandt, N.M. Johnson, R.J. Molnar, R. Singh and T.D. Moustakas, unpublished
13. B. Monemar, O. Lagerstedt and H.P. Gislason, J. Appl. Phys. 51, 625 (1980)
14. J.I. Pankove and J.A. Hutchby, J. Appl. Phys. 47, 5387 (1976)
15. M.R.H. Khan, Y. Ohshita, N. Sawaki and I. Akasaki, Sol. State Comm. 57, 405 (1986)
16. J. Baur, K. Maier, M. Kunzer, U. Kaufmann, J. Schneider, H. Amano, I. Akasaki, T. Detchprohm and K. Hiramatsu, Appl. Phys. Lett. 64, 857 1994)
17. K. Maier, M. Kunzer, U. Kaufmann, J. Schneider, B. Monemar, I. Akasaki and H. Amano, Defects in Semiconductors, ed. by H. Heinrich and W. Jantsch, Tans. Tech. 1994, Vol. 143-147, p.93
18. For a compilation of data see A. Zunger, Solid State Phys. 39, 275 (1987)
19. B. Clerjaud, J. Phys.C 18, 3615 (1987)
20. U. Kaufmann, H. Ennen, J. Schneider, R. Woerner, J. Weber and F. Koehl, Phys. Rev. B 25, 5598 (1982)
21. M.S. Skolnick, P.J. Dean, M.J. Kane, Ch. Uihlein, D.J. Roberts, W. Hayes, B. Cockayne and W.R. Mac Ewan, J. Phys. C 16, L767 (1983)

ACCEPTOR BINDING ENERGY AND BAND LINEUP OF III-V NITRIDE ALLOYS AND MOCVD GROWTH OF GaN ON GaAs - OR GaP-COATED Si

YOSHIHIRO UETA, SHIRO SAKAI, YASUSHI KAMIYA AND HISAO SATO

Tokushima University, Department of Electrical and Electronic Engineering, Minami-josanjima, Tokushima 770, Japan.

ABSTRACT

The acceptor binding energy is calculated to find out the best acceptor impurity in InN, GaN and AlN. Be is predicted to be the shallowest acceptor and the next are Mg and Zn. Group IV elements such as C or Si are very deep. Band lineup is calculated to be $\Delta Ec : \Delta Ev = 2.1$ eV : 0.76 eV = 0.73 : 0.27 = 2.8 : 1 for GaN/AlN and $\Delta Ec : \Delta Ev$ =0.88 eV : 0.66 eV = 0.57 : 0.43 = 1.3 : 1 for GaN/InN. GaN is grown on GaAs and GaP-coated Si substrate by MOCVD. GaAs intermediate layer gives better GaN compared to GaP intermediate layer. It is suggested that the lower bulk modulus of GaAs than that of GaP gives this difference.

Introduction

Although light emitting diodes in blue region is realized by GaN material system, the difficulties regarding this material are too deep acceptor level that limits doping in p-GaN, band lineup which is important in device designing and the problems associated with sapphire substrate. Mg has widely been used as a shallow acceptor, however, there is no theoretical background in selecting a suitable acceptor in GaN, InN and AlN. First part of this paper deals with the impurity levels of simple substitutional acceptors in nitride compounds. The primarily interest of this calculation is to look for the best impurity in GaN, InN and AlN. The valence band energy of nitrides is then calculated by the Harrison model using the effective bond length of aluminum compounds. The last part of this paper is related to the substrate that can be an alternative to sapphire. Silicon coated by crystalline GaAs and GaP are used to grow GaN by MOCVD, since the direct growth of GaN on silicon is prevented by the formation of amorphous SiN at the interface. Additional advantage of the use of GaAs or GaP intermediated layer is that more dislocation is expected to be formed in the intermediate layer than in GaN, since bulk modulus of GaN is much larger than those of GaAs or GaP. The material characterization results of GaN on Si is presented and compared with those of GaN on sapphire.

Acceptor Binding Energy in Nitrides

The impurity level in a crystal is most simply calculated by the hydrogen model which is $Ea = m^*/\varepsilon^2$ 13.6 eV. The hydrogenic energy for several materials are shown in Table 1. Effective mass m^* do not change significantly from material to material and is linearly proportional to Ea, but dielectric constant ε which effects on Ea in square is fairly small in the nitride compounds. It is this small value that makes Ea of nitrides deep. The reason for this small dielectric constant is related to the atomic structure of nitrogen atom. Since nitrogen atom has only K and L shells, the electrons are tightly bounded to atomic core making electronic polarization and hence dielectric constant small. Although the hydrogen model reveals an essential problem associated with acceptor level in nitride compounds, it does not give quantitative Ea, because the effective Bohr radius a^* in nitrides is as small as the lattice spacing of the crystal.

Mat. Res. Soc. Symp. Proc. Vol. 339. ©1994 Materials Research Society

Table 1. Acceptor binding energy calculated by the hydrogen model.

	GaAs	GaP	InN	GaN	AlN
ε	13.1	11.1	9.3	5.8	4.8
m*	0.45	0.6	0.8[a)]	0.8	0.8[a)]
Ea (meV)	36	66	126	323	472
a* (nm)	1.5	0.9	0.6	0.4	0.2

a) Value of GaN.

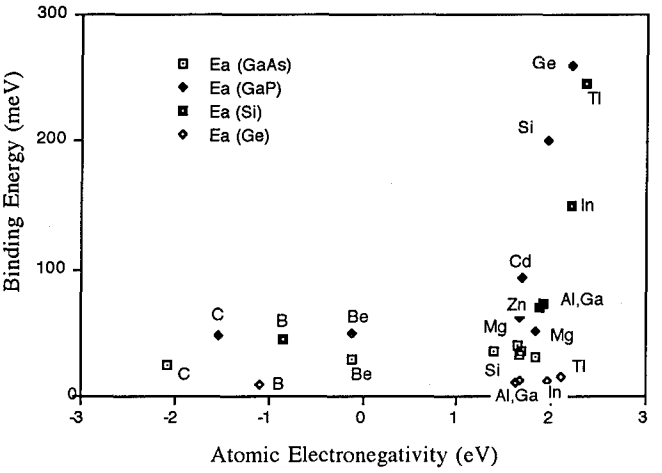

Fig.1 Acceptor binding energy in GaAs, GaP, Si and Ge as a function of atomic electronegativity (difference in p-state energy of host and impurity atoms).

The chemical trend of impurity atom can be included by considering difference in electronic structure of impurity and host atoms as discussed by Phillips[1] and Jaros.[2] Due to ref.1, the activation energy E_a of the acceptor is expressed as $E_a - E_h$ = const. $[X_I - X_{C,A}]^2$, where E_h is hydrogenic energy, X_I is the electronegativity of impurity atom and $X_{C,A}$ is the electronegativity of anion or cation which is replaced by the impurity. Jaros's theory also expresses activation energy as a function of atomic electronegativity which is the difference in p-state energy of impurity and host atoms. The dependence of the energy in this theory, however, is not a simple square function but is derived after some calculation. Although both theories do not give an accurate absolute value of the impurity level, they correctly indicate the chemical trend of many impurity atoms in known crystals. Jaros's plot for Si, Ge, GaP and GaAs is shown as a function of atomic electronegativity in Fig.1, where Hartree-Fock atomic term values are used as p-state energy[3]. The energy becomes suddenly deep when atomic electronegativity value exceeds about 1.5 eV, and the energy is constant for the smaller electronegativity value. This behavior of binding energy is qualitatively the same as the that predicted by the theory, and do not change from one material to the other. The binding energy for small value of electronegativity is determined by the long range potential (hydrogenic model like) and is different from material to material, however, the behavior of Fig.1 in certain material is independent on the host crystal, and therefore, the chemical trend in an unknown crystal can roughly be estimated by the atomic electronegativity value. The electronegativity values in InN, GaN and AlN are summarized in Table 2. The shallowest acceptor impurity in all of the three crystals is predicted to be Be. Mg, Zn and Cd might be shallow in InN, but is uncertain in GaN and AlN, since the values are at just the onset of increase in binding energy. These prediction is consistent with the recent experimental

results in GaN. (Mg = 155 meV[4], Zn = 210 meV[4] and Cd = 500 meV[5].) Group IV impurities are predicted to be very deep in all nitride compounds. The big difference of nitrides from other III-V compounds such as GaAs and GaP in which C and Si are shallow comes from large p-state energy of nitrogen atom.

Table 2. Calculated electronegativity of impurity atoms in InN, GaN and AlN. Units are in eV.

	Be	Mg	Zn	Cd	C	Si
InN	-0.42	1.53	1.36	1.39	2.77	6.26
GaN	-0.12	1.83	1.66	1.69	2.77	6.26
AlN	-0.08	1.87	1.7	1.73	2.77	6.26

Band Lineup of AlN, GaN and InN

The valence band energy of several binary compounds which include B an N was calculated[6] by the Harrison model.[7] Although this model is convenient to calculate energy in unknown materials, it gives the error for aluminum compounds. This error can be compensated by considering the effective bond length of aluminum compounds as pointed out by Gonda.[8] The bond length of BN, GaN and InN lines up on a straight line as shown in Fig.2 together with As and P compounds, but only aluminum compounds deviate from the lines. It was empirically shown that the effective bond lengths of AlAs and AlP which were the interpolated values on the straight lines gave correct valence band energy of Harrison model.[8] We apply the same method to obtain correct energy for AlN whose effective bond length is 1.76 Å. The calculated energy (top of the valence band and bottom of the conduction band) is shown as a function of bond length in Fig.3. The most important values for the practical application must be the band discontinuities at GaN/AlN and GaN/InN. The results are ΔEc : ΔEv = 2.1 eV : 0.76 eV = 0.73 : 0.27 = 2.8 : 1 for GaN/AlN and ΔEc : ΔEv = 0.88 eV : 0.66 eV = 0.57 : 0.43 = 1.3 : 1 for GaN/InN. Both interfaces are type I. The value, ΔEv = 0.76 eV at GaN/AlN, is in reasonable agreement with that of Albanesi et al (0.85 eV)[9].

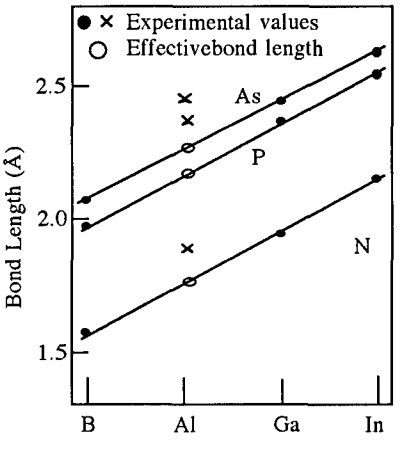

Fig.2 Bond length of several binary compounds.

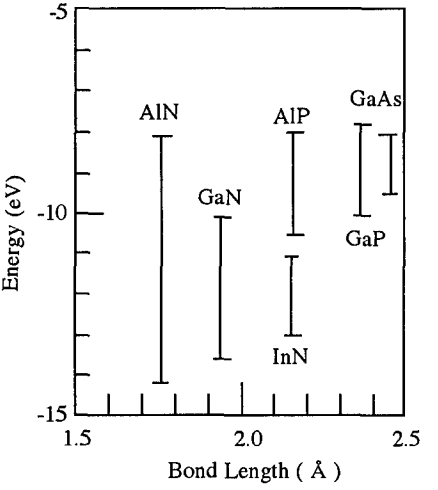

Fig.3 Top of the valence band and bottom of the conduction band for several binary compounds.

Growth of GaN on GaAs and GaP-coated Si Substrates

Silicon is a useful substrate to grow GaN and its heterostructures, but the direct growth of nitrides on Si is prevented by the formation of amorphous SiN at the interface. The alternative way is to use the intermediate layer of crystalline GaAs or GaP between GaN and Si. GaAs or GaP are first grown on Si (100) 4 ° off Si substrate by MOCVD, and then GaN are grown. The effects of intermediate layers on GaN crystal quality are investigated.

GaAs are grown in the separate MOCVD system. The Si substrates is annealed prior to the growth, and thin (about 50 nm) GaAs is grown at 450 °C. Some samples are taken out from the system to grow GaN on low-temperature-grown GaAs in the separate MOCVD system. The growth of GaAs is continued for other samples at 750 °C. The thickness of GaAs layer is changed from 0.2 to 2 μm. GaAs grown at 450 °C and 750 °C on Si are poly-crystalline and single crystalline, respectively. GaP is grown in the same MOCVD system as that used for GaN growth. The growth condition is almost the same as that of GaAs, except that the growth rate is reduced and the V/III ratio is increased to obtain mirror surface.

No strong relation between crystal quality of GaN and the thickness of the intermediate layers is observed. The X-ray diffraction curves from GaN (0002) face for three samples grown on different substrates (GaAs on Si, GaP on Si and sapphire) are compared in Fig.4. The FWHM is smallest on sapphire substrate (9 min which is the resolution of the apparatus). The next is GaAs on Si (12 min), and GaP on Si results in the broadest FWHM(18 min). This result is qualitatively understood by the difference in bulk modulus of GaAs, GaP and GaN. The dislocations tend to be formed in the material that has the smaller bulk modulus. Since GaAs has smaller bulk modulus than GaP, more dislocations are formed in GaAs reducing the dislocation density in GaN. The X-ray FWHM obtained in this work can be compared with those of the other works that use Si substrates; Lei et al[10] (60 min), Watanabe et al. [11] (12.8 min) and Hirosawa et al.[12] (18 min).

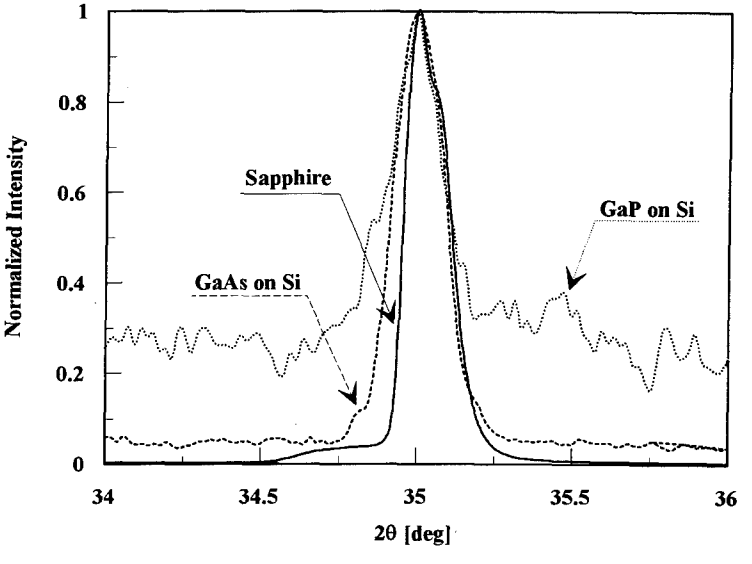

Fig.4 X-ray diffraction curves from GaN (0002) plane grown on sapphire, GaP on Si and GaAs on Si substrates.

Summary

The acceptor binding energy is investigated to find out the best acceptor impurity in InN, GaN and AlN. It was pointed out that the small dielectric constant due to small atomic number of N is the main reason of the deeper acceptor levels in nitrides compared to the other III-V compounds. Be is predicted to be the shallowest acceptor, and the next are Mg, Zn and Cd. Group IV elements such as C or Si are very deep.

Valence band energy of nitride compounds is calculated by the Harrison model using the effective bond length of aluminum compounds. The results are $\Delta Ec : \Delta Ev = 2.1$ eV : 0.76 eV = 0.73 : 0.27 = 2.8 : 1 for GaN/AlN and $\Delta Ec : \Delta Ev = 0.88$ eV : 0.66 eV = 0.57 : 0.43 = 1.3 : 1 for GaN/InN. Both interfaces are type I.

GaN is grown on GaAs and GaP-coated Si substrate by MOCVD. GaAs intermediate layer gave better GaN compared to GaP intermediate layer. It was suggested that the lower bulk modulus of GaAs than that of GaP gave this difference. However, GaN layers grown on these substrates are still inferior to the layer grown on sapphire substrates.

References

1. J.C.Phillips, Bonds and Bands in Semiconductors, (Academic Press, New York, 1973) Chapt.9.
2. M. Jaros, Deep Levels in Semiconductors, (Adam Hilger Ltd., Bristol, 1982) Chapt. 9.
3. W.A.Harrison, Electronic Materials, ed. by J.R.Chelikowsky and A.Franciosi, (Springer-Verlag, Berlin, 1991) 9.
4. H.Amano and I. Akasaki, Oyobutsuri 60 (1991) 163 (in Japanese).
5. S.Nakamura, N.Iwasa and S.Nagahama, Jpn. J. Appl. Phys. 32 (1993) L338.
6. S.Sakai, Y.Ueta and Y.Terauchi, Jpn. J. Appl. Phys. 32 (1993) 4413.
7. W.A. Harrison, J. Vac. Sci. Technol. 14 (1977) 1016.
8. S.Gonda, Solid State Communications 60 (1986) 249.
9. E.A.Albanesi, W.R.Lambrecht and B.Segall, MRS 1994 Spring Meeting (1994) D4.4.
10. T.Lei and T.D.Moustakas, J. Appl. Phys. 71 (1992) 4933.
11. A.Watanabe, T.Takeuchi, K.Hirosawa, H.Amano, K.Hiramatsu and I.Akasaki, J. Crystal Growth 128 (1993) 391.
12. K.Hirosawa, K.Hiramatsu, N.Sawaki and I.Akasaki, Jpn. J. Appl. Phys. 32 (1993) L1039.

THERMALLY ANNEALED GaN NUCLEATION LAYERS AND THE MOCVD GROWTH OF Si-DOPED GaN FILMS ON (00.1) SAPPHIRE

D. K. WICKENDEN, J. A. MIRAGLIOTTA, W. A. BRYDEN, AND T. J. KISTENMACHER
Applied Physics Laboratory, The Johns Hopkins University, Laurel, MD 20723-6099

ABSTRACT

The effect of epitaxial growth temperature in the range 985 - 1050°C on the preparation of device quality Si-doped GaN layers on self-nucleated (00.1) sapphire has been explored. Not unexpectedly, several device-related properties monotonically improve with increasing growth temperature, including: (a) carrier density; and, (b) volume fraction of heteroepitaxial domains. However, a number of equally important device-related properties show a local maximum or minimum and include: (a) optical second-harmonic generation intensity; (b) structural coherence; and, particularly (c) surface morphology. The antecedents of the first class is found in an increase in surface and bulk diffusion and a reduction in film defect incorporation and stress at the GaN/GaN (nucleation layer)/α-Al_2O_3 heterointerface (even for overlays with thicknesses near 1μm). The second class apparently stems from the limited range over which the thermally annealed GaN nucleation layer stimulates pseudo two-dimensional growth of the overlayer.

INTRODUCTION

To a large degree, the recent and rather remarkable improvement in the morphological and physical (structural, optical and electrical) characteristics of heteroepitaxial thin films of gallium nitride (GaN) deposited on (00.1) oriented sapphire (α-Al_2O_3) can be attributed to the utilization of a predeposited nucleation layer. Without this nucleation layer, the extremely large lattice mismatch between GaN and (00.1) oriented sapphire generally results in films with pronounced hexagonal features, owing to a three-dimensional (3D) island growth mechanism. Thus far, nucleation layers consisting of either lattice-mismatched aluminum nitride (AlN; -2.2%) [1,2] or zinc oxide (ZnO; -1.9%) [3] or lattice-matched GaN [4-6] itself have been investigated. In each instance, it has been suggested that the seed layer provides a significant increase in nucleation density for the subsequent GaN overgrowth and in the process converts the growth mechanism from 3D to pseudo two dimensional (2D).

As the nucleation layers are usually deposited at temperatures below that of the overlayer, it became essential that data be accumulated on the effect of thermal annealing on the nucleation layers and, obviously, on the succeeding overlayer. In this regard, we have recently described [7] the evolution of the structural and optical properties with thermal annealing of GaN nucleation layers on (00.1) sapphire and demonstrated that the as-deposited layers have a measurable epitaxial component, although the crystallite size is quite small. Upon annealing to higher temperatures, the crystallite size increased significantly through solid-phase epitaxy and the crystal perfection improved markedly.

Herein, we describe studies of self-nucleated, Si-doped thin films (~0.7-8μm) of GaN grown with a variety of device applications in mind. It was certainly anticipated that the self-nucleated overgrowth of GaN (a process that is thermally and metrically matched) should exemplify the concepts outlined above. In fact, while the data offered here supports that view, a simple caveat emerges that is crucial to the preparation of device quality, self-nucleated GaN films for optoelectronic applications.

Mat. Res. Soc. Symp. Proc. Vol. 339. ©1994 Materials Research Society

EXPERIMENTAL RESULTS AND DISCUSSION

The samples were prepared in a vertical spinning disc MOCVD reactor operating at 70 torr. Trimethylgallium (TMG) and ammonia (NH_3) gases were used as precursor chemicals and nitrogen (N_2) gas as the carrier. Prior to loading into the reactor, precisely oriented (0001) sapphire substrates were cleaned and lightly etched. Immediately before growth, the surfaces were further processed by heating in situ at 850°C for 5 minutes. The nucleation layers were deposited for 180 seconds at 540° to give a thickness near 450Å. The substrates were then ramped at a constant rate in flowing NH_3 and N_2 gases to growth temperatures in the range 985°C to 1050°C. Overlayers were grown for 45 minutes using a TMG flow rate of 54 μmol/min, an NH_3 flow rate of 6.7×10^{-2} mole/min and a N_2 flow of 4.0 slm. During growth the samples were doped with silicon by flowing SiH_4 at a rate of 1.1×10^{-3} μmol/min.

X-ray data were collected on a Phillips APD diffractometer (step resolution 0.005°) employing graphite-monochromatized CuKα radiation and using the precession method and Zr-filtered MoKα radiation. The nonlinear second-harmonic generation (SHG) measurements were performed utilizing the 1.064μm output of a Nd:YAG laser at a peak power density of 10MW/cm^2 -- well below the damage threshold of the GaN film. The p-polarized incident beam was set at an angle of 55° to the air/GaN interface to maximize the SHG signal, and as the film thickness is less than the coherence length (~2.5μm for GaN), the reported peak intensities have been normalized by the square of the film thickness. Room-temperature electrical resistivity and Hall effect (in 0.5T) were measured using a four-probe van der Pauw technique. The surface morphology of the films were investigated in polarized light utilizing a Vickers Photoplan metallographic microscope.

As a means of reference for the present data, it is recalled that earlier work [7] has shown that as-deposited GaN nucleation layers on (00.1) sapphire are comprised of a mixture of crystalline and amorphous domains. These deductions were initially inferred by contrasting the optical absorption spectra of as-deposited and thermally annealed (to simulate overlayer growth conditions) nucleation layers. As the temperature is increased, these crystallites undergo solid-state epitaxy and their size is augmented by Ostwald ripening. A quantitative measure of this increased crystallinity, as determined from the absorbance data, is obtained by subtracting the absorbance curve of the as-deposited sample from those of the annealed samples and taking the gradient of the resulting difference curves. The maximum of the absorbance gradient of the difference curves as a function of anneal temperature was subjected to an Arrhenius-type analysis, yielding an apparent energy for the crystallization of the GaN nucleation layers of 0.9±0.1 eV (22±2 kcal/mole). This value compares favorably to typical activation energies for steady state self-diffusion in alloys and suggests that possible mechanisms for the recrystallization include the movement of vacancies or dislocations, self diffusion within the bulk material, creep and grain boundary diffusion. [8]

The presence of a crystalline component in GaN nucleation layers (for both as-deposited and post-deposition annealed layers) was confirmed by the detection of well-defined, essentially Lorentzian $\theta/2\theta$ X-ray diffraction peaks. An as-deposited GaN nucleation layer had a measured (00.2) d-spacing of 2.603 Å and a full-width at half maximum (FWHM) of an unresolved α_1-α_2 doublet of 0.35°. The increase in crystallinity with annealing temperature was confirmed, for example, by a monotonic reduction in tensile strain ($\Delta c/c_o$, where c_o = 5.1850Å is the equilibrium cell constant for thick GaN films [9,10]) in the nucleation layer as the anneal temperature is increased. In fact, by an anneal temperature of 900°C, the nucleation layers are essentially fully relaxed, and by an

anneal temperature of 1050°C the FWHM has decreased to near 7 arc minutes. These results further indicate that not only do the crystallites of the GaN nucleation layer continue to grow but their degree of orientation to the substrate improves as well.

In the present study, the structural properties of GaN overlayers deposited at various growth temperatures (in the range 985 - 1050°C) on self-nucleated (00.1) sapphire substrates is presented. **[11]** Initially, the structural coherence of these films normal to the substrate (parallel to the growth direction) was examined by conventional $\theta/2\theta$ X-ray scans. These data are illustrated in Figure 1 and show that: (a) the (00.1) plane of

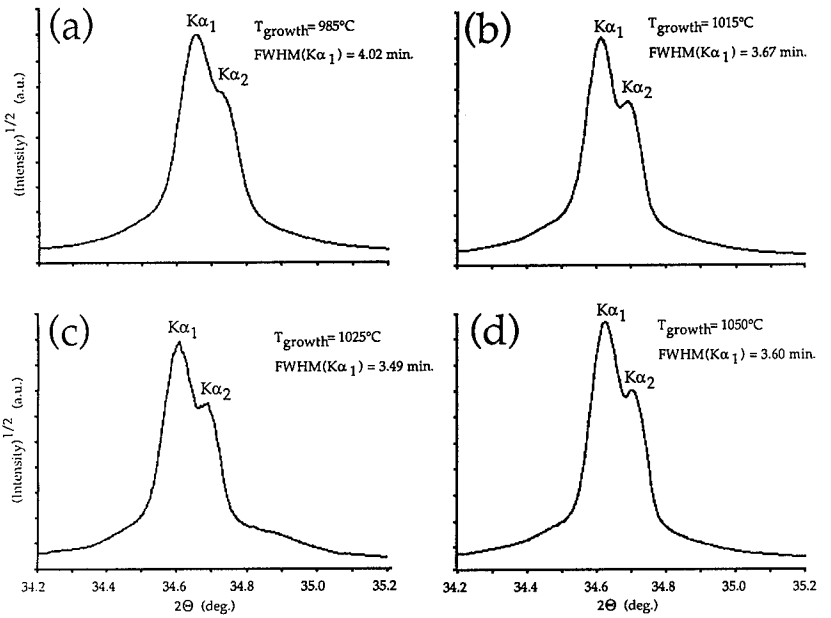

Figure 1. X-Ray diffractometry ($\theta/2\theta$ scan, 0.005° step resolution) of four GaN overlayers deposited on self-nucleated (00.1) sapphire at various growth temperatures.

the GaN overlayer parallels that of the sapphire substrate and, not surprisingly, the GaN nucleation layer as well; (b) the structural coherence parallel to the growth direction is excellent, as demonstrated by a clear separation in the $K\alpha_1/K\alpha_2$ doublet for $(00.2)_{GaN}$ and a Lorentzian fit to the $K\alpha_1$ component that yields a FWHM near 4 arc min or less; (c) the film stress is minimal as the uniformly deduced d spacing for $(00.2)_{GaN}$ at 2.589(1)Å is identical to that reported for thick GaN films. **[9-10]** It is also noted, as can be seen in Figure 2, that the temperature dependence of the integrated intensity for the $(00.2)_{GaN}$ reflection exhibits a functional dependence reminiscent of an activated (Arrhenius-type) process. Given the discussion outlined above, the ripening of the predeposited nucleation layer is a likely precursor to this trend. In a similar vein, the electrical transport properties of these films improve monotonically with growth temperature as exemplified by the n-type carrier density which also shows an Arrhenius-type behavior. **[11]** However, not all parameters display such a simple dependence on growth temperature. For example, as depicted in Figure 3, there is a shallow but discernible minimum in the FWHM at the penultimate growth temperature of 1025°C (a point to which we shall return).

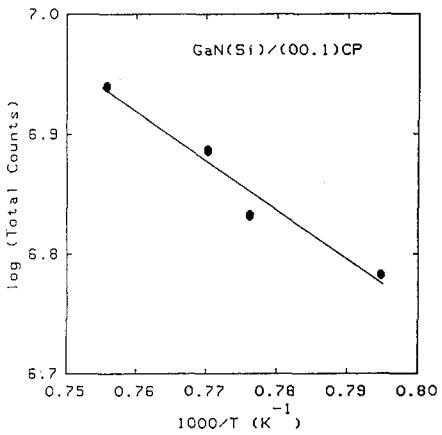

Figure 2. Arrhenius plot of the logarithm of the intensity of the (00.2)GaN reflection.

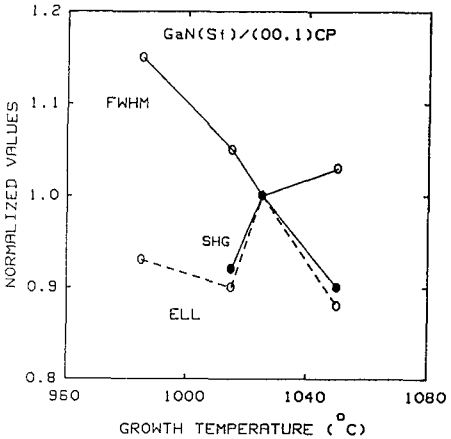

Figure 3. Plot of normalized values for several parameters with temperature.

Employing the X-ray precession method, the in-plane heteroepitaxy of these films [$(10.0)_{GaN}$//$(21.0)_{sapphire}$] has also been ascertained and shown to be equally robust; typical results for the film grown at 1025°C are presented in Figure 4. From photographs

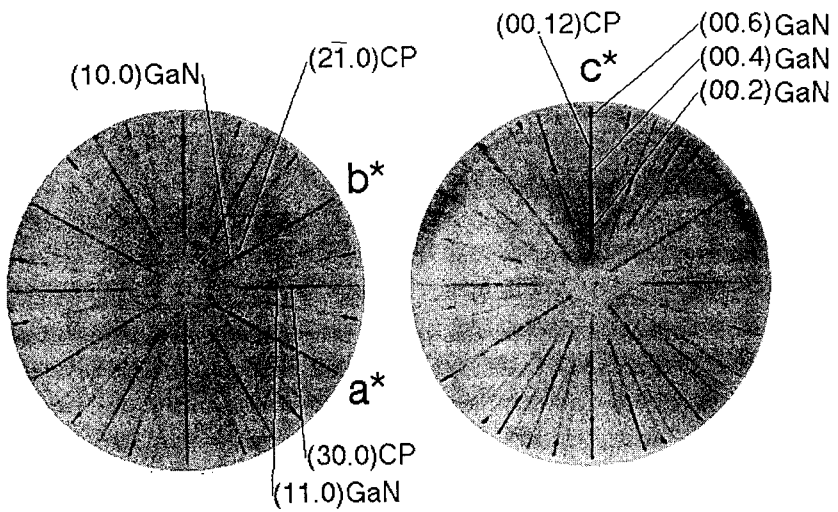

Figure 4. X-Ray precession photographs for the GaN overlayer deposited at 1025°C.

such as these, the mean ellipticity (defined as the ratio of the reflection width in the $\theta/2\theta$ scan direction to that in the ω scan direction and denoted as ELL in Figure 3) has been measured for the family of reflections {11.0} from the GaN films. **[12]** On an absolute scale, the ellipticities for the reflections from the GaN film rival those from the (00.1)

sapphire substrate, and the best ratio (indicating in large measure a superior mosaic spread) is found for the film grown at 1025°C as indicated in Figure 3 and in coincidence with the implication of the FWHM measurements.

Finally, a study of the in-plane morphology of the GaN overlayer has been undertaken as a function of growth temperature. Optical micrographs of the films are given in Figure 5. It is first noted that the film grown at 985°C is such that it is nearly

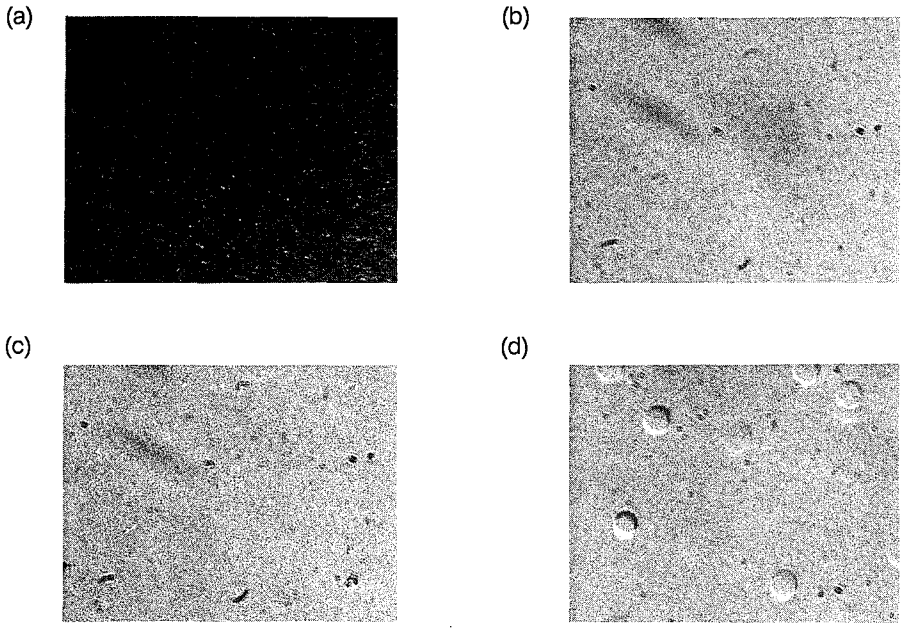

Figure 5. Phase contrast optical images of the surface of the GaN overlayers deposited at (a) 985°C; (b) 1015°C; (c) 1025°; and, (d) 1050°C.

opaque in visible light due to scatter from a dense matrix of three-dimensional islands. The other three films are all transparent in visible light; however, the optical micrographs of Figure 5 show specular surfaces and, therefore, pseudo 2D growth only for the films deposited at 1015 and 1025°C. By a growth temperature of 1050°C, an island growth mode reemerges and a featured surface reappears as shown in Figure 5(d). In parallel, results from the nonlinear optical studies shows a SHG intensity that is optimized for a growth temperature of 1025°C, presented once again in Figure 3.

The unanticipated trends for the SHG intensity, the structural coherence of the epitaxial volume (FWHM), and the reflection ellipticity, and particularly the surface morphology surely lie in the altered overlayer growth mode engendered by the presence of the nucleation layer. We attributed this latter result to a coarsening of the GaN crystallites to the point of a premature coalescence of GaN mesa islands at a growth temperature of 1050°. Apparently then, this coarsening of the GaN nucleation layer at higher temperatures leads to a critical increase in island size, a decrease in nucleation density, and a return to a 3D island growth mechanism for the GaN overlayer, and an optimal growth temperature for self-nucleated GaN films, especially for optoelectronic and device processing applications, that lies in a narrowly defined regime.

SUMMARY

In summary, it has been shown that Si-doped GaN thin films grown on self-nucleated (00.1) sapphire exhibit excellent in-plane and out-of-plane structural coherence and are virtually free of residual stress. Moreover, the dependence of the properties of these films on growth temperature seems to directly stem from that of the GaN nucleation layers predeposited at 540°C. These results can be interpreted within the model proposed by Akasaki and coworkers [13] for AlN-seed layers, where it was suggested that the as-deposited AlN nucleation layers are largely amorphous but anneal and crystallize to a random columnar microstructure upon the thermal ramp to the GaN overlayer deposition temperature. This model further implies that the GaN overlayer nucleates on the AlN columns, and that a preferred overlayer heteroepitaxy dominates initial and subsequent stages of the GaN film. As described, the as-deposited GaN nucleation layers also have a measurable crystalline component, although the crystallite size is very small. Upon annealing to the growth temperature, the crystallite size and crystal perfection of the nucleation layer improves until it approaches that of a heteroepitaxial GaN thin film. Finally, GaN overlayers deposited at growth temperatures in excess of 900°C mimic the excellent structural coherence of the mature GaN nucleation layer. However, beyond a critical crystallite size for the nucleation layer, a three-dimensional growth mode and a textured surface reemerges and the GaN overlayer is less than optimal for optoelectronic applications.

ACKNOWLEDGMENTS

This work was supported by the U. S. Department of the Navy under Contract N00039-91-C-5301. We are indebted to Professor C. L. Chien for diffractometer time.

REFERENCES AND FOOTNOTES

1. S. Yoshida, S. Misawa and S. Gonda, Appl. Phys. Lett. **42**, 427 (1983).
2. H. Amano, N. Sawaki, I. Akasaki and Y. Toyoda, Appl. Phys. Lett. **48**, 353 (1986).
3. T. Detchprohm, K. Hiramatsu, H. Amano and I. Akasaki, Appl. Phys. Lett. **61**, 2688 (1992).
4. S. Nakamura, Jap. J. Appl. Phys. **30**, L1705 (1991).
5. D. K. Wickenden, T. J. Kistenmacher, W. A. Bryden, J. A. Morgan and A. Estes Wickenden, Mat. Res. Soc. Symp. Proc. **221**, 167 (1991).
6. R. J. Molnar, T. Lei, and T. D. Moustakas, Appl. Phys. Lett. **62**, 72 (1993).
7. A. Estes Wickenden, D. K. Wickenden, and T. J. Kistenmacher, J. Appl. Phys., in press.
8. A.E.D.M. van der Heijden and J.P. van der Eerden, J. Crystal Growth **118**, 14 (1992).
9. H. P. Maruska and J. J. Tietjen, Appl. Phys. Lett. **15**, 327 (1969).
10. K. Hiramatsu, T. Detchprohm and I. Akasaki, Jap. J. Appl. Phys. **32**, 1528 (1993).
11 . D. K. Wickenden, J. A. Miragliotta, W. A. Bryden, and T. J. Kistenmacher, J. Appl. Phys., in press.
12. S. J. Andrews, J. E. Hails, M. M. Harding, and D. W. J. Cruickshank, Acta Crystallogr. A **43**. 70 (1987); W. W. Arndt and B. T. M. Willis, Single Crystal Diffractometry (Cambridge University Press, Cambridge, 1966), Ch. 8.
13. I. Akasaki, H. Amano, Y. Koide, K. Hiramatsu and N. Sawaki, J. Crystal Growth **98**, 209 (1989).

GROWTH AND CHARACTERIZATION OF GaN ON Si(111)

A. Ohtani, K.S. Stevens, and R. Beresford
Division of Engineering and Center for Advanced Materials Research
Brown University, Providence, RI 02912, USA

ABSTRACT

Wurtzite GaN films on AlN buffer layers were grown on Si (111) by electron cyclotron resonance microwave plasma assisted MBE (ECR-MBE). High resolution x-ray diffraction studies indicate that the mosaic disorder decreases with increasing growth temperature. The grain size is related to the growth temperature. The best (0002) diffraction peak full width at half maximum was 22 min. for a film 1.7 μm thick. Prominent exciton luminescence is observed at 3.46 eV at 10 K.

The plasma I-V characteristics were measured with a Langmuir probe near the growth position. The nitrogen ion density has been extracted from the data, and is a strong function of the N_2 flow rate, the microwave power and the aperture size of the ECR source. The crystal quality of AlN is strongly affected by the plasma conditions.

INTRODUCTION

Gallium nitride is one of the most important targets among the wide bandgap nitrides for future optical devices. GaN-based *p-n* junction blue light-emitting diodes [1, 2] have already been fabricated using sapphire substrates and commercial introductions in Japan have begun. From the standpoint of a prospective device technology, sapphire poses severe problems as a substrate material because it is hard to cleave, relatively expensive, not amenable to *in situ* homoepitaxy and cannot be made conductive. Silicon solves all these difficulties. Availability of wide bandgap light emitters and detectors on Si would be a significant benefit to nitrides and potentially will have a big impact on Si integrated circuit technology as well.

Research on GaN films on Si substrates dates to 1991[3–6]. The difficulties in achieving good crystal quality of GaN on Si come from the large differences in lattice constants, thermal expansion coefficients, and surface chemistry. In recent reports [4–6], chemical vapor deposition, vapor-phase epitaxy, and ECR-MBE methods were tried using SiC, AlN, or low-temperature-grown GaN as buffer layers to overcome those obstacles.

In this paper, the first detailed investigation of wurtzite GaN growth on Si (111) using AlN buffer layers by ECR-MBE is reported. Apparently also the material is the first optically active GaN on Si. The mosaic structure and grain size are studied using x-ray diffractometry. This project is based on the simple observation that along the (111) direction in the diamond structure, 2-D triangular nets are stacked in the sequence *ABCABC...*, whereas along the *c* axis in the wurtzite structure, similar triangular nets are stacked in the *ABAB....* sequence. Thus, in an ideal layer-by-layer growth mode, wurtzite overlayers can in effect be lattice matched to a diamond or zincblende (111) face. GaN on Si (111) unfortunately constitutes a –17% mismatch ($\sqrt{2}a_{GaN} / a_{Si} - 1$). Nonetheless, substantial progress toward high-quality epitaxy has been demonstrated. The presence of the thin AlN layer is very helpful, as without it, the GaN growth becomes disordered. This difference may be due to the formation at the interface of Si_3N_4 or other silicon nitrides. To make further progress, the activity of the drift plasma from the ECR source is a key issue in control of the crystal quality. For the first time in the nitride ECR-MBE process, *I-V* characteristics of the drift plasma were measured. Some interesting features of the drift plasma related to the efforts to optimize film growth are shown, namely that the ion energy and especially the density are strong functions of the microwave power, nitrogen flow rate, and the aperture size of the ECR plasma source.

Mat. Res. Soc. Symp. Proc. Vol. 339. ©1994 Materials Research Society

EXPERIMENTAL PROCEDURES

The EPI Model 930 MBE system with Astex Compact ECR plasma source was used for this work. Prior to the growth, the *p*-type (B doped, 1-10 Ω-cm, miscut approximately 2.6° toward (100)) Si (111) substrates were cleaned using a standard RCA process, then outgassed in the deposition chamber at 850 °C for 60 minutes to remove the native oxide. After cooling to the growth temperature, the 7-fold surface reconstruction and prominent Kikuchi lines were confirmed in the electron diffraction pattern indicating a high-quality Si surface.

The AlN buffer layers and GaN films were deposited with substrate temperatures over the range of 500 to 800 °C, a microwave power input of 40 W, an N_2 flow rate of 2 sccm and a deposition chamber pressure of 2.0×10^{-5} torr. The thickness of the AlN buffer layers is about 10 nm. The crystallographic structures of AlN buffer layers and GaN films were examined by reflection high energy electron diffraction (RHEED), and double-crystal 4-bounce x-ray diffractometry with a line-focused x-ray generator. The x-ray wavelength is 1.540 Å (Cu Kα). The x-ray beam width is 1.2 mm for theω scanning mode and 0.2 mm for the θ–2θ scanning mode. To study the optimum plasma conditions, AlN films were grown with different microwave powers and nitrogen flow rates, and with two different exit apertures on the ECR source.

RESULTS AND DISCUSSION

X-ray measurements

According to the theory of x-ray diffraction from thin films of mosaic structure [7, 8], the full width at half maximun of the ω scanning mode, ($\Delta\theta_\omega$) is attributed to the superposition of the orientation distribution ($\Delta\theta_1$), the distribution of the lattice spacing ($\Delta\theta_2$), and the finite size of crystallites and/or the finite thickness of film ($\Delta\theta_3$). Therefore $\Delta\theta_\omega \sim (\Delta\theta_1 + \Delta\theta_2 + \Delta\theta_3)$. On the other hand, the FWHM of the θ–2θ scanning mode with a narrow x-ray beam is $\Delta\theta_{2\theta} \sim 2(\Delta\theta_2 + \Delta\theta_3)$. The relation between $\Delta\theta_3$ and the mean dimension, D, the grain size or the thickness of the thin film was given by Scherrer [9],

$$D = \frac{K\lambda}{2(\cos\theta_B)(\Delta\theta_3)} \tag{1}$$

where K is a constant related to the crystallite shape, θ_B is the Bragg angle, and λ is the x-ray wavelength. The value of K was given as 0.7 for microcrystallites [10, 11], and 0.89 for thin films [12].

The $\Delta\theta_\omega$ of the GaN samples depends on the growth temperature (Fig. 1). The value of $(1/2)\Delta\theta_{2\theta}$ is smaller than that of $\Delta\theta_\omega$. This result implies that the GaN films have a mosaic structure that improves as the growth temperature increases. In fact, $(1/2)\Delta\theta_{2\theta}$ decreases as the growth temperature increases. The theoretical value of $(1/2)\Delta\theta_2$ for GaN is very small, 20.5 s [8]. The FWHM from the finite thickness of the film (eq. 1) is also negligible compared to the measured $\Delta\theta_{2\theta}$. Therefore the temperature dependence of $\Delta\theta_{2\theta}$ reflects the temperature dependence of the grain size of the microcrystallites. The surface morphology observed by scanning electron microscopy corresponds to the above x-ray analysis, that is, the size of the hills on the GaN surface increases with growth temperature.

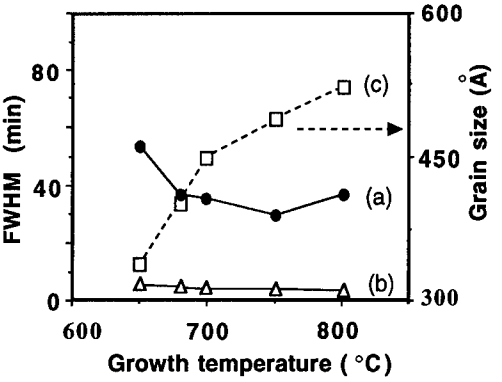

Figure 1. FWHM from GaN(0002) vs. growth temperature. $\Delta\theta_\omega$ (a); $\Delta\theta_{2\theta}$ (b); grain size from equation 1 (c). The film thickness is 0.6-0.7 μm.

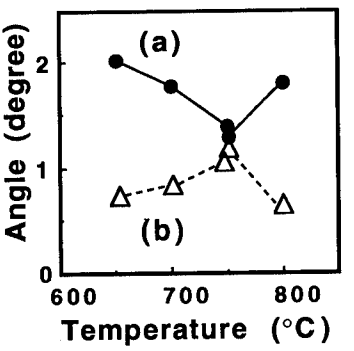

Figure 2. Tilt angle vs. growth temperature. Angle between GaN(0002) and Si(111) (a); angle between GaN(0002) and surface normal (b).

The alignment of the GaN(0002) direction with respect to the Si(111) and the surface normal shows a temperature dependence as in Fig. 2. The (0002) axis tends to align to Si(111) and away from the surface normal as the growth temperature increases up to 750 °C. From these results, we get an optimum growth temperature of 750 °C. When the growth temperature exceeds 750 °C, the sublimation rate of GaN from the film becomes comparable to the growth rate. This decomposition of the film is correlated with an increase in $\Delta\theta_\omega$ and the reorientation of GaN(0002) away from Si(111).

Photoluminescence

The photoluminescence spectrum of GaN at 10 K is shown in Fig. 3. Five different types of emissions are recorded. The most efficient emission is obtained at 3.46 eV with 23 meV full-width and is identified as the donor bound exciton [13–15]. The peaks at 3.40 and 3.30 eV may be LO-phonon replicas of the lowest free exciton [15]. More detailed study is needed for an identification of the peak at 3.35 eV. A broad peak near 2.27 eV has been ascribed to deep-donor / deep-acceptor recombination [13]. The growth conditions for this sample were a substrate tempertature of 750 °C , a microwave power of 20 W, and a film thickness of 1.0 μm. The observation of photoluminescence only from films grown at this reduced microwave power strongly suggests that the more energetic plasma species are damaging to the growth of optically active films.

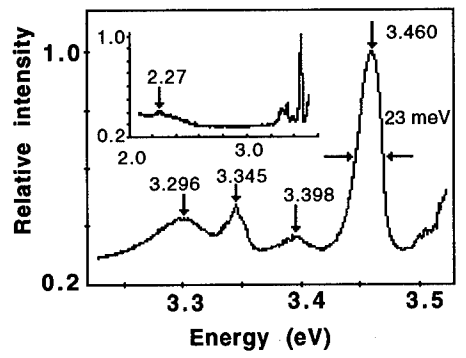

Figure 3. Photoluminescence spectrum.

Plasma I-V characteristics

Molecular nitrogen gas is supplied to the ECR active region (Fig. 4), where active and ionic nitrogen are created through electron collision. Some of the active N_2^*, ionic N_2^+ species and electrons migrate through the aperture of the ECR source and hit the sample surface. Among those species, the positively charged N_2^+ ions potentially cause surface damage due to their high mass and the high kinetic energy obtained from acceleration through the plasma potential.

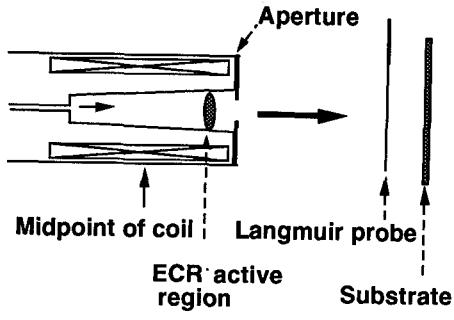

Figure 4. The ECR plasma configuration showing location of the probe.

Powell *et. al.* reported that the bombardment of high energy nitrogen ions (kinetic energy ≥ 60 eV) in a reactive-ion MBE system causes severe damage to GaN film quality [16]. In order to optimize growth conditions, the activity of the plasma was studied via the *I-V* characteristics measured near the growth position by a conventional Langmuir probe of 0.127 mm diameter and 4.445 cm length.

The qualitative behavior of the *I-V* characteristics is explained as follows. For a low density plasma and a small probe, the standard theory of "orbital motion" described by Langmuir [17] gives the positive ion current, I_p , when the probe radius r_p is much less than the Debye length λ_D . In this work, r_p / λ_D was always less than 0.2. The ion current is

$$I_p = eAn \left(\frac{-2e(V_p - V_s)}{\pi^2 m_p} \right)^{\frac{1}{2}} \qquad (2)$$

where e is the electron charge, n the density of ions, A the probe area, V_s the space potential for the ion, and m_p the mass of the ion. The ion number density and the plasma potential are analyzed by plotting I_p^2 vs V_p .

The plasma data are shown in Fig. 5. The density of ions inferred from the ion current increases sharply with the nitrogen flux and the microwave power. From these data, a microwave power of 40 W and nitrogen flow rate of 2 sccm for an aperture diameter of 12 mm seems to be a moderate condition in terms of the plasma bombardment of the sample surface. Using this plasma condition and a growth temperature of 750 °C, we were able to grow at a rate of 0.12 μm/hr. Unless otherwise noted, these conditions were used for the GaN growths reported here. In order to reduce the ion density at the growth surface, we installed a smaller aperture (4 mm diameter) in the ECR source. By doing so, the density of ions becomes one order of magnitude smaller, which is the same order as the reduction in the aperture area. The ionic N_2^+ species that hit the aperture surface seem to cool down, relaxing or recombining to N_2 or N_2^* . The density of ions increases as the microwave power increases in the same way for both apertures. But the density dependence on the flow rate is contrary between those two apertures (Fig. 5a). Since the nitrogen molecule pressure inside the ECR tube is a function of the nitrogen flow rate and the aperture size, and the ionization collision frequency is related to the nitrogen pressure, there is an optimum nitrogen pressure for the creation of the ionized nitrogen. From Fig. 5b, this optimum pressure is about 3 mtorr. The space potential (Fig. 6) of the 12 mm aperture is almost independent of the nitrogen pressure and microwave power. To the contrary, the space potential of the 4 mm aperture increases as the microwave power increases, and decreases as the nitrogen flow rate increases. In the case of the 4 mm aperture

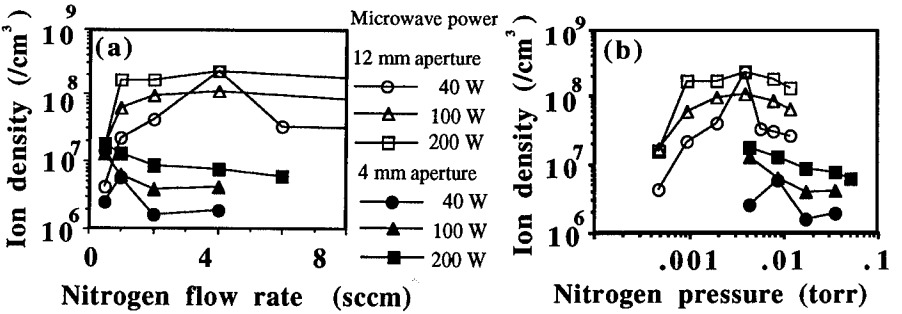

Figure 5. Ion density vs. nitrogen flow rate (a). Ion density vs. calculated nitrogen pressure inside ECR tube (b). The ion production is maximized at about 3 mtorr.

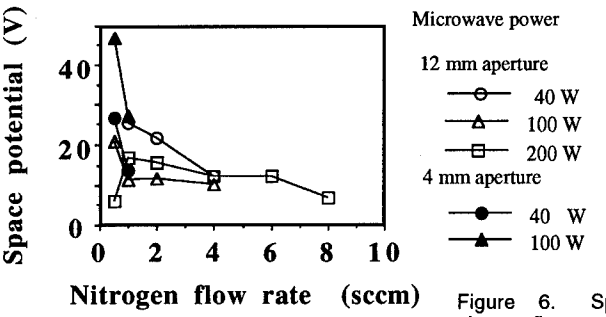

Figure 6. Space potential vs. nitrogen flow rate. The flow should be above about 2 sccm to limit the nitrogen ion energy (4 mm aperture).

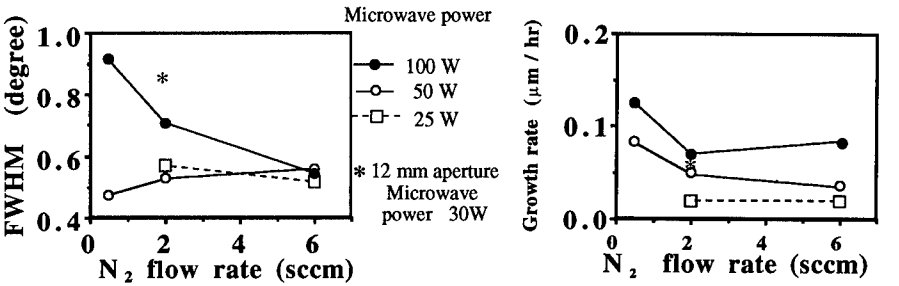

Figure 7. FWHM of AlN vs. plasma condition for the 4 mm aperture. The AlN crystal quality is improved compared to 12 mm aperture. The deposition time is 3 hr. The growth temperature is 750°C.

Figure 8. Growth rate vs. plasma condition (4 mm aperture). The growth rate is reduced compared to the 12 mm aperture.

and a flow rate of more than 2 sccm, the use of an *I-V* curve to estimate the space potential is unreliable.

The FWHM of the AlN (0002) x-ray peak (Fig. 7) indicates that under the plasma conditions of high ion density (10^7 cm^{-3}) and high ion kinetic energy ($\geq$ 40 eV) (0.5 sccm, 100 W) the crystal quality of AlN deteriorates. On the other hand, the growth rate of AlN increases under plasma conditions of higher ion density (Fig. 8). The ion flux for a nitrogen flow of 2 sccm and a microwave power of 50 W is about 10^{12} cm^{-2} sec^{-1} assuming the ion kinetic energy is equivalent to the space potential of 10 eV infered from Fig. 7. The typical growth rate of 0.06 μm/hr corresponds to a nitrogen flux of 8×10^{13} cm^{-2} sec^{-1} that is one order of magnitude greater than the ion flux. Thus, these data suggest that the growth rate is not limited by the ion flux. Instead, the flux of active nitrogen limits the growth rate. With the 4-mm aperture, the growth rate is about a factor of 2 smaller, even though the ion density is ten times smaller.

CONCLUSION

We have grown single-crystal GaN films on Si (111) by ECR plasma-assisted MBE using AlN buffer layers. The samples have a mosaic structure, and this mosaic-type disorder decreases with increasing temperature (less than 750 °C) . The grain size of the mosaic structure is related to the growth temperature. The plasma particle density and energy were characterized by analysis of the Langmuir probe *I-V* data. The density of positively charged nitrogen ions of the drift plasma is a strong function of the microwave power and the nitrogen flow rate. The ionic nitrogen hinders good crystal quality of AlN films.

ACKNOWLEDGMENTS

The work reported here is supported by the National Science Foundation under the Materials Research Group award DMR-9121747. The photoluminescence data was kindly provided by Minna Hovinen and Prof. A.V. Nurmikko.

REFFERENCES

1. S. Nakamura, T. Mukai, and M. Senoh, Jpn. J. Appl. Phys. **30**, L1998 (1991).
2. N. Koide, H. Kato, M. Sussa, and K. Manabe, J. Cryst. Growth. **115**, 639 (1991).
3. K.S. Stevens, A. Ohtani, A.F. Schwartzman, and R. Beresford, J. Vac. Sci. Technol. B (to appear Mar/Apr 1994).
4. T. Takeuchi, H. Amano, K. Hiramatsu, N. Sawaki, and I. Akasaki, J. Cryst. Growth. **115**, 634 (1991).
5. T. Lei and T.D. Moustakas, J. Appl. Phys. **71**, 4933 (1992).
6. Z. Sitar, M.J. Paisley, B. Yan, and R.F. Davis, Mater. Res. Soc. Symp. Proc. **162**, 537 (1990).
7. N. Itoh and K. Okamoto, J. Appl. Phys. **63**, 1486 (1988).
8. Y. Koide, N. Itoh, K. Itoh, N. Sawaki, and I. Akasaki, Jpn. J. Appl. Phys. **27**, 1156 (1988).
9. P. Scherrer, Göttinger Nachr. **2,** 98 (1918).
10. A. L. Patterson, Z. Kirst. **66,** 637 (1928).
11. F.W. Jones, Proc. Roy. Soc. **A166**, 16 (1938).
12. W.L. Bragg, The Crystalline State, Vol. I. A General Survey, G.Bell and Sons, London, Vol.1, 189. (1919).
13. H.G. Grimmiss and B. Mnemar, J. Appl. Phys. **41,** 4054 (1970).
14. M. Ilegems, R. Dingle, and R.A. Logan, J. Appl. Phys. **43,** 3797 (1971).
15. R. Dingle, D.D. Sell, S.E. Stokowski, and M. Ilegems, Phys. Rev. B. **4,** 1211 (1971).
16. R.C. Powell, N.E. Lee, Y.W. Kim, and J.E. Greene, J. Appl. Phys. **73,** 189 (1993).
17. H. M. Mott-Smith and I. Langmuir, Phys. Rev. **28** , 727 (1926).

EFFECT OF ALUMINUM NITRIDE BUFFER LAYER TEMPERATURE ON GALLIUM NITRIDE GROWN BY OMVPE

L. B. ROWLAND†, K. DOVERSPIKE†, D. K. GASKILL†, AND J. A. FREITAS JR.†*
†Laboratory for Advanced Material Synthesis, Naval Research Laboratory, Washington, DC 20375-5347
*Naval Research Laboratory, Washington, DC 20375 and Sachs-Freeman Associates, Landover, MD 20785-5396

ABSTRACT

Gallium nitride layers were grown by organometallic vapor phase epitaxy on AlN buffer layers deposited in the range of 450-650°C. The GaN growth conditions were kept constant so that changes in film properties were due only to changes in the buffer layer growth temperature. A monotonic improvement in relative crystallinity as measured by double-crystal X-ray diffraction corresponded with a decrease in buffer layer growth temperature. Improvements in GaN electron transport at 300 and 77 K were also observed with decreasing AlN buffer layer temperature. Photoluminescence spectra for the lowest temperatures studied were dominated by sharp excitonic emission, with some broadening of the exciton linewidth observed as the buffer layer growth temperature was increased. The full width at half maximum of the excitonic emission was 2.7 meV for GaN grown on a 450°C buffer layer. These results indicate that minimizing AlN buffer layer temperature results in improvements in GaN film quality.

INTRODUCTION

Gallium nitride (GaN) is a promising material for electronic and optoelectronic devices. The immediate need for a lattice-matched substrate for GaN has been somewhat alleviated by the use of low-temperature buffer layers of AlN [1-3] or GaN [3-5] deposited on sapphire (Al_2O_3) prior to GaN growth at elevated temperatures. This 200-500 Å thick buffer layer has a dramatic effect on the properties of subsequently grown GaN films. These films have exhibited greatly improved electrical properties including a reduction of the net n-type carrier concentration by two orders of magnitude. Previous studies of the effect of GaN [5] or AlN [6] buffer layer growth temperature on the GaN film were conducted at 600-1000°C. In both accounts, optimal properties were reported for buffer layers deposited at the lowest temperatures studied (600°C). This raises the possiblity that GaN film properties may be further improved as the buffer layer growth temperature is lowered below 600°C.

In this work, the (0001) GaN films are grown by organometallic vapor phase epitaxy (OMVPE) on AlN buffer layers deposited on (0001) Al_2O_3 substrates. The effect of varying the buffer layer growth temperature in the range of 450°-650°C on properties of the resultant film will be discussed.

EXPERIMENTAL

An inductively-heated, water cooled, vertical OMVPE reactor operated at 57 torr was used for growth as previously described [9]. The AlN buffer layers of 375 Å thickness were formed in the range of 450°C to 650°C using 1.5 μmol/min triethylaluminum (TEAl), 2.50 slm NH_3, and 3.50 slm H_2. Buffer layer thickness was independently calibrated by growing buffer layers under these conditions to 0.3-0.5 μm thickness followed by measurements using cross-sectional scanning electron microscopy. The buffer layers were then annealed in 2.50 slm NH_3 and 3.50 slm H_2 for 10 min at 1025°C. Growth occurred at 1050°C using 25.7 μmol/min TMGa, 2.50 slm NH_3, and 1.75 slm H_2, with a resultant growth rate of 1.9 μm/hr.

Mat. Res. Soc. Symp. Proc. Vol. 339. ©1994 Materials Research Society

To prevent GaN decomposition, samples were cooled after growth in NH_3/H_2 until they were near room temperature.

Sample thickness was measured using interference fringes obtained via infrared reflectance spectroscopy and all samples were 2.8 ± 0.1 μm. Surface morphology was examined using Nomarski optical microscopy. Van der Pauw Hall measurements (2240 G) using a clover-leaf geometry were performed on the samples at 300 K and 77 K using either In or In-6% Ge as ohmic contacts. Double-crystal x-ray diffractometry (DCXRD) using Cu Kα radiation was used to assess crystallinity of these films. Selected films were examined by low-temperature (6 K) photoluminescence (PL) using the 325 nm line of a He-Cd laser as the excitation source.

RESULTS

Figure 1 shows the surface morphology of the resultant GaN grown on AlN buffer layers deposited at (a) 450°C, (b) 550°C, and (c) 650°C. Other than semicircular features present on all samples, which may be due to gas-phase reaction, GaN films grown on AlN buffer layers formed at 450°C were quite smooth. A similar morphology was observed for GaN grown on 500°C buffer layers. The roughness of GaN films increased with increasing AlN buffer layer growth temperature as indicated by the increased roughness present in films on buffer layers deposited at (b) 550°C and (c) 650°C.

The relative crystal quality of the GaN films was then assessed using DCXRD. Figure 2 shows the full width at half-maximum (FWHM) for (0002) diffraction of GaN films as a function of AlN buffer layer growth temperature. The FWHM decreased monotonically from about 8 min for buffer layers grown at 650°C to 5 min for buffer layers grown at 450°C. Thus improved crystallinity and decreased surface roughness occured when AlN buffer layers are formed at lower temperatures.

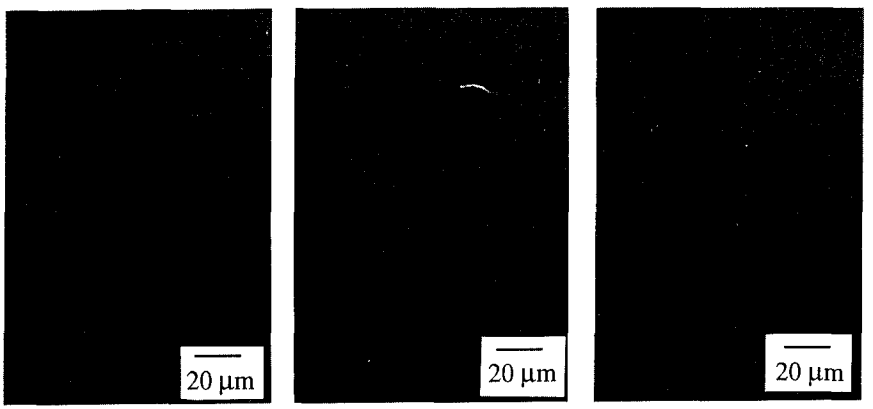

(a) (b) (c)

Figure 1. Nomarski optical micrographs of GaN films grown at 1050°C on AlN buffer layers deposited at (a) 450°C, (b) 550°C, and (c) 650°C.

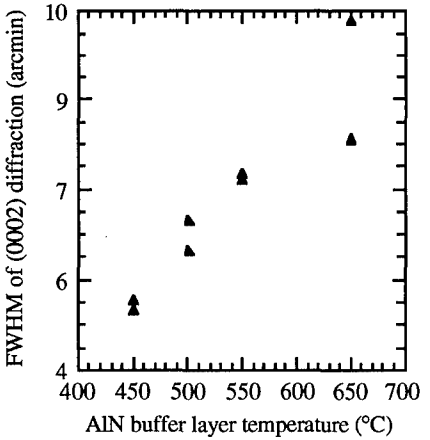

Figure 2. Relative crystallinity as measured by DCXRD for GaN films as a function of buffer layer growth temperature.

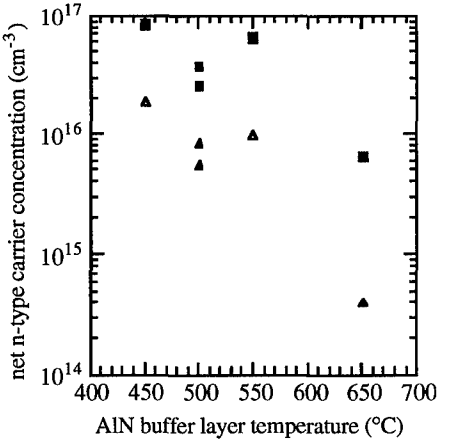

Figure 3. Net n-type carrier concentration determined by van der Pauw Hall measurements as a function of buffer layer growth temperature. Solid squares denote 300 K measurements, while triangles denote 77 K measurements.

The GaN layers were n-type and the free carrier concentration as a function of AlN buffer layer growth temperature at 300 and 77 K are plotted in Figure 3. Figure 4 shows the Hall mobility plotted as a function of AlN buffer layer temperature at (a) 300 K and (b) 77 K. The

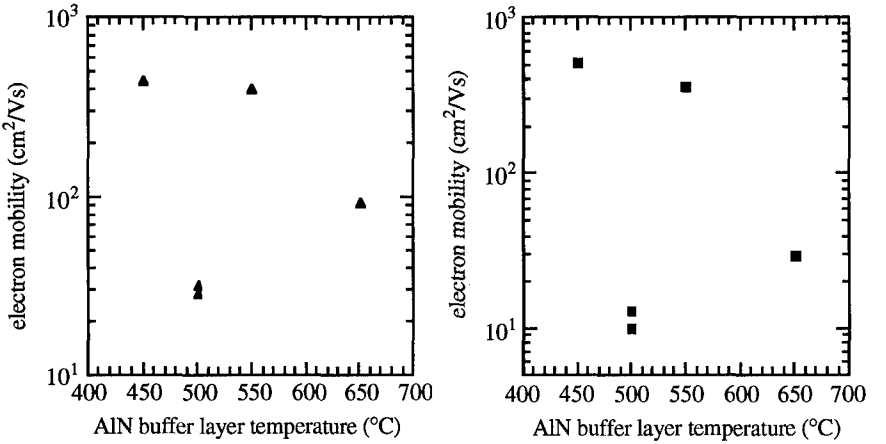

Figure 3. Electron Hall mobility as measured by van der Pauw Hall measurements at (a) 300 K and (b) 77 K.

highest carrier concentrations and the highest mobility values occurred for films grown on AlN buffer layers deposited at the lowest temperature studied. Suppressed mobility and carrier concentration values were consistently observed in films grown on AlN buffer layers formed at 500°C for reasons not understood at this time.

Photoluminescence spectra measured at 6K for the films are shown in Figure 4. The spectrum of GaN grown on 450°C AlN buffer layer (spectrum (a)) was dominated by sharp excitonic emission. Examination of this emission with higher spectral resolution gives a FWHM of 2.7 meV, indicative of high quality material. The exciton linewidth is only slightly broader for films on buffer layers grown at 500°C (not shown) and 550°C (spectrum (b)), but is substantially broader (FWHM = 5.8 meV) for GaN grown on buffer layers grown at 650°C (spectrum (c)). Additional features are observed in PL spectra of GaN films grown on AlN buffer layers formed at (b) 550°C and (c) 650°C in the spectral range between 3.41 and 3.04 eV. To our knowledge, these spectral features do not correspond to any previously reported or identified in the literature. Photoluminescence studies as a function of temperature and excitation intensity will be examined in the near future in an attempt to identify these features.

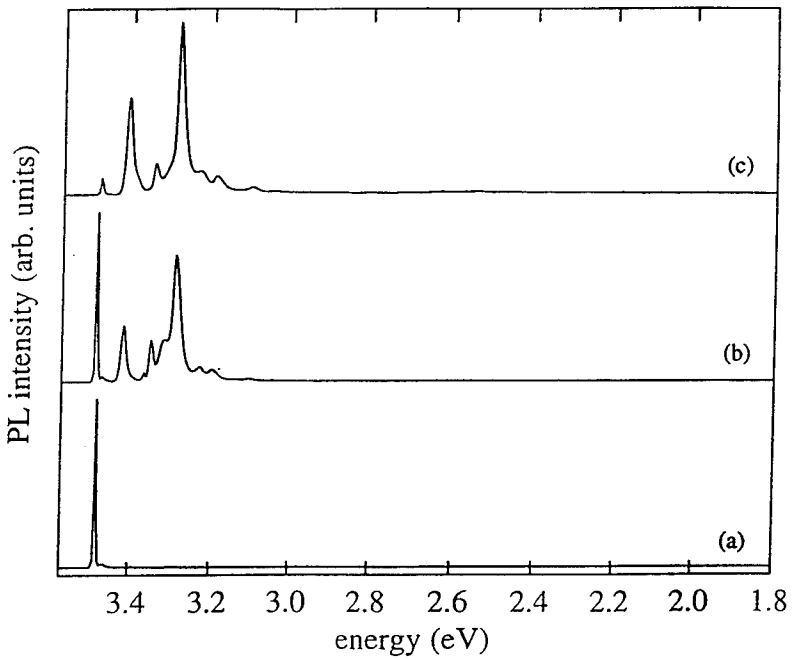

Figure 4. Low-temperature (6K) photoluminescence spectra of 2.8 μm-thick GaN films on AlN buffer layers grown at 450°C (spectrum (a)), 550°C (spectrum (b)), and 650°C (spectrum (c)). Previously unreported spectral features are located at 3.415 eV, 3.364 eV, 3.350 eV, 3.314 eV, 3.290 eV, 3.228 eV, 3.197 eV, and 3.105 eV in spectrum (b).

DISCUSSION

Based on the results presented, it is evident that a reduction in AlN buffer layer growth temperature from 650 to 450°C results in an improvement in film properties. A previous study which included AlN buffer layer temperature as a variable [6] concluded that the lowest buffer layer temperature studied (600°C) resulted in improvements in electrical transport properties, crystallinity and surface morphology. This trend is continued in the present work. As the *only* variable in this study was the buffer layer growth temperature, the vast difference in GaN film properties can only be due to physical differences which result as the buffer layer growth temperature is varied. Two mechanisms are proposed which could influence the characteristics of the GaN films. It is possible that the GaN film is seeded differently depending on the buffer layer growth temperature, thus affecting its properties. A second mechanism is that impurities incorporated in the buffer layer as a function of growth temperature diffuse into the growing AlN film, thus modifying its properties. Some evidence exists that lends support to each of these mechanisms.

First, we consider the nucleation mechanism. Previously, 500 Å buffer layers grown at 600°C using trimethylaluminum (TMAl) and NH_3 were found to be at least partially crystalline [2]. Also, oriented crystalline AlN layers using these precursors have been reported at temperatures as low as 400°C [8]. Conversely, AlN buffer layers formed using TEAl and NH_3 (the same precursors as used in this work) at 550°C were amorphous prior to annealing [3]. It is reasonable from these studies to believe the cystallinity of AlN buffer layers, especially the surface, can be dependent on growth conditions. In this fashion, the GaN film nucleates differently depending on the buffer layer growth temperature. The nucleation of the resulting film therefore may determine the overall morphology, crystallinity, transport, and optical properties as shown in this work.

Next, we consider the impurity mechanism. Possible impurities in the TEAl or NH_3 sources could be incorporated in the AlN buffer layer. Likewise, impurities from incomplete decomposition of sources could be incorporated Furthermore, OMVPE growth kinetics are known to be extremely temperature sensitive [9]. Impurity atoms present on the top surface could affect the GaN nucleation and the resulting growth as discussed above. If these impurities are present in sufficient concentration, they may diffuse into the GaN film and serve as compensating centers and may also affect film crystallinity. In the near future, secondary ion mass spectrometry will be utilized to determine the concentration of impurities in the films as a function of buffer layer growth temperature.

SUMMARY

Gallium nitride layers were grown at 1050°C by organometallic vapor phase epitaxy on AlN buffer layers of 375 Å thickness deposited in the range of 450-650°C. Changes in GaN film properties were due only to changes in the buffer layer growth temperature. Improvements in surface morphology, relative crystallinity, and electron transport were observed with a decrease in buffer layer temperature. Photoluminescence spectra for the lowest temperatures studied were dominated by sharp excitonic emission. The exciton emission became broader and less intense as the buffer layer temperature was increased, and several as yet unidentified spectral features dominated the spectra at the highest buffer layer growth temperatures studied. It is proposed that the effect observed in this study was due to differences in nucleation on the buffer layer or impurities present in the buffer layer.

ACKNOWLEDGEMENTS

The authors would like to acknowledge A. Giordana and L. Shirey for assistance with Hall measurements and scanning electron microscopy. One of the authors (LBR) would like to acknowledge support from a NRC-NRL Cooperative Research Associateship.

REFERENCES

1. S. Yoshida, S. Mizawa, and S. Gonda, Appl. Phys. Lett. **42,** 427 (1983).
2. H. Amano, N. Sawaki, I. Akasaki, and Y. Toyoda, Appl. Phys. Lett. **48**, 353 (1986).
3. J. N. Kuznia, M. A. Khan, D. T. Olson, R. Kaplan, and J. A. Freitas, Jr., J. Appl. Phys. **73**, 4700 (1993).
4. S. Nakamura, Jpn. J. Appl. Phys. **30**, L1705 (1991).
5. D. K. Wickenden, T. J. Kistenmacher, W. A. Bryden, J. S. Morgan, and A. Estes Wickenden, Mat. Res. Soc. Symp. Proc. **221**, 167 (1991).
6. I. Akasaki, H. Amano, Y. Koide, K. Hiramatsu, and N. Sawaki, J. Cryst. Growth **98**, 209 (1989).
7. L. B. Rowland, K. Doverspike, A. Giordana, M. Fatemi, D. K. Gaskill, M. Skowronski, and J. A. Freitas, Jr., to be published in Proceedings of the International Conference on Silicon Carbide and Related Materials, 1994.
8. Z. J. Yu, J. H. Edgar, A. U. Ahmed, and A. Rys, J. Electrochem. Soc. **138**, 196 (1991).
9. G. B. Stringfellow, Organometallic Vapor Phase Epitaxy: Theory and Practice (Academic Press, New York, 1989).

Fundamental Materials-Issues involved in the Growth of GaN by Molecular Beam Epitaxy

N. Newman, T.C Fu, X. Liu, Z. Liliental-Weber, M. Rubin, J.S. Chan, E. Jones,
J. T. Ross, I. Tidswell, K. M. Yu, N. Cheung and E. R. Weber
Lawrence Berkeley Laboratory, Berkeley, CA 94720

Abstract

Gallium nitride is one of the most promising materials for ultraviolet and blue light-emitting diodes and lasers. Both Molecular Beam Epitaxy (MBE) and Metal-Organic Chemical Vapor Deposition (MOCVD) have recently made strong progress in fabricating high-quality epitaxial GaN thin films. In this paper, we review materials-related issues involved in MBE growth. We show that a strong understanding of the unique meta-stable growth process allows us to correctly predict the optimum conditions for epitaxial GaN growth. The resulting structural, electronic and optical properties of the GaN films are described in detail.

Introduction

The fabrication of high-quality single crystal GaN has been a formidable challenge to researchers to date. In order to produce GaN, it has been experimentally realized that high temperatures, activated nitrogen species and/or high nitrogen pressures are necessary to overcome the large kinetic barriers of formation. For this reason, conventional bulk and thin-film growth technologies which are commonly-used to produce III-V semiconductors such as GaAs and InP can not all be directly transferred to GaN production. Only the MOCVD technique operates under analogous principals when growing GaN and other III-V semiconductors. In this report, we highlight the important issues involved in the MBE growth process which we have reported in journal articles.[1,2] We also include more detailed characterization of the films using a number of techniques including Transmission Electron Microscopy (TEM), ion-channeling Rutherford Backscattering (RBS), Cathodoluminescence (CL), and Photoluminescence (PL)

Standard bulk growth techniques such as Czochralski, Bridgeman and Float-zone are not practical alternatives for the growth of GaN because experimental techniques have not been developed which can contain the high equilibrium nitrogen pressures at the melt temperature. In fact, even when contained at pressures possible with diamond anvil cell technology, melting of GaN has not been achieved. Single crystals have been produced by solution growth in a predominantly Ga melt under high pressure (~ 2 GPa) and high temperature (~1500 C) conditions.[3]

In contrast to bulk growth, the successful use of both MBE and MOCVD to fabricate high-quality epitaxial GaN thin films by a large number of groups is striking. MOCVD is grown under conditions which GaN is the stable phase.(Fig. 1a) Typically pressures of 0.1-1.0 atmospheres and temperatures of ~1300 K are used. Since the growth temperature is less than 50% the theoretically-predicted melt temperature (2793 K)[4], the kinetic barriers of epitaxial growth may be limiting the quality of the growing film. For comparison, device quality GaAs is fabricated using MOCVD at ~950 K which is ~63% of the melting temperature(1511 K).

Chemistry of GaN Growth by MBE

Essential conditions for growth: In contrast to all III-V MOCVD growth and MBE growth of conventional III-V compounds, MBE growth of GaN occurs under metastable conditions. Fig.1b shows the equilibrium phase diagram for the reaction of Ga(l) and N_2(g) to form GaN(s), as well as the conditions under which successful MBE growth occurs.[1] The figure clearly shows that the conditions of growth fall below the critical stability line(solid line). This indicates that

Mat. Res. Soc. Symp. Proc. Vol. 339. ©1994 Materials Research Society

additional energy is required to drive the forward synthesis reaction. The use of a more reactive species such as activated nitrogen or nitrogen ions provides sufficient energy to form GaN.[1]

Since the growth occurs in the unstable region of the phase diagram, decomposition will also occur during growth.[1] Fig. 2 compares the rate at which nitrogen ions arrive at the growing

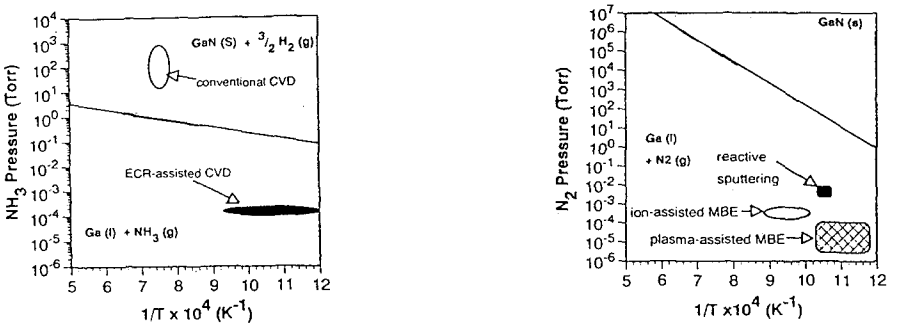

Fig. 1. Phase diagram for the reactions: (a) Ga (l) + NH_3(g) → GaN (s) +$^3/_2$ H_2 (g) and (b) Ga (l) + $^1/_2$ N_2 (g) → GaN (s). Also shown are typical gas pressure and substrate temperature used for the successful production of GaN. From Ref. 1.

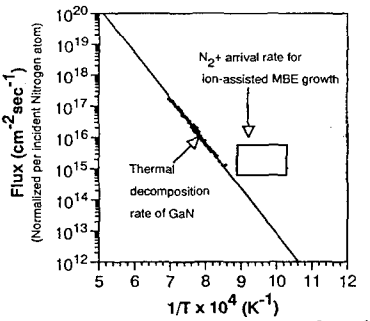

Fig. 2. A comparison of the flux of N_2+ at the growth surface during MBE growth and the N_2 flux from the experimentally-determined sublimation rate[5] of GaN in vacuum. From Ref. 1.

GaN surface with the rate of thermal decomposition, as measured by Munir and Searcy.[5] Note that film growth by MBE only occurs when the rate of arrival of the activated species (i.e. the maximum rate at which the forward reaction could occur) is greater than the thermal rate of decomposition (the minimum rate at which the reverse reaction could occur). As is illustrated, the growth process is controlled by a competition between the forward reaction which depends on the arrival of activated nitrogen species at the growing surface and the reverse reaction whose rate is limited by the unusually large kinetic barrier of decomposition of GaN.[1]

Experimental parameters of growth

Substrate temperature: The effect of substrate temperature on the electrical properties of the GaN films is shown in Fig. 3.[1] Consistent with our analysis, the large kinetic barrier of decomposition allows crystalline film growth up to substrate temperatures of approximately

800 °C. As the temperature was reduced to 600 °C, the carrier concentration decreased to $10^{14}/cm^3$ and the mobility rose to 1200 cm^2/V sec. This is strong evidence that at the higher substrate temperatures, the enhanced rate of decomposition results in the formation of a significant concentration of the auto-doping donor levels, presumably the non-stoichiometric defect, V_N. For substrate temperatures below 600 °C, epitaxial films are not obtained, presumably because the thermal energy was not sufficient to overcome the kinetic barriers of compound formation and epitaxial growth.

Plasma/Ion energy: The requirement that activated Group V species are present during the growth of GaN by MBE is distinctly different than that for other III-V compounds such as GaAs and InP. This requirement may limit the quality possible with this technique due to

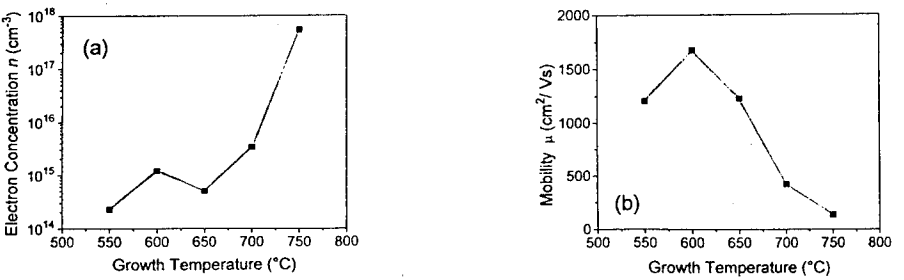

Fig. 3. (a) Hall carrier concentration and (b) Hall mobility versus growth temperature for unbiased undoped n-GaN films. From Ref. 2.

several different processes. The reverse decomposition rate can be significantly enhanced by the impinging flux of energetic ions, electrons, atoms and molecules.[1] Also, damage can be produced by energetic species, resulting in defects in the growing film.[2] Brice et. al.[6] reported that subsurface damage is found when ions with kinetic energies of ~3 times the cohesive energy of the film.[6] This is on the order of ~20 eV for GaN. Also, the presence of the ion beam or plasma results in much less stringent control of contamination due to sputtering of absorbed gas and the system components.

In order to minimize ion-impact damage and decomposition during the film growth, a source which can produce a high flux of activated species with a small, but well defined, kinetic energy is required. A Kauffman Ion Source is used for these experiments because it superior to ECR sources for the production of low-energy monoenergetic species. In order to reduce the kinetic energy of the impinging ions with a Kauffman Ion Source, the substrate to anode potential should be kept small. The minimum anode potential of + 30 V combined with a substrate bias of + 18 V is expected to reduce the impinging N_2+ ion kinetic energy to ~10 V. Because the Kauffman source typically uses a tungsten filament for the production of the plasma and a nickel or carbon grid for the extraction of the ions, it is inherently higher in contamination. An activated ion source which can produce a high-flux low-energy monoenergetic ion-beam with low levels of contamination is clearly needed in this field.

When the substrate bias was used in combination with low temperature and high N_2^+ flux, p-GaN was obtained without intentional doping.[2] Hall measurements indicate a hole concentrations of $5x10^{11}$ cm^{-3} and hole mobilities of over 400 cm^2/V s at 250 K. These electrical parameters compare quite well with values for GaAs when adjusted for the strength of

the electron-phonon coupling and the Debye temperature, despite the higher level of impurities in our ion-beam MBE system compared to conventional GaAs MBE and the wider x-ray peaks of the GaN films.

Properties of the epitaxial films

In this section, we give a brief overview of the properties of the films grown in our laboratory.

Structural Properties: Θ-2Θ X-ray diffraction data (Fig. 4a) indicate that the films are single phase with the hexagonal structure and the c-axis is parallel to the growth direction.

Fig. 5a shows the RBS channeling yield as a function of depth when the beam is aligned perpendicular to the film. The channeling data for bulk GaAs is also plotted for comparison. Note that the 200 nm closest to the surface show a low minimum yield (5%), indicating a reasonably perfect crystal. The significant slope starting at 200 nm indicates that the material contains a significantly larger density of extended defects closer to the substrate/semiconductor surface. The TEM study described below indicates the density and nature of the extended defects responsible for this observation. Off-axis X-ray Φ-scans (Fig. 4b) and off-axis RBS channeling data (Fig. 5b) show that the film is well-oriented in-plane, indicating the films are single crystalline.

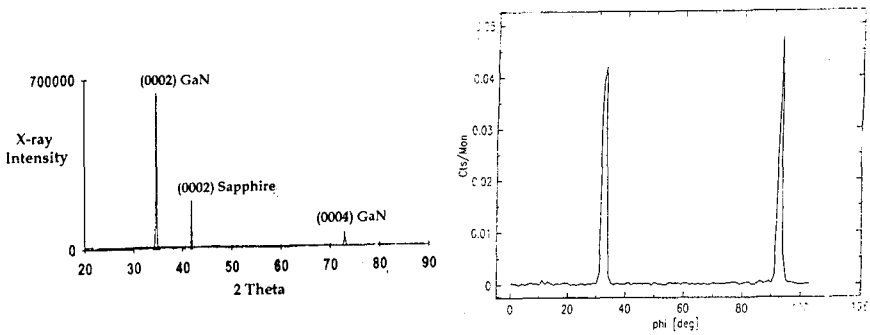

Fig. 4. X-ray diffraction data. (a) Θ-2Θ scan illustrating that the GaN films are predominantly c-axis oriented and (b) Φ-scan for the $(1\bar{1}02)$ diffraction condition illustrating that there is a high degree of in-plane epitaxy (i.e. a-b plane) with no detectable high angle grain boundaries.

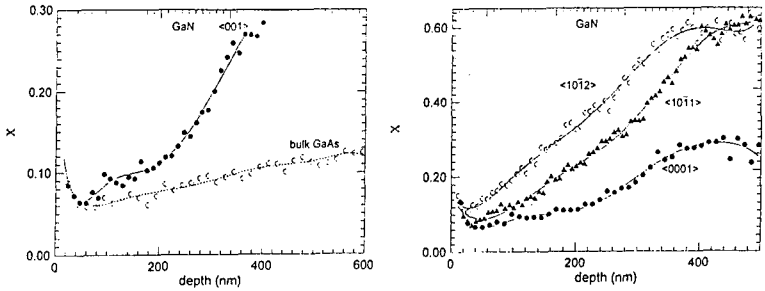

Fig. 5. RBS channeling yield for the beam directed along the normal (001) direction (a) and along off-axis $(10\bar{1}2)$ and $(10\bar{1}1)$ directions (b).

Transmission Electron Microscopy of plan-view and cross-section samples confirm the conclusions from the RBS study that the GaN thin films are high quality crystalline material. A Topcon 002B microscope was used for the TEM studies. The high resolution micrograph (Fig. 6a) from a plan-view sample shows the six-fold symmetry characteristic of the hexagonal structure. Diffraction patterns obtained from the plan-view samples indicate that the thin films are monocrystalline. The $(1\bar{1}00)$ planes of the GaN layers are parallel to the $(2\bar{1}\bar{1}0)$ sapphire planes with [0001] Al_2O_3 || [0001] GaN and show about 13% mismatch between these two materials, as predicted theoretically from bulk lattice constants.

The most common defects in the GaN layers are low angle grain boundaries. The average grain size is on the order of 800 nm. In cross-sectioned samples, a significant concentration of two other defects are also found. Fig. 6b is a high resolution micrograph which shows both of these defects. The defects perpendicular to the interface are twins and are initiated at the interface and extend through the entire layer thickness. Their width is of the order of 8-10 nm and the distance between them is about 20 nm. Their contrast disappears for the (0001) diffraction vector. These defects appear to be the same as the double positional boundaries described by Paisley and Davis[7]. Image simulation is in progress in order to determine the detailed atomic nature of these defects.

The second type of defects observed in cross-section samples form domains terminated by stacking faults parallel to the (0001) growth surface. Their contrast disappear for the diffraction vector parallel to $[\bar{1}010]$GaN. In the area close to the interface, the distance between the stacking fault is of the order of 50 nm and this distance increases to 200 nm when the GaN layer thickness is larger than 300 nm. The smaller concentration of these defects away from the substrate/semiconductor interface can explain the RBS data that indicates the crystal quality improves near the surface of the film.

Optical properties: Fig. 7 shows cathodoluminescence spectra for typical undoped (a) and Mg-doped (b) samples at 90 K. For the undoped sample, the spectrum is dominated by near-band edge exciton emission at 362 nm (3.43 eV). Note the absence of significant emission from deep-levels. In the Mg-doped sample, the near-band edge emission at 372 nm (3.33 eV) is associated with donor-acceptor pair transitions. Also, a strong emission from deep levels is observed at 550 nm (2.2 eV). Other groups typically report emission at similar energies, even in undoped films. The physical origin of this defect has not been directly identified, although our data suggests the presence of Mg during growth can induce the formation of this deep defect.

Electrical properties; Achieving p-type doping: Diffusion of Mg into unintentionally doped n-type GaN films resulted in conversion to p-type material.[2] The films were grown at 600 °C without substrate bias. The diffusion was performed in a sealed ampoule for 80 hours at atmospheric N_2 pressures and 800 °C. Hall measurements at room temperature indicated a hole concentration of $2x10^{16}/cm^3$ and a mobility of 12 cm^2/Vs at room temperature. Higher diffusion temperatures resulted in the removal of the film by decomposition and evaporation. Lower diffusion temperatures were not successful in converting the material to p-type.

Finally, a Knudsen cell for direct in-situ co-evaporation of Mg was used.[2] At a Mg source temperature of 180 °C and a substrate bias of 18 V, the films were found to exhibit hole conduction. Hall measurements indicated a hole concentration of $2x10^{17}$ $/cm^3$ and hole mobilities of <1 cm^2/V s at room temperature.

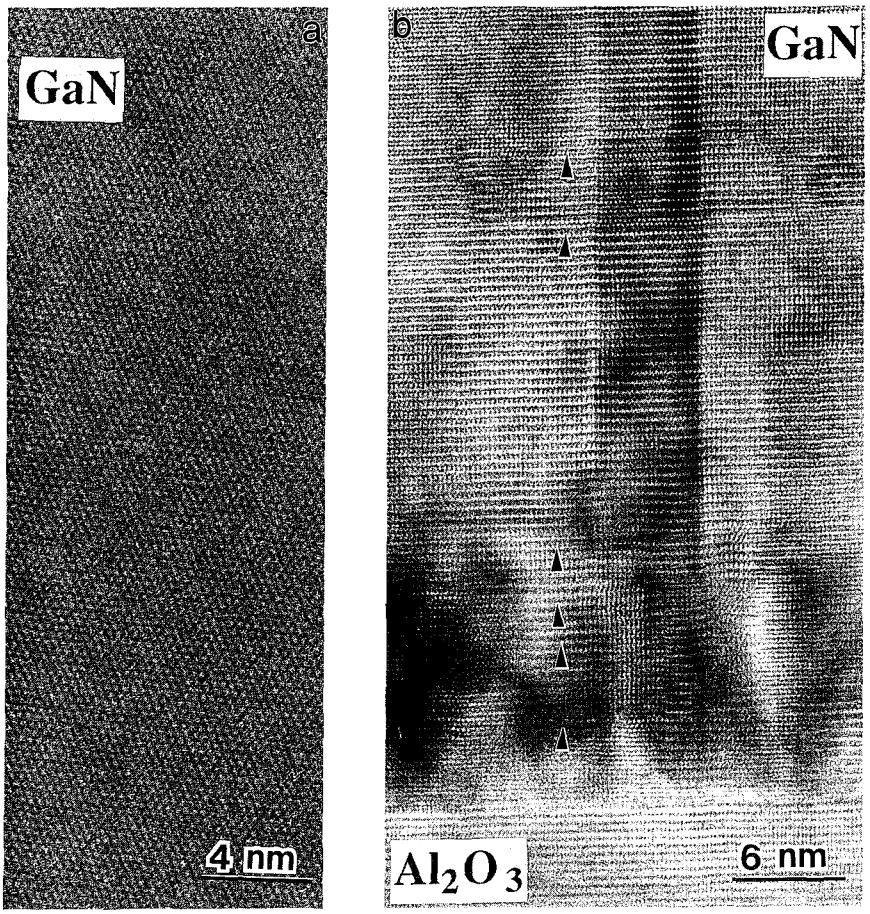

Fig. 6. (a) High resolution plan-view TEM micrograph. (b) High resolution cross-sectional TEM micrograph illustrating a defect which lies perpendicular to the substrate surface and extends throughout the thickness of the film and defects (marked by arrows) which lie parallel to the substrate surface. The concentration of the latter defect is found to decrease with distance from the substrate/film interface.

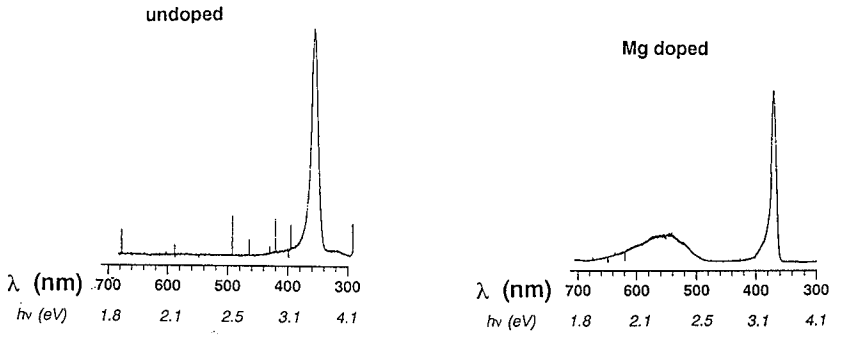

Fig. 7. Cathodoluminescence data for an undoped (a) and Mg-doped (b) GaN film at 90 K.

Summary

We show that an understanding of the unique meta-stable growth process allows us to correctly predict the optimum conditions for the epitaxial growth of GaN with MBE.[1] Using this method, high-quality GaN epitaxial thin films are routinely fabricated.[2] We have also demonstrated that the control of hole-doping lies primarily in reducing the defects in the base material.[2]

Acknowledgments: This work was supported by the Laboratory Director's Research and Development (LDRD) program of the U.S. Department of Energy under Contract No. DE-AC03-76SF00098. J. Chan and T. Fu are partly supported by the Air Force Office of Scientific Research (AFOSR/JSEP) under contract # F49620-90-C-0029. T.C. Fu is partly supported by an NDSEG fellowship. We thank Dr. P. Dreszer for assistance with characterization, Prof. K. Gustafson, Prof. E.E. Haller, and Prof. S. Smith for helpful discussions and use of equipment.

References.

1. N. Newman, J. Ross and M. Rubin, *Appl. Phys. Lett.* **62**, 1242 (1993); *Appl. Phys. Lett.***63**, 424 (1993).
2. M. Rubin, N. Newman, J. S. Chan, T. C. Fu and J. T. Ross, *Appl. Phys. Lett.***64**, 64 (1994).
3. P. Perlin, J. Gorczyca, N. E. Christensen,, I. Grzegory, H. Teisseyve and T. Suski, Phys. Rev. B 45, 13307 (1992); J. Karpinski, J. Jun and S. Porowski, *Journal of Crystal Growth* **66**, 1 (1984).
4. J. A. Van Vechton, *Phys. Rev.* **B4**, 1479 (1973).
5. Z. A. Munir and A. W. Searcy, *J. Chem. Phys.* **42**, 4223 (1968).
6. D. K. Brice, J. Y. Tsao and S. T. Picraux, *Nucleur Instruments and Methods in Physics Research* **B44**, 68 (1989).
7. M. J. Paisley and R. F. Davis, *J. of Crystal Growth* **127**, 136 (1993).

STRUCTURAL CHARACTERIZATION OF GaN GROWN BY ELECTRON CYCLOTRON RESONANCE-METALORGANIC MOLECULAR BEAM EPITAXY (ECR-MOMBE)

S. Bharatan, K.S. Jones, S.J. Pearton, C.R. Abernathy, F. Ren*,
University of Florida, Gainesville, FL 32611
* AT&T Bell Laboratories, Murray Hill, NJ 07974

ABSTRACT

Electron cyclotron resonance-metalorganic molecular beam epitaxy (ECR-MOMBE) has been used to deposit cubic and hexagonal gallium nitride (GaN) on various substrates, namely GaAs, ZnO and Al_2O_3. This paper will report on the effect of the growth rate of the GaN layer on the surface morphology, as analyzed using scanning electron microscopy (SEM). Structural characterization of this material was conducted using cross-sectional transmission electron microscopy (XTEM) and x-ray diffraction. Conditions such as pre-deposition annealing, growth rate and growth temperature are critical in determining the phase and crystallinity of the deposited layers. These parameters were optimized to obtain the cubic GaN phase on GaAs substrates and single crystal wurtzitic GaN on ZnO and Al_2O_3 substrates.

INTRODUCTION

The growth of GaN is becoming increasingly important due to its potential for application in optoelectronic and high-power devices. Though a great deal of information is available regarding GaN growth by metalorganic chemical vapor deposition (MOCVD) and molecular beam epitaxy (MBE)[1-3], little is known about the deposition of nitride based compounds using electron cyclotron resonance-metalorganic molecular beam epitaxy (ECR-MOMBE)[4-6], where the advantages of both MOCVD and MBE can be utilized.

A variety of substrates such as Si[7-9], GaAs[5,10], GaP[6], α-SiC[8], β-SiC[11], MgO[12], TiO_2[8], ZnO[8] and variously oriented Al_2O_3[13,14] have been used for the deposition of GaN thin films. Depending on the substrate symmetry, GaN crystallizes in either a wurtzitic structure having lattice constants a= 3.189Å and c= 5.185Å[15], or a zincblende structure with a lattice constant a= 4.52Å[3]. In general, wurtzitic GaN grows on substrates with a hexagonal symmetry and the zincblende polytype grows on substrates with cubic symmetry. Because the wurtzite and zincblende polytypes differ only in the stacking order of the zincblende <111> planes, the wurtzite having an ABABAB... sequence and zincblende an ABCABC... sequence, they have similar physical properties[3].

In this paper, we will discuss the deposition and structural characterization of GaN films grown on Al_2O_3, ZnO and GaAs substrates. The resulting microstructure of the wurtzitic and cubic GaN films are subsequently presented.

Mat. Res. Soc. Symp. Proc. Vol. 339. ©1994 Materials Research Society

EXPERIMENTAL

Samples were grown on 2" diameter (100) GaAs using In-free mounting and (0001) Al_2O_3 or (0001) ZnO using In-mounting in an INTEVAC Gas Source Gen II. Triethylgallium (TEG) and trimethylamine alane (TMAA) were used as the Ga and Al sources respectively and were transported with either H_2 or He carrier gas. Prior to growth of the GaN on GaAs a 1000Å homoepitaxial buffer layer was deposited. AsH_3 decomposed in a catalytic cracker held at 1100°C was used as the As source. The nitrogen beam used for deposition of the nitrides was derived from a nitrogen plasma generated from 2-13 sccm of N_2 at 200W in a Wavemat ECR MPDR610. Film thicknesses ranged from 4000Å to 9000Å and were grown at rates of either 60 or 140Å/min. GaN layers were deposited directly on the ZnO substrates at 700°C using 7 sccm of N_2. All other substrates were first exposed to a nitrogen plasma at 500°C or 700°C for 15-30 min followed by deposition of a low temperature AlN or GaN buffer layer at 425° - 500°C. Surface morphologies were examined using Nomarski optical and scanning electron (SEM) microscopes . X-ray diffraction (XRD) scans were obtained using CuK_α radiation in a single-crystal powder diffractometer. Transmission electron microscopy (JEOL 200CX) and high resolution electron microscopy (JEOL 4000FX) were used for the structural characterization of the layers by analysis of selected area diffraction patterns (SADP), cross-sectional bright field microphotographs and high resolution lattice images. Cross-sectional samples were prepared using standard techniques[16].

RESULTS AND DISCUSSIONS

When observed under SEM, the surface of GaN films grown on (0001) Al_2O_3 at a rate of 140Å/min appears rough and faceted, indicating that the deposited layers are polycrystalline in nature (Fig.1a-1c). However, when the growth rate was reduced to 60Å/min, epitaxial GaN with a specular surface was observed (Fig.1d).

Fig.2a shows a low magnification cross-section view of a GaN sample deposited at 700°C and 60Å/min on (0001) Al_2O_3 with an AlN buffer layer. It is clear that the defect density is lower in the GaN film than in the AlN buffer layer. The vertical defects, perpendicular to the (0001) planes are believed to be misfit dislocations and antiphase domain boundaries[8]. Also, the defect density decreases with distance from the GaN/AlN interface. This is also seen in the microstructure of wurtzitic GaN grown directly on (0001) ZnO (Fig3a). The HREM image (Fig3b) also shows a series of microtwins close to the interface.

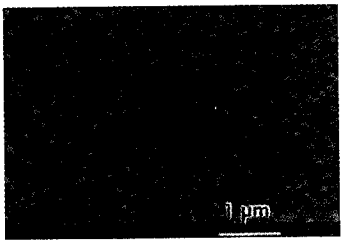

Fig1a) GaN/Al_2O_3
T_{GaN}=700°C

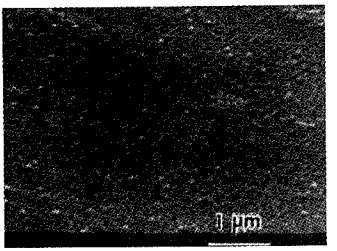

Fig1b) GaN/GaN/Al_2O_3
$T_{buff.}$=500°C, T_{GaN}=700°C

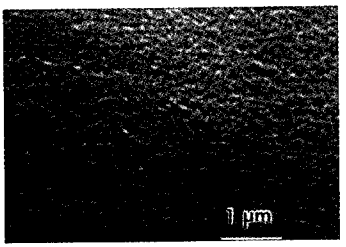

Fig1c) GaN/AlN/Al_2O_3
$T_{buff.}$=425°C, T_{GaN}=700°C

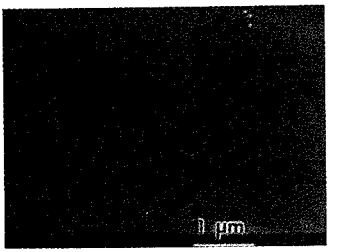

Fig1d) GaN/AlN/Al_2O_3(low growth rate)
$T_{buff.}$=425°C, T_{GaN}=700°C

Fig1: Surface morphology of GaN/(0001) Al_2O_3 grown under different conditions.

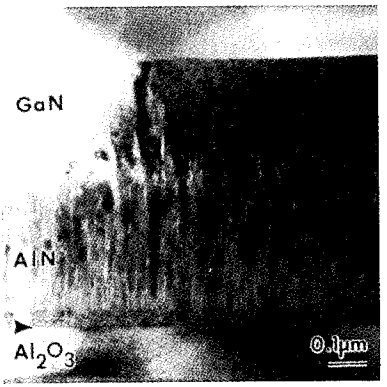

Fig2a) BF image of GaN/AlN/Al_2O_3(low growth rate) g=$(10\bar{1}0)$

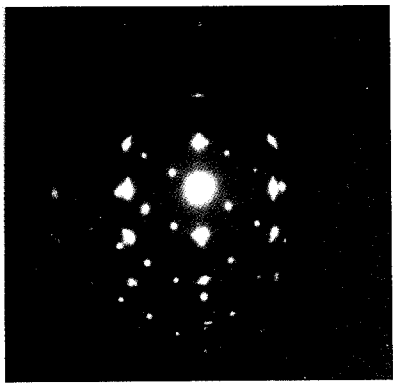

Fig2b) SADP from GaN/AlN/Al_2O_3 interfaces
The orientation relationship is
$(0001)_{nit}//(0001)_{sub}$; $[10\bar{1}0]_{nit}//[11\bar{2}0]_{sub}$

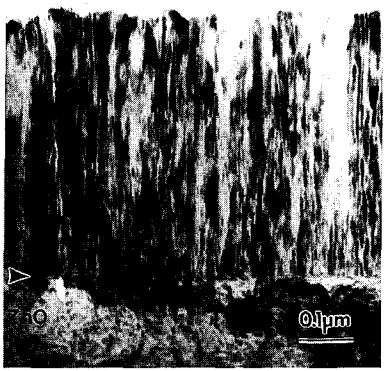

Fig 3a) BF image of GaN/(0001)ZnO T_{GaN}=700°C

Fig 3b) HREM of GaN/(0001)ZnO interface

In order to take advantage of the processing, materials and device technologies already in place, it is desirable to deposit GaN on another III-V substrate such as GaAs. Due to the large mismatch (~20%) between GaN and GaAs, large defect densities are often observed in the epilayer[2,17]. Hence, careful control of the initial nucleation conditions is required to grow single crystal cubic GaN. Table I lists the GaN samples grown on (100) GaAs under various conditions. All samples show a highly oriented polycrystalline columnar structure with grain size from 300Å-900Å. Just as in the growth of wurtzitic GaN on Al_2O_3, it appears that incorporation of a low temperature buffer layer improves the crystalline quality of GaN on GaAs. Use of a GaN buffer layer grown at 500°C helped in nucleation of cubic GaN at the interface. However, there is a transition to the hexagonal phase with increasing distance from the interface. It is clear from the table that when the in-situ anneal time under nitrogen plasma at 700°C prior to deposition is increased from 15 min to 30 min the cubic phase is dominant. This implies a structural change of the GaAs surface upon exposure to the nitrogen plasma. The formation of cubic GaN on the surface seems to be the most probable explanation[18]. This was confirmed by examination of a GaAs substrate exposed to nitrogen plasma for 30 min at 700°C in TEM. A 150Å cubic GaN layer was observed at the surface, along with misfit dislocations.

CONCLUSIONS

The dependence of the GaN phase on the substrate utilized for growth has been investigated. The effect of nucleation condition on film quality, as determined by surface morphology and cross-section TEM, has been studied. It was shown that single crystal wurtzitic GaN can be grown on (0001) Al_2O_3 with an AlN buffer layer at low growth rates. All of the samples deposited on GaAs appear to be highly oriented polycrystalline with 300Å to 1000Å grain size. Incorporation of a low temperature buffer layer and nitrogen pre-annealing helps in nucleation of the cubic phase but there is a transition to the hexagonal phase with increasing film thickness.

Table I

Initial Treatment	Buff. layer	Final layer	Thickness(μm)	XRD,cubic	XRD,hex.	SADP,cubic	SADP,hex
N2 anneal,15min,700°C	GaN,5min.,525°C	GaN,700°C	0.44	yes	yes	yes	yes
N2 anneal,30min,700°C	GaN,5min.,525°C	GaN,700°C	0.86	yes	no	yes	no
N2 anneal,15min,700°C	GaN,500°C	GaN,800°C	0.8	no	yes	no	yes
N2 anneal,15min,700°C	GaN,500°C	GaN,700°C	0.9	yes	yes	yes	no
N2 anneal,15min,700°C	none	GaN,700°C	0.44	yes	yes	no	yes

Table I: GaN samples grown on (100) GaAs under various initial nucleation conditions.

ACKNOWLEDGEMENTS

This work was supported by the ONR/ARPA URI program, grant no N00014-92-J-1895.

REFERENCES

1. R. F. Davis, Proceedings of the IEEE, Vol. 79, 702 (1992).
2. S. Strite and H. Morkoc, Journal of Vacuum Science and Technology B 10, 1237 (1992).
3. S. Strite, M. E. Lin and H. Morkoç, Thin Solid Films 231, 197 (1993).
4. C. R. Abernathy, Journal of Vacuum Science and Technology A 11,869 (1993).
5. P. W. Wisk, C. R. Abernathy, S. J. Pearton, F. Ren, J. R. Lothian, A. Katz and K. Jones in Chemical Perspectives of Microelectronic Materials III, edited by C.R. Abernathy, C.W. Bates, D.A. Bohling and W.S. Hobson (Mater. Res. Soc. Proc. **282**, Boston, MA, 1992) pp. 599-604.
6. S. Bharatan, K. S. Jones, C. R. Abernathy, S. J. Pearton, F. Ren, P. W. Wisk and J. R. Lothian, Journal of Vacuum Science and Technology, in press.
7. P. J. Born and D. S. Robertson, Journal of Materials Science 15, 3003 (1980).
8. Z. Sitar, M. J. Paisley, B. Yan and R. F. Davis in Diamond, Silicon Carbide and Related Wide Bandgap Semiconductors, edited by J.T. Glass, R.F. Messier and N. Fujimori (Mater. Res. Soc. Proc. **162**, Boston, MA, 1989) pp. 537-541.
9. T. Lei, T. D. Moustakas, R. J. Graham, Y. He and S. J. Berkowitz, Journal of Applied Physics 71, 4933 (1992).
10. Z. Q. He, X. M. Ding, X. Y. Hou and X. Wang, Applied Physics Letters 64, 315 (1994).
11. T. Takeuchi, H. Amano, K. Hiramatsu, N. Sawaki and I. Akasaki, Journal of Crystal Growth 115, 634 (1991).
12. R. C. Powell, G. A. Tomasch, Y.-W. Kim, J. A. Thornton and J. E. Greene in Diamond, Silicon Carbide and Related Wide Bandgap Semiconductors, edited by J.T. Glass, R.F. Messier and N. Fujimori (Mater. Res. Soc. Proc. **162**, Boston, MA, 1989) pp. 525-530.
13. N. Kuwano, T. Shiraishi, A. Koga, K. Oki, K. Hiramatsu, H. Amano, S. Itoh and I. Akasaki, Journal of Crystal Growth 115, 381 (1991).
14. T. D. Moustakas, R. J. Molnar, T. Lei, G. Menon and C. R. Eddy Jr. in Wide Bandgap Semiconductors, edited by T.D. Moustakas, J.I. Pankove and Y. Hamakawa (Mater. Res. Soc. Proc. **242**, Boston, MA, 1991) pp. 427-432.
15. H. P. Maruska and J. J. Tietjen, Applied Physics Letters 15, 327 (1969).
16. M. K. Summerville and J. B. Posthill, Journal of Electron Microscopy Technique 12, 56 (1989).
17. S. Strite, J. Ruan, Z. Li, A. Salvador, H. Chen, D. J. Smith, W. J. Choyke and H. Morkoç, Journal of Vacuum Science and Technology B 9, 1924 (1991).
18. S. Fujieda and Y. Matsumoto, Japanese Journal of Applied Physics 30, L1665 (1991).

ECR-ASSISTED REACTIVE MAGNETRON SPUTTERING OF InN

W. A. BRYDEN,* S. A. ECELBERGER,* M. E. HAWLEY,** and T. J. KISTENMACHER*

*Milton S. Eisenhower Research Center, Applied Physics Laboratory
The Johns Hopkins University, Laurel, Maryland 20723
**Los Alamos National Laboratory, Los Alamos, New Mexico 87545

ABSTRACT

The growth of high-quality thin films of the Group IIIA nitrides is exceedingly difficult given their propensity for nonstoichiometry and the lack of suitable substrates for either homoepitaxial or heteroepitaxial growth. A novel deposition technique, ultrahigh vacuum electron cyclotron resonance-assisted reactive magnetron sputtering, has been developed for the preparation of Group IIIA nitride thin films. Thus far, thin films of the semiconductor InN have been deposited on AlN-seeded (00.1) sapphire substrates, and the properties (structural, morphology, and electrical transport) of these films studied as a function of growth temperature. Comparison to InN thin films grown by conventional reactive magnetron sputtering shows enhanced Hall mobilities (from about 50 to over 100 cm^2/V-sec), a decreased carrier concentration (by about a factor of 2-3), an increased optical bandgap, and an apparent reduction in homogeneous strain that is in part to be due to film relaxation induced by the ECR beam and in part to enhanced nitrogen content and more nearly stoichiometric films.

INTRODUCTION

Two of the main obstacles limiting the utilization of thin films of the Group IIIA nitrides (AlN, GaN, InN) in wide bandgap electronic and photonic devices [1] are deviations from stoichiometry (typically nitrogen deficiency and oxygen incorporation) and residual film strain (arising from poor lattice and thermal expansion matches). The introduction of seeded substrates (in particular, AlN [2] and GaN [3] nucleation layers) has done much to increase the nucleation density and lateral growth rate and reduce residual strain. In parallel, one novel method of increasing the nitrogen content has been developed around ECR-assisted molecular beam epitaxy (MBE), using conventional gas sources [4-9] and metal-organic sources. [10]

Similarly, reactive sputtering has been widely employed for the preparation of AlN, GaN and InN thin films, [11] and generally high carrier concentration (in excess of 10^{20} cm^{-3}) are observed. Thus, off stoichiometry remains a problem in these sputter deposited films, and data from the reactive magnetron sputtering of InN films in an ultrahigh vacuum chamber and *in situ* electrical transport measurements indicate that oxygen incorporation can be minimized. [12] Prompted by the success of the ECR-assisted MBE growth technique, an ECR source has been added to this ultrahigh vacuum (UHV) deposition chamber to yield what is believed to be a unique growth facility [13], and additional results are reported here for InN films grown on AlN-nucleated (00.1) sapphire.

Mat. Res. Soc. Symp. Proc. Vol. 339. ©1994 Materials Research Society

EXPERIMENTAL

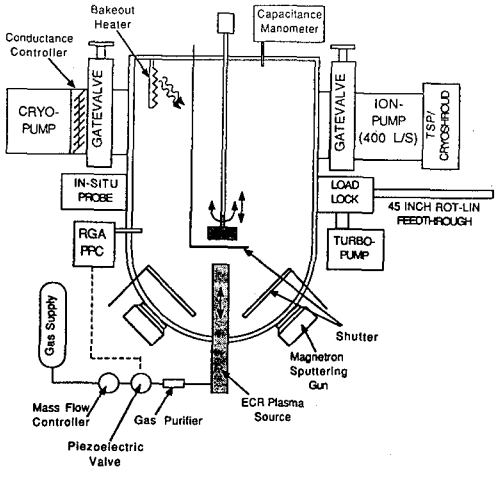

Figure 1. Schematic drawing of ECR-assisted reactive magnetron sputtering system.

A UHV stainless steel chamber forms the core of the ECR-assisted magnetron sputtering system (Figure 1). The chamber is equipped with a combination of turbo-, ion- and cryo-pumps and typically achieves a base pressure of 5 x 10^{-11} Torr. [12] A Wavemat™ Inc. ECR source [Model MPDR 610] is aligned parallel to the rotation axis of the substrate/heater assembly and normal to the substrate surface, here (00.1) sapphire. The magnetron sputtering guns are at an angle of 45° to this common axis, and to facilitate uniform film thickness, the substrate/heater assembly is incrementally rotated through ±180° during deposition. Under typical sputtering conditions, the substrates (after initial chemical cleaning) were heated to 850°C in vacuum and then cooled to 600°C where a 400Å nucleation layer of AlN was dc sputtered from a high-purity Al target in 5 mTorr of N_2. Subsequently, the seeded substrates were ramped to the growth temperature (100 - 400°C), the ECR source activated (150W, N_2 flow of 50 sccm) and InN deposited for 90 min by the reactive sputtering (100W, rf) of a high-purity In target.

Ex situ, the InN films were characterized by a variety of physical techniques. The structural coherence and strain normal to the film plane was ascertained from X-ray data collected on a Phillips APD diffractometer employing graphite-monochromatized CuKα radiation. Analogous in-plane structural parameters were derived from X-ray data collected using the precession method and Zr-filtered MoKα radiation. Room-temperature electrical resistivity and Hall effect (in a magnetic field of 0.5 T) were measured using the four-probe van der Pauw technique. The optical bandgap was derived from absorption spectra using a Perkin-Elmer Model 330 dual-beam spectrophotometer. Finally, surface morphology was examined with a Digital Nanoscope III: in AFM (atomic force microscope) mode employing both commercial triangular Si_3N_4 cantilever tips and high aspect ratio Si tips; and in STM (scanning tunneling microscopy) mode using Ir-Pt dip etched and cut tips.

RESULTS AND DISCUSSION

As for conventionally grown materials [14], the InN thin films deposited by ECR-assisted magnetron sputtering have their (00.1) planes parallel to the (00.1) plane of the sapphire substrate [$(00.1)_{InN}//(00.1)_{sapphire}$]. Using normal-beam X-ray diffractometry, the structural coherence and strain along the film growth direction have been studied, and Figure 2 shows the θ/2θ profile of the (00.2) reflection from an ECR-assisted magnetron sputtered InN thin film. The full-width at half-maximum (FWHM) for this reflection is quite small

at 0.12° [reduced by about 0.1° compared to a standard film growth] and there is a distinct indication of the resolution of the $K\alpha_1$,$K\alpha_2$ doublet. Both of these aspects of the diffraction profile confirm the excellent structural coherence of the film in the growth direction and imply a considerable reduction in inhomogeneous strain. Similarly, the apparent homogeneous strain normal to the growth surface has been estimated [$(d_{(00.2)}^{obs} - d_{(00.2)}^{bulk})/d_{(00.2)}^{bulk}$] and a comparison of the results from conventionally grown films is displayed in Figure 3. Apparently, the homogeneous strain in the ECR-assisted films is measurably reduced from that found in the conventionally grown films. In a cautionary note, however, there is a distinct possibility that some of the shift in measured d-spacing may arise from an enhanced nitrogen content and not from reduced strain.

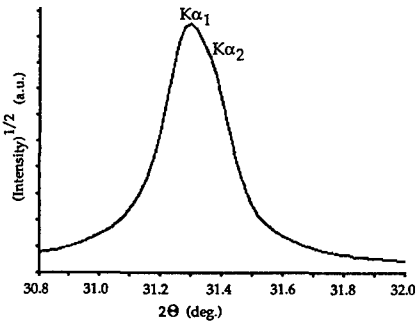

Figure 2. X-ray profile (θ/2θ) of the (00.2) reflection from an InN film grown at 325°C.

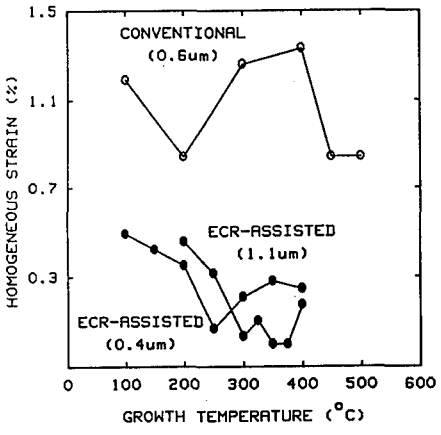

Figure 3. Derived homogeneous strain as a function of growth temperature for two ECR-assisted and conventional InN films.

The surface morphology of the ECR-assisted magnetron sputtered InN thin films has been investigated by scanned probe techniques, and a typical STM micrograph from a film grown at 325°C is shown in Figure 4. On a fine scale, these films show highly orientated grains with diameters on the order of a few hundred angstroms. On a larger scale, there is clear evidence of Ostwald ripening to yield well-defined islands with diameters on the order of 1μm. This is in marked contrast to conventionally grown films where there is no evidence of island formation, only the dense packing of micrograins. Finally, the X-ray scattering from the (00.1) planes of the InN film and the sapphire substrate [$(10.0)_{InN}//(21.0)_{sapphire}$] is illustrated in Figure 5. Here, it is evident from the nearly circular shape of the diffraction maxima that the misorientation of grains is quite small (near 0.5°), improved by about a factor of two compared to the best conventionally grown films. Much of the improvement in in-plane misorientation likely follows from the island formation indicated in Figure 4.

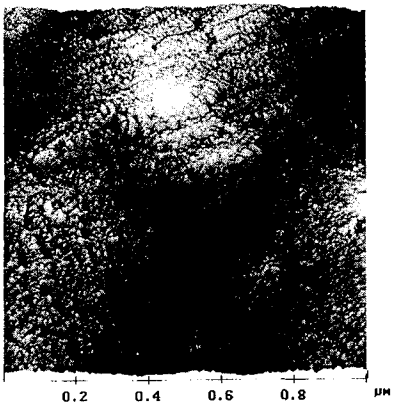

Figure 4. Morphology of an InN film on (00.1) sapphire grown at 325°C.

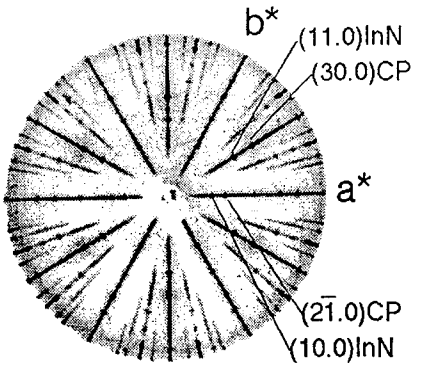

Figure 5. X-ray scattering from the (00.1) planes of the InN film and the sapphire substrate.

The effects of the ECR plasma on the magnetron sputter growth of InN films are also well illustrated by comparing the electrical transport properties of the present films to those grown by conventional reactive magnetron sputtering. In Figure 6, the room-temperature

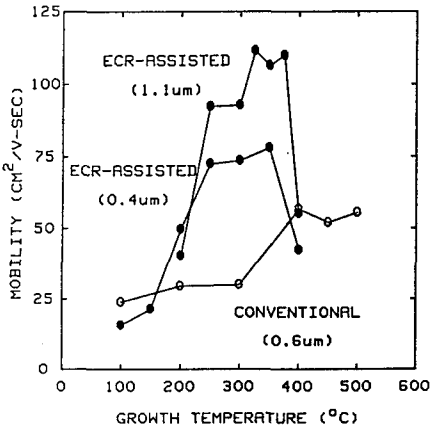

Figure 6. Dependence of the electrical mobility on growth temperature.

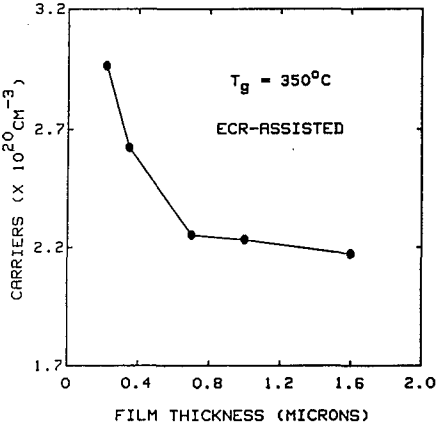

Figure 7. Variation in carrier density as a function of InN film thickness.

Hall mobility as a function of growth temperature is presented for both conventional [14] and two sets (one with a mean thickness of 0.4μm and one with a mean thickness of 1.1μm) of ECR-assisted sputtered films of InN. It is apparent, except at the very lowest and the very

highest growth temperatures, that the mobility of the InN thin films deposited by ECR-assisted sputtering are enhanced, by factors as large as 3-4. It is also evident that the thicker ECR-assisted films (~1.1μm) generally show a higher mobility compared to the thinner films (~0.4μm), especially in the intermediate temperature regime. The improved mobility for the thicker films in large measure arises from a distinct thickness dependence to the carrier concentration as shown in Figure 7 for a series of films grown at 350°C. It can be speculated that the reduction in importance of surface and interfacial scattering states lead to trend observed in Figure 7. However, another major contributor to the enhanced mobility is a reduction in nitrogen defect sites, especially at grain boundaries. Here, as for other polygrained films, the improvement in mobility probably originates from diminished charge-carrier trapping and a reduction in scattering from localized defects at intergrain boundaries. Finally, in parallel with these observations, the sharpening of the optical absorption spectrum and an increase in magnitude of the optical bandgap for these ECR-assisted InN films further attests to the reduction in sub-bandgap carriers.

In summary, heteroepitaxial thin films of InN have been deposited on AlN-seeded (00.1) sapphire substrates by ultrahigh vacuum ECR-assisted reactive magnetron sputtering and the properties of these films studied as a function of growth temperature. Contrasting these InN films to those grown by conventional reactive magnetron sputtering shows enhanced Hall mobilities, decreased carrier concentrations and increased optical bandgaps, and increased structural coherence and an apparent reduction in homogeneous strain that is in part be due to film relaxation and in part to more nearly stoichiometric films.

ACKNOWLEDGMENTS

This work was supported in part by the U. S. Department of the Navy under Contract N00039-91-C-0001. We are indebted to Professor C. L. Chien for diffractometer time to undertake some of the X-ray scattering experiments.

REFERENCES

1. See, for example: R. F. Davis in *The Physics and Chemistry of Carbides, Nitrides and Borides*, edited by R. Freer (Kluwer Academic Publishers, Dordrecht, 1990), pp. 653-669; S. Strite and H. Morkoç, J. Vac. Sci. Technol. B 10, 1237 (1992).
2. H. Amano, N. Sawaki, I. Akasaki, and Y. Toyoda, Appl. Phys. Lett. 48, 415 (1988). D. K. Wickenden, T. J. Kistenmacher, W. A. Bryden, J. S. Morgan, and A. E. Wickenden, Proc. Mater. Res. Soc. 221, 167 (1991); S. Nakamura, Jpn. J. Appl. Phys. 30, L1705 (1991).
4 Z. Sitar, M. J. Paisley, D. K. Smith and R. F. Davis, Rev. Sci. Instrum. 61, 2407 (1990).
5. T. Lei, M. Fanciulli, R. J. Molnar, T. D. Moustakas, R. J. Graham, and J. Scanlon, Appl. Phys. Lett. 59, 944 (1991).
6. S. Strite, J. Ruan, Z. Li, A. Salvador, H. Chen, D. J. Smith, W. J. Choyke and H. Morkoç, J. Vac. Sci. Technol. B 9, 1924 (1991).
7. M. E. Lin, G. Xue, G. L. Zhou, J. E. Greene, and H. Morkoç, Appl. Phys. Lett. 63, 932 (1993).
8. Cheng Wang and R. F. Davis, Appl. Phys. Lett. 63, 990 (1993).
9. L. B. Rowland, R. S. Kern, S. Tanaka, and R. F. Davis, Appl. Phys. Lett. 62, 3333 (1993).

10. S. J. Pearton, C. R. Abernathy, P. W. Wisk, W. S. Hobson, and F. Ren, Appl. Phys. Lett. 63, 1143 (1993).
11. H. J. Hovel and J. J. Cuomo, Appl. Phys. Lett. 20, 71 (1972); T. L. Tansley and C. P. Foley, Electr. Lett. 20, 1066 (1984); T. J. Kistenmacher and W. A. Bryden, Appl. Phys. Lett. 59, 1844 (1991); N. Newman, J. Ross, and M. Rubin, Appl. Phys. Lett. 62, 1242 (1993).
12. W. A. Bryden, S. A. Ecelberger, and T. J. Kistenmacher, Mat. Res. Soc. Symp. Proc. 280, 509 (1993).
13. W. A. Bryden, S. A. Ecelberger, and T. J. Kistenmacher, Appl. Phys. Lett., submitted.
14. T. J. Kistenmacher, S. A. Ecelberger, and W. A. Bryden, J. Appl. Phys. 74, 1684 (1993).

RAMAN SCATTERING AND X-RAY DIFFRACTION STUDIES OF GALLIUM NITRIDE FILMS GROWN ON (100) GALLIUM ARSENIDE

S. W. BROWN*, S. C. RAND*, C.-H. HONG**, AND D. PAVLIDIS**
*University of Michigan, Applied Physics Program,
500 E. University Ave., Ann Arbor, MI 48109
**University of Michigan, Solid State Electronics Laboratory,
Department of Electrical Engineering and Computer Science, Ann Arbor, MI 48109

ABSTRACT:

Raman spectroscopy and x-ray diffraction are used to characterize Gallium Nitride (GaN) films grown on (100) Gallium Arsenide (GaAs) substrates. Reflection X-ray diffraction data from (200) planes of GaAs and cubic GaN are presented. The linewidth of the cubic GaN diffraction peak is shown to be a strong function of the growth temperature. Raman spectra are presented for a series of samples grown at different temperatures. Raman scattering is characterized by strong peaks at 560 cm^{-1} and at 736 cm^{-1}, corresponding to TO and LO phonon modes of cubic GaN, respectively. An additional, unexplained feature at 768 cm^{-1} is clearly observed in Raman spectra of c-GaN samples grown at lower temperatures. The polarization dependence of the intensity of the GaN LO phonon mode is presented and compared with the GaAs LO phonon mode to establish the relative orientation of the c-GaN epitaxy on GaAs.

INTRODUCTION:

Gallium nitride (GaN) is a direct gap, III-V semiconductor which crystallizes in both wurtzitic and cubic form. High-quality wurtzitic GaN has been grown successfully on a variety of substrates, in particular basal plane sapphire [1-4]. Cubic GaN has also been grown on a variety of substrates, including silicon and GaAs [5-9]. Use of GaAs or silicon as substrates for the growth of GaN is desirable for reduction of interfacial defects and impurities as well as for device processing and integration of GaN-based devices into existing silicon and GaAs-based systems. Potential optical and electronic device applications of these materials have been reviewed by Davis [10] and Strite and Morkoç [11], among others.

Previous polarized Raman scattering studies of wurtzitic GaN have identified an A_1(TO) mode at 533 cm^{-1}, an E_1(TO) mode at 559 cm^{-1}, and an E_2 mode at 568 cm^{-1} [12-14]. In addition, Raman studies of cubic GaN films have identified a TO phonon mode with a frequency

Mat. Res. Soc. Symp. Proc. Vol. 339. ©1994 Materials Research Society

of 556 cm^{-1} and an LO mode with a frequency of 737 cm^{-1} [9, 15-16]. In this work, Raman scattering results from cubic GaN are presented. We compare results of Raman shifts and intensities versus temperature as well as the polarization dependence of the Raman scattering with the earlier work, using X-ray diffraction measurements to confirm the cubic phase of the GaN films.

EXPERIMENT:

GaN films were grown by MOCVD on (100)-oriented GaAs substrates. Substrates were degreased and cleaned using standard procedures prior to loading into the MOCVD reactor. Prior to growth, the substrate was annealed in H_2 and AsH_3 for 5 minutes at 670 °C to remove the surface oxide. The substrate was then brought to the growth temperature; growth temperatures ranged from 530 °C to 700 °C in this study. Sample heating is provided by halogen lamps. The sample temperature, measured by a thermocouple mounted on the sample holder, was continuously monitored and actively stabilized. Nitridation of the substrate with a 10 minute exposure to ammonia preceded every growth. High purity trimethylgallium was then introduced through a hydrogen bubbler in addition to the NH_3 at a fixed V/III ratio of 3300 for GaN growth. System pressure was kept at 60 Torr during film deposition. The growth rate was on the order of 0.65 μm/hr at 600 °C. Film thicknesses ranged from 2500 to 4000 Å, depending upon the growth temperature.

Reflection X-ray diffraction studies used a conventional single-axis goniometer in θ-2θ geometry. The Cu Kα line (λ=1.537 Å) was used as an x-ray source.

Raman scattering measurements were performed in a backscattering geometry. For excitation, 100 mW of 488 nm radiation from an argon ion laser was focused onto the sample with a 150 mm focal length lens. A small pick-off mirror steered the light onto the sample. Care was taken to ensure that incident light was perpendicular to the plane of the sample and that only light scattered into a solid angle of 0.04 pi steradians about the backscattering direction reached the spectrometer. An intensified diode array coupled with a signal digitizer allowed for rapid signal averaging; typically, 500 scans of one second duration were averaged. The accuracy of the system, referenced to both the GaAs substrate and a CCl_4 standard, was estimated to be better than 5 cm^{-1}. The polarization of the incident light was controlled with a polarization rotator. A polarizer in front of the entrance slits to the spectrometer analyzed the scattered polarization. Finally, samples were mounted on a calibrated rotation stage for rotation of the samples in the plane perpendicular to the wavevector of the incident light.

RESULTS AND DISCUSSION:

X-ray diffraction results for a GaN film grown at a substrate temperature of 600 °C are shown in Figure 1. The diffraction peak at 39.8° originates from the (200) cubic GaN plane, giving a lattice constant of 4.52 Å. Analysis of the linewidth of the GaN diffraction peak as a function of growth temperature is presented in Figure 2. The width of the cubic peak at 39.8° shows a strong 2θ minimum of 1° for a growth temperature of 600 °C. For comparison, the width of the (200) GaAs peak is less than 0.25°. The increased width of the GaN diffraction peak relative to the GaAs peak is an indication of disorder in the material. TEM measurements have also confirmed the cubic phase of the GaN [17].

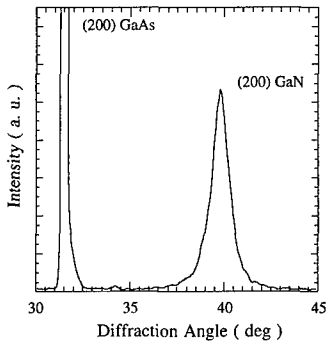

Figure 1. X-ray diffraction pattern of GaN film grown at 600 °C on (100) GaAs.

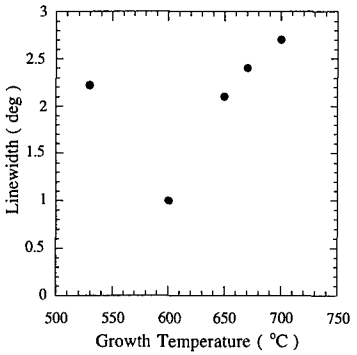

Figure 2. Dependence of the linewidth of the (200) GaN x-ray diffraction peak on the growth temperature.

Typical z(xx)z and z(xy)z Raman spectra from c-GaN films are shown in Figure 3. Co-polarized Raman spectra are characterized by a strong peak at 736 cm^{-1}, a small shoulder at 768 cm^{-1}, and a weak continuum extending from 700 cm^{-1} to 500 cm^{-1} with a second peak at 560 cm^{-1}. The shoulder at 768 cm^{-1}, the second peak at 560 cm^{-1}, and the continuum are shown more clearly in the cross-polarized spectrum, where the intensity of the 736 cm^{-1} feature is reduced by a factor of three. These results are consistent with previous work on cubic GaN [16] and sharply contrast recent Raman results from wurtzitic GaN films [4]. The peaks at 736 cm^{-1} and 560 cm^{-1} are consistent with cubic LO and TO phonon energies; the peak at 768 cm^{-1} is assumed to be defect-related, although it is close in energy to quoted wurtzitic LO phonon

energies [12]. There are two contributions to the background continuum, one arising from second order Raman scattering from GaAs in the 600 cm^{-1} region, the other from disorder-activated first order Raman scattering from GaN [18]. A disorder-activated contribution to the Raman spectrum is consistent with x-ray diffraction results; the width of the GaN diffraction peak is also indicative of disorder in the material.

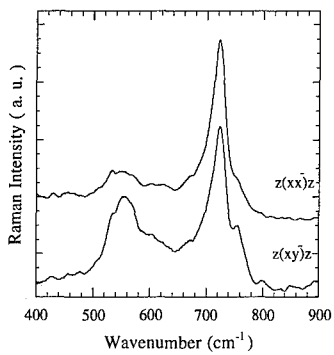

Figure 3. Co- and cross-polarized Raman spectra from a GaN film grown on (100) GaAs.

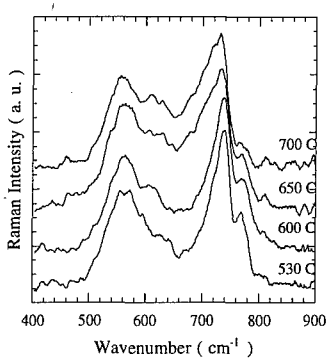

Figure 4. Cross-polarized Raman spectra from GaN films grown at different temperatures.

Figure 4 shows the temperature dependence of the cross-polarized Raman signal. The intensity of the 768 cm^{-1} peak decreased strongly as the growth temperature was increased, while the 736 cm^{-1} feature broadened and shifted to lower energy. The strength of symmetry forbidden transitions from the GaAs substrate also increased with the growth temperature, indicating increased interfacial disorder at higher growth temperatures.

The polarization dependence of scattering from c-GaN LO phonon modes GaN at 736 cm^{-1} and GaAs modes at 292 cm^{-1} are plotted in Figure 5. In this experiment, the incident polarization was rotated while the detector polarization remained fixed; the sample was oriented such that the (100) crystallographic direction is along the x-direction. The disorder-induced TO phonon mode from the GaAs substrate at 270 cm^{-1} and the 560 cm^{-1} and 768 cm^{-1} modes from the GaN showed no polarization dependence. The LO phonon modes from GaAs and cubic GaN show similar polarization dependence, and agree well with theoretical predictions [19]. In a second experiment, the incident and scattered polarizations were kept fixed, while the sample was rotated 180° in the plane of polarization of the incident and scattered light. Co-polarized results are shown in Figure 6; cross-polarized results are similar. These data are reflect a distribution in the orientation of grains with respect to the GaAs substrate. The polarization-

dependent Raman data are consistent with recent TEM results of GaN films grown on (100) GaAs [17, 20].

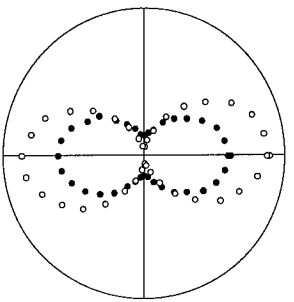

Figure 5. Polarization dependence of the GaN and GaAs LO phonon intensity as the incident polarization is rotated. $\theta = 0$ corresponds to the co-polarized signal for the GaAs aligned along a (100) direction.

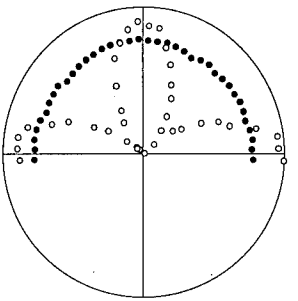

Figure 6. Polarization dependence of the co-polarized GaN and GaAs LO phonon intensity as the sample is rotated. $\theta = 0$ corresponds to (100)-oriented GaAs.

In summary, we have observed an X-ray diffraction peak at 39.8 degrees corresponding to a cubic GaN (200) reflection and a lattice constant of 4.52 Å in thin films grown on (100) GaAs. A 1° minimum in the linewidth of the x-ray diffraction peak was observed for a growth temperature of 600 °C, reflecting the high quality of the material. Unpolarized Raman features from c-GaN were seen at 560 cm^{-1} and 768 cm^{-1}. A strong polarization-dependent Raman peak associated with the LO phonon was observed at 736 cm^{-1}. An unpolarized continuum reflecting the phonon density of states in the region between 500-700 cm^{-1} was also observed and attributed to a combination of second-order scattering from the GaAs substrate and disorder-induced scattering from the GaN.

ACKNOWLEDGEMENTS: The author's acknowledge helpful discussions with R. Merlin, C. Taylor, and R. Clarke. S. Brown acknowledges partial support by the NSF Center for Ultrafast Optical Science (STC PHY 8920108). This work is supported by ONR Contract No. N00014-92-J-1552.

REFERENCES:

[1] T. Sasaki and S. Zembutsu, J. Appl. Phys. **61**, 2533 (1987).

[2] H. Amano, I. Akasaki, K. Hiramatsu, N. Koide, and N. Sawaki, Thin Solid Films **163**, 415 (1988).

[3] C. R. Eddy, T. D. Moustakas, and J. Scanlon, J. Appl. Phys. **73**, 448 (1993).

[4] C.-J. Sun and M. Razeghi, Appl. Phys. Lett. **63**, 973 (1993).

[5] T. Lei, M. Fanciulli, R. J. Molnar, T. D. Moustakas, R. J. Graham, and J. Scanlon, Appl. Phys. Lett. **59**, 944 (1991).

[6] D. Pavlidis, J. Singh, C.-H. Hong, and K. Wang, ONR Progress Report N00014-92-J-1552 (1993).

[7] T. D. Moustakas, T. Lei, and R. J. Molnar, Physica B **185**, 36 (1993).

[8] S. Strite, J. Ruan, Z. Li, A. Salvador, H. Chen, D.J. Smith, W. J. Choyke, and H. Morkoç, J. Vac. Sci. Technol. B **9**, 1924 (1991).

[9] S. Miyoshi, K. Onabe, N. Ohkouchi, H. Yaguchi, R. Ito, S. Fukatsu, and Y. Shiraki, J. Crystal Growth **124**, 439 (1992).

[10] R. F. Davis, Proc. IEEE **79**, 702 (1991).

[11] S. Strite and H. Morkoç, J. Vac. Sci. Technol. B **10** , 1237 (1992).

[12] D. D. Manchon, Jr., A. S. Barker, Jr., P. J. Dean, and R. B. Zetterstrom, Solid State Comm. **8**, 1227 (1970).

[13] V. Lemos, C. A. Arguello, and R. C. Leite, Solid State Comm. **11**, 1351 (1972).

[14] A. Cingolani, M. Ferrara, M. Lugara, and G. Scamarcio, Solid State Commun. **58**, 823 (1986).

[15] T. P. Humphreys, C. A. Sukow, R. J. Nemanich, J. B. Posthill, R. A. Rudder, S. V. Hattangady, and R. J. Markunas, Mat. Res. Soc. Symp. Proc. **162**, 531 (1990).

[16] S. Murugkar, R. Merlin, T. Lei, and T. D. Moustakas, Abstract from the American Physical Society Meeting, March 1992.

[17] C.-H. Hong and D. Pavlidis, Private Communication, submitted for publication.

[18] R. Carles, A. Zwick, M. A. Renucci, and J. B. Renucci, Solid State Comm. **41**, 557 (1982).

[19] J. B. Hopkins and L. A. Farrow, J. Appl. Phys. **59**, 1103 (1986). K. Mizoguchi and S. Nakashima, J. Appl. Phys. **65**, 2583 (1989).

[20] N. Kuwano, Y. Nagatomo, K. Kobayashi, K. Oki, S. Miyoshi, H. Yaguchi, K. Onabe, and Y. Shiraki, Jpn. J. Appl. Phys. **33**, 18 (1994).

BUFFER LAYER THICKNESS AND THE PROPERTIES OF InN THIN FILMS ON AlN-SEEDED (00.1) SAPPHIRE AND (111) SILICON

T. J. KISTENMACHER, S. A. ECELBERGER AND W. A. BRYDEN
Milton S. Eisenhower Research Center, Applied Physics Laboratory
The Johns Hopkins University, Laurel, Maryland 20723-6099

ABSTRACT

Introduction of a buffer layer to facilitate heteroepitaxy in thin films of the Group IIIA nitrides has had a tremendous impact on growth morphology and electrical transport. While AlN- and self-seeded growth of GaN has captured the majority of attention, the use of AlN-buffered substrates for InN thin films has also had considerable success. Herein, the properties of InN thin films grown by reactive magnetron sputtering on AlN-buffered (00.1) sapphire and (111) silicon are presented and, in particular, the evolution of the structural and electrical transport properties as a function of buffer layer sputter time (corresponding to thicknesses from ~50Å to ~0.64μm) described. Pertinent results include: (a) for the InN overlayer, structural coherence and homogeneous strain normal to the (00.1) growth plane are highly dependent on the thickness of the AlN-buffer layer; (b) the homogeneous strain in the AlN-buffer layer is virtually nonexistent from a thickness of 200Å (where a significant X-ray intensity for (00.2)AlN is observed); and (c) the n-type electrical mobility for films on AlN-nucleated (00.1) sapphire is independent of AlN-buffer layer thickness, owing to divergent variations in carrier concentration and film resistivity. These effects are in the main interpreted as arising from a competition between the lattice mismatch of the InN overlayer with the substrate and with the AlN-buffer layer.

INTRODUCTION

The heteroepitaxial growth of thin films of the Group IIIA nitrides (AlN, GaN, and InN) has come under extensive study [1] owing to their potential micro- and opto-electronic applications. For many studies, (00.1) sapphire has been the substrate of choice because of its device oriented optical and dielectric properties. However, a generally large lattice mismatch leads to a low density of nucleation sites, three-dimensional island growth, and thin films composed of a mosaic of columnar grains exhibiting low-angle grain boundaries. Much recent effort has focussed on the predeposition of a nucleation layer, and the earliest study of growth of a Group IIIA nitride thin film on a modified substrate was that by Yoshida [2] on reactive molecular beam epitaxy of GaN on AlN-coated (00.1) sapphire. More recently, Amano and Akasaki have grown smooth, high mobility films of GaN on AlN-nucleated (00.1) sapphire using metal-organic vapor phase epitaxy [3] and fabricated the first GaN p-n junction diode. [4] Additionally, Nakamura [5] and Wickenden [6] have shown that self-nucleated GaN films on (00.1) sapphire display similarly enhanced structural and electrical properties.

In parallel, growth by reactive magnetron sputtering of InN thin films on AlN-nucleated (00.1) sapphire, see Figure 1, has also yielded [7] enhanced structural coherence and electrical transport. Recently, these studies have been extended to include the deposition of InN onto AlN-nucleated (111) silicon, and in particular the effect of substrate bias was examined. [8] Herein, a comparison is given of the effect of buffer layer thickness on the structural and electrical properties of InN overlayers deposited onto AlN-nucleated (00.1) sapphire and (111) silicon substrates.

Mat. Res. Soc. Symp. Proc. Vol. 339. ©1994 Materials Research Society

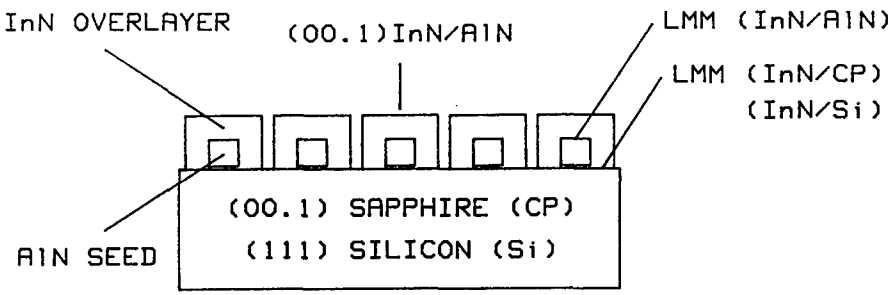

Figure 1. Schematic diagram of the overgrowth of InN onto AlN-seeded (00.1)CP or (111)Si. In each case, the (00.1) plane of InN lies parallel to the substrate surface.

EXPERIMENTAL

The reactive sputtering system employs planar magnetron sources mounted in the sputter-up configuration. The targets were high-purity Al or In disks and growth was carried out in pure N_2 gas at a pressure of 5mTorr. In a typical deposition sequence, chemically-polished (00.1) sapphire [(00.1)CP, nominal resistivity of $>10^{16}$ Ω-cm] and (111) silicon [(111)Si, nominal resistivity of 5 milli-Ω-cm] substrates were cleaned and loaded into the deposition chamber and subsequently heated to 900°C in vacuo. The temperature was then reduced to 600°C and the AlN layer was dc sputtered (150W; 15min presputter; sputter time from 2min to 4hr; buffer layer thickness from ~50Å to 0.64μm). Subsequently, the AlN-seeded substrates were cooled to the film growth temperature (400°C) and an InN overlayer deposited for 1hr (rf, 50W; 30min presputter; substrate bias -90V). The clear, reddish-brown films were examined in reflection using a Read X-ray camera [V-filtered CrKα radiation] and a Phillips APD powder diffractometer [graphite-monochromated CuKα radiation] and in transmission employing a Buerger precession X-ray camera [Zr-filtered MoKα radiation]. Room-temperature electrical resistivity and Hall effect (in a magnetic field of 0.5T) were measured using the van der Pauw technique. Film thickness was determined using a stylus profilometer.

RESULTS AND DISCUSSION

The variation in total bilayer film thickness with AlN seed layer sputter time is presented in Figure 2. Previous independent measurements on AlN and InN films on both (00.1)CP and (111)Si substrates demonstrated a linear relationship between film thickness and deposition time. Utilizing these independent data to obtain growth rates (approximately 25Å/min for AlN films and 100Å/min for InN films), bilayer film thicknesses as a sum of each estimated layer thickness have been computed and are shown as dotted lines in Figure 2, to guide an explanation of the data. It is first noted that parallel

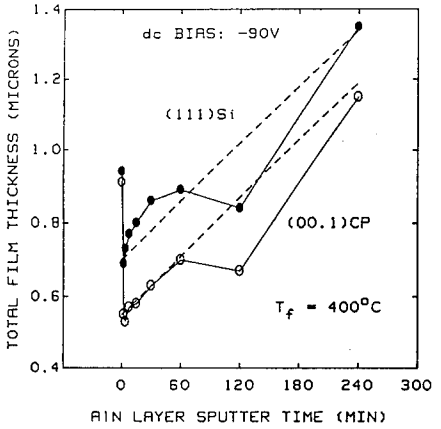

Figure 2. Dependence of film thickness on growth time of the AlN buffer layer.

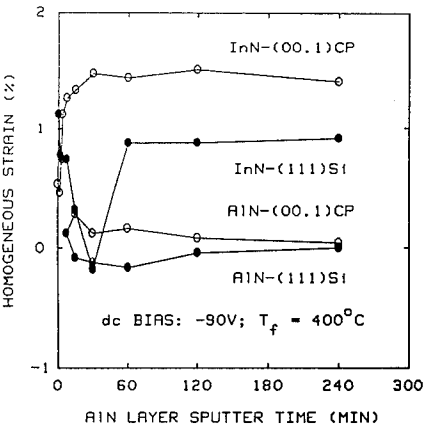

Figure 3. Variation in homogeneous strain with growth time of the AlN buffer layer.

experimental trends are observed for deposition onto both substrates. Secondly, there is in each case a sharp reduction in film thickness (due to in-plane densification) even at the thinnest AlN-nucleation layer (estimated at 50Å). At intermediate AlN layer sputter times (up to one hour; approximately 1600Å), deposition onto (00.1)CP well matches the linear dependence based on the simple addition of layer thicknesses. The match is obviously less robust for growth on (111)Si. There remains, however, a monotonic increase in total film thickness for deposition onto (111)Si for growth times for the AlN buffer layer up to 60min. Finally, there is a rather sharp drop from the projected total film thickness at a sputter time of 2hr (~0.32μm) and a return to projection at a sputter time of 4hr (~0.64μm). No simple explanation for this anomalous behavior at larger AlN buffer layer thicknesses has been advanced at this time. Whatever the factors are that determine the observed thickness variation, these same factors are apparently significant in determining trends in the electrical transport properties, as will be exposed below.

Structurally, the films grown on (00.1)CP fall exclusively into one of two classes. In the absence of the AlN-nucleation layer, scattering from a roughly equal mixture of broadly heteroepitaxial [(00.1)InN//(00.1)CP; (10.0)InN//(11.0)CP] and textured [(00.1)InN//(00.1)CP, only] domains is observed. However, for AlN-nucleation layers with thicknesses from ~50Å to 0.64μm, the InN overlayers are nearly (~95%) completely composed of heteroepitaxial domains. The variation in structural quality is considerably more varied for growth on AlN-nucleated (111)Si. In the absence of an AlN-nucleation layer, the X-ray scattering is typical of a mixture of polycrystalline and textured [(00.1)InN//(111)Si] domains. With the deposition of a 50Å AlN-nucleation layer, the InN film becomes simply textured, and by a 100Å AlN-nucleation layer a considerable heteroepitaxy [(00.1]InN//(111)Si and (21.0)InN//(220)Si] component is achieved, although there is evidence in the X-ray precession photographs of a sizeable (3-4°) mosaic spread. The heteroepitaxial growth of InN overlayers on AlN-nucleated (111)Si improves modestly for layer thicknesses of 400Å and beyond. Although, a return to simple texture at an AlN-layer thickness of 0.64μm is observed.

The structural coherence and homogeneous strain parallel to the growth direction for these AlN/InN bilayer films have been estimated from conventional $\theta/2\theta$ X-ray

diffractometer scans. The derived homogeneous strain $[(d_{(00.2)}^{obs} - d_{(00.2)}^{bulk})/d_{(00.2)}^{bulk}]$ is shown in Figure 3 for both the AlN buffer layer and the InN overlayer. It is evident that the homogeneous strain for the AlN buffer layer (at least for thickness beyond about 200Å where the (00.2) reflection is well above background) is insignificant for either substrate and at any buffer layer thickness. As for the degree of heteroepitaxial volume, the homogeneous strain in the InN overlayer for growth on AlN-buffered (00.1)CP is immediately increased, even for an AlN-nucleation layer as thin as 50Å. This probably reflects the large discrepancy between the lattice mismatches for AlN (13%) and InN (29%) and (00.1) sapphire and the preference in this instance for homogeneous growth of InN on AlN seeds (lattice mismatch of 13%). Once again, however, the situation is more complex for growth of InN on AlN-nucleated (111)Si. In that case, the lattice mismatch between AlN and (111)Si is -19%, while that for InN and (111)Si is only -8% -- a value even smaller in magnitude that the lattice mismatch between AlN and InN. For the films on AlN-nucleated (111)Si, there is a gradual decrease in homogeneous strain for buffer layers up to about a 1000Å, beyond which there is sufficient coverage for the lattice mismatch to be dominated by the AlN buffer layer and for the homogeneous strain to approach that for growth on AlN-nucleated (00.1)CP.

To complete the structural discussion, the full-width at half maximum (FWHM) for the (00.2) reflections from the AlN-buffer layers and the InN overlayers are compared in in Figures 4 and 5 for both substrates. As shown in Figure 4, there is a smooth decrease

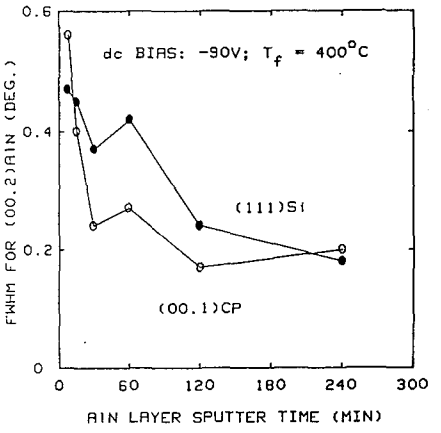

Figure 4. Dependence of FWHM (AlN buffer) on growth time of the AlN buffer layer.

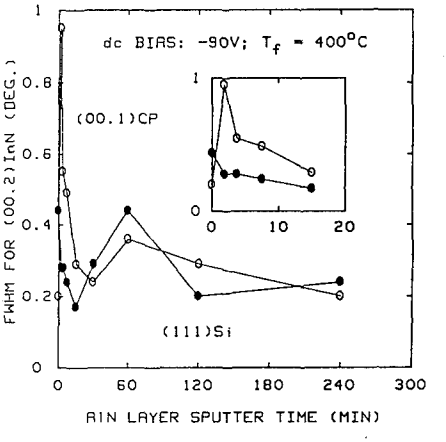

Figure 5. Variation in FWHM (InN film) with growth time of the AlN buffer layer.

in the width of the X-ray line as a function of increasing film thickness, and therefore it is expected that the linewidth is dominated by finite size effects for up to 2hrs of sputtering time (about 1600Å). In contrast, linewidths for the InN overlayer were anticipated to be considerably less dependent on crystallite size, as these overlayers have a thickness near 0.5-0.6μm over the series. Thus, the early results of Figure 5 are probably dominated by inhomogeneities owing to the competing lattice mismatches illustrated in Figure 1 and the emergence of films with mixtures of textured and heteroepitaxial domains.

Finally, the electrical properties of the InN films deposited on AlN-nucleated (00.1) sapphire substrates are presented in Figures 6 and 7. As can be seen, the Hall mobility

increases from ~0.1 cm^2/V-sec for deposition on native (00.1)CP to ~60 cm^2/V-sec immediately upon the deposition of a 50Å AlN-nucleation layer (and the achievement of heteroepitaxy), and then remains constant with nucleation layer thickness. Interestingly, this constant Hall mobility arises from divergent trends in the film resistivity and

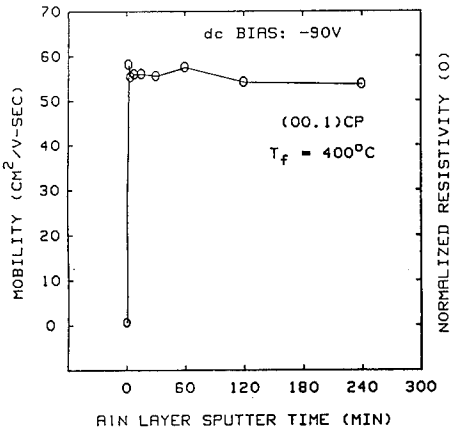

Figure 6. Dependence of the mobility (InN) on growth time of the AlN buffer layer.

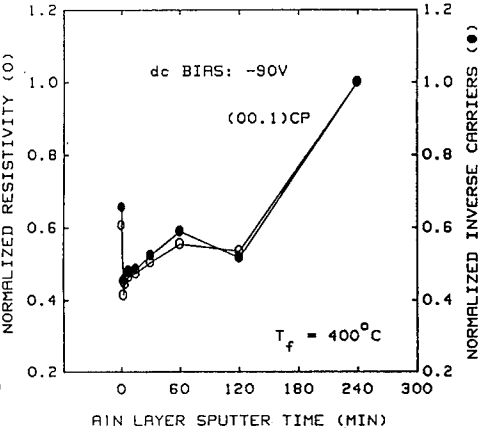

Figure 7. Variation in resistivity and inverse carriers on growth time of the AlN layer.

carrier concentration as seen in Figure 7. And it is particularly note worthy that the normalized trends shown in Figure 7 parallel those for the film thickness in Figure 2, suggesting that volume dependent effects, such as the number of grain boundaries, dominate the electron scattering cross section. In fact, it has been widely conjectured that the observed (often degraded) electrical transport found in oriented polygrained films (e. g., a dense matrix of grains with a random heteroepitxay, as for polycrystalline silicon [9] or diamond [10] films, or a common heteroepitaxy, as for the present films) has its origins in grain boundary effects such as charge-carrier trapping or scattering from localized defects. Finally, other factors expected to be of importance to the electrical properties of the present films are impurity band conduction or hopping conductivity, donor impurity compensation (especially from nitrogen atom defects) and surface trapping and scattering (possibly due to a generally higher surface oxygen content).

SUMMARY

In summary, a significant extension of the recently improved growth characteristics of GaN and InN overlayers on AlN-nucleated (00.1) sapphire has been achieved for the growth of InN by reactive magnetron sputtering on AlN-nucleated (111) silicon. Pertinent results include: (a) for the InN overlayer, structural coherence and homogeneous strain normal to the (00.1) growth plane are highly dependent on the thickness of the AlN-buffer layer; (b) the homogeneous strain in the AlN-buffer layer is virtually nonexistent; and (c) the n-type electrical mobility for films on AlN-nucleated (00.1) sapphire is independent of AlN-buffer layer thickness, owing to divergent variations in carrier concentration and film

resistivity. Characterization of the structural properties of AlN-nucleated InN overlayers indicates the very narrow range of parameters over which the growth is heteroepitaxial on (111) silicon compared to (00.1) sapphire. Bounding the limits for heteroepitaxial growth on (111) silicon is a crucial first step on the path to device arrays capable of incorporating both sources or detectors and processing elements.

ACKNOWLEDGMENTS

This work was supported by the U. S. Department of the Navy under Contract N00039-91-C-0001. We are indebted to Professor C. L. Chien for diffractometer time to undertake some of the X-ray scattering experiments.

REFERENCES

1. For recent thin film results, see: R. C. Powell, N.-E. Lee, and J. E. Greene, Appl. Phys. Lett. **60**, 2505 (1992); J. S. Foresi and T. D. Moustakas, Appl. Phys. Lett. **62**, 2859 (1993); C. R. Abernathy, J. Vac. Sci. Tech. A **11**, 869 (1993); W. J. Meng, J. A. Sell, T. A. Perry, and G. L. Eesley, J. Vac. Sci. Tech. A **11**, 1377 (1993); S. Nakamura, M. Senoh, and T. Mukai, Appl. Phys. Lett. **62**, 2390 (1993); M. E. Lin, B. Sverdlov, G. L. Zhou, and H. Morkoc, Appl. Phys. Lett. **62**, 3479 (1993); M. A. Khan, A. Bhattarai, J. N. Kuznia, and D. T. Olsen, Appl. Phys. Lett. **63**, 1214 (1993); C. Wang and R. F. Davis, Appl. Phys. Lett. **63**, 990 (1993); H. Amano, N. Watanabe, N. Koide, and I. Akasaki, Jpn. J. Appl. Phys. **32**, L1000 (1993); W. P. Lin, P. M. Lundquist, G. K. Wong, E. P. Rippert, and J. B. Ketterson, Appl. Phys. Lett. **63**, 2875 (1993); Y. Bu, L. Ma, and M. C. Lin. J. Vac. Sci. Tech. A **11**, 2931 (1993); J. Miragliotta, D. K. Wickenden, W. A. Bryden, and T. J. Kistenmacher, J. Opt. Soc. Am. B **10**, 1447 (1993); M. Rubin, N. Newman, J. S. Chan, T. C. Fu, and J. T. Ross, Appl. Phys. Lett. **64**, 64 (1994).
2. S. Yoshida, S. Misawa, and S. Gonda, Appl. Phys. Lett. **42**, 427 (1983).
3. H. Amano, N. Sawaki, I. Akasaki, and Y. Toyoda, Appl. Phys. Lett. **48**, 415 (1988).
4. H. Amano, M. Kito, K. Hiramatsu, and I. Akasaki, Jpn. J. Appl. Phys. **28**, L2112 (1989).
5. S. Nakamura, T. Mukai, and M. Senoh, J. Appl. Phys. **71**, 5543 (1992).
6. D. K. Wickenden, T. J. Kistenmacher, W. A. Bryden, J. S. Morgan, and A. E. Wickenden, Proc. Mater. Res. Soc. **221**, 167 (1991).
7. T. J. Kistenmacher, S. A. Ecelberger, and W. A. Bryden, J. Appl. Phys. **74**, 1684 (1993).
8. T. J. Kistenmacher and W. A. Bryden, Appl. Phys. Lett. **62**, 1221 (1993).
9. See, for example: T. I. Kamine, J. Appl. Phys. **42**, 4357 (1971); J. Y. W. Seto, J. Appl. Phys. **46**, 5247 (1975).
10. D. M. Malta, J. A. von Windheim, and B. A. Fox, Appl. Phys. Lett. **62**, 2926 (1993).

DEPOSITION AND CHARACTERIZATION OF CNx FILMS

X.T. CUI, Z.H. ZHANG, Q.Y. CHEN, F. ROMERO-BORJA, J.R. LIU, Z.S. ZHENG, D.W. PAN, L.T. WOOD AND W.K. CHU
Department of Physics and Texas Center for Superconductivity at University of Houston, Houston, TX 77204-5932, USA

ABSTRACT

CNx films with x around 1.0 have been made by inverted cylindrical DC magnetron sputtering. RBS, XPS, IR spectroscopy, ERD and SEM were used to characterize the composition and bonding properties of the films, while X-ray diffraction was used for crystal structure determination. XPS data indicated the existence of the tetrahedral C_3N_4 phase in the CNx films, which was consistent with the C-N single bond suggested by IR spectra. The annealing effect on CNx films will also be discussed.

INTRODUCTION

Solid carbon nitride was first predicted by Liu and Cohen[1] to have some extraordinary mechanical and thermal properties comparable to diamond. Due to this prediction, several research groups have tried to grow carbon nitride thin films [2-9] over the past few years. The amorphous carbon nitride thin films made by conventional DC or RF magnetron sputtering reportedly have nitrogen content ranging from 0 to 40 at% [2-4]. We have increased the nitrogen content in the CNx films up to or even above 50% (x>1) using an inverted cylindrical DC magnetron sputtering system with He-N_2 mixed gas and a graphite target. In this paper, we report the deposition and characterization of these CNx films by Rutherford backscattering spectrometry (RBS), X-ray photoemission spectroscopy (XPS), Infra-red spectroscopy, SEM and X-ray diffraction (XRD). We also discuss the composition changes of the CNx film after annealing.

EXPERIMENTAL

CNx films were made by an inverted hollow cylindrical magnetron sputtering system (Fig. 1). The advantage of this system is that the substrate is outside the plasma, thus reduces the re-sputtering. A high purity graphite (99.999%) ring target was sputtered in a gas mixture of high purity nitrogen (99.999%) and helium (99.995%). The total gas pressure was kept around 240mTorr while the nitrogen content varied from 5% to 100% of the total pressure. A bias voltage ranging from -50 volts to -250 volts was applied to the substrate to increase the particle mobility on the substrate surface. The substrate holder was fixed and kept at ambient temperature. Substrates used were single and double-side polished Si(100) wafers, Zr, Corning 2947 glass and Si_3N_4 films. Double-side polished Si(100) wafers were used for IR absorption studies. Substrates other than silicon wafers were used to investigate the adhesive properties of the CNx films. In our experiment, we did not observe significant difference in the adhesion of CNx films to different substrates.

Atomic compositions were measured by 3.3 to 3.5 Mev He RBS. Chemical bonding information was measured by XPS and IR absorption. The thickness was measured by an α-stepper machine. The thicknesses of most films were around 1μm. The surface morphology of the films were examined by SEM. Elastic Recoil Detection (ERD) technique was used to measure the hydrogen content in the films.

RESULTS AND DISCUSSION

Mat. Res. Soc. Symp. Proc. Vol. 339. ©1994 Materials Research Society

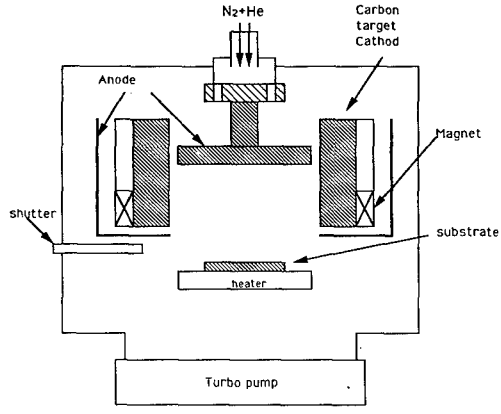

Figure 1: Schematic of the Inverted Cylindrical DC Magnetron Sputtering system

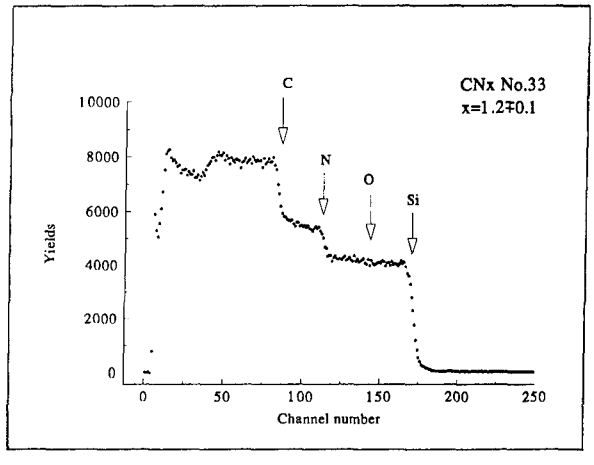

Figure 2: 3.5 MeV He^{+2} elastic scattering spectrum of CNx film deposited on a Si wafer. The thickness of the film is 1 μm. Plasma power is 9W and total pressure is 200 mTorr(N_2: 93%, He:7%). Bias: -90V.

Fig.2 shows the RBS spectrum of an CNx film deposited on Si wafer. RBS measurements were conducted on a NEC Model 5SDH-2 tandem accelerator. Non-Rutherford elastic scattering

with He ions of 3.3 to 3.5 Mev energy were employed to increase the sensitivity for the nitrogen, oxygen and carbon measurements. The measured nitrogen content was above 50% in CNx film (x>1.0) and oxygen content was below 7%. The nitrogen content in our films is higher than those reported made with conventional sputtering system. We have also observed hydrogen in the films up to several percent by Elastic Recoil Detection method (ERD). The oxygen and hydrogen contamination were suspected to come from the target rather than from residual molecules in the vacuum chamber with a base pressure of $6x10^{-6}$ torr. Fig.3 shows the nitrogen and carbon composition ratio of CNx films as a function of nitrogen partial pressure of the sputtering N_2-He gas mixture. As the sputtering yield of carbon by He ions was very low, only energetic nitrogen particles could effectively sputter carbon away from the target. This may be part of reason why, although the deposition rate increased slightly, the N/C ratio of the films was not sensitive to the increasing N_2 partial pressure.

XPS measurements were carried out *ex situ* in a Perkin-Elmer Model 550 using Mg Kα X-rays at 0.5 eV spectrometer resolution. Typical C1s and N1s XPS lines are shown in Fig. 4 for a carbon nitride film. Based on a study by D. Marton et al. [10], these two lines can be deconvoluted into four distinguishable peaks for carbon and three peaks for nitrogen. Such analysis has been conducted on a batch of CNx films [10] in which consistent chemical shifts that indicated the presence of tetrahedral type C-N coordination were observed. Carbon XPS peaks at 286.4eV and 287.8eV have been curve-fitted and identified as two different binding states between carbon and nitrogen. Correspondingly, there are two nitrogen peaks at 399.7eV and 398.6eV for these two binding states. Such binding energy assignments, following Ref [10], were based on the XPS data from well-studied compounds, pyridine and urotropine (hexamethylene-tetramine). Pyridine consists of a planar sp^2 hybrid orbital π-bonded aromatic ring with one nitrogen, which shows C1s at 285.5eV and N1s at 399.8eV. On the other hand, urotropine contains nitrogen and carbon atoms arranged in close resemblance to the predicted β-C_3N_4 structure, with the C1s peak at 286.9eV and N1s at 399.4eV. These chemical shifts suggest the more polar nature of the tetrahedral type aromatic arrangements. For the C_3N_4 phase, the extent of chemical shifts should be even larger. Because the nitrogen atoms for C_3N_4 are in trigonal sites and thus the 1s electrons should be better shielded than the urotropine case in which the nitrogen atoms are in the tetrahedral sites. It is thus reasonable to assert that the peaks at 287.8eV (C1s) and 398.6 eV (N1s) arise from the tetrahedral C_3N_4 structure. Meanwhile, the

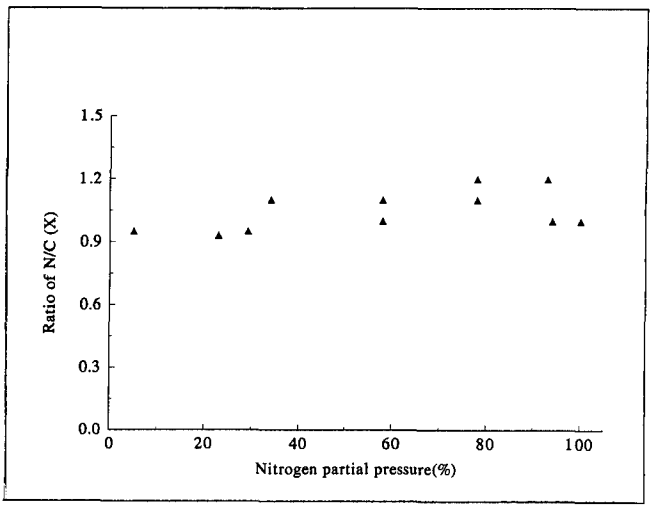

Figure 3: Changes of the N/C ratio with nitrogen partial pressure in sputtering processes. Plasma power and total pressure may not be the same.

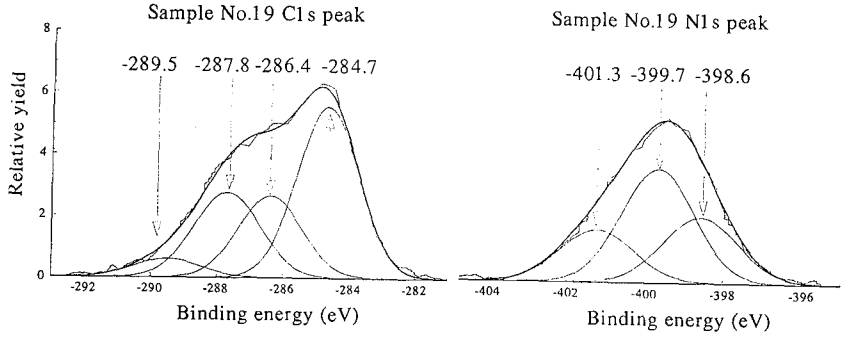

Figure 4: Nitrogen and carbon 1s XPS spectra. The intensity scales for the N and C spectra are not the same.

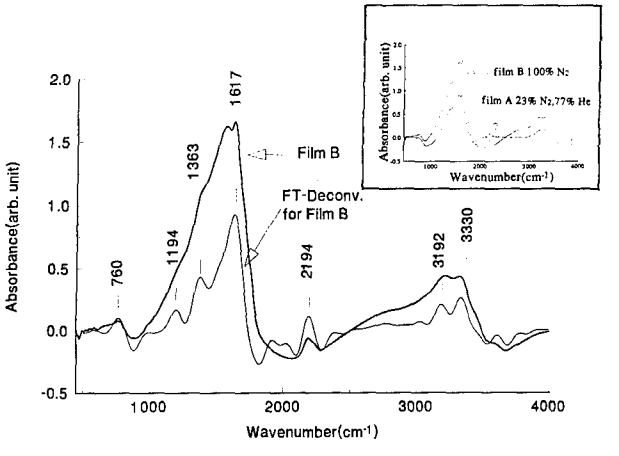

Figure 5: Infrared absorption spectra of CNx films deposited under different nitrogen partial pressures. For one of the films, the FT-deconvoluted spectrum is also shown. On the top right are the IR absorption spectra of films A and B as obtained.

peaks at 286.4eV for C1s and 399.7eV for N1s represent the sp^2 type bonding for the regions where the nitrogen content is low. While more evidences would be helpful in drawing a more definite conclusion, the possibility of existing C_3N_4 structure can not be ruled out. Based on the integrated intensity of the associated C1s and N1s peaks, the percentage for the tetrahedral C_3N_4 in the film was estimated to be 30 at%.

Infrared absorbance spectra were obtained for two CNx thin film samples on thin double-side polished silicon wafers. The FTIR spectrometer used was a Bomem DA8 equipped with a MCT detector and a KBr beam splitter. The low spectral resolution of $16cm^{-1}$ was selected for the measurement in order to minimize interference effects in the spectrum (due to the thin silicon substrate), but it is still good enough to resolve spectral features common in this type of solid material. Two films for IR measurements were produced with different concentrations of N_2/He gas mixture. The mixture partial pressure for film A was: 23% N_2 and 77% He, and, for film B: 100% nitrogen and no helium. Figure 5 shows the absorption spectra for the films as obtained in the spectral range from 500 to $4000cm^{-1}$ (20 to 2.5μm). Also shown is a FFT deconvoluted spectrum using a Bessel apodization filter. This operation helped us identify the principal bands comprising a more complex band with overlapping features. In figure 5, it is easy to observe the effect that different nitrogen partial pressures have on the infrared absorbance. As discussed in references [4] and [11], the complex spectral feature around $1600cm^{-1}$ grows with increasing N_2 concentration and can be related to the Raman active G ($1588cm^{-1}$) and D ($1360cm^{-1}$) bands; stretching vibrations from C=C and C=N occur, in this fingerprinting region as well. The relatively narrow band observed in the $2190cm^{-1}$ region has been identified [11,12] with the stretching vibrations of the groups C-N, C-C triple bonds or N=C=O bond. The band centered at $760cm^{-1}$ has only been mentioned in reference [11] as a bending mode for the graphitelike domains after nitrogen incorporation. Alternative assignments for this band are the out-of-plane bending mode for C-H or the stretching vibration modes for C-C or C-N. The bands observable after deconvolution at the frequencies 1000 and 1190 cm^{-1} are characteristic for phenyl C-H deformations. Finally, the bands in the 3200-3300 cm^{-1} region have been typically observed in carbon nitride samples prepared from hydrocarbons and correspond to stretching vibrations of C-H and N-H. Since the samples analyzed in this paper were neither prepared from hydrocarbons

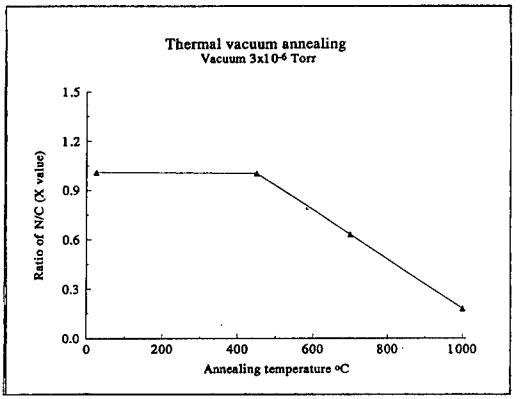

Figure 6: Changes of the N/C ratio with annealing temperatures

nor intentionally hydrogenated during preparation, a possible explanation for the appearance of these bands in the absorbance spectra would be potential contamination of the samples and/or substrate, as could be presumed from the ERD measurements .

We have annealed some samples from 450°C to 1000°C in vacuum. Nitrogen content consistently decreased with the increasing annealing temperature, as shown in Fig.6. The thickness of the films decreased too. After 1000°C high temperature vacuum annealing for 30 minutes, the nitrogen content or x decreased from 1.0 to 0.2, in agreement with a previous report [13].

As far as the microstructures of the films are concerned, we have observed some small particles in the CNx films by SEM. The particle sizes were around 0.4 to 1 μm for a 2 μm thick film. While more measurements are being conducted using electron diffraction to determine their crystal structures, it is reasonable to conjecture that, based on the X-ray diffraction data, most of the film was amorphous CNx matrixs with crystalline C_3N_4 inclusion, supportive of what was reported in reference [5].

CONCLUSION

Our results show that CNx films, with nitrogen content higher than 50%, can be obtained by reactive sputtering deposition using an inverted cylindrical DC magnetron sputtering system. XPS study suggested that a part of the nitrogen in the CNx films was bonded with carbon to form tetrahedral C_3N_4 phase. The CNx films studied here were not stable at elevated temperatures, as the nitrogen content decreased upon heating.

ACKNOWLEDGEMENTS

This work was supported in part by ARPA through ONR under contract number MDA972-90-J-001 and by the State of Texas through the Texas Center for Superconductivity at the University of Houston. The authors would like to thank Dr. D. Marton for the XPS measurements and Mr. X.Y. Li for X-ray diffraction measurements.

REFERENCES

1. A.Y. Liu and M.L. Cohen, Phys. Rev. B. **41**,10727(1990-II).
2. M.Y. Chen, D.Li, X. Lin, V.P. Dravid, Y.W. Chung, M.S. Wong and W.D.Sproul, J.Vac.Sci. Technol. A **11**, 521(1993).
3. He-Xiang Han and Bernard J. Feldman, Solid State Commun. **65**,921(1988).
4. J.H. Kaufman, S. Metin and D. D. Saperstein, Phys. Rev.B,**39**(1989)13053.
5. Kin Man Yu, M.L. Cohen, B.E. Haller, W.L. Hansen, Amy Y. Liu and I.C. Wu,Phys. Rev. B. **49**,5034(1994)
6. F. Fujimoto and K. Ogata, Jpn. J. Appl. Phys. **32**,L420 (1993)
7. J.F.D. Chubaci, T. Sakai, T. Yamamoto, K. Ogata, A. Ebe. F. Fujimoto, Nucl. Instr. Methods, B **80/81**, 463 (1993)
8. C. Niu,Y.Z. Lu and C.M. Lieber, Science **261**,334 (1993).
9. Michael R. Wixom, J. Am. Ceram. Soc. **73**(7), 1973 (1990).
10. D. Marton, K.J. Boyd, A.H. Al-Bayati, S.S. Todorov and J.W. Rabalais, submitted to Phys. Rev. Letter (1994).
11. N.Nakayama, Y.Tsuchiya, S. Tamada, K. Kosuge, S.Nagata, K.Takahiro and S.Yamaguchi, Jap. J. Appl. Phys. II (1994)L1465
12. M.Y. Chen, X. Lin, V.P. Dravid, Y.W. Chung, M.S. Wong and W.D.Sproul, Surf. Coat. Tech. **54/55**(1992)360
13. J.J. Cuomo and W. Reuter, IBM Tech. Discl. Bull. Vol.**19**,No.2, p.742(1976).

PART VIII

Doping, Impurities and Properties

NMR SPIN LATTICE RELAXATION IN NITROGEN-DOPED 6H SILICON CARBIDE

J. STEPHEN HARTMAN, ARJUN NARAYANAN AND YOUXIANG WANG
Department of Chemistry, Brock University, St. Catharines, Ontario L2S 3A1, Canada

ABSTRACT

Nuclear magnetic resonance (NMR) spin lattice relaxation is highly sensitive to the nature, amount, and homogeneity of unpaired-electron-containing impurities in silicon carbide and similar solids, and is a promising tool for the study of dopants and impurities. In nitrogen-doped 6H silicon carbide, ^{13}C and ^{29}Si NMR spin lattice relaxation is highly site-dependent. Not only do carbon sites relax much more rapidly than the corresponding silicon sites, but also there are unprecedented differences in relaxation efficiency among the different carbon (and silicon) sites, consistent with much higher unpaired electron density at the higher-symmetry (Types A and B) sites than at the lowest-symmetry (Type C) site. In contrast, all sites relax at equivalent rates in undoped samples and in commercial abrasive grade material with high levels of impurities, although there are large differences in relaxation efficiency among samples. The change in the nature of the relaxation process, from exponential in high-purity to stretched exponential in lower-purity samples, is apparently related to changes in unpaired-electron mobility.

INTRODUCTION

Nuclear magnetic resonance (NMR) spectroscopy has recently become an important technique in materials research, and is used for the characterization of a wide range of inorganic materials.[1] There are many NMR-active nuclei, each with its own chemical shift range, and the technique is applicable to both crystalline and amorphous species. Using the technique of Magic Angle Spinning to increase resolution, even very similar nuclear environments such as the crystallographically distinct sites of 6H silicon carbide give rise to well-separated NMR signals.[2] Thus 6H silicon carbide gives three equal-intensity ^{29}Si signals, one for each silicon site, and also three equal-intensity ^{13}C signals, one for each carbon site (each of which is isostructural to one of the silicon sites).[2] By single crystal NMR work we have been able to determine that the central peak in the ^{29}Si spectrum, but the low field peak in the ^{13}C spectrum, arises from the lowest-symmetry (Type C) site (Figure 1).[3]

NMR peak positions (chemical shifts) are not appreciably sensitive to dopant concentration. However dopants and impurities can have very large effects on spin lattice relaxation behaviour. Spin lattice relaxation involves the return of spin magnetization to thermal equilibrium after a disturbance (such as applying a train of radiofrequency pulses to destroy the

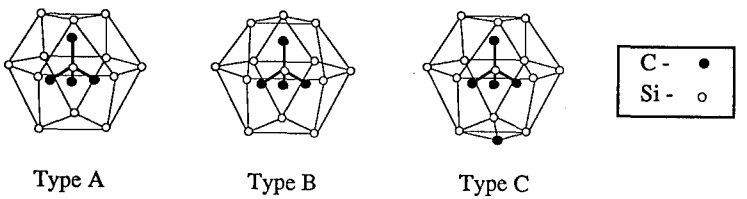

Figure 1. Local site designations for the first and second neighbour environments of the three types of silicon (and carbon). Type C has the lowest-symmetry second-neighbour shell.

Mat. Res. Soc. Symp. Proc. Vol. 339. ©1994 Materials Research Society

z-axis spin magnetization in the saturation-recovery experiment).[4] The recovery of z-axis spin magnetization is frequently (but not always) exponential:

$$[1] \qquad M_z(t) = M_z(\infty)[1 - e^{-t/T_1}]$$

where $M_Z(t)$ is the z-axis magnetization after time t, $M_Z(\infty)$ is the equilibrium z-axis magnetization, and T_1 is the spin lattice relaxation time. For dilute spin-1/2 nuclei in rigid solids such as silicon carbide, there is no intrinsic mechanism of spin lattice relaxation. Instead, interaction with the unpaired electrons of impurities is the dominant relaxation process. The resulting strong impurity dependence of spin lattice relaxation provides a promising approach to studying dopants and impurities. We now report our use of nitrogen-doped 6H silicon carbide as a model system to explore this approach. Further aspects of spin lattice relaxation in 6H silicon carbide will be reported elsewhere.[5]

EXPERIMENTAL PROCEDURES

Materials. Nitrogen-doped semiconductor grade 6H silicon carbide samples from Cree Research, Inc., with dopant levels determined by the capacitance-voltage technique, were used. Other impurities were reported to be at or below the 2 ppm level.

NMR Spectra. ^{29}Si and ^{13}C Magic Angle Spinning NMR spectra were obtained on powdered samples on Bruker AC-200 (4.7 T) and AM-500 (11.7 T) multinuclear Fourier transform NMR instruments. On the 4.7 T instrument, samples were spun at 3.0 - 3.6 kHz at an angle of 54°44' to the magnetic field. Spectra were obtained with 8K data points, frequencies of 39.76 MHz (^{29}Si) and 50.3 MHz (^{13}C) , and spectral widths between 10 and 50 KHz. The 90° pulse was close to 25 μs for both nuclei. On the 11.7 T instrument, a Doty high speed Magic Angle Spinning probe was used, with spinning speeds of up to 8 KHz. Spectra were obtained with 8K data points, a frequency of 99.3 MHz (^{29}Si) and 125.7 MHz (^{13}C) and spectral widths between 30 and 50 KHz. The 90° pulse width was close to 6 μs for both nuclei. Variations in spinning speed between 1 and 8 KHz had little effect on the efficiency of spin lattice relaxation.

The saturation recovery method, in which a train of pulses (progressive saturation sequence) saturates the nuclear magnetization, was used for determination of spin lattice relaxation behaviour. Because of very slow relaxation , only a single scan was obtained for each delay time τ whenever possible. Four scans were required to obtain usable ^{13}C spectra of even the best silicon carbide samples at 4.7 tesla. Less pure samples with broad and poorly resolved peaks required additional scans.

Fitting Procedures and Error Analysis. Spin lattice relaxation does not always follow the exponential rate law [1], but instead a stretched exponential expression may be necessary:

$$[2] \qquad M_z(t) = M_z(\infty)[1 - e^{-(t/T')^n}]$$

The time constant T′, and the exponent n indicating the degree of stretch of the stretched exponential decay function, were obtained from four parameter least squares fits. Because two parameters rather than one must be determined, data sets of at least 15 to 20 τ values were used whenever possible. A function of the form

$$[3] \qquad y = a - be^{-(\tau/T')^n}$$

was fitted to the data to estimate T′ and n, using a standard nonlinear least squares approach.[6] Despite good fits to the stretched exponential function, a problem with stretched exponential curve fitting is that the values of T′ and n are often correlated, with only a shallow minimum, so that there are often large errors in both. Because of this, only our best data sets give values

of n that are accurate to within ± 0.1, and values of T′ to within ±10%. Nevertheless many low-purity silicon carbide samples relax in a clearly stretched-exponential manner. Our error analysis work on stretched exponential spin lattice relaxation will be published elsewhere.

RESULTS AND DISCUSSION

Undoped high-purity 6H silicon carbide relaxes extremely inefficiently, with time constants T_1 of several hours, and it is very difficult to obtain the full relaxation curve. What is clear, however, is that all six sites (three ^{29}Si and three ^{13}C) have similar relaxation behaviour.

The situation is very different with nitrogen-doped samples. Spin-lattice relaxation is exponential and is essentially independent of magnetic field, but is highly dependent on both the nitrogen concentration and the individual site, with great differences even between different sites of the same nucleus in the same sample. Figure 2 shows saturation recovery ^{29}Si and ^{13}C NMR spectra of nitrogen-doped samples after different recovery times τ. The top spectra were obtained after allowing adequate time for full relaxation and all three peaks have equal intensities, corresponding to the equal populations of the sites. The middle and bottom spectra were obtained after much shorter recovery times. Total signal intensity is less, due to incomplete recovery of z-axis magnetization, but it is particularly noteworthy that in both the ^{29}Si and ^{13}C spectra one of the three signals is much less intense than the other two, indicating much less efficient spin lattice relaxation. In both cases the slow-relaxing signal is the one that we previously[3] assigned to the Type C site. Figure 3 shows a plot of signal intensity vs. saturation recovery delay time τ for each of the three ^{13}C peaks, from which T_1 values can be determined for each of the sites.

Table I gives ^{29}Si and ^{13}C spin lattice relaxation times T_1 for three nitrogen-doped samples with dopant concentrations differing by more than an order of magnitude. In each of the samples there is a consistent difference of a factor of about 20 between the T_1 values of the low-field ^{13}C peak and the other two ^{13}C peaks, and a factor of about 4 between the T_1 values of the middle ^{29}Si peak and the other two ^{29}Si peaks. Moreover, the slowest-relaxing ^{13}C peak has similar T_1 values to the fastest-relaxing ^{29}Si peaks, giving a factor of 80 overall between the relaxation efficiencies of the slowest-relaxing ^{29}Si and the fastest-relaxing ^{13}C sites. This must arise from large differences in conduction band unpaired electron densities at the sites.

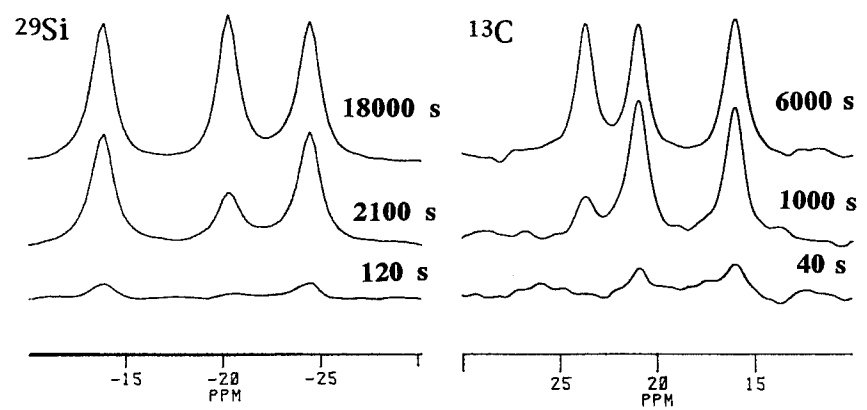

Figure 2. 11.7 Tesla ^{29}Si and ^{13}C Magic Angle Spinning NMR spectra of nitrogen-doped 6H silicon carbide samples, obtained by the saturation recovery method. Saturation recovery delay times τ are given. Spectra are calibrated in ppm to high frequency of tetramethylsilane.

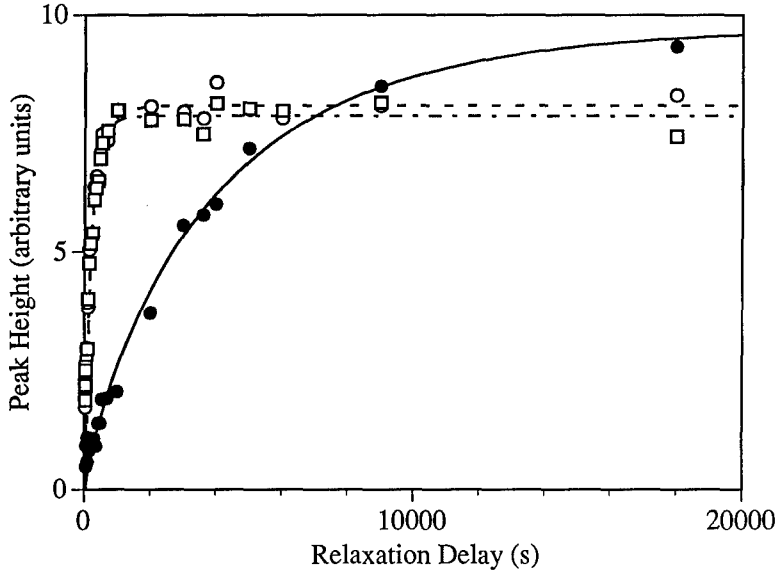

Figure 3. Plot of MAS NMR peak intensity vs. saturation recovery delay time t for the three ^{13}C peaks of a 6H silicon carbide sample doped with nitrogen at a level of 4.5 x 10^{17} atoms/cm^3. ●, 23 ppm peak; ○, 20 ppm peak; □, 15 ppm peak.

Table I Spin-Lattice Relaxation Parameters for N-Doped 6H SiC Samples.

	(a) 11.7 Tesla				**(b) 4.7 Tesla**			
		^{29}Si		^{13}C		^{29}Si		^{13}C
[N] atoms/cm^3	Peak at (ppm)	T_1 (s)	Peak at (ppm)	T_1 (s)	Peak at (ppm)	T_1 (s)	Peak at (ppm)	T_1 (s)
9.0 x 10^{16}	-14	12300	23	24800	-14	14700	23	18400
	-21	24700	20	1700	-21	28900	20	1700
	-25	12500	15	1800	-25	18100	15	1900
4.5 x 10^{17}	-14	3700	23	4000	-14	4500	23	4200
	-21	12200	20	220	-21	11800	20	250
	-25	3200	15	220	-25	4500	15	220
1.4 x 10^{18}	-14	1340	23	1400	-14	1400	23	1500
	-21	5600	20	80	-21	5000	20	90
	-25	1200	15	80	-25	1100	15	90

Charge density effects in silicon carbide have been calculated by Qteish, Heine, and Needs and used to rationalize the number of NMR peaks and the range of NMR chemical shifts observed in silicon carbide polytypes.[7] They find that the intrinsic dipole moments in any silicon carbide polytype except 3C lead to substantial electric fields, and these lead to variations in electrical potential at the different sites. They propose that mobile carriers would be sufficiently localized to take advantage of the differences in potential at different sites, and would therefore tend to occupy the sites of lowest potential. Our spin lattice relaxation work, indicating very different unpaired electron densities at different sites, supports their proposal.

Further evidence that the electronic environments about the different carbon sites must differ considerably comes from ESR work on nitrogen-doped 6H silicon carbide, showing that nitrogen donors in the hexagonal (h) carbon site have only about one-tenth the unpaired electron spin density of that of nitrogen donors in the two quasicubic sites.[8]

Lower-purity samples behave quite differently: (i) all sites, both ^{29}Si and ^{13}C, relax very similarly, and (ii) the relaxation process is no longer exponential but is stretched exponential (eq [2]), indicating a very different impurity-based relaxation mechanism. Stretched exponential processes are frequently encountered in disordered systems such as glasses,[9] and stretched exponential spin lattice relaxation is known in solid state NMR of rigid solids where relaxation is caused by fixed paramagnetic centres.[10] Some NMR-active nuclei are nearer than others to the fixed paramagntic centres and are more readily relaxed. In *e.g.* silicate minerals n normally takes the value of 0.5[10,11] (when n = 1, relaxation is exponential), but in silicon carbide we commonly obtain values intermediate between 0.5 and 1. This is consistent with competition between relaxation by mobile conduction band electrons (giving exponential relaxation) and fixed paramagnetic centres (giving stretched exponential relaxation).

Table II gives spin lattice relaxation parameters (including n, the "degree of stretch" of the stretched exponential) for high-impurity-level samples. Note that in abrasive grade samples, which contain a wide range of impurities, relaxation is very inefficient. It would appear that the numerous deep level defects capture electrons, thereby eliminating the mobility of conduction

Table II ^{29}Si Spin-Lattice Relaxation Parameters for Lower Purity 6H SiC Samples[a].

Sample	Peak at (ppm)	T′ (s)	n
B,Al,N-Doped	-14	100	0.71
	-20	110	0.70
	-24	120	0.73
Abrasive Grade (BGW43)	-14	4,600	0.6
	-20	4,600	0.9
	-24	4,400	0.5
American Matrix Platelets	-14	7,900	0.6
	-20	12,000	0.6
	-24	9,600	0.7
NBS 112b[b]	very slow - no reliable numbers		

[a] 4.7 Tesla; ^{13}C values where available are similar
[b] mixture of polytypes

band electrons and quenching the mechanism of spin lattice relaxation that is predominant in the semiconductor-grade samples.

CONCLUSIONS

The order-of-magnitude differences in relaxation efficiency at different sites in N-doped 6H silicon carbide, apparently arising from great differences in conduction band unpaired electron densities at the sites, illustrate the potential of NMR spin-lattice relaxation in studying local variations in conduction band structure. The shift from exponential to stretched-exponential relaxation behaviour in less pure samples, as localized paramagnetic sites take over from mobile electrons in relaxing the nuclei, suggests that NMR will have a role in the study of variations in electron mobility in semiconductors. Spin lattice relaxation experiments are time-consuming, especially for high-purity samples, because of extremely slow relaxation and the need for many data points in order to convincingly distinguish between exponential and stretched-exponential relaxation, so the method is unlikely to become routine. Nevertheless a wealth of information on electron density and mobility seems to be accessible.

ACKNOWLEDGEMENTS

We thank Prof. Mary Frances Richardson (Brock University) and Prof. Alex D. Bain (McMaster University) for helpful discussions, Prof. Robert. F. Davis (North Carolina State University) for helpful discussions and for providing samples, Mr. Tim Jones (Brock), Mr. Brian Sayer and Dr. Don Hughes (McMaster) for assistance with the instrumentation, our colleagues at Brock for allowing us to tie up large blocks of NMR instrument time, and the Natural Sciences and Engineering Research Council of Canada for financial support.

REFERENCES

1. H. Eckert, Prog. NMR Spectrosc. **24,** 159 (1992).
2. J. S. Hartman, M. F. Richardson, D. Guo, and B. G. Winsborrow, J. Am. Chem. Soc. **109,** 6059 (1987).
3. M. F. Richardson, J. S. Hartman, D. Guo, and B. G. Winsborrow, Chem. Mater. **4,** 318 (1992).
4. E. Fukushima and S.B.W. Roeder, Experimental Pulse NMR. A Nuts and Bolts Approach, (Addison-Wesley: Reading, MA. 1981), Chapter III.
5. J. S. Hartman, A. Narayanan, and Y. X. Wang, J. Am. Chem. Soc., in press.
6. W. H. Press, S. A. Teulosky, W. H. Vetterling, and B. P. Flannery, Numerical Recipies in C: The Art of Scientific Computing, 2nd ed. (Cambridge University Press, Cambridge, 1992), Chapter 15.
7. A. Qteish, V. Heine, and R. J. Needs, Physica B. Condensed Matter **185,** 366 (1993).
8. J. Schneider and K. Maier, Physica B, Condensed Matter **185,** 199 (1993), and references therein.
9. W. Siebrand and T. A. Wildman, Acc. Chem. Res. **19,** 128 (1986).
10. I. J. Lowe and D. Tse, Phys. Rev. **166,** 279 (1968); H. E. Rorschach, Jr., Physica **30,** 38 (1964).
11. J. S. Hartman and B. L. Sherriff, J. Phys. Chem. **95,** 7575 (1991).

IR–ABSORPTION SPECTRA OF IMPURITIES IN 6H–SiC

F. ENGELBRECHT AND R. HELBIG
Institute of Applied Physics, University of Erlangen-Nürnberg, Staudtstr. 7, 91058 Erlangen, Germany

ABSTRACT

We performed infrared absorption and reflectivity measurements on serveral 6H-SiC samples at variable temperatures between T=5K and T=300K. From the temperature dependence of the observed absorption lines we separated electronic from vibronic transitions. The electronic transitions are assumed to be due to transitions from the neutral nitrogen donor occupying the three different carbon lattice sites in 6H–SiC into excited states. We determined polarization and the oscillator strengths of these transitions. From the temperature dependence of the electronic transitions we determined the valley-orbit-splitting energy and we demonstrated the influence of compensation. For the different vibronic transitions we determined the Grüneisen constants.

INTRODUCTION

Infrared impurity excitation spectra in 6H–SiC were reported by several authors since the early seventies [1],[2]. However both the measured absorption spectra and their interpretation do not agree in some points. So additional information is necessary to identify the origin of the observed absorption lines (separation of electronic and vibronic transitions, determination of line symmetry). For this purpose we performed absorption and reflectivity measurements of different 6H–SiC samples at different temperatures between 200 cm^{-1} and 6000 cm^{-1}.

EXPERIMENTAL PROCEDURE

The samples used here were supplied by Siemens Research Laboratories in Erlangen, Joffe Institute St. Petersburg and Norton Company Germany (Acheson samples). The identification of the polytype was performed by measuring low temperature photoluminescence due to bound excitons at neutral nitrogen donor atoms. The samples used for measurements of electronic transitions were n–type 6H–SiC modified Lely crystals doped with nitrogen. The free electron density at room temperature in these crystals was between $2.0 \cdot 10^{16}$ cm^{-3} and $7.0 \cdot 10^{17}$ cm^{-3}. An optical cryostat with two exchangeable cooling fingers for transmission and reflectivity measurements was used to perform the measurements between T=5K and T=300K. The spectra were recorded using a Nicolet infrared fourier transform spectrometer type FTIR 740 at a resolution of 1 cm^{-1} or 2 cm^{-1}. The absorption constant was calculated using equation (2.58) of ref. [4], with reflectivity computed from the parameters in ref. [6].

EXPERIMENTAL RESULTS: VIBRATIONAL MODES

Non intrinsic infrared absorption lines in SiC can be attributed either to vibrational modes (localized vibrational modes (LVM) and gap modes) or to electronic transitions of impurities. Absorption lines which appear both at T=5K and at T=300K are possible candidates for LVM. We found five of them in Acheson and in n– and p–type 6H–SiC modified Lely material and determined the wavenumber shift $\Delta\omega$ of these lines with temperature. The peak maxima of the lines 625.7, 727 and 737 cm^{-1} (measured at T=5K) decrease with temperature, whereas the peak maxima ω of the lines 683.6, 691.3 cm^{-1} show no significant temperature dependence

Mat. Res. Soc. Symp. Proc. Vol. 339. ©1994 Materials Research Society

Table 1: Gap modes in 6H–SiC and 4H–SiC: $E \perp c$

energy [1/cm]	6H-Acheson	6H-Lely:N	6H-Lely:Al	4H-Lely:N [5]	Grüneisen
625.7	+	+	+	+	2.0 ±0.5
683.6	+	+	+	+	0.0 ±0.5
691.3	+	+	+	not observed	0.0 ±0.5
727	+	not observed	not observed	+	3.2 ±0.5
737	+	+	+	+	2.7 ±0.5

within the errorbars, i. e. the GRÜNEISEN constants

$$\gamma \approx -\frac{\partial \ln \omega}{\partial \ln V} = -\frac{1}{\omega} \frac{\frac{\partial \omega}{\partial T}}{\alpha_V} \tag{1}$$

of these lines are different (V means the crystal volume, α_V the thermal volume expansion coefficient). We conclude that there are different coupling mechanisms of these gap modes to the SiC–lattice, which are attributed to different chemical impurities. Götz et. al. [5] found some of these lines (625, 683, 728 and 738 cm^{-1}) in n-type modified Lely 4H-SiC material (T=7K), but they were regarded as electronic transitions of nitrogen donors in this material. The fact that these lines are observable in different polytypes strongly confirms their vibronic character, because the lattice potentials of the different SiC polytypes are very similar. Table 1 summarizes known gap–mode absorption lines in SiC, but the chemical nature of these impurities is not well known at the moment. From the (electric active) nitrogen concentration dependence there is some evidence that the absorption line 625.7 cm^{-1} is nitrogen correlated. For more precise statements isotope doped samples are necessary.

EXPERIMENTAL RESULTS: ELECTRONIC TRANSITIONS

We measured various 6H–SiC samples with different nitrogen concentrations at T=5K. The Acheson material samples showed no discrete absorption lines additional to those described before. However in modified Lely material we found a lot of discrete absorption lines which are either polarized $E \perp c$ or $E \parallel c$ (Fig. 2 a–c).

Additionally we found one line in the low temperature reflectivity spectrum of SiC samples with nitrogen concentrations of $\approx 1.0 \cdot 10^{18}$ cm^{-3}. All these absorption lines are assumed to be due to electronic transitions of the neutral N impurity center occupying the three inequivalent lattice sides in 6H–SiC. They are listed in Tab. 2 and 3.

Oscillatorstrengths of electronic transitions:

After substracting the background lattice absorption we used the absorption spectra to determine the corresponding oscillator strengths of the electronic transitions. Regarding the broad lineshape of the absorption lines we used gaussians for fitting them. The oscillator strengths were then obtained from the integral of the attributed gaussian and are listed in Fig. 1. Looking carefully at the spectra one can recognize that some lines are due to several overlapping lines. Especially line 332 cm^{-1} which has an asymmetric form seems to be build up of three single lines. We took this into account by decomposing this line in three lines (310, 332, 342 cm^{-1}). We stress that these two additional lines, especially their exact energetic positions, were only obtained by the fitting procedure. At the moment we have no

Table 2: Electronic Transitions in 6H–SiC: $E \parallel c$

Energy [cm^{-1}]	Energy [meV]	Polarization
332	41.13	$E \parallel c$
382	47.33	$E \parallel c$
405	50.18	$E \parallel c$
429	53.15	$E \parallel c$
632	78.31	$E \parallel c$

Table 3: Electronic Transitions in 6H–SiC: $E \perp c$

Energy [cm^{-1}]	Energy [meV]	Polarization
559	69.26	$E \perp c$
571	70.75	$E \perp c$
579	71.74	$E \perp c$
581	71.99	$E \perp c$
614	76.07	$E \perp c$
622.5	77.13	$E \perp c$
667	82.64	$E \perp c$
907	112.4	$E \perp c$
1124	139.3	$E \perp c$
1162	144.0	$E \perp c$

clear experimental evidence for them. The two line complexes (559, 571, 579, 581 cm^{-1}) and (614, 622.5 cm^{-1}) are partly overlapping but in this case we were able to identify all peak positions experimentally. We estimate the uncetainty in determining the relative oscillator strengths to be about $\pm$ 20 % .

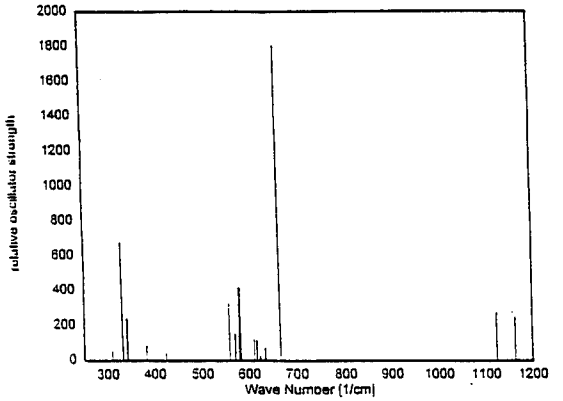

Figure 1: Relative oscillator parameters of electronic transitions in 6H–SiC

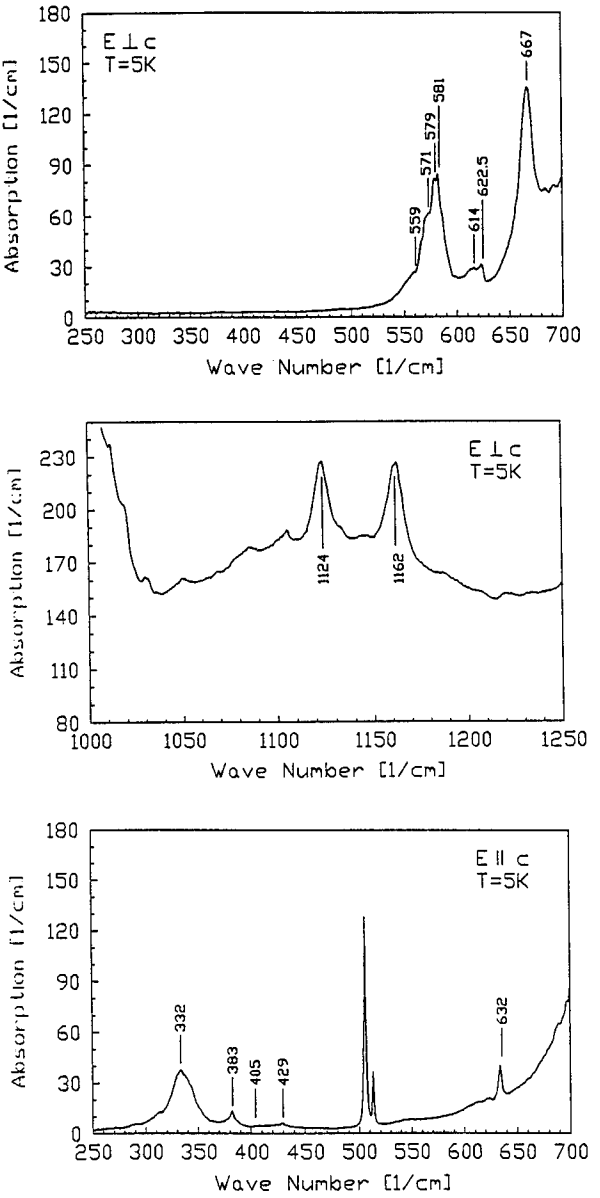

Figure 2: Absorption lines for electronic transitions of the nitrogen donor at T=5K a) $E \perp c$ (250cm^{-1}–700cm^{-1}) b) $E \perp c$ (1000cm^{-1}–1250cm^{-1}) c) $E \parallel c$ (250cm^{-1}–700cm^{-1})

Temperature dependence of electronic absorption:

Temperature dependence of electronic absorption strongly depends on sample quality. Some of the samples show electronic absorption lines up to T=200 K. No line broadening of electronic absorption lines is observed up to T=120K in this kind of samples. However at higher temperatures lines are getting broader. At T=200K only broad structures instead of sharp lines can be observed. Additionally above T=30K lines already observable at T=5K begin to decrease whereas new lines appear whose energy is exactly 105cm^{-1} or 13meV lower as the corresponding lines at T=5K. We attribute these lines to transitions from the thermally populated $1s(E)$ state of the nitrogen donor, which is split off from $1s(A)$ ground state by valley-orbit energy E_{VO} =13.0 meV (or 104.8 cm^{-1}) as determined by Colwell et. al. from electronic raman scattering experiments [7]. From the temperature dependent ratio of absorption constants

$$\frac{\alpha(1s(E) \rightarrow f)}{\alpha(1s(A) \rightarrow f)} \propto \frac{N_E}{N_A} = \frac{g_E}{g_A} \exp(-\frac{\Delta E_{VO}}{k_B T}) \tag{2}$$

(N_i means the occupation number of the state i which has the degeneracy g_i) of two corresponding absorption lines $1s(E) \rightarrow f$ and $1s(A) \rightarrow f$ we determined the valley-orbit-splitting energy E_{VO} as

$$\Delta E_{VO} = 14meV \pm 1.4meV \tag{3}$$

in very good agreement with the value from electronic raman measurements. We also found some samples which showed a quite different temperature dependence of electronic absorption. Here no electronic absorption could be observed in the energy range E $\leq$ 700 cm^{-1} at temperatures higher than 56K. Transitions from $1s(E)$ state, which is separated from $1s(A)$ ground state by valley-orbit-splitting energy E_{VO} cannot be observed. On the other hand the electronic transitions at 1124 cm^{-1} and 1162 cm^{-1} can be still observed at T=80K. The low temperature (T=1.8K) PL-spectrum of this sample shows the typical donor–acceptor–pair (DAP) spectrum and the characteristic lines for the Al complex. Furthermore we know from Hall effect measurements that these samples are strongly compensated. It is assumed that the different degree of compensation is responsible for the different temperature dependence of the electronic absorptions reported above, because the fermi level which determines the occupation of impurities depends on compensation. From the relation

$$N_E = N_A \cdot \frac{g_E}{g_A} \exp\left(-\frac{\Delta E_{VO}}{k_B T}\right) \tag{4}$$

one can draw some conclusions. For temperatures $k_B T > E_{VO}$ the occupation ratio $\frac{N_E}{N_A}$ is

$$\frac{N_E}{N_A} = \frac{g_E}{g_A} \tag{5}$$

which means equal distribution weighted by $\frac{g_E}{g_A}$ of the ground states 1s(E) and 1s(A). For temperatures $k_B T \leq E_{VO}$ occupation of 1s(E) state depends on the occupation of 1s(A) state, which is governed by the fermi level and therefore by the compensation. In the case of high compensation the ground state is depopulated at relatively low temperatures. In this case the occupation of 1s(E) state is so small that it cannot be observed by absorption measurements.

CONCLUSIONS

We measured absorption and reflectivity spectra of several 6H–SiC single crystals at different

temperatures ranging from T=5K up to T=300K. Using the different temperature dependence of the various lines we separated vibronic from electronic transitions. We found five gap modes in 6H-SiC and determined their Grüneisen constants. Various electronic transitions were observed at low temperature, which are attributed to transitions between discrete energy levels of the nitrogen donor occupying the three different carbon lattice sites in 6H-SiC. We determined the polarization dependence and oscillator strengths of these transitions. However due to lacking information about the line symmetry it is not possible to identify the observed electronic transitions uniquely at the moment. So we do not try to propose an energy scheme for these transitions. We demonstrated the effect of valley-orbit-splitting of the 1s ground state on the spectra. Using semiconductor statistics, LT-photoluminescence and Hall effect measurements the effect of high compensation on the spectra is shown.

ACKNOWLEDGEMENTS

We are indebted to S. Leibenzeder and Dr. R. A. Stein of the Siemens Research Laboratories Erlangen, Prof. V. Tsvetkov formerly LETI St. Petersburg and Norton Company Germany for supplying the samples. We thank C. Peppermüller for performing the LT-photoluminescence and A. Schöner for the Hall effect measurements. This work was supported by Deutsche Forschungsgemeinschaft through Sonderforschungsbereich 292.

References

[1] O. V. Vakulenko and O. A. Guseva, Sov. Phys. Semicond. **15**, 886 (1981) and references in there

[2] W. Suttrop et. al. J. Appl. Phys. **72**, 3708 (1992)

[3] G. Ziegler, P. Lanig, D. Theis and C. Weyrich, IEEE Trans. Electron. Dev. ED. **30**, 277 (1983)

[4] M. Balkanski. Optical Properties due to Phonons, in: T. S. Moss, Handbook on Semiconductors Vol. 2, North-Holland Publishing Company 1980

[5] W. Götz et. al. J. Appl. Phys. **73**, 3332 (1994)

[6] F. Engelbrecht and R. Helbig, Phys. Rev. **B48**, 15698 (1993)

[7] P. J. Colwell and M. V. Klein, Phys. Rev. **B6**, 498 (1972)

ELECTRON SPIN RESONANCE STUDIES OF DONORS IN BULK AND THIN FILM β-SiC

W.E. CARLOS[a], J.A. FREITAS, JR.[b], J.C. PAZIK[a,c], L.M. IVANOVA[d], YU.M. ALTAISKII[e] AND V.L. ZUEV[e]
[a]Naval Research Laboratory, Washington, D.C. 20375
[b]Sachs Freeman Associates, Landover, MD 20785
[c]Current address; Office of Naval Research, Arlington, VA 22217
[d]A.A. Baikov Institute of Metallurgy, Russian Academy of Sciences, Moscow, Russia
[e]Kiev Polytechnic Institute, Kiev, Ukraine.

ABSTRACT

We have investigated the electron spin resonance of donors in bulk and thin film β-SiC at T = 10K to 40K. In both, two donor spectra are resolved; a three line spectrum associated with nitrogen on the carbon site and a broader line of unidentified origin. The observable hyperfine splitting decreases with increasing temperature due to a small valley-orbit splitting, in qualitative agreement with photoluminescence results. The lineshape has a significant lorentzian character even at the lowest temperatures, indicating exchange interactions with residual conduction electrons, possibly from a shallower donor. We find a lower concentration of both donors in the bulk material and a different temperature dependence of the lineshape for the two samples.

INTRODUCTION

The zincblende polytype of SiC (β-SiC) shows promise as a semiconductor material for high power, high frequency or high temperature applications. Thin films (<10μm) grown on various substrates such as Si or α-SiC are envisioned for most applications. Recently there has been renewed interest in bulk growth of various polytypes of SiC, including β-SiC, primarily for use as substrates. The undoped film and bulk materials are invariably n-type and often highly compensated (N_D-N_A~$10^{17}cm^{-3}$).[1,2] Dean and coworkers' optical measurements on the best Lely-grown bulk samples indicated one donor level at 54meV below the conduction band edge.[3] This level has been associated with substitutional nitrogen on a carbon site and a N-bound exciton spectrum is also observed in the thin films.[4] Hall measurements on thin film and bulk samples from several sources suggest another donor about 15meV below the conduction band edge. ^{14}N is the only near 100% abundant nucleus with I=1 and so a three-line electron spin resonance (ESR) spectrum serves as a fingerprint of nitrogen. Our measurements reveal two donor signals, a three line spectrum with a weak isotropic nuclear hyperfine splitting, indicating a diffuse orbital centered on the nitrogen atom, e.g., a shallow donor, and a broader overlapping line of comparable intensity. We note that a third, rather dilute, donor at about 47meV below the conduction bandedge has also been observed in infra-red measurements.[5] However, we are not able to resolve an ESR line due to that donor.

The thin films, which were free standing, were initially deposited onto a silicon on insulator substrate using a horizontal reactor. Reactant gases were high purity, undiluted ethylene and 1% SiH_4 diluted in H_2. The bulk crystals were grown by a vapor phase process utilizing the thermal decomposition of CH_3SiCl_3 in H_2 at 1700°C onto a graphite substrate. Details of the growth

Mat. Res. Soc. Symp. Proc. Vol. 339. ©1994 Materials Research Society

processes have been described previously.[6,7] Here we focus on two samples whose exceptionally well resolved features permitted us to follow the lineshape parameters as a function of temperature. The ESR measurements were performed on a Bruker ESP300 x-band spectrometer using a liquid helium flow cryostat to control the sample temperature. Microwave power levels between 10nW to 1μW were used to avoid saturation effects.

LOW TEMPERATURE SPECTRA

Figure 1 shows the low temperature (20K) ESR spectra of the thin film and bulk samples. Aside from differences in the signal to noise level, the two spectra appear virtually identical and do not depend significantly on temperature below about 25K. Both can be fit with three equal intensity Voigt functions (convolutions of lorentzian and gaussian functions) plus another Voigt function to simulate the broad line. The two components for the bulk sample are also shown in figure 1. At low temperatures the two components have comparable intensities in either sample. The total excess donor density is about an order of magnitude higher in the film. The identification of the triplet spectrum with an N_c shallow donor is based on three observations. (1) The Landé g value is isotropic and about the expected value for a shallow donor in β-SiC. This suggests that the broad line which has a similar g value is also a donor. (2) The hyperfine splitting agrees with our effective mass calculations for a N_c donor. (3) The width of the three lines agrees with our estimate based on Si:P.

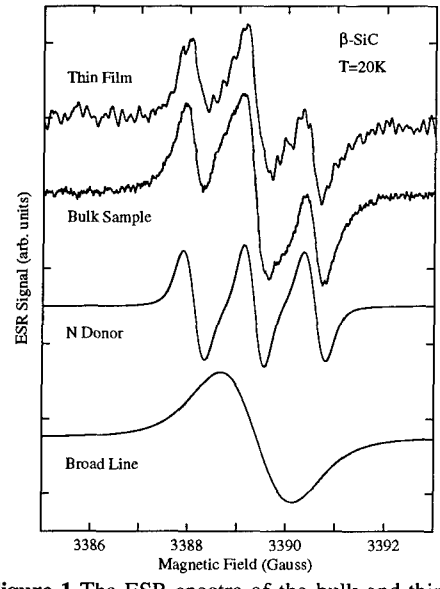

Figure 1 The ESR spectra of the bulk and thin film β-SiC samples. The spectrum of the thin film has been shifted to compensate for the difference in resonant frequency. The two lower traces are the components of the bulk sample spectrum.

The donor wave function is a Bloch sum of conduction band wave functions, we therefore expect that the g value of the donor will simply be that of the appropriate conduction band minimum (X_1 for β-SiC). A simple linear combination of atomic orbitals is appropriate for SiC because of the symmetry of the zinc-blende lattice and the simplicity of the atomic structure of carbon. A simple two band model gives[8] $g = \frac{1}{3}g_{\|} + \frac{2}{3}g_{\perp}$, where $g_{\|} - g_e = 2\delta/E_{1\text{-}5}\,(m_e/m_t - 1)$ and $g_{\perp} - g_e = 2\delta/E_{1\text{-}5}\,(m_e/m_l - 1)$ and $\delta = 0.010$meV,[9] $E_{1\text{-}5} = 6.4$eV,[10] $m_t/m_e = 0.247$ and $m_l/m_e = 0.677$.[11] This yields g=2.0062 compared to the measured value of 2.0050.

The effective mass approximation (EMA) has been successfully applied to a number of problems regarding donors and acceptors in semiconductors. The donor wave function is comprised of contributions from each of the equivalent conduction band minima. For a C-site donor β-SiC the lowest minima have X_1 symmetry and the irreducible representations are a

singlet and a doublet. The singlet state wave function has a maximum at the donor and is the lowest energy state. In the EMA the hyperfine splitting is given by;[12]

$$\Delta H = \frac{8\pi}{3}\frac{\mu_D}{I_D}|\psi(0)|^2 \iota\eta\,, \qquad (1)$$

where μ_D and I_D are the nuclear magnetic moment and spin of the donor, ι is the number of equivalent conduction band minima (3) and η is the ratio of the amplitude of the conduction band wave function at a lattice site to its average value over a unit cell. This parameter is estimated from the nuclear spin-lattice relaxation time data of Alexander.[13] $\eta = 227$ which corresponds reasonably well to $\eta = 186$ for the Si:P system.[14] Equation (1) then yields $\Delta H = 1.05$G which is in reasonably good agreement with the measured value of 1.24G. One would expect the measured ΔH to be somewhat higher than the calculated value due to the valley-orbit interaction.

We consider the linewidth of donors in β-SiC by analogy with the Si:P system. The linewidth of donors in Si is about 2.5G primarily due to unresolved ^{29}Si hyperfine interactions with atoms on the same face centered cubic sublattice while the contribution from those on the opposite sublattice is zero.[13] The inhomogeneous linewidth of the N-donor in β-SiC is only 0.7G due to hyperfine interaction with ^{13}C nuclei. ^{29}Si is 4.7% abundant while ^{13}C is only 1.1% abundant but has a magnetic moment 27% larger than that of ^{29}Si. From the ratios of abundances and magnetic moments of these isotopes, we estimate that a donor in SiC should have a linewidth approximately one third that of one in Si.

TEMPERATURE DEPENDENCE OF THE DONOR RESONANCES

The ESR signal was monitored from T=10K to 40K. As mentioned above, the low temperature spectra contains two resolvable components, a triplet due to electrons on isolated nitrogen donors and a broad line due to an unidentified donor. The lineshape changes due to a number of effects. Electrons are promoted from the 1S(A) state into the d-like 1S(E) state; this weakens the observed central hyperfine interaction due to an averaging of the singlet state and the doublet state which has a node at the central N atom. Exchange interactions between electrons in the conduction band and those on donor sites will enhance the lorentzian character of both lines and eventually yield a single resonance line.

In figure 2a and 2b we show the evolution of the ESR spectrum with temperature for the bulk and thin film samples, respectively. To remove the effect of the variation of the magnetization with temperature the ESR signals have been scaled by multiplying by the temperature. All of the spectra were taken at 100 nW of microwave power which is low enough to avoid saturation effects at all but the lowest temperatures. The appearance of the data in figures 2a and 2b is somewhat deceptive. As previously mentioned, a derivative ESR spectrum emphasizes sharp rather than broad features, while the concentration is proportional to the second integral of the spectrum. There is some decrease in intensity with increasing temperature; however, the dominate effects are changes in lineshape rather than in the line intensity. Therefore, information gained from the temperature dependence of the ESR spectra came primarily from analysis of the lineshape. The isolated N-donor was simulated by three Voigt functions of equal intensity and equal separation; the outer lines ($m_I=\pm1$) are more perturbed by differences in local environment

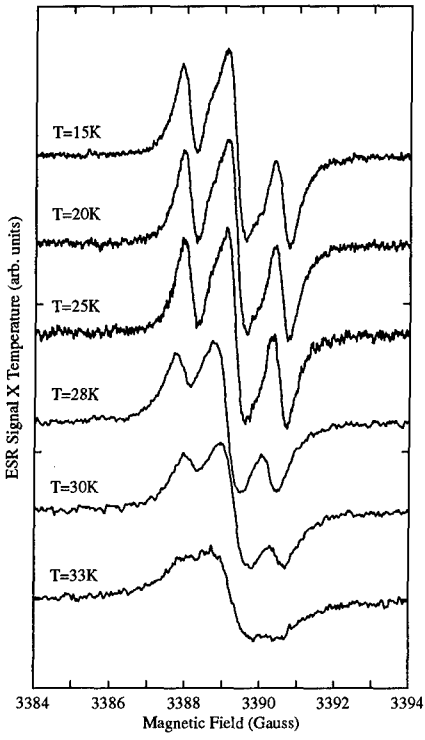

Figure 2a The thermal evolution of the donor resonances in the bulk sample of β-SiC.

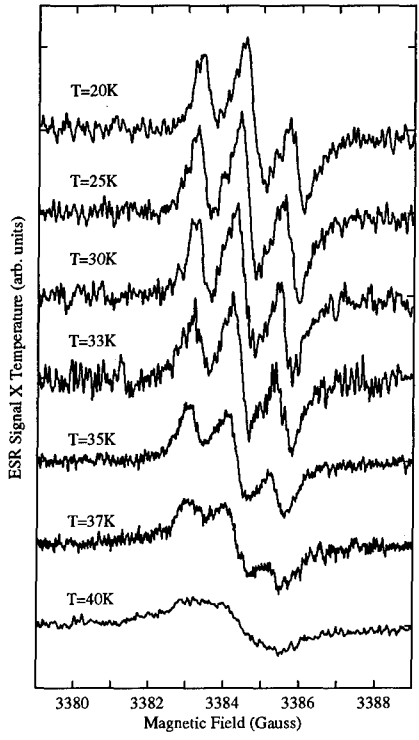

Figure 2b The thermal evolution of the donor resonance for the thin film sample of β-SiC.

which could result in a distribution of central hyperfine interactions and somewhat larger gaussian linewidths. At low temperatures the lorentzian linewidths are due to exchange interactions between the donor electrons and conduction electrons which involve the hyperfine interaction, yielding larger lorentzian linewidths for the outer lines. There are then a total of seven parameters representing this portion of the spectrum (intensity, central position, hyperfine separation and the four linewidths). In practice, the gaussian width of the outer lines is, at most, only modestly larger than that of the central line. The broad line is fit by a single Voigt line at a similar (although not necessarily identical) position to the triplet. At low temperatures donor ESR lines are inhomogeneously broadened and therefore yield primarily gaussian lineshapes, while at higher temperatures, exchange interactions give an increasingly lorentzian character to the lineshape.

Even without elaborate lineshape fitting we see that the individual components of the triplet become less well resolved with increasing temperature. Furthermore, it is obvious that these changes take place at significantly lower temperatures (5-7K) for the bulk crystal compared to the thin film. In addition to the increasingly lorentzian character two other effects also contribute to this behavior. The hyperfine splitting of the triplet becomes weaker with increasing temperature and the broad line becomes relatively stronger and its linewidth increases.

The reduction in the hyperfine splitting is due to the averaging of the splitting of the 1S(A) and the d-like 1S(E) states.[14] The temperature dependence of the observed hyperfine interaction is given by;

$$A = A_0 (1 - e^{-2\Delta/kT}), \qquad (2)$$

where A_0 is the hyperfine splitting of the 1S(A) state and Δ is the valley-orbit interaction. The fit to equation 2 shown in figure 3 give $A_0 = 1.24$ G which, as previously noted, is good agreement with theoretical expectations. We obtain $\Delta = 8.5$ meV which is consistent with the value of 6.5 meV obtained by Dean and coworkers[3] in their photoluminescence measurements.

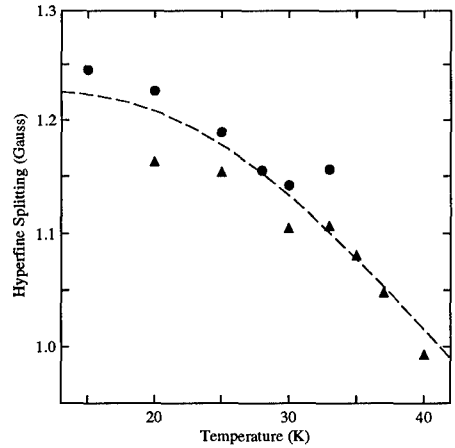

Figure 3 The hyperfine splitting for the bulk (circles) and thin film (triangles) samples of β-SiC. The dashed line is a fit to equation 2.

With increasing temperature the N donor line intensity decreases while the intensity of the broad line, when compensated for changes in magnetization, remains almost constant. This indicates that the broad line is due to a deeper donor than N_c. The decrease in the N donor line is apparently due to ionization with the resonance due to conduction electrons presumably too broad to be easily observed. The increase in the conduction electron density does result in an increase in the lorentzian character of either donor line due to exchange interaction with the conduction electrons. Because of the differences in intensity this result is most obvious in the broad line, with the results shown in figure 4 in which we display the lorentzian linewidths for the two samples as a function of temperature. The lorentzian linewidth is proportional to the conduction electron density which at low temperatures is given by;

$$n_0 \approx N_C \beta \left(\frac{N_D}{N_A} - 1\right) e^{(-E_D/kT)}, \qquad (3)$$

where N_C and β are the conduction band density of states and degeneracy, respectively, N_D and N_A are the donor and acceptor concentrations and E_D is the donor binding energy. When this ratio approaches one (the sample is highly compensated) the exponential (i.e., the temperature) must be relatively large to give the same carrier density as would be seen in a lightly compensated sample at a lower temperature. This indicates that since the bulk sample's linewidth

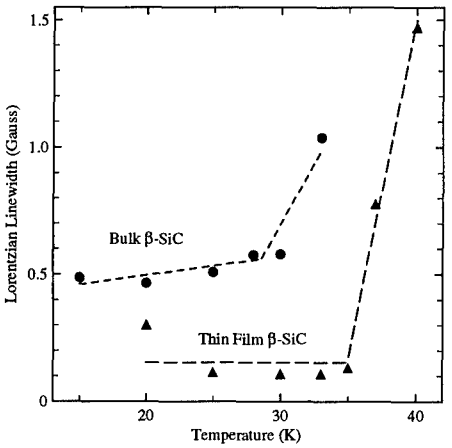

Figure 4 The temperature dependence of the lorentzian width of the broad line. The dashed lines are meant as an aid to the eye.

starts to broaden at a significantly lower temperature, as seen in figure 2a and 2b, it more lightly compensated than the thin film sample. Also because of the higher compensation level in the thin film there are fewer free carriers at low temperature and, hence, a smaller lorentzian component to the linewidth for T<25K.

SUMMARY

In both bulk and thin film β-SiC, two donor spectra are resolved; a three line spectrum due to nitrogen on the carbon site and a broad line due to a deeper donor. The hyperfine splitting of the N donor decreases with increasing temperature due to a valley-orbit interaction of about 8.5 meV, which is in reasonable agreement with photoluminescence results. The lineshape has a significant lorentzian character even at the lowest temperatures, indicating exchange interactions with residual conduction electrons, possibly from a shallower donor. However, we are not able to resolve any resonance due to such a donor. We find a lower concentration of both donors in the bulk material and the different temperature dependence of the lineshape indicates that the bulk sample is less compensated than the thin film material.

REFERENCES

1. W.J. Moore, J. Appl. Phys. **74**, 1805 (1993).
2. B. Segall, S.A. Alterovitz, E.J. Haugland, and L.G. Matus, Appl. Phys. Lett. **49**, 584 (1986).
3. P.J. Dean, W.J. Choyke and L. Patrick, J. Lumin. **16**, 299 (1977).
4. J.A. Freitas, Jr., S.G. Bishop, A. Adamiano, P.H. Klein, H.J. Kim and R.F. Davis in *Proceedings of the Materials Research Society Symposia*, edited by N.M. Johnson, S.G. Bishop and G.D. Watkins (Materials Research Society, Pittsburgh, PA, 1985), Vol. 46, p. 581.
5. W.J. Moore, Pj. Lin-Chung, J.A. Freitas, Jr., Y.M. Altaiskii, V.L. Zuev and L.M. Ivanova, Phys. Rev. B **48**, 12289 (1993).
6. J.C. Pazik, G. Kelner and N. Bottka, Appl. Phys. Lett. **58**, 1419 (1991).
7. A.A. Pletyushkin, L.M. Ivanova and T.N. Sultanova, Inorg. Mater. (USSR) **16**, 966 (1980).
8. L.M. Roth, Phys. Rev. **118**, 1534 (1960)
9. R.G. Humphreys, D. Bimderg and W.J. Choyke, J. Phys. Soc. Jpn. **49** Suppl. A, 519 (1980).
10. Yuan Li and P.J. Lin-Chung, Phys. Rev. B **36**, 1130 (1987).
11. R. Kaplan, R.J. Wagner, H.J. Kim and R.F. Davis, Solid State Commun. **56**, 67 (1985).
12. W. Kohn and J.M. Luttinger, Phys. Rev. **97**, 883 (1955).
13. Michael N. Alexander, Phys. Rev. **172**, 331 (1968).
14. R.G. Shulman and B.J. Wyluda, Phys. Rev. **103**, 1127 (1956).
13. G. Feher, Phys. Rev. **114**, 1219 (1959).
14. Daniel J. Lépine, Phys. Rev. B **2**, 2429 (1970).

DYNAMICS OF THE NITROGEN BOUND EXCITONS IN 6H AND 3C SiC

J. P. Bergman, C. I. Harris, O. Kordina, A. Henry, and E. Janzén
Department of Physics and Measurement Technology
Linköping University, S-581 83 Linköping, SWEDEN

Abstract

We have measured the photoluminescence decay time of the bound excitons at the neutral nitrogen donors in the 6H and 3C polytypes of SiC. At 2K the decay times are 8.0 ns, 1.8 ns and 1.5 ns, for the P, R and S bound excitons in 6H SiC. For the nitrogen exciton in 3C, we find a decay time of 160 ns. These values are faster than previously reported for shallow donors in other indirect bandgap materials such as Si or GaP. Each of the observed decay times is found to be independent of the doping level in the sample, is temperature independent at low temperatures but decrease when the bound excitons are thermally ionised. The decay time related to different donor levels in 6H exhibits a strong dependence on the donor binding energy. We suggest that the dominant mechanism responsible for the observed decay time is a phonon-less Auger process. In high-purity 6H samples we have also measured the free exciton decay time at low temperatures to be 12 ns.

Introduction

The growing interest in SiC during the last years is due to its potential as a material for high performance devices in optoelectronic, high temperature, high frequency, and power applications. By recent efforts and achievments in crystal growth it is now possible to produce both epitaxial and bulk SiC material of high quality. SiC is also interesting as a model material for fundamental studies. The possibility to produce high quality material of several different polytypes, having different bandstructures (and thus different bandgaps ranging from 2.3 eV for 3C to 3.3 eV for 2H) makes it possible to study the behaviour of fundamental electronic properties as well as properties of defects, in a way not possible in other semiconductor materials.

Nitrogen is the most common residual impurity in 6H and 3C SiC. In 6H SiC there are three inequivalent carbon sites. Nitrogen atoms occupying substitutional carbon sites give rise to three different donor levels in the bandgap. The energy positions of these levels have recently been determined by infrared absorption spectroscopy to be 81.0 meV (h), 137.6 meV (c1), and 142.4 meV (c2) below the conduction band level [1]. In 3C SiC there is only one possible carbon site, with a donor energy level of 54 meV [2].

The near bandgap low temperature photoluminescence (PL) spectrum of both 6H and 3C SiC, is normally dominated by sharp lines due to the recombination of excitons bound at these nitrogen donors. The no-phonon (NP) lines of the donor bound excitons (DBE) associated with nitrogen in 6H are usually labelled P_0, R_0 and S_0. The recombination energies at 2K are 3.0070 eV, 2.9924 eV and 2.9906 eV [3], respectively, and correspond to DBE binding energies of 16.0 meV, 30.6 meV, and 32.4 meV, if the free exciton (FE) bandgap is taken as 3.023 eV [4]. At slightly lower photon energies (Fig. 1.), the phonon replicas of the P_0, R_0 and S_0 lines are shown. The recombination energy for the nitrogen DBE in 3C SiC is at 2.3779 eV, which, with the FE energy at 2.3877 eV, gives an exciton binding energy of 9.8 meV.

Mat. Res. Soc. Symp. Proc. Vol. 339. ©1994 Materials Research Society

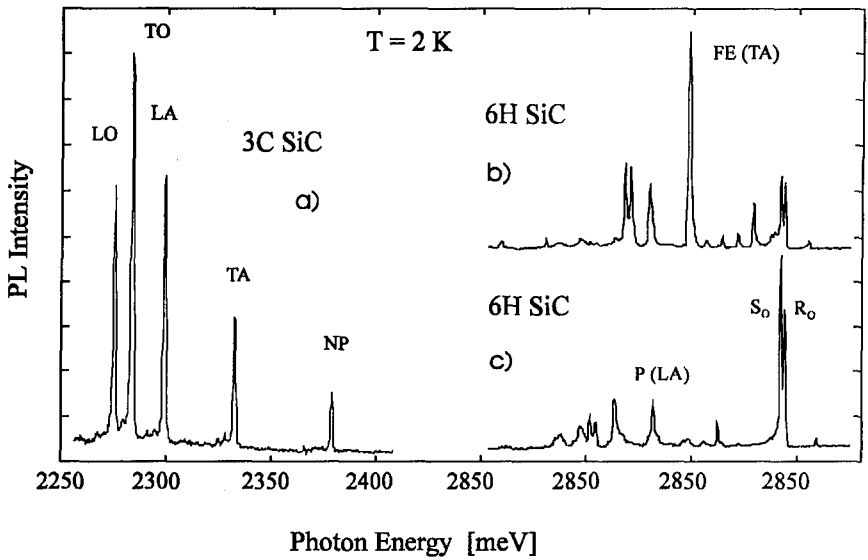

Figure. 1. PL spectrum at 2K in the near bandgap region of three different SiC samples. a) is a 3C sample. b) is a high purity 6H epitaxial layer, and c) is high doped 6H bulk sample.

In this paper we present decay measurements of the different nitrogen related DBE's in the 6H and 3C polytype of SiC. To our knowledge, no time resolved measurements of the DBE's in 6H SiC have been published. An experimental value for the decay time of the bound exciton in 3C has previously been reported [5], but is not in agreement with our results.

Experimental

Experimental results will be shown for two different 6H samples, one modified Lely substrate with a high doping level of $2x10^{18}$ cm^{-3}, and one high purity epitaxial layer, with a doping level of less than $5x10^{14}$ cm^{-3}, grown by chemical vapour deposition (CVD) [6]. The 3C SiC sample is epitaxial grown by CVD on a 6H on-axis substrate. Further samples, both bulk and epitaxial, have also been studied for comparison.

The PL and PL time resolved measurements were performed using pulsed excitation from a dye laser synchronously pumped by a mode-locked Ar^+-laser. The pulses, with a width of <10 ps and a photon wavelength about 7400 Å, were frequency doubled with a $LiIO_3$ crystal producing excitation at about 3700 Å (3.5 eV). The frequency doubled average power was in the order of 1 mW, while the repetition frequency is varied with a cavity dumper from 1 MHz to 10 MHz depending on the decay time of the PL. Some PL spectra were obtained with continuous wave (CW) excitation using the UV lines from an Ar^+-laser.

The PL was dispersed with a 0.6 m double monochromator (Jobin Yvon HRD). The time decays were measured with a time correlated photon counting system with a total time resolution better than 200 ps.

Results

Figure 1 shows the low temperature near bandgap PL spectrum from three different samples obtained with CW excitation. Figure 1c shows the spectrum from the highly doped 6H bulk sample, which is dominated by the recombination of the three different nitrogen bound excitons. In addition to the NP line, each exciton has a corresponding spectrum of phonon replicas involving the TA (46.3 and 53.5 meV), LA (77.0 meV), TO (95.6 meV) and LO (104.2 and 107.0 meV) phonons. Figure 1b shows the spectrum from the high purity epitaxial sample. This spectrum is dominated by the recombination of the phonon replicas of the FE. The NP line of the FE is not observed due to the indirect bandgap. The spectrum for the 3C SiC sample is shown in Figure 1a, and shows the NP line as well as the four dominant phonon replicas, TA, LA, TO and LO.

The decay time of the three different excitons in 6H SiC has been measured separately at 2.0K and is found to be 1.5 ± 0.1 ns, 1.8 ± 0.1 ns and 8.0 ± 0.5 ns, for the S, R, and P, respectively. The corresponding decay curves are shown in Figure 2. The larger experimental error for the P exciton is related to difficulties in evaluating the slower and weaker signal from this exciton, which has a spectrally overlapping contribution from the faster R and S excitons. The reported value of the decay time of the R and S DBE was measured with detection at the recombination wavelength of the NP line, while the value for the P exciton was measured in the strongest phonon replica (LA, 77.0 meV) since the NP line has much lower intensity. We have also measured the decay in the NP of the P exciton as well as in different phonon replicas of all the three excitons. As expected, the same value for the decay time in the NP line and in all related phonon replicas is observed. The observed decay times for the DBE's in 6H do not differ between samples with different doping levels, in the range of 10^{16} to 10^{18} cm^{-3}.

We have also measured the temperature dependence of the decay time. The measured decay time is found to be constant up to a certain temperature above which it decreases rapidly. This can most simply be described with the introduction of an additional temperature activated non

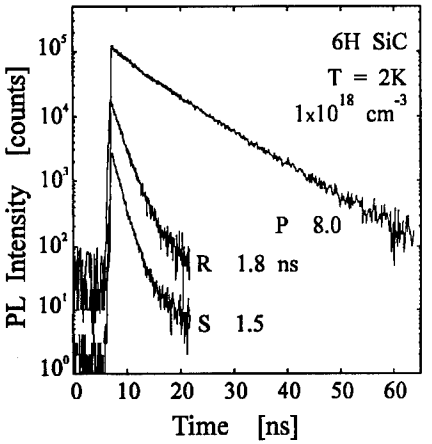

Figure 2. Decay curves at 2K of the P, R and S DBE in a 6H SiC sample with high nitrogen concentration.

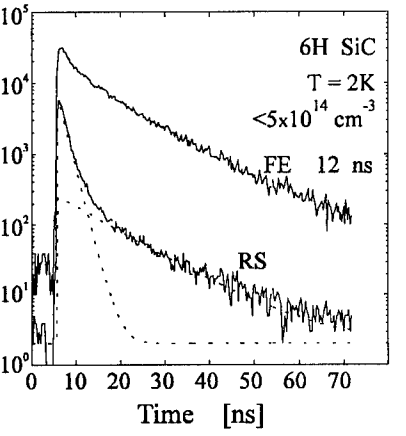

Figure 3. Decay curves at 2K of the FE and RS DBE in a high purity 6H SiC sample.

radiative recombination channel. The experimentally expected decay time τ_m is then expressed as

$$\tau_m = \left(\frac{1}{\tau_{BE}} + \frac{1}{\tau_{NR}} \exp^{(-\Delta E/k_B T)} \right)^{-1} \quad (1)$$

where τ_{BE} is the decay time of the DBE, τ_{NR} the decay time of the non radiative channel for the DBE, and ΔE the activation energy. This model gives good agreement with the experimental values obtained from the highly doped sample. The line corresponding to the RS exciton, defined as the combined signal from the R and S DBE, shows the best fit of the experimental values with equation 1, using ΔE and τ_{NR} as variational parameters. The activation energies of 30.2 meV and 15.3 meV, obtained for the RS and P exciton are very close to the corresponding DBE binding energy. From this we draw the conclusion that the DBE in this sample is thermally released as FE's. The expression above is valid under the assumption that the nonradiative recombination of the upper level, assumed to be the FE, is faster than the capture to the donors. In this case no recapture back to the DBE occurs. This assumption is reasonable since the FE is not at all observed in the PL spectrum in these samples.

This is, however, not the case in the high purity sample where the FE is observed in the PL spectrum. In this sample the decay time of the FE recombination is 12 ns. The decay curve of the RS DBE in the same sample is different from the sample with higher doping level, as seen in Figure 3. The decay curve has two components, one fast corresponding to the previously observed decay of ~ 1.5 ns and a slower component identical to the decay time of the FE. This reflects the fact that the DBE is formed by capture of a FE onto the neutral nitrogen donor. The creation of DBE's will continue as long as there exists a population of FE's, and since the recombination time of the DBE is faster (1.5 ns), the observed lifetime will be determined by the lifetime of the FE population.

The observed decay time of the exciton in 3C SiC is considerably longer, 160 ± 5 ns, as shown in Figure 4. We have obtained the same value for the decay time in several samples, in both bulk and epitaxial layers.

Discussion

The observed values for the decay time in both 6H and 3C are considerably faster than expected for a radiative recombination in a semiconductor with an indirect bandgap like SiC. To our knowledge, no measurement or estimation of the expected radiative recombination probability has been made in SiC, but a comparison can be made with other semiconductors with indirect bandgap. In GaP and Si, the radiative recombination time are estimated to be 10 and 75 μs, from calculations of the absorption due to DBE's [7]. The experimentally observed photoluminescence decay times have in both these cases been several orders of magnitude

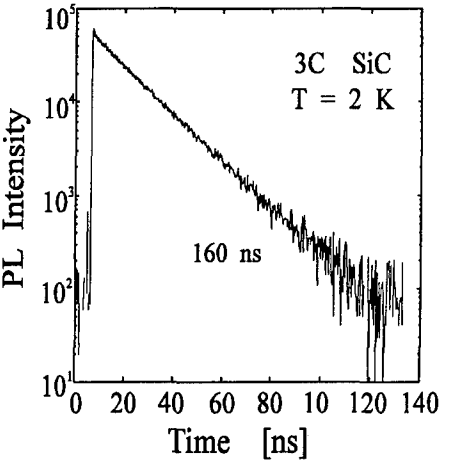

Figure 4. Decay curve at 2K of the nitrogen DBE in 3C SiC.

lower, which we also observe for SiC. It appears that non radiative recombination is the dominant mechanism that reduces the BE population. From these decay time measurements - fast recombination, temperature independence at low temperatures, no dependence on doping concentration, correlation between decay time and energy level of the corresponding donor - we conclude that the most probable non-radiative process is a phonon-less Auger process [8-9].

The donor bound exciton consists originally of three particles, two electrons and one hole. In the Auger process one of the electron recombines with the hole leaving the excess energy and momentum to the second electron. This electron, labelled as the Auger particle, is then excited up into the conduction band with an energy close to the bandgap energy and with an additional wave vector determined by the separation of the electron and hole in momentum space.

In 6H SiC, the hole is located at the valence band top, which is located at the Γ-point in the zone center, whereas the two electrons are located at the conduction band minimum (assumed to be at or close to the M-point at the zone edge). This means that the Auger electron receives an additional wave vector corresponding to the indirect bandgap, and that the final state of the Auger electron in k-space will be in the vicinity of the zone center. Existing bandstructure calculations [10] show that the bandgap at the Γ-point is close to or larger than twice the minimum indirect bandgap. The exact value of the zone center bandgap is in this case very important, since the recombination rate is strongly dependent on whether the final energy of the Auger particle is located below or above the Γ-point band gap. According to our measurements the recombination process is very fast (in the low ns range) and we thus conclude that the direct bandgap is less than twice the indirect bandgap.

The nitrogen donor levels in 6H SiC are relatively deep causing a strong localisation for the primarily bound electron. This will consequently lead to a delocalized wavefunction in k-space and a higher probability of Auger recombination for final state wavevectors different from k=0. This is further demonstrated by the observed decrease in decay time with increasing energy for the three nitrogen donor levels.

The same assumption of a dominating phonon-less Auger process can not be made for 3C SiC. Since only one exciton is observed in our material, a similar comparison as in 6H with excitons at different donor levels can not be made. There are experimental [11] and theoretical [10,12] results indicating that the direct bandgap in 3C is larger than twice the indirect bandgap, making the final state for the Auger particle inside the forbidden gap. If this is the case the, Auger process must be phonon-assisted or it must be assumed that the spread of the DBE wavefunction in momentum space is large enough to make other final states accessible. Figure 5 shows a comparison between the decay time of the DBE and the corresponding donor level in different indirect bandgap materials. A relation according to $\tau \sim E_D^{-4}$ is expected from theoretical calculations in Si [8], and is also observed for our results in 6H SiC as well

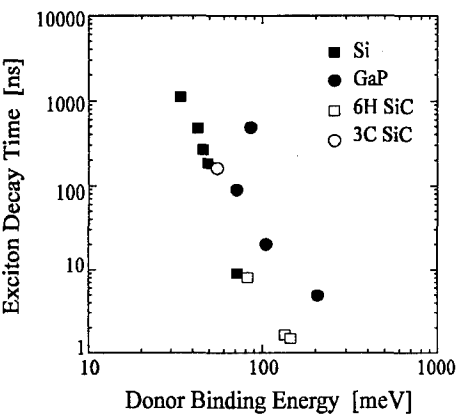

Figure 5. The decay time of the DBE as a function of the corresponding donor energy level, in different indirect bandgap materials.

as in previous measurements in Si and GaP [8,13].

Summary

We have measured the decay time of the recombination of excitons bound at the neutral nitrogen donor in different 6H and 3C SiC samples. We have found very fast decay times at low temperatures with values of 1.5 ns, 1.8 ns, and 8.0 ns for the S, R and P DBE in 6H SiC. The observed decay time for the DBE in 3C SiC is much longer, 160 ns. The observed decay time is independent of temperature, at low temperatures, and independent of the doping level in the sample. We have also observed a strong relation between the decay time and the energy of the corresponding donor level, with a decrease of the decay time with increasing donor energy. From our experimental results in 6H SiC we conclude that the dominating recombination mechanism is a phonon less Auger process.

In low doped samples, where the FE is present in PL, we have found that the observed decay time of the DBE recombination is determined by the lifetime of the FE and not by the recombination rate of the Auger process. We have furthermore concluded that the direct bandgap at the zone center must be less than two times the indirect bandgap to account for the fast Auger recombination process.

Acknowledgement

Financial support for this work was provided by the Swedish Natural Research Council (NFR).

References

1) W. Suttrop, G. Pensl, W. J. Choyke, R. Stein, and S. Leibenzeder, J. Appl. Phys. **72**, 3708, (1992).
2) P. J. Dean, W. J. Choyke, and L. Patrick, J. Lumin. **15**, 299 (1977).
3) P. J. Dean, and R. L. Hartman, Phys. Rev. B. **5**, 4911 (1972).
4) W. J. Choyke, D. R. Hamilton, and L. Patrick, Phys. Rev. A. **139**, 1262 (1965).
5). R. L. Hartman, and P. J. Dean, Phys. Rev. B. **2**, 951 (1970).
6) O. Kordina, C. Hallin, R. C. Glass, A. Henry, and E. Janzén, Proc. Int. Conf. on Silicon Carbide and Related Materials, Washington DC, USA 1-3:th Nov. 1993.
7) D.F. Nelson, J.D. Cuthbert, P.J. Dean, and D.G. Thomas, Phys. Rev. Lett. **17**, 1262 (1966).
8) W. Schmid, Phys. Stat. Sol. **84**, 529 (1977).
9) G. C. Osbourn, and D. L. Smith, Phys. Rev. B. **16**, 5426 (1977).
10) V. I. Gavrilenko, A. V. Postnikov, N. I. Klyui, and V. G. Litovchenko, Phys. Stat. Sol. **162**, 477 (1990).
11) B. E. Wheeler, Solid State Commun. **4**, 173 (1966).
12) C. H. Park, Byoung-Ho Cheong, Keun-Ho Lee, and K. J. Chang, Phys. Rev. B. 49, 4485 (1994).
13) P. J. Dean, R. A. Faulkner, S. Kimura, and M. Ilegems, Phys. Rev. B **4**, 1926 (1971).

RAMAN AND PHOTOLUMINESCENCE STUDIES OF UNDOPED AND MAGNESIUM-DOPED GAN FILMS ON SAPPHIRE

JAIME A. FREITAS, JR.* AND M. ASIF KHAN**
* Sachs/Freeman Assoc. Inc., 1401 McCormick Dr., Landover, MD 20785
Naval Research Laboratory: Contract #N00014-93-C-2227
** APA Optics Inc., 2950 N.E. 84th Lane, Blaine, MN 55434

ABSTRACT

Room temperature Raman scattering measurements performed on undoped GaN films indicate that high crystalline quality wurtzite material has been deposited on the basal plane of sapphire. Photoluminescence study of these films show that thicker films ($t > 4\mu m$) are homogeneous along the growth direction. The PL spectra of Mg-doped films are dominated by an intense emission band around 3.1 eV associated with recombination processes involving donor-acceptor pairs.

INTRODUCTION

Recent advances in heteroepitaxy growth of GaN by either metalorganic chemical vapor deposition (MOCVD) or molecular beam epitaxy (MBE) have demonstrated that high quality films can be grown on several types of substrates [1]. Nominally undoped films deposited over the basal plane sapphire substrate are characterized by a residual *n*-type conduction. The carrier densities and mobilities at room temperature are typically around $1x10^{17}/cm^3$ and 350 cm^2/V s, respectively [2]. Although the donor identity has not been fully established [3,4,5], insulating and *p*-type films have been fabricated [6,7].

In this work we report the optical characterization of the crystalline quality, impurity, and defect content of thin film wurtzite GaN as determined by room temperature Raman scattering (RS) and low temperature photoluminescence (PL) spectroscopies. After a brief description of the deposition procedure for undoped and Mg-doped films, we will discuss the use of Raman measurements of undoped films to identify the crystal structure and to assess the material crystalline quality. We will also discuss PL studies of undoped and Mg-doped films, grown with either GaN or AlN buffer layers, to verify the incorporation of native defects and the activation of impurities.

EXPERIMENTAL

We have used basal plane sapphire substrates (1.25 cm x 1.25 cm) and a low pressure MOCVD (LPMOCVD) system operating at 76 Torr for deposition of undoped and Mg-doped films. Triethylgallium (TEG), triethylaluminum (TEA), and ammonia were used as the precursors. A detailed discussion of substrate preparation, precursor fluxes, and growth sequences steps is presented in Ref. 8. To reduce the large lattice mismatch between the GaN film and the sapphire substrate a thin (~ 400 Å) buffer layer of either AlN or GaN were deposited at 550 °C.

Mat. Res. Soc. Symp. Proc. Vol. 339. ©1994 Materials Research Society

This was followed by the deposition of GaN at a growth temperature of 1000 °C. The room temperature (RT) carrier concentration for films with thickness from 0.5 to 10.6 μm varied from 1.1 to $2.6x10^{17}/cm^3$ [3]. The Mg-doped film was deposited under conditions identical to those of the undoped films. The doping level was modulated by the flux of Mg precursor. Post deposition the Mg dopant species were activated using a thermal annealing under conditions identical to those used previously [5].

The RS measurements were carried out with a 0.85 m double grating (1200 gr/mm) spectrometer (spect. #1) coupled to a GaAs photomultiplier with a UV window, operated in a photocounting mode. We use the 488.0 nm laser line of an Argon ion laser and a spectrometer band pass of about 3.0 cm^{-1} for the room temperature RS experiments. The low temperature PL spectra were obtained with the samples placed in a continuous flow liquid helium cryostat and the temperature was kept constant at 6K. The samples were excited with the 351.1 nm (3.53 eV) and/or 325.0 nm (3.81 eV) lines from an argon ion laser and He-Cd laser, respectively. The emitted radiation was analyzed by the double spectrometer fitted with a 1200 gr/mm (spect. #1) or with a 1800 gr/mm (spect. #2) grating set. The spectral band pass at 500 nm was ≤0.1 meV and ≤1.1 meV for the high resolution (band edge emission) and low resolution (large spectral range), respectively. The PL measurements performed with spect. #1 show an enhanced instrumental response at the visible spectral range of the PL spectra. The PL spectra presented here have not been corrected for spectrometer responses.

RESULT AND DISCUSSIONS

Hexagonal GaN has the wurtzite crystal structure and belongs to the symmetry group C(6v) with two molecules in the unit cell. Therefore nine optical branches are expected, namely:

$$1A_1(TO)+1A_1(LO)+2B_1+1E_1(TO)+1E_1(LO)+2E_2$$

The TO and LO refers to transverse and longitudinal optics modes, respectively. The A_1 and E_1 modes are simultaneously Raman and IR active. The two B_1 modes are inactive (silent) and the two E_2 modes are only Raman active. All six allowed optical phonons has been observed previously by Raman spectroscopy [9,10].

The RS experiment was carried out using the film as thin-film waveguide [9]. With this geometry the laser beam propagates through the film parallel to the spectrometer entrance slit, increasing the scattering volume and the collection efficiency of the scattered light. A typical RS spectrum of GaN film is represented in Fig. 1. The polarization of the laser light was parallel to the c-axis. Only four lines associated with the GaN are clearly observed, corresponding to the $A_1(TO)$, $E_1(TO)$, E_2, and $E_1(LO)$, with Raman shift of 534.6 cm^{-1} (66.3 meV), 560.8 cm^{-1} (69.5 meV), 569.6 cm^{-1} (70.6 meV), and 742.2 cm^{-1} (92.0 meV), respectively. The phonons observed at 380.6 cm^{-1}, 419.9 cm^{-1}, and 646.1 cm^{-1} are due to the sapphire substrate. The high intensity, line shape, linewidth, and peak position of the phonon lines suggest that the material studied has high crystalline quality and exhibits the wurtzite structure.

The PL spectra of nominally undoped GaN films are characterized by an intense sharp line at about 3.472 eV and a broad band which peaks around 2.2 eV. The former has been assigned to excitons bound to shallow donor [3,11,12] and the latter may be associated with structural defects [5]. The thinner films (<4.0 μm) showed an additional band in the spectral range between 2.9 and 3.3 eV, which has been assigned to donor-acceptor (DA) pair recombination [13]. Since the relative intensity of these bands seems to vary from sample to sample, we carried out detailed PL study on a set of samples covering a range of film thickness from 0.5 to 11 μm. Although we have measured films deposited on GaN and AlN buffer layers, we will show only

spectra of films with AlN buffer layer. To verify if the defect incorporation is limited to the GaN/buffer layer interface region we performed PL measurements with illumination at the *front surface* (GaN growth surface) and *back surface* (GaN/buffer layer interface surface).

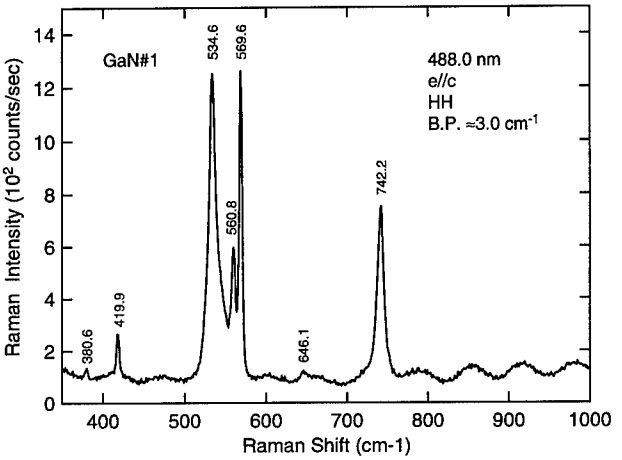

Fig. 1. Raman spectrum of an undoped GaN film at room temperature. Polarizations are listed in the figure.

The PL spectra of *front surface* (full line) and *back surface* (broken line) of a 3.3 μm thick film are represented in Fig. 2. The peak intensity of the edge emission in the *front surface* spectrum is about 68 times larger then the peak intensity of the edge emission in the spectrum of the *back surface*, the latter having broader linewidth then the former.

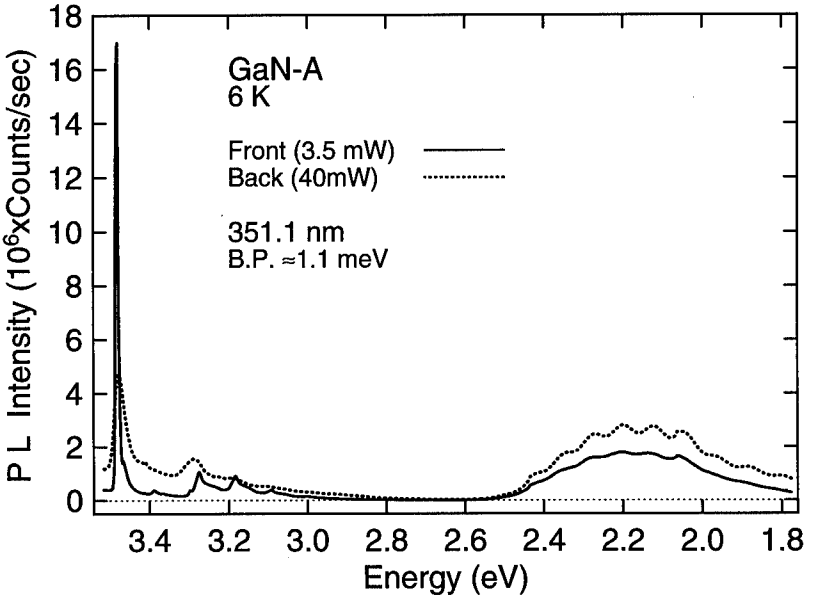

Fig. 2. PL spectra of a 3.3 μm undoped film. The continuous line and dashed line spectra represent the *front* and *back surfaces*, respectively.

In Fig. 3 we show the PL spectra of a 10.6 μm thick film, where the spectrum of the *back surface* has been normalized to the edge emission intensity of the *front surface* spectrum. The normalization factor was 1.36. Note that the linewidth of the edge emission and the peak intensity of the 2.2 band in both spectra have about similar values.

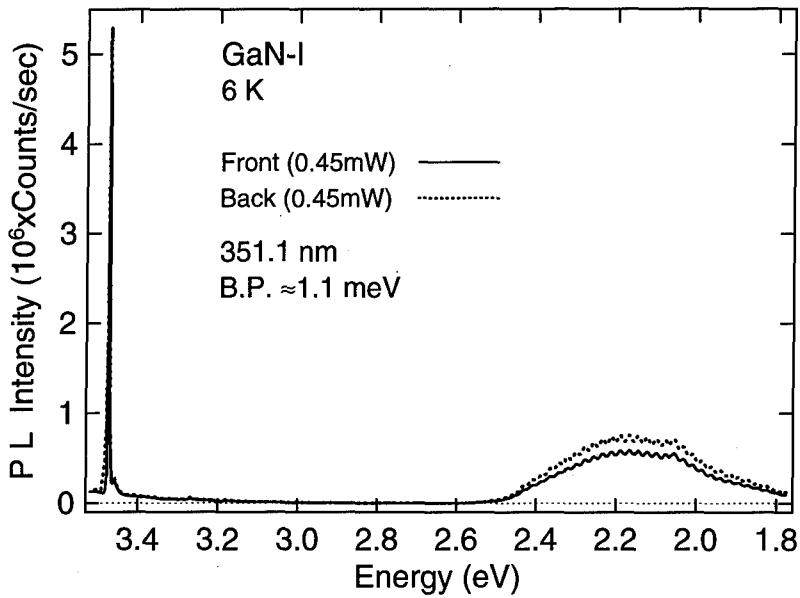

Fig. 3. PL spectra of a 10.6 μm undoped film. The *back surface* spectrum has been normalized to the edge emission of the *front surface* spectrum.

The exciton peak intensity ratio between *front* and *back surfaces* (I_f/I_b) increases with increasing film thickness and reaches a maximum value at film thicknesses ~ 4.0 μm. However, the ratio for the ~10 μm thick film; $I_f/I_b \approx 1$. We have also observed a systematic shift of the exciton peak position to higher energies and a reduction of the exciton full width at half maximum (FWHM) with increasing film thickness. The broad band at 2.2 eV was observed in all films independent of film thickness. However, this band intensity becomes weaker in both the *back* and *front surface* spectra with increasing film thickness. This behavior is evident in Fig. 3. Therefore the thin films are not homogeneous, but the homogeneity improves as the films grow thicker, presumably as a result of annealing at the growth temperature. Note that the donor-acceptor band between 2.9 and 3.3 eV, although weak, is still observed. This band's intensity relative to the edge emission is large only in the very thin films, suggesting that these defects are incorporated mostly during the initial growth, which we believe are different from the defects associated with the edge and the 2.2 eV emissions. To emphasize the high quality of thick films, we show in Fig. 4 the high resolution PL spectrum of the edge emission of the sample represented in Fig. 3. The linewidth of 2.7 meV is one of the narrowest reported to date for high quality GaN films.

Fig. 5 shows the PL spectra of the *back* and *front surface* of a Mg-doped GaN film. The largest differences between the two spectrum are the complete quenching of the 3.472 eV and the 2.2 emission bands observed in the *back surface* spectra. An intense band centered around 3.1eV

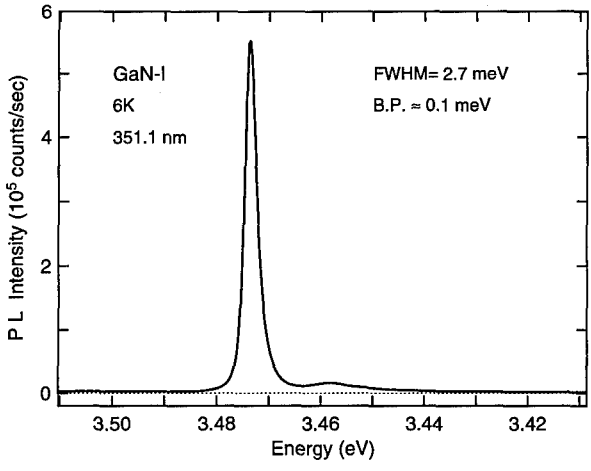

Fig. 4. High resolution PL spectrum of the band edge emission of the sample represented in Fig.3.

dominates the *front surface* spectrum. This band is made up of a strong zero phonon line (ZPL) at 3.260 eV associated with distant DA pairs and its LO-phonon replicas (separated by 92 meV). We also observed weak features associated with excitons bound to neutral Mg-acceptors and one phonon replica. Due to the high quality of the film, both spectra in Fig. 5 are modulated by the interference fringes. Equivalent spectrum for Mg-doped GaN has been reported previously [15].

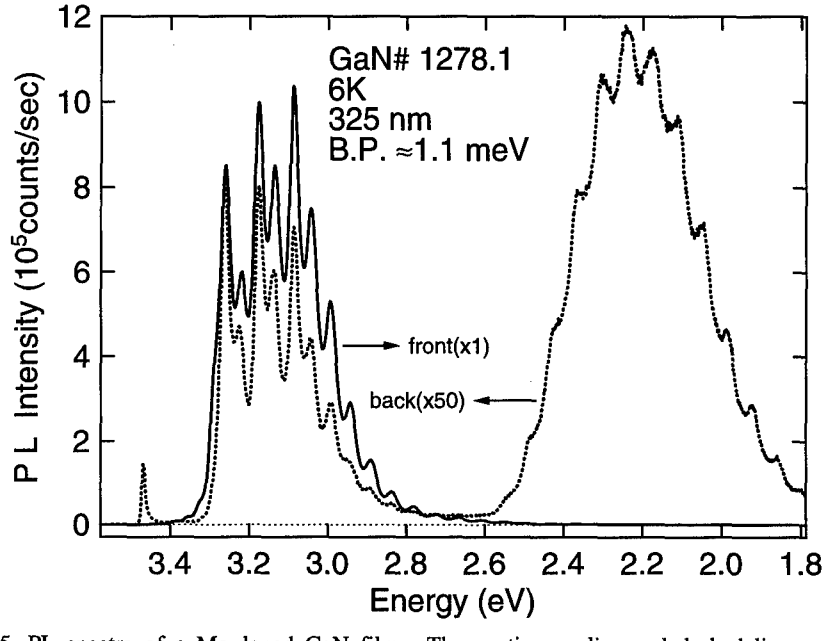

Fig. 5. PL spectra of a Mg-doped GaN film. The continuous line and dashed line spectra represent the *front* and *back surfaces*, respectively. The *back surface* spectrum intensity was normalized to the ZPL intensity of the *front surface* spectrum.

SUMMARY

We have presented results of our RS and PL measurements on nominally undoped and Mg-doped GaN films deposited onto sapphire substrates. The Raman results shown that high crystalline quality wurtzite GaN films have been deposited. The PL studies of undoped films indicate that the quality and homogeneity of the growth layers improve with increasing film thicknesses. Although we presented only results on films deposited with AlN buffer layers, we have observed the same behavior for the films deposited with GaN buffer layers [4,14]. The PL spectra of Mg-doped films is characterized by an intense emission band associated with DA recombination processes.

ACKNOWLEDGMENTS

This work was partially supported by Navy Contract No. N00014-91-C-0065 and was monitored by Max Yoder of the Office of Naval Research.

REFERENCES

1. For a detailed review on III-V nitrides, see S. Strite and H. Morkoç, J. Vac. Sc. Technol. B **10**, 1237 (1992).
2. M.A. Khan, J.N. Kuznia, J.M. Van Hove, and D.T. Olson, Appl. Phys. Lett. **58**, 526 (1991).
3. M.A. Khan, D.T. Olson, J.N. Kuznia, W.E. Carlos, and J.A. Freitas, Jr., J.Appl. Phys. **74**, 5901 (1993).
4. W.E. Carlos, J.A. Freitas, Jr., M.A. Khan, D.T. Olson, and J.N. Kuznia, Phy. Rev. B **48**, 17878 (1993).
5. E.R. Glaser, T.A. Kennedy, H.C. Crookham, J.A. Freitas, Jr., M.A. Khan, D. T. Olson, and J.N. Kuznia, Appl. Phys. Lett. **63**, 2673 (1993).
6. M.A. Khan, R.A. Skogman, J.M. Van Hove, D.T. Olson, and J.N. Kuznia, Appl. Phys. Lett. **60**, 1366 (1992).
7. H. Amano, M. Kito, and K. Hiramatsu, Jpn. J. Appl. Phys. **28**, L2112 (1989).
8. M.A. Khan, J.N. Kuznia, J.M. Van Hove, and D.T. Olson, Appl. Phys. Lett. **58**, 526 (1991).
9. G. Burns, F. Dacol, J.C. Marinace, B.A. Scott, and E. Burstein, Appl. Phys. Lett. **22**, 356 (1973).
10. A. Cingolani, M. Ferrara, M. Lugarà, and G. Scarmacio, Sol. St. Comm. **58**, 823 (1983).
11. R. Dingle, D.D. Sell, S.E. Stokowski, M. Ilegems, Phys. Rev. B **4**, 1211 (1971).
12. H.G. Grimmeis and B. Monemar, J. Appl. Phys. **41**, 4054.
13. R. Dingle and M. Ileglems, Sol. St. Commun. **9**, 175 (1971).
14. W.E. Carlos, J.A. Freitas, Jr., M.A. Khan, D.T. Olson, and J.N. Kuznia in Defects in Semicondoctors 17, edited by H. Heinrich and W. Jantsch, (Trans Tech Publications, Switzerland; Mat. Sc. Forum, **143-147**, 1994), pp. 99-104.
15. M. Ilegems and R. Dingle, J. Appl. Phys. **44**, 4234 (1973).

REDISTRIBUTION OF HYDROGEN IN GaN, AlN, and InN

J. M. Zavada*, R. G. Wilson**, S. J. Pearton*** and C. R. Abernathy***
* U.S. Army Research Office, Research Triangle Park, NC 27709
** Hughes Research Laboratories, Malibu, CA 90265
*** Department of Materials Science & Engineering, University of Florida, Gainesville, FL 32611

ABSTRACT

Hydrogen incorporation during gas-phase growth of III-V nitrides is thought to play an important role in determining the apparent doping efficiency, due to unintentional passivation of dopants. Hydrogen implantation can also be used for electrical and optical isolation of neighboring devices, as in other III-V materials such as GaAs. We have implanted ^2H at 40 keV to doses of 5 x 10^{15} cm^{-2} at room temperature into epitaxial layers of GaN, AlN and InN grown by MOMBE on GaAs substrates, and measured the ion ranges and hydrogen redistribution upon subsequent furnace annealing. The hydrogen profiles remain unchanged for annealing temperatures up to 800-900°C for GaN and AlN, and 600° for InN. Samples were also deuterated from an ECR plasma at 250 or 400°C for 30 min, producing ^2H incorporation depths of $\leq$ 1 μm in GaN. With annealing, there is no significant hydrogen redistribution observed at temperatures up 800°C. Hydrogen concentrations remain in the range ~ 10^{19} cm^{-3} under these conditions. At 900°C considerable hydrogen outdiffusion to the surface occurs. The thermal stability of hydrogen in these III-V nitride films indicates the need for post-growth annealing at high temperatures to achieve appreciable doping efficiencies.

INTRODUCTION

Recently, III-V nitride semiconductors have attracted considerable interest due to their potential applications including blue light emitting devices, high temperature electronics, and highly stable encapsulant films on semiconductor devices[1-6]. Two main difficulties prevent their further development. First is the lack of suitable substrate materials and the other is the difficulty of achieving useful p-type doping levels, on the order of 10^{18} cm^{-3}, particularly in GaN. Amano et al.[3] and Nakamura et al.[7] found that a low energy electron beam irradiation treatment after metal organic chemical vapor deposition growth of Mg-doped GaN produced higher p-type doping levels. Thermal annealing of these films in a N_2-ambient led to dramatic decreases in resistivity (from 10^6 Ω cm to 2 Ω cm) for temperatures between 500 - 700°C.[5] This increase in effective p-type doping level may be due to dehydrogenation of passivated Mg acceptors[8,9]. Similarly, hydrogenation at 500°C of p-type GaN films grown by molecular beam epitaxy has been shown to reduce hole concentrations by an order of magnitude[10].

Hydrogen is likely to be a common impurity in III-V nitride materials due to incorporation during gas-phase growth, plasma-enhanced chemical vapor deposition, proton implantation for device isolation, and wet or dry etching processes. All of these procedures have been shown to produce significant hydrogen concentrations in other III-V

Mat. Res. Soc. Symp. Proc. Vol. 339. ©1994 Materials Research Society

materials[11]. Clearly, the electrical effects as well as the thermal stability of hydrogen in III-V nitride semiconductor epilayers is of interest.

Here we report on the incorporation of hydrogen in III-V nitrides and its redistribution upon subsequent furnace annealing. The work is aimed at clarifying the thermal stability of hydrogen in III-V nitride semiconductor epilayers. Hydrogen was incorporated in the epilayers either by implantation or plasma treatment. Hydrogen implantation into III-V compound semiconductor crystals generally leads to a neutralization of charge carriers, primarily through induced crystal damage. Plasma hydrogenation of the same crystal materials also results in a reduction of charge carriers, but through a passivation mechanism involving hydrogen-dopant atom complexes. Consequently, the physical characteristics of material methods are different after these two techniques.

EXPERIMENTAL PROCEDURES AND SIMS ANALYSIS

The III-V nitride epilayers were grown on semi-insulating GaAs substrates at ~500°C using a metalorganic source, molecular beam epitaxy (MOMBE) machine. Group III metalorganics, triethylgallium, trimethylindium and trimethylamine alane, were used for the Ga, In, and Al sources, respectively. Atomic nitrogen was generated by a 200 W, 2.45 GHz electron cyclotron resonance (ECR) source (Wavemat MPDR) on an Intevac gas source Gen II molecular beam epitaxy system[12]. Optical emission spectroscopy of the ECR N_2 plasmas confirms the presence of a significant atomic nitrogen density at the sample position. The films were polycrystalline with a mixture of hexagonal and cubic phases in each case. There is a large lattice mismatch between the nitride epilayers and the GaAs substrate, nearly 45 % for either GaN or AlN, and about 30 % for InN. Both the GaN and AlN were insulating while the InN was strongly n-type (~ 3×10^{20} cm^{-3}), which may be due to N vacancies[13]. Layer thickness were 1 - 1.5 μm for each material.

Atomic deuterium (^2H) was introduced into GaN, AlN, and InN epilayers either by implantation or plasma treatment. The nitride samples were implanted with $^2H^+$ ions at 40 keV to a dose of 5×10^{15} cm^{-2} at room temperature. Companion samples exposed to a pure $^2H^+$ plasma for 30 min at either 250 or 400°C using the ECR source on the MOMBE system. The applied microwave power was 200 W, the deuterium flow rate 20 standard cubic centimeters per minute and the pressure ~ 5×10^{-5} Torr. Annealing was performed under a flowing N_2 ambient for 20 min at temperatures up to 900°C in the conventional proximity geometry. Depth profiles of the deuterium were obtained from secondary ion mass spectrometry (SIMS) measurements using a Cs^+ ion beam and detecting negative secondary ions. The background subtracted detection sensitivity for ^2H in the III-V nitrides was approximately 10^{17} cm^{-3}. The depths were determined based on surface profilometry of the SIMS craters, with an error of about 7%.

Figure 1 displays the SIMS depth profiles of implanted ^2H in GaN. There is a change in the SIMS Ga sensitivity factor between the GaN epilayer and the GaAs substrate. This is indicated by the decrease in the Ga level at a depth of about 0.8 μm, which is the apparent thickness of the epilayer. The shoulder on the bulk side of the ^2H profile at the same approximate location may be due to crystal imperfections or SIMS yield variations. Post-implant annealing up to 800°C did not lead to any redistribution of the deuterium, but approximately 90% of the deuterium was lost upon 900°C annealing. The original ^2H profile shape is retained, indicating that the deuterium appears to decorate

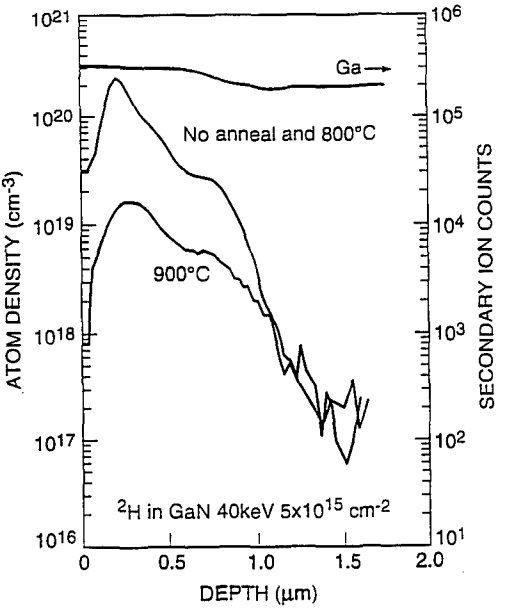

Fig. 1. SIMS depth profiles of ^{2}H implanted into GaN at an energy of 40 keV and at a dose of 5 x 10^{15} cm^{-2}, followed by annealing at 800 and 900°C.

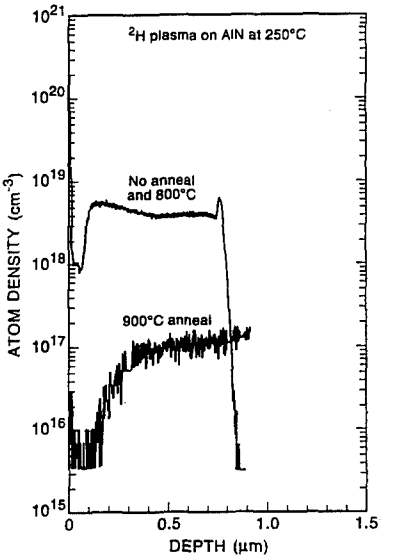

Fig. 2. SIMS depth profiles of ^{2}H in AlN after exposure to a deuterium plasma for 30 min at 250°C, and after subsequent furnace annealing at 800 and 900°C.

the residual implant damage, as was reported previously for GaAs[14]. Ion-induced nuclear stopping damage apparently is also quite stable in GaN and high annealing temperatures (well in excess of 900°C) may be necessary for good electrical activation of implanted dopants.

The redistribution of implanted ^2H in GaAs crystals is in marked contrast to the behavior shown in Fig. 1. In GaAs, redistribution of implanted ^2H begins at about 250°C and terminates at about 650°C[14]. The more rapid redistribution in GaAs appears related to its smaller bandgap and larger crystal lattice.

Figure 2 shows the ^2H depth profiles in deuterium plasma-treated AlN. In this case, the samples were protected from oxidation by the presence of a thin (0.1 μm) GaN cap layer. During hydrogenation at 250°C, the ^2H ions penetrated easily into the AlN and reached concentrations as high as $5x10^{18}$ cm^{-3}. It is assumed that the ^2H atoms are bonded to residual impurities or native defects in the AlN epilayer. While the ^2H atoms permeated the entire AlN layer, only a very small amount diffused into the substrate. There was a slight accumulation of ^2H at the AlN/GaAs interface. This accumulation is due to the large density of defects in this region and has been previously observed in hydrogenated GaAs epilayers grown on a Si substrates[15]. There is little accumulation of ^2H at the GaN/AlN interface, which is nearly lattice matched. While there was no significant redistribution of ^2H with annealing up to 800°C, most of it outdiffused to the surface at 900°C.

These results are also very different from similar studies in GaAs. Hydrogen depth profiles in plasma-treated GaAs typically show concentrations on the order of 10^{18} cm^{-3} over a depth of several μms. Annealing for 5 min at 350°C has been shown to lead to significant ^2H redistribution indicating relatively weak bonding between ^2H and the crystal defects[16].

SIMS depth profiles for implanted ^2H in InN are shown in Fig. 3. The InN epilayer was uncapped. Post-implantation annealing at 600°C failed to produce any appreciable ^2H redistribution in InN. Since the equilibrium vapor pressure of N_2 over InN at 600°C is several Torr, annealing at higher temperatures would require substantial N_2 overpressures and was not performed. The thermal stability of the ^2H profiles in these materials is again very high compared to other III-V semiconductors[14].

We measured similarly high thermal stabilities in the III-V nitrides for other normally rapidly diffusing species in III-V materials, such as Be. This emphasizes the ability of these nitrides to act as stable encapsulants for other semiconductors during high temperature processing. It is likely that dopant diffusion in nitride heterojunctions should be less of an issue than in more conventional III-V semiconductors, where rapid diffusion of Be, Mg. Zn, and Cd during epitaxial growth or subsequent processing, of laser or heterojunction bipolar transistor structures, leads to junction displacement and severe deterioration of the device performance.

DISCUSSION

Our results show that of all the III-V and group IV semiconductors investigated to date, the nitrides exhibit the greatest thermal stability for retaining hydrogen. This stability of hydrogen in GaN, AlN, and InN suggests that the amount of hydrogen in the growth or processing ambient for these materials should be minimized to avoid unintentional passivation effects. This may be less of a problem in conventional molecular beam

epitaxy where there is only a residual background component of hydrogen in the growth chamber. In metal-organic based growth techniques, the role of hydrogen in passivating dopants could be substantial, as indicated by the results of Nakamura et al.[5] The use of NH_3 as the nitrogen source is also a potential supplier of significant quantities of hydrogen.

In summary, we have investigated the redistribution of ^2H in GaN, AlN, and InN epilayers in which incorporation of ^2H was accomplished through ion implantation and plasma treatment. In either case, relatively high annealing temperatures were required to cause ^2H redistribution. Annealing in the range 500-600°C did not produce any motion of implanted ^2H in the nitride films. Only with annealing at temperatures ~ 800-900°C did ^2H redistribution occur. In the plasma-exposed nitride films, it was found that ~ 1 μm thick layers are completely permeated within 30 min at 250 or 400°C. The deuterium does not show any significant redistribution upon subsequent annealing until ~900°C. These results are consistent with the post-growth annealing experiments where dopant reactivation occurred at ≤700°C, since this requires only a breaking of the hydrogen-dopant bond and does not result in macroscopic movement of the hydrogen. The high thermal stability of hydrogen in the III-V nitrides combined with its ready entry into these materials suggests that unintentional hydrogen passivation occurring during growth or processing is likely to be a significant effect.

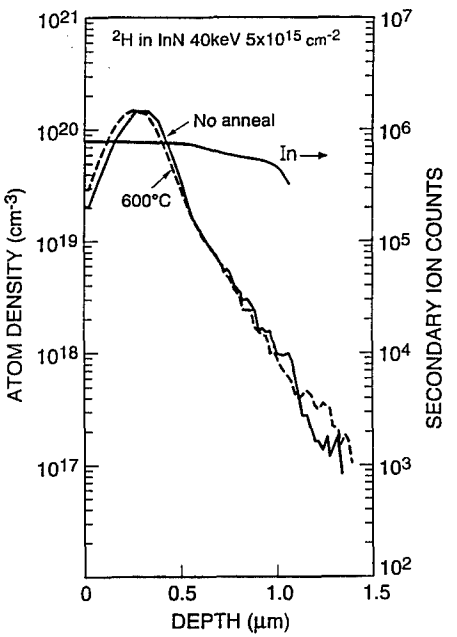

Fig. 3. SIMS depth profiles of ^2H implanted into InN at an energy of 40 keV and at a dose of 5 x 10^{15} cm^{-2}, followed by furnace annealing at 600°C.

ACKNOWLEDGMENTS

The authors acknowledge the support of their colleagues C.W. Magee (Evans East, Inc.), F. Ren and P. Wisk (AT&T Bell Laboratories) during the course of this work. Portions of this work were supported by the U.S. Army Research Office.

REFERENCES

1. S. Strite and H. Morkoc, J. Vac. Aci. Technol. B**10**, 1237 (1992).
2. T. Matsuoka, T. Sasaki and A. Katsui, Optoelectronics - Devices and Technologies **5**, 53 (1990).
3. H. Amano, M. Kito, K. Hiramatsu, and I. Akasuki, Jap. J. Appl. Phys. **28**, L2112 (1989).
4. M.A. Khan, J.N. Kuznia, D.T. Olson, M. Blasingame and A.R. Bhattarai, Appl. Phys. Lett. **63**, 2455 (1993).
5. S. Nakamura, T. Mukai, M. Senoh and N. Iwasa, Jap. J. Appl. Phys. **31**, L139 (1992).
6. R.F. Davis, Proc. IEEE **79**, 702 (1991).
7. S. Nakamura, M. Senoh, and T. Mukai, Jap. J. Appl. Phys. **30**, L1708 (1991).
8. S. Nakamura, N. Iwasa, M. Senoh and T. Mukai, Jap. J. Appl. Phys. **31**, 1258 (1992).
9. J.A. Van Vechten, J.D. Zook, R.D. Horning, and B. Goldenberg, Jap. J. Appl. Phys. **31**, 3662 (1992).
10. M. S. Brandt, N. M. Johnson, R. J. Molnar, R. Singh, and T. D. Moustakas, Appl. Phys. Lett. (To be published).
11. See for example, Hydrogen in Compound Semiconductors, edited by S.J. Pearton (Trans-Tech Publishers, Zurich 1993).
12. C.R. Abernathy, P. Wisk, S.J. Pearton and F. Ren, J. Vac. Sci. Technol. B**11**, 179 (1993).
13. J. I. Pankove, Mat. Res. Soc. Conf. Proc. **162**, 515 (1990).
14. J.M. Zavada and R.G. Wilson, in Hydrogen in Compound Semiconductors, edited by S.J. Pearton (Trans-Tech Publishers, Zurich 1993).
15. J. M. Zavada, S. J. Pearton, R. G. Wilson, C. S. Wu, M. Stavola, F. Ren, J. Lopata, W. C. Dautremont-Smith, and S. W. Novak, J. Appl. Phys. 65 347 (1989).
16. S. J. Pearton, W. C. Dautremont-Smith, J. Lopata, C. W. Tu and C. R. Abernathy, Phys. Rev. B**36**, 4260 (1987).

INFRARED LUMINESCENCE FROM MOCVD GaN

M. W. LEKSONO, C. H. QIU, W. MELTON, AND J. I. PANKOVE
Department of Electrical and Computer Engineering, University of Colorado, Boulder, CO 80309-0425

ABSTRACT

An infrared emission peak at 1.25 eV is observed from a GaN film which exhibits strong yellow luminescence peaking at 2.15 eV. It is most efficient at a temperature of 160 K. The full width at half maximum (FWHM) of the IR peak is 0.17 ± 0.01 eV, which is about 1/3 that of the yellow peak.

INTRODUCTION

GaN is a potentially important wide band-gap semiconductor for high temperature electronics and blue/UV emitters [1-3]. Such applications are encouraged by the successful demonstration of p-type doping in GaN [4,5]. GaN would be additionally useful in optical fiber communication if optical emission at 1.3 μm or 1.5 μm could be obtained from GaN. Yellow luminescence at 2.15 eV is frequently observed in undoped GaN; it originates either from some defects (such as those due to ion implantation and thermal annealing [6]) or from carbon impurities [7]. We note that Ogino and Aoki [7] attributed the yellow emission to electron recombination from the conduction band edge to a level 0.86 eV above the valence band edge. It is thus interesting to investigate the possibility of optical emission from this level to the valence band, since it would produce an emission at 1.44 μm. Furthermore, the origin of the infrared luminescence peak at 1.3 eV, observed by Pankove et al. from undoped GaN [8], was not understood.

EXPERIMENTAL RESULTS

Thin films of GaN were grown in a cold-wall low pressure metalorganic chemical vapor deposition (MOCVD) system. Before deposition, the R-plane sapphire and basal plane sapphire substrates were degreased and cleaned in boiling phosphoric acid. They were rinsed in deionized water and blown dry before loading into the load lock. The base pressure of the MOCVD reactor is in the low 10^{-8} torr. The substrate was pretreated at 1100 °C in hydrogen. The triethylgallium (TEG) is transported into the reactor by hydrogen carrier gas. The ammonia flow rate is 500-1000 times that of the hydrogen carrier gas. The total pressure during deposition is around 3 torr. Typical deposition rate is 1μm/h. The deposited films are epitaxial GaN as shown by X-ray diffraction. Their

Mat. Res. Soc. Symp. Proc. Vol. 339. ©1994 Materials Research Society

appearance is slightly yellowish and milky. Hall measurements indicate n-type conduction, with a carrier mobility of 10-50 $cm^2/Vsec$ and an electron concentration of 10^{18}-10^{20} $/cm^3$.

The cathodoluminescence (CL) is excited by a model VP-052 electron gun (Thermionics), with a beam current of 12.5 μA and an accelerating voltage of 15 kV. The vacuum during measurement is usually better than 10^{-6} torr. The visible-UV luminescence is detected by an RCA 31025 photomultiplier, while the infrared-visible luminescence is detected by a PbS photodetector cooled by dry ice.

In the visible-UV region, most samples exhibit at room temperature a strong yellow luminescence peaking at 2.15 eV with a FWHM of 0.45-0.51 eV, and a sharp and weaker edge luminescence peaking at 3.40 eV. In the near infrared region, an emission peak at 1.25 eV can be observed (Fig. 1). The yellow peak appears red-shifted to 2.06 eV, because the PbS detector is less responsive to photons with higher energies. The signal to noise ratio improves when the sample is cooled to T<200K.

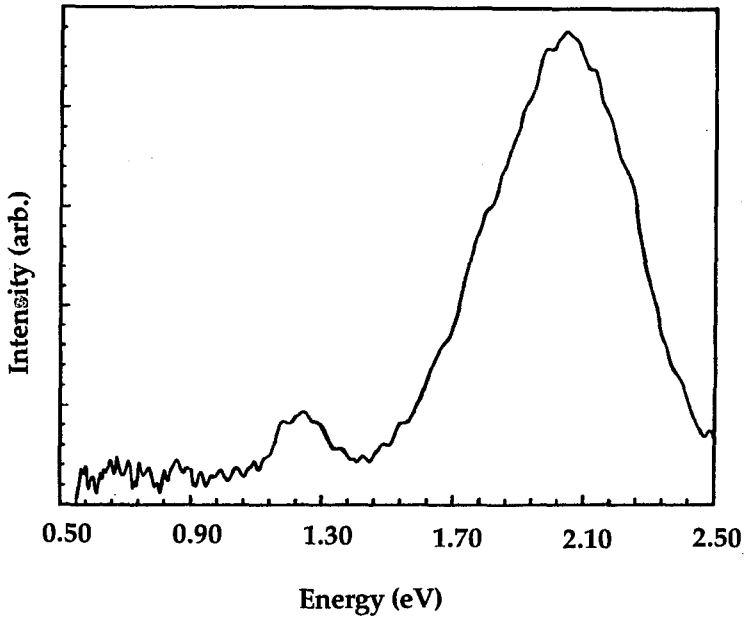

Fig. 1. CL spectrum at 160K from a GaN film deposited on R-plane sapphire.

At the lowest temperature measured (8K), the IR emission peaks at 1.27 eV. As the temperature increases to 300 K, the peak position decreases slightly to 1.24 eV. Over the temperature region of 8K-300K, the IR emission peak is much narrower than the yellow emission peak. The FWHM is 0.17±0.01 eV.

The intensity of the IR emission peak, as well as the intensity ratio of the IR peak to the yellow peak (I_{IR}/I_{yellow}), are shown in Fig. 2 as a function of temperature. The IR emission is most efficient at around 160 K, and becomes less efficient at either lower or higher temperatures. The yellow peak decreases slightly in intensity with increasing temperature, as reported previously by Ogino and Aoki [7]. The intensity ratio I_{IR}/I_{yellow} is slightly higher at higher temperatures. Note that the detector response is not corrected in Fig. 2. Since the detector is less responsive to the higher energy photons, we expect that the actual intensity ratio I_{IR}/I_{yellow} should be smaller than that in Fig. 2.

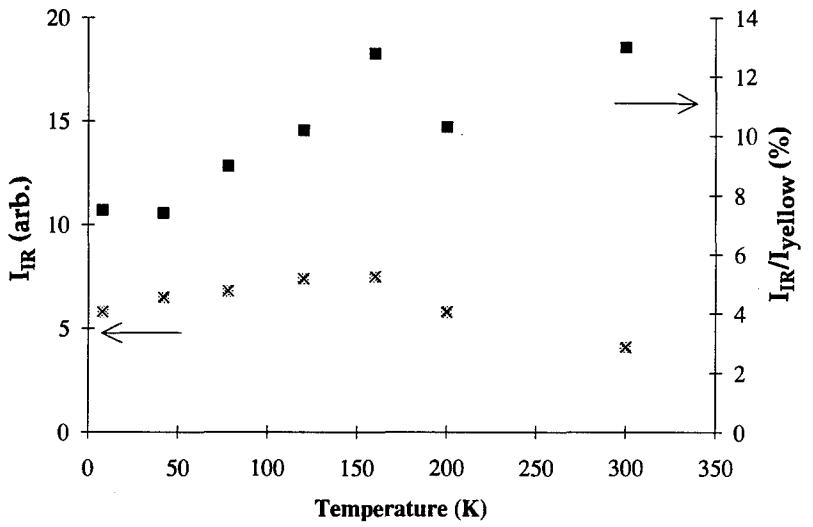

Fig. 2. The temperature dependencies of the peak intensity of the infrared luminescence, and the intensity ratio of the infrared to the yellow emission peaks.

DISCUSSION

Note that the IR peak was only observed from a sample which exhibits strong yellow luminescence. The IR peak may be the same IR peak at 1.3 eV as observed in 1970 by Pankove et al. [8]. Since last summer, our film growth has improved so that even the yellow luminescence peak is quite weak, which makes the observation of the IR peak difficult because the PbS detector is not sensitive enough.

We tentatively suggest that the IR emission is the complementary step to the yellow luminescence. The sum of the peak energies, 2.15 eV (yellow)+1.25 eV (IR), matches closely the edge luminescence at 3.40 eV. The much narrower IR peak might indicate that only a narrow portion of the defect states is involved in the IR emission. A schematic diagram of the recombination process is shown in Fig. 3.

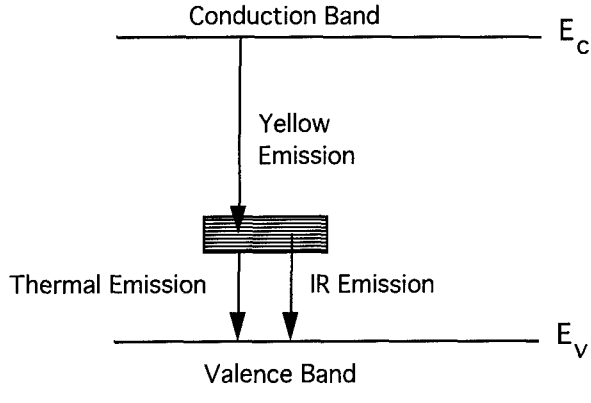

Fig. 3. Proposed diagram for the luminescence scheme.

In our model, only transitions from the top portion of the defect band to the valence band gives rise to infrared emission. We can interpret the temperature dependence of the IR emission in the following way. At low temperatures, most of the electrons thermalize to the bottom of the defect band. As the temperature increases, some of the electrons are excited to the top portion of the defect band and lead to an increase in the IR emission. When the temperature is increased above 160 K, the thermal emission from the defect band to the valence band becomes important, hence the IR emission efficiency decreases.

Now, we would like to point out what caution one needs to take in order to derive the position of a defect level from the temperature dependence of the intensity of a luminescence peak. An Arrhenius plot of the intensity dependence usually measures the activation energy of the non-radiative process that competes with the radiative process. This is not a determination of the energy level with respect to the band edges. In fact, the procedure used by Ogino and Aoki may not be valid. This argument is demonstrated by the following derivation.

The electron occupation probability f_n of the defect level is [9]:

$$f_n = (e_p + nb_n)/ (e_n + e_p + nb_n + pb_p) \qquad (1a),$$

where n is the electron density in the conduction band, p is the hole density in the valence band, e_n is the emission coefficient of an electron from the defect level to conduction band, e_p is the emission coefficient of a hole from the defect level to valence band, b_n is the electron capture coefficient of the defect level, and b_p is the hole capture coefficient of the defect level. *Note that both e_n and e_p contain thermal and optical contributions.* Since the defect level is more than 2 eV away from the conduction band, one may neglect the thermal contribution to e_n in the temperature region. Thus, we have

$$f_n = 1/[1 + 1/r] \qquad (1b),$$

where

$$r=(e_p + nb_n)/pb_p \qquad (1c).$$

The hole occupation probability of the defect level f_p is:

$$f_p = 1 - f_n = 1/[1 + r] \qquad (2).$$

To use equation (2) to deduce the energy position of the defect level, one needs to assume that both nb_n and pb_p terms do not depend on temperature. In addition, one needs to assume that e_p is the thermal emission coefficient without any optical contribution.

CONCLUSIONS

An infrared emission peak at 1.25 eV is observed from a GaN film which exhibits strong yellow luminescence peaking at 2.15 eV. We tentatively suggest that the IR emission is the complementary step to the yellow luminescence.

ACKNOWLEDGMENT

This work was supported by DARPA-URI grant UFLOR-OCG0845B and monitored by Dr. A. M. Goodman of ONR.

REFERENCES

1. J. I. Pankove, Mat. Res. Soc. Symp. Proc. **97**, 409 (1987).
2. J. I. Pankove, RCA Review **34**, 336(1973).
3. J. I. Pankove, IEEE Transactions on Elec. Devices Ed **22**, 721(1975).
4. H. Amano, M. Kito, K. Hiramatsu, and I. Akasaki, Jpn. J. Appl. Phys. **28**, L2112(1989).
5. S. Nakamura, M. Senoh, and T. Mukai, Jpn. J. Appl. Phys. **30**, L1708(1991).
6. J. I. Pankove and J. A. Hutchby, J. Appl. Phys. **47**, 5387(1976).
7. T. Ogino and M. Aoki, Jpn. J. Appl. Phys. **19**, 2395(1980).
8. J. I. Pankove, J. E. Berkeyheiser, H. P. Maruska, and J. Wittke, Solid State Commun. **8**, 1051(1970).
9. C. Qiu and D. Han, Phys. Rev. B**37**, 10912(1988).

ELECTRONIC STRUCTURE OF DIAMOND, SILICON CARBIDE, AND THE GROUP-III NITRIDES

WALTER R. L. LAMBRECHT
Department of Physics, Case Western Reserve University, Cleveland, OH 44106-7079

ABSTRACT

This paper describes the trends in the electronic structure of diamond, silicon carbide, the group-III nitrides and some related materials. The relationships between the electronic band structures in the zincblende and wurtzite structures are adressed. For SiC, the discussion is extended to other polytypes. The trends with ionicity and atomic number are explained. The purpose of this discussion is to help identify the similarities and differences between the various classes of wide bandgap semiconductors. The strain effects on the band structure are discussed and calculated elastic constants are given for SiC, GaN and AlN. Spectroscopic probes of the band structure such as photoemission and UV-reflectivity are discussed for GaN and SiC. Materials with the formula II-IV-N_2 are proposed to be an interesting complement to the III-N's. In particular, $BeCN_2$ is a direct gap semiconductor with elastic properties close to those of diamond and may also be useful as a bufferlayer for diamond growth.

INTRODUCTION

Diamond, silicon carbide and the group-III nitrides are all recognized as promising materials for novel semiconductor applications because of their wide band gaps. Their intrinsic properties related to their wide band gaps, often summarized in the Johnson [1] and Keyes [2] figures of merit, give them clear potential advantages over silicon and gallium arsenide for high-speed, high-power, and high-temperature devices. In addition, they are "hard" materials in the sense of having high elastic constants and large cohesive energies and are generally resistant to harsh environments, including radiation. In the area of optoelectronics, they may fulfill the need for materials emiting light of short wave lengths. Blue light emission is needed for full color displays and UV emission is optimal for optical communications because of its higher information density.

While each of these materials clearly has advantages over silicon and other more traditional III-V and II-VI semiconductors, the question arises how they compare relative to each other. Specifically, what are their similarities and differences which may give one of these a unique advantage for a particular application? This paper attempts to provide at least partial answers to this question by describing the trends in basic physical properties among these and related materials. An important question in this context is: How well do we actually know the basic properties of these materials? Often the properties quoted in the literature are based on early measurements on materials of poor quality. We believe that now that materials growth and purity problems are being solved, the time is ripe to re-carefully evaluate the basic properties of these materials. In some cases, the intrinsic materials properties can at present be calculated from first-principles accurately enough to set the standard for what high-quality material should achieve. This is, for example, the case for elastic constants and band-structure deformation potentials. The computational aspects and theoretical framework will be described along with the results. Besides the better materials quality, another aspect makes it worthwile to restudy the fundamental properties such as the electronic structure of these materials. Compared to the situation at the time of the pioneering studies on these materials, the theoretical capabilities have greatly improved. For example, comparison between calculated and experimental photoemission

Mat. Res. Soc. Symp. Proc. Vol. 339. ©1994 Materials Research Society

Table I: Some key properties* of diamond, SiC, GaN and AlN

	diamond-C	SiC	GaN	AlN
ELECTRONIC				
E_B (10^5 V/cm)	100	40	20	
v_{sat} (10^7 cm/s)	2.7	2.5 (for 3C)	2.0	
E_g (eV)	5.5	2.4–3.3	3.5	6.3
	indirect	indirect	direct	direct
THERMAL AND DIELECTRIC				
κ (W/cm K at 300 K)	20	5	1.5	3.2
ϵ_0	5.5	9.7	9.5	9.1
ϵ_∞	5.5	6.5	5.0	4.8
COHESIVE AND ELASTIC				
bond strength (eV/bond)	3.7	3.2	2.2	2.9
B (10^2 GPa)	4.4	2.2	2.0	
STRUCTURAL				
bond length (Å)	1.54	1.88	1.95	1.89
π bonded structures	yes	no	no	no
number of known polytypes	2	~100	2	2

* E_B, v_{sat}, κ, ϵ_0 from [3], bond energies from [4] remaining quantities from [5].

and UV-reflectance spectra allowed us to probe many-body effects beyond the single particle band-structure picture.

This paper is mainly concerned with the intrinsic properties of the materials. Of course, many practical problems remain to be solved to achieve the promise of these materials. As such, the present state of progress of each of the above identified classes of materials is quite different and each has its own set of problems which are most immediate. We will only briefly comment on those because we here want to emphasise the long-term perspective and address the question for which areas each of one of these materials may ultimately find a unique advantage.

RELATIONSHIPS AMONG FUNDAMENTAL PROPERTIES

To start our comparison of diamond, silicon carbide and the group-III nitrides, we consider some of the key properties of interest for electronic devices given in Table I for diamond, silicon carbide and two representative III-nitrides: GaN and AlN

Johnson [1] proposed that the key parameters for high-frequency and high-power transistors are the breakdown field and the saturation drift velocity (for SiC, the latter depends on the polytype with the highest value corresponding to cubic SiC). The saturation drift velocity is a rather complex quantity depending on various scattering processes and details of the band structure. A complete theory of how to calculate it from first principles is not available. We may note that it appears to be of the same order of magnitude for diamond, SiC and GaN. From the first part of Table I, one would conclude that diamond has a factor of two or more advantage over other wide gap semiconductors mainly as a result of its higher breakdown field. Breakdown again is a complex phenomenon involving avalanche ionization of defects. The ideal Zener breakdown field, however, is directly proportional to the magnitude of the band gap and from this point of view, we would seem to want gaps as large as possible. As far as the gaps themselves are concerned, nitrides seem to be leading with gaps as high as 6.3 eV for AlN and even 6.4 eV for

c-BN. Furthermore, the wurtzite compounds AlN, GaN and InN all have direct gaps while SiC, diamond and c-BN all have indirect gaps. This is an important advantage for optoelectronic light-emitting devices and we will thus discuss in some detail what determines the directness or indirectness of the gaps.

Also, the question arises whether a material closer in overall properties to diamond exists which would have a direct gap. We have recently shown [6, 7] that $BeCN_2$ in the chalcopyrite structure indeed has a direct gap. This material, which combines only elements of the second row of the periodic table has a volume per atom and elastic properties intermediate between diamond and BeO, i.e. it is more diamond-like than silicon-carbide-like. It remains to be synthesised, but calculations of the energy of formation of it and related beryllium compounds suggest this should be possible [8]. We expect π-bonding to be supressed in this case because of the higher ionicity. Indeed, π-bonded structures also do not occur for BeO [9]. We note that an entire class of materials with formula II-IV-N_2, with the group-II element being Be or Mg and the group-IV one either C or Si, has quite interesting band structures and may deserve some more experimental attention [7].

Keyes [2] argued that ultimately the limiting factor for high frequency high-power devices is how fast the heat can be dissipated, thus placing strong emphasis on the thermal conductivity κ. Also, the speed with which charge can be moved around in space in a device is roughly speaking inversally proportional to the dielectric constant. Again, we see that diamond has important advantages from this point of view with a factor four to its nearest competitor (SiC) in thermal conductivity and a factor two in the static dielectric constants. The main reason why the other materials have larger static dielectric constants (ϵ_0) is that they have an ionic contribution related to the motion of the ions. Their high frequency dielectric constants (ϵ_∞) are roughly inversally proportional to the gap and thus also of the order of 5–6, i.e. comparable to that of diamond.

Since these materials are insulating their high thermal conductivity is clearly phonon-mediated. The intrinsic materials quantities determining the heat-conductivity are thus the sound velocities, which are high because of the high elastic constants. Following Slack [10], the thermal conductivity κ at room temperature scales with $\bar{M}\delta\theta_D^3$ where $\bar{M}$ is the average mass per atom, δ is half the effective cubic lattice constant and θ_D is the Debye temperature. The latter is proportional to $B^{1/2}$ with B the bulk modulus, which gives a convenient measure for the elastic strength of the materials. The latter and the high cohesive energy is also what provides all these materials' resistance to adverse environments and radiation damage. In fact, a number of processes leading to damage such as vacancy production, dislocation kink formation and migration, all scale with the bond strength. This is also of crucial importance for high power operation because of thermal creation of defects often limits performance and lifetime of devices. The bulk modulus of diamond (and c-BN) is larger than that of SiC by a factor 2 and also its bond energy (cohesive energy per bond with respect to neutral atoms) is significantly higher than for the other materials. It is indeed well-known that diamond is the hardest material known and as such finds numerous applications of a mechanical nature. This is closely related to its short bond length and hence high number density.

From the above, it appears that diamond has significant advantages over the other materials, except for the indirectness of the gap. From a structural point of view, however, carbon has an important disadvantage. That is the occurence of a competing structure, namely graphite. In fact, there exists a whole series of forms of carbon such as fullerenes, which are all characterized by π bonding. BN also has a layered graphite-like structure with π bonding (namely h-BN) while this is not the case for SiC or the other III-nitrides. In several respects, in fact, BN is more similar to diamond than to the other III-nitrides. This indicates that the key to understanding their properties is the fact that C, B and N all are from the second row of the periodic table while the other compounds contain one element from this row combined with elements from other rows of the periodic table. Below, we will discuss how this is reflected in more detail in the trends in

the band structure.

The existence of π bonded structures for C and BN and absence of it for the other materials is arguably the major factor holding up progress in crystal growth of diamond and c-BN. In fact, for these materials heteroepitaxial growth of single crystal films is still a major challenge. Recent calculations suggest that the interplay between graphitic and tetrahedral bonding may play an important role in the nucleation step of diamond [11]. Hydrogen saturation essentially converts planar hexagonal sp^2 bonding into sp^3 bonding. When this happens at the edge of a graphite layer, it leads to a curling of the graphite sheet in such a way that it can bond to the next graphite layer. The resulting hydrogenated prism-plane surface structure forms an ideal nucleus for subsequent diamond-growth. Experimental evidence that the nucleation step of diamond occurs through a graphitic intermediate in the manner described above is still accumulating. For example, Fallon and Brown [12] using energy electron loss spectroscopy (EELS) in a scanning transmission electron microscope found evidence for graphitic amorphous carbon trapped at grain boundaries in diamond films. Although this does not prove that this layer originates from the nucleation step, it is suggestive of it. Very interestingly, Davidson and Pickett [13] recently predicted that diamond surface layers may graphitize near steps. This suggests that step growth on diamond may take place through a graphitic intermediate as well. Relatedly, Koizumi and Inuzuka [14] have shown that in diamond growth on c-BN, graphitic carbon can be detected near steps in the early stages.

Another major impediment for diamond epitaxial growth is its very high surface energy and the lack of any tetrahedrally bonded substrate with close lattice matching besides c-BN which itself suffers from the same problems as diamond. The above mentioned $BeCN_2$ and related tetrahedrally bonded new materials with lattice constants intermediate between SiC and diamond may be helpful in this context.

For SiC, another structural problem is the existence of a large number of closely related crystal structures, called polytypes, corresponding to slightly different stackings of what are the {111} layers in the cubic polytype (3C) (sometimes called β-SiC) and the {0001} layers in hexagonal polytypes (collectively denoted α-polytypes). While this may seem a disadvantage, it may actually turn out to be an advantage if the polytype growth can be controlled. They are in some sense natural superlattices of a special type, namely superlatttices with twin planes as boundaries. Important progress has been made not only in understanding the origin of polytypism [15], but also in its empirical control during growth [16]. This does not imply that one follows from the other! At present, polytype control is still a largely empirical achievement without guidance from first principles thermodynamics. Surface step control, purity, surface diffusion controlled by surface temperature, etc. seem to play a more important role in the growth than does bulk thermodynamics. In the present paper, we explore some of the consequences of polytypism for the electronic structure. Although the nitrides naturally occur in the (hexagonal) wurtzite form (referred to as 2H in the case of SiC), the zincblende form can be stabilized epitaxially. We will show that the changes in band structure between wurtzite and zincblende are very similar in diamond, SiC and the nitrides and are an important ingredient in understanding the directness or indirectness of the gaps.

There are many other relationships among the properties of these materials that are worthwhile exploring. For example, the bond strengths clearly must play a role in the ease with which native defects are produced and as such in the ease with which these materials can be doped. The band-structure alignment at heterojunctions and in alloys plays also a role in the doping problem. Other papers in this conference deal with the doping issue. Phonons and electron-phonon coupling are important for the high-temperature electronic transport. We have only just started to explore this by evaluating some of the band-structure deformation potentials [17, 18].

In summary, diamond (and c-BN) have intrinsically superior properties than the other wide-gap semiconductors, but are much more difficult to grow. The III-nitrides (AlN, GaN, InN)

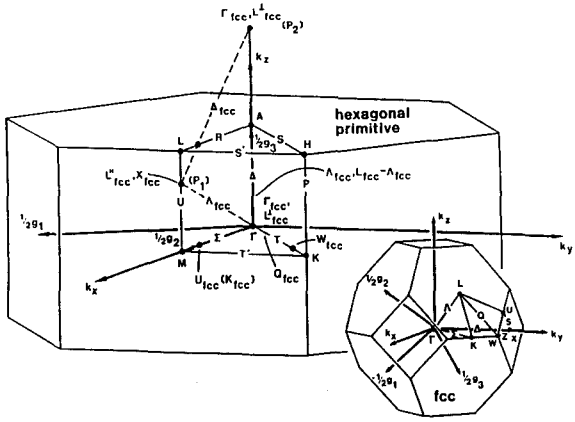

Figure 1: Relation between hexagonal and cubic Brillouin zones

have an important advantage for optoelectronics because of their direct gaps. Materials quality, however, is at present highest for SiC. It is the only material for which large high-purity single crystal films can presently be fabricated. Because of the close lattice match between SiC and the nitrides, one may expect that SiC will also play an important role as substrate for the III-nitrides. There is thus ample reason to study each of these materials in detail.

STRUCTURAL EFFECTS ON THE ELECTRONIC BAND STRUCTURE

In this section, we focus on the effects of polytypism on the electronic band structure. Since these are most complex in SiC, we focus on it. We first review the basics about polytypism. The two "extreme" polytypes are zincblende (pure cubic stacking) and wurtzite (pure hexagonal stacking). While commonly the stacking is described by ABC for cubic and AB for wurtzite, it is important to notice that actually it is sufficient to inspect the bonding between two succesive layers to distinguish cubic from hexagonal stacking. For hexagonal stacking, the bonds are eclipsed and the hexagonal rings joining the layers are "boat"-shaped, while for the cubic stacking, the bonds are staggered and the rings are all "chair"-shaped. (Of course, the fact that we already attach bonds in a certain direction on the second layer, implies the position of the atoms in the third, so there is no contradiction!) In fact, associating a fictitious spin to each layer, one may then describe two hexagonally stacked layers by a change in spin direction, while cubic stacking corresponds to parallel spins. Wurtzite is then described as $\uparrow\downarrow$ periodically repeated, while cubic is described by $\uparrow\uparrow\downarrow$ periodically repeated. In a similar manner, the common hexagonal polytypes of SiC, 4H and 6H, and the rhombohedral polytype 15R are respectively described by $\uparrow\uparrow\downarrow\downarrow$, $\uparrow\uparrow\uparrow\downarrow\downarrow\downarrow$, and $\uparrow\uparrow\uparrow\uparrow\downarrow$, periodically repeated. A single spin-flip in an otherwise cubic structure corresponds to a twin boundary. It is thus sufficient to tell the number of parallel spins or distance between succesive twin boundaries to identify a polytype. This is the principle of the Zhdanov [19] notation, in which 2H is described as $\langle 1 \rangle$, 4H as $\langle 2 \rangle$, 6H as $\langle 3 \rangle$, 15R as $\langle 23 \rangle$ and 3C as $\langle \infty \rangle$. The overall structure in some cases has hexagonal symmetry (denoted by nH) and in some cases rhombohedral (denoted by nR) The number in front of the H or R notation indicates the translationally periodic repeat length in the c-direction perpendicular to the layers.

Inside each layer, the crystal structure consists of chair-shaped hexagons in each case. By aligning the hexagons in the layers in cubic and hexagonal structures, the reciprocal spaces can

be related and provide a common framework for comparing band structures among polytypes. Among the various hexagonal polytypes, the nH polytype has a repeat length along the c-axis of $n/2$ times that of the wurtzite structure. Thus, its Brillouin zone (BZ) is essentially a $n/2$ times folded version of the wurtzite one in the c-direction. We can either fold the wurtzite bands $n/2$ times or unfold the 4H and 6H bands to make the comparison. The relation between the cubic and wurtzite conventional Brillouin zones is slightly more involved [20] because it involves a rotation of coordinate axes from the usual cubic ones to a frame in which the cubic [111] direction is parallel to the hexagonal [0001] direction and the cubic $[10\bar{1}]$ is parallel to the hexagonal $[11\bar{2}0]$ direction. Since the wurtzite primitive cell contains two formula units and the zincblende only one this leads to a somewhat complicated folding of the zincblende band structure in the wurtzite Brillouin zone. See Fig. 1. For example, going along the [111] direction, one goes from $\Gamma_c \equiv \Gamma_h$ to A_h to the $L_c \equiv \Gamma_h$ point. Thus both L_c and Γ_c eigenvalues appear at Γ_h. The subscripts c and h here denotes cubic or hexagonal. Because a particular L point or [111] direction among the eight equivalent ones is chosen along the [0001] direction, it and its counterpart in the $[\bar{1}\bar{1}\bar{1}]$ are denoted as $L_\perp$ (i.e. perpendicular to the basal plane). The other six L points are denoted $L_\parallel$ and are folded onto the hexagonal $M - L_h$ or U_h axis. They occur at 2/3 of the height from M to L for the ideal c/a ratio. This point is indicated as P_1 in Fig. 1. The cubic X_c points are also folded onto these $U_h(2/3) \equiv P_1$ points. The $L - W_c$ or Q_c axis is folded along with the Σ_c or $\Gamma - K_c$ axis on the hexagonal T_h or $\Gamma - K_h$ axis. W appears at 3/4 the $\Gamma - K_h$ distance while K_c lies outside the first BZ along this direction. The cubic K_c point also appears on the hexagonal $\Gamma - M_h$ axis at 3/4 of the distance. Finally, we note that the hexagonal polytypes contain a six-fold screw axis along the c-axis (with varying pitch for the different polytypes) and thus have non-symmorphic space groups. As a result of this and time-reversal [21], there is a degeneracy of the bands on the BZ face perpendicular to the c-axis. Armed with this background, we can now describe the changes in the band structure with polytype.

The calculations of the electronic band structure were performed using the linear muffin-tin orbital method in the atomic sphere aproximation (ASA) [22]. Empty spheres were chosen in the manner described in [23] and differ for the various polytypes. For example, the 2H polytype contains a large open channel which is best represented by two large empty spheres. The spacing between the two atoms eclipsing each other near a twin boundary only leaves space for a small empty sphere. Similar elongated interstitial spaces exist in 4H and 6H. The calculations also include the combined correction and are performed for the ideal c/a ratio and experimental volume per atom. The potential is determined self-consistently within the local density functional approximation (LDA) [24] using Hedin-Lundqvuist parametrization [25]. For the k-point sampling 12–24 special k-points were used for the hexagonal polytypes and 10-16 for the cubic case. Tests showed that the k-point sampling was adequately converged. For 2H-SiC we also performed so-called full-potential (FP) calculations, i.e. all-electron calculations without any shape approximation, using the approach described by Methfessel [26].

Fig. 2 shows the bands of 3C, 2H, 4H and 6H SiC. Comparing first 2H and 4H-SiC, one may notice that essentially the bands in the 2H $A - L - H$ plane (surface of the 2H-BZ) are folded onto the $\Gamma - M - K$ plane of the 4H-BZ. However, the forced degeneracy is lifted and leads to a small splitting. A non-symmorphic symmetry related degeneracy appears on the new 4H $A - L - H$ plane. Similarly, the bands of 6H are folded in three. This implies that the eigenvalues of the $L - A - K_{2H}$ plane are folded onto the new $L - A - K_{6H}$ plane while the new eigenvalues appearing in the $\Gamma - M - K$ plane correspond to the eigenvalues in a plane at 2/3 of the height along the c-direction of the 2H-BZ. This is illustrated in Fig. 3 for the lowest conduction bands along the $M - L$ axis. The reason for emphasizing this part of the band structure is that this is the region of the BZ where the minimum band gap occurs for all polytypes considered except for 2H. One may notice that a band-crossing in 2H along this axis appears to be lifted by a gradually increasing interaction going from 4H to 6H. We may also notice that the occurence of an odd

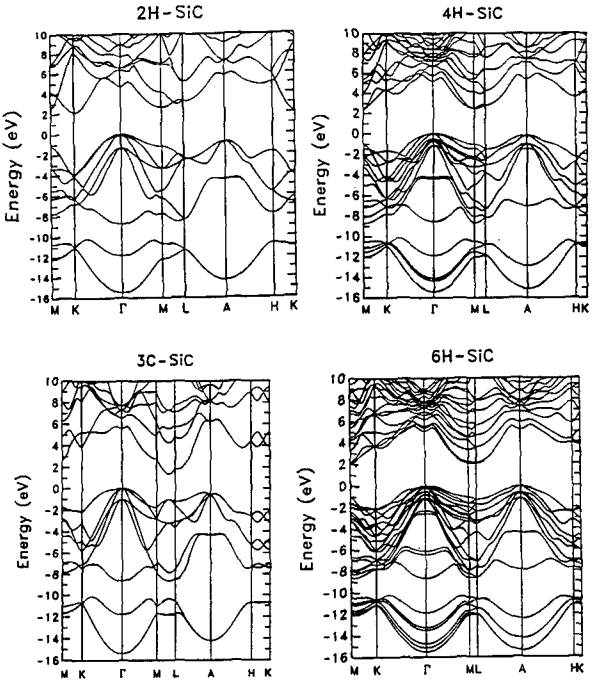

Figure 2: Band structure of 3C, 2H, 4H, and 6H SiC

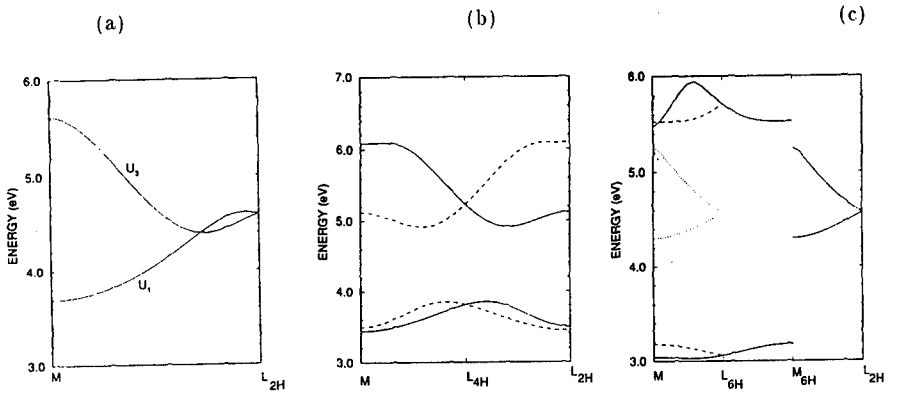

Figure 3: Conduction bands along $M - L_{2H}$ for (a) 2H-SiC, (b) 4H-SiC, and (c) 6H-SiC; (folding indicated by dashed lines).

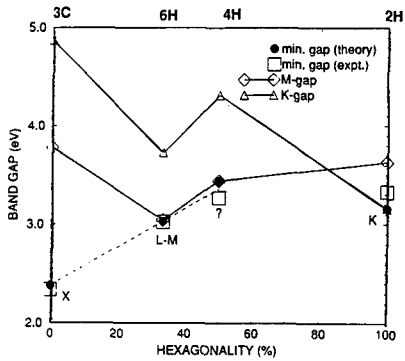

Figure 4: Band gaps in SiC polytypes

or even number of foldings of the bands of the 2H zone makes a qualitative difference. Indeed, this leads to a degeneracy at the folded out L_{2H} point for 6H but not for 4H. These symmetry constraints on the band-structure have an important effect on where the minimum occurs. For 4H we find two closely spaced minima at M (one related to M_{2H} and one to L_{2H}). For 6H, the minimum lies along the $L-M$ axis (leading to 6 instead of 3 equivalent valleys) but stays close to M. The minimum in 3C occurs at the X_c point, or, on $M-L$ 2/3 of the way to L. We note that for 4H, there are indirect experimental indications that the minimum may lie at an even lower symmetry point with 12 equivalent minima [27]. This is based on the number and spacing of phonon replicas in photoluminescence spectra from the N-donor. We do not find evidence for this in our present band structure. We note, however, that the present band structure for 4H was calculated within the ASA. For 2H, for which we did both ASA and FP calculations, the bands along $M-L$ are found to be rather insensitive to the non-spherical corrections to the potential. Nevertheless, we cannot completely exclude the possibility that the minimum for 4H would occur at a point of lower symmetry. FP calculations are in progress to sort this out.

For 2H-SiC, the minimum gap occurs at the K point instead of along the $M-L$ line. We found it essential to perform a FP-LMTO calculation to obtain this result. In the ASA, the minima at M and K are nearly degenerate. Fig. 2 show the bands of 3C in the 2H-BZ for easy comparison to the other polytypes. Comparing 3C and 2H, one notices that the conduction band state X_{1c}^{zb} moves up going from 3C to 2H while the state K_{2c}^{wz} moves up going from 2H to 3C. Here the subscript indicates the symmetry representation of the particular state with c indicating that it is a conduction band state and the superscript indicates that the k-point notation is for the zincblende (zb) or wurtzite (wz) structure irrespective of whether the structure actually is 3C or 2H. In both cases, the gap is larger for the structure in which the corresponding k-point has a reduced symmetry. Inspection of the wavefunction of the K_2^{wz} state shows that it is a purely $p_{x,y}$ state in 2H, i.e. only contain p-orbitals perpendicular to the c-axis. In the 3C structure, the symmetry of this k-point is reduced and the eigenvector contains also s and p_z components. (We ignore d-components throughout this discussion.) The lower symmetry allows for more interactions with valence band states and apparently leads to the the upward shift of this state. Fig. 4 shows an overview of the minimum gaps as a function of hexagonality of the polytype. (Hexagonality is defined as the fraction of sites with local hexagonal stacking.) We note that hexagonality alone does not completely describe the differences in the band structure

in the sense that the band gaps do not vary monotonically with it. For example, the $\Gamma - K$ gap is closer to that of 2H in 6H than in 4H. Also, while the minimum gap along the $M - L$ axis indeed varies nearly linearly with hexagonality, there are qualitative changes in the bands depending on whether the number of foldings of the 2H-zone is even or odd. This will lead to different effective mass tensors, differences in possible scattering mechanisms between equivalent or nearly equivalent minima and hence in the mobilities. We note that important differences between the mobilities between 4H and 6H SiC, and particularly, their anisotropy were reported at this meeting by Schaffer *et al.* [28]. Our present band structures for 6H predicts a larger anisotropy of the effective mass than in 4H, the $m_{||}$ being roughly twice that in the c-direction in 6H than the $m_{\perp}$ masses of either 6H or 4H. The nearness of the equivalent U-valleys at positive and negative k_z along the c-axis in 6H and the shallow barrier between them suggests that one might effectively treat them as a single (double minimum) valley with an even larger mass $m_{||}$. This corresponds to the assumption that scattering between such nearby valleys is easy and would lead to the prediction of an even a larger anisotropy in the mobilities than that due to the masses in each U-valley alone. At present, however, we cannot yet provide a quantitative description of this effect. These differences in the conduction band minimum energy surface will also influence the nature of shallow donor states. A complete theory of these effects remains to be constructed.

For the nitrides, the same systematic shifts occur for eigenvalues at K_h, M_h and X_c. Their trends will be discussed in the next section. The same changes also occur between lonsdaleite (hexagonal packing) and diamond (cubic stacking) as shown by Salehpour and Satpathy [20]. Even for BeO, the same trends persist [29]. This strongly indicates that it is a genuine structural effect, largely independent of the atomic potentials.

TRENDS WITH IONICITY AND ATOMIC NUMBER

As mentioned earlier, the key feature shared by diamond, SiC and the group-III-Nitrides is that they contain an element of the second row of the periodic table. Since the latter (C and N) do not have p-like core-states below the 2p valence level, they have rather deep valence levels with rather compact orbitals. In fact, the 2s and 2p orbitals have about equal spatial extent as opposed to later rows where the p-like valence orbitals tend to be more diffuse than the s-like orbitals. This plays a role in why π bonding is favored for the second row elements [30]. Indeed, it means that there is less advantage in $s-p$ promotion to form directed bonds because π bonding between p-orbitals is an alternative effective way to strengthen the bonds. It means that these elements have a choice between sp^3 hybridisation or sp^{3-n} hybridization complemented by n π bonds. It is also the basic reason why the covalent component of the bonding is stronger than for other group-IV or III-V semiconductors. This leads to small lattice constants, high cohesive energies and large elastic constants and hence "hardness" in a general sense.

Table II: $X_1^c - X_3^c$ splitting (in eV) as a function of polarity (α_p).

	α_p	$\lvert X_1^c - X_3^c \rvert$ (eV)
BP	0.018	0.25
SiC	0.473	3.27
AlN	0.807	7.29

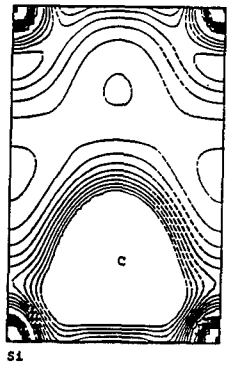

Figure 5:Total charge density of 3C-SiC in {110}-plane

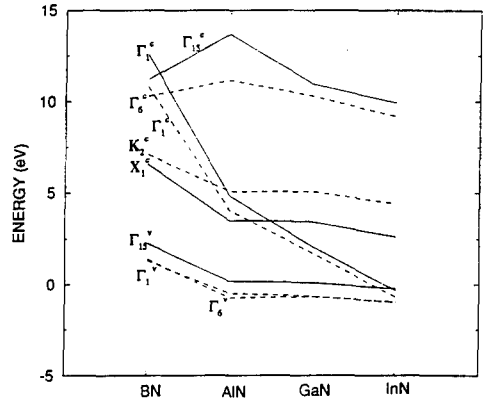

Figure 6: Trends in the eigenvalues of the group-III nitrides solid lines: zincblende, dashed lines: wurtzite

It also leads to large gaps, not only because of the high covalent component, but also because of the large ionic component. Even in SiC, a IV-IV compound, the bonding has a significantly ionic character because of the large energy difference between the Si (3s, 3p) and C (2s, 2p) valence levels. A plot of the charge density (calculated using the ASA for the potential but not for the final charge density), displayed in Fig. 5 clearly shows the strong asymmetry between Si and C. This ionic component is even stronger in the nitrides because of the additional effect of the valency difference. Interestingly, for the borides [31] (BP, BN, BAs) there is instead a reduction in ionicity. This results from the fact that it is the group-III element (normally the cation!) that comes from the second row of the periodic table and hence has a low-lying level. As a result, the ionicity of BP and BAs is so low that the ionic character is reversed: *i.e.* B becomes the anion, in the sense that it draws more charge around it than P or As. This has been noted to have important effects for the bonding at interfaces between these and related materials [31]. It also can be seen clearly in certain band splittings, *e.g.* the $X_1^c - X_3^c$ splitting in these compounds in the zincblende structure as can be seen in Table II.

Next, we consider the trends of the eigenvalues with cation in the series of nitrides as shown in Fig. 6. Full details of the calculations of the band structures of these compounds can be found in [34]. Fig. 6 shows the important eigenvalues near the gap, i.e. the valence band maximum Γ_{15}^v for ZB or Γ_1^v and Γ_6^v for wurtzite, the conduction band Γ_1^c and K_2^c for WZ and X_1^c for ZB which are "competing" for the minumum. The conduction band Γ_1^c states in both wurtzite and zincblende are mostly s-like (actually purely s-like in ZB) and, being antibonding states, have important cation-s components. One may see that these states show the largest variation with atomic number, and, in particular, are monotonically decreasing with increasing atomic number. Of course, the above statement requires that we compare the different band structures with respect to the same reference level. The natural reference level used here is the ASA zero of energy [32] which coresponds to the average of the point charge electrostatic potential and is close to the average potential in the interstitial region. This is not sufficiently accurate to determine band-offsets because that requires consideration of charge transfer but is sufficient for our present qualitative discussion. The reason for the downward trend with atomic number is well known and also ocurs for example in the series C-Si-Ge-Sn. It is simply due to the fact that s-orbitals have a

Table III: Polarities (α_p) calculated from TB-ASA-LMTO potential parameters.

	SiC	BN	AlN	GaN	InN	BP	AlP	GaP	AlAs	GaAs
α_p	0.473	0.475	0.807	0.771	0.792	0.018	0.490	0.451	0.443	0.404

non-zero value at the nucleus and as such feel the $-Z/r$ potential. Thus, heavier elements have lower s-levels with respect to corresponding p-levels. Since the Γ_1 state is s-like and the X_1^c-level in zincblende (or diamond) is a mixture of s and p-like components and the K_2^c state in wurtzite or londaleite is purely p-like, this explains why diamond, SiC and BN are indirect gap materials in either zincblende or wurtzite structure while GaN and InN are direct in both. AlN turns out to be indirect in the zincblende structure and direct in the wurtzite. Even in WZ, however, the indirect and direct gap in AlN are close to each other. Fig. 6 shows that the variation of Γ_1^c is linear from Al to In but has a different slope between B and Al. This emphasizes again the peculiar role of the second row elements. In addition, the Γ_{15}^c state is lower in c-BN than the Γ_1^c state. This again is a manifestation of the relative energies of p and s-levels and thus a result, once again of the absence of a p-like core for 2p wave functions. We note that the levels shown are LDA levels and that the latter is known to underestimate conduction band levels. This problem is well understood. As will be discussed in a later section, the difference between the self-energy of quasiparticles and the LDA exchange-correlation potential to a good approximation leads to a constant upward shift of the conduction bands. It is noteworthy that for zb-InN, the LDA gap is actually negative while the real gap is 1.9 eV. The latter is thus almost entirely due to the self-energy correction.

The tight-binding ASA-LMTO method may be used to define a polarity or ionicity scale [33]. The polarities of some of the compounds of interest here are given in Table III. It shows that BN has an ionicity close to that of SiC and distinctly lower than that of the other nitrides. This is a consequence of the low-lying 2p-level in the second row group-III element B as discussed above. This is also probably related to the fact that for BN the zb structure is more stable than the wz, while all other nitrides prefer the wz structure. Ionicity indeed is known to favor wurtzite [15, 35]. Ionicity also explains why the bandgap variation is so much stronger in the III-N series than in the III-As or III-P series. The reason is that the high ionicity makes the cation component of the Γ_1^c state relatively more important. The lower ionicity of GaP compared to GaN, for example, explains why GaP has an indirect gap. Indeed, the Γ_1^c state having a smaller Ga (heavy element) component is less sensitive to the nuclear potential and lies relatively higher with respect to the Ga_p–P_s like X_1^c state. By the time we get to GaAs, the anion is also a heavier element and thus it also tends to bring the Γ_1^c state down with respect to p-like states. Ionicity also explains why SiC is indirect in both structures while AlN is only direct in wurtzite. The reason is that SiC being less ionic has a relatively smaller component of the Si (i.e. "heavier" element) in the conduction band Γ_1^c state. We note that even for Si, the p-like Γ_{15}^c state lies below the s-like Γ_1 state.

Obviously, these insights in the trends are important for the understanding of alloys and heterostructures. We have performed calculations for SiC–AlN [34], SiC–BP [8], diamond–c-BN [36] and AlN–GaN alloys [37] and heterojunctions [31, 38, 39]. We briefly mention here that charge re-arrangements are generally found to be more important in the heterovalent systems. They lead to important dipole contributions to the offset and to extemely large bowings for the band gap variation with concentration. For $Al_xGa_{1-x}N$, on the other hand, the bowing is very small [37]. In that case, the above discussed trends help to explain the cross-over from direct to indirect gaps.

Table IV: Calculated cubic elastic constants (in GPa) for AlN, GaN, and SiC and Γ_{TO} phonon frequencies ($\hbar\omega_{TO}$) (in cm^{-1}); experimental values in parentheses

	AlN	GaN	SiC
C_{11}	304 (328)[a]	296 (264)[a]	420 (390)[b]
C_{12}	152 (139)	154 (153)	126 (142)
C_{44}	199 (133)	206 (68)	287 (256)
$\hbar\omega_{TO}$	702 (668)[c]	603 (550)[d]	796 (796)[e]

[a] Sherwin and Drummond [43]
[b] Arlt and Schodder [44]
[c] Sanjurgo *et al.* [41]
[d] Using wurtzite data from Perlin *et al.* [45].
[e] Olego and Cardona [46].

ELASTIC CONSTANTS AND STRAIN EFFECTS

Elastic constants being integral total energy properties are rather insensitive to the details of the band structure. Thus, it is a good approximation to derive the elastic constants for wurtzite from those of zincblende by transforming the tensor with the appropiate coordinate rotation. Martin [40] showed that the difference between the nearest neighbor tetrahedra in the two cases, which are twinned with respect to each other, can easily be taken account as a correction. This correction is in fact small for the materials considered here. Similarly [41], one can define an effective cubic TO-phonon frequency by $\omega_{TO}^2 = [\omega_{TO}^2(A_1) + 2\omega_{TO}^2(E1)]/3$ in terms of the wurtzite A_1 and E_1 phonon modes. Elastic constants have been calculated in our group using full-potential LMTO for zincblende SiC, [17], GaN [18], AlN and InN [42]. In all cases the best or only direct experimental data available are for hexagonal polytypes. The experimental values shown below are derived from those by the inverse tensor transformation.

In contrast to the other elastic constants and to ω_{TO}, the C_{44} are not in good agreement with experimental data for AlN and GaN. For GaN this is probably due to the fact that the experimental values quoted are not based on sound velocity measurements, which normally give the most accurate elastic constants, but on indirect methods such as X-ray diffraction linewidths [47] measured on powders. For AlN, the crystalline quality may have been a problem. Because of the excellent agreement (10 %) of our calculations with experiment for the related total energy quantities, such as the cubic Γ_{TO} phonon freqeuncy, we believe that our calculated values are more accurate than currently available measurements for the elastic constants. This suggests an important need to redetermine elastic constants on high-quality crystals of these materials. The availability of better crystals and new techniques for working with smaller samples are promising for this purpose.

The band structure changes under uniaxial and hydrostatic strains are important for two reasons. First, epitaxial films are often subject to biaxial strains due lattice mismatch to the substrate. Second, uniform strains correspond to the long-wavelength limit of acoustic phonons. The acoustic deformation potentials, which are obtained from the band-structure shifts due to these strains, can be shown to give the strength of the long-wavelength electron-acoustic-phonon coupling. Since electron scattering by phonons is dominant at high temperatures, these deformation potentials play an important role in high-temperature electronic transport theory. We have calculated the important deformation potentials for Si (as a test) [42], SiC [17, 48] and GaN[18] and are currently working on those for AlN and InN.

SPECTROSCOPIC PROBES OF THE ELECTRONIC BAND STRUCTURE

While band structures can nowadays be calculated from first principles, a reality check by comparison to spectroscopic data remains important. Furthermore, the various spectroscopic probes provide information on the many-body effects beyond the standard LDA treatment used for the band-structure calculations. We illustrate this here with the photoemission and UV-reflectivity studies of GaN.

Ga3d and In4d effects

Within a simple single-particle picture, X-ray photoemission spectroscopy (XPS) probes the density of occupied states. An interesting aspect of the GaN band structure is the overlap of the Ga3d bands with the N2s. This hybridization is important for a correct description of the total energy properties and has been the subject of discussion between pseudopotential and all-electron calculation practioners for GaN [49, 50, 51]. While the Ga3d also play a role in GaAs, their effect is more pronounced in GaN because of their overlap with the relatively deep N2s band. This leads to a significant dispersion of the Ga3d levels into bands. In addition, the relatively short distance between Ga atoms in GaN causes significant dispersion of the Ga3d bands by direct Ga-Ga interactions. We have performed calculations for GaN in two distinct ways: one treating Ga3d as a core level, and one as a valence band. Treating the Ga3d as a core level in our calculation means imposing atomic-like boundary conditions on it at the atomic sphere radius. The core level and its associated charge density are allowed to relax towards self-consistency and thus to adjust to the lattice constant. One should realize that this treatment is different from a "frozen core" (or frozen overlapping core [50]) approximation which is more closely related to the pseudopotential treatment as has been discussed in detail by Fiorentini *et al.* [50]. What happens in our Ga3d core-like treatment is that the core wave functions are artificially compressed in the small Ga spheres and thus have too high kinetic energy. The system can lower its energy by expanding the lattice constant. Hence in our Ga3d core-like treatment we find a lattice constant which is about 2 % too large. Relatedly, the bulk modulus is 3 % too small (compared to the calculation which includes Ga3d band dispersion.) Since the hydrostatic bandgap deformation potential is negative, the erroneous expansion results in an underestimate of the gap by -0.4 eV. Including slight adjustments in the self-consistent potential due to the treatment of the Ga3d as core, the effect is actually smaller, only -0.2 eV. The direct effect of the Ga3d on the valence band maximum is actually small as is obvious from perturbation theory since it lies more than a Rydberg away. In fact, if one recalculates the bands with the potential determined self-consistently including the effect of Ga3d as bands fixed but with a basis set that does not include Ga3d, one finds a gap which is reduced by only 0.1 eV. The latter effecively corresponds to a "two-panel" calculation of the bands. Our conclusions on the effects of treating Ga3d as a core state differ from what is obtained in pseudopotential treatments or frozen core treatments. As explained by Fiorentini *et al.* [50] the main additional error made by the pseudopotential method is linearizing core-valence exchange. Even when this is corrected for, the frozen core approximation leads to a slight underestimate of the lattice consant. In pseudopotential calculations, somewhat arbitrary details on how exactly the pseudopotential is constructed (e.g. the choice of cut-offs in local and non-local parts) and the convergence of the basis set can make a difference. Similar effects occur for the In4d in InN.

The question now arises: can this Ga3d be seen to overlap with N2s in XPS? The answer turns out to be no. This can be seen in Fig. 7, which shows the XPS spectrum compared to the DOS including the Ga3d band dispersion. It shows that in the XPS-spectrum the Ga3d peak occurs a $\sim$4 eV below the N2s band. The reason for this is that XPS does not exactly probe the densities of

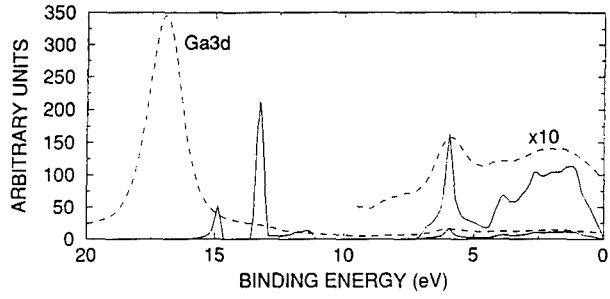

Figure 7: X-ray photoemission spectrum of zb-GaN compared to calculated DOS with inclusion of Ga3d as valence orbitals.

states as we calculate it in Kohn-Sham LDA theory. The eigenvalues in Kohn-Sham LDA theory are only intermediate quantities used to obtain the total energy of the groundstate but do not have the meaning of quasiparticle excitations as probed by XPS. In particular, for narrow bands, the difference between quasiparticle excitation energies and Kohn-Sham eigenvalues can be large. In that case, a more accurate calculation consists in subtracting total energies with and without a core-hole. This is called the ΔSCF procedure because it consists in taking the difference between two self-consistent field (SCF) energies. Because on the time scale of the photoemission experiment, the hole does not have time to delocalize by hopping to the neighbors, one has to treat the core-hole as a localized excitation, i.e. like an impurity. In this treatment, one first of all corrects for the incomplete cancellation of the self-interaction in the Hartree and exchange terms in the local density approximation. Indeed, the latter treats exchange in an average manner instead of an "orbital-specific" manner as does Hartree-Fock. ΔSCF calculations for a free Ga atom in the LDA indicate that the Ga3d binding energy is larger than the absolute value of the Kohn-Sham eigenvalue by 8.5 eV. Secondly, the other orbitals of the system, are polarized by the external perturbation presented by this local core-hole and lead to so-called final state screening shifts. This effect can be treated in the so-called "excited atom" model [52]. In fact, most of the screening in the solid occurs within an atomic radius because the dielectric function $\epsilon(q)$ decays with a characteristic length of the Thomas-Fermi wave vector q_{TF}. As shown elswehere, one can thus mimic the effects of the induced screening charge density by adding an electron to the lowest unoccupied atomic state for every core electron removed. The combination of the two effects gives a net shift of $\sim$4 eV from the LDA eigenvalue. This is in good agreement with experiment.

UV-reflectance

For many years UV-reflectance has been an important tool in determining band structures. Frequently, it has been used in conjunction with the semi-empirical pseudopotential method by identifying critical point transition energies at symmetry points with experimental features and adjusting the pseudopotential so as to reproduce the measured transition energies. The problem with that approach is that the assignment of features to critical points may not be unique. We have recently started analyzing measured UV-reflectivities for SiC polytypes and the group-III nitrides by means of explicit calculations of the optical response functions from the first-principles band structures.

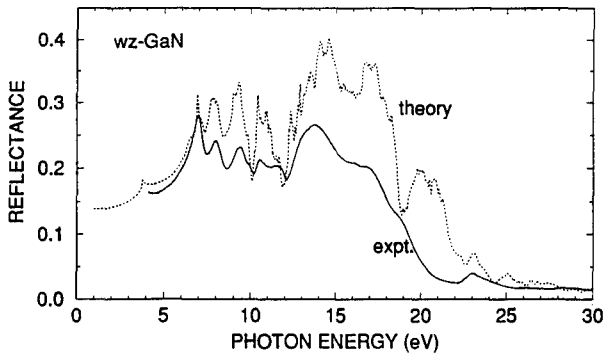

Figure 8: Measured and calculated UV-reflectance spectrum of wz-GaN: a rigid upward shift of the calculated spectrum by 0.98 eV is used in order to correct for the LDA band gap error.

The imaginary part of the dielectric function in the random phase approximation

$$\epsilon_2^j(\omega) = \frac{e^2}{m^2\omega^2\pi} \sum_{v,c} \int_{BZ} d^3k |\langle v\mathbf{k}|\frac{\hbar}{i}\partial_j|c\mathbf{k}\rangle|^2 f_v^k(1-f_c^k)\delta(E_v^{\mathbf{k}} - E_c^{\mathbf{k}} - \hbar\omega) \qquad (1)$$

was calculated using an expansion of the wavefunctions in muffin-tin orbitals for the calculation of the dipole matrix elements. Here, $E_v(\mathbf{k})$ and $E_c(\mathbf{k})$ are the occupied and unoccupied energy bands respectively with the Fermi function occupation numbers $f_v^k = 1$ and $f_c^k = 0$ at zero temperature. The real part $\epsilon_1(\omega)$ is then obtained by the Kramers-Kronig transformation from $\epsilon_2(\omega)$ and the normal incidence reflectance is calculated from the Fresnel equations.

Fig. 8 shows a comparison between calculated UV-reflectance and recent experimental data [53] . We note that the agreement in peak positions between theory and experiment is excellent. It should be mentioned that the theory spectrum was shifted upwards by 0.98 eV, this shift being chosen so as to adjust the minimum bandgap to experiment. The good agreement means that the self-energy corrections are indeed very well approximated by a constant k-independent and energy independent shift. The constant shift approximation works well to within a few 0.1 eV. We found the same to be true for SiC where in addition the correction is found to be essentially independent of polytype [54].

Analysis of the partial contributions to the imaginary part of the dielectric function ϵ_2 show that the peaks do generally not coincide with high symmetry critical points, but rather with more or less extended regions of parallel bands in the interior of the BZ. Thus, many of the critical point assignments given in the older literature have to be revised. Details are still under study and will be published elsewhere.

CONCLUSION

The similarities and differences between the various classes of wide-band gaps semiconductors involving early elements of the periodic table such as carbon, nitrogen, boron and beryllium were reviewed. We have emphasised fundamental properties and their relation to the underlying electronic structure. Their relevance to electronic devices was pointed out. The main purpose of the first-principles calculations presented here was to provide a deeper understanding of the

trends in the band-structures with polytype, ionicity and atomic number. Their use in the study of other physical properties, such as elastic constants and optical properties was also illustrated.

ACKNOWLEDGEMENTS

I wish to thank Prof. B. Segall, A. G. Petukhov, E. A. Albanesi, K. Kim and C. H. Lee for collaborations on various aspects of the work. I also wish to express appreciation to M. Alouani, M. van Schilfgaarde and M. Methfessel for providing computer programs, J. C. Angus for collaborations on diamond, W. J. Choyke and R. P. Devaty and coworkers for collaborations on SiC, J. Rife and coworkers for UV-reflectance work on GaN, and H. Morkoç and coworkers for XPS work on GaN, and S. Satpathi for allowing me to reproduce Fig. 1. The nitride work was supported by NSF DMR-92-22387, the diamond work by the NSF-MRG DMR-89-03527 and ONR N-00014-89-J-1631 and the SiC work by Wright-Laboratories (Contract No. F33615-93-C-5347). Part of the computations were done a the Ohio Supercomputer Center.

REFERENCES

1. E. O. Johnson, *RCA Rev.* **26**, 163 (1965).
2. R. W. Keyes, *Proc. IEEE*, **60**, 225 (1972).
3. R. F. Davis, Z. Sitar, B. E. Williams, H. S. Kongs, H. J. Kim, J. W. Palmour, J. A. Edmond, J. R. Yu, J. T. Glass, and C. H. Carter, Jr., *Mater. Sci. and Eng.* **B1**, 77 (1988).
4. CRC Handbook of Chemistry and Physics, edited by R. C. Weast, (CRC Press, Inc., Boca Raton, FL 1988), 68th Edition.
5. *Numerical Data and Functional Relationships in Science and Technology*, edited by E. O. Madelung, Landolt-Börnstein, new series, Group III, Vol. 17a (Springer, Berlin, 1982).
6. W. R. L. Lambrecht and B. Segall, *Phys. Rev. B* **45**, 1485 (1992).
7. A. G. Petukhov, W. R. L. Lambrecht and B. segall, *Phys. Rev. B* **49**, 4549 (1993).
8. W. R. L. Lambrecht, unpublished.
9. R. M. Wentzcovitch, A. Continenza, and A. J. Freeman, in *Diamond, Silicon Carbide and Related Wide Bandgap Semiconducors*, ed. J. T. Glass, R. Messier, N. Fujimori, Mater. Res. Soc. Symp. Proc. Vol. 162, (MRS, Pittsburgh 1990), p. 611.
10. G. A. Slack, *J. Phys. Chem. Solids* **34**, 321 (1973).
11. W. R. L. Lambrecht, C. H. Lee, B. Segall, J. C. Angus, Z. Li, and M. Sunkara, *Nature* **364**, 607 (1993).
12. P. J. Fallon and L. M. Brown, *Diamond and Related Materials*, **2**, 1004 (1993).
13. B. N. Davidson and W. E. Pickett, these proceedings.
14. S. Koizumi, and T. Inuzuka, *Jpn., J. Appl. Phys.***32**, 3920 (1993).
15. V. Heine, C. Cheng, G. E. Engel, and R. J. Needs, in Wide Band Gap Semiconductors, ed. T. D. Moustakas, J. I. Pankove, and Y. Hamakawa, Mater. Res. Soc. Symp. Proc. Vol. 242, (MRS, Pittsburgh, 1992), p. 507.

16. H. Matsunami, these proceedings.

17. W. R. L. Lambrecht, B. Segall, M. Methfessel, and M. van Schilfgaarde, *Phys. Rev. B* **44**, 3685 (1991).

18. K. Kim, W. R. L. Lambrecht, and B. Segall, submitted to *Phys. Rev. B* (1994).

19. G. S. Zhdanov, *C. R. Acad. SCi. USSR*, **48**, 43 (1945).

20. M. R. Salehpour and S. Satpathy, *Phys. Rev. B* **41**, 3048 (1990).

21. C. Herring, *J. Franklin Inst.* **233**, 525 (1942).

22. O. K. Andersen, O. Jepsen, and M. Šob, in *Electronic Band Structure and its Applications*, edited by M. Yussouff, (Springer, Heidelberg, 1987) and refs. therein.

23. V. I. Gavrilenko, A. V. Postnikov, N. I. Klyui, and V. G. Litovchenko, Phys. Stat. Sol. (b) **162**, 477 (1990).

24. W. Kohn and L. J. Sham, *Phys. Rev.* **140**, A1133 (1965).

25. L. Hedin and B. I. Lundqvist, *J. Phys. C* **4**, 2064 (1971).

26. M. Methfessel, *Phys. Rev. B* **38**, 1537 (1988).

27. L. Patrick, W. J. Choyke, and D. R. Hamilton, *Phys. Rev.* **137**, A1515 (1965).

28. W. J. Schaffer, G. H. Negley, K. G. Irvine, and J. W. Palmour, these proceedings.

29. K. J. Chang, S. Froyen, and M. L. Cohen, *J. Phys. C: Solid State Phys.* **16**, 3475 (1983).

30. J. Harris, in *The electronic structure of complex systems*, ed. P. Phariseau and W. M. Temmerman, NATA-ISI Series, (Plenum, New York, 1984).

31. W. R. L. Lambrecht and B. Segall, *Phys. Rev. B* **43** 7070 (1991).

32. W. R. L. Lambrecht, B. Segall, and O. K. Andersen, Phys. Rev. B **41**, 2813 (1990).

33. W. R. L. Lambrecht and B. Segall, *Phys. Rev. B* **41**, 2832 (1990).

34. W. R. L. Lambrecht and B. Segall, in *Properties of the Group-III Nitrides*, edited by J. H. Edgar, EMIS Data Review Series, (IEE, Stevenage Herts, UK 1994), in press.

35. C.-Y. Yeh, Z. W. Lu, S. Froyen and A. Zunger, *Phys. Rev. B* **46**, 10086 (1992).

36. W. R. L. Lambrecht and B. Segall, *Phys. Rev. B* **47** , 9289 (1993)

37. E. A. Albanesi, W. R. L. Lambrecht, B. Segall, *Phys. Rev. B* **48**, 17841 (1993).

38. E. A. Albanesi, W. R. L. lambrecht, and B. Segall, *J. Vac. Sci. Technol. B* (1994), accepted, (PCSI-21 Proceedings).

39. E. A. Albanesi, W. R. L. Lambrecht, and B. Segall, these proceedings.

40. R. M. Martin, *Phys. Rev. B* **6**, 4546 (1972).

41. J. A. Sanjurgo, E. López-Cruz, P. Vogl, and M. Cardona, *Phys. Rev. B* **28**, 4579 (1983).

42. K. Kim, W. R. L. Lambrecht, unpublished.

43. M. E. Sherwin and T. J. Drummond, *J. Appl. Phys.* **69**, 8423 (1991).

44. G. Arlt, and G. R. Schodder, *J. Acoust. Soc. Am.* **37**, 384 (1965).

45. P. Perlin, C. Jauberthie-Carillon, J. P. Itie, A. San Miguel, I. Grzegory, and A. Polian, *Phy. Rev. B* **45** 83 (1992)

46. D. Olego and M. Cardona, *Phys. Rev. B.* **25**, 1151 (1982).

47. V. A. Savastenko and A. U. Sheleg, *Phys. Stat. Sol. (a)* **48** K135 (1978); A. U. Sheleg and V. A. Savastenko, *Inorg. Mater.* **15** 1257 (1979).

48. W. R. L. Lambrecht, E. A. Albanesi, and B. Segall, in *Proc. International Conference on Silicon Carbide and Related Materials*, Washington DC, November 1993, in press.

49. W. R. L. Lambrecht and B. Segall, in *Wide band GAp Semiconductors*, ed. T. D. Moustakas, J. I. Pankove, and Y. Hamakawa, Mater. Res. Soc. Symp. Proc. Vol. **242** (MRS, Pittsburg, 1992) p. 367.

50. V. Fiorentini, M. Methfessel, and M. Scheffler, Phys. Rev. B **47**, 13353 (1993)

51. A. F. Wright and J. S. Nelson, these proceedings.

52. A. R. Williams and N. D. Lang, *Phys. Rev. Lett.* **40**, 954 (1978).

53. J. Rife, W. R. Hunter, W. R. L. Lambrecht,, B. Segall, and D. K. Wickenden, *Bull. Am. Phys. Soc.* **39**, 211 (1994); and unpublished.

54. W. R. L. Lambrecht, B. Segall, W. Suttrop, M. Yonagathan, R. P. Devaty, W. J. Choyke, J. A. Edmond, J. A. Powell, and M. Alouani, *Appl. Phys. Lett.* **63**, 2747 (1993); and unpublished.

TUNABLE SECOND-HARMONIC STUDIES OF GaN FILMS NEAR THE FUNDAMENTAL BANDEDGE

JOSEPH MIRAGLIOTTA, WAYNE A. BRYDEN, THOMAS J. KISTENMACHER, AND DENNIS K. WICKENDEN
The Johns Hopkins University, Applied Physics Laboratory, Johns Hopkins Road, Laurel, MD 20723-6099

ABSTRACT

Tunable second-harmonic (SH) transmission measurements were performed on a series of GaN films epitaxially deposited onto (0001)-oriented sapphire. Analysis of the nonlinear response showed an increase in the second-order nonlinear susceptibility ($\chi^{(2)}_{ijk}$) when the photon energy of the SH field was tuned above the absorption edge in each respective film. Specifically, the magnitude of the $\chi^{(2)}_{zxx}$ element in $\chi^{(2)}_{ijk}$ reached a maximum of 0.5×10^{-7} e.s.u. just above the the fundamental bandgap with a dispersion similar to the predicted nonlinear response in wide-bandgap cubic zincblende II-VI semiconductors such as ZnSe.

INTRODUCTION

Under ambient conditions, gallium nitride (GaN) crystallizes in a hexagonal wurtzite structure which possesses a 6mm point group symmetry. The noncentrosymmetric nature of this crystal symmetry assures that second-order nonlinear optical phenomena, such as second-harmonic (SH) generation, will occur in the bulk region of the material. In fact, previous nonlinear studies have shown the intrinsic second-order susceptibility of GaN, $\chi^{(2)}_{ijk}$, (27 element tensor of rank 3) to be sensitive to the crystalline symmetry and orientation of epitaxial thin films deposited on sapphire substrates [1].

In this paper, we report the results of a tunable SH investigation from a series of epitaxial GaN thin films that were grown on a (0001)-oriented sapphire substrate using metal organic chemical vapor deposition (MOCVD). This work is an extension of an earlier SH study of GaN/sapphire samples in which the nonresonant contribution to $\chi^{(2)}_{ijk}$ between 375 and 545nm was observed to be an order of magnitude greater than the second-order nonlinearity in quartz or KDP [2]. In the present investigation, the transmitted SH intensity was measured as a function of the incident polarization and the SH wavelength in the range of 342 to 380nm. Analysis of the SH intensity profile determined a resonant enhancement in the the magnitude of the $\chi^{(2)}_{zxx}$ element in $\chi^{(2)}_{ijk}$ at SH photon energies above the bandgap energy of the GaN crystal (λ_{SH} <365nm). In addition, the dispersive characteristics of $\chi^{(2)}_{zxx}$ in this photon range was qualitatively similar to previous SH calculations of $\chi^{(2)}_{xyz}$ in wide-bandgap cubic zincblende semiconductors [3,4].

EXPERIMENTAL PROCEDURE

The procedure used in the MOCVD deposition of an epitaxial GaN film on sapphire has been discussed in Wickenden et al [5]. The epitaxial films were grown on a pre-deposited GaN nucleation layer at 1050° C so as to provide a relatively strain- and defect-free crystalline sample. X-ray analysis verified the crystalline nature of the epitaxial films as well as the parallel alignment of the film and substrate the optical axes (parallel to the surface normal).

The SH transmitted intensity from a series of GaN/sapphire samples was measured as a function of the SH wavelength and photon energy. Stimulated Stokes Raman scattering of

Mat. Res. Soc. Symp. Proc. Vol. 339. ©1994 Materials Research Society

tunable dye laser radiation (570 to 750nm) in a high pressure volume of H_2 gas (10 atmospheres, 2 meter beam path) produced a high peak-power, fundamental light source in the 750 to 1090nm wavelength range. The laser radiation was linearly polarized (s- or p-polarized) and incident at an angle of 45^0 at the air/GaN interface of all samples. Typical incident power densities were ~ 1 MW/cm^2, well below any observable damage threshold. The transmitted SH light was observed to be p-polarized for either s- or p-polarized inputs with no detectable nonlinear contribution from the sapphire substrate. The harmonic light was detected with a photomulitiplier tube and analyzed with a gated boxcar integrator. The SH signal from the GaN sample was normalized to the SH intensity generated from a nonlinear reference crystal (quartz, $\chi^{(2)}= 1.9\times10^{-9}$ e.s.u. [17]) so as to allow a quantitative determination of $\chi^{(2)}_{ijk}$.

THEORY

In hexagonal GaN, the 6mm point group symmetry of the sample reduces the number of nonvanishing tensor elements in $\chi^{(2)}_{ijk}$ from 27 to 3: $\chi^{(2)}_{zzz}$, $\chi^{(2)}_{xzx}$, and $\chi^{(2)}_{zxx}$, where the z-axis (x-axis) is parallel (perpendicular) to the surface normal of the GaN film. The alignment of the optical axis and the high refractive index in the film prevents efficient coupling to the $\chi^{(2)}_{zzz}$ element, limiting the contribution from this nonlinearity to ~5% of the total SH response in this investigation. For this reason, this susceptibility element was neglected in the analysis of the nonlinear response. The crystalline structure was assumed to be an ideal wurtzite phase which equated the magnitude and dispersion of the $\chi^{(2)}_{xzx}$ and $\chi^{(2)}_{zxx}$ tensor elements. The wurtzite geometric relationship between $\chi^{(2)}_{zxx}$ and $\chi^{(2)}_{xzx}$ is supported by previous experimentally observations in nonresonant SH studies of GaN [1,2] and resonant SH examinations of CdS and CdSe [6]. Under these assumptions, the nonlinear polarization induced with p-polarized (xz-plane) incident radiation at a distance z into the film is

$$P_x^{(2)}(2\omega,z) = 2\chi_{zxx}(2\omega)E_z(\omega,z)E_x(\omega,z)$$

$$P_z^{(2)}(2\omega,z) \approx \chi_{zxx}(2\omega)\, E_x^{\,2}(\omega,z) \qquad (1)$$

where $P_i(2\omega,z)$ and $E_i^2(\omega,z)$ are the ith components of the induced polarization and incident field at position z, respectively. For an s-polarized input (y-axis), the induced nonlinear polarization is

$$P_z^{(2)}(2\omega,z) = \chi_{zxx}(2\omega)\, E_y^{\,2}(\omega,z) \qquad (2)$$

From the expressions for the induced polarization, it is clear that the nonlinear response will be polarized in the xz plane (p-polarized) for either s- or p-polarized inputs.

To model the SH transmitted intensity, tractable solutions to Maxwell's equations in the nonlinear media were deduced from the usual boundary conditions for the electromagnetic fields at the plane interfaces between the nonlinear and linear media. For the purposes of brevity, the calculations for the nonlinear response using s-polarized incident radiation will be discussed. The details of the electromagnetic response from a nonlinear film using a p-polarized incident source can be found in Bloembergen et al [7], and Miragliotta et al [1]. For an ω light source incident at the air(n=1)/GaN interface, the SH signal transmitted through the sapphire/air interface is

$$I_{2\omega} = 2\pi c T_{13}^2 \{f_1 \exp(i\phi) + f_2\}^* \{f_1 \exp(i\phi) + f_2\} \left|\chi^{(2)}_{zxx}\right|^2 \qquad (3)$$

where

$$f_1 = \frac{\dfrac{(Q_4\cos\theta_t - Q_3 n_t)R_{12}\exp(i\phi)}{(n_{2\omega}\cos\theta_t + n_t\cos\theta_{2\omega})} - \dfrac{(Q_1 n_1 + Q_2\cos\theta_1)}{(n_1\cos\theta_{2\omega} + n_{2\omega}\cos\theta_1)}}{1 + R_{12}R_{23}\exp(2i\phi)} \tag{4a}$$

$$f_2 = \frac{(Q_4\cos\theta_{2\omega} + Q_3 n_{2\omega})}{n_{2\omega}\cos\theta_t + n_t\cos\theta_{2\omega}} \tag{4b}$$

with

$$Q_{1(3)} = \frac{-E_y^2(0(d))n_\omega^2\sin\theta_\omega\cos\theta_\omega}{n_{2\omega}^2(n_\omega^2 - n_{2\omega}^2)} \tag{4c}$$

$$Q_{2(4)} = \frac{-E_y^2(0,(d))n_\omega\sin\theta_\omega}{n_\omega^2 - n_{2\omega}^2} \tag{4d}$$

In these expressions, n_1, $n_{2\omega}$, and n_t are the refractive indices at 2ω of the incident media, the GaN film, and sapphire substrate, respectively, with n_ω the refractive index of the GaN film at the fundamental frequency. R_{12}, R_{23}, T_{31}, and T_{23} are the Fresnel coefficients which account for reflection (2ω) at the air/GaN and GaN/sapphire interfaces and transmission (2ω) across the sapphire/air and GaN/sapphire interfaces, respectively. $E_y(\omega,0(d))$ is the fundamental optical source at the front (back) surface of the sample which contains the phase factors associated with the propagation of this field in the film. ϕ is the optical phase of the SH field at the GaN/sapphire interface which is linearly dependent on the film thickness, d. The optical response in the film at ω and 2ω was characterized by the ordinary value of the refractive index since the birefringence in GaN is very small [8].

EXPERIMENTAL RESULTS AND ANALYSIS

The transmitted SH signal from a series of GaN samples using a s-polarized incident light source is shown in Figures 1(a)-(d) as a function of the SH wavelength and photon energy. In each spectrum, most noticeable for the 6.1 μm film, the SH signal displayed an oscillatory behavior throughout for SH photon energies below the fundamental bandedge. The oscillations are attributed to the wavelength dependence of the phase velocity mismatch between the free and bound second-harmonic waves and has been observed in a number of previously investigated nonlinear materials, notably illustrated in the work of Jerphagnon and Durtz [9] and Maker et al [10]. The period associated with maximum interference between the second-harmonic waves, i.e., the energy separation between SH minimum intensity, was observed to increase with decreasing photon energy due to the increase in the nonlinear optical coherence length of the GaN film. The phase mismatch oscillations terminated for 2ω photon energies $> E_g$ due to the strong absorption of the SH field in the film. In this energy range, the signal was observed to have oscillations which were a result of the multibeam interference pattern in the fundamental beam. Figures 2(a)-(d) show the results for the transmitted SH signal using a p-polarized incident light source. The spectra are qualitatively similar to the corresponding results shown in Figure 1; however, the p-polarized input generated a signal intensity that was approximately a factor of 8 larger than the s-polarized incident source due to the respective difference in the coupling efficiency to $\chi^{(2)}_{ijk}$. We note that under the room temperature conditions of this investigation there was no observation of valence band splitting near the bandedge or additional resonances in the spectrum, e.g, bandedge excitonic effects.

An examination of Eqs.(3)-(4) show that the photon energy dependence and absolute magnitude of $\chi^{(2)}_{zxx}$ can be determined from the detected SH signal if the film thickness and

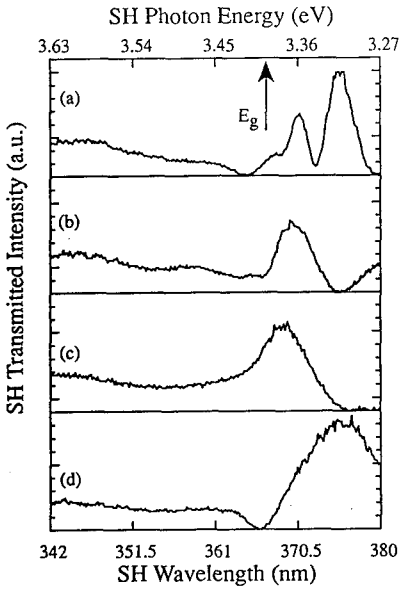

Figure 1. Transmitted SH intensity from a (a) 6.1μm, (b) 2.6μm, (c) 1.3μm, (d) and 0.85μm GaN film. Incident field was s-polarized and generated SH field was p-polarized.

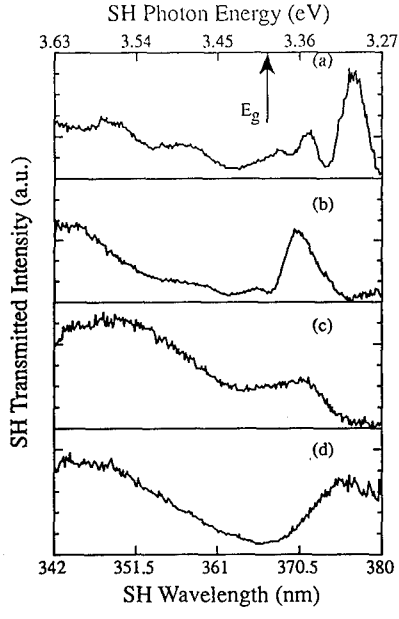

Figure 2. Transmitted SH intensity from a (a) 6.1μm, (b) 2.6μm, (c) 1.3μm, (d) and 0.85μm GaN film. Incident and generated fields were p-polarized. Intensity scale is a factor of 8 larger than the corresponding scale in Figure 1.

$n_\omega(2\omega)$ can be independently evaluated using other optical investigations. For photon energies below E_g, these parameters were determined with a series of linear reflectance and transmission measurements. Near and above the fundamental absorption edge ($2h\omega > 3.2$ eV), values for the real and imaginary parts of $n_{2\omega}$ were taken from the literature [11]. In Figure 3, the spectrum of $\chi^{(2)}_{zxx}$, obtained from the SH intensity in Figure 1(b), shows the magnitude and dispersion of this nonlinearity in the bandedge region. The scan was generated by normalizing the square root of the SH intensity to the square root of the scale factor $2\pi c(f_1+f_2\exp(i\phi))T^2_{13}$ (see Eq.(3)), where c is the speed of light. As is evident from the spectrum, the experimentally derived result exhibited an enhancement for SH photon energies above the absorption edge, reaching a maximum value of ~0.5 x 10^{-7} e.s.u. It is interesting to note that the spectrum of $\chi^{(2)}_{zxx}$ exhibitied a 70% increase in the 380 to 342nm wavelength range while the corresponding change in the linear dielectric function, $\varepsilon(2\omega)$, is only on the order of ~ 14%. The variational differences can be attributed to the photon energy dependence of the linear (E_ω^{-3}) versus nonlinear (E_ω^{-5}) response in the GaN film. As has been discussed in prevous nonlinear theoretical studies [3,4], the photon energy dependence of $\chi^{(2)}_{zxx}$ phenomena allow low-energy interband transitisons,

e.g., the fundamental absorption edge, to be more readily observable than in the linear dielectric response.

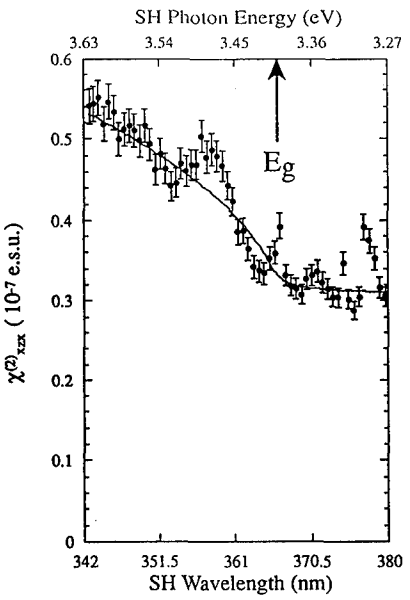

Figure 3. Spectrum of $\chi^{(2)}_{zxx}$ as determined from the SH transmission spectrum in Figure 1(b). The solid line is a rough fit to the data. E_g is the bandgap energy.

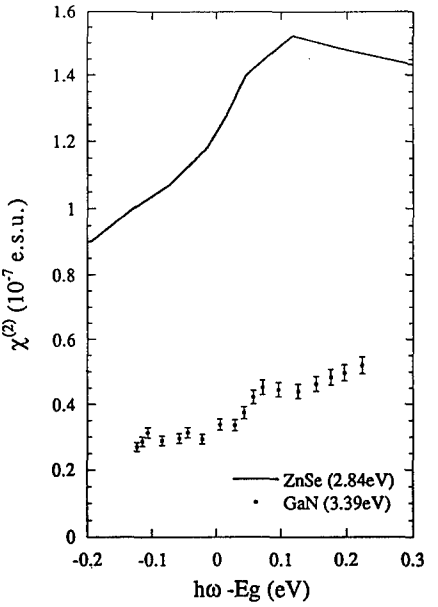

Figure 4. Comparison of $\chi^{(2)}_{zxx}$ in GaN (experimentally derived) with the theoretical predictions of $\chi^{(2)}_{xyz}$ in ZnSe [3] as a function of the difference in SH photon and bandgap energies.

At the present time, it is not possible to compare the nonlinear experimental results in Figure 3 with a wurtzite band structure calculation of $\chi^{(2)}_{zxx}$. However, the similarites in the electronic properties of hexagonal and zincblende phase GaN [12,13] should allow a reasonable comparison with previous nonlinear zincblende predictions [3,4]. Specifically, recent band structure calculations by Ghahramani et al [3] and Ching et al [4] of $\chi^{(2)}_{xyz}$ for cubic II-VI materials such as ZnS, ZnSe, and ZnTe have determined magnitudes on the order of 10^{-7} e.s.u. near the respective bandgap energies of these semiconductors, similar to the experimental results for GaN in Figure 3. In addition, large variations were predicted in $\chi^{(2)}_{xyz}$ as the SH photon energy was tuned through the fundamental bandgap region. A direct comparison between $\chi^{(2)}_{zxx}$ in Figure 3 with the predicted results of $\chi^{(2)}_{xyz}$ in ZnSe [3] are shown in Figure 4 where the spectra are plotted as a function of the energy difference between the SH photon energy and E_g. ZnSe was chosen as an appropriate candidate since, like GaN, it has a direct valence to conduction band transition at the fundamental absorption edge. The density of states in ZnSe and GaN have upper valence band states that are dominated by the p-orbitals of the anion (Se or N) and a lower conduction band region dominated by the s-orbitals of the cation (Zn or Ga). Therefore, critical points in the joint density of states, e.g., the fundamental absorption edge, are very similar in these two materials [14, 15] provided the effect of spin-orbit coupling (s-o) is neglected in ZnSe. In fact, the calculations of $\chi^{(2)}_{xyz}$ in ZnSe [3,4] did not include relativistic effects such as s-o coupling which should generate an electronic structure that closely resembles the absorption

edge region in wurtzite GaN (weak s-o splitting on the order of ~0.02 eV [16]). The comparison in Figure 4 shows similar wavelength dependences for $\chi^{(2)}_{zxx}$ of GaN and $\chi^{(2)}_{xyz}$ of ZnSe at photon energies in the bandedge region, i.e., similar dispersion. The magnitude of $\chi^{(2)}_{xyz}$ is approximately 3 times the value of $\chi^{(2)}_{zxx}$ in hexagonal GaN. In part, this difference can be attributed to issues associated with orbital overlap, e.g., ionicity, which have a tendency to reduce the second-order nonlinearity with decreasing covalency. Previous nonresonant bond-charge calculations have determined a $\chi^{(2)}$ magnitude in ZnSe that was a factor of two larger than that in GaN [18]. Also, we note that the higher bandgap energy in GaN lowers the magnitude of $\chi^{(2)}_{zxx}$ with respect to $\chi^{(2)}_{xyz}$ by an amount that is equal to the ratio of the GaN and ZnSe bandgap energies to the fifth power [3].

In summary, we have measured the transmitted SH intensity from a series of GaN thin films on a sapphire substrate. The magnitude of $\chi^{(2)}_{zxx}$ was observed to be enhanced at 2ω photon energies above the fundamental bandedge. The dispersion in the bandedge region was found to be qualitatively similar to previous band structure calculations of ZnSe, a II-VI cubic zincblende wide-bandgap semiconductor.

REFERENCES

1. J. Miragliotta, D. K. Wickenden, T. J. Kistenmacher, and W. A. Bryden, J. Opt. Soc. Am. B, **10**, 1447 (1993).
2. J. Miragliotta, W. A. Bryden, T. J. Kistenmacher, and D. K. Wickenden, in Proceedings of the 5th ICSCRM, edited by R. Devaty and W.T. Choyke (1993).
3. E. Ghahramani, D.J. Moss, and J. E. Sipe, Phys. Rev. B, **43**, 9700 (1991).
4. W. Y. Ching and M.-Z. Huang, Phys. Rev. B, **47**, 9479 (1993).
5. D. K. Wickenden, T. J. Kistenmacher, W. A. Bryden, J. S. Morgan, and A. Estes-Wickenden, Mat. Res. Soc. Symp. Proc., **221**, 167 (1991).
6. F. G. Parson, E. Yi Chen, and R. K. Chang, Phys. Rev. Lett., **27**, 1436 (1971).
7. N. Bloembergen and P. S. Pershan, Phys. Rev., **128**, 606 (1962).
8. E. Ejder, Phys. Status Solidi a, **6**, 442 (1971).
9. J. Jerphagnon and S. K. Durtz, J. Appl. Phys., **41**, 1667 (1970).
10. P. D. Maker, R. W. Terhune, M. Nisenoff, and C. M. Savage, Phys. Rev. Lett., **8**, 21 (1962).
11. H. Amano, N. Watanabe, N. Koide, and I. Akasaki, Jpn. J. Appl. Phys., **32**, L1000 (1993).
12. S. Bloom, J. Phys. Chem. Solids, **32**, 2027 (1971); S. Bloom, G. Harbeke, E. Meier, and I. B. Ortenburger, Phys. Stat. Sol. (b), **66**, 161 (1974).
13. Y.-N. Xu and W. Y. Ching, Phys. Rev. B, **48**, 4335 (1993); K. Miwa and A. Fukumoto, Phys. Rev. B, **48**, 7897(1993); W. R. L. Lambrecht and B. Segall, Mat. Res. Soc. Symp. Proc., **242**, 367 (1992).
14. S. Adachi, Phys. Rev. B, **43**, 9569 (1991).
15. Y.-N. Xu and W. Y. Ching, Phys. Rev. B **48**, 4335 (1993).
16. R. Dingle, D. D. Sell, S. E. Stokowski, and M. Ilegems, Phys. Rev. B, **4**, 1211 (1971).
17. R. Boyd, *Nonlinear Optics*, (Academic Press, 1992), pg 52.
18. B. F. Levine, Phys. Rev. B, **7**, 2600 (1973).

CORRELATIONS BETWEEN ELECTRICAL AND MATERIAL PROPERTIES OF CVD DIAMOND

C. White[a], S. Zhao, K.K. Gan[a], H. Kagan[a], R. Kass[a], R. Malchow[a1], F. Morrow[a], W. Palmer[a], S. Han[b2], D. Kania[b], L.S. Pan, S. Schnetzer[c], R. Stone[c], R. Teserek[c], J. Angus[d], S.J. Ma[d], Y. Sugimoto[e]

[a]Department of Physics, The Ohio State University, Columbus, OH 43210
[b]Laser Division, Lawrence Livermore National Laboratory, Livermore, CA 94550
[c]Department of Physics, Rutgers University, Piscataway, NJ 08854
[d]Department of Chemical Engineering, CWRU, Cleveland, OH 44106
[e]KEK National Laboratory, Tsukuba-shi, Ibaraki-ken, Japan 305
[1]Current address: Colorado State University, Fort Collins, CO 80523
[2]Current address: Los Alamos National Lab, Los Alamos, NM 87545

ABSTRACT

The electrical properties associated with diamond charged particle- and photo-detectors were studied using charged particle-induced conductivity (CPIC) and photo-induced conductivity (PIC). The collection distance d, the product of the excess carrier mobility μ, excess carrier lifetime τ and electric field E, was used to characterize the diamonds. X-ray diffraction, Raman spectroscopy, photoluminescence, SEM and TEM were performed on CVD diamond detectors to investigate the limitations of the electrical properties. Correlations were found between the electrical properties and the material characterizations.

INTRODUCTION

The detection of charge particles and photons using Chemical Vapor Deposited (CVD) diamond as the detector medium is being actively pursued. This is primarily due to diamond's extreme properties: radiation hardness, high mobility and large band gap [1]. Detector performance is directly associated with the quality of the CVD diamond films. The collection distance, a characteristic of the electrical properties of diamond, was studied as a function of film thickness, visual transparency, lattice constant, X-ray diffraction peak width, Raman line width, and growth rate to try to understand the significant improvements in the collection distance which have been achieved in the past few years.

EXPERIMENTS AND RESULTS

Two methods were employed to study the electrical properties of the CVD diamond samples, charged particle induced conductivity (CPIC) and photon induced conductivity (PIC). For the CPIC studies, electric contacts were deposited on either side of the diamond film to form an ionization chamber. For PIC studies, the contacts were deposited on the same side of the diamond film with a 1mm gap. The electrode configurations are shown in Figure 1. Ohmic contacts were prepared using sputtered Ti/Pt/Au [2, 3] or thermally evaporated Cr/Au metalization [4].

The CPIC measurements were performed using a radioactive source (^{90}Sr) which produces electrons with a β-decay spectrum and maximum energy of 2.28MeV [5]. The charged particles traverse the diamond film depositing a well defined and uniform quantity of energy along the track through the film [5]. For this analysis, we used a value of 13 eV as the average energy to create an electron-hole pair [6]. The CPIC technique probes the bulk of the diamond film and measures the collection distance averaged over the material along the columnar direction.

Mat. Res. Soc. Symp. Proc. Vol. 339. ©1994 Materials Research Society

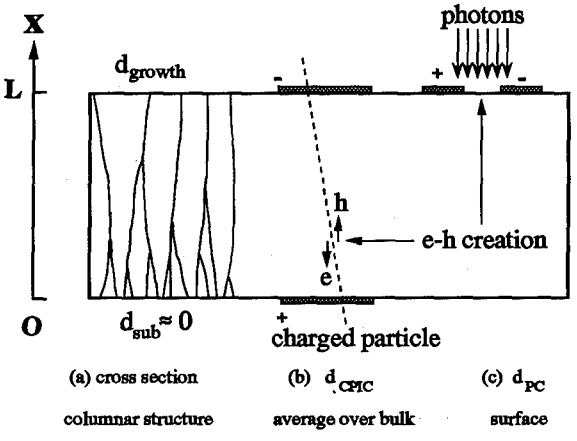

Figure 1: *Cross section view of a CVD particle detector.*

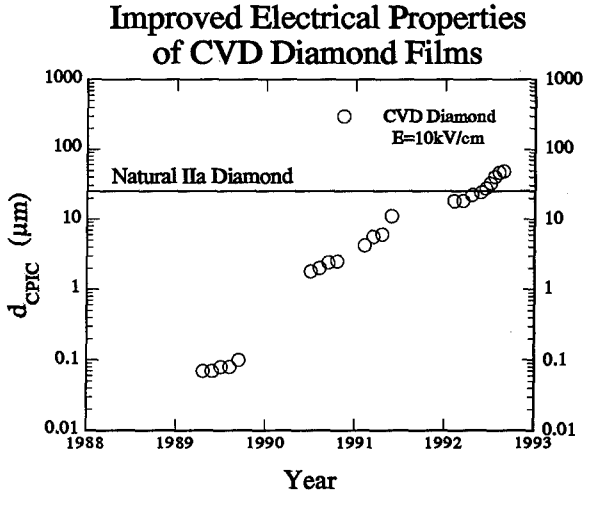

Figure 2: *Improvement in the CPIC collection distance for CVD films as a function of time.*

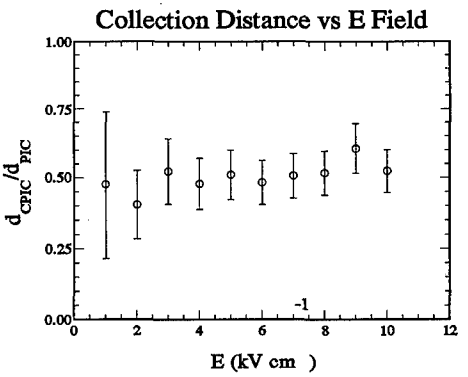

Figure 3: *The ratio of d_{CPIC}/d_{PIC} as a function of the electric field E.*

Photoconductivity measurements were performed using dye lasers pumped with a YAG laser. Photons with $E_\gamma = 6.11$eV were obtained. The absorption depth (1/e) for the photon is approximately $1 \sim 2\mu$m thus the electron hole pair creation occurs in a region near the surface [7]. Therefore, the PIC technique provides information about the surface of the diamond film.

When a charged particle passes through the diamond film ionizing the material, or when a photon with E_γ greater than the band gap is absorbed, excess electron hole pairs ($Q_{\rm ion}$) are produced. In each case, the number of pairs created is calculated directly from the amount of energy absorbed [4, 8, 9]. When a voltage is applied to the contacts, the electric field, E, causes motion of the excess carriers which induces image charges ($Q_{\rm ind}$) on the electrodes. In either CPIC or PIC measurements, the measured collection distance, $d_{\rm meas}$ ($d_{\rm CPIC}$ or $d_{\rm PIC}$), is given by

$$d_{\rm meas} = \frac{Q_{\rm ind}}{Q_{\rm ion}} L$$

where L is the electrode spacing; $Q_{\rm ind}$ is measured from the integration of the current pulse; and $Q_{\rm ion}$ is the number of excess electron hole pairs produced by the radiation. Over the past few years there has been a dramatic improvement in the collection distance [4] as shown in figure 2.

SEM studies show that polycrystalline CVD diamond typically grows in cone shaped columnar structures. The substrate side of the films begin with small grains, typically 1μm or less. The average grain size on the growth side of the films increases with film thickness and is typically about 40 μm for the thickest samples. The grains exhibit a preferred crystal orientation, usually (110), which was determined from x-ray diffraction studies. With the columnar structure along the growth direction, it is possible for the electrical properties to change with the film thickness. To investigate this possibility, samples were grown to 500μm thickness and then cut into pieces. A slow mechanical lapping process was used to remove varying amounts of material from the substrate side of each piece. In this way, a series of samples with differing thickness was created to measure the depth profile of the electrical properties.

For single crystal natural type IIa diamond, the CPIC measurements of the collection distance averaged over the bulk material and the PIC measurements of the surface collection distance give identical results indicating uniform electrical properties throughout the single crystal diamond [3, 4, 8, 10]. Our data indicate that for CVD diamond films, the collection distance averaged over the bulk of the material is not equal to the collection distance near the surface of the material. This implies that the collection distance is not a constant along the columnar direction. A

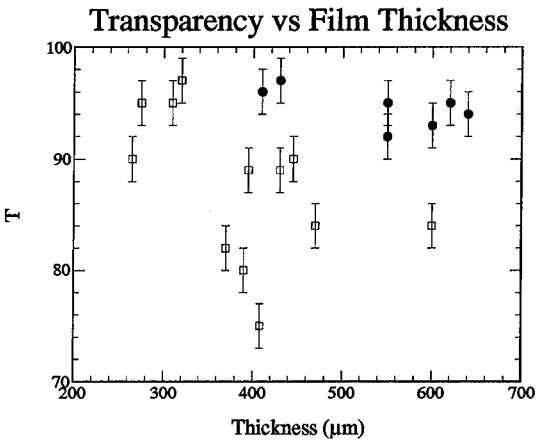

Figure 4: *Transparency as a function of film thickness. The dark points are for CVD samples with large collection distance ($25\mu m < d < 35\mu m$ at an electric field of 10 kV cm^{-1}), while the open points are for CVD samples with small collection distances ($d < 5\mu m$ at an electric field of 10 kV cm^{-1}).*

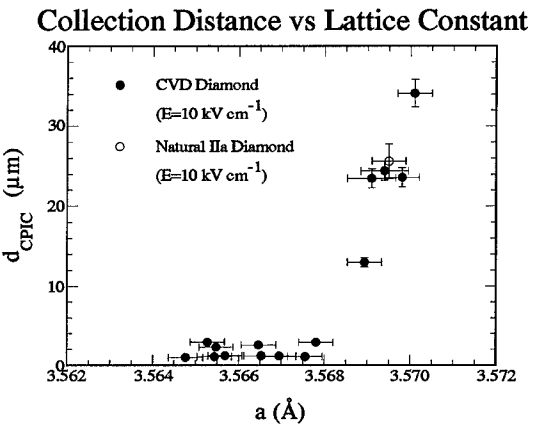

Figure 5: *Collection distance as a function of the measured lattice constant, the scale is not absolutely calibrated. The value for a type IIa natural diamond is shown for reference.*

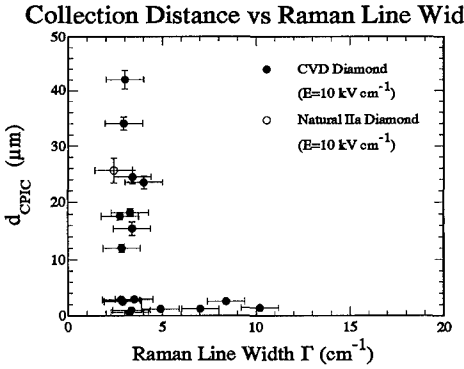

Figure 6: *Collection distance as a function of the measured Raman line width. A natural type IIa diamond has also been measured and is shown for reference.*

linear change in the collection distance with depth is observed. A weighted fit of the data yields $d_{\mathrm{CPIC}} \approx (0.51 \pm 0.07)\, d_{\mathrm{PIC}}$. This indicates that the bulk properties are approximately the average of those at the two surfaces of the film, consistent with $d_{\mathrm{CPIC}} \approx 0.5\ d_{\mathrm{PIC}}$. In figure 3 we plot d_{CPIC}/d_{PIC} for an individual CVD sample indicating that the result is independent of the electric field.

The collection distance was also found to be correlated with several physical characteristics of the CVD films. Visual observations were used to quantify the transparency of each diamond film with a value assigned from 0 (opaque) to 100 (translucent). The transparency as a function of the film thickness is shown in figure 4. Notice that films with a large collection distance have high transparency, but not all high transparency films have a large collection distance. In addition, the transparency for diamonds with superior electrical properties is only weakly dependant on the film thickness, while diamonds with poor electrical properties are transparent only when thin.

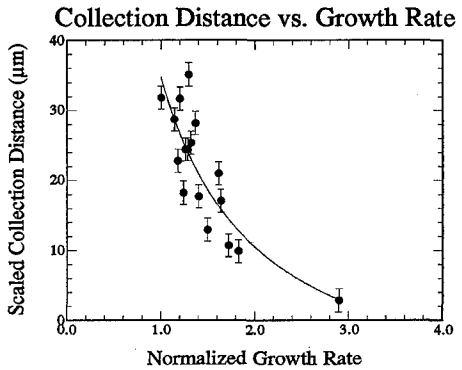

Figure 7: *The collection distance as a function of the normalized growth rate. The values are scaled to account for variations due to varying sample thicknesses.*

Correlations were also found between the collection distance and the X-ray diffraction peak width and lattice constant. As shown in figure 5, the collection distance increases with lattice constant. Furthermore, samples with larger collection distances have narrower X-ray diffraction peak widths. A narrow peak is not sufficient for a large collection distance, however. These studies indicate that film quality is important for electrical properties in CVD films. Raman line width provides a further indication of overall film quality. Broader line widths indicate higher defect rates within the film. The collection distance has been measured as a function of the Raman line width and is shown in figure 6. Again, a narrow Raman line width is necessary but not sufficient to guarantee a large collection distance.

Although the impurity density is not likely to be affected by the growth rate of the CVD film, the defect rate may vary significantly. To study the effects on electrical properties, sample were grown at various rates and their collection distances measured. Due to variations in the collection distance with sample thickness, values were scaled to a uniform electric field (10 kV cm^{-1}) and film thickness (400 μm). The data (figure 7) show a strong correlation between the growth rate and collection distance. The inverse relation between growth rate and collection distance provides further evidence that defect densities influence the electrical properties of CVD films.

SUMMARY

A gradient in electrical properties has been observed in polycrystalline CVD diamond, increasing linearly from the substrate side to the growth side of the film. The material properties also show a gradient; the average grain size increases with film thickness. The collection distance has been found to be correlated with visual transparency, lattice constant, X-ray diffraction peak width, Raman line width, and growth rate. From these correlations, we conclude that a low defect density is required for high quality electrical properties.

ACKNOWLEDGEMENTS

This work is supported, in part, by grants from the Texas National Research Laboratory Commission (RGFY9164, RGFY9264, and RGFY93251), and the Department of Energy through the SSC Research Program (92/32100), and the Department of Energy through a grant to Lawrence Livermore National Laboratory (W-7405-ENG-48).

REFERENCES

1. R. W. Keyes, Proc. IEEE **60**, 225 (1972); A. Johnson, RCA Rev. **26**, 163 (1965).
2. K. L. Moazed *et al.*, J. Appl. Phys., **68**, 2246 (1990).
3. L. S. Pan *et al.*, J. Appl. Phys., **74**, 1086 (1993).
4. S. Zhao, Ph. D. thesis, The Ohio State University (1994).
5. B. Rossi, *High Energy Particles* (Prentice-Hall, New York, 1952); E. Serge, *Nuclei and Particles* (Benjamin, New York, 1965).
6. C. Canali *et al.*, Nucl. Instr. and Meth., **160**, 623 (1990).
7. E. L. Palik, *Handbook of Optical Constants of Solids* (Academic, New York, 1985), pp. 665-673; B. L. Henke *et al.*, At. Data Nucl. Data Tables **27**, 1 (1982).
8. M. Franklin *et al.*, Nucl. Instr. and Meth., **A315**, 39 (1992).
9. M. A. Plano *et al.*, Appl. Phys. Lett., **64**, 193 (1994).
10. L.S. Pan *et al.*, Mat. Res. Soc. Symp. Proc., **Vol 302** (1993).

CONDUCTIVITY ANISOTROPY IN EPITAXIAL 6H AND 4H SiC

WILLIAM J. SCHAFFER, G.H. NEGLEY, K.G. IRVINE and J.W. PALMOUR
Cree Research, Inc., 2810 Meridian Parkway, Durham, NC 27713

ABSTRACT

A measure of the electron mobility anisotropy in n-type 4H and 6H-SiC has been obtained using the Hall effect over the temperature range 80K<T<600K. Hall mobility and resistivity data are collected from appropriately oriented bar patterns fabricated into high quality epitaxial material grown on $(1\bar{1}00)$ or $(11\bar{2}0)$ surfaces having total impurity concentrations 10^{17}-10^{18} cm^{-3}. The observed mobility ratio for 4H is $\mu_{[11\bar{2}0]}/\mu_{[0001]} = 0.83$ and is independent of temperature. For 6H, the ratio $\mu_{[1\bar{1}00]}/\mu_{[0001]}$ decreases from ~6.2 at 80K to ~5.0 at 150K and is essentially constant (~4.8) above 200K. A donor level near 0.6 eV is occasionally observed in 4H which reduces the high temperature electron mobility and introduces an apparent temperature dependence to the mobility ratio if nonuniformly distributed.

INTRODUCTION

Epitaxial 6H and 4H-SiC materials are currently receiving considerable attention for electron device applications requiring high temperature, high power and high frequency performance. Because of the hexagonal symmetry, the electron transport properties differ between the basal plane of the crystal and the c-axis and the anisotropy differs from polytype to polytype as the unit cell dimension in the [0001] direction changes.[1] A direct measure of the mobility anisotropy in both polytypes is required for device modeling and integrated circuit design. It will be possible to optimize the performance of electron devices in which the current flow is primarily one dimensional by choosing an appropriate orientation of the device with respect to the crystal structure.

Previous measurements[2,3] of the bulk resistivity ratio, $\rho_{\parallel}/\rho_{\perp}$, have been reported on various polytypes of SiC using Schnabel's method.[4] The technique requires current and potential point contacts to be arranged in pairs on either side of a slab sample and determines the resistivity ratio from terminal resistances and tabulated functions derived from equipotential calculations. The measured resistivity ratio for 6H was 2.0 - 3.7 and ≈1 for 4H at T≈1000K for samples with $N_D+N_A > 5x10^{18}$ cm^{-3}. Since these measures of the anisotropy were obtained from highly doped material and because Schnabel's technique does not provide independent measures of the mobility or the ability to account for extrinsic effects, Hall effect data from high quality epitaxial material is used in this experiment to provide a better measure of the intrinsic anisotropy.

The quantity of interest is the ratio of the Hall mobilities,

$$\frac{\mu_{H\perp c}}{\mu_{H\parallel c}} = \frac{\mu_{\perp c}}{\mu_{\parallel c}} = \frac{n_{\parallel c}\rho_{\parallel c}}{n_{\perp c}\rho_{\perp c}} = \frac{m^*_{\parallel}}{m^*_{\perp}}. \qquad (1)$$

Mat. Res. Soc. Symp. Proc. Vol. 339. ©1994 Materials Research Society

When the Hall factor is isotropic, the Hall (μ_H) and drift (μ) mobility ratios are equal. The resistivity ratio ($\rho_\parallel/\rho_\perp$) requires scaling if the free carrier concentrations (n) differ between samples oriented parallel and perpendicular to the c-axis. From the mobility ratio, a measure of the ratio of effective masses (m^*) is obtained. The individual mobility curves provide qualitative insight into any nonuniformity in the scattering mechanisms between directions.

EXPERIMENT

Hall measurements using the van der Pauw[5] technique are appropriate only when the resistivity is isotropic in the plane of the measurement, e.g., the basal plane of the hexagonal polytypes of SiC. If the carrier transport properties are anisotropic in the plane, the Hall current must be constrained to the desired measurement direction. This is accomplished using bar geometries with aspect ratios of ~10:1. For hexagonal symmetry, it is possible to measure the anisotropic transport properties in a single epitaxial layer if the growth plane contains both the [0001] direction (c-axis) and a basal plane direction.

For 4H and 6H-SiC, the $[11\bar{2}0]$ and $[1\bar{1}00]$ directions lie in the basal plane and include a 30° angle. Consequently, the $[11\bar{2}0]$, $[1\bar{1}00]$ and [0001] directions, or their equivalents, will form an orthogonal set. High quality material can be produced with the [0001] and $[11\bar{2}0]$ or $[1\bar{1}00]$ directions in the surface plane by growing epitaxial layers on either the $(1\bar{1}00)$ or $(11\bar{2}0)$ surfaces. Anisotropic transport properties are then determined from Hall effect measurements on perpendicularly oriented bar patterns such as those shown in Figure 1. Since the mobility data from two different sites will be ratioed, it is important to verify uniformity by requiring that the free carrier concentration curves be identical. If the impurity ionization curves differ, the resistivity or mobility must be scaled for different carrier concentrations and different impurity densities.

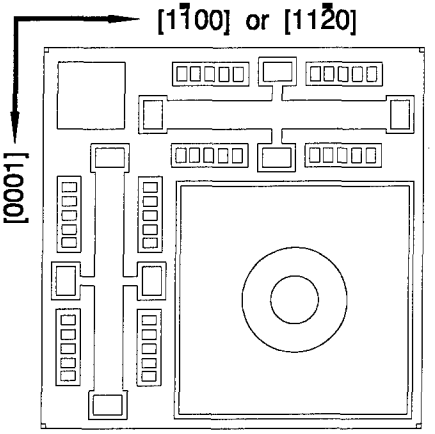

Figure 1 4mm x 4mm die for anisotropic Hall, contact resistance and C(V) measurements.

In this experiment, 4H and 6H-SiC boules have been oriented to within ±¼° of $[1\bar{1}00]$ or $[11\bar{2}0]$, wafered and polished for epitaxial growth. Layers 3-6 μm thick are grown onto buffer layers of the opposite conductivity type to eventually provide pn junction isolation of mesa etched devices for either van der Pauw (cloverleaf) or Hall bar (Figure 1) geometries. The layer thicknesses and uniformity are monitored by SIMS profiling since the optimum epitaxial growth parameters vary significantly for different growth faces. Ohmic contacts are formed by alloying aluminum or nickel into p or n-type material. After metallization, the sample is wire bonded into a Joule-Thomson refrigerator (80K<T<600K) and data is taken under computer control in a magnetic field of 0.4 T. Analysis of the temperature dependence of the free carrier concentration curves provides measures of the total impurity concentration, density of compensating impurities

Table I Caughey-Thomas parameters for basal plane mobilities in 4H and 6H SiC.

Material	μ_{max} (cm^2/Vs)	μ_{min} (cm^2/Vs)	N_{ref} (cm^{-3})	γ
N:4H	947	0.0	$1.94x10^{17}$	0.61
N:6H	415	0.0	$1.11x10^{18}$	0.59
Al:4H	124	15.9	$1.76x10^{19}$	0.34
Al:6H	99	6.8	$2.10x10^{19}$	0.31

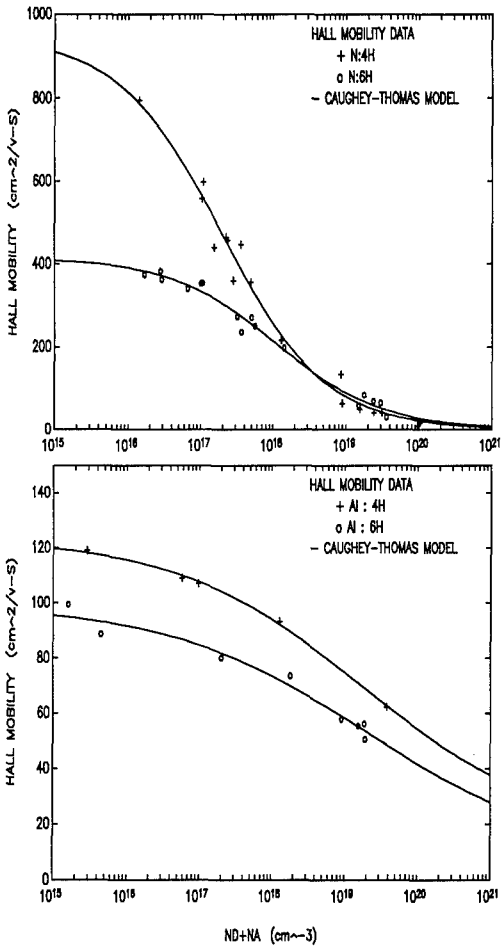

Figure 2 Mobility in the (0001) plane for nitrogen and aluminum doped epitaxial 4H and 6H-SiC at 300K. Solid curves are least squared error fits to Eqn (2) using the parameters in Table I.

and impurity energy levels.[6]

RESULTS

Basal plane Hall mobility data obtained at 300K from van der Pauw patterns is summarized in Figure 2. The solid lines are least squared error fits (Table I) to an empirical relation suggested by Caughey and Thomas[7] for silicon,

$$\mu = \mu_{min} + \frac{\mu_{max} - \mu_{min}}{1 + \left(\frac{N_D+N_A}{N_{ref}}\right)^{\gamma}} . \qquad (2)$$

From these data, the electron mobility in 4H-SiC is twice that of 6H for total impurity concentrations less than $\approx 10^{17}$ cm^{-3}. Further, the hole mobility in 4H-SiC is 20-30% higher than in 6H over the entire impurity range.

The temperature dependence of the free carrier concentration and mobility for a 4.7 μm thick epitaxial layer of nitrogen doped 4H-SiC grown on the $(1\bar{1}00)$ surface are given in Figures 3 and 4. The inset in Figure 3 shows an expanded linear plot of the high temperature portion of the ionization curve. There is an additional donor level in this sample which is estimated to be 0.55-0.6 eV below the conduction band edge. A higher density of these deeper donors is seen in the free carrier curve from the bar

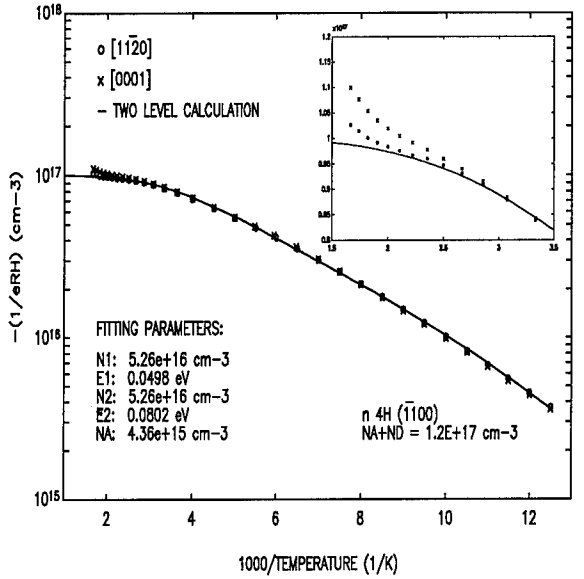

Figure 3 Ionization curves for n-type 4H-SiC grown on ($1\bar{1}00$) from patterns aligned along [0001] and [11$\bar{2}$0].

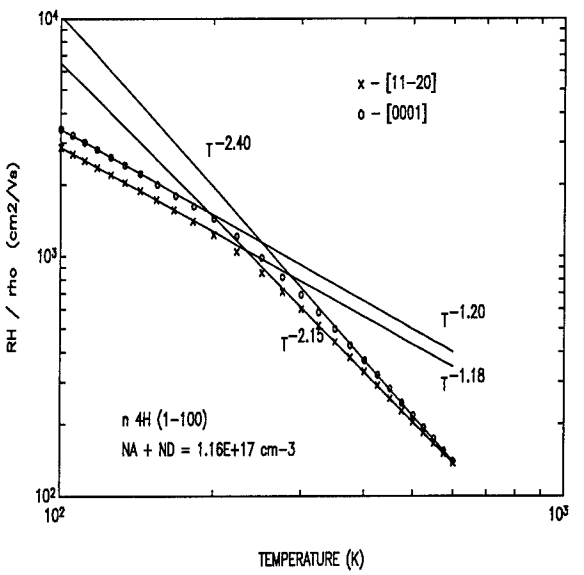

Figure 4 Mobility anisotropy in n-type 4H-SiC measured in the [0001] and [11$\bar{2}$0] directions.

oriented in the [0001] direction and is associated with a steeper high temperature mobility characteristic, presumeably due to additional ionized impurity scattering. As a result, the ratio of the mobilities at the two sites appears temperature dependent, as seen in Figure 6. The mobility ratio measured from a different wafer showing no evidence of this deeper level is also given in Figure 6 for comparison. No temperature dependence of the mobility is observed for the sample without the deeper level.

Similar data from epitaxial 6H-SiC grown on the (11$\bar{2}$0) surface with a total impurity concentration of 1.0×10^{17} cm^{-3} are shown in Figures 5 and 6. In this sample, the free carrier concentration curves are identical and show no deeper levels. The temperature dependence of the mobility is the same at both measurement sites for higher temperatures, but the mobility in [0001] begins to saturate below 150K, causing an increase in the mobility ratio below this temperature. A result from an additional sample with a total impurity concentration of 1.1×10^{18} cm^{-3} is given in Figure 6 and shows identical behaviour.

REMARKS

Barrett and Campbell[8] reported that the temperature dependence of the electron Hall mobility in SiC above 300K is T^{-n} with $n \approx 2.4$ and suggested, from data on 15R-SiC prepared by the sublimation technique, that

samples of higher purity (i.e. lower doping) would show even larger values of n. Patrick[9] argued from this data and also from modeling results obtained by Long[10] on n-type Si, that the dominant high temperature scattering mechanisms in n-type SiC are acoustic phonon and intervalley scattering.

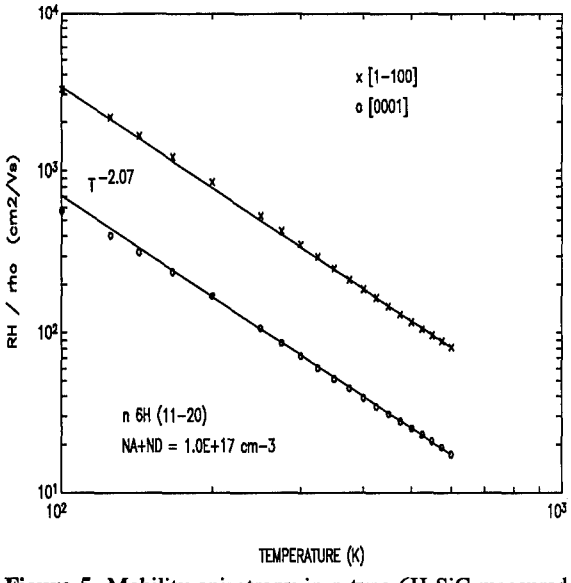

Figure 5 Mobility anisotropy in n-type 6H-SiC measured in the [0001] and [1$\bar{1}$00] directions.

The current results are contrary to Barrett and Campbell's conclusion. From the data in Figures 3 and 4, it appears that a higher density of the deeper level is associated with a larger exponent. From all the data (over 100 6H and 4H epitaxial wafers), samples in which 1) a high temperature mobility asymptote can be clearly identified and 2) no evidence of a deeper level is detected in the high temperature portion of the free carrier concentration curve, n is always ≤2.0, with a minimum of n=1.80 in an exceptional n-type 4H sample. The issue appears to be the magnitude of the contribution of ionized impurity scattering to the total mobility for T>300K. Using the Brooks-Herring[11] formula for an estimate of μ_I and the Bardeen-Schockley[12] formula for μ_L (albeit the band minimum is not at the center of the zone in n-type SiC), the magnitudes of the theoretical mobilities are comparable near 300K for $N_I \approx 1x10^{18}$ cm^{-3}. Combining these mobilities using the approach of Debye and Conwell[13] and comparing the result to the observed mobility, our estimate is that the steeper temperature dependence near 300K can result from increased ionized impurity scattering in either heavily doped material or material with a

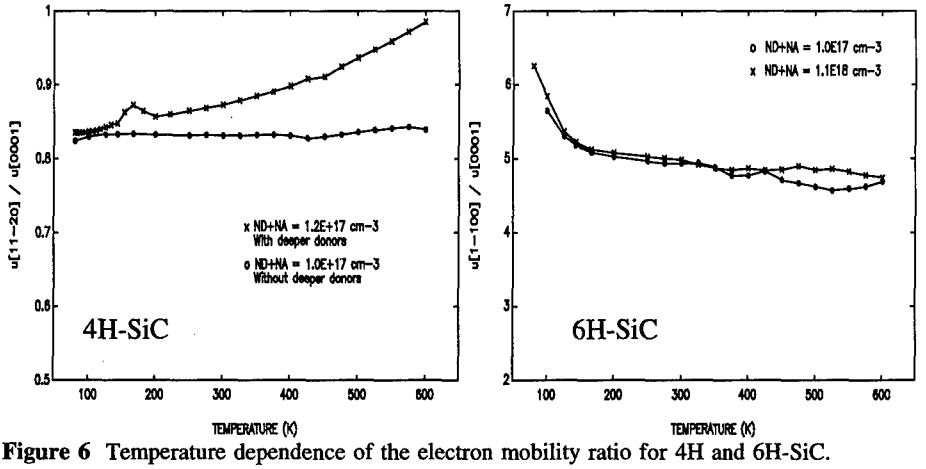

Figure 6 Temperature dependence of the electron mobility ratio for 4H and 6H-SiC.

significant concentration of impurities near 0.6 eV. The mobility estimates are preliminary and require thorough analysis, which is now underway.

The conclusion regarding the high temperature dependence of the mobility in low doped, low compensation n-type SiC with no ionizeable levels near room temperature is that the mobility varies as $T^{-1.80}$. Since this temperature dependence is nearly characteristic of acoustic phonon scattering, it appears that intervalley scattering contributes less to limit the mobility than previously anticipated.

A Hall mobility ratio $\mu_{[11\bar{2}0]}/\mu_{[0001]} = 0.83$ is measured for 4H SiC and is temperature independent in homogeneous samples. These results are in qualitative agreement with previous measurements and quantitative agreement with recent results[14] on bulk 4H and 6H-SiC. There is no clear evidence that the conductivity effective mass ratio changes over this temperature range. The ratio $\mu_{[1\bar{1}00]}/\mu_{[0001]} = 4.8$ is measured for 6H and shows an increase to ~6.2 at 80K. Since similar curves are obtained for two impurity densities with similar compensation levels (N_A ~ $8x10^{14}$), it is unlikely that the effect is associated with ionized impurity scattering. Likewise, since the free carrier concentration curves are nearly identical, anisotropic effects of nonuniform neutral impurity scattering should be insignificant. Preferential dislocation scattering should be minimal in these high quality layers. Whether preferential scattering due to extrinsic defects (e.g., striations in point defects or doping) or a temperature dependence of the effective mass ratio has been observed in 6H SiC is undecided.

ACKNOWLEDGEMENTS AND REFERENCES

This work was supported by BMDO through Wright Laboratories (Contract No. F33615-93-C-2340) and NIST (Award No. 70NAN132H1252). Additional support was provided by the Office of Naval Research (Contract Nos. N00014-92-C-0083 and N00014-93-C-0071) and NASA (Contract No. NAS3-26927). It is a pleasure to acknowledge valuable discussions with Prof. Gerhard Pensl.

1. L.A. Patrick, Mat. Res. Bull. **4**, 129 (1969).
2. G.A. Lomakina and Yu.A. Vodakov, Fiz. Tverd. Tela [Leningrad] **15**, 123 (1973) [Sov. Phys. Solid State **15**, 83 (1973)].
3. G. Bosch, J. Phys. Chem. Solids **27**, 795 (1966).
4. P. Schnabel, Philips Res. Repts. **19**, 43 (1964).
5. L. van der Pauw, Philips Res. Repts. **13**, 1 (1958).
6. W. Schaffer, H. Kong, G. Negley, J. Palmour, Proc. 1993 ICSCRM, Phys. Stat. Solidi, (in press).
7. D.M. Caughey and R.E. Thomas, Proc. IEEE **55**, 2192 (1967).
8. D.L. Barrett and R.B. Campbell, J. Appl. Phys. **38**, 53 (1967).
9. L.A. Patrick, J. Appl. Phys. **38**, 50 (1967).
10. D. Long, Phys. Rev. **120**, 2024 (1960).
11. H. Brooks, Phys. Rev. **83**, 879 (1951).
12. J. Bardeen and W. Schockley, Phys. Rev. **80**, 72 (1950).
13. P.P. Debye and E.M. Conwell, Phys. Rev. **93**, 693 (1954).
14. G. Pensl (private communication).

DIFFUSION OF IMPURITIES UNDER BIAS IN CVD DIAMOND FILMS

G. POPOVICI*, T. SUNG*, M. A. PRELAS*, S. KHASAWINAH*,
AND R. G. WILSON**
*Nuclear Engineering Department, University of Missouri, Columbia, MO 65211
** Hughes Research Laboratories, Malibu, CA 90265

Abstract

The diffusion of oxygen, lithium, chlorine, and fluorine in CVD diamond films was performed under bias at 700 and 1000 ^{o}C. SIMS and Auger analyses were used to determine the impurity concentration. After diffusion, the concentrations of Li and O in the diamond films were found to be of the order of (3-4)$\times 10^{19}$ cm^{-3}. The fluorine concentration was of order of (1-2)$\times 10^{17}$ cm^{-3}. The conductivity was p-type. The change in the resistivity due to diffusion was nearly nine orders of magnitude for the sample diffused under electric field, and six orders of magnitude for the samples diffused without field. No dependence of the impurity concentration on the applied bias was observed except for fluorine. The fluorine concentration dependence on the electric field indicates that fluorine may have formed a shallow level in the diamond band gap. The fact that large concentrations of impurities can be diffused into diamond films at relatively low temperatures indicates the presence in the films of many lattice defects (including grain boundaries).

Introduction

The development of an electronic technology based on diamond thin films requires solving the problem of reproducible doping by donor and acceptor impurities to obtain p-n junctions, which form an essential part of many electronic devices. It is well known that p-type conductivity can be obtained by boron doping. Obtaining n-type conductivity is a more difficult problem.

The basic difficulties of diamond doping are caused by lattice rigidity and the small covalent radius of carbon.[1] Thus, only boron and nitrogen of all prospective substitutional dopants have covalent radii small enough to enter the diamond lattice. The boron atom is electrically active in diamond and can be described by the hydrogen-like model. Nitrogen does not form a shallow donor in the diamond band gap.[2-3] Other impurities such as substitutional phosphorus, or interstitial lithium and sodium have been tried for n-type doping. The results on phosphorus doping are contradictory. Earlier papers reported a shallow level.[4] Later, a number of researchers found that phosphorus forms a deep (0.8 to 0.9 eV) level in the band gap.[5-6] Doping by lithium has been done by ion implantation,[7-8] during growth[9] and by diffusion.[8, 10-11] Reports on Li diffusion into diamond are inconsistent. In reference 10, it was reported that Li atoms diffused at temperatures between 400 and 900 ^{o}C as measured using secondary ion mass spectrometry (SIMS) analysis. In reference 11,

Mat. Res. Soc. Symp. Proc. Vol. 339. ©1994 Materials Research Society

opposite results were obtained. No diffusion of implanted Li was detected after annealing at 1400 °C for several hours. In reference 12, implanted Li did not redistribute during 1000 °C thermal treatment.

Theory predicts a very low solubility of potential n-type impurities in the diamond lattice.[13] Taking into account the high rigidity of the diamond lattice, high temperatures would be required for effective diffusion of impurities.[1] It is known that interstitial impurities, like Cu, Li, and Na are fast diffusing and can be introduced into semiconductor lattices at lower temperatures than substitutional impurities.[14] For instance, Li diffuses in Si in the relatively low temperatures range (300-500 °C), which is lower than the temperature of diffusion for substitutional impurities (800-1100 °C).[14]

In this paper, a study of lithium, oxygen, and chlorine diffusion in CVD diamond films is reported. An electric field was used to enhance diffusion of those impurities that could be ionized at the diffusion temperature. Positive ions are accelerated to the negative electrode and negative ions to the positive electrode. To our knowledge no experimental results on the field-assisted diffusion have been reported yet for diamond. The field-enhanced diffusion of Li into diamond lattice should be effective,[1] if the predictions of theory, that Li forms a shallow donor level in the diamond band gap with activation energy ΔE=0.1 eV,[13] is correct. (Li atoms would be nearly totally ionized at 1000 °C). In our experiments we have not detected any influence of electric field on the diffusion of Li. We have to conclude that Li must form a deeper level in the diamond band gap than the theory predicts.

Experimental

Free standing diamond films, received from Norton Co, 230 μm thick, with medium size crystallites of the order of tens micrometers, and polished on both sides have been used in this work. Samples B, as well as samples C, were of the same batch. Raman spectra of the samples showed the diamond line only. The lines of graphite and amorphous carbon were absent from the Raman spectra. The films were mounted on a graphite base with an imbedded tungsten heater. The base temperature was monitored using a chromel-alumel thermocouple. The experimental conditions of diffusion are listed in Table I.

Table I. Experimental conditions of diffusion

Sample	Dopant Source	Temperature (°C)	Time (min)	Applied Voltage (V)	Current (mA)
C5	$LiClO_4$	700	100	100	0.5-0.9
C6	$LiClO_4$	990	180	30	2.5
B4	Li_2CO_3	1000	190	200	0.5
B5	Li_2CO_3	1000	190	-200	0.5
B6	Li_2CO_3	1000	190	0	0

The dopant sources, $LiClO_4$ and Li_2CO_3, were of analytical purity (99%). During the diffusion process dc potential of 100 and 30 V were applied to samples C5 and C6, respectively. The negative terminal of the source was applied to the graphite base. The positive terminal was applied to the dopant source placed on the upper surface of the sample. A graphite rod served as the upper contact. The resulting field should push the positive ions into the sample. The diffusion was performed in a hydrogen atmosphere.

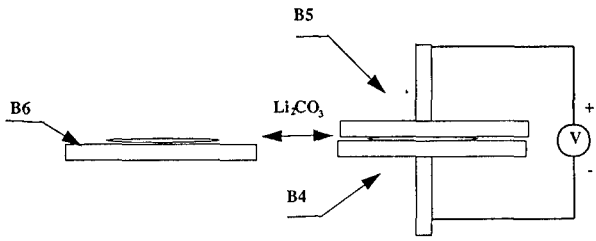

The samples of the B series were arranged as shown in Fig. 1. The applied field should have pushed the positive ions into sample B4 and negative ions into sample B5. The control sample, B6, had no electric field applied. The diffusion was performed in an argon atmosphere.

Fig. 1. Experimental arrangement for the diffusion

After diffusion, the samples were boiled in a Cr_2O_3+HSO_4 mixture for 20 min and washed in deionized water. The resistivity was measured at room temperature. Depth profiles of O and Cl were performed on the C samples using Auger measurements. Depth profiles of H, Li, O, and F on the B series were measured using SIMS. The primary beam was 14.5-keV Cs and secondary negative ions were measured for H, O and F. Li was measured using 8-keV primary O_2 beam and positive secondary ions, in a separate profile. Quantification was carried out using implanted standards for all these elements in crystalline diamond.

Result and Discussions

The resistivity of pristine samples at room temperature was 10^{14} Ω cm. After diffusion, the resistance was measured and was found to be ~10^5 Ω for the B and C samples diffused under electric field, and 10^8 Ω for the sample B6 diffused without an electric field. Supposing that the diffused conducting layer was 2-5 micrometers thick, one can estimate that the layer resistivity of the samples diffused under electric field was approximately 20-50 Ω cm. The change in resistivity was nearly twelve orders of magnitude. The samples diffused under electric field exhibit p-type conductivity as measured using a thermal probe. We did not succeed in determining the type of conductivity of sample B6 diffused without electric field , as the sample resistance was too high for the thermal probe test equipment.

Concentration profiles of the impurities in the C samples were determined using Auger spectroscopy. The samples were gradually sputtered to a depth of 1600 Å. The results for oxygen and chlorine are shown in Fig. 2. A chlorine concentration of 0.1 at. % was achieved. An oxygen concentration at 1500 Å of approximately 0.1at. % in sample C6 was

found, and 0.01 at %, in sample C5.

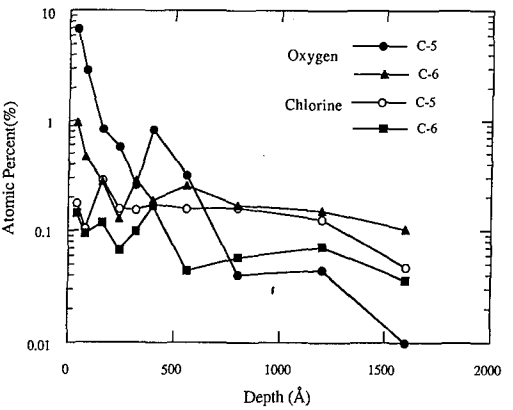

The quantity of oxygen near the surface is larger for lower diffusion temperature (700 C) than for a higher diffusion temperature (990 °C). This can be explained in the following way. $LiClO_4$ decomposes at 430 °C. Oxygen reacts with hydrogen more readily at higher temperatures, and diffusion has been performed in a hydrogen atmosphere. Lithium was not found in the sample, but the sensitivity of the Auger method to Li is very low. Hydrogen can not be detected by Auger analysis.

Fig.2 Auger profiles of oxygen and chlorine in the samples C5 and C6

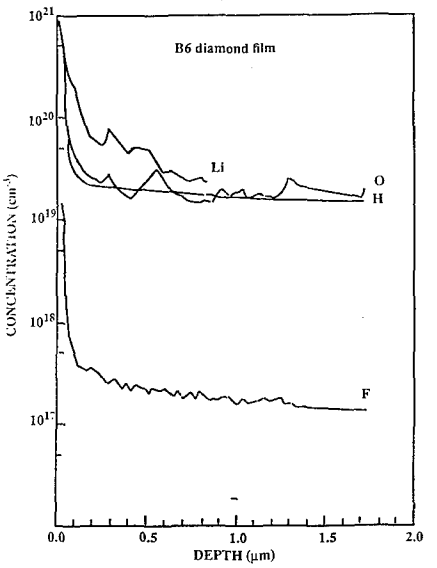

Fig.3 SIMS profiles of Li, O, H and F

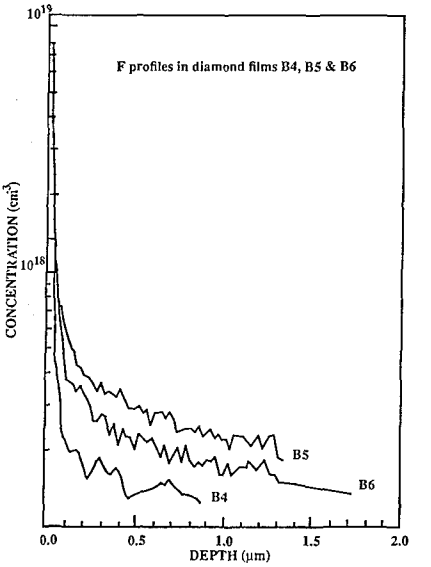

Fig. 4. SIMS profiles of fluorine

The results of SIMS analysis for sample B6 are shown in Fig. 3. The results are shown only for sample B6, as there was no difference in the doping profiles for any of the B samples (except for fluorine, see Fig. 4). Oxygen, hydrogen, lithium, and fluorine were found to be

present in the diamond lattice. Fluorine was present as an impurity in the diffusion source , as its purity was of only 99%. Oxygen and hydrogen concentrations of approximately 3×10^{19} cm^{-3} were found. We did not check the presence of hydrogen in the sample before the diffusion. However, the presence of hydrogen of the order of 0.1at% in CVD diamond films has been reported earlier.[8,15] We should not exclude the possibility of hydrogen diffusion from graphite, as earlier experiments have been done in hydrogen atmosphere. Li diffused into the diamond films to ~3×10^{19} cm^{-3}. No dependence of diffusion on bias was detected for Li, implying that the fraction of ionized Li atoms is small, if any. The Li level must be deeper, than the theory predicts (0.1eV).[13] Li probably diffuses mostly on the grain boundaries, as it was shown earlier.[8, 11]

Only the fluorine concentration was found to be possibly influenced by the electric field, applied during diffusion. The quantity of fluorine that entered the lattice is smaller for the negatively biased and larger for positively biased sample as compared with the unbiased one. Fluorine appears to, at least partially, diffuse as negative ions. In the unbiased B6 sample, the fluorine concentration is ~1×10^{17} cm^{-3} (at the depth of 0.7μm). In the positively biased B5 sample, the concentration is approximately doubled, while in negatively biased B4 sample the concentration is ~0.5×10^{17} cm^{-3}. In order to be partially ionized at 1300 K, fluorine should have in the diamond band gap a shallow level with an energy of the order of $2kT \approx 0.22$ eV. Impurities of the seventh group of the periodical table, F and Cl, in interstitial positions should act as shallow acceptors in covalent semiconductors. One can speculate that the p-type conductivity in the samples after diffusion is due to fluorine or chlorine atoms in interstitial sites. However, quantitatively the difference in the fluorine concentration does not explain the differences in conductivity obtained for samples diffused under electric field and those without it.

As was discussed earlier, the solubility and diffusion rate of impurity atoms into the perfect diamond lattice should be low. However, experimentally, a large concentration of impurities was seen to be diffused into these diamond films at relatively low temperatures. This means that the CVD diamond films are not perfect. Large quantities of lattice defects (including grain boundaries) are present in the films. It might be that the cause of the contradictory results obtained by different authors on diffusion of lithium into diamond films is due to the different content of lattice defects in the diamond films.

Conclusions

The diffusion of impurities under bias in CVD diamond films was performed at 700 °C and 1000 °C. $LiClO_4$ and Li_2CO_3 were used as diffusion sources. After diffusion, the concentrations of Li and O in the diamond films were found to be of the order of $(3\text{-}4)\times10^{19}$ cm^{-3} while Cl was ~10^{20} cm^{-3}. No dependence of the impurity concentration on the applied bias was observed, except for fluorine. Fluorine was present as an impurity in the diffusion sources. Its concentration dependence on the electric field indicates that fluorine may have formed a shallow level in the diamond band gap. The decrease in resistivity due to diffusion was larger for the samples diffused under electric field than for the sample diffused without an electric field. The fact that large concentrations of impurities can be diffused into diamond

films at relatively low temperatures indicates the presence in the films of many lattice defects (including grain boundaries).

Acknowledgements

The authors are thankful to Dr. B. Spitsyn for providing the diamond films studied here. The authors also like to thank Mr. J. Chamberlain for the Raman measurements. The authors wish to express their appreciation to the Department of Energy for providing funds for the project.

References

1. G. Popovici and M. A. Prelas, Diamond-Film Semiconductors, Proc. SPIE Conference, OE/LASE'94, January 1994, Los Angeles, to be publ.
2. W. J. P. van Enkevort and E. H. Versteegen, J. Phys. : Condens. Matter v. 4, p. 2361, 1992
3. R. G. Farrer, Solid State Comm. v. 7, p. 685, 1969
4. B. V. Spitsyn and A. E. Alexenko, Diamond materials, Proc. of the SecondInt. Symposion of Electochem. Soc., 1991 ed. by A. J. Purdes, J. C. Angus, R. F. Davis, B. M. Meyerson, K. E. Spear, and M. Yoder, p.597
5. N. Setaka, Technology Update on Diamond, Extended Abstracts (EA-19), ed. P. P. H. Chang, D. Nelson and A. Hiraki, 1989 Materials Research Society,
6. M. Kamo, H. Yarimoto, T. Ando, and Y. Sato, New Diamond Science and Technology, 1991 MRS Int. Conf. Proc., editors R. Messier, J. T. Glass, J. E. Butler, R. Roy, p. 637-641
7. V.S. Vavilov: Phys. Stat. Solidi (a)31, 11 (1975)
8.. M. I. Landstrass, M. A. Plano, D. Moyer, S. P. Smith, and R. G. Wilson, Diamond Materials, Electrochem. Soc., ed. A. J. Purdes, J. C. Angus, R. F. Davis, B. M. Meyerson, K. E. Spear, and M. Yoder, 1991, p. 574-579
9. G. G. Fountain, R. A. Rudder, D. P. Malta, S. V. Hattangady, R. G. Alley, G. C. Hudson, J. B. Posthill, R. J. Markunas, T. P. Humphreys, R. J. Nemanich, V. Venkatesan and K. Das, Diamond Materials, Proc. Second Symp. Electochem. Soc. ed. A. J. Purdes, J. C. Angus, R. F. Davis, B. M. Meyerson, K. E. Spear, and M. Yoder, 1991, p. 523
10. K. Okumura, J. Mort, and M. Machonkin, Appl. Phys. Lett. v.57, p. 1907, 1990
11. C. Cytermann, R. Brener, and R. Kalish, to be published in Diamond and Related Materials.
12. R. G. Wilson, Surface and Coatings Technol. 47, 559 (1991)
13. J. Bernholc, S. A. Kajihara, and A. Antonelli, New Diamond Science and Technology, 1991 MRS Int. Conf. Proc., editors R. Messier, J. T. Glass, J. E. Butler, R. Roy, p. 923
14. B. L. Sharma, Diffusion in semiconductors, Trans Tech Publishers, Germany, 1970, p. 25-62
15. S. Khasawinah, T. Sung, B. Spitsyn, W. H. Miller, G. Popovici, M. A. Prelas, E. J. Charlson, E. M. Charlson, J. M. Meese, T. Stacy, G. Mannig, S. K. Loyalka, R. V. Tompson, J. Chamberlain, and H. White, Diamond Materials, ed. J. P. Dismukes and K. V. Ravi, Electrochemical Society Proc. v.93-17, 1993, p. 1032-1035

BAND-OFFSETS BETWEEN GROUP-III-NITRIDES

E. A. Albanesi, W. R. L. Lambrecht and B. Segall
Department of Physics, Case Western Reserve University, Cleveland, OH-44106-7079

ABSTRACT

The valence-band offset at the zincblende AlN/GaN, AlN/InN and InN/GaN (110) interfaces are calculated self-consistently by means of the linear muffin-tin orbital method using up to 5+5 layer supercells. All interfaces have a type I-offset. Assuming interface orientation and polytype effects on the valence-band maximum to be reasonably small, a type I offset can also be expected for wurtzite interfaces. Our results are in very good agreement with experimental values for AlN/GaN, the only nitride interface for which they are available.

Subject index terms: band offsets, interfaces, heterojunctions, superlattices, III-nitrides.

INTRODUCTION

The group-III-nitride heterojunctions show great promise for short wavelength light-emiting devices because of their wide and direct band gaps. Important progress in the growth and doping of these materials has recently lead to the first successfull fabrication of blue/violet light emitting devices based on $GaN/Al_xGa_{1-x}N$ (for recent reviews, see [1, 2]). The single most important parameter for the design of quantumwell devices is the band-offset. Here, we report the first comprehensive theoretical study of the band-offsets among the group-III nitrides.

While the nitrides GaN, AlN and InN occur naturally in the wurtzite structure, the closely related zincblende phase differs from it by only a very small energy [3] and has already been stabilized for GaN [4, 5, 6] and InN [7]. Although zincblende AlN has an indirect gap (with conduction-band minimum at X), alloys with up to 60 % Al were found to be direct in our recent study of these alloys' electronic structure [8]. Because of its non-polar nature, the (110) interface between zincblende structures is the simplest interface for which to determine the band-offsets. In view of the above, it is of interest both in itself and as a first step in the understanding of the offsets for other interface orientations. We note that interface orientation effects on the average valence-band offsets at isovalent heterojunctions have generally been found to be small [9]. Also, if interdiffusion takes place at real interfaces (even at only a monolayer scale) the specific interface bonding effects would be averaged out [10]. The valence-band maxima in wurtzite and zincblende have a very similar wave function character. One may thus to a good first approximation assume that the average valence-band offsets are polytype and interface orientation independent.

The actual offsets are then expected to be largely determined by the "generic" (110) zincblende offset plus appropriate bulk strain effects on the valence-band maximum and polytype induced changes in the conduction-band minimum. The differences in the conduction-band minimum for the different polytypes are important and are well understood for the semiconductors under consideration [11]. A study of the hydrostatic deformation potential and on further details of the electronic structure for the group-III-nitrides interfaces are in progress [12]. A study of the composition dependence of the bandgaps of $Al_xGa_{1-x}N$ alloys has been reported elsewhere [8].

COMPUTATIONAL METHOD

In the supercell approach, the interface under consideration is periodically repeated in an artificially periodic system with a large unit cell. The charge density of the latter is obtained self-consistently, and from it the layer averaged electrostatic potential profile at the interface. The interface dipole D is defined to be the difference between the asymptotic values of this potential on the two sides of the interface. Our convention is to take D as the difference between the potential on the first minus the second compound. This, combined with the positions of the

Mat. Res. Soc. Symp. Proc. Vol. 339. ©1994 Materials Research Society

bands with respect to the appropriately averaged electrostatic potential in each solid, obtained from a standard bulk band-structure calculation, straightforwardly yields the band-offsets. Here, the linear muffin-tin orbital method [13] is used in the atomic sphere approximation (ASA) including the so-called combined correction, and, in the usual manner, empty spheres at the tetrahedral interstices. The local density approximation (LDA) is used with the Hedin-Lundqvist parametrization of exchange and correlation [14]. The value of the average electrostatic potential in an infinite solid is not uniquely defined [15]. It is given relative to an arbitrary reference energy. Our specific choice for this (arbitrary) reference is the so-called ASA level, which is the average of the electrostatic potential of the point charges associated with the atomic spheres [15]. We found for the {110} interface that five layers of each material are sufficient to obtain reasonable convergence to bulk values for the relevant properties (charge and average point charge electrostatic potential) of the central layer in each half cell. Each layer contains both a cation and an anion and two different types of empty spheres and is neutral for the bulk solids. The layer-averaged net charge and electrostatic potential provide concise information on the interface dipole formation. The present unit cell is large enough that good k-point sampling convergence of the charge density is obtained with four special k-points [16]. The Ga3d and In4d states in GaN and InN respectively are treated as band states since their LDA eigenvalues overlap with the N2s band and were found to be important for obtaining correct ground state charge densities [11].

While GaN and AlN are closely lattice matched ($\sim$ 3% mismatch), InN has a significant mismatch with the other two compounds. In this initial investigation, we nevertheless use a common lattice constant of 4.435 $\AA$ for GaN/AlN, 4.670 $\AA$ for AlN/InN, and 4.735 $\AA$ for InN/GaN. These correspond to the averages of the bulk lattice constants of the parent compounds for each pair.

In our previous work on the GaN/AlN interface [17], we estimated the strain effects on the band offsets to be smaller than 0.2 eV using the absolute hydrostatic deformation potential calculated within the dielectric midgap energy (DME) model [18]. For heterojunctions with In^N, we expect the effects to be somewhat larger. However, since strain effects are dependent on the substrate/film configuration, interface orientation, and polytype, they should be treated separately for each case. We prefer to incorporate these effects later as perturbations due to the deformation potentials of the bulk compounds. The calculation of the needed deformation potentials is in progress. Results for GaN are available in [19].

RESULTS

The (110) layer is neutral in the bulk and at the interface has equal number of III(A)-N and III(B)-N bonds with A and B corresponding to Al, Ga, In. The largest deviations from charge neutrality for this (110) interface occur on the layers immediately adjacent to the interface, and the bulk value (zero) is approached rapidly and is nearly achieved on the third layer of the 5+5 supercells we have used.

The initial offset is $\Delta E_v^0 = E_v(\mathrm{A}) - E_v(\mathrm{B})$ corresponding to the valence band alignment from the band positions relative to the ASA-reference levels in A and B. The final self-consistent value, $\Delta E_v = \Delta E_v^0 + \mathrm{D}$, where $\mathrm{D} = V_{av}(A) - V_{av}(B)$ provides the interface dipole in terms of the local average ASA potentials on the central layers of each half cell. The conduction-band offsets for the zincblende structures, $\Delta E_c^{zb} = E_c^{zb}(\mathrm{A}) - E_c^{zb}(\mathrm{B})$, are obtained by adding to the valence band maxima, the values of the energy gap of each compound. The LDA is well-known to underestimate the band gaps. Thus, we here prefer to use the experimental bandgaps adjusted to the appropriate lattice constant and corresponding to the zincblende crystal structure. The resulting band gaps [20] are 3.2 eV for GaN, 4.9 eV for AlN for the indirect $\Gamma_{15}^v - X_1$ gap, and 1.66 eV for InN. A similar expression is obtained for the conduction-band offset for the wurtzite structure, ΔE_c^w, with experimental direct band gaps of 3.65 eV for GaN, 6.28 eV for AlN and

2.05 eV for InN. The latter are the zero temperature gaps at the equilibrium lattice constant. As mentioned earlier, the character of the wave function at the valence-band maximum (at Γ) in wurtzite is similar to that for the corresponding zincblende crystal. Since, the bonding is also similar, the dipole due to the charge transfer is expected to be similar. It is thus reasonable to assume that the valence-band offsets will be nearly the same in the two structures apart from the symmetry induced splitting of the valence-band maximum in wurtzite. Spontaneous polarization effects due to the polar nature of the {0001} wurtzite interfaces are presently ignored. They will require a separate investigation. From all these considerations, the resulting values for the dipoles and offsets are as follows:

	D	ΔE_v^0	ΔE_v	ΔE_c^{zb}	ΔE_c^w
GaN/AlN	−0.11	0.96	0.85	−0.81	−1.78
AlN/InN	2.16	−3.26	−1.09	2.15	3.14
InN/GaN	−2.08	2.58	0.51	−1.07	−1.09

We note that the values given for wurtzite are expected to be somewhat more approximate than those for zincblende because of the additional approximations involved. Also, the values for the cases involving InN may be subject to strain corrections slightly larger than 0.2 eV, the estimated maximum for the GaN/AlN interface, because of the larger lattice-mismatchs involved.

In Fig. 1 we plot the different interface band offsets, which all turn out to be of type I. In these pictures, we have also included the Γ_1 states for zincblende *AlN*. This state is similar in character to the Γ_1 minimum of the conduction band for the wurtzite structure. As can be seen in the figure, their energies are indeed close.

As an example of interfacial strain effects, we note that if InN is grown on bulk GaN, one would expect the lattice constant in the interface plane to be that of GaN instead of the average of the two. The system will compensate this lateral compression by expanding the lattice constant in the InN film in the direction perpendicular to the interface according to the Poisson ratio. The latter depends on the crystallographic orientation. As an example, consider the experimentally most relevant interface for wurtzite, the basal plane, or the closely related zincblende {111} interface. The Poisson ratio for this direction is ∼0.3 for both GaN and AlN, and we thus also expect that value for InN. This value is obtained from $\sigma_{111} = 2(C_{11} + 2C_{12} - 2C_{44})/(C_{11} + 2C_{12} + 4C_{44})$ and the calculated elastic constants for zb-GaN and AlN by Kim et al. [19]. This implies that the parallel lattice constant $a_{\|}$ of InN would be decreased by about 10 % from its bulk equilibrium value while the perpendicular lattice constant $a_{\perp}$ would be increased by about 3 %. The net volume change is thus a decrease by 16.6 % corresponding to an effective cubic lattice constant change of −5.8 %. This corresponds closely to the average lattice constant that we used. Thus the hydrostatic deformation potential induced change from our present band-offset would be expected to be small. The uniaxial strain component in the ⟨111⟩ direction in this case would be ∼4 %. Assuming that the deformation potentials are similar in GaN and InN, this would lead to an increase in the valence-band maximum by 0.2–0.3 eV. In fact, the uniaxial strain splits the level as follows: $\delta E_v = \{2\sqrt{3/2}d_5\eta_5, -\sqrt{3/2}d_5\eta_5\}$, with $d_5 \approx -5$ eV and $\eta_5 \approx 0.04$. The subscript here refers to the irreducible representation using the notations of Kane [21] and η_5 is the strain tensor component and d_5 the corresponding deformation potential. Thus, we conclude that the band alignment at the wurtzite interface will remain type I even when strain effects are included, at least for the case of the {0001} interface discussed here. Since the valence-band offsets with AlN are of the order of 0.8-1.0 eV, it is unlikely that strain effects would invert them. Thus, the conclusion that the offsets are all of type I appears to be rather robust. We also note that the conduction band offsets in the wurtzite systems make larger relative contributions to the gap discontinuities than do their zincblende counterparts. The zincblende/wurtzite difference in the conduction bands is clearly most dramatic for AlN where it is about 1 eV.

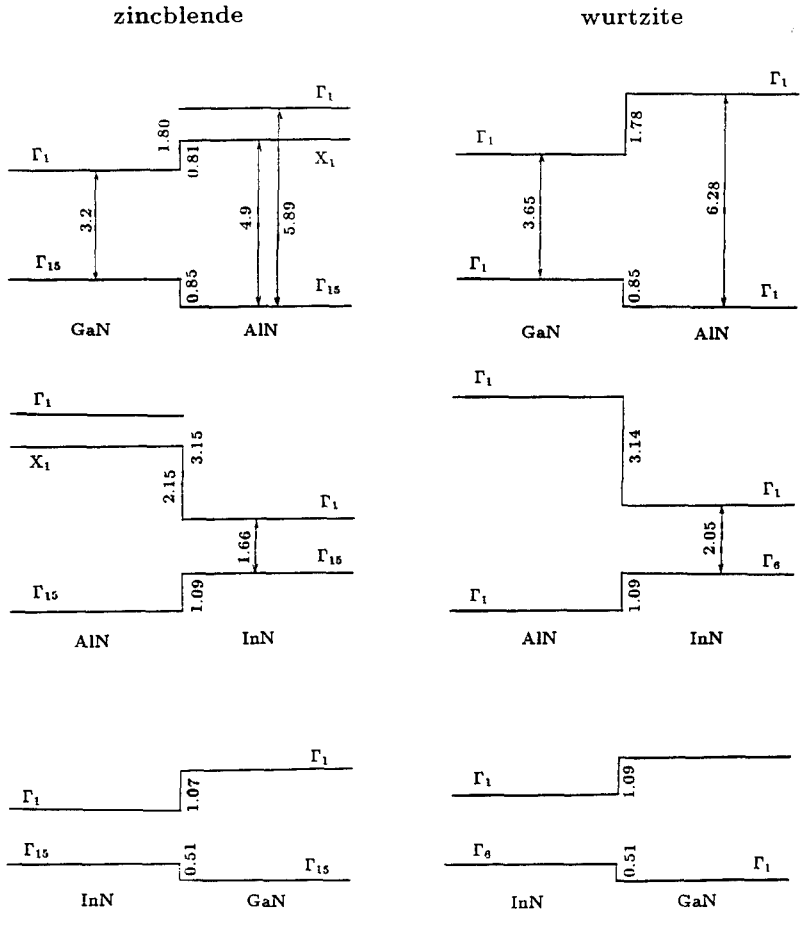

Figure 1: Band-offsets calculated for the zincblende {110} interfaces and estimated for the wurtzite interfaces

Our previous results for GaN/AlN [17] have shown that there are no interface states in the main band gap. This is to be expected for a well-matched interface which preserves the tetrahedral bonding. We anticipate that this will also be the case for the other interfaces. According to the transitivity rule, one has $\Delta E_v(A/B) + \Delta E_v(B/C) + \Delta E_v(C/A) = 0$. In the present case, this rule is violated by 0.27 eV. We note, however, that for each interface considered here, another (appropriate average) lattice constant was used. This probably plays a role in the origin of this violation. We note, however, that there is actually no *a-priori* justification for this rule within the self-consistent supercell approach. It is, of course, obeyed by construction within any linear offset model such as the DME approach.

DISCUSSION

Martin *et al.*[22] measured the valence-band discontinuity for a wurtzite GaN/AlN (0001) heterojunction by means of X-ray photoemission spectroscopy and obtained a value of (0.8±0.3)eV with a type I alignment. This is in very close agreement with our calculation for the GaN/AlN interface. Schneider [23] has also estimated this band-gap offset by aligning in the two semiconductors the level positions of a transition metal (Fe) impurity with respect to the band edges and using the semi-empirical Langer-Heinrich rule [24]. His value of (0.53±0.1) eV is in fair agreement with our calculations, especially with the result obtained in [17] with the DME model. This is not surprising because the justification of the Langer-Heinrich rule is precisely that transition metal levels are pinned at a midgap level such as the DME level.

Ren and Dow [25] have studied the size quantization effect on the valence and conduction band minima in $GaN/Al_xGa_{1-x}N$ wurtzite superlattices as a function of the repeat period and an assumed ratio of the valence-band offset to the band gap discontinuity, $R = \Delta E_v/\Delta E_g$. They did this for the various x for which experimental optical data on the blue shift of the gap were available, i.e. data for $x = 1$ by Sitar *et al.*[26] and for $x = 0.1$ by Itoh *et al.*[27]. Their best fit to the data corresponded to $R = 0.4$ for both cases. This corresponds to a band-offset for pure GaN/AlN of 1.05 eV. Our calculations predict a ratio of $R = 0.32$ rather than 0.4 for wurtzite. We note, however, that the method used by Ren and Dow to determine R has a significant uncertainty. For example, using effective mass approximation calculations, Sitar *et al.*[26] concluded from the same data at $x = 1$ that the band-gap discontinuity was about equally divided between valence and conduction-band offsets, corresponding to $R \approx 0.5$. Itoh *et al.*[27] using a Kronig-Penney model analysis of their optical data on quantum wells concluded that the offset occurs mostly between the conduction bands. Thus, this approach seems rather unreliable for a precise determination of the offsets. It is very plausible that our R value may yield equally satisfactory agreement with the optical data. We plan to investigate this hypothesis in future work. To the best of our knowledge, no experimental data are presently available for the heterojunctions involving InN.

CONCLUSIONS

The valence-band offsets at the zincblende AlN/GaN, AlN/InN and InN/GaN (110) interfaces were calculated by means of the self-consistent supercell approach at the average lattice constant of the constituents. A back-of-the envelope estimate of the strain effects shows that deviations from these offsets for specific strain situations may be expected to be of order 0.2–0.3 eV. The band alignments are all of type-I. This leads to confinement of both electrons and holes in the material with the smaller gap, which is favorable for light-emission from quantum wells devices. While our calculation were for zincblende (110) interfaces, the similarity in the wave function character of the valence-band maxima of wurtzite and zincblende, allows us to extend our results to wurtzite offsets. Our band-offset for GaN/AlN appears to be consistent with XPS experimental data [22] while the interpretation of optical data is presently unclear.

ACKNOWLEDGEMENTS

This work was supported by N.S.F. Grant No. DMR-92-22387. E. A. A. also acknowledges financial support from the Consejo Nacional de Investigaciones Científicas y Técnicas, Argentina.

REFERENCES

1. *Wide-band-gap Semiconductors*, ed. C. G. Van de Walle, Proc. Seventh Trieste ICTP-IUPAP Semiconductor Symposium (1992), (North-Holland, Amsterdam 1993), also published as *Physica B* **185**, (1993).

2. *Wide Band Gap Semiconductors*, Ed. T. D. Moustakas, J. H. Pankove, and Y. Hamakawa, Mater. Res. Symp. Proc. Vol. 242, (MRS, Pittsburgh, 1992).

3. C.-Y. Yeh, Z. W. Lu, S. Froyen and A. Zunger, *Phys. Rev. B* **46**, 10086 (1992)

4. M. Mizuta, S. Fujieda, Y. Matsumoto, and T. Kawamura *Jpn. J. Appl. Phys.* **25**, L945 (1986).

5. G. Martin, S. Strite, J. Thornton, and H. Morkoç *Appl. Phys. Lett.* **58**, 21 (1991)

6. M. J. Paisley, Z. Sitar, J. B. Posthill, and R. F. Davis, *J. Vac. Sci. Technol. A* **7**, 701 (1989).

7. S. Strite, D. Chandrasekhar, D. J. Smith, J. Sariel, H. Chen, N. teraguchi, and H. Morkoç, [J. Cyrstal Growth vol. 127 (1993) p. 204-208]

8. E. A. Albanesi, W. R. L. Lambrecht, and B. Segall, *Phys. Rev. B* **48**, 17841 (1993).

9. W. R. L. Lambrecht and B. Segall, *Phys. Rev. B* **41**, 8353 (1990).

10. R. Resta, A. Baldereschi, and S. Baroni, *J. chimie physique* **86**, 789 (1989).

11. W. R. L. Lambrecht and B. Segall, in [2], p. 367.

12. E.A. Albanesi, W.L. Lambrecht and B. Segall, to be published.

13. O. K. Andersen, O. Jepsen, and M. Šob, *Electronic Band Structure and its Applications*, Ed. M. Yussouff, Springer, Heidelberg, 1987, p. 1

14. L. Hedin and B. I. Lundqvist *J. Phys. C* **4**, 2064 (1971).

15. W. R. L. Lambrecht, B. Segall, and O. K. Andersen, *Phys. Rev. B* **41**, 2813 (1990).

16. H. J. Monkhorst and J. D. Pack, *Phys. Rev. B* **13**, 5188 (1976).

17. E.A. Albanesi, W.L. Lambrecht and B. Segall, in press, *J. Vac. Sci. Technol. (1994).*

18. M. Cardona and N. E. Christensen, *Phys. Rev. B* **35**, 6182 (1987).

19. K. Kim, W. R. L. Lambrecht and B. Segall, *Bull. Am. Phys. Soc.* **39**, 334 (1994), and to be published.

20. W. R. L. Lambrecht and B. Segall, in *Properties of the Group-III Nitrides*, edited by J. H. Edgar, EMIS Data Review Series, (IEE, Stevenage Herts, UK 1994), in press.

21. E. O. Kane, *Phys. Rev.* **178** 1368 (1969).

22. G. Martin, S. Strite, A. Botchkarev, A. Agarwal, A. Rockett, W. Lambrecht, B. Segall and H. Morkoç, to be published in *Appl. Phys. Lett., 1994.*

23. J. Schneider, private communication.

24. J. M. Langer and M. Heinrich, *Phys. Rev. Lett.* **55**, 1414 (1985).

25. S.Y. Ren and J.D. Dow, Mat. Res. Soc. Symp. Proc., **281**, 775 (1992).

26. Z. Sitar, M. J. Paisley, B. Yan, R. F. Davis, J. Ruan, and W. J. Choyke, *Thin Solid Films* **200**, 311 (1991).

27. K. Itoh, T. Kawamoto, H. Amano, K. Hiramatsu, and I. Akasaki, *Jpn. J. Appl. Phys.* **30**, 1924 (1991).

PERTURBED -ANGULAR -CORRELATION SPECTROSCOPY ON INDIUM- AND CADMIUM- COMPLEXES IN SILICON CARBIDE

J. MEIER, D. FORKEL- WIRTH, T. LICHT, U. REISLÖHNER, M. UHRMACHER*, W. WITTHUHN AND ISOLDE COLLABORATION**
Physikalisches Institut der Universität Erlangen-Nürnberg, D- 91058 Erlangen, Germany
*2.Physikalisches Institut, Universität Göttingen, D- 37037 Götttingen, Germany
** CERN / PPE, CH-1211 Geneva 23, Switzerland

ABSTRACT

Complex formation at indium and cadmium impurities implanted into samples of 3C-, 4H- and 6H- SiC was investigated by means of Perturbed Angular Correlation (PAC)-Spectroscopy. After annealing at 1600 K up to five different configurations characterized by their specific electric field gradients (EFG(i)) were observed in 6H- SiC, only four complexes in 4H- SiC; in the 3C- modification no complex was observed. All EFG`s are axially symmetric and are oriented along the c- axis of the crystal. In a highly nitrogen doped 6H- SiC epi- layer an new EFG was observed. It is tentatively assigned to a close indium- nitrogen pair.

INTRODUCTION

The application of semiconductors to devices at high temperatures is restricted by material properties. Since there are great demands on the devices like high temperature resistivity (T>500°C), high mechanical and chemical stability, high temperature conductivity and high break-down voltage, one has to take into account wide-band-gap semiconductors like silicon carbide.

Investigations on the electronical properties of SiC were made by means of Hall effect-, DLTS- and optical measurements like infra-red absorption [1]. More specific on the atomic scale are nuclear probe methods like EPR, Mössbauer spectroscopy or PAC- spectroscopy. EPR and Mössbauer spectroscopy are restricted essentially to lower temperatures and thus cannot yield information about the high temperature behaviour of the measured material. On the contrary, the study of close probe complexes by PAC spectroscopy enables in favourable cases a direct monitoring of the environment of the probe atoms without limitations by temperature.

This nuclear technique is based on the time differential detection of an aniostropic radiation pattern of a γ-γ-cascade. The correlation between the direction of the first and the second emitted radiation quantum depends on the nuclear spins and the multipolarities of the radiation fields involved. The quadrupole hyperfine interaction between the quadrupole moment Q of the isomeric state and the electric field gradient (EFG) at the probe atoms results in a time dependent perturbation of this correlation.

The EFG characterizes the electric charge distribution in the neighbourhood of the radioactive probe atom. The product of the largest component V_{zz} of the EFG-tensor and the

Mat. Res. Soc. Symp. Proc. Vol. 339. ©1994 Materials Research Society

nuclear quadrupole moment Q determines the quadrupole coupling constant $\nu_Q = eQV_{zz}/h$. The other components of the traceless tensor are combined to the asymmetry parameter $\eta = |V_{xx} - V_{yy}|/V_{zz}$ with $0 \leq \eta \leq 1$.

The measured coincidence spectra of the γ-γ cascade are combined to the ratio R(t). In this time spectrum the probe specific environment (e.g.: defect, specific lattice site, etc.) creates characteristic modulations described by frequency triplets ω_1, ω_2, ω_3. From each EFG specific triplet it is possible to calculate the value of ν_Q and the symmetry of the EFG. The relative amplitudes of the three frequencies yield information about the orientation of the EFG as a function of the crystal orientation with respect to the detector system. The relative fraction of the decorated probe atoms can be seen in the amplitude of the modulation pattern. Further theoretical background on the PAC method is given in [2], information concerning its application in semiconductor research is reviewed in [3].

EXPERIMENT and RESULTS

In the present experiment the PAC measurements were performed at the isomeric $5/2^+$ level of ^{111}Cd ($t_{1/2}$ = 84 ns). Most of the measurements were carried out with the parent activity ^{111}In, which decays to ^{111}Cd ($t_{1/2}$ = 2,8 d). The SiC crystals were implanted with ^{111}In ions with an energy of 350 keV at the Göttingen IONAS facility resulting in an indium profile with a maximum concentration of about 10^{18}cm^{-3} centred 100 nm beneath the surface.

The ^{111m}Cd-atoms ($t_{1/2}$ = 49 min) were implanted with the on line isotope separator ISOLDE at CERN. The lower implantation energy of 60 keV results in a profile with a maximum concentration of about 10^{18}cm^{-3} centred 25 nm beneath the surface.

The annealing behaviour of the SiC samples was investigated by encapsulating the samples in quartz ampoules filled with Argon. After a temperature treatment in a furnace the samples (within the quartz ampoules) were quenched in water. The following PAC- measurements were all performed at T_m = 295K.

Indium:

In the *3C- SiC* samples no distinct electric field gradient was revealed by the PAC- spectra. The fraction of probe atoms which are located in nearly cubic surroundings increases from 0 % directly after the implantation to 30% after an annealing step at 1600 K for 10 minutes.

In the hexagonal *6H-SiC* polytype different electric field gradients were observed. During the annealing procedure up to 1500 K five different modulations could be detected in the R(t)-spectra.

In the *4H- SiC* polytype up to four different EFGs appeared after an analogous annealing procedure. Typical PAC- spectra are shown in figure 1a for the 4H- polytyp (n-type, [N]= $3*10^{16}$cm^{-3}) and in figure 1b for the 6H- modification (n-type, [N]= $8*10^{18}$cm^{-3}) after annealing steps at 1500 K for 90 minutes and 180 minutes, respectively.

All these spectra were obtained in a standard geometry between the c- axis of the crystal and the detector system. In this case the frequency triplet degenerates to a doublet ω_1, ω_2 for axially symmetric (η=0) EFGs oriented along the c- axis of the crystal.

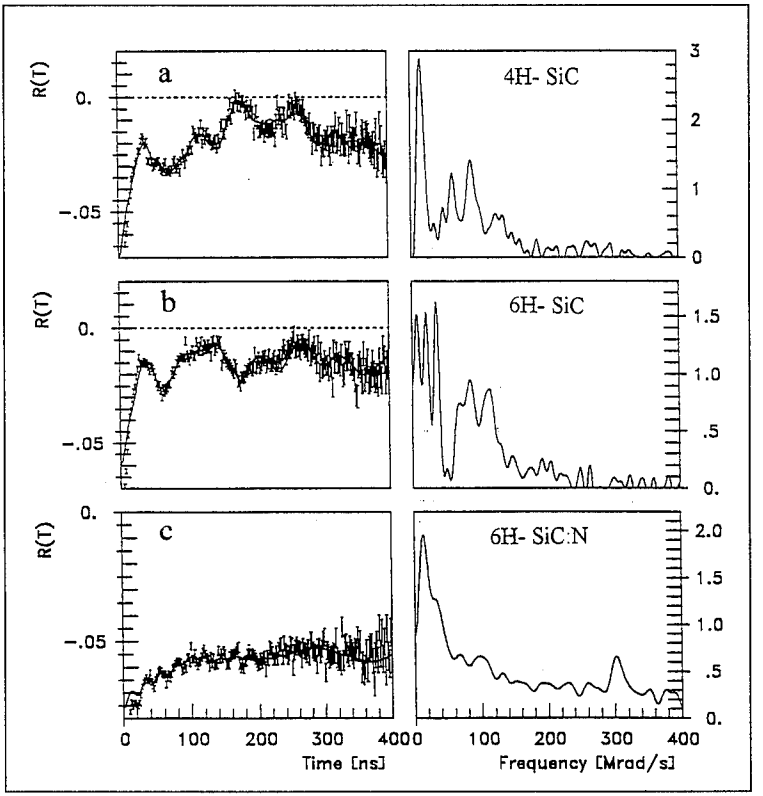

Figure 1: (a) PAC- spectrum of 4H- SiC after an annealing step at 1500 K for 90 minutes
(b) PAC- spectrum of 6H- SiC after an annealing step at 1500 K for 180 minutes
(c) PAC- spectrum of 6H- SiC:N (epi-layer sample)after an annealing step at 1500 K for 30 minutes

The PAC- parameters of the electric field gradients obtained at Indium/Cadmium probe atoms are summarized in table 1.

The fractions of the probe atoms, which were exposed to these EFGs increase with the annealing temperature. In 6H- SiC three of them can be detected only for annealing temperatures above 1300 K (see figure 2: EFG(3), (4) and (5)). The other two, EFG(1) and EFG(2), appear at an annealing temperature higher than 1000 K.

	4H-SiC			6H-SiC		
	ν_Q(/MHz)	η	orientation	ν_Q(/MHz)	η	orientation
EFG(1)	15(2)	0(.2)	c-axis	22(2)	0(.2)	c-axis
EFG(2)	-	-	-	36(1)	0(.2)	c-axis
EFG(3)	62(2)	0(.1)	c-axis	73(2)	0(.1)	c-axis
EFG(4)	92(2)	0(.2)	c-axis	89(3)	0(.2)	c-axis
EFG(5)	135(5)	0(.2)	c-axis	113(4)	0(.2)	c-axis
EFG(6)				300(2)	(0)	?

Table 1: EFG parameters of the complexes at Indium/Cadmium probe atoms in SiC

In the 6H- polytype the electric field gradients show a different behaviour on the measuring temperature (see figure 3). EFG(1) and EFG(2) were found between temperatures of 30 K and 900 K. Their PAC- parameters do not change significantly up to a temperature of 700 K. The other three electric field gradients show a strong temperature dependence. In this modification EFG(3) was observed between 30 K and 500 K, EFG(4) between 265 K and 700 K and EFG(5) was observed between 30 K and 900 K.

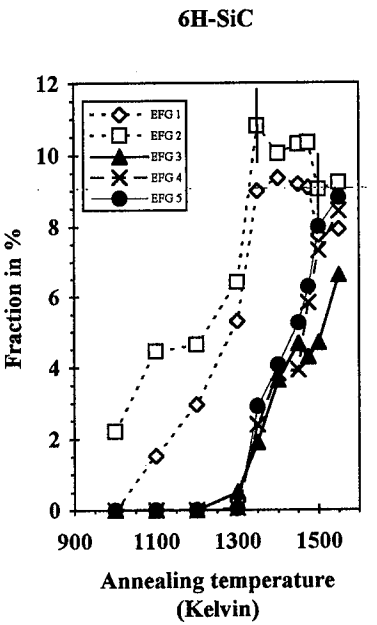

Figure 2: Annealing behaviour of 6H-SiC

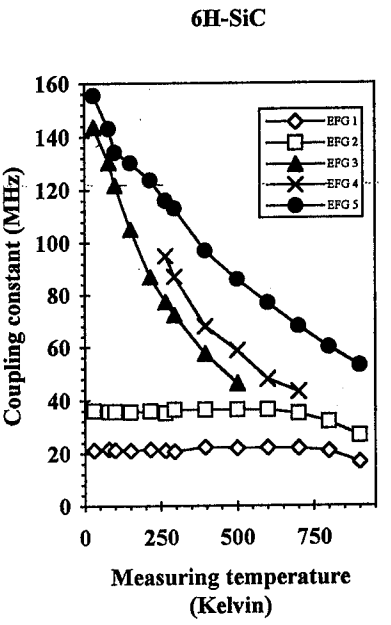

Figure 3: Dependence of the quadrupole coupling constant on measuring temperature

In a 6H- SiC epi layer with a nitrogen content of $3*10^{19}cm^{-3}$ another distinct EFG was found at annealing temperatures above 1425 K, see figure 1c. Because of the small fraction of probe atoms experienced to this EFG(6), its PAC- parameters can not be deduced unambigiously. Assuming axial symmetry the quadrupole coupling constant is 300(2) MHz.

Cadmium

In the ^{111m}Cd implanted 6H- SiC samples only the first three electric field gradients were observed; the identical PAC-parameters strongly indicate that the Cd and In atoms occupy identical lattice sites after the implantation and annealing process. The fractions of probe atoms experienced to EFG(1) and EFG(2) were greater than in the case of ^{111}In probe atoms.

DISCUSSION

The first question is concerned with the lattice site occupied by the indium or cadmium probe atoms. At present, however, details of the nature of the bonds between silicon and carbon in silicon carbide are still discussed controversially [5],[6]. Regardless of this open question carbon atoms should be charged negatively, silicon atoms positively, with the charge distribution depending on the bonding model. An isolated In- or Cd- impurity should act as a negatively charged acceptor in silicon carbide, corresponding to other group III elements, like B, Al, or Ga [7]. Like these elements Cd and In impurities are expected to occupy Si-sites in silicon carbide.

A probe atom at a substitutional site in the cubic 3C- modification experiences no EFG generated by the lattice. The surroundings of such a probe atom show tetraedric symmetry. Our PAC- measurements indicate, that 30% of the ^{111}In probe atoms have a only weakly disturbed cubic environment after an annealing step at 1600 K. So the conclusion can be drawn, that about 30% of the probe atoms are located at a weakly disturbed substitutional site; there may be a fraction of probe atoms on interstitial sites showing cubic symmetry, too.

In contrary to the 3C- polytype the local environment around a lattice site in 4H- and 6H-SiC shows a noncubic symmetry. Therefore a probe atom at a substitutional or an interstitial site in the hexagonal polytypes experiences a lattice EFG oriented parallel to the c- axis of the crystal. EFG(1) and EFG(2) are assigned to substitutional probe atoms experiencing the lattice EFG, because they were detected in the temperature range from 30K to 1000K. Their quadrupole coupling constants ν_Q show no significant temperature dependence (see figure 3) up to 700 K.

In the temperature region above 1300 K segregation of carbon to the silicon carbide surface takes place [8]. The produced carbon vacancies in the carbon sublattice are expected to be the dominant defects in this temperature region. The PAC- measurements show the appearance of three EFGs (EFG(3)-(5)) in 6H- and two EFGs (EFG(3)-(4)) in 4H- SiC at this temperature. The fraction of decorated probe atoms rises with the annealing temperature. This leads to the straightforward interpretation of an indium carbon-vacancy complex. This assignment is strongly supported by the three complexes in 6H- and the two configurations in 4H-SiC, since in the 6H- SiC three nonequivalent lattice sites -and therefore nonequivalent In-V_C complexes - are expected. In the 4H polytype only two nonequivalent sites are present. Against this

interpretation, however, one has to recognize that all measured EFGs show orientations parallel to the c-axis. This points to a lattice and not to a defect induced EFG. A definite conclusion on the basis of the present data can not be given; here additional experiments are required.

In the highly N-doped silicon carbide EFG(6) (see table 1) was found. It is assigned to a close In-N-pair, where the indium is located at a silicon site and the nitrogen on a carbon site. This interpretation is suggested since in the SiC crystals the nitrogen atoms should prefer the carbon lattice site [4]. An isolated In or Cd impurity should act as a negatively charged acceptor in SiC prefering the silicon lattice site, corresponding to other group III-elements like B, Al or Ga [5].

ACKNOWLEDGEMENT

The SiC epi-layers were kindly made available by Prof. Dr. R Helbig, University of Erlangen-Nürnberg. This work was supported financially by the German Federal Minister for Research and Technology (BMFT).

REFERENCES

/1/ G. Pensl, R. Helbig
Festkörperprobleme **30**, 133, (1990).

/2/ H. Frauenfelder, H.M. Steffen
in Alpha, Beta, and Gamma Ray Spectroscopy, **Vol. 2**
Editor: K.Siegbahn
(North Holland, Amsterdam, 1965), 997.

/3/ T. Wichert, N. Achtziger, H. Metzner, R. Sielemann
in Hyperfine Interactions in Semiconductors
Editor: G. Langouche
(North Holland, Amsterdam, 1992).

/4/ H.H. Woodbury, G.W. Ludwig
Physical Review **124**, 1083, (1961).

/5/ R.T. Holm, P.H. Klein, P.E.R. Nordquist
J. Appl. Phys. **60**, 1479, (1986)

/6/ W.F. Knippenberg
Philips Res. Rep. **18**, 161, (1963)

/7/ W.J. Choyke, L. Patrick
Physical Review **B2**, 4959,(1970).

/8/ L.Muehlhoff, M.J. Bozack, W.J. Choyke, J.T. Yates, Jr.
J. Appl. Phys. **60** (7), 2558, (1986).

A SPIN RESONANCE STUDY OF THE 2.9 eV LUMINESCENCE CENTERS IN NATURAL AND SYNTHETIC DIAMOND

D. M. HOFMANN*, W. STADLER*, B. K. MEYER*,
L. PEREIRA**, L. SANTOS**, AND E. PEREIRA**
* Physics Department E 16, Technical University of Munich, D-85747 Garching, Germany
** Departamento e Centro de Fisica (INIC), University of Aveiro, 3800 Aveiro, Portugal

ABSTRACT

Time resolved photoluminescence and optically detected magnetic resonance experiments were performed on the 2.985 eV (N_3) luminescence band in natural diamond and the 2.964 eV luminescence center in synthetic diamonds. For the N_3 luminescence the resonance occurs in the ^2E excited state of the center. On the 2.964 eV luminescence a strongly anisotropic resonance signal is observed. The frequency response of the magnetic resonance signals confirms the time resolved photoluminescence measurements.

INTRODUCTION

In synthetic and natural diamonds a large number of luminescence centers can be observed in the visible spectral range [1,2]. Most of these centers are thought to be impurity related. Also the common nitrogen related centers emit in this spectral range. As there is some superposition of luminescence and luminescence excitation spectra of these centers they can not be separated under steady state conditions. However, time resolved PL and optically detected magnetic resonance (ODMR) should be able to discriminate between these centers and to establish a correlation of the luminescence and defect properties.

In this study we concentrate on the luminescence of the prominent N_3 center in natural diamond which is located at 2.985 eV and the 2.964 eV center luminescence which occurs in natural and synthetic diamonds [3,4]. The ODMR experiments reveal a asymmetrical resonance for the N_3 center, whereas a strongly anisotropic signal is observed in the 2.964 eV emission band. Time resolved ODMR experiments show similar decay times as obtained by time resolved PL which correlates the ODMR signals to the respective PL bands.

EXPERIMENTAL

The optically detected magnetic resonance experiments were carried out in a magneto-optical cryostat (0-2 Tesla) at temperatures of 1.6 K. For these experiments the samples were excited with the 325 nm line of a HeCd laser. The emission was analyzed by a single monochromator (Spex 1680) in combination with a photomultiplier. The samples were placed in the center of a TE_{011} resonator allowing optical excitation and detection of the emitted light. The available microwave power was 400 mW at frequencies around 36 GHz. For detection of the ODMR signals by lock-in technique the microwaves were squarewave on/off modulated. The frequency response was measured by varying the modulation frequency.

Time resolved PL spectra and lifetime measurements were performed with a Spex 1934C phosphorimeter, delivering light pulses of approx. 10 μs from a Xe arc lamp. The temperature could be controlled in the range from 10 to 300 K.

Mat. Res. Soc. Symp. Proc. Vol. 339. ©1994 Materials Research Society

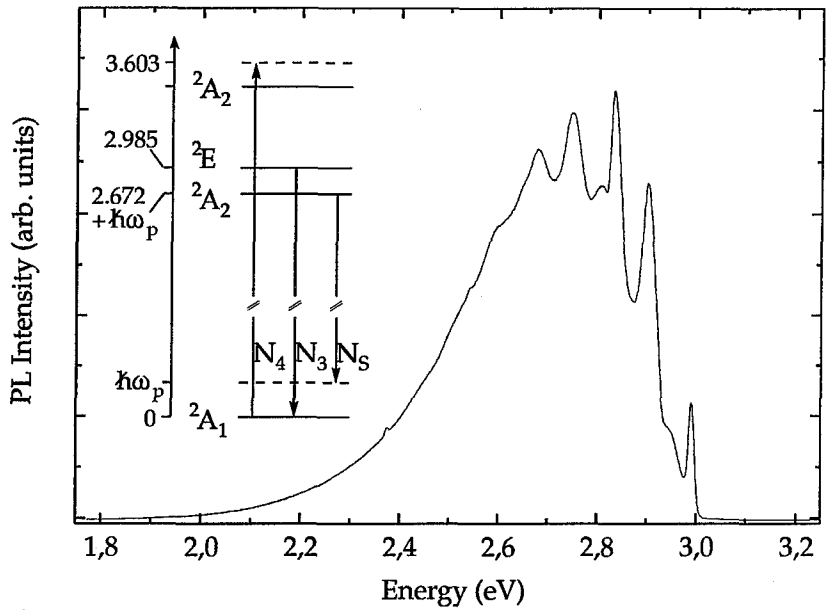

Fig. 1: Photoluminescence Spectrum of the N_3 center in natural diamond excited via the N_4 absorption (2 K). The inset shows a simplyfied level scheme of the N_3 center.

RESULTS AND DISCUSSION

a) The N3 center

The N_3 center is known to be due to three substitutional nitrogen atoms bound to a common carbon atom or a vacancy, the ground state being a $^2A_1$ (or $^2A_2$). The excited state of the 2.985 eV luminescence is a ^2E state. For excitation in the N_3 absorption band the prompt luminescence decay is exponential and equal to 40 ns. Long living components can be observed by excitation in the energy range of the N_4 absorption. For such excitation conditions and temperatures below 170 K beside the 2.985 eV PL another emission with a first peak at 2.672 eV was observed and attributed to a $^2A_2$ excited state (labeled N_S in the original paper [3]). Fig. 1 shows a typical luminescence spectrum of the N_3 center emission where both luminescence bands overlap, the inset shows a simplified energy level diagram. Time resolved PL measurements have shown that the 2.985 eV emission has a single exponential decay of (0.4 ± 0.1) ms. The PL decay of the 2.672 eV band is best described by two exponentials with decay times of (0.8 ± 0.1) ms and (6.8 ± 0.5) ms and relative intensities of 1 to 4.

Performing ODMR experiments the resonance shown in Fig. 2 is observed as an increase of the PL intensity. In general one expects to observe Gaussian- or Lorentzian-lineshapes for ODMR resonances, dependent on wether the lineshape results from lifetime or inhomogenious broadening. The asymmetrical lineshape of the resonance shown in fig. 2 is somewhat unusual and could be caused by a superposition of two close lying

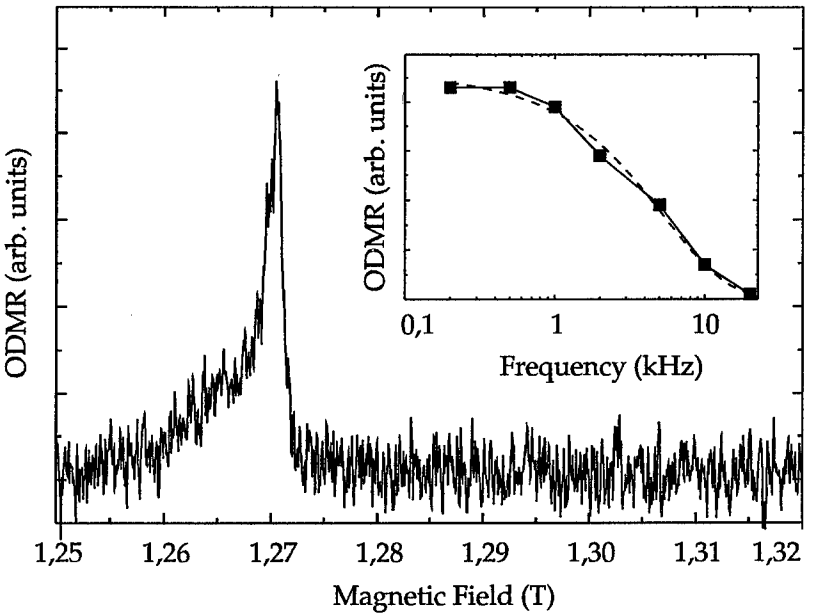

Fig. 2: Optically detected magnetic resonance spectrum of the ^2E excited state of the N_3 center in natural diamond. The inset shows the modulation frequency dependence of the ODMR signal intensity (36 GHz, 2 K).

resonances of different origin. In order to get more insight we performed time resolved ODMR measurements by varying the on/off modulation frequency of the microwaves from 0.1 to 100 kHz. The result was that the signal intensity decreases for frequencies above 1 kHz (inset in fig.2) without changing the lineshape. The inverse of the frequency decay corresponds to a lifetime of 0.2±0.05 ms. Assuming that the spin relaxation time is short, it reflects the PL decay time and is thus close to the luminescence decay time of the ^2E -> $^2A_1$ transition as measured by time resolved PL. Further evidence that the ODMR signal originates from the ^2E excited state of the N_3 center and not from the $^2A_2$-state was found by changing the sample orientation with respect to the magnetic field. The resonance showed a clear angular dependence, in contrast to an $^2A_2$-state resonance which is expected to be isotropic. Unforunately a precise analysis of the rotation pattern was prevented by the fact that no diamond sample cut in high symmetry crystal directions was available. An unusual lineshape of a ^2E-state resonance was also observed for Cr^{3+} in MgO and it was shown that it originates from random strain present in the sample [5].

b) The 2.964 eV luminescence center

A photoluminescence spectrum of a synthetic diamond in the spectral range from 1.75 eV to 3.00 eV is shown in fig. 3. Below 2.6 eV the emission is dominated by the recombination of a center which is thought to be related to substitutional Ni [6]. At higher energies the emission of the 2.964 eV center is visible. Its intensity and width of the ZPL line, which is hardly visible in fig. 3, is very sample dependent. PL lifetime measurements

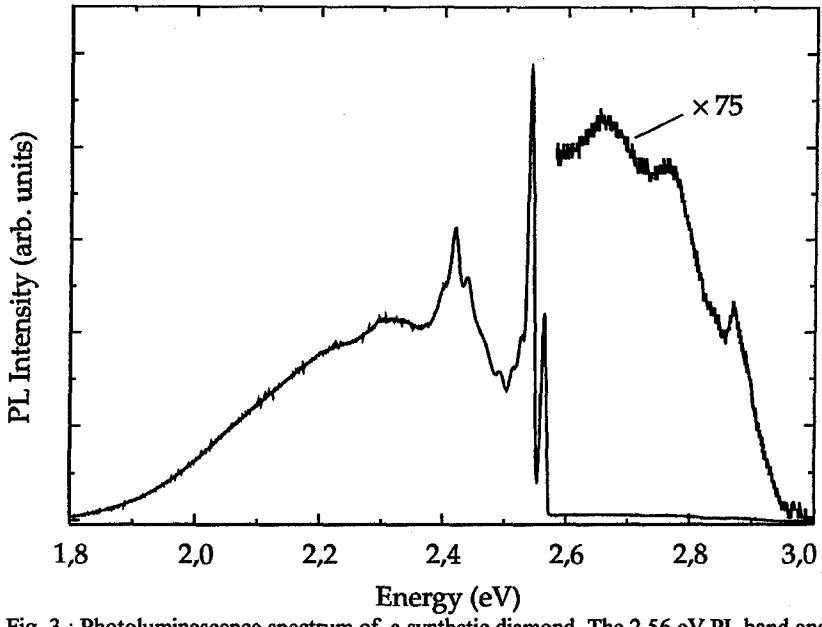

Fig. 3 : Photoluminescence spectrum of a synthetic diamond. The 2.56 eV PL band and magnified the 2.964 eV PL band (2 K)

show that the PL decay is 40 μs and mono-exponential below 15 K, between 30 and 150 K the decay is still exponential but slows down to 130 μs. The PL and time resolved PL features of this center are discussed in detail in ref. [4].

The optically detected magnetic resonance spectrum observed on the 2.964 eV emission is shown in fig. 4. A single line appears as an increase of the luminescence intensity. The resonance position changes from B || [110] at 0.84 T to 1.02 T at B || [110] + 25 degress (rotating towards [111]). Its intensity decreases rapidly for crystal orientations out off the [110] orientation and for angles larger than 25° it vanishes in the noise. No other resonance lines appear. The line width is about 8 Gauss reflecting inhomogenous broadening due to hyperfine interaction of surrounding nuclei.

Again a direct correlation of the ODMR signal to the time resolved PL measurements is obtained by measuring the modulation frequency response of the ODMR (inset in fig. 4). The ODMR signal intensity is constant up to 4 kHz for higher frequencies the signals decreases. The data are well fitted by a single exponential decay frequency of $f_0 = 21.3 \pm 3$ kHz. From this value a lifetime $t = 1/f_0 = 47 \pm 3$ μs results in good agreement with the PL-lifetime measurements.

A precise identification of the defect responsible for the 2.964 eV luminescence band is yet not possible. This luminescence band has been found in natural and synthetic diamonds which have as a common impurity Al [4]. Unfortunately no Al hyperfine splitting was observed in our ODMR experiments. The striking anisotropy of the ODMR line does not point to a defect with a vacancy-type structure with g-values usually around g = 2. More consistent would be a fine structure splitting in the excited state as a result from a high spin state. Indeed the rapid decrease of the ODMR signal intensity for sample orientations a few

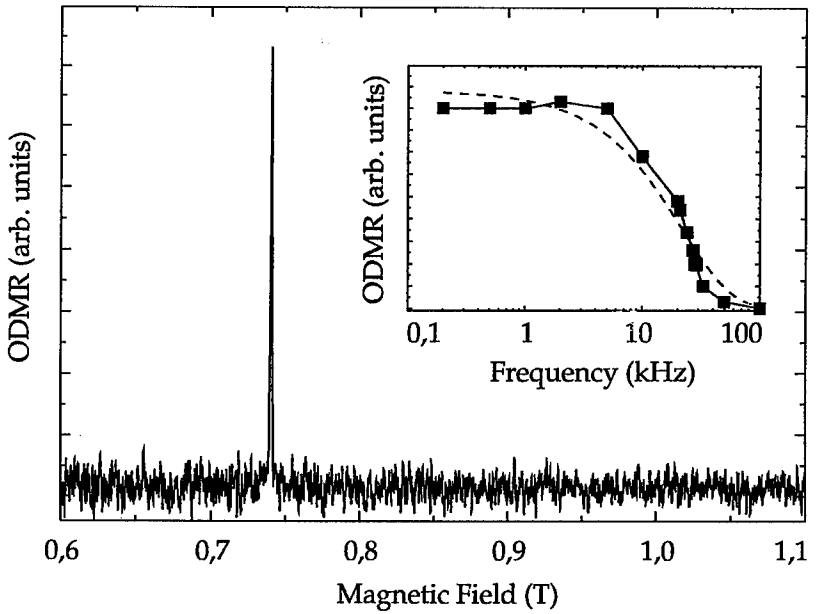

Fig. 4: Optically detected magnetic resonance spectrum measured on the 2.964 eV PL band in synthetic diamond (36 GHz, 2 K). The modulation frequency dependence of the ODMR signal intensity is shown in the inset

degrees from the high symmetry (110) plane indicated spin forbidden transitions. The participation of singulet and triplet excited states was also concluded from time resolved PL measurements [4].

CONCLUSIONS

Time resolved photoluminescence and optically detected magnetic resonance experiments allowed to distinguish between the N_3 luminescence (2.985 eV) and the 2.964 eV luminescence in diamond. Both techniques showed that the radiative lifetime for the 2.964 eV band is in the order of 40μsec. The low temperature lifetime of the N3 PL excited via the N_3 absorption is about 0.4 ms which is confirmed by the frequency response of the ^2E excited state spin resonance.

REFERENCES

[1] J. F. Field, The properties of natural and synthetic Diamonds, Academic Press, 1992
[2] J. Walker, Rep. Prog. Phys. **42**, 108 (1979)
[3] E. Pereira and T. Monteiro, J. of Luminescence **45**, 443 (1990)
[4] E. Pereira and L. Santos, Physica **B 185**, 222 (1993)
[5] L. L. Chase, Phys. Rev. **168**, 341 (341)
[6] A. T. Collins and P. M. Spear, J. Phys. **D 15**, L183 (1982)

NICKEL RELATED ABSORPTION LINES IN HIGH-PRESSURE SYNTHETIC DIAMOND

M. H. NAZARÉ*, J. C. LOPES* AND H. KANDA**
* Departamento de Física, Universidade de Aveiro, 3800 Aveiro, Portugal
** National Institute for Research in Inorganic Materials, Namiki 1-1, Tsukuba, Japan

ABSTRACT

Diamonds grown by the temperature gradient method using a nickel catalyst show an optical absorption band, extending from 2.5 eV to 2.56 eV, with a zero-phonon line at 2.51 eV. At 4 K this line exhibits fine structure; it is made up of 3 components at 2.509 eV, 2.510 eV and 2.511 eV. In absorption the fine structure components have the same relative intensity at different temperatures. We report on the effects of uniaxial stress on the zero-phonon transition at 77 K. We propose an interpretation of the results according to which the optical defect has a tetrahedral symmetry, and the 2.51 eV line occurs between two T_2 states.

INTRODUCTION

Transition metals, particularly Ni, Co, Fe and their alloys, are used as solvent catalysts to fabricate bulk diamonds. Synthetic diamonds grown using a nickel-solvent catalyst, and only these, exhibit optical absorption bands with zero-phonon lines at 1.22 eV, 1.4 eV, 1.885 eV, 2.51 eV and 3.15 eV [1,4]. The relative strengths of these bands depend not only on the Ni concentration but also on the nitrogen content of the diamond.

The 1.4 eV system is dominant in diamonds of low nitrogen content and has been associated with a Ni^+ distorted along a <111> direction. This system presents fine structure which is caused by the different isotopes of natural nickel [2,3]. Recently it was proposed that the 1.22 eV transition occurs also at the 1.4 eV defect but in a different charge state [4]. The 1.885 eV center is stronger in diamonds grown without nitrogen getters and is dominant in diamonds with a nitrogen content greater than 50 ppm. This transition occurs at a defect with tetrahedral symmetry from a T_2 ground state [5]. Also present in the visible absorption spectrum of diamonds grown without nitrogen getters is the 2.51 eV center. In absorption the band extends from 2.5 to 2.56 eV and the zero-phonon line (ZPL) presents fine structure.

In this paper we describe absorption experiments which show that the fine structure is not due to a split ground state and cannot be accounted for in terms of the natural abundances of the different nickel isotopes. We also describe uniaxial stress measurements from which we infer the symmetry of the center. We tentatively suggest that at 77 K the results are consistent with a tetrahedral symmetry for the optical defect, the 2.51 eV line occurring at this defect between two T_2 states.

Mat. Res. Soc. Symp. Proc. Vol. 339. ©1994 Materials Research Society

EXPERIMENTAL

The samples used in this work were synthetic diamonds grown by the Japanese Institute for Research in Inorganic Materials using a nickel-containing solvent catalyst without nitrogen getters. Spectroscopic measurements were made using a 1 m SPEX spectrometer, fitted with a 1200 grooves/mm grating. Absorption measurements were made using a 10 W quartz-halogen tungsten lamp. Light that passed through the sample was detected with a RCA photomultiplier. Measurements at 4 K were done using a CF1204 He flow cryostat from Oxford Instruments.

For the uniaxial stress measurements the samples were polished into cuboids with (111), $(11\bar{2})$ and $(1\bar{1}0)$ and(001), (110) and $(1\bar{1}0)$ faces. Uniaxial stresses were applied using push rods driven by oil pressure, the samples being cooled by liquid nitrogen.

RESULTS AND DISCUSSION

Absorption measurements

In figure 1 we show absorption spectra between 2.48 eV and 2.56 eV of a synthetic diamond recorded at three different temperatures. In the absorption we can detect a ZPL around 2.51 eV.

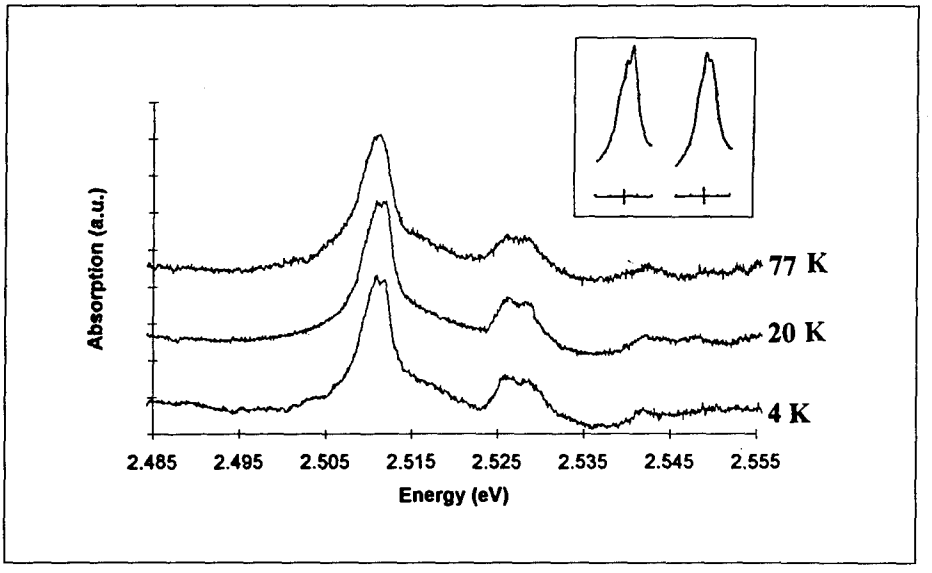

Figure 1- *Absorption spectra of a synthetic diamond recorded at three different temperatures. Inset: Absorption at 4 K, with light propagating perpendicularly to <110>, viewed through a polarizer paralel (left) and perpendicular (right) to <110>.*

This ZPL is replicated twice by phonons peaking at 15 meV from the ZPL. At 4 K the ZPL is made up of three components at 2.509 eV, 2.510 eV and 2.511 eV. These fine-structure components have the same relative intensities measured in absorption up to about 40 K. Above this temperature phonon broadening effects occur and the fine structure can no longer be separated. If the fine structure were to arise from a split ground state, the relative intensities of the two main components in the absorption spectra would change by a factor of 10 when the temperature increases from 4 K to 20 K. This change is not observed. Also the intensity ratios are polarization-dependent -- see inset in figure 1; this shows that the fine structure of the ZPL is not due to isotopic splitting.

Uniaxial stress measurements

Results

Compressive stresses of up to 2.0 GPa were applied along the <001>, <111> and <110> axes of the synthetic diamonds. The ZPL responds to the applied stress as shown in figures 2 and 3.

At 77 K the presence of the fine structure on the ZPL could no longer be detected and from now on we refer to the energy of the envelope line as the ZPL energy. Considering the number and polarization of the *stress split components*, the best assumption we could make was that the 2.51 eV is a transition between two T_2 states at a tetrahedral defect T_d point group.

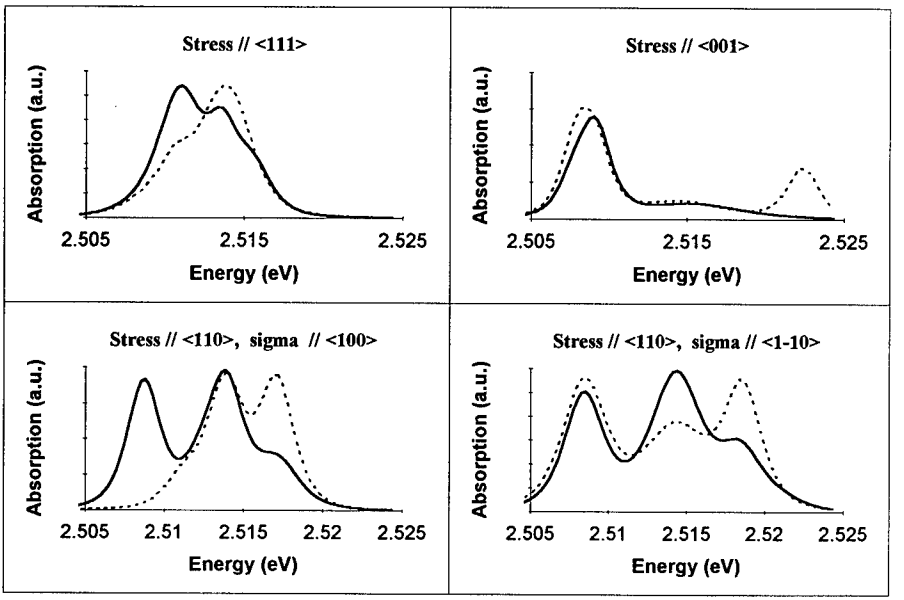

***Figure 2** -Absorption spectra in the ZPL region recorded at 77 K for stresses along <001>, <111> and <110>. Full and broken lines are used to show spectra taken in π and in σ polarization respectively.*

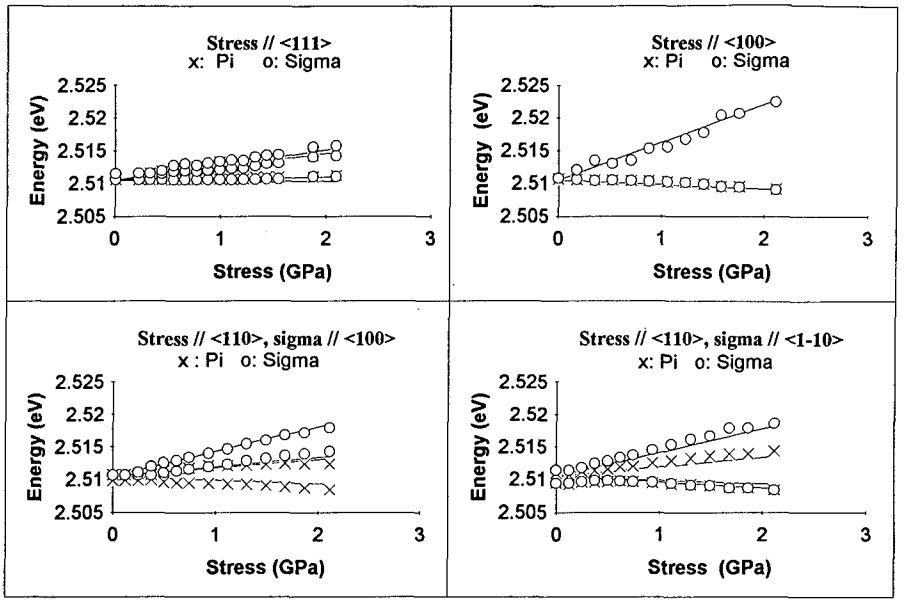

***Figure 3** - Perturbation of the 2.51 eV line under <001>, <111> and <110> uniaxial compressions. Crosses represent data points recorded for π and circles for σ polarization. Full lines show calculated energies using the best fit values for stress parameters of equation 2, with theory described in the text. For stresses along <110>, the highest-energy π component was not considered as the model cannot account for it.*

Analysis

Stresses along <001> reduce the T_d symmetry for D_{2d} and consequently the T_2 state splits into B_2+E. For <111> stress the symmetry is lowered from T_d into C_{3v}, the T_2 splits into A_1+E. <110> stresses produce a C_{2v} symmetry with T_2 breaking into B_1+B_2+A_1. Selection rules determine the polarization and intensity of the transitions occurring between the stress-split components as is shown in figure 4. Comparision of figures 2 and 4 shows that the observed and the theoretical splitting patterns are very similar; however, the intensity ratios don't match.

We define the stress Hamiltonian as:

$$H_S = c_{A_1} s_{ii} + c_{E_\theta} s_\theta + c_{E_\varepsilon} s_\varepsilon + c_{T_{2,z}} s_{xy} + c_{T_{2,y}} s_{xz} + c_{T_{2,x}} s_{yz} \qquad (1)$$

where s_{ij} are the stress tensor components, $s_{ii} = s_{xx} + s_{yy} + s_{zz}$, $s_\theta = 2s_{zz} - s_{xx} - s_{yy}$, $s_\varepsilon = \sqrt{3}(s_{xx} - s_{yy})$, and c_{A_1}, c_{E_θ}, c_{E_ε} and $c_{T_{2,i}}$ are electronic operators transforming as indicated by the subscripts in the T_d point group. For the T_2 ground (superscript g) and excited (superscript e) states we define the following stress parameters:

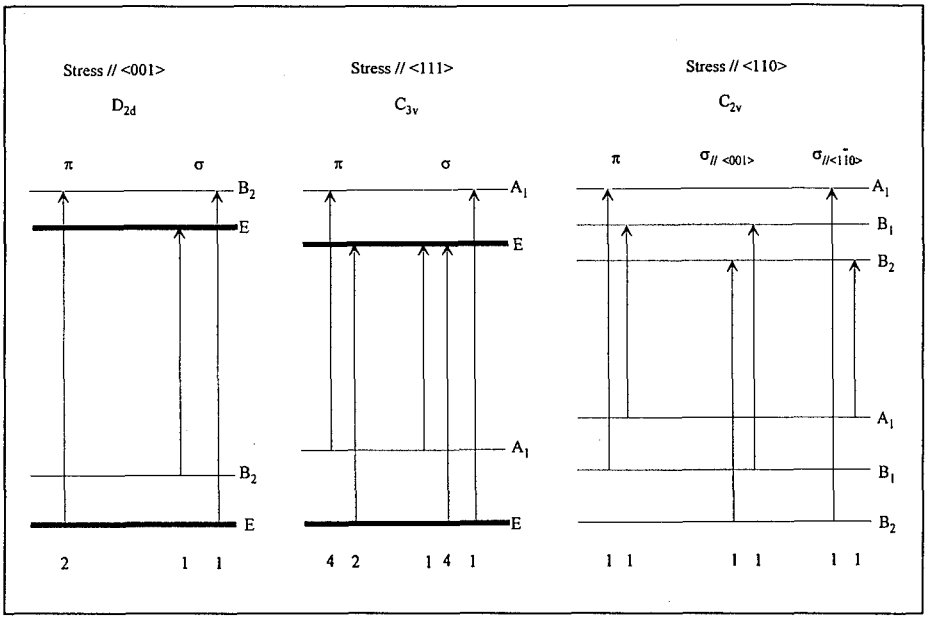

***Figure 4** - Splitting pattern of a T_2 to T_2 transition at a T_d center under uniaxial stresses along the major crystallographic directions.*

$$A^g = \left\langle T^g_{2,x} \middle| c_{A_1} \middle| T^g_{2,x} \right\rangle,\ B^g = \left\langle T^g_{2,z} \middle| c_{E_\theta} \middle| T^g_{2,z} \right\rangle,\ C^g = \left\langle T^g_{2,x} \middle| c_{T_2} \middle| T^g_{2,z} \right\rangle,$$

$$A^e = \left\langle T^e_{2,x} \middle| c_{A_1} \middle| T^e_{2,x} \right\rangle,\ A^e = \left\langle T^e_{2,z} \middle| c_{E_\theta} \middle| T^e_{2,z} \right\rangle,\ C^e = \left\langle T^e_{2,x} \middle| c_{T_2} \middle| T^e_{2,z} \right\rangle. \qquad (2)$$

Experimentally we can only determine the differences in the responses to totally symmetric perturbations of the ground and excited states. Consequently we define $A = A^e - A^g$.

In terms of the stress parameters the secular matrix for either the ground or the excited state is given by:

$$\begin{bmatrix} As_{ii} + \frac{B}{2}(\sqrt{3}s_\varepsilon - s_\theta) & Cs_{xy} & Cs_{xz} \\ Cs_{xy} & As_{ii} - \frac{B}{2}(\sqrt{3}s_\varepsilon + s_\theta) & Cs_{yz} \\ Cs_{zx} & Cs_{yz} & As_{ii} + Bs_\theta \end{bmatrix} \qquad (3)$$

For each direction of the applied stress the secular matrices for both states can be diagonalized and the difference between their eigenvalues, taking into account the selection rules in figure 4, gives the perturbation, relative to the zero-stress situation, to the energy difference between the excited and ground states of the transition. Comparison of the calculated energies for the stress split components and data is shown by lines on figure 3. For stresses along <110> the highest-

energy component should not be seen in π polarization nor should the middle-energy component in σ // $\langle 1\bar{1}0 \rangle$. However, in both cases the lines are present in the absorption spectra. The best fit to the data on figure 3 is obtained with the following values for the stress parameters: A = 1.45 meV/GPa; B^e = 2.15 meV/GPa; B^g =0; C^e = -2.28 meV/GPa and C^g = -0.35 meV/GPa. These values are of the same order of magnitude as those obtained for other absorption bands known to be related with nickel.[3,5]

CONCLUSIONS

In this paper we have shown that the 2.51 eV absorption band is made up of a ZPL near 2.51 eV replicated twice by phonons of 15 meV. The ZPL exhibits fine structure. At 4 K the ZPL can be separated into 3 components at 2.509 eV, 2.510 eV and 2.511 eV. The relative intensities of these components are the same in the temperature range from 4 K to 40 K. This can be interpreted as evidence to the existence of a split excited state. The origin of this splitting is not yet clear.

At 77 K the fine structure can no longer be detected and the line at 2.51 eV splits under uniaxial stress as a transition between two T_2 states at a T_d center, even though the relative intensities observed do not match the predicted ones. This requires further investigation. Also the stress parameters obtained from this model are consistent with those of other nickel-related centres.

Work is in progress to determine the origin of the fine structure on the ZPL and uniaxial stress experiments are being carried at 4 K.

REFERENCES

1. A.T. Collins, H. Kanda, and R.C. Burns, *Phil.Mag. B* **61**, 797 (1990).
2. G. Davies, A.J. Neves, and M.H. Nazaré, *Europhys. Lett.* **9**, 47 (1989).
3. M.H. Nazaré, A. J. Neves, and G. Davies, *Phys. Rev. B* **43**, 196 (1991).
4. S.C. Lawson, H. Kanda, and M. Sekita, *Phil. Mag.* **68**, 39 (1993).
5. M.H. Nazaré and L.M. Rino, *Materials Science and Engineering B* **21**, 329 (1993).

FREE CARRIER ABSORPTION IN N–TYPE 6H–SiC

F. ENGELBRECHT AND R. HELBIG
Institute of Applied Physics, University of Erlangen-Nürnberg, Staudtstr. 7, 91058 Erlangen, Germany

ABSTRACT

Free carrier absorption (FCA) in n-type 6H–SiC doped with nitrogen has been studied in the energy range 50–250 cm^{-1} using samples of different free carrier concentrations ranging from $2.0 \cdot 10^{16} cm^{-3}$ to $7.0 \cdot 10^{17} cm^{-3}$. The index of wave number dependence of FCA p varies between -1.4 and -0.55 depending on free carrier concentration and electron mobility. The experimental results are in good agreement with the classical expression for the FCA coefficient. Quantum mechanical expressions for the FCA coefficient do not reproduce the measured p values. It is supposed that this is due to fact that the requirement for the application of perturbation theory $\omega\tau \gg 1$ is not fulfilled. We investigated the anisotropy of FCA with respect to the c–axis and find a strong difference between $\alpha_\perp$ and $\alpha_\parallel$.

INTRODUCTION

Analysis of the optical properties of semiconductors due to free carriers can provide useful information about bandstructure, scattering processes and free carrier concentration. However, in 6H–SiC. the situation is complicated due to the high ionization energies E_i of the impurities (E_i of the nitrogen donors is $\approx$ 100 meV). So at room temperature there is only partial ionization of the impurities. For optical energies $\hbar\omega \geq E_i$, always the total absorption due to free carriers and photoionization are measured. At T=300K the absorption due to photoionization is stronger than the absorption due to free carriers. This was shown by Imai [1], who demonstrated that the absorption of n–type α–SiC crystals decreases with the rise in temperature from T=300K to T=500K in the range 1 to 5 μ. The normal way to measure pure FCA is to use high temperatures (T$\approx$1000K) so that all impurities are ionized. However, in this case, the strong increase of multiphonon absorption bands and infrared radiation emission of the sample according to Planck's law disturb the measurement. Therefore only the energy range 50–250 cm^{-1} was examined which lies well below the ionization energy E_i of the nitrogen impurities and where the background absorption due to phonon processes is low.

EXPERIMENTAL PROCEDURE

The samples were n–type 6H–SiC crystals doped with nitrogen grown by the SIEMENS process after Ziegler [2]. The free electron density at room temperature was determined by Hall effect measurements and found to be between $2.0 \cdot 10^{16}$ cm^{-3} and $7.0 \cdot 10^{17}$ cm^{-3}. The identification of the polytype was performed by measuring low temperature photoluminescence due to bound excitons at neutral nitrogen donor atoms. The absorption spectra were recorded at T=300K using a Nicolet infrared Fourier transform spectrometer type FTIR 740 at a resolution of 2 cm^{-1}. The absorption constant was calculated using equation (2.58) which can be found in ref. [3]. Herein reflectivity was calculated from the parameters in ref. [4]. This is confirmed experimentally since in the above mentioned samples no change in

Mat. Res. Soc. Symp. Proc. Vol. 339. ©1994 Materials Research Society

Table 1: FCA: Index of wave number dependence p (50 cm^{-1} - 250 cm^{-1}): $E \perp c$

sample	n [cm^{-3}]	μ [$\frac{cm^2}{Vs}$] (T=300 K)	p	
1	$2.0 \cdot 10^{16}$	230	-1.4	
2	$3.1 \cdot 10^{16}$	300	-1.4	
3	$4.3 \cdot 10^{16}$	169	-1.4	group I
4	$4.3 \cdot 10^{16}$	320	-1.4	
5	$8.0 \cdot 10^{16}$	170	-1.35	
6	$5.0 \cdot 10^{16}$	17	-1.1	group II
7	$5.0 \cdot 10^{16}$	18	-0.55	
8	$1.2 \cdot 10^{17}$	235	-0.95	group III
9	$8.5 \cdot 10^{17}$		-0.6	

reflectivity due to plasma effects was observed.

EXPERIMENTAL RESULTS

Index of wave number dependence

Various 6H-SiC samples doped with nitrogen were examined (table 1). After correcting for background absorption due to phonon processes it was found that the index of wave number dependence p of the absorption ($\alpha \propto \omega^p$) is between -1.4 and -0.55.
Using the logarithmic derivative of $\alpha_{FCA} \propto \omega^p$,

$$p = \frac{\partial \ln \alpha}{\partial \ln \omega} = \frac{\partial \ln \alpha}{\partial \alpha} \cdot \frac{\partial \alpha}{\partial \omega} \cdot \frac{\partial \omega}{\partial \ln \omega} = \frac{\omega}{\alpha} \cdot \frac{\partial \alpha}{\partial \omega} \tag{1}$$

we find that p is nearly independent of ω. The obtained results are summarized in Table 1. One can see from Table 1 that p is -1.4 if the doping concentration is less than $1.0 \cdot 10^{17}$ cm^{-3} and the electron mobility μ at T=300K is ≥ 200 $\frac{cm^2}{Vs}$ (group I). However, in samples with doping concentrations above $1.0 \cdot 10^{17}$ cm^{-3} (group II) or in samples with low electron mobility (group III), the absolute value of p strongly decreases.

Optical cross section

The samples 1–5 which all had the same value of p were used to determine the optical cross section $\sigma(\omega)$ of free carrier absorption according to

$$\alpha = n\sigma + \alpha_0 \tag{2}$$

with n as the free carrier density at T=300K and α_0 as a constant background absorption. The experimental data at $\omega = 200$ cm^{-1} were fitted using $\sigma = 5.9 \cdot 10^{-16} cm^2$ and $\alpha_0 = 9 cm^{-1}$ (Figure 1).

Anisotropy

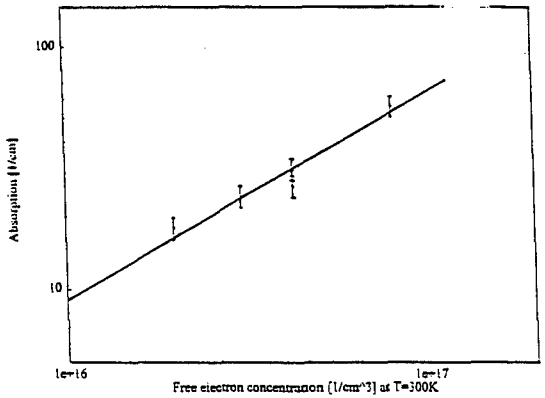

Figure 1: Optical cross section σ of FCA in 6H–SiC at ω=200 cm^{-1} for $E \perp$ c

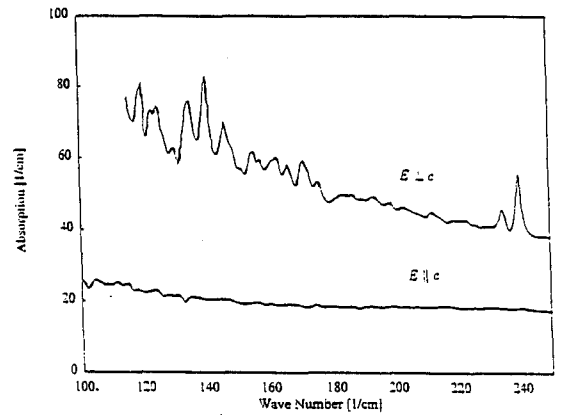

Figure 2: Anisotropy of FCA (absorption due to phonons is not corrected here)

In the investigated energy region we found that the absorption due to free carriers is strongly anisotropic with respect to the c–axis (Figure 2). In all crystals $\alpha_\perp$ exceeded $\alpha_\parallel$ at least by a factor of two. We assume that the anisotropic absorption is not due to macroscopic crystal defects (micropipes) along the c–axis but due to anisotropic scattering processes in the crystal, because anisotropic absorption was also found in the best crystals which had almost no macroscopic defects.

THEORY

Classical theory

The classical Drude electron model was used to calculate the FCA coefficient, which is given

by [6],

$$\alpha = \frac{\omega}{n_r c}\epsilon_2 = \frac{\omega'^2\tau}{n_r c(1+\omega^2\tau^2)} \quad , \quad \omega'^2 = \frac{4\pi e^2 n}{m^*} \quad . \tag{3}$$

Here, n is the free carrier concentration, n_r the refraction index, m_* the effective electron mass and $1/\tau$ the inverse damping constant. In the case $\omega\tau \to \infty$ one obtains $\alpha \propto \omega^2$, in case $\omega\tau \to 0$, α is constant. This can also easily be seen from the logarithmic derivative $\frac{\partial \ln\alpha}{\partial \ln\omega}$ which gives for the index of wavenumber dependence $p(\omega)$:

$$p = (-2) \cdot \frac{\omega^2\tau^2}{1+(\omega\tau)^2} \tag{4}$$

$p(\omega)$ for the Drude model is plotted in Figure 3. One can see from this figure that the expe-

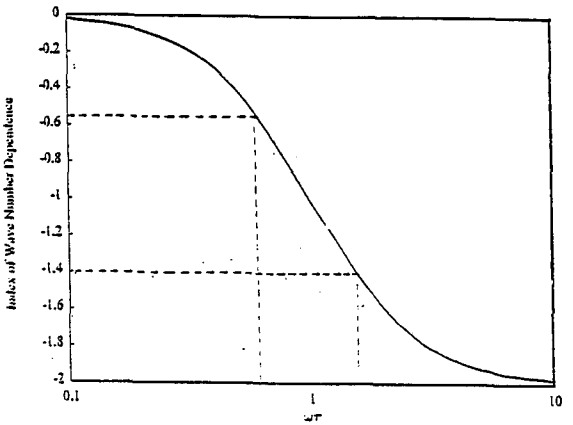

Figure 3: Index of wave number dependence p for the classical Drude model

rimentally observed values for p between -0.55 and -1.4 belong to values of $\omega\tau \approx 1$. The variation of p for different samples can be explained by different values of the scattering time τ. From the experiments we conclude that the scattering time τ is lowered either by high doping concentrations ($n \geq 1 \cdot 10^{17}\text{cm}^{-3}$) or in the case of low crystal quality (low electron mobility at room temperature).

Quantum theory

The quantum mechanical expressions of α_{FCA} for different absorption mechanisms can be obtained from second order perturbation theory (impluse conservation requires three particle processes). They are scaled by the corresponding electron scattering matrix elements (Table 2).

For the isotropic, parabolic, one band model α_{FCA} can be calculated analytically for the different scattering mechanisms. The corresponding expressions can be found ref. [5].

Since many of the parameters in these formualae are unkown in 6H–SiC only the spectral dependence but not absolute values of α are calculated.
These expressions can be expanded in classical ($\frac{\hbar\omega}{k_B T} \to 0$) and quantum mechanical ($\frac{\hbar\omega}{k_B T} \to \infty$) limit. The index of wavenumber dependence p for these two cases is listed in Table. 3

Scattering process	Scattering matrix element
Acoustic Phonon	$\frac{\Xi^2 k_B T}{2V c_L}$
Optical Phonon	$\frac{D_0^2 \hbar}{2V\rho\omega_0} \left\{ \begin{array}{c} n(\omega_0) \\ n(\omega_0)+1 \end{array} \right\}$
Polar optical Phonon	$\frac{e^2\hbar\omega_0}{2V\epsilon_p q^2} \left\{ \begin{array}{c} n(\omega_0) \\ n(\omega_0)+1 \end{array} \right\}$
Piezoelectric	$\frac{e^2 K_{av}^2 k_B T}{2V\epsilon q^2}$
Charged impurity	$\frac{Z^2 e^4 N_I}{V\epsilon^2 q^4}$

Table 2: Scattering matrix elements for different scattering processes of electrons. Ξ, D_0 are the deformation potentials for the acoustic and optic phonon scattering, K_{av} the electromechanical coupling coefficient, N_I the ionized impurity density and q the wave vector

Table 3: FCA: Index of Wave Number Dependence:

Mechanism		$\frac{\hbar\omega}{k_B T} \to 0$	$\frac{\hbar\omega}{k_B T} \to \infty$
Acoustic phonons	(ADP)	-2	-1.5
Optical phonons	(ODP)	-2	-1.5
Polar optical phonon	(POP)	-2	-2.5
Piezoelectric	(PIE)	-2	-2.5
Ionized Impurity	(IIS)	$\frac{1}{\omega^2}\ln(\frac{\hbar\omega}{2k_B T})$	-3.5

for the different scattering mechanisms. One recognizes that significant differences in $p(\omega)$ between the scattering mechanisms only exist in the quantum limit. $p(\omega)$ was evaluated numerically using the logarithmic derivative $\frac{\partial \ln\alpha}{\partial \ln\omega}$ and taking into account the wave number dependent refraction index $n_r(\omega)$ of 6H-SiC according to ref. [4]. The result is plotted in fig. 4. It can be seen that there is a strong difference between the experimental results for p ($-1.4 \leq p \leq -0.55$) and the quantummechanical result $p \approx -2$ in the investigated frequency region. We assume that in the investigated frequency region the condition $\omega\tau \gg 1$ which is necessary for application of quantum mechanical perturbation theory is not fulfilled.

CONCLUSIONS

FCA in 6H-SiC in the energy range 50–250 cm^{-1} can be used for material characterization by analyzing the index of wave number dependence p of α_{FCA}. In the above mentioned energy range $p \approx -1.4$ is found. In samples with doping concentrations over $1.0 \cdot 10^{17} cm^{-3}$ or with low electron mobility the absolute value of p decreases. The relation $\alpha_{FCA} = N\sigma + \alpha_0$ can be used to determine the free carrier concentration by an easy optical measurement. It is shown that the classical Drude model provides reasonable results whereas the quantum mechanical description of FCA by second order perturbation theory is not applicable in the the energy range 50–250 cm^{-1}. The energy region of the quantum limit $\frac{\hbar\omega}{k_B T} \gg 1$ is difficult

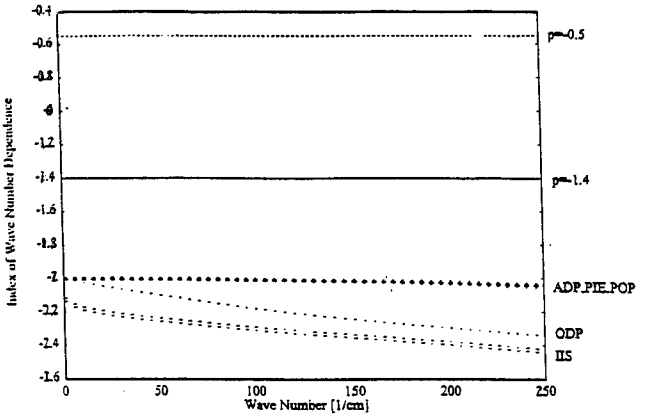

Figure 4: Index of wave number dependence p for different scattering processes

to analyze due to the overlap of FCA with impurity photoionization.

ACKNOWLEDGEMENTS

The authors are indebted to S. Leibenzeder and Dr. R. A. Stein of the SIEMENS Research Laboratories Erlangen for supplying the samples. We also thank C. Peppermüller and Dr. C. Haberstroh for performing the LT-photoluminescence and Dr. A. Schöner for the Hall effect measurements. This work was supported by Deutsche Forschungsgemeinschaft through Sonderforschungsbereich 292.

References

[1] A. Imai, J. Phys. Soc. Japan **21**, 2610 (1966).

[2] G. Ziegler. P. Lanig, D. Theis and C. Weyrich, IEEE Trans. Electron. Dev. **30**, 277 (1983).

[3] M. Balkanski. Optical Properties due to Phonons, in T. S. Moss, Handbook on Semiconductors Vol. 2, North-Holland Publishing Company 1980.

[4] F. Engelbrecht and R. Helbig, Phys. Rev. **B48**, 15698 (1993).

[5] B. K. Ridley. Quantum Processes in Semiconductors, Clarendon Press Oxford (1982)

[6] C. R. Pidgeon, Free Carrier Optical Properties of Semiconductors, in T. S. Moss, Handbook on Semiconductors Vol. 2, North-Holland Publishing Company 1980.

ELECTRICAL CHARACTERIZATION OF ALUMINUM NITRIDE FILMS ON SILICON GROWN BY CHEMICAL VAPOR DEPOSITION

A.H. KHAN, J.M. MEESE, T. STACY, E.M. CHARLSON, E.J. CHARLSON, G. ZHAO
Electrical and Computer Engineering, University of Missouri, Colombia, MO 65211
G. POPOVICI AND M.A. PRELAS
Nuclear Engineering, University of Missouri, Columbia, MO 65211.

ABSTRACT

Aluminum nitride (AlN) films were grown on silicon (Si) substrates by chemical vapor deposition (CVD). The films were characterized by scanning electron microscopy (SEM) and x-ray diffraction (XRD). The refractive index of the AlN films was determined by ellipsometry. Current-voltage and current-temperature characteristics were performed on metal-AlN-p^+ Si structures with Pt, Au and Al as metal electrodes. The characteristics showed that at high field and high temperature the carrier conduction mechanism in the film was dominated by Frenkel-Poole emission. The relative dielectric constant of the AlN films was estimated to be 9.66 ± 0.3 from capacitance-voltage-frequency (C-V-f) measurements on Au-AlN-p^+ Si.

INTRODUCTION

Aluminum nitride (AlN) has generated interest in electronic applications due to its unique properties. It possesses a wide band gap of 6.2 eV, high thermal conductivity, high breakdown voltage, highest reported surface acoustic wave velocity, high melting temperature, low coefficient of thermal expansion, is chemically inert and possesses a high mechanical strength. All these properties makes AlN a potential candidate for UV photonic devices, and for electrically insulating and passivating layers for other semiconductors. Also the metal-AlN-Si MIS structure has potential use for surface acoustic wave (SAW) devices. Therefore it is essential to understand the electronic conduction mechanisms of AlN films in order to explore its electronic applications.

In this paper the current conduction mechanisms of AlN films grown on silicon substrates are studied through measurements of the current-voltage, current-temperature and capacitance-voltage-frequency characteristics of metal-AlN-p^+ Si structures.

EXPERIMENTAL

Aluminum nitride films were grown on (111)-oriented n^+ and (100)-oriented p^+ silicon substrates by the chemical reaction of $AlCl_3$ and NH_3 in the presence of hydrogen in a horizontal tube CVD apparatus previously reported [1]. Prior to the growth the silicon substrates were organically cleaned with the solvent sequence trichloroethylene, acetone,

Mat. Res. Soc. Symp. Proc. Vol. 339. ©1994 Materials Research Society

methanol, and deionized (DI) water in an ultrasonic bath. Then the substrates were dipped in 10% hydrofluoric acid to etch off the silicon native oxide. Finally they were cleaned in warm HCl and HNO_3 and rinsed in DI water. After air drying, the substrates were briefly heated to 600°C in flowing H_2 in the CVD apparatus to remove the surface native oxide of silicon. The substrate temperature was then raised to the desired growth temperature and the reactants were introduced to initiate the deposition process. AlN films of different thicknesses ($\sim$0.2 μm to 1 μm) were grown. During the growth the substrate temperature was maintained at $\sim$750-800°C and the chamber pressure was $\sim$35-40 Torrs.

The thickness of the grown samples were estimated by SEM and by a Gaertner ellipsometer with a wavelength of 6328 Å and an incident angle of 70°. The ellipsometer were also used to measure the refractive index of the AlN films.

The electrical measurements were performed on a metal-AlN-Si structure. Au, Pt (deposited by sputtering) and Al (deposited by thermal evaporation) dots of 2 mm diameter were used as metal electrodes. The I-V characteristics were taken using a Hewlett-Packard model 4140B picoammeter with a DC voltage source interfaced with a desk-top computer by an IEEE 488 interface control board. A Hewlett-Packard 4192A LF impedance analyzer was used to perform C-V-f measurements.

RESULTS AND DISCUSSION

Figure 1(a) shows an SEM of the surface of $\sim$1 μm thick AlN film deposited on silicon. The surface appeared to be coated with small particulates having a grain size of about 0.2 μm. The AlN films exhibit conformal growth as observed in the cross-sectional SEM in Fig. 1(b).

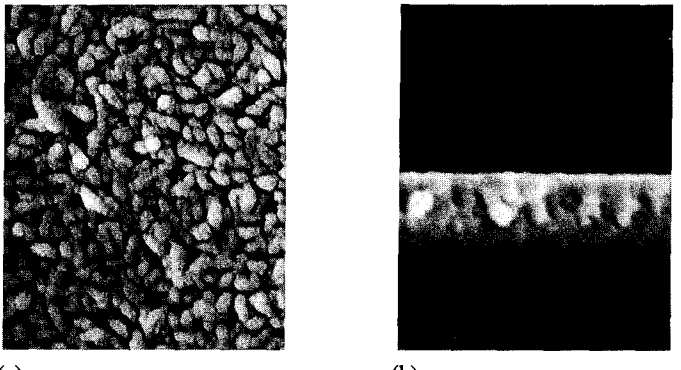

(a) (b)

Figure 1. Scanning electron micrograph of (a) surface (b) cross-section

A typical X-ray diffraction pattern of the deposited film is presented in Fig. 2. The XRD study shows three diffraction peaks at 2θ=33.04°, 36.2° and 37.5° due to (100), (002) and (101) oriented AlN. The d(hkl) values estimated for these peaks are consistent with the values of the ASTM card [2]. The refractive index of the deposited AlN films measured by ellipsometry at 6328 Å radiation showed an index value of 2.196 ± 0.1 which is comparable to the reported value of single crystal AlN [3].

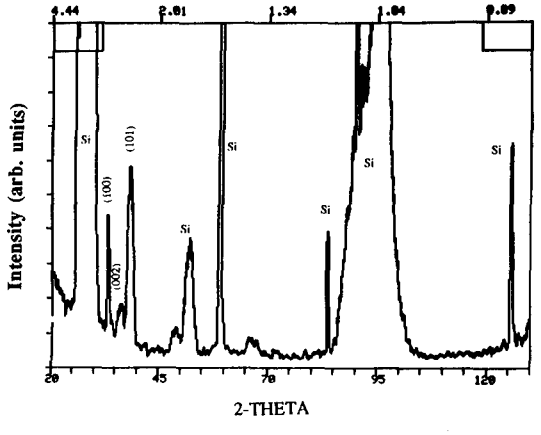

Figure 2. A typical X-ray diffraction of the grown film.

Figure 3(a), 3(b) and 3(c) respectively shows typical I-V characteristics of Pt-AlN-p^+ Si, Au-AlN-p^+ Si and Al-AlN-p^+ Si structures. All three structures had ~2000 Å thick AlN films. The curves of all the three structures appeared similar, where the current had linear relationship to the voltage at low applied field. The resistivity estimated at low field for all the structures is of the order of 10^{10}-10^{11} Ω-cm, which is smaller than the thicker(~1μm) AlN films. The resistivity of the thicker AlN films were measured to be around 10^{13} Ω-cm. This behavior is typical for films grown by the nucleation process where thin films are more likely to have in holes and defects.

In order to clarify the current transport mechanisms in the high applied field region, the ln I vs. $E^{1/2}$ plots, obtained from Figs. 3(a), 3(b) and 3(c) are shown in Figs. 4(a), 4(b) and 4(c) respectively. All three structures showed identical behavior where the current showed a linear relationship on the ln I vs. $E^{1/2}$ plot at high electric fields. This kind of behavior was reported by Bauer *et. al.* [4] for a Al-AlN-Si structure where Frenkel-Poole conduction was dominant. Thus it can be concluded that at high electric field, in all three structures the current transport mechanism is dominated by Frenkel-Poole conduction and the currents are bulk controlled rather than electrode-controlled as in Schottky-barrier diodes.

Figure 5 shows a plot of ln I vs. 1/T of an Au-AlN-p^+Si structure with an applied

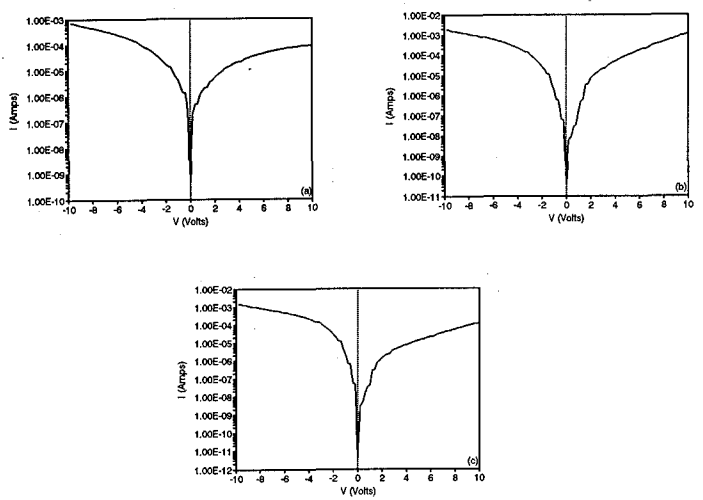

Figure 3. Current-voltage characteristics of (a) Pt-AlN-p^+ Si structure (b) Au-AlN-p^+ Si structure (c) Al-AlN-p^+ Si structure.

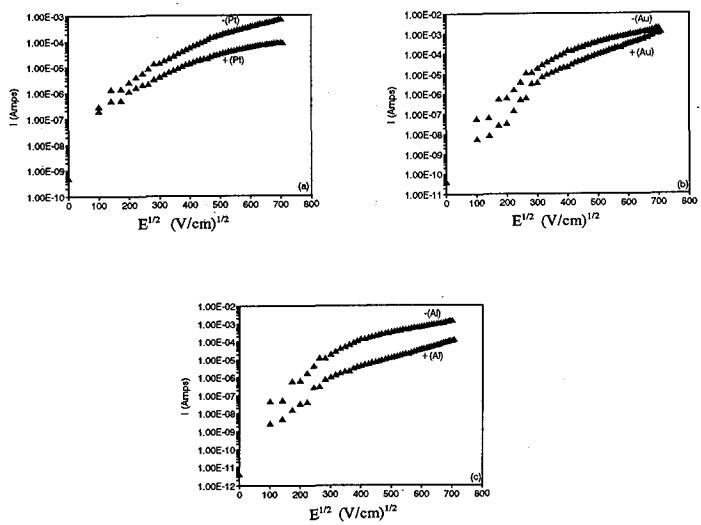

Figure 4. ln I vs. $E^{1/2}$ plots of (a) Pt-AlN-p^+Si structure (b) Au-AlN-p^+ Si structure (c) Al-AlN-p^+ Si structure.

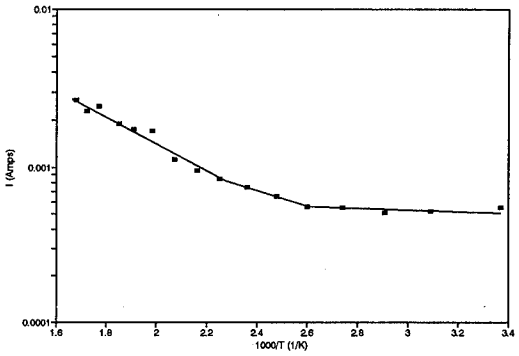

Figure 5. Current-reciprocal temperature characteristics of Au-AlN-p^+ Si structure.

field of - 4.5×10^5 V/cm. The curve shows that the current conduction increases more rapidly at higher temperatures. This kind of behavior has been previously observed in other insulators where Frenkel-Poole emission dominates at high temperatures and high fields [5].

The C-V-f characteristics at frequencies ranging from 10 kHz to 1 MHz of an Au-AlN-Si MIS structure is shown in Fig. 6. The curve showed distinctive accumulation, depletion and inversion regions. It was also observed that the accumulation capacitance decreases with the increase in frequency. This kind of behavior, although not completely understood, presumably is due to the varying time constants of surface states. The dielectric constant of AlN estimated

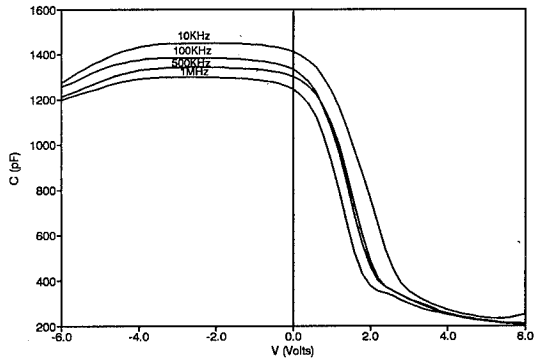

Figure 6. Capacitance-voltage-frequency characteristics of Au-AlN-p^+ Si structure.

from the capacitance in the accumulation region is 9.66 ± 0.3 which is in good agreement with the reported value estimated by reflectivity measurements [6].

CONCLUSIONS

Aluminum nitride films were grown by the CVD method utilizing $AlCl_3$ and NH_3 as source materials. The ellipsometry study showed the deposited films are of good optical quality and had a refractive index of 2.196 ± 0.1 which is comparable to the single crystal value. The study of current-voltage and current-temperature characteristics on metal-AlN-p^+ Si structures with Pt, Au and Al as metal electrodes showed at high fields the current transport mechanism is bulk controlled and is dominated by Frenkel-Poole emission. The C-V-f measurements on Au-AlN-p^+ Si showed the ideal behavior of an MIS structure while the estimated relative dielectric constant of AlN from C-V-f measurement is 9.66 ± 0.3.

ACKNOWLEDGEMENTS

This study is supported by the Department of Energy under Contract DE FG02-91ER12107. The authors would like to thank Mr. Louis M. Ross and Mr. Naiya Zhao for their assistance in SEM and XRD studies.

REFERENCES

1. A. H. Khan, M. F. Odeh, J. M. Meese, E. M. Charlson, E. J. Charlson, T. Stacy, G. Popovici, M. A. Prelas, and J. L. Wragg, accepted for publication in *J. Mater. Sci.*
2. ASTM card 25-1133.
3. J. Pastrnak and L. Roskovcova, *Phys. Stat. Sol.*, **14**, K5 (1966).
4. J. Bauer, L. Biste, and D. Bolze, *Phys. Stat. Sol.*, **A 39**, 173 (1977).
5. S. M. Sze, Physics of Semiconductor Devices, (J. Wiley Publishers, India, 1986), chapter 7.
6. A. T. Collins, E. C. Lightowlers, and P. J. Dean, *Phys. Rev.*, **158**, 833 (1967).

CONDUCTIVITY AND FTIR MEASUREMENTS OF THE HYDROGEN CONTENT OF HEAT TREATED DIAMOND FILMS

T. SUNG*, S. KHASAWINAH*, G. POPOVICI*, M. A. PRELAS*, B. V. SPITSYN*, G. MANNING**, S. LOYALKA**, AND R. V. TOMPSON**
*Nuclear Engineering Department, University of Missouri, Columbia, MO 65211
**Particulate Systems Research Center, University of Missouri, Columbia, MO 65211

ABSTRACT

The content of bonded hydrogen in hot filament grown diamond films was determined by Fourier transform Infrared (FTIR) measurements before and after annealing. The quantity of bonded hydrogen was found to remain unchanged on annealing in diamond films with high amounts of microcrystalline diamond and amorphous carbon. The hydrogen content was found to decrease on annealing ~9 times in diamond film of good crystalline quality. The change of the bulk hydrogen content did not seem to be linked to changes in resistivity of the samples.

INTRODUCTION

Hydrogen in molecular and atomic states is a main constituent of the vapor phase of chemical vapor deposition (CVD) diamond growth systems. The hydrogen content of diamond films depends on the growth conditions and was found to vary over a wide range, from 0.01 to a few at.%. [1,2] Landstrass and Ravi reported that the resistivity of natural diamond decreases nearly 8 orders of magnitude after hydrogenation in the plasma. [3] The resistivity increased back to ~10^{14} Ω cm after annealing at 780 °C in a flowing nitrogen ambient. [3] The authors concluded that annealing causes dehydrogenation, resulting in electrical activation of deep traps with an associated increase in resistivity. Albin and Watkins made similar observation by treating annealed diamond in hydrogen plasma [4]. No direct measurements of hydrogen concentration were made in these studies. Celli et al [5] used nuclear resonance reaction analysis to determine the total (bonded and unbonded) hydrogen content in CVD diamond. They attempted to correlate the electrical resistivity of CVD diamond with the hydrogen content. They found that the change in resistivity observed on nitrogen annealing (of several orders of magnitude) cannot be explained by the difference in hydrogen content, as no significant change in the hydrogen content was observed on annealing. Zhang et al. [6] used IR absorption measurements to study the bonded hydrogen in diamond films. They observed a two to three fold decrease in hydrogen content due to annealing to 400 °C in nitrogen atmosphere.

To verify whether the amount of bonded hydrogen changes on annealing, FTIR spectroscopy was used in this work. Resistivity measurements were also performed to verify the influence of the change of the hydrogen content in the bulk upon the electrical behavior of the films.

Mat. Res. Soc. Symp. Proc. Vol. 339. ©1994 Materials Research Society

EXPERIMENTAL

The samples were grown by hot filament CVD method as described elsewhere.[1] For this work three samples were selected, grown at relatively low substrate temperatures (650, 682 and 690 °C) with a high hydrogen content. Two of the samples were free standing films grown on molybdenum substrates. The films had peeled off the substrates due to poor adhesion. The third sample was grown on silicon substrate.

XRD measurements were performed on a Scintag diffractometer. Raman spectra were measured by using an argon ion laser operated 514.5 nm.

The annealing processes were performed either in argon flow at atmospheric pressure or in air. Before electrical measurements, the films were cleaned by boiling in a saturated solution of Cr_2O_3 in H_2SO_4 at 200 °C for 20 min to eliminate non-diamond carbon phases. One mm^2 point aquadag contact on one side and a larger area aquadag contact on the other side of the sample were used to measure the bulk resistance through the sample. The I-V curves were measured with a picoamperemeter.

The procedures of measurement were as follows : 1. cleaning the sample, 2. measuring the resistance of the sample, 3. measuring the FTIR transmission spectra, 4. annealing the sample, 5. cleaning the sample, 6. measurig the resistance of the sample, 7. measuring the the FTIR transmission spectra. The samples were not polished. As measurements before and after annealing were made on the same sample, the roughnesss effects in FTIR relative transmission measurements should not matter.

RESULTS AND DISCUSSION

In diamond films of good crystalline quality (grown under optimal conditions, with the diamond line present only in the Raman spectra), the hydrogen content is usually low and cannot be detected by FTIR measurements. The hydrogen content of our diamond samples of good crystalline quality was determined by neutron scattering and was found to be (0.01-0.1 at%) [1].

All three films had diamond lines only in their XRD patterns. The Raman spectra of the samples are presented in Fig. 1. The Raman spectrum of Sample 1 grown at a substrate temperature of 650 °C has only a broad band due to amorphous carbon and no detected diamond line. Sample 2 grown at 682 °C also has no observed diamond line, but has a line due to microcrystalline diamond at ~1150 cm^{-1} and a line due to amorphous carbon. The Sample 3 grown at 690 °C has both a diamond line and a line due to amorphous carbon.

The FTIR absorption curves before and after annealing are shown in Fig. 2. The main hydrogen peaks observed in the diamond Sample 2 and 3 (at 2850 cm^{-1} and 2920 cm^{-1}) are due to sp^3 CH_2 bonding [4]. Sample 1 has a band at 3300 cm^{-1} due to sp^1CH bonding [7] along with the two peaks due to the sp^3CH_2 bonding.

The conditions and results of annealing are presented in the Table I. There was no change in the measured hydrogen content nor in the relative intensity of different peaks after annealing in the Sample 1 and 2, of poor crystalline quality. A change in resistivity due to annealing was observed for Sample 2, but was not observed for Sample 1. This indicates that the change in resistivity was not caused by a change in the amount of bonded hydrogen in the films. A decrease in hydrogen content after annealing was observed only for Sample 3, which was of a better crystalline quality. For this sample an increase in resistivity was also

observed. The conclusion is drawn that the observed change in the conductivity on heat treatment can not be due to the bonded in the bulk hydrogen. On the other hand, it is highly plausible that all hydrogen captured into the film during growth is bonded because the C-H bond (99 kcal/mole [8]) is stronger than C-C bond (83 kcal/mole [8]). The observed change in conductivity on heat treatment probably a surface effect, rather than a bulk effect.

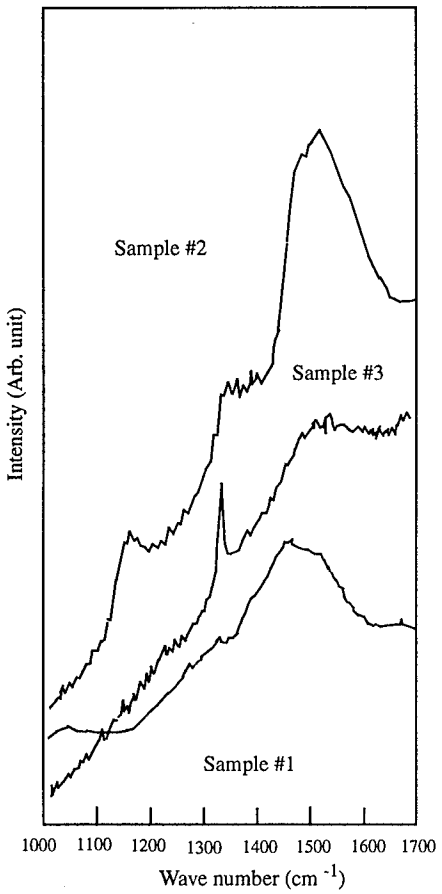

Fig. 1 Raman spectra excited at 514.5 nm

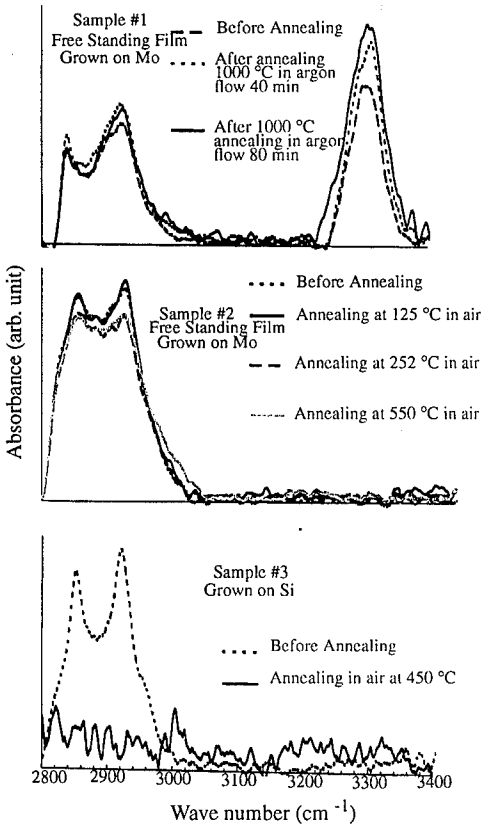

Fig. 2 FTIR spectra before and after annealing

Table I. Conditions and results of annealing

Sample	thickness (μm)	atmosphere	Annealing temp. (°C)	time (min)	Change in H content	Resistance (Ω) before annealing	after annealing
1	19	air	600	60	no	10^7	10^7
1	19	argon	1000	80	no	10^7	10^7
2	9	air	600	60	no	10^7	$>10^{12}$
3	9	air	450	60	decreas ~ 9 times	10^9	$>10^{12}$

CONCLUSIONS

The hydrogen content of diamond films grown by the HF CVD method was studied before and after annealing. Diamond films of good quality have a low hydrogen content. The hydrogen content can be high in films grown at relatively low substrate temperature (650-690 °C) and having large amount of amorphous and microcristalline disorder. The hydrogen bonded in these films cannot be removed by annealing at the temperatures up to 1000 °C. A decrease in hydrogen content on annealing was observed in a film of better crystalline quality. The change in resistivity of the films due to annealing can not be linked to the change of the bulk hydrogen content.

REFERENCES

1. S. Khasavinah, T. Sung, B. Spitsyn, W. H. Miller, G. Popovici, M. A. Prelas, E. J. Charlson, E. M. Charlson, J. Meese,T. Stacy, G. Mannig, S. Loyalka, R. V. Tomson, J. Chamberlain and H. White,*Diamond Materials*, ed. J. P. Dismukes and K. V. Ravi, Electrochemical Societ y Proc. v.**93-17**, 1993, p. 1032-1035
2. M. Kamo, H. Yurimoto, T. Ando, and S. Sato, *New Diamond Science and Technology*, Proc. Second Int. Conf., 1990, Washington D.C., MRS, p.637 - 641
3. M. I. Landstrass and K. V. Ravi, Appl. Phys. Lett. 55, 1391 (1989).
4. F. G. Celii, A. J. Purdes, B. E. Gnade and D. L. Weathers, *New Diamond Science and Technology*, 631 (1991).
5. Sacharia Albin and Linwood Watkins, IEEE Electron Devices 11, 159 (1990).
6. Wenjun Zhang, Fangqing Zhang, Quanzhong Wu and Guanghua Chen, Material Letters , 15, 292 (1992).
7. T. A. Geissman, *Principles of Organic Chemistry*, W. H. Freeman and Co, San Francisco, 1977, p. 392-400
8. T. R. Anthony, Proc. MRS Symposium, MRS 1990, v. 162 p. 61

BLUE LIGHT ELECTROLUMINESCENCE FROM DOPED μc-SiC PREPARED BY EXCIMER (ArF) LASER CRYSTALLISATION

S.P. LAU, J.M. MARSHALL, T.E. DYER, A.R. HEPBURN AND J.F. DAVIES
Department of Materials Engineering, University College of Swansea, Singleton Park, Swansea, SA2 8PP, United Kingdom.

ABSTRACT

A novel method has been developed to prepare highly conductive and wide band gap doped (B_2H_6/PH_3) microcrystalline silicon carbide (μc-SiC) by excimer (ArF) laser crystallisation. Doped a-SiC:H films were prepared by Plasma Enhanced Chemical Vapour Deposition (PECVD), both with and without H_2 dilution. After crystallisation, this material has Tauc gap of around 2.0 eV and exhibits a dark conductivity as high as 20 $(\Omega cm)^{-1}$, more than ten orders of magnitude higher than before the laser irradiation. This is shown to be mainly due to the formation of SiC microcrystallites in the laser crystallised a-SiC:H.

In this paper, we report that this material can be utilised not only as the carrier injection layer in a-SiC:H based Thin Film Light Emitting Diodes (TFLEDs) but also as a luminescent layer. Blue light emission has been observed from a laser crystallised (LC) doped μc-SiC based electroluminescent device, the peak wavelength is around 490nm.

The simplicity of excimer (ArF) laser crystallisation and its capability to fabricate poly-Si TFTs, makes this a promising novel method to realise fully integrated Si large area multi-colour displays.

INTRODUCTION

It is of great importance to develop highly conductive wide band gap doped μc-SiC material which can be utilised as a window layer in heterojunction solar cells[1], and carrier injection layers in a-SiC:H[2] and porous silicon[3] based light emitting diodes. Excimer laser crystallisation of undoped and doped a-Si:H is a useful technique to fabricate polycrystalline silicon thin film transistors (poly-Si TFTs) for applications including active-matrix flat panel display systems[4,5]. Lau et al[6] first reported a novel method for preparing doped μc-SiC with conductivity as high as 2 $(\Omega cm)^{-1}$ utilising excimer (ArF) laser crystallisation. The resulting conductivity is comparable to that obtained by Electron Cyclotron Resonance (ECR) PECVD. It was also proposed that this material can be utilised as a carrier injector in TFLEDs.

Recently, carrier injection type TFLEDs consisting of a-SiC:H p-i-n junctions have been successfully developed[7]. In this type of device, emission in the red, orange, yellow and green are obtained by controlling the optical band gap of the luminescent layer. For large area multi-colour displays to become realistic, a blue light emitter has to be developed. Although blue light emission from an a-C:H based mutilayered intrinsic thin film electroluminescent (EL) device has been observed [8], the driving voltage was too high (300 V_{rms}) for any practical application.

Mat. Res. Soc. Symp. Proc. Vol. 339. ©1994 Materials Research Society

EXPERIMENTAL

Material Preparation and Characterisation

The preparation conditions of the doped (PH_3/B_2H_6) and undoped a-SiC:H as well as the laser crystallisation method were described in a previous publication[6]. In order to maximise the optical band gap of the material at around 2.0 eV, n and p-type a-SiC:H films with typical dopant ratios 0.43% and 0.044% respectively were fabricated, except when otherwise shown. Samples were deposited on Corning 7059 glass for structural and optoelectronic characterisation, and on polished silicon wafers for infrared measurement.

The microcrystalline structure of the films was revealed by transmission electron microscopy and electron diffraction TEM/TED. The surface texture and the micro-porosity of the specimen before and after laser crystallisation were examined by scanning electron microscopy (SEM). Fourier Transform Infrared (FTIR), in the transmission mode, reveals the Si-C, Si-O-Si and Si-H related bonds of the doped μc-SiC before and after laser processing. Measurement of dark conductivity σ_{dc}, over the temperature range 120-400K, was performed in a coplanar configuration with electrode gap ~0.1mm.

Electroluminescent Device Fabrication

Indium tin oxide (ITO) (Cerac 90 mol % In_2O_3 - 10 mol % SnO_2 99.999%) was sputtered onto the 7059 substrate and then annealed at 400 ^{0}C for 2 hours in order to optimise its optoelectronic properties[10]. The resulting resistivity and transmission at 500 nm are 10^{-3} Ωcm and ~80% respectively. Two types of EL devices were fabricated, their schematic structure is shown in Figure 1. For Type I devices, after laser crystallisation of the p layer, the substrate is returned to the PECVD system to deposit the i and n layers. Finally, an Al top electrode with a circular area 1.8 mm^2 was deposited on both Type I and II devices by thermal evaporation through a metal mask. The EL intensity was measured by placing the device in front of a calibrated Newport Model 818-SL silicon detector.

RESULTS AND DISCUSSION

Electrical Characterisation

The results of dc conductivity measurements on doped μc-SiC are shown in Fig. 2. σ_{dc} was increased to 20 $(\Omega cm)^{-1}$ and 10^{-2} $(\Omega cm)^{-1}$ at room temperature for n and p type μc-SiC respectively. Doped a-SiC:H was prepared as a function of methane gas ratio ($CH_4/CH_4 + SiH_4$) from 70% to 90%. There are no significant differences in σ_{dc} after laser irradiation for the various methane ratios, even though the conductivity in the amorphous state varied from 10^{-4} to 10^{-9} $(\Omega cm)^{-1}$. For n-type μc-SiC prepared from

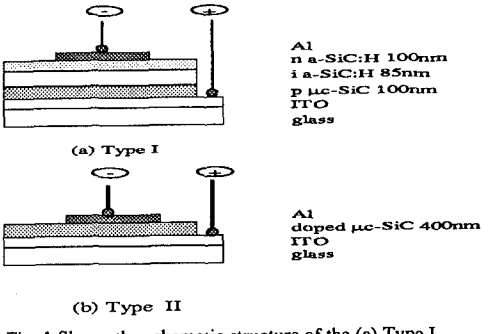

Fig. 1 Shows the schematic structure of the (a) Type I and (b) Type II EL devices.

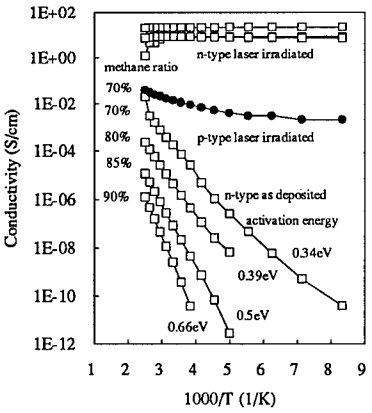

Fig. 2 Temperature dependence of σ_{dc} of p and n-type a-SiC:H and μc-SiC as a function of methane ratio

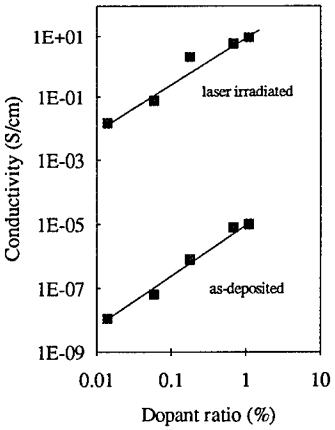

Fig. 3 Room temperature conductivity of p-type a-SiC:H and μc-SiC as a function of dopant ratio.

the highest methane ratio a-SiCH, σ_{dc} was increased by more than 10 orders of magnitude. The conductivities of all the n-type μc-SiC samples are almost independent of temperature between 120 to 400K. The activation energy is of the order of 10^{-2} eV. This indicates that the Fermi levels are located within the conduction band (i.e. a degenerate band structure has been formed)[10]. It has been argued that such a large increase in σ_{dc} and decrease in activation energy may be due to laser induced melting and consequent activation of dopant atoms[5] . If this was the case, the σ_{dc} of the μc-SiC films would depend on the initial dopant concentration in the films. To investigate this possibility, n and p -type a-SiC:H films were prepared as a function of dopant gas ratio (PH_3 or B_2H_6/SiH_4 $+CH_4$). Figure 3 shows the conductivity of p-type μc-SiC before and after laser processing as a function of dopant ratio. Evidently, the ratio of $\sigma_{laser\ irradiated}/\sigma_{as\text{-}deposited}$ is unchanged for doping ratios ranging from 0.044 to 1%, undoped μc-SiC also exhibits the same ratio (not shown). This implies that the increase in σ_{dc} is not predominately due to the activation of dopant atoms.

Structural Properties

After laser processing, all the doped, undoped, diluted and undiluted a-SiC:H films exhibit a microcrystalline structure. Figure 4 shows the planar bright-field TEM and TED images of a laser crystallised p-type μc-SiC film where the a-SiC:H precursor was prepared with H_2 dilution. The grain sizes are found to be between 50 and 200nm for both n and p type μc-SiC. A clear (200) ring, which is characteristic of crystalline SiC, is revealed in the TED micrograph[11]. The considerable increases in σ_{dc} described in the previous section can hence be ascribed to the formation of a SiC microcrystalline phase. This is in contrast to μc-SiC grown from ECR-PECVD, where the enhanced conductivity was mainly attributed to the formation of Si microcrystalline phase[1].

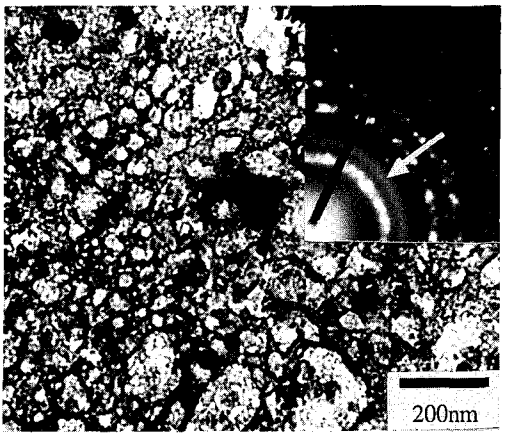

Fig. 4 TEM/TED micrographs of p-type μc-SiC prepared under H_2 dilution. The (200) ring is indicated by an arrow

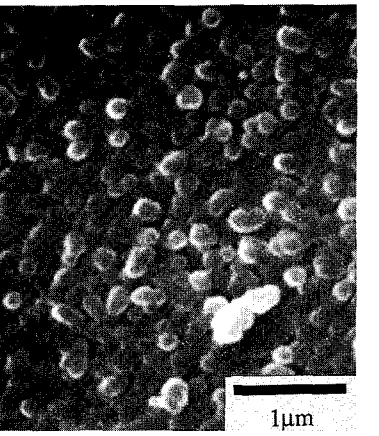

Fig. 5 SEM images of typical laser crystallised p-type μc-SiC surface morphology.

Figure 6 shows the transmittance FTIR spectra of diluted and undiluted p type a-SiC:H and μc-SiC. After laser crystallisation two strong features are evident in the spectrum at 780cm^{-1} and 1050cm^{-1}. These have been attributed to the Si-C stretching vibration and Si-O modes respectively[12]. Additionally, we find that the SiH modes at 650 and 2090cm^{-1} are weakened. The formation of the Si-O modes is mainly attributable to the fact that the specimens were crystallised in air. Thus, oxygen atoms are expected to be incorporated in the films during laser melting. The sharp features associated with the Si-C mode confirm the formation of crystalline SiC.

After laser irradiation, hydrogen related modes disappear from the spectrum, showing that most of the hydrogen atoms are released during laser crystallisation[3]. The explosive hydrogen evolution during the laser melting results a very rough surface morphology. The surface morphology of a typical laser crystallised μc-SiC film is shown in Fig. 5. Micro-pores of the order of 50nm are observed.

EL Device Characterisation

In order to demonstrate that doped μc-SiC can be utilised as a carrier injection layer in a-SiC:H based TFLEDs, a Type I device was fabricated with μc-SiC as a hole injector. Fig. 7 shows the EL spectrum of this device. The EL exhibits a broad band output with peak emission at 490nm (2.5eV) and full width half maximum (FWHM) 0.5eV. No EL spectrum can be measured from our TFLEDs with p type

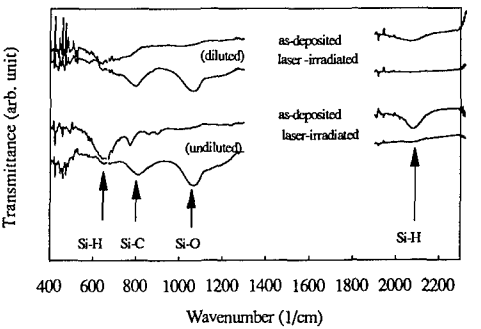

Fig. 6 FTIR spectra of p-type diluted and undiluted a-SiC:H before and after laser irradiation.

amorphous SiC:H as a hole injector because of its low and unstable EL output.

An EL intensity improvement and blue shift of light emission was observed from a similar device structure with a p type μc-SiC layer as a hole injector prepared using ECR-PECVD[12]. However the peak wavelength of this device is at 600nm with FWHM = 0.5eV. Highly conductive and wide band gap p type μc-SiC prepared by ECR may give rise to an increase in the injection level of holes, as well as a decrease of the barrier height for tunnelling of holes and electrons. Such a model has been used to explain the EL improvement and blue shift of EL spectra[12] using this fabrication technique. Orange-white emission from TFLEDs with a n type μc-SiC as a electron injector prepared by ECR-PECVD have also been reported[13]. In this study it was found that the light emission was actually higher than the optical band gap of the intrinsic layer. It is difficult to explain the origin of such high energy electroluminescence.

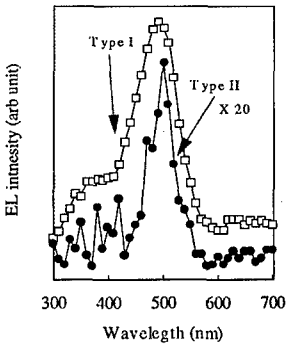

Fig. 7. EL spectrum of Type I and II devices.

For the purpose of explaining the origin of the blue emission from our Type I device, a Type (II) device was fabricated. Surprisingly, we observed light emission from this single layer μc-SiC device, sandwiched between an ITO and Al electrode. The EL spectrum of this Type II device is shown in Fig. 7. The EL intensity of the Type I device is 20 times higher than that obtained from the Type II device. However, the peak wavelength of both devices is around 500nm. Similar electroluminescence can also be observed from the Type I device deposited on a semi-transparent Au substrate, indicating that the EL does not originate from the ITO. Similar I-V characteristics are also observed for both types of devices (Fig. 8). This indicates that the electroluminescence may originate from the μc-SiC only. One possible explanation for the EL observed is that our μc-SiC emits light in a similar fashion to porous silicon/silicon carbide[14,15]. Indeed, if one compares the FTIR spectrum of porous silicon treated in boiling water[14] with our doped μc-SiC, very similar features are observed. Blue light emitting porous silicon shows strong Si-O modes at 1040cm^{-1} and two very weak SiH related peaks at 640m^{-1} and 2090cm^{-1}. There are also many pores in our μc-SiC surface as revealed by SEM (Fig. 5) and the structure is similar to porous Si[16]. Hence, the blue light emission from the doped μc-SiC may be explained by the formation of porous SiC after laser crystallisation.

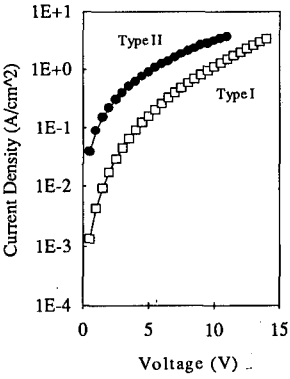

Fig. 8 I-V characteristics of Type I and II devices.

CONCLUSIONS

Excimer (ArF) laser crystallisation is a novel method for preparing highly conductive and wide band gap μc-SiC. The considerable increase in conductivity is mainly due to the formation of a crystalline SiC phase. The blue light emission from the μc-SiC based EL devices is possibly related to the formation of porous SiC by laser crystallisation/texturisation. The structural and

optoelectronic properties of this novel material have some similarities to porous silicon. Further efforts have to be made to investigate the laser crystallisation mechanism, and the origin of the radiative recombination.

Acknowledgements

The authors would like to thank Mr M.Williams for his assistance with the TEM and SEM characterisation, and Professor W.J. Jones (Department of Chemistry) for access to the FTIR spectrometers. We also wish to acknowledge the C.V.C.P for an Overseas Research Studentship awarded to one of us (S.P. Lau). This work was carried out under SERC contracts GR/G49999 and GR/H71819.

REFERENCES

1. Y. Matsumoto, G. Hirata, H. Takakura, H. Okamoto and Y. Hamakawa, J. App. Phys. **67**, 6538 (1990).
2. D. Kruangam, T. Toyama, Y. Hattori, M.Deguchi, H.Okamoto and Y. Hamakawa, J. of Non-Cryst. Solids **98&98** 293 (1987).
3. T. Futagi, T. Matsumoto, M.Katsuno, Y.Onta, H. Mimura, and K. Kitamura in Microcrystalline Semiconductors: Materials Science & Devices, edited by P.M. Fauchet, C.C. Tsai, L.T. Canham, I. Shimizu and Y. Aoyagi (Mater. Res. Soc. Proc. **283**, Pittsburgh, PA, 1993) 389.
4. T.E. Dyer, J.M. Marshall, W. Pickin, A.R. Hepburn and J.F. Davies, J. Non-Cryst. Solids **164-166** 1001 (1993).
5. T. Sameshima (Mater. Res. Soc. Proc. **283**, Pittsburgh, PA, 1993) 679.
6. S.P. Lau, J.M. Marshall, T.E. Dyer, A.R. Hepburn and J.F. Davies, J. Non-Cryst. Solids **164-166** 813 (1993).
7. D. Kruangam, T. Endo, M. Deguchi, W.G. Pu, H. Okamota and Y. Hamakawa, Optoelectronics-Devices and Technologies **1** 67 (1986).
8. M. Yoshimi, H. Shimizu, K. Hattori, H. Okamoto and Y. Hamakawa. Optoelectronics-Devices and Technologies **7** 69 (1992).
9. M. Martinez, J. Herrero and M.T. Gutierrez, Solar Energy Materials and Solar cells **26** 309 (1992).
10. S.M. Sze, Semiconductor Devices, Physics and Technology (John Wiley & Sons, New York, 1985), p. 225.
11. S. Nishino and J. Saraie, in Amorphous and Crystalline Silicon Carbide and Related Materials, edited by G.L. Harris and C.Y. -W. Yang (Springer-Verlag, Berlin Heidelberg, 1989) p. 186.
12. F. Demichelis, C.F. Pirri, and E. Tresso, J. Appl. Phys **72** 1327 (1992).
13. T. Futagi, N. Ohtani, M. Katsuno, K. Kawamura, Y. Ohta, H. Mimura and K. Kitamura, J. of Non-Cryst. Solids **137** 1271 (1991).
14. X.Y. Hou, G. Shi, W. Wang, F.L. Zhang, P.H. Hao, D.M. Huang, X.F. Jin and X. Wang, (Mater. Res. Soc. Proc. **283**, Pittsburgh, PA, 1993) 89.
15. T. Matsumoto, J. Takahashi, T. Tamaki, T. Futagi H. Mimura and Y.Kanemitsu, J. Appl. Lett **64** 226 (1994).
16. W.B. Dubbelday, D.M. Szaflarski, R.I. Shimabakuro and S.D. Russell, (Mater. Res. Soc. Proc. **283**, Pittsburgh, PA, 1993) 161.

THE EFFECTS OF FRICTION AND WEAR ON PECVD DIAMOND FILMS,

M.L. Languell, J.L. Davidson, And J.J. Wert,
Departments of Mechanical Engineering and Materials Science Engineering, Vanderbilt University, Nashville, TN 37212
and
M.A. George, W.E. Collins and A. Burger,
Department of Physics, Fisk University, Nashville, TN 37208,

ABSTRACT

The effects of friction and wear were examined on plasma enhanced chemical vapor deposition (PECVD) diamond films deposited on tungsten substrates. The tribology of diamond on diamond was studied and the changes in surface roughness and the bearing ratio were determined before and after wear. The (111) textured heteroepitaxial films were studied morphologically by scanning electron microscopy (SEM) and atomic force microscopy (AFM). The changes in morphology involved a transition from the large as grown diamond crystallites with a mean diameter of 10 μm to a surface with grains as small as 100 nm. The nature of the wear-modified films will be discussed regarding the possible mechanisms for the surface changes.

Work partially supported by NASA Lewis Research Center grant NAG3-1430.

INTRODUCTION

The high hardness of diamond minimizes the plastic deformation and contact area, contributing to low frictional traction and low wear rates.[1] Low friction and wear make diamond coatings an attractive candidate for tribological applications. Previous studies on the tribological response of polycrystalline diamond films (PDF) have mostly focused on point-contact geometries (pin-on-disk) in mixed systems (i.e., sapphire slider on PDF counterface, steel slider on PDF counterface, single crystal diamond slider on PDF counterface, etc.).[2-6] Various investigators have examined the effects of gas and ambient air, variations in temperature, applied pressure and initial film structure on the wear behavior of diamond films. Of particular interest is the resulting modifications in composition, friction and morphology[7-11]. It is of critical importance to examine these parameters in order to understand the mechanistic behavior of friction and wear on diamond films. In this study, the morphology and nanostructure of the films are examined before and after wear and are correlated to experimental conditions.

EXPERIMENTAL

Tungsten substrates were diamond coated to about 10μm with the plasma enhanced chemical vapor deposition (PECVD) technique. Tungsten sliders and counterfaces, were

Mat. Res. Soc. Symp. Proc. Vol. 339. ©1994 Materials Research Society

diamond coated, using a microwave PECVD ASTeX® reactor. Details for the process are reported by Davidson et al.[12] To evaluate the tribological response of the diamond coating, an extended point contact geometry (cylinder-on-flat) was used to better simulate real contact between mechanical components. The system studied was PDF on PDF to eliminate differences in hardness and chemical reactivity between the slider and counterface. Tribological testing was performed on a reciprocating tribometer without lubrication. The frictional forces were sampled and converted to a coefficient of friction for each sliding cycle to monitor changes in the tribological response. The diamond films were characterized before and after tribotesting for compositional and surface morphological changes. Raman spectroscopy was used to describe film quality. Scanning electron microscopy (SEM) and atomic force microscopy (AFM) using a Nanoscope II were employed to discern changes in surface morphology.

RESULTS

Figure 1 contains representative SEM micrographs of the diamond films deposited on the slider and counterface substrates. Raman spectra of the diamond films were excited by an argon ion laser at 514.5 nm. The Raman data were characterized by fitting the spectra to a model function using the curve fitting routines of Lab Calc®. The line shape function consists of four components: the first order Raman line of crystalline diamond, at 1333 cm^{-1}, a band, centered at ~1550 cm^{-1}, attributed to the sp^2 bonded forms of carbon, a broadening of the diamond peak, believed to be associated with the defect content, and a broad photoluminescence (PL) background underlying the entire spectra. The ratio of the area of the diamond peak to that of the sp^2 bonded carbon band was used as a figure of merit for the diamond content of the film.

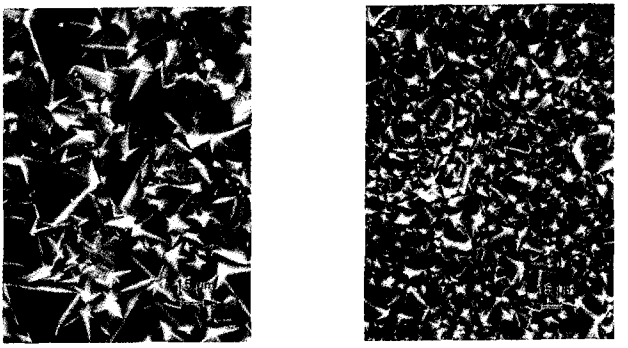

(A) (B)

Figure 1. Representative scanning electron micrographs of the as-deposited diamond film on tungsten substrates highlighting grain size and surface morphology. (A) Slider, (B) Counterface. (Magnification 1.000x)

Figure 2 is a plot of the original spectrum, the curve fit function, and the four model components. The diamond to graphite area ratio is the figure of merit used to describe the diamond film quality.

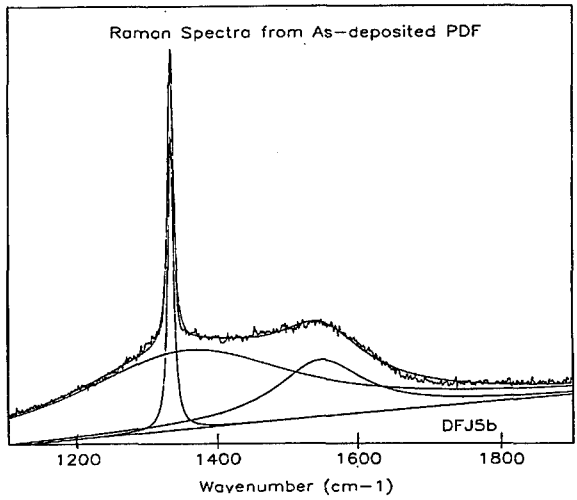

Figure 2. Original Raman spectrum of as-deposited diamond film with model line shape function. The line shape function consists of four components: a linear photoluminescence background, a symmetric diamond peak at ~1332 cm^{-1}, a band centered at 1550 cm^{-1} from sp^2-bonded carbon structures, and a broadening of the diamond peak tails attributed to defect content.

In comparing the diamond to graphite peak ratio, shown in figure 3, the data after obtaining spectra from many samples, both before and after wear, was inconsistant since in as many cases as the graphite content was indicated to have increased, the reverse was also true.

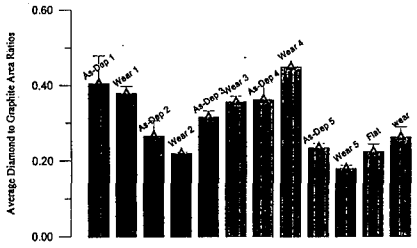

Figure 3. Diamond to graphite peak ratios from Raman spectra from as-deposited and worn PDF.

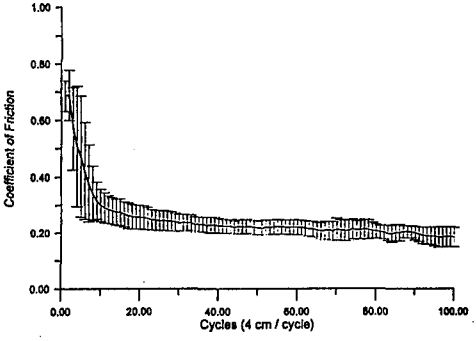

Figure 4. Average of all tribosets with a normal load of 3.56 Newtons in dry nitrogen.

Tribotesting consisted of linear cyclic dry sliding of a right cylinder on a flat surface in a dry nitrogen atmosphere. The relative motion between the slider and counterface was held constant at 19.05 centimeters per minute, except for reversals. This motion generates frictional forces when the slider is brought into contact with the counterface under an applied normal load. Details of the tribotesting system have been reported previously[13]. The normal applied load was 3.56 N, corresponding to a mean Hertzian pressure of 0.2 GPa. During tribotesting, the coefficient of friction was sampled and stored by microcomputer for each cycle. Figure 4 is an average plot of the coefficient of friction versus cycle for five tribotests with standard deviation error bars.

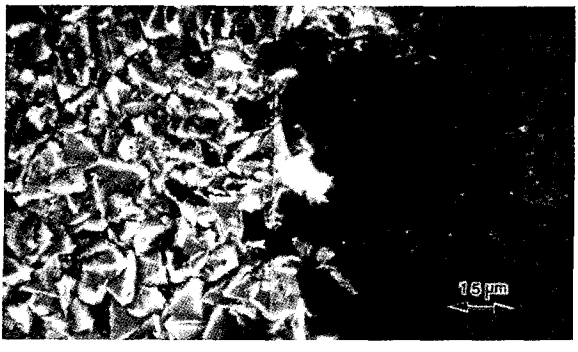

Figure 5. Composite scanning micrograph showing interface between PDF and wear track on diamond coated slider (1000x).

After tribotesting, the wear track of the slider was characterized with Raman spectroscopy, SEM, and AFM. Figure 5 is a SEM micrograph of the interfacial region on the PDF slider between the wear track and as-deposited diamond film.

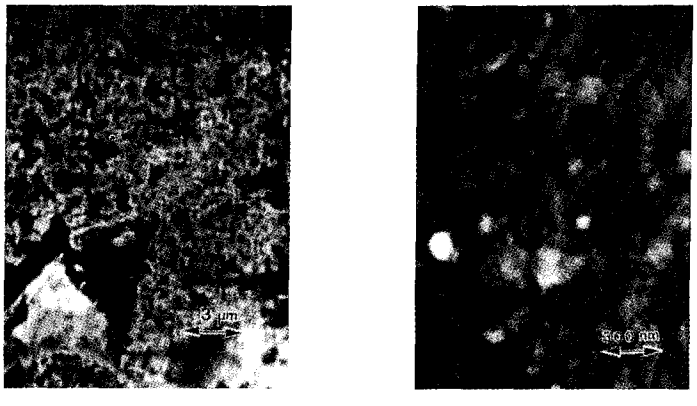

(a) (b)

Figure 6. SEM micrograph of diamond surface after 100 sliding cycles (Magnification (a) 5,000x and (b) 50,000x).

Figure 6 contains high magnification SEM micrographs of the slider wear track. AFM imaging of the as-deposited and worn diamond revealed surface topographies, as shown in

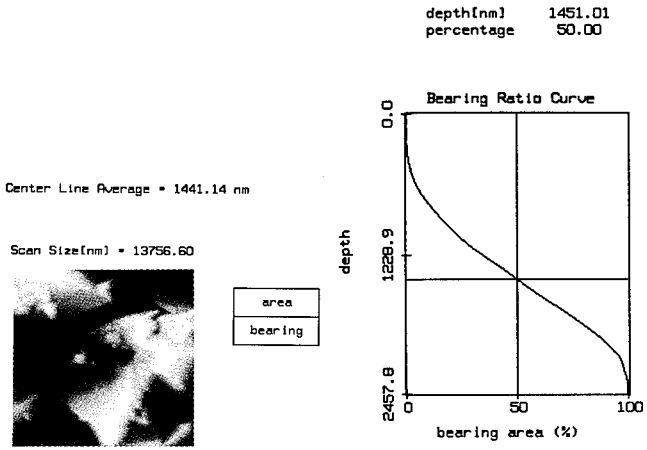

Figure 7. Bearing ratio and centerline average roughness from AFM scan of as-deposited diamond film.

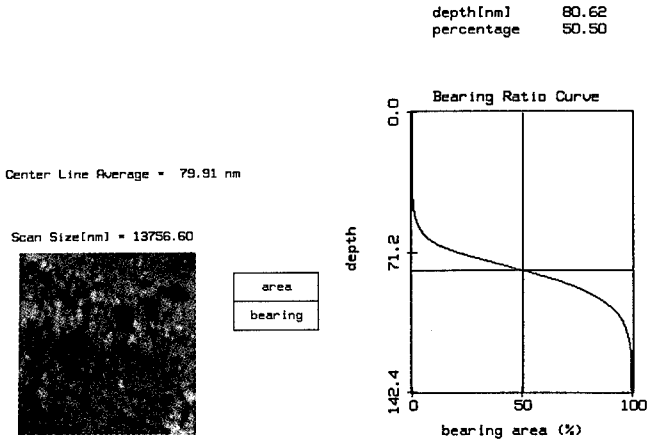

Figure 8. Bearing ratio and centerline average roughness from AFM scan of worn diamond film.

Figures 7 and 8, consistent with the previous SEM micrographs. The bearing area ratio and center line average roughness (R_a) were calculated by image analysis of the scans. Figure 9 contains high magnification AFM scans of the worn PDF.

DISCUSSION

The coefficient of friction (COF) data taken during tribotesting (Figure 4) indicates a well defined break-in period. The initial COF is high (~0.65) but decays to a steady state value (~0.25) within the first 20 cycles. The interlocking of the rough (as-deposited) diamond film of the slider and counterface causes a high initial COF. However, subsequent sliding reduces the asperity tips via fracture. This reduction of the surface roughness is clearly seen by comparing Figures 7 and 8 and is quantified by the bearing ratio curves. The slope of the bearing ratio curve is an indication of the asperity height distribution; a steeper slope represents a narrower height distribution. Thus, the dry sliding of PDF produces a uniform and smoother surface. The wear debris generated during the break-in period can be seen in the as-deposited half of Figure 5. The large angular black areas in the worn portion represent intergranular boundaries while the fractured tops of the worn diamond grains are characterized by random pits. The randomness of these pits suggest little to no plastic deformation during the dry sliding, as expected for diamond.

Pitting is also seen on the surface of single crystal diamonds that have been polished using a metal-bonded wheel containing diamond powder about 30 μm in size.[14] The scale of the pitting seen on these single crystal diamonds is, however, an order of magnitude finer than that evidenced in Figure 6. The polishing of single crystal diamonds may occur along specific crystallographic planes, and account for the difference in scale since the grains of the PDF are randomly oriented perpendicular to the substrate with respect to one another. The pitting may arise from graphitization of the diamond at the asperity junctions, as proposed by previous authors.[8,10] However, results from the Raman survey in this study do not support this hypothesis, since the graphitic content of the worn samples varied from sample to sample. This does not preclude that graphitization is occurring, but its detection with Raman spectroscopy is not conclusive.

Inspection of the high magnification AFM images (Figure 9) reveal a nodular structure with features as small as 50 nm.

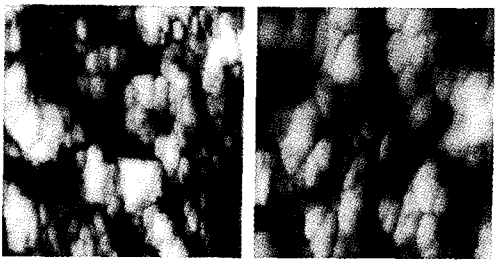

(a) (b)

Figure 9. High magnification AFM scans of worn diamond film, (a) is 1350 X 1350 nm and (b) is 700 X 700 nm.

This nodular structure is very similar to AFM images obtained at the interface between the substrate and PDF as demonstrated in a nucleation study by M.A George et al[15]. The nodular structure they observed was attributed to the initial formation of a diamond like carbon precursor layer onto which diamond crystallites nucleate and grow. Thus one may conclude that the nodular structure of the worn diamond film results from wear of the coating to the PDF/substrate interfacial region. However, the geometry of the slider and the diamond film thickness employed for the tribotesting make this unlikely. Microabrasion of the slider surface from wear debris (Recall Figure 5) and /or the counterface PDF could account for the scale of the nodular structure. However, abrasion of diamond is generally accompanied by brittle fracture which would produce an angular surface morphology with a larger mean grain size. One explanation for the nodular structure observed in Figure 9 is that the smoothed PDF is being microabraded followed by a tribochemical reaction that reduces the sharp fracture surfaces. The possible tribochemical reactions are oxidation, graphitization and the formation of amorphous carbon. Graphitization, as discussed earlier, was not indicated; however, the graphite produced might be below the Raman resolution limit or is removed by subsequent sliding. Though the tribotest chamber was purged with dry nitrogen, a small quantity of oxygen may have remained, thus preclusion of oxidation is not feasible. Furthur studies are planned to determine the composition of the worn diamond film surface.

References

1. M.T. Dugger, D.E. Peebles, and L.E. Pope, "Counterface and Ambient Atmosphere - Role in the Tribological Perforance of Diamond Films." in Surface Science Investigation in Tribology : Experimental Approaches, p. 72. Edited by Y.W. Chung, A.M. Homola, and G.B. Street. ASC Symposium Series No. 485, American Chemical Society, Washington DC 1992.
2. D. Tabor in The Properties of Diamond, edited by E. Field , Academic Press, 1979, Chap. 10, pp 345-349.
3. P.J. Blau, C.S. Yust, L.J. Heatherly and R.E. Clausing " Morphological Aspects of the Friction of Hot-Filament-Grown Diamond Films" in Mechanics of Coatings, Leeds-Lyon 16, Tribology Series, 17, pp 399-407. Edited by D. Dowson, C.M. Taylor, M. Godat. Elsevier Science B.V., 1990.
4. I.P. Hayward and I.L. Singer, *2nd Int. Conf. on the New Diamond Science and Technology*, Washington, DC, Sept. 25-27, 1990.
5. M.N. Gardos and B.L. Soriano, " The Effect of Environment on the Tribological Properties of Polycrystalline Diamond Films." pp 2599-2609. *J. Mater. Res.*, **5**, 1990.
6. J.F. Braza and T.S. Sudarshan "Tribological Behavior of Diamond and Diamond-like Carbon Films: Status and Prospects" in Surface Modification Technologies V, pp. 801-819. Edited by T.S. Sudarshan and J.F. Braza, The Institue of Materials, 1992
7. I.P. Hayward, *The Friction and Strength Properties of Diamond*; Ph.D. Thesis, University of Cambridge, 1987; pp. 71-94.
8. S. Jahanmir, D.E. Deckman, L.K. Ives, A.Feldman, E. Farabaugh, *Wear,* **1989,** *133*, pp.73-81
9. T. Evans in The Properties of Diamond edited by E. Field, Chapter 13, pp 403-423. Academic Press, 1979.
10. M.N. Gardos and B.L. Soriano, *J. Mater. Res.*, **5**, 1990 pp 2599-2609.

11. I.P. Hayward, I.L. Singer, L.E. Seitzman, "Effect of Roughness and Surface Chemistry on Friction of CVD Diamond Films," presented at the 17th Int. Conf. on Metallurgical Coatings and 8th Int. Conf. on Thin Films, San Diego, CA, April 2-6, 1990.
12. J.L. Davidson, C. Ellis and R. Ramesham, *J. of Elec Mats*, **18** (6) 1989 p. 711-715.
13. M.L. Languell, J.J. Wert, J.L. Davidson, and B.K. Wagner,"Transient and Steady State Tribological Response of Diamond Films in Dry Sliding Contact" in the Proceedings from the VIIth Int. Conf. on Surface Modification Technologies, Nov. 1 - 3, 1993, Nagaoka JAPAN.
14. J. Wilkes and E. Wilkes, Properties and Applications of Diamond, 1990, pp 245-248, Butterworth and Heinmann, Oxford.
15. M.A. George, A. Burger, J.L. Davidson, A.V. Barnes and N.J. Tolk, Submitted March, 1994, *J. Appl. Phys.*

PART IX

Defects

RECOMBINATION PROCESSES OF THE BROADBAND AND 1.681 eV OPTICAL CENTERS IN DIAMOND FILMS

L. BERGMAN, M.T. MCCLURE, J.T. GLASS AND R.J. NEMANICH
Department of Physics and Department of Materials Science and Engineering,
North Carolina State University, Raleigh, North Carolina 27695-8202

ABSTRACT

Micro- and macro-photoluminescence techniques were employed in this research to investigate the role of nitrogen-doping on the optical spectra of chemical vapor deposited diamond films and to determine whether the origin of the broadband luminescence is due to vibronic interaction of the nitrogen centers. The temperature behavior of the broadband PL and of the 1.681 eV silicon related optical center were analyzed. The intensity of the broadband was found to exhibit a temperature dependence characteristic of optical emission from a continuous distribution of gap states while the temperature dependence of the 1.681 eV band followed the Boltzmann quenching process.

I. INTRODUCTION

This research investigates the broadband, nitrogen-related, and 1.681 eV optical defects in chemical vapor deposited diamond films. A broadband luminescence extending from approximately 1.5 to 2.5 eV and centered at ~ 2 eV has been observed in various photoluminescence (PL) studies of diamond films grown by various chemical vapor deposition (CVD) methods [1,2]. A complete model has yet to be formulated to explain the origin of this broadband PL. Studies utilizing cathodoluminescence (CL) and absorption spectroscopy of crystal diamonds of types Ia and Ib which contain nitrogen have shown that similar luminescence has its origin in the electron-lattice coupling (vibronic interaction) of nitrogen related centers with zero phonon lines (ZPL) at 1.945 and 2.154 eV [3,4]. Luminescence studies on natural brown diamonds [5] have shown that the brown diamonds luminesce in the yellow and in the red region of the spectrum. The luminescence appears in the optical spectra as wide bands centered at ~ 2.2 eV and at ~ 1.8 eV and is very similar to the one observed in the spectra of the CVD diamond films. The origin of the PL bands of the brown diamonds has also been determined to be of vibronic nature with numerous ZPL the principal ones at 2.721 and at 2.145 eV.

An alternative mechanism which could give rise to the broadband PL in the CVD diamond films is the amorphic phase of the sp^2-bonded carbon (also called the graphitic phase), the presence of which has been widely confirmed. The PL of amorphous carbon films exhibit emission centered at ~ 1.8-2 eV which is of similar line shape to that observed in the CVD diamond films [6,7]. According to the general model of the state distribution of amorphous materials [8], the distortions of bond angles and of bond lengths which constitute the amorphous phase introduce a continuous state distribution in the optical band gap of the material. The PL of amorphous carbon films has been determined to originate in the optical transitions of an in-gap state-distribution related to the disordered forms of the sp^2 carbon bonding. In this paper we establish the presence of an in-gap state-distribution in CVD diamond films and suggest that it is the likely cause of the broadband luminescence. We also present an analysis of the temperature characteristics of the 1.681 eV PL band. The 1.681 eV optical center is commonly accepted to be associated with a Si impurity introduced into the diamond matrix during growth [1,2].

II. EXPERIMENT

Diamond samples were grown on Si (100) substrates using an ASTeX microwave plasma CVD system. The plasma power, temperature and pressure were maintained at 900 watts, 850°C

Mat. Res. Soc. Symp. Proc. Vol. 339. ©1994 Materials Research Society

and 25 Torr respectively. Two samples involved in the nitrogen study were subjected to $H_2/CH_4/N_2$ flow rates of 500/5/0 sccm and 500/5/0.5 sccm and will be referred to as the 0% and 0.1% nitrogen-doped samples respectively according to their gas phase N_2/H_2%. The growth time was 5 hours and the morphology consist of diamond grains. A third undoped diamond continuous sample about 2 μm thick (described in our previous study [2]) was also used and will be referred to as the 20h sample, reflecting its growth time. The micro-PL analysis of the 0% and the 0.1% nitrogen-doped samples was carried out at room temperature employing Argon-ion laser excitation (514.5 or 457.9 nm) which was focused on the sample to a spot of ~ 5 μm in diameter. Focusing was facilitated by using an Olympus BH-2 microscope. The macro PL analysis of the 20h sample was carried out employing a JANIS CCS-350 closed cycle refrigerator system. The laser was focused to a line of ~ 2 mm x 100 μm on the sample. In both studies, an ISA U-1000 scanning double monochrometer was used to analyze the signal.

III. RESULTS AND DISCUSSION

The first part of our work focused on obtaining the PL spectra of nitrogen-doped and undoped diamond films, identifying the nitrogen-related PL bands and examining the influence of the nitrogen on the broadband PL. In Figure 1 the PL spectra of the 0.1% and of the 0% nitrogen-doped diamond films are shown. Both spectra were obtained utilizing the 514.5 nm green line of the Argon laser. The PL spectra are shown in absolute energy scale. The PL spectra of the undoped diamond film exhibits the fairly smooth broadband line shape centered at ~ 2.05 eV, and also exhibits the 1.681 eV band which has been attributed to an optical transition in a Si complex center [9]. However, the spectra of the nitrogen-doped film indicates a red-shift of the broadband luminescence center as well as a line-shape change. Furthermore, the nitrogen-related bands at 2.154 and 1.945 eV are present. Studies carried out by Davies et al. [4] have suggested that the 1.945 eV band is due to the substitutional nitrogen-vacancy optical center. Collins et al. [3] proposed that the 2.154 eV band is the result of a transition in a center consisting of a single substitutional nitrogen atom with one or more vacancies. Yet another PL band at 1.967 eV is also present in the spectra (barely distinguishable from the 1.945eV band), which might also be due to a nitrogen-related center.

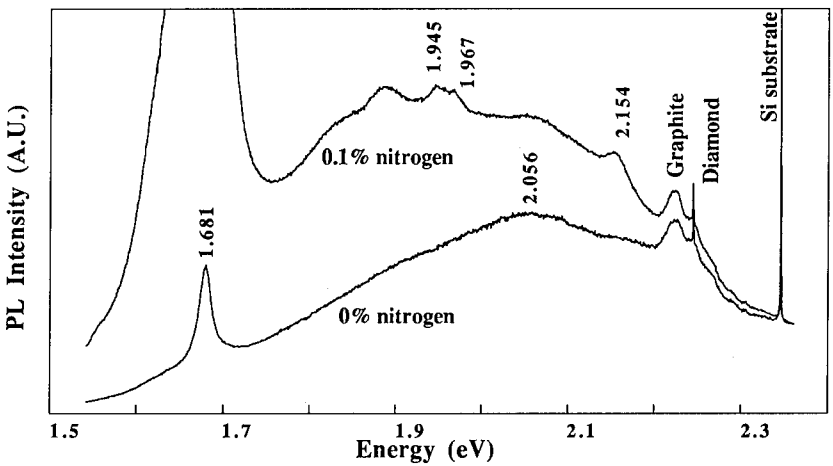

Figure 1. The PL spectra of the diamond films utilizing the 514.5 nm (2.41 eV) laser line.

In order to examine in further detail the line-shape of the broadband PL, the 457.9 nm blue laser line was used for excitation. Figure 2 shows the spectra of the 0% and of the 0.1% nitrogen-doped diamond films for this laser frequency. The broadband PL of the undoped

diamond film retained its relatively unstructured line-shape; however, the maximum intensity is shifted towards higher energy and is centered at ~ 2.2 eV. The spectra of the nitrogen-doped diamond film exhibits the nitrogen-related bands at 2.154 and at 1.967 eV. The 1.945 eV band, which appeared with the 1.967 eV band as a doublet in the spectra obtained using the green laser line, can not be clearly distinguished in the spectra taken using the blue line. This overlapping of the two bands is a resolution artifact of the scaling of the spectra using the blue laser line. A relatively wide band with line-width ~ 0.3 eV centered at 2.46 eV is also present. Similar wide-band luminescence has been observed in both natural and synthetic diamonds, and is commonly referred to as "band A" luminescence [10]. This band has variable peak energy and line-width depending on the concentration of the nitrogen in the diamond and on the diamond type. The band A luminescence has been suggested to originate from donor-acceptor recombination process. Our observation of the three nitrogen-related bands in the spectra may indicate that the paramagnetic (1.945, 2.154 eV) as well as the non-paramagnetic (band A) forms of nitrogen centers can exist simultaneously in the CVD diamond films. It is also evident from the spectra that the incorporation of nitrogen caused a distortion in the line-shape of the underlying broadband luminescence. If the broadband PL had been due to the nitrogen-lattice interaction, the line-shape would have been invariant, and a change in the intensity would have been anticipated.

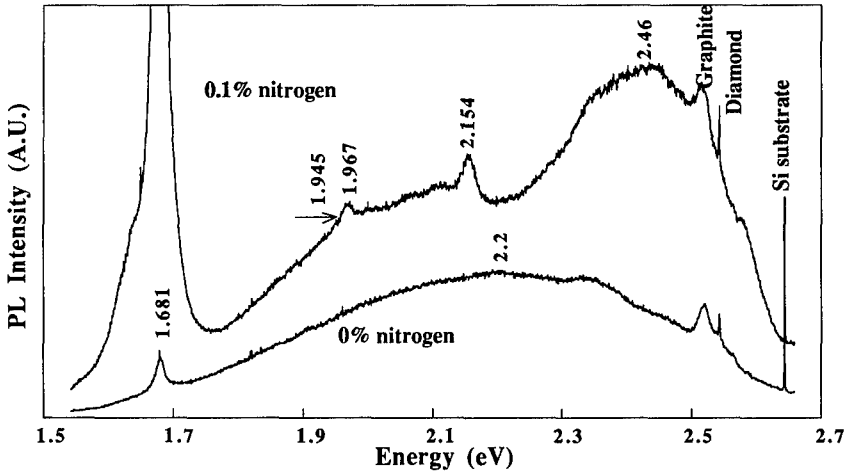

Figure 2. The PL spectra of the diamond films utilizing the 457.9 nm (2.71 eV) laser line.

A second series of experiments and analysis were conducted to further rule out the possibility of the broadband PL being of vibronic origin. According to the theoretical model of the electron-lattice interaction [11], the total band intensity which includes the zero-phonon line and its vibronic sideband is expected to be independent of temperature. As the temperature increases the zero-phonon line intensity decreases, and the vibronic band intensity is expected to increase so as to keep the total intensity constant with temperature (where the ZPL and sideband intensities are taken relative to the total band intensity). The width of the vibronic band is also expected to increase with temperature. However, as shown in Figure 3 we found instead that the broadband PL intensity of the 20h sample exhibits a ~ 60% decrease with increasing temperature without any significant change in the band width. Furthermore no ZPL lines were present at the low temperature spectra. However, the ZPL responsible for the vibronic band in brown diamonds as well as the ZPL of nitrogen centers are known to be sharp and well-pronounced in low-temperature spectra [5,10]. The temperature dependence we observed is thus not characteristic of a vibronic interaction.

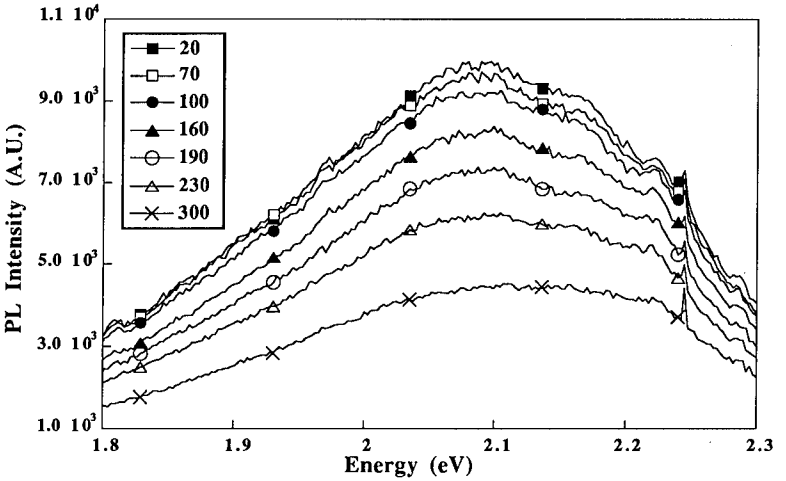

Figure 3. The spectra of the broadband PL of the 20h sample at various temperatures.

Figure 4 shows the correlation between the Raman intensity of the graphitic phase and the intensity of the broadband PL. This correlation was found and described in detail in a previous study [2]. It was found that, as a function of growth time, as the graphitic phase increases so does the intensity of the broadband PL. We have suggested that the amorphic graphitic phase introduces a state distribution in the band gap which provides transition centers for the photo-excited carriers, thus resulting in the broadband PL.

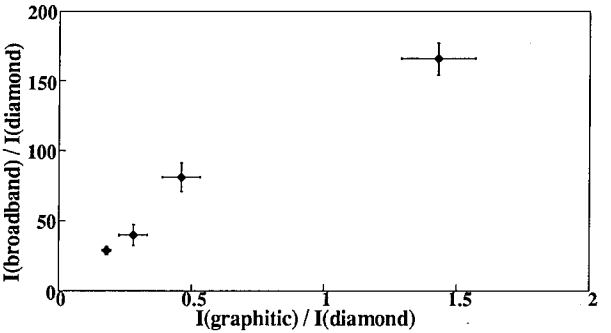

Figure 4. Correlation between the intensities of broadband and the graphitic phase.

We now present the results of a further investigation of the broadband PL obtained from the 20h undoped diamond film. We establish that it has PL characteristics similar to those found in amorphous materials. In general the PL process can be expressed by the following equation

$$I / I_0 = P_R / (P_R + P_{NR}) \qquad (1)$$

where P_R and P_{NR} are the probabilities for the radiative and the nonradiative recombination respectively [12], I is the PL intensity, and I_0 is the PL intensity for the temperature approaching absolute zero. If there exists a single activation energy E_A for P_{NR} for which the thermal quenching of the PL is of the form of a Boltzmann activated process then Eq.(1) becomes:

$$P_{NR} / P_R = [I_0 / I(T)] - 1 \sim \exp(- E_A / k_B T) \quad (2)$$

By plotting $\log((I_0 / I(T) - 1))$ vs $1/T$ a straight line should be obtained from which E_A can be evaluated. Figure 5 shows this plot for our experimental data, I(T), the inset in the figure shows I(T) vs. temperature. The continuous curve of figure 5 indicates the existence of a continuous distribution of activation energies E(T) rather than a single E_A associated with one energy level of a specific defect. Such a continuous distribution of activation energies E(T) indicates in turn a corresponding distribution of localized energy states in the band gap of the CVD diamond film. E(T) may thus be viewed as corresponding to the binding energies of these localized states. The data in Figure 5 can be fitted by the equation

$$[I_0 / I(T)] - 1 \sim \exp(T/T_0) \quad (3)$$

for which T_0 is a constant to be determined. This form of quenching of the PL which we find in our studies has also been observed and its theory developed by Street et al. [13] in their extensive work on amorphous Si:H. We note that the broadband PL intensity in the diamond films exhibits a much slower decrease with increasing temperature than the PL intensity reported for a-Si:H. A smaller dependence on temperature was also reported for amorphous C:H [7] with temperature dependence of the form of Eq.3, consistent with our findings. According to the model developed by Street et al. for amorphous materials T_0 is a measure of the width of an exponential in-gap state distribution from which optical transitions can occur [13]. More extensive experiments need to be carried out to further quantify and model the state distribution and to determine the bands involved in the optical transitions. In amorphous carbon material the sp^2 bonding creates sigma-bands (σ, σ^*) and pi-bands (π, π^*) for which optical transitions can occur [6]. At present we hypothesize that the π-π^* band transitions are responsible for the broadband PL; these bands constitute allowable optical transitions and are in the energy range closest to our laser excitation energy [14].

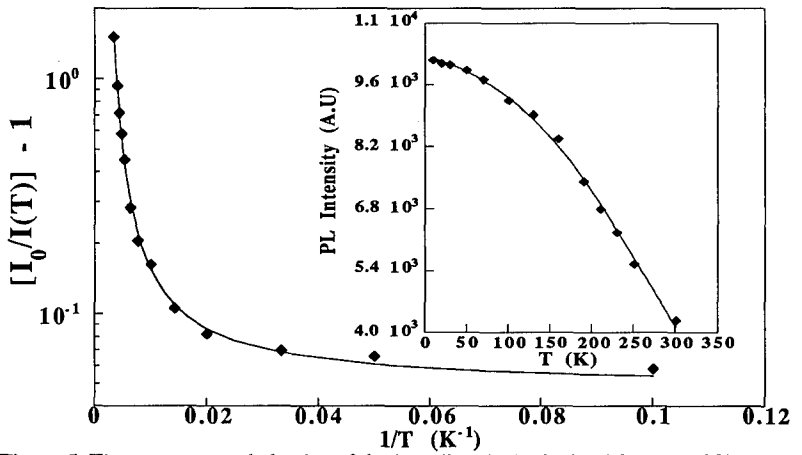

Figure 5. The temperature behavior of the broadband PL obtained from the 20h sample.

Figure 6 shows the temperature dependence of the 1.681 eV PL intensity. It can be seen that the PL intensity in the temperature range 10-100K is approximately constant whereas a strong quenching of the PL takes place at T > 100K. The data in Figure 6 can be fitted by Eq.2, with an activation energy E_A = 90 meV (±10 meV). Thus ~ 90 meV is the energy needed to channel the photo-carriers from the excited state to the nonradiative path. The substantially different temperature dependence of the broadband PL and the 1.681 eV band, suggests that different non-radiative recombination mechanisms are involved. This may imply that these two optical centers do not directly communicate.

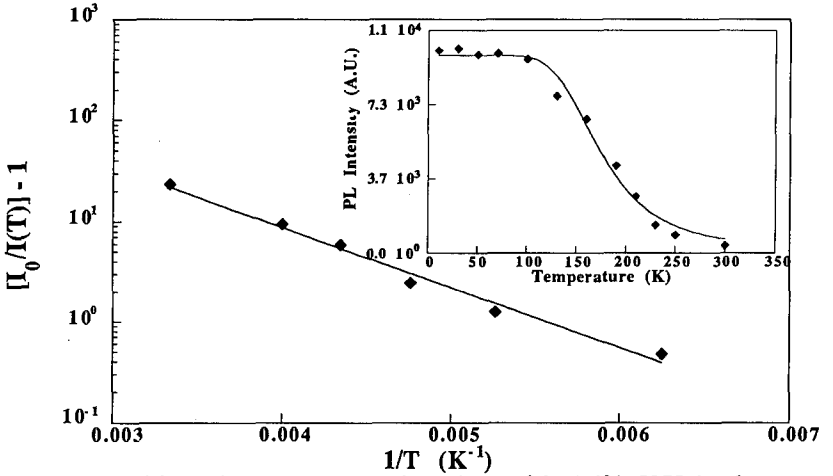

Figure 6. The temperature dependence of the 1.681 eV PL band

In conclusion, the spectra of both nitrogen-doped and undoped films exhibited the broadband PL; the nitrogen-doped sample, however, had a distortion of the line-shape of the underlying broadband PL due to the vibronic interaction of the nitrogen centers. The nitrogen optical centers at 2.154, 1.945 and at 2.46 eV (band-A) were observed, as well as a new possibly nitrogen-related center at 1.967 eV. The temperature behavior of the broadband PL indicates that the band does not originate from a vibronic interaction. Morever, the intensity of the broadband PL was found to exhibit a temperature dependence characteristic of optical emission from a continuous distribution of gap states. In light of the above findings and from the correlation of the PL intensity to the graphitic phase we suggest that the broadband PL in CVD diamond films is due to the optical transitions in an in-gap state distribution, where the in-gap state distribution is introduced by the amorphous phase of the sp^2 hybrid bondings. The temperature-behavior of the 1.681 PL band found to exhibit characteristic of Boltzmann activation process with an activation energy of nonradiative transition $E_A \sim 90$ meV.

REFERENCES

1. J.A. Freitas, Jr., J.E. Butler, and U. Strom, J. Mater. Res. **5**, 2502 (1990).
2. L.Bergman, B.R. Stoner, K.F. Turner, J.T. Glass, and R.J. Nemanich, J. Appl. Phys. **73**, 3951 (1993).
3. A.T. Collins and S.C. Lawson, J. Phys.: Condens. Matter **1**, 6929 (1989).
4. G. Davies and M.F. Hamer, Proc. R. Soc. Lond. A. **348**, 285 (1976).
5. M.E. Pereira, M.I. Jorg, and M.F.Thomaz, J. Phys. C: Solid State Phys. **19**, 1009 (1986).
6. J. Robertson, Advances In Physics **35**, 317 (1986).
7. R.C. Fang, J. Lumin. **48/49**, 631 (1991).
8. N.F. Mott and E.A. Davis, Electronic Processes in Non-Crystalline Materials (Clarendon Press, Oxford, 1979).
9. A.T. Collins, M.Kamo, and Y.Sato, J. Mater. Res. **5**, 2507 (1990).
10. Gordon Davies, Chemistry and Physics of Carbon **13**, 2 (1977).
11. Gordon Davies, Rep. Prog. Phys. **44**, 787 (1981).
12. D. Curie, Luminescence in Crystals (John Wiley and Sons, 1963).
13. R.A. Street, Advances in Physics **30**, 593 (1981).
14. G.S. Painter and D.E. Ellis, Phys.Rev.B **12**, 4747 (1970).

ON THE NATURE OF THE NATIVE DEFECT ESR IN THIN DIAMOND FILMS

J. Shinar,*† H. Jia,*† D. P. Lang,*‡ and M. Pruski*‡
*Ames Laboratory - USDOE, Iowa State University, Ames, Iowa 50011
†Department of Physics and Astronomy, Iowa State University, Ames, Iowa 50011
‡Department of Chemistry, Iowa State University, Ames, IA 50011

ABSTRACT

The X-band ESR of thin diamond films deposited from 99.5% H_2/0.5% CH_4 is compared to that of films similarly prepared from D_2/CD_4 and $H_2/^{13}CH_4$. The main line and the satellites at ±7.2 G are unaffected by annealing at T ≤ 1100°C, but their intensity is reduced upon annealing at T ~ 1200°C. As the satellites are absent from the deuterated films, they are attributed to newly identified dangling bond-H centers, either on internal microvoid surfaces or embedded in the tetrahedral network. This is consistent with the ^{13}C spin-lattice relaxation rate, which indicates that the distribution of paramagnetic centers is homogeneous to within ~0.04 μm. However, they may be nonuniformly distributed on a finer scale, consistent with the concentrations in multivacancies or stacking faults recently suggested by Fanciulli and Moustakas.

INTRODUCTION

Extensive studies on thin diamond films have been reported since the discovery that they could be deposited on hot substrates by thermally-assisted chemical vapor deposition (CVD) of CH_4 heavily diluted by H_2 [1,2]. Relatively modest efforts, however, have been directed towards establishing a detailed picture of the structural and electronic properties of these films in general and their native defects in particular [1-6]. This work focusses on the nature of the ESR that is invariably observed in these films, and is thus evidently due to a native defect. This ESR includes a central line that usually appears to be the sum of narrow ($\Delta H_{ppn} = 1.4 \pm 0.2$ G) and broad Lorentzians ($3.0 \leq \Delta H_{ppb} \leq 6.1$ G) [4-7], or a narrow Lorentzian and a broad Gaussian [8]. In many cases, but not all, two partially resolved satellites are observed at $\Delta g \approx \pm 4 \times 10^{-3}$ ($6.0 \leq |\Delta H| \leq 7.5$ G at the X-band frequency of 9.33 GHz) [3-6]. We show below that the main line and the satellites are unaffected by annealing at T ≤ 1100°C, but their intensity is reduced upon annealing at T ~ 1200°C. As the satellites are strikingly absent from the ESR of films deposited from 99.5% D_2/0.5% CD_4 or 99.5% D_2/0.5% CH_4, they are attributed to dangling bond-H centers. To the best of our knowledge, these centers have not been previously identified in either natural [7], synthetic [7], or CVD diamond. Comparison with NMR studies indicate that they are bulk defects, probably located either on a multivacancy or stacking fault surface as suggested by Fanciulli and Moustakas [8], or isolated in the tetrahedral diamond network.

EXPERIMENTAL PROCEDURE

Thin diamond films were grown by flowing a 99.5 % H_2/0.5% CH_4 or a similar D_2/CD_4 mixture as described elsewhere [13]. Following the deposition, the Si substrate was removed by dissolving it in HF, to yield free-standing films. X-ray diffraction spectra yielded sharp diamond diffraction peaks only.

Mat. Res. Soc. Symp. Proc. Vol. 339. ©1994 Materials Research Society

The samples were oven annealed in either open quartz tubes in an Ar flow, or in sealed evacuated quartz tubes, or by an oxyacetylene torch in an open quartz tube in an Ar flow.

No nitrogen ESR, identifiable by the ^{14}N hyperfine-split components at ±25 - ±30 G from the main line [4], could be detected by the Bruker DSR 200 ESR spectrometer.

The ^{1}H and ^{13}C NMR are also described elsewhere [14]. The ^{13}C NMR of naturally (1.1%) abundant as well as of 99% ^{13}C-enriched films indicated that no more than 0.5% of the carbon atoms were in a nondiamond configuration [14]. Scanning electron microscopy (SEM) showed that the crystallites at the top surface of the film were several microns across. The ^{1}H NMR spin count, however, suggested that if the hydrogen was confined to the crystallite surfaces and essentially covered them, then the average crystallite should be less than ~0.5 μm across [14]. This apparent discrepancy could be due to the observation that the crystallite size increases during film growth [9,10,15] and the smaller crystallites near the substrate cannot be seen in SEM images. These smaller crystallites could account for the larger amount of hydrogen detected by NMR. This issue is discussed further below.

RESULTS AND DISCUSSION

Typical X-band derivative ESR spectra of samples A and B deposited from H_2/CH_4, the former grown over 30 hrs, the latter over 146 hours, are shown as the solid lines in Figures 1(a) and 1(b), resp. The total integrated intensities yield spin densities of $3.1x10^{16}$ and $2.7x10^{17}$ spins/gm, or 0.6 and 5.4 ppm, resp. The observation that the spin density of the thicker film B is greater than that of the thinner one A is interesting. Although not firmly established, it is consistent with the interpretation of the ESR results discussed below. Following Redwing et al. [5], the spectra were fit to the sum of four Lorentzians (shown as the dotted lines in Fig. 1), of g-values, amplitudes, and linewidths summarized in Table I. The central narrow and broad Lorentzians, invariably observed in all films, have been attributed to exchange-narrowed clusters and isolated carbon dangling bonds at spinless ^{12}C nuclei, resp. [5]. These tentative assignments are in general agreement with the recent analysis of Fanciulli and Moustakas [8]. The satellites were suggested to result from hyperfine coupling of carbon dangling bonds with central or adjacent ^{13}C nuclei, or with neighboring ^{1}H [5]. The former interpretation, however, is problematic: (i) The 1.1% natural abundance of the ^{13}C nuclei is too low to account for the in-

Table I. *The spin densities N_s of the samples whose ESR spectra are shown in Figure 1, the derivative peak-to-peak linewidth and fractional integrated intensity of the central narrow (ΔH_{ppn} and I_n, resp.) and broad (ΔH_{ppb} and I_b, resp.) Lorentzians, and those of the satellites (ΔH_{ppsat} and I_{sat}, resp.). In all cases, the g-values of the central Lorentzians are 2.0028 ± 0.005, and the satellites are split from them by ΔH = 7.2 ± 0.2 G.*

Sample	A	B	B	B	C	D	E
Spectrum	1(a)	1(b)	1(c)	1(d)	1(e)	1(f)	1(g)
$N_s(gm^{-1})$	$3.1x10^{16}$	$2.7x10^{17}$	$2.7x10^{17}$	$6.2x10^{16}$	$1.1x10^{18}$	$1.4x10^{18}$	$3.6x10^{17}$
N_s(ppm)	0.6	5.4	5.4	1.2	22	28	7.8
ΔH_{ppn}(G)	2.4	2.6	2.6	1.9	2.8	2.9	---
I_n(%)	12	13	15	10	44	35	---
ΔH_{ppb}	7.5	7.8	7.5	5.8	8.7	10.1	---
I_b(%)	83	83	78	81	56	65	---
ΔH_{ppsat}	2.4	2.9	3.0	2.7	--	--	---
I_{sat}(%)	5	4	7	9	--	--	---

tensity of the satellites relative to that of the central resonances, which increases to $I_{sat}/I_c \sim 0.09$ upon annealing (see below). (ii) Hyperfine coupling with ^{13}C should lead to a constant value of I_{sat}/I_c, i.e., in contrast to its temperature dependence in this work and its variation among different samples. Indeed, in some cases [8], notably those involving oxygen-containing precursors [3,6], their intensity is negligible. (iii) Although measured at similar microwave frequencies, the splitting of these satellites from the main Lorentzians is $\Delta H \approx \pm 6$ G as reported by Redwing et al. [6], but ±7.2 G in the samples studied in this work, .

Previous ^1H NMR measurements have indicated that most of the hydrogen in thin diamond films resides on the crystallite surfaces, and most of it is removed after ~2 hr annealing at ~850°C [5,9-12]. Sample B was therefore annealed in 1 hour steps, and its ESR was measured after each step. Yet in spite of annealing in an Ar flow at 740, 765, 790, 830, 867, 905, 935, 965, 1013, 1057, and 1085°C, then crushing it to a powder and annealing it in an evacuated quartz tube at 828, 865, and 970°C, and then crushing the powder further and annealing it in an Ar flow at 805, 875, 965, 1015, and 1112°C, the ESR lineshape and spin density did not change (Fig. 1(c)). Finally, the sample was heated for 20 minutes in an Ar flow by an oxyacetylene torch at T ≥ 1200°C (an optical pyrometer indicated T ≈ 1500°C, but that temperature is considerably above the softening point of quartz). The resulting ESR is shown in Figure 1(d). Interestingly enough, while the overall spin density decreased by a factor of ~4.5, the relative intensity of the satellites actually slightly *increased* with respect to the main lines (Table I).

Figure 1(e) shows the ESR spectrum of sample C similarly deposited from 99.5% D_2/0.5% CD_4. As clearly seen from the figure and Table I, the satellites are completely absent from this sample. Also striking is the increased intensity of the central narrow Lorenztian relative to the broad component. It is suspected, however, that this is due to the contribution of unresolved ^2D-hyperfine-split dangling bonds.

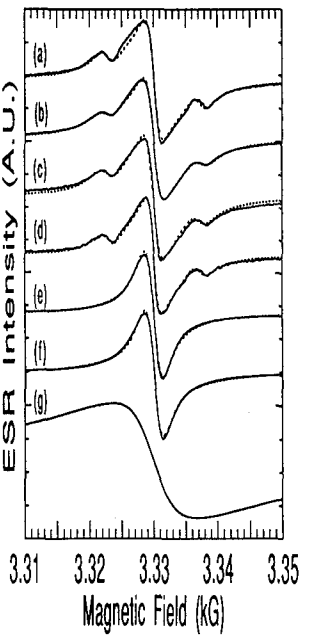

Figure 1. *X-band ESR spectra (solid lines) of thin diamond films. The dotted lines are the sum of four (spectra (a) - (d)) or two (spectra (e) and (f)) Lorentzians, of g-values, amplitudes, and linewidths listed in Table I. (a) Sample A, as deposited for 30 hours from 99.5% H_2/0.5% CH_4 (see text for details). (b) Sample B, as deposited under the same conditions, but for 146 hours. Note that the satellites are weaker relative to the central resonances than in (a). (c) Sample B following 1 hr annealing steps (see text) at T ≤ 1112°C. (d) Same sample, after annealing by an oxyacetylene torch for 20 min at ~1200°C in an Ar flow. (e) Sample C, as deposited from 99.5 % D_2/0.5% CD_4. Note the absence of the satellites from spectra (e) and (f) Sample D, as deposited from 99.5% D_2/0.5% CH_4. (g) Sample E, as deposited from 99.5% H_2/0.5% $^{13}CH_4$. Note the inhomogeneous broadening due to the hyperfine coupling of the dangling bonds with the ^{13}C nuclei.*

Fig. 1(f) shows the ESR of sample D deposited from 99.5% D_2 and 0.5% CH_4. As in Fig. 1(e), the satellites are absent from this film as well, and the central narrow Lorentzian is relatively much more intense than in Figs. 1(a) - 1(d). Finally, Fig. 1(g) shows the ESR of the fully ^{13}C-enriched film (sample E). Its inhomogeneously broadened structureless lineshape ($\Delta H_{pp} \approx 13$ G) is clearly due to the hyperfine coupling of the dangling bonds to the central and neighboring ^{13}C nuclei.

^{13}C NMR relaxation measurements on the fully ^{13}C-enriched sample E and naturally abundant (1.1%) ^{13}C sample F, each deposited under conditions similar to those of sample B, yielded an exponential recovery of the free induction decay in all cases. Their paramagnetic spin densities were 3.6×10^{17} and 4.4×10^{17} gm^{-1} (7.8 and 8.8 ppm), resp. and the ^{13}C T_1's were 8 ± 1 and 67 ±3 s, resp. Spin diffusion [16] to these defects is believed to be the dominant ^{13}C relaxation mechanism in these samples. The ^{13}C spin diffusion constant in diamond can be estimated to be $D \approx 0.15\gamma^2 hd$ [17], where γ is the ^{13}C gyromagnetic ratio and d is the mean ^{13}C - ^{13}C distance. This yields $D_E \approx 4 \times 10^{-13}$ and $D_F \approx 0.85 \times 10^{-13}$ cm^2/s for samples E and F, resp. Hence, during time T_1 the ^{13}C magnetization is transported over a distance of $\sim\sqrt{6DT_1} \sim 0.05$ μm in both samples. However, this value is much smaller than the average crystallite size, which are at least 0.12 and 0.43 μm, as estimated from the measured H conent and assuming that the hydrogen essentially covers the crystallite surfaces. The actual distribution of crystallite sizes is apparently very broad, from a fraction of a micron near the substrate to several microns near the top surface [9,10,14,15]. Therefore, confinement of the dangling bonds to the crystallite surfaces should result in a striking deviation from an exponential relaxation, in contrast to the observed behavior [14]. It is thus concluded that the paramagnetic centers are homogeneously distributed over length scales significantly greater than ~0.04 μm.

The foregoing ESR results clearly show that the satellites are due to carbon dangling bonds hyperfine coupled to adjacent protons. The hyperfine coupling constant of these H-dangling bond complexes is equal to the field splitting between the two satellites, i.e., about 14.5 G (13.5×10^{-4} cm^{-1}). Their intensity indicates a density of about 0.03 - 0.2 ppm (Table I), i.e., they are a minute fraction of the total H content, which was 0.56 and 0.15 at.% in samples E and F, resp., as determined by ^1H NMR [14].

The stability of the satellites upon annealing at $T \leq 1100°C$ for extended periods strongly suggests that the H-dangling bond complexes are not located on any crystallite surface. However, the reduction of the satellites and the main line by a factor of ~4.5 after ~20 min annealing at $T \geq 1200°C$ is consistent with the evolution of most of the hydrogen from these centers. We therefore consider two types of bulk hydrogen-dangling bond centers: A center on an internal surface, and a center trapped in the tetrahedral diamond network.

As mentioned above, SEM images showed that the average crystallite is several microns across at the top surface of the films. Yet if the hydrogen is essentially confined to the crystallite surfaces, then the ^1H NMR spin count indicates that the average crystallite is less than 0.5 μm across [14]. As mentioned above, this discrepancy may be resolved by previous observations which showed that the crystallite size rapidly increases during film growth [9,10,15]. It therefore does not allude to the existence of internal surfaces within the observed crystallites. However, such internal surfaces and/or microvoids are to be expected within the kinetic model described by Anthony [18]. In this model, the hydrogenated surface is constantly etched and repassivated by H atoms, but occasionally a methyl radical [19] attaches to an exposed carbon dangling bond, providing the fundamental diamond network growth step. Such dynamical processes may yield considerable internal defect structures and (micro)surfaces. Fanciulli and Moustakas have indeed recently invoked multivacancies and (111) stacking faults to explain the properties of the ESR of their diamond films [8]. However, hydrogen that resides on the surfaces of such voids which are connected to the crystallite surface will be released within a few

hours at ~850°C. In addition, a dangling bond on a largely hydrogen-decorated surface should generally be adjacent to more than one H atom. We therefore turn to the model of a dangling bond-H center which is embedded in the tetrahedral network.

In the simplest approach, substitution of a C by an H atom should result in an H atom terminating one dangling bond and an interacting system of the 3 other dangling bonds. The ground state of this system should probably be an unpaired sp^3 electron slightly overlapping the reconstructed paired wavefunction of the other two, as carbon bonds pair on diamond surfaces [18,20,21]. However, this model should be verified by a calculation of the defect wavefunction which would yield a ^1H hyperfine splitting in agreement with the observed value. Given the strong C-H bond and the surrounding tetrahedral diamond network, the stability of these centers at $T \leq 1100°C$ is not surprising, but needs to be substantiated by appropriate calculations. At the same time, the reduction in their intensity after 20 min at ~1200°C (Table I) is consistent with evolution of hydrogen from these centers at such high temperatures.

The dynamics of the main lines appear to be similar to those of the satellites (Fig. 1(b) - 1(d) and Table I). The slight but unambiguous weakening of the central lines relative to the satellites after annealing at ~1200°C is consistent with the suggestions of Fanciulli and Moustakas [8]: Although annealing should have little effect on the defects in isolated multivacancies, those at the stacking faults should probably weaken after annealing at ~1200°C.

The absence of the ^1H-coupled dangling bonds from some films prepared by CVD from oxygen-containing precursors [3,6] suggests that these precursors, under appropriate conditions, prevent the formation of such H-dangling bond centers. It also indicates that the H-dangling bond center probably does not include an oxygen atom. It should be noted, however, that density of such centers was also negligible in the films studied by Fanciulli and Moustakas, which were also synthesized from $H_2 + CH_4$ only.

Finally, Figure 1(e) showed that the ^1H-hyperfine coupled dangling bonds are absent from films deposited from 99.5% D_2 and 0.5% CH_4. This suggests that the probability of incorporation of H or D is unrelated to its source. It also then suggests that most of the H or D atoms that are found on the surfaces of the diamond crystallites are due to the H_2 or D_2 gas, rather than to the hydrogen attached to the carbon-containing precursor.

SUMMARY

In summary, the X-band ESR of thin diamond films deposited from 99.5% H_2/0.5% CH_4 invariably exhibits Lorentzian satellites at $\Delta H \approx 7.2 \pm 0.2$ G from the main line at $g \approx 2.0028 \pm 0.0005$, which is the sum of narrow ($\Delta H_{ppn} \approx 2.4 \pm 0.2$ G) and broad ($\Delta H_{ppb} \approx 7.6$ G) Lorentzians. As the ESR of films deposited from 99.5% D_2/0.5% CD_4 or 0.5% CH_4 does not exhibit the satellites, they are assigned to dangling bond-H complexes. The main lines and the satellites are unaffected by annealing at $T \leq 1100°C$, but are reduced after ~20 min at ~1500°C. The complexes are thus discussed in relation to newly identified dangling bond-H centers on internal surfaces, or embedded in the bulk of the diamond crystallites. The latter scenario appears to be more plausible if confirmed by a calculation of the defect wavefunction which would yield a ^1H hyperfine splitting in agreement with the observed value of $\sim 13.5 \times 10^{-4}$ cm^{-1}.

ACKNOWLEDGEMENTS

We thank Drs. K. K. Gleason, S. Mitra, R. Shinar, S. T. Pantelides, W. Trahanovsky, K. M. Ho, and R. Biswas for valuable discussions. Ames Laboratory is operated by Iowa State University for the US Department of Energy under Contract W-7405-Eng-82. This work was supported by the Director for Energy Research, Office of Basic Energy Sciences.

REFERENCES

1. J. T. Glass, R. Messier, and N. Fujimori, editors, *Diamond, Silicon Carbide, and Related Wide Bandgap Semiconductors* (Mat. Res. Soc. Proc. **162**, Pittsburgh, PA, 1990).
2. T. D. Moustakas, J. I. Pankove, and Y. Hamakawa, editors, *Wide Band Gap Semiconductors* (Mat. Res. Soc. Proc. **242**, Pittsburgh, PA, 1992).
3. I. Watanabe and K. Sugata, Jap. J. Appl. Phys. **27**, 1808 (1988).
4. M. Hoinkis, E. R. Weber, M. I. Landstrass, M. A. Plano, S. Han, and D. R. Kania, Appl. Phys. Lett. **59**, 1870 (1991).
5. J. M. Redwing, T. W. Root, and W. F. Banholzer, J. Appl. Phys. (submitted).
6. H. Jia, J. Shinar, S. Mitra, and K. K. Gleason, unpublished results.
7. J. H. N. Loubser and J. A. van Wyk, Rep. Prog. Phys. **41**, 1201 (1978).
8. M. Fanciulli and T. D. Moustakas, Phys. Rev. B **48**, 14982 (1993).
9. K. M. McNamara, D. H. Levy, K. K. Gleason, and C. J. Robinson, Appl. Phys. Lett. **60**, 580 (1992).
10. K. M. McNamara, K. K. Gleason, and C. J. Robinson, J. Vac. Sci. Tech. A **10**, 3143 (1992).
11. D. H. Levy and K. K. Gleason, J. Phys. Chem. **96**, 8125 (1992).
12. S. Mitra and K. K. Gleason, Diamond and Related Materials **2**, 126 (1993).
13. H. Jia, J. Shinar, D. P. Lang, and M. Pruski, Phys. Rev. B **48**, 17595 (1993).
14. M.Pruski, D. P. Lang, S. J. Hwang, H. Jia, and J. Shinar, Phys. Rev. B **49**, xxxx (1994); J. Shinar, M.Pruski, D. P. Lang, S. J. Hwang, and H. Jia, this volume.
15. Ch. Wild, N. Herres, and P. Koidl, J. Appl. Phys. **68**, 973 (1990).
16. A. Abragam, *Principles of Nuclear Magnetism,* Oxford University Press, Oxford, 1961, Chap. 9.
17. M. Goldman, Phys. Rev. **A138**, 1675 (1965).
18. T. R. Anthony, in ref. 1, p. 61.
19. M. R. Pederson, K. A. Jackson, and W. E. Pickett, *ibid.*, p. 91.
20. S. T. Pantelides, private communication.
21. W. Trahanovsky, private communication.

ON THE STRUCTURE OF THIN DIAMOND FILMS: A ^{1}H AND ^{13}C NUCLEAR MAGNETIC RESONANCE STUDY

J. Shinar,*† M. Pruski,*‡ D. P. Lang,*‡ S.-J. Hwang,*‡ and H. Jia*†
*Ames Laboratory - USDOE, Iowa State University, Ames, Iowa 50011
†Department of Physics and Astronomy, Iowa State University, Ames, Iowa 50011
‡Department of Chemistry, Iowa State University, Ames, IA 50011

ABSTRACT

The ^{1}H and ^{13}C nuclear magnetic resonance (NMR) of thin diamond films deposited from naturally abundant (1.1 at.%) as well as 50% and 100% ^{13}C-enriched CH_4 heavily diluted in H_2 is described and discussed. Less than 0.6 at.% of hydrogen is found in the films which contain crystallites up to ~15 μm across. The ^{1}H NMR consists of a broad 50-65 kHz wide Gaussian line attributed to H atoms bonded to carbon and covering the crystallite surfaces. A narrow Lorentzian line was only occasionally observed and found not to be intrinsic to the diamonds. The ^{13}C NMR demonstrates that >99.5% of the C atoms reside in a quaternary diamond-like configuration. The ^{13}C spin-lattice relaxation times T_1 are four orders of magnitude shorter than in natural diamond and believed to be due to ^{13}C spin diffusion to paramagnetic centers, presumably carbon dangling bonds. Analysis of T_1 indicates that within the ^{13}C spin diffusion length of ~0.05 μm, these centers are uniformly distributed in the diamond crystallites, possibly concentrated on the internal surfaces of a relatively dense system of nanovoids.

INTRODUCTION

In spite of the extensive studies of thin diamond films deposited by thermally-assisted CVD of CH_4 heavily diluted in H_2 [1,2], the detailed picture of the chemical structure and electronic properties of the films and their native defects is incomplete [3-6] Similarly, the role of hydrogen, a ubiquitous impurity, and its possible bonding sites, are not completely understood [7]. In this study, nuclear magnetic resonance (NMR) of ^{1}H and ^{13}C, electron spin resonance (ESR), and scanning electron microscopy (SEM) were used to examine natural and ^{13}C enriched CVD films grown on a silicon wafer substrate.

Previous NMR studies of thin diamond films and diamond powders have been reported by Gleason and coworkers [4-6,8] and Henrichs et al. [9]. The NMR had shown that the H content is typically 0.1 - 0.5 at.% [5,8], that the H atoms predominantly "decorate" the crystallite surfaces [8] and that the ^{13}C relaxation rates are much faster than those found in natural diamonds [9] This study confirms some of these earlier conclusions, but it also provides new insight into the nature of the polycrystalline films: (i) the narrow ~5 kHz wide Lorentzian ^{1}H NMR line typically observed on top of the main >50 kHz wide Gaussian line and attributed to rotating methyl groups [6], is found to represent hydrogen that is not intrinsic to the films studied in this work. (ii) Analysis of the ^{13}C relaxation rates in the CVD films, which are indeed much faster than found in natural crystals, indicates that the dangling bonds are homogeneously distributed in the diamond crystallites on a scale larger than ~0.05 μm. They may, however, be clustered on a finer scale, or concentrated on nanovoids such as multivacancies or stacking faults as suggested by Fanciulli and Moustakas [10].

EXPERIMENTAL PROCEDURE

(a) Samples. The films were grown at ~0.5 μm/h by flowing a mixture of ~99.5% H_2 and ~0.5% CH_4 at a pressure of ~50 Torr through a tungsten filament heated to ~2000°C onto a silicon wafer substrate heated to 850°C. Following the deposition, the substrate was dissolved in HF to yield free-standing films. About 15 mg of film A was grown over 13 h using 100% ^{13}C enriched methane at a flow rate of ~200 sccm. Film B was grown for 80 h from natural

Mat. Res. Soc. Symp. Proc. Vol. 339. ©1994 Materials Research Society

^{13}C-abundant CH_4 at the same flow rate to yield ~70 mg. Film C was grown over 21 hours under the same conditions using 50% ^{13}C enriched methane. SEM images showed that the top crystallites of film B were much larger than those of A [11], consistent with the observations [6,8,12] that the crystallite size increases with the distance, i.e. growth time, from the substrate.

(b) NMR. Proton NMR spectra at 100-300 K were acquired using a 250 MHz home-built spectrometer. Room temperature ^{13}C spectra were obtained using a second home built spectrometer operating at 100.06 MHz for ^1H and 25.15 MHz for ^{13}C. The ^{13}C spin-lattice relaxation time T_1 for each diamond film was measured without magic angle spinning (MAS). Additional details of the NMR measurement techniques are given elsewhere [11].

(c) ESR. Electron spin resonance spectra were obtained using a commercial Bruker ESR 200 spectrometer, with a sensitivity of ~10^{11} spins/Gauss. The spin densities of samples A and B, determined by comparing their ESR with known DPPH standards sealed in evacuated quartz tubes, were ~7.8 and ~8.8 ppm, resp. (see Table I).

RESULTS AND DISCUSSION

(a) ^1H NMR lineshape. A typical ^1H NMR spectrum of film B, consisting of a broad $\Delta H_{1/2} = 65 \pm 5$ kHz Gaussian, is shown in Figure 1. Similar Guaussian lines of widths 50 ± 5 and 65 ± 5 kHz were observed in samples A and C, respectively. The total hydrogen content in films A and B calculated to be ~0.56 and ~015 at.%, resp., and the ^1H NMR lineshape parameters, are given in Table I. These H contents are comparable to previously reported values [5,8]. However, as they yield less than $5x10^{18}$ ^1H spins per sample, accurate NMR measurements were challenging. Thus, special precautions were taken to accurately eliminate the background signal [11].

As described and discussed elsewhere [11], the ^1H NMR linewidth and lineshape is clearly attributable to rigid dipolar coupled proton spins in a densely packed environment. If the H atoms were homogeneously distributed within the film, the linewidth $\Delta H_{1/2}$ would be less than 1 kHz for the measured ^1H densities [11]. As the ESR spin densities were ~8 ppm (Table I), the homonuclear proton-proton dipolar coupling was clearly the dominant line broadening mechanism. The Van Vleck equation [11,13] then yields Gaussian lineshapes of $\Delta H_{1/2} \approx 70$, 40, and 30 kHz for H atoms uniformly passivating unreconstructed (100), (110), and (111) diamond surfaces. A superposition of these lines can be easily used to fit the broad portion of the ^1H NMR spectra, which suggests that the model of hydrogen stabilizing the (100), (110) and (111) surfaces by forming a mono-layer of C-H species is reasonable. The change in surface texture between films A and B, visible in the SEM images [11], results from differences in the deposition time and film thickness [6,8,12]. Although assuming a single crystal orientation does not allow us to describe the broad resonance, the contributions from different crystal orientations cannot be quantitatively determined due to the low signal-to-noise and the number of parameters involved. Note, however, that in samples B and C $\Delta H_{1/2} = 65 \pm 5$ kHz, which strongly indicates that the (100) is the dominant surface.

In earlier studies [5,6,8] a narrow ($2 \leq \Delta H_{1/2} \leq 6$ kHz) Lorentzian ^1H line was also observed. This component, due to a small fraction of the hydrogen, suggested another environment with weaker dipolar coupling due either to mobility or isolation from neighboring spins, e.g., rotating CH_3 groups on the crystallite surface [6,8]. Indeed, it had been postulated earlier that

Sample	Film A	Film B
% ^{13}C	100	1.1
at. % ^1H_T	0.56	0.15
$\Delta H_{1/2}$ (kHz)	50	65
N_H (spins/gm)	$2.6x10^{20}$	$7.3x10^{19}$
S (nm^2/gm)	$8.7x10^{18}$	$2.4x10^{18}$
a (μm)	0.2	0.7
N_e (spins/gm)	$3.6x10^{17}$	$4.4x10^{17}$
N_e (ppm)	7.8	8.8
R_{es} (nm)	4.9	2.3
R_{ev} (nm)	9.3	8.6

Table I. *NMR and ESR parameters of the thin diamond films: ^{13}C enrichment (at. %); H content (at. %) ^1H_T; full width at half- maximum of the ^1H NMR spectrum, $\Delta H_{1/2}$; proton spin density, N_H; average surface area per gram, S; estimated average diamond crystallite size, a; electron spin density, N_e; average distance between radicals if confined to the surface, R_{es}; average distance between radicals if they are distributed uniformly within the bulk, R_{ev}.*

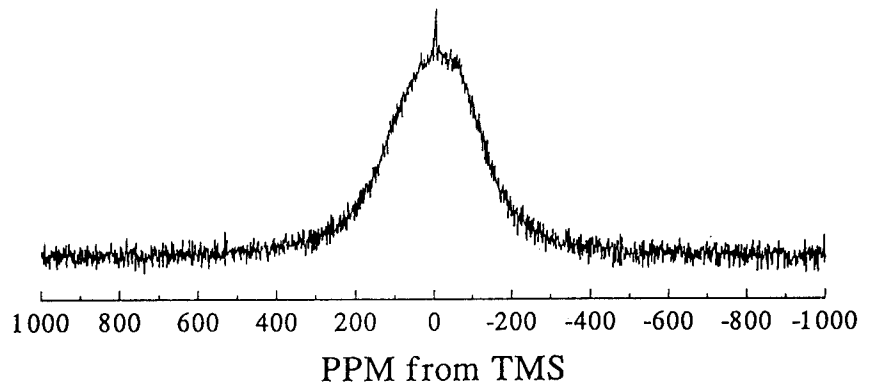

Figure 1. *Solid-state ^1H NMR spectrum of diamond film B. The broad Gaussian component represents densely packed hydrogen bonded to carbon on crystallite surfaces.*

radicals, in particular CH_3 and H, control the gas-phase chemistry of CVD diamond growth [14] and could hence be important as propagating and/or passivating units.

A narrow 2 - 6 kHz resonance was also found in some of the spectra obtained in this work. However, it could not be unambiguously assigned to hydrogen in the films. The residual background signal consisted of a narrow peak superimposed on a broad feature and could not be completely eliminated [11]. Since its intensity remained comparable to that of the samples, a residual narrow feature, representing between 0 and 10% of the total intensity, remained in some spectra after background subtraction, either as a small peak (see Figure 1) or a 'hole'. In addition, measurements on sample B from 100 to 300 K showed that below 200 K the Lorenztian component broadened and could not be distinguished from the Gaussian even with the background signal. This behavior disqualified a hypothesis involving rotating CH_3, as the ^1H NMR linewidth of such a group rotating around its C_3 axis at 300 K should be ~20 kHz, which is half the rigid lattice width [15], and the narrowing occurs at $100 \leq T \leq 150$ K [15,16]. Hence, the ~5 kHz-wide resonance observed in this work would imply a more isotropic motion, which is highly improbable. Also, the presence of CH_3 groups could not be unambiguously detected by FT-IR [11]. Since no evidence of adsorbed water was found in the IR spectrum, its presence was also unlikely. Furthermore, we considered the existence of residual concentration of hydrogen gas trapped inside the crystallites, and exhibiting restricted thermal reorientation. This possibility was also excluded by the temperature dependence of the Lorentzian. Finally, the possibility of methane molecules remaining trapped in the microvoids of crystallites was investigated. To that end we prepared a diamond film using a mixture of H_2 and deuterated methane CD_4, but observed no change in the NMR spectra.

In summary, at least 95% of the ^1H NMR intensity originated from strongly coupled H atoms localized on the crystallite surfaces, and the narrow Lorenztian observed in some spectra could not be attributed to hydrogen intrinsic to the diamond films.

(b) H content. Using ^1H NMR spectroscopy for measuring hydrogen concentration implies that all of the proton spins are detected in the NMR experiment and that the intensity of the FID at t = 0 is correctly determined. The precautions that were exercised are described elsewhere [11], and yielded the H concentrations N_H given in Table I.

Also listed in Table I are other parameters of samples A and B measured or determined as described elsewhere [11]: the calculated average surface area per gram, S; average crystallite size, *a*; the ESR spin densities, N_e; and the average distances between unpaired electrons R_{es} and R_{ev} calculated assuming uniform distribution on the surface or in the bulk, respectively.

The NMR spin count results show that the hydrogen concentration in diamond film A is higher than in film B. Assuming that the hydrogen essentially covers the crystallite surfaces, the previous result is in agreement with the SEM images which show that the top of diamond film A consists of smaller diamond particles. We also observe that for both samples the calculated

crystallite sizes are considerably smaller than those observed on the surfaces of the films, which are several μm across. This is probably due to a distribution of crystallite sizes in the diamond films with generally larger crystallites growing at greater heights from the silicon substrate [6,8,12]. Also, as suggested earlier, the existence of internal surfaces within the crystallites should not be excluded. Thus, the values of a given in Table I should only be considered as the lower limit of the average crystallite size. We will refer to these values below in the discussion of spin diffusion and relaxation.

(c) ^{13}C magic angle spinning (MAS) NMR. ^{13}C MAS direct excitation (Bloch decay) spectra of diamond films A and B are presented in Figures 2a and 2b respectively. A single isotropic peak centered at 36 ± 2 ppm is observed, characteristic of carbon in the tetrahedrally symmetric environment of natural diamond [9,17] and diamond films studied previously [4,5]. For the ^{13}C enriched sample (Fig. 2a) a central peak ($\Delta H_{1/2}$ ~ 600 Hz) is accompanied by spinning sidebands resulting from ^{13}C-^{13}C homonuclear dipolar coupling which is only partly eliminated by MAS at 4.5 kHz (a dipolar powder pattern width of ~10 kHz was measured in a static experiment). At least 99.5% of the carbon in sample A is determined to reside in an sp^3 diamond-like configuration. The static spectrum of diamond film B (not shown) exhibited a linewidth $\Delta H_{1/2}$ ~ 300 Hz which resulted from residual chemical shift anisotropy and magnetic susceptibility. This spectrum was narrowed by MAS to ~75 Hz (Fig. 2b).

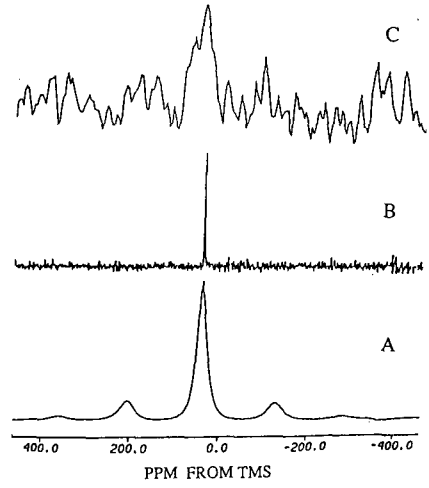

Figure 2. *^{13}C MAS NMR spectra of the diamond films: (A) Bloch decay spectrum of 100% ^{13}C-enriched sample A; (B) Bloch decay spectrum of sample B with natural abundance of ^{13}C; (C) Cross polarization (CP)/MAS spectrum of sample A after 80,000 scans.*

(d) ^{13}C cross polarization (CP)/MAS NMR. In this experiment, the polarization of carbon nuclei is achieved indirectly via the ^1H-^{13}C dipolar interaction, and the obtained spectra represent primarily those ^{13}C spins which are less than three bond distances away from the nearest proton. Fig. 2c shows the spectrum from the ^{13}C- enriched sample A after 80,000 cross polarization scans. The single distinguishable feature is a resonance centered at 36 ± 5 ppm, similar to that of Fig. 2a. This important result confirms that the majority of ^{13}C spins in film A which are polarized by hydrogen reside in sp^3 diamond-like sites. Furthermore, it shows that the reconstruction of the diamond surface, which would result in a graphitic-like structure [7], is prevented by atomic hydrogen surrounding the diamond during the thermally-assisted CVD synthesis.

(e) ^{13}C longitudinal relaxation. ^{13}C relaxation times T_1 were measured with the progressive saturation method, as described elsewhere [11], to yield 8 ± 1, 67 ± 5, and 17 ± 2 s in samples A, B and C, resp. By comparing the ^{13}C NMR intensities measured in this experiment to that of a calibrated standard we determined that within the experimental error (±20%) all of the ^{13}C nuclei in samples A, B, and C were detected in the relaxation studies.

The T_1 values measured in this work are 10^4 times shorter than of natural diamonds [9]. This result and the high ESR spin densities (Table I) strongly suggest that the interaction of ^{13}C spins with paramagnetic centers is the primary relaxation mechanism in thin diamond films. A detailed analysis of this relaxation mechanism [11] clearly shows that the distribution of these centers is uniform on a scale larger than the spin diffusion length which is $\sim\sqrt{6DT_1} \sim 0.05$ μm, where D is the spin-diffusion constant. An alternative model with the paramagnetic centers concentrated primarily on the crystallite faces is incompatible with the results for several reasons. If the paramagnetic centers were confined to the crystallite surfaces only, then (a) assuming the crystallite size from Table I, there is insufficient time for the spin diffusion to transport carbon magnetization toward the surface of a crystallite; (b) a non-exponential decay of magnetization

would be expected, in contrast to the observed recovery (see Figure 3) and (c) a discrepancy between the observed values of R_{es} of samples A and B would be difficult to explain [11].

(f) Consequences of the spin distribution. As claimed above, the conclusion that the distribution of paramagnetic centers is homogeneous is very significant. If they are embedded in the tetrahedral network, a determination of their structure is required, and is not obvious. While a dangling bond may easily be envisioned in the distorted tetrahedral network of amorphous C (a-C) or Si (a-Si), that is not the case in the ordered network found in the thin diamond films. For example, a carbon vacancy would probably result in a spinless pairing of the four sp^3 electron orbitals directed towards the vacancy. If the dangling bonds are not isolated centers embedded in the tetrahedral network, then one may speculate that they are located on the internal surfaces of nanovoids which are embedded in the crystallites. Such nanovoids may possibly be as small as a di- or tri-vacancy, as indeed hypothesized by Fanciulli and Moustakas [10], and perhaps viewed as such a complex of dangling bonds partially passivated by H atoms or methyl groups. This picture then implies that the system of these nanovoids is sufficiently dense so that the distribution of the dangling bonds appears homogeneous on the length scale of ~0.05 μm. If neither of these scenarios can be established, the possibility that these paramagnetic centers are not carbon dangling bonds would clearly have to be considered.

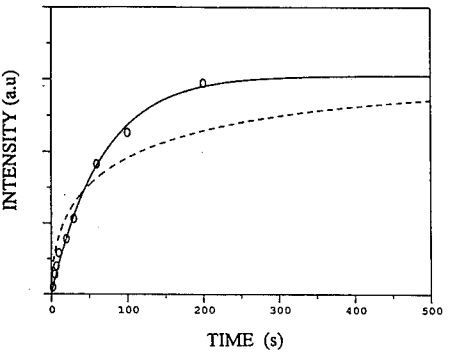

Figure 3. *^{13}C signal intensity versus time in the progressive saturation experiment [11]. The solid and dashed curves represent least-square fits to $M(t) = M_0\{1-exp[-(t/T_1)^n]\}$ with n=1 and n = 0.5, resp.*

The postulated nanovoids are plausible for another reason as well: The average crystallite size calculated from the ^1H NMR spin count assuming coverage of surfaces by hydrogen is ~0.2 and ~0.7 μm for samples A and B, resp. Yet the top crystallites in sample B are up to 15 μm across. That would imply that the crystallites growing at the early and intermediate stages of the deposition process would be unreasonably small. A potential resolution of this problem might be such a system of internal nanovoids and microvoids in which the carbon dangling bonds are nearly, but not totally, terminated by H atoms. The H atoms which are sufficiently far from the remaining dangling bonds would then contribute to the observed ^1H NMR.

SUMMARY AND CONCLUDING REMARKS

Using ^1H NMR, hydrogen concentrations below 0.6 at.% were determined for the diamond films. The observed hydrogen resonances had linewidths in the 50 - 65 kHz range and are consistent with hydrogen-covered crystallite surfaces. The presence of significant concentrations of methyl groups, adsorbed water, trapped methane molecules and isolated hydrogen atoms in the diamond films studied in this work was excluded.

^{13}C NMR measurements indicated that over 99.5% of all carbon resided in a quaternary diamond-like environment, and only carbon in a similar configuration was detected in CP/MAS.

The decay of the ^{13}C magnetization yielded an exponential function with a T_1 of 8 , 17, and 65 s for films with ^{13}C concentrations of 100%, 50%, and 1.1%, resp. These rates, which are 10^4 times faster than those in natural diamond, implied that the dominant relaxation mechanism is spin diffusion to paramagnetic centers, whose density was ~$4x10^{17}$ gm^{-1} (~8 ppm). Analysis of the measured rates indicated that the paramagnetic centers are uniformly distributed within the

resolution of the ^{13}C spin diffusion length of ~0.05 μm. This result is very significant if the paramagnetic centers are carbon dangling bonds, because it is difficult to envision such defects in an otherwise ordered regular tetrahedral network. It therefore raises the specter of dangling bonds located at the internal surfaces of nanovoids, possibly as small as multivacancy complexes. As the distribution is homogeneous to within ~0.05 μm, their content would be sufficient to strongly impact the electronic and mechanical properties of these films.

The scenario of nanovoids and microvoids may also contribute to the large discrepancy between the average crystallite size calculated from the ^{1}H NMR and the observed crystallite sizes which are several microns across. While this discrepancy is partially accountable by a high content of small crystallites at the bottom and intermediate layers of the films, the required average size of 0.2 and 0.7 μm would entail a large fraction of unreasonably small crystallites. The possibility that a significant fraction of the hydrogen is residing in internal nanovoids and microvoids should therefore be seriously considered. This scenario is, however, clearly speculative and additional results are required for its confirmation or refutation.

ACKNOWLEDGEMENTS

The authors are indebted to Dr. B.C. Gerstein of the Iowa State University Chemistry Department for invaluable advice and to M.J. Robertson for his assistance with the FT-IR measurement. One of the authors (S. H.) wishes to acknowledge the financial support from the Phillips Petroleum Company. Ames Laboratory is operated by Iowa State University for the US Department of Energy under Contract W-7405-Eng-82. This work was supported by the Director for Energy Research, Office of Basic Energy Sciences.

REFERENCES

1. J. T. Glass, R. Messier, and N. Fujimori, editors, *Diamond, Silicon Carbide, and Related Wide Bandgap Semiconductors* (Mat. Res. Soc. Proc. **162**, Pittsburgh, PA, 1990).
2. T. D. Moustakas, J. I. Pankove, and Y. Hamakawa, editors, *Wide Bandgap Semiconductors* (Mat. Res. Soc. Proc. **242**, Pittsburgh, PA, (1992).
3. H. Jia, J. Shinar, D. P. Lang, and M. Pruski, Phys. Rev. B **48**, 17595 (1993).
4. K. M. McNamara and K. K. Gleason, J. Appl. Phys. **71**, 2884 (1992), and references therein.
5. K. M. McNamara, K. K. Gleason, D. J. Vestyck, and J. E. Butler, Diamond and Related Materials **1**, 1145 (1992).
6. K. M. McNamara, D. H. Levy, K. K. Gleason, and C. J. Robinson, Appl. Phys. Lett. **60**, 580 (1992).
7. T. R. Anthony, in ref. 2, p. 61.
8. K. M. McNamara, K. K. Gleason, and C. J. Robinson, J. Vac. Sci. Technol. A **10**, 3143 (1992).
9. P. M. Henrichs, M. L. Cofield, R. H. Young, and J. M. Hewitt, J. Magn. Reson. **58**, 85 (1984).
10. M. Fanciulli and T. D. Moustakas, Phys. Rev. B **48**, 14982 (1993).
11. M. Pruski, D. P. Lang, S.-J. Hwang, H. Jia, and J. Shinar, Phys. Rev. B **49**, xxxx (1994), and references therein.
12. Ch. Wild, N. Herres, and P. Koidl, J. Appl. Phys. **68**, 973 (1990).
13. A. Abragam, *Principles of Nuclear Magnetism,* Oxford University Press (Oxford, 1961), ch. IV.
14. S. J. Harris and A. M. Weiner, J. Appl. Phys. **67**, 6520 (1990).
15. N. Bloembergen, E. M. Purcell, and R. V. Pound, Phys. Rev. **73**, 679 (1948).
16. H. S. Gutowsky and G. E. Pake, J. Chem. Phys. **18**, 162 (1950).
17. M. J. Duijvestijn, C. van der Lugt, J. Smidt, R. A. Wind, K. W. Zilm, and D. C. Staplin, Chem. Phys. Lett. **102**, 25 (1983).

ENERGIES AND ATOMIC STRUCTURES OF GRAIN BOUNDARIES IN DIAMOND: COMPARISON WITH GRAIN BOUNDARIES IN SILICON

M. KOHYAMA*, H. ICHINOSE**, Y. ISHIDA** AND M. NAKANOSE***
* Department of Material Physics, Osaka National Research Institute, AIST, 1-8-31, Midorigaoka, Ikeda, Osaka 563, Japan.
** Department of Materials Science, University of Tokyo, 7-3-1, Hongo, Bunkyo-ku, Tokyo 103, Japan.
*** Nissan Motor Company Ltd., Aerospace Div., 3-5-1, Monomi, Suginami-ku, Tokyo 168, Japan.

ABSTRACT

Fairly different features of grain boundaries in diamond from those in Si were experimentally observed in diamond thin films. As the first step in order to understand the fundamental properties of grain boundaries in diamond, the energy and atomic structure of the {122} Σ=9 tilt boundary have been calculated for the first time by using the tight-binding electronic theory. The results have been compared with the calculations of the same boundary and the {111} Σ=3 boundary in Si. It has been shown that the Σ=9 boundary in diamond has a very large interfacial energy caused by the large bond rigidity as compared with the boundaries in Si and the {111} Σ=3 boundary in diamond. This point should be related to the observation that the {122} Σ=9 boundary is rarely found in diamond thin films.

INTRODUCTION

Diamond thin films have received considerable interest for various applications such as high-temperature devices or coating films, because diamond has remarkable chemical and physical properties such as high thermal conductivity, extreme hardness, high Young's modulus, wide band gap, high saturated electron velocity, and so on. Usually, diamond thin films are obtained as polycrystalline films by the CVD techniques. Thus, it is of much importance to understand the fundamental properties of grain boundaries in diamond. However, there exist only few studies [1] about grain boundaries in diamond at the atomic and electronic level.

On the other hand, polycrystalline Si or Ge is used for solar cells or thin film transistors (TFT's), and a lot of studies have been performed about grain boundaries in Si or Ge [2]. In particular, significant advances have been made in the understanding of the atomic and electronic structures of CSL (coincidence site lattice) tilt boundaries in Si or Ge [2-11]. Many high-resolution transmission electron microscopy (HRTEM) observations have indicated that such tilt boundaries are constructed by arranging the structural units consisting of atomic rings such as five-membered or seven-membered rings without any coordination defects [2-5]. And many theoretical studies using band calculations have shown that such interfaces can exist stably and contain no electronic states inside the minimum band gap [6-11].

Recently, Ichinose, Nakanose, Itoh and Ishida [12] have performed the HRTEM observation of grain boundaries in diamond thin films. They have found the predominance of the <011> tilt boundaries in the diamond films as well as those in usual Si films, which may be related to a predominance <011> texture. However, they have found fairly different features of grain boundaries in diamond from those in Si. Firstly, the {122} Σ=9 boundaries are rarely found in diamond, although there exist a lot of {111} Σ=3

Mat. Res. Soc. Symp. Proc. Vol. 339. ©1994 Materials Research Society

boundaries in diamond. This is consistent with the previous observation in diamond films [1], where the {122} Σ=9 boundaries often split into two {111} Σ=3 boundaries. This is in remarkable contrast to the observations in Si, where both the {122} Σ=9 and {111} Σ=3 boundaries are typical CSL tilt boundaries frequently found. Secondly, they have obtained the images of several CSL tilt boundaries in diamond indicating fairly different atomic configurations from those in Si observed previously. Thirdly, there exist a lot of boundaries with disordered configurations in the diamond films.

These points might be dependent on the growth conditions of the films or the presence of other species such as hydrogen. However, it is possible that the observed features of grain boundaries in the diamond films are dominated by the nature of diamond or carbon itself such as its large bond rigidity in four-coordinated structure or its ability to form chemical bonds with a variety of coordination numbers from two to four, which is quite different from the nature of Si or Ge. Thus, we think that grain boundaries in diamond possibly have fairly different features from those in Si or Ge.

In this paper, as the first step in order to understand the fundamental properties of grain boundaries in diamond, we deal the {122} Σ=9 boundary. We perform theoretical calculations of the energy and atomic and electronic structure of the {122} Σ=9 boundary in diamond by using the transferable tight-binding (TB) method for carbon. The results are compared with those of the same boundary and the {111} Σ=3 boundary in Si calculated by the transferable TB method for Si. And we discuss the reason why the {122} Σ=9 boundary is rarely found in diamond as compared with the {111} Σ=3 boundary.

METHOD OF CALCULATIONS

The transferable TB method

For grain boundaries in Si and in diamond, we use the transferable TB method for Si developed by Sawada [13], and the transferable TB method for carbon developed by Xu, Wang, Chan and Ho [14]. Nowadays, new techniques in ab initio calculations have begun to be applied to complex systems such as grain boundaries. Nevertheless, tractable numbers of atoms are at present still limited to be small in such calculations of first-row elements such as carbon. The semi-empirical TB method [6,8-10] can easily deal with hundreds of atoms of Si or carbon. And by the development of new transferable methods, the accuracy in the TB approach has been much advanced.

In these transferable TB methods, the total energy is given as a sum of the band structure energy E_{bs} and the remaining repulsive energy E_{rep} as well as in the usual TB method [6,8-10]. E_{bs} is obtained by the TB band calculation with the valence atomic orbital basis, and E_{rep} is obtained by short-range inter-atomic repulsive potentials. However, the transferable methods can deal with variously coordinated structures of Si and of carbon more correctly than the usual TB method. This can be attained by modifying the behavior of the two-center integrals in the Hamiltonian and that of the repulsive inter-atomic potentials for large distances, and by introducing proper devices in calculating E_{rep}. In the method for Si, the inter-atomic repulsive potential has the dependence on the local environment through the effective coordination numbers. In the method for carbon, E_{rep} is not a simple sum of the repulsive potentials, but a sum of terms of respective atoms that are obtained for each atom as a function of a sum of the repulsive potentials between that atom and its neighboring atoms.

We have examined the ability of the respective methods. As shown in [15], the method for Si can well reproduce the energies and equilibrium volumes of

variously coordinated phases of Si as compared with the ab initio results [16], by using the parameters readjusted in [15]. About the method for carbon, we have examined that the energies and equilibrium volumes of variously coordinated phases can be well reproduced as compared with the ab initio results [17], by using the parameters and functional forms given in [14]. These methods can reproduce the elastic properties of the diamond structures. The calculated bulk moduli of Si and of diamond are 0.92Mbar and 4.70Mbar, respectively, which are reasonable as compared with the experimental values, 0.99Mbar and 4.42Mbar.

We have examined the applicability of the methods to the graphitic structure. For graphite, the calculated equilibrium bond length is 0.1417nm and the energy decrease against diamond is 0.016eV/atom, which are reasonable as compared with the experimental values, 0.1421nm and 0.025eV/atom. For graphitic Si, the calculated bond length is 0.2197nm and the energy increase against the diamond structure is 0.63eV/atom, which are reasonable as compared with the ab initio results, 0.2249nm and 0.71eV/atom [18].

About the weak points of the present methods, the energy of hexagonal diamond is not properly reproduced by the method for carbon. We have found that hexagonal diamond is more stable than cubic diamond by 0.007eV/atom by the present method for carbon, although the ab initio calculation indicates that cubic diamond is more stable by 0.03eV/atom [17]. On the other hand, the present method for Si can reproduce reasonably the energy of hexagonal diamond Si, which is higher than that of cubic diamond Si by 0.013eV/atom [15]. And the ab initio result of the difference between the two structures of Si is 0.016eV/atom [16].

By this problem, it is not proper to perform calculations of the {111} Σ=3 boundary in diamond by the present method for carbon, because the interface of this boundary consists of atomic rings common to hexagonal diamond as shown in the following section. Thus, in this paper, only the {122} Σ=9 boundary in diamond is dealt with by the present method for carbon, and the energy of the Σ=3 boundary in diamond is only estimated, although both the Σ=3 and Σ=9 boundaries in Si are dealt with by the present method for Si.

Atomic models and the supercell technique

The {122} Σ=9 and {111} Σ=3 boundaries are typical CSL tilt boundaries in the diamond structure. The former and the latter are constructed by rotating two crystals around the <011> axis by 38.9° and by 70.5°, respectively. The boundary planes {122} and {111} are parallel to the rotation axis.

We deal with the atomic models for Si from the previous observations and theoretical studies [2-8,10], and deal with the same models for diamond. The Σ=9 boundary consists of zigzag arrangement of five-membered and seven-membered rings without any coordination defects, and contains glide plane symmetry. The Σ=3 boundary consists of boat-shaped six-membered rings without any coordination defects, and contains mirror symmetry.

Calculations of boundaries are performed by using the supercell technique. Periodicity normal to the interface is imposed by stacking symmetric boundary planes alternately in addition of the two-dimensional periodicity of CSL boundary. Thus the conventional technique of band calculations can be used. The supercell of the Σ=9 boundary contains 144 atoms, where the interfaces are repeated between 72 atomic layers. The distance between the interfaces is about 3.26nm in Si and about 2.13nm in diamond. The supercell of the Σ=3 boundary contains 48 atoms, where the interface are repeated between 24 atomic layers. The distance between the interfaces is about 3.76nm in Si.

In the present calculations, electrostatic interactions are included self-consistently through the form of a Hubbard-like Hamiltonian, although this

effect is negligibly small in the present cases where all the atoms are four-coordinated. The parameter U is 2eV for Si [11] and 4eV for carbon [14]. In lattice relaxations, atomic forces are calculated via the Hellmann-Feynman theorem after the self-consistent iterations, which are terminated if the differences between input and output atomic occupancies are all kept within 10^{-4} electrons.

The rigid-body translations between the two grains have been determined by iterating the relaxations of the smaller supercells for saving computing time. These are the 80-atom cell for the Σ=9 boundary and the 24-atom cell for the Σ=3 boundary. In both the boundaries, only the translations normal to the interface are permitted by the symmetry. The optimized translation for the Σ=9 boundary in Si is a dilatation of 0.006nm, and that for the Σ=3 boundary in Si is a dilatation of 0.001nm. The optimized translation for the Σ=9 boundary in diamond is a dilatation of 0.008nm.

RESULTS AND DISCUSSION

The boundaries in Si

Fig. 1 shows the relaxed configuration of the {122} Σ=9 boundary in Si. The interfacial energy E_{gb} is 0.32J/m^2. The bond-length and bond-angle distortions range from -1.6% to +1.5% and from -16.2° to +20.8°, respectively. E_{gb} and the ranges of bond distortions are similar to the previous results of the same boundary [6,7,10]. Bond-angle distortions of which the absolute values are larger than 10° are all associated with the five-membered and seven-membered rings at the interface. The distortions of -16.2° and of +20.8° exist at the five-membered rings and at the seven-membered rings, respectively. Bond-length distortions of which the absolute values are larger than 1% are also associated with the atomic rings and the back bonds at the interface.

Recently, Kohyama and Yamamoto [11] have performed the comparison between the tilt and twist boundaries in Si by using the same theoretical method. It can be said that the energy and bond distortions of the Σ=9 boundary are relatively small as compared with twist boundaries or general boundaries.

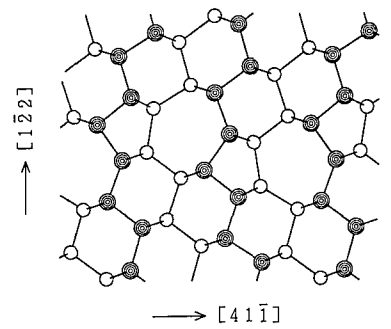

Fig. 1. Relaxed configuration of the {122} Σ=9 boundary in Si. Atoms are projected along the <011> axis. Open and closed circles indicate the atoms with the two different atomic heights along the <011> axis.

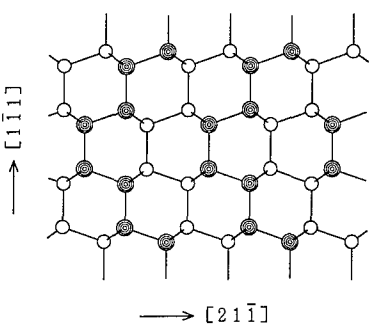

Fig. 2. Relaxed configuration of the {111} Σ=3 boundary in Si. Atoms are projected along the <011> axis. Open and closed circles indicate the atoms with the two different atomic heights along the <011> axis.

Fig. 2 shows the relaxed configuration of the {111} Σ=3 boundary in Si. E_{gb} is 0.062J/m^2, which is similar to the value by the usual TB method [8]. The maximum absolute values of the bond-length and bond-angle distortions are 0.13% and 0.04°, respectively. This interface is especially stable with negligible bond distortions. The six-membered rings at the interface are common to those in the hexagonal diamond structure. Thus, the interfacial energy can be explained by the energy difference between cubic diamond Si and hexagonal diamond Si, which is 0.013eV/atom by the present method, although the energy of the Σ=9 boundary is mainly caused by the bond distortions. The energy increase by the insertion of two atomic layers of hexagonal diamond Si is estimated to be 0.026eV per interfacial bond. This value is close to the calculated energy value per bond of the Σ=3 boundary, which is 0.025eV.

The present results of the relatively small energies and bond distortions of the Σ=9 and Σ=3 boundaries in Si are consistent with the existence of both the boundaries in polycrystalline Si. And it should be noted that the energy and bond distortions of the Σ=9 boundary are similar to those of other CSL tilt boundaries in Si [8,9], because of similar configurations consisting of atomic rings. This should cause the observed predominance of the CSL tilt boundaries in polycrystalline Si as discussed in [11].

The boundaries in diamond

Fig.3 shows the relaxed configuration of the {122} Σ=9 boundary in diamond. E_{gb} is 1.68J/m^2. The bond-length and bond-angle distortions range from -3.7% to +2.7% and from -15.0° to +19.0°, respectively. Bond-angle distortions of which the absolute values are larger than 10° are all associated with the five-membered and seven-membered rings at the interface. The distortions of -15.0° and of +19.0° exist at the five-membered rings and at the seven-membered rings, respectively. Large bond-length distortions are also associated with the atomic rings and the back bonds at the interface. The ranges of bond distortions are similar to those in Si, although the range of bond-length distortions is somewhat larger and that of bond-angle distortions is somewhat smaller than those in Si.

E_{gb} of the Σ=9 boundary in diamond is very large. It is about 5.2 times larger than that in Si. This is caused by the large bond rigidity of diamond. The energy increase per one period of the interface in diamond is 1.99eV, although that in Si is 0.89eV. It can be said that the similar bond distortions in diamond generate the energy increase about 2.2 times larger than that in Si. The present interfacial energy can be explained by this point coupled with the inverse-squared ratio of the lattice constant, 2.3.

About the {111} Σ=3 boundary in diamond, it is possible to estimate E_{gb} by using the energy difference between cubic diamond and hexagonal diamond as the above analysis in Si, although the present TB method for carbon cannot deal with this problem. From the relation between the ab initio values of the differences in Si and in diamond, 0.016eV/atom [16] and 0.03eV/atom [17], coupled with the relation between the lattice constants, E_{gb} is estimated to be about 4.4 times larger than that in Si. This is about 0.27J/m^2.

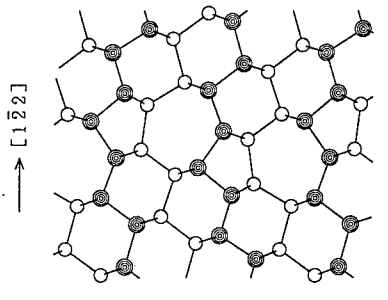

Fig. 3. Relaxed configuration of the {122} Σ=9 boundary in diamond.

Discussion

About the reason why the {122} Σ=9 boundaries are rarely found in diamond, it is probable that the present large interfacial energy itself is mainly responsible. In diamond films, it is possible that the generation of the Σ=9 boundary is suppressed by its large interfacial energy, or that the dissociation of the Σ=9 boundary is promoted by its large interfacial energy.

Of course, the relation between the energies of the Σ=9 and Σ=3 boundaries is of much importance. It is also possible that Herring's criterion [19] for the triple point of one Σ=9 boundary and two Σ=3 boundaries forces the Σ=9 boundary to split into the Σ=3 boundaries as discussed in [1], although this criterion is valid only for equilibrium systems where boundary energies are not dependent on the orientation. By this criterion, the ideal ratio of the energy of the Σ=9 boundary to that of the Σ=3 boundary is 1.15. The ratio from the calculated values in Si is 5.2, and that from the calculated and estimated values in diamond is 6.2. Thus, from this point of view, the Σ=9 boundary in diamond also seems to be more unstable than that in Si.

Finally, the present energy value for diamond is about one half of the value obtained by the empirical inter-atomic potential, 3.6J/m^2 [1]. We think that our results are more reliable because our calculations include directly the effects of the electronic structure of boundaries.

REFERENCES

1. J. Narayan and A.S. Nandedkar, Phil. Mag. B63, 1181 (1991).
2. J. Thibault, J.L. Rouviere and A. Bourret, in Materials Science and Technology, edited by R.W. Cahn, P. Haasen and E.J. Kramer (VCH, Weinheim, 1991), Vol.4, p.321.
3. A. Bourret and J.J. Bacmann, Surf. Sci. 162, 495 (1985).
4. Y. Ishida and H. Ichinose, in Polycrystalline Semiconductors, edited by H.J. Moller, H.P. Strunk and J.H. Werner (Springer, Berlin, 1989), p.42.
5. M. Elkajbaji and J. Thibault-Desseaux, Phil. Mag. A58, 325 (1988).
6. R.E. Thomson and D.J. Chadi, Phys. Rev. B29, 889 (1984).
7. D.P. DiVincenzo, O.L. Alerhand, M. Schluter and J.W. Wilkins, Phys. Rev. Lett. 56, 1925 (1986).
8. A.T. Paxton and A.P. Sutton. Acta Metall. 37, 1693 (1989).
9. M. Kohyama, R. Yamamoto, Y. Watanabe, Y. Ebata and M. Kinoshita, J. Phys. C21, L695 (1988).
10. M. Kohyama, S. Kose, M, Kinoshita and R. Yamamoto, J. Phys. Condens. Matter 2, 7809 (1990).
11. M. Kohyama and R. Yamamoto, in Amorphous Silicon Technology-1993, edited by E.A. Schiff, M.J. Thompson, A. Madan, K. Tanaka and P.G. LeComber (Mat. Res. Soc. Symp. Proc. 267, Pittsburgh, PA, 1993), p177; to be published in Phys. Rev. B (1994).
12. H. Ichinose, M. Nakanose, K. Itoh and Y. Ishida, to be published in the proceedings of the 3rd IUMRS International Conference on Advanced Materials, Tokyo, Japan, 1993.
13. S. Sawada, Vacuum 41, 612 (1990).
14. C.H. Xu, C.Z. Wang, C.T. Chan and K.M. Ho, J. Phys. Condens. Matter 4, 6047 (1992).
15. M. Kohyama, J. Phys. Condens. Matter 3, 2193 (1991).
16. M.T. Yin and M.L. Cohen, Phys. Rev. B26, 5668 (1982).
17. S. Fahy and S.G. Louie, Phys. Rev. B36, 3373 (1987).
18. M.T. Yin and M.L. Cohen, Phys. Rev. B29, 6996 (1984).
19. J.P. Hirth and J. Lothe, Theory of Dislocations, 2nd ed. (Wiley, New York, 1982), p.698.

NATIVE DEFECTS AND IMPURITIES IN CUBIC AND WURTZITE GaN

JÖRG NEUGEBAUER AND CHRIS G. VAN DE WALLE
Xerox PARC, 3333 Coyote Hill Road, Palo Alto, CA 94304

ABSTRACT

Using state-of-the-art total energy calculations we investigate defect formation energies and electronic structure for native defects in wurtzite and cubic GaN. The defect formation energies and electronic structures are very similar in both structures. The main difference is a split in the p-like defect states in wurtzite GaN, which are degenerate in cubic GaN. The role of the Ga $3d$ electrons on the chemical bonding in GaN is discussed in detail. We explain why the deep lying Ga $3d$ electrons have a remarkably strong influence on defect formation energies and atomic relaxation for some of the defects.

INTRODUCTION

Very recently GaN has attracted widespread attention for producing blue light-emitting diodes and as a promising candidate for blue lasers and high-temperature or high-power devices. These applications are related to distinct properties of GaN: a large direct band gap and very strong interatomic bonds. A major problem in the technological application is that of doping. As-grown GaN is usually n-type, and p-type conductivity has been difficult to obtain.[1,2] The origin of the n-type conductivity is commonly associated with the nitrogen vacancy. An understanding, however, of the role of native defects and impurities in compensation and doping is still in its infancy.

GaN can be grown both in the wurtzite and cubic structure; different defect properties may be expected in the two phases. Following this idea it has been speculated that cubic GaN can be more easily doped than wurtzite GaN.[3,4]

The aim of the present contribution is to determine the dominant native defects in GaN. In particular we study the differences in defect formation energies (defect concentrations) and electronic structure for both phases of GaN. One methodical aspect which will be addressed is the role of the Ga $3d$ electrons on the chemical bonding in GaN.

METHODICAL ASPECTS

For calculating the defect energies and the electronic structure we performed first density-functional theory (DFT) energy calculations using a supercell approach with 32 atoms per cell, a plane wave basis set with an energy cutoff of 60 Ry, and soft Troullier-Martins pseudopotentials.[5] Details of the method and convergency checks are described elswhere.[6,7]

The effect of the Ga $3d$ electrons on the bonding in GaN is only poorly understood. In most of the previous theoretical studies the $3d$ electrons were treated as core electrons, i.e., they were not allowed to relax. This was justified by the fact that the band of the Ga $3d$ electrons lies about 14 eV below the top of the valence band. A more pragmatic reason is that the numerical task is strongly reduced by taking the d electrons as core states. A

Mat. Res. Soc. Symp. Proc. Vol. 339. ©1994 Materials Research Society

systematic study of the role of the $3d$ electrons in GaN was performed by Fiorentini *et al.*,[8] however, this study was restricted to bulk properties of cubic GaN. They concluded that, although the main effect of the Ga $3d$ electrons can be described by the non-linear exchange-correlation correction (nlcc),[9] the relaxation of the $3d$ electrons also plays an important role; a neglect of this effect results in a lattice constant which is too small by about 3 %. In agreement with Ref. [8] we find an improvement of the lattice constant from −3.1 % (nlcc) to −0.7 % (explicit treatment of the Ga $3d$ electrons) compared to the experimental lattice constant.

The formation energy of a charged defect is defined as:

$$E^f(q) = E^{\rm tot}(q) - n_{\rm Ga}\mu_{\rm Ga} - n_{\rm N}\mu_{\rm N} - qE_F \quad . \tag{1}$$

Here q is the charge state of the defect, E_F the Fermi energy and $\mu_{\rm Ga}$ ($\mu_{\rm N}$) are the chemical potentials for Ga (N). $n_{\rm Ga}$ and $n_{\rm N}$ are the number of Ga and N atoms. The chemical potentials for Ga ($\mu_{\rm Ga}$) and N ($\mu_{\rm N}$) are not independent, since both species are in equilibrium with GaN: $\mu_{\rm Ga} + \mu_{\rm N} = \mu_{\rm GaN}$. Since we are interested here only in a comparison between the cubic and wurtzite phase, we choose as a reference for the chemical potentials the total energy of a free atom. In the remainder of this discussion we focus on the Ga vacancy, where we observed a particularly strong effect. Table 1 summerizes formation energies and relaxation geometry for the Ga vacancy in a neutral charge state. Results are shown from calculations with and without explicit treatment of the $3d$ electrons; in both cases, the calculations are carried out at the appropriate theoretical lattice constant. The calculations "without" $3d$ electrons used the non-linear core correction.[9]

Table 1: *Defect formation energy E^f, energy gain due to atomic relaxation $E^{\rm rel}$ and distance of the nearest neighbors from the center of the vacancy. r_1 is the distance to the three nearest neighbors arranged in one plane perpendicular to the c axis. r_2 is the distance to the nearest neighbor along the c axis. Calculations were performed for a 16 atom supercell in the wurtzite structure. "rel." indicates whether atomic relaxation was included ((y)es or (n)o) and "3d" whether the 3d electrons are treated explicitly.*

rel.	3d	E^f (eV)	$E^{\rm rel}$ (eV)	r_1 (Å)	r_2 (Å)
n	n	10.37	–	1.89	1.89
y	n	9.49	0.88	2.12	2.17
n	y	11.81	–	1.94	1.94
y	y	11.55	0.26	2.05	2.05

The results listed in Table 1 clearly indicate that the $3d$ electrons are important both for the formation energy and the atomic relaxation. They increase the formation energy and decrease the atomic relaxation. The increase in formation energy can be explained in terms of additional bonds between the Ga $3d$ orbitals and the N orbitals: the breaking of bonds to create a vacancy costs more energy. Taking the Ga $3d$ electrons as core electrons

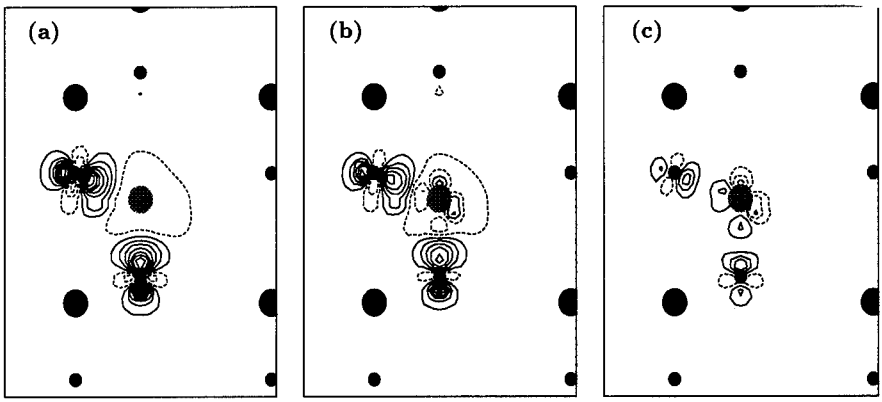

Figure 1: *Contour plot of the charge redistribution* ($\rho = \rho^{\text{bulk}} - \rho^{\text{Ga-vac}} - \rho^{\text{Ga-atom}}$) *around a Ga vacancy.* ρ^{bulk}, $\rho^{\text{Ga-vac}}$ *and* $\rho^{\text{Ga-atom}}$ *are the charge density for GaN bulk, the Ga vacancy and a Ga atom, respectively. (a) shows the charge redistribution if the Ga* 3*d electrons are treated as core electrons, (b) if they are allowed to relax. (c) is the difference of (a) and (b). The large dots mark the positions of the Ga atoms, the small dots those of the N atoms. The large gray dot in the center is the position of the Ga vacancy. Dashed lines mark negative contour lines, solid lines positive contour lines. The contour spacing is* $0.01\,bohr^{-3}$.

results in a large relaxation. The outward displacement of the nearest neighbor nitrogen atoms is more than 0.2 Å and the energy gain is nearly 0.9 eV. Introducing the 3*d* electrons makes the system stiffer: the outward displacement of the surrounding nitrogen atoms is reduced to 0.1 Å and the energy gain to 0.26 eV. The *d* electrons prevent the Ga-N bond length becoming too short.

The question remains why a level 14 eV below the top of the valence band has such a strong influence on bonding properties. In order to identify the mechanism we consider the charge redistribution around a gallium vacancy as shown in Fig. 1. The most striking feature is the strong localization of the charge redistribution around the vacancy; it is restricted to nearest neighbors around the vacancy. The charge depletion around the vacancy can be understood considering that Ga in bulk GaN is positively charged. Thus, by creating a vacancy a back charge transfer from the nitrogen orbitals into the Ga atom occurs. The charge redistribution for the frozen core approximation (Fig. 1(a)) and with an explicit treatment (Fig. 1(b)) are qualitatively similar. The main difference is the relaxation of the Ga 3*d* electrons (visible as the perturbations around the Ga vacancy in Fig. 1(b)) indicating a bond between the Ga 3*d* electrons and the nitrogen orbitals. Also a weaker hybridization of the nitrogen orbitals is observed by explicitly treating the Ga 3*d* electrons. These features become even more visible in the difference plot (Fig. 1(c)). The relaxation of the 3*d* electrons has only a second order effect on the total energy. However, the change in the hybridization of the surrounding nitrogen has important effects both on formation energy and on atomic relaxation. Thus, the influence of the 3*d* electrons is not simply realized by a relaxation of this orbital but by changing the hybridization of the neighboring atoms. By this indirect mechanism the deep lying 3*d* states can modify states

near the Fermi level. We note that this effect is only important for *some* of the defects; for instance the defect properties of the nitrogen vacancy are virtually independent of the Ga $3d$ electrons.

COMPARISON OF DEFECTS IN CUBIC AND WURTZITE GaN

In Ref. [6] we discuss formation energy and electronic structure for all the native defects in GaN. Here we will investigate in which way the structure of GaN (cubic or wurtzite) modifies defect properties such as formation energy, atomic relaxation and electronic structure. This question is interesting for device engineering as well as from a more fundamental point of view. Since the first deviation of the wurtzite and cubic structure lies in the 3rd nearest neighbor shell a distinction between short and long range order effects is possible.

For the following discussion we will focus on vacancies, since (as shown in Ref. [6]) these are the dominant defects in GaN. For the comparison we treat the Ga $3d$ electrons as core states, considering that the differences between both phases are long range. Table 2 lists the results for the nitrogen and gallium vacancies.

Table 2: *Defect formation energy E^f, energy gain due to atomic relaxation E^{rel} and distance of the nearest neighbors from the center of the vacancy after relaxation for cubic (c) and wurtzite (w) GaN. The calculations were performed in a 32 atom cell with a $2 \times 2 \times 2$ Monkhorst-Pack[10] mesh. r_1 and r_2 are the nearest neighbor distances to the neighboring atoms from the center of the vacancy after atomic relaxation (see Table 1).*

vac.	structure	E^f (eV)	E^{rel} (eV)	r_1 (Å)	r_2 (Å)
Ga	(w)	9.86	0.70	2.05	2.06
Ga	(c)	10.12	0.78	2.07	2.07
N	(w)	12.61	0.03	1.88	1.87
N	(c)	12.65	0.03	1.88	1.88

For the nitrogen vacancy we find only minor differences for the defect formation energy and for the atomic relaxation. The remaining deviations are within the expected error of our calculations. For the Ga vacancy the deviations are larger but on an absolute scale still small. The origin of the larger deviations for the Ga vacancy is related to the stronger perturbation in charge density and effective potential of the Ga vacancy compared to the N vacancy. Since our calculations are based on a supercell approach, defect-defect interactions occur which are stronger if the defect-induced perturbation is less localized. Due to the lower symmetry of the wurtzite structure a split in the relaxations occurs, which is however very small (< 0.01 Å).

Figure 2 plots the calculated defect levels for the neutral vacancies. In both structures the Ga vacancy is a triple acceptor; the nitrogen vacancy is a single donor. The donor level of the nitrogen vacancy lies in the conduction band. The main difference is a small split in

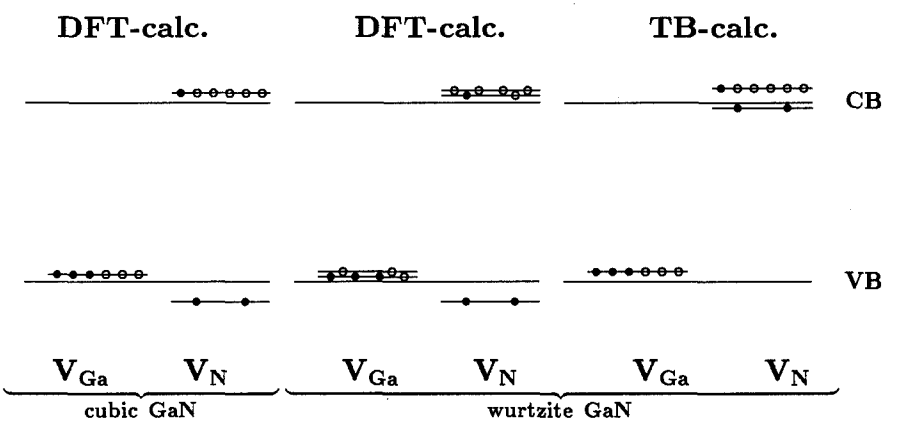

Figure 2: *Electronic structure of the neutral gallium and nitrogen vacancies in cubic and wurtzite GaN. For comparison the results of a tight-binding calculation by Jenkins and Dow*[11] *are shown.*

the p-like vacancy states for the wurtzite structure. An analysis of the corresponding wave functions revealed that the doubly degenerate state originates from a linear combination of the dangling bonds located on the three equivalent neighbors around the vacancy. The single state belongs to the remaining atom. Thus, the split is related to the lower symmetry of the wurtzite compared to the cubic structure.

A comparison of our results for the electronic defect structure with recent tight-binding calculations by Jenkins and Dow[11] shows good agreement for the Ga vacancy. For the nitrogen vacancy, however, a qualitative difference exists: Whereas our calculations predict the nitrogen vacancy to be a *single* donor, according to the tight-binding calculations it is a *triple* donor. The main difference is that our calculations show a large split (more than 4 eV) between the s and p-like vacancy states. Due to this split the doubly occupied s-like state lies in the valence band. The split between the defect levels is usually explained in terms of an interaction of the dangling bonds located at the 4 neighboring atoms of the vacancy. Since these atoms are second nearest neighbors a small interaction and thus a small split might be expected. The large split, however, indicates a large interaction between the Ga atoms.

This strong interaction can be understood in terms of the large mismatch between the covalent radii of Ga ($r^{Ga} = 1.26$ Å) and N ($r^N = 0.75$ Å); we note that the radius of Ga is nearly twice that of N. Due to the large mismatch the Ga-Ga distance in GaN is reduced, compared to GaAs by some 20 %. In order to examine the Ga-Ga interaction in GaN in more detail we removed all the nitrogen atoms, obtaining hexagonal closed-packed Ga bulk. Surprisingly, we find that the calculated Ga-Ga distance for this structure is only 1 % smaller than in GaN, indicating again an unusually strong interaction of the Ga cations in GaN. Consequently, the Ga-Ga interaction is comparable to the Ga-N interaction, which explains the large split in the defect levels, but also the failing of the tight-binding calculations[11] where only the nearest-neighbor Ga-N interaction was taken into account.

The unusually strong Ga-Ga interaction also has important consequences for defect formation energies as discussed in Ref. [6].

CONCLUSIONS

We have calculated formation energies, atomic relaxations and electronic structure for defects in GaN using first principles total energy calculations. We have identified a mechanism by which the deep lying Ga $3d$ electrons modify formation energy and atomic relaxation for some of the defects. This effect has to be taken into account in future calculations.

A comparison of defect properties for wurtzite and cubic GaN showed only minor deviations. Thus, we expect that *if* point defects are a source of doping problems, they will exist in both structures. We note, however, that the quality of the GaN epilayers can depend strongly on the structure (number of dislocations, stacking faults, etc.). In this way differences between both structures may occur, despite the fact that the microscopic point defect structure is the same.

ACKNOWLEDGMENTS

This work was supported in part by the DAAD (German Academic Exchange Service) and by the AFOSR.

REFERENCES

1. H. Amano, M. Kito, K. Hiramutsu, I. Akasaki, Jpn. J. Appl. Phys. **28**, 2112 (1989).
2. R. Madar, G. Jacob, J. Hallais, and R. Fruchart, J. Cryst. Growth **31**, 197 (1975).
3. J. I. Pankove, MRS Symp. Proc. **162**, 515 (1990).
4. T. Lei, M. Fanciulli, R. J. Molnar, T. D. Moustakas, R. J. Graham, and J. Scanlon, Appl. Phys. Lett. **59**, 944 (1991)
5. N. Troullier and J. L. Martins, Phys. Rev. B **43**, 1993 (1991).
6. J. Neugebauer and C. G. Van de Walle, to be published.
7. R. Stumpf and M. Scheffler, Computer Phys. Commun. to be published.
8. V. Fiorentini, M. Methfessel, and M. Scheffler, Phys. Rev. B **48**, 13353 (1993).
9. S. G. Louie, S. Froyen and M.L. Cohen, Phys. Rev. B **26**, 1739 (1982).
10. H. J. Monkhorst and J. D. Pack, Phys. Rev. B **13**, 5188 (1976).
11. D. W. Jenkins and J. D. Dow, Phys. Rev. B **39**, 3317 (1989).

NATIVE DEFECTS IN WURTZITE GaN AND AlN

P.BOGUSLAWSKI,* E. BRIGGS, T. A. WHITE, M. G. WENSELL, AND J. BERNHOLC
North Carolina State University, Raleigh, NC 27695-8202

Abstract

The results of an extensive theoretical study of native defects in GaN and of vacancies in AlN are presented. We have considered cation and anion vacancies, antisites, and interstitials. The computations were carried out using quantum molecular dynamics, in supercells containing 72 atoms. Due to the wide gap of nitrides, the formation energies of defects depend strongly on the position of the Fermi level. The N vacancy in GaN introduces a shallow donor level that may be responsible for the n-type character of as-grown GaN. Other defects introduce deep states in the gap, with strongly localized wave functions.

1. Introduction

Wide gap nitrides hold substantial promise for electronic applications. Since the electronic quality of a semiconductor is largely determined by the nature and number of its native defects and impurities, it is important to understand their properties. In wide gap semiconductors, impurity-induced shifts in the Fermi level position will have a major effect on the abundance of native defects, and thus on self-compensation and diffusion. Therefore, they will also affect growth and processing.

In GaN, $n-$ and recently also $p-$type doping has been achieved [1, 2]. The quality of the material could still be improved, and the role of native defects needs to be understood, in particular for light-emitting applications, where a presence of recombination centers could lead to severe degradation. AlN has so far resisted any doping attempts, either n- or p-type. This may be due to its very wide band gap (6.3 eV), or be caused by a presence of a large number native defects.

We have embarked on a comprehensive study of native defects and impurities in GaN and AlN, focusing on identifying the dominant native defects, stoichiometry effects, and a search for effective dopants. In the following, we describe our first results regarding the electronic structure and formation energetics of point defects. We have also considered substitutional impurities and contaminants. These results will be presented elsewhere.

2. Calculations and Theoretical Aspects

The calculations were carried out using *ab initio* molecular dynamics (MD) [3] and the local density approximation (LDA). A soft non-local pseudopotential for N was generated according to the procedure of Lee and Rabii [4], while for Ga a standard non-local potential was used [5]. The kinetic energy cutoff for the plane wave basis set was 30 Ry. The accuracy of the pseudopotentials was tested by computing the lattice constants, the cohesive energies, and the bulk moduli of zinc-blende GaN and AlN. The results were in good agreement with previous calculations and experimental data [6]. Calculations for defects were carried out in a large supercell that would contain 72 atoms in the case of the perfect crystal. Due to the size of the cell, only the Γ point was used for Brillouin zone summations. To speed up the search for minimum energy configurations, the atoms were relaxed according to an efficient scheme that uses Newtonian dynamics with a special friction force for the atoms [7], while the electrons follow the motion of the atoms according to the Car-Parrinello equations [3].

Considering the limitations of the above approach, the use of supercells allows for the application of the powerful *ab initio* MD formalism, but results in broadening of the defect-

*Permanent address: Institute of Physics, Polish Academy of Sciences, 02-668 Warsaw, Poland.

Mat. Res. Soc. Symp. Proc. Vol. 339. ©1994 Materials Research Society

and impurity-induced energy levels. This leads to an uncertainty in level positions of up to 0.5 eV in the supercell we are using. (The total energy and thus the calculated formation energies converge much more rapidly with supercell size.) The remaining source of error is due to the use of local density theory, which seriously underestimates band gaps and overestimates the cohesive energy. Even when the positions of the levels are measured from the nearest band edge, the band gap problem introduces an *additional* uncertainty of the order of 0.5 eV for deep levels. The overbinding problem is less severe, affecting the formation energies by less than 10%.

For the purposes of the present paper, we define the formation energy E_{form} of a neutral defect, *e.g.*, a nitrogen vacancy, as

$$E_{form} = E[GaN : V_N] + E_{at}(N) + \mu(N) - E[GaN], \quad (1)$$

where E is the total energy of the supercell, E_{at}(N) is the total energy of the isolated N atom, and μ is taken as the experimental cohesive energy of the solid [8] except for N, where we use the binding energy of N_2.

For charged defects, the formation energy depends on the position of the Fermi level E_F as

$$E_{form}(\Delta n) = E^0_{form} - E_F \Delta n, \quad (2)$$

where E^0_{form} is the formation energy for the neutral defect, and Δn is its charge.

One should stress that the definition of the formation energy (1) is not unique, since it depends on the chemical potential(s) of the atom(s). These, in turn, depend on the conditions at which the defects form during growth, processing, or annealing. If the growing solid can be assumed to be in local equilibrium with other solid phases, one can constrain the variation of the chemical potential in (1) to a range determined by the difference in the cohesive energy of the compound and that of its elements [9, 10, 7]. In some cases, the assumption of a good quality material (*i.e.*, with a low concentration of defects), restricts the values of the chemical potential to a narrow range [7, 11].

Provided that the growth proceeds under quasi-equilibrium conditions, the concentration of a defect is given by

$$Conc = N_{sites} exp(S_{form}/k_B - E_{form}/k_B T) \quad (3)$$

where N_{sites} is the number of available sites and S_{form} is the formation entropy. Usually, the formation entropy is in the range of 4-10 k_B and the formation energy dominates.

It should be pointed out that the local equilibrium with competing solid phases may not be maintained. This is especially true if the growth process involves local excitations with ion sources and/or energetic beams, or specific kinetic conditions, *e.g.*, those corresponding to atomic layer epitaxy. In CVD, the use of complex precursors may also preclude the attainment of local equilibrium with the solid phases. In annealing experiments, the chemical potentials are determined by the nature and pressure of the gases in the annealing ampoule, rather than by equilibrium with the solid phases [11]. We postpone the investigation of these effects to a future publication and use equation (1) as a benchmark for an approximate comparison of the energetics of formation of various types of defects.

Turning to crystal symmetry issues, it is convenient to analyze the results obtained for the wurtzite structure in terms of zinc-blende symmetry with a superimposed hexagonal perturbation. In the zinc-blende structure, a substitutional defect, *e.g.*, a vacancy, has four equivalent nearest neighbors, which may be subject to both fully symmetric (breathing mode) and asymmetric relaxations. In the wurtzite structure, the atom along the c axis relative to the defect (called here type-1 neighbor) becomes inequivalent to the three remaining neighbors (called here type-2 neighbors). The lowering of the point symmetry is also reflected in the electronic structure: the defect states that are three-fold degenerate in the zinc-blende structure split into singlets and doublets in the wurtzite structure. In the following, we refer to such singlet and doublet pairs as quasi-triplets.

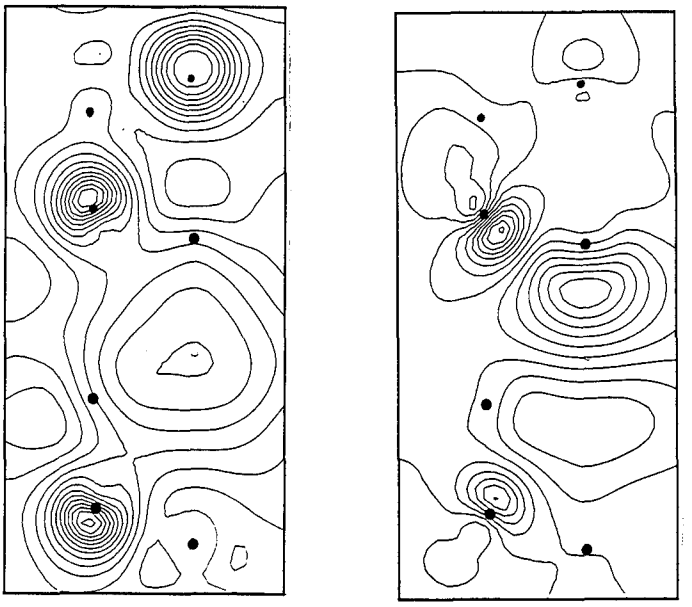

Figure 1: Contour plots of the wave functions of V_N a) the shallow donor state; and b) the conduction band resonance.

3. Native Defects in GaN

3.1. Nitrogen vacancy

The nitrogen vacancy has long been thought to be the dominant native defect in GaN, responsible for the n-type character of as-grown crystals. Our results show that the neutral N vacancy is indeed a shallow donor, with a level just below the conduction band edge. The effective-mass character of this state follows not only from the position of its energy level, but also from its wave function, which is mainly built up from wave functions at bottom of the conduction band of the perfect GaN, see Fig. 1a. This is what one expects for a shallow donor state from the effective mass theory.

The dangling-bond-like quasi-triplet state expected for the vacancy is a resonance in the conduction bands. The hexagonal symmetry results in a 0.5 eV splitting, with the singlet being lower than the doublet. The singlet is located 0.8 eV above the bottom of the conduction band. In the dangling bond model of the vacancy, the quasi-triplet level, which would have held six electrons in the perfect GaN, should contain one electron once the vacancy was created by removing the five-valent N atom. However, since the quasi-triplet is a resonance, the electron autoionizes to the bottom of the conduction bands, where it forms an effective mass state bound by the Coulomb tail of the vacancy potential.

The lattice relaxation around V_N is not very pronounced. The Ga nearest neighbor shell relaxes outwards, by 0.407 and 0.125 a.u. for type-1 and type-2 neighbors, respectively. For the neutral vacancy, the energy gain is 0.38 eV and the computed formation energy becomes 4.8 eV. It will be strongly reduced in p-type material by electron transfer from its donor level to the Fermi level. In n-type GaN, the high formation energy of V_N would indicate that it cannot be formed in sufficient concentration to account for the n-type character of the as-grown material. However, the assumption of phase equilibrium during growth may not be valid for GaN, since MBE growth involves supplying highly excited N_2 to the surface

(N_2 in its ground state is unreactive) which could result in N-deficient material. In CVD, thermal equilibrium should be easier to achieve, but thermal decomposition of TGM and ammonia may involve complicated intermediates, making simple formation energy estimates less reliable. Attainment of local equilibrium between the various solid phases also requires that the diffusion rate in the surface layers be faster than the deposition rate. At this time little is known about the mechanisms of growth of GaN, and thus the reliability of formation energy arguments cannot be assessed.

Recent high-pressure measurements in as-grown n-type GaN show that when high pressure is applied, the electrons that were initially in the conduction bands become localized [12]. This result indicates the presence of a resonant state in the conduction bands that emerges into the forbidden gap as the bottom of the conduction bands moves up with pressure. The electrons in the conduction bands would then become trapped in the just emerged deep level, rendering the sample insulating. We have performed calculations for V_N under pressure, and found that the quasi-triplet indeed emerges into the gap in agreement with the experimental data. The wave function of the lower (singlet) level is shown in Fig. 1b. Additional results regarding the pressure calculations will be published elsewhere.

Obviously, further data are needed for a final identification, but the good agreement between the theoretical and experimental results suggests that N vacancies are present in the samples of Ref. [12].

3.2. Gallium Vacancy

Since the formation of the Ga vacancy creates N dangling bonds, its levels should be close to the top of the valence bands. Indeed, the quasi-triplet is located about 0.4 eV above the valence bands edge, and the hexagonal splitting is only 0.1 eV. Since the quasi-triplet is populated by 3 electrons in the neutral charge state, V_{Ga} can trap both electrons and holes. In spite of the proximity to the valence band, the quasi-triplet wave functions are very localized. The wave function of the singlet is composed mainly of the p_z(N) orbital of the type-1 neighbor. The contributions of the type-2 neighbors are smaller by an order of magnitude. The wave functions of the doublet are built up from the p(N) orbitals of the type-2 neighbors. In this case, the contribution of the type-1 neighbor is negligible.

The formation energy of the neutral V_{Ga} is very high, 8 eV. However, since V_{Ga} can release or accept three electrons, its formation energy depends very strongly on the position of the Fermi level. In particular, in n-type samples the formation energy of V_{Ga}^{-3} may become very low. The thermodynamic levels for 0/-, -/2-, and 2-/3- transitions are at 0.5, 0.8, and 1.3 eV above the top of the valence band, respectively.

3.3. Nitrogen antisite, N_{Ga}

In the neutral charge state, N_{Ga} introduces a doubly occupied singlet at E_v+0.4 eV, and an empty doublet at E_c-0.2 eV. For both levels, the contribution of the type-1 neighbor is about 5 times smaller than those of type-2 neighbors. However, the singlet and the doublet do not originate from one quasi-triplet. In the initial unrelaxed configuration, there is a resonant quasi-triplet located at 0.3 eV above the bottom of the conduction band, with a vanishing hexagonal splitting. After relaxation, the splitting becomes 2.3 eV and the doublet moves to E_c-0.2 eV.

The dominant contribution of the type-1 neighbor is due to a strong distortion of N_{Ga} along the c axis. Specifically, the bond distance to the type-1 neighbor is reduced by 29% (from 3.70 to 2.62 a.u.) and becomes comparable with the bond length in the N_2 molecule, 2.07 a.u. Due to the distortion, the remaining bond lengths increase by 11%. The relaxation energy is 0.6 eV.

The formation energy of the neutral N_{Ga} is 7.3 eV. This value can be slightly reduced in strongly p-type samples, due to electron transfer to the Fermi level. The empty doublet at E_c–0.2 eV cannot be occupied even by one electron, due to the large value of the electron-electron repulsion parameter for this level (0.95 eV).

3.4. Gallium antisite, Ga_N

The gallium antisite introduces a quasi-triplet close to the middle of the band gap. In the neutral charge state, the singlet at E_v+1.4 eV and the doublet at E_v+2.1 eV contain two electrons each. The wave function of the singlet is mainly a bonding combination of the p_z orbitals of Ga_N with the orbitals of the type-1 neighbor. Similarly, the doublet is mainly a bonding combination of $p_{x,y}$ of Ga_N with p orbitals of the type-2 neighbors. However, the p orbitals from the second neighbor N atoms contribute considerably to both the singlet and the triplet.

As expected, we find an outward relaxation around Ga_N, with a large relaxation energy of 3.9 eV. The bond lengths with type-1 and type-2 neighbors are 4.12 and 4.27 a.u., respectively. The formation energy of Ga_N in the neutral state is 6.0 eV, but it is reduced strongly in highly doped samples due to electron transfer to/from the Fermi level.

3.5. Interstitials

For substitutional defects, the local topologies of zinc-blende and wurtzite lattices are similar, since in both cases each atom has four first neighbors with tetrahedral symmetry. The difference between the two structures begins at the second shell of neighbors. This is why the electronic structures of vacancies and interstitials in both structures are similar. In contrast, the local topologies of interstitials are quite different in the two lattices. In zinc-blende crystals there are two interstitial sites with tetrahedral symmetry, surrounded by four cations and four anions, respectively. In the wurtzite structure, there are two high-symmetry interstitial positions, referred to as 'tetrahedral' (T) and 'octahedral' (O) in the literature [13]. These terms are misleading, since they do not correspond to the actual point group symmetry, which is C_{3v} in both cases. In the ideal wurtzite lattice, an atom at the O site has six first neighbors, three cations and three anions. An atom at the T site has two first neighbors, one cation and one anion, and six second neighbors (three anions and three cations). Due to the point symmetry, neither T nor O can be the equilibrium position of an interstitial defect, except by accident. In particular, a relaxation along the c axis is expected.

Indeed, we find that both T and O positions are highly unstable for native interstitials. The interstitials move towards the first neighbor of the same kind. For the N interstitial, starting from both T and O positions leads to the same final configuration. At present, we are investigating whether an analogous effect also holds for the Ga interstitial.

After relaxation, N_I assumes a bridge-bond configuration similar to the bridge-bond geometry of As interstitial in GaAs, as discussed by Chadi [14] . The N-N bond length is 2.64 a.u., which is very close to the N-N distance in the case of N_{Ga}. Both N atoms move off the c-axis, and the resulting configuration is asymmetric. The relaxation energy is 7.6 eV, due to interstitial motion of over 2 a.u. Considering the electronic structure, N_I introduces two closely spaced deep levels at about E_v+1.0 eV, separated by 0.06 eV. Both are built up from the orbitals of the N-N pair and are occupied by three electrons. The formation energy of N_I^0 is 2.9 eV, but it will be strongly reduced in highly doped samples.

The Ga_I, initially at the T position, undergoes a displacement of 1.2 a.u., which leads to an energy gain of 8.9 eV. As mentioned above, the equilibrium configuration is similar to the bridge-bond geometry of interstitial Ga found by Chadi, but in GaN both Ga atoms are exactly along the c axis. The Ga-Ga distance is 4.17 a.u., which is close to the average Ga-Ga distance for Ga_N.

Turning to the electronic structure, Ga_I^0 introduces a deep level at E_v+0.5 eV, occupied by two electrons, and a resonance at E_c+0.8 eV. The remaining Ga electron autoionizes from the resonance and is trapped in a shallow, effective mass state. The deep Ga_I state is composed of displaced host Ga orbitals and the three N neighbors. The formation energy of a neutral Ga(T) is 5.1 eV, but it will be strongly reduced in p-type samples.

4. Vacancies in AlN

We have extended the computations to the second important nitride, AlN, and considered both vacancies. Their electronic structures and formation energies are very close to the corresponding values in GaN. Specifically, V^0_{Al} introduces a quasi-triplet at E_v+0.4 eV, split by 0.05 eV. It is occupied by 3 electrons. Its formation energy is 8.05 eV, which is smaller by 0.05 eV from that of V^0_{Ga}. V_N introduces a quasi-triplet at E_c+0.2 eV. The hexagonal splitting is 0.6 eV and the singlet is below the bottom of the conduction band. The formation energy of V^0_N is 5.4 eV, compared to 5.0 eV in GaN.

5. Summary

We have calculated the electronic structure and formation energies of native defects in wurtzite GaN by *ab initio* molecular dynamics. In most cases, the relaxation around the defect is substantial, strongly influencing the energy levels and formation energies. This is particularly true for interstitials. We have investigated two possible high-symmetry interstitial sites, the so-called T and O. In these high-symmetry positions both Ga and N interstitials are highly unstable. After a displacement of 1-2 a.u., both atoms form split interstitial configurations that are lower in energy by 5-9 eV. Due to the large value of the forbidden gap, formation energies depend strongly on the position of the Fermi level. The low-formation energy defects are V_{Ga}, Ga_N, and N_I in n-type samples, and V_N, Ga_N, Ga_I, and N_I in p-type samples. Our results confirm the widely held hypothesis that V_N is a shallow donor, which may be responsible for the n-type character of as-grown GaN. We have also considered common dopants and contaminants in GaN and AlN. The results of these investigations will be presented elsewhere.

This work is supported by ONR and NSF.

6. References

1. R. F. Davis, Physica B **185**, 1 (1993).
2. S. Strite and H. Morkoc, J. Vac. Sci. Technol. B **10**, 1237 (1992).
3. R. Car and M. Parrinello, Phys. Rev. Lett. **55**, 2471 (1985).
4. G. Li and S. Rabii, preprint.
5. G. B. Bachelet, D. R. Hamann, and M. Schluter, Phys. Rev. B **26**, 4199 (1982); X. Gonze, R. Stumpf, and M Scheffler, Phys. Rev. B **44**, 8503 (1991).
6. R. W. L. Lambrecht and B. Segall, Mat. Res. Soc. Symp. Proc. **242**, 367 (1992); V. Fiorentini, M. Methfessel, and M. Scheffler, Phys. Rev. **47**, 13353 (1993); K. Miwa and A. Fukumoto, Phys. Rev. B **48**, 7897 (1993).
7. C. Wang, Q.-M. Zhang, and J. Bernholc, Phys. Rev. Lett. **69**, 3789 (1992).
8. C. Kittel, Introduction to Solid State Physics, Wiley and Sons, New York (1986).
9. S. B. Zhang and J. E. Northrup, Phys. Rev. Lett. **67**, 2339 (1991).
10. D. B. Laks, C. G. Van De Walle, G. F. Neumark, and S. T. Pantelides, Phys. Rev. Lett. **66**, 648 (1991).
11. B. Chen, Q.-M. Zhang, and J. Bernholc, Phys. Rev. B **49**, 2985 (1994).
12. P. Perlin, H. Teysseire, and T. Suski, to be published.
13. R. Boyn, Phys. Stat. Solidi (b) **148**, 11 (1988). M. A. Robertson and S. K. Estreicher, Mat. Res. Soc. Symp. Proc. **242**, 355 (1992), denote these sites by T and R, respectively.
14. J. D. Chadi, Phys. Rev. B **46**, 9400 (1992).

FAST RECOMBINATION OF EXCESS CARRIER IN 6H-SiC

R.TOMASHIUNAS*, E.VANAGAS*, M.PETRAUSKAS*, A.ZHINDULIS*, M.WILLANDER**, Q.WAHAB**, H.BERGNER***
*Vilnius University, Semiconductor Physics Department, Sauletekio 10, 2054 Vilnius, Lithuania
**Linköping University, Department of Physics, S-581 83 Linköping, Sweden
***Friedrich-Schiller-Universität Jena, 07743 Jena, Germany

ABSTRACT

Fast carrier recombination phenomena in 6H-SiC has been investigated. Evaluation of carrier recombination in nitrogen doped n-type 6H-SiC grown by the Lely method have been carried out using picosecond photoconductivity, time-resolved photoluminescence and dynamic gratings (DG) techniques. From photoluminescence measurements the hole capture by neutral (nitrogen) donors is discussed. The hole capture times and capture cross sections 820 ps, 2.32 ns and $1.5 \cdot 10^{-15} cm^2$, $1.2 \cdot 10^{-15} cm^2$, respectively, by each of the inequivalent donor were evaluated. From the photoconductivity measurements the electron lifetimes ~ 1.5 μs at 300 K and $(3.5 \div 6.5) \mu$s at 125 K were obtained. The ambipolar diffusion coefficient 1.4 $cm^2 \cdot s^{-1}$ obtained from dynamic gratings measurements is in good coincidence with the calculated values.

INTRODUCTION

Non-equilibrium charge carrier (NCC) recombination and their diffusion are the main processes applying the n-type 6H-SiC in opto- and microelectronic devices. Very recent works concerning the evaluation of minority carrier lifetimes and their diffusion in 6H-SiC pn structures [1, 2, 3] have been done. Most of the methods used were electrical and for the ultrafast process investigation they have significant shortcomings (limited high frequency bandwidth, contact influence). Our goal was using the picosecond laser technique to investigate NCC fast transitions ($1 <$ ns) in nitrogen doped 6H-SiC.

EXPERIMENT

Single-crystals of n-type 6H-SiC were grown by the Lely method at $T > 3000^0$C by subliming 6H-SiC powders. The sample surface was (0001) orientated. Nitrogen as a donor was present during the growth. The doping concentration is 10^{17} cm^{-3}.

The experimental arrangements of picosecond dynamic gratings measurements (DG) is described in [4]. A passive mode-locked phosphate glass Nd^{3+} laser ($\tau_L = 12$ ps, $h\nu = 1.17$ eV and 2.3 eV, first and second harmonics) was used. After amplification and frequency doubling the 0.53 μm radiation was split into two pump beams of the same intensity (I_{ex}). The pump beams crossing in the sample at an angle Θ made a DG in the direction parallel to the sample surface with a period $\Lambda = \lambda_{ex}(2 \cdot \sin\Theta/2)$, where λ_{ex} is the wavelength of the pump beams. The subsequent temporal decay of this transparent grating was studied by directing probe pulses of the non-exciting 1.06 μm radiation to the same spot, with various settings of this beam's delay line, and measuring the intensity of the probe pulse first-order diffraction.

Mat. Res. Soc. Symp. Proc. Vol. 339. ©1994 Materials Research Society

Photoluminescence measurements were carried out at 300 K by using an argon ion laser (τ_L=100 ps, repetition rate 123 MHz, $h\nu$=4.82 eV). The radiant averaged power was 3 mW. The laser beam was focused into a ~100 μm spot. The photoluminescence was detected using a fast photomultiplier coupled to spectrometer with spectral resolution of 3 nm. The data were collected by a measuring set SPC 100 with time resolution of 150 ps.

For photoconductivity measurements Ni microstrip structure matched to 50 Ω line with a narrow gap for optical excitation was evaporated and annealed 5 min. at 1100°C. This is a technology of making ohmic contacts on n-type 6H-SiC [5,6]. In order to measure the photoconductivity in a range of 125K<T<300K the sample was placed in a cryostat. Photoconductivity kinetics were measured with an oscilloscope.

Assuming that the instantaneous decay times τ_M of the NCC density are longer than the optical pulse duration, the light induced NCC density was calculated: $\Delta N=\beta(1-R)(1-e^{-\alpha d})E(h\nu \cdot d_{eff})^{-1}$, where β is the quantum efficiency, R is the reflectivity, α is the absorption coefficient, E is the excitation pulse energy per unit area, d is the sample thickness, d_{eff} is the effective depth of NCC generation.

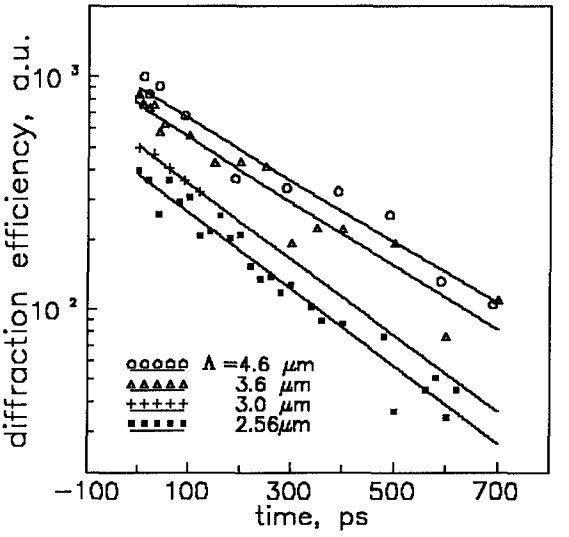

Figure 1. Dependence of diffraction efficiency η on delay time Δt for different grating periods Λ.

RESULTS

In order to select an appropriate intensity for DG experiments, the lux-diffraction characteristic (LDC) was measured. The diffraction efficiency is defined as $\eta=I_{1pr}/I_{pr}$, where I_{pr} is the probe beam intensity, I_{1pr} is the probe beam first order diffraction intensity. For small modulation phase gratings and in the case of one photon absorption ($\Phi \ll 1$, where $\Phi=2\pi\cdot\Delta n\cdot d\cdot\lambda_{pr}^{-1}$, where Δn is the light induced change of the refractive index, d is the grating depth, λ_{pr} is the wavelength of the probe beam) the diffraction efficiency $\eta(t)\approx(\Phi(t)/2)^2\sim\Delta n^2(t)\sim(I_{ex})^2$ (for two photon absorption $\sim(I_{ex}^2)^2$) [7-9]. For $0.5<I_{ex}<2$ GW/cm^2, a slope $f\approx 4$ of the LDC was obtained. This corresponds to a two-photon or two-step interband absorption. The direct band gap manifested in 6H-SiC at 4.6 eV [10-12] provided the two-photon absorption ($2h\nu$= 2·2.34 eV= 4.68 eV). From the slope of $\eta=f(\Delta t)$, where Δt denotes the delay of the probe beam, it is possible to determine the erasure time τ_e of the DG. The DG erasure is described by the diffusion equation, whose solution gives information on ΔN and the DG decay time τ_e: $\tau_e^{-1}=\tau_R^{-1}+\tau_D^{-1}$ [13], where τ_R is the ΔN decay time; $\tau_D=(2\pi/\Lambda)^2 D_a^{-1}$

is the diffusive decay time, D_a is the ambipolar diffusion coefficient. Experimental results of the diffraction efficiency versus probe delay time for different DG periods are shown in Fig.1. By solving the diffusion equation a best fit for each grating period (Λ) using one erasure time τ_e= 656; 628; 530; 488 ps for Λ= 4.6; 3.6; 3.0; 2.56 μm, respectively, is achieved. Using the expressions above for τ_e and D_a, we determined the ΔN decay time 820 ps and the ambipolar diffusion coefficient $D_a \approx 1.4$ cm^2s^{-1} at $\Delta N \approx 3 \cdot 10^{17}$ cm^{-3}.

Photoluminescence measurements were carried out on the same samples at 300 K Fig.2(insert). It appears similar to the luminescence spectra of unintentionally doped 6H-SiC samples with the luminescence maximum near the band edge [14]. The peak at 417 nm is caused by the nitrogen impurities. Weaker luminescence peaks resolved at 425-430 nm can be characterized by other donor assisted transitions. The luminescence intensity decay measured at 417 nm after the excitation of ΔN up to $2 \cdot 10^{16}$ cm^{-3} is shown in Fig.2. The experimental points are well approximated by a sum of two exponential decays 820 ps and 2.3 ns with different weights, as shown by the straight lines in the figure.

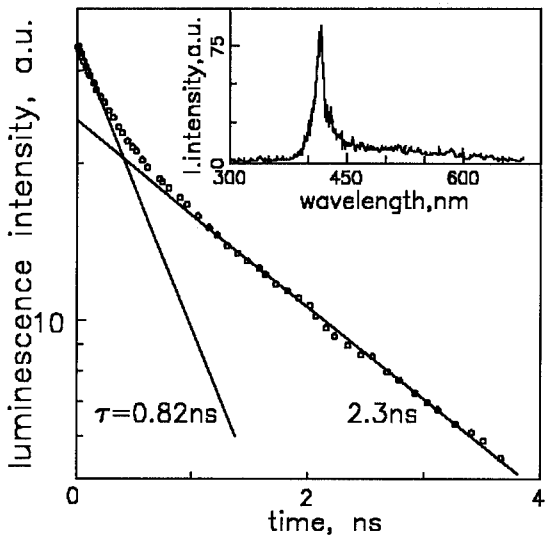

Figure 2. Decay of luminescence intensity at 417 nm. The inset shows the luminescence spectra of nitrogen doped 6H-SiC at 300 K.

The instantaneous decay times τ_M of photoconductivity kinetics induced by picosecond light pulse excitation are shown in Fig.3. Values of τ_M were defined as $\tau_M^{-1} = -\delta[\ln(\Delta U(t)]/\delta t$, were $\Delta U(t)$ is the voltage signal on the 50 Ω load resistance. The kinetics were analyzed and some of them at different excitation intensities and quantum energies are shown in the figure. Each line presents one analyzed kinetic. The resistivity of the samples were ~ 15 Ω (300 K) and 45 Ω (125 K). Due to low resistivity values weak electrical fields (approximately 7 $V \cdot cm^{-1}$ (300 K) and 15 $V \cdot cm^{-1}$ (125 K)) were applied. Band-to-band excitation kinetics show a relative slow decay time of ~ 1.5 μs at 300 K, which increases ($4 \div 7$ μs) at 125 K. The analysis of extrinsic photoconductivity with 1.15 eV and 2.3 eV excitation quantum energies displayed a different slope of $\tau_M(\Delta U/U_s)$ decay, and it is evident that the steeper lines are for higher quantum energies.

DISCUSSION

The NCC density decay time 820 ps obtained by DG and photoluminescence

measurements indicates a relative fast excess carrier capture. In the case of an electron-hole pair photogeneration ($h\nu$= 3.45 eV) both the electrons and holes can be captured by impurities, though it's known that for single crystal silicon carbide a distinct expressed type of conductivity is defined by a strong capture of minority carriers [15]. As it is calculated from the carrier diffusion length measurements the minority carrier lifetimes in n-type 6H-SiC are (200÷400) ps in nitrogen doped (10^{18} cm^{-3}) single crystals [15], and up to 7÷10 ns for epitaxial layers [1,2,3]. From our DG and photoluminescence measurements we concluded, that the minority carriers, i.e. holes, are rapidly captured by neutral donors. This defines their short lifetime value 820 ps. The rate of phonon assisted electron capture by the ionized donors is respectively weak. From the photoluminescence measurements we assume that the capture of photoexcited holes by two nitrogen inequivalent donor levels [16] determines the two exponential luminescence decay times 820 ps and 2.32 ns. The ratio of the concentrations of these donors is approximately $N_{N,1}$:$N_{N,2}$=1:2 (the ionization energies of the donor levels are $\Delta E_{N,1}$= 85.5 meV, $\Delta E_{N,2}$= 125 meV) [16]. So, in our case each donor concentration is of $3\cdot10^{16}cm^{-3}$ (N,1) and $7\cdot10^{16}cm^{-3}$ (N,2), respectively. Assuming, that deeper donor levels capture holes more rapidly, for a mean temperature of holes 300 K and hole mass m_h= $1\cdot m_0$, V_{th} = $(3kT/m_h)^{1/2}$ = $1.17\cdot10^7 cm\cdot s^{-1}$, the hole capture cross section by nitrogen for the both of donor levels is found:

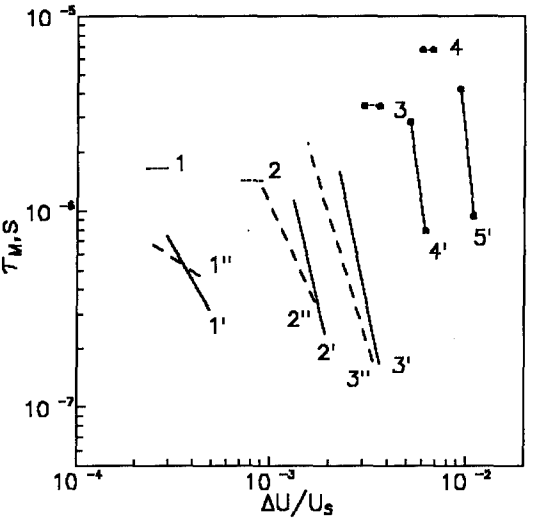

Figure 3. Instantaneous photoconductivity decay time versus $\Delta U/U_s$. Each line corresponds to one typical kinetic at excitation intensities: 1) 0.012, 2) 0.037, 3) 0.023, 4) 0.056, 1') 0.088, 2') 0.2, 3') 0.4, 4') 0.47, 5') 1, 1'') 0.16, 2'') 1, 3'') 2.2 $GW\cdot cm^{-2}$. Lines correspond to 2.3 eV, dashed lines - 2.3 eV, fine dashed (1,2,3,4) - 3.45 eV quantum energies. Marked lines - measurements at 125 K.

$$\sigma_{N,1}(N) \approx 1.2\cdot10^{-15}cm^2,$$
$$\sigma_{N,2}(N) \approx 1.5\cdot10^{-15}cm^2$$

The precision of $\sigma_p(N)$ certainly could be improved by a quantitative determination of the distribution of occupied donors. The influence of non-radiative recombination is considered to be respectively weak.

Assuming a significant difference between the values of electron and hole mobilities, 400 and 40 $cm^2\cdot V^{-1}\cdot s^{-1}$ [16,17], respectively, the photocurrent in 6H-SiC is determined by electron

drift. The photoconductivity kinetics are described by photoexcited electron density decay. The shortest instantaneous lifetime value for electrons evaluated after band-to-band excitation is ~ 1.5 μs at 300 K. The increase of electron lifetimes up to $(3.5 \div 6.5)$ μs at 125 K is determined by a respective decrease of ionized donor concentration. At high excitation intensities, using impurity ionization quantum energies 2.3 eV, 1.15 eV $< E_g$, an increase of electron capture by the ionized donors, i.e. τ_M decrease, with the excitation intensity has been observed. For high extrinsic excitation condition, it appears that $\tau_M^{-1} \sim \Delta n$ [18].

The experimentally determined ambipolar diffusion coefficient D_a can be compared to calculated values: $D_a = D_p D_n (n+p)(nD_n + pD_p)^{-1}$, where $n = n_0 + \Delta n$; $p = p_0 + \Delta p$; n_0, D_n and p_0, D_p are the equilibrium concentrations and the diffusion coefficients of electrons and holes, respectively. Assuming the mobility values and using the Einstein relation for electrons and holes, $D_{p,n} = (kT/e) \cdot \mu_{p,n}$, the ambipolar diffusion coefficient 1.7 $cm^2 \cdot s^{-1}$ in the case of total donor ionization, and 1.9 $cm^2 \cdot s^{-1}$ in the case of full occupied donors, at NCC density $3 \cdot 10^{17} cm^{-3}$ were calculated. The coincidence between the calculated and measured (1.4 $cm^2 \cdot s^{-1}$) values is quite good. The slight discrepancy we attribute to the impurity distribution fluctuations which appear during the growth.

ACKNOWLEDGMENTS

We would like to thank Prof.G.Jushka for useful discussions. Two of the authors (R.Tomashiunas, M.Petrauskas) greatfully acknowledge the support of the International Science Foundation under the Emergency Grants for Individuals.

REFERENCES

1. M.Anikin, A.M.Strelchuk, A.L.Syrkin and V.E.Chelnokov, to be published in the Proceedings of ICSCRM, Washington DC, 1993, p.I-52; A.M.Strelchuk, A.I.Syrkin, V.E.Chelnokov, A.E.Cherenkov and V.A.Dmitriev, ibid., p. II-21.
2. M.M.Anikin, A.A.Lebedev, I.V.Popov, A.M.Strelchuk, A.V.Suvorov, A.L.Syrkin and V.E.Chelnokov, Sov. Phys. Semicond. **5**(20), 844(1986).
3. A.V.Naumov and V.I.Sankin, Sov. Phys. Semicond. **6**(23), 1009(1989).
4. I.Rückmann, J.Kolenda, F.Henneberger and M.Petrauskas, Phys. Status Solidi **150**, 735(1988).
5. A.Naumov, S.Nikitin, A.Ostroumov and V.Vodakov, Sov. Phys. Semicond. **21**, 37 (1987).
6. S.Nishino, A.Ibaraki, H.Matsunami and T.Tanako, Jap. J. Appl. Phys. **19**, L353 (1980).
7. H.J.Eichler, P.Gunter and D.W.Pohl, Laser-Induced Dynamics Grating, (Springer, Berlin,1985)
8. A.L.Smirl, Semiconductor Probed by Ultrafast Laser Spectroscopy, edited by R.R.Alfano Vol.1 (Academic Press,1984), p.198.
9. C.A.Hoffman, K.Jarasiunas, H.J.Gerritsen and A.V.Nurmiko, Appl. Phys. Lett. **33**, 536(1978).
10. W.J.Choyke, Mater. Research Bullet. **4**, 141(1969).
11. V.V.Makarov, Sov. Phys. Semicond. **9**(6), 1556(1972).
12. B.F.Wheeler, Sol. St. Communic. **4**, 173(1966).
13. R.J.Manning, A.Miller, A.M.Fox and J.H.March, Electron. Lett. **20**, 601(1984).
14. V.V.Evstropov, I.Vn.Linkov, Ya.V.Morozenko and F.G.Pikus, Physica B **185**, 313(1993).

15. V.S.Balandovich and G.N.Violina, Sov. Phys. Semicond. **8**(15), 1650(1981).
16. G.Pensl and W.J.Choyke, Physica B **185**, 264(1993).
17. P.A.Ivanov and V.E.Chelnokov, Semicond. Sci. Technol. **7**, 863(1992).
18. S.M.Ryvkin, Photoelectronic effects in semiconductors, (Consultants Bureau, New York, 1964), p.494.

RADIATION DEFECTS IN SiC - ELECTRON IRRADIATION WITH DIFFERENT ENERGIES

D.Volm, B.K. Meyer, E.N. Mokhov* and P.G. Baranov*

Physikdepartment E16, Technical University Munich, D-85747 Garching, Germany,
*Ioffe Physico-Technical Institute, St. Petersburg, Russia

ABSTRACT

Radiation defects in 6H SiC introduced by electron irradiation at energies of 400 keV and 1 MeV are studied by low-temperature photoluminescence and Zeeman spectroscopy. We observe a new two line spectrum at 2.547 and 2.528 eV which dominates in the spectrum of the sample irradiated at 400 keV. For 1 MeV irradiation numerous recombination lines are observable and also the well known D_1 center lines appear. Annealing the sample at 1100 °C leads to the disappearance of almost all lines but the D_1 lines are still present.

INTRODUCTION

The study of lattice defects in SiC introduced by ion implantion, electron or neutron irradiation is an ongoing subject for nearly twenty years. The isolated Si-vacancy has been identified quite recently by electron paramagnetic resonance (EPR) in 3C and 6H SiC following neutron irradiation [1,2]. However there is no correlation to optical and electrical properties of the samples. With the method of Deep Level Transient Spectroscopy (DLTS) six electron irradiation induced traps are found, Z_1 and Z_2 acceptors at E_c-620 meV and E_c-640 meV are thought to be related to double vacancies (V_{Si}-V_C). For the E_1/E_2 and E_3/E_4 levels at E_c-350 meV and E_c-570 meV no definite assignment can be made [3]. The observation of two levels very close in energy could imply that the defects reside at cubic and hexagonal lattice sites in 6H SiC. Annealing at around 800 °C leads to the disappearance of the isolated vacancy and secondary radiation defects can be formed [4]. The most prominent one is the so called D_1-center as observed in photoluminescence and studied by Zeeman spectroscopy [5,6,7]. Double vacancies and V_{Si}-N_C, a Si-vacancy Nitrogen-donor complex have been put forward as microscopic structure models for the D_1-center. Here we report on a new two line spectrum labelled G_1 and G_2 already introduced at an electron energy of 400 keV without performing additional high temperature treatments.

EXPERIMENTAL

Electron irradiation at room temperature was performed on 6H SiC epitaxial layers grown on 6H SiC substrates. The low temperature luminescence studies employed a 1 m Jarrel Ash monochromator with a resolution better than 0.1 nm in

Mat. Res. Soc. Symp. Proc. Vol. 339. ©1994 Materials Research Society

the investigated range from 400 to 450 nm. Detection was performed with a cooled photomultiplier. For the Zeeman measurements the sample was located in the center of a 12 T solenoid type superconducting magnet, excitation by the UV line of a HeCd laser (325 nm) and emission from the sample was guided by an optical fiber.

EXPERIMENTAL RESULTS

Irradiation at 400 keV: Fig.1 gives an overview of the recombination lines found after 400 keV electron irradiation. Not all of them are due to radiation damage. For example close to the band gap of 6H SiC at around 3 eV the excitons bound to the Nitrogen donor are seen followed by their phonon replicas at 2.9 eV.

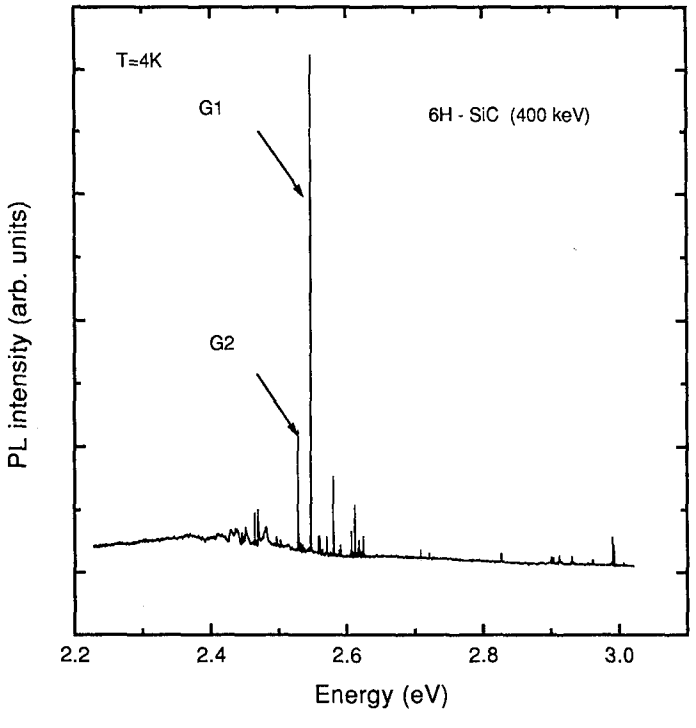

Fig.1: Photoluminescence spectrum of 6H SiC after electron irradiation with 400 keV electrons. The two arrows mark the positions of the G_1 and G_2 lines.

The strongest lines appear at 2.547 eV (G_1) and 2.528 eV (G_2). They are followed by TA and LO phonon replicas around 2.35 eV (for more details see table 1) and prove that they are zero-phonon-lines. The three lines (L_1, L_2 and L_3) of the D_1 center are hardly visible. These two lines were studied in more detail. At 4 K the intensity ratio of G_1 to G_2 is ~5:1, note that at this temperature a new line appears at 2.537 eV which was not present at low temperatures. Around and above 20 K all lines decrease in intensity (G_2 is already absent) and for temperatures above 30 K can not be observed any longer with this spectrometer resolution.

The photoluminescence spectrum has markedly changed for the sample irradiated with 1 MeV electrons. A forest of lines appears between the D_1 center line at the highest energy and the G_2 line. The L_1, L_2 and L_3 lines of the D_1 center corresponding two cubic and one hexagonal sites in 6H SiC are now observed in comparable intensity (see fig.2c). Identifying all or at least part of them would be a very tedious job. Annealing at 1100 °C leads to a destruction of most of the defects or defect pairs as can be seen in fig.2.b. As already mentioned in earlier works [5,7] the D_1 center is stable up to that temperatures and is prominent in the low temperature photoluminescence spectra.

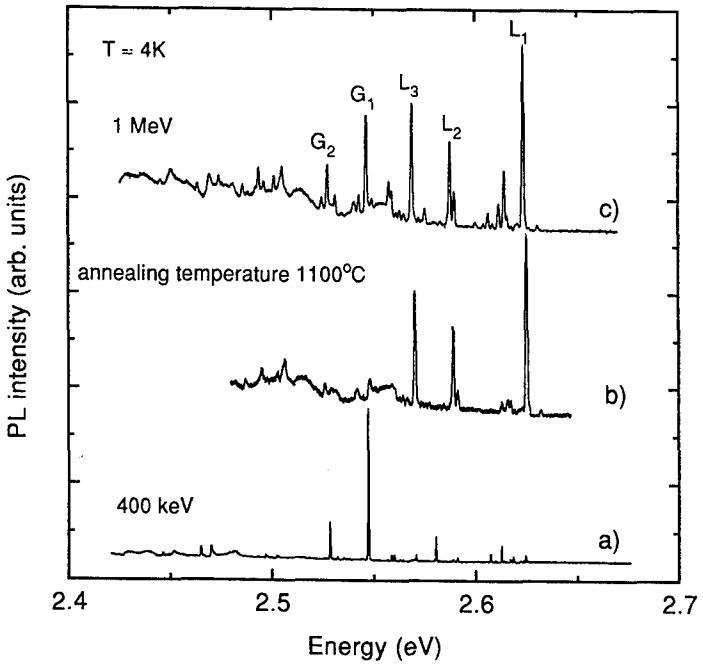

Fig.2: Photoluminescence spectra for 400 keV (a) and 1 MeV (c) electron irradiated 6H SiC; b) irradiated at 1 keV and annealed at 1100°C.

Zeeman spectroscopy: To obtain further insight into the microscopic structure of a defect, i.e electronic level structure, site and symmetry, perturbation spectroscopy resolving stress or Zeeman splittings in the ground and excited states is an appropriate tool. The extremely narrow lines observed for the G_1 and G_2 lines favour Zeeman spectroscopy.

In fig. 3 we present the evolution of the G_1 line for magnetic fields from 0 to 11 T. At 4 T a small shoulder appears at the low energy side which continously shifts to lower energies as a function of the applied field. At 11 T both lines now have equal intensity. It also clear from fig. 5 that one component of the sublevels is independent of the magnetic field. The measured field dependence shown in fig. 3 was for the magnetic field parallel to the c-axis. With the magnetic field perpendicular to the c-axis only a shift to lower energies is found without any splitting of the line. The G_2 line instead showed for all magnetic fields neither splittings nor a shift.

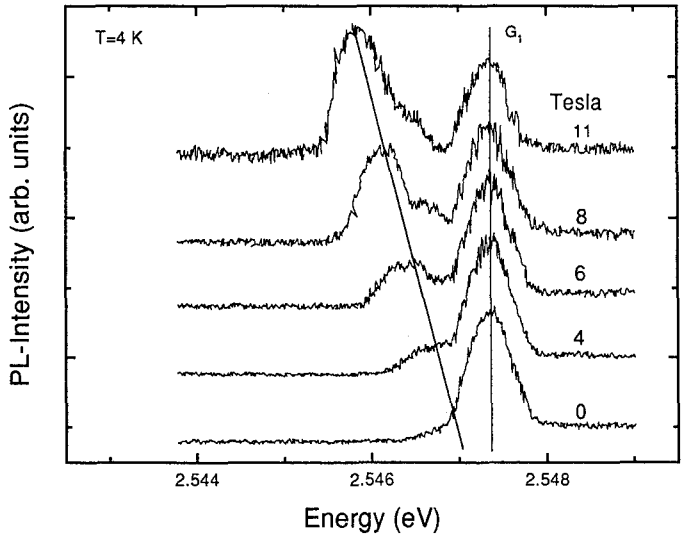

Fig.3: Evolution of the Zeeman splittings for the G_1 line as a function of magnetic field (6H SiC, 400 keV)

DISCUSSION AND CONCLUSION

The G-line spectrum behaves in many aspects quite similar to the D_1-center. There are small but distinct differences. The D1-center gives rise to three recombination lines [5,7] at low temperatures connected to the three sites in 6H SiC. Five magnetic subcomponents with site-independent splittings were

observed on L_1, L_2 and L_3. The high temperature modifications H_1, H_2 and H_3 were magnetically inactive. The recombination lines were explained by assuming exciton recombination at a deep neutral center where the exciton is bound by short range forces. Coupling of a J=1/2 state for the electron and a J=3/2 for a hole leads to exciton states with total angualar momentum of J=2 and J=1, the J=1 being higher in energy. At low temperatures the J=2 states is observed and its five fold degeneracy gives rise to the five magnetic subcomponents seen in Zeeman spectroscopy. The J=1 state corresponding to the high temperature lines of the D_1 center is magnetically inactive as found in the experiment.

The two newly observed G-lines are obviously no site dependent lines of one and the same defect. The observation of the same phonon replica spectrum however proofs that they are zero phonon lines (see table 1). In magnetic fields the G_2 line remains unsplit and unshifted implying either spin singulet to spin singulet recombination or the equality of g-values of electron and hole in the excited state [8].

The G_1 line is accomponied by a high temperature line (the line at 2.5374 eV) and in magnetic field it shows at least three magnetic subcomponents. The failure to observe transition moving to higher energies can easily be explained by the thermalisation into the lower sublevels. The strong increase in intensity of the low energy transition (see fig.4) as a function of the magnetic field is a clear indication for such a behaviour. The multiple splitting together with a field independent transition within the G_1 line supports the exciton model proposed by Dean et al [6] for the D_1 line. In contrast to the Zeeman work on the D_1 line [6] we do not observe a zero field splitting caused by the hexagonal crystal field. It was of the order of 0.3 meV and hence may be hidden within the linewidth of the transitions.

The isolated Silicon vacancy has been identified in particle irradiated 6H SiC by electron paramagnetic resonance (EPR). Ligand hyperfine interactions with nearest Si and next nearest C atoms surrounding the vacancy were resolved and gave firm evidence for the structure model. No distortion i.e. an isotropic spectrum was found in EPR in contrast to the vacancies in Si [9]. The EPR also showed no indications for additional lines due to the possible different sites. For a deep level with the spin density distributed over a few lattice constants (typically 4-6 A) this is quite reasonable. We can expect that low energetic electron irradiation creates primary defects such as the Carbon or Silicon vacancy. They can exist in several charge states also in the neutral one were exciton binding can occur. Hence the G_1 line might arise from exciton recombination at the neutral Si vacancy. At higher energies (1 MeV) EPR showed in addition to the Nitrogen donor resonance the appearance of a new line which is radiation induced. Its identification has to be awaited for.

Mode	Energy (meV)	Lattice (6 H) (meV)	G_1 (2.547 eV) (meV)	G_2 (2.528 eV) (meV)
Resonant LA	68		67	
Zone edge LA	76	76	77	77
Localized (Gap)	83		82	81
Zone center TO	98	98	98	
Resonant LO	110-112		110-113	
Zone center LO	120	120	119-122	

Table 1: Phonon energies (and assignment) observed as replicas on the G_1 and G_2 zero phonon lines

References

1. H. Itoh, M. Yoshikawa, I. Nashiyama, S. Misawa, H. Okumara and S. Yoshida, EEE Trans. Nucl. Sci. 37, 1732 (1990).
2. L.A. de S. Balona and J.H.N. Loubser, J. Phys. C 3, 2344 (1970).
3. G. Pensl and W.J. Choyke, Physica B, 264 (1993).
4. H. Itoh, N. Hayakawa, I. Niashiyama and E. Sakuma, J. Appl. Phys. 66, 4529 (1989).
5. L. Patrick and W.J. Choyke, Phys. Rev. B 5, 3253 (1972)
6. P.J. Dean, D. Bimberg and W.J. Choyke, Inst. Phys. Conf. Ser. 46, 447 (1979).
7. W.J. Choyke and L. Patrick, Phys. Rev. B 4, 1843 (1971).
8. D.G. Thomas and J.J. Hopfield, Phys. REv. 128, 2153 (1962).
9. G.D. Watkins, 7th Int. Conf. on the Physics of semiconductors, Dunod, Paris, (1965).

CHARACTERIZATION OF DEFECTS IN N-TYPE 6H-SiC SINGLE CRYSTALS BY OPTICAL ADMITTANCE SPECTROSCOPY

A.O. EVWARAYE*, S.R. SMITH**, and W.C. MITCHEL
Wright Laboratory, Materials Directorate, WL/MLPO, Wright-Patterson Air Force Base, Ohio 45433-7707.

ABSTRACT

Optical admittance spectroscopy is a technique for measuring the conductance and capacitance of a junction under illumination as a function of the wavelength of the light and the frequency of the measuring AC signal. This technique has been applied to characterize deep defect levels in 6H-SiC:N. Nitrogen is a donor atom in 6H-SiC which substitutes for carbon in three inequivalent sites (h, k_1, k_2). giving rise to n-type conduction. Deep defect levels attributable to transition metal impurities have also been identified in 6H-SiC:N. We have examined persistent photoconductance in this material by optical admittance spectroscopy.

INTRODUCTION

The unique physical and electronic properties of silicon carbide make it an ideal choice for high-power, and high-operating temperature devices, and devices that are radiation resistant. The frequency of device operation depends on the minority carrier lifetime, which, in turn, is controlled by deep traps that act as recombination centers. Furthermore, the development of semi-insulating materials requires the introduction of a trap near mid gap in sufficient quantities to compensate shallow donors, e.g. Cr in GaAs.

Nitrogen can be introduced into the growth ambient when it is de-adsorbed from the graphite components of the growth chamber, or it may be intentionally added as a dopant via the growth ambient. It is incorporated into the SiC lattice at a hexagonal site(h) and two cubic sites(k_1,k_2), gives rise to n-type conduction, and three shallow levels[1,2].

In order to electrically characterize traps that lie near mid gap in wide band gap semiconductors(e.g., 6H-SiC) by thermal techniques such as Deep Level Transient Spectroscopy(DLTS), or Admittance

Mat. Res. Soc. Symp. Proc. Vol. 339. ©1994 Materials Research Society

Spectroscopy, it is necessary to raise the temperature of the specimen to high temperatures. A method that has the sensitivity of the capacitance techniques, but that does not require the use of high temperatures would be useful. Therefore, we have studied the deep levels in n-type(N-doped) 6H-SiC by using optical admittance spectroscopy on Schottky diodes.

DISCUSSION

Admittance spectroscopy was first introduced by Losee to study deep traps in compound semiconductors [3]. The details of the technique have been worked out by him and others[4,5]. The optical variation of this technique was introduced by Vincent, et al.[4], and further developed by Duenas, et al.[6].

Thermal admittance spectroscopy detects the effect of thermal emission of carriers from deep centers on the conductance of a diode, optical admittance spectroscopy detects the effect of carriers that have been optically excited from trap level(s) to the conduction band. During an optical experiment the temperature is held below the point where the trap level crosses the Fermi level.

Traps introduce into the measurement, a conductance G_T, given by[4]

$$G_T = \frac{e_n \omega^2}{e_n^2 + \omega^2} \frac{N_T}{n} A \left(\frac{\varepsilon q N^+}{2V} \right)^{\frac{1}{2}},$$

and a capacitance given by

$$C_T = \frac{e_n}{e_n^2 + \omega^2} \frac{N_T}{n} A \left(\frac{\varepsilon q N^+}{2V} \right)^{\frac{1}{2}},$$

where e_n is the emission rate, n is the number of free carriers in the bulk, N_T is the number of deep traps, N^+ is the number of ionized deep centers, ω is the measurement frequency, ε is the bulk dielectric coefficient, A is the area of the diode, and q is the electronic charge. N^+ can then be manipulated optically.

Schottky diodes were fabricated on SiC intentionally doped with nitrogen to make it n-type. The material was prepared for fabrication by being oxidized and etched to yield a clean, ordered, surface. Actual metallization consisted of sputtering Ni onto one side of the material and

annealing at 900 C for five minutes in forming gas(95% N_2, 5% H_2) to produce ohmic contacts. Schottky diodes were fabricated by evaporating Al dots 600μm in diameter onto the other side of the wafer. The diodes that were formed by this process were evaluated by examining the C^{-2} vs V behavior. The capacitance and conductance were measured using an HP4270A Multifrequency LCR Meter, operated in the high resolution mode.

RESULTS

Five peaks were seen in the spectrum obtained from the SiC specimens, as shown in figure 1. The energies of the transitions indicated by the peaks are shown in the figure. Consideration of the transition energies rules out the possibility that any of these peaks are related to nitrogen in any other manner than a complex of some sort. The band-to-band transition for 6H-SiC is clearly seen along with two peaks that are attributable to deep levels in SiC arising from the transition metal impurity vanadium; and two peaks that are as yet unidentified. These results are reported elsewhere.[7,8]

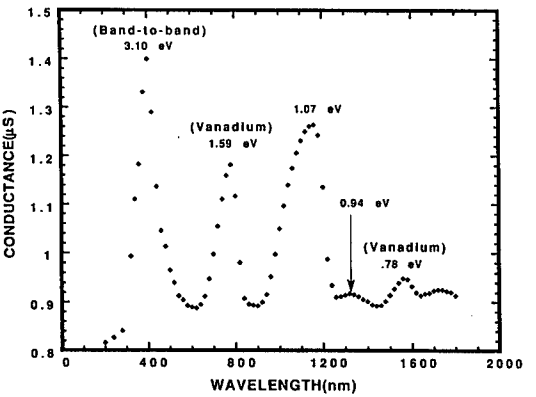

FIGURE 1. Optical admittance spectrum reveals peaks attributable to band-to-band transitions, vanadium, and two as yet unidentified deep levels.

Figure 2 shows the results of an experiment wherein the conductance was monitored as a function of time when the light was turned off. As can be seen from this graph, the time constant was very long. This phenomenon can be called persistent photoconductance since current was not being measured. This figure shows the result of fitting a straight line to the ln G vs t data. The decay constant in the linear portion of the curve was calculated to be 0.088 $\mu S\text{-}min^{-1}$.

When further experiments were performed by setting the wavelength of the light to produce the maximum conductance of one of the peaks seen in figure 1, and then, after the signal reaches equilibrium, shifting the wavelength either up or down, to a value that corresponds to a minimum in the conductance, the decay constant was seen to vary depending on the direction of the shift. Figure 3 shows the decay when

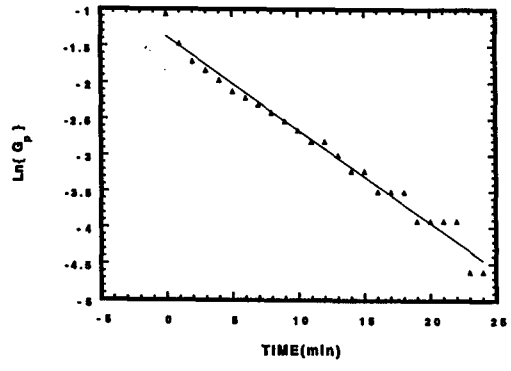

FIGURE 2. A logarithmic plot of the conductance decay reveals an exponential character with a time constant of 0.088 $\mu S\text{-}min^{-1}$.

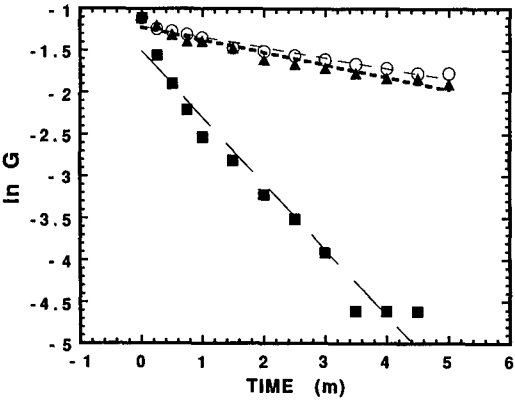

FIGURE 3. Fits to the logarithmic plots of the decay indicate that differences in the decay of the conductance signal occur when the wavelength is shifted to shorter wavelengths(■), longer wavelengths(▲), or allowed to decay in the dark(O).

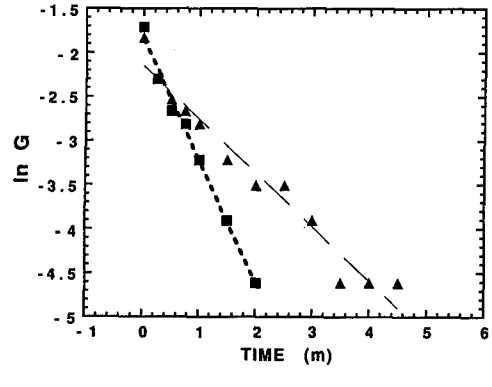

FIGURE 4. Logarithmic plot of the photoconductance decay from the 780 nm peak: (■) when the light was turned off, (▲) when the wavelength was shifted to shorter values.

the experiment was performed with λ_p = 400nm. The triangles are the data obtained by shifting to longer wavelengths, the circles are the data obtained when the shutter was closed and the conductance allowed to decay in the dark, and the squares are the data obtained by shifting to shorter wavelengths. It is apparent that the decay constant is different depending on the direction of the wavelength shift. Furthermore, there are apparently two distinct decay constants in each curve.

Figure 4 shows the results of shifting to shorter wavelengths (600nm) when the peak was centered at 780 nm, compared to closing the shutter. This peak has been identified with vanadium in SiC, whereas the peak at 400 nm is undoubtedly the band-to-band transition.

CONCLUSIONS

We conclude that transition metal impurities give rise to persistent photoconductance in 6H-SiC. This result may be indicative of lattice relaxation. We believe that it is more likely that these larger atoms would cause lattice relaxation than would N atoms, which are more the size of C atoms.

ACKNOWLEDGEMENTS

We would like to acknowledge the work of Mr. Paul Von Richter, Mr. Robert V. Bertke, and Mr. Gerald Landis in preparing the specimens for these experiments. The work of SRS was supported by Air Force contract no. F33615-91-C-5603.
*Visiting Scientist, Permanent address, Physics Department, University of Dayton, Dayton, Ohio 45469-2314, **University of Dayton Research Institute, Dayton, Ohio 45469-0178.

REFERENCES

1. W. Suttrop, G. Pensl, W.J. Choyke, R. Stein, S. Liebenzeder, J. Appl. Phys. **27**, 3708(1992)
2. A. O. Evwaraye, S. R. Smith, and W. C. Mitchel, J. Appl. Phys. 1APR1994.
3. D. L. Losee, J. Appl. Phys. **46**, 2204(1975)
4. G. Vincent, D. Bois, and P. Pinard, J. Appl. Phys. **46**, 5173(1975)
5. W. D. Oldham and S. S. Naik, Solid State Electron. **15**, 1085(1972)
6. S. Duenas, M. Jaraiz, J. Vicente, E. Rubio, L. Bailon, and J. Barbolla, J. Appl. Phys. **61**, 2541(1987)
7. T.H. Stiasny, R. Helbig, and R.A. Stein, Springer Proc. in Phys. **V71**, p210, 1992.
8. A.O. Evwaraye, S.R. Smith, and W.C. Mitchel, Materials Research Society Fall Meeting 1993, Boston, MA, Symposium L, L6.9, Proceedings in publication.

PROPERTIES OF CRYSTALLINE 3*C*-SIC GROWN FROM METHYL TRICHLOROSILANE

W. J. MOORE[a], R. KAPLAN[a], J. A. FREITAS, Jr.[b], Y. M. ALTAISKII[c], V. L. ZUEV[c], and L. M. IVANOVA[d]
[a]Naval Research Laboratory, Washington, DC 20375
[b]Sachs/Freeman Associates, Landover, MD 20785
[c]Kiev Polytechnic Institute, Kiev, Ukraine
[d]A. A. Baikov Institute of Metallurgy, Moscow, Russia.

ABSTRACT

Cubic silicon carbide grown by thermal decomposition of methyl trichlorosilane in hydrogen has been studied in infrared (IR) transmission, cyclotron resonance (CR), and photoluminescence (PL). Sample characteristics include: The nitrogen concentration, determined from CR and IR can be of the order of 10^{15} cm^{-3} or less. Ionized impurity concentrations determined from the linewidths of CR and IR spectra can be less than 7×10^{14} cm^{-3}. Low temperature electron mobilities from CR are near 10^5 cm^2 v^{-1} s^{-1}. Carrier freeze-out is consistent with either uncompensated donors with activation energy near 50 meV or heavily compensated donors with 20 meV activation energy. The latter choice, however, is excluded by the low ionized impurity concentration. These high quality samples show little or no evidence of the apparently shallow (< ~20 meV) donor which usually dominates the low temperature conductivity of 3C-SiC grown on Si. Nitrogen donor excitation spectra are in excellent agreement with effective mass theory. Only nitrogen donors at 54.2 meV and an unidentified effective-mass donor at 47.8 meV are observed. If material with the characteristics described above can be reliably reproduced then there is substantial expectation that high quality electronic devices based on 3*C*-SiC can be fabricated.

INTRODUCTION

Wide bandgap semiconductor materials present potential advantages over silicon in many device applications. For example, control electronics for high temperature operating environments such as engines and furnaces, electronic circuitry in nuclear radiation environments, and high density integrated circuitry combining high operating temperatures with the need for high thermal conductivity all could benefit from wide bandgap materials. Of the currently studied wide bandgap materials, e.g., SiC, diamond, and the III-V nitrides, the cubic SiC described in this paper most nearly approximates Si with respect to achievable material purity with current technology. If these material properties can be reproduced in large volume then cubic SiC will be an attractive candidate for device applications.

Cubic SiC has presented several perplexing characteristics. Most recent studies have used epitaxial samples grown on Si or on 6H-SiC. This epitaxial growth on Si or 6H-SiC entails unavoidable problem with strains from the lattice mismatch with the substrate and the purity of the resulting material appears to be marginal. A part of the marginal purity may be the difficulty in reconciling the apparently conflicting material parameters. For example, most Hall effect studies on 3C-SiC grown on Si indicate that the wafers are dominated by conduction originating from

Mat. Res. Soc. Symp. Proc. Vol. 339. ©1994 Materials Research Society

a shallow donor with an activation energy in the 10 to 20 meV range [1-4]. This has been interpreted to be due to a high nitrogen donor concentration and high compensation [1]. In contrast, mobility analysis of samples appearing to be highly compensated in Hall effect [3] suggest that the ionized impurity concentrations are much lower than thought [5]. In addition, the published data on which the assumed dependence of the nitrogen binding energy as a function of nitrogen concentration was based has been questioned [6].

These problems have not been encountered in our studies of the high quality 3C-SiC samples grown from methyl trichlorosilane which we describe here. This may be, in part, due to the very low nitrogen concentration in the samples that we have chosen to study. The properties of samples with high nitrogen concentration grown in this way have not yet been determined.

EXPERIMENT

This report describes results of infrared (IR) transmission, cyclotron resonance (CR), and photoluminescence (PL) studies of small samples of 3C-SiC grown by thermal decomposition of a single precursor, methyl trichlorosilane, in a hydrogen atmosphere. Decomposition took place on a graphite filament and the crystals were self-seeding. The resulting samples typically have two parallel planar faces, one larger than the other, and a variably shaped circumference. Areas of the parallel faces range from 1 mm^2 to about 10 mm^2. Crystalline orientation with faces perpendicular to (100) and (111) has been observed.

Selected samples were packed into an aperture in a brass plate with pure In and clamped as a window over a gallium-doped Ge photoconductor cooled to near 4.2 K for low temperature IR transmission. Measurement with the sample at an unknown higher temperature was accomplished by gluing the sample over an aperture by one corner with a small amount of insulating varnish. Infrared spectra were acquired with an Fourier transform spectrometer.

Cyclotron resonance was carried out with the sample attached to a heated block in a superconducting magnet. In this system the transmission of a submillimeter laser (0.667 mm) is measured while the magnetic field is scanned through the resonance. The minimum temperature for which the free electron concentration exceeded our threshold for reliable measurement was 28K. Above 53 K the absorption at resonance was sufficiently saturated that reliable quantitative absorption strength determination was not possible.

Photoluminescence studies were carried out with the sample immersed in cooling helium vapor/liquid with several laser sources and excitation powers. Measurements at low power/high resolution and at high power/low resolution were made.

RESULTS

A typical IR transmittance spectrum is shown in Fig. 1. There are two sequences of donor excitation absorption lines, a sharp sequence with the $1s(A_1)$ - $2p_0$ line at 32.54 meV and a broad one with $1s(A_1)$ - $2p_0$ line at 38.99 meV. The broad sequence is identified as nitrogen on the carbon site while the sharp one is an unknown donor. The strong absorption in the neighborhood of the lattice optical phonons is seen to the right of the Fig. As a result of this strong absorption and the strong two-phonon bands at greater energies, a large part of the mid IR is inaccessible for transmission studies. However, we can see from Fig. 1 that there are no excitation lines from donors with binding energies greater than the N donor but smaller than about 90 meV. Similar spectra at energies to 10 meV also show no observable additional donors. From this data alone

we can determine that there are two donors present with binding energies near the expected value for an effective mass single donor and no other donors in appreciable concentrations in this sample with binding energies less than about 90 meV. This result is characteristic of the material discussed here.

A portion of this spectrum is given in Fig. 2 as an absorption coefficient spectrum. Several excitation transitions are identified with the designations of the final state of the transition. Both sequences in this spectrum originate on the $1s(A_1)$ ground state of the relevant donor. An unusual feature of these spectra is the prominent line at high energy labeled $4f_{\pm}$. This transition appears in most published spectra to be weaker than its neighbors [7] but is identified as strong in photo-thermal excitation spectra of Ge donors [8] and appears in Fig. 2 at a position which agrees much better with theory [9] than any other choice. Thus this designation appears to be the preferred one.

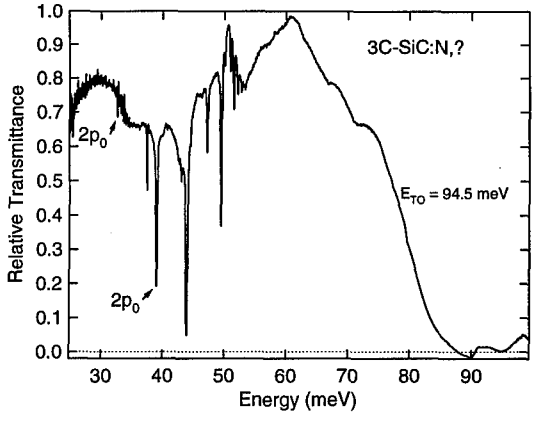

Fig. 1. A typical infrared transmittance spectrum. Features appearing above about 80 meV may not be observed due to the strong phonon absorptions.

Transition energies and binding energies for the excited states have been tabulated [10]. These data, when fitted to theory [9] give an activation energy of 54.2 meV for N and 47.8 meV for the shallow, essentially effective mass, donor (EMD). The narrow line widths, especially in the sharp sequence, and modest absorption strength indicate that the material is unusually pure for 3C-SiC. These observations will be quantified below. Similar spectra taken on a warmed sample exhibit transitions originating on the 1s(E) ground state, indicating an 8.34 meV valley-orbit splitting. These 1s(E) transitions are somewhat broader than those originating on the $1s(A_1)$ ground state at the same temperature and suggest that the 1s(E) ground state may be split. One possible source of 1s(E) ground state splitting would be a conduction band minimum slightly off the X-point in the Brillouin zone.

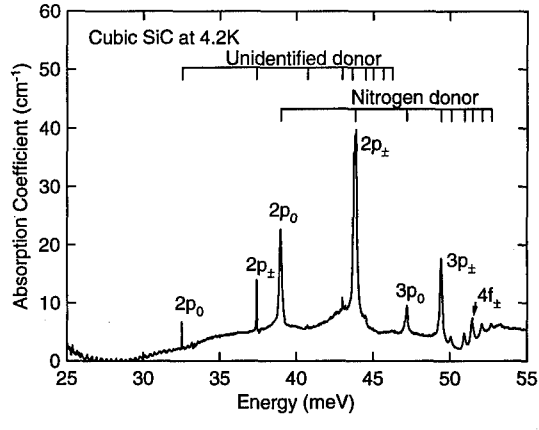

Fig. 2. Absorbance of 3C-SiC near 4.2K. The difference in linewidth for the broad (N) transitions and the sharp (EMD) transitions is clearly seen.

The free electron concentration and the electron scattering time/mobility can be calculated from the cyclotron resonance absorption strength and linewidth, respectively. The free electron concentration as a function of temperature determined from CR [11] can be modeled as due to thermal excitation of donors in the same way that carrier concentrations from Hall effect are modeled [1]. The CR line strength as a function of temperature is consistent with either a heavily compensated very shallow donor near 15 meV or with an essentially effective mass donor and low compensation.

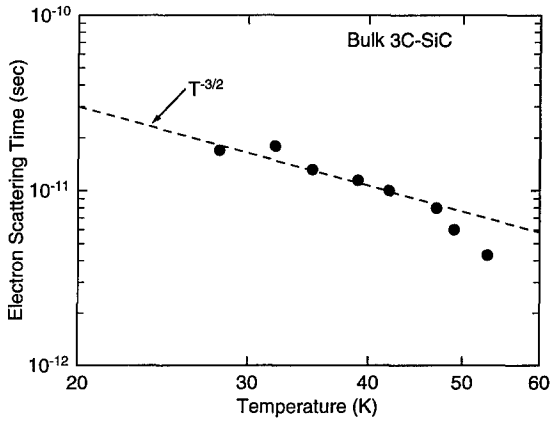

Fig. 3. Electron scattering time as a function of temperature from the cyclotron resonance linewidth. The data follow an approximate $T^{-3/2}$ dependence.

The electron scattering time from the cyclotron resonance line width is given in Fig. 3 as a function of temperature. The slope of the temperature dependence is consistent with the expected $T^{-3/2}$ for acoustic phonon scattering and quite different from the $T^{+3/2}$expected for ionized impurity scattering. Therefore, the observed scattering times are a lower limit on the ionized impurity scattering times . If the electron scattering time indicated at 30 K in Fig. 3 were entirely due to ionized impurity scattering, then the ionized impurity concentration calculated by the Brooks-Herring formalism would be about 4×10^{14} cm^{-3} [11]. An analogous result has been found for 3C-SiC grown on Si [5]. Ionized impurity scattering also can be estimated from the widths of the donor excitation transitions. The actual numerical result depends on presently unknown details of the impurity state wavefunctions. However, ionized impurity concentrations can be estimated based on results for phosphorous in Si which has a binding energy approximating that of N in SiC. These estimates yield a maximum ionized impurity concentration of 7×10^{14} cm^{-3} for the sample of Fig. 3 [12]. Thus the two techniques yield similar results and both ionized impurity concentration estimates are much too low to be consistent with a compensated

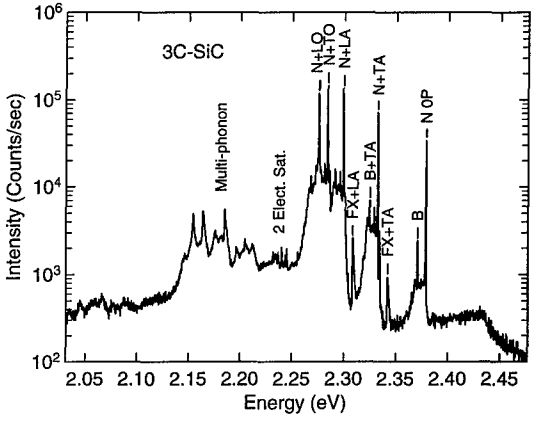

Fig. 4. Photoluminescence at high power. Zero-phonon, one-phonon, two-phonon, and two-electron satellites are seen.

shallow donor near 15 meV. Therefore it is concluded that conduction due to the two donors near 50 meV dominates and the total concentration of these donors is less than 1.4 x 10^{15} cm^{-3}. The electron scattering times in Fig. 3 correspond to an acoustic phonon limited mobility of 91,000 cm^2 v^{-1} s^{-1} at 30K and extrapolate to 2,900 cm^2 v^{-1} s^{-1} at 300K.

Photoluminescence at a high level of excitation is given in Fig. 4. The intensity scale is logarithmic in order to show both efficient and inefficient processes. This spectrum shows features similar to those observed by others on 3C-SiC [13, 14]. The principal features here include, beginning at high energy, the no-phonon nitrogen bound exciton (N 0P), bound multi-exciton complexes (BMEC), beginning with the strong two-exciton emission line traditionally labeled B. Free excitons do not luminescence without momentum conserving phonons so the first free exciton observed is the TA replica (FX+TA). This is followed by an unlabeled TA replica of a feature, previously observed but unidentified, which we assign to the TA replica of an exciton bound to the unidentified effective mass donor, EMD. Next are regions dominated by the LA, TO and LO phonon replicas of features observed at higher energies. The sharp lines around 2.24 eV are TO and LO replicas of two-electron satellite transitions leaving N in an excited state. Finally, there are the two-phonon replicas.

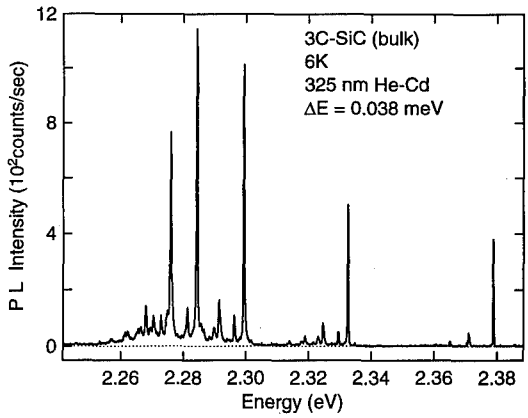

Fig. 5 Photoluminescence at high resolution.

Many of these features are also shown in Fig. 5 which was taken at high resolution but low power. Although the power is too low to see the free exciton, the BMEC lines are present, even in the no-phonon region. The TA phonon spectrum reveals a new sequence not present without phonon participation. This sequence, denoted the MCP series, appears to be a BMEC-like series which is observed only with the momentum conserving phonons. Its identification is not yet clear. All observed features, including the MCP series, are consistent with association with either N or EMD. The positions of the observed features have been determined from this high resolution spectrum and are tabulated in Table I.

SUMMARY

Infrared transmission, cyclotron resonance and photoluminescence studies of 3C-SiC grown from thermal decomposition of methyl trichlorosilane indicate that the material is of very high purity. No donors other than nitrogen and an unidentified effective mass donor are seen by any of these techniques. These studies indicate that the total neutral N plus EMD concentration is 1 x 10^{15} cm^{-3} or less and the ionized impurity concentration is in the 10^{14} cm^{-3} range. This material appears to be the purest SiC presently available.

This work was supported in part by the Office of Naval Research.

Table I, Positions and identifications of the stronger luminescence lines.

Position (eV)	Identification	Position (eV)	Identification
2.3788	BMEC-1	2.2962	MCP-1 + LA(x)
2.3709	BMEC-2	2.2914	BMEC-2 + LA(x)
2.3649	BMEC-3	2.2897	MCP-2 + LA(x)
2.3346	EMD-1 + TA(x)	2.2843	BMEC-1 + TO(X)
2.3325	BMEC-1 + TA(x)	2.2812	MCP-1 + TO(x)
2.3294	MCP-1 + TA(x)	2.2759	BMEC-1 + LO(x)
2.3246	BMEC-2 + TA(x)	2.2728	MCP-1 + LO(x)
2.3229	MCP-2 + TA(x)	2.2704	BMEC-3 + TO(x)
2.3188	BMEC-3 + TA(x)	2.2679	BMEC-2 + LO(x)
2.2993	BMEC-1 + LA(x)		

Notes: All bound excitons are bound to nitrogen unless designated EMD, indicating the unidentified effective mass donor. BMEC indicates bound multiexciton complex and is followed by the number of bound excitons. MCP indicates the BMEC-like series observed only with momentum conserving phonons.

REFERENCES

1. B. Segall, S. A. Alterovitz, E. J. Haugland, and L. G. Matus, J. Appl. Phys. **74**, 584 (1986).
2. A. Suzuki, A. Uemoto, M. Shigeta, K. Furukawa, and S. Nakajima, Appl. Phys. Lett. **49**, 450 (1986).
3. B. Segall, S. A. Alterovitz, E. J. Haugland, and L. G. Matus, Appl. Phys. Lett. **50**, 1533 (1987).
4. A. Suzuki, A. Uemoto, M. Shigeta, K. Furukawa, and S. Nakajima, Appl. Phys. Lett. **50**, 1534 (1987).
5. A. Suzuki, A. Ogura, K. Furukawa, Y. Fujii, M. Shigeta, and S. Nakajima, J. Appl. Phys. **64**, 2818 (1988).
6. W. J. Moore, J. Appl. Phys. **74**, 1805 (1993).
7. A. K. Ramdas and S. Rodriguez, Rep. Prog. Phys. **44**, 1297 (1981).
8. E. E. Haller, W. L. Hansen, and F. S. Goulding, Adv. Phys. **30**, 93 (1981).
9. R. A. Faulkner, Phys. Rev. **184**, 713 (1969).
10. W. J. Moore, P. J. Lin-Chung, J. A. Freitas, Jr., Y. M. Altaiskii, V. L. Zuev, and L. M. Ivanova, Phys. Rev. B, **48**, 12289 (1993).
11. R. Kaplan, W. J. Moore, J. A. Freitas, Jr., Yu. M. Altaiskii, V. L. Zuev, and L. M. Ivanova, presented at ICSCRM'93, Washington, DC, 1993 (unpublished).
12. W. J. Moore, J. A. Freitas, Jr., Yu. M. Altaiskii, V. L. Zuev, and L. M. Ivanova, presented at ICSCRM'93, Washington, DC, 1993 (unpublished).
13. P. J. Dean, W. J. Choyke, and L. Patrick, J. Luminescence **15**, 299 (1977).
14. P. J. Dean, D. C. Herbert, D. Bimberg, and W. J. Choyke, Phys. Rev. Lett. **37**, 1635 (1976).

CHARACTERIZATION OF SiC LAYER FORMED BY C ION IMPLANTATION (ESR AND IR STUDIES)

Y. SHOW, T. IZUMI, M. DEGUCHI*, M. KITABATAKE* AND T. HIRAO*
Department of Electronics, Faculty of Engineering, Tokai University, 1117 Kitakaname, Hiratsuka, Kanagawa, 259-12, Japan
*Central Research Laboratories, Matsushita Electric, Industrial Co., Ltd., 3-4 Hikaridai, Seika, Soraku, Kyoto, 619-02, Japan

ABSTRACT

Characterization of C ion implanted silicon layers were performed by fourier transformation infrared (FT-IR) spectroscopy and electron spin resonance (ESR) methods. Microcrystalline β-SiC including amorphous Si are formed in the Si surface region by annealing at 1200 ℃ following hot (450 ℃) implantation. The ESR analysis revealed the presence of two kinds of defect centers in SiC layer formed by implantation, i.e. Si dangling bond (g=2.0060, ΔH_{pp}=6 Oe) in the amorphous Si and Si dangling bond with C atom neighbors (g=2.0032, ΔH_{pp}=3 Oe). Heating substrate during implantation prevents the formation of carbon clusters on the Si surface.

INTRODUCTION

SiC is an interesting semiconductor material because its wide band gap together with its thermal and chemical stability make it suitable for the fabrication of devices that can operate at high temperature and high radiation. One technique of the SiC formation is to implant a silicon wafer with a high dose of carbon ions [1, 2]. This technique has the advantage that SiC is able to be formed in the low temperature range as compared with CVD method. The structures of SiC formed by implantation strongly depends on the implantation temperature [3]. However, up to now very few investigations have been made into the effects of implantation temperature on the structural properties of the formed SiC films. In this paper, we report the characterization of SiC formed by low energy and high dose C ion implantation into silicon surface for low implantation temperature range.

EXPERIMENTAL

The specimens used in this study were made of p-type silicon with resistivity in the range of 1 - 10 Ωcm. Mass-separated carbon ions with 30 keV to 1×10^{17} - 5×10^{17}/cm^2 were implanted into the silicon substrates. The substrates were kept at room temperature (R.T.) or at 450 ℃ during implantation. The pressure of the chamber was 1×10^{-6} torr during C^+ ion implantation into the Si substrate. The average C^+ ion current density was 5 μA/cm^2. The samples were annealed in the temperature range of room temperature - 1200 ℃ in an argon atmosphere. Formation of Si-C bonds in ion implanted and annealed layer, was observed by FT-IR measurement at room temperature. The distribution of the implanted C atoms into the Si substrate was measured by Auger electron spectroscopy (AES). Moreover, defect structures were analyzed by an ESR measurement at room

Mat. Res. Soc. Symp. Proc. Vol. 339. ©1994 Materials Research Society

temperature. ESR measurements were performed using the X-band spectrometer. The g-value, line width (ΔH_{PP}) and signal intensity were determined using the signal of Mn^{2+} or DPPH as calibration reference.

RESULTS AND DISCUSSION

As-implanted state

Fig. 1 shows IR absorption spectra for <111> Si samples which were implanted with 30 keV C ions to a dose of $1\times10^{17}/cm^2$. The broad IR absorption spectra were observed at 730 cm^{-1} for Si implanted at room temperature and at 760 cm^{-1} for Si implanted at a substrate temperature of 450 ℃, respectively. The broad absorption spectrum at around 730 cm^{-1} originated from Si-C bonds, which were in a weak binding state within high dose C ion implanted layer. When the substrate temperature increased to 450 ℃, the peak position of the spectrum shifted to 760 cm^{-1} without increase of IR intensity. This result implies that hot implantation leads to the formation of tighter Si-C bonds in the Si surface than the R.T. implantation [4].

Fig. 2 shows the ESR signals of as-implanted samples. The g-value of the signals were 2.0046 for R.T. implantation and 2.0041 for hot implantation. These signals result from amorphous SiC formed in the implanted silicon surface layer. Shimizu reported the ESR signals observed from a-Si_XC_{1-X} films prepared by RF sputtering, and the g-value of the ESR signal is varied from 2.0057 at X=0 to 2.0028 at X=0.5 [5]. Furthermore, C. O'Raifertaigh et al reported that the g value shifted from 2.0037 to 2.0029, as the 200 keV C ion dose increased from 7.5×10^{17} to 2.3×10^{18} [6]. The observed ESR signal with g-value of 2.0041 and 2.0046, therefore, arises mainly from a dangling bond in a silicon-rich amorphous SiC layer formed by C ion implantation.

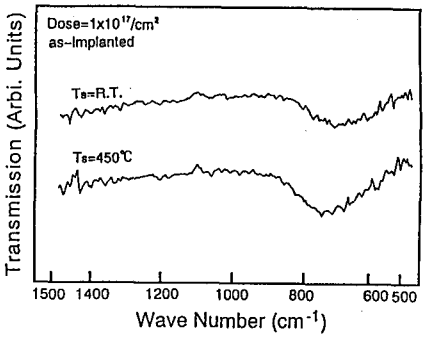

Fig. 1. Infrared absorption spectra of silicon implanted with $1\times10^{19}/cm^2$ at 30 keV. (T_S: substrate temperature)

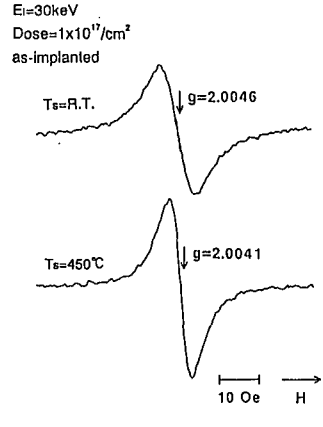

Fig. 2. ESR signals of as-implanted silicon.

Annealed state

When the samples used in Fig. 1 were annealed at 1200 ℃, the IR absorption peak shifted to 800 cm^{-1} with decreasing its full width at half-maximum (FWHM) as shown in Fig. 3(a) and (b). Moreover, the intensity of absorption spectrum of Fig. 3(b) is stronger than that of Fig. 3(a). This implies that loose Si-C bonds in C ion implanted layer are varied to tighter Si-C bonds and a crystalline SiC are formed in the implanted layer [7, 8]. Next, the defect structures of implanted layer were investigated by ESR measurement.

Fig. 4 shows the typical ESR signal for the R.T. and hot implanted samples annealed at 1200 ℃. While the signal of Fig. 4(a) is an unsymmetrical line shape, the ESR signal, which is identical with that of Fig. 4(b) is observed after thermal treatment at 400 ℃ in oxygen atmosphere as shown in Fig. 5. We decomposed the ESR signal of Fig. 4(b) into two kinds of ESR lines as shown in Fig. 6 using computer simulation. The ESR line with a g-value of 2.0060 in Fig. 6(a) is identical with the signal in the amorphous silicon that is known as the a-center [9]. The ESR line in Fig. 6 had a g-value of 2.0034, which arises from Si dangling bond with C atom neighbors in the SiC region formed by annealing at 1200 ℃ [10]. In general, the a-center created by ion implantation into silicon disappeared at annealing above 650 ℃ and implanted damaged layer is recrystallized. However, an amorphous silicon region remained stable in the implanted layer even after annealing at 1200 ℃ in this case.

From the above results, the formed β-SiC region seems to be a microcrystal with amorphous silicon clusters.

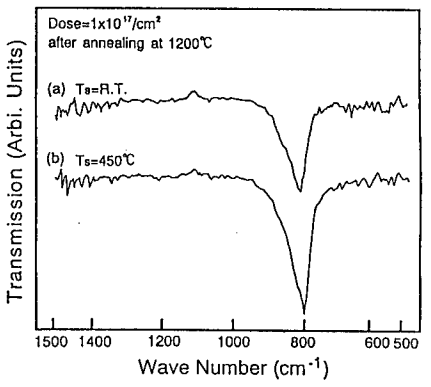

Fig. 3. Infrared absorption spectra for the samples after annealed at 1200 ℃.

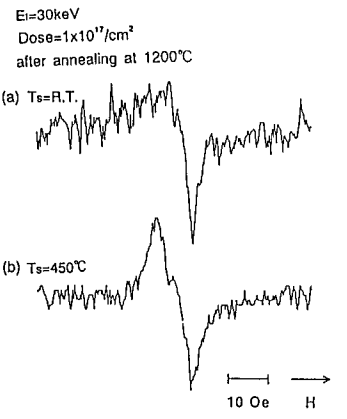

Fig. 4. ESR signals for the samples after annealed at 1200 ℃.

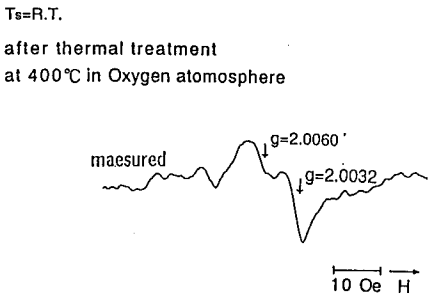

Fig. 5. ESR signal for the sample (used in Fig. 4(a)) after thermal treatment at 400 ℃ in oxygen atmosphere.

Fig. 7 shows the depth profiles of the C and Si atoms measured by Auger electron spectroscopy (AES) for the as-implanted and the annealed samples. The distribution of the C atoms coincided with the Gaussian distribution predicted from LSS (Lindhard, Scharff and Schiott) theory. The concentration of C atoms in the implanted layer reached the maximum value of 1×10^{22} atoms/cm^3 at around 1000 Å from the substrate surface. The C atoms of R.T. implantation diffused toward the surface much more than those of hot implantation.

The factors affecting the ESR signal by the thermal treatment in oxygen atmosphere could be as follows: The weak Si-C bonds were formed by C ion implantation into Si at R.T. The implanted C atoms diffused toward the surface to form a carbon cluster together with formation of β-SiC.

Carbon cluster, including with amorphous carbon (a-C) and graphite, which reacted the oxygen atoms, removed from the surface as carbon monoxide etc. by thermal treatment at 400 ℃ in oxygen atmosphere [11]. Only the microcrystalline β-SiC remained in C ion implanted layer. In contrast, the C atoms of hot implantation hardly diffuse toward the surface and prevent the formation of carbon clusters in the surface region after annealing.

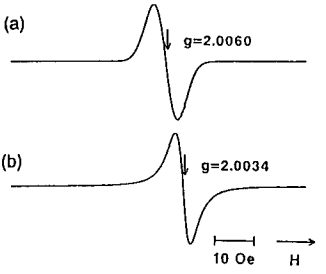

Fig. 6. The ESR signal of Fig. 4(b) was decomposed into two kinds of ESR lines using computer simulation.
(a) Si-dangling bonds in the amorphous layer created by implantation (a-center, g=2.0060).
(b) Si-dangling bond with C atom neighbors (g=2.0034).

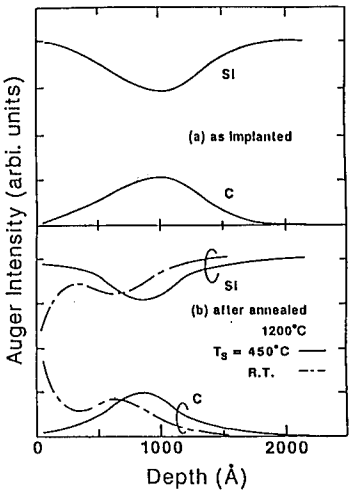

Fig. 7. AES depth profiles of C and Si atoms for as-implanted and annealed sample.

High-dose implanted Si surface state

With increasing C^+ ion dose to $5\times10^{17}/cm^2$, a symmetrical ESR signal with g=2.0032 was observed for hot implanted sample as shown in Fig. 8(a). However, the a-center is not observed. Intensity of the ESR signal decreased by annealing at 1200 ℃ in argon atmosphere. Moreover, the IR absorption spectrum at 800 cm^{-1} and the decreased FWHM were also observed for the annealed samples. At the dose of 5×10^{17} ions/cm^2, the maximum concentration of C atoms in Si was 5×10^{22} atoms/cm^3, which correspond to a C/Si atomic ratio of 1. These results suggest that the crystalline SiC was formed with annealing at 1200 ℃ and high C^+ ion dose of hot implantation.

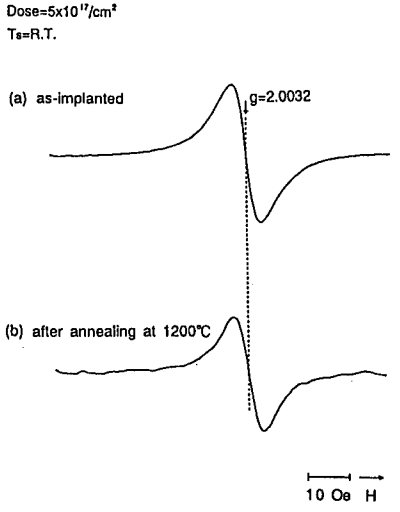

Fig. 8. ESR signals for as-implanted and annealed samples. The 30 keV C ion with $5\times10^{17}/cm^2$ were implanted into Si substrate.

SUMMARY

We have studied the characterization of β-SiC formed by R.T. and hot implantation into Si surface using IR and ESR measurements. The silicon surface layer changed into Si-rich amorphous SiC for as-implanted state. However, microcrystalline β-SiC with amorphous Si is formed in the Si surface region after annealing at 1200 ℃. Furthermore, amorphous carbon on the SiC layer is removed by thermal treatment at 400 ℃ in the oxygen atmosphere. The ESR analysis revealed the presence of two kinds of defect centers in the SiC layer formed by C ion implantation, that is Si dangling bond,which is known as the a-center (g=2.0060) of amorphous silicon and Si dangling bond with C atom neighbors (g=2.0032).

The authors wish to thank Mr. M. Iwase and Mr. N. Arai for useful discussions and Mr. M. Takahashi, Miss M. Sugita and Mr. A. Aizawa for experimental supports.

REFERENCES

[1] J. A. Borders, S. T. Picraux and W. Beezhold; Appl. Phys. Lett., **18**, 509(1971)
[2] M. Deguchi, A. Yoshida, M. Kitagawa and T. Hirao; Jpn. J. Appl. Phys., **29**, L1493(1990)
[3] P Martin, B. Baudin, M. Dupuy, A. Ermolieff, M. Olivier, A. M. Papon and G. Rolland; J. Appl. Phys., **67**, 2908(1990)
[4] M. Deguchi, M. Kitabatake, T. Hirao, N. Arai and T. Izumi; Jpn. J. Appl. Phys., **31**, 343(1992)
[5] T. Shimizu, M. Kumeda and Y. Kiriyama; Solid. State. Commun., **37**, 699(1981)
[6] C. O'Raifertaigh, R. C. Barklie, K. Reeson and P. L. F. Hemment; Semicond. Sci. Technol., **5**, 78(1990)
[7] W. G. Spitzer, D. A. Kleinman and C. J. Frosch; Phys. Rev., **113**, 127(1959)
[8] W. G. Spitzer, D. A. Kleinman and C. J. Frosch; Phys. Rev., **113**, 133(1959)
[9] B. L. Crowder, R. S. Title, M. H. Brodsky and G. D. Pettit; Appl. Phys. Lett., **16**, 205(1970)
[10] G. W. Wagner, B. Na and A. Vannice; J. Phys. Chem., **93**, 5061(1989)
[11] H. Minagawa, R. O. Vina, T. Kadowaki, S. Mizuno, H. Tochihara, K. Hayakawa; Jpn. J. Appl. Phys., **31**, L1707(1992)

INVESTIGATION OF STRUCTURAL DEFECTS IN 4H SiC WAFERS

M. TUOMINEN[1,2], R. YAKIMOVA[1], R.C. GLASS[1], T. TUOMI[3] AND E. JANZÉN[1]
1 Department of Physics and Measurement Technology, Linköping University, Sweden
2 Outokumpu Semitronic AB, Bromma, Sweden
3 Optoelectronics Laboratory, Helsinki University of Technology, Finland

ABSTRACT

For high-power device applications SiC has better physical and electronic properties than the traditional semiconductor materials Si and GaAs. In this work, structural defects of 4H SiC wafers have been studied and partly compared with results from a previous study of 6H material. Optical microscopy, scanning electron microscopy, high-resolution X-ray diffraction and synchrotron X-ray topography were used for structural studies of 4H SiC. Optical micrographs show micropipes and larger specific defects - tubes and cracks. X-ray rocking curve peaks are broad and split revealing the mosaicity of the material. Synchrotron X-ray topographs show areas having a large number of defects, images of cracks and micropipes, and misorientated regions close to the micropipes.

INTRODUCTION

SiC has different properties depending on the polytypic structure. For power applications 4H may be preferred to 6H because of its higher mobility and theoretically higher breakdown electric field. Commercially available 4H SiC material is grown with a seeded modified-Lely technology in a similar manner as 6H wafers, and may therefore contain similar structural variations.

In this work, by using several non-destructive structure sensitive techniques, an attempt is made to reveal specific imperfections of the crystal structure of 4H SiC material. We have studied modified Lely grown 4H SiC wafers, with a (0001) basal plane orientation. The wafers were 1 3/16 inch in diameter, from Cree Research, Inc., Durham, NC, USA. In addition, Lely grown 4H SiC platelets with the same basal plane were studied to compare with the same material but different sublimation growth process.

EXPERIMENTAL TECHNIQUES

The sample surface was investigated by means of an optical microscope and a scanning electron microscope (SEM). The samples were examined with a Nikon Metallurgical Microscope in the reflection mode. Nomarski contrast and polarization were used. SEM pictures were taken with Cambridge Instruments Stereoscan MK3 microscope. The accelerating voltage was 15 kV and the working distance was 10 mm. The samples were only slightly tilted and pictures were produced in the secondary electron mode.

Synchrotron white beam X-ray topography [1] was applied to make section and large-area transmission topographs. Reflection topographs were taken as well. In section topography the sample was exposed to the beam at an angle of 26° between incident beam and the sample surface. The beam size was limited with a horizontal slit having a typical height and width of 15 μm and 5 mm, respectively. Transmission Laue patterns were imaged on a high resolution film behind the sample. In the large-area topography, sample surfaces were orientated perpendicularly to a 3x3 mm^2 incident beam. Finally, in reflection mode the sample surface was placed at an angle of 1° to the incident beam, while the beam spot size varied up to 12 mm in width.

Mat. Res. Soc. Symp. Proc. Vol. 339. ©1994 Materials Research Society

High resolution X-ray diffraction measurements were carried out with a Philips MRD 1880/HR equipped with a 3 kW Cu X-ray source. Rocking curves (ω and $2\theta/\omega$) and high-resolution topographs were exploited. The measurement technique has been described elsewhere [2].

RESULTS AND DISCUSSION

Initially, the samples were examined by optical microscopy in the reflection mode. In the modified Lely samples cracks and micropipes were found, some of them being visible to the naked eye. Since the material is transparent, it was possible to follow micropipes through the whole wafer. We observed that some holes did not go through the sample but were connected to each other forming a tube in the basal plane. These tubes were located at different depths in the material and the holes they connected did not necessarily have an orientation parallel to the c-axis. In the Lely samples no such defects were found, however, some did contain basal plane defects inside the sample.

Similar results were obtained from SEM studies. In the modified Lely samples cracks, micropipes, holes and pits were observed. Often the defects, except long cracks, were gathered in certain areas surrounded by a boundary containing holes and pits (Figure 1). The dimensions of these areas were of the order of millimeters, while individual hole diameters were either tens of micrometers or 1 to 2 μm, the average density being 10^2-10^3 cm^{-2}. The diameter of the pits observed was about 0.5 μm.

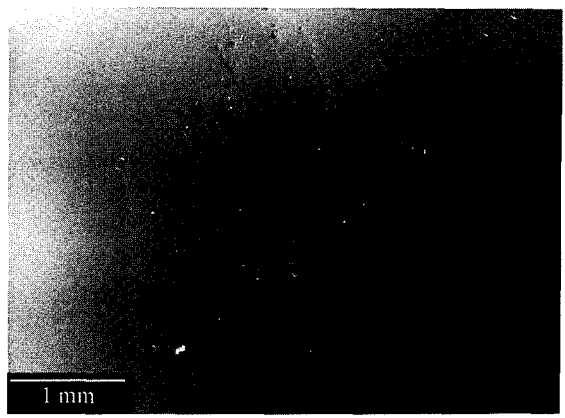

Figure 1 SEM image of defect clustering in modified Lely grown 4H SiC.

Cracks from a half mm to 2 mm long were observed. It seemed that the cracks were always associated with hexagonally shaped holes, which we believe are micropipes (Figure 2). Only a few cracks were found in the middle part of the wafer but they could frequently be found at the edges. By comparison, the surface of Lely samples appeared to be free of structural defects. This is believed to result from the orientation of the basal plane defects reducing their visibility on the surface.

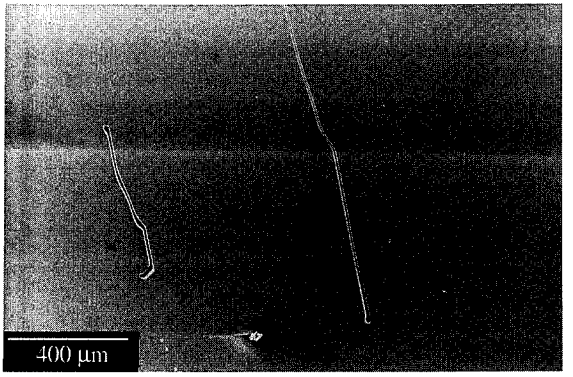

Figure 2 SEM image of cracks in modified Lely grown 4H SiC.

Figure 3a shows a synchrotron topograph of one 4H SiC Lely grown sample. In the picture a damaged area having high dislocation density and a group of voids is seen. These particular areas were in contact with the graphite crucible where the platelets nucleated. Further away from the defect area the material has higher quality, but dislocation networks can still be seen in the section topographs (Figure 3b). In transmission and reflection topographs these defects image as black strain contrast on the grey background image. In some topographs taken outside of the damaged area one can observe fringes due to the interference of wave fields inside the material. These Pendellösung fringes indicate that material quality is very high.

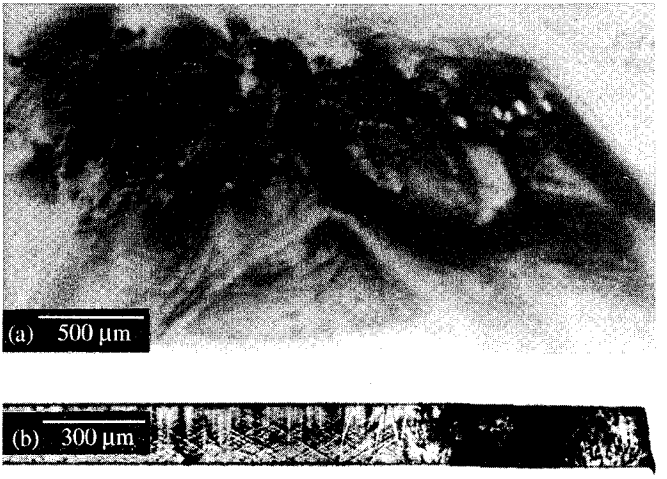

Figure 3 (a) Synchrotron X-ray reflection topograph taken from a damaged area of Lely grown 4H SiC platelet, (b) Section topograph showing the damaged area and the dislocation network.

The synchrotron X-ray topographs taken from the modified Lely grown sample are more complicated than the pictures taken from the Lely samples due to a relatively higher defect density giving rise to dark kinematical contrast. However, micropipes are clearly seen in the reflection picture as white circles or ellipses because the hollow cores do not diffract any of the beam (Figure 4).

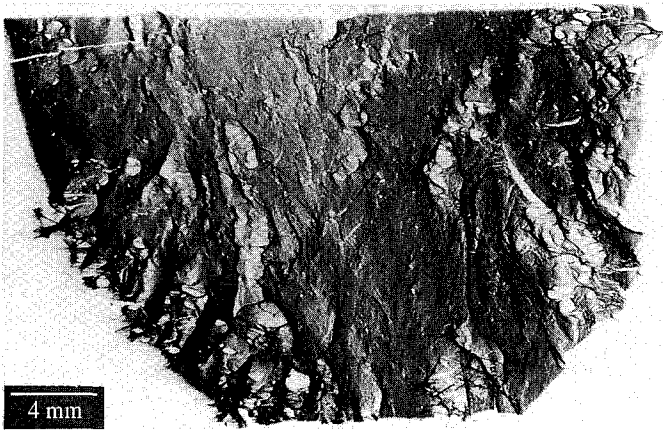

Figure 4 Synchrotron X-ray reflection topograph of modified Lely 4H SiC wafers.

Similarly, micropipes with a diameter larger than the resolution of the film are seen as a white spot in transmission topographs, and they can easily be recognized by the black strain contrast, i.e. an increased X-ray intensity, arising in the crystal around them. In the section topograph (Figure 5), where the image is a sum of through and near surface strain effects, the micropipes image as a black stripe going through the wafer, while the crack image is white. Occasionally, a white spot is visible in the middle of the black stripe as the positive and negative strain fields are imaged on either side of the micropipe. In the section topographs the effect of misorientation is clearly seen as a bend in the photo image. A perfect crystal images as a straight line, while misoriented regions reflect the beam to different places and bend the stripe. In our samples the bending starts, where a micropipe is observed.

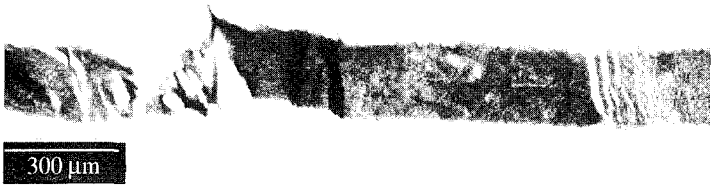

Figure 5 Synchrotron X-ray section topograph of modified Lely 4H SiC wafer.

In the transmission large-area topograph, a micropipe is seen as a large dark spot appearing in several different planar reflections. There are also black stripes emerging from the spot, which are thought to be glide dislocations. In these topographs, very little strain contrast is associated with the cracks, which suggests that these defects arise from strain relaxation. The cracks appear as a white area in the pictures.

In the rocking curves taken of the modified Lely samples mosaicity is observed as a splitting of the ω rocking curve (Figure 6). The crystal consists of domains which are slightly misoriented to each other. These domains satisfy the Bragg conditions at slightly different orientations to one another, and the broad peak is a superposition of their individual diffraction peaks. This is illustrated by rocking curves taken with different beam spot sizes. As one can see, the main peak intensity does not increase very much compared to the width of the curve even with increasing spot size (and concomitantly increasing domain coverage). It is to be noticed that the shape of rocking curves taken from defective areas and defect free areas, are similar. Additional evidence

can be obtained from the diffraction topographs, which are images of the diffracted beam. Topographs corresponding to different peaks in the rocking curve image different areas. Similar phenomenon has been observed in modified Lely grown 6H SiC wafers [2].

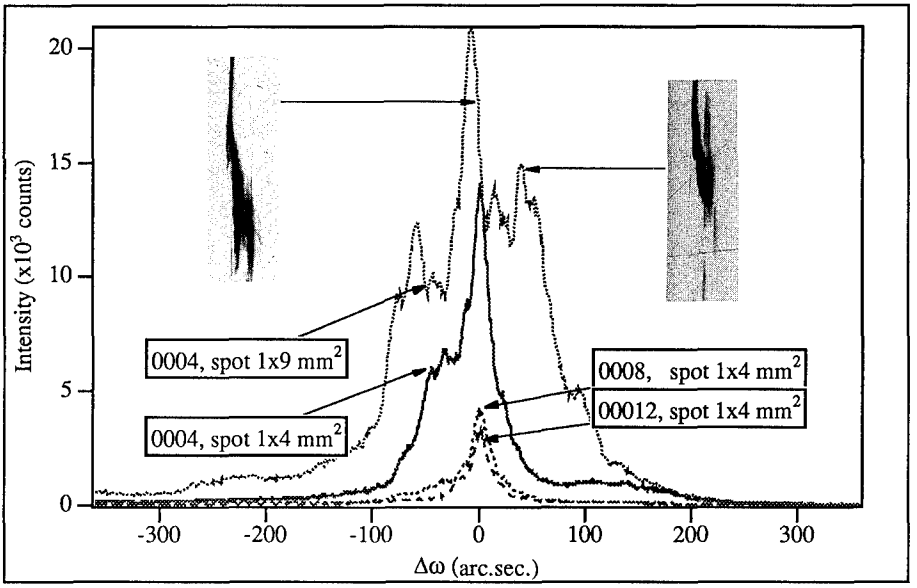

Figure 6 Rocking curves and the (0004) diffraction topographs of modified Lely wafer.

The rocking curves taken from the good quality region of the Lely samples show sharp peaks with higher intensity than typically seen in modified Lely sample rocking curves. However, focusing the beam on the distorted part of the crystal one can see similar diffraction peak splitting as in the modified Lely material.

Rocking curves (ω and $2\theta/\omega$) were studied with (0004, 0008 and 00012) reflections. Comparing the ratios of the experimental full widths at half maximum, W_{hm}, with the theoretical values one can draw additional information about the defect structure within the crystal [3,4]. For the modified Lely material, the values of the W_{hm} ratios obtained from the RC($2\theta/\omega$) for the same reflections are smaller than the theoretical ones for randomly distributed dislocations of high density and suggest most probably a mosaic domain structure (Table I). Similar results are obtained for the rocking curves taken from the damaged area in the Lely sample.

Table I Theoretical and experimental values of the (00012, 0008, 0004) reflection W_{hm} ratios.

	W_{hm12}/W_{hm4}	W_{hm12}/W_{hm8}	W_{hm8}/W_{hm4}
Randomly distributed high density dislocations	7.0	3.0	2.3
Mosaic domain structure with dislocation boundaries	2.4	2.0	1.2
Experimental	3.6	2.4	1.5

The comparison of the ω rocking curve W_{hm} values for different reflections shows that they become smaller as the 2θ angle increases and the beam penetrates deeper into the sample. A possible explanation is that finally the beam hits only one domain at the higher order reflection. However in the highly distorted area of the Lely sample W_{hm} for the (00012) reflection is larger than for the (0008) reflection, which is consistent with the synchrotron X-ray topographic images. This "mosaicity" in the Lely sample also reduces the intensity of the reflection compared to the better areas in the same sample but still this intensity is of the same order of magnitude as recorded in the modified Lely sample.

CONCLUSIONS

In conclusion, by using a variety of structure sensitive techniques we have been able to obtain independent evidence of some specific structural defects in 4H SiC. Several types of defects have been observed in the modified Lely 4H SiC wafers: micropipes, pits, basal plane tubes, dislocation lines, strains and cracks. Furthermore, from the high-resolution X-ray diffraction measurements it appears that mosaicity with domain misorientation is a dominant imperfection in the modified Lely grown 4H wafers.

A comparison has been made with the crystal structure of Lely grown platelets. The results obtained suggest that the growth direction plays an important role in crystal defect formation. The investigation of structural defects in 4H SiC wafers has shown some similarity with the 6H material as far as micropipes and mosaicity are concerned.

ACKNOWLEDGEMENTS

The authors wish to thank Dr T. Wroblewski for providing help during the measurements at HASYLAB-DESY in Hamburg, Germany, L.O. Björketun for SEM measurements at Linköping University and Dr I. Nikitina for providing information about differential X-ray diffraction technique. Financial support for this work was provided by the Swedish Board for Industrial and Technical Development (NUTEK) / Asea Brown Boveri (ABB) Power Device Program, the Swedish Council for Engineering Sciences (TFR), NUTEK, and the NUTEK / Swedish Natural Science Research Council (NFR) Material Consortium on Thin Film Growth.

REFERENCES

1. T. Tuomi, K. Naukkarinen and P. Rabe, Phys. Stat. Sol. (a) **25**, 93 (1974).

2. R.C. Glass, L.O. Kjellberg, V.F. Tsvetkov, J.E. Sundgren and E. Janzén, J. Cryst. Growth **132**, 504 (1993).

3. I.P. Nikitina, R.C. Glass, E. Janzén, N.B. Guseva, A.A. Mal'tsev, 1994 (unpublished).

4. R.N. Kjutt, R. Shol'ts, S.S. Ruvimov, T.S. Argunova, A.A. Budza, S.V. Ivanov, P.S. Kop'ev, L.M. Sorokin, M.P. Scheglov, Fizika Tv. Tela **35**, 724 (1993).

X-RAY TOPOGRAPHIC STUDIES OF DEFECTS IN PVT 6H-SiC SUBSTRATES AND EPITAXIAL 6H-SiC THIN FILMS

S. Wang,* M. Dudley,* C.H. Carter, Jr.,** and H.S. Kong **
* Dept. of Materials Science & Engineering, SUNY, Stony Brook, NY 11794-2275;
**Cree Research, Inc., 2810 Meridian Parkway, Durham, NC 27713.

ABSTRACT

Synchrotron white beam X-ray topography has been used to characterize defect structures in (0001) 6H-SiC substrates grown by the sublimation physical vapor transport (PVT) technique as well as in 6H-SiC epitaxial thin films grown on these substrates. Defects revealed in 6H-SiC substrates include super screw dislocations and basal plane dislocations. It has been found that back-reflection topographs are particularly suitable for imaging such super screw dislocations as well as basal plane dislocations whenever transmission topography is not applicable. Epitaxial 6H-SiC thin films grown on such (0001) substrates (tilted a few degrees towards the a-axis) were also examined by using surface sensitive grazing Bragg-Laue topography. It has been shown that super screw dislocations were replicated in the epitaxial thin films but no basal plane dislocations were revealed in the thin films. Results from various topographic techniques are discussed.

INTRODUCTION

SiC has attracted much attention as a wide bandgap semiconductor in recent years from both fundamental research and industrial research and development points of view [1, 2]. Although the crystalline perfection of commercial 6H-SiC single crystal wafers is adequate for the fabrication of many types of devices, defect densities, primarily dislocation densities, in these wafers are still high, ranging from 10^3 to 10^4 cm^{-2}. Among the defects present in the crystals, the so-called "micropipes" [3, 4] running approximately parallel to the ⟨0001⟩ direction in PVT 6H-SiC crystals are considered to be most detrimental to device performance. Characterization of these "micropipes" as well as other structural defects in PVT SiC single crystals has been carried out by optical microscopy, etch-pit techniques [4] and transmission electron microscopy (TEM) [5], with the two latter techniques being destructive in nature.

We have previously reported [6] preliminary results of the characterization of defect structures in PVT 6H-SiC (0001) single crystal wafers primarily obtained by using synchrotron white beam X-ray topography (SWBXT) as a non-destructive technique [7, 8] and provided evidence that the "micropipes" are actually Frank-type open core super screw dislocations [9]. In the present paper, results from X-ray topographic studies carried out mainly on standard, commercially available (0001) 6H-SiC wafers as well as epitaxial 6H-SiC thin films are presented. Recently, a back-reflection diffraction geometry was developed for SWBXT, which has been found suitable for mapping the super screw dislocations in the standard (0001) wafers. Since the active regions of most semiconductor devices, such as diodes and transistors, are located within a very small depth (usually of the order of a few microns) beneath the wafer surfaces, the study of defects in the near-surface regions of wafers (with or without epitaxial layers) is very important for achieving desired device performance. To this end, defects in 6H-SiC epitaxial thin films grown on 6H-SiC (0001) wafers were exclusively imaged by employing a surface sensitive Bragg-Laue diffraction geometry.

Mat. Res. Soc. Symp. Proc. Vol. 339. ©1994 Materials Research Society

EXPERIMENTAL

The 6H-SiC substrates are standard (0001) wafers of one inch in diameter and about 300μm in thickness cut from crystal boules. The wafers were in fact cut a few degrees off the exact (0001) plane towards the a-axis to facilitate homo-epitaxy of 6H-SiC. Most of the substrate wafers examined were polished on one side and lapped on the other side, which prevents one from using the transmission geometry in X-ray topographic studies because strong contrast associated with the strains due to lapping superimposes with that associated with other crystal lattice defects. As a result, the reflection geometry has to be employed. Among the available reflection techniques, the grazing incidence Bragg-Laue geometry using synchrotron white X-rays [10] is particularly suitable for imaging defects in the near-surface region. The penetration depth of the X-rays in this technique is varied by selecting different grazing incidence angles for a given reflection at a given wavelength. Defects in epitaxial thin films can, therefore, be exclusively imaged by making the X-ray penetration depths less than the thickness of the epitaxial layer.

In addition, a back-reflection geometry, rarely used in X-ray diffraction topographic techniques, was developed for the synchrotron white beam aiming to achieve a better spatial resolution for imaging the super screw dislocations or "micropipes" as well as other defects in the SiC wafers whenever transmission X-ray topography is not applicable.

RESULTS

X-ray back-reflection topographs were recorded from 6H-SiC wafers, an example of which is shown in figure 1(a) (principal reflection **g**=00036, λ=0.98 Å). On the topograph, the

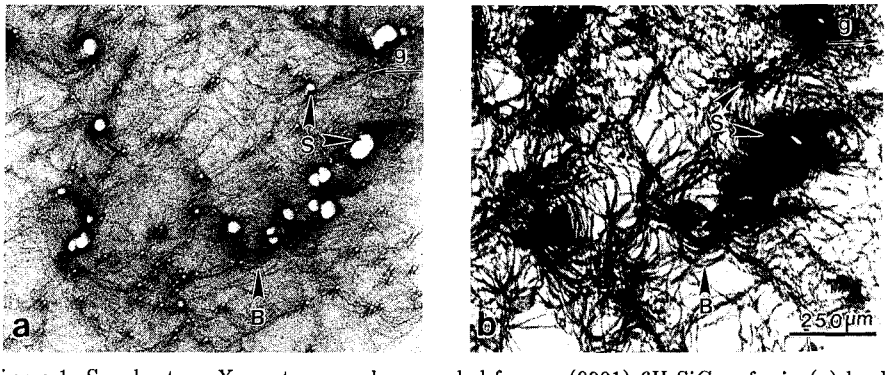

Figure 1. Synchrotron X-ray topographs recorded from a (0001) 6H-SiC wafer in (a) back-reflection (principal **g**=00036 and λ=0.98 Å) and (b) transmission (**g**=$1\bar{1}01$, λ=0.78 Å), respectively, showing super screw dislocations (**S**) as well as basal plane dislocations (**B**).

circular white features of various diameter correspond to super screw dislocations. Some of these super screw dislocations, the ones exhibiting large circular white contrast features on the back-reflection topograph, were observed, using stereo optical microscopy, as "micropipes" running approximately parallel to the wafer surface normal, i.e. ⟨0001⟩. The larger the "micropipe" diameter (proportional to the square of the magnitude of the Burgers vector of the super screw dislocation associated with it in thermodynamic equilibrium [9]) observable through stereo microscopy, the larger the diameter of the circular white contrast

feature on the corresponding back-reflection topograph. The faint, dark lines connecting the circular features, **B**, on the back-reflection topograph are associated with dislocations lying in the basal plane. A transmission topograph ($\mathbf{g}=1\bar{1}01$, λ=0.78 Å) recorded from the same area of the wafer (polished on both sides) is also shown in figure 1(b), where the dark dots of various sizes correspond to the super screw dislocations, e.g. the one indicated by **S** on both topographs, and the linear features comprising a network are associated with basal plane dislocations.

Back-reflection topographs were also recorded from those wafers polished only on one side. An example is shown in figure 2(a) (principal reflection $\mathbf{g}=00036$ and λ=0.98 Å). Apparently, there are some broad, dark line features (e.g. indicated by **L**) associated with

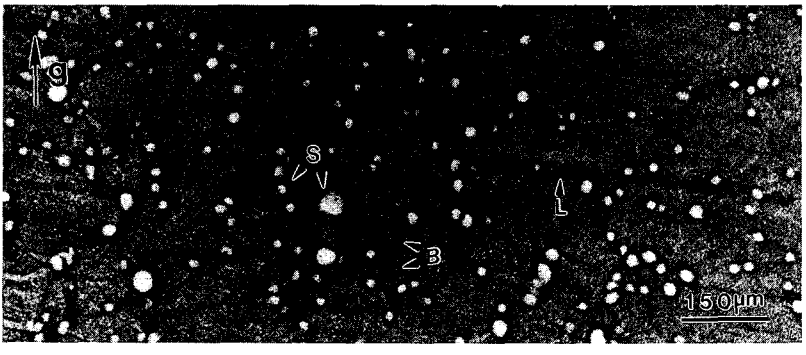

Figure 2. Back-reflection topograph (principal reflection $\mathbf{g}=00036$, λ=0.98 Å) recorded from a (0001) 6H-SiC wafer polished only on one side showing that contrast associated with lapping marks (**L**) does not affect contrast associated with both super screw dislocations (**S**) and basal plane dislocations (**B**).

strains resulting from the lapping marks on the backside of the wafer. However, super screw dislocations as well as some basal plane dislocations were clearly imaged, even in the regions where the contrast associated with the lapping marks superimposes on the contrast associated with the dislocations. This is in contrast to the situation in transmission topography for wafers polished on one side only, where contrast features due to lapping marks are much more extensive and hence overwhelm other features such as dislocation images, making transmission topographs effectively unusable for such standard commercial SiC wafers.

X-ray topographs were also recorded in the grazing incidence Bragg-Laue geometry from the 6H-SiC substrate wafers. An example of such a reflection topograph from a 6H-SiC substrate wafer is shown in figure 3(a), where $\mathbf{g}=11\bar{2}6$, λ=1.10 Å and the X-ray penetration depth (absorption depth) is 5.6 μm. The elliptical white features on the topograph are associated with super screw dislocations and the faint, dark lines connecting the elliptical white features are associated with basal plane dislocations. The X-ray topograph shown in figure 3(b) was recorded from the same region of the wafer under the same diffraction conditions as that of the topograph shown in figure 3(a) after a 6H-SiC epitaxial layer of about 6 μm thick was deposited on it. Since the penetration depth of X-rays for this topograph was also controlled to about 5.6 μm, defect structures in the epitaxial layer were revealed exclusively. By comparing these two topographs, one can easily find that each of

the super screw dislocations observed in the substrate were replicated in the epitaxial layer, i.e. the elliptical white features on both topographs. However, the basal plane dislocations in the near-surface region of the substrate, the dark lines on the topograph in figure 3(a),

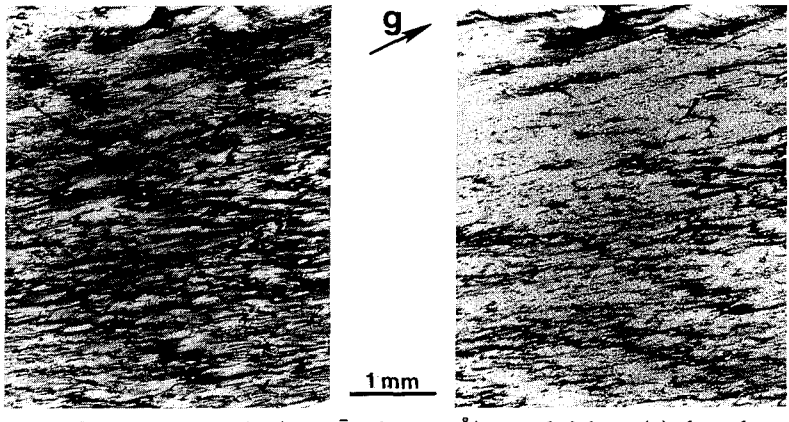

Figure 3. Reflection topographs ($\mathbf{g}=11\bar{2}6$, $\lambda=1.10$ Å) recorded from (a) the substrate and (b) the epitaxial layer, showing that super screw dislocations (the elliptical white features) in the substrate were replicated in the epitaxial layer and basal plane dislocations (the faint line features) were not observed in the epitaxial layer.

were not observed on the topograph recorded from the epitaxial layer shown in figure 3(b). The elimination of basal plane dislocations in the epitaxial thin films is certainly significant and highly desirable.

DISCUSSION

Back-Reflection Topography

In a previous report [6], a ray-tracing topography technique was used to show that there are significant crystal lattice rotations around "micropipes" and the senses of such lattice rotations are opposite on the two diametrically opposed sides of a "micropipe", indicating that they have are significant lattice strains associated with them. Growth spirals were routinely observed using Nomarski optical microscopy on as-grown surfaces of PVT 6H-SiC boules and holes of a tenth of a micron to a few microns in diameter were observed at the centers of the growth spirals using scanning electron microscopy (SEM), both of these features always correlating with the positions of the topographic images of the "micropipes". This evidence suggests that the so-called "micropipes" are indeed Frank-type super screw dislocations with open cores. It is also evident that there were many super screw dislocations of various smaller magnitudes of Burgers vector that had no visible (via optical microscopy or SEM) open cores associated with them. Device yield results indicate that the super screw dislocations with smaller Burgers vectors are not detrimental to device performance. The back-reflection topographs presented here not only support the conclusions drawn earlier, but also clearly indicate that the majority of the super screw dislocations actually have the same magnitude of Burgers vector, most probably equal to the lattice parameter c, simply because the diameters of the majority of the circular white features on the back-reflection

topographs shown, which are proportional to the lattice strains and hence proportional to the magnitudes of the Burgers vectors of the super screw dislocations, are almost exactly the same. The nearly circular symmetry of contrast features associated with "micropipes" on the back-reflection topographs reflects the cylindrical symmetry of the screw dislocation displacement field. It should be pointed out, however, that the distortion of some circular white features on the back-reflection topographs, particularly the larger ones, is due to the interaction of strains between the super screw dislocations and the basal plane dislocations around them and between adjacent super screw dislocations.

While back-reflection Laue geometry is routinely used to determine crystal orientations, it has rarely been used for defect imaging using X-ray topography. From the topographs presented in the previous section, one can see that the spatial resolution of back-reflection topographs is better than that of both transmission topographs and "forward" reflection topographs, judging from the image widths of basal plane dislocations. Since back-reflection topographs are usually recorded with Bragg angles of about 80 degrees or more, and the diffracted beams exit almost normal to the wafer surface, such topographs have little geometric distortion, while "forward" reflection topographs often require sacrifices to be made of spatial resolution in order to correct the geometric distortion of the images. Moreover, back-reflection topographs are superior for imaging super screw dislocations in (0001) 6H-SiC wafers because the images associated with super screw dislocations are more well-defined than that in other geometries and the magnitudes of super screw dislocations Burgers vectors are reflected directly by the diameters of the circular white features.

Defect Reduction in Epitaxial Thin Films

Although super screw dislocations in the SiC substrates examined were found to be replicated in the epitaxial thin films, no growth spirals were observed to be associated with the surface intersections of the super screw dislocations on the as-grown surfaces of the epitaxial thin films. However, triangular-shaped growth features were often observed at these surface intersections. The absence of observable spirals is believed to be due to fact that the step density on the as-grown vicinal surfaces of the epitaxial thin films resulting from the off-cut of the substrates away from the (0001) plane (a few degrees towards the a-axis) is much higher than that of the vicinal hill around a screw dislocation so that spirals developed around super screw dislocations during epitaxial growth merge with steps resulting from the off-cut. In fact, spirals can only be observed at regions of as-grown surfaces where the local surface orientations are very close with respect to the (0001) plane (on the order of a tenth of a degree). Recently, with controlled etching of (0001) 6H-SiC wafers, Takahashi [11] managed to show that there were spirals around many etch-pits, small and large, that mark the emergence points of "micropipes" or super screw dislocations on the etched wafer surfaces.

The replication of super screw dislocations in the epitaxial thin films grown on (0001) substrates is inevitable because such super screw dislocations are approximately parallel to the growth direction and therefore cannot grow out of the crystal. The absence of basal plane dislocations in the thin films may be explained based on the surface relaxation mechanism for generation of basal plane dislocations reported earlier [6], in which basal plane dislocations, slip dislocations, are believed to be generated by super screw dislocations through surface relaxation during the PVT growth process at high temperatures at which the yield stress of the crystals is very low. In the epitaxial growth of thin films, however, the growth

temperatures are at least several hundred degrees lower than that for PVT bulk 6H-SiC crystal growth and hence the yield stress of SiC crystals is higher, so that the stress due to surface relaxation is not sufficient to generate basal plane dislocations.

CONCLUSIONS

Dislocations in commercial 6H-SiC (0001) substrate wafers as well as in epitaxial thin films were imaged and studied by SWBXT techniques. Back-reflection topography using a synchrotron white beam was developed for imaging defects in crystal wafers polished only on one side. It was found that back-reflection topographs were especially suitable for imaging super screw dislocations. Epitaxial 6H-SiC thin films grown on the substrates were examined using a surface-sensitive grazing incidence Bragg-Laue reflection technique, in which X-ray penetration depths were reduced to less than the thicknesses of the epitaxial layers so that defects in the epitaxial layers could be exclusively imaged. Preliminary results showed that super screw dislocations in the substrates were replicated in the epitaxial layers whereas basal plane dislocations, present in the substrate, were not observed in the epitaxial layers. The absence of basal plane dislocations in thin films is attributed to the fact that the temperatures for epitaxial growth of 6H-SiC thin films are at least several hundred degrees lower than that for PVT bulk 6H-SiC crystals, so that the stress due to surface relaxation is not sufficient to exceed the yield stress and to generate basal plane dislocations.

ACKNOWLEDGMENTS

Research supported by NIST through the Advanced Technology Program via Cree Research, Inc. and by ARO (contract monitor Dr. John T. Prater). Topography carried out at the Stony Brook Synchrotron Topography Facility, Beamline X-19C at the NSLS, supported by DOE.

REFERENCES

[1] P.A. Ivanov and V.E. Chelnokov, Semiconductor Science and Technology, **7**, 863 (1992).

[2] J.W. Palmour, J.A. Edmond, H.S. Kong, and C.H. Carter, Jr., Physica **B, 185**, 461-465 (1993).

[3] G. Ziegler, P. Lanig, D. Theis and C. Weyrich, IEEE Trans. Electron. Devices **ED-30**, 277 (1983).

[4] H.M. Hobgood, J.P McHugh and R.H. Hopkins, presented at International Conference on SiC and Related Materials-1993, Wachington D.C., November 1993.

[5] J.W. Yang, Ph.D. Thesis, Case Western Reserve University (1993).

[6] S. Wang, M. Dudley, C. H. Carter, Jr., D. Asbury and C. Fazi, in *Applications of Synchrotron Radiation Techniques to Materials Science*, D.L. Perry, N.D. Shinn, R.L. Stockbauer, K.L. D'Amico, and L.J. Terminello (Eds.), Mat. Res. Soc. Symp. Proc., **307**, 249 (1993).

[7] T. Tuomi, K. Naukkarinen, and P. Rabe, Phys. Status Solidi, **A 25**, 93-106 (1974).

[8] M. Hart, J. Appl. Crystallogr., 8, 436 (1975).

[9] F.C. Frank, Acta Cryst., 4, 497 (1951).

[10] G.-D. Yao, M. Dudley and J. Wu, X-Ray Sci. Tech. 2, 195 (1990).

[11] J. Takahashi, M. Kanaya and Y. Fujiwara, J. Cryst. Growth, **135**, 61-70 (1994).

SOLID-STATE NMR STUDIES OF THE BONDING STRUCTURE OF DIAMONDLIKE AMORPHOUS CARBON FILMS

SUSAN M. HOLL*, ROBERT D. JOHNSON*, VLAD. J. NOVOTNY*, JEFFREY L. WILLIAMS**, CATHERINE E. CALEY**, MARK HOINKIS**, and ROBERT E. JONES**

* IBM Research Division, Almaden Research Center, 650 Harry Road, San Jose, CA 95120
** IBM Corporation, Storage Systems Division, 5600 Cottle Road, San Jose, CA 95193

ABSTRACT

Amorphous carbon films are (a-C:H) of interest because of their useful physical properties. They are extremely hard and chemically inert, resisting degradation by both acids and alkalis. They are insoluble and can be conformably coated onto virtually any substrate. These properties make the films ideal protective coatings on magnetic disks and tools. We have studied several thin (one to two micron) films prepared by plasma enhanced chemical vapor deposition with varying radiofrequency fields strengths to determine structural differences at the atomic level. Several properties of the films, such as hardness and wear rate, are dependent on deposition power. We have found that the sp^2/sp^3 ratio increases with increasing deposition power. Thus, films that are harder are more "graphitic" and less "diamondlike". The films studied here contain 11-16 atomic percent hydrogen, most of which is associated with sp^3 carbon sites. At least two distinct phases of hydrogens exist. Variable temperature studies reveal that, in contrast to amorphous hydrogenated silicon, proton linewidths in carbon films are temperature dependent, suggesting some molecular motion is present at room temperature.

INTRODUCTION

In an effort to understand the physical basis for the film properties, many studies of the atomic structure of amorphous carbon films have been undertaken. Key to this understanding is the characterization of the carbon and hydrogen chemical bonds. Nuclear magnetic resonance (NMR)[1-5], infrared (IR) and Raman spectroscopy[6], and Auger electron spectroscopy[7] have been used to quantify the sp^2/sp^3 ratio of carbon binding sites. The goals of these studies were to quantify the hydrogen content and bonding in the film, and to enumerate the types of carbon bonding environments and the relative ratios of the environments in the films. Other studies have assigned some of the chemical shifts of the different types of carbon environments that can form in plasma polymerized films.[8] Nuclear magnetic resonance has several distinct advantages in characterizing carbon films. NMR is very sensitive to local spin environments and can provide quantitative measurements of these chemical sites. The analysis is usually straightforward and model independent. Long-range molecular order is not necessary for NMR experiments, and these experiments are non-destructive, as opposed to other techniques that rely on high energy ion or electron bombardment. The area of NMR resonances are proportional to the number of chemically distinct atoms giving rise to each resonance, and so yield quantitative information about the distribution of these environments. This is in contrast to other techniques such as IR spectroscopy.[9] We have applied solid-state NMR experiments to characterize the carbon bonding

Mat. Res. Soc. Symp. Proc. Vol. 339. ©1994 Materials Research Society

environments, the extent of hydrogenation, and the role of oxygen in these films. These results and their dependence on deposition power are reported.

EXPERIMENTAL

Three samples (20 watt, 30 watt, and 50 watt powers) of a-C:H were prepared by plasma enhanced chemical vapor deposition onto aluminum targets and silicon wafers mounted to the aluminum targets. The film thicknesses were 1-2 microns. Cyclohexane at 80 microns pressure was the process gas. After deposition and prior to NMR measurements, the carbon films were removed from the aluminum by dissolving the metal in 50 % hydrochloric acid.

All NMR spectra were obtained on a Bruker MSL NMR spectrometer (Bruker Instruments, Billerica, MA) equipped with high power amplifiers and a two channel broadband probe. The spectrometer operates at 300 MHz for protons. Approximately 40 mg of sample were packed into 4 mm zirconia rotors. Proton spectra (32 transients each) were obtained using the solid echo pulse sequence[10] with a delay time of 70 μs. Carbon spectra (5000 transients) were obtained with cross-polarization and dipolar decoupling from protons. Quantitive NMR spectra were ensured by varying the contact time of the cross-polarization and implementing the PASS technique for controlling spinning sidebands while preserving their intensities[11]. Interrupted decoupling experments[12] used decoupling delays of 70 μs to allow non-protonated carbons to dephase. Radiofrequency field strengths of 50 kHz for both channels during cross-polarization and 100 kHz for proton decoupling were used. Magic angle spinning was at 3 kHz or 14 kHz for the carbon experiments and the proton spectra which were obtained without spinning. Variable temperature proton NMR spectra were taken over a 220 K range using a fluoroptic thermometer (Luxtron Inc., Mountain View, CA) to measure the temperature.

Rutherford forward (proton content) and backscattering (oxygen and carbon) measurements were used in conjuction with NMR to determine atomic composition. Measurements were made on a General IonX spectrometer; the incident energy of the He beam is 2.01 MeV.

RESULTS AND DISCUSSION

Carbon Spectra

Radiofrequency (rf)-power plasma polymerized films have varying physical properties based on the rf power that was used. In general, higher power samples are harder and wear better than their softer low-power counterparts. Figure 1 shows the ^{13}C cross-polarization, magic-angle spinning (CPMAS) spectra of three amorphous carbon films made at different deposition powers. The spectra of Figure 1 were obtained with high power dipolar decoupling and 14 kHz magic-angle spinning frequency. This speed is fast enough to average the chemical shift anisotropy and remove all spinning sidebands. The sp^2 and sp^3 carbon geometries are well resolved and easily integrated. A peak at about 210 ppm, which has not been noted in previous NMR experiments on carbon films, is indicative of oxygenated carbons. The sp^2/sp^3 ratio of carbon sites increases with increasing deposition power. Diamond has a carbon chemical shift of 39 ppm[13] and graphite falls at 158 ppm[14] in the carbon spectrum. Thus it is the harder films that are more "graphitic" and less "diamondlike". Unlike in polymers, CPMAS experiments on films show that the relative ratio of carbon sites is independent of cross-polarization contact time from 0.5 to 15 ms. This indicates

that these compounds are amenable to quantitative study without the necessity of performing many relaxation experiments.

There has been a trend in NMR to perform experiments at progressively higher applied magnetic fields. The advantages of higher field are twofold. Sensitivity is improved with increasing field strength, and, since the chemical shift scales with the field, resolution is also improved. However, higher fields are a complication in the study of solids because the anisotropy of the chemical shift also scales with the applied field. As a result, spectral resolution is inhibited by the presence of overlapping spinning sidebands, which complicate the interpretation of spectra and the quantitative evaluation of spectral components. The easiest way to remove spinning sidebands is by ultrafast magic-angle spinning (Figure 1), but this can cause complications in cross-polarization experiments, which are necessary to obtain quality spectra of dilute spins systems such as ^{13}C in a more reasonable amount of time.

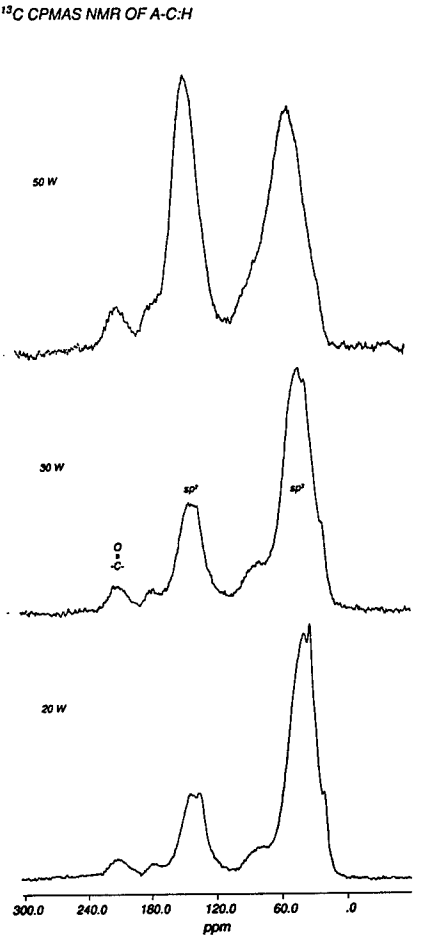

Figure 1. ^{13}C CPMAS NMR of a-C:H. The rf deposition powers are indicated.

As the spinning rate becomes an appreciable fraction of the static interaction among the abundant spins in cross-polarization experiments, the dynamics of polarization transfer between abundant and rare spins can be significantly modulated. Several pulse sequences have been suggested in the past two years to broaden the matching condition,[15-17] which is typically one or two kHz wide at spinning speeds of about 10 kHz. An alternative approach[11] to sideband suppression consists of combining echo spectra (typically 3 or 4 kHz MAS) with phase-alternated spinning-sidebands (PASS). This method has two advantages over the high speed approach. High-speed spinning assemblies, rotors and hardware are not required. The sidebands are not permanently eliminated, so information about the chemical shift anisotropy is retained. PASS experiments work well at high field despite the larger spectral width. Sideband intensities are recovered by re-phasing and adding spectra and are added to the intensities of the isotropic peaks. Using PASS, the sp^2/sp^3 ratios of the 50 W, 30 W, and 20 W samples were determined to be 0.83, 0.41, and 0.33, respectively.

Delayed Decoupling

A pulse sequence to suppress signals from NMR signals from protonated carbons in solids samples was first introduced by Opella and Frey.[18] This sequence and other modifications of it[19] involve the brief interruption of the proton spin decoupling after cross-polarization and before data acquisition. In a sample with random distribution of spin orientations, dipolar interactions will nearby protons cause the carbon magnetization to dephase. The 70 μs time for the dephasing delay was chosen based on the dephasing behavior of model compounds at the 3 kHz spinning rate used here. Figure 2 shows a pair of the spectra, with and without decoupling delays, of the 30 W sample. In contrast to plasma-enhanced CVD films that were prepared at lower pressures and higher power[3], these films have lower proton content (11-14 at%), and a much lower percent of the sp^2 sites are protonated. The relative amounts of protonated and nonprotonated carbons for the three samples are given in Table 1. There is a big difference of the sp^2/sp^3 ratios between samples, but very little difference between the protonated carbon fraction of sp^2 and sp^3 carbon geometries. The numbers in Table 1 should be considered preliminary and accurate to within a few percent. More detailed studies using several dephasing delays are being undertaken.

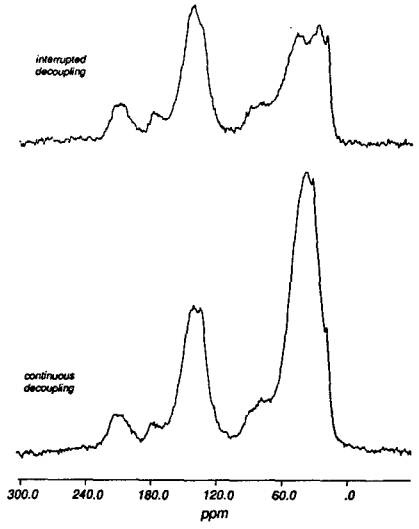

Figure 2. ^{13}C CPMAS NMR with delayed decoupling. Decoupling interruption is 70 us.

Table 1. Sample composition. All numbers are given in fractions. Proton and oxygen content is in atom fraction. The remaining atom fraction is carbon.

Sample	H content	O content	sp^2/sp^3 ratio	protonated sp^2	protonated sp^3
20 W	0.15	0.09	0.33	0.16	0.48
30 W	0.13	0.10	0.41	0.21	0.52
50W	0.12	0.13	0.83	0.17	0.42

Proton Spectra

The proton linewidth in solids is due almost entirely to dipolar interactions. Narrowing in proton lines occurs when the protons do not experience the full field effects of each other. This situation occurs when either the protons are far away from each other (the magnitude of the interaction is inversely proportional to the distance cubed) or there is enough molecular motion that the fields experienced by each nucleus vary with time, producing an averaging effect. There are at least two phases of protons in these carbon films. The proton spectra (Figure 3) can be deconvoluted into a broad Gaussian (35 kHz at half-maximum) and a narrower Lorentzian (4 kHz). The nature of the phase of protons that are responsible for the narrow spectral component was investigated using variable temperature NMR.

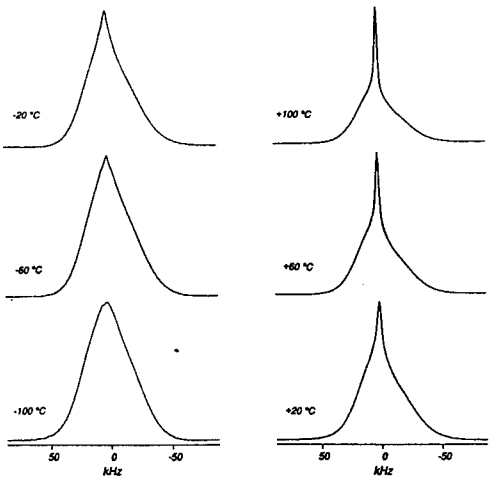

Figure 3. ^1H Solid Echo Spectra of a-C:H. Acquisition temperatures are indicated.

Variable temperature proton NMR spectra are shown in Figure 3. In these films the narrow Lorentzian component is indicative of high segmental molecular motion. As the samples were cooled, the molecular motion in the sample slows and line broadening occurs as the protons experience larger effective fields from each other. As the samples were heated, the mobile fraction of protons remains constant at about 15% for all the samples. While the most obvious

change is in the narrow spectral component, the width of the Gaussian component also varies with temperature.

In the absence of large amplitude molecular motion, the proton spin densities can be calculated from the lineshapes and widths. This kind of analysis was performed on amorphous hydrogenated silicon films.[20] Even though amorphous silicon and amorphous carbon films have similar proton spectra at room temperature, proton lineshapes of amorphous silicon are independent of temperature over a broad range. Since this is not true for the carbon samples, we conclude that a-(C:H) and a-(Si:H) have different structures and there are hydrocarbon moieties that are quite mobile at room temperature in amorphous hydrogenated carbon films.

Film Changes with Time

All three films were observed to change over time, with the sp^2/sp^3 ratio apparently increasing and incorporated oxygen reacting to form oxygenated carbon species. The oxygen may have been a contaminant or may diffuse through the film with time. The number of dangling bond defects (free radicals) decreases with time. We suggest that the sp^2 concentration is not really growing, but the nuclear spin coupling to the free electrons initially prevent the detection of some of the double-bonded carbons.

REFERENCES

1. G. Beamson, W. J. Brennan, N. J. Clayden, and R. C. K. Jennings, J. Polym. Sci.: Part B: Polym. Phys. **31**, 1205 (1993).
2. R. Kleber, W. Dworschak, J. Gerber, A. Krueger, K. Jung, H. Ehrhardt, S. Schultze, I. Muehling, S. Deutschmann, W. Scharff, F. Engelke, and H. Metz, Mater. Sci. Eng. **A140**, 775 (1991).
3. U. Schwerk, F. Engelke, R. Kleber, and D. Michel, Thin Solid Films **230**, 102 (1993).
4. A. Grill, B. S. Meyerson, V. V. Patel, J. A, Reimer and M. A. Petrich, J. Appl. Phys. **61** (8), 2874 (1987).
5. S. Kaplan, F. Jansen, and M. Machonkin, Appl. Phys. Lett. **47** (7), 750 (1985).
6. B. Dischler, A. Bubenzer, and P. Koidl, Solid State Commun. **48**, 105 (1983).
7. A. Fuchs, J. Scherrer, K. Jung, and H. Ehrhardt, Thin Solid Films **232**, 51 (1993).
8. A. Dilks, S. Kaplan, and A. Van Laeken, J. Polym. Sci. Polym. Chem. Ed. **19**, 2987 (1981).
9. W. Jacob and W. Moeller, Appl. Phys. Lett. **63** (13), 1771 (1993).
10. J. Lowe, Bull. Am. Phys. Soc **2**, 344 (1957).
11. W. T. Dixon, J. Chem. Phys. **77** (4), 1800 (1982).
12. S. J. Opella and M. H. Frey, J. Am. Chem. Soc. **101**, 5854 (1979).
13. P. M. Henrichs, M. L. Cofield, R. H. Young, and J. M. Hewitt, J. Magn. Reson. **58**, 85 (1984).
14. H. L. Retcofsky and R. A. Friedel, J. Phys. Chem. 77, 68 (1973).
15. S. Hediger, B. H. Meier, and R. R. Ernst, Chem. Phys. Lett. **213**, 627 (1993).
16. O. B. Peerson, X. Wu, I. Kustanovich, and S. O. Smith, J. Magn. Reson. A **104**, 334 (1993).
17. T. M. Barbara, and E. H. Williams, J. Magn. Reson. **99**, 439 (1992).
18. S. J. Opella and M. H. Frey, J. Am. Chem. Soc. **101**, 5854 (1979).
19. L. B. Allemany, D. M. Grant, T. D. Alger, and R. G. Pugmire, J. Am. Chem. Soc. **105**, 6697 (1983).
20. F. R. Jeffrey and M. E. Lowry, J. Appl. Phys. **52** (9), 5529 (1981).

GROWTH OF BETA SILICON CARBIDE FILM ON Si BY HOT-FILAMENT CVD

Zhang Rong, Shi Hongtao, Yu Shidong, Zheng Youdou, He Yuliang and Liu Xiangna,

DEPARTMENT OF PHYSICS, NANJING UNIVERSITY, NANJING 210008, CHINA

ABSTRACT

In this paper, we will report fabrication and structure study of single crystal β-SiC film on Si substrate by hot-filament chemical vapor deposition(HFCVD). The reaction sources are hydrogen-diluted methane(CH_4) and Silane(SiH_4). The wafer surface temperature is about 650°C. The typical growth rate is 200nm/h. Raman scattering spectrum shows a peak centering at 960cm^{-1} with a full width at half magnitude (FWHM) of 75cm^{-1}. At room temperature, the photoluminescence spectrum gives a wide band at 580nm (2.2eV) with a FWHM of 55nm. Fourier transmission infrared (FT-IR) spectrum exhibits an absorption peak at 12.6 μm. XRD and XPS analysis indicate that the epilayer is a stoichiometrical single crystal cubic silicon carbide film.

I. INTRODUCTION

Silicon Carbide (SiC) is recently attracting much interest as a promising candidate for fabricating high temperature, radiation hardness, high frequency/high power and non volatile memory devices, because of its excellent physical and chemical stability, high breakdown electrical field, high thermal conductivity and compatibility with Si ULSI technology [1]. In order to develop hybrid circuits and to share advantages of integrated technique, single crystalline SiC films must be grown on Si substrate. So far the main methods for growing single crystal SiC film on Si substrate are chemical vapor deposition (CVD), sublimation, molecular beam epitaxy (MBE) and radiative magnetron sputtering[2-6]. Among them CVD is favorable because it runs near thermal equilibrium. The CVD method have several version according to different type of heating energy source and operating pressure in chamber, such as rapid thermal CVD (RTCVD), electron cyclotron

Mat. Res. Soc. Symp. Proc. Vol. 339. ©1994 Materials Research Society

resonance plasma CVD(ECRCVD), low pressure CVD (LPCVD) and atmosphere pressure CVD (APCVD). In these techniques, high temperature (usually more than 1000°C) and high vacuum or ultrahigh vacuum system have to be maintained in the reaction chambers during the whole deposition process. Generally high temperature induces tensile stress in the epitaxial films and the thermal damages strongly affect the crystal quality of the deposited films. These factors greatly reduce the feasibility of SiC-related device processes and applications. One also can see the disadvantage of high temperature process from the other viewpoint of hybrid integration of Si and SiC devices. Therefore for obtaining high throughout production and developing hybrid integrated circuits, an economical low temperature growth method is practically required to fabricate high quality single crystal SiC films on Si substrates. Up to now, a successful test for decreasing the growing temperature have been done by using LPCVD technique at 750°C with methylsilane ($SiCH_3H_3$) as the only reaction source gas [7].

In this paper we report here, for the first time the successful deposition of SiC film on the Si substrate at temperature as low as 600-700°C by hot-filament assisted chemical vapor deposition (HFCVD). X-ray diffraction and Raman method confirm that the epilayer is a single crystal β-SiC film. x-ray photoelectron spectroscopy analysis indicate that the epilayer is a stoichiometric β-SiC film. At room temperature, the photoluminescence spectrum gives a wide band at 580nm (2.2eV) with FWHM of 55nm.

II. THE ROLE OF HOT FILAMENT IN HFCVD

Usually the reaction source gases in CVD growth of SiC are simple carbides such as methane(CH_4) or propane(C_3H_8), and silicides such as silane (SiH_4), disilane (Si_2H_6) and so on. The total CVD growth process can be divided in three stages as (i) decomposition of reaction source gas; (ii) bonding between Si and C atoms and (iii) migration on growing surface. If we take the methane-silane system as an example, the chemical reaction in the CVD chamber can be abstractly written as

$$SiH_4 \rightarrow Si + 2H_2 \quad (1)$$

$$Si + CH_4 \rightarrow SiC + 2H_2 \quad (2)$$

The active energy of the reaction (1) is lower than the reaction (2), for example, the active energy of (1) of 1atm is 30kCal/mol[8], otherwise the active energy of (2) at 1atm is as high as 99kCal/mol[8]. Therefore high temperature in CVD technique is needed for driving the reaction (2), the key problem to decrease the deposition temperature is Si-C bonding. I.Golecki et al[7] used $SiCH_3H_3$ as the only reaction source gas, and grew high quality SiC film at temperature as low as 750°C. This result confirms the technical approach suggested above.

According to the experimental results and the analysis made in the last section, if the Si-C bond has formed, the following process could be run at the "lower" temperature. So an approach is possible that runs the main chemical reactions at the "higher" temperature and keeps the substrate at the "lower" temperature. The hot-filament assistant chemical vapor deposition (HFCVD) technique is just suitable for that purpose. HFCVD is usually used to fabricate diamond films. It has advantages on high temperature of the hot wire, generally higher than 1500°C, and the relatively lower temperature of the substrate, which is different in various cases.

III. GROWTH AND CHARACTERIZATION

The apparatus used in this study is schematically shown in Fig.1. The details of the HFCVD system was described elsewhere [8]. Si with orientation of (100) or (111) was used as substrate, and Hydrogen (H_2), 15% H_2-dilute methane (CH_4) and 10% H_2-dilute silane (SiH_4) were used as the reaction source gases with the flow rate as 150, 20 and 10sccm, respectively. Before the growth of SiC, H_2 and CH_4 were loaded into the chamber for "carbonizing" the Si substrate for 10min. During the whole process, the operation pressure in the chamber was 0.3Torr and the substrate temperature was kept in the range of 600-750°C. The typical growth rate was 200nm/h.

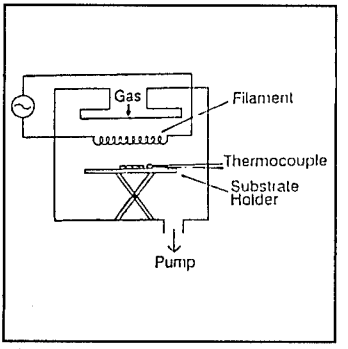

Fig. 1 The schematic diagram of HFCVD.

Fig.2 was a typical x-ray diffraction (XRD) spectrum of the β-SiC/Si(111) sample grown by the HFCVD method. In the range of

2θ=20° to 70°, there were only two XRD peaks observed at 28.5° and 35.64°. The low-angle peak came from the diffraction of Si(111) substrate and the high-angle peak was from the diffraction of the SiC epilayer which had a lattice constant of 0.4345nm. It indicated a β-SiC film and good crystallinity.

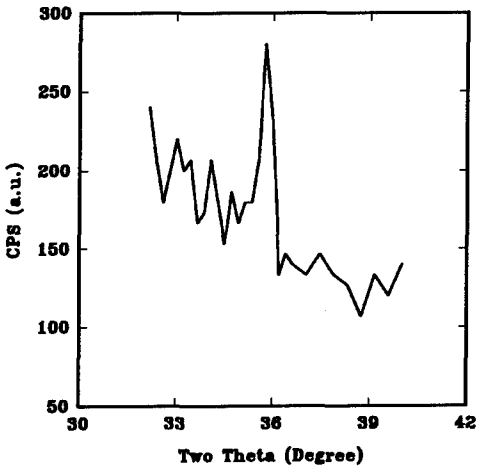

Fig.2 X-ray diffraction spectrum of β-SiC film.

Fig.3 Shows a Raman scattering spectrum of the same sample at room temperature. The experimental data were obtained using a backscattering geometry, where the incident light was normal to the surface and the scattered light was collected with a small angle to the incident light. The incident light wave length was 488nm and the incident power was 20mW on the sample surface. It could be seen that the characteristic Raman peak located at 975cm^{-1} with a FWHM of 76cm^{-1}. The relatively wide Raman peak relates mainly to the lattice mismatch between Si and SiC, as high as 20%, and very low energy for generating stack faults.

XPS characterization technique was used to analyze the chemical composition in the epilayer and the results were shown in fig.4. (a) and (b) were XPS spectra of Si_{2p} and C_{1s} combined with their decomposed curves by assuming Gaussian type peak shape. It was found in fig. 4(a) that two Si_{2p} peaks located at 99.9eV and 101.5eV, respectively. We assigned the 99.9eV peak to the Si substrate and the 101.5eV peak to the SiC epilayer. Correspondingly, as

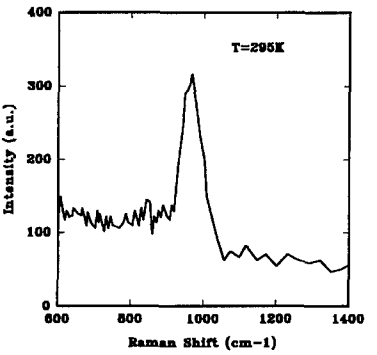

Fig.3 Raman scattering spectrum of β-SiC film.

shown in Fig 4(b), the SiC component of C_{1s} peak located at 283.5eV and the higher energy part of C_{1s} peak was due to the CH_x compounds, coming from the organic contamination of the measured system. The energy difference between the C_{1s} and Si_{2p} binding energy was 182.0eV, which agreed well with the literature[9].

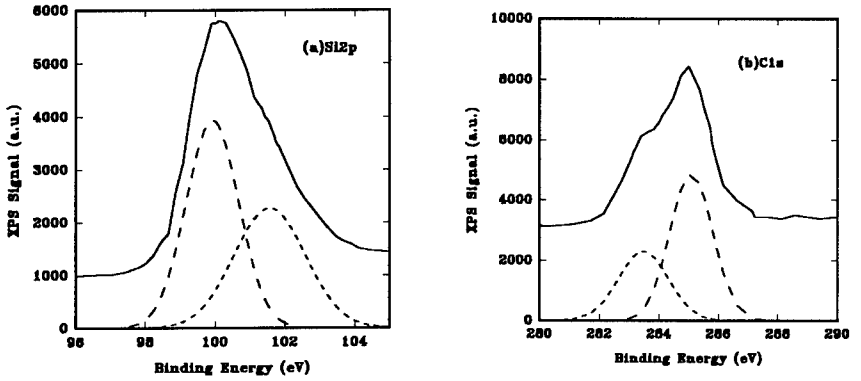

Fig.4 XPS spectra of β-SiC film. (a)Si_{2p}, (b)C_{1s}.

As a sensitive probe to evaluate the material quality, photoluminescence (PL) measurement was carried out on the epitaxial β-SiC films grown on Si substrates with different orientation. At room temperature those PL spectra peak at 580nm, with a FWHM of 60nm. A typical curve was given in Fig.5. The wide band structure and asymmetric characteristics of PL peak originated obviously from the defects in the epilayer.

IV. SUMMARY

HFCVD technique for growing SiC films have been reported in this paper and successfully used to fabricate SiC films on Si substrates at low temperature in the range of 600-750°C. Results of XRD, XPS, Raman scattering spectroscopy demonstrate a good single crystal structure of the epilayers. PL measurements show visible light emitting from the SiC film. Those results indicate that HFCVD is a powerful tool for depositing single crystal SiC film on Si at low temperature.

REFERENCES

[1] P. A. Ivanov and V. E. Chelnokov, Semicond. Sci. Technol., **1**, 863(1992)

[2] J. W. Palmour, J. A. Edmond, H. S. Kong and C. H. Carter Jr, Physica B, **185**, 461(1993)

[3] G. Ziegler, P. Lanig, D. Theis and C. Weyrich, IEEE Trans Electron Devices, **ED-30**, 277(1983)

[4] T. Sugii, T. Aoyama and T. Ito, J. Electrochem. Soc., **3**, 989(1990)

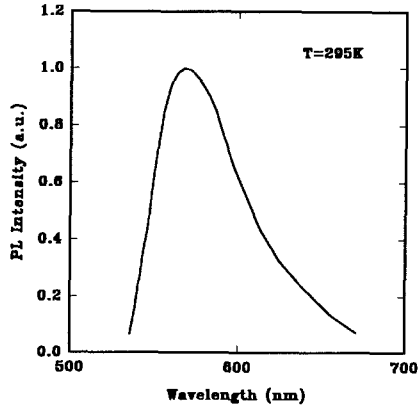

Fig.5 Photoluminescence spectrum of β-SiC film taken at room temperature.

[5] Q. Wahab, R. C. Glass, I.P. Ivanov, J.Birch, J.-E. Sundgren and M. Willander, J. Appl. Phys., **74**, 1663(1993)

[6] A. J. Steckl and J. P. Li, Appl. Phys. Lett., 60, 2107(1992)

[7] I. Golecki, F. Reidinger and J. Marti, Appl. Phys. Lett., 60, 1703(1992)

[8] R. Zhang, H. Shi, S. Yu, Y. Zheng, Y. He and X. Liu, High Tech Letters (in press)

[9] I. Kusunoki and Y. Igari, Appl. Surf. Sci., 59, 95(1992)

Author Index

Abelson, J.R., 435
Abernathy, C.R., 179, 491, 553
Ager, R., 393
Ailey, K.S., 351
Akasaki, I., 443
Albanesi, E.A., 607
Alexander, W. Brock, 301
Altaiskii, Yu.M., 535, 717
Amano, H., 443
Angus, John C., 285, 589
Askew, R.F., 329

Bächli, A., 247
Bachmann, Peter K., 3, 267, 285
Bailon, L., 151
Bandis, Christos, 33, 75
Banholzer, W., 307
Baranov, P.G., 453, 705
Barbolla, J., 151
Baumann, Peter K., 69
Beerling, T.E., 203
Beesabathina, D. Prasad, 363
Benjamin, M.C., 81
Beresford, R., 471
Bergman, J.P., 541
Bergman, L., 663
Bergner, H., 699
Bernholc, J., 693
Bharatan, S., 491
Black, D., 307
Boguslawski, P., 693
Boudreau, Marcel, 381
Boumerzoug, Mohamed, 381
Bozack, M., 329
Briggs, E., 693
Brown, S.W., 339, 503
Bryden, Wayne A., 465, 497, 509, 583
Buchwald, W., 145
Burdette, H., 307
Burger, A., 653
Burgess, Jr., D.R.F., 429
Burm, J.W., 163

Caley, Catherine E., 741
Carlos, W.E., 535
Carter, Jr., C.H., 133, 735
Casas, L.M., 145, 429
Cassidy, William D., 285
Chan, J.S., 223, 483
Chao, C.H., 325
Charlson, E.J., 191, 325, 637
Charlson, E.M., 191, 637
Chen, J.S., 247
Chen, Q.Y., 515
Cheung, N.W., 223, 483
Chien, F.R., 399
Choo, S.K.L., 417
Chu, P., 223
Chu, W.K., 515

Clarke, R., 339, 345
Collaboration, Isolde, 613
Collins, W.E., 653
Coston, R., 411
Cui, X.T., 515

D'Evelyn, Mark P., 89, 279
Davidson, Brian N., 27
Davidson, J.L., 653
Davies, J.F., 647
Davis, Robert F., 81, 351
Deguchi, M., 723
Deneuville, A., 185
Doering, Patrick, 301
Doverspike, Kathleen, 313, 477
Dreifus, David L., 109
Dubey, M., 145
Dudley, M., 735
Dyer, T.E., 647

Ecelberger, S.A., 497, 509
Engelbrecht, F., 529, 631
Evans, Edward A., 285
Evwaraye, A.O., 711

Fekade, K., 363
Feng, Z.C., 411, 417
Fitzner, M.P., 435
Flemish, J.R., 145
Foo, Y.G., 417
Forkel-Wirth, D., 613
Foulon, F., 185
Fountain, G.G., 39
Fox, Bradley A., 235
Franklin, M., 121
Freitas, Jr., Jaime A., 313, 477, 535, 547, 717
Frenklach, Michael, 255
Fröjdh, Christer, 215
Fu, T.C., 223, 483
Fujino, D., 121
Furukawa, Atsuhiko, 45

Gan, K.K., 121, 589
Ganesan, D., 319
Gaskill, D.K., 477
George, M.A., 653
George, T., 163
Gheeraert, E., 185
Gilbert, Donald R., 301
Gillen, G., 429
Gilman, R., 121
Glass, J.T., 291, 663
Glass, R.C., 405, 729
Glesener, J.W., 241
Gold, J.S., 63

Hagemann, Hans-Jürgen, 267, 285
Haggerty, David, 33, 75
Hajsaid, M., 191

Hallin, C., 405
Han, S., 121, 589
Hangas, J., 393
Harkness, S.D., 127
Harris, C.I., 541
Harris, V.G., 241
Hartman, J. Stephen, 523
Hartsell, M.L., 235
Hawley, M.E., 497
He, Yuliang, 747
He, Z., 191
Heera, V., 197
Helbig, R., 387, 529, 631
Helms, C.R., 203
Hemmingsson, C., 405
Henry, A., 405, 541
Hepburn, A.R., 647
Hewett, C.A., 97
Hirao, T., 723
Hng, H.H., 411
Hoff, H.A., 241
Hofmann, D.M., 619
Hoinkis, Mark, 741
Holl, Susan M., 741
Holmes, Joseph S., 109
Hong, C.-H., 503
Hu, R., 411, 417
Hu, Xiao, 15
Hudson, G.C., 39, 51
Hultman, L., 157
Humphreys, T.P., 39, 51, 69
Hwang, S.-J., 675

Ichinose, H., 681
Irvine, K.G., 595
Ishida, Y., 681
Ivanova, L.M., 535, 717
Izumi, T., 723

Janzén, E., 405, 541, 729
Jaraiz, M., 151
Jessop, Paul E., 381
Jia, H., 669, 675
Jing, Z., 57
Johnson, David L., 423
Johnson, Robert D., 741
Jones, E., 483
Jones, K.S., 491
Jones, Robert E., 741

Kagan, H., 121, 589
Kamiya, Yasushi, 459
Kanda, H., 625
Kanda, S., 121
Kania, D.R., 121, 307, 589
Kao, Chien-Teh, 109
Kaplan, R., 717
Kass, R., 121, 589
Kern, R.S., 81, 351
Kester, D.J., 351
Khan, A.H., 191, 637
Khan, M. Asif, 163, 547
Khasawinah, S., 601, 643
Kidner, S., 339, 345
Kim, S.K., 121
Kimoto, Tsunenobu, 369
Kistenmacher, Thomas J., 465, 497, 509, 583
Kitabatake, M., 723
Kögler, R., 197
Kohyama, M., 9, 681
Kong, H.S., 735
Konstantinov, A.O., 405
Kordina, O., 405, 541
Kreider, K.G., 429
Krishnankutty, S., 163
Kumbartski, G., 121
Kuznia, J.N., 163

Lade, Hartmut, 267
Lambrecht, Walter R.L., 565, 607
Lang, D.P., 669, 675
Languell, M.L., 653
Lannon, Jr., J.M., 63
Lareau, R., 429
Lau, S.P., 647
Lee, Dong-Gu, 127, 301
Lee, M.H., 121
Leers, Dieter, 267, 285
Leksono, M.W., 559
Licht, T., 613
Liew, S.C., 417
Liliental-Weber, Z., 483
Liu, J.R., 515
Liu, X., 223, 483
Lopes, J.C., 625
Lothian, J.R., 179
Loyalka, S., 643
Lui, W., 291
Lundberg, Nils, 229

Ma, S.J., 589
Malchow, R., 121, 589
Malta, D.P., 39, 51
Malta, Dean M., 109
Manning, G., 643
Mantini, M.J., 39
Markunas, R.J., 39, 51
Marshall, J.M., 647
Mascher, Peter, 381
Matsunami, Hiroyuki, 3, 369
Matthai, C.C., 21
McClure, M.T., 663
McLane, G., 145
Meese, J.M., 191, 325, 637
Meier, J., 613
Melton, W., 559
Meyer, B.K., 453, 619, 705
Miragliotta, Joseph A., 465, 583
Mitchel, W.C., 711
Mokhov, E.N., 453, 705
Moore, W.J., 717
Moran, G.J., 21
Moreno, M.M., 307
Morkoc, Hadis, 3
Morozov, B., 121
Morrison, I., 21

Morrow, F., 589
Moyer, M.D., 307

Nakamura, Shuji, 173
Nakanose, M., 681
Narayanan, Arjun, 523
Nazaré, M.H., 625
Negley, G.H., 595
Nemanich, R.J., 69, 81, 663
Neugebauer, Jörg, 687
Newman, N., 223, 483
Ng, W.E., 417
Nguyen, R., 97
Nicolet, M-A., 247
Nilsson, Hans-Erik, 215
Nilsson, S., 453
Nordquist, K.J., 133
Novotny, Vlad. J., 741
Nutt, S.R., 399

Ohtani, A., 471
Ohuchi, Fumio S., 15
Olson, D.T., 163
Östling, Mikael, 209, 229

Palmer, W., 121, 589
Palmour, John W., 133, 595
Pan, D.W., 515
Pan, L.S., 121, 307, 589
Pankove, J.I., 559
Pappas, D.P., 241
Pate, Bradford B., 33, 75
Patton, Martin O., 423
Pavlidis, D., 503
Pazik, J.C., 535
Pearton, S.J., 179, 491, 553
Pelaz, Lourdes, 151
Pereira, E., 619
Pereira, L., 619
Petersson, C. Sture, 215
Petrauskas, M., 699
Picht, Frederike, 267
Pickett, Warren E., 27
Piltch, Nancy D., 423
Pirouz, Pirouz, 423
Plano, Linda S., 109
Plano, M.A., 307
Pochet, T., 185
Poindexter, B.D., 393
Popovici, G., 325, 601, 637, 643
Posthill, J.B., 39, 51
Prelas, M.A., 191, 325, 601, 637, 643
Pressel, K., 453
Pruski, M., 669, 675

Qiu, C.H., 559

Ramesham, R., 329
Rand, S.C., 339, 503
Rawles, Robin E., 89, 279
Reislöhner, U., 613
Ren, F., 179, 491
Rimai, L., 393
Robins, L., 307
Romero-Borja, F., 515
Rose, M.F., 329
Ross, J.T., 223, 483
Rottner, K., 387
Rowland, L.B., 477
Roychoudhury, R., 191
Rubin, M.D., 223, 483
Rudder, R.A., 39, 51
Ruiz, R.P., 247
Rutt, P., 121

Sakai, Shiro, 459
Sakamoto, Yoshifumi, 45
Salamanca-Riba, L., 363
Sannes, F., 121
Santos, L., 619
Sato, Hisao, 459
Schaff, W.J., 163
Schaffer, William J., 595
Schnetzer, S., 121, 589
Segall, B., 607
Shamamian, Vasgen A., 313
Sharma, S.C., 319
Shechtman, D., 297
Shi, Hongtao, 747
Shinar, J., 669, 675
Shirafuji, Junji, 45
Show, Y., 723
Shur, M.S., 163
Singh, Rajiv K., 127, 301
Sitar, Z., 351
Skogman, R.A., 163
Skorupa, W., 197
Smith, L., 351
Smith, S.R., 711
Somalwar, S.V., 121
Son, N.T., 405
Spencer, M.G., 363
Spitsyn, B.V., 643
Stacy, T., 191, 637
Stadler, W., 619
Stan, Mark A., 423
Stevens, K.S., 471
Stinespring, C.D., 63
Stoemenos, J., 197
Stone, R., 121, 589
Stoner, Brian R., 109, 291
Struck, Lisa M., 89
Subramaniam, V., 339
Sugimoto, Y., 121, 589
Sugino, Takashi, 45
Sundgren, J.-E., 157
Sung, T., 601, 643

Tan, K.L., 411
Tanaka, S., 351
Tang, S.H., 417
Tarlov, M.J., 429
Taylor II, C.A., 339, 345
Tesarek, R.J., 121, 589
Tessmer, Alison J., 109
Thomas, R.E., 39, 51

Thomson, G.B., 121
Thungström, Göran, 215
Tidswell, I., 483
Tin, C.C., 411, 417
Tomashiunas, R., 699
Tompson, R.V., 643
Tuomi, T., 729
Tuominen, M., 729
Turan, R., 157

Ueta, Yoshihiro, 459
Uhrmacher, M., 613

Vanagas, E., 699
Van de Walle, Chris G., 687
Vicente, J., 151
Vithana, Hemasiri K.M., 423
Volm, D., 453, 705

Wahab, Q., 157, 699
Wang, C., 81, 351
Wang, S., 735
Wang, Yaxin, 285
Wang, Youxiang, 523
Warner, Joseph D., 423
Watena, G.L., 241
Weber, E.R., 483
Weber, W.H., 393
Wee, A.T.S., 411
Weitzel, C.E., 133
Wensell, M.G., 693
Wert, J.J., 653
Wetzel, C., 453
White, C., 121, 589
White, T.A., 693
Whitten, J.L., 57
Wickenden, Dennis K., 465, 583
Wiechert, Detlef U., 267, 285
Wight, S., 429
Willander, M., 157, 699
Williams, J., 417
Williams, Jeffrey L., 741
Wilson, Howard, 267
Wilson, R.G., 553, 601
Withuhn, W., 613
Wolter, S.D., 291
Wongchotigul, K., 363
Wood, L.T., 515
Wynands, Henry A., 235

Xiangna, Liu 747
Xie, K., 145

Yakimova, R., 729
Yamamoto, R., 9
Yan, Hong, 15
Yang, Jinwei, 423
Yang, P.C., 291
Yoder, Max N., 3
Yoo, W.S., 399
Yu, K.M., 483
Yu, Shidong, 747
Yue, K.T., 417

Zavada, J.M., 553
Zeidler, J.R., 97
Zetterling, Carl-Mikael, 209
Zhang, Rong, 747
Zhang, Z.H., 515
Zhao, G., 191, 637
Zhao, J.H., 145
Zhao, S., 121, 589
Zheng, Youdou, 747
Zheng, Z.S., 515
Zhindulis, A., 699
Zuev, V.L., 535, 717

Subject Index

absorption, 625
acceptor binding energy, 459
a-C:H, 741
acid cleaning, 89
activated nitrogen, 483
adsorption on SiC, 21
Al/beta-SiC, 15
AlGaN, 163
AlGaN/GaInN DH, 443
AlGaN/GaN DH, 443
AlN, 81, 351, 363, 459, 553, 637, 693
AlN
  buffer layer, 477
  growth, plasma conditions, 471
  seeded, 509
  SiC, 81
amorphization, 197
amplifier, 109
anisotropy, 595
annealing, 69, 515
antisites, 693
atomic force microscopy, 89, 653

backscattering spectrometry, 247
band
  lineup, 459
  offsets, 607
$BeCN_2$, 565
bias-enhanced nucleation, 291
blue light emitting diodes, 163, 173
bonding structure, 741
boron nitride, 351
  cubic, 339, 345
  hexagonal, 339
broadband luminescence, 663
buffer layer, 509, 547

C ion implantation, 723
cadmium impurities, 613
calorimeter, 121
capacitance(-), 711
  voltage, 209, 235, 637
capture(-)
  cross section, 699
  emission, 151
carbon
  dangling bonds, 675
  films, 741
  solubility, gas phase, 285
carrier
  mobility, 185
  recombination, 699
cathodoluminescence, 307, 339
C-C surface species, 63
charge particle detectors, 589
chemisorption of CH_2, 57
C-H-F diagram, 285
chlorine, 601
C-H-O diagram, 285
cleaning processes, 69
cluster model, 57
CN_x, 515
cobalt silicide/6H-SiC, 229
cold cathode emitters, 81
complex formation, 613
conductance, 711
conductivity and FTIR, 643
contact resistance, 223, 229
copper/diamond, 241
crystallographic defects, 297
current-
  temperature, 637
  voltage, 235, 637
cyclotron resonance, 717

dangling bond-H centers, 669
DC
  arc, 127
  magnetron sputtering, 515
decay time, 541
device performance, 387
diamond, 27, 39, 45, 51, 57, 89, 191, 203, 235, 241, 247, 675, 681
  carrier
    concentration, 97
    mobility, 97
  CVD, 267
  electronic
    devices, 97, 109
    structure, 565
  epitaxy, 291
  etching, 279
  FET, 97
  films
    deuterated, 669
    heat treatment, 643
    tribology, 653
  grain boundaries, 681
  growth
    chemical reactions, 255
    combustion flame, 313
    compositional diagrams, 267
    CVD, 185, 285, 297, 301, 589, 663
    d.c. biased, 325
    ECR, 301
    effect of oxygen, 329
    gas compositions, 267
    HFCVD, 319
    homoepitaxial, 301, 307
    kinetics, 279
    nickel substrate, 329
    nucleation, 291
    rates, 285
  heteroepitaxy, 63
  impurities, 601
  powder, 319
  resistivity, 97
  surface, 33, 69, 127

diamond (continued)
synthetic, 619, 625
TiO interface, 75
/tungsten, 121
diffusion
coefficient, ambipolar, 699
of impurities, 601
dimer
bond length, 57
energy, 57
direct bandgap, 163
ditertiary butyl silane, 381
donors, 535
dopant(s)
and impurities, 523
incorporation, 97
double-modulation mass spectrometry, 435

ECR(-), 145, 179
aperture size, 471
assisted, 497
microwave plasma assisted MBE, 471
MOMBE, 491
plasma CVD, 381
source, 345
electric breakdown field, 133
electrical
properties, 589
transport, 497
electroluminescence, 647
electroluminescent device, 647
electron
emission, 39
energy loss, 477
irradiation, 705
spin resonance, 535, 723
electronic
components, high
frequency, 163
power, 163
temperature, 163
structure, 565
enclosed chamber, 313
energetic ions, 345
etching rate, 127
excitonic emission, 477
excitons, 541

fcc-iron, 241
field-effect transistors, 109
Fizeau interferometry, 89
free carrier adsorption, 631
Frenkel-Poole emission, 637

GaN, 173, 223, 351, 453, 459, 491, 547, 559, 583, 693
cubic, 687
electronic structure, 565
growth
(100) GaAs, 503
metallic-organic CVD, 483
organometallic VPE, 477
hydrogen incorporation, 553
Mg-doped, 547
on Si(111), 471
Si doped, 465
wurtzite, 687
gap modes, 529
grain boundaries, 9
graphitic, 27

H
plasma, 45
vibration frequencies, 27
Hall effect, 595
heteroepitaxy, 163
heterojunctions, 607
heterostructure(s), 363
double, 175
high frequency MESFETs, 133
higher order twin boundaries, 297
homoepitaxy, 279
hot filament CVD, 325, 747
hydrogen, 643
absorption, 33, 291

ideality factor, 151
III-nitrides, 607
implantation, 51
impurities, 529, 693
indium, 613
infrared
absorption, 529
luminescence, 559
properties, 631
spectroscopy, 89
transmission, 717
InGaAlN, 179
InGaN, 163
InGaN/AlGaN, 173
InN, 459, 553
growth, 497, 509
interface(s), 607
stoichiometry, 9
traps, 235
interfacial energy, 681
internal
microvoid, 669
surfaces, 675
interstitials, 693
ion
beam, 197
assisted deposition, 351
bombardment, 203
damage, 203
milling, 179
ionized impurity concentration, 717
ionizing particle detector, 121

Kelvin probe, 45

laser
ablation, 393, 423
crystallization, 647
deposition, 423
processed, 429

lattice misfit, 329
LEDs, 173
lithium, 601
low-voltage threshold, 345

magnetron sputtering, 339
mesa diodes, 387
meta-stable growth, 483
microcrystalline-SiC, 647
micropipes, 735
microstructure, 363
microwave plasma, 329
mobility, 595
MOCVD, 465
molecular
  beam epitaxy, 351, 483
  dynamics, 21
MOMBE, 179
MOS, 235
  capacitor, 157
MOVPE, 443
multivacancies, 669

nanovoids, 675
native defects, 687, 693
negative electron affinity, 39, 69, 75, 81
nickel, 625
nitrogen-doping, 523, 535, 541, 663, 717
NMR, 523
  of diamond films, 675
nonlinear susceptibility, 583
nucleation, 369
  precursors, 63
numerical simulation, 387

O(-)
  adlayer, 63
  plasma, 45
ohmic contact, 97, 223, 229
optical
  admittance spectroscopy, 711
  confinement, 443
optically detected magnetic resonance, 619
oxidation, 209
oxy-acetylene, 313
oxygen, 601
ozone and oxygen, 127

PAC-spectroscopy, 613
Panel Discussion, 3
PECVD, 653
phase transformation, 325
photoconductor, 185
photo-detectors, 589
photoluminescence, 313, 405, 453, 477, 547, 663, 705, 717
  micro/macro, 663
photoresponse, 191
planarization, 127
plasma
  etching, 145
  I-V characteristics, 471
Polle-Frenkel, 151
power MOSFETs, 133
protective coatings, 741

quantum efficiencies, 191

radiation
  damage, 197
  detector, 185
Raman spectroscopy, 503, 547
reactive
  ion etching, 145, 179, 203
  magnetron sputtering, 157, 435, 497
reconstruction, C(100), 57
recrystallization, 197
refractive index, 443
refractory metal substrates, 291
RF power density, 133

Sigma=3 twins, 297
sapphire, 465
Schottky
  barrier height, 69, 191
  diodes
    diamond, 191
    SiC, 215
second-harmonic, 583
self-nucleated, 465
sensors, 429
SiC, 21, 351, 363, 369, 387, 429, 613, 631, 705
  3C, 157, 417, 541
  3C/Si(100), 411
  2H, 423
  4H, 133, 595, 729
  6H, 133, 145, 197, 209, 215, 229, 405, 453, 523, 529, 541, 595, 631, 699, 735
    nitrogen, 711
  beta, 9, 399, 535, 717, 747
  electronic structure, 565
  growth, 381, 747
    CVD, 387, 405, 411, 417
    epitaxial, 393
    low doped, 405
  MESFETs, 133
  microcrystalline, 647
  p-n junctions, 151
SiC(001), beta, surfaces, 15
$Si_{1-x}C_x$ growth, 435
silicon/tungsten calorimeters, 121
SiO_2, 157
smooth diamond films, 325
solid(-)
  phase reaction, 247
  state NMR, 741
spin
  diffusion, 675
  lattice relaxation, 523, 669
sputtering, 345
stacking fault(s), 669
  configurations, 399
  energy, 399
step(-)
  controlled epitaxy, 369
  dynamics, 369

stimulated emission, 443
structural
  characterization, 491
  defects, 729
  morphology, 497
superlattices, 607
super screw dislocations, 735
surface
  electronic structure, 15
  fermi level, 45
  kinetics, 369
  preparation, 51
  step, 27
synchrotron, 735
  topography, 729

tetrahedral C_3N_4, 515
textured diamond, 329
thermal stability, 553
thyristors, 133
tight-binding
  electronic theory, 681
  method, self consistent, 9
tilt boundary, 681
time resolved photoluminescence, 619
total energy calculations, 687
transient photoconductivity, 307
transition metal impurities, 711
transmission
  electron microscopy, 363
  line, 223
tribology, 653
tungsten thin films, 247

uniaxial stress, 625
uv(-)
  and x-ray detectors, 81
  photoelectron spectroscopy, 33, 39
  visible light emitter, 163

vacancies, 693
valley-orbit splitting, 535

WC, 247
W_2C, 247
wrong bonds, 9

x-band ESR, 669
x-ray, 417, 729
  diffraction, 453, 503
  topographs, 307, 735

yellow luminescence, 559

Zeeman spectroscopy, 705